XIV International Conference on Computational Plasticity. Fundamentals and Applications

COMPLAS 2017

5 - 7 September 2017, Barcelona, Spain

E. Oñate, D.R.J. Owen, D. Peric and M. Chiumenti (Eds.)

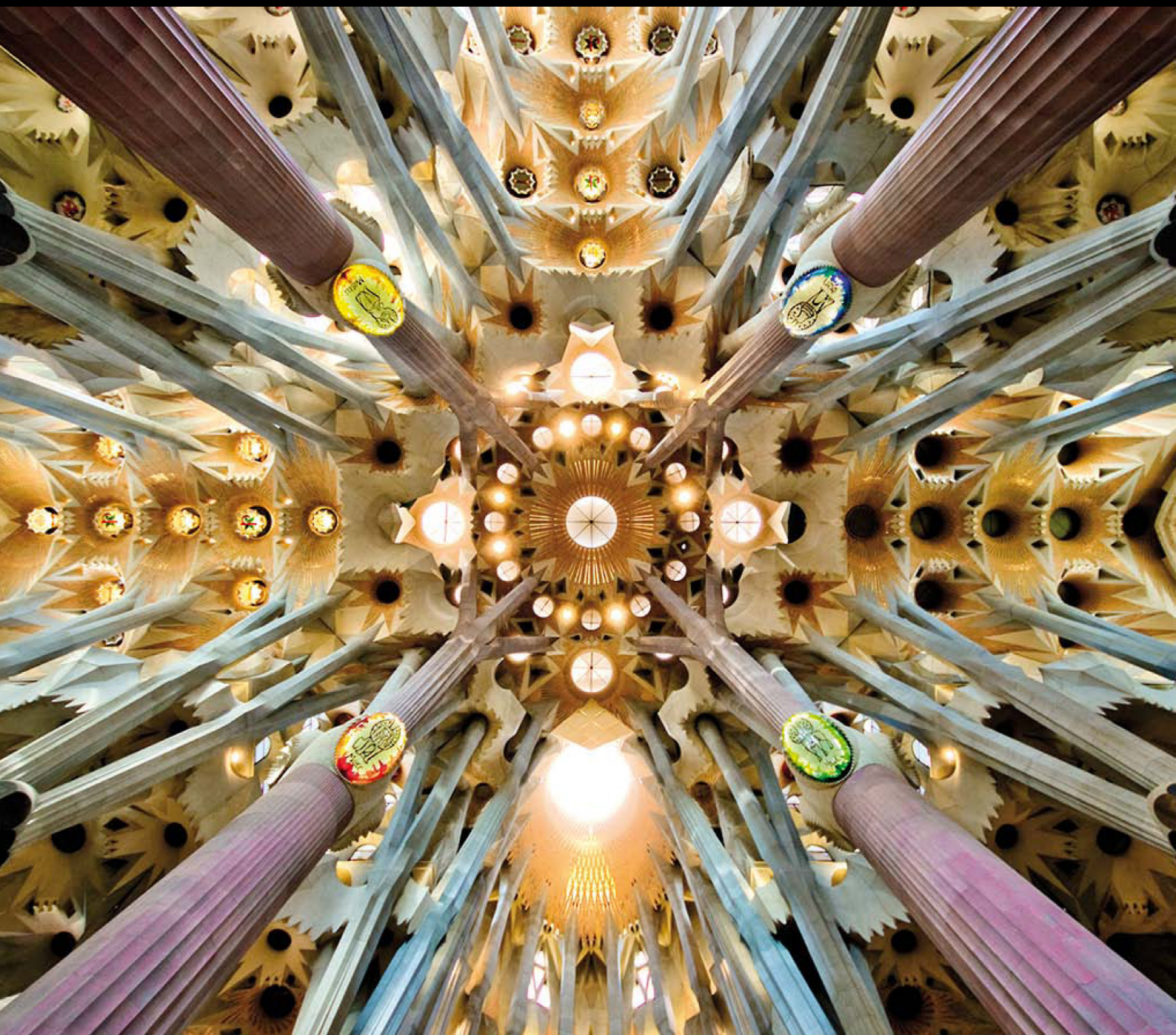

COMPUTATIONAL PLASTICITY XIV
Fundamentals and Applications

Proceedings of the XIV International Conference on Computational Plasticity – Fundamentals and Applications held in Barcelona, Spain
5-7 September 2017

Edited by:

E. Oñate
CIMNE / Universitat Politècnica de Catalunya, Spain

D.R.J. Owen
Swansea University, United Kingdom

D. Peric
Swansea University, United Kingdom

M. Chiumenti
CIMNE / Universitat Politècnica de Catalunya, Spain

A publication of:

International Center for Numerical Methods in Engineering (CIMNE)
Barcelona, Spain

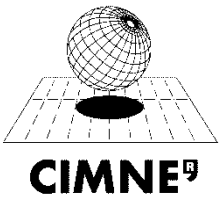

International Center for Numerical Methods in Engineering (CIMNE)
Gran Capitán s/n, 08034 Barcelona, Spain
www.cimne.com

Computational Plasticity XIV – Fundamentals and Applications

E. Oñate, D.R.J. Owen, D. Peric and M. Chiumenti (Eds.)

First edition, July 2017

Printed by: Artes Gráficas Torres S.A., Huelva 9, 08940 Cornellà de Llobregat, Spain

ISBN: 978-84-946909-6-9

TABLE OF CONTENTS

PREFACE

This volume contains the full papers accepted for presentation at the XIV International Conference on Computational Plasticity (COMPLAS 2017), held in Barcelona on 5-7 September, 2017. The first thirteen conferences of the series were also held in Barcelona; in April 1987, September 1989, April 1992, April 1995, March 1997, September 2000, April 2003, September 2005, September 2007, September 2009, September 2011, September 2013 and September 2015.

COMPLAS 2017 will be a special occasion as we will be celebrating the 30^{th} anniversary of the first COMPLAS conference.

The ever increasing rate of development of new engineering materials required to meet advanced technological needs poses fresh challenges in the field of constitutive modelling. The complex behaviour of such materials demands a closer interaction between numerical analysts and material scientists in order to produce thermodynamically consistent models which provide a response, while keeping with fundamental micromechanical principles and experimental observations. This necessity for collaboration is further highlighted by the continuing remarkable developments in computer hardware which makes the numerical simulation of complex deformation responses increasingly possible.

The developments that have taken place in these directions are illustrated by the contents of the papers included in these Proceedings. A stronger interaction between the phenomenological and micromechanical modelling of plasticity behaviour is apparent. The development of efficient and accurate computational methods for plasticity problems continues to be challenging goal, while it is interesting to note the permanence of element modelling as a research issue. The blending of classical FEM with new particle-based and discrete element methods appears as one of the more prominent areas of research. Industrial forming processes, geo-mechanics, bio-mechanics, steel, concrete and masonry structures form the core of the applications of the different numerical methods presented.

The organizers would like to thank all authors for submitting their contributions, as well as the supporting organizations for their help in making COMPLAS XIV possible.

Eugenio Oñate

Michele Chiumenti

Universitat Politècnica de Catalunya
Barcelona, Spain

Roger Owen

Djordje Peric

Swansea University
Swansea, Wales
United Kingdom

ACKNOWLEDGEMENTS

The conference organizers acknowledge the support towards the organization of COMPLAS 2015 to the following organizations:

International Center for Numerical Methods in Engineering (CIMNE)

Universitat Politècnica de Catalunya (UPC)

Swansea University

European Community on Computational Methods in Applied Sciences (ECCOMAS)

International Association for Computational Mechanics (IACM)

We thank the **Plenary Speakers** and the **Invited Sessions Organizers** for their help in the setting up of a high standard Scientific Programme.

ORGANIZERS AND COMMITTEES

Conference Co-Chairmen

E. Oñate, *Universitat Politècnica de Catalunya*, Spain

D. R. J. Owen, *Swansea University*, United Kingdom

D. Peric, *Swansea University*, United Kingdom

M. Chiumenti, *Universitat Politècnica de Catalunya*, Spain

Scientific Committee

C. Agelet de Saracibar, Spain
O. Allix, France
C. Andrade, Spain
E. Artioli, Italy
A. H. Barbat, Spain
K-J. Bathe, USA
Z. Bazant, USA
Y. Bazilevs, USA
E. Benvenuti, Italia
A. Benzerga, USA
M. Bischoff, Germany
R. Borja, USA
P-O. Bouchard, France
I. Carol, Spain
D. Cendon, Spain
M.Čermák, Czech Republic
M. Cervera, Spain
J. César de Sá, Portugal
J. S. Chen, USA
J. L. Chenot, France
F. Chinesta, France
D. Coutellier, France
E. Cueto, Spain
R. de Borst, Netherlands
A. de Jesus, Portugal
L. De Lorenzis, Germany
R. A. de Sousa, Portugal
F. Dufour, France
E. Dvorkin, Argentina
J. Eberhardsteiner, Austria
A. Eskandarian, USA
R. Feijoo, Brazil
S. Forest, France
L. Fourment, France
M. Galic, Croatia
A. Gens, Spain
C. Hellmich, Austria
G. Holzapfel, Austria
A. Huerta, Spain
T. J.R. Hughes, USA
A. Ibrahimbegovic, France
T. Iizuka, Japan
T. Jefferson, UK
D. Juhre, Germany
M. Kleiber, Poland
B. Klusemann, Germany
D. Kochmann, USA
T. Kuboki, Japan
P. Ladevèze, France
T. Laursen, USA
A. Ledesma, Spain
C. Li, UK
C. Linder, USA
L-E. Lindgren, Sweden
W. K. Liu, USA
J. Llorca, Spain
Y. Maday, France
G. Maier, Italy
H. Mang, Austria
A. Maniatty, USA
P. Marovic, Croatia
E. Martínez Pañeda, Denmark
H. Matthies, Germany
I. Mihai, UK
N. Moës, France
C. Morin, Francia
J. Mosler, Germany
H. Naceur, France
R. Natal, Portugal
A. Needleman, USA
C. F. Niordson, Denmark
R. Ohayon, France
J. Oliver, Spain
S. Oller, Spain
M. Ortiz, USA
A. Pandolfi, Italy
M. Papadrakakis, Greece
M. Pastor, Spain
R. H. J. Peerlings, Netherlands
U. Perego, Italy
B. Pichler, Austria
G. Pijaudier-Cabot, France
F. Pires, Portugal
J-P. Ponthot, Belgium
P. Prat, Spain
E. Ramm, Germany
A. Reali, Italy
D. Reddy, South Africa
S. Reese, Germany
P. Roca, Spain
T. Rodic, Slovenia
A. Rodriguez-Ferran, Spain
B. Rosic, Germany
G. Ruiz, Spain
K. Runesson, Sweden
B. Schrefler, Italy
J. Schröder, Germany
S. W. Sloan, Australia
L. Stainier, France
E. Stein, Germany
S. Sysala, Czech Republic
R. L. Taylor, USA
K. Terada, Japan
V. Tvergaard, Denmark
R. A. F. Valente, Portugal
M. Vaz Júnior, Brazil
G. Ventura, Italia
N. E. Wiberg, Sweden
P. Wriggers, Germany
G. Yagawa, Japan
Y. Yuan, China
Z. Zhuang, China

SUMMARY

CONTENTS

PLENARY LECTURE

INVITED SESSIONS

IS - Advances in Meshless and Weakened Weak Formulations in Computational Mechanics

IS - Applications of Computational Methods to Product and Process Design for Industry

IS - Computational Biomechanics

IS - Computational Modeling of Ductile Fracture at Multiple Scales

IS - Computational Modeling of Material Forming Processes

IS - Computational Scale Bridging

IS - Computational Strategies for Metal Cutting & Forming Operations

IS - Evolving Microstructures in Solids

IS - Irreversible Material Phenomena in the Presence of Uncertainty: Constitutive Modelling and Computational Approaches

IS - Modelling of Shrinkage Cracking in Porous Media

IS - Multiscale Modeling of Concrete and Concrete Structures

IS - Size-effects in Metal Plasticity

Advanced Material Models

Biomechanics and Bio-Medicine

Composites

Contact and Crash

Damage, Fracture and Fatigue

Environment and Geosciences

Forming Processes Simulations

Geomaterials and Concrete

Industrial Applications

Innovative Computational Methods

Multi-Physics Problems

Multi-Scale Material Models

Nano-Mechanics

Parallel and Real Time Computing Techniques

PLENARY LECTURE

XIV International Conference on Computational Plasticity. Fundamentals and Applications
COMPLAS 2017
E. Oñate, D.R.J. Owen, D. Peric and M. Chiumenti (Eds)

SIMULATION OF PENETRATION PROBLEMS IN GEOMECHANICS

ANTONIO GENS*, MARCOS ARROYO*, JOSEP M. CARBONELL*, MATTEO CIANTIA†, LLUÍS MONFORTE*

*Centre Internacional de Mètodes Numèrics en Enginyeria (CIMNE)
Departament d'Enginyeria Civil i Ambiental
Universitat Politècnica de Catalunya
Jordi Girona 1-3, Campus Nord UPC, 08034 Barcelona, Spain
e-mail: antonio.gens@upc.edu,marcos arroyo@upc.edu, cpuigbo@cimne.upc.edu, lluismonforte@gmail.com
Web page: https://www.etcg.upc.edu/
†Department of Civil and Environmental Engineering
Imperial College, London SW7 2AZ, UK
e-mail: m.ciantia@imperial.ac.uk Web page : http://www.imperial.ac.uk/civil-engineering

Key words: Discrete Element Method, Particle Finite Element Method, Cone penetration, Crushable sands, Clays.

Abstract. The simulation of penetration problems in geomaterials is a challenging problem as it involves large deformations and displacements as well as strong non-linearities affecting material behaviour, geometry and contact surfaces. The paper presents examples of modelling of the cone penetration test using two procedures: a discrete approach and a continuum approach. The discrete approach is based on the Discrete Element Method where a granular material is represented by an assembly of separate particles. Cone penetration has been successfully simulated for the case of crushable sands. For the continuum approach, the Particle Finite Element Method has been adopted. The procedure has been effectively applied to the modeling of undrained cone penetration into clays. Although not exempt of problems, both approaches yield realistic results leading to the possibility of a closer examination and an enhanced understanding of the mechanisms underlying penetration problems in geomechanics.

1 INTRODUCTION

Penetration problems are encountered very frequently in geotechnical engineering and other geomechanical applications. Some examples are the use of tube samplers to recover soil specimens, the installation of driven piles in the ground or a variety of penetration probes for site investigation purposes. A realistic numerical simulation of those type of problems would yield important advantages concerning the understanding of the processes involved during penetration possibly leading to a more rational approach for, among others, in-situ test interpretation, assessment of sampling disturbance and pile design.

However, the numerical simulation of penetration problems faces significant challenges as it involves large deformations and displacements as well as strong non-linearities affecting material behaviour, geometry and contact surfaces. A variety of computational techniques are

available to tackle this kind of problems [1]. They can be classified into two main categories: discrete and continuum.

In this paper, both types of numerical modelling are applied to the same penetration problem: the cone penetration test (CPT). The CPT is a widely used site investigation tool for geomechanical applications. The test consists of the introduction of a cone, of standard dimensions, into the ground at a constant rate of penetration. The unit cone resistance is measured in a quasi-continuous manner during penetration. Normally, lateral friction and pore pressures are also measured but here attention is mainly focused on cone resistance. In this contribution, two examples of application are presented: the Discrete Element Method (DEM) for cone penetration in crushable sands and the Particle Finite Element Method (PFEM) for the undrained analysis of cone penetration in clays.

2 DEM MODELLING OF CONE PENETRATION IN CRUSHABLE SANDS

In the DEM modelling, the granular soil is represented by a number of finite size particles that interact through their contacts. The method tracks the motion of those particles subjected to a series of forces transmitted by the adjacent particles through the contacts [2]. The method has certainly important limitations bus also a considerable number of advantages [3]. Among the limitations are the generally oversimplified geometrical representation of the particles (often assumed to be spheres) and the need to scale up their size, especially in boundary value problems such as the cone penetration analyses. The main advantage is that large strains, displacements and rotations are readily accommodated in the analyses. Also, it is possible to bypass the need for quite sophisticated constitutive models for sands; instead, only the contact law between pairs of individual particles is usually required. It should be noted, however, that there is considerable uncertainty over the precise form of those contact laws and their parameters are generally calibrated comparing the macroscopic response of a DEM model and the results of analogous laboratory tests.

The modeling of cone penetration in materials made up of weak grains (e.g. calcareous sands) is especially interesting because it has been observed [4] that the pattern of cone resistance increase with relative density is notably different in calcareous crushable sand compared to non-crushable silica sand. This difference results in difficulties when correlations developed for silica sands are applied to materials with crushable grains [5-6]. In this context, the application of DEM analysis is appealing because it allows the isolation of the effects of grain strength and crushability. It is applied to an extreme case, reported in [7], where the cone resistance observed in calibration chamber tests was insensitive to relative density (Figure 1). The material is volcanic pumice sand the grains of which are porous themselves.

To model such materials, it is necessary to introduce particle crushing into the DEM formulation. Here, an efficient formulation recently developed has been adopted [8-9]. The main features of this approach can be summarized as follows: a particle failure criterion inspired by the analytical work of [10-11], a particle spawning procedure based on Apollonian packing and upscaling rules for particle strength and contact stiffness parameters. As in many multigenerational approaches, mass is not conserved after particle splitting but the missing mass of broken particles is allocated, during post-processing, to finer fractions according to a fractal distribution. In this way, it is possible to track evolving porosity and grain size distribution.

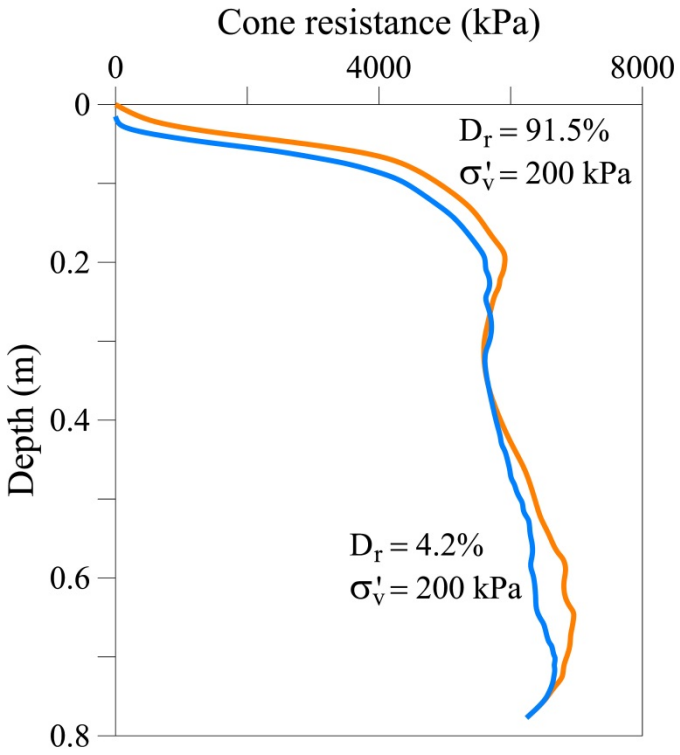

Figure 1: CPT results observed in cone penetration tests on pumice sand performed in a calibration chamber [7]

The corresponding virtual calibration chamber (Figure 2) has been constructed with the same procedure and scaling reported in [12]. The zero-strain radial lateral condition of the physical chamber was replicated by the model. The DEM model has been calibrated against oedometer and triaxial tests on the pumice sand used in the calibration chamber tests [7]. Selected results of the DEM analyses are presented in Figure 3 where it is apparent that the cone penetration values are quite insensitive to the density of the sand, as observed in the physical experiments.

Parallel DEM calculations assuming uncrushable grains were also performed so that the effects of particle crushability could be readily identified. Results in terms of ratio of cone penetration resistance of uncrushable and crushable granular materials are collected in Figure 4. It can be noted that the pattern of variation with relative density agrees well with reported experimental results. No DEM results are available for densities below about 40% due to the difficulty of constructing very loose virtual specimens. In any case, it appears that the use of the new DEM formulation for crushable materials provides a good tool to further explore penetration problems in this type of materials. More information on this study is given in [13].

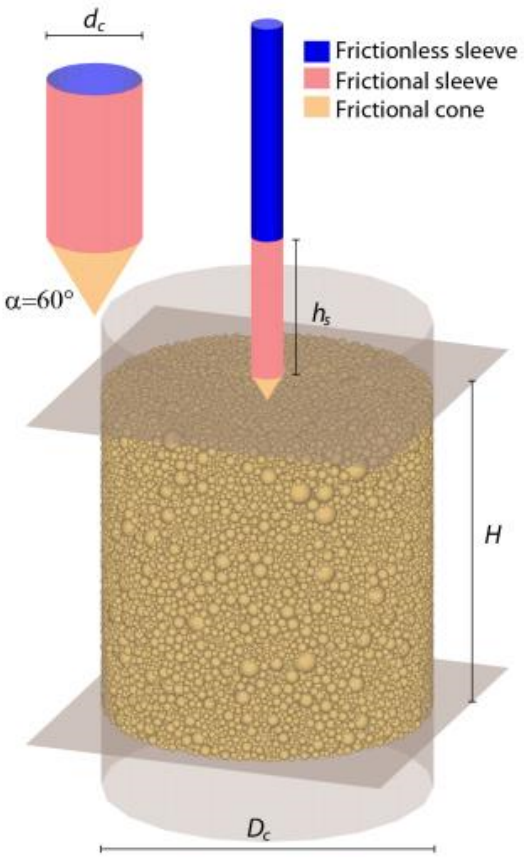

Figure 2: Scheme of DEM analysis: virtual calibration chamber and cone

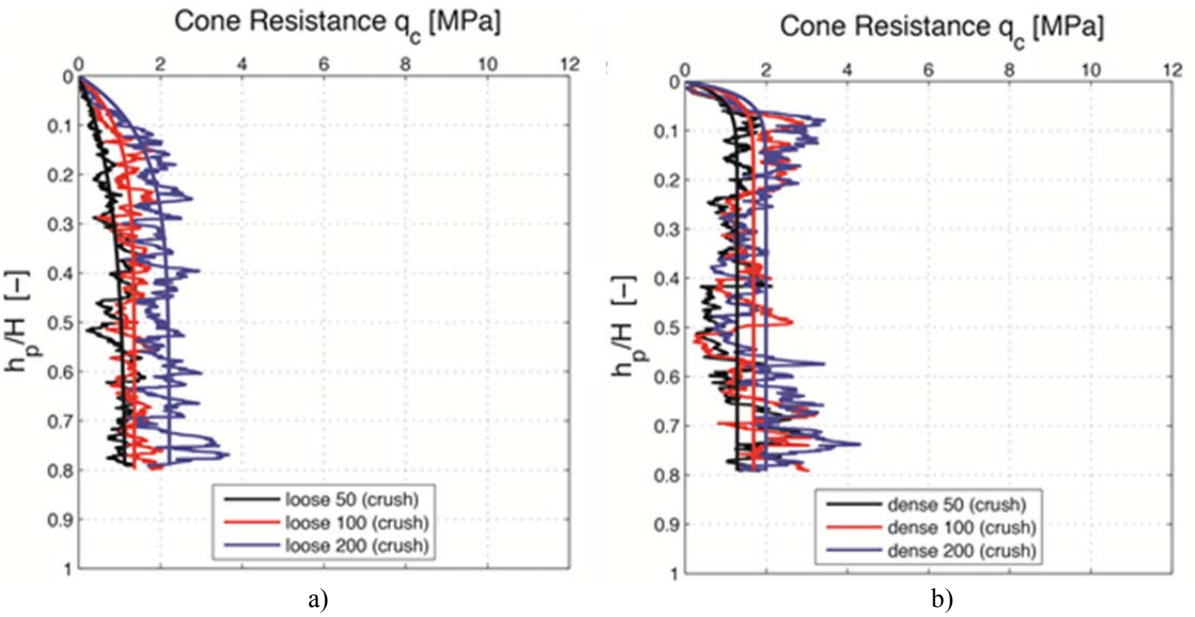

a) b)

Figure 3: Computed cone resistance in simulated cone penetration on pumice sand at different stress values
a) Loose specimen, b) Dense specimen

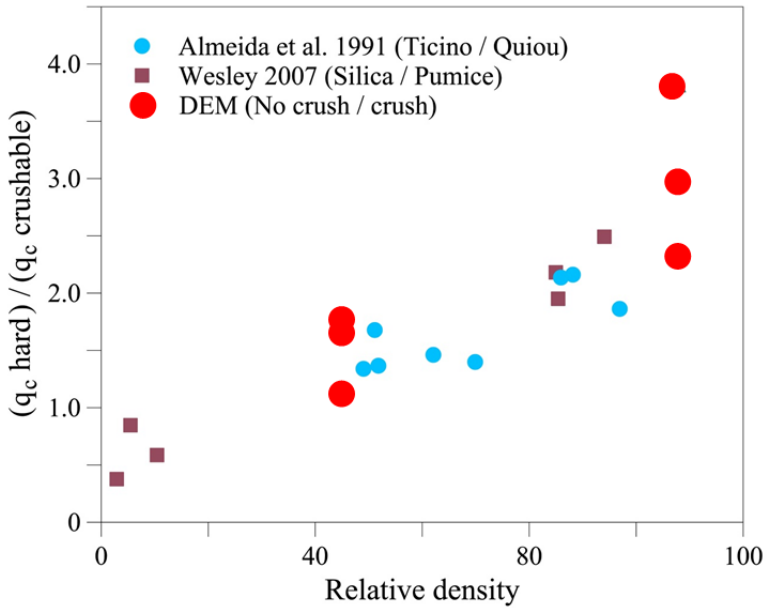

Figure 4: Effect of crushability on cone resistance for different relative densities. Experimental and DEM results

3 PFEM MODELLING OF UNDRAINED CONE PENETRATION IN CLAYS

The continuum modelling of the cone penetration test has been performed using the Particle Finite Element Method, PFEM [14-16]. The method uses a Finite Element approximation to compute the movement of the particles within an updated Lagrangian framework. In this method, particles and nodes coincide and the mesh is updated when required to prevent excessive distortions; Delaunay tessellation is used for this purpose. The mesh nodes are considered particles that carry mass and the state variables and, being particles, they can separate from the main domain giving rise to new boundaries. Although the method was initially developed for fluid-solid interaction problems, there have already been some applications to geotechnical problems [17-19].

Figure 5 shows a scheme of the method that can be summarised in the following steps: i) A cloud of particles, C_n, is defined at a time $t=t_n$, ii) identify the boundaries defining the analysis domain, iii) discretise the domain with a finite element mesh, iv) solve the governing equations within a Lagrangian formulation and compute the state variables at the next updated configuration at t_{n+1}, v) move the nodes to the new position C_{n+1}, vi) go back to step i).

In a purely undrained case the soil can be considered as a single phase medium and only the linear momentum balance equation (equilibrium) needs to be solved. Accordingly, a total-stress Tresca constitutive model has been adopted to represent the soil whereas the tangential contact with the rigid cone has been simulated with a von Mises yield criterion. The analyses presented here have been performed with a rigidly index, Ir = 100. The geometry of the problem and the computation domain are shown in Figure 6a.

The cone penetration analyses have been carried out using values of cone-soil adhesion ratio (α = adhesion/undrained shear strength) ranging from 0 to 0.7. The results in terms of cone penetration (normalized as cone factor N_{kt}) and friction sleeve resistance are plotted in Figure 6b. As expected, the friction sleeve resistance coincides with the specified adhesion

and the cone resistance increases modestly with the value of adhesion. Figure 7 shows more explicitly the variation of cone factor with the value of adhesion. The gradient of the variation of the cone factor as roughness increases is 1.8; this value is within the range of other analyses.

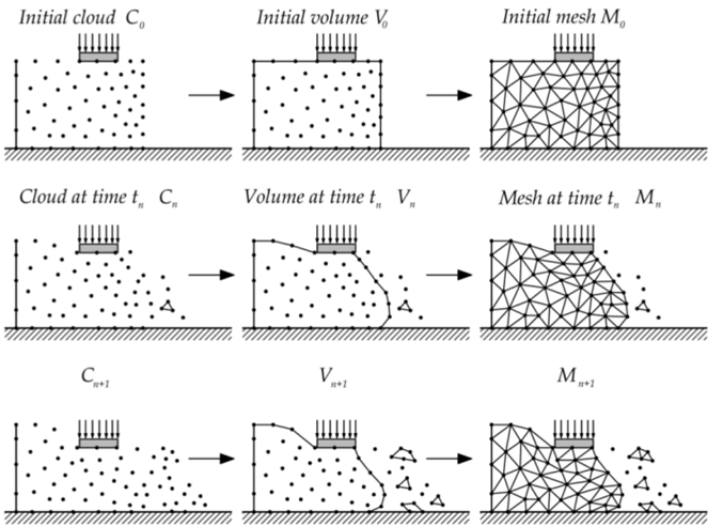

Figure 5: Scheme of a PFEM computational step

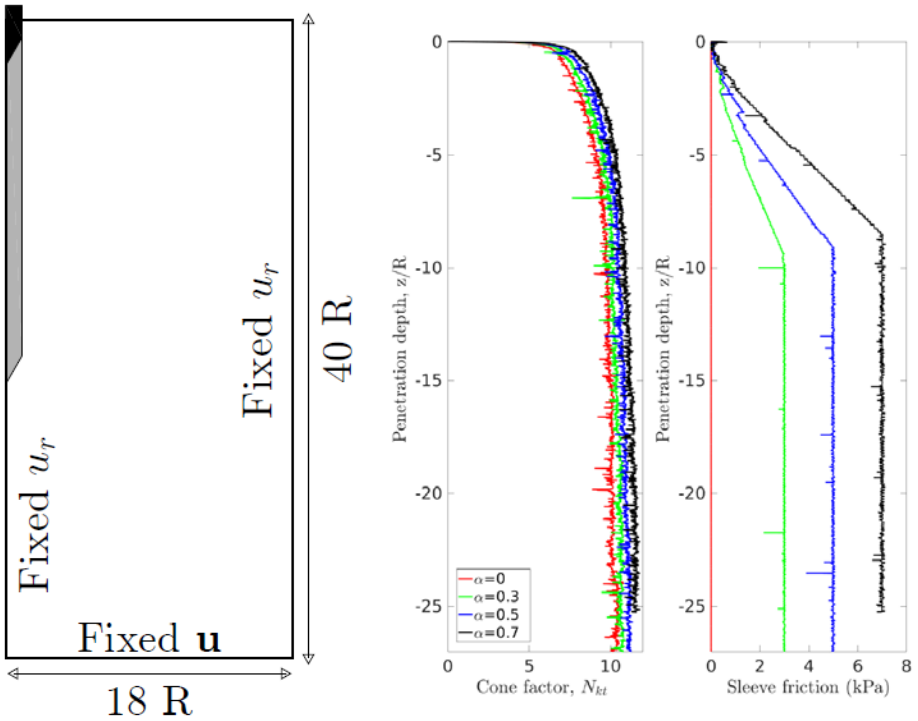

a) b)

Figure 6: a) Geometry and computational domain of the PFEM analysis of cone penetration. b) Cone factor and friction sleeve resistance for different values of adhesion

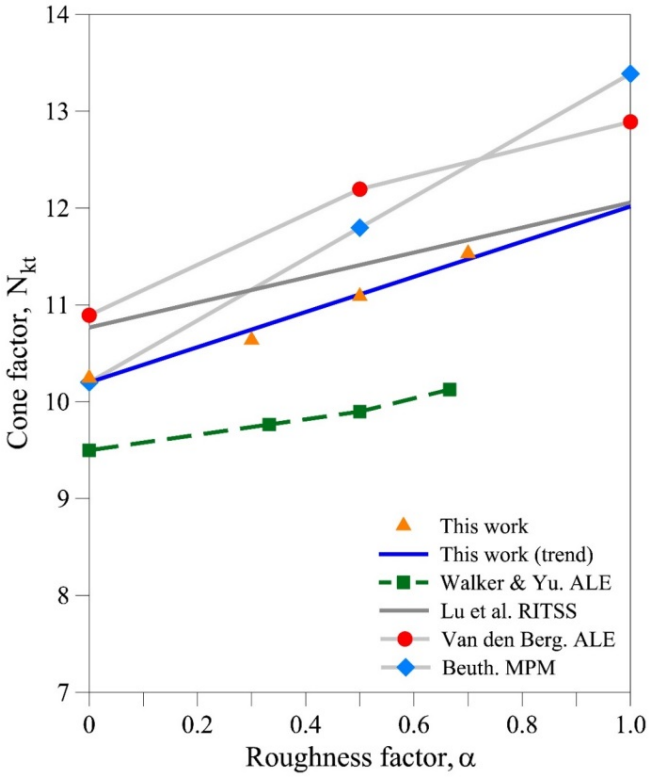

Figure 7: Influence of contact roughness on cone factor N_{kt}

To illustrate further the performance of the method, Figure 8 shows the PFEM meshes (and mean stress contours) at the start and the end of the analysis. It can be readily noted how the mesh refinement has adapted to the advance of the cone accommodating, without undue element distortions, the large displacements associated with the penetration of the cone. More information on this analysis is given in [20].

4 CONCLUDING REMARKS

Two different approaches have been presented for the modelling of the cone penetration test that attempt to overcome the considerable difficulties associated with the simulation of penetration problems, i.e. large displacements, large strains and rotations, severe domain distortion as well as geometrical, material and contact nonlinearities. Both the DEM and PFEM procedures have shown their capabilities in this respect although some significant challenges and shortcomings remain. They constitute, however, areas of intense development and research that should lead to an increasingly realistic description of the process of cone penetration in all its complexity. Consequently, it can be envisaged that more rational-based procedures for the interpretation of the test should ensue. More generally, these numerical procedures open up the prospect of efficient simulations of a wide range of penetration problems in geomechanics.

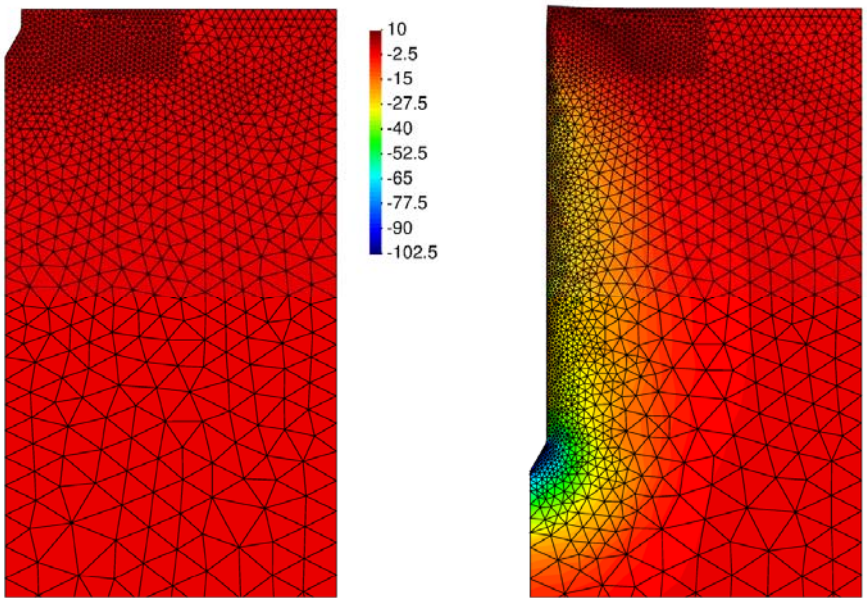

Figure 8: PFEM meshes and mean stress contours at the start (left) and at the end (right) oh the analysis

ACKNOWLEDGEMENTS

The support of the Ministerio de Economía y Competividad of Spain through research grants BIA2011-27217 and BIA2014-59467-R is gratefully acknowledged.

REFERENCES

[1] Gens, A., Arroyo, M., Butlanska, J., Carbonell, J.M., Ciantia, M., Monforte, L. and O'Sullivan, C. Simulation of the cone penetration test: discrete and continuum approaches. *Australian Geomechanics* (2016) **51**(4):169-182.

[2] Cundall, P. A. and Strack, O. D. L.. Discrete numerical model for granular assemblies. *Géotechnique* (1979) **29**(1): 47-65.

[3] O'Sullivan, C. *Particle-Based Discrete Element Model-ing: A geomechanics perspective.* Hoboken, NJ: Taylor & Francis (2011).

[4] Almeida, M., Jamiolkowski, M. and Peterson, R.. Preliminary results of CPT tests in calcareous Quiou sand. *Proceedings of the International Symposium on Calibration Chamber Testing*: 41-53. New York: Elsevier (1991).

[5] Ahmed, S. M., Agaiby, S. W. and Abdel-Rahman, A. H. A unified CPT–SPT correlation for non-crushable and crushable cohesionless soils. Ain Shams Engineering Journal (2014) **5**: 63-73

[6] Moss, R.E.S. A Critical State framework for seismic soil liquefaction triggering using CPT, *3rd International Symposium on Cone Penetration Testing, CPT14*, Las Vegas, Nevada, Paper 2#20 (2014).

[7] Wesley L. D. Geotechnical characteristics of a pumice sand. In Tan et al. (ed.) *Characterisation and Engineering properties of Natural Soils*: 2449-2473. London: Taylor & Francis (2007).

[8] Ciantia, M. O., Arroyo, M., Butlanska, J. and Gens, A. DEM modelling of a double-

porosity crushable granular material. In K. Soga et al. (Ed.), *Proc. Int. Symp. on Geo-mechanics from Micro to Macro*: 269-274. London: Taylor & Francis (2014.

[9] Ciantia, M. O., Arroyo, M., Calvetti, F. and Gens, A. An approach to enhance efficiency of DEM modelling of soils with crushable grains. *Géotechnique* (2015) **65**: 91–110.

[10] Russell, A. R. and Muir Wood, D. Point load tests and strength measurements for brittle spheres. *Int. J. of Rock Mech. and Mining Sciences* (2009) **46:** 272–280

[11] Russell, A. R., Muir Wood, D. and Kikumoto, M.. Crushing of particles in idealised granular assemblies. J. Mech. Phys. Solids (2009) **57**: 1293–1313.

[12] Arroyo, M., Butlanska, J., Gens, A., Calvetti, F., and Jamiolkowski, M. Cone penetration tests in a virtual calibration chamber. *Géotechnique* (2011) **61**: 525-531.

[13] Ciantia, M. O., Arroyo, M., Butlanska, J. and Gens, A. DEM modelling of cone penetration test in a double-porosity crushable granular material. *Computers and Geotechnics*. (2016) **73**:109-127.

[14] Idelsohn, S.R., Onate, E. and Del Pin, F. The particle finite element method: a powerful tool to solve incompressible flows with free-surfaces and breaking waves. *Int J Numer Meth Eng.* (2004) **61**:964–89.

[15] Onate, E., Idelsohn, S.R., Del Pin, F. and Aubry, R. The particle finite element method an overview. *Int J Comput Meth*. (2004) **1**:267–307.

[16] Carbonell, J.M.. *Modeling of ground excavation with the Particle Finite Element Method*. Ph.D. Thesis. Universitat Politècnica de Catalunya, Barcelona (2009).

[17] Carbonell J.M., Onate, E. and Suarez, B. Modeling of ground excavation with the Particle Finite Element Method. *Journal of Engineering Mechanics, ASCE* (2010) **136**: 455-463.

[18] Zhang, X., Krabbenhoft, K., Pedroso D.M., Lyamin, A.V., Sheng, D., da Silva, M.V. and Wang, D. Particle finite element analysis of large deformation and granular flow problems. *Computers and Geotechnics* (2013) **54**: 133-142.

[19] Zhang, X., Krabbenhoft, K., Sheng, D. and Li., W. Numerical simulation of a flow-like landslide using the particle finite element method. *Computational Mechanics* (2015) **55**: 167-177.

[20] Monforte, L., Arroyo, A., Carbonell J.M. and Gens A. Numerical simulation of undrained insertion problems in geotechnical engineering with the Particle Finite Element Method (PFEM) Computers and Geotechnics (2017) **82**: 144-156.

XIV International Conference on Computational Plasticity. Fundamentals and Applications
COMPLAS XIV
E. Oñate, D.R.J. Owen, D. Peric & M. Chiumenti (Eds)

ON THE ROLE OF PARTICLES AND RADIAL BASIS FUNCTIONS IN A FINITE ELEMENT LEVEL SET METHOD FOR BUBBLE DYNAMICS

JUAN LUIS PRIETO[*] [†]

[†] Departamento de Ingeniería Energética
Escuela Técnica Superior de Ingenieros Industriales
Universidad Politécnica de Madrid
c/ José Gutiérrez Abascal, 2, 28006 Madrid, Spain
e-mail: juanluis.prieto@upm.es
ORCID® iD: orcid.org/0000-0001-5085-0482

Key words: Finite Element Method, Level Set, Particles, Radial Basis Functions, Bubbles, Non-Newtonian Flows.

Abstract. The aim of this presentation is to highlight the role that Particle-based simulations and Radial Basis Functions (RBFs) have played in the development of a computationally efficient, level-set, Finite Element method for the simulation of Newtonian and non-Newtonian interface flows. First, we introduce the mathematical formulation and the interface-capturing technique used in the simulation of multiphase flows, underscoring the influence of marker particles on the enhanced definition of the interface. Then, we explore the effect of adding polymer particles to the domain to perform Brownian Dynamics Simulations of polymer flows. Finally, we leverage RBFs to reconstruct, in an almost free-independent way the polymer stress tensor retrieved from the polymer particles.

Numerical simulations of pure advection flows and bubble dynamics simulations of complex flows on two-dimensional configurations emphasize the improvements offered by this hybrid, Finite Element/RBF/Particle-based method.

1 INTRODUCTION

From its inception, the contribution of meshfree methods to the solution of complex scientific and engineering problems has proven remarkable; at this point in its history, particle and meshless methods offer a viable alternative to more traditional methods [1, 2, 3, 4, 5]. The purpose of this work is to highlight some recent advances made in the field of Multiphase Flows and non-Newtonian Fluid

Dynamics by combining particle methods and Radial Basis Functions with the Finite Element Method in a semi-Lagrangian approach.

2 MATHEMATICAL FORMULATION

Since we aim with this work to illustrate the role of particles in multiphase flows, and more precisely, in bubble dynamics simulations, we succinctly describe here the numerical tools used, referring the reader elsewhere for additional details.

2.1 Marker particles for free-surface representation

As an improvement over the level set method, marker particles can be added to better represent the interface between the two fluids. The idea is to advect the massless particles and provide each of them with a variable radius $r_{\min} \leq r_p \leq r_{\max}$ so that the particle surface, whenever possible, remains in contact with the free-surface; otherwise, the particle will have a minimum or maximum radius. Then, we carry out a three-stage procedure based on error identification, error quantification and error correction, with local level set functions ϕ_p defined at each of the massless particles according to:

$$\phi_p(\mathbf{x}_i) = s_p^n \left(\left| \mathbf{x}_i - \mathbf{x}_p^n \right| - r_p^n \right),$$

with $s_p^n \equiv sign\left\{\phi_h^n(\mathbf{x}_p^n)\right\}$. These particles help in correcting the global level set function ϕ whose zero isocontour represents the interface. For details, see [6].

2.2 Polymer particles in Brownian Dynamics simulations

As an alternative to the constitutive modeling of non-Newtonian fluids, the micro-macro (stochastic) approach uses polymer particles that carry the internal degrees of freedom of the viscoelastic fluid; these particles are advected by the flow, contributing to the incompressible, Navier-Stokes equations through the extra-stress tensor computed by taking moments of the configurations. In this work, we use the Hookean and FENE ('Finitely Extensible, Nonlinear Elastic') kinetic models, each of them represented by two dumbbells connected by a spring of force $\mathbf{F}$, so that the stochastic differential equation ruling the configurations $\mathbf{Q}$ of the dumbbells are integrated by a (weak) second-order algorithm, as in [7, 8]. Further, the cubic equation for the FENE model is efficiently solved with the method proposed in [9]. Variance-reduction techniques are applied using N_{ens} ensembles each of them containing N_d dumbbells, as described in [6].

2.3 CSRBFs for polymer stress tensor reconstruction

Compactly-Supported Radial Basis Functions offer a way of handling, in an efficient and mesh-independent manner, the problem of image reconstruction

from a set of points [10]. In our context, their usefulness directly relates to the reconstruction of the polymer stress tensor: as data set we have the values of each of the components of the polymer stress tensor τ_{pij}^{i} at a certain ensemble i, along with the position of the ensembles themselves $\{\mathbf{x}_i\}$. We choose to use the CSRBFs of minimal degree obtained by Wendland [11], solving the linear systems resulting after imposing the orthogonality conditions using the techniques described in [12].

3 ILLUSTRATIVE EXAMPLES

In this section, we highlight the usefulness of particles and RBFs for improving interface shape, modeling non-Newtonian fluids, and reconstructing the polymer, extra-stress tensor, by a series of numerical tests.

3.1 Star-shaped droplet in vortex flow

We consider the pure advection test recently proposed in [13] to check the ability of the method to deal not only with stretching filaments and quite possibly with topological changes, but also with a multi-layered structure that must be recovered at the end of the periodic simulation. A star-shaped droplet is placed at the center of a square $[0,1]\times[0,1]$ domain, with the interface given in polar coordinates by $r(\theta) = a + b\cos(m\theta)$, with $a = 0.3, b = 0.1$ and $m = 5$. The imposed, periodic ($T_p = 4$) vortex flow is defined by the stream function $\psi = \frac{1}{\pi}\sin^2(\pi x)\sin^2(\pi y)\cos(\pi t/T_p)$, so that the velocity field is obtained as

$$\begin{cases} u = -\sin^2(\pi x)\sin(2\pi y)\cos(\pi t/T_p)\,, \\ v = \sin^2(\pi y)\sin(2\pi x)\cos(\pi t/T_p)\,. \end{cases} \tag{1}$$

Next, we use our SLEIPNNIR method [6] to retrieve the interface at the final instant of the simulation, for a variable number of marker particles scattered in the domain $N_p = \{0, 10^4, 5\times10^4, 10^5\}$; a second-order, eikonal-based reinitialization procedure is used every other time step to ensure that no numerical instabilities propagate away from the interface; the fixed time step size is $\Delta t = 0.01$. A uniform, unstructured mesh refinement was carried out to ascertain the influence of the mesh size h, with h successively halving from $h = 8\times10^{-2}$ down to $h = 5\times10^{-3}$. The shapes of the droplet are pictured in Fig.1: we observe how the addition of marker particles notably improves shape preservation, strikingly so for the coarsest mesh ($h = 8\times10^{-2}$) in which the addition of even a small amount of marker particles ($N_p = 10^4$) enhances the final shape from a rather amorphous interface when no marker particles are used, to a quite precise final shape.

Table 1 conveniently collects the mesh size h, number of elements NE, number of mesh nodes NC, and number of particles N_p used in each simulation, along with the errors measured in the L^2 and L^∞-norms, percentage of mass loss at the end

Figure 1: Shape of a star-shaped droplet in a square $[0,1] \times [0,1]$ domain under a periodic ($T_p = 4$) vortex flow, under uniform mesh refinement. Panels from left to right, and from top to bottom: $h = \left\{8 \times 10^{-2}, 4 \times 10^{-2}, 10^{-2}, 5 \times 10^{-3}\right\}$. For each panel, a variable number of marker particles is used: $N_p = 0$ (green), $N_p = 10^4$ (orange), $N_p = 5 \times 10^4$ (blue) and $N_p = 10^5$ (purple); the initial solution is represented in black.

of the simulation and maximum memory demanded during the simulation. For a fixed mesh size, increasing the number of particles results in a behavior resembling the law of diminishing returns: the benefits of the addition of marker particles are remarkable, while increasing the number offers increasingly small improvements. Nevertheless, the computational cost of the marker particles in terms of memory spent during the simulation, is modest in the coarser meshes and negligible in the finer meshes.

In Fig.2 we plot the evolution of the e_{L^2} error for the three finer meshes and an increasing number of marker particles. As we can observe, the maximum value is reached at the moment of the largest deformation of the flow, decreasing again when particles are added, and slowly increasing in time if no marker particles are used. Again, the same trend of diminishing returns is observed throughout the simulations.

Table 1: Average size h of the unstructured, uniform mesh; number of marker particles N_p; number of elements NE; number of mesh-points NP; error in the Euclidean norm e_{L^2}; error in the infinity norm e_{L^∞}; mass loss percentage; and maximum memory used during the simulation of a periodic ($T_p = 4$) star-shaped droplet under a vortex flow. Values collected at the end of the simulation ($t = 4$).

h	N_p	NE	NC	Error e_{L^2}	Error e_{L^∞}	$A_{\text{loss}}(\%)$	Mem (MB)
$8E{-}2$	0	360	773	$3.1647E{-}1$	$1.1128E{-}1$	$3.81E{-}2$	39.86
$8E{-}2$	10000	362	777	$5.4471E{-}2$	$3.2967E{-}3$	$1.30E{-}2$	40.38
$8E{-}2$	50000	362	777	$6.3726E{-}2$	$4.5122E{-}3$	$6.32E{-}2$	46.87
$8E{-}2$	100000	360	773	$6.9271E{-}2$	$5.3317E{-}3$	$4.02E{-}2$	55.98
$4E{-}2$	0	1484	3069	$2.9478E{-}1$	$9.6547E{-}2$	$2.53E{-}1$	63.44
$4E{-}2$	10000	1484	3069	$3.1659E{-}2$	$1.1137E{-}3$	$3.77E{-}3$	63.39
$4E{-}2$	50000	1484	3069	$2.9832E{-}2$	$9.8883E{-}4$	$9.81E{-}3$	67.47
$4E{-}2$	100000	1484	3069	$2.4658E{-}2$	$6.7557E{-}4$	$8.59E{-}3$	77.23
$2E{-}2$	0	5846	11893	$2.8022E{-}1$	$8.7248E{-}2$	$2.51E{-}3$	142.08
$2E{-}2$	10000	5846	11893	$4.4221E{-}2$	$2.1728E{-}3$	$6.76E{-}2$	142.06
$2E{-}2$	50000	5846	11893	$1.2143E{-}2$	$1.6383E{-}4$	$4.42E{-}4$	142.10
$2E{-}2$	100000	5846	11893	$1.1652E{-}2$	$1.5085E{-}4$	$6.64E{-}4$	142.17
$1E{-}2$	0	23384	47169	$2.1471E{-}1$	$5.1223E{-}2$	$3.61E{-}2$	514.41
$1E{-}2$	10000	23384	47169	$2.0051E{-}2$	$4.4672E{-}4$	$1.88E{-}4$	514.31
$1E{-}2$	50000	23384	47169	$1.1636E{-}2$	$1.5043E{-}4$	$2.27E{-}4$	514.38
$1E{-}2$	100000	23384	47169	$1.0572E{-}2$	$1.2418E{-}4$	$7.75E{-}5$	514.41
$5E{-}3$	0	94330	189461	$9.1740E{-}2$	$9.3514E{-}3$	$3.57E{-}3$	2,029.47
$5E{-}3$	10000	94330	189461	$1.9352E{-}2$	$4.1612E{-}4$	$2.16E{-}4$	2,029.37
$5E{-}3$	50000	94330	189461	$1.0243E{-}2$	$1.1657E{-}4$	$5.29E{-}5$	2,029.48
$5E{-}3$	100000	94330	189461	$8.3215E{-}3$	$7.6941E{-}5$	$5.62E{-}5$	2,029.46

3.2 Viscoelastic droplet in shear flow

We now proceed with a problem in which the viscoelastic effects are present, namely, the behavior of a viscoelastic droplet in a Newtonian, viscous fluid. This situation has been thoroughly investigated (see e.g. [14, 15, 16]) in studies strongly suggesting that droplet viscoelasticity prevents deformation to a certain degree The schematics are showed in Fig.3, in which a droplet of radius a is placed at the center of a domain $[2L \times 2H]$, with $H = 4a$ and $L = 8a$. The no-slip boundary condition is imposed at the bottom and top lids of the domain, which move at a velocity V in opposite directions, giving rise to a shear rate $\dot{\gamma} = V/H$, here taken as $\dot{\gamma} = 1$. For details on the numerical model, refer to the uncorrelated computations found in [6] and [17].

The viscoelastic drop is modeled by Hookean dumbbells (equivalent to the Oldroyd-B constitutive equation), and is immersed in a Newtonian, ambient fluid. The flow is suddenly started at $t = 0$ with shear rate $\dot{\gamma} = 1$, using a mesh with 80×40 elements and $N_p = 10^7$ uncorrelated, polymer particles (dumbbells) uniformly placed inside the droplet; the flow is continued until dimensionless time

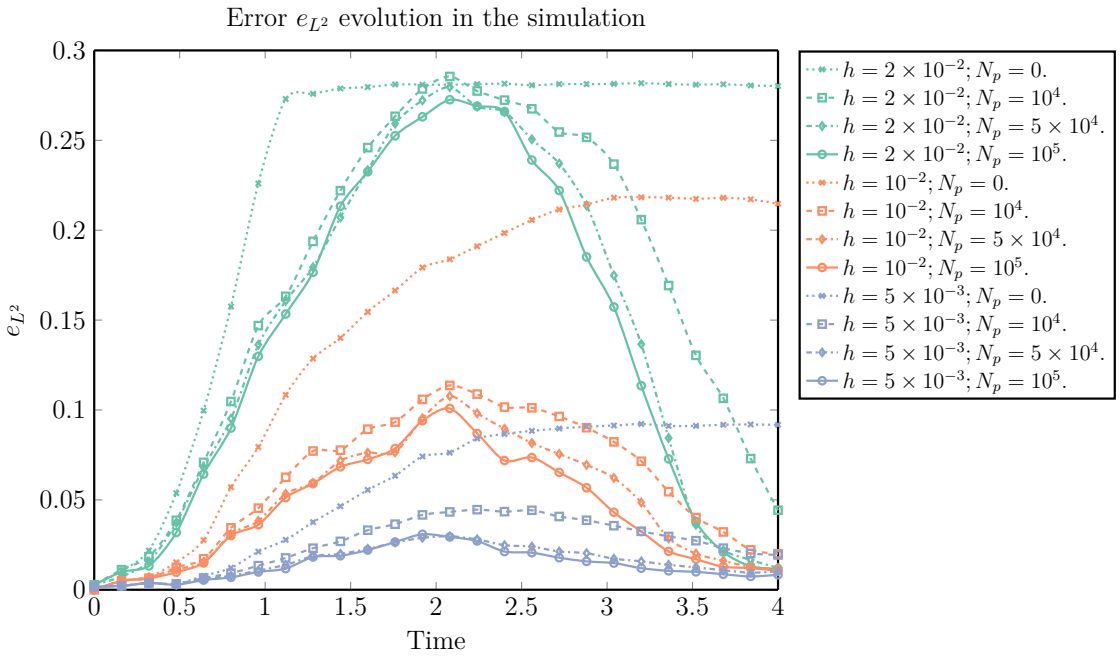

Figure 2: Evolution of the e_{L^2} error during the simulation of a star-shaped droplet in a square $[0,1] \times [0,1]$ domain under a periodic ($T_p = 4$) vortex flow, under uniform mesh refinement $h = \{2 \times 10^{-2}, 10^{-2}, 5 \times 10^{-3}\}$ and variable number of marker particles $N_p = \{0, 10^4, 5 \times 10^4, 10^5\}$.

$t^* = t\dot{\gamma} = 10$, with a small time step to accurately solve the internal configurations of the dumbbells ($dt = 1/200$), taking $N_t = 2000$ time steps to finish each simulation; the number of marker particles to improve the definition of the interface is $N_{mp} = 2.5 \cdot 10^5$. The effects of the Reynolds prove to be of utmost importance, in the sense that, if the method is not able to deal with extremely low Re (creeping flows), the inertial effects become relevant when small time steps are used, thus affecting the history of the flow and, consequently, that of the dumbbells: it is for this reason that $Re = 10^{-5}$ is chosen. The rest of the dimensionless parameters are those found in [14] (also referenced henceforth as "Yue et al. PoF05"): $Fr \to \infty$, $We = 10^{-6}$ so that the Capillary number $Ca = 0.1$; our concentration parameter c, according to the characteristic scales chosen in that article, corresponds to $c = 1 - \beta$, with $\beta = 0.5$ the retardation parameter of the Oldroyd-B fluid; the Deborah numbers studied are $De = \{0.25; 0.5; 1; 2\}$; and the density and viscosity ratios between the droplet and the outer ambient fluid (matrix) are $\rho_2/\rho_1 = \mu_2/\mu_1 = 1$.

We perform a set of simulations to obtain the evolution of the droplet deformation, and compare the results with those by Yue et al. in their Fig.1; the results are collected in Fig. 4. Despite the rather coarse mesh used, the not-so high number of dumbbells, and the totally different approach taken by the two techniques compared (their diffuse-interface method along with a phase-field approach ruled

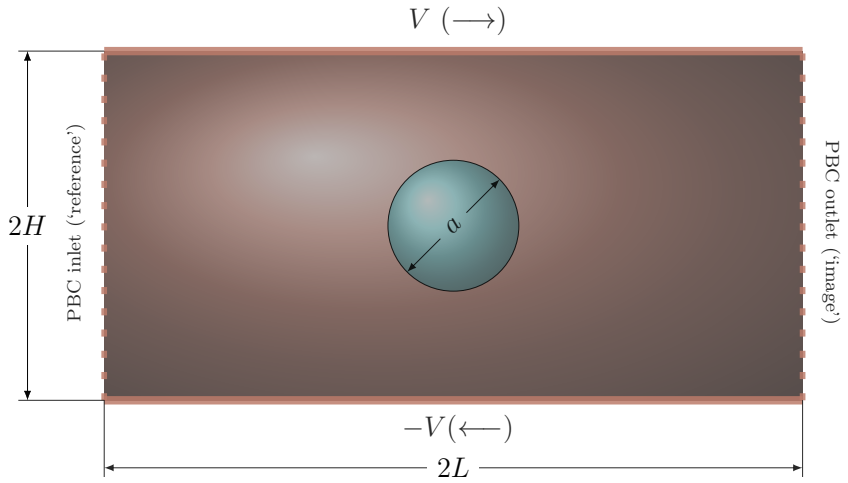

Figure 3: Viscoelastic droplet in Newtonian matrix under a shear flow. Sketch.

by Cahn-Hilliard dynamics to study the Newtonian/non-Newtonian problem in a unified way; and our micro-macro, semi-Lagrangian, Particle Level-Set Finite Element method) the results are in remarkably good agreement, especially the steady state values of the deformation parameter D, defined as $D = (L - B) / (L + B)$, with L and B being the longest and shortest lengths from the center of the droplet to the interface (corresponding also to the major and minor axes of the ellipse), respectively. The transient behavior shows a noteworthy resemblance as well, with the overshoot appearing for sufficiently high De values, and the evolution of $De = 2$ being for $t \lessapprox 4$ being higher than those for $De = 1$. In any case, we notice the effect of the droplet viscoelasticity as a means to reduce the deformation of the interface; plots of the actual shape of the interface (not included here) show this same trend. Finally, we would like to point out that more refined meshes would be needed to prevent some of the oscillation from appearing in the Figure; apart from the stochastic noise (we are using here totally uncorrelated dumbbells), the modification of the interface by the correction stage of the marker particles and the mass conservation step add somewhat to this oscillatory behavior in D, which is explicitly computed from the discrete interface; additional results with a better mesh indeed confirm this fact.

3.3 Reconstruction of polymer stress tensor

Finally, to show the ability of the CSRBFs to reconstruct the extra-stress tensor in non-Newtonian fluids, we perform some numerical tests in a two-dimensional configuration using SLEIPNNIR [6] where a Newtonian bubble rises in a non-Newtonian ambient fluid. A very fine, uniform mesh with grid size $h = 1/320$ is used, with $N_{ens} = 3 \times 10^4$ ensembles being scattered in the viscoelastic fluid,

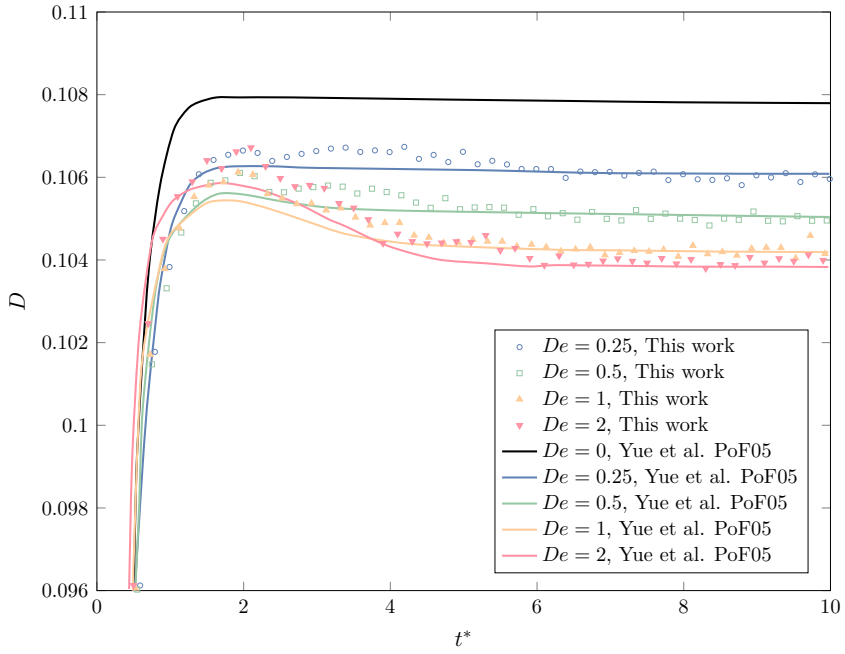

Figure 4: Evolution of the deformation parameter D for a viscoelastic droplet in a Newtonian matrix under a shear flow, for increasing values of the Deborah number De. Comparison with Fig. 1 of [14].

each of them carrying $N_d = 25 \times 10^3$ dumbbells for variance-reduction effects. The dimensionless numbers defining the problem are: Reynolds $Re = 35$, Weber $We = 10$, concentration parameter $c = 5$, Deborah number $De = 3$, density and viscosity ratios $\rho_1/\rho_2 = 10 = \mu_1/\mu_2$; the kinetic FENE ($b = 50$) model is used, with the efficient solution to the resulting cubic equation proposed in [9], and the simulation is continued until dimensionless time $t = 3$ is reached. Four different Compactly-Supported Radial Basis Functions proposed by Wendland are used, with different degree of smoothness represented by the number of continuous derivatives, $\varphi_{sk} \in \mathcal{C}^{2k}(\mathbb{R})$ with convergence rate $h^{s/2+k+1/2}$, and a support size $\chi = 65$. We observe that increased smoothness is beneficial to the reconstruction of well-defined surfaces, with a sufficiently high number of ensembles; see Fig. 5 for the final shapes of the bubbles, in which a nice convergence is noticed for $\varphi_{31}, \varphi_{32}$ and φ_{33}. Additionally, Fig. 6 plots the reconstruction of the shear component of the polymer stress tensor at the end of the simulations; the previous comments may be applied here as well. For additional details about the effect of ensembles and dumbbells per ensemble, see [12].

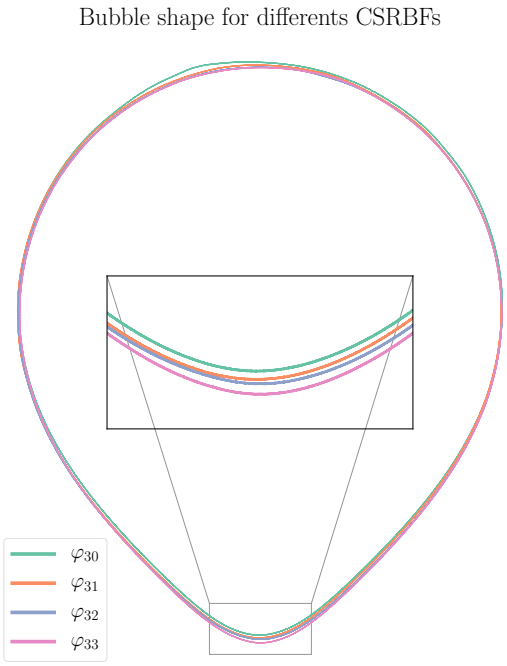

Figure 5: Final shape of bubble using differents CSRBFs: $\varphi_{30}, \varphi_{31}, \varphi_{32}, \varphi_{33}$.

4 CONCLUSIONS

The purpose of this work has been to underscore the role of particles in the context of numerical methods for multiphase flow problems, showing their relevance in a three-fold way:

- Improvement of mass conservation and enhancement of shape preservation, by means of *marker particles*.
- Modeling of non-Newtonian fluids in complex, multiphase flows, using *polymer particles* along with Brownian Dynamics simulations.
- Reconstruction the polymer, extra-stress tensor, leveraging smooth Compactly-Supported Radial Basis Functions.

All these effects have been addressed in a series of numerical simulations that prove the potential of such an approach. Future work involves Adaptive Mesh Refinement techniques, with preliminary results recently communicated in [18].

5 ACKNOWLEDGMENTS

Financial support from grant MTM2015-67030-P from Ministerio de Economía y Competitividad is acknowledged.

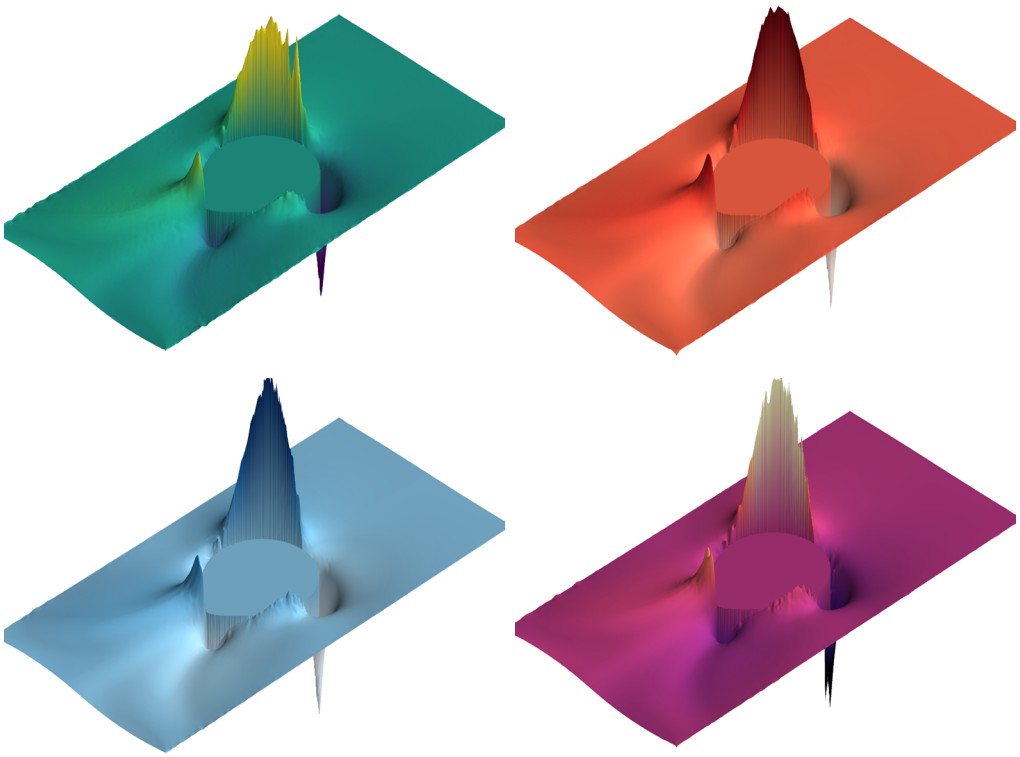

Figure 6: Reconstruction of the shear component τ_{p12} of the polymer stress tensor at the end of a bubble dynamics simulation, for different Wendland's CSRBFs. Panels from left to right, and from top to bottom: $\varphi_{30}, \varphi_{31}, \varphi_{32}, \varphi_{33}$.

REFERENCES

[1] Ferreira, A.J.M. , Roque, C.M.C. and Jorge, R.M.N. Free vibration analysis of symmetric laminated composite plates by FSDT and radial basis functions. *Comput. Methods Appl. Mech. Engrg.* (2005) **194**(39-41):4265–4278.

[2] Nguyen, V.P., Rabczuk, T., Bordas, S. and Duflot, M. Meshless methods: A review and computer implementation aspects. *Mathematics and Computers in Simulation* (2008) **79**(3):763–813.

[3] Liu, G. R. *Meshfree methods: moving beyond the finite element method*. CRC press, (2009), ISBN: 9781420082098.

[4] Belinha, J., Dinis, L.M.J.S. and Jorge, R.M.N., The natural radial element method. *Int. J. Numer. Meth. Engrg.* (2013) **93**(12):1286–1313.

[5] Griebel, M. and Schweitzer, M.A. (Eds.). *Meshfree Methods for Partial Differential Equations VIII*. Springer, (2017), ISBN: 978-3-319-51954-8.

[6] Prieto, J.L., SLEIPNNIR: A multiscale, particle level set method for Newtonian and non-Newtonian interface flows. *Comput. Methods Appl. Mech. Engrg.* (2016) **307**:164–192.

[7] Öttinger, H.C. *Stochastic Processes in Polymeric Fluids*. Springer, (1996), ISBN: 978-3-642-58290-5.

[8] Prieto, J.L., Stochastic particle level set simulations of buoyancy-driven droplets in non-Newtonian fluids. *J. Non-Newtonian Fluid Mech.* (2015) **226**:16–31.

[9] Prieto, J.L., Multi-scale Simulation of Newtonian and Non-Newtonian Multiphase Flows. In: Ibrahimbegovic, A. (Ed.). *Computational Methods for Solids and Fluids: Multiscale Analysis, Probability Aspects and Model Reduction*. Springer, Computational Methods in Applied Sciences series, Vol. 41 (2016):379–398. ISBN: 978-3-319-27996-1.

[10] Ohtake, Y., Belyaev, A. and Seidel, H-P. 3D scattered data interpolation and approximation with multilevel compactly supported RBFs. *Graphical Models* (2005) **67**:150–165.

[11] Wendland, H. *Scattered Data Approximation*. Cambridge University Press, (2005), ISBN: 0521843359.

[12] Prieto, J.L., An RBF-reconstructed, polymer stress tensor for stochastic, particle-based simulations of non-Newtonian, multiphase flows. *J. Non-Newtonian Fluid Mech.* (2016) **227**:90–99.

[13] Chenl, X. and Yang, V., Thickness-based adaptive mesh refinement methods for multi-phase flow simulations with thin regions. *J. Comput. Phys.* (2014) **269**:22–39.

[14] Yue, P., Feng, J.J., Liu, C. and Shen, J. Transient drop deformation upon startup of shear in viscoelastic fluids. *Phys. Fluids* (2005) **17**:123101.

[15] Aggarwal, N. and Sarkar, K. Effects of matrix viscoelasticity on viscous and viscoelastic drop deformation in a shear flow. *J. Fluid Mech.* (2008) **601**:63–84.

[16] Verhulst, K., Cardinaels, R., Moldenaers, P., Afkhami, S. and Renardy, Y. Influence of viscoelasticity on drop deformation and orientation in shear flow. Part 2: Dynamics. *J. Non-Newtonian Fluid Mech.* (2009) **156**(1-2):44–57.

[17] Prieto, J.L., Numerical simulations of buoyancy-driven droplets in non-Newtonian media using a variance-reduced, micro-macro, particle-level set

method. In: Kádár, R. (Ed.). *Annual Transactions of the Nordic Rheology Society* (2017) **25**:233–235.

[18] Prieto, J.L. and Carpio, J. Accurate and Efficient, Multiscale Simulations of Newtonian and non-Newtonian Free-Surface Flows. In: Papadrakakis, M. and Oñate, E. and Schrefler, B. (Eds.). *Proc. VII International Conference on Computational Methods for Coupled Problems in Science and Engineering* (2017) (7 pages).

XIV International Conference on Computational Plasticity. Fundamentals and Applications
COMPLAS XIV
E. Oñate, D.R.J. Owen, D. Peric & M. Chiumenti (Eds)

BIFURCATION ANALYSIS BASED ON A MATERIAL MODEL WITH STRESS–RATE DEPENDENCY AND NON–ASSOCIATED FLOW RULE FOR FRACTURE PREDICTION IN METAL FORMING

Tetsuo Oya*, Jun yanagimoto, Koichi Ito†, Gen Uemura† and Naomichi Mori†**

* Graduate School of Science and Technology, Keio University
3-14-1 Hiyoshi, Kohoku-ku, Yokohama, Japan
e-mail: oya@sd.keio.ac.jp

**Institute of Industrial Science, The University of Tokyo, Tokyo, Japan

†M &M Research Inc., Tokyo, Japan

Key words: Metal Forming, Fracture Prediction, Bifurcation Theory, Plastic Constitutive Equation, Stress–rate Dependency, Non–associated Flow Rule

Abstract. Recent increasing application of advanced high-strength metals causes growing demand for accurate fracture prediction in metal forming simulation. However, since the construction of objective and reliable fracture prediction method is generally difficult, essential progress in fundamental theory that supports evolution of fracture prediction framework is required.

In this study, a fracture prediction framework based on the bifurcation theory is presented. The main achievement is a novel material model based on stress-rate dependency related with non-associate flow rule. This model is based on non-associated flow rule with independent arbitrary higher-order yield function and plastic potential function for any anisotropic materials. And this formulation is combined with the stress-rate dependency plastic constitutive equation, which is known as Ito-Goya model, to construct a generalized plastic constitutive model in which non-normality and non-associativity are reasonably considered. Then, by adopting the three-dimensional bifurcation theory, which is known as the 3D localized bifurcation theory, more accurate prediction of the initiation of shear band is realized, leading to general and reliable construction of forming limit diagram. Then, by using virtual material data, numerical simulation is carried out to exhibit fracture limit diagram for demonstrating the generality and reliability of the proposed methodology. In particular, the effect of stress-rate dependency on the bifurcation analysis is investigated, and the order of the yield function is used to investigate the influence on the forming limit prediction.

1 INTRODUCTION

Recent increasing application of advanced high-strength metals causes growing demand for accurate fracture prediction in metal forming simulation. However, since the construction of objective and reliable fracture prediction method is generally difficult, essential progress in fundamental theory that supports evolution of fracture prediction framework is required. For example, many fracture prediction criteria have been proposed based on the concept of the ductile fracture model. This methodology uses criteria on the basis of physical observation by subjective or intuitive way. This is the reason why there are many criteria to predict the onset of fracture for various materials and forming types. However, the mechanism of the onset of fracture should be constructed free from material type and forming type to achieve accurate, physically reasonable and objective, and user-friendly fracture prediction framework. To realize this aim, because fracture is a terminal phenomena happens at the end of large plastic deformation, the authors considered that reliable and useful fracture prediction scheme should be invented faithfully based on the theory of plasticity.

For constructing reliable fracture prediction model, the bifurcation theory has been adopted in this research, and a novel material model to conduct bifurcation analysis was developed. Although the onset of localized bifurcation is not equivalent to the rapture of a material, this phenomena is closely related with material fracture particularly in sheet metal. Therefore, building an analytical methodology for fracture prediction based on the bifurcation theory is meaningful. The bifurcation theory as a fracture prediction method is advantageous in terms of generality and objectivity, but it is known that the bifurcation analysis using conventional material models sometimes exhibit poor result. General bifurcation theory was established by Hill [1] for plastic materials, followed by many researches based on it. These were based on plane-stress condition and on normality rule; under these assumptions, accurate prediction of the initiation of shear band, which is considered as a sign of fracture, is almost impossible. Even with the S-R (Stören-Rice) theory [2] in which stress-rate dependency is considered, there is still a restriction of plane-stress condition. Thus, to conduct bifurcation analysis appropriately, a new framework that can deal with three-dimensional bifurcation mode and abrupt change in stress field should be created.

In this study, a material model based on stress-rate dependency related with non-associate flow rule is presented. This model is based on non-associated flow rule with arbitrary higher order yield function and plastic potential function for any anisotropic materials [3][4]. And this formulation is combined with the stress-rate-dependency plastic constitutive equation, which is known as the Ito-Goya plastic constitutive equation [5], to construct a generalized plastic constitutive model in which non-normality and non-associativity can be reasonably included. Then, by adopting the three-dimensional bifurcation theory [5], more accurate prediction of the initiation of shear band is realized, leading to general and reliable construction of forming limit diagram.

In this paper, the above-mentioned theoretical framework is described. Then, by using virtual material data, numerical simulation is carried out to exhibit fracture limit diagram

for demonstrating the effectiveness of the proposed methodology.

2 PROPOSED MODEL AND FRAMEWORK FOR FRACTURE PREDICTION

2.1 Material model

First, the material model proposed by the authors[3][4], which plays an essence role in this research, is described. This model is constructed to express deformation anisotropy and yield stress anisotropy by using non-associated flow rule formulation with the number of material constants same as that of Hill's 1948 model. The following is the definition of the yield function and the plastic potential function and the equivalent plastic strain increment.

In the proposed model, we defined the yield function $f(\boldsymbol{\sigma})$ as being equal to the equivalent stress; namely, the expression is

$$f(\boldsymbol{\sigma}) = \bar{\sigma} = \sqrt[2m_y]{\frac{3}{2(F+G+H)}\left(\boldsymbol{s}_{m_y}\cdot\boldsymbol{A}\cdot\boldsymbol{s}_{m_y}\right)}. \tag{1}$$

Here, the matrix $\boldsymbol{A}$ has the anisotropic parameters in its diagonal terms; and the pseudo-vector $\boldsymbol{s}_{m_y}$ is a set of deviatoric stress components to the power of m_y. This higher-order function preserves the form of Hill's quadratic yield function, that is, it contains the same anisotropic parameters F, G, H, L, M, and N. This feature is important because it is possible to construct a higher-order yield function by changing the power value m_y without increasing the number of undetermined variables.

In our non-associated flow rule-based formulation, a function different from the yield function is adopted as a plastic potential function, which provides the direction of the plastic strain increment of the subsequent state of current stress. In this study, the previously introduced function $f(\boldsymbol{\sigma})$ is used as the yield function, and another function $g(\boldsymbol{\sigma})$ that takes the same form as $f(\boldsymbol{\sigma})$ but has different anisotropic parameters F^*, G^*, H^*, L^*, M^*, and N^* is adopted as the plastic potential function. In this expression, asterisks are used to distinguish $f(\boldsymbol{\sigma})$ from $g(\boldsymbol{\sigma})$. For example, the anisotropy matrix $\boldsymbol{A}$ is changed to $\boldsymbol{A}^*$, in which the original parameters F, G, H, L, M, and N are also changed to F^*, G^*, H^*, L^*, M^*, and N^*, respectively. To express another order of the function, the power variable m_p is used instead of m_y. Thus, the plastic potential function of the proposed model takes the form of

$$g(\boldsymbol{\sigma}) = \bar{\sigma}^* = \sqrt[2m_p]{\frac{3}{2(F^*+G^*+H^*)}\left(\boldsymbol{s}_{m_p}\cdot\boldsymbol{A}^*\cdot\boldsymbol{s}_{m_p}\right)}. \tag{2}$$

From the definition of the plastic work, an explicit expression for the equivalent plastic strain increment is obtained as

$$d\bar{\varepsilon}^p = \frac{m_p\overline{\sigma}^{*m_p}}{\overline{\sigma}}\sqrt{\frac{2(F^*+G^*+H^*)}{3}\left(\boldsymbol{D}'^*_{m_p}\cdot d\boldsymbol{e}^p\right)^T\cdot\left\{\boldsymbol{A}^*\cdot\left(\boldsymbol{D}'^*_{m_p}\cdot d\boldsymbol{e}^p\right)\right\}}. \tag{3}$$

The main disadvantage of the non-associated flow rule models would be the increase in the number of unknown variables. Usually, these variables can be specified from experiments such as tensile tests; therefore, the use of the non-associated flow rule model could lead to an increased burden of experiments and measurements. In addition, if a higher-order function is required, the burden increases, making this approach impractical. Thus, to enjoy the benefits of the non-associated flow rule model, an increase in the numbers of unknown variables should be avoided, and this demand is considerably achieved with the proposed model.

The plastic anisotropy characteristics of materials are classified into two categories; namely, plastic flow stress anisotropy and plastic deformation anisotropy. The former and latter should be incorporated in the yield function and the plastic potential function, respectively. Consider cold-rolled metal sheets under a plane stress state. Under the plane stress condition, the number of variables is halved. The anisotropic variables that must be determined are F, G, H, and N and F^*, G^*, H^*, and N^*. The former set expresses the yield stress anisotropy and the latter set expresses the deformation anisotropy.

The parameters about stress anisotropy, F, G, and H, are determined by the yield stresses that are obtained by tensile test in rolling direction, transverse direction, and equibiaxial test. The parameters about deformation anisotropy, F^*, G^*, H^*, and N^*, are determined by the r-values in the direction of rolling, diagonal, and transverse. The remaining parameter N is determined by optimization using the tensile test data in the diagonal direction. Note that the diagonal yield stress, usually denoted as σ_{45}, is not used because the directions except for the rolling and transverse directions are not anisotropic principal axis and it is difficult to separate with the shear component. The order of the functions, m_y and m_p, should be determined before these anisotropic parameters are determined because these values specify the function type, and have own physical meaning different from the anisotropic parameters.

2.2 Ito-Goya's plastic constitutive model

Local bifurcation brings abrupt change on the current strain rate direction. Since the classical J_2 theory does not allow the rotation of the strain rate direction caused by the subsequent stress rate direction, it is not appropriate to the bifurcation problems. Therefore, in this study, Ito-Goya's plastic constitutive equation [5] is applied, because this model can take the dependency of the strain rate direction on the stress rate direction into account. Ito-Goya's plastic constitutive equation is represented as

$$d\boldsymbol{\varepsilon}^p = \Lambda \left(\boldsymbol{n}_F : \boldsymbol{l}_p \right) |d\boldsymbol{\sigma}'| \left[K_C \boldsymbol{l} + (1 - K_C) \boldsymbol{n}_N \right], \tag{4}$$

where $\boldsymbol{n}_N$ is an unit tensor called natural direction. This tensor indicates the direction of the deviatoric stress rate that is identical to that of the plastic strain rate. The unit tensor $\boldsymbol{n}_F$ is the direction of the gradient of the yield function and $\boldsymbol{l}$ is the direction of current deviatoric stress. In Eq. (4), the parameter K_C, which takes a value between 0 and 1, shows the dependency of the direction of the strain rate on stress rate. When K_C is equal to 1, the Ito-Goya's constitutive equation becomes the J_2 flow theory.

2.3 3D local bifurcation theory

Based on Hill's general bifurcation theory, bifurcation occurs at when the following condition is satisfied.

$$I[\Delta \boldsymbol{v}] = \int \Delta \boldsymbol{L} : \Delta \dot{\boldsymbol{S}} dV = 0, \tag{5}$$

where $\Delta \boldsymbol{v}$ is velocity field, $\boldsymbol{L}$ and $\dot{\boldsymbol{S}}$ are velocity gradient tensor and 1st Piola-Kichhoff stress tensor rate, respectively. $\dot{\boldsymbol{S}}$ can be represented by the Cauchy stress tensor as

$$\dot{\boldsymbol{S}} = \boldsymbol{D} : \dot{\varepsilon} + \boldsymbol{\omega} \cdot \boldsymbol{\sigma} - \boldsymbol{\sigma} \cdot \boldsymbol{\omega} - \boldsymbol{L} \cdot \boldsymbol{\sigma} = \boldsymbol{A} : \boldsymbol{L}, \tag{6}$$

where $\dot{\boldsymbol{\varepsilon}}$, $\boldsymbol{\omega}$, $\boldsymbol{D}$ are strain rate tensor, spin tensor, and tangent stiffness tensor, respectively. And $\boldsymbol{A}$ is a fourth rank tensor that relates the nominal stress rate and velocity gradient tensor $\boldsymbol{L}$. To characterize the bifurcation mode, the velocity gradient tensor is allowed to be discontinuous when the velocity gradient tensor crosses the bifurcation border Γ. $\boldsymbol{L}$ can be represented by the normal vector $\boldsymbol{n}$ on the bifurcation border and the local deformation mode vector $\boldsymbol{m}$ that is normal to $\boldsymbol{n}$ as

$$\boldsymbol{L} = \boldsymbol{m} \otimes \boldsymbol{n}. \tag{7}$$

The mode vector $\boldsymbol{m}$ can be composed of two different vectors in the Γ plane; namely, $\boldsymbol{m}_{\mathrm{SH}}$ and $\boldsymbol{m}_{\mathrm{SV}}$ are the vectors in horizontal and vertical direction, respectively. These vectors are expressed with three angle parameters; ϕ, ψ and θ, as shown in Fig.1. Specific expressions for these vectors are as follows.

$$\boldsymbol{n} = (\sin\phi\cos\psi,\ \sin\phi\sin\psi,\ \cos\phi)\,, \tag{8}$$
$$\boldsymbol{m}_{\mathrm{SH}} = (-\sin\phi,\ \cos\psi,\ 0)\,, \tag{9}$$
$$\boldsymbol{m}_{\mathrm{SV}} = (\cos\phi\cos\psi,\ \cos\phi\sin\psi,\ -\sin\phi)\,, \tag{10}$$
$$\boldsymbol{m} = \boldsymbol{m}_{\mathrm{SH}}\cos\theta + \boldsymbol{m}_{\mathrm{SV}}\sin\theta. \tag{11}$$

Substituting Eq. (6) and (7) into (5), we have the following bifurcation criterion

$$I[\boldsymbol{m}, \boldsymbol{n}; \boldsymbol{\sigma}] = hH[\boldsymbol{m}, \boldsymbol{n}; \boldsymbol{\alpha}] - \sigma\Sigma[\boldsymbol{m}, \boldsymbol{n}; \boldsymbol{\alpha}], \tag{12}$$

where the first and second term of this functional are described as

$$H[\boldsymbol{m}, \boldsymbol{n}; \boldsymbol{\alpha}] = \boldsymbol{m} \cdot \boldsymbol{n} \cdot \overline{\boldsymbol{D}}(\boldsymbol{s}) \cdot \boldsymbol{n} \cdot \boldsymbol{m}, \quad \text{where} \quad \overline{\boldsymbol{D}}(\boldsymbol{s}) \equiv \boldsymbol{D}(\boldsymbol{s})/h, \tag{13}$$
$$\Sigma[\boldsymbol{m}, \boldsymbol{n}; \boldsymbol{\alpha}] = \frac{1}{2}\left[\boldsymbol{m} \cdot \boldsymbol{\alpha} \cdot \boldsymbol{m} - \boldsymbol{n} \cdot \boldsymbol{\alpha} \cdot \boldsymbol{n}\right]. \tag{14}$$

In an elasto-plastic material subjected to large strain, ignoring elastic deformation, the tangent stiffness tensor can be assumed to be proportional to the hardening rate h.

Then, the current stress is represented by

$$\boldsymbol{\sigma} = \sigma\boldsymbol{\alpha}, \quad \sigma = \sqrt{\boldsymbol{\sigma} : \boldsymbol{\sigma}}, \quad \boldsymbol{\alpha} = \boldsymbol{\sigma}/\sigma, \tag{15}$$

where σ and $\boldsymbol{\alpha}$ are the norm of the current stress tensor and normalization tensor which gives stress ratios for each stress component, respectively.

Based on these relations, finally have the following local bifurcation criterion.

$$\left(\frac{\sigma}{h}\right)_{\mathrm{cr}} = \min\left(\frac{H[\boldsymbol{m},\boldsymbol{n};\boldsymbol{\alpha}]}{\Sigma[\boldsymbol{m},\boldsymbol{n};\boldsymbol{\alpha}]}\right). \tag{16}$$

The bifurcation criterion represented by Eq.(16) indicates that the local bifurcation, which is specified by the mode vectors $\boldsymbol{m}$ and $\boldsymbol{n}$ that are based on the current stress ratio tensor $\boldsymbol{\alpha}$, should be identified by the ratio σ/h that means the ratio of the stress level to the work-hardening. Mechanically, stress σ means the intensity of fracture initiation, and the hardening coefficient h means the material's resistance against fracture. Therefore, the formability represented in the σ/h plane is free from the strain-path-dependency that is usually observed in a typical FLD (Forming Limit Diagram) represented in strain space. Thus, because exhibiting forming limits on the σ/h plane is mechanically reasonable, this new expression is called SHFLD.

The fracture limits in the SHFLD can show 3D local bifurcation limits. The probable fracture would be lie between the lower bound represented by the S-R limit and the upper bound represented by the 3D local bifurcation limit.

3 BIFURCATION ANALYSIS

By using the theoretical framework described in the previous section, numerical analyses have been conducted to investigate the characteristics of the proposed method. In this analysis, assuming plane-stress condition, an isotropic material was considered with the following constants; $F = G = H = F^* = G^* = H^* = 1$, $L = M = N = L^* = M^* = N^* = 3$, Young ' s modulus = 210 GPa, Poisson ' s ratio $\nu = 0.3$, $n = 0.2$ and $K = 5.0 \times 10^8$ in the n-power law for material hardening. The order of the yield function and the plastic potential function, m_y and m_p, were set to 1. Parameters used in this investigation were the K_C value in the Ito-Goya model, and a strain value ε_h which determines the evaluation point of work-hardening coefficient included in the parameter Λ in Equation (4). In the construction of the tangent stiffness tensor in Equation (13), the component of the original tensor $\boldsymbol{D}$ was assumed linear in terms of hardening coefficient h; however, the tensor $\boldsymbol{D}$ is not actually linear with h. In this study, instead of dealing with the tensor $\boldsymbol{D}$ as nonlinear one, we assumed this as a linear tensor as for the hardening h for computational simplicity and investigated the effect of the hardening term on the analysis.

Bifurcation analyses were conducted as follows. The minimum value of the functional represented in the right-hand-side of Equation (16) was searched by changing the variables included in the fracture mode vectors, $\boldsymbol{m}$ and $\boldsymbol{n}$. The simulated annealing algorithm was adopted in this optimization process. To calculate the yield function in the used equations, a stress ratio α was used to control the stress condition; for example, $\alpha = 0$ for uniaxial, $\alpha = 1$ for equi-biaxial stress condition. The obtained minimum values were used to show the bifurcation initiation as the possible fracture onset in the fracture limit diagram exhibited in the σ/h plane, as shown in the following figures.

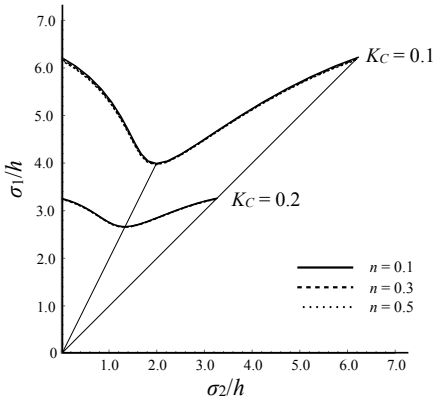

Figure 1: SHFLD for different n values.

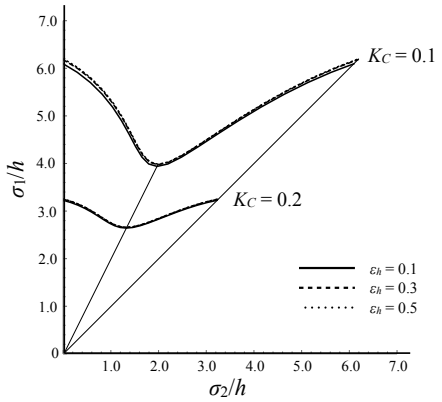

Figure 2: SHFLD for different work-hardening evaluation point ε_h.

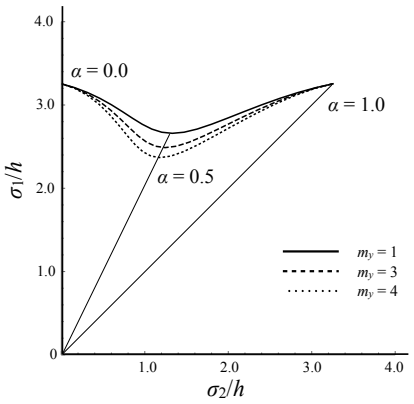

Figure 3: SHFLD for different m_y values.

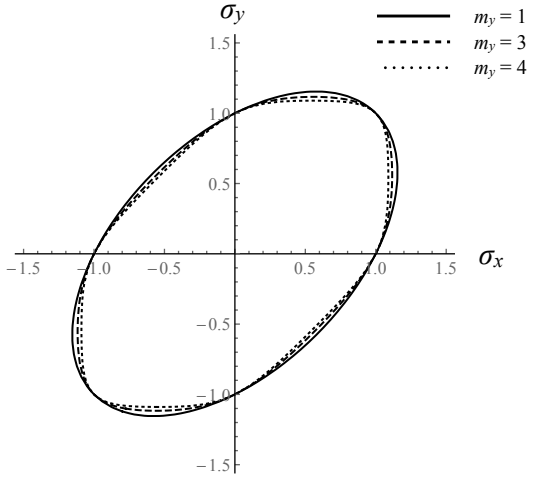

Figure 4: Yield surfaces for different m_y values.

In Figure 1, the effect of the n value on the fracture limit curve is shown. And in Figure 2, the effect of the work-hardening evaluation strain ε_h on the fracture limit curve is shown. In both figures, there are two sets of curves that are calculated with different K_C values (0.1 and 0.2). From these figures, as a apparent tendency, work-hardening properties do not affect the shape of curves and the only parameter that changes the curve is K_C value. In other words, the fracture limit curve exhibited on the SHFLD is almost independent from the material's hardening characteristics. This means the predicted limit is free from the strain path. Furthermore, this results support our assumption that the hardening property does not affect the minimum search and show that the linearization procedure explained above is valid. Then, the influence of the K_C value on fracture prediction is confirmed. Generally, as the K_C value increases, fracture limit deteriorates because of the growing stress-rate dependency. As seen in these figures, the fracture limit lines descend with the increased K_C value. This means the conducted bifurcation analyses were valid and shows physically reasonable tendency.

In Figure 3, the effect of the order of the yield surface on the limit curve is investigated. Since setting $m_y = 2$ brings same result with $m_y = 1$, the parameter m_y is varied as 1, 3 and 4. Clear descent of the curves can be observed around the plane-strain situation ($\alpha = 0.5$), on the other hand, no difference can be seen at tensile ($\alpha = 0$) and equi-biaxial ($\alpha = 1.0$) conditions. This result is quite reasonable because the stress level drops at the plane-strain condition, as shown in Figure 4, in the case of higher order yield function.

4 CONCLUSION

This paper has described the proposed fracture prediction framework that consists of the anisotropic material model based on non-associated flow rule, the Ito-Goya ' s stress-rate dependent constitutive equation, and the 3D bifurcation theory. And a new concept of fracture limit exhibition, which is called SHFLD, has been introduced. Numerical investigations have been carried out with virtual material data to show the effectiveness of the proposed method. Physically reasonable results were obtained from these analyses and the authors have confirmed that the assumptions made in this study is valid. There are many possible situations that have not tested yet; therefore, more numerical exploration and mechanical considerations would be conducted.

REFERENCES

[1] Hill, R., *J. Mech. Phys. Solids*, **7**, 209, (1959).

[2] Stören, S. and Rice, J. R., *J. Mech. Phys. Solids*, **23**, 421, (1975).

[3] Oya, T., Yanagimoto, J., Ito, K., Uemura, G. and Mori, N., *Procedia Engineering*, **81**, 1210, (2014).

[4] Oya, T., Yanagimoto, J., Ito, K., Uemura, G. and Mori, N., *MATEC Web of Conferences*, **80**, 05003, (2016).

[5] Ito, K., Sato, K., Goya, M. and Yoshida, T., *Int. J. Mech. Sci*, **42**, 2233, (2000).

XIV International Conference on Computational Plasticity. Fundamentals and Applications
COMPLAS 2017
E. Oñate, D.R.J. Owen, D. Peric and M. Chiumenti (Eds)

EFFECT OF TOOL DESIGN ON FORMABILITY IN DEEP DRAWING BY APPLYING COMPRESSIVE FORCE ON FLANGE

SHOHEI KAJIKAWA*, TAKASHI KUBOKI* AND TAKASHI IIZUKA†

* The University of Electro-Communications (UEC)
Department of Mechanical and Intelligent Systems Engineering
1-5-1 Chofu Gaoka, Chofu-shi, Tokyo, Japan
e-mail: s.kajikawa@uec.ac.jp, kuboki@mce.uec.ac.jp, www.uec.ac.jp/eng/

† Kyoto Institute of Technology (KIT)
Faculty of Mechanical Engneering
Matsugasaki Goshokaido-cho, Kyoto-shi, Kyoto, Japan
email: tiizuka@kit.ac.jp, www.kit.ac.jp/en/

Key words: Sheet metal, Deep drawing, Compression, Aluminum, FEM.

Abstract. This paper presents a new deep drawing process which applies compressive force on a flange for forming a deep cup effectively. This method uses a punch with a convex and a die, and optimum tool design was investigated using the finite element method (FEM) in order to prevent the formation of defects. First, the effect of the punch configuration was investigated. As a result, a cup with a uniform side wall thickness was obtained under the condition that the punch convex length was greater than the blank thickness and the punch top corner radius was appropriate. It was possible to obtain the deep cups by decreasing the clearance between the punch convex and the die. However, dimensional accuracy decreased with the decrease in the clearance. Based on these results, two-steps process using a backward punch was proposed, and deep cups having high dimensional accuracy was formed successfully by this method.

1 INTRODUCTION

Various products are manufactured from sheet metals in the industrial fields, such as for automotive components, household electronics, medical instruments and so on. Deep drawing is one of the sheet metal forming methods, and cup shaped products are obtained by this method [1]. Cup-shaped products are used for beverage cans, automobile body panels, motor or battery housings and so on. Although deep drawing is a very popular method, it is difficult to form a deep cup with a wide flange. In deep drawing, the material is drawn from a blank holder into a die by a punch press. This method breaks material easily because the material is stretched by tensional force. Forming a cup becomes difficult when the flange portion is expanded because the tensional force increases with an increase in frictional force on the flange. Therefore, deep cups are generally manufactured by multi stage process [2]. In addition, the deep drawn cup is welded to a holed flange when the flange portion is needed.

Reduction of the tensional force is important for improvement of the forming limit in deep drawing. For example, the tensional force can be reduced by reducing the frictional force on

the flange portion. Lubrication is important for reducing the frictional force. Horikoshi et al. developed a method using a high-pressure water jet as lubricant [3]. Hatanaka et al. increased the forming limit by reducing the frictional force using a blank having a shape similar to a petal [4]. Other alternatives for the reduction of the tensional force would be methods which apply compressive force on the flange portion. In Maslennikov's method, a deep cup was formed by repetitively compressing the flange using a rubber ring without the punch [5]. Hassan et al. performed a deep drawing with incremental flange compression using a tapered blank holder divided into four segments [6]. However, much time is wasted because the deep cup is formed by iterative compression. In a previous study, the authors developed a new deep drawing method applying compressive force on the flange [7]. In this method, a very deep cup was formed using simple tools in only one step. However, dimensional accuracy of the formed cup was low.

This study investigated the effects of forming parameters, such as a punch configuration and clearance between the punch and die, by the finite element method (FEM) in order to optimize the tool design for improvement of the dimensional accuracy of the formed cup. First, the optimum punch configuration was investigated for suppression of forming defects. Next, the possibility of forming the deep cup was investigated by decreasing the clearance, and dimensional accuracy was evaluated. Based on these results, a two-step process was proposed for suppression of defects and improvement of the dimensional accuracy.

2 DEEP DRAWING BY APPLYING COMPRESSIVE FORCE

Figure 1 shows a schematic illustration of deep drawing by applying compressive force on the flange. Main tools are die and punch with convex, as shown in Fig. 1 (a). The blank is initially stretched into the die by the punch convex, as shown in Fig. 1 (b). After that, the flange portion of the blank starts to be compressed between the punch and the die, then the material in the flange portion is drawn into the die, as shown in Fig. 1 (c). Height of the cup could be controlled by changing the compression amount of the flange. In this processing method, products were formed only by compressive force. Therefore, it is considered that the forming limit is high compared to the general deep drawing method.

In this method, the punch shape is important. For example, when the punch convex length L_p was too long, the blank ruptured during the initial stretching. On the other hand, the material flow could not be controlled when L_p was too short. The clearance c determines the side wall

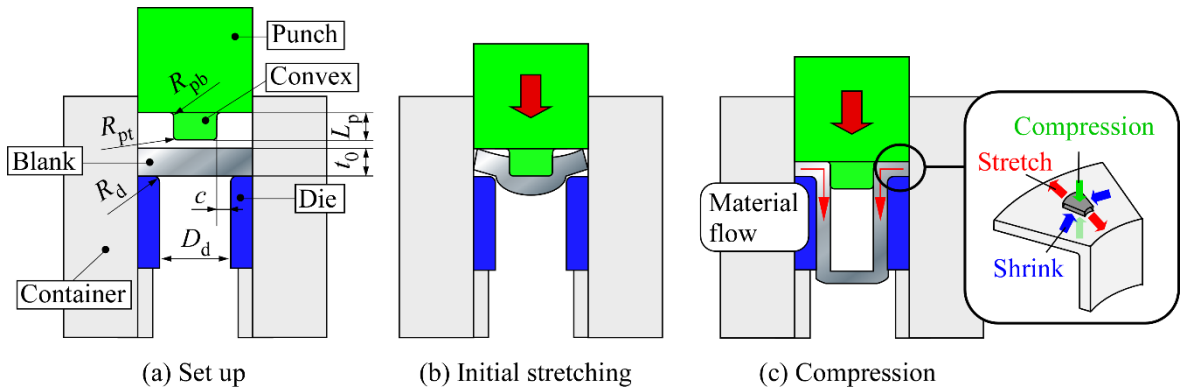

Figure 1: Schematic illustration of deep drawing applying compressive force on flange

thickness of the product. A very deep cup with thin side walls could be produced when c is set at a small value.

3 ANALYSIS

An elastic-plastic analysis was carried out by using commercial code ELFEN for FEM (Rock field Software Limited, Swansea). Figure 2 shows the schematic illustration of the model, and Table 1 shows the analysis conditions. The model is two dimensional with axisymmetry. The von Mises yield criterion was adopted, and the normality principle was applied to the flow rule. The constraints were determined by the penalty function method, and an explicit scheme was adopted. Three-node triangular elements with three integration points and adaptive meshing scheme were adopted. During the analysis, we changed punch shape, such as convex length L_p and top corner radius R_{pt}, and clearance c between the punch convex and die. c was aligned by changing the die diameter D_d while the punch convex diameter D_{pc} remained constant. The thicknesses of the side wall t_s and the flange t_f, and height h were measured for evaluating the dimensional accuracy of the formed cup as shown in Fig. 3. Aspect ratio α and compression ratio of the flange thickness β_f and was defined by the following expression.

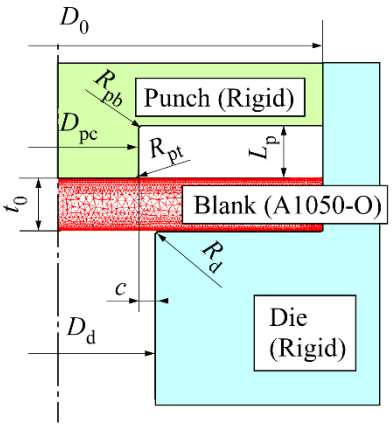

Figure 2: Schematic illustration of analytical model

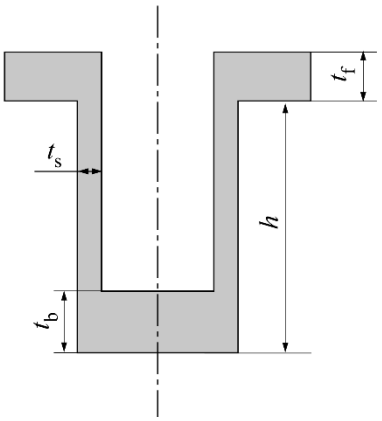

Figure 3: Evaluation of the formd cup

Table 1: Analysis conditions

Material	Blank material	Aluminum (A1050-O)
	Blank diameter D_0 [mm]	30
	Blank thickness t_0 [mm]	3.0
Punch	Diameter D_p [mm]	30
	Convex diameter D_{pc} [mm]	9.0
	Convex length L_p [mm]	1.0~5.0
	Base corner radius R_{pb} [mm]	0.2
	Top corner radius R_{pt} [mm]	0.2~1.0
Die	Diameter D_d [mm]	10~15
	Corner radius R_d [mm]	0.2
	Clearance c [mm]	0.5~3.0
Friction coefficient		0.1

$$\alpha = \frac{h}{D_d} \tag{1}$$

$$\beta_f = \frac{t_0 - t_f}{t_0} \tag{2}$$

4 RESULTS AND DISCUSSION

4.1 Effect of punch convex length

In this experimental series, the effect of the punch convex length L_p was investigated in order to reveal the appropriate punch shape for forming the product without defects. The clearance c was set at 2.0 mm, and the punch top corner radius R_{pt} was set at 0.2 mm. Figure 4 shows the typical cups formed in this investigation. Side wall curved, and thickness t_s was uneven and thicker than the clearance c when L_p was shorter than the blank thickness t_0, as shown in Fig. 4 (a). When L_p was equal to t_0, t_s was uniform and equal to c as shown in Fig. 4 (b). However, a dent was seen at the corner of the bottom due to local thinning during the initial stretching. The thickness at the dent decreased with an increase in L_p, and the blank ruptured when L_p was 5 mm as shown in Fig. 4 (c).

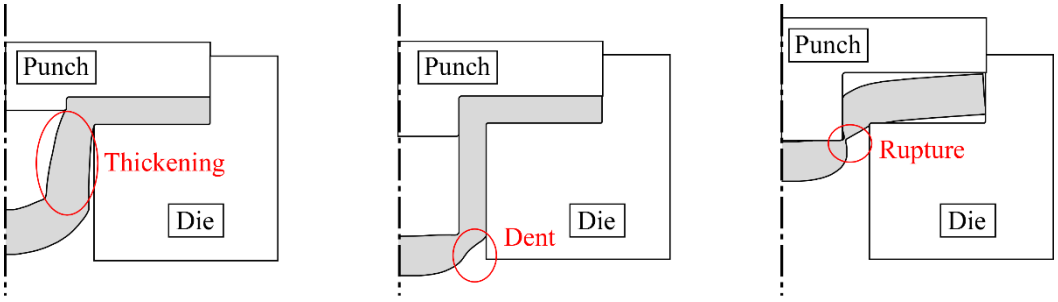

(a) L_p=1.0 mm (b) L_p=3.0 mm (c) L_p=5.0 mm

Figure 4: Typical configuration of formed cup (c=2.0 mm, R_{pt}=0.2 mm)

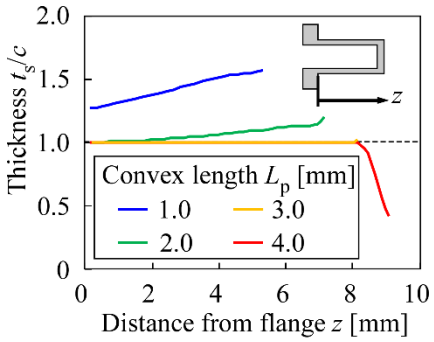

Figure 5: Side wall thickness distribution (c=2.0 mm, R_{pt}=0.2 mm, β_f=0.33)

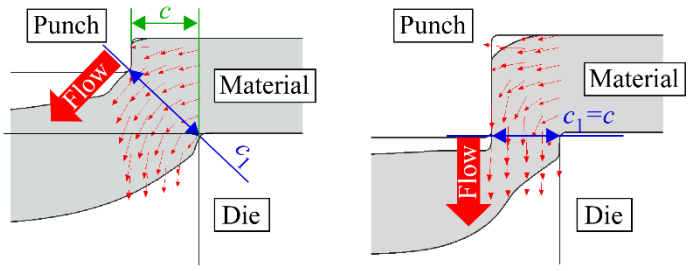

(a) L_p=1.0 mm (b) L_p=3.0 mm

Figure 6: Material flow during flange compression (c=2.0 mm, R_{pt}=0.2 mm)

Figure 5 shows the distribution of the side wall thickness t_s/c when the flange compression ratio β_f was 0.33. t_s/c increased toward the bottom of the cup when L_p was shorter than t_0. The material flowed out from the clearance c_1 between the punch convex corner and the die corner during the compression of the flange as shown in Fig. 6, and the material flow direction and t_s are determined by c_1. When L_p is shorter than t_0, c_1 is larger than c when the flange compression starts as shown in Fig. 6 (a), and c_1 decreases to c while the punch convex approaches the die. When L_p is larger than t_0, a cup with uniform distribution of t_s was produced because c_1 is equal to c during the flange compression, as shown in Fig. 6 (b). However, t_s/c drastically decreases due to the local thinning at the corner of the cup when L_p is long compared to t_0 as shown in Fig. 5. Thus, L_p should be t_0 approximately for forming a cup with good dimensional accuracy.

4.2 Effect of punch top corner radius

Suppression of the dent was attempted by increasing the punch top corner radius R_{pt}. The clearance c was set at 2.0 mm, and the punch convex length L_p was set at 3.0 mm. Figure 7 shows the cup bottom shape when R_{pt} was changed. The dent was suppressed under the condition that R_{pt} was over 0.6 mm by preventing the localized deformation at the portion near the corner of the punch top. However, the side wall thickness t_s/c was large near the bottom in the case of R_{pt}=1.0 mm as shown in Fig. 8. When the flange compression starts, the clearance c_1 between the punch convex corner and the die corner increases with an increase in R_{pt} as shown in Fig. 9. Therefore, the side wall thickened and curved just like the case that the punch convex length L_p was short. From this investigation, the appropriate R_{pt} is 0.6 mm for suppression of the dent.

4.3 Production of deep cup by changing clearance

Production of the deep cup was conducted by decreasing the clearance c. The punch convex length L_p and corner radius R_{pt} were set at 3.0 mm and 0.6 mm, respectively based on the above results. Maximum flange compression ratio β_f was set at 0.83 which reduces the flange thickness to 0.5 mm. Figure 10 shows the maximum aspect ratio α of the formed cup without

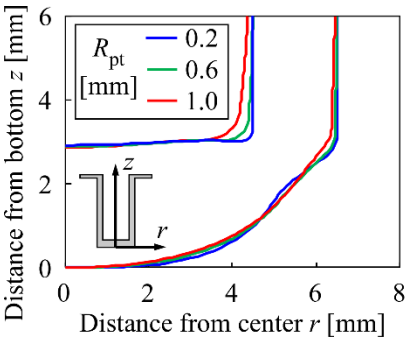

Figure 7: Effect of punch top corner radius on bottom shape of cup (c=2.0 mm, L_p=3.0 mm)

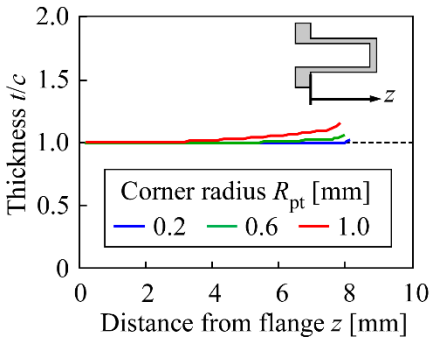

Figure 8: Effect of punch top corner radius R_{pt} on side wall thickness distribution (c=2.0 mm, L_p=3.0 mm, β_f=0.33)

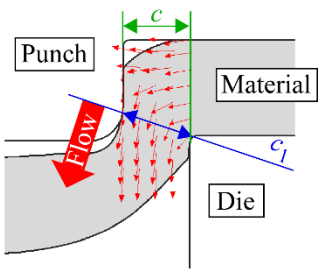

Figure 9: Material flow during flange compression (c=2.0 mm, L_p=3.0 mm, R_{pt}=1.0 mm)

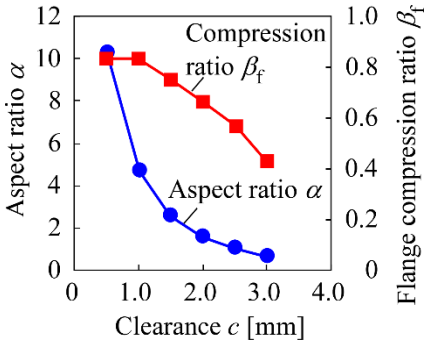

Figure 10: Aspect ratio and flange thickness variations with change in clearance (L_p=3.0 mm, R_{pt}=0.6 mm)

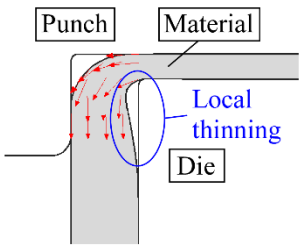

Figure 11: Thinning of side wall near flange (c=2.0 mm, L_p=3.0 mm, R_{pt}=0.6 mm)

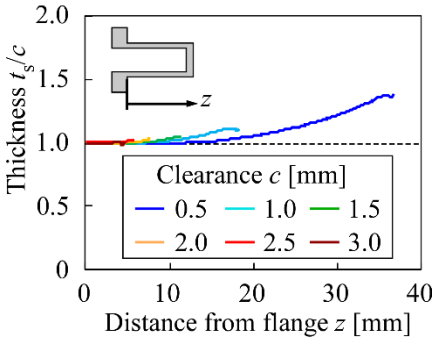

Figure 12: Effect of clearance c on side wall thickness distribution (L_p=3.0 mm, R_{pt}=0.6 mm, β_f=0.33)

defects. α increases by thinning of the side wall and large compression of the flange. When c was 0.5 and 1.0 mm, it was possible to compress the flange at the maximum compression ratio β_f=0.83, and maximum α is 10.2 under the condition of c=0.5 mm in this investigation.

When c was over 1.5 mm, local thinning occurred on the side wall near the flange when the flange thickness t_f was small compared to c as shown in Fig. 11. This defect occurs because the thickness of the material, which flows from the flange portion, becomes gradually thinner than c with the flange compression. Therefore, β_f should be controlled under a certain value with c in order to suppress this local thinning.

Figure 12 shows the side wall thickness distribution with the change of c. Thickness t_s/c increased with a decrease in c, because the clearance c_1 between the punch top corner and the die corner become large compared to c when c is small as shown in Fig. 9. Thus, it is possible to obtain the deep cup by decreasing c, although the dimensional accuracy is low.

4.4 Two-step process for improving the dimension accuracy

A two-step process was proposed in order to improve the dimensional accuracy of the formed cup as shown in Fig. 13. In first step, a fixed backward punch is used. The blank was stretched into the die with compression between the punch convex and the backward punch, as shown in Fig. 13 (a); this way, the local thinning at the punch top corner is suppressed by compression. After the first step, the backward punch was removed, and the flange was compressed as shown in Fig. 13 (b). Figure 14 shows the tool's position after the first step. Compression ratio of the thickness of the cup bottom portion β_b was controlled by changing the position of the backward punch, and β_b is calculated by the following expression.

$$\beta_b = \frac{t_0 - t_b}{t_0} \tag{3}$$

Here, t_0 is the initial blank thickness, and t_b is the bottom thickness of the cup as shown in Fig. 3. The punch convex length L_p was set at 3.8 mm as total length of the blank thickness t_0= 3.0 mm, the die corner radius R_d= 0.2 mm and the punch top corner radius R_{pt}= 0.6 mm for preventing the change of the clearance c_1 in Fig. 9 during the flange compression.

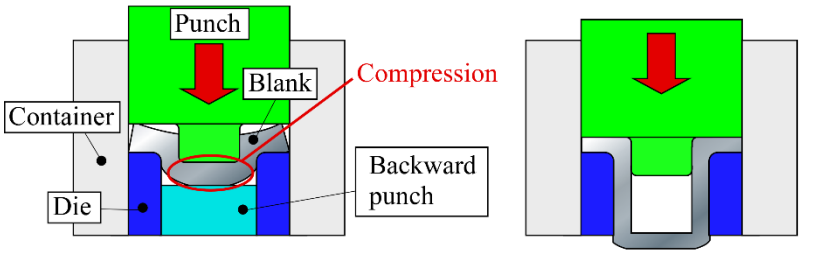

Figure13: Schematic illustration of the two-step process

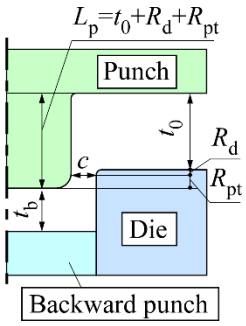

Figure 14: Tooling for the two-step process

At first, appropriate β_b was investigated. Figure 15 shows the appearance of the cup after the first step using the backward punch under the condition that the clearance c was 1.0 mm. The material was stretched without the local thinning when the compression amount β_b was appropriate as shown in Fig. 15 (b). The local thinning appeared when β_b was too small as shown in Fig. 15 (a). Folding appeared due to the material flow from the cup bottom when β_b was too large as shown in Fig. 15 (c). Table 2 shows the formability in the first step using backward punch. Appropriate range of the bottom compression ratio is narrow when the clearance c was small, because the local thinning is easy to occur during the first step.

Based on the above result, two-step process was conducted. Figure 16 shows the appearance of the formed cup by the two-step process using the backward punch, and Fig. 17 shows the side wall distribution compared with the one-step process without the backward punch. Appearance of the formed cup was ideal, and the side wall thickness was equal to c and completely uniform.

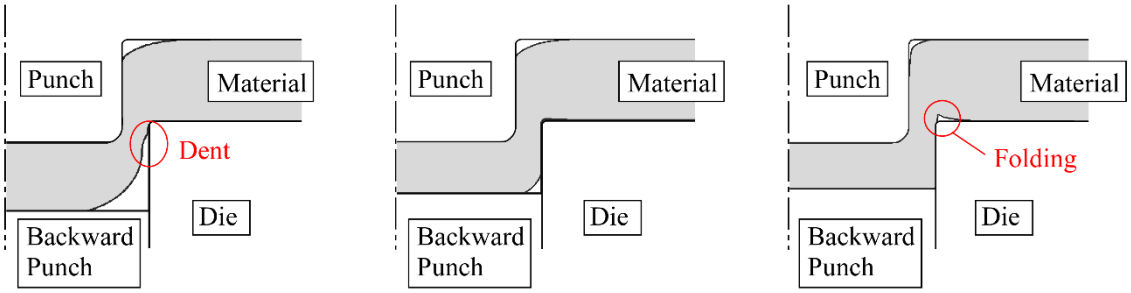

Figure 15: Effect of bottom compression ratio β_b on the cup shape after first step (c=1.0 mm)

Table 2: Formability in first step using backward punch

Clearance c [mm]	Bottom compression ratio β_b						
	0.17	0.23	0.25	0.27	0.30	0.37	0.43
0.5		△	○	×			
1.0	△	○	○	○	○	○	×
○:Success △:Dent ×:Folding							

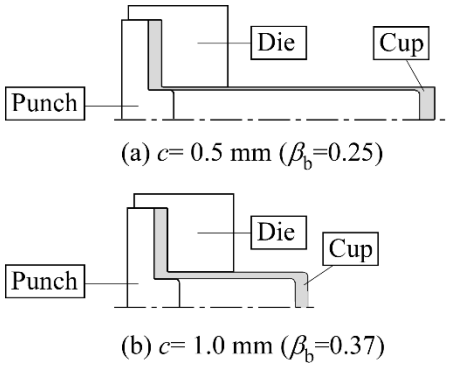

Figure 16: Appearance of the cup formed by two-step process (c=1.0 mm, L_p=3.8 mm, R_{pt}=0.6 mm, β_f=0.33)

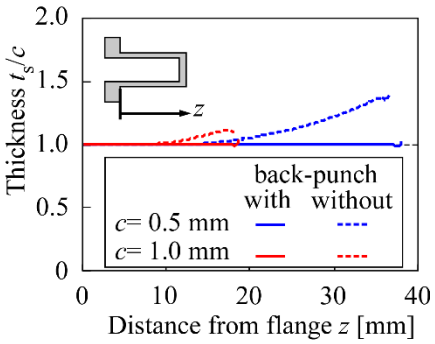

Figure 17: Side wall thickness distribution of the cup formed by one-step and two-step processes with backward punch (c=1.0 mm, L_p=3.8 mm, R_{pt}=0.6 mm, β_f=0.33)

5 CONCLUSIONS

- This paper presents a new deep drawing method that applies compressive force on the flange, and an investigation of the tool design was conducted using the FEM for improving the dimensional accuracy of the formed cups.
- The proposed method is composed of initial stretching and flange compression. The main tools are a punch with convex and a die.
- The punch convex length should be over the blank thickness for a cup with uniform side wall thickness.
- Local thinning is prevented by increasing the punch top corner radius, but side wall thickness becomes uneven when the punch top corner radius is too large.
- A deep cup could be obtained by decreasing the clearance between the punch convex and the die, and a maximum aspect ratio of 10.2 was obtained in this study. However, the dimensional accuracy decreases with a decrease in the clearance.
- A two-step process using a backward punch was proposed for the improvement of the dimensional accuracy when the clearance is small. A cup with uniform side wall thickness was successfully formed by the two-step process.

REFERENCES

[1] Doege, E., Hallfeld, T. Metal Working: Stretching of Sheets. *Encyclopedia of Materials: Science and Technology (Second Edition)* (2001): 5518-5521.

[2] Harada, Y., Maeda, Y., Ueyama, M. and Fukuda, I. Improvement of formability for multistage deep drawing of Ti-15V-3Cr-3Sn-3Al alloy sheet. *Procedia Engineering* (2014) **81**:819-824.

[3] Horikoshi, Y., Kuboki, T., Murata, M., Matsui, K., Tsubokura, M. Die design for deep drawing with high-pressured water jet utilizing computer fluid dynamics based on Reynolds' equation. *Journal of Materials Processing Technology* (2015) **218**: 99-106.

[4] Hatanaka, N., Waki, S., Iizuka, T. Deep drawing of square cup with airtight using developed blank of 1100 aluminum sheet. *Journal of The Japan Institute of Light Metals* (2014) **64**-8: 361-367. (in Japanese)

[5] Maslennikov, N.A. Russian developed punchless drawing. *Metalwork Production* (1957) **16**: 1417-1420.
[6] Hassan, M.A., Suenaga, N., Takakura, N., Yamaguchi, K. A novel process on friction aided deep drawing using tapered blank holder divided into four segments. *Journal of Materials Processing Technology* (2005) **159**: 418-425.
[7] Iizuka, T., Hatanaka, N., Takakura, N. Deep Drawing of High Cup of Magnesium Alloy AZ31 by Compressive Force, *Steel Research International* (2010) **81**-9: 1247-1250.

XIV International Conference on Computational Plasticity. Fundamentals and Applications
COMPLAS 2017
E. Oñate, D.R.J. Owen, D. Peric and M. Chiumenti (Eds)

EXAMINATION OF WORKING CONDITION FOR REDUCING THICKNESS VARIATION IN TUBE DRAWING WITH PLUG

TAKASHI KUBOKI*, SHUNSUKE TASAKA* AND SHOHEI KAJIKAWA*

* Department of Mechanical Engineering & Intelligent Systems
The University of Electro-Communications
1-5-1 Chofu Gaoka, Chofu-shi, Tokyo, 182-8585, Japan
e-mail: kuboki@mce.uec.ac.jp

Key words: Tube Drawing, Thickness variation, Plug, Die angle.

Abstract. The present research carried out a series of analyses using the finite element method (FEM). The analyses investigated the effect of working condition on thickness variation after drawing a tube with initial thickness distribution. As a result, it was notably revealed that application of dies with small half angle below 5 degrees was prominently effective for levelling the thickness variation. This effect was strengthen by employing tubes with thicker walls and larger diameters. Moreover, the mechanism of levelling the thickness variation was also examined. The small die angle affects the contact length at die approach, and the contact length at thinnest side becomes longer than that at the thickest side. The difference of the contact lengths equalizes the thicknesses of the thinnest and thickest sides. The analyses also predicted the thickness variation should almost be zero under an optimum condition.

1 INTRODUCTION

Drawing is a common and general process, which is placed in one of the last stages for manufacturing elongated products of bars, wires and tubes. Drawing process determines many characteristics of the products, including mechanical properties, hardness, residual stresses, surface integrities, straightness and so on. Although straightener, which is placed after drawing, improves straightness and alleviates residual stresses, these properties should previously be improved in the drawing process for stable manufacturing.

There are many research works for drawing, assuming that drawing should be conducted in an axisymmetric manner. Some drawing methods were proposed for levelling residual stresses in bar drawing. Application of light reduction in area at the final drawing stage is very effective for levelling residual stresses [1]. This light reduction drawing is effective for copper, aluminum, high carbon steel as well as medium carbon steel [2]. Shape optimization of die was conducted and it was revealed that double-tapered die with light angle at the second taper was also effective for levelling residual stresses [3]. It was also pointed out that high reduction in thickness is effective for levelling residual stresses in tube drawing using plug [4].

There are some research works on asymmetric phenomena in bar or tube drawing. One of the concerns is straightness. It was found that there are two ranges of reduction in area which effectively improve straightness in bar drawing [5]. Another concern is thickness variation in the case of tube drawing. The thickness variation derives from the tube fabrication processes.

Tubes and pipes are fabricated by either (1) electric resistance welding process (ERW process) or (2) seamless tube fabrication. The ERW process used a sheet metal which is rolled in advance, and the rolling process inevitably yields thickness variation. The seamless tube fabrication process is composed of piercing, mandrel-mill rolling and reducing-mill rolling, and these processes also yield thickness variation [6]. It has been desired that the drawing process should eliminate or reduce the thickness variation, which is yield by the tube fabrication processes. Foadian et al. proposed a unique drawing method using tilting die according to the thickness variation [7]. However, the amount and the direction of thickness variation in hoop direction should be known in advance for the arrangement of the die orientation.

The present research conducts a series of analyses using the finite element method (FEM) for the investigation of the effect of working condition on thickness variation after drawing tubes with a plug. In particular, this research focuses upon the effect of die angle, and tries to find the optimum condition. Furthermore, the mechanism of thickness change during drawing and the effects of the thickness reduction are also examined.

2 ANALITICAL CONDITION FOR TUBE DRAWING WITH PLUG

2.1 Drawing condition and FEM model

A schematic illustration of drawing a tube with a plug is shown in Fig. 1 and the drawing condition is shown in Table 1. The die has an approach of straight tapered shape. The thickness variation is assumed to exist in the initial tube. The plug is a straight cylinder, which is supported by an elongated rod. The plug should freely and flexibly move in the orthogonal direction to the rod axial direction due to elastic deformation as it is actually longer than or equal to 10,000 mm in the industry.

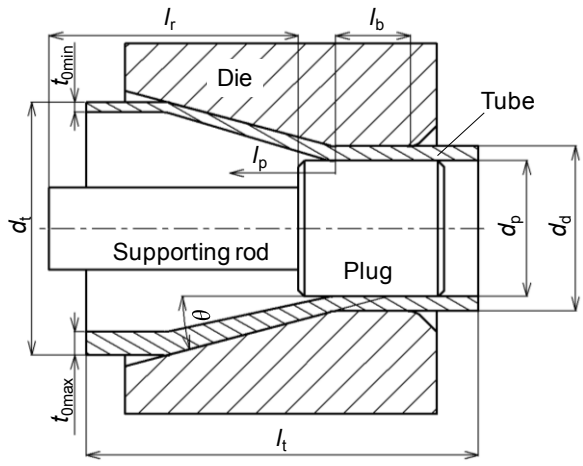

Figure 1: Drawing a tube with a plug

Table 1: Drawing condition

Die	Type		Rigid
	Die hole diameter d_d /mm		30
	Die half angle θ /°		4.5 - 10
	Bearing length l_b /mm		4
Plug	Type		Elastic
	Plug diameter d_p /mm		24.4
	Average clearance bw die & plug C_L $C_L = (d_d - d_p)/2$ /mm		2.8
Tube	Type		Plastic
	Material of tube		A1070
	Tube outer diameter d_t /mm		31.5
	Tube thickness on average t_{0ave} /mm Thickness reduction R_{dt} (%) $R_{dt} = (t_{0ave} - C_L)/ C_L$		2.9 - 3.2 3.5 -14.3
	Length of tube l_t /mm		170
	Initial thickness variation $\Delta t_0 = t_{0max} - t_{0min}$ /mm		0.2
	Division in FEM	Axial	0.5 mm/div
		Radial	7div. (progressive)
		Hoop	15 deg./div
Friction coefficient			0.07

The FEM model is shown in Fig. 2. A half model is employed due to the symmetricity on the y-z plane. All nodes on the y-z plane are constrained in the x direction. The upper side of the tube cross section is thin and the lower side is thick, and the shape of the cross section is constant in the tube axial direction for the straight part of the tube which is denoted by [A] in Fig. 2(a). The supporting rod is much shorter than the actual one in the manufacturing line in the industry. The end face of the rod is constrained in the z direction, but free in y direction as shown in Fig. 2(a). Therefore, the plug freely moves in the y direction just as in the manufacturing line. The nodes of the tube are located between the nodes on the tools in the hoop direction so that the nodes should freely move in the hoop direction as shown in Fig. 2(c).

The finite element analyses were conducted using the commercial code ELFEN, which was developed by Rockfield Software Limited, Swansea. An elastic-plastic analysis was carried out using an implicit scheme. A von Mises' yield criterion was adopted, and the normality principle was applied to the flow rule. Constraints were dealt with by the penalty function method. A hexahedral element was used because of the simplicity of the material deformation. The F-bar method was applied to the element for overcoming volumetric locking with simple 8-node hexahedral elements [8].

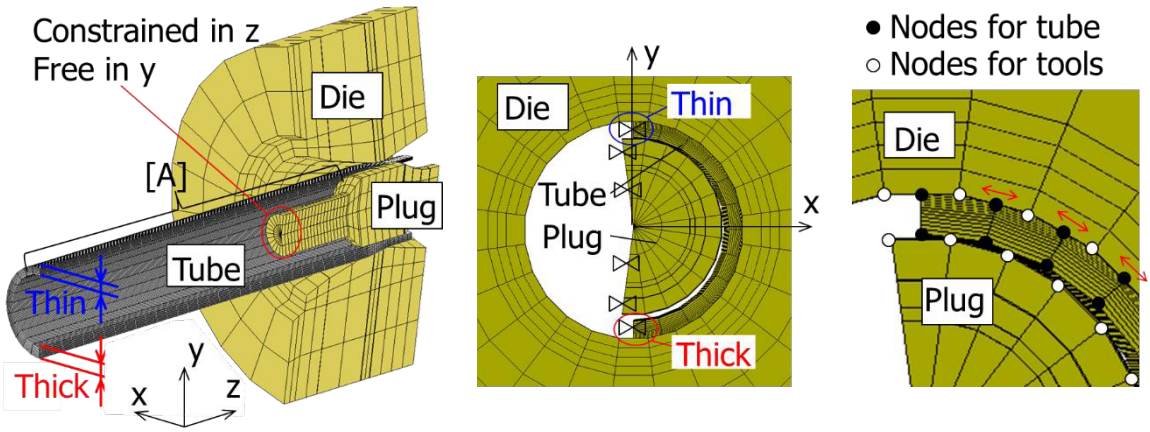

(a) Bird-eye view (b) Rear view (c) Magnified rear view

Figure 2: FEM model for drawing

2.2 Evaluation method of dawn tube

The thickness variation ratio E_c was defined by the following equation, and the comparison was made between the values before and after drawing:

$$E_c = \frac{\Delta t}{t_{ave}} = \frac{t_{max} - t_{min}}{(t_{max} + t_{min})/2} \tag{1}$$

where t_{max} is the maximum tube thickness and t_{min} is the thinnest one.

The change of thickness must be affected by stresses during drawing. Average stresses in the thickness direction was used for examination of the mechanism as the thickness change should appear as a result of the total deformation in the thickness direction. The average stresses σ are calculated by the following equation:

$$\sigma = \sum_{i=1}^{N_{dr}} \left(\frac{(y_{i+1} - y_i) \times (\sigma_{i+1} + \sigma_i)/2}{(y_{i+1} - y_i)} \right) \tag{2}$$

where i is the node number, N_{dr} is the number of elements y direction, y_i is the node position in y direction and σ_i is the stress at node i. The nodes for calculation of average stress is shown in Fig. 3.

The thickness variation ratio and the average stress are calculated during and after drawing. Figure 4 shows the definition of the position l_a after drawing and l_p during drawing where the thickness variation or the average stress were evaluated. The vertical position of plug, which would dominates the thickness variation was evaluated according to the drawing stroke l_d.

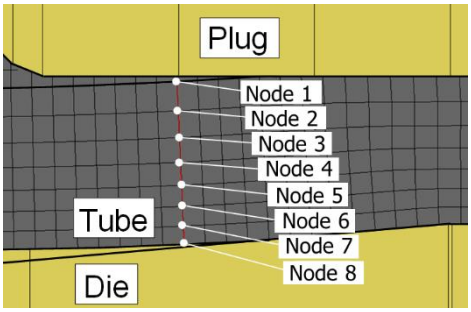

Figure 3: Nodes for calculation of average stress in the thickness direction

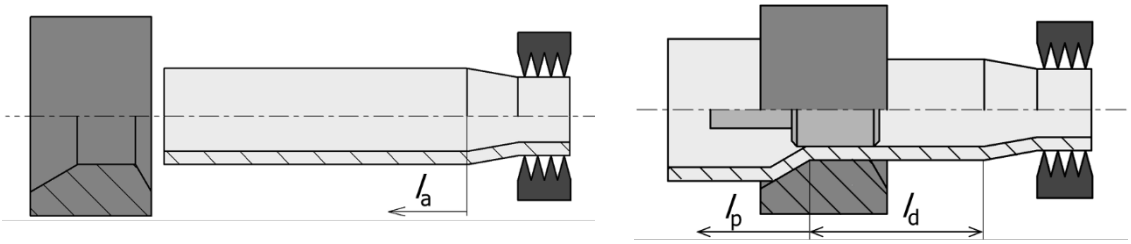

(a) After drawing (b) During drawing

Figure 4: Definition of positions for evaluating thickness variation and average stress in thickness

3 RESULTS OF THE FINITE ELEMENT ANALYSIS

3.1 Effect of die angle and thickness reduction on thickness variation

Figure 5 shows the effect of die half angle on thickness variation after drawing. The thickness variation E_c changes from the head to the tail of the tube. The change of the thickness variation should be attributed to gradual position change of plug in vertical direction (y) during drawing. If a longer tube is used, the position of plug will become stable at the tail side, resulting in a stable thickness variation. The effect of die angle is prominent at the tail side, and the thickness variation E_c was effectively levelled when the die half angle θ was lower than or equal to 5

degrees.

Figure 6 shows the effect of initial average thickness on the thickness variation E_c after drawing for the low die half angle of 5 degrees. The effect of initial average thickness t_{0ave} is prominent at the tail side, and the thickness variation E_c effectively decreased with the increase of initial average thickness t_{0ave}. When the initial average thickness is larger than or equal to 3.1mm, in other words, when average thickness reduction R_{dt}, which was defined inside Table 1, is larger or equal to about 10 %, the thickness variation was effectively levelled.

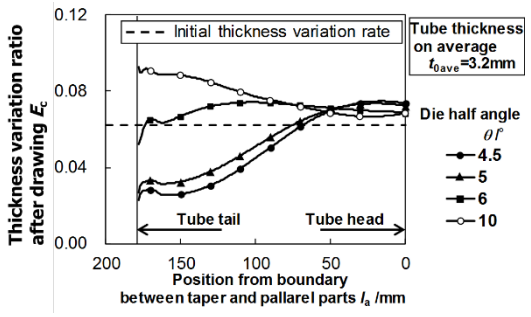

Figure 5: Effect of die angle on thickness variation after drawing

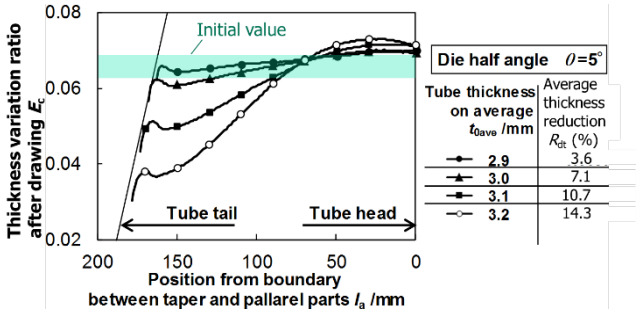

Figure 6: Effect of average thickness on thickness variation after drawing

3.2 Mechanism on decrease of thickness variation by applying the low die angle

Figures 7 shows the mechanism of levelling thickness variation when the die half angle was low and the thickness reduction was large. There are three regions, (a), (b) and (c), which feature the change of thickness variation as follows:

- Region (a): Gradual decrease of thickness variation.

The inner surface does not contact with the plug surface. Compressive force must appear in the hoop direction of tube, and the hoop compressive stress should be higher at the thin side than that at the thick side. As a result, the thickness should increase more at the thin side than at the thick side, resulting in gradual decrease of thickness variation.

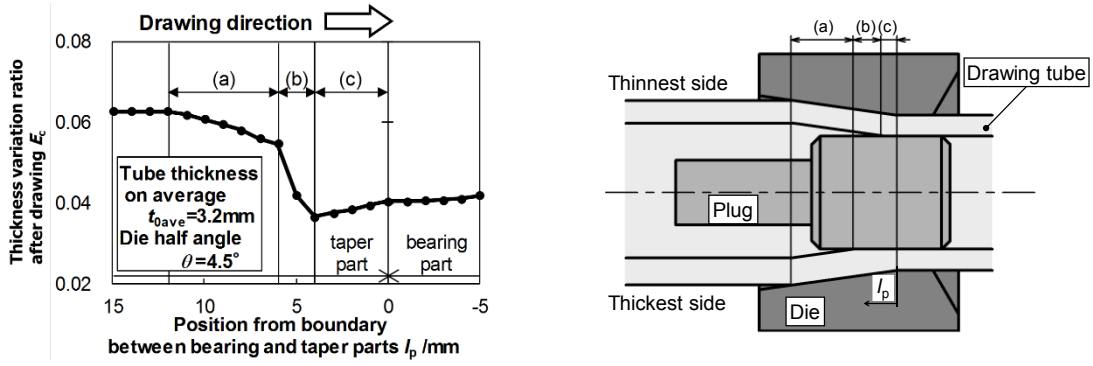

Figure 7: Thickness variation change during drawing
(die half angle θ=4.5°, initial average thickness t_{0ave}=3.2mm)

- Region (b): Rapid decrease of thickness variation.

The thicker side of the inner surface contacts with the plug surface, but the thinner side does not. The thickness on the thicker side decreases as the tube wall is constrained between the plug and the die. On the other side, the thickness of the thinner side does not change much. As a result, the thickness variation rapidly decreases.

- Region (c): Slight increase of variation ratio.

The thicker and thin sides of the inner surface contacts with the plug surface. The tube wall at both of the thicker and thinner sides is constrained by the die and the plug. Therefore, the absolute value of the thickness variation, t_{max}-t_{min} does not change, while the thickness itself decreases at this region with decrease of the die diameter along z axis. As a result, the thickness variation ratio E_c slightly increases.

Figure 8(a) shows deviatoric hoop stress which dominates plastic deformations in hoop direction. Deviatoric hoop stresses of the thickest and thinnest sides are compressive at the region (a), and that means the tube shrinks in the hoop direction. However, that of the thickest side changes to almost zero at the region (b), where the thickest side is constrained by the die and the plug. That means the thinnest side continues to shrink while the thickest stops to deform in the hoop direction at the region (b).

Figure 8(b) shows deviatoric radial stress which dominates plastic deformation in thickness direction. Deviatoric radial stress of the thinnest side is larger than that of the thickest side at the region (a) with the drop of the value at the thickest side at [A]. That means thickness of the thinnest side increases more than that of the thickest side, resulting in the decrease of the thickness variation. The negative value of deviatoric radial stress of the thinnest side is smaller than that of the thickest side at the region (b), and that means thickness of the thickest side decreases more than that of the thinnest side, resulting in the decrease of the thickness variation. Therefore, both of the regions (a) and (b) have the effect of levelling thickness variation.

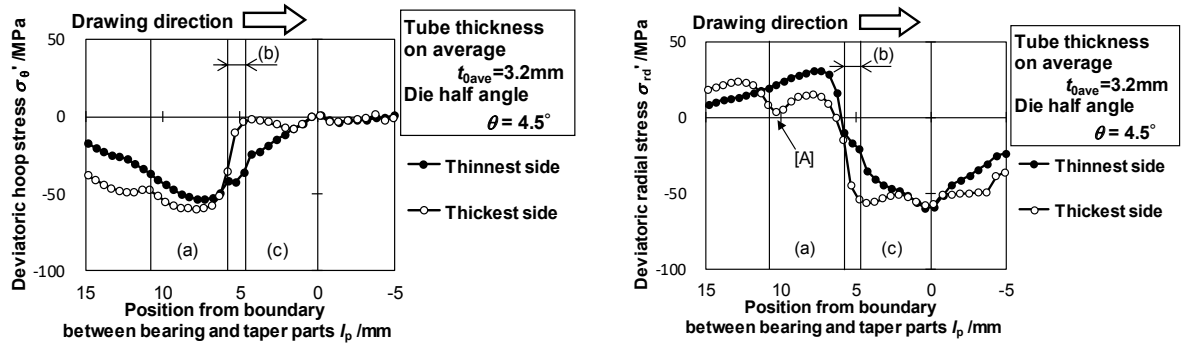

(a) In hoop direction (b) In radial direction

Figure 8: Distribution of deviatoric stresses
(die half angle θ=4.5°, initial average thickness t_{0ave}=3.2mm)

3.3 Effect of die angle on the mechanism of levelling thickness variation

Figure 9 shows the effect of the die half angle on the distribution of thickness variation during drawing. The final thickness variation at the exit of the region (c) decreased with the decrease of the die half angle θ. The effect of the die angle is attributed to the length of the regions (a) and (b), which have the effect of levelling thickness variation as explained in Figs. 7 and 8. The dies with low die half angles of 4.5 and 5 degrees have much longer regions of (a) and (b). Therefore, when the die half angle is less than or equal to 5 degrees, the thickness variation is effectively suppressed.

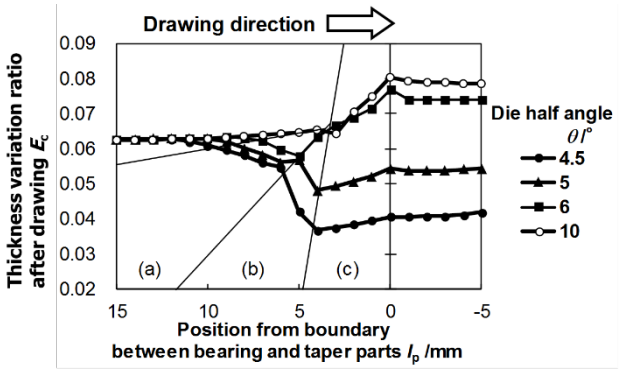

Figure 9: Effect of die angle on distribution of thickness variation during drawing (initial average thickness t_{0ave}=3.2mm)

3.4 Effect of initial average thickness on the mechanism of levelling thickness variation

Figure 10 shows the effect of the initial average thickness on the distribution of thickness variation. The final thickness variation at the exit of the region (c) decreased with the increase of the initial average thickness t_{0ave}. Even though the lengths of the regions (a) and (b) are not affected by t_{0ave}, thickness variation ratio E_c decreased for large t_{0ave}.

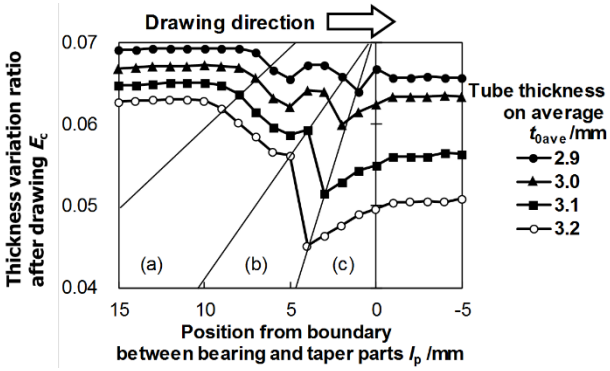

Figure 10: Effect of initial thickness on distribution of thickness variation during drawing (die half angle θ = 5 degrees, plug free in y)

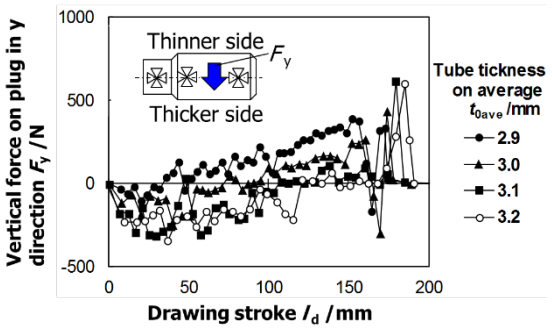

Figure 11: Effect of initial thickness on vertical force on plug (θ = 5 degrees, plug fixed in y for constant thickness variation)

Figure 11 shows the effect of the initial average thickness t_{0ave} on the vertical force F_y on plug in vertical direction (y). In this analysis, the plug was fixed in the vertical direction and the plug position in y direction δ_y was determined so that the thickness variation ratio E_c should be constant before and after drawing. The force F_y was defined as positive for the downward direction, and then the larger F_y of positive value means less thickness variation E_c should be realized when the plug is free in vertical direction (y). It is noteworthy that the vertical force F_y increased with increase of t_{0ave}, and that means larger t_{0ave} should lead to less thickness variation E_c when the plug is free in y.

4 OPTIMUM CONDITION

The previous sections revealed that the optimum conditions should be low half die angle θ less than or equal to 5 degrees and large thickness reduction R_{dt} larger than or equal to 10 %. It would be also predicted that larger initial tube diameter would be desirable because it would enlarge the region (a), which has the effect of levelling thickness variation.

FEM analyses was conducted for the verification under the condition in Table 2 for comparison between the optimum condition (B) and another condition (A). The FEM results are shown in Fig. 12 with a long and elastic plug, the end of which is constrained in 3 directions. The optimum condition certainly levelled the thickness variation to zero at the latter end of the tube.

Table 2: Optimum condition and its comparison

Drawing condition		(A) For comparison	(B) Optimum
Die	Die half angle θ /°	10	5
Tube	Tube outer diameter d_t /mm	31.5	33
	Average tube thickness t_{0ave} /mm	2.9	3.2
	Average thickness reduction R_{dt} (%)	3.6	14.3
	(Initial thickness variation rate E_0)	(0.0690)	(0.0625)

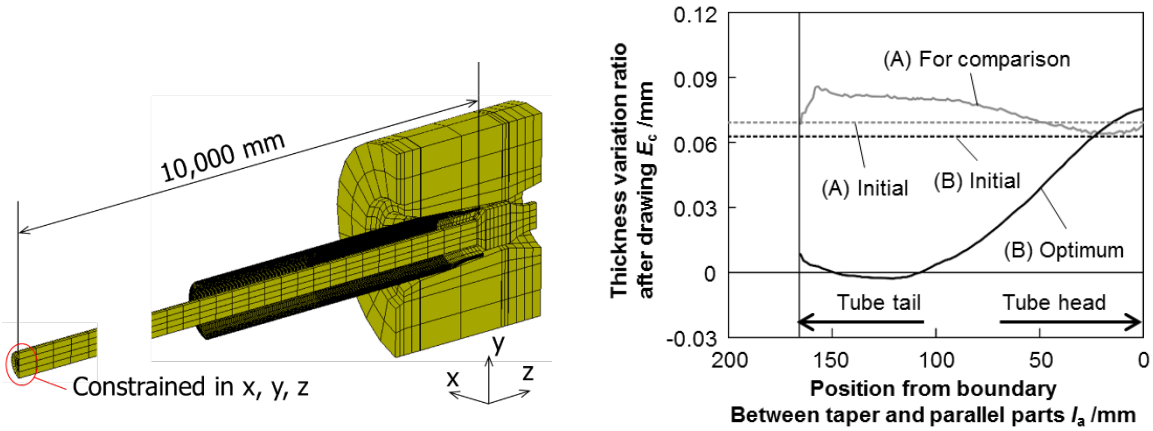

(a) Model with long and elastic plug (b) Thickness variation

Figure 12: Thickness variation for optimum condition and for a compared condition

5 CONCLUSIONS

- The present research carried out a series of analyses using the finite element method (FEM) for the investigation of the effect of working condition on thickness distribution after drawing tubes.
- It was notably revealed that application of dies with low half die angle smaller than or equal to 5 degrees was prominently effective for levelling the thickness variation.
- This effect was strengthen by employing tubes with thicker walls with thickness reduction larger than or equal to 10 %.
- It was also suggested that the effect was also strengthen by employing tube with large diameter.
- Moreover, the mechanism of levelling the thickness variation was also examined.
- The FEM also predicted the thickness variation should almost be levelled to zero under the optimum condition.

REFERENCES

[1] Kuboki, T., Akiyama, M., Neishi, Y., Kuroda, K. Effect of final drawing with light reduction on the levelling of residual stress distribution in cold bar drawing, *Proc. Instn Mech. Engrs, Part C, J. of Mech. Eng. Sci.*, (2000) **214**-12:1389-1400.

[2] Kuboki, T., Kawakami, I., Neishi, Y., Kuroda, K., Akiyama, M. A study on the influence of mechanical properties on the distribution of axial residual stress after cold drawing of metallic bars, *J. of Materials Science Research International*, (2001) **7**-1:41-46.

[3] Kuboki, T., Neishi, Y., Kuroda, K., Akiyama, M. Influence of mechanical properties of metallic material on the reducing effect of axial residual stress after cold drawing by a double-taper die, *J. Jpn. Soc. Technol. Plast.*, (2001) **42**-486:705-709.

[4] Kuboki, T., Nishida, K., Sakaki, T., Murata, M. Effect of plug on levelling of residual stress in tube drawing, *J. Mater. Process. Technol.*, (2008) **204**:162-168.

[5] Kuboki, T., Furuta, H., Akiyama, M. Suppression of bending after steel bar drawing by heavy-reduction pass, *Proc. Inst. Mech. Eng. Part B J. Eng. Manuf.*, (2004) **216**-12:1461-1470.

[6] Okui, T., Yamada, M., Yamada, T. Deformation analysis of a three-roll reducing mill, *J. Jpn. Soc. Technol. Plast.*, (1997), **38**-432:76-80,in Japanese.

[7] Foadian, F., Carrado, A., Palkowski, H. Precision tube production: influencing the eccentricity and residual stresses by tilting and shifting, *J. Mater. Process. Technol.*, (2003) **1**:17-24.

[8] de Souza Neto, E.A., Peric, D., Dutko, M., Owen, D.R.J. Design of simple low order finite elements for large strain analysis of nearly incompressible solids, *Int. J. Solids Struct.*, (1996) **33**-20-22:3277-3296.

XIV International Conference on Computational Plasticity. Fundamentals and Applications
COMPLAS 2017
E. Oñate, D.R.J. Owen, D. Peric and M. Chiumenti (Eds)

FEM Analysis on Fundamental Relationship between Hydrostatic Stress and Strain Obtained from Uniaxial Tensile Test Using Axially symmetric Tapered Specimen

Hiromu Sakamoto*, Takashi Iizuka†

* Department of Mechanical and System Engineering
Kyoto Institute of Technology
Matsugasaki Goshokaido-cho, Sakyo-ku, Kyoto 606-8585, Japan
E-mail: m7623111@edu.kit.ac.jp

† Faculty of Mechanical Engineering
Kyoto Institute of Technology
Matsugasaki Goshokaido-cho, Sakyo-ku, Kyoto 606-8585, Japan
E-mail: tiizuka@kit.ac.jp

Key words: FEM analysis, Tensile properties, Axially symmetric tapered specimen, Forming limit

Abstract. In sheet metal forming, we can recognize most deformed states by using in-plane biaxial deformation and can predict the occurrence of fracture by a forming limit diagram. However, in the case of axially symmetric tensile specimens, it is known that the magnitude of hydrostatic stress or stress triaxiality largely affects the occurrence of fracture. In this study, we investigated the history of hydrostatic stress and stress triaxiality by using an axially symmetric tapered tensile specimen.

1 INTRODUCTION

In sheet metal forming, it is very important to understand the forming limit for various in-plane strain paths [1], [2]. A method to obtain a forming limit diagram was decided in the ISO standard [3]. However, the changes in hydrostatic stress depend on the strain path. It is known that the magnitude of hydrostatic stress largely affects the occurrence of fracture. Therefore, to evaluate the forming limit for each strain path more precisely, a new evaluation method considering hydrostatic stress would be beneficial. With a new method to test the uniaxial tension state, various hydrostatic stress states could be differentiated by using axially symmetric specimens of various shapes. However, few studies have investigated new methods. Thus, in this study, we used axially symmetric tapered tensile specimens to evaluate the forming limit of the uniaxial tension state in various hydrostatic stress states.

Using finite element method (FEM) analyses, we investigated the hydrostatic stress-strain responses for elastic and plastic deformation of axially symmetric tapered tensile specimens during the uniaxial tensile test. By changing the taper angle, the possibility to control the hydrostatic stress in tensile tests was also examined.

In the elastic deformation region, it was found that the hydrostatic stress could be controlled by changing the taper angle of the axially symmetrical specimen. The hydrostatic stress

increased with increasing taper angle. In the plastic deformation region, the hydrostatic stress at the center of the specimen varied nonlinearly. The nonlinear curve of hydrostatic stress and equivalent stress became larger by increasing the taper angle. Trials of varying taper angles were conducted to correlate the equivalent strain to the hydrostatic stress, and possible methods were considered to evaluate the forming limit at various hydrostatic stress states by using axial symmetry tapered specimens.

2 THEORY

2.1 Relationship between hydrostatic stress and pre-strain

According to Ohji [4], hydrostatic stress does not affect occurrence of void; however, the stress largely affects the growth of a void. He also concluded that, as the strain grows, the void is stretched in the axial direction rather than in the radial direction. Therefore, it seems that hydrostatic stress after the occurrence of a void affects the growth of the void and the occurrence of fracture. Figure 1 shows the relationship between hydrostatic stress and pre-strain. Here, we define σ as stress and ε as strain.

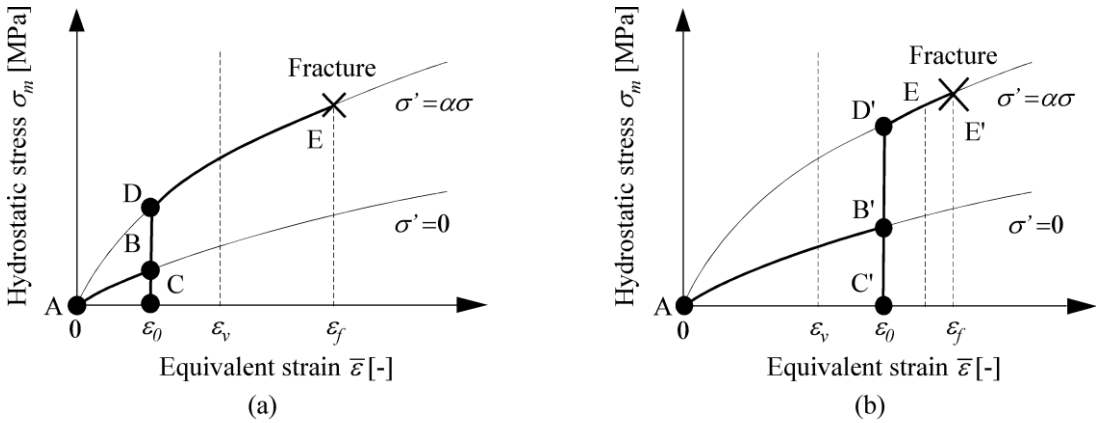

Figure 1: Relationship between hydrostatic stress and equivalent strain
(a) Pre-strain $\varepsilon_0 < \varepsilon_v$, (b) Pre-strain $\varepsilon_0 > \varepsilon_v$

In Figure 1, we define ε_0 as pre-strain, ε_v as equivalent strain when void is caused and ε_f as fracture equivalent strain. Figure 1 (a) shows ε_0 is smaller than ε_v. Figure 1 (b) shows ε_0 is larger than ε_v. It appears that ε_f in Figure 1 (b) is larger than ε_f in Figure 1 (a), because hydrostatic stress affects the growth of the void.

2.2 Relationship between stress triaxiality and equivalent strain

According to Oyane [5], the relative density of the material of a specimen decreases due to void growth during deformation. He proposed criteria for ductile fracture based on the relative density of the material. To predict the forming limit, Takuda [6] proposed criteria for ductile fracture using the following equation, which is used along with finite element analysis.

$$I = \frac{1}{b}\int_0^{\varepsilon_f}\left(\frac{\sigma_m}{\bar{\sigma}} + a\right)d\bar{\varepsilon} \tag{1}$$

In equation (1), the integral value I is composed of equivalent strain and stress triaxiality. Stress triaxiality is given by the following equation in the case of $\sigma_1>\sigma_2=\sigma_3$ by assuming uniaxial tensile test. We can judge fracture when the integral value I becomes 1. The stress triaxiality in equation (2) is given in equation (3) by assuming $\sigma_2=\sigma_3=0$, i.e., using non-tapered specimen, or equation (4) by assuming $\sigma_2 = \sigma_3 = \alpha\bar{\sigma}$, i.e., using tapered specimen.

$$\frac{\sigma_m}{\bar{\sigma}} = \frac{\sigma_1 + \sigma_2 + \sigma_3}{3\bar{\sigma}} = \frac{1}{3} + \frac{\sigma_2}{\bar{\sigma}} \tag{2}$$

$$\frac{\sigma_m}{\bar{\sigma}} = \frac{1}{3} \tag{3}$$

$$\frac{\sigma_m}{\bar{\sigma}} = \frac{1}{3} + \alpha \tag{4}$$

Figure 2 shows relationship between stress triaxiality and equivalent strain.

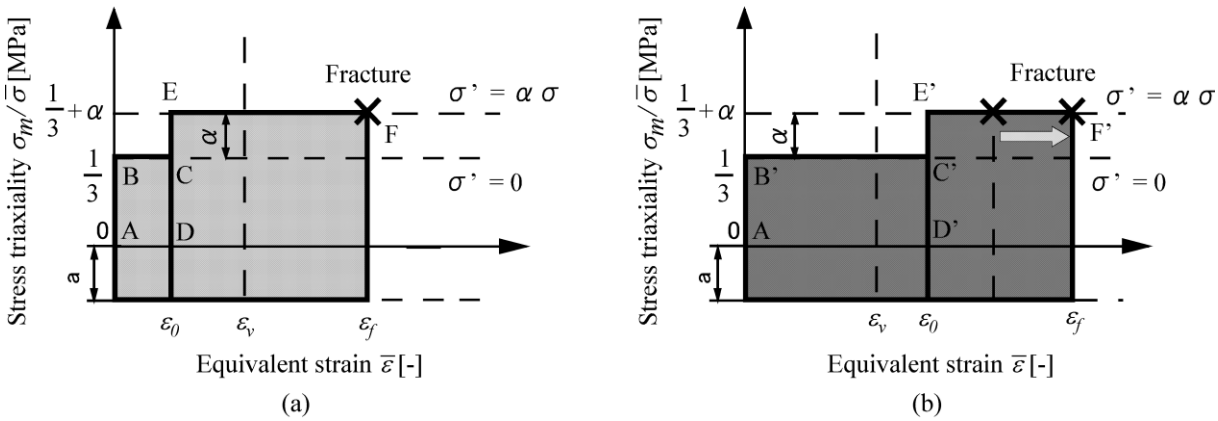

Figure 2: Relationship between stress triaxiality and equivalent strain
(a) Pre-strain $\varepsilon_0 < \varepsilon_v$, (b) Pre-strain $\varepsilon_0 > \varepsilon_v$

In Figure 2, the gray area in Figure 2 (b) is larger than that in (a). Therefore, ε_{fb} is larger than ε_{fa}.

2.3 Relation between stress triaxiality and pre-strain

Similarly to hydrostatic stress, stress triaxiality affects the growth of a void. Therefore, we can rewrite equation 1) as follows by changing the integration range when the void is caused by ε_v.

$$I' = \frac{1}{b'} \int_{\varepsilon_v}^{\varepsilon_f} \left(\frac{\sigma_m}{\bar{\sigma}} + a' \right) d\bar{\varepsilon} \tag{5}$$

Figure 3 shows the relationship between equations 3), 4) and 5).

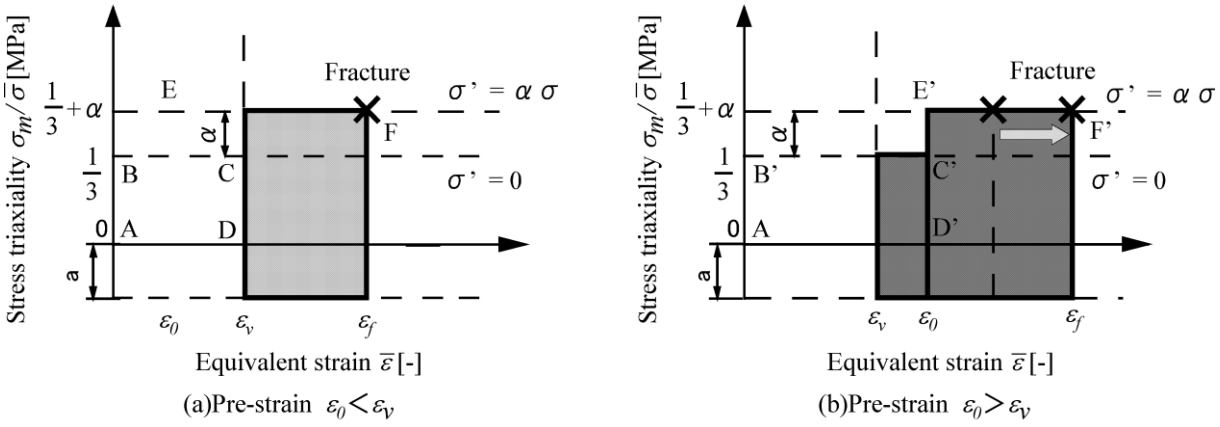

Figure 3: Relationship between stress triaxiality and equivalent strain after occurrence of void (a) Pre-strain $\varepsilon_0 < \varepsilon_v$, (b) Pre-strain $\varepsilon_0 > \varepsilon_v$

Figure 2 shows that ε_{fb} is larger than ε_{fa}.

3 EXPERIMENT

3.1 Experimental conditions

An experiment was conducted with axially symmetric tensile specimens made of aluminum (A1070). Figure 4 shows the specimen shape before the axial tensile test to give pre-strain.

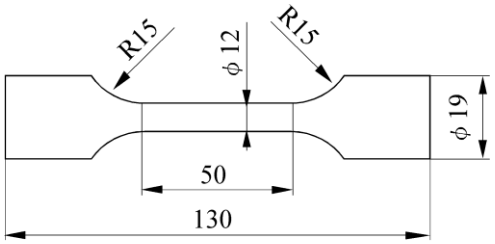

Figure 4: Specimen for pre-straining

The axial tensile test is conducted with the specimen in Figure 4. Figure 5 shows the load-stroke curve.

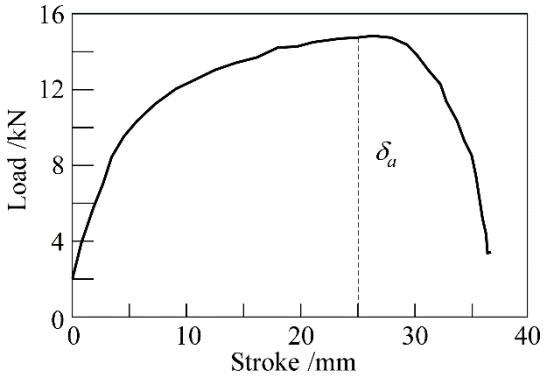

Figure 5 : Tensile test to give pre-strain

In Figure 5, the void caused at stroke = 25 mm is due to necking. Therefore, from the result of the tensile test, the specimen is pre-strained when the stroke is 25 mm. The value of the pre-strain is 0.05413. Furthermore, the specimen shape is changed by additional process. Figure 6 shows the specimen shapes after processing. Here, θ is tapered angle in Figure 6 (b).

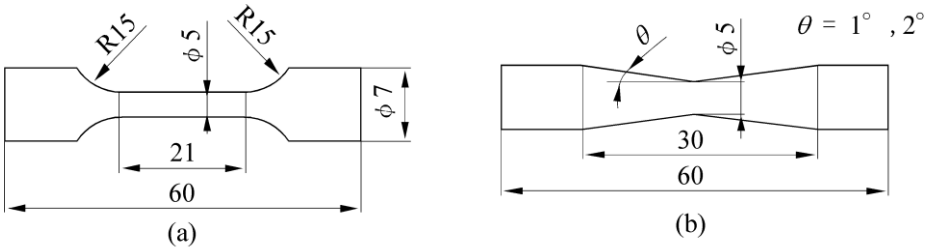

Figure 6: Specimen before and after pre-straining and processing (a) Non-tapered (b) Tapered

3.2 Experimental results

Figure 7 shows the fracture surfaces after the axial tensile test with specimen in Figure 6.

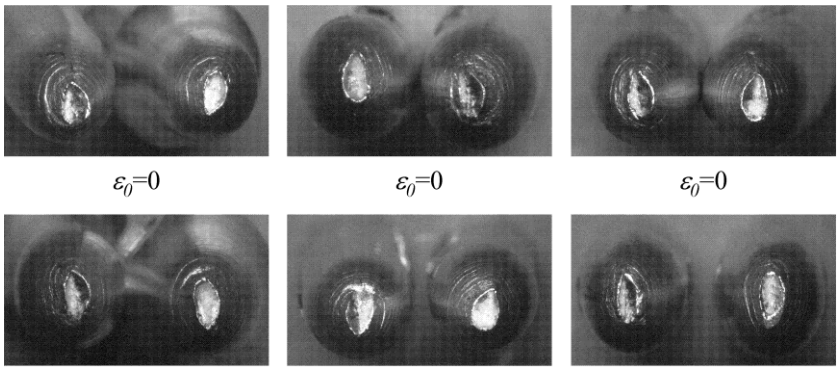

Figure 7 : The fracture surface (a)θ=0° (b)θ=1° (c)θ=2°

In Figure 7, all surfaces are cup and cup. Therefore, it seems that the void is stretched in the axial direction in the tensile test. The fracture point is at the center of the specimen in Figure 7 (b), where θ=1° and Figure 7 (c), where θ=2°. However, the fracture point is not at the center of the specimen in Figure 7 (a), where θ=0°. The fracture equivalent strain can be calculated by the following equation. Here, we define A_0 as cross-sectional area before tensile test and A as it after tensile test.

$$\varepsilon_{eq}' = -\ln\left(\frac{A}{A_0}\right) \tag{6}$$

The fracture equivalent strains are listed in Table 1.

Table 1: Fracture strain before and after axially symmetric tensile test

Fracture strain	θ=0°	θ=1°	θ=2°
$\varepsilon_0 = 0$	2.458	2.250	2.165
$\varepsilon_0 = 0.05413$	2.340	2.195	1.949

4 ANALYSIS

4.1 Analytical condition

The analysis is conducted by simfact forming. Figure 9 shows the analysis model and Table 2 shows the analysis condition.

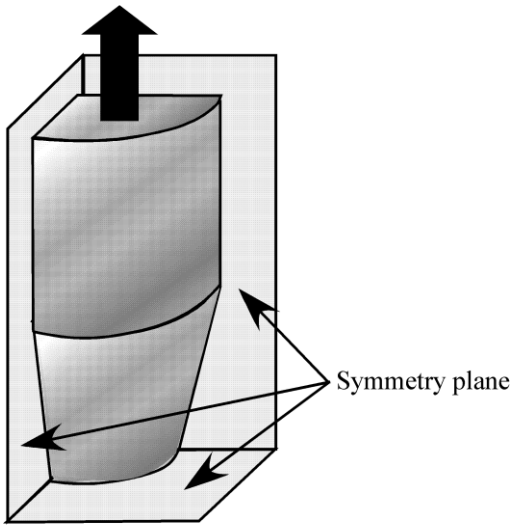

Figure 8 : 1/8 specimen model

Table 2: The material should be the first listed

Flow curve	$\sigma = F\varepsilon^n$
Young's modulus / GPa	71
Poisson's ratio	0.33
Material	A1070
Pre-strain	0
Work hardening exponent	0.0161
Plastic coefficient / MPa	119

In Figure 8, the 1/8 symmetry model is used to reduce the analytical time and expense. However, the tensile part has a fine mesh in order to observe the area in detail. In Table 2, the

mechanical properties were calculated using a tensile test. In the analysis of the axial tensile test, the data output interval was 0.005 mm, and the equivalent strain at the center of the specimen was 3.0.

4.2 Analytical results

Figure 9 shows the relationship between equivalent strain and hydrostatic stress or stress triaxiality.

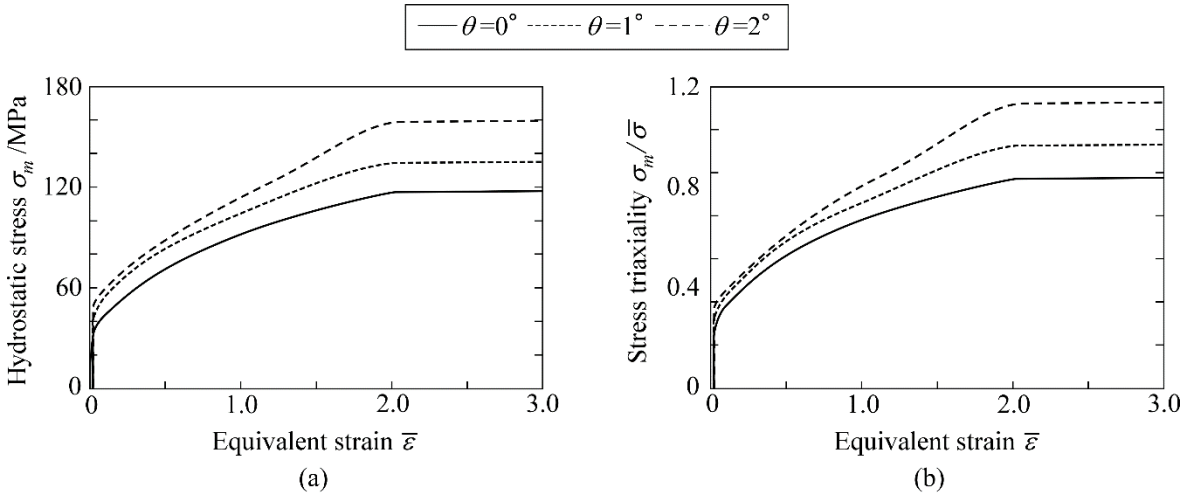

Figure 9 : Relationship between equivalent strain and (a) hydrostatic stress (b) stress triaxiality

In Figure 9, hydrostatic stress and stress triaxiality increase with increasing taper angle. Therefore, the stress states at the center of the specimen are changed by the taper angle. Furthermore, in the plastic deformation region, hydrostatic stress at the center of the specimen varies nonlinearly. The nonlinear curve of hydrostatic stress and equivalent stress becomes larger with increasing taper angle.

5 CONCLUSIONS

- In the experiment, unlike the theory, the fracture equivalent strain of a specimen with pre-strain is smaller than it is without pre-strain.
- The work-hardening exponent of the material in this study is very small. Therefore, the uniform elongation region is very short in the tensile test. Essentially, the material needs to have uniform deformation in the length region. Furthermore, the void grows too large because the stroke in the tensile test is excessive for pre-straining a specimen. Detailed observation of the specimen cross section during the tensile test is required.
- In the analysis, the results suggest a possible method to evaluate the forming limit at various hydrostatic stress states by using axially symmetry tapered specimens.

REFERENCES

[1] C. Karadogan, M.E. Tamer, “Development of a new and simplified procedure for the experimental determination of forming limit curves”, CIRP annuals, 64, 265-268, (2015).
[2] Y. Hanabusa, H. Takizawa, T. Kuwabara, “Evaluation of accuracy of stress measurements determined in biaxial stress tests with cruciform specimen using numerical method”, Steel Research International, 81, 1376-1379, (2010). Y. Hanabusa, H. Takizawa, T. Kuwabara, “Evaluation of accuracy of stress measurements determined in biaxial stress tests with cruciform specimen using numerical method”, Steel Research International, 81, 1376-1379, (2010).
[3] ISO 12004-2:2008(E).
[4] K. Ohji, K Ogura, Y. Mutoh, “The effect of hydrostatic pressure on the basic mechanisms of ductile fracture”, Transactions of the JSME, 42, 31-37, (1976).
[5] M. Oyane, “On criteria for ductile fracture”, Transactions of the JSME, 75, 596-601, (1972).
[6] H. Takuda, K. Mori, T. Hirose, N. Hatta, “Prediction of Forming Limit in Axisymmetric Deep Drawing of Steel/Aluminium Alloy Laminated Sheets Using a Simple Criterion for Ductile Fracture”, Journal of Japan Society for Technology of Plasticity, 37, 509-514, (1996).

XIV International Conference on Computational Plasticity. Fundamentals and Applications
COMPLAS 2017
E. Oñate, D.R.J. Owen, D. Peric and M. Chiumenti (Eds)

FEM ANALYSIS ON THE DEFORMATION BEHAVIOR OF FLANGE PORTION DURING EARLY STAGE IN DEEP DRAWING OF DUPLEX EMBOSSED SHEET METAL

WUYANG.LIU*, TAKASHI. IIZUKA†

* Department of Mechanical Design
Kyoto Institute of Technology
Matsugasaki Goshokaido-cho, Sakyo-ku, Kyoto 606-8585, Japan
e-mail: liuwuyangkit@gmail.com

† Faculty of Mechanical Engineering
Kyoto Institute of Technology
Matsugasaki Goshokaido-cho, Sakyo-ku, Kyoto 606-8585, Japan
Email: tiizuka@kit.ac.jp

Key words: Duplex embossed sheet, FEM Analysis, Flange deformation behavior, Deep drawing.

Abstract. Duplex embossed sheet metals are very useful due to their high rigidity. Furthermore, it is very interesting that the periodic configurations given by embossing brings a new macroscopic feature into a sheet metal. In this study, in order to confirm the effect of only sub-macroscopic structure, which was the configuration given to sheet metal by duplex embossing process, the material was set to isotropy, and FEM simulation was carried out to investigate about the deformation behavior of flange portion during the early stage in deep drawing of duplex embossed sheet.

1 INTRODUCTION

In the recent decades, the energy conservation is more and more demanded. And around this opinion, many strategies of lightweight were proposed. One of the representatives is using the thinner sheet metal. However, the rigidity and forming ability of thinner sheet metal become poor when compare with the thick sheet metal. To overcome this problem, embossing process was proposed due to their high rigidity.

As the sheet metal subjected to duplex embossing process which the sheet metal subjected to embossing process on both sides. The cross section changed to be wave, and the sheet metal will be given a periodic convex-concave structure. It is considered that there will have a new anisotropy depends on this sub-macroscopic structure. Until now, uniaxial tensile properties have been investigated, and peculiar features of duplex embossed sheet have been reported [1]-[3]. One of the features is the low Lankford value (r-value). According to the classical theory, this means that deep drawability could become lower in embossed sheets than that in a plane sheet. However, there is only a few investigations about the deep drawability of embossed sheet metal [4]. And in some cases, contrary experimental results have been reported [5].

Here, in this present study, in order to confirm what happens at flange portion during early stage in deep drawing deformation of duplex embossed sheet, simulation of deep drawing test was conducted by FEM analysis carried out using SIMUFACT 13.0. In this FEM analysis, 1/4 symmetry model was used to reduce the analytical time and expense. And in order to confirm the effect of sub-macro structure on flange deformation behavior, which was the configuration given to sheet metal by duplex embossing process, the material was set to isotropy. The punch force-stroke response in the deep drawing deformation, the average strains in both radial and circumferential directions, the equivalent strain increment distribution map are evaluated numerically at early stage in deep drawing. From these results, the flange deformation behavior was investigated. And also it affirms the results of previous experimental results[6].

2 DUPLEX EMBOSSING PROCESS

Figure 1 shows the schematic of analytical models of duplex embossing process in this study. As shown in this figure, about the duplex embossing process, only upper die is movable in vertical direction. The embossing height h is defined as the half of upper die stroke. Moreover, it is considered that the mechanical characteristics of regular sheet metal depend on the aggregate structure caused by rolling process. And as it subjected to duplex embossing process, the apparent mechanical characteristics of duplex embossed sheet metal changed to depend on this convex-concave structure. So, it is necessary to define the relationship between the rolling direction and embossing direction. Firstly, about the embossing direction, the direction which the same orientation (convex or concave) became linear was defined as embossing angle is 0°. The angle between this embossing direction and the rolling direction was defined as γ. Furthermore, the distance between the centers of adjacent convex and concave bosses was defined as 3mm.

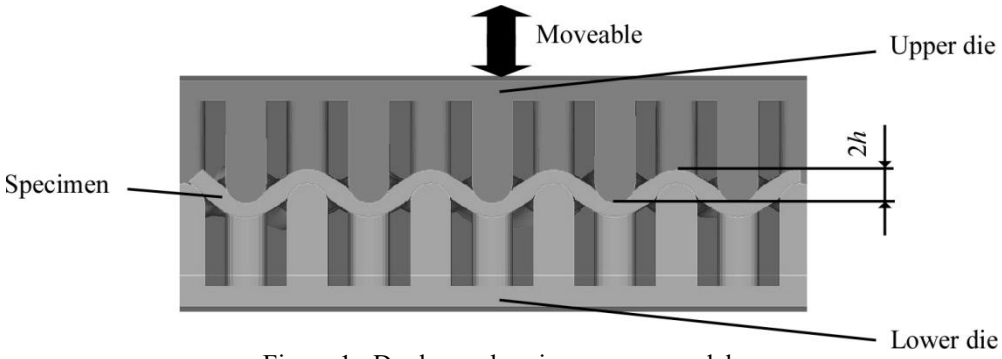

Figure 1 : Duplex embossing process models

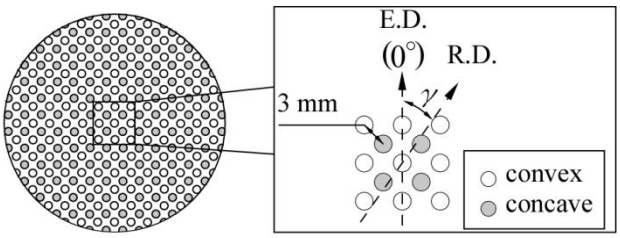

Figure 2 : Definition of the relationship between embossing direction

3 ANALYSIS

3.1 Analytical condition

In fact, the work hardening is existed in the duplex embossed sheet metal caused by this process. So, in order to as far as possible simulate the deep drawing test using duplex embossed sheet accurately. The analysis of duplex embossing process is also essential. Here, in this present study, the analysis of duplex embossing process was conducted firstly. Moreover, in this FEM analysis, 1/4 symmetry model was used to reduce the analytical time and expense. Figure 3 shows about the 1/4 specimen used in this FEM analysis of deep drawing test.

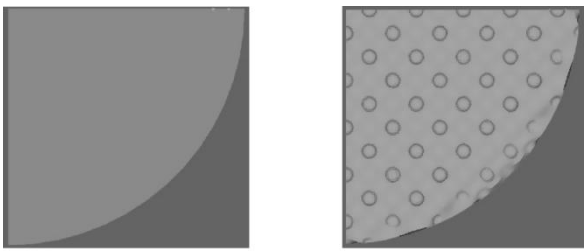

(a) (b)

Figure 3: 1/4 specimen model (a) Plane sheet (b) Duplex embossed sheet

Analytical conditions are listed in Table 1. The diameter of the circular specimen (before duplex embossing process) was set to be 60mm. And the material of specimen was set to be Aluminum alloy. The specific information of this material (Young modulus, n-value, F-value) were also listed in this table. About the γ, in this study, the material was set to isotropy, it can be approximately considered that it is similar to γ=0°. The embossing height *h* was 1mm, and the thickness of the sheet metal before duplex embossing process was 1.0mm. Furthermore, the mesh size of specimen model was set to 0.5.

Table 1: Analytical condition

Specimen	Φ60
Material	Aluminum
γ/°	0
Embossing height *h*/mm	1, 0(plane)
Thickness (before embossing process)/mm	1
Young modulus/ GPa	69
n-value	0.2757
F-value/ MPa	155
Mesh size	0.5

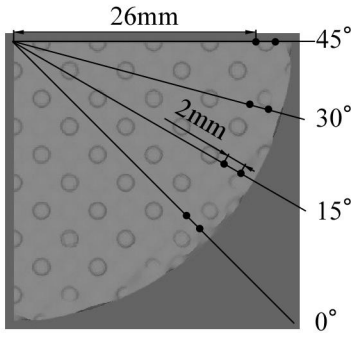

Figure 4 : Measured positions

Next, Figure 4 introduces the flange deformation measurement method in this study. The measured portions in this analysis were set to 26mm and 28mm from the center of specimen respectively. Because the material was set to be isotropy in this present study. It is considered that there only have one kind of anisotropy which depends on the periodic embossing structure. So in the circumferential direction, the measure points were established from

embossing direction is 0° to 45° by 15° interval of 1/8 specimen as the symmetric of embossing structure.

About the deep drawing test set-up, here, the flat head punch was used to conduct the test, and diameter and shoulder radius of it was 29 mm and 3mm respectively. Moreover, due to the apparent thickness of plane sheet and duplex embossed sheet metal (distance between convex and concave bosses) is different from each other. Focus on this issue, in this analysis, the die was set the same as the experiment which was conducted previously. In case of plane sheet, the inner diameter of die was 31.5 mm. And in case of duplex embossed sheet, the inner diameter of die was changed to be 33.5 mm. About the conditions of deep drawing test, the blank holder force was set to be 3kN, and the friction coefficient was set to 0, it can be considered to similar with perfect lubricated state.

3.2 Calculation method

In this present study, the strain component in the radial and circumferential direction were calculated in order to evaluated the flange deformation behavior. First, about the radial direction strain, it was calculated from average variations of the length of two measurement points in the same embossing direction. On the other hand, about the circumferential direction strain component, it was calculated from the average circumferential length with radius r_{ave} of the center point of the two measurement points in the same embossing direction. The r_{ave} can be calculated by the following equation.

$$r_{ave} = \frac{r_0 + 2(r_{15} + r_{30} + r_{45} + r_{60} + r_{75}) + r_{90}}{12} \quad 1)$$

Where the r_α denotes the average radius of the corresponding embossing direction. Because it is considered that the embossed sheet metal is 1/8 symmetry in case of the material is isotropy. So, r_{ave} could be calculated by the following equation simply.

$$r_{ave} = \frac{r_0 + 2r_{15} + 2r_{30} + r_{45}}{6} \quad 2)$$

After the calculation of r_{ave}, the average circumferential length L could be calculated easily by the following equation.

$$L = 2\pi r_{ave} \quad 3)$$

In the end, this average length was used to calculate the average circumferential strain.

4 RESULTS

Figure 5 shows the punch force-stroke curves in deep drawing test of plane sheet and duplex embossed sheet. Comparing these two curves, it can be easily found that the punch force of embossed sheet in case of h=1mm is smaller than that of plane sheet no matter how much the punch stroke is. It is considered that the deep drawing deformation resistance of embossed sheet is smaller than that of plane sheet.

Figure 6 shows the variations of center points coordinate of the two measurement points in case of different embossing directions and punch stroke. From these figures, it can be found that at the beginning of the analysis of deep drawing test (stroke=0~4mm), the positions of these center points are almost the same with each others. And from the punch stroke is 6mm, it was confirmed that the moving toward center speed of plane sheet is faster than that of duplex embossed sheet metal. It is considered that in the radial direction, the duplex embossed

sheet metal can be deformed more easily than plane sheet because of the existence of rotatable portion. Next, from the punch stroke is 16mm, it can be found that the difference of the center points positions coordinate between plane sheet and duplex embossed sheet started to become smaller as punch stroke is increased. It can be thought that the tendency can be reversed in the end of deep drawing test. In other words, about the cup height, duplex embossed sheet will be smaller than that of plane sheet.

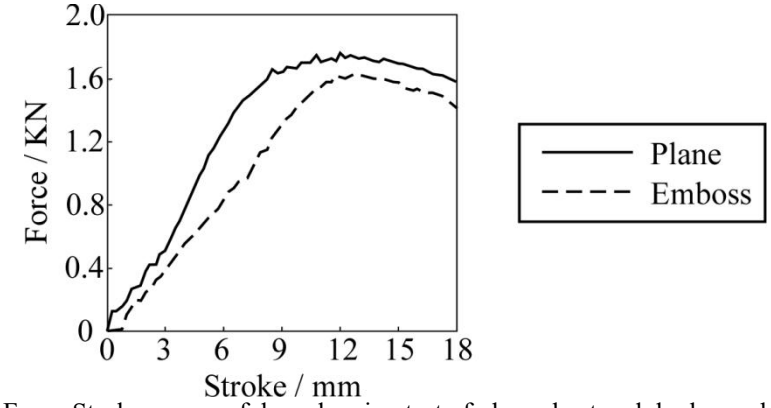

Figure 5: Force-Stroke curves of deep drawing test of plane sheet and duplex embossed sheet

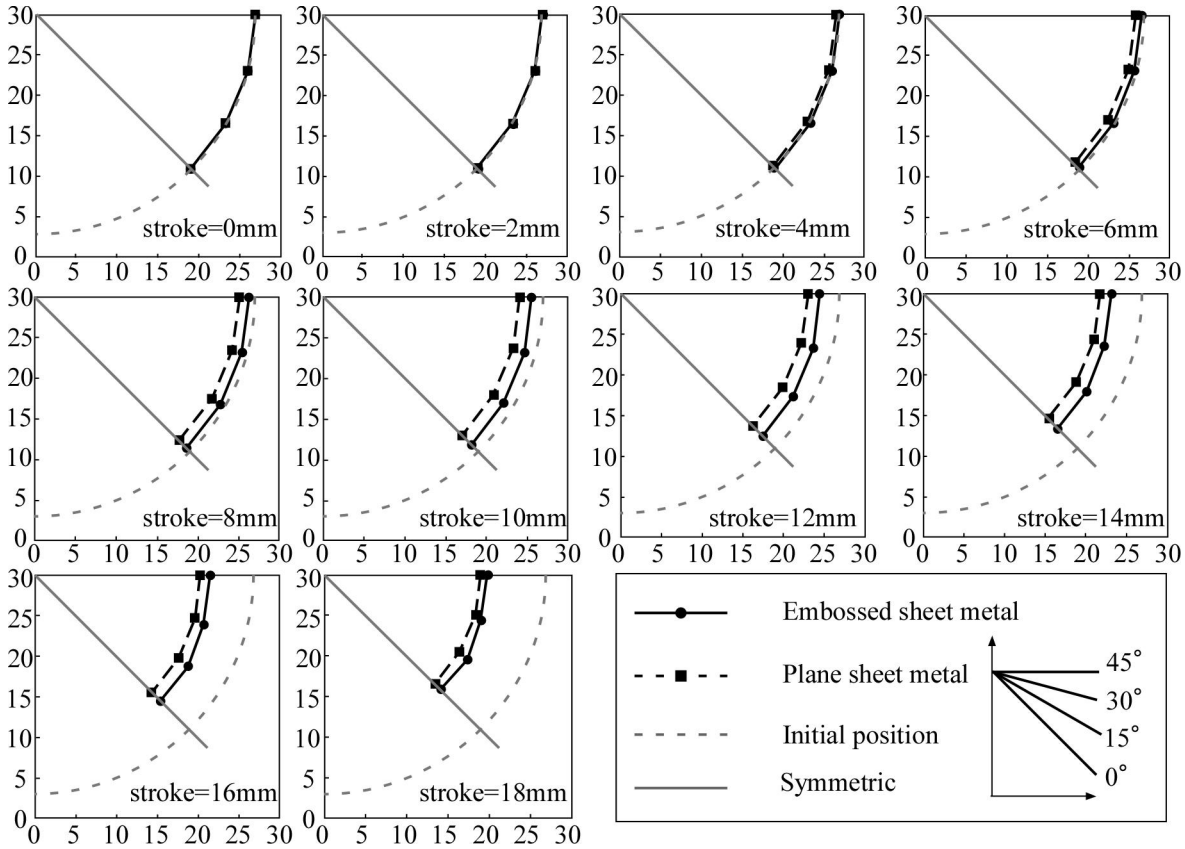

Figure 6: Variations of the center points coordinate of two measurement points in case of different embossing directions and punch stroke

Figure 7 shows the variations of strain distribution of the flange portion deformation in deep drawing. Figure 7 (a) is the relationship between radial direction logarithmic strain and punch stroke. From this result, it can be found that about the radial direction logarithmic strain, plane sheet is the same as duplex embossed sheet metal at the beginning of deep drawing deformation (stroke=0~2mm). Next, as the punch stroke is developed, the radial direction logarithmic strain of them were increased altogether. Moreover, the embossed sheet is smaller than that of plane sheet. And then there have a tendency that this strain of plane sheet will be decreased as the stroke increased and become smaller than that of duplex embossed sheet.

Figure 7 (b) shows the relationship between circumferential and radial direction logarithmic. Here, in this present analysis, it can be found that about the plane sheet, these two kinds of strain changed in the same degree. It is considered that the strain ratio is approximated to be -1. And as the deep drawing test is developed, it final stage of deep drawing, the strain ratio become larger. It it thought that the thickness of flange portion will be increased. On the other hand, about the duplex embossed sheet, it could be found that the slope of the curve is bigger than that of plane sheet. It can be considered that the thickness increase of duplex embossed sheet is larger than that of plane sheet. Therefore, it is also considered to be the reason which lead to the cup heights are different with each other.

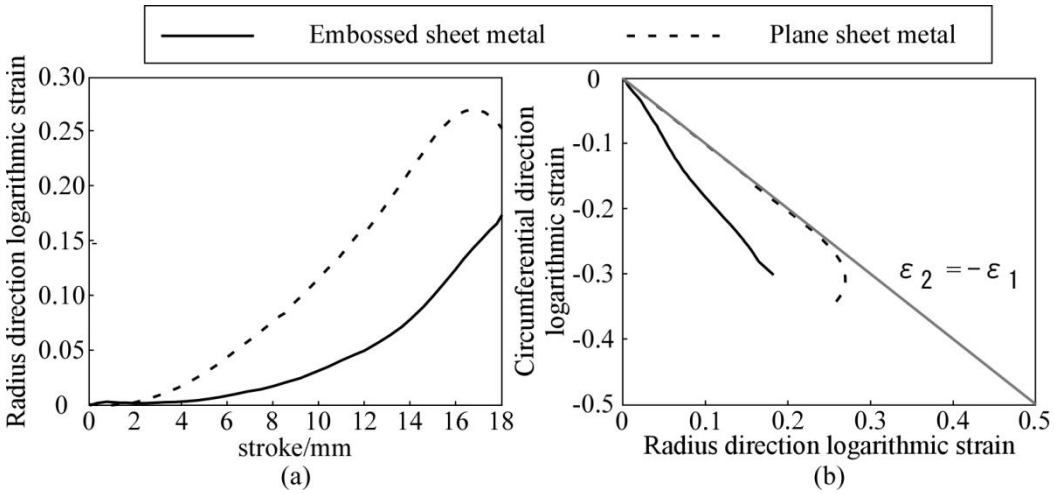

Figure 7: Variations of strain distribution (a) Relationship between radius direction logarithmic strain and punch stroke; (b) Relationship between circumferential and radius direction logarithmic

Finally, Figure 8 shows the equivalent strain increment distribution maps in case of different punch stroke. Figure 8(a) is the sequence of deformation of plane sheet. Paying attention to the flange portion, it can be found that the flange portion of plane sheet deformed uniformly as the punch stroke is increased. And the equivalent strain increment became maximum at the shoulder portion of die. On the other hands, Figure 8(b) is the distribution maps of duplex embossed sheet. It can be confirmed that at the flange portion of duple embossed sheet, the portion near the place where the embossing direction is 0° become the largest. It can be considered that it is derived from the anisotropy depend on embossing distribution. And because of the existence of rotatble part, the variation is not uniform, the

portion between bosses is the largest relatively. And at the last half of the deep drawing, the difference depend on embossing direction became not very obvious.

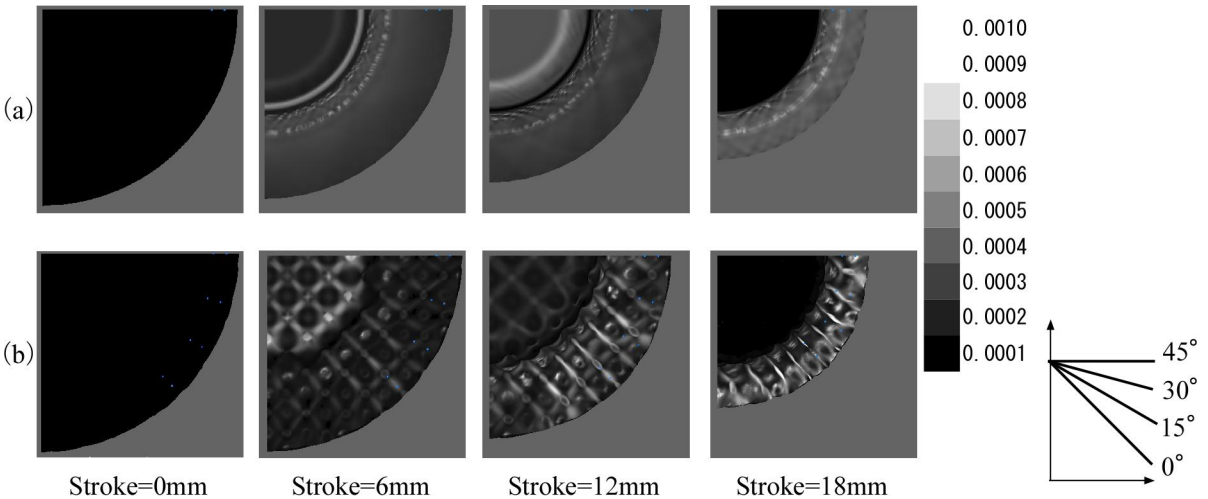

Figure 8: Variations of equivalent strain increment in case of different punch stroke
(a) Plane sheet ; (b) Duplex embossed sheet

5 CONCLUSIONS

In the present study, the flange portion deformation behavior of duplex embossed sheet metal was investigated numerically. The results obtained from this study are summarized as following.

- The deep drawing deformation resistance of embossed sheet (h=1mm) is smaller than that of plane sheet.
- About the moving toward center of the flange portion in deep drawing, when the punch stroke is increased, plane sheet is larger than that of duplex embossed sheet. And in the second half of the deep drawing, the embossed sheet start to be larger than that of plane.
- As punch stroke is developed, the radial direction logarithmic strain of both of plane sheet and duplex embossed sheet increased. Furthermore, duplex embossed sheet is smaller than that of plane sheet. However, in the second half of the deep drawing, the strain of plane sheet started to decrease.
- Strain ratio of duplex embossed sheet is larger than that of plane, it is considered that the apparent thickness increase of flange portion in deep drawing deformation of duplex embossed sheet is larger than that of plane sheet.
- About the equivalent strain increment distribution, duplex embossed sheet is different from that of plane sheet, it was deformed not uniformly, and become the largest as at the embossing direction is 0°.

REFERENCES

[1] T. Iizuka, S. Yamagata, N. Hatanaka, N. Takakura, “Fundamental Study on Deformation and In-plane Anisotropy of Stainless Steel Sheet Subjected to Embossing on Both Sides”

Steel Research International, 79-2, 669-676 (2008)
[2] W.Y. Liu, T. Iizuka, Variation of Apparent Mechanical Anisotropy of Cold-formed Embossed Sheet by Annealing, The 19th European Scientific Association for Material Forming, Nantes, AIP conf.Proc. 1769 200003(2016)
[3] T. Iizuka, T. Aso, Fundamental FEM Analysis on Tensile Deformation of the Sheet Metal Embossed on Both Sides of the Plane, Proceeding of The 13th International Conference on Computational Plasticity , Barcelona (2015), 78-84
[4] W.Y. Liu, T. Iizuka, "Try of Deep Drawing Test using Duplex Embossed sheet "The Proceedings of the 67th Japanese Joint Conference for the Technology of Plasticity, 2016, pp.613-614.
[5] C.S. Namoco, T.Iizuka, K. Narita, N. Takakura, K. Yamaguchi "Effects of Embossing and Restoration process on the Deep Drawablity of Aluminum Alloy Sheets" Journal of Material Processing Technology, 187-188, 202-206(2007)
[6] W.Y. Liu, T. Iizuka. : The 20th European Scientific Association for Material Forming, Dublin, 127 (2017)

XIV International Conference on Computational Plasticity. Fundamentals and Applications
COMPLAS XIV
E. Oñate, D.R.J. Owen, D. Peric & M. Chiumenti (Eds)

INVERSE FORM FINDING WITH H-ADAPTIVITY AND AN APPLICATION TO A NOTCH STAMPING PROCESS

M. CASPARI*,†, P. LANDKAMMER† AND P. STEINMANN†

† Institute of Applied Mechanics
Friedrich-Alexander University Erlangen-Nuremberg
Egerlandstr. 5, 91058 Erlangen, Germany
*e-mail: michael.caspari@fau.de
web page: http://www.ltm.uni-erlangen.de; http://www.tr-73.de

Key words: Inverse form finding, Shape optimization, H-adaptivity, Metal forming

Abstract. The aim is to determine the optimized semi-finished workpiece geometry to its given target geometry after a forming process. Hereby, a novel approach for inverse form finding, a type of a shape optimization, is applied to a notch stamping process. As a special feature, h-adaptive mesh refinement is considered within the iteratively performed forming simulation.

1 INTRODUCTION

Metal forming processes are classified into sheet forming with plane stress conditions and bulk metal forming with three dimensional stress conditions. Recently a new class of forming process called Sheet-Bulk Metal Forming (SBMF) has been introduced by [9]. SBMF combines three dimensional plastic flow with sheet metal forming operations, whereby the focus is placed on functional integration. It gains to form local shape elements normal to the sheet plane with a magnitude similar to the original sheet thickness. This leads to even higher requirements in regards to shape optimization. Numerical shape optimization is beneficial to reduce experimental costs, since trail-and-error methods and subsequent finishing operation steps, respectively, are minimized. In this contribution, shape optimization is applied by means of an inverse form finding strategy.

According to Chenot et. al. [4], the forming simulation, with quantities prescribed in the material configuration, is defined as a direct problem. Whereby shape optimization is referred to an inverse problem, which seeks to determine the optimal workpiece geometry based on the prescribed forming process and a target geometry.

For this purpose, a parameter-free (node-based), form finding algorithm is introduced by Landkammer and Steinmann [8]. It includes nodal positions as design variables and an objective function as minimization criterion. An iterative optimization strategy to update the workpiece geometry is implemented in a non-invasive fashion. This implicates independence of the algorithm to the constitutive behavior and the simulation tool. The

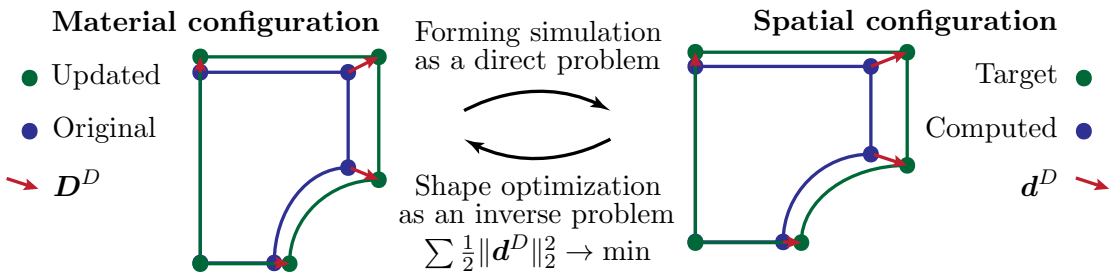

Figure 1: Inverse shape optimization procedure with material configuration, target spatial configuration and the computed spatial configuration

procedure is realized via subroutines, which translate information between the forming simulation (direct problem) and the optimization algorithm (indirect problem), see Fig. 1.

Shape optimization suffers from the contradiction to be efficient but accurate in same time. Due to large deformations within the forming simulation, a fine mesh is required in order to avoid serve mesh distortions of the finite element (FE) mesh. Adaptive strategies are required to decrease computational costs and minimize the discretization error. Here, an h-adaptive strategy is applied to locally refine the mesh during the simulation. It leads to a refinement of highly exposed regions and an efficient mesh is generated.

The implementation of adaptive remeshing techniques requires detailed investigation due to the applied node-based optimization strategy. The challenge of the inverse optimization process with h-adaptivity is caused by newly emerging nodes and elements within the model. This issue can be mastered by adjusting the subroutines, which translates information between the forming simulation (direct problem) and the optimization algorithm (inverse problem).

Due to the advantages of h-adaptivity, it is possible to optimize more complex geometries and to cope with large plastic strains. It even enables to include penetration of a sharp edge tool into the forming simulation.

The paper is structured as follows: In the sequel, basics of nonlinear continuum mechanics are introduced in Sec. 2 and FE discretization clarification is outlined in Sec. 3. The detailed algorithm for inverse form finding, formulated as an optimization problem, follows in Sec. 4. Afterwards, h-adaptive mesh refinement is described in Sec. 5. A example in Sec. 6, is presented to demonstrate the application of the mesh adaptivity within inverse form finding. Finally, Sec. 7 recaps the findings.

2 BASICS OF NONLINEAR CONTINUUM MECHANICS

A general description of nonlinear continuum mechanics is required for a discussion regarding inverse shape optimization and further the description of the h-adaptive refinement strategy. More detailed description of nonlinear continuum mechanics can be found in [1] among others.

2.1 Kinematics

Fig. 2 depicts a continuous setting of the material configuration $\mathcal{B}_0$ at time $t = 0$ and the spatial configuration $\mathcal{B}_t$ at time $t > 0$. A placement of a physical body into the Euclidean space $\mathbb{E}^3$ with $\boldsymbol{E}_i \equiv \boldsymbol{e}_i$ and $i = 1, 2, 3$ is assumed.

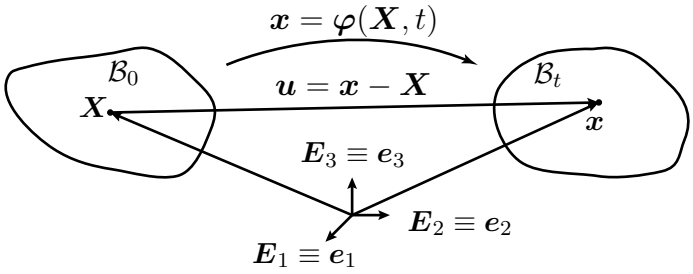

Figure 2: Kinematics of a nonlinear continuum with the undeformed (material) and the deformed (spatial) configuration

The deformation map $\boldsymbol{\varphi}$ maps positions $\boldsymbol{X}$ of a material configuration $\mathcal{B}_0$ to positions $\boldsymbol{x}$ of a spatial (deformed) configuration $\mathcal{B}_t$:

$$\boldsymbol{x} = \boldsymbol{\varphi}(\boldsymbol{X}, t) \quad : \mathcal{B}_0 \to \mathcal{B}_t \tag{1}$$

The displacement field $\boldsymbol{u}$ occurs to the difference of the position vectors at spatial and material configurations:

$$\boldsymbol{u}(\boldsymbol{X}, t) = \boldsymbol{\varphi}(\boldsymbol{X}, t) - \boldsymbol{X} \tag{2}$$

The gradient $\boldsymbol{F}$ of the deformation map with respect to material coordinates renders a linear map from the material tangent space $T\mathcal{B}_0$ to the spatial tangent space $T\mathcal{B}_t$:

$$\boldsymbol{F} = \frac{\partial \boldsymbol{\varphi}(\boldsymbol{X})}{\partial \boldsymbol{X}} \quad : T\mathcal{B}_0 \to T\mathcal{B}_t \tag{3}$$

2.2 Weak Piola formulation

In the following, the body forces are neglected due to its minor influence in contrast to forming forces.

An equilibrium in the Piola formulation is given by the boundary value problem with Dirichlet and Neumann boundary conditions (Eq. 5):

$$\mathrm{Div}\boldsymbol{P} = \boldsymbol{0} \tag{4}$$

$$\boldsymbol{\varphi} = \bar{\boldsymbol{\varphi}} \quad \text{on} \quad \partial\mathcal{B}_0^{\boldsymbol{\varphi}} \qquad \text{and} \qquad \boldsymbol{P} \cdot \boldsymbol{N} = \boldsymbol{T} \quad \text{on} \quad \partial\mathcal{B}_0^{\boldsymbol{T}} \tag{5}$$

The balance equation (Eq. 4), formulated with the first Piola-Kirchhoff stress $\boldsymbol{P}$, results from the balance of linear momentum, including the divergence operator with respect to material coordinates.

This system of equations is solved by an application of the principle of virtual work. Therefore, virtual displacements $\delta\boldsymbol{\varphi}$ are introduced. With corresponding initial conditions, the weak formulation is written as:

$$\int_{\mathcal{B}_0} \boldsymbol{P} : \delta\boldsymbol{F}\mathrm{d}V = \int_{\partial\mathcal{B}_0^t} \delta\boldsymbol{\varphi} \cdot \boldsymbol{T}\mathrm{d}A \qquad \forall\delta\boldsymbol{\varphi} \text{ admissible} \tag{6}$$

3 FINITE ELEMENT DISCRETIZATION

Discretization is required to solve the weak formulation in Eq. 6 for a continuum body $\mathcal{B}$. The body itself and likewise the field values are approximated. Gauss-integration is typically performed for solving integrals over a finite element. Linearization enables the use of efficient iterative solution methods for the system of nonlinear equations.

3.1 Discretization of a body into finite elements

The body $\mathcal{B}$ is discretized into n_{elem} elements:

$$\mathcal{B}_0 \approx \mathcal{B}_0^{\text{h}} = \bigcup_{e=1}^{n_{\text{elem}}} \mathcal{B}_0^e \qquad \text{and} \qquad \mathcal{B}_t \approx \mathcal{B}_t^{\text{h}} = \bigcup_{e=1}^{n_{\text{elem}}} \mathcal{B}_t^e \tag{7}$$

Accordingly, coordinates of material and spatial configurations are prescribed as discretized values through:

$$\boldsymbol{X}^{\text{h}} = \bigcup_{e=1}^{n_{\text{elem}}} \boldsymbol{X}^e \qquad \text{and} \qquad \boldsymbol{x}^{\text{h}} = \bigcup_{e=1}^{n_{\text{elem}}} \boldsymbol{x}^e \tag{8}$$

Within the isoparametric concept, all kinematic quantities are approximated by the same shape functions $N^i(\boldsymbol{\xi})$ for each element node ($i = 1 \dots n_{\text{en}}$), which are defined on a reference element $\mathcal{B}_\square$ with isoparametric coordinates $\boldsymbol{\xi} \in [-1, 1]^{n_{\text{dim}}}$. The element coordinates $\boldsymbol{X}^e$ and $\boldsymbol{x}^e$ depend on the nodal positions $\boldsymbol{X}^i$ and $\boldsymbol{x}^i$:

$$\boldsymbol{X}^e(\boldsymbol{\xi}) = \sum_{i=1}^{n_{\text{en}}} \boldsymbol{X}^i N^i(\boldsymbol{\xi}) \qquad \text{and} \qquad \boldsymbol{x}^e(\boldsymbol{\xi}) = \sum_{i=1}^{n_{\text{en}}} \boldsymbol{x}^i N^i(\boldsymbol{\xi}) \tag{9}$$

The deformation map and further the deformation gradient follows the discretization with:

$$\boldsymbol{x}^{\text{h}} = \boldsymbol{\varphi}(\boldsymbol{X}^{\text{h}}, t) \quad : \mathcal{B}_0^{\text{h}} \to \mathcal{B}_t^{\text{h}} \quad \text{and} \quad \boldsymbol{F}^{\text{h}} = \frac{\partial\boldsymbol{\varphi}(\boldsymbol{X}^{\text{h}})}{\partial\boldsymbol{X}^{\text{h}}} \quad : T\mathcal{B}_0^{\text{h}} \to T\mathcal{B}_t^{\text{h}} \tag{10}$$

The Jacobians

$$\boldsymbol{J}^e(\boldsymbol{\xi}) = \sum_{i=1}^{n_{\text{en}}} \boldsymbol{X}^i \otimes \frac{\partial N^i(\boldsymbol{\xi})}{\partial\boldsymbol{\xi}} \qquad \text{and} \qquad \boldsymbol{j}^e(\boldsymbol{\xi}) = \sum_{i=1}^{n_{\text{en}}} \boldsymbol{x}^i \otimes \frac{\partial N^i(\boldsymbol{\xi})}{\partial\boldsymbol{\xi}} \tag{11}$$

are used for the mapping from the reference element to the element of spatial or material configuration. The deformation gradient $\boldsymbol{F}^e$ yields:

$$\boldsymbol{F}^e(\boldsymbol{\xi}) = \boldsymbol{j}^e(\boldsymbol{\xi}) \cdot \boldsymbol{J}^e(\boldsymbol{\xi})^{-1} = \left[\sum_{i=1}^{n_{\text{en}}} \boldsymbol{x}^i \otimes \frac{\partial N^i(\boldsymbol{\xi})}{\partial \boldsymbol{\xi}}\right] \cdot \left[\sum_{i=1}^{n_{\text{en}}} \boldsymbol{X}^i \otimes \frac{\partial N^i(\boldsymbol{\xi})}{\partial \boldsymbol{\xi}}\right]^{-1} \tag{12}$$

Relations between an element in material, spatial and reference configuration are depicted in Fig. 3.

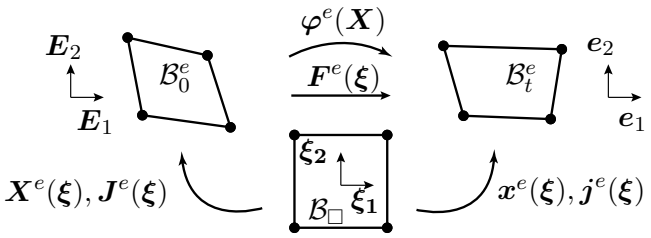

Figure 3: Mapping of a reference element to the material and the spatial configuration.

3.2 Discretization and linearization of the weak formulation

Neglecting dynamics, the weak formulation (Eq. 6) contains internal and external virtual work. The prescribed discretization and linearization is required and demonstrated exemplary for the internal virtual work.

$$\begin{aligned} \delta W_{0\,\text{int}} &= \int_{\mathcal{B}_0} \left[\boldsymbol{F}^{\mathsf{T}} \cdot \frac{\partial\, \delta\boldsymbol{\varphi}}{\partial \boldsymbol{X}}\right]^{\text{sym}} : \boldsymbol{S}\mathrm{d}V \\ &\approx \delta W^{\text{h}}_{0\,\text{int}} = \delta\boldsymbol{\varphi}^I \mathop{\mathsf{A}}_{e=1}^{n_{\text{elem}}} \int_{\mathcal{B}_0^e} \boldsymbol{F} \cdot \boldsymbol{S} \cdot \frac{\partial N^i}{\partial \boldsymbol{X}} \mathrm{d}V^e = \delta\boldsymbol{\varphi}^I \cdot \boldsymbol{f}^I_{\text{int}} \end{aligned} \tag{13}$$

Hereby $\delta\boldsymbol{\varphi}$ denotes the virtual displacement, discretized in the same way as the deformation map (Eq. 9), which is referred to as the Galerkin Method. The same procedure for external virtual work results in an external force vector:

$$\boldsymbol{f}^I_{\text{ext}} = \mathop{\mathsf{A}}_{e=1}^{n_{\text{elem}}} \int_{\delta\mathcal{B}_0^e} N^i \bar{\boldsymbol{T}}\, \mathrm{d}A^e \tag{14}$$

This leads further to a system of equations which is represented node wise as:

$$\boldsymbol{r}^I = \boldsymbol{f}^I_{\text{int}} - \boldsymbol{f}^I_{\text{ext}} = \boldsymbol{0} \qquad \forall I = 1, ..., n_{\text{nodes}} \tag{15}$$

The residuum $\boldsymbol{r}_I$ has to be solved for each node I. For a solution, the linearization of this equation is needed. It consequently follows for one element:

$$\delta\boldsymbol{\varphi}^{e\mathsf{T}} \cdot \boldsymbol{K}^e \cdot \Delta\boldsymbol{\varphi}^e = \delta\boldsymbol{\varphi}^{e\mathsf{T}} \cdot \boldsymbol{f}^e \tag{16}$$

4 INVERSE FORM FINDING

A node-based approach is pursued to solve the inverse form finding problem. Therefore, coordinates of selected design nodes serve as design variables for the optimization algorithm, introduced by [8].

The objective function

$$\delta(\mathbf{X}^{\mathrm{D}}, \mathbf{x}^{\mathrm{D}}_{\mathrm{tg}}) = \sum_{D=1}^{n_{\mathrm{dsgn}}} \delta^D \left(\boldsymbol{x}^D_{\mathrm{tg}}, \boldsymbol{\varphi}(\boldsymbol{X}^D) \right) \tag{17}$$

summarizing the local squared error

$$\delta^D = \frac{1}{2} \boldsymbol{d}^{D\mathsf{T}} \cdot \boldsymbol{d}^D \tag{18}$$

with nodal differences

$$\boldsymbol{d}^D = \boldsymbol{x}^D_{\mathrm{tg}} - \boldsymbol{\varphi}(\boldsymbol{X}^D) \tag{19}$$

between the current spatial configuration $\boldsymbol{\varphi}(\boldsymbol{X}^D)$ and the prescribed target positions $\boldsymbol{x}^D_{\mathrm{tg}}$ determined at each design node $D = 1, \ldots, n_{\mathrm{dsgn}}$. The positions are stored in the column vectors $\mathbf{X}^{\mathrm{D}} = \left[\boldsymbol{X}^{1\top} \cdots \boldsymbol{X}^{n_{\mathrm{dsgn}}\top} \right]^\top$ and $\mathbf{x}^{\mathrm{D}} = \left[\boldsymbol{x}^{1\top} \cdots \boldsymbol{x}^{n_{\mathrm{dsgn}}\top} \right]^\top$.

The optimization strategy results in a minimization of the objective function, which is satisfied at the optimal configuration:

$$\left. \frac{\partial \delta(\mathbf{X}^{\mathrm{D}}, \mathbf{x}^{\mathrm{D}}_{\mathrm{tg}})}{\partial \mathbf{X}^{\mathrm{D}}} \right|_{\mathbf{X}^{\mathrm{D}}_{\mathrm{opt}}} \stackrel{!}{=} \mathbf{0} \tag{20}$$

In use of the approximation by Taylor series, Eq. 20 reads:

$$\frac{\partial \delta\left(\mathbf{X}^{\mathrm{D}}, \mathbf{x}^{\mathrm{D}}_{\mathrm{tg}}\right)}{\partial \mathbf{X}^{\mathrm{D}}} + \frac{\partial^2 \delta\left(\mathbf{X}^{\mathrm{D}}, \mathbf{x}^{\mathrm{D}}_{\mathrm{tg}}\right)}{\partial \mathbf{X}^{\mathrm{D}} \partial \mathbf{X}^D} \cdot \left[\mathbf{X}^{\mathrm{D}}_{\mathrm{opt}} - \mathbf{X}^{\mathrm{D}} \right] \stackrel{!}{=} \mathbf{0}\,, \tag{21}$$

The Taylor series is terminated after the first term. This leads to an iteration step as:

$$\mathbf{X}^{\mathrm{D}}_{k+1} = \mathbf{X}^{\mathrm{D}}_k - \frac{\partial^2 \delta\left(\mathbf{X}^{\mathrm{D}}, \mathbf{x}^{\mathrm{D}}_{\mathrm{tg}}\right)}{\partial \mathbf{X}^{\mathrm{D}} \partial \mathbf{X}^{\mathrm{D}}}^{-1} \cdot \frac{\partial \delta\left(\mathbf{X}^{\mathrm{D}}, \mathbf{x}^{\mathrm{D}}_{\mathrm{tg}}\right)}{\partial \mathbf{X}^{\mathrm{D}}} \tag{22}$$

Motivated by the mentioned node-wise optimization approach, Eq. 22 is written as an iteration step for each design node as:

$$\boldsymbol{X}^D_{k+1} = \boldsymbol{X}^D_k - \alpha \frac{\partial^2 \delta^D\left(\boldsymbol{X}^D, \boldsymbol{x}^{\mathrm{h}}_{\mathrm{tg}}\right)}{\partial \boldsymbol{X}^D \partial \boldsymbol{X}^D}^{-1} \cdot \frac{\partial \delta^D\left(\boldsymbol{X}^D, \boldsymbol{x}^{\mathrm{h}}_{\mathrm{tg}}\right)}{\partial \boldsymbol{X}^D} \tag{23}$$

This iteration includes a linesearch parameter α, controlled by Armijo-Backtracking [7], which ensures a suited update without serve mesh distortions. A complete update step is now written as:

$$\boldsymbol{X}^D_{k+1} = \boldsymbol{X}^D_k - \alpha\, \tilde{\boldsymbol{F}}^{D-1} \cdot \boldsymbol{d}^D \tag{24}$$

Table 1: The node-based optimization problem for inverse form finding [7].

Objective funct.:	$\delta\big(\mathbf{X}^{\mathrm{D}}, \mathbf{x}^{\mathrm{D}}_{\mathrm{tg}}\big) = \sum_{D=1}^{n_{\mathrm{design}}} \frac{1}{2}\|\boldsymbol{d}^D\|_2^2$
Design variables:	Material positions $\boldsymbol{X}^D$ of the design nodes
State equation:	Motion $\boldsymbol{\varphi} : \mathbf{X}^{\mathrm{D}} \in \mathcal{B}^{\mathrm{h}}_0 \rightarrow \mathbf{x}^{\mathrm{D}} \in \mathcal{B}^{\mathrm{h}}_{\mathrm{t}}$

Yet, the earlier introduced discretized deformation gradient in Eq. 10 performs the mapping of the difference vectors from the spatial to the material configuration as a smoothed gradient $\tilde{\boldsymbol{F}}$. Eq. 12 introduces an element-wise deformation gradient which is evaluated on the integration points. To obtain the smoothed deformation gradient $\tilde{\boldsymbol{F}}^D$ for a certain node, all adjacent elements are evaluated and smoothing techniques are applied to map quantities from integration points to element nodes. The used recovery technique is the widespread global Least-Squares (L^2-) Smoothing proposed by Hinton and Campbell [6].

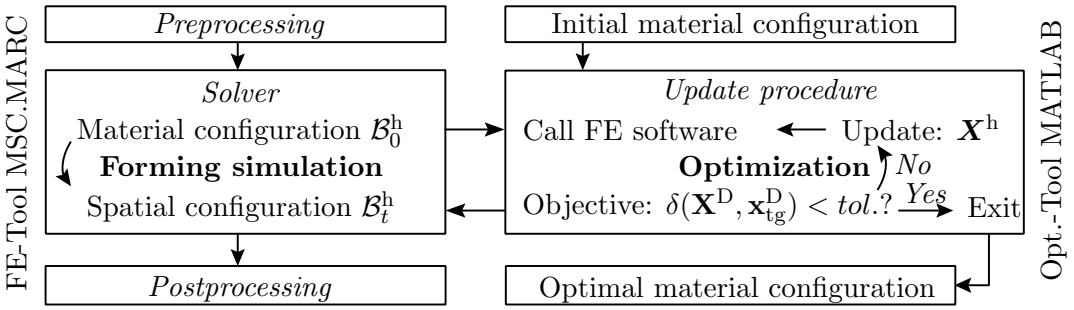

Figure 4: The iterative strategy for inverse form finding, separated into forming simulation (direct problem) and shape optimization (inverse problem) [7].

5 H-ADAPTIVE FINITE ELEMENT REFINEMENT STRATEGY

The main task of adaptive mesh refinement strategies is to control the discretization error in sense of minimization and additionally to compensate it over the area of interest. However, the quantity of the error and the area of the highest gradient is not available prior and has to be computed during the simulation [13]. Within this obstacle, particular error estimators have been established ([5], [3]).

After detecting the area of high errors or distorted elements an adaptivity strategy is applied. Typically h-, p- and r-adaption is available.

As pictured in Fig. 5(**c**) the r-refinement induces a moving of nodes by which the mesh density is concentrated to a particular place. Due to the refinement caused by a p-adaptivity Fig. 5(**b**), the polynomial degree of the element in the particular place is raised. One common used r-adaptive method is the Arbitrary-Lagrangian-Eulerian adaptivity [2].

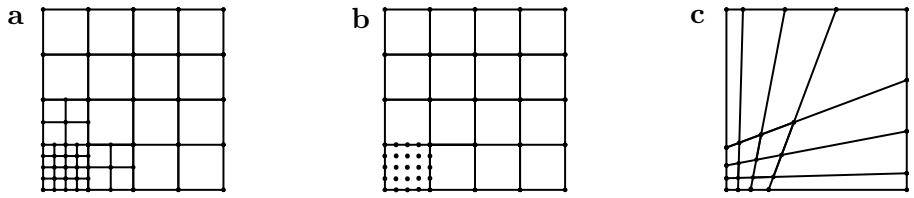

Figure 5: H-adaptivity (**a**) with a level two refinement, p-adaptivity (**b**) for one element and a global r-adapted mesh (**c**)[13]

Besides no occurrence of irregular nodes, a benefit of p- and r-adaptivity is given by no modification of connectivity during the refinement process.

H-adaption Fig. 5(**a**) means an adaption of the element size with respect to prescribed criterion, whereby the problem size rises during the implementation of new element nodes [13]. Regarding to [10], there are two different kinds of nodes within the adapted grids. The first one is the *regular* node which is standard for non adapted grids but also part of the refinement. The second is the *irregular* node generated by the refinement. The *regular* nodes are corners of the undisturbed elements. Remaining nodes are called *irregular*. By definition, all corners being part of a boundary are called *regular* nodes. As pictured in Fig. 6, the refinement of the top-right part of the structure causes some *irregular* nodes. To ensure a continuity of the solution, despite of the existence of *irregular* nodes, the solution is constrained to obtain interpolated values of surrounded *regular* nodes.

For a geometrical simple refinement depicted in Fig. 6, a mathematical description is needed, which has been introduced by [5]. Recap Eq. 16, a description between node displacement values, stiffness matrix, and node force values for one element are prescribed.

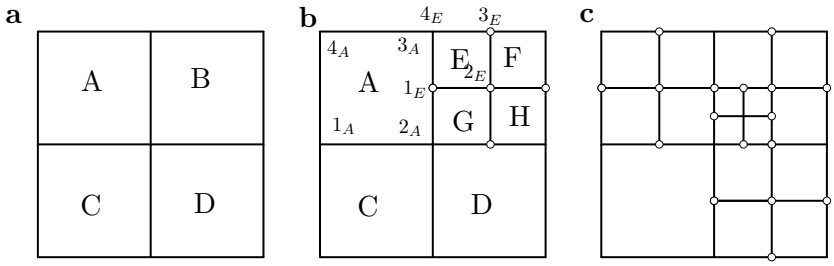

Figure 6: H-refinement of a quadrilateral element set (**a**) with level one (**b**) and level two (**c**) refinement [5].

During the refinement procedure, a 4-noded quadrilateral element is divided into four new smaller elements. Nodal values for new element nodes are required. For the newly irregular node $\mathbf{1}_E$ a relation depending on regular nodes is introduced by:

$$\mathbf{1}_E = \frac{1}{2}[\mathbf{3}_A + \mathbf{2}_A] \tag{25}$$

In conjunction with regular nodes, the transformation of nodal values is prescribed:

$$\boldsymbol{\varphi}_E = \boldsymbol{P}_E \cdot \bar{\boldsymbol{\varphi}}_E \tag{26}$$

$$\begin{bmatrix} \mathbf{1}_E \\ \mathbf{2}_E \\ \mathbf{3}_E \\ \mathbf{4}_E \end{bmatrix} = \begin{bmatrix} \frac{1}{2} & 0 & 0 & \frac{1}{2} \\ 0 & 1 & 0 & 0 \\ 0 & 0 & 1 & 0 \\ 0 & 0 & 0 & 1 \end{bmatrix} \cdot \begin{bmatrix} \mathbf{2}_A \\ \mathbf{2}_E \\ \mathbf{3}_E \\ \mathbf{4}_E \end{bmatrix} \tag{27}$$

Furthermore the variational node values $\delta\boldsymbol{\varphi}_E$ for one element are transformed with the same requirement:

$$\delta\boldsymbol{\varphi}_E = \boldsymbol{P}_E \cdot \delta\bar{\boldsymbol{\varphi}}_E \tag{28}$$

In consideration of Eq. 26 and Eq. 28, Eq. 16 is written as:

$$\delta\bar{\boldsymbol{\varphi}}_E^{\mathsf{T}} \cdot \boldsymbol{P}_E^{\mathsf{T}} \cdot \boldsymbol{K}_E \cdot \boldsymbol{P}_E \cdot \bar{\boldsymbol{\varphi}}_E = \delta\bar{\boldsymbol{\varphi}}_E^{\mathsf{T}} \cdot \boldsymbol{P}_E \cdot \boldsymbol{f}_E \tag{29}$$

Therefore, a new and again symmetric, stiffness matrix and also an updated force vector for the E-th element results in:

$$\overline{\boldsymbol{K}}_E = \boldsymbol{P}_E^{\mathsf{T}} \cdot \boldsymbol{K}_E \cdot \boldsymbol{P}_E \qquad \text{and} \qquad \overline{\boldsymbol{f}}_E = \boldsymbol{P}_E \cdot \boldsymbol{f}_E \tag{30}$$

The same procedure is applied for elements F, G and H. Subsequent, the global stiffness matrix is routinely assembled. For a second level refinement in element G in Fig. 6(**c**), element D and A has to be refined at first, otherwise two irregular nodes appear between two regular nodes, which is prohibited.

6 EXAMPLES

The iterative optimization includes a forming simulation within each step. The notch stamping process is reduced to a two dimensional and a half notch model, in order to decrease the computational costs. Symmetry conditions are applied on the right side of the model, which is depicted in Fig. 9(**a**). Beside the symmetry boundary condition, the

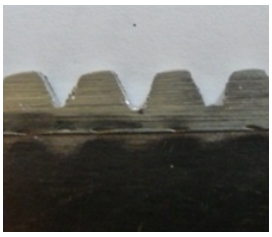

Figure 7: Workpiece of a notch stamping process as in [11]

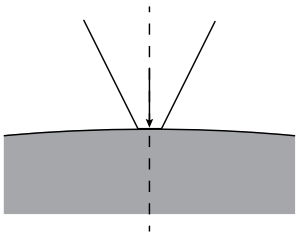

Figure 8: Sketch of the notch stamping process [11]

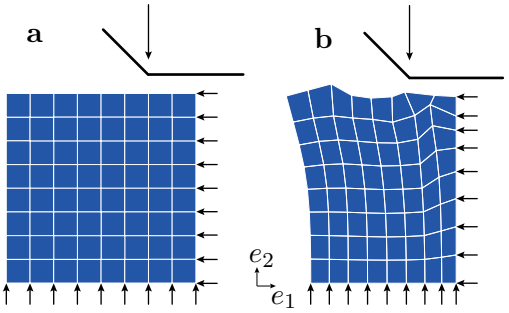

Figure 9: The original discretized material configurations (**a**) and the optimized material configuration (**b**)

bottom is fixed in e_2-direction. All four sides (width: 50 mm) of the rectangle quadratic solid body are discretized by 9 nodes, which results in 81 nodes and 64 quadrilateral elements (plane stress) for the whole model. The dual phase steel DP600 with a nonlinear

isotropic hardening and corresponding parameters, investigated by [14], is used. The notch is composed by a 12.5 mm horizontal line and a 45° line connected without a fillet radius. The resultant sharp edge is of special interest concerning the influence of the h-adaptivity to the simulation output. The initial gap between notch and solid body prevents an initial penetration during a further iteration step. A constant velocity is applied to the notch to reach a fixed solid body penetration of 25 mm. A friction factor of 0.07 is specified between the notch and the solid body. Furthermore, a contact control of the shear arctangent type is used to represent the contact behavior. This is originated by an investigation of [12] to improve the material flow during a forming process. The factor represents the application of the water based non-poisonous lubricant (Beruforge BF 150 DL) with wax particles and high viscosity. The h-adaptivity is applied with a *node in region*-option and use two regions moving along in conjunction with the notch. This constraint ensures a refinement of every element within this region and therefore includes those elements close to the notch. The configuration in Fig. 10(**a**) serves as the material start configuration of the first iteration.

The target configuration in Fig. 10(**d**) is defined by a rectangle quadratic box (width: 50 mm) that includes an exact shape of the impressed notch. A total number of 18 design nodes $\boldsymbol{X}^D$ enter the objective function $\delta(\mathbf{X}^{\mathrm{D}})$.

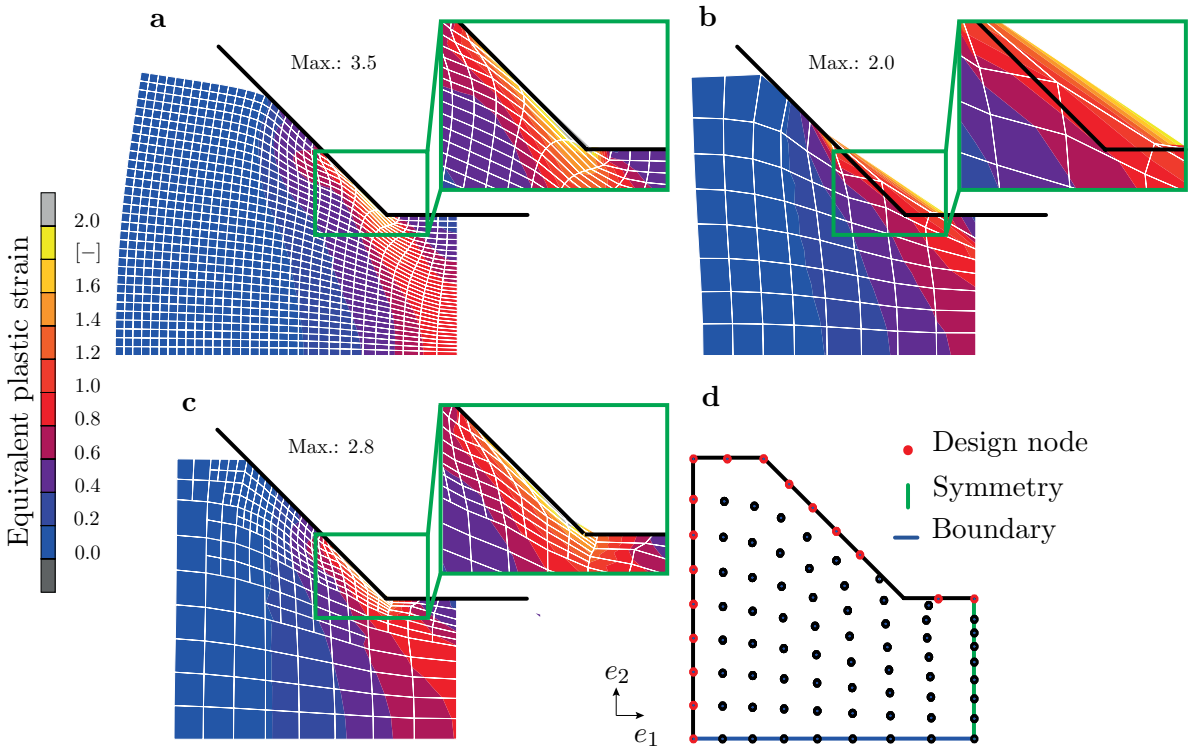

Figure 10: Deformed spatial configurations when inputting the globally refined (**a**), the optimized coarse (**b**) and the optimized h-adaptively refined (**c**) mesh, beside the prescribed target configuration (**d**)

Fig. 10 shows three examples of the deformed configuration after forming simulations. Fig. 10(**a**) is the simulation result using a refined mesh throughout the whole body without applying adaptive method. Hereby, the imprint of the notch fits proper and an h-adaptivity would not improve the result in that particular area. However, a major drawback is the excessive long computational time. The simulation takes six times longer compared to a simulation with a locally adapted coarse mesh. Consequently, adaptivity improves computational cost by factor six. Fig. 10(**b**) shows an optimized spatial configuration of a model without mesh adaptivity. The desired target configuration is not achieved. Two nodes slide along the sharp edge of the notch. As a consequence the notch penetrates the element edge. Thus, the computational results are not significant.

Finally, the spatial configuration in Fig. 10(**c**) belongs to the optimized material configuration depicted in Fig. 9(**b**). It results by applying h-adaptivity with four iteration steps. In comparison to the global mesh refinement Fig. 10(**a**) the adverse time effect is improved. In addition, compared to the coarse meshed model Fig. 10(**b**), the mesh is more accurate. The objective function, including the mean squared error of nodal differences between computed spatial and the target configuration, is thereby reduced from 5.45 (first iteration) to 0.3 (fourth iteration). This is an improvement by factor 4.6, compared to the final optimized coarse meshed model Fig. 10(**b**) with a mean squared error of 1.39.

7 CONCLUSION

An inverse form finding algorithm with material nodal positions acting as design variables is prescribed. The iterative procedure determines an optimized deformed (spatial) configuration. The commonly used h-adaptivity is applied to ensure satisfying numerical result despite of a sharp edge at the geometry of the contact body. For demonstration purposes, the shape of a semi-finished workpiece geometry, belonging to a notch stamping process, is optimized. The minimization criterion, an objective function representing the differences between the spatial computed and the target configuration, is significantly reduced. Further research will be pursued regarding mesh adaptivity in conjunction with the inverse form finding algorithm.

Acknowledgement: This work is part of the collaborative research project *Manufacturing of complex functional components with variants by using a new metal forming process - Sheet-Bulk Metal Forming* (SFB/TR73: www.tr-73.de).

REFERENCES

[1] Altenbach, H.: *Kontinuumsmechanik: Einführung in die materialunabhängigen und materialabhängigen Gleichungen.* Springer Vieweg (2015)

[2] Aymone, F., Lufs, J.: Mesh motion techniques for the ALE formulation in 3D large deformation problems. *Int. J. Numer. Methods Eng.*, **59**(14), 1879-1908 (2004)

[3] Babuvska, I., Rheinboldt, W.C.: Error estimates for adaptive finite element computations. *SIAM J. Numer. Anal.*, **15**(4), 736-754 (1978)

[4] Chenot, J.L., Massoni, E., Fourment, J.: Inverse problems in finite element simulation of metal forming processes. *Eng. Comput.*, **13**(2/3/4), 190-225 (1996)

[5] Demkowicz, L., Devloo, P., Oden, J.: On an h-type mesh-refinement strategy based on minimization of interpolation errors. *Comput. Methods Appl. Mech. Eng.*, **53**(1), 67-89 (1984)

[6] Hinton, E., Campbell, J.: Local and global smoothing of discontinuous finite element functions using a least squares method. *Int. J. Numer. Methods Eng.*, **8**(3), 461-480 (1974)

[7] Landkammer, P., Söhngen, B., Steinmann, P., Willner, K.: On gradient-based optimization strategies for inverse problems in metal forming. *GAMM-Mitt. - Special Issue: Comput. Manuf., (accepted)* (2017)

[8] Landkammer, P., Steinmann, P.: A non-invasive heuristic approach to shape optimization in forming. *Comput. Mech.*, **57**(2), 169-191 (2016)

[9] Merklein, M., Allwood, J., Behrens, B.A., Brosius, A., Hagenah, H., Kuzman, K., Mori, K., Tekkaya, A., Weckenmann, A.: Bulk forming of sheet metal. *CIRP Ann. - Manuf. Technol.*, **61**(2), 725-745 (2012)

[10] Rheinboldt, W.C., Mesztenyi, C.K.: On a data structure for adaptive finite element mesh refinements. *ACM Trans. Math. Softw.*, **62**, 166-187 (1980)

[11] Sieczkarek, P., Wernicke, S., Gies, S., Martins, P.A.F., Tekkaya, A.E.: Incipient and repeatable plastic flow in incremental sheet-bulk forming of gears. *Int. J. Adv. Manuf. Technol.*, **9-12** (2016)

[12] Vierzigmann, U., Koch, J., Merklein, M., Engel, U.: Material flow in Sheet-Bulk Metal Forming. *Key Eng. Mater.*, **Vols. 504-506**, 1035-1040 (2012)

[13] Wriggers, P.: *Nichtlineare Finite-Element-Methoden.* Berlin: Springer (2001)

[14] Yin, Q., Soyarslan, C., Güner, A., Brosius, A., Tekkaya A.E.: A cyclic twin bridge shear test for the identification of kinematic hardening parameters. *Int. J. Mech. Sci.*, **59**, 31-43 (2012)

XIV International Conference on Computational Plasticity. Fundamentals and Applications
COMPLAS 2017
E. Oñate, D.R.J. Owen, D. Peric and M. Chiumenti (Eds)

MEASUREMENT OF STRAIN DISTRIBUTION ON SHEET SPECIMEN IN TENSION TEST VALIDATING TRANSITION OF STRAIN DISTRIBUTION PREDICTED BY FEM

MASAYOSHI AKIYAMA[*], RYO MORIMOTO[†]

[*] Research Institute for Applied Science (RIAS),
49 Tanaka-Ooi-cho, Sakyo-ku, Kyoto, 606-8202, Japan
e-mail: makiyama@rias.or.jp, web page: http://www.rias.or.jp/

[†]2-20-9, Tomatsucho, Amagasaki-shi, Hyogo, 661-0003, Japan
e-mail: rmorimoto0@gmail.com

Key words: Stress-Strain Curve, Tension Test, Sheet Specimen, FEA, Strain Distribution, Transition of Strain, .

Summary *In the present research work the authors tried to measure the non-uniformity of strain on the specimen throughout tension test to validate the results of FEA. Flat specimen of JIS5 was used to investigate the transition process of strain distribution. The material was pure iron. A cast ingot was elongated by hot forging to make a round bar which is 4 times as long as the ingot. The bar was subjected to thermal treatment to homogenize the grain size before flat specimens were sectioned from the bar. Strain gauges were placed on the specimen to monitor the transition of largest strain. An extensometer was also placed to measure the average strain between the two gauge points. Result of FEA analysis predicted that the largest value of strain is observable at the shoulder portion at the initial stage of yielding. The position of largest strain moved to an intermediate portion when the average strain increased and finally moved to the centre portion. The result validated the predicted result by FEA.*

1 INTRODUCTION

Tension test has a long history and has been widely acknowledged as the most common method for evaluating the mechanical properties of materials and it has been used on both academia and industry sides [1]. Major purpose of tension test is obtaining mechanical properties of the material such as a stress-strain curve of the material. Yield stress or Elastic characteristics such as Young's modulus are measured depending upon the customers' request. Stress is calculated by dividing force by the cross sectional area of specimen and strain is calculated by measuring the change in gauge length of the measuring device such as a strain gauge or an extensometer. It is important to note that uniform distribution is assumed of the stress on the cross sectional plane and of the strain in the two gauge points, and the cross sectional plain and the segment connecting two gauge points cross each other. The authors showed that there are cases where these assumptions do not apply**.** Uniformity of stress and

strain distribution is important to ensure the precision of measured curve of stress-strain. The authors showed by using FEA that there is a non-uniform distribution of stress and strain in tension test and there is a transition of peak stress and strain according to the progress of tension test [2]. In COMPLAS2015 the authors presented experimental results to show that these peak shifts might affect the shift of rupture point in tension test and proposed a geometry to ensure the centre rupture [3]. In the present work experimental result is shown to validate the result of FEA on tension test of sheet specimen. Strain gauges were placed on the specimen and transition of the intensity of strain on the specimen was compared with the numerical result.

2 NUMERICAL ANALYSIS

Elastic-plastic FEA was carried out on a sheet specimen subjected to tension test focusing attention on the transition of stress and strain distribution according to the progress of the test. The code used was ELFEN [4] developed at Swansea University.

2.1 Preparations

The geometry of sheet specimen is illustrated in Figure 1. It is basically a JIS5 specimen. Symmetry was taken into consideration and only a quarter in the first quadrant was subjected to the analysis. It was a plane-stress analysis and displacement in X-direction was applied on the nodes in the gripping portion.

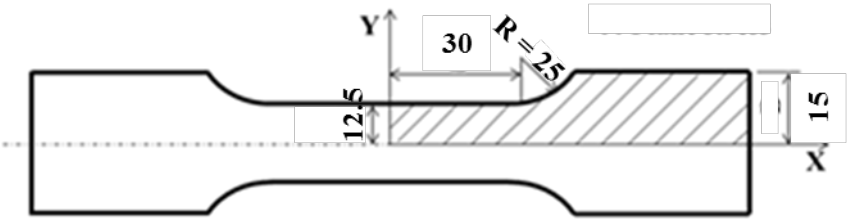

Figure 1: Geometry of specimen and first quadrant subjected to FEA.

Four types of stress-strain curve adopted in the analysis are shown in Figure 2; two types of yield stress and two types of work-hardening ratio. Young's modulus E and Poisson's ratio ν were 210Gpa and 0.3 respectively and were not changed throughout the analysis. Influences of yield stress and work-hardening ratio on the transition of the distributions of stress and strain on the specimen were evaluated.

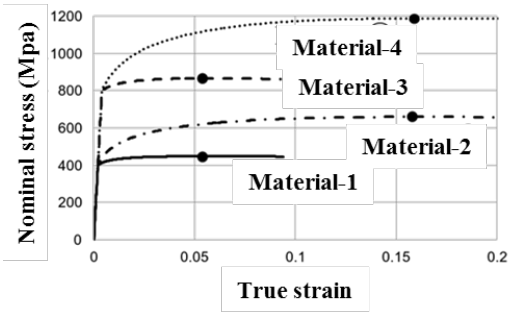

Figure 2: Stress-strain curve used in FEA.

4.2 Result

For the case of material-1 transitions of axial stress and axial strain are illustrated in Figure 3 and 4. Plastic deformation starts in the vicinity of the shoulder portion and new poastic zone suddenly appears on X-axis in between the centre and the shoulder. Finally the highest value of strain moves to the centre and almost uniform distribution of axial stress and axial strain are obtainable in the vicinity of specimen centre. Little influence of work-hardening ratio was observed on the distribution patterns of stress and strain.

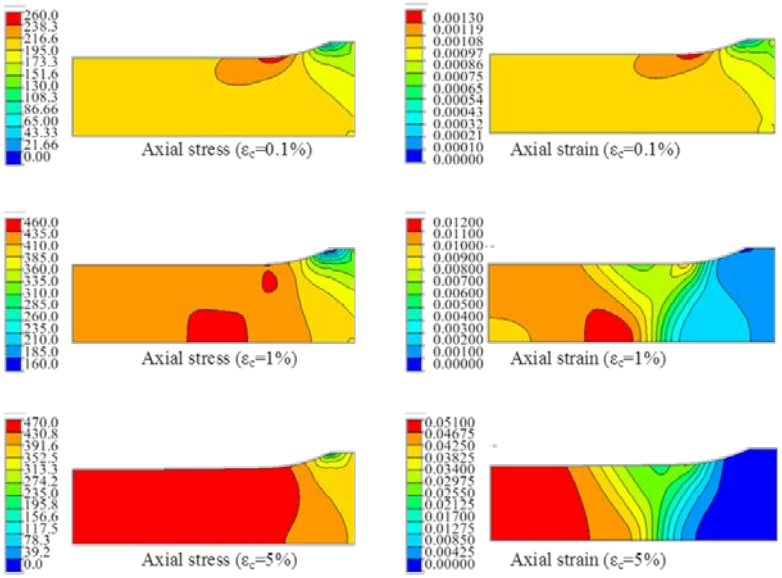

Figure 3: Transition of axial stress and axial strain according to tension test

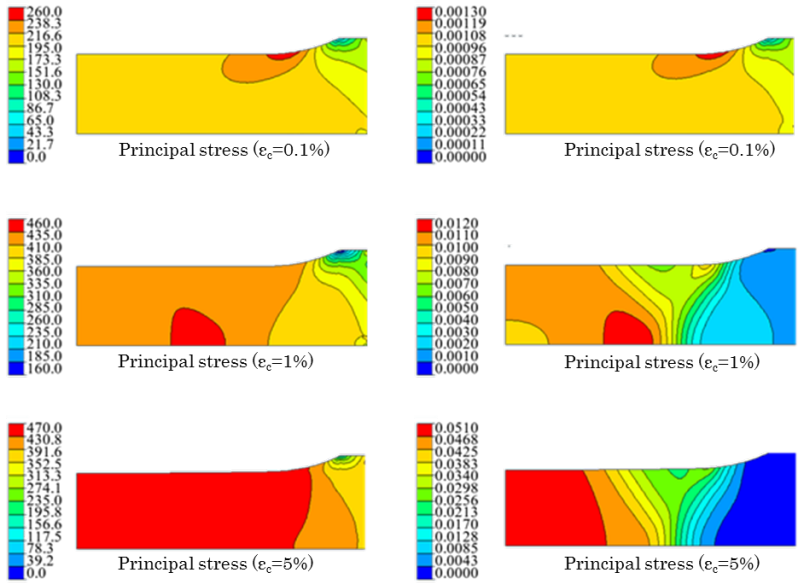

Figure 4: Transition of principal stress and strain according to tenstion test.

3 EXPERIMENT

3.1 Preparations

A 50Kg round ingot of pure iron was cast of which geometry was 310mm in height, 180mm and 130mm in upper and lower diameters. After cooling, the ingot was put in an electric furnace in order to homogenise the grain size. Then specimen for tension test was sectioned from it bu wire cutting. The specimen was JIS5 of which geometry is given in Figure 5. In order to measure the distribution of axial strain, 5 strain gauges were placed in the axial direction on both edges and on the centre line. The number of strain gauges were 15 on both sides of the front and rear surface. The gauges placed on the specimen were plastic gauges which are capable of measuring strain up to 20%. The grid size was 1.5mm wide and 5mm in length and the base size was 3mm wide and 11.5mm in length.

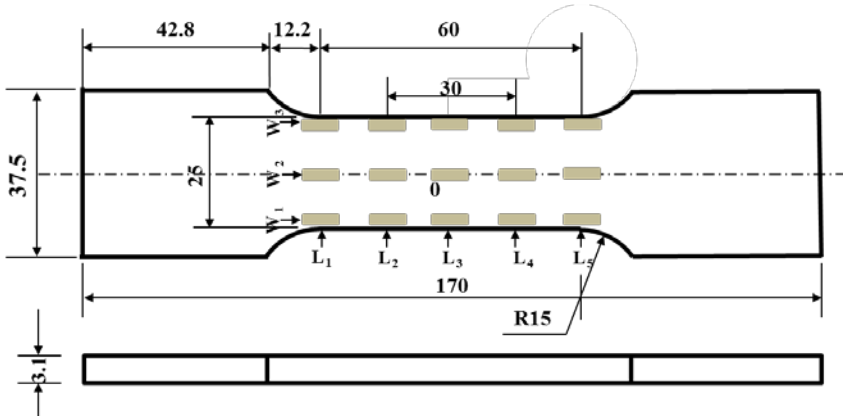

Figure 5: Geometry of sheet specimen of JIS5 and placement positions of strain gauges.

View of the tension test is given in Figure 6. The testing was carried out by using an Instron testing machine with capacity of 200KN. The cross head speed was 2mm/min. The deformation of strain gauges hit 20%, which is the lowest limit of measurable strain of the strain gauge, in the course of the test but the test was carried out until rupture.

Initial setting Testing Necking

Figure 6: View of tension test.

3.2 Result

Measured stress-strain curve obtained by extensometer is shown in Figure 7.

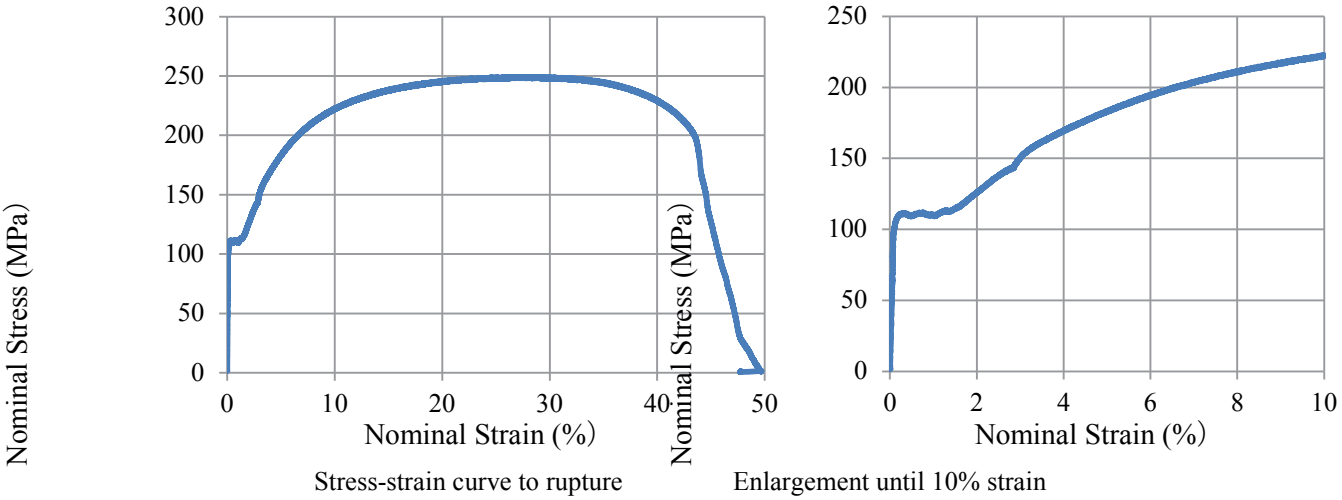

Stress-strain curve to rupture Enlargement until 10% strain

Figure 7: Measured stress-strain curve by load and extensometer.

Increase in the strain on each observation point, i.e. point where strain gauge was placed , is shown in Figure 8. It is shown that shoulder portion immediately respond as soon as tension test starts. Then intermediate portion starts to deform and the plastic strain exceeds that of shoulder portion. Finally the centre portion starts to deform. Extensometer picks up the average value which gradually approaches to the strain at the centre portion. It is curious to note that the axial strain at centre is smaller than those of intermediate and edge portions until the time reaches 200 sec.

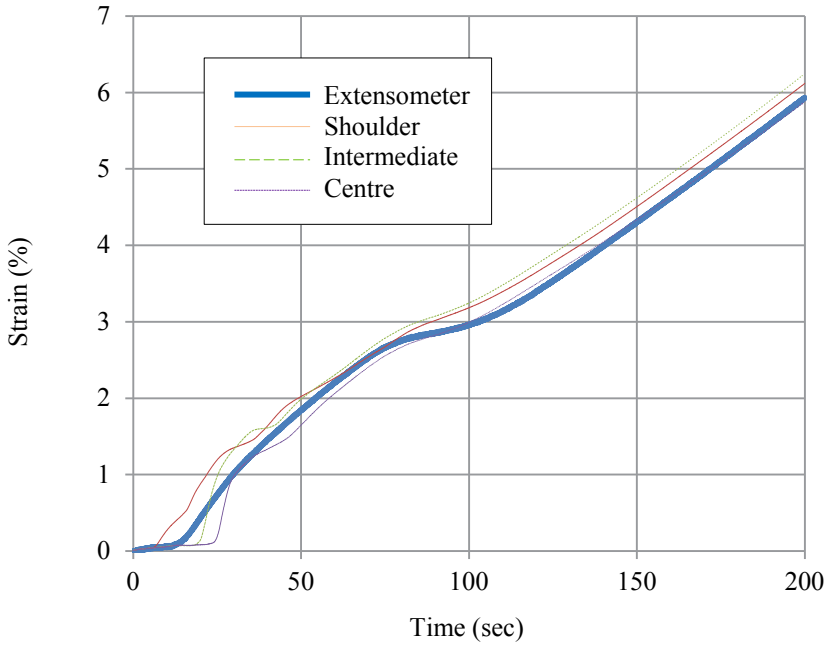

Figure 8: Transition of axial strain according to tension test.

Distribution of strain measured by strain gauges are shown in Table 1. The axial strain on the centre of shoulder portion (b) is 4.45 and is much smaller than those of other observation points, but this is because of the constraint of the gripped portion as it was shown in Figure 4. On the centre plane the distribution of axial strain (Axdial-3(Centre)) is deemed uniform in the width direction, but at the intermediate portion the axial strain on one edge of specimen (c) is considerably smaller than those on the other edge (a) and on the centre line (b). Unfortunately some gauges placed on the intermediate ceentgre plane peeled off after 200 seconds and it was not observed that the peak of strain shifts to the centre. It may be better to carry out more numher of tension test in the same manner.

Table 1: Distribution of axial stress (Time:200sec)

Position	Edge (a)	Centre (b)	Edge (c)
Axial-1(End)	6.39	4.45	5.84
Axial-2(Intermediate)	6.23	6.25	5.75
Axial-3(Centre)	5.82	5.88	5.58

4 CONCLUSIONS

Elastic-plastic FEA was carried out on tension test of sheet speccimen followed by an experiment for validation. Analytical result showed that peak value of axial strain appears at the beginning stage of the test and as soon as the plastic deformation starts on the parallel portion the position of peak strain moves to the intermediate portion, and finally the axial strain at the centre becomes largest. Result of experiment validated that the shoulder portion immediately responds as soon as the test starts but as soon as the plastic strain starts to cover the specimen the peak strain shifts to the intermediate portion as it was predicted by FEA. By repeating tension in the same manner peak shift of axial strain to the centre plane will be observed as was predicted by FEA.

ACKNOWLEDGEMENT

The authors would like to thank Ministry of Economy Trade and Industry, Japan for the experimental part of the present work was supported by the fund titled “Development of a method for the next generation on the measurement and evaluation of steel” in the fiscal year 2016.

REFERENCES

[1] ASTM E8 / E8M - 16a, Standard Test Methods for Tension Testing of Metallic Materials
[2] R. Morimoto and M. Akiyama, Propagation Mechanism of Non-uniform Distribution of Stress and Strain in Tension Test, COMPLAS-XII, 631 (2013).
[3] R. Morimoto and M. Akiyama, Proposal of New Specimen Geometry for Tension Test Restraining Non-Uniform Deformation, COMPLAS-XIII, 968 (2015).
[4] ELFEN : Rockfield Software Limited

XIV International Conference on Computational Plasticity. Fundamentals and Applications
COMPLAS XIV
E. Oñate, D.R.J. Owen, D. Peric & M. Chiumenti (Eds)

ATOMISTIC SIMULATION OF THE CHANGE IN MICROSTRUCTURE OF A POLYCRYSTALLINE FCC METAL UNDER COMPRESSION

TAKUYA UEHARA*

* Department of Mechanical Systems Engineering
Yamagata University
Jonan 4-3-16, Yonezawa 992-8510, Japan
e-mail: uehara@yz.yamagata-u.ac.jp
web page: http://uhlab.yz.yamagata-u.ac.jp

Key words: Microstructure, Deformation, Molecular Dynamics, Computer Simulation, Grain Boundary

Abstract. In this study, the change in microstructure during large deformation is simulated using molecular dynamics method. A polycrystalline fcc model consisting of four grains with periodic boundary condition is prepared, and a compressive external force is imposed on the model. The plastic deformation behavior, such as change in grain shape, motion of grain boundary, generation of dislocation and slip, are investigated. Initial orientation of every grain and the combination of the adjacent grains are varied, and the dependency of the crystallographic conditions on the change in microstructure along with the stress-strain relation are investigated. As a result, grain refinement due to generation of grain boundaries revealed to strongly depend on the relation between the original crystal orientation and imposed load direction.

1 INTRODUCTION

Mechanical properties of a material depend strongly on the microstructure, and hence various methods have been developed to improve the microstructure. One of the most simple indicators representing the state of microstructure is grain size, and the strength of the material is generally stronger as the grain size is smaller. This relation is well known as Hall-Petch relation, and to refine the grain size is generally effective to make the material stronger. Therefore, sustained effort have been devoted to refine the crystal grains; some of the successful schemes are equal-channel angular pressing (ECAP)[1], accumulative roll bonding (ARB)[2], and asymmetric rolling[3] methods, and these processes have been applied to industrial purposes. The common condition in these processes is that the material is subjected to severe plastic deformation, and especially compressive load is the key factor. However, the mechanism of the grain refinement is not straightforward, and many kinds of researches have been ongoing. Experimental observation of

the microstructure using electron backscatter diffraction (EBSD) method is quite effective to investigate the change in microstructure, but the dynamic mechanism is not directly observed. Several kinds of electron microscopy have made it possible to observe the atomistic real image, but the dynamic motion is not yet observable. Therefore, computer simulation is indispensable for clarification of the mechanism, and the molecular dynamics (MD) method is the most suitable for the purpose. A great number of researches have been reported on the deformation mechanism of polycrystalline materials based on MD simulations, and various kind of fundamental plastic behaviors such as generation and motion of dislocation, grain-boundary migration, change in crystal orientation, and their relation and interactions [4-8]. The author has demonstrated MD simulations on plastic deformation and related phenomena such as grain-boundary stability and change in shape of a polycrystalline material [9], shape-memory behavior [10], and transformation-induced plasticity [11]. We are now motivated to investigate the mechanism of grain refinement due to large deformation. In our previous report [12], change in microstructure under tensile load was simulated, and grain-boundary migration and change in grain shape were observed. In this study, supposing the grain refinement, a large compression is imposed to the same model, and the change in grain shape and size is investigated.

2 MODEL AND CONDITIONS

2.1 Fundamental equations

In this study, a classical molecular dynamics method is used. The fundamental equation is the following Newton's equation of motion, and the force $\boldsymbol{F}_i$ acting on the i-th atoms is assumed to be represented by a Lennard-Jones-type interatomic potential function ϕ.

$$\frac{\mathrm{d}^2\boldsymbol{r}_i}{\mathrm{d}t^2} = \boldsymbol{F}_i, \quad \boldsymbol{F}_i = -\sum_{j\neq i}^{N} \frac{\mathrm{d}\phi}{\mathrm{d}r}\frac{\boldsymbol{r}_{ij}}{|\boldsymbol{r}_{ij}|}, \tag{1}$$

with

$$\phi = 4\varepsilon\left((\frac{\sigma}{r_{ij}})^{12} - (\frac{\sigma}{r_{ij}})^{6}\right) \tag{2}$$

Here, $\boldsymbol{r}_i$ is the position vector of the i-th atoms from the origin, and $\boldsymbol{r}_{ij} = \boldsymbol{r}_j - \boldsymbol{r}_i$. The variables in LJ potential ε and σ are the material parameters in the dimension of energy and length, respectively. For a generalized analysis, the equations are non-dimensionalized. Then the potential parameters are diminished, and other physical quantities including stress and temperature are all shown in the non-dimensional values in this paper.

2.2 Simulation model

A simplified polycrystalline model is used to capture the fundamental feature of the grain refinement. Figure 1 represents the schematic illustration of the model; two types are prepared, each of which consists of four grains while the grain arrangement differs from each other: a transversal grain boundary is perpendicular to the loading direction in Type A, while they are parallel in Type B. Periodic boundary conditions are applied in all

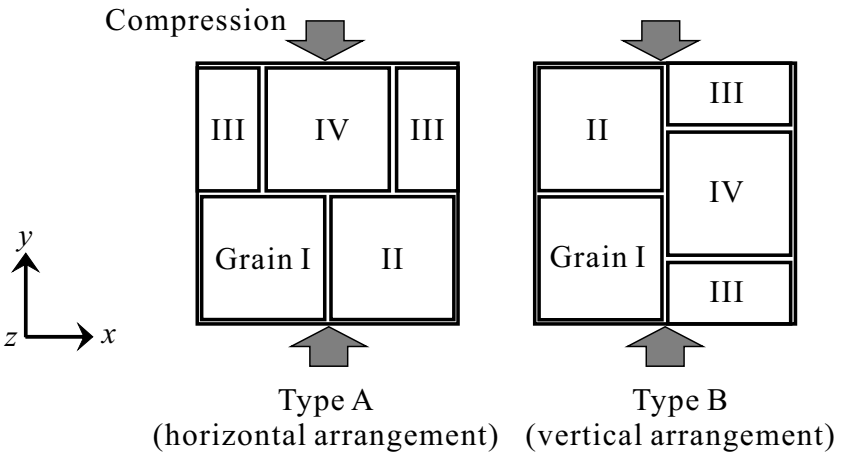

Figure 1: Illustration of the simulation model.

directions. The thickness of the model in the z direction is taken very small; every grain corresponds to infinitely long columnar one. A compressive load is imposed by decreasing the length L_y in the y direction. The lengths L_x and L_z in the x and z directions are adjusted so that the average stress component σ_{xx} and σ_{zz} are kept at zero, while the model retains rectangular parallelepiped.

The atoms are set on the lattice points of fcc crystal so that the (001) plane is on x-y plane and [100] direction is along the x axis, and the number of unit cells are 50×50×5 in the x, y and z directions. Then the atoms are rotated around the z axis by angle θ_k, in which k identify the grain number from I to IV in Fig. 1. The values in the angles are varied, and the results for the combination represented in Table 1 are shown in this paper.

Table 1: Grain angles and their combination for the simulation models presented in this paper.

Model ID \ Grain No.	I	II	III	IV
A1, B1	26.6°	-26.6°	18.4°	-18.4°
A2, B2	26.6°	-18.4°	18.4°	-26.6°
A3, B3	26.6°	18.4°	-26.6°	-18.4°

$26.6^\circ = \tan^{-1}1/2$, $18.4^\circ = \tan^{-1}1/3$

Grain boundaries constructed in Models A1-A3 and B1-B3 are mostly coincident site lattice (CSL) boundaries. For example, in Model A1 and B1, the grain boundaries between Grain I and II, and between III and IV are typical CSL boundaries indicated by low-index sigma values.

2.3 Conditions

The initial configuration of atoms are relaxed for 15000 time steps under constant temperature at T=0.1 and no stress condition. Then compressive load is applied in the y direction by decreasing the edge length L_y in the y diction at a constant decrement $\Delta L_y/t_s$. Here, ΔL_y is the total shrinkage in length and t_s is time steps of the compression period, the these values in this study are taken as ΔL_y=25.0 and t_s=50000. Actually, the initial length L_y^0 at the relaxation period is slightly different for every models, but nearly L_y^0=73.0. Accordingly, the total compressive strain is about 0.34. After the loading period of 50000 time steps, the model is unloaded; the average stress in the y direction is also released, and 5000-step relaxation period is assigned.

3 RESULTS AND DISCUSSION

3.1 Change in microstructure

Simulation results for Model A1 is shown in this section. Figure 2 represents the snapshots of the atomic configuration projected on the x-y plane. The color indicates potential energy of each atom; the atoms in bulk grain have low energy, depicted in blue, whereas the atoms at grain boundaries have higher energy, and depicted in green or yellow.

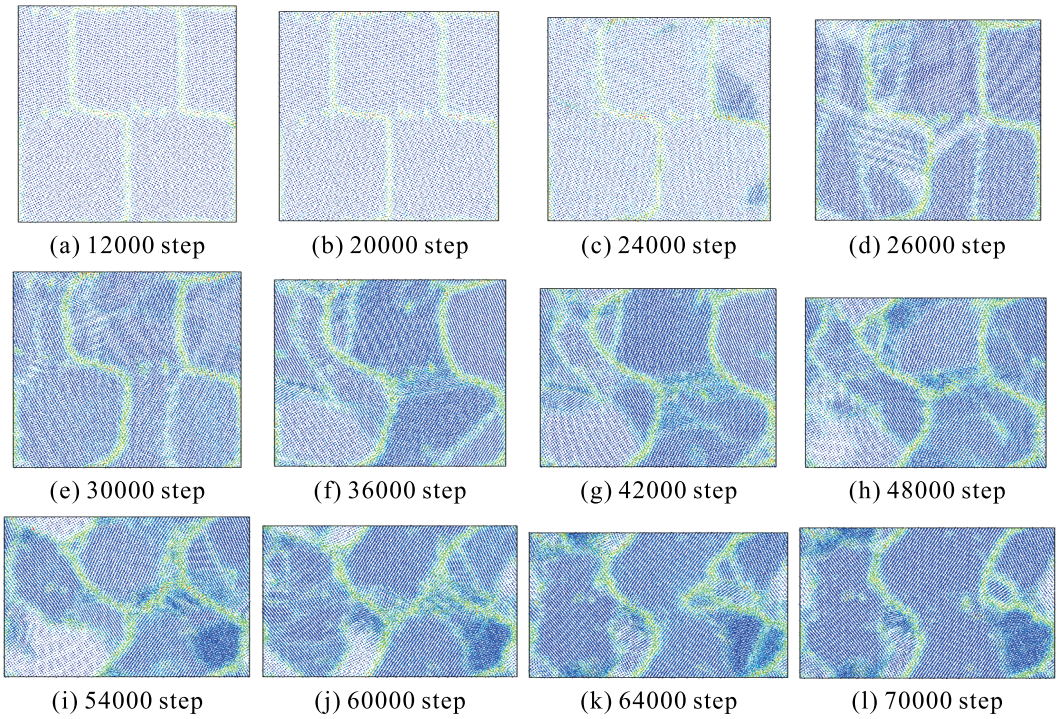

Figure 2: Configuration of atoms for Model A1, in which the color indicates the potential energy of every atom; green and yellow show grain-boundary region.

Figure 2(a) shows a stabilized state by the relaxation period, which represents all grains mostly retain square shape.

Then the compressive load is imposed from the 15000th time step. No specific change is observed at the 20000th time step, but an apparent change is observed at the 24000th time step at the left bottom corner in Grain III; The color is the same in blue but looks denser. This is due to the projection angel on the x-y plane; i.e. initially the z direction is exactly [001] in all grain and all atoms align straight, but the alignment changed when rotation or change in orientation change occurs. Therefore, Figure 2(c) indicates that orientation change is initiated in Grain III. A small change is also observed in right bottom corner in Grain II. These orientation change spread inward grain quickly by the 26000th time step as shown in Fig. 2(d). Simultaneously various changes are observed in other grains; New grain boundaries depicted in green color, are generated. In all of the four grains, a vertical boundary at the middle is observed, while some of which are temporally appeared, and are not observed at the 30000th time step, as shown in Fig. 2(e).

The initial grain shape and grain boundaries are mostly maintained at the 30000th time step, but extreme deformation occurs thereafter: the original square shapes are almost completely unobservable at the 36000th time step shown in Fig. 2(f), and small grains surrounded by the new boundaries is generated.

The main grain boundaries which originate from the initial ones retain even though the grain shapes changed, and depicted in clear and relatively wide lines at the 48000th time step. However, as further compression is imposed, some of them become apparent, and the Grain II and IV is finally unified at the central domain in the model at the 64000th time step. The reason is, however, not only the large strain but may be the influence of the periodic boundary condition. The model height becomes smaller and periodic boundary makes one grain sandwich another, and strong restriction may affect too much. Final unloading makes overall slight recovery in model height in the y direction, but apparent change in microstructure is not observed.

3.2 Stress-strain curve

The variation of the overall stress is shown in Fig. 3 (a), in which the length in the y direction is also drawn. As the compression starts at the 15000th time step, compressive stress increases monotonously by the 24000th time step. Along with the result shown in Fig. 2 that no specific change in the configuration of atoms is observed, the deformation is elastic region, and the gradient corresponds to the elastic coefficient.

The stress drops drastically between the 24000th and 26000th time steps. This is the initiation of the plasticity, as crystallographic irregularity is observed in Figs. 2(c) and (d). Then the stress starts increasing again, and a similar behavior as the initial elastic region is exhibited by the second peak in stress at the 3000th time step. After the following stress drop, the stress increase and drastic drop are not clearly appeared, whereas gradual increase by the 45000th time step, and mostly flatten at the about σ_y=2.0. The compression is stopped at the 65000th time step, and stress is released. In the stress-strain curve shown in Fig. 3(b), elastic recovery by the unload process is clearly represented.

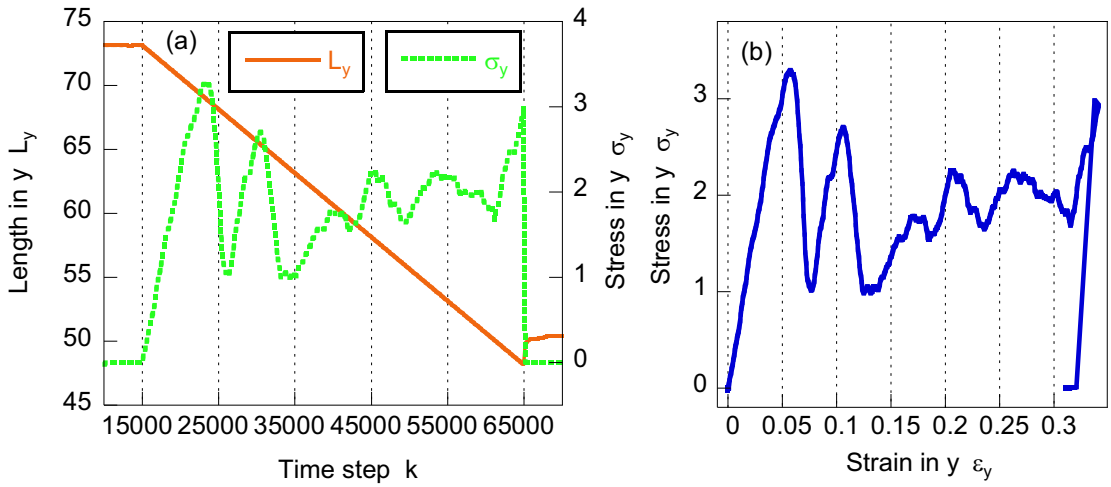

Figure 3: Simulation result for Model A1. Variation of the length in the y direction and stress in y (a), and stress-strain curve (b) .

3.3 All results

The results for the other models are summarized in Figs. 4 and 5. Figure 4 shows the snapshots at the 48000th time step, and Fig. 5 shows stress-strain curves. Grain refinement is observed for every case, and the original square grain shape has disappeared. Only the retained feature of the initial grain feature is a straight grain boundary which transects the model in Models A3 and B3. These boundaries are both constructed by two CSL boundaries between $\pm 26.5^\circ$ and $\pm 18.4^\circ$ which are very stable and seems unaffected by the large straining.

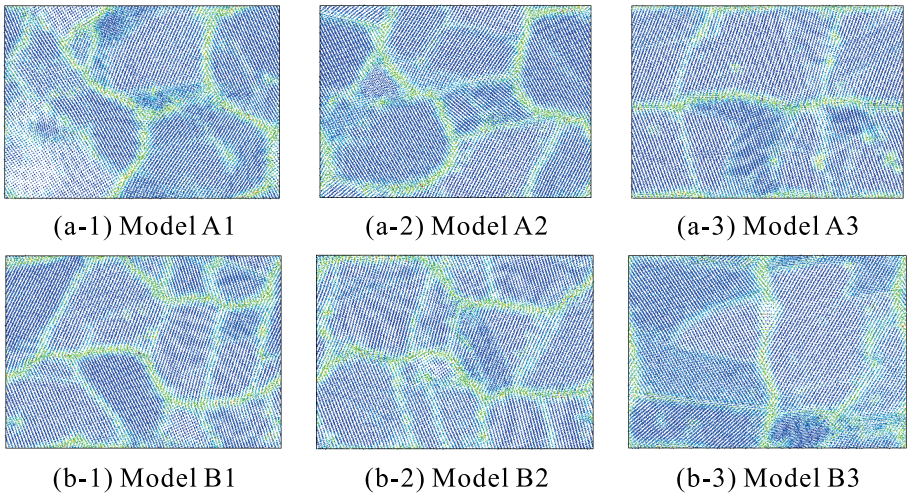

Figure 4: Configuration of atoms at the 48000th time step for all models, in which the color indicates the potential energy of every atom.

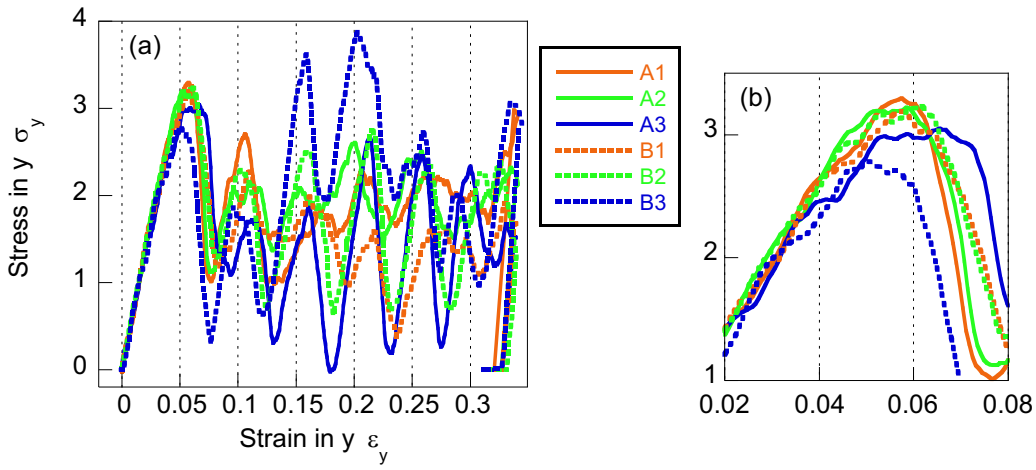

Figure 5: Stress-strain curves for all models (a) and the magnified plots around the first peaks around between ε=0.02 to 0.08 (b).

Stress-strain relation is overall common to all cases; the stress increases monotonically at first, drastically drops following the first peak, and thereafter, gradual increase and drastic drop are intermittently repeated. However, the peak values and the event interval are not identical. For example, the first peak, which is assumed to be the yielding stress, differs as shown in the magnified diagram in Fig. 5(b). Models A1, A2, B1 and B2 have almost identical peak value of σ_y=3.1, while Models A3 and B3 show lower value. The former 4 models commonly exhibit continuously smooth round peak from mostly linear elastic region to the stress drop. In Models A3 and B3, on the contrary, the curve deviate from the elastic curve once at $sigma_y$=2.1 for B3 and 2.4 for A3, and increase again till the peak values of $sigma_y$=2.8 for B3 and 3.0 for A3. In the configuration of atoms, specific features are observed for these two models, as discussed above, and such features may affect the overall stress-strain relation. Detailed investigation on the bases of atomic arrangement, crystal orientation, and grain-boundary structures will be discussed in our future work.

4 CONCLUSIONS

In this study, molecular dynamics simulations were carried out on the atomistic behavior of a polycrystalline fcc material under large compressive deformation. A simplified model with four grains is prepared, and six models which are different in grain arrangement and crystal orientation. All the model consist of typical CSL grain boundaries, while some are different. As a result, change in microstructure is observed for all models when a large compressive strain is imposed. Some of the grains are divided into two or more subgrains, and grain refinement was observed for all cases. The dependence of the grain boundary structure was inferred by a specific behavior found for two models which commonly have straight CSL boundary traversing the model. Further investigation including much more variation of grain arrangement, structure of grain boundaries, and

combination of crystal orientations is necessary to clarify the mechanism of the grain refinement. This study, nevertheless, revealed the effectiveness of the model for the purpose, and hence we will continue the research using the present model.

REFERENCES

[1] Segal, V.M. Equal channel angular extrusion: from macromechanics to structure formation. *Mater. Sci. Eng. A* (1999) **271**: 322-333.

[2] Saito, Y., Utsunomiya, H., Tsuji, N. and Sakai,T. Novel ultra-high straining process for bulk materials — development of the accumulative roll-bonding (ARB) process. *Acta Mater.* (1999) **47**: 579-583.

[3] Sidor, J., Miroux, A., Petrov, R. and Kestens, L. Microstructural and crystallographic aspects of conventional and asymmetric rolling processes. *Acta Mater.* (2008) **56**: 2495-2507.

[4] Van Swygenhoven, H., Caro, A. and Farkas, D. A molecular dynamics study of polycrystalline fcc metals at the nanoscale: grain boundary structure and its influence on plastic deformation. *Mater. Sci. Eng. A* (2001) **309-310**: 440-444.

[5] Wolf, D., Yamakov, V., Phillpot, S.R., Mukherjee, A. and Gleiter, H. Deformation of nanocrystalline materials by molecular-dynamics simulation: relationship to experiments? *Acta Mater.* (2005) **53**: 1-40.

[6] Trautt, Z.T. and Mishin, Y. Grain boundary migration and grain rotation studied by molecular dynamics. *Acta Mater.* (2012) **60**: 2407-2424.

[7] Farkas, D. Atomistic simulations of metallic microstructures. *Current Opinion in Solid State and Mater. Sci.* (2013) **17**: 284-297.

[8] Hahn, E.N. and Meyers, M.A. Grain-size dependent mechanical behavior of nanocrystalline metals. *Mater. Sci. Eng. A* (2015) **646**: 101-134.

[9] Uehara, T., Wakabayashi, N., Hirabayashi, Y. and Ohno, N. An atomistic study of grain boundary stability and crystal rearrangement using molecular dynamics techniques. *Int. J. Mech. Sci.* (2008) **50**: 956–965.

[10] Uehara, T., Asai, C. and Ohno, N. Molecular dynamics simulation of shape-memory behaviour using a multi-grain model. *Model. Simul. Mater. Sci. Eng.* (2009) **17**: 035011.

[11] Uehara, T. Molecular dynamics simulation on transformation-induced plastic deformation using a Lennard-Jones model. *Key Eng. Mater.* (2015) **626**: 414-419.

[12] Uehara, T. Molecular dynamics simulation of the variation in the microstructure of a polycrystalline material under tensile load. *Key Eng. Mater.*, to appear.

XIV International Conference on Computational Plasticity. Fundamentals and Applications
COMPLAS 2017
E. Oñate, D.R.J. Owen, D. Peric and M. Chiumenti (Eds)

THREE-DIMENSIONAL NUMERICAL ANALYSIS OF ROTARY PIERCING PROCESS

KOJI YAMANE†, KAZUHIRO SHIMODA† AND AKIHITO YAMANE†

† Research and Development, Process Research Laboratories
Nippon Steel and Sumitomo Metal Corporation
1-8 Fuso-Cho, Amagasaki, Hyogo, 660-0891, Japan
e-mail: yamane.6nq.kohji@jp.nssmc.com

Key words: Rotary Piercing, Seamless Tube, FEM, Toe Angle, Feed Angle, Shear Strain.

Abstract. Three-dimensional numerical analysis of the rotary piercing process was performed by the rigid plastic finite element method. Rotary piercing, also known as the Mannesmann piercing process, is a hot rolling process that manufactures seamless tubes. In this process, the heated round billet is rotated by the rolls and pierced by the plug as an internal tool. Numerical analysis was conducted to investigate the deformation behaviour during rotary piercing and redundant shear deformation specific to this process. This paper discusses the effect of various rolling parameters on redundant shear deformation.

1 INTRODUCTION

The rotary piercing process is one method for manufacturing seamless tubes that are used for oil country tubular goods and so forth. It is also known as the Mannesmann piercing process, the concept of which was invented by the Mannesmann brothers in Germany in 1886. More than 100 years later, a cone-type piercing mill with a high toe angle was developed by Sumitomo Metal Industries, Ltd. In this process, the heated round billet is rolled by a pair of rolls and held by a pair of guide rolls. The axes of the rolls are inclined opposite to each other in order to advance the round billet. The round billet is rotated by the rolls and pierced by the plug as an internal tool. While the round billet is rotated helically, the wall thickness is reduced by rolling with the rolls and the plug. As previously described, the tube is subject to large deformation in this process. Moreover, little study has been done concerning complex boundary conditions in this process: the round billet has a free surface, the billet-roll contact area is narrow, and the direction of the friction forces affecting the billet-roll contact surface often changes. It was thus difficult to model the numerical analysis of the rotary piercing process. Therefore, the boundary conditions were investigated in a hot rolling experiment. Setting the boundary conditions that match the experimental results, the three-dimensional numerical analysis model of the rotary piercing process was developed by the rigid plastic finite element method in 2006. The developed numerical analysis was undertaken in order to investigate the deformation behaviour during rotary piercing and redundant shear deformation specific to this process. Such redundant shear deformation is considered to be one of the parameters that may cause propagation defects on the internal surface of the tube. This paper puts its focus on the effect of various rolling parameters on redundant shear deformation.

2 NUMERICAL ANALYSIS MODEL

Three-dimensional deformation analysis was performed by the rigid plastic finite element method using DEFORM-3D. The numerical analysis model of the rotary piercing process is shown in **Fig. 1**. The rolls rotate in the same direction with a constant rotational velocity of 60 rpm, the disc guide rolls rotate in the opposite directions with a constant rotational velocity of 4.0 rpm, and the plug is rotated by the rolled billet. All the tools were modeled as rigid bodies, the billet was modeled as Lagrange tetrahedral elements, the billet material was carbon steel C45, and the billet temperature was 1200°C. This numerical analysis assumed a mechanical calculation scheme. To investigate the boundary conditions, the deformation behavior of the tube was analyzed in the hot rolling experiment. This experimental results showed that the circumferential velocity of the rolled material was slightly lower than that of the roll. Since hardly any metal relative to the roll slipped, the friction model of the roll was approximated to sticking. Assuming that the friction model depends on the metal slipping velocity relative to the tool, the shear friction coefficient m for the roll was set to 1.0.

In the hot rolling experiment and the developed numerical analysis, the toe angle γ and the feed angle β were varied. The toe angle γ is the opening angle of the roll axis with respect to the pass line. As shown in **Fig. 2**, the roll diameter varies depending on the toe angle γ to keep the roll face angle α constant. **Figure 3** shows the feed angle β that is the inclination angle of the roll axis with respect to the pass line. As the feed angle β is increased, the advance direction velocity of the rolled material increases.

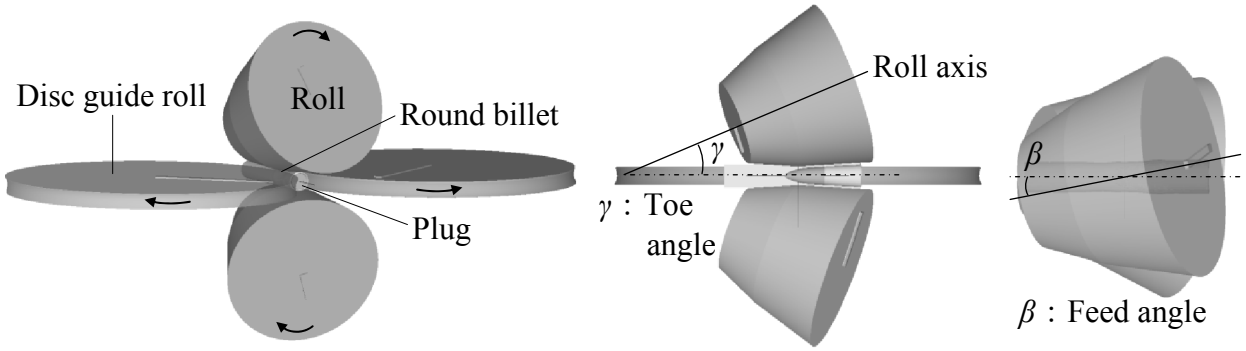

Figure 1: Numerical analysis model of the rotary piercing process.

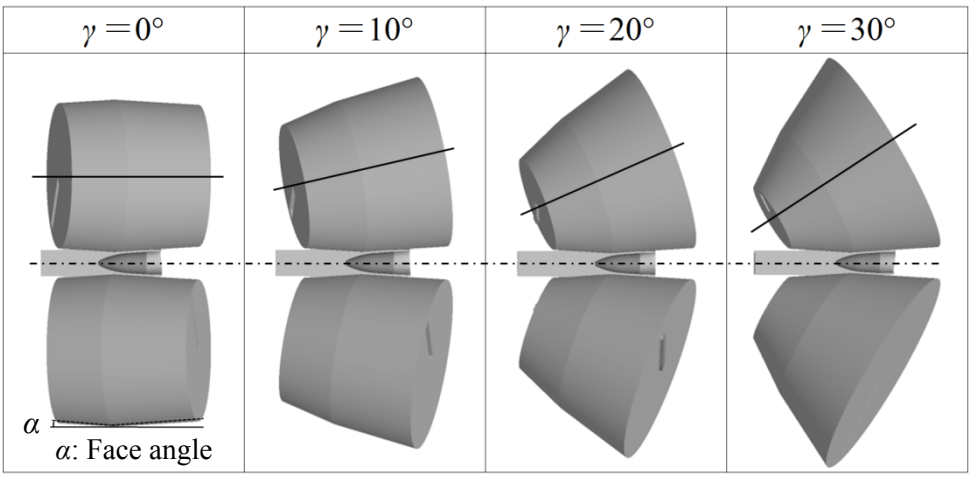

Figure 2: Schematic of the toe angle γ (at the feed angle β = 10°).

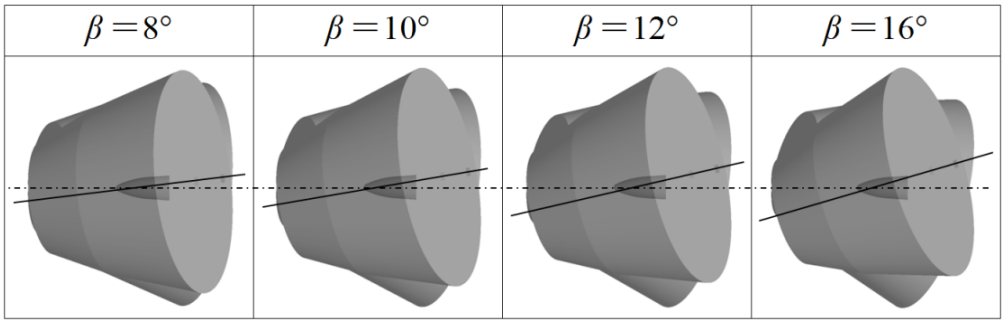

Figure 3: Schematic of the feed angle β (at the toe angle $\gamma = 20°$).

3 NUMERICAL ANALYSIS MODEL VALIDATION

3.1 Dimensional accuracy

To validate the developed numerical analysis model, the dimensions of the tube in the numerical analysis were compared with those of the hot rolling experiment. **Figure 4** shows both the longitudinal and transverse sections of the semi-finished product. The upper part shows the experimental results and the lower part shows the numerical analysis results. The numerical analysis results agree with the experimental results concerning the shape of the semi-finished product. As shown in **Fig. 5**, the difference in the circumferential length of the semi-finished product between the experiment and the numerical analysis was less than 2%.

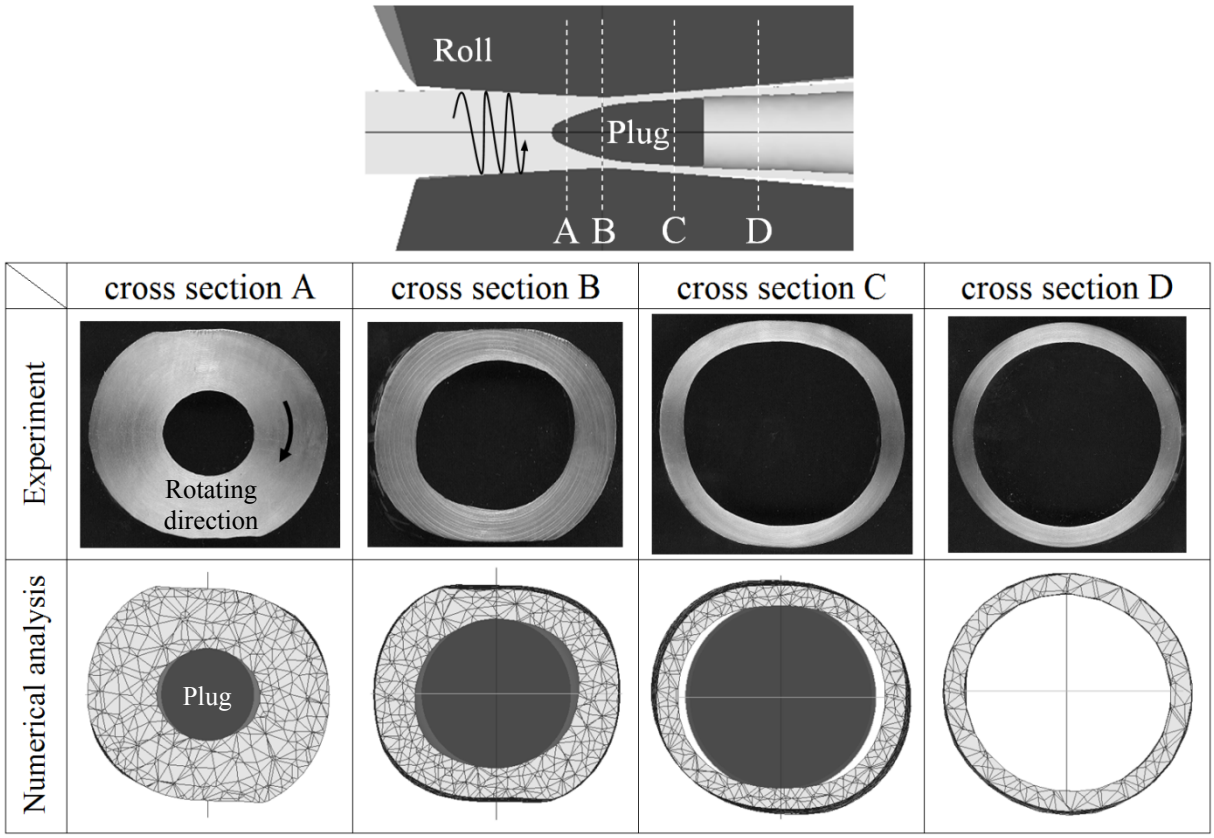

Figure 4: Shape of the semi-finished product during rotary piercing.

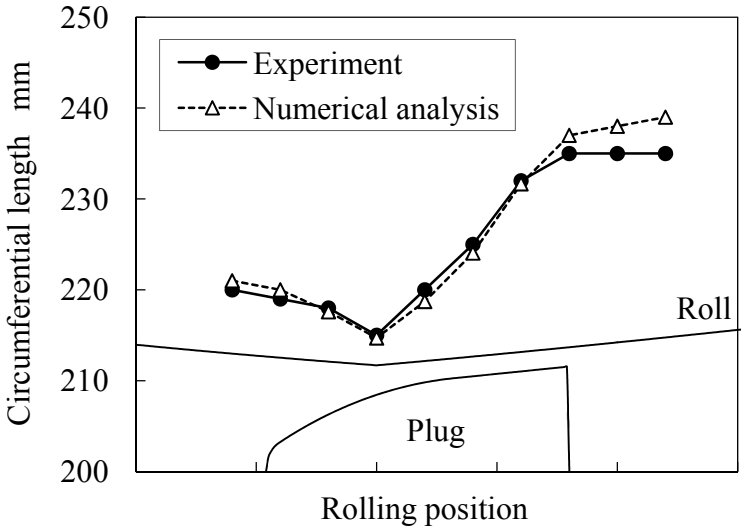

Figure 5: Comparison of the circumferential length of the semi-finished product between the experiment and the numerical analysis.

3.2 Circumferential shear deformation

In the rotary piercing process, the external surface of the rolled material follows the roll, whereas its internal surface follows the plug. Since the external surface velocity is larger than the internal surface velocity, the circumferential velocity difference between the external surface of the rolled material and its internal surface is generated. As a result, redundant shear deformation occurs in the circumferential direction when the round billet is rolled by the rolls and the plug. The measurement of circumferential shear strain $\gamma_{r\theta}$ is illustrated in **Fig. 6**. In the experiment, the twist angle θ in the circumferential direction was investigated by rolling a billet filled with Kanthal wire. In the numerical analysis, the twist angle θ in the circumferential direction was investigated by measuring the material flow in the rolling cross section. **Figure 7** shows the comparison of the twist angle θ in the circumferential direction between the experiment and the numerical analysis in each rolling cross section. The twist angle θ in the experiment was 30° and the twist angle θ in the numerical analysis was 32°. The developed numerical analysis results show agreement with the experimental results concerning circumferential shear strain $\gamma_{r\theta}$.

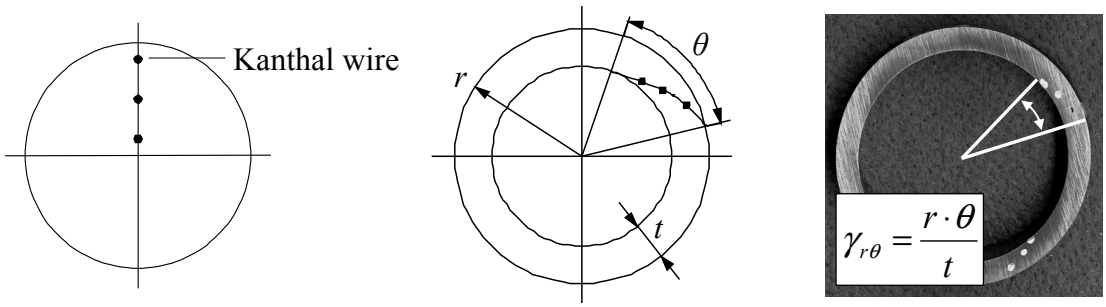

Figure 6: Measurement of circumferential shear strain $\gamma_{r\theta}$.

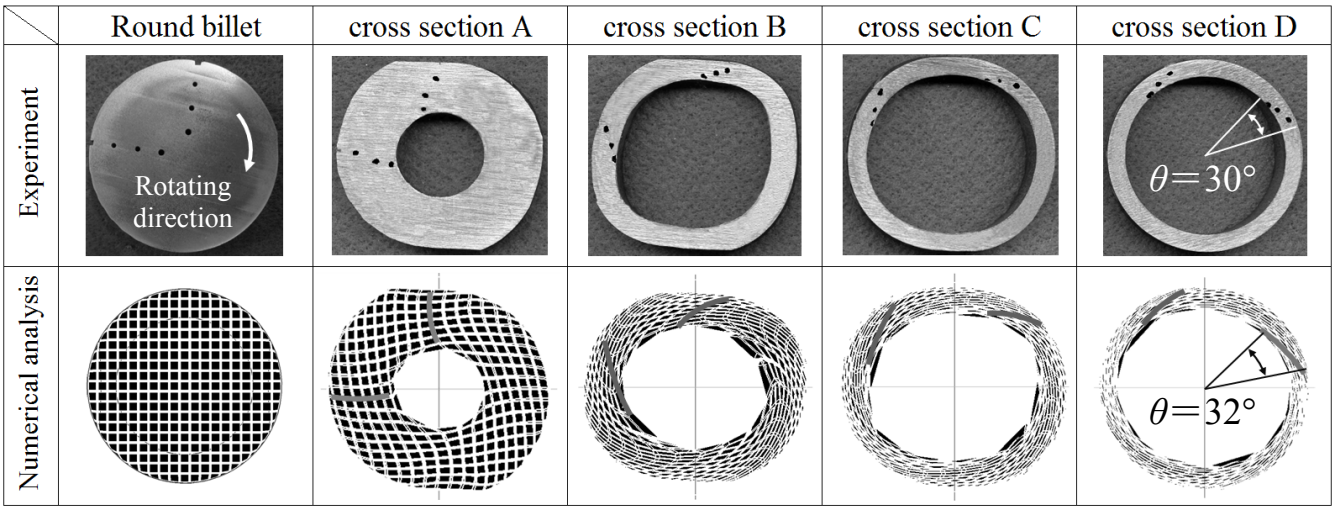

Figure 7: Comparison of the twist angle θ in the circumferential direction between the experiment and the numerical analysis.

4 RESULTS AND DISCUSSION

4.1 Effect of toe angle γ on circumferential shear strain $\gamma_{r\theta}$

Figure 8 shows the effect of the toe angle γ on circumferential shear strain $\gamma_{r\theta}$. The rolling conditions were the feed angle β = 10°, the elongation ratio (rolled length L' / billet length L) = 3.0, and the diameter expansion ratio (rolled diameter D' / billet diameter D) = 1.06. In the experiment and the numerical analysis, circumferential shear strain $\gamma_{r\theta}$ was suppressed as the toe angle γ was increased. The cause of this phenomenon was that the roll diameter varied due to the toe angle γ. As the toe angle γ is increased, the roll diameter on the inlet side is smaller. At the high toe angle, the small roll diameter on the inlet side allows a decrease in the external surface velocity of the rolled material. On the other hand, the internal surface velocity of the rolled material is affected by the plug geometry. Taking these results into account, on the inlet side of the roll, the circumferential velocity difference between the external surface of the rolled material and its internal surface decreases as the toe angle γ is increased.

Figure 9 shows the increment of the twist angle θ in the circumferential direction during rotary piercing. The numerical analysis confirmed that the twist angle θ increased on the inlet side of the roll. On the inlet side of the roll, decreasing the plug diameter led to an increase in the circumferential velocity difference of the rolled material. Reducing the wall thickness of the tube under the condition that the circumferential velocity difference of the rolled material was large, the twist angle θ increased significantly. On the outlet side of the roll, increasing the plug diameter led to a decrease in the circumferential velocity difference of the rolled material. Additionally, since the wall thickness of the tube was slightly redused, the twist angle θ hardly increased. Consequently, the twist angle θ in the toe angle γ = 0° was twice as large as the twist angle θ in the toe angle γ = 30°. It is interpreted from this study that decreasing the circumferential velocity difference of the rolled material on the inlet side of the roll due to the toe angle γ suppresses circumferential shear strain $\gamma_{r\theta}$.

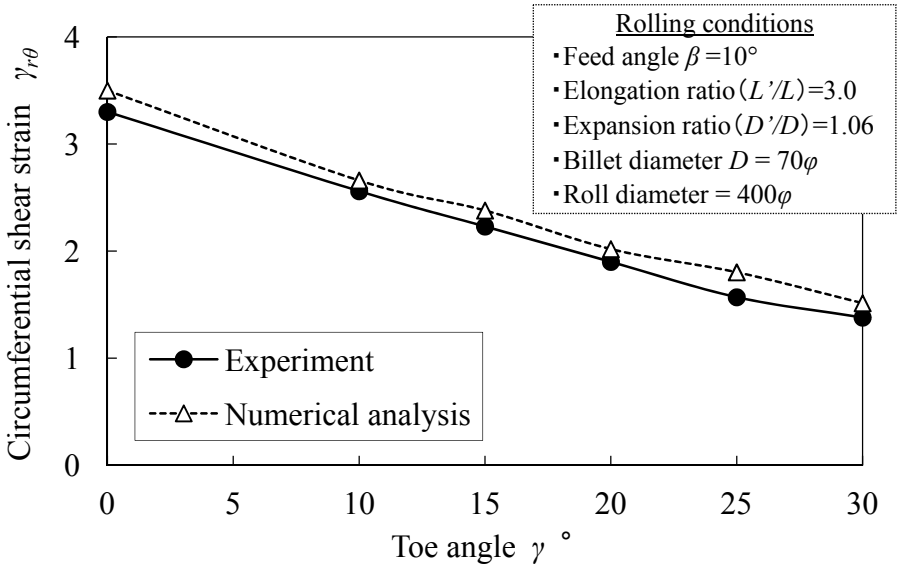

Figure 8: Effect of the toe angle γ on circumferential shear strain $\gamma_{r\theta}$.

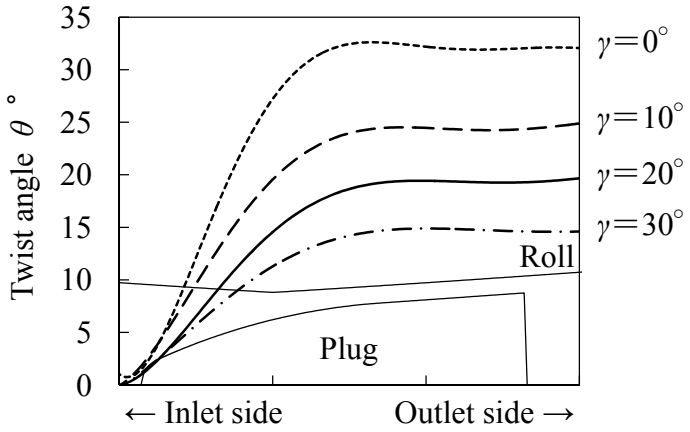

Figure 9: Increment of the twist angle θ in the circumferential direction during rotary piercing in the numerical analysis.

4.2 Effect of feed angle β on circumferential shear strain $\gamma_{r\theta}$

Figure 10 shows the effect of the feed angle β on circumferential shear strain $\gamma_{r\theta}$. The rolling conditions were the toe angle γ = 20°, the elongation ratio (rolled length L' / billet length L) = 3.0, and the diameter expansion ratio (rolled diameter D' / billet diameter D) = 1.06. In the experiment and the numerical analysis, circumferential shear strain $\gamma_{r\theta}$ was suppressed as the feed angle β was increased. This phenomenon was attributed to that the advance direction velocity of the rolled material increased in proportion to sin β. Therefore, the number of rolling times decreased as the feed angle β was increased. The effect of the feed angle β on the number of rolling times is shown in **Fig. 11**. The numerical analysis confirmed that most of circumferential shear strain $\gamma_{r\theta}$ occured when the tube was rolled by the rolls and the plug. The results from this study indicates that decreasing the number of rolling times due to the feed angle β suppresses circumferential shear strain $\gamma_{r\theta}$.

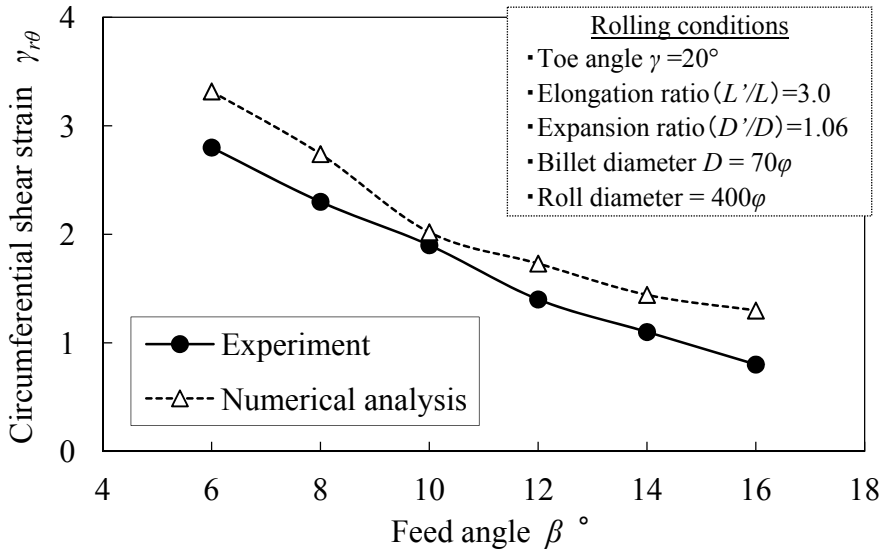

Figure 10: Effect of the feed angle β on circumferential shear strain $\gamma_{r\theta}$.

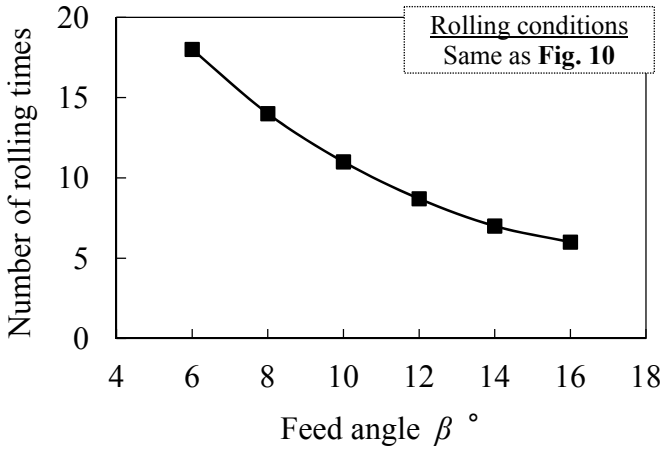

Figure 11: Effect of the feed angle β on the number of rolling times.

5 CONCLUSIONS

- The three-dimensional numerical analysis of the rotary piercing process was performed by the rigid plastic finite element method. The agreement of the numerical analysis results with the experimental results concerning circumferential shear strain $\gamma_{r\theta}$ confirms the validity of the developed numerical analysis model.
- The experiment and the numerical analysis clarified the effect of the toe angle γ and the feed angle β on circumferential shear strain $\gamma_{r\theta}$. As the toe angle γ or the feed angle β was increased, circumferential shear strain $\gamma_{r\theta}$ was suppressed. This paper clearly shows that the cone-type piercing mill with the high toe angle has an advantage of suppressing redundant shear deformation.

REFERENCES

[1] C.Hayashi and T.Yamakawa , Influences of Feed and Cross Angle on Rotary Forging Effects and Redundant Shear Deformation in Rotary Piercing Process , *ISIJ Int.* , (1997) **37**: 146-152.

[2] C.Hayashi and T.Yamakawa , Comparison of Double and Single Piercing Process in Seamless Steel Tube Manufacture , *Materials Science Research International* , (1997) **3**: 143-150.

[3] C.Hayashi and T.Yamakawa , Influences of Feed and Cross Angle on Inside Bore and Lamination Defects in Rotary Piercing for Materials with Poor Hot Workability, *ISIJ Int.* , (1997) **37**: 153-160.

[4] E.Erman , The influence of the processing parameters on the performance of the two-roll piercing operation , *Journal of Mechanical Working Technology* , (1987) **15**: 167-179.

[5] K.Mori , H.Yoshimura and K.Osakada , Simplified three-dimensional simulation of rotary piercing of seamless pipe by rigid-plastic finite-element method , *Journal of Materials Processing Technology* , (1998) , **80-81**: 700-706.

[6] R.Kawalla , E.Höfer , G.Lehmann and W.Lehnert , Use of finite element method for deeper analysis of rotary piercing , *Metal Forming 2000* , (2000) , 229-235.

[7] Hansgeorg Schoß , Nutzung der FEM beim Schrägwalzlochen , *Meform 2001 TU Bergakademie Freiberg* , (2001) , 317-331.

[8] E.Ceretti , C.Giardini , A.Attanasio , F.Brisotto and G.Capoferri , Rotary tube piercing study by FEM analysis: 3D simulations and experimental results , *Tube & Pipe Technology* , (2004) , 155-159.

[9] J.Pietsch and P.Thieven , FEM simulation of the rotary tube piercing process , *MPT International* , (2003) **26**: 52-60.

[10] K.Komori , Simulation of Mannesmann piercing process by the three-dimensional rigid-plastic finite-element method , *International Journal of Mechanical Sciences* , (2005) **47**: 1838-1853.

[11] Diego A.Berazategui , Miguel A.Cavaliere , Luca Montelatici and Eduardo N.Dvorkin , On the modelling of complex 3D bulk metal forming processes via the pseudo-concentrations technique. Application to the simulation of the Mannesmann piercing process , *Int. J. Numer. Meth. Engng* , (2006) **65**: 1113-1144.

[12] Z.Pater , J.Kazanecki and J.Bartnicki , Three dimensional thermo-mechanical simulation of the tube forming process in Diescher's mill , *Journal of Materials Processing Technology* , (2006) **177**: 167-170.

[13] R.Pschera , J.Klarner and C.Sommitsch , Finite-Elemente-Modellierung des Schrägwalzens , *Berg- und Hüttenmännische Monatshefte* , (2007) **152**: 205-211.

[14] A.Ghiotti , S.Fanini , S.Bruschi and P.F.Bariani , Modelling of the Mannesmann effect , *CIRP Annals – Manufacturing Technology* , (2009) **58**: 255-258.

[15] K.Komori and K.Mizuno , Study on plastic deformation in cone-type rotary piercing process using model piercing mill for modeling clay , *Journal of Materials Processing Technology* , (2009) **209**: 4994-5001.

[16] R.Krux and M.Zemko , FEM-modelling of Barrel-type Cross-roll Piercing and Analysis of the Induced Rotational Motion of the Plug Bar , *ICTP* , (2011) , 143-148.

[17] Z.Pater and J.Kazanecki , Complex Numerical Analysis of the Tube Forming Process Using Diescher Mill , *Archives of Metallurgy and Materials* , (2013) **58**: 717-724.

XIV International Conference on Computational Plasticity. Fundamentals and Applications
COMPLAS XIV
E. Oñate, D.R.J. Owen, D. Peric & M. Chiumenti (Eds)

COMPUTATIONAL MODELLING OF VOID GROWTH IN SWELLED HYDROGELS

L. SIAD*, M. ELKOLLI† AND S.C. GANGLOFF*

* Biomatériaux et Inflammation en Site Osseux (BIOS)
Université de Reims
UFR Pharmacie, 1 rue du Maréchal Juin, 51100 Reims, France
e-mail: {larbi.siad,sophie.gangloff}@univ-reims.fr, web page: http://www.univ-reims.fr/

†Laboratoire PMA des Matériaux Polymériques Multiphasiques (LPMAMPM)
Université Ferhat Abbas Sétif-1
Faculté de Technologie, 19000 Sétif, Algérie
e-mail: elkolli@hotmail.com - Web page: http://www.univ-setif.dz

Key words: Gels, Microvoid Growth, Multiscale Simulation, Porous Polymeric Biomaterials, Swelling.

Abstract. The nature and the large notable distinguishing features of polymeric gels explain their pervasive use as biomaterials in both regenerative medicine and tissue engineering. With regard to their biocompatibility, their ability to withstand large deformation and their significant capacity of solvent absorption, these biomaterials are often selected owing to their versatile mechanical properties and especially the closeness to soft biological tissues, amongst others. A finite-strain theory for the study of the overall behaviour of a porous polymeric gel where microvoids are present is presented. The swollen polymeric gel is modeled as a two-component body composed of two incompressible components, namely, an elastic porous polymer imbibed with a solvant. The chemical equilibrium is assumed to be preponderate at the interface between the porous polymer and the environment where the chemical potential of the solvent is fixed. The initially dry porous polymer undergoes large deformation induced by absorption of a solvent from the environment and mechanical loading. In this paper an attempt is made towards obtaining an estimation of the macroscopic responses of the swollen porous polymer to prescribed proportional loadings. To this end, a two-level representation of the material at hand for which the Representative Volume Element (RVE) imbibed with a solvent is a simple axisymmetric cylinder composed of a homogeneous matrix surrounding a spherical void, is considered. The computational study addresses the situation where the RVE is subjected to prescribed axial and lateral overall stresses under conditions of constant overall stress triaxiality. For fixed values of the Flory-Huggins parameter and the nominal concentration of the solvent, the overall stress-strain behaviour of the RVE model, the influence of the initial porosity, and the prescribed stress triaxiality ratio have been outlined.

1 INTRODUCTION

Hydrogels are pervasive in biology and have been turned out to be nearly optimal for interfacing with dynamic systems. By way of illustration, they are used as biomaterials in order to enhance stem cell transplantation by addressing, in particular, the mechanical aspects associated with each stage of the transplantation process [1, 17]. The characteristic soft ability of these polymeric biomaterials makes them strongly resembling the extracellular matrix (ECM) which encapsulates cells in their native environment. Regarding tissue engineering, scaffolds made of hydrogels, just like ECM, act as a structural support and are able to accommodate biomechanical signals to control cell function and eventually their fate [13]. Nowadays, it is trite to claim that stem cells are known to respond to mechanical cues in their microenvironment by changing their morphology, dynamics, proliferation rate, migration speed, and differentiation potential [7, 27]. The physical process of mechanosensitivity is realized through the contact and adhesion between cells and their microenvironment.

Hydrogels, a cross-linked polymers immersed in water, are an interesting class of materials that are able to undergo significantly large deformation which can also be triggered by external stimuli through appropriate change of constituents [26]. Solvent molecules migrate in a gel by self-diffusion. When hydrogels are subjected to mechanical loadings or also when the chemical potential of the environment changes, the polymer chain network deforms and the solvent molecules migrate to reach the thermodynamic equilibrium [28]. This equilibrium is reached as soon as the chemical potential of the solvent equals to that in the external solution. The mechanical, thermodynamic and kinetic properties of various environmentally sensitive hydrogels have been modeled and analyzed to study the different interesting phenomena exhibited, namely the phase transition and instability during swelling [2, 6, 20]. The interaction of mechanics and absorption of a swelling solvent in polymeric gels encompasses many important phenomena like environmental stress cracking, phase transformations, and cavitation to quote few. Very useful and recent presentations of the subject, based on continuum theories, may be found in a series of publications [3, 6, 9, 8, 12, 20, 36, 39] and references cited therein.

Poor toughness of soft porous biomaterials may results in failure which is an issue of importance to both engineering and medical practice [23, 37, 4]. An understanding of failure mechanisms turns out to be crucial in the study of fracture of these biomaterials. Cavitation is an important failure mode in elastomeric materials which includes situations where failure is mediated by environmental factors. Because of its close connection with material failure inception, cavitation has received much attention from the materials and mechanics communities [4, 16, 18, 21, 25]. Physical evidence showed that sufficiently large tensile loads can induce the sudden appearance of internal microvoids in elastomeric solids. Gent and Lindley [18] considered cavitation as the result of unlimited elastic expansion of a pre-existing microvoid. They used the elastic theory of void inflation to successfully correlate the critical load for cavitation with the corresponding one necessary for the unbounded growth of a microvoid in

an infinite medium. These authors conducted experimental investigations showing that the critical load for cavitation was directly related to the elastic modulus. On the other hand, the occurrence of such instabilities can also be attributed to the growth of pre-existing defects into finite sizes. In Ball's approach [4] cavitation is the start of a traction-free void within a nonlinear elastic solid as the consequence of reaching a critical load. Reviews as well as further details dealing with cavitation can be found for example in [16, 21]. Pence and Tsai [35] have extended the Ball's approach to account for the absorption of a swelling solvent resulting in volumetric changes at a fixed degree of swelling. They concluded that a Treloar material [38] always supports cavitation under uniform swelling provided that the load is sufficiently large. Duda *et al.* [12, 11] have shown that there is a critical value for the interaction parameter χ below which a Treloar material does not support cavitation regardless of the magnitude of the load. In addition, Zimberlin *et al.* [41], using a syringe needle to prescribe an internally pressurized void within a gel material, have proposed a method named "cavitation rheology testing" allowing the determination of the local modulus of the gel material. From these very short comments regarding the quantitative prediction of the occurrence of cavitation in real soft materials, it can be kept in mind that fundamental problems dealing with this subject remain largely unresolved [30, 29].

In addition to this, let us mention briefly that the toughness of a material depends on the ability of the microstructure to dissipate energy without propagation of defects like initiated microvoids or cracks [23, 37]. Subsequently, the understanding of failure mechanisms would also provide insight and afterwards enhancement into the production of tissue-engineering scaffolds with properly appropriate architecture and tailored properties. Scaffolds can be designed as porous structure (sponges) or in forms of hydrogels. Sponges facilitate cell adhesion and the pore size variation affects cell adhesion, migration and deposition. Hydrogels support the transportation of cells and bioactive agents and can suspend cells in a three dimensional environment. Keeping the focus on the porosity, among the essential characteristics that ideal scaffolds should share in order to be successful are the following [33, 32, 31] : i) the scaffolds should have high permeability to enable adequate diffusion of nutrients for the cells and the removal of waste products; ii) the cell supports porosity should be sufficiently high to allow for the ingress of cells and provide the cells space to proliferate and form the ECM; iii) they should have a large surface area; and iv) the pore size should be fine-tuned to the cells type applied.

As regard overall properties, the presence of those microscopic defects can have drastic consequences at the macroscopic level. In this computational study, the growth of a small spherical void within a polymeric gel is viewed through the prism of micromechanics [10, 34, 14] and finite element analysis. A two-level representation of the material at hand is considered. The mesoscopic scale is treated through an axisymmetric representative volume element (RVE) composed of two phases: a homogeneous void free matrix and spherical void. The behaviour of the RVE is appropriately averaged to provide the so-called macroscopic behaviour of the material considered as homogeneous. The calculations are very similar to many earlier similar simulations,

the prototype of which is due to Koplik and Needleman [24]. The boundary conditions of the RVE are prescribed under proportional stressing in such a way that the isotropically invariant stress triaxiality keeps a constant prescribed value throughout the loading displacement controlled history. The paper is organized as follows. Following [6, 12, 20, 22, 35], a general framework for studying the uptake of a solvent by a polymeric elastic solid is summarized in Section 2 where the basic constitutive equations are recollected. A brief presentation of the multiscale analysis and the description of the RVE model for the considered material are introduced in Section 3. Some of the obtained numerical results are presented in Section 4. Finally, concluding remarks are given in Section 5.

2 Governing equations

The problem formulation and material modelling of hydrogels are briefly presented in this section. Closely following works in [6, 12, 20, 22, 35], the governing equations and corresponding boundary conditions for equilibrium swelling deformation of this material are described. They serve as the basis for the numerical studies presented in the subsequent sections.

2.1 Kinematics and balance equations of finite growth

Consider a hydrogel body (current state) of volume Ω enclosed by a surface Γ, subjected to body force, $\underline{\mathbf{b}}$, and surface traction, $\underline{\mathbf{t}}$. Due to immersion of the hydrogel body in a solvent environment of chemical potential μ (per solvent molecule), a transport of the solvent molecules occurs within Ω and across Γ. In addition, part of the surface Γ may be mechanically constrained (*e.g.*, bounded to a rigid body) and/or chemically isolated from the solvent. Due to large deformation, it is more appropriate to use nominal quantities referring to a reference state with fixed volume Ω_o and surface Γ_o. A generic material particle occupying position $\underline{\mathbf{X}}$ at the reference state moves to position $\underline{\mathbf{x}}(\underline{\mathbf{X}}, t)$ at the current state at time t. The deformation gradient tensor maps both reference states, namely,

$$F_{iK} = \frac{\partial x_i(\underline{\mathbf{X}}, t)}{\partial X_K} \quad \text{with} \quad J := \det \underline{\underline{\mathbf{F}}} > 0 \tag{1}$$

While the choice of the reference state is arbitrary in general, we choose the dry state of the hydrogel as the reference state in the present study. Such a choice is necessary for the use of a specific free energy function. However, let us mention from now that a numerical challenge has to be circumvented in finite element analysis by using an intermediate configuration for which $J \neq 1$. The equation of force balance in terms of the nominal stress $\underline{\underline{\mathbf{s}}}$ and boundary conditions can be set as follows

$$\frac{\partial s_{iK}(\underline{\mathbf{X}}, t)}{\partial X_K} + B_i(\underline{\mathbf{X}}, t) = 0 \quad \text{and} \quad \underline{\mathbf{X}} = \bar{\underline{\mathbf{X}}} \text{ or } s_{iK} N_K = \bar{T}_i^o \tag{2}$$

where $\bar{\underline{\mathbf{T}}}^o$ is traction per unit area of the reference surface with the unit outward normal $\underline{\mathbf{N}}$ and the barred quantities are prescribed. In the circumstance of absence of

any chemical reaction, the conservation of the number of injected small molecules at the chemical potential μ into the gel, in the vicinity of $\underline{\mathbf{X}}$, read

$$\frac{\partial C(\underline{\mathbf{X}},t)}{\partial t}+\frac{\partial J_K(\underline{\mathbf{X}},t)}{\partial X_k}=r(\underline{\mathbf{X}},t) \tag{3}$$

where r is the number of the small molecules per unit time injected into a volume element dV, $J\,N_K\,dA$ is the number of the small molecules per unit time crossing an element of area $\underline{\mathbf{N}}\,dA$, and C be the concentration of the solvent number. The polymers and the individual small molecules are assumed to be incompressible, which is reflected in the incompressibility condition

$$1+v\,C(\underline{\underline{\mathbf{F}}},C)=J \tag{4}$$

where v is the volume per small molecule and $v\,C$ is the volume of the small molecules in the gel divided by the volume of the dry polymers.

2.2 Constitutive equations

Standard reasoning in thermodynamics accounting for condition of molecular incompressibility through the use of a field of Lagrange multiplier Π results in (refer *e.g.*, [6, 19, 39] and also to above mentioned references)

$$s_{iK}=\frac{\partial W(\underline{\underline{\mathbf{F}}},C)}{\partial \underline{\underline{\mathbf{F}}}}-\Pi\,JH_{iK}\quad,\quad \mu=\frac{\partial W(\underline{\underline{\mathbf{F}}},C)}{\partial C}+\Pi\,v \tag{5}$$

where W is the free energy of the gel and $\underline{\underline{\mathbf{H}}}$ is the transpose of the inverse of the deformation gradient $\underline{\underline{\mathbf{F}}}$, , namely, $H_{iK}F_{iL}=\delta_{KL}$ and $H_{iK}F_{jK}=\delta_{ij}$ [1].

For the dissipation due to solvent migration, we can correlate the solvent flux, $\mathbf{J}$, to its driving force, the chemical potential gradient, as

$$\mathbf{J}=-\mathbf{M}\boldsymbol{\nabla}_{\mathrm{X}}\mu \tag{6}$$

The spatial differential operator $\boldsymbol{\nabla}_{\mathrm{X}}$ is taken with respect to the reference configuration. The kinetic tensor $\mathbf{M}$ may not be constant in general, but is all positively definite.

The choice of an explicit form of the free-energy function W for elastomers and soft tissues is a controversial problem. This choice is needed in order to solve the initial value problem under consideration. Following Flory and Rehner [15], W has the form $W(\underline{\underline{\mathbf{F}}},C)=W_s(\underline{\underline{\mathbf{F}}},C)+W_m(C)$ reflecting the stretching network of the polymers, W_s, and the mixing of the polymers and the small molecules, W_m. These two terms are taken to be

$$\begin{aligned} W_s(\underline{\underline{\mathbf{F}}},C) &= \frac{1}{2}\,NkT(F_{iK}F_{iK}-3-2\log J)\\ W_m(C) &= -\frac{kT}{v}\left[vC\log\left(1+\frac{1}{vC}\right)+\frac{\chi}{1+vC}\right] \end{aligned} \tag{7}$$

[1] Algebraic identity: $\dfrac{\partial\,(\det\mathbf{F})}{\partial F_{iK}}=\det\mathbf{F}H_{iK}$

where N is the number of polymer chains in the gel per unit volume of the dry polymers, v is the volume per solvent molecule, T is the absolute temperature, and k is the Boltzmann constant. The first term inside the bracket comes from the entropy of mixing, and the second from the enthalpy of mixing. The Flory interaction parameter χ is a dimensionless measure of the enthalpy of mixing, with representative values $\chi = 0 - 1.2$. For applications that prefer gels with large swelling ratios, materials with low χ values are used. The enthalpy of mixing motivates the small molecules to enter the gel if $\chi < 0$, but motivates the small molecules to leave the gel if $\chi > 0$. The chemical potential and stresses are normalized by kT and kT/v, respectively. The material properties of the hydrogel is fully determined by three parameters: NkT, $\frac{kT}{v}$, and χ. The first two combine to give one dimensionless parameter, Nv. It is well known that NkT defines the initial shear modulus of the polymer network, with the number N proportional to the crosslink density ρ_c,[39, 38]. A representative value of the volume per molecule is $v = 10^{-28}\,\mathrm{m}^3$. At room temperature, $kT = 4 \times 10^{-21}\,\mathrm{J}$ and $kT/v = 4 \times 10^{7}\,\mathrm{Pa}$. In the numerical examples below, we will take the values $Nv = 10^{-3}$ and $\chi = 1.2$. The normalized chemical potential is mimicked by a temperature-like variable, which is uniform in the polymeric gel, and is incremented as a loading parameter. The whole governing equations and the thorough approach have been implemented into Abaqus via a UHYPER subroutine. [20, 22, 40].

3 THE AXISYMMETRIC RVE MODEL

The voids are assumed to be uniformly distributed inside the matrix material as shown in Figure 1-a. Specifically, the position of these voids are presumed to form a hexagonal crystal lattice in such a way that the shape of the unit microstructure is a prism with hexagonal basis face with inner radius R_o, height $2\,L_o$, and containing an initially spherical void with radius r_o. In order to reduce the effort of calculations to a two-dimensional analysis, the cross section of the unit microstructure has been simplified as a cylinder, as done in [5, 24]. Due to this approximation, the axisymmetric RVE is shown in Figure 1-d for which a cylindrical reference coordinate system with radial coordinate R, circumferential angle Θ and axial coordinate Z is used for the analysis. In the initial undeformed configuration, the RVE model is a cylinder with diameter $2\,R_o$ and height $2\,L_o = 2\,R_o$ (for the sake of simplicity). The initial axisymmetric RVE geometry is then simply characterized by the initial void volume fraction f_o given by $f_o = \frac{2}{3}\left(\frac{r_o}{R_o}\right)^3$. The RVE model is assumed to be subjected to axisymmetric deformations with constant prescribed overall triaxiality so that all field quantities are independent of Θ.

As a consequence of the lattice periodicity all outer planes of the unit cell have to move as rigid planes in coordinate directions during the process of loading (Figure 2). The faces at $R = R_o$ and $Z = L_o$ will have a uniform normal displacements and their mutual orientations will be maintained. These requirements impose the RVE model to remain, during the finite strain deformation process, a cylinder which is

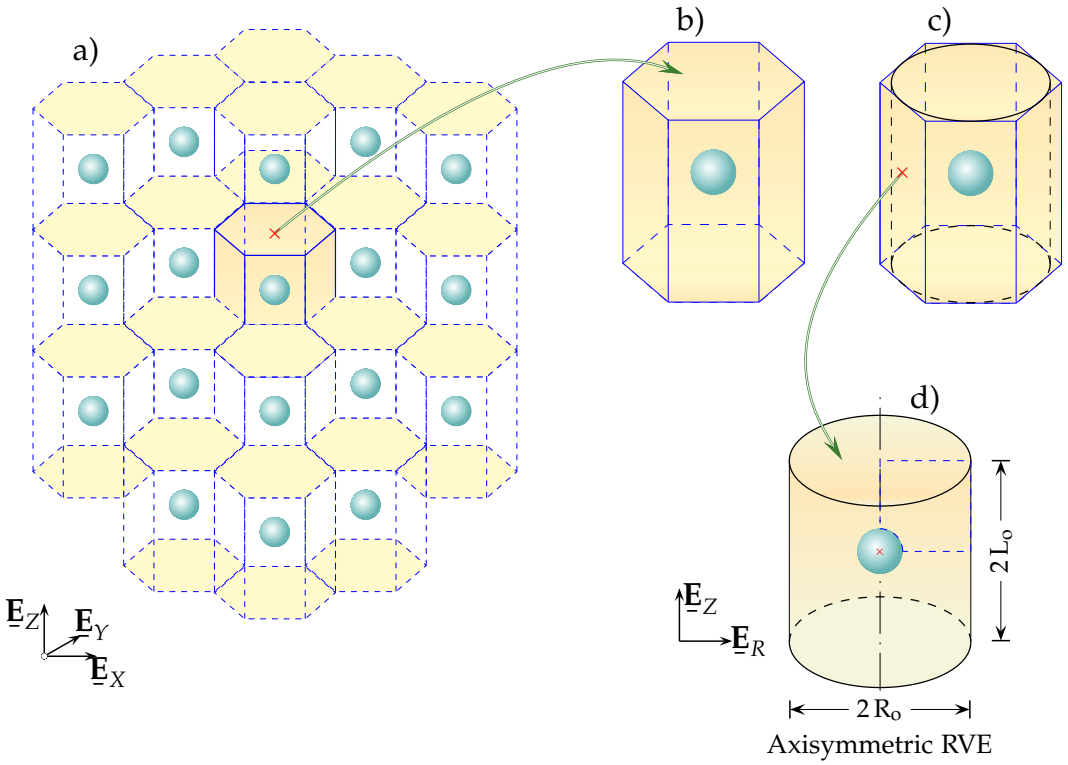

Figure 1: Three-dimensional hexagonal arrangement of spherical voids. a) Schematic representation of a porous polymeric gel which is considered as an array of unit hexagonal RVEs, each containing a single spherical void. The porous unit hexagonal microstructure shown in (b) is approximated by the axisymmetric RVE model displayed in (d).

thus characterized in an arbitrary state by $\ell_R = R_o + u_R^A$ and $\ell_Z = L_o + u_Z^A$ where u_R^A and u_Z^A are the radial and axial components displacement of the upper right corner **A**. Because of these constraints, only one quarter geometry of the RVE model ($0 \leq R \leq R_o$, $0 \leq Z \leq L_o$) needs to be analyzed and is drawn in Figure 2.

The overall deformation of the RVE model can be calculated from the normal displacements of the outer faces. The macroscopic total logarithmic strain tensor and Cauchy stress tensor possess the same principal directions, which are the radial and axial directions. The effective strain E_e defined by $E_e = \frac{2}{3}|E_Z - E_R|$ where E_R and E_Z are the macroscopic principal strains, is chosen as the overall deformation of the RVE model and the independent variable for presenting most results. The effective von Mises stress Σ_e , hydrostatic stress Σ_h, and the overall stress triaxiality $\mathcal{T}$ result from

$$\Sigma_e = |\Sigma_Z - \Sigma_R| \ , \ \Sigma_h = \frac{1}{3}(\Sigma_Z + 2\Sigma_R) \ , \ \mathcal{T} := \frac{\Sigma_h}{\Sigma_e} = \frac{1}{3}\frac{(\Sigma_Z + 2\Sigma_R)}{|\Sigma_Z - \Sigma_R|} \tag{8}$$

where Σ_R is the remote macroscopic principal stresses in both R and Θ directions, and Σ_Z in the Z-one. The RVE model is presumed to be remotely loaded with predominant axial stress; that is the axial direction is assumed to be the maximum prin-

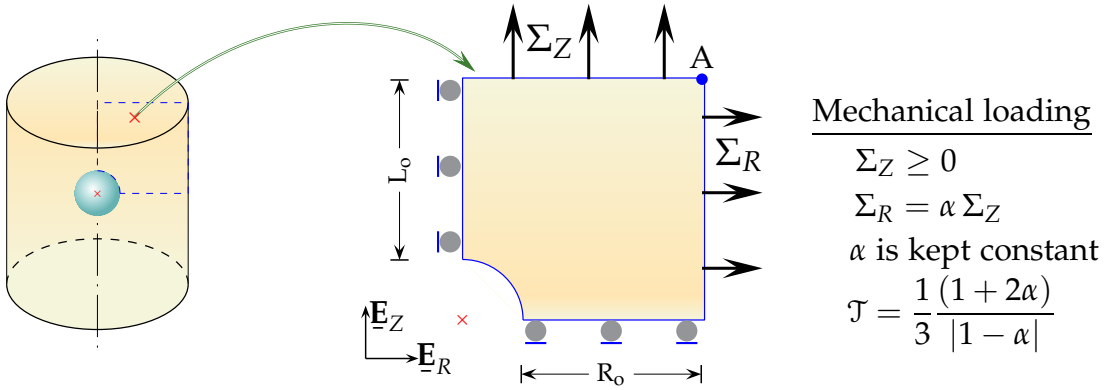

Figure 2: Axisymmetric RVE model containing an isolated spherical void and to be FE analyzed.

cipal direction and the components of the overall stress tensor $\underline{\underline{\Sigma}}$ are then such that $\Sigma_Z \geq \Sigma_R$.

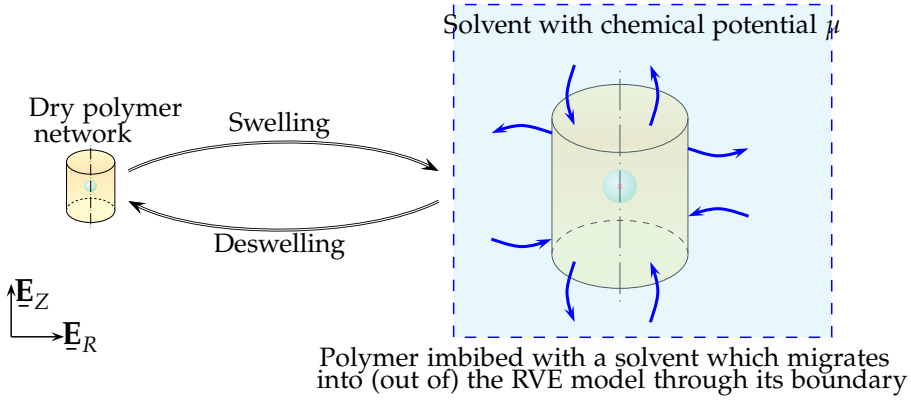

Figure 3: Swelling-deswelling of the axisymmetric RVE model. After swelling the porosity is maintained constant.

For metal, it is a well known fact that the stress triaxiality ratio $\mathcal{T}$ is the most important driving force to void growth in porous materials [5, 24]. On that account, a general problem in RVE model computations is to maintain $\mathcal{T}$ constant in the course of loading irrespective of the large displacement of the cell faces and the unstable stiffness behaviour. The finite elements used were eight-nodes quadrilateral isoparametric elements. The mesh surrounding the void is slightly refined and it was judged to be sufficiently refined for this study (800 Q8 elements). Care has been taken to insure that the meshes were sufficiently refined and that the results were independent of the degree of refinement. The Riks's arc-length method in Abaqus is used in order to handle the inevitable instability of the RVE and to proceed with further calculations. The overall stress and strain rates are directly computed from the reaction forces and the applied displacement rates. The actual void volume fraction f corresponding to

the evolution of the microvoid is calculated using numerical integration from the updated coordinates of the nodes at the void-matrix interface during the deformation of the RVE model. The initial conditions and loading rate of the RVE model are chosen such that inertial effects are negligible. No artificial damping has been used in all computations. The value of the imposed axial displacement u_z^A depends essentially upon the value of f_o and the fixed stress triaxility $\mathcal{T}$ as well. In addition, the imposed boundary conditions have to be ramped up using a function of time over the first part of calculation (typically the first 1-10%).

Before to proceed further, it is important to mention that the prevalent approach of modeling the porous biomaterial at hand as an assemblage of axisymmetric unit RVEs reduces the amount of work required for the multiscale analysis. This convenience comes with an approximation since this assemblage cannot patently fill the space continuously, and then is only suited for moderate porosity. Furthermore, the used axisymmetric RVEs do not allow the adjustment of arbitrary stress ratios in three directions.

4 NUMERICAL RESULTS

For the simulation presented hereafter, the chosen hydrogel properties are the following: initial polymer volume fraction $\phi_o = 0.90$, degree of cross-linking $N\nu = 0.0010$, and parameter $\chi = 0.10$. At the reference state corresponding to an initially swollen hydrogel of properties ϕ_o, $N\nu$ and χ, its initial chemical potential is prescribed by μ_o/kT given by $\mu_o/kT = N\nu(\phi_o^{1/3} - \phi_o) + \ln(1-\phi_o) + \phi_o + \chi\phi_o^2 = -1.3216$. This prescribed value is accounted for in Abaqus as an initial condition [40]. The porosity f_o takes on values $0.10, 0.50, 1.0, 2.0, 5.0$ and 10.0%. The stress triaxiality $\mathcal{T}$ ranges from $1/3$ (pure tension) to 2 (severe stress state for soft materials). However, in the interest of place, hereafter only the value $f_o = 5\%$ is considered.

The swelling-mechanical loading of the RVE model at hand may be summarised as follows: (a) the polymer network of the RVE model with initial porosity f_o is first imbibed with solvent as shown in Figure 3. Subsequently, homogeneous swelling occurs and the size of the RVE model changes a lot irrespective of the value of f_o. At equilibrium the chemical potential μ is homogeneous throughout the RVE model which porosity after swelling turns out to be practically equal to f_o. (b) The swelled RVE model is then subjected to axial and lateral overall stresses under conditions of constant prescribed overall stress triaxiality. Contour plots at the end of calculations of the lagrangian strain component LE_{22} are shown in Figure 4 for $\mathcal{T} = \frac{1}{3}, 1$ and 2. For each of these values of $\mathcal{T}$, the evolution of the normalized effective stress, $\frac{\Sigma_e}{kT}$ and the porosity f are displayed in Figure 5 as a function of the equivalent strain E_e.

It is to be noted that for moderate stress triaxiality (*e.g.*, $\mathcal{T} = \frac{1}{3}$ corresponding to a tensile test), the equivalent stress Σ_e continuously increases with equivalent strain E_e. The same applies to the variations of void volume fraction f in terms of E_e, (red curves in Figure 5). By way of example, it can be observed from Figure 5 that for $\mathcal{T} = 1$ (magenta curve) beyond the peak stress corresponding to $E_e = 0.39$, $(\frac{\Sigma_e}{kT})^{max} = 1.22 \times$

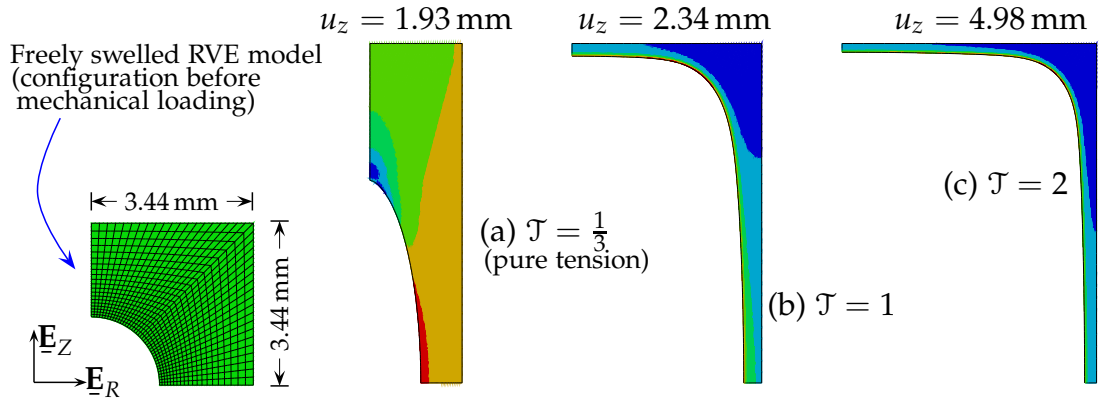

Figure 4: Distribution of lagrangian strain component LE_{22} at the end of calculations and final deformation shape of the RVE model for $f_o = 0.05$. The hydrogel properties are $\phi_o = 0.90$, $Nv = 0.0010$, and $\chi = 0.10$. The mechanical loading of the freely swelled RVE model has been performed under constant stress triaxiality ratio $\mathcal{T} = \frac{1}{3}$ (a), 1 (b), and 2 (c).

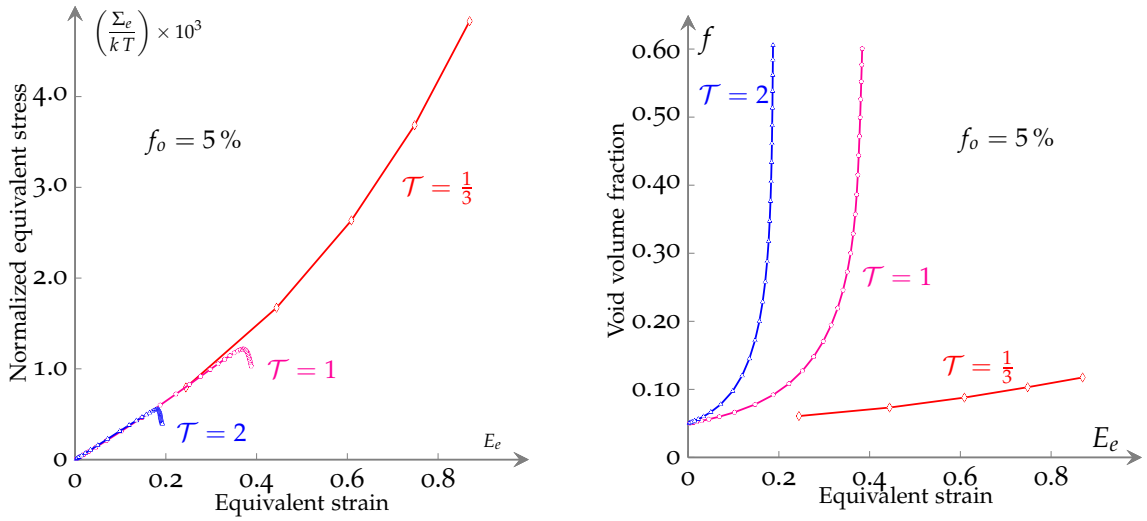

Figure 5: Evolution of the normalized equivalent stress $\frac{\Sigma_e}{kT}$ and the void volume fraction f in terms of the macroscopic equivalent strain E_e of the RVE model. The initial value of the void volume fraction is $f_o = 0.050$ and along the whole process of deformation the overall stress triaxiality $\mathcal{T}$ is kept constant.

10^{-3}, and $f = 38.6$ %, the void volume fraction increases very quickly. Figures 6–8 shows the deformation of the RVE model and the evolution during the whole process

of loading of the lagrangian strain component LE_{22} for $\mathcal{T} = 1/3$ (a), $\mathcal{T} = 1$ (b) and $\mathcal{T} = 2$ (c), respectively.

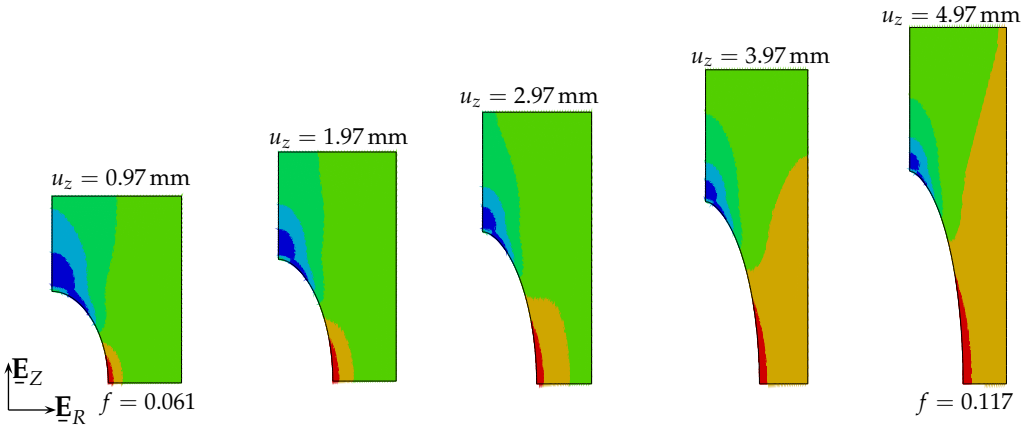

Figure 6: Deformation of the RVE model and evolution of contours of the lagrangian strain component LE_{22}. The initial porosity is $f_o = 0.050$ and along the whole process of loading the triaxiality is kept constant: $\mathcal{T} = 1/3$ (pure tension).

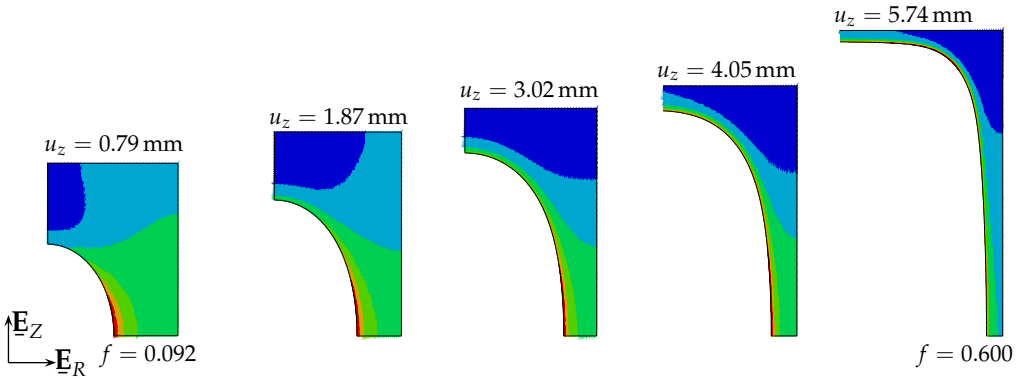

Figure 7: Deformation of the RVE model and evolution of contours of the lagrangian strain component LE_{22}. The initial porosity is $f_o = 0.050$ and along the whole process of loading the triaxiality is kept constant: $\mathcal{T} = 2$.

Figure 9 displays similar results as those shown in Fig. 5 for f_o ranging from 0.1 % to 10.0 %. It is to be noted that for $\mathcal{T} = 1$, each curve macroscopic equivalent stress versus macroscopic equivalent strains has a maximum depending on the initial value of the void volume fraction. Lower the initial value f_o of the void volume fraction, higher the reached value of the relevant peak stress. Table 1 shows the obtained associated values of $\left(\frac{\Sigma_e}{kT}\right)^{max}$, E_e, f, and the imposed axial displacements u_Z for $f_o = 0.1$, 0.5, 1.0, 2.0, 5.0 and 10.0 %. Beyond macroscopic peak stresses, the void volume fraction rapidly

increases. In this connection, it should be kept in mind that special care would be considered after maximum load occur in the vicinity of the boundary of void. Indeed, it is well known that strong softening of the material result in localized deformation and consequently the mesh size dependence. After the peak macroscopic stresses the equivalent stress drops abruptly and the validity of the numerical results is expected to quickly deteriorate because of mesh excessive distortion. In addition, it should be important to keep in mind that for the analysis presented above a criterion for the final failure of the intervoid ligament is clearly missing.

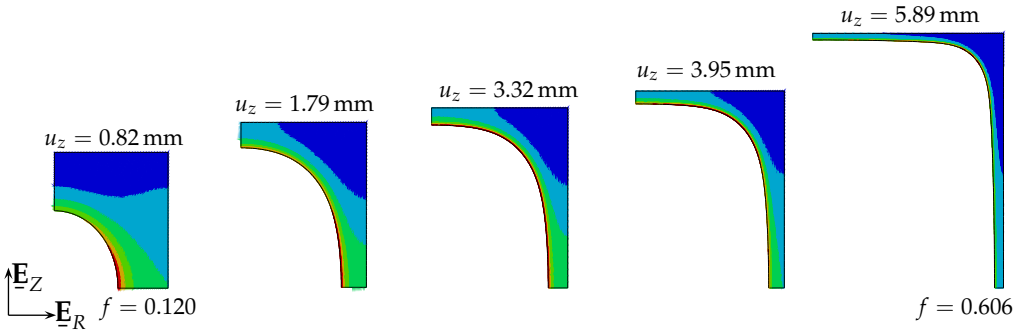

Figure 8: Deformation of the RVE model and evolution of contours of the lagrangian strain component LE_{22}. The initial porosity is $f_o = 0.050$ and along the whole process of loading the triaxiality is kept constant: $\mathcal{T} = 2$.

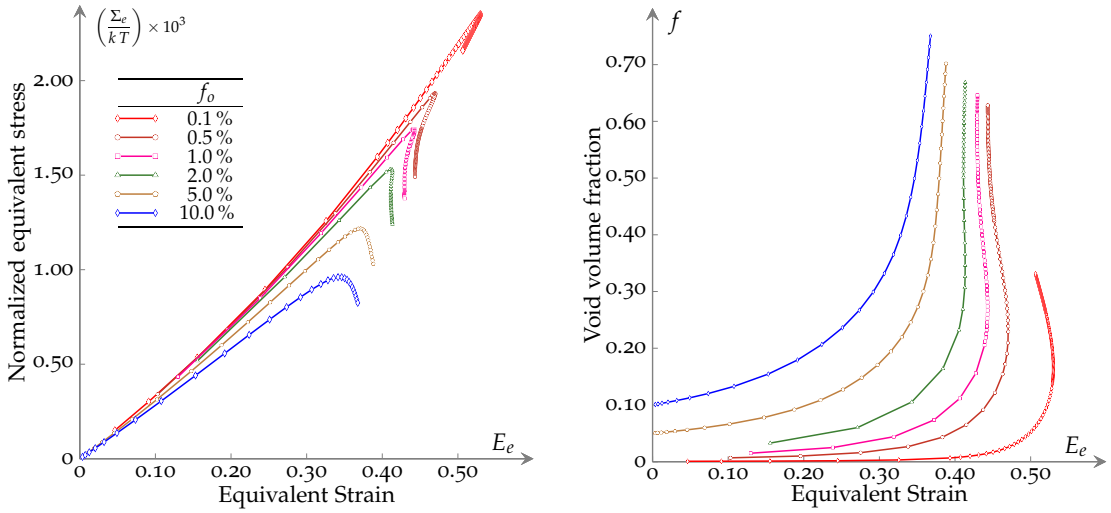

Figure 9: Evolution, for $\mathcal{T} = 1$, of the normalized effective stress and the void volume fraction in terms of the macroscopic effective strain E_e of the RVE model.

Table 1: Normalized maximum macroscopic equivalent stresses $\left(\frac{\Sigma_e}{k\,T}\right)^{max}$ and the corresponding macroscopic equivalent strain E_e, void volume fraction f, and axial displacements u_Z. The stress triaxiality $\mathcal{T}$ is equal to 1.

f_o (%)	$\left(\frac{\Sigma_e}{k\,T}\right)^{max}$	f (%)	E_e	u_Z (mm)
0.1	2.35×10^{-3}	15.8	0.53	2.75
0.5	1.93×10^{-3}	20.9	0.47	2.50
1.0	1.74×10^{-3}	23.9	0.44	2.40
2.0	1.53×10^{-3}	26.9	0.41	2.23
5.0	1.22×10^{-3}	38.6	0.37	2.33
10.0	0.96×10^{-3}	46.7	0.34	2.32

5 CONCLUDING REMARKS

This study focuses on the mechanical behaviour of porous polymeric gels intended for use in tissue engineering and regenerative medicine as scaffolds. Following Hong *et al.* [20] and Koplik and Needleman [24], we present a computational framework for investigating the growth of microvoids initially assumed to be spherical and uniformly distributed inside the matrix material. The evolution of the size and the shape of the microvoid has been obtained under the conditions that i) the ambient chemical potential of the solvent is fixed, ii) the chemical equilibrium prevails at the interface between the polymer and the environment interface, and iii) the mechanical loading of the RVE is such that the stress triaxiality ratio is maintained constant throughout the whole process of deformation. The following conclusions are drawn:

- For a porous polymeric gel, the amount of solvent molecules inside the material is related to the chemical potential of the environment. The degree of swelling is obtained by solving equations that account for the simultaneous interaction of mechanics and absorption. It can be determined with a free swelling stretch, using a finite element analysis.
- As an expected result, the value of the initial void volume fraction has a large influence on the overall mechanical behaviour of a porous polymeric gel. Higher the initial value of the void volume fraction, lower the resistance (maximum equivalent stress) of the polymeric gel.
- The size of the swollen axisymmetric porous RVE model does not depend on the initial value of the void volume fraction and the porosity is kept constant after

swelling.
- For moderate stress triaxiality, *e.g.*, $\mathcal{T} = \frac{1}{3}$, the macroscopic equivalent stress continuously increases with macroscopic equivalent strain. The same applies to the variations of the void volume fraction.
- For high stress triaxiality, the curves macroscopic equivalent stress *vs* macroscopic equivalent strain display maximum depending on both the initial porosity and the fixed value of the overall triaxiality.
- Finally, so far for the analysis presented above a criterion for the final failure of the intervoid ligament is clearly missing.

The investigation of the effects of the constitutive parameters entering the theory, namely, the number N of polymer chains per unit volume of the dry polymers, the volume per solvent molecule v, and the Flory interaction parameter χ, on the overall behaviour of a porous polymeric gel are contemplated as a future research work. The fact of the matter is that this preliminary study could be of some relevance in regard to failure of responsive polymeric gels. Numerous tissues and organs are hydrogel-like in nature and several issues related to the mechanics of hydrogels remain open (a short list is given in the review [28]). With increment of biomedical applications, computational modelling to predict the performance of these biomaterials for use in regenerative medicine and tissue engineering proves to be a valuable aid in assisting understanding of the behaviour of hydrogels and their optimization as well.

REFERENCES

[1] Artmann, G.M. and Chien, S. (eds) *Bioengineering in Cell and Tissue Research.* Springer, Heidelberg, Berlin, (2008).

[2] Baek, S. and Srinivasa, A.R. *A thermo-mechanically coupled theory for fluid permeation in elastomeric materials: Application to thermally responsive gels. International Journal of Nonlinear Mechanics* (2004) **39**:201-2018.

[3] Baek, S. and Pence, T.J. *Inhomogeneous deformation of elastomer gels in equilibrium under saturated and unsaturated conditions. Journal of the Mechanics and Physics of Solids* (2011) **59**:561-582.

[4] Ball, J.M. *Discontinuous equilibrium solutions and cavitation in nonlinear elasticity. Phil. Trans. Royal Soc., London. Series A* (1982) **306**:557-611.

[5] Brocks, W. Sun, D.Z. and Hönig, A. *Micromechanics of coalescence in ductile fracture. International Journal of Plasticity* (1995) **11**:971-989.

[6] Chester, A.S. and Anand, L. *A thermo-mechanically coupled theory for fluid permeation in elastomeric materials: Application to thermally responsive gels. Journal of the Mechanics and Physics of Solids* (2011) **59**:1966-2006.

[7] Disher, D. *et al.*, *Biomechanics: Cell research and applications for the next decade. Annals of Biomedical Engineering* (2009) **37**:847–859.

[8] Doi, M. *Gel dynamics. Journal of the Physical Society of Japan* (2009) **78**:052001-1–052001-19.

[9] Doi, M. *Soft Matter Physics.* Oxford University Press, Oxford, (2013).

[10] Dormieux, L. Kondo, D. and Ulm, F.-J. *Microporomechanics.* John Wiley & Sons, Ltd., Chichester, (2006).

[11] Duda, F.P. Souza, A.C. and Fried, E. *Theory for species migration in a finitely strained solid with application to polymer network swelling. Journal of the Mechanics and Physics of Solids* (2010) **58**:515-529.

[12] Duda, F.P. Souza, A.C. and Fried, E. *Solvent uptake and cavitation. Journal of the Mechanics and Physics of Solids* (2011) **59**:2341–2354.

[13] Fernandes, P.R. and Bártolo, P.J. (eds), *Tissue Engineering: Computer Modeling, Biofabrication and Cell Behavior.* Springer, Dordrecht, Heidelberg, (2014).

[14] Fish, J. *Practical Multiscaling.* John Wiley & Sons Ltd., Chichester, (2014).

[15] Flory, P.J. and Rehner, J. *Statistial mechanics of cross-linked polymer networks II. Swelling.* textitJ. Chem. Phys. (1943 **11**:521-526.

[16] Fond, C. *Cavitation criterion for rubber materials: a review of void-growth models. Journal of Polymer Science B: Polymer Physics* (2001) **33**:2081-2096.

[17] Foster, A.A. Marquardt, L.M. and Heilshorn, S.C. *The diverse roles of hydrogel mechanics in injectable stem cell ... Current Opinion in Chemical Engineering* (2017) **15**:15-23.

[18] Gent, A.N. and Lindley, P.B. *Internal rupture of bonded rubber cylinders in tension. Proc. R. Soc. Lond. A* (1959) **249**:195-205.

[19] Holzapfel, G.A. and Ogden, R.W. (eds) *Mechanics of Biological Tissue.* Springer, Berlin, Heidelberg, (2006).

[20] Hong, W. Liu, Z.S. and Suo Z.G. *Inhomogeneous swelling of a gel in equilibrium with a solvent and mechanical load. International Journal of Solids Structures* (2009) **46**:3282-3289.

[21] Horgan, C. O. and Polignone, D. A. *Cavitation in nonlinearly elastic solids: A review. Appl. Mech. Rev.* (1995) **48**: 471-485.

[22] Kang, M.K. and Huang, R. *A variational approach and finite element implementation for swelling of polymeric hydrogels under geometric constraints. Journal of Applied Mechanics* (2010) **77**:061004.

[23] Koh, C.T. Strange, D.G.T. Tonsomboon, K. and Oyen, M.L. *Failure mechanisms in fibrous scaffolds. Acta Biomaterialia* (2013) **9**:7326-7334.

[24] Koplik, K. and Needleman A. *Void growth and coalescence in porous plastic solids. International Journal of Solids Structures* (1988) **24**:835-853.

[25] Lefèvre, V. Ravi-Chandar, K. and Lopez-Pamies O., *Cavitation in rubber: an elastic instability or a fracture phenomenon? International Journal of Fracture* 2015) **192**:1-23

[26] Li, H. *Smart Hydrogel Modelling.* Springer, Dordrecht, (2009).

[27] Zheng, X. Li, S. and Kohles, S.S. *Multiscale Biomechanical Modeling of Stem Cell-Extracellular Matrix Interactions.* in: S. Li and B. Sun, (eds.), *Advances in Cell Mechanics, Chapter 2* Springer, Heidelberg, (2011):27-53.

[28] Liu, Z.S. Toh, W. and Ng T.Y. *Advances in mechanics of soft materials: large deformation behavior of hydrogels. International Journal of Applied Mechanics* (2015) **7**:35.

[29] Lopez-Pamies, O. *Onset of cavitation in compressible, isotropic, hyperelastic solids. Journal of Elasticity* (2009) **94**:115-145.

[30] Lopez-Pamies, O. *An exact result for the macroscopic response of particle-reinforced Neo-Hookean solids. Journal of Applied Mechanics* (2010) **77**:021016-1-021016-5.

[31] Ma, P.X. *Scaffolds for tissue fabrication. Materialstoday* (2004) **7**:30-40.

[32] Mauli Agrawal, C. Ong, J.L. Appleford, M.R. and Mani, G. *Introduction to Biomaterials.* Cambridge University Press, Cambridge UK, (2014).

[33] Migliaresi, C. and Motta, A. (eds) *Scaffolds for Tissue Engineering. Biological Design, Materials, and Fabrication.* Pan Stanford Publishing Pte. Ltd., Singapore, (2014).

[34] Nemat-Nasser, S. and Hori, M. *Micromechanics: overall properties of heterogeneous materials.* North-Holland, Elsevier, Amsterdam, 2nd edition, (1999).

[35] Pence, T.J. and Tsai, H. *Swelling-induced cavitation of elastic spheres. Mathematics and Mechanics of Solids* (2006) **11**:527-551.

[36] Rajagopal, K.R. *Diffusion through polymeric solids undergoing large deformations. Materials Science and Technology* (2003) **19**:1175-1180.

[37] Stella, J.A. D'Amore, A. Wagner, W.R. and Sacks, M. S. *On the biomechanical function of scaffolds for engineering load-bearing ... Acta Biomaterialia* (2010) **6**: 2365-2381.

[38] Treloar, L.R.G. *The Physics of Rubber Elasticity.* Oxford University Press, Oxford (1975).

[39] Volokh, K. *Mechanics of Soft Materials.* Springer, Singapore (2016).

[40] Wong, W.H. *Instability study of soft materials-Modelling and simulation.* PhD thesis, National University of Singapore, Singapore, (2011).

[41] J.A. Zimberlin, G.N. Tew, N. Sanabria-Delong, A.J. Crosby, *Cavitation rheology fo soft materials. Soft Matter* (2007) **3**: 763-767.

XIV International Conference on Computational Plasticity. Fundamentals and Applications
COMPLAS XIV
E. Oñate, D.R.J. Owen, D. Peric & M. Chiumenti (Eds)

CRACK PHASE-FIELD MODELING OF ANISOTROPIC RUPTURE IN FIBROUS SOFT TISSUES

O. GÜLTEKİN[1], H. DAL[2] AND G.A. HOLZAPFEL[1,3]

[1]Institute of Biomechanics, Graz University of Technology
Stremayrgasse 16/II, 8010, Graz, Austria
e-mail: {gueltekin|holzapfel}@tugraz.at, web page: http://www.biomech.tugraz.at/

[2]Department of Mechanical Engineering, Middle East Technical University
Dumlupınar Bulvarı No. 1, Çankaya, 06800, Ankara, Turkey
e-mail: dal@metu.edu.tr, web page: http://www.me.metu.edu.tr/meweb/

[3]Faculty of Engineering Science and Technology
Norwegian University of Science and Technology (NTNU), 7491 Trondheim, Norway
e-mail: gerhard.holzapfel@ntnu.no, web page: https://www.ntnu.no/ansatte/gerhard.holzapfel

Key words: Fracture, Crack phase-field, Failure criteria, Fibrous soft tissue, Aorta

Abstract. The estimation of rupture in fibrous soft tissues has emerged as a central task in medical monitoring and risk assessment of diseases such as aortic dissection and aneurysms. In an attempt to address the challenges we have established a computational framework within the context of crack phase-field modeling and proposed an energy-based anisotropic failure criterion based on the distinction of isotropic and anisotropic material responses. Numerically we compare that criterion with other anisotropic failure criteria, in particular we analyze their capability to describe an admissible failure surface and how a crack can be propagated. A canonical rate-dependent setting of the crack phase-field model is formulated and solved in a weak sense by a standard Galerkin procedure featuring a one-pass operator-splitting algorithm on the temporal side. The anisotropic failure criteria are tested according to their performance on reflecting an admissible initiation, and crack propagation with an emphasis placed upon the aortic dissection.

1 INTRODUCTION

Rupture of fibrous soft tissues involves tangled series of coupled biomechanical processes imposing conspicuous limits on computational models to characterize physically relevant failure. In this respect, mathematical models can help physicians to better assess the risk of rupture involved in diseases such as aneurysms (Humphrey and Holzapfel [7]). In an attempt to address the related issues we have established a mathematical framework within the context of crack phase-field and proposed a novel energy-based failure criterion based on a distinction of isotropic and anisotropic material responses (Gültekin et al. [3]).

To date several contributions on failure criteria have been reported in the literature for both isotropic and anisotropic materials, see, e.g., Hill [5] and Tsai and Wu [13]. However, an account on their numerical performance, i.e. their capability to describe an admissible failure surface and a crack propagation, is not yet presented, the main objective of this communication. An anisotropic phase-field approach is formulated, enforcing the crack growth along the direction of fibers. A rate-dependent setting of the crack phase-field formulation is proposed which not only enhances the algorithmic stability upon macro-cracking but also becomes physically justifiable as, e.g., the aortic dissection is observed to be rate-dependent (Tong et al. [12]).

2 THEORY

This section deals with phase-field modeling of fracture in solids at finite strains featuring the primary field variables, namely the deformation map $\boldsymbol{\varphi}$ and the crack phase-field d in relation to the balance of linear momentum and the crack evolution, respectively.

2.1 The primary field variables of the multi-field problem

The coupled problem of fracture is described by $\boldsymbol{\varphi}$ and d, i.e.

$$\boldsymbol{\varphi}_t(\mathbf{X}) : \begin{cases} \mathcal{B} \times \mathcal{T} & \rightarrow & \mathcal{S}, \\ (\mathbf{X}, t) & \mapsto & \mathbf{x} = \boldsymbol{\varphi}(\mathbf{X}, t), \end{cases} \qquad d : \begin{cases} \mathcal{B} \times \mathcal{T} & \rightarrow & [0,1], \\ (\mathbf{X}, t) & \mapsto & d(\mathbf{X}, t), \end{cases} \tag{1}$$

where $\boldsymbol{\varphi}$ maps a material point $\mathbf{X} \in \mathcal{B} \subset \mathbb{R}^3$ in the reference configuration onto $\mathbf{x} \in \mathcal{S} \subset \mathbb{R}^3$ located in the spatial configuration, while the crack phase-field d interpolates between the intact ($d = 0$) and the ruptured ($d = 1$) state of the material. A key aspect is to provide a diffusive crack topology by smearing out the sharp crack surface over a solid domain using the length-scale parameter l (Miehe et al. [10, 8]). The sharp crack surface topology at time t can be denoted by $\Gamma(t) \subset \mathbb{R}^2$ in the solid $\mathcal{B}$, with the definition $\Gamma(d) = \int_\Gamma \mathrm{d}A$. In contrast, a diffusive crack simply approximates the sharp crack surface by a volume integral in the form of the regularized crack surface functional

$$\Gamma_l(d) = \int_{\mathcal{B}} \gamma(d, \nabla d) \mathrm{d}V, \qquad \gamma(d, \nabla d) = \frac{1}{2l}(d^2 + l^2 |\nabla d|^2), \tag{2}$$

where $\nabla[\bullet]$ denotes the gradient operator with respect to the reference coordinates, and γ is the isotropic volume-specific crack surface. This can be extended to a class of anisotropic materials via the introduction of an anisotropic volume-specific crack surface γ up to first order, i.e.

$$\gamma(d, \mathbf{Q} \star \nabla d) = \gamma(d, \nabla d), \qquad \forall \mathbf{Q} \in \mathcal{G} \subset \mathcal{O}(3), \tag{3}$$

where $\mathbf{Q}$ denotes the rotations in the symmetry group $\mathcal{G}$, a subset of the orthogonal group $\mathcal{O}(3)$ containing rotations and reflections, and $\star$ denotes a transformation operator. The anisotropy is accounted by a second-order structure tensor $\boldsymbol{\mathcal{L}}$ such that

$$\boldsymbol{\mathcal{L}} = l^2[\mathbf{I} + \omega_{\mathrm{M}}(\mathbf{M} \otimes \mathbf{M}) + \omega_{\mathrm{M}'}(\mathbf{M}' \otimes \mathbf{M}')], \tag{4}$$

which aligns the evolution of the crack according to the orientation of fibers in the continuum using the anisotropy parameters ω_{M} and $\omega_{\mathrm{M}'}$ that regulate the transition from weak to strong anisotropy. The anisotropic volume-specific crack surface can now be represented by the alternative form

$$\gamma(d, \nabla d; \mathcal{L}) = \frac{1}{2l}(d^2 + \nabla d \cdot \mathcal{L} \nabla d). \tag{5}$$

2.2 Kinematics

The fundamental deformation measure at finite strain kinematics is the deformation gradient, i.e.

$$\mathbf{F} = \nabla \boldsymbol{\varphi}. \tag{6}$$

Manifolds are equipped with the covariant reference metric tensor $\mathbf{G}$ and the spatial metric tensor $\mathbf{g}$ transforming the co and contravariant objects in the Lagrangian and Eulerian manifolds, respectively. Exploiting the multiplicative decomposition of $\mathbf{F}$ into a volumetric part $\mathbf{F}_{\mathrm{vol}}$ and an isochoric part $\overline{\mathbf{F}}$, with $\det\overline{\mathbf{F}} = 1$, we have

$$\mathbf{F} = \mathbf{F}_{\mathrm{vol}}\overline{\mathbf{F}} \qquad \text{with} \qquad \mathbf{F}_{\mathrm{vol}} = J^{1/3}\mathbf{I}, \qquad \overline{\mathbf{F}} = J^{-1/3}\mathbf{F}, \tag{7}$$

where the Jacobian $J = \det\mathbf{F} > 0$ characterizes the volume map of an infinitesimal reference volume element onto the associated spatial element. Subsequently, we define the unimodular part of the left Cauchy-Green tensor $\overline{\mathbf{b}}$ and its first invariant $\bar{I}_1$ as

$$\overline{\mathbf{b}} = \overline{\mathbf{F}}\mathbf{G}^{-1}\overline{\mathbf{F}}^{\mathrm{T}}, \qquad \bar{I}_1 = \mathrm{tr}\overline{\mathbf{b}}. \tag{8}$$

The anisotropic structure of fibrous soft tissues makes it necessary to consider additional invariants. Hence, we introduce two reference unit vectors $\mathbf{M}$ and $\mathbf{M}'$ representing the mean fiber orientations, with their spatial counterparts $\mathbf{m} = \mathbf{F}\mathbf{M}$ and $\mathbf{m}' = \mathbf{F}\mathbf{M}'$ idealizing the micro-structure. Following this, we describe the additional invariants

$$I_4 = \mathbf{g} : (\mathbf{m} \otimes \mathbf{m}), \qquad I_6 = \mathbf{g} : (\mathbf{m}' \otimes \mathbf{m}'), \tag{9}$$

expressed by the structure tensors $\mathbf{A}_{\mathbf{m}} = \mathbf{m} \otimes \mathbf{m}$ and $\mathbf{A}_{\mathbf{m}'} = \mathbf{m}' \otimes \mathbf{m}'$.

2.3 Constitutive modeling of artery walls

The effective Helmholtz free-energy function Ψ_0 describes the local anisotropic mechanical response of the intact solid. We assume a specific form which comprises the effective volumetric part U_0, the isotropic part Ψ_0^{iso} and the anisotropic part Ψ_0^{ani} according to

$$\Psi_0(\mathbf{g}, \mathbf{F}, \mathbf{A}_{\mathbf{m}}, \mathbf{A}_{\mathbf{m}'}) = U_0(J) + \Psi_0^{\mathrm{iso}}(\mathbf{g}, \overline{\mathbf{F}}) + \Psi_0^{\mathrm{ani}}(\mathbf{g}, \mathbf{F}, \mathbf{A}_{\mathbf{m}}, \mathbf{A}_{\mathbf{m}'}), \tag{10}$$

in the sense of Dal [1]. It needs to be underlined that in (10) the multiplicative decomposition of $\mathbf{F}$ is only used upon the matrix response; in other words, we omit the multiplicative decomposition of $\mathbf{F}$ for the fiber response. The effective volumetric part is given by

$$U_0(J) = \kappa(J - \ln J - 1), \tag{11}$$

while Ψ_0^{iso} and Ψ_0^{ani} are functions of the invariants according to

$$\Psi_0^{\text{iso}}(\mathbf{g}, \overline{\mathbf{F}}) = \hat{\Psi}_0^{\text{iso}}(\bar{I}_1), \qquad \Psi_0^{\text{ani}}(\mathbf{g}, \mathbf{F}, \mathbf{A_m}, \mathbf{A_{m'}}) = \hat{\Psi}_0^{\text{ani}}(I_4, I_6), \tag{12}$$

which take on the neo-Hookean and exponential models according to Holzapfel et al. [6]

$$\hat{\Psi}_0^{\text{iso}}(\bar{I}_1) = \frac{\mu}{2}(\bar{I}_1 - 3), \qquad \hat{\Psi}_0^{\text{ani}}(I_4, I_6) = \frac{k_1}{2k_2} \sum_{i=4,6} \{\exp[k_2(I_i - 1)^2] - 1\}, \tag{13}$$

representing the elastic response of the ground matrix and the two distinct families of collagen fibers, respectively. To give an account of the parameters, κ denotes the bulk modulus in (11), while μ indicates the shear modulus in $(13)_1$. The parameters k_1 and k_2 in $(13)_2$ denote a stress-like and a dimensionless parameter, respectively. The anisotropic part contributes to the mechanical response only when a family of fibers is under extension, i.e. $I_4 > 1$ and $I_6 > 1$ [6]. The derivations of the corresponding constitutive response, i.e. the effective Kirchhoff stress tensor $\boldsymbol{\tau}_0$ and the effective elasticity tensor $\mathbb{c}_0$ can be found in Gültekin et al. [4].

2.4 Variational formulation based on power balance

For a degrading anisotropic solid with two families of fibers, the Helmholtz free-energy function Ψ can be written as

$$\Psi(\mathbf{g}, \mathbf{F}, \mathbf{A_m}, \mathbf{A_{m'}}; d) = g(d)\Psi_0(\mathbf{g}, \mathbf{F}, \mathbf{A_m}, \mathbf{A_{m'}}), \tag{14}$$

where Ψ_0 is the effective free energy of the hypothetically intact solid according to (10). The explicit form of the monotonically decreasing quadratic degradation function g is

$$g(d) = (1 - d)^2, \tag{15}$$

which describes the degradation of the solid as d evolves, along with appropriate growth conditions [2, 3, 4]. Hence, the volumetric, isotropic and anisotropic parts of the free-energy function $\Psi = U + \hat{\Psi}^{\text{iso}} + \hat{\Psi}^{\text{ani}}$ for a degenerating material become

$$U(J, d) = g(d)U_0(J), \quad \hat{\Psi}^{\text{iso}}(\bar{I}_1; d) = g(d)\hat{\Psi}_0^{\text{iso}}(\bar{I}_1), \quad \hat{\Psi}^{\text{ani}}(I_4, I_6; d) = g(d)\hat{\Psi}_0^{\text{ani}}(I_4, I_6), \tag{16}$$

respectively. We now write the rate of the energy storage functional $\mathcal{E}$ by considering the time derivative of the isotropic and the anisotropic contributions of $(16)_{2,3}$ integrated over the domain, i.e.

$$\mathcal{E}(\dot{\boldsymbol{\varphi}}, \dot{d}; \boldsymbol{\varphi}, d) = \int_{\mathcal{B}} (\boldsymbol{\tau} : \mathbf{g}\nabla_x \dot{\boldsymbol{\varphi}} - f\dot{d}) \mathrm{d}V, \tag{17}$$

where $\nabla_x[\bullet]$ denotes the gradient operator with respect to the spatial coordinates. We have defined the Kirchhoff stress tensor $\hat{\boldsymbol{\tau}}$ and the energetic force f such that

$$\boldsymbol{\tau} = g(d)(\boldsymbol{\tau}_0^{\text{iso}} + \boldsymbol{\tau}_0^{\text{ani}}), \qquad f = -\partial_d[U(J, d) + \hat{\Psi}^{\text{iso}}(\bar{I}_1; d) + \hat{\Psi}^{\text{ani}}(I_4, I_6; d)], \tag{18}$$

where $\boldsymbol{\tau}$ is essentially obtained via the effective isotropic and anisotropic Kirchhoff stresses $\boldsymbol{\tau}_0^{\text{iso}}$ and $\boldsymbol{\tau}_0^{\text{ani}}$, respectively. Meanwhile, f can be interpreted as the work conjugate quantity to $\dot{d}$. The external action on the body gives the external power functional $\mathcal{P}$, i.e.

$$\mathcal{P}(\dot{\boldsymbol{\varphi}}) = \int_{\mathcal{B}} \rho_0 \tilde{\boldsymbol{\gamma}} \cdot \dot{\boldsymbol{\varphi}} \mathrm{d}V + \int_{\partial \mathcal{B}_t} \tilde{\mathbf{t}} \cdot \dot{\boldsymbol{\varphi}} \mathrm{d}a, \tag{19}$$

where ρ_0, $\tilde{\boldsymbol{\gamma}}$ and $\tilde{\mathbf{t}}$ represent the material density, the prescribed body force and the spatial surface traction, respectively. In what follows, the dissipation functional $\mathcal{D}$ accounts for the dissipated energy in the body is given as

$$\mathcal{D}(\dot{d}) = \int_{\mathcal{B}} g_{\mathrm{c}}[\delta_d \gamma(d, \nabla d; \mathcal{L})] \dot{d} \mathrm{d}V, \tag{20}$$

where $\delta_d \gamma$ defines the variational derivative of the volume-specific crack surface γ, whereas g_{c} is the critical fracture energy (Griffith-type critical energy release rate), see Miehe et al. [10, 8] and Gültekin et al. [3].

Concerning thermodynamics, $\mathcal{D}$ has to be non-negative for all admissible deformation processes, a primary demand of the second law of thermodynamics. This inequality is *a priori* fulfilled by a the local form of (20) featuring a positive and convex propensity (Miehe et al. [10]). The local form of (20) can be stated by the principle of maximum dissipation via the following constrained optimization problem

$$g_{\mathrm{c}}[\delta_d \gamma(d, \nabla d; \mathcal{L})] \dot{d} = \sup_{\beta \in \mathbb{E}} \beta \dot{d}, \tag{21}$$

which can be solved by a Lagrange method yielding

$$g_{\mathrm{c}}[\delta_d \gamma(d, \nabla d; \mathcal{L})] \dot{d} = \sup_{\beta, \lambda \geq 0} [\beta \dot{d} - \lambda t_{\mathrm{c}}(\beta; d, \nabla d)], \tag{22}$$

where the local driving force β, dual to $\dot{d}$, and the Lagrange multiplier λ enforce the constraint. In addition, the threshold function t_{c} delineating a reversible domain $\mathbb{E}$ is

$$\mathbb{E}(\beta) = \{\beta \in \mathbb{R} \,|\, t_{\mathrm{c}}(\beta; d, \nabla d) = \beta - g_{\mathrm{c}}[\delta_d \gamma(d, \nabla d; \mathcal{L})] \leq 0\}. \tag{23}$$

Finally, the extended dissipation functional $\mathcal{D}_\lambda$ reads

$$\mathcal{D}_\lambda(\dot{d}, \beta, \lambda; d) = \int_{\mathcal{B}} [\beta \dot{d} - \lambda t_{\mathrm{c}}(\beta; d, \nabla d)] \mathrm{d}V. \tag{24}$$

2.4.1 Mixed rate-independent variational formulation based on power balance

The sum of the functionals (17), (19) and (24) describes a rate-type potential giving rise to the power balance, i.e.

$$\Pi_\lambda = \mathcal{E} + \mathcal{D}_\lambda - \mathcal{P}. \tag{25}$$

On the basis of the rate-type potential (25), the mixed saddle point principle for the quasi-static process states

$$\{\dot{\boldsymbol{\varphi}}, \dot{d}, \beta, \lambda\} = \operatorname{Arg}\left\{\inf_{\dot{\boldsymbol{\varphi}}\in\mathcal{W}_{\dot{\varphi}}} \inf_{\dot{d}\in\mathcal{W}_{\dot{d}}} \sup_{\beta,\lambda\geq 0} \Pi_\lambda\right\}, \tag{26}$$

with the admissible domains for the primary variables $\mathcal{W}_{\dot{\varphi}} = \{\dot{\boldsymbol{\varphi}} \mid \dot{\boldsymbol{\varphi}} = \mathbf{0} \quad \text{on} \quad \partial\mathcal{B}_\varphi\}$ and $\mathcal{W}_{\dot{d}} = \{\dot{d} \mid \dot{d} = 0 \quad \text{on} \quad \partial\mathcal{B}_d\}$. By considering the variation of Π_λ we obtain the Euler-Lagrange equations describing the mixed multi-field problem for the rate-independent fracture of an anisotropic hyperelastic solid, i.e.

$$\boxed{\begin{array}{ll} 1: & J\operatorname{div}(J^{-1}\boldsymbol{\tau}) + \rho_0\tilde{\boldsymbol{\gamma}} = \mathbf{0}, \\ 2: & \beta - f = 0, \\ 3: & \dot{d} - \lambda = 0, \end{array}} \tag{27}$$

along with the Karush-Kuhn-Tucker-type loading-unloading conditions ensuring the principal of maximum dissipation in case of an evolution of the crack phase-field parameter d, i.e. $\lambda \geq 0$, $t_\mathrm{c} \leq 0$ and $\lambda t_\mathrm{c} = 0$.

2.4.2 A mixed rate-dependent variational formulation based on power balance

Now we deal with the viscous extension of the variational approach and introduce a Perzyna-type viscous extension of $\mathcal{D}$ such that

$$\mathcal{D}_\eta(\dot{d}, \beta; d) = \int_\mathcal{B} \left[\beta\dot{d} - \frac{1}{2\eta}\langle t_\mathrm{c}(\beta; d, \nabla d)\rangle^2\right] \mathrm{d}V, \tag{28}$$

where the viscosity η determines the viscous over-force governing the evolution of $\dot{d}$. In (28) the positive values for the threshold function t_c are filtered out by the ramp function $\langle x\rangle = (x + |x|)/2$. The corresponding viscous rate-type potential reads

$$\Pi_\eta = \mathcal{E} + \mathcal{D}_\eta - \mathcal{P}. \tag{29}$$

On the basis of the rate-type potential (29), we establish a mixed saddle point principle for the quasi-static process, i.e.

$$\{\dot{\boldsymbol{\varphi}}, \dot{d}, \beta\} = \operatorname{Arg}\left\{\inf_{\dot{\boldsymbol{\varphi}}\in\mathcal{W}_{\dot{\varphi}}} \inf_{\dot{d}\in\mathcal{W}_{\dot{d}}} \sup_{\beta\geq 0} \Pi_\eta\right\}, \tag{30}$$

with the admissible domains for the primary state variables. One can retrieve the coupled set of Euler-Lagrange equations for the rate-dependent fracture by simply taking the variation of Π_η, i.e.

$$\boxed{\begin{array}{ll} 1: & J\operatorname{div}(J^{-1}\boldsymbol{\tau}) + \rho_0\tilde{\boldsymbol{\gamma}} = \mathbf{0}, \\ 2: & \beta - f = 0, \\ 3: & \dot{d} - \langle t_\mathrm{c}(\beta; d, \nabla d)\rangle/\eta = 0, \end{array}} \tag{31}$$

The explicit form of the threshold function t_c recasts the equality $(31)_3$ in the form

$$f = \eta\dot{d} + g_\mathrm{c}\delta_d\gamma(d, \nabla d). \tag{32}$$

2.5 Crack driving function and failure Ansatz

Focusing on the rate-independent case in (32), where $\eta \to 0$, we elaborate on the energetic force $(18)_2$. Accordingly, we substitute (15) and (16) into $(18)_2$ to arrive at

$$f = 2(1-d)(U_0 + \hat{\Psi}_0^{\text{iso}} + \hat{\Psi}_0^{\text{ani}}) = 2(1-d)\Psi_0. \tag{33}$$

By substituting (33) into (32) for the rate-independent case we obtain (the calculation of the variational derivative can be found in Gültekin et al. [3])

$$2(1-d)\frac{\Psi_0}{g_c/l} = d - \nabla \cdot (\mathcal{L}\nabla d). \tag{34}$$

With this notion at hand, we can define the dimensionless crack driving function

$$\boxed{\overline{\mathcal{H}} = \frac{\Psi_0}{g_c/l}.} \tag{35}$$

As discussed in Miehe et al. [9] the dimensionless characteristics of $\overline{\mathcal{H}}$ allows the incorporation of different failure criteria. A particular form of the failure Ansatz is postulated in accordance with two significant conditions, i.e. the irreversibility of the crack and the positiveness of $\overline{\mathcal{H}}$ ensuring that the crack growth solely takes place upon loading, i.e.

$$\boxed{\mathcal{H}(t) = \max_{s\in[0,t]} \left[\langle \overline{\mathcal{H}}(s) - 1 \rangle\right].} \tag{36}$$

With these adjustments (34) takes on the following form

$$\boxed{2(1-d)\mathcal{H} = d - \nabla \cdot (\mathcal{L}\nabla d).} \tag{37}$$

Bearing this in mind, we recall the rate-dependent case for $\eta \neq 0$, i.e.

$$\boxed{2(1-d)\mathcal{H} = d - \nabla \cdot (\mathcal{L}\nabla d) + \eta\dot{d},} \tag{38}$$

which compares to (32) with the replacement of the dimensional energetic force by the dimensionless failure Ansatz, the cornerstone of the crack phase-field modeling.

2.6 Anisotropic failure criteria

The dimensionless crack driving function (35) already reflects an energy-based criterion for a general isotropic material. However, we know that most fibrous soft tissues exhibit an anisotropic morphology, thereby an anisotropic mechanical response is expected. We, therefore, provide a short description of anisotropic failure criteria which may manifest the rupture phenomena in coherence with clinical observations. For simplicity, the ensuing formulations are established according to the assumption that the principal axes of anisotropy lie on the axes of reference. Nonetheless, transformation of stress components can be achieved without much effort [4].

2.6.1 Energy-based anisotropic failure criterion

Two distinct failure processes are assumed to govern rupture of the ground matrix and the fibers as suggested by Gültekin et al. [3]. Accordingly, the energetic force $(18)_2$ can be additively decomposed into an isotropic part f_{iso} and an anisotropic part f_{ani} such that

$$f_{\text{iso}} = 2(1-d)(U_0 + \hat{\Psi}_0^{\text{iso}}), \qquad f_{\text{ani}} = 2(1-d)\hat{\Psi}_0^{\text{ani}}, \tag{39}$$

which, in their turn, modify (34) into two distinct fracture processes which are

$$(1-d)\overline{\mathcal{H}} = d - \frac{1}{2}\nabla\cdot(\mathcal{L}\nabla d), \qquad \text{with} \qquad \overline{\mathcal{H}} = \overline{\mathcal{H}}^{\text{iso}} + \overline{\mathcal{H}}^{\text{ani}}, \tag{40}$$

where the dimensionless crack driving functions are defined as

$$\overline{\mathcal{H}}^{\text{iso}} = \frac{\hat{\Psi}_0^{\text{iso}}}{g_{\text{c}}^{\text{iso}}/l}, \qquad \overline{\mathcal{H}}^{\text{ani}} = \frac{\hat{\Psi}_0^{\text{ani}}}{g_{\text{c}}^{\text{ani}}/l}. \tag{41}$$

Therein, $g_{\text{c}}^{\text{iso}}/l$ and $g_{\text{c}}^{\text{ani}}/l$ are the distinct critical fracture energies over the length scale for the ground matrix and for the fibers, respectively. Finally, we provide the modified forms of the rate-dependent and rate-independent cases for the crack evolution, i.e.

$$(1-d)\mathcal{H} = d - \frac{1}{2}\nabla\cdot(\mathcal{L}\nabla d), \qquad (1-d)\mathcal{H} = d - \frac{1}{2}\nabla\cdot(\mathcal{L}\nabla d) + \eta\dot{d}. \tag{42}$$

For more details regarding the derivations see [3, 4].

2.6.2 Stress-based anisotropic Tsai-Wu failure criterion

The Tsai-Wu criterion is based on the strength of the material at which the stress space intercepts the assumed failure surface (Tsai and Wu [13]). Accordingly, the dimensionless crack driving function with respect to the effective Cauchy stress tensor $\boldsymbol{\sigma}_0$ assumes a composition of two scalar functions, i.e.

$$\overline{\mathcal{H}} = \mathbf{T} : \boldsymbol{\sigma}_0 + \boldsymbol{\sigma}_0 : \mathbb{T} : \boldsymbol{\sigma}_0, \tag{43}$$

where $\mathbf{T}$ and $\mathbb{T}$ denote the second and fourth-order strength tensors, respectively. Through assumptions and simplifications introduced by symmetry relations we end up with

$$T_{ii} = \frac{1}{(\sigma_i^{\text{u}})^2} \tag{44}$$

for the diagonal terms of the fourth-order strength tensor related to ultimate normal and shear stresses σ_i^{u}, with $i \in \{1,\dots,6\}$.

2.6.3 Stress-based anisotropic Hill failure criterion

Considered as the anisotropic extension of the von Mises–Huber criterion, the Hill criterion (Hill [5]) uses a quadratic form of $\overline{\mathcal{H}}$ such that

$$\overline{\mathcal{H}} = \boldsymbol{\sigma}_0^{\mathrm{vm}} : \mathbb{T} : \boldsymbol{\sigma}_0^{\mathrm{vm}}, \tag{45}$$

where $\boldsymbol{\sigma}_0^{\mathrm{vm}}$ represents the effective von Mises stress tensor. The components of $\boldsymbol{\sigma}_0^{\mathrm{vm}}$ can be defined in terms of general stress components, i.e.

$$\begin{aligned} \sigma_{0_1}^{\mathrm{vm}} &= \sigma_{0_1} - \sigma_{0_2}, & \sigma_{0_2}^{\mathrm{vm}} &= \sigma_{0_2} - \sigma_{0_3}, & \sigma_{0_3}^{\mathrm{vm}} &= \sigma_{0_3} - \sigma_{0_1}, \\ \sigma_{0_4}^{\mathrm{vm}} &= \sigma_{0_4}, & \sigma_{0_5}^{\mathrm{vm}} &= \sigma_{0_5}, & \sigma_{0_6}^{\mathrm{vm}} &= \sigma_{0_6}. \end{aligned} \tag{46}$$

The fourth-order strength tensor $\mathbb{T}$ pertains to the effective normal stresses and shear stresses [4].

2.6.4 Principal stress criterion

Developed on the basis of principal stresses the criterion by Raina and Miehe [11] reports on the spectral decomposition of the effective Cauchy stress tensor and takes the positive principal stresses into account, i.e.

$$\boldsymbol{\sigma}_0^{+} = \sum_{i=1}^{3} \langle \sigma_{0_i} \rangle \mathbf{n}_i \otimes \mathbf{n}_i, \tag{47}$$

where σ_{0_i} denote the effective principal stresses, and $\mathbf{n}_i$ are the corresponding eigenvectors for $i \in \{1, 2, 3\}$. Accordingly, $\overline{\mathcal{H}}$ is rewritten as

$$\overline{\mathcal{H}} = \boldsymbol{\sigma}_0^{+} : \mathbb{T} : \boldsymbol{\sigma}_0^{+}, \tag{48}$$

where the fourth-order strength tensor $\mathbb{T}$ reads in the index notation

$$(\mathbb{T})_{ijkl} = \frac{1}{4\sigma_{\mathrm{crit}}^2}(A_{ik}A_{jl} + A_{il}A_{jk}), \tag{49}$$

where σ_{crit} denotes the reference critical stress associated with uniaxial loading in a certain axis that can be conceptually replaced by an ultimate stress. Therein, $\mathbf{A}$ is expressed in index notation for $i, j, k, l \in \{1, 2, 3\}$, for which details are provided in [11].

3 NUMERICAL EXAMPLES

We now briefly demonstrate the performance of the proposed model applied to fracture of a fibrous soft tissue for which the crack initiation and propagation associated with different failure criteria are compared for simple yet representative numerical examples.

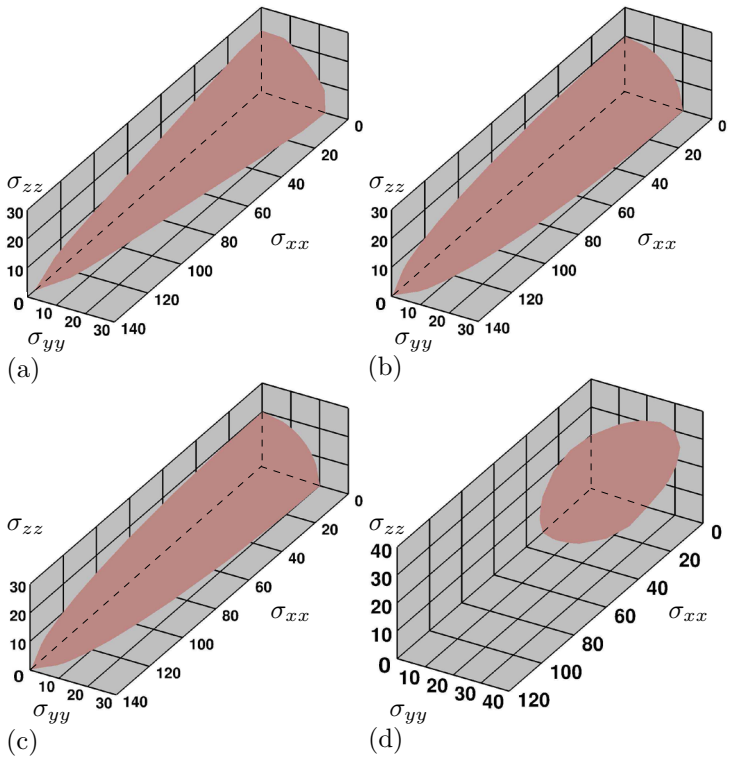

Figure 1: Failure surfaces in regard to Cauchy stresses σ_{xx}, σ_{yy} and σ_{zz} in kPa at which the failure conditions are satisfied, leading to $d > 0$ for (a) the energy-based; (b) the Tsai-Wu; (c) the maximum principal stress; (d) the Hill failure criterion (adopted from Gültekin et al. [4]).

3.1 Numerical investigation of the failure surfaces

The first example deals with the onset of micro-cracking with regard to distinct failure criteria, as mentioned in Section 2.6. The problem setup involves a homogeneous case with a unit cube discretized by one hexahedral element resolving the analytical solution for the deformation and stress. The sample, regarded as transversely isotropic, undergoes a series of uniaxial and biaxial deformations (for details see Gültekin et al. [4]).

Figures 1(a),(b) and (c) illustrate the resulting failure surfaces at the instance when $d \neq 0$ for the energy-based, Tsai-Wu and the principal stress criterion, respectively. The results conspicuously retrieve ellipsoidal failure surfaces. Figure 1(d) indicates the failure surface for the Hill criterion. In fact, this criterion induces surfaces diverging from being elliptic. In particular, the isotropic failure envelope on the yz-plane eventually becomes discernable, see Fig. 1(d), which recovers the von Mises–Huber criterion, as expected.

3.2 Peel test investigated with different failure criteria

The second example shows a peel test alluding to aortic dissection. This benchmark, with an initial tear, models a hypothetical artery comprised of a single family of fibers with orientation $\mathbf{M}$ (again for more details see [4]).

The two arms of the strip are separated by an initial tear and pulled apart in opposite

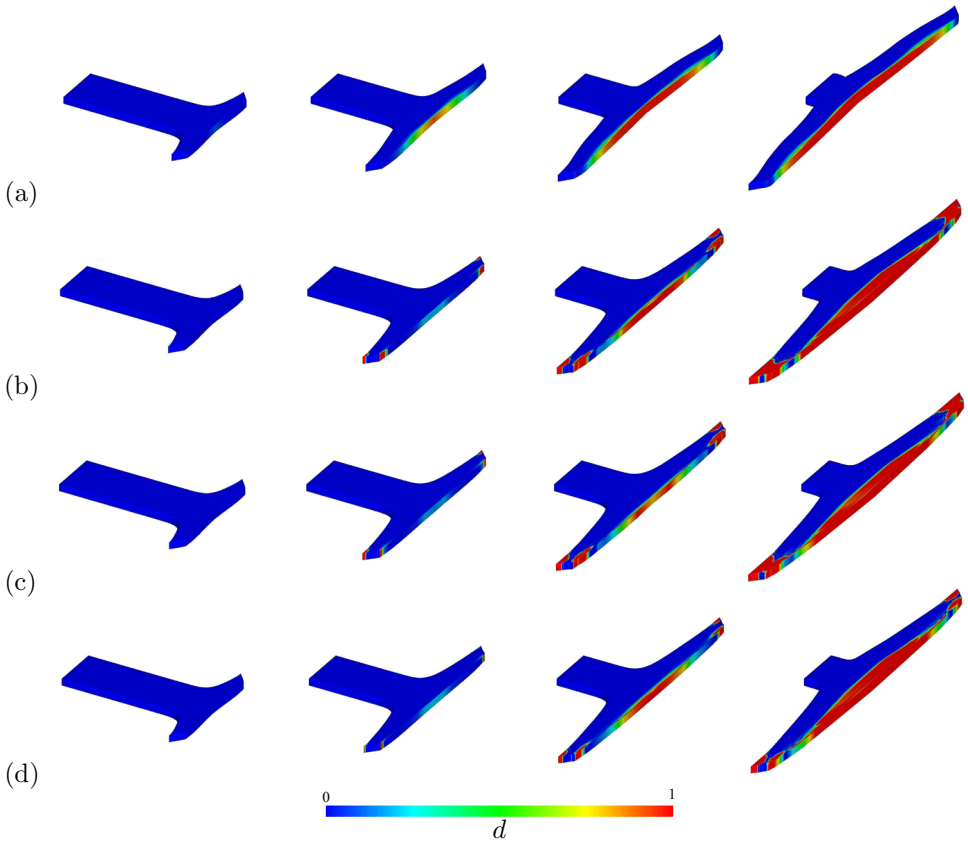

Figure 2: Evolution of the crack phase-field d for (a) the energy-based; (b) the Tsai-Wu; (c) the principal stress criterion, as the arterial tissue with an initial tear is being pulled in two opposite directions.

directions, see Fig. 2. Analysis results render the stress-based criteria susceptible to instabilities in terms of crack growth upon the initiation of macro-cracks in the material thereby the convergence of the algorithm becomes problematic. Moreover, the use of stress-based criteria leads to a crack propagation susceptible to boundary effects not observed in the case of the energy-based criterion.

4 CONCLUSION

A number of anisotropic failure criteria, essentially based on free energy or stress, was compared in terms of their capability to manifest admissible anisotropic failure surfaces and crack propagations for simple boundary-value problems (BVPs). On the theoretical side, the anisotropic crack phase-field model, established according to a continuous variational setup due to a power balance, provided the backbone of our modeling endeavors. On the numerical side, we focused on the failure surfaces of the used criteria induced for a homogeneous problem subjected to uniaxial and planar biaxial deformations. A peel test was also analyzed and the respective dissections were examined. Results favor the energetic-based criterion to accomplish a stable crack growth for the analyzed 3D BVPs blended with anisotropy at finite strains.

REFERENCES

[1] H. Dal. Quasi-incompressible and quasi-inextensible element formulation for transversely anisotropic materials. *Int. J. Numer. Meth. Engng*, 2017. submitted.

[2] O. Gültekin. A Phase Field Approach to the Fracture of Anisotropic Medium. Master's Thesis, University of Stuttgart, Institute of Applied Mechanics (CE), 2014.

[3] O. Gültekin, H. Dal, and G. A. Holzapfel. A phase-field approach to model fracture of arterial walls: theory and finite element analysis. *Comput. Meth. Appl. Mech. Eng.*, 312:542–566, 2016.

[4] O. Gültekin, H. Dal, and G. A. Holzapfel. Numerical aspects of anisotropic failure in soft biological tissues favor energy-based criteria: A rate-dependent mixed crack phase-field model. *Comput. Meth. Appl. Mech. Eng.*, 2017. submitted.

[5] R. Hill. A theory of the yielding and plastic flow of anisotropic metals. *Proc. R. Soc. Lond. A*, 193:281–297, 1948.

[6] G. A. Holzapfel, T. C. Gasser, and R. W. Ogden. A new constitutive framework for arterial wall mechanics and a comparative study of material models. *J. Elasticity*, 61:1–48, 2000.

[7] J. D. Humphrey and G. A. Holzapfel. Mechanics, mechanobiology, and modeling of human abdominal aorta and aneurysms. *J. Biomech.*, 45:805–814, 2012.

[8] C. Miehe, M. Hofacker, and F. Welschinger. A phase field model for rate-independent crack propagation: Robust algorithmic implementation based on operator splits. *Comput. Meth. Appl. Mech. Eng.*, 199:2765–2778, 2010.

[9] C. Miehe, L.-M. Schänzel, and H. Ulmer. Phase field modeling of fracture in multi-physics problems. Part I. Balance of crack surface and failure criteria for brittle crack propagation in thermo-elastic solids. *Comput. Meth. Appl. Mech. Eng.*, 294:449–485, 2015.

[10] C. Miehe, F. Welschinger, and M. Hofacker. Thermodynamically consistent phase-field models of fracture: Variational principles and multi-field FE implementations. *Int. J. Numer. Meth. Engng*, 83:1273–1311, 2010.

[11] A. Raina and C. Miehe. A phase-field model for fracture in biological tissues. *Biomech. Model. Mechanobiol.*, 15:479–496, 2016.

[12] J. Tong, T. Cohnert, P. Regitnig, J. Kohlbacher, R. Birner-Gruenberger, A. J. Schriefl, G. Sommer, and G. A. Holzapfel. Variations of dissection properties and mass fractions with thrombus age in human abdominal aortic aneurysms. *J. Biomech.*, 47:14–23, 2014.

[13] S. W. Tsai and E. M. Wu. A general theory of strength of anisotropic materials. *J. Compos. Mater.*, 5:58–80, 1971.

XIV International Conference on Computational Plasticity. Fundamentals and Applications
COMPLAS XIV
E. Oñate, D.R.J. Owen, D. Peric & M. Chiumenti (Eds)

A THERMODYNAMICALLY CONSISTENT COHESIVE DAMAGE MODEL FOR THE SIMULATION OF MIXED-MODE DELAMINATION

FEDERICA CONFALONIERI* AND UMBERTO PEREGO*

* Department of Civil and Environmental Engineering
Politecnico di Milano
Piazza Leonardo da Vinci, 32, Milano, Italy
e-mail: federica.confalonieri@polimi.it - umberto.perego@polimi.it

Key words: Mixed-mode delamination, cohesive model, isotropic damage

Abstract. This work is devoted to the formulation of a new cohesive model for mixed-mode delamination. The model is based on a thermodynamically consistent isotropic damage formulation, with consideration of an internal friction mechanism that governs the interaction between normal and shear opening modes.

1 INTRODUCTION

Delamination, i.e. the progressive decohesion between two layers, is one of the main causes of failure for laminated composites. Delamination often develops under the presence of concurrent interlaminar tensile and shear stresses, leading to mixed-mode loading conditions with variable mode ratios. Several experimental works [1, 2, 3] have shown that the micro-mechanical mechanisms involved in the delamination phenomenon vary with the mixed-mode ratio, with a transition from pure mode I loading characterized by matrix cleavage and fiber pull-out, to mode II conditions dominated by the formations of cusps and hackles. At the macroscopic scale, this causes the fracture energy to increase in passing from Mode I to Mode II, as confirmed by results of experimental tests performed on many different composite materials (see, for instance, [4, 5]). As an example, Figure 1 shows the values of fracture energy at different mode ratios reported in [6] and deriving from different experiments performed with the Mixed Mode Bending test apparatus [7] on AS4/3501-6 carbon/epoxy composite. Empirical relationships have been proposed in the literature to define a failure locus able to interpolate the toughness variation over the full mixed-mode range. Among them, it is worth mentioning the Power Law [8] and the BK law [4], widely employed as delamination criteria.

Robust numerical simulation tools are mandatory to obtain accurate predictions of the onset and propagation of delamination in real-life problems, characterized by variable loading paths. The finite element simulation of the decohesion between layers is often addressed by means of interface elements, whose constitutive behavior is modeled by a

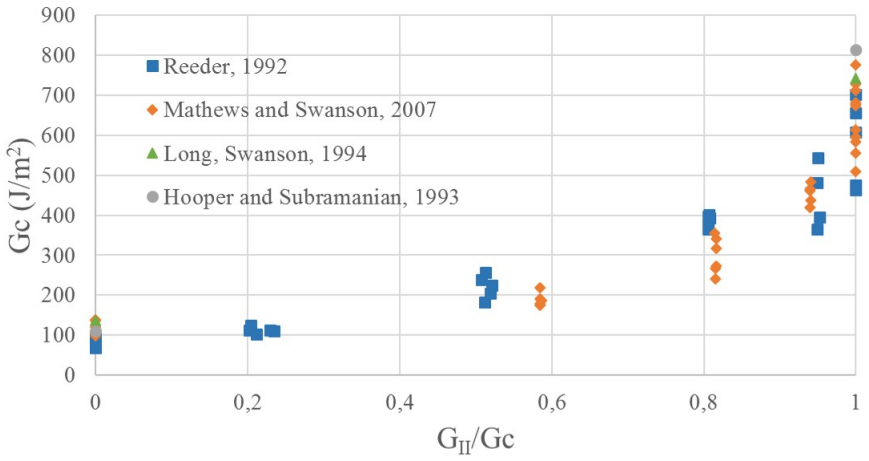

Figure 1: AS4/3501-6: fracture energy vs mode mixity

cohesive law. In the literature, one can find a huge number of works on the cohesive modeling of delamination, (see, for instance, [9, 10, 11]). However, many of them exhibit some limitations, such as the need of assumptions on the loading path, the lack of thermodynamic consistency, or the inability to ensure the correct energy dissipation in case of non-proportional loading paths. These drawbacks may affect the reliability of the numerical results when mixed-mode loading conditions with variable mode mixity ratios and/or non-proportional loading are considered.

This work proposes a new cohesive model, based on a thermodynamically consistent formulation with isotropic damage. An internal friction parameter is introduced to handle the coupling between normal and shear stresses. The overall fracture energy at any mode ratio is an outcome of the model, without the need to introduce any empirical laws to define the fracture energy variation with the mode-mixity ratio.

2 FORMULATION

Let us consider the zero-thickness 2D interface element with four nodes shown in Figure 2. Under the hypothesis of small openings, the relative displacement vector $\boldsymbol{\delta}$ is computed as the difference between the displacements of two corresponding points belonging to the top and bottom edges respectively:

$$\boldsymbol{\delta} = \boldsymbol{\delta}^{+} - \boldsymbol{\delta}^{-} \tag{1}$$

A local reference frame is introduced in order to identify the normal and the tangential directions. Superscripts n and s will denote the normal and the shear components, respectively, of tractions and opening displacements.

The starting point of the formulation is the introduction of the free energy per unit surface Ψ, defined as:

$$\Psi = \frac{1}{2} K \left(\langle \delta^n \rangle_-\right)^2 + \frac{1}{2} \left(1-d\right) K \left(\langle \delta^n \rangle_+\right)^2 + \frac{1}{2} \left(1-d\right) K \left(\delta^s\right)^2 \tag{2}$$

where K is the elastic stiffness of the interface and d the isotropic damage variable.

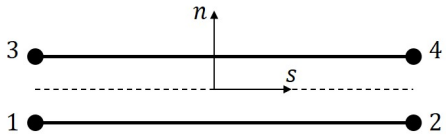

Figure 2: 4-node interface element

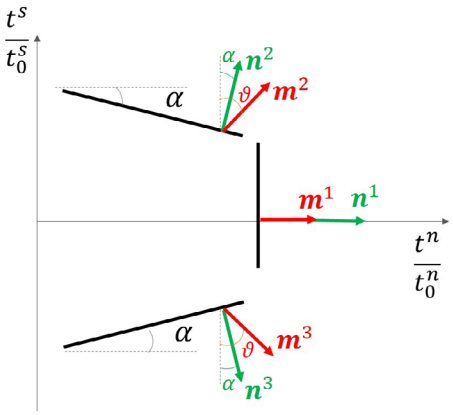

Figure 3: Damage modes

The same elastic stiffness is considered in the normal and in the shear directions. The Macauley brackets $\langle\ \rangle$ are introduced to distinguish between the negative and the positive part of the normal opening displacement, so that the unilateral effect is accounted for. The cohesive tractions t^n and t^s and the strain energy release rate Y per unit damage growth are obtained through the state equations:

$$t^n = \frac{\partial \Psi}{\partial \delta^n} = K\langle\delta^n\rangle_- + (1-d)\,K\langle\delta^n\rangle_+ \qquad t^s = \frac{\partial \Psi}{\partial \delta^s} = (1-d)\,K\delta^s \tag{3}$$

$$Y = -\frac{\partial \Psi}{\partial d} = \tfrac{1}{2}K\left(\langle\delta^n\rangle_+\right)^2 + \tfrac{1}{2}K\left(\delta^s\right)^2 \tag{4}$$

For the sake of simplicity, in the following only the tensile case, i.e. $\delta^n \geq 0$, will be considered.

The model is based on the definition of three different damage modes in the plane of non-dimensional cohesive tractions, identified by the normal unit vectors $\mathbf{n^1}$, $\mathbf{n^2}$ and $\mathbf{n^3}$ (see Figure 3), whose interaction governs the cohesive interface evolution under mixed-mode loading conditions. As can be seen from Figure 3, $\mathbf{n^1}$ defines the opening-dominated mode, while $\mathbf{n^2}$ and $\mathbf{n^3}$ the two shear-dominated modes. The three normals are collected in matrix $\mathbf{N}$:

$$\mathbf{N} = \begin{bmatrix} \mathbf{n^1} \\ \mathbf{n^2} \\ \mathbf{n^3} \end{bmatrix} = \begin{bmatrix} 1 & 0 \\ \sin\alpha & \cos\alpha \\ \sin\alpha & -\cos\alpha \end{bmatrix} \tag{5}$$

where the angle α, playing the role of a parameter of internal friction, defines the inclination of the two shear-dominated damage modes.

A vector of effective cohesive stresses $\mathbf{s} = [s^1\ s^2\ s^3]^T$ is defined by projecting the vector of dimensionless cohesive traction $\overline{\mathbf{t}}$ along the three normals:

$$\mathbf{s} = \mathbf{N}\overline{\mathbf{t}} \tag{6}$$

where:

$$\overline{\mathbf{t}} = \begin{bmatrix} \overline{t}^n \\ \overline{t}^s \end{bmatrix} = \begin{bmatrix} \frac{t^n}{t_0^n} \\ \frac{t^s}{t_0^s} \end{bmatrix} \tag{7}$$

being t_0^n and t_0^s the strengths in pure Modes I and II. Thus, eqn. 6 becomes:

$$\begin{aligned} s^1 &= \overline{\mathbf{t}}^T\mathbf{n^1} = \overline{t}^n \\ s^2 &= \overline{\mathbf{t}}^T\mathbf{n^2} = \overline{t}^n\sin\alpha + \overline{t}^s\cos\alpha \\ s^3 &= \overline{\mathbf{t}}^T\mathbf{n^3} = \overline{t}^n\sin\alpha - \overline{t}^s\cos\alpha \end{aligned} \tag{8}$$

Let us now introduce the effective opening displacements $\mathbf{w} = [w^1\ w^2\ w^3]^T$, representing the kinematic variables conjugated to the effective cohesive stresses $\mathbf{s}$ in the expression of the free energy density Ψ and defined as the projection of the dimensionless relative displacements vector $\overline{\boldsymbol{\delta}}$ onto a structural vector $\mathbf{m^i}$ (see Figure 3). In matrix form:

$$\mathbf{w} = \mathbf{M}\overline{\boldsymbol{\delta}} \tag{9}$$

where:

$$\overline{\boldsymbol{\delta}} = \begin{bmatrix} \overline{\delta}^n \\ \overline{\delta}^s \end{bmatrix} = \begin{bmatrix} \frac{\delta^n}{\delta_0^n} \\ \frac{\delta^s}{\delta_0^s} \end{bmatrix} \tag{10}$$

being δ_0^n and δ_0^s the relative displacements at the onset of delamination, i.e. corresponding to t_0^n and t_0^s. $\mathbf{M}$ is the matrix gathering the components of the three structural vectors $\mathbf{m^i}$:

$$\mathbf{M} = \begin{bmatrix} \mathbf{m^1} \\ \mathbf{m^2} \\ \mathbf{m^3} \end{bmatrix} = \begin{bmatrix} a & 0 \\ b\sin\theta & b\cos\theta \\ b\sin\theta & -b\cos\theta \end{bmatrix} \tag{11}$$

being θ the angle defining the orientation of $\mathbf{m^2}$ and $\mathbf{m^3}$. As shown in Figure 3, $\mathbf{m^1}$ is aligned to $\mathbf{n^1}$ for symmetry considerations. The two unknown constants a and b are determined by imposing that the elastic strain energy density Ψ remains the same in passing from the direct to the effective variables, i.e.

$$\frac{1}{2}\mathbf{t}^T\boldsymbol{\delta} = \frac{1}{2}\left(s^1w^1 + s^2w^2 + s^3w^3\right) \tag{12}$$

From eqn. 12, one obtains:

$$a = (t_0^n\delta_0^n - t_0^s\delta_0^s\tan\alpha\tan\theta) \qquad b = \frac{t_0^s\delta_0^s}{2\cos\alpha\cos\theta} \tag{13}$$

Thus,

$$\begin{aligned} w^1 &= \overline{\boldsymbol{\delta}}^T\mathbf{m^1} = (t_0^n\delta_0^n - t_0^s\delta_0^s\tan\alpha\tan\theta)\,\overline{\delta}^n \\ w^2 &= \overline{\boldsymbol{\delta}}^T\mathbf{m^2} = \tfrac{t_0^s\delta_0^s}{2\cos\alpha\cos\theta}\left(\sin\theta\overline{\delta}^n + \cos\theta\overline{\delta}^s\right) \\ w^3 &= \overline{\boldsymbol{\delta}}^T\mathbf{m^3} = \tfrac{t_0^s\delta_0^s}{2\cos\alpha\cos\theta}\left(\sin\theta\overline{\delta}^n - \cos\theta\overline{\delta}^s\right) \end{aligned} \tag{14}$$

Based on the definitions 6 and 9 of effective stresses and relative displacements, the overall strain energy density can be decomposed into the sum of three distinct contributions, each one associated to a damage mode as:

$$\Psi = \frac{1}{2}\mathbf{t}^T\boldsymbol{\delta} = \underbrace{\frac{1}{2}s^1w^1}_{\Psi^1} + \underbrace{\frac{1}{2}s^2w^2}_{\Psi^2} + \underbrace{\frac{1}{2}s^3w^3}_{\Psi^3} \tag{15}$$

By exploiting the decomposition of eqn. 15, three effective strain energies Y^i released per unit growth of damage can also be defined through the state equations as:

$$\begin{aligned} Y^1 &= -\frac{\partial\Psi^1}{\partial d} = \frac{1}{2}\left(t_0^n\delta_0^n - t_0^s\delta_0^s\tan\alpha\tan\theta\right)\left\langle\overline{\delta}^n\right\rangle^2 \\ Y^2 &= -\frac{\partial\Psi^2}{\partial d} = \frac{1}{4}t_0^s\delta_0^s\left[\tan\alpha\tan\theta\left\langle\overline{\delta}^n\right\rangle^2 + \left\langle\overline{\delta}^s\right\rangle^2 + \left(\tan\alpha+\tan\theta\right)\overline{\delta}^n\overline{\delta}^s\right] \\ Y^3 &= -\frac{\partial\Psi^3}{\partial d} = \frac{1}{4}t_0^s\delta_0^s\left[\tan\alpha\tan\theta\left\langle\overline{\delta}^n\right\rangle^2 + \left\langle\overline{\delta}^s\right\rangle^2 - \left(\tan\alpha+\tan\theta\right)\overline{\delta}^n\overline{\delta}^s\right] \end{aligned} \tag{16}$$

It can be observed that:

$$Y^1 + Y^2 + Y^3 = \frac{1}{2}t_0^n\delta_0^n\left\langle\overline{\delta}^n\right\rangle^2 + \frac{1}{2}t_0^s\delta_0^s\left\langle\overline{\delta}^s\right\rangle^2 = Y \tag{17}$$

with $t_0^n = K\delta_0^n$ and $t_0^s = K\delta_0^s$. The decomposition of the strain energy release rate Y into its three components Y^i depends on the ratio $\frac{t_0^n\delta_0^n}{t_0^s\delta_0^s}$ and on the angles α and θ. In the applications, it will be assumed that:

$$\theta = \arctan\left(\frac{t_0^n\delta_0^n}{t_0^s\delta_0^s}\tan\alpha\right) \tag{18}$$

so that Y^1 is always positive for any positive value of δ^n. Under this hypothesis, either Y^2 or Y^3 can be negative, but their sum $Y^2 + Y^3 = \frac{1}{2}\left[\tan\alpha\tan\theta\left\langle\overline{\delta}^n\right\rangle^2 + \left\langle\overline{\delta}^s\right\rangle^2\right]$, representing the fraction of the strain energy release rate associated to the shear-dominated damage modes, is always positive.

An energy criterion is considered to express the damage activation function:

$$\varphi = \left(\frac{Y^1}{\chi_0^1+\chi^1}\right)^k + H(Y^2)\left(\frac{Y^2}{\chi_0^2+\chi^2}\right)^k + H(Y^3)\left(\frac{Y^3}{\chi_0^3+\chi^3}\right)^k - 1 \leq 0 \tag{19}$$

where $H()$ is the Heavyside function introduced to exclude possible negative contribution of Y^2 or Y^3 to damage activation, the exponent k is a parameter of the proposed cohesive model and $(\chi_0^i + \chi^i)$ represents the current threshold of the $i-th$ damage mode, being χ_0^i its initial value and χ^i an internal variable governing its evolution with damage and determining the shape of the softening branch. In this work, a model exhibiting a bilinear traction-separation law in pure Modes I and II (see Figure 5) is considered, although other choices of the functional form of the traction-separation curves (e.g. with an exponential strength decay) are in principle allowed. Figure 4 shows the damage activation surface at the onset of decohesion, for increasing values of the internal friction angle α and $k = 2$

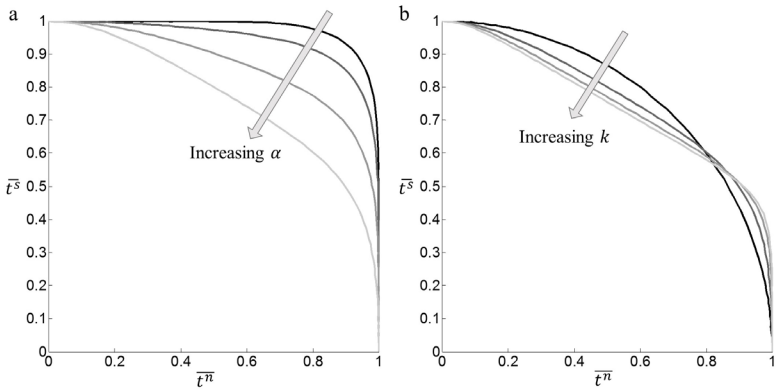

Figure 4: First activation domain: a) for increasing values of α and $k = 2$; b) for increasing values of k and $\alpha = 30°$

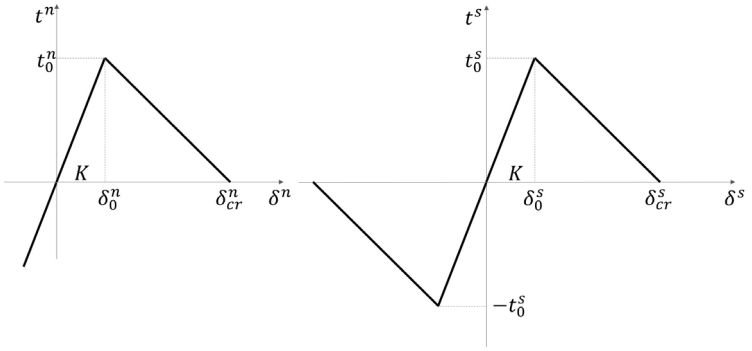

Figure 5: Bilinear cohesive laws in pure Modes I and II

(a) and for increasing values of the exponent k, while maintaining a constant value of the angle $\alpha = 30°$ (b).

The expressions of χ_0^i and χ^i for the bilinear law can be found by considering the behavior in pure loading Modes. At first, let us consider a pure Mode II case, characterized by $\delta^n = 0$ and $\delta^s \neq 0$. Under this hypothesis, it holds that (subscripts mI and mII denote pure Mode I and Mode II loading conditions):

$$\begin{aligned} Y_{mII}^1 &= 0 \\ Y_{mII}^2 &= \tfrac{1}{4} t_0^s \delta_0^s \left(\overline{\delta}^s\right)^s \\ Y_{mII}^3 &= \tfrac{1}{4} t_0^s \delta_0^s \left(\overline{\delta}^s\right)^s \end{aligned} \tag{20}$$

Because of the symmetry of the two shear dominated damage modes, it turns out that $Y_{mII}^2 = Y_{mII}^3$, $\chi_0^2 = \chi_0^3$ and $\chi^2 = \chi^3$. The initial thresholds χ_0^2 and χ_0^3 can be determined by imposing that the activation function is zero at the onset of delamination, i.e. for $\overline{\delta}^s = 1$. Thus,

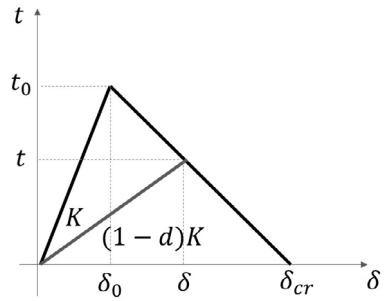

Figure 6: Pure mode bilinear law

$$\phi = \left(\frac{Y^2_{mII}|_1}{\chi^2_0}\right)^k + \left(\frac{Y^3_{mII}|_1}{\chi^3_0}\right)^k = 2\left(\frac{Y^2_{mII}|_1}{\chi^2_0}\right)^k - 1 = 0 \quad \rightarrow \quad \chi^2_0 = \chi^3_0 = 2^{\frac{1}{k}}\frac{1}{4}t^s_0\delta^s_0 \tag{21}$$

Analogously, by considering a generic point along the softening branch, it is possible to find the expressions of χ^2 and χ^3 as:

$$\phi = \left(\frac{Y^2_{mII}}{\chi^2_0+\chi^2}\right)^k + \left(\frac{Y^3_{mII}}{\chi^3_0+\chi^2}\right)^k - 1 = 0 \quad \rightarrow \quad \chi^2 = \chi^3 = 2^{\frac{1}{k}}\frac{1}{4}t^s_0\delta^s_0\left[\left(\overline{\delta}^s\right)^2 - 1\right] \tag{22}$$

If a pure mode case is considered, the relationship between the relative displacement and the damage variable can be obtained on the basis of purely geometrical considerations, given the triangular shape of the cohesive law depicted in Figure 6.

$$\delta = \frac{\delta_{cr}\delta_0}{\delta_{cr} - (\delta_{cr} - \delta_0)d} \tag{23}$$

By substituting eqn. 23 into eqn. 22, one obtains:

$$\chi^2 = \chi^3 = 2^{\frac{1}{k}}\frac{1}{4}t^s_0\delta^s_0\left[\frac{\delta^s_{cr}}{\delta^s_{cr} - (\delta^s_{cr} - \delta^s_0)\,d}\right]^2 - \chi^2_0 \tag{24}$$

While in pure Mode II one has $Y^1_{mII} = 0$, in a pure Mode I case, i.e. for $\delta^n \neq 0$ and $\delta^s = 0$, Y^2_{mI} and Y^3_{mI} are also non-zero:

$$\begin{aligned} Y^1_{mI} &= \tfrac{1}{2}\left(t^n_0\delta^n_0 - t^s_0\delta^s_0\tan\alpha\tan\theta\right)\left(\overline{\delta}^n\right)^2 \\ Y^2_{mI} &= \tfrac{1}{4}t^s_0\delta^s_0\left(\tan\alpha\tan\theta\overline{\delta}^n\right)^s \\ Y^3_{mI} &= \tfrac{1}{4}t^s_0\delta^s_0\left(\tan\alpha\tan\theta\overline{\delta}^n\right)^s \end{aligned} \tag{25}$$

At delamination onset (i.e. for $\overline{\delta}^n = 1$), it holds that:

$$\phi = \left(\frac{Y^1_{mI}|_1}{\chi^1_0}\right)^k + \left(\frac{Y^2_{mI}|_1}{\chi^2_0}\right)^k + \left(\frac{Y^3_{mI}|_1}{\chi^3_0}\right)^k - 1 = 0 \quad \rightarrow \quad \chi^1_0 = \frac{1}{2}\frac{\left(t^n_0\delta^n_0 - t^s_0\delta^S_0\tan\alpha\tan\theta\right)}{\left[1-(\tan\alpha\tan\theta)^k\right]^{\frac{1}{k}}} \tag{26}$$

while, by imposing that the activation function is zero for a generic dimensionless opening displacement $\overline{\delta}^n$, i.e.

$$\phi = \left(\frac{Y^1_{mI}}{\chi^1_0 + \chi^1}\right)^k \left(\frac{Y^2_{mI}}{\chi^2_0 + \chi^2}\right)^k + \left(\frac{Y^3_{mI}}{\chi^3_0 + \chi^2}\right)^k - 1 = 0 \tag{27}$$

one obtains:

$$\chi^1 = \frac{\left(t^n_0 \delta^n_0 - t^s_0 \delta^S_0 \tan\alpha \tan\theta\right)}{\left\{1 - \left[\left(\frac{\delta^n_{cr}}{\delta^s_{cr}} \frac{\delta^s_{cr} - (\delta^s_{cr} - \delta^s_0)d}{\delta^n_{cr} - (\delta^n_{cr} - \delta^n_0)d}\right)^2 \tan\alpha \tan\theta\right]^k\right\}^{\frac{1}{k}}} \frac{1}{2} \left(\frac{\delta^n_{cr}}{\delta^n_{cr} - (\delta^n_{cr} - \delta^n_0)d}\right)^2 - \chi^1_0 \tag{28}$$

The formulation of the proposed cohesive model is completed by the introduction of the evolution law, expressing the damage rate as:

$$\dot{d} = -\frac{\frac{\partial\phi}{\partial\delta^n}\dot{\delta}^n + \frac{\partial\phi}{\partial\delta^s}\dot{\delta}^s}{\frac{\partial\phi}{\partial d}} = \frac{\sum_{i=1}^3 \left(\frac{\partial\phi}{\partial Y^i}\frac{\partial Y^i}{\partial\delta^n}\right)\dot{\delta}^n + \sum_{i=1}^3 \left(\frac{\partial\phi}{\partial Y^i}\frac{\partial Y^i}{\partial\delta^s}\right)\dot{\delta}^s}{\sum_{i=1}^3 \left(\frac{\partial\phi}{\partial\chi^i}\frac{\partial\chi^i}{\partial d}\right)} \tag{29}$$

together with the classical loading/unloading conditions:

$$\phi \leq 0 \qquad \dot{d} \geq 0 \qquad \phi\dot{d} = 0 \tag{30}$$

Using a classical argument, based on the Clausius-Duhem inequality for isothermal processes, the mechanical dissipation can be proven to be always non-negative:

$$D = Y^1\dot{d} + Y^2\dot{d} + Y^3\dot{d} = \left(Y^1 + Y^2 + Y^3\right)\dot{d} = Y\dot{d} \geq 0 \tag{31}$$

The definition of the proposed cohesive model requires the following input parameters: the fracture energies G_{Ic}, G_{IIc} and the peak tractions t^n_0, t^s_0 in pure Modes I and II, the internal friction angle α and the exponent k appearing in the activation function ϕ. These parameters can be identified based on the results of standard experimental tests, i.e. one Double Cantilever Beam (DCB) test for pure Mode I, one End Notch Flexure (ENF) test for pure Mode II and a set of Mixed Mode Bending (MMB) tests [7] for varying mode-mixity ratio, from which a curve describing the evolution of the fracture energy with the mode mixity ratio can be constructed.

3 NUMERICAL EXAMPLES

The accuracy of the proposed model is assessed at a material point level by prescribing the two components of the relative displacement along different paths, for a number of different parameter sets.

3.1 Consistency tests: proportional path

Radial loading conditions with varying separation angles are enforced by imposing $\delta^n = (1-\beta)\,\gamma$ and $\delta^s = \beta\gamma$, γ being a multiplier linearly increasing from 0 to $\gamma_{max} = 0.1$ mm and $\beta \in [0,1]$ a parameter defining the mode-mixity. Pure Modes I and II are recovered for $\beta = 0$ and $\beta = 1$, respectively. Identical cohesive properties are here assumed for the pure Modes, considering $G_{Ic} = G_{IIc} = 0.1$ kJ/m^2 and $t^n_0 = t^s_0 = 6$ MPa.

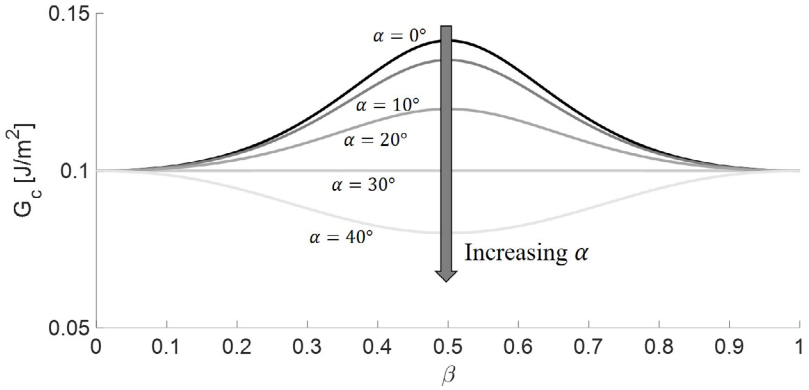

Figure 7: Fracture energy vs mode mixity for $k = 2$, $G_{Ic} = G_{IIc}$, $t_0^n = t_0^s$ for increasing values of angle α

Under these hypotheses, it is possible to show analytically that the softening branch is linear for any value of β (note that this is not the case for $\beta \neq 0$ and $G_{Ic} \neq G_{IIc}$, even when the traction-separation curves are bilinear in pure modes). Moreover, for an exponent $k = 2$ (i.e. quadratic damage activation surface), the response is symmetric with respect to $\beta = 0.5$, i.e. the response is the same for β_1 and $\beta_2 = 1 - \beta_1$. Figure 7 shows the evolution of the overall fracture energy G_c with the mode mixity parameter β, computed as the sum of the areas beneath the traction-separation curves. Increasing the internal friction α has the effect of reducing the peak value, without changing its position because of symmetry. It is noteworthy that for $\alpha = 30°$, the model is able to reproduce the case of constant fracture energy. This result can be found also analytically, by imposing that the activation function is zero at the onset of delamination and at complete decohesion, so that the two corresponding values of γ_0 and γ_{cr} are obtained:

$$\gamma_0 = \frac{\delta_0}{\left[(1-\beta)^4 + 6\beta^2 (1-\beta)^2 \tan\alpha^2 + \beta^4\right]^{\frac{1}{4}}}, \qquad \gamma_{cr} = \gamma_0 \frac{\delta_{cr}}{\delta_0} \tag{32}$$

For $\alpha = 30°$, one obtains:

$$\gamma_0 = \frac{\delta_0}{\sqrt{1 - 2\beta + 2\beta^2}}, \qquad \gamma_{cr} = \frac{\delta_{cr}}{\sqrt{1 - 2\beta + 2\beta^2}} \tag{33}$$

The fracture energy turns out to be independent of β, i.e.:

$$G_c = \frac{1}{2} K (1-\beta)^2 \gamma_0 \gamma_{cr} + \frac{1}{2} K \beta^2 \gamma_0 \gamma_{cr} = \frac{1}{2} K \delta_0 \delta_{cr} = \text{const.} \tag{34}$$

3.2 Consistency test: non-proportional path

The non-proportional, zig-zag loading path proposed in [12] and depicted in Figure 8a is considered in this example. The adopted cohesive properties are listed in Table 1. Figure 8b shows the evolution of the damage variable: since a monotonically increasing separation is applied, the damage increases monotonically as expected. The resulting traction-separation curves are shown in Figure 9.

Table 1: Non proportional zig-zag path: cohesive properties

t_0^n MPa	t_0^s MPa	G_{Ic} $\frac{J}{m^2}$	G_{IIc} $\frac{J}{m^2}$	α	k
10	10	100	100	30	4

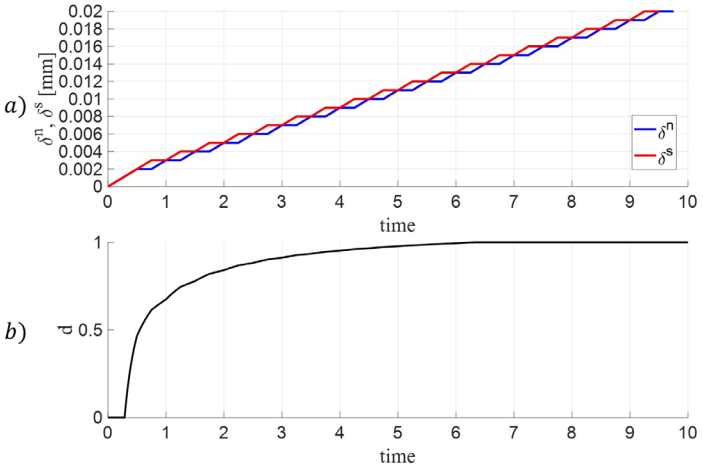

Figure 8: Zig-zag path: a) relative displacement history, b) damage variable evolution.

3.3 Mixed-mode bending (MMB) tests

The experimental data of the Mixed Mode Bending (MMB) tests performed by Reeder [8] on three different fibre reinforced composites, namely AS4/PEEK, AS4/3501-6 and IM7/977-2, are here considered to assess the capability of the proposed model to reproduce the mixed-mode behaviour over the full range of mode-mixity ratios. The adopted cohesive properties are reported in Table 2. The internal friction angle α and the exponent k are the values that guarantees the best fitting of the experimental data. The fracture energy is computed as the sum of the areas beneath the normal and shear traction-separation curves, obtained with a series of radial paths in the $\delta^n - \delta^s$ plane, with increasing mode-mixity ratio. In figure 10 the numerical prediction of the fracture energy for varying mode-mixity ratio is compared with the experimental data and with the results obtained with a Power Law, whose exponents have been calibrated in [8]: the dots corresponds to the experimental points, the red dashed lines are obtained with the empirical Power Law and the solid lines are the results of the present model. In all the three cases, the model is able to reproduce correctly the non-monotonic growth of the fracture energy with the mode mixity ratio and the numerical results are very close to the best fitting obtained by Reeder, without the need of adopting any empirical law.

4 CONCLUSIONS

A new isotropic damage cohesive model has been proposed for the simulation of delamination under mixed-mode loading conditions. The model is based on the introduction of

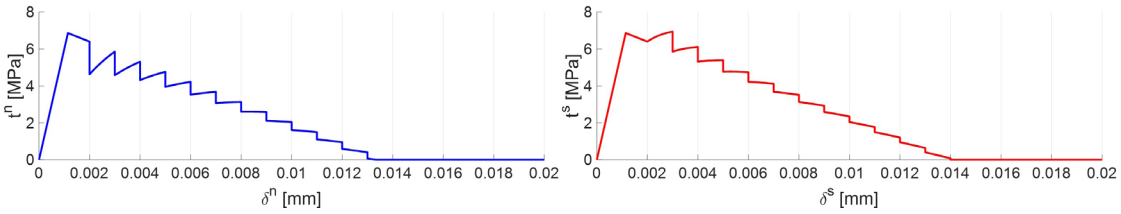

Figure 9: Zig-zag path: traction-separation laws.

Table 2: Cohesive properties

	t_0^n MPa	t_0^s MPa	G_{Ic} $\frac{J}{m^2}$	G_{IIc} $\frac{J}{m^2}$	α	k
AS4/PEEK	80	100	779	1142	24	1.6
AS4/3501-6	45	48	90	600	25	12
IM7/977-2	70	130	310	1410	28	12

an internal friction dissipation mechanism, which allows to handle the coupling between normal and shear damage modes. The resuting mixed-mode fracture energy is the outcome of modes interaction, without the need to define a-priori any empirical law. The model is thermodynamically consistent, even under arbitrary non proportional loading paths, with variable mode ratio.

5 Acknowledgements

The financial support of Tetra Pak Packaging Solutions is gratefully acknowledged.

REFERENCES

[1] Hibbs, M.F. and Bradley, W.L. Correlations between micromechanical failure processes and the delamination toughness of graphite/epoxy systems. *Fractography of Modern Engineering Materials: Composites and Metals, ASTM International* Vol. 948, (1987)

[2] Greenalgh, E.S. and Rogers, C. and Robinson, P. Fractographic observations on delamination growth and the subsequent migration through the laminate. *Composites Science and Technology* (2009) **69**:2345–2351.

[3] Marat-Mendes, R. and de Freitas, M. Fractographic analysis of delamination in glass/fibre epoxy composites. *Journal of Composite Materials* (2013) **47**:1437–1448.

[4] Benzeggagh, M.L. and Crews, J.H. Measurement of mixed-mode delamination fracture toughness of unidirectional glass/epoxy composites with mixed-mode bending apparatus. *Composites Science and Technology*, (1996) **56**:439–449.

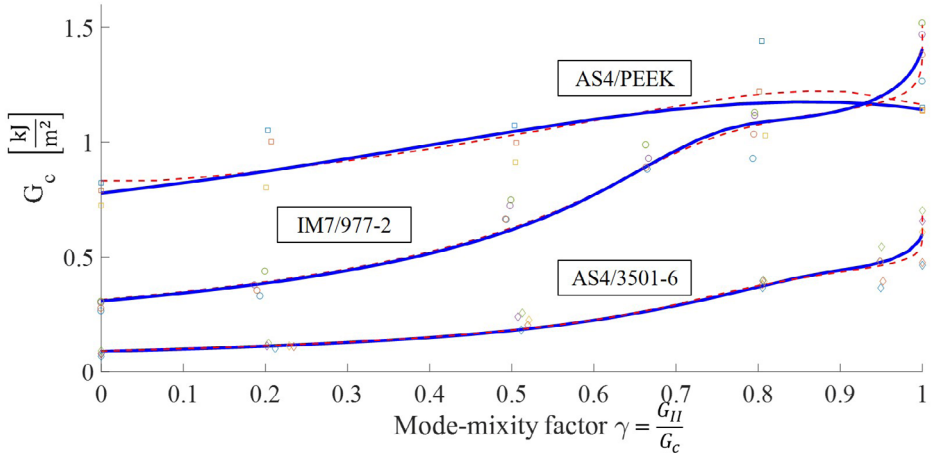

Figure 10: Experimental vs numerical mixed-mode fracture energies. Dots: experimental data [8]. Dashed line: Power Law [8]. Solid line: result of the present model.

[5] Davidson, B.D. and Zhao, W. An accurate mixed-mode delamination failure criterion for laminated fibrous composites requiring limited experimental input. *Journal of Composite Materials* (2007) **41**: 679–702.

[6] Mathews, M. J., and Swanson, S. R. Characterization of the interlaminar fracture toughness of a laminated carbon/epoxy composite. *Composites Science and Technology* (2007) **67**: 1489–1498.

[7] Reeder, J.R. and Crews, J.H. Mixed-mode bending method for delamination testing. *AIAA Journal* (1990)**28**:1270-1276.

[8] Reeder, J.R., An Evaluation of Mixed-Mode Delamination Failure Criteria. *NASA Technical Reports* (1992) **ID:19920009705**:1-50.

[9] Camanho, P.P and Davila, C.G. and de Moura, M.F. Numerical Simulation of Mixed-mode Progressive Delamination in Composite Materials. *Journal of Composite Materials* (2003) **37**:1415–1438.

[10] Van den Bosch, M.J. and Schreurs, P. J. G. and Geers, M. G. D. An improved description of the exponential Xu and Needleman cohesive zone law for mixed-mode decohesion. *Engineering Fracture Mechanics* (2006) **73**:1220–1234.

[11] Park, K. and Paulino, G. H. and Roesler, J. R. A unified potential-based cohesive model of mixed-mode fracture. *Journal of the Mechanics and Physics of Solids* (2009) **57**:891-908.

[12] Park, K. and Choi, H. and Paulino, G. Assessment of cohesive traction-separation relationships in ABAQUS: a comparative study. *Mechanics Research Communications* (2016) **78**:71–78

XIV International Conference on Computational Plasticity. Fundamentals and Applications
COMPLAS 2017
E. Oñate, D.R.J. Owen, D. Peric and M. Chiumenti (Eds)

COMPARISON OF GURSON AND LEMAITRE MODEL IN THE CONTEXT OF BLANKING SIMULATION OF A HIGH STRENGTH STEEL

FLORIAN GUTKNECHT, KERIM ISIK,

TILL CLAUSMEYER AND A. ERMAN TEKKAYA

Institute of Forming Technology and Lightweight Construction (IUL)
Technical University Dortmund
Baroper Str. 303, 44227 Dortmund, Germany
Email: Florian.Gutknecht@iul.tu-dortmund.de, www.iul.eu

Key words: sheet metal, blanking, damage model, parameter identification, simulation.

Abstract. The process of blanking takes place in a short band with high accumulated strain undergoing various stress triaxialities. Enhanced implementations for shear and compressive loads of Gurson's and Lemaitre's model are directly compared for the same blanking setup. For a dual phase steel DP600 the Lemaitre parameters are identified completely by an inverse strategy, while the parameters of the Gurson's porous plasticity model are predominantly gained from analysis with a scanning electron microscopy (SEM). The models are validated by comparison of force-displacement curves, time point and location of crack initiation. Advantages and disadvantages of both approaches are discussed with respect to prediction accuracy and costs of parameter identification. Both of the models deliver an exact prediction for the location of the crack and a good prediction of the punch displacement at the onset of cracking.

1 INTRODUCTION

In recent decades, numerous improvements of early damage models have been made. Research in this field follows basically two different approaches. On the one hand, there are microscopicly motivated damage models which go back to the idea of Gurson [1], Tvergaard and Needleman [2]. These are referred to as "porous plasticity", as the measure for material degradation is the void volume fraction, which leads to softening due to this degradation. On the other hand, there are phenomenological models (e.g. Lemaitre [3]) which are often derived within the context of thermodynamics. As these models are not linked to microstructure the quantity associated to material degradation is an internal variable called "damage" instead of a void volume fraction. As most internal variables in thermodynamics, the "damage" is not necessarily directly measureable as void volume fraction. Thus coefficients in the evolution equations (e.g. material parameters) must be determined via inverse parameter identification.

Both approaches need intense amount of effort for parameter identification. The microscopically motivated models need several hours of scanning electron microscopy (SEM) and an experienced operator to obtain meaningful and reliable results. The phenomenological models need a series of different experiments and computing capacity for inverse identification.

As a consequence it is of significant interest for users, as well as researchers in this field to have some comparative results to identify the advantages and disadvantages of both approaches.

Vaz et al. [4] recently compared modern implementations of Lemaitre and Gurson models, but focused on identification strategy and finally applied the models to uniaxial tension. Hambli [5] compared basic versions of Lemaitre and Gurson models in the context of blanking. He found the Lemaitre model to yield better predictions in terms of crack initiation and propagation. Since then several modifications for the Gurson model have been proposed. Nahshon and Hutchinson [6] suggested to add a term for void growth due to shear load. This enhanced porous plasticity model is used by the authors in [7] for the simulation of a blanking process. Along the way further modifications for Lemaitre's model have been proposed. Desmorat and Cantournet [8] suggested a modification to consider the effect of negative triaxialities. A similar approach presented by Soyarslan and Tekkaya [9] to account for the coupling of orthotropic plasticity and damage is used by the authors in [10] for the simulation of a blanking process. As both studies had different purposes they had different setups and focused on different aspects for validation. In this study, both approaches are directly compared for the same blanking setup.

The following section briefly introduces the experiments and microscope analysis that are necessary for the comparison. Section 3 addresses the aspects of simulation (i.e. material model and parameter identification). In section 4, the simulation results are compared to the experimental data and discussed. The paper ends with a conclusion in section 5.

2 EXPERIMENTS

After a brief summary of the investigated material the setup of experiments for parameter identification and process validation are presented in section 2.1. Section 2.2 briefly describes how material parameters for Gurson model were measured. The material investigated is a dual phase steel, DP600 with a thickness of 2 mm. The chemical composition and basic mechanical properties measured in standard tensile test are given in Table 1.

Table 1: Mechanical properties from uniaxial test and chemical composoition of DP600.

Modulus of Elasticity in MPa	**Poisson's ratio**	**Anisotropy**			**Yield strength in MPa**	**Swift hardening (eq. 3.4)**		
		r_0	r_{45}	r_{90}		K *in* MPa	e_0	n
201400	0.3	0.974	0.972	1.217	359	983	0.00232	0.190

C	**Mn**	**Cu**	**Ni**	**P**	**Cr**	**Mo**	**Al**	**Ti**	**S**	**Si**	**Fe**
0.081	1.45	0.056	0.071	0.021	0.212	0.00	0.029	0.002	0.005	0.255	balance

2.1 Tests (Macro level)

For this study, three experiments are necessary. Notched tensile tests and biaxial Nakajima tests are conducted for parameter identification and blanking tests are run in a universal testing

machine for validation. The notched tensile tests have a twofold use. On the one hand, they are used for direct measurement of void volume fraction and void nucleation in the Gurson model (section 2.2) and on the other hand, they are used for inverse identification of the Lemaitre model parameters (section 3.3). The notched tensile specimen has a width of 20 mm and length of 235 mm. Notches with a radius of 10 mm are cut with a laser from both sides at the centre of the long side. Thus the minimum width is 10 mm. The specimens are elongated with a constant strain rate of 0.0025 s^{-1}. The displacement field in the notched area is captured with optical camera system GOM Aramis. The biaxial specimen is one of the Nakajima geometries used for the identification of forming limit curve. Standard DIN EN ISO 12004-2 defines the specimen geometries and testing methodology for forming limit curves. Testing setup consist of the hemispherical punch with radius of 50 mm, blankholder and die. The circular blank without any notch has a radius of 100 mm and results in the deformation path close to equibiaxial deformation till necking. The force-displacement curves taken from the experiments are used as the objective function for the inverse parameter identification methodology. The test is conducted till final fracture to cover forming behaviour beyond necking.

The blanking experiments were conducted with a punching module (Figure 1) that is attached to universal testing machine Zwick 250. Thus intermediate stops of the punch are possible and the force and displacement of the punch can be recorded for validation. The cylindrical punch has radius of 8 mm. The tip of punch and die have edge radii of 25 µm. The cutting clearance is 80 µm, which corresponds 4% of sheet thickness.

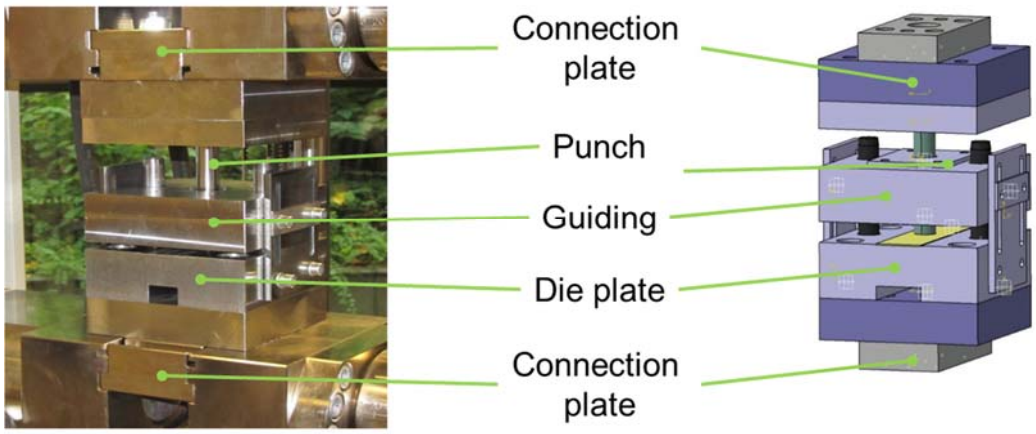

Figure 1: Punching module (left) and schematic representation (right) used for validation of blanking process simulation.

2.2 Tests (Micro level)

The samples for micrographs are detached with a precision cut-off machine. Afterwards an ion-etch-system is used to prepare the samples' surface by using ion beam slope cutting. With this method, it is possible to observe voids with an area as small as 0.05 µm². Details of the method are presented in [11]. This approach makes it possible to directly quantify the initial void volume fraction f_0 assuming that the void volume fraction approximately equals the void area fraction and thus can be obtained by the ratio of surface area of the voids to the total area of that surface. Furthermore, the method proposed in [12] makes it possible to identify the

parameters for void nucleation f_N, S_N and e^p_N (cf. eq. 3.9) with the analysis of a notched tensile specimen. Therefore one half of the notched region is divided into eight zones. Each of these zones corresponds to a certain equivalent plastic strain and has a characteristic mean void size. The voids having a smaller size than the mean size of the neighbouring zone, which has a lower deformation is counted as newly nucleated void for that zone. Thus one gets a uniform distribution of nucleated void volume fraction and can fit the parameters to that distribution (Table 2).

3 SIMULATIONS

This section starts with an introduction to the common framework of both materials models used. Afterwards characteristics of the used Gurson and Lemaitre type models are given. Section 3.2 presents the model setup of the blanking process and experiments for inverse identification. This section closes with information about the numerical identification strategy.

3.1 Material models

Both material models in this study fall in the context of continuum damage mechanics. The framework uses a multiplicative split of the total deformation gradient

$$\mathbf{F} = \mathbf{F}^{\mathrm{e}} \bullet \mathbf{F}^{\mathrm{p}} \tag{3.1}$$

into elastic $\mathbf{F}^{\mathrm{e}}$ and plastic part $\mathbf{F}^{\mathrm{p}}$ as proposed by Lee [13]. The kinematic formulation of the model relies on an approximation for the logarithmic, elastic stretch $\mathbf{U}^{\mathrm{e}}$, which arises in the context of the polar decomposition $\mathbf{F}^{\mathrm{e}} = \mathbf{R}^{\mathrm{e}} \bullet \mathbf{U}^{\mathrm{e}}$, with $\mathbf{R}^{\mathrm{e}}$ the elastic rotation tensor. As demonstrated in [14] one obtains

$$\frac{d}{dt}\ln(\mathbf{U}^{\mathrm{e}}) = \mathbf{R}^{\mathrm{e}} \bullet \mathbf{D} \bullet \mathbf{R}^{\mathrm{e}\mathrm{T}} - \mathbf{D}^{\mathrm{P}} \tag{3.2}$$

$$\dot{\mathbf{R}}^{\mathrm{e}} = \mathbf{W} \bullet \mathbf{R}^{\mathrm{e}} - \mathbf{R}^{\mathrm{e}} \mathbf{W}^{\mathrm{P}} \tag{3.3}$$

for small elastic strain, i.e. $|\ln(\mathbf{U}^{\mathrm{e}})| << 1$. The rate of total deformation $\mathbf{D} = \mathrm{sym}(\mathbf{L})$ is given in terms of the "velocity gradient" $\mathbf{L} = \dot{\mathbf{F}}^{\mathrm{p}} \bullet \mathbf{F}^{-1}$. Consequently, $\mathbf{D}^{\mathrm{p}} = \mathrm{sym}(\mathbf{L}^{\mathrm{p}}) = \mathrm{sym}(\dot{\mathbf{F}}^{\mathrm{p}} \bullet \dot{\mathbf{F}}^{-1})$ and $\mathbf{W}^{\mathrm{p}} = \mathrm{skw}(\mathbf{L}^{\mathrm{p}})$ represent the rate of plastic rotation and the plastic spin, respectively. The assumption $\mathbf{W}^{\mathrm{P}} \approx \mathbf{0}$ is justified for the investigated metals, such that the material axes rotate with the continuum. The associative flow rule

$$\mathbf{D}^{\mathrm{P}} = \dot{\gamma} \partial_{\mathbf{T}} \Phi^{\mathrm{P}} \tag{3.4}$$

determines the rate of plastic deformation depending on the specific choice of the yield function Φ^{P} and the magnitude of the plastic multiplicator $\dot{\gamma}$. The Cauchy stress tensor is denoted by $\mathbf{T}$, and its principal stresses are T_i. Stress triaxiality is defined as $\eta = -p/\sigma_{\mathrm{eq}}$ with hydrostatic pressure $-p = \sigma_{\mathrm{m}} = 1/3\,\mathrm{tr}[\mathbf{T}]$ and equivalent von Mises stress σ_{eq}. The next paragraph presents a short summary of the coupled elasto-plastic damage models used in this comparative study.

Enhanced Gurson Model

The yield function of the Gurson model has the general form:

$$\Phi^{P} = \left(\frac{\sigma_{\mathrm{eq}}}{\sigma_{\mathrm{y}}}\right)^{2} + 2q_1 f^{*} \cosh\left[\frac{3}{2}\frac{q_2\sigma_{\mathrm{m}}}{\sigma_{\mathrm{y}}}\right] - (1 - q_3 f^{*2}) = 0 \tag{3.5}$$

where q_1, q_2 und q_3 are material parameters [15], [16] and e^p is the equivalent plastic strain. $\sigma_y = \sigma_y [e^p]$ is the flow stress and for the Swift type isotropic hardening with material parameters K, e_0 und n, it reads:

$$\sigma_{\mathrm{y}}[e^{\mathrm{p}}] = K\,(e_0 + e^{\mathrm{p}})^{n} \tag{3.6}$$

The void volume fraction is modified to f^*, due to the accelerating effects of the void coalescence as follows [2]:

$$f^{*} = \begin{cases} f & f \le f_{\mathrm{c}} \\ f_{\mathrm{c}} + \dfrac{f_{\mathrm{u}}^{*} - f_{\mathrm{c}}}{f_{\mathrm{f}} - f_{\mathrm{c}}}\left(f - f_{\mathrm{c}}\right) & f > f_{\mathrm{c}} \end{cases} \tag{3.7}$$

where critical void volume fraction at incipient coalescence and the void volume fraction at final fracture are denoted by f_c and f_f, respectively. $f_u^*=1/q_1$ is the maximal value of the modified void volume fraction f^* at which the stress carrying capacity vanishes macroscopically. This corresponds to the trigger for the element deletion to model fracture.
The change in the void volume fraction $\dot{f}$ has contributions due to the nucleation of the new voids $\dot{f}^{\mathrm{n}}$, void growth due to hydrostatic stresses $\dot{f}^{\mathrm{g}}_{\mathrm{hyd}}$ and void growth due to the shear stresses $\dot{f}^{\mathrm{g}}_{\mathrm{shr}}$:

$$\dot{f} = \dot{f}^{\mathrm{n}} + \dot{f}^{\mathrm{g}}_{\mathrm{hyd}} + \dot{f}^{\mathrm{g}}_{\mathrm{shr}} \tag{3.8}$$

The nucleation of the voids is given by:

$$\dot{f}^{\mathrm{n}} = A_{\mathrm{N}}\dot{e}^{\mathrm{p}}, \quad A_{\mathrm{N}} = A_{\mathrm{N}}(e^{\mathrm{p}}) = \frac{f_{\mathrm{N}}}{S_{\mathrm{N}}\sqrt{2\pi}}\exp\left[-\frac{1}{2}\left(\frac{e^{\mathrm{p}} - e^{\mathrm{p}}_{\mathrm{N}}}{S_{\mathrm{N}}}\right)^{2}\right] \tag{3.9}$$

where the material parameters are: f_N nucleated void volume fraction, S_N standard deviation of the distribution of the nucleated voids and e^pN mean equivalent plastic strain at the incipient nucleation [17].
The void growth due to hydrostatic stresses is given by:

$$\dot{f}^{\mathrm{g}}_{\mathrm{hyd}} = (1 - f)\,\mathrm{tr}(\mathbf{D}^{\mathrm{p}}) \tag{3.10}$$

The void growth due to shear stress is:

$$\dot{f}^{\mathrm{g}}_{\mathrm{shr}} = k_{\mathrm{w}} f \frac{w\left(\mathrm{dev}\left[\mathbf{T}\right]\right)}{\sigma_{\mathrm{eq}}}\mathrm{dev}\left[\mathbf{T}\right] : \mathbf{D}^{\mathrm{p}} \tag{3.11}$$

according to [6]. Here, k_w is a material parameter and $w(\mathrm{dev}[\mathbf{T}])$ is a stress dependent function depending on the third invariant of the deviatoric stress tensor J_3 as follows:

$$w\left(\mathrm{dev}\left[\mathbf{T}\right]\right) = 1 - \left(\frac{27 J_3}{2\sigma_{\mathrm{eq}}^3}\right)^2 \tag{3.12}$$

The factor inside the eq. 3.12 is known as the Lode angle parameter ξ. The Lode angle θ distinguishes the stress state between axisymmetric and shear stress state. It is related to the normalized third deviator stress invariant J_3 as follows [18]:

$$\xi = \frac{27}{2}\frac{J_3}{\sigma_{\mathrm{eq}}{}^3} = \cos\left(3\theta\right) \tag{3.13}$$

For further details of the model regarding nucleation of the voids and the growth due to hydrostatic stresses, model implementation and related model parameters readers are referred to [19].

Enhanced Lemaitre Model

Similar to the Gurson type models with the void volume fraction, the effect of ductile damage is considered by the damage variable $D \in [0,1]$. It accounts for the deterioration of the load bearing capacity due to the evolution of the defect structure. The effective stress $\tilde{\mathbf{T}} = \mathbf{T} / (1 - D)$ represents the stress acting on the fictitious undamaged area, as opposed to the stress $\mathbf{T}$ acting on the total area. The plastic potential is given by $\Phi^{\mathrm{p}}(\mathbf{T}, q, D) = \tilde{\sigma}_{\mathrm{eq}} - q = \sqrt{3/2\ \mathrm{dev}(\tilde{\mathbf{T}}) : \mathrm{dev}(\tilde{\mathbf{T}})} - q$, where $\tilde{\sigma}_{\mathrm{eq}}$ represents the effective equivalent stress. The damage potential

$$\Phi^{\mathrm{d}} = \frac{S}{(\delta+1)}\left\langle\frac{Y - Y_0}{S}\right\rangle^{\delta+1}\frac{1}{(1-D)^{\beta}} \tag{3.14}$$

depends on the driving force $Y := Y^+$ and the material parameters S, β, δ and Y_0. $\langle x\rangle = (|x| + x)/2$ represents the Macauley bracket. In the context of blanking simulations it is important to consider that the evolution of damage under compressive stress states is different than under tensile stress states. Therefore, the weighting factor h is introduced

$$Y^+ = \frac{1+\nu}{2E}\left\{\sum_{i=1}^{3}\left[\left\langle\tilde{T}_i\right\rangle^2 + h\left\langle-\tilde{T}_i\right\rangle^2\right]\right\} - \frac{9\nu}{2E}\left\{\sum_{i=1}^{3}\left[\left\langle\tilde{p}\right\rangle^2 + h\left\langle-\tilde{p}\right\rangle^2\right]\right\} \tag{3.15}$$

to consider the effect of compressive stress states on the driving force. Here, $\tilde{T}_i$ represent the principle stresses of $\tilde{\mathbf{T}}$ and $\tilde{p} := 1/3\ \mathrm{tr}(\tilde{T})$ the hydrostatic pressure. Differentiation of (3.14), with respect to Y reveals the particular form of the damage evolution

$$\dot{D} = \lambda\left\langle\frac{Y - Y_0}{S}\right\rangle^{\delta}\frac{1}{(1-D)^{\beta}} \tag{3.16}$$

The model is implemented via the user material interface into Abaqus/Explicit. For details of

the model formulation and the implementation the reader is referred to [9]. The standard damage model of Lemaitre [3] does not distinguish between compressive stresses and tensile stresses for the evolution of damage. This is in contrast to experimental observations, e.g. of Bao et al. [20], such as a cut-off value of the stress triaxiality -1/3, below which fracture does not occur. With the original Lemaitre model, i.e. $h = 1$ in (3.14), one obtains a fracture curve which does not consider the sign of triaxiality. In general, for technical metals, fracture occurs at higher strains for compressive stresses. Thus the fracture strain for η = -1/3 tends asymptotically to infinity in the current model for the limiting case of $h = 0$.

In order to modify the cumulative damage for Lemaitre Model according to the shear stress states, the shear fracture related parameter of the fracture model in [21] is introduced to the damage evolution rate of the model. Then the damage evolution equation in eq. 3.15 reads:

$$\dot{D} = \lambda \left(\frac{2\tau_{\max}}{\sigma_{eq}} \right)^{\kappa} \left\langle \frac{Y - Y_0}{S} \right\rangle^{\delta} \frac{1}{\left(1 - D\right)^{\beta}} \tag{3.17}$$

The relation between selected factor and Lode angle θ can be shown as [22]:

$$\frac{2\tau_{\max}}{\sigma_{eq}} = \frac{2}{3}\left(\cos\theta - \cos\left(\frac{4}{3}\pi - \theta \right) \right) \tag{3.18}$$

3.2 Modelling of experiments

All experiments (i.e. notched tensile test, biaxial Nakajima test and blanking process) are modelled in the commercial software Abaqus/Explicit with a VUMAT implementation of the described material models. Failure of the material is represented by the deletion of those elements, at which the void volume fraction f, or the damage variable D reaches the critical value f_f, or D_c respectively.

The blanking process was simulated using a two-dimensional axisymmetric model with bilinear CAX4R elements. The mesh size in the process zone is set to 25 µm and maintained constant with an Arbitrary-Lagrange-Euler (ALE) approach (Figure 2). Punch and die are modelled as rigid bodies.

The notched tensile test and biaxial Nakajima test are modelled in 3D space using trilinear C3D8R elements. For the notched specimen all three symmetry planes are used and for the Nakajima specimen a quarter model is used. The mesh size of the models for parameter identification is taken as 1 mm. Because the required mesh size for the blanking process is much finer than this value, one of the model parameters, S for Lemaitre model and k_w for Gurson Model are manually scaled for the mesh size of 25 µm. The model parameters for the mesh size of 25 µm are tabulated in Table 3.

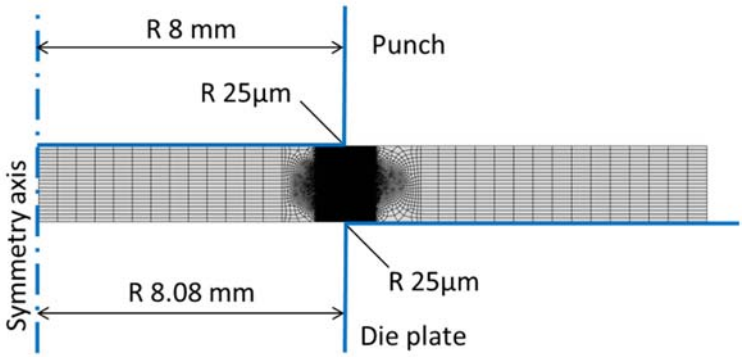

Figure 2: Simulation model of the blanking process.

3.3 Parameter identification strategy

The parameters for the elasto-plastic regime are obtained directly from uniaxial tensile test (Table 1). For the parameters related to material softening a distinction of cases is necessary. Parameter of the Gurson model are determined predominantly directly from microscopic analysis. Yet some parameters need to be identified inversely. The parameter related to void growth due to shear k_w (cf. eq. 3.10) is obtained a posteriori by fitting to the force displacement curve of the blanking process.

In the case of Lemaitre's model all parameters related to softening (i.e. S, β, δ, κ and Y_0) have to be identified by an inverse strategy. The critical damage D_c may be determined a posteriori. For the inverse identification the force displacement curve of the notched tensile and biaxial Nakajima test are used. The target function

$$e = \sum_{i=1}^{N} \sqrt{\left(F(u_i)_{\exp}^{R10} - F(u_i)_{sim}^{R10} \right)^2} + \sum_{i=1}^{N} \sqrt{\left(F(u_i)_{\exp}^{G0} - F(u_i)_{sim}^{G0} \right)^2} \tag{3.19}$$

needs to be minimized. $F(u_i)$ is the force vector with respect to the displacement. R10 denotes the notched tensile test and G0 the Nakajima test. The identification optimization itself is performed manually. The parameters for both models are tabulated in Table 2.

4 RESULTS

In the context of blanking special attention must be paid to use material models which are appropriate to treat evolution of material degradation with respect to all of the occurring stress states. The application to blanking is a challenging task, one of the reasons being that the triaxiality η takes values between - 2/3 and + 2/3 for a closed cut line [10]. The representatives of both model families should be able to account for these stress states. Therefore it is expected that the comparison is fair.

The simulations of both models yield a fair prediction of force-displacement curve. The solution of the Lemaitre model is very close to the experimental measured one. The deviation in maximum force is less than 2%. The results of the Gurson model are significantly improved compared to the previous study of Hambli [5].

Table 2: Identified material parameters for both models.

Enhanced Gurson model [15], [16], [12]									
f_0	q_1	q_2	q_3	f_N	s_N	e^p_N	f_c	f_f	k_w
0.0008	1.5	1.0	2.25	0.00062	0.1283	0.5421	0.015	0.07	1.2

Enhanced Lemaitre model						
Y_0 in MPa	S in MPa	β	δ	κ	h	D_c
1.06	6	15	2	1	0	0.2

This is probably due to the enhancement for shear activated void growth. Yet the solution accuracy is lower than for the enhanced Lemaitre model. The maximum force predicted is 4.4% below the maximum force in experiment. Despite these results the Gurson model predicts the onset of the first crack very well, with respect to both punch displacement and place of initiation (Figure 3).

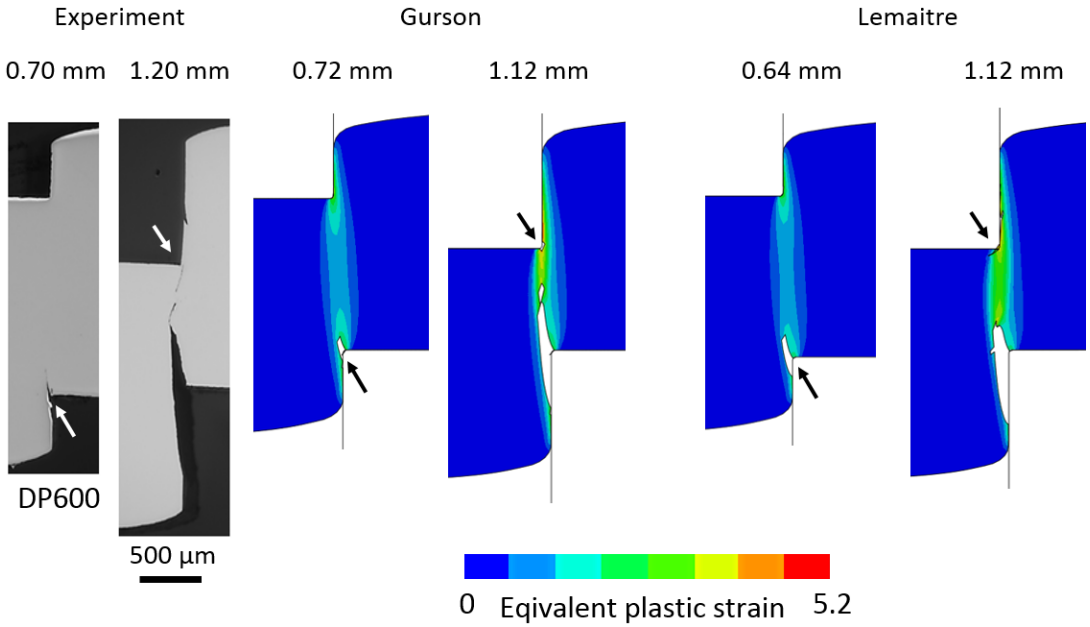

Figure 3: Occurence of initial crack and total rupture. Experiment and results for Gurson model from [7].

The Lemaitre model also predicts the place of initiation correctly on the lower side of blank, but the punch displacement for this event is predicted too early and slightly worse than with the Gurson model. Prediction of the second cracking from the upper side of the blank is achieved with both models similarly well.

5 CONCLUSION

Two modern implementations of different continuum damage mechanics models have been applied to a complex process simulation. Parameters for the Gurson model have been identified

predominantly with a scanning electron microscope, while parameters for Lemaitre have been identified completely by an inverse strategy. Both models have shown good prediction accuracy. On the one hand the Lemaitre model predicted the punch force during the process almost excellently, on the other hand the Gurson model yielded better results for predicting the onset of damage, which is important for determining the amount of burnish and fracture on the cut surface.

Concerning the effort of parameter identification the inverse strategy is considerably superior. At first the preparation of samples for SEM in order to observe voids in the nanometer scale is time consuming. Secondly, it takes a lot of time for the user of SEM to distinguish voids from other artefacts. In contrast the experiments for inverse strategy can be conducted easily. Due to the short simulation time of these experiments (one Nakajima simulation needed roughly two hours) the parameters could be identified manually. If the inverse identification were run automated as presented in [10] the complete procedure would probably have needed between one and four days, depending on the number of used computing cores.

On the other hand the processing of microscope images might be automated at least partially, as well. Moreover, the Gurson's model reveals quantities (e.g. void volume fraction) directly comparable to microstructural information. This information might give a better insight in the physics on microstructure level and will be used in future validations.

ACKNOWLEDGEMENT

The authors gratefully acknowledge funding by the German Research Foundation (DFG) within the scope of the Transregional Collaborative Research Centre on sheet-bulk metal forming (SFB/TR 73) in the project C4 'Analysis of load history dependent evolution of damage and microstructure for the numerical design of sheet-bulk metal forming processes'.

Furthermore, the authors would like to thank Florian Nürnberger and Gregory Gerstein for optical as well as scanning electron microscopy and corresponding discussions.

REFERENCES

1. Gurson, A.L., *Continuum Theory of Ductile Rupture by Void Nucleation and Growth .1. Yield Criteria and Flow Rules for Porous Ductile Media.* Journal of Engineering Materials and Technology-Transactions of the Asme, 1977. **99**(1): p. 2-15.
2. Tvergaard, V. and A. Needleman, *Analysis of the Cup-Cone Fracture in a Round Tensile Bar.* Acta Metallurgica, 1984. **32**(1): p. 157-169.
3. Lemaitre, J., *A Continuous Damage Mechanics Model for Ductile Fracture.* Journal of Engineering Materials and Technology-Transactions of the Asme, 1985. **107**(1): p. 83-89.
4. Vaz, M., et al., *Considerations on parameter identification and material response for Gurson-type and Lemaitre-type constitutive models.* International Journal of Mechanical Sciences, 2016. **106**: p. 254-265.
5. Hambli, R., *Comparison between Lemaitre and Gurson damage models in crack growth simulation during blanking process.* International Journal of Mechanical Sciences, 2001. **43**: p. 2769-2790.
6. Nahshon, K. and J.W. Hutchinson, *Modification of the Gurson Model for shear failure.* European Journal of Mechanics a-Solids, 2008. **27**(1): p. 1-17.
7. Isik, K., et al. *Investigations of ductile damage in DP600 and DC04 deep drawing steel sheets during punching*. in *21st European Conference on Fracture (ECF21)*. 2016. Catania, Italy: Procedia Structural Integrity.
8. Desmorat, R. and S. Cantournet, *Modeling microdefects closure effect with isotropic/anisotropic damage.* International Journal of Damage Mechanics, 2008. **17**(1): p. 65-96.

9. Soyarslan, C. and A.E. Tekkaya, *A damage coupled orthotropic finite plasticity model for sheet metal forming: CDM approach (vol 48, pg 150, 2010).* Computational Materials Science, 2010. **48**(4): p. 875-876.
10. Gutknecht, F., et al. *Advanced material model for shear cutting of metal sheets*. in *COMPLAS XIII*. 2015. Barcelona, Spain: CIMNE.
11. Gerstein, G., et al., *The effect of texture in modeling deformation processes of bcc steel sheets.* Materials Letters, 2016. **164**: p. 356-359.
12. Isik, K., et al., *Evaluation of Void Nucleation and Development during Plastic Deformation of Dual-Phase Steel DP600.* steel research international, 2016. **87**(12): p. 1583-1591.
13. Lee, E.H., *Elastic-Plastic Deformation at Finite Strains.* Journal of Applied Mechanics, 1969. **36**(1): p. 1-&.
14. Clausmeyer, T. and B. Svendsen, *Comparison of two models for anisotropic hardening and yield surface evolution in bcc sheet steels.* European Journal of Mechanics - A/Solids, 2015. **54**: p. 120-131.
15. Tvergaard, V., *Influence of Voids on Shear Band Instabilities under Plane-Strain Conditions.* International Journal of Fracture, 1981. **17**(4): p. 389-407.
16. Tvergaard, V., *On Localization in Ductile Materials Containing Spherical Voids.* International Journal of Fracture, 1982. **18**(4): p. 237-252.
17. Chu, C.C. and A. Needleman, *Void Nucleation Effects in Biaxially Stretched Sheets.* Journal of Engineering Materials and Technology-Transactions of the Asme, 1980. **102**(3): p. 249-256.
18. Bai, Y.L. and T. Wierzbicki, *Application of extended Mohr-Coulomb criterion to ductile fracture.* International Journal of Fracture, 2010. **161**(1): p. 1-20.
19. Soyarslan, C., et al., *An Experimental and Numerical Assessment of Sheet-Bulk Formability of Mild Steel DC04.* Journal of Manufacturing Science and Engineering-Transactions of the Asme, 2011. **133**(6).
20. Bao, Y. and T. Wierzbicki, *On fracture locus in the equivalent strain and stress triaxiality space.* International Journal of Mechanical Sciences, 2004. **46**(1): p. 81-98.
21. Isik, K., et al., *Enhancement of Lemaitre Model to Predict Cracks at Low and Negative Triaxialities in Sheet Metal Forming.* Key Engineering Materials, 2015. **639**: p. 427-434.
22. Lou, Y., et al., *New ductile fracture criterion for prediction of fracture forming limit diagrams of sheet metals.* International Journal of Solids and Structures, 2012. **49**(25): p. 3605-3615.

XIV International Conference on Computational Plasticity. Fundamentals and Applications
COMPLAS 2017
E. Oñate, D.R.J. Owen, D. Peric and M. Chiumenti (Eds)

HARDENING EFFECTS ON FORMABILITY LIMIT PREDICTION BASED ON GURSON-TYPE DAMAGE MODELS AND BIFURCATION ANALYSIS

H. CHALAL[*] AND F. ABED-MERAIM[*,†]

[*] Laboratoire d'Étude des Microstructures et de Mécanique des Matériaux
LEM3, UMR CNRS 7239, Arts et Métiers ParisTech
4 rue Augustin Fresnel, 57078 Metz Cedex 3, France
e-mail: farid.abed-meraim@ensam.eu, hocine.chalal@ensam.eu, www.ensam.eu

[†] Laboratory of Excellence on Design of Alloy Metals for low-mAss Structures
DAMAS, Université de Lorraine
Ile du Saulcy 57045 Metz, Cedex 1, France
e-mail: farid.abed-meraim@ensam.eu, www.ensam.eu

Key words: Bifurcation analysis, GTN-type damage model, Formability limits, Hardening effects, Void nucleation mechanism, Micromechanics-based calibration.

Abstract. In this work, ductility limits of metallic materials, associated with the occurrence of strain localization, are predicted using the GTN damage model coupled with bifurcation theory. The resulting approach is implemented into the finite element code ABAQUS within the framework of large plastic strains and a fully three-dimensional formulation. A parametric study with respect to damage and hardening parameters is conducted in order to identify the most influential material parameters on strain localization. The analysis shows that the damage parameters have a significant impact on the predicted ductility limits, while the effect of hardening parameters on strain localization depends on the choice of void nucleation mechanism.

1 INTRODUCTION

It is well known that in sheet metal forming processes, different types of defects may occur, which are usually associated with operating conditions and/or material characteristics. Plastic instabilities, corresponding to the occurrence of zones of highly localized plastic strain, are examples of these undesirable phenomena. To characterize the formability of thin sheet metals, the concept of forming limit diagram has been introduced [1]. Among the most influential constitutive features on the formability limits of thin sheet metals, the damage development is of particular importance. In this context, Gurson-type damage models have been developed, among which the GTN model [2], which is adopted in this work to describe the initiation of ductile damage and its evolution during loading. This model is coupled with the bifurcation analysis [3,4] to predict the occurrence of strain localization in metallic materials. The present work investigates the respective effect of damage and hardening parameters on the prediction of ductility limits using different void nucleation mechanisms. In

addition, an alternative modeling approach is explored for the analysis of hardening effects on strain localization, which consists in adopting a micromechanics-based calibration for the GTN q-parameters.

2 GTN DAMAGE MODEL

The ductile damage model adopted in this work is based on the Gurson model, which accounts for void nucleation and growth. This model has been subsequently modified in the literature leading to the following well-known GTN yield potential (see, e.g., [2]):

$$\Phi = \left(\frac{\sigma_{eq}}{\sigma_Y}\right)^2 + 2q_1 f^* \cosh\left(\frac{3}{2} q_2 \frac{\sigma_m}{\sigma_Y}\right) - \left(1 + q_3 f^{*2}\right) \leq 0 , \tag{1}$$

where q_1, q_2 and q_3 are material parameters; σ_m is the hydrostatic stress defined by $\sigma_m = \boldsymbol{\sigma} : \mathbf{1}/3$, with $\boldsymbol{\sigma}$ being the Cauchy stress tensor and $\mathbf{1}$ the second-order identity tensor; σ_{eq} is the von Mises equivalent stress defined by $\sigma_{eq} = \sqrt{3\mathbf{S} : \mathbf{S}/2}$, with $\mathbf{S}$ being the deviatoric part of the Cauchy stress; σ_Y is the flow stress, function of the equivalent plastic strain $\bar{\varepsilon}_{\mathrm{m}}^{\mathrm{pl}}$ of the fully dense matrix; $f^*(f)$ is the modified void volume fraction, function of the actual void volume fraction f, which is defined by

$$f^*(f) = \begin{cases} f & \text{for} \quad f \leq f_{cr}, \\ f_{cr} + \delta_{GTN}\left(f - f_{cr}\right) & \text{for} \quad f_{cr} < f \leq f_R, \end{cases} \quad \text{with} \quad \delta_{GTN} = \frac{f_u^* - f_{cr}}{f_R - f_{cr}}, \tag{2}$$

where the damage parameters f_{cr} and f_R are the critical void volume fraction, at which the coalescence stage starts, and the void volume fraction at final fracture, respectively. According to Eq. (2), $f^*(f)$ reaches its ultimate value f_u^* when $f = f_R$.

The tensile flow stress σ_Y of the fully dense matrix material is assumed to be governed by an isotropic hardening law, as given by the following rate expression:

$$\dot{\sigma}_Y = h \dot{\bar{\varepsilon}}_{\mathrm{m}}^{\mathrm{pl}} , \tag{3}$$

where h is the plastic hardening modulus of the fully dense matrix material. The plastic flow rule follows the classical normality law, which defines the plastic strain rate $\mathbf{D}^{\mathrm{p}}$ as

$$\mathbf{D}^{\mathrm{p}} = \dot{\lambda} \frac{\partial \Phi}{\partial \boldsymbol{\sigma}} , \tag{4}$$

where $\dot{\lambda}$ is the plastic multiplier, and $\partial\Phi/\partial\boldsymbol{\sigma}$ is the direction of the plastic flow. The evolution of void volume fraction depends on both growth of pre-existent voids and nucleation of new ones. For the nucleation of new voids, the model proposed by Chu and Needleman [5] is adopted in this work. This model involves the contribution of both the flow stress rate of the dense matrix and the hydrostatic stress rate. The final expression of the incremental change in void volume fraction is given by

$$\dot{f} = \underbrace{(1 - f)\mathbf{D}^{\mathrm{p}} : \mathbf{1}}_{\text{growth}} + \underbrace{\left[\left(A_N / h\right) + B_N\right]\dot{\sigma}_Y + B_N \dot{\sigma}_m}_{\text{nucleation}} . \tag{5}$$

In the above equation, the constants A_N and B_N allow characterizing the void nucleation model, which is strain controlled for $A_N > 0$ and $B_N = 0$, and stress controlled for $A_N = 0$ and $B_N > 0$. Their expressions follow normal distribution laws as proposed in [5]

$$A_N = \frac{f_N}{s_N\sqrt{2\pi}}\exp\left[-\frac{1}{2}\left(\frac{\bar{\varepsilon}_{\mathrm{m}}^{\mathrm{pl}} - \varepsilon_N}{s_N}\right)^2\right],\quad B_N = \frac{f_N}{s_N\sigma_0\sqrt{2\pi}}\exp\left(-\frac{1}{2}\left(\frac{\sigma_Y + \sigma_m - \sigma_N}{s_N\sigma_0}\right)^2\right), \tag{6}$$

where ε_N and σ_N are the mean strain and the mean stress for nucleation, respectively; s_N is the standard deviation on ε_N; f_N is the volume fraction of void-nucleating particles; σ_0 is the initial yield stress of the matrix surrounding the voids. In the co-rotational frame, which is associated with the Jaumann objective derivative, the Cauchy stress rate is expressed using the following hypoelastic law:

$$\dot{\boldsymbol{\sigma}} = \mathbf{C}^e : \left(\mathbf{D} - \dot{\lambda}\frac{\partial \Phi}{\partial \boldsymbol{\sigma}}\right) = \mathbf{C}^{ep} : \mathbf{D}, \tag{7}$$

where $\mathbf{D}$ is the strain rate tensor, $\mathbf{C}^e$ is the fourth-order elasticity tensor, and $\mathbf{C}^{ep}$ is the elastic–plastic tangent modulus. Using the consistency condition $\dot{\Phi} = 0$, together with the above equations, the plastic multiplier $\dot{\lambda}$ writes

$$\dot{\lambda} = \frac{1}{H_\lambda}\mathbf{E} : \mathbf{C}^e : \mathbf{D}, \tag{8}$$

where

$$\mathbf{E} = \frac{\partial \Phi}{\partial \boldsymbol{\sigma}} + \frac{B_N}{3}\frac{\partial \Phi}{\partial f^*}\frac{\partial f^*}{\partial f}\mathbf{1}, \tag{9}$$

$$H_\lambda = \mathbf{E} : \mathbf{C}^e : \frac{\partial \Phi}{\partial \boldsymbol{\sigma}} - \frac{h}{(1-f)}\frac{\boldsymbol{\sigma} : \dfrac{\partial \Phi}{\partial \boldsymbol{\sigma}}}{\sigma_Y}\left[\frac{\partial \Phi}{\partial \sigma_Y} + \left(\frac{A_N}{h} + B_N\right)\frac{\partial \Phi}{\partial f^*}\frac{\partial f^*}{\partial f}\right] - (1-f)\frac{\partial f^*}{\partial f}\frac{\partial \Phi}{\partial f^*}\frac{\partial \Phi}{\partial \boldsymbol{\sigma}} : \mathbf{1}. \tag{10}$$

By replacing the plastic multiplier $\dot{\lambda}$ (see Eq. (8)) into the hypoelastic law (Eq. (7)), the elastic–plastic tangent modulus of the GTN model writes

$$\mathbf{C}^{ep} = \mathbf{C}^e - \left(\mathbf{C}^e : \frac{\partial \Phi}{\partial \boldsymbol{\sigma}}\right) \otimes \left(\mathbf{E} : \mathbf{C}^e\right) \Big/ H_\lambda. \tag{11}$$

It can be observed that, in the case of strain-controlled nucleation (i.e., $A_N > 0$ and $B_N = 0$), the above elastic–plastic tangent modulus becomes symmetric and the normality of the plastic flow rule holds. In the case of stress-controlled nucleation (i.e., $A_N = 0$ and $B_N > 0$), the elastic–plastic tangent modulus is non-symmetric and the normality of the plastic flow rule does not hold.

3 BIFURCATION CRITERION

In this section, the constitutive equations described above are coupled with a plastic

instability criterion, as proposed by Rudnicki and Rice [3] and Rice [4], in order to predict the occurrence of strain localization. This criterion is based on bifurcation theory, where the incipience of plastic flow localization in the form of an infinite band is associated with the loss of uniqueness for the solution of the rate equilibrium equations. According to this criterion, the critical condition, which also corresponds to the loss of ellipticity of the associated boundary value problem, is related to the singularity of the acoustic tensor $\mathbf{A}$, defined as $\mathbf{A} = \mathbf{n} \cdot \mathbf{L} \cdot \mathbf{n}$, where $\mathbf{n}$ is the normal to the localization band and the tangent modulus $\mathbf{L}$ writes

$$\mathbf{L} = \mathbf{C}^{ep} + \mathbf{Z}_1 - \mathbf{Z}_2 - \mathbf{Z}_3, \tag{12}$$

where $\mathbf{Z}_1$, $\mathbf{Z}_2$ and $\mathbf{Z}_3$ are fourth-order tensors that consist of Cauchy stress components. These additional tensors originate from the large-strain framework and their complete expressions can be found in [6,7]. The critical condition is then given by

$$\det(\mathbf{A}) = \det(\mathbf{n} \cdot \mathbf{L} \cdot \mathbf{n}) = 0. \tag{13}$$

4 PREDICTION OF DUCTILITY LIMITS

In this section, the GTN model is coupled with the bifurcation analysis to predict strain localization in porous materials subjected to in-plane loading conditions. The resulting approach is implemented into the finite element code ABAQUS/Standard within the framework of large plastic strains and a fully three-dimensional formulation. The effect of hardening and damage parameters, as well as the choice of nucleation modeling, on the prediction of ductility limits is analyzed.

4.1 Strain-controlled nucleation model

In this section, nucleation of new voids is taken strain-controlled, by considering $A_N > 0$ and $B_N = 0$ in the GTN model (see Eq. (5)). It is worth noting that, in this case, the normality of the plastic flow rule holds and the elastic–plastic tangent modulus $\mathbf{C}^{ep}$ is symmetric, while the acoustic tensor $\mathbf{A}$ is non-symmetric due to the convective stress components (Eq. (12)).

The material considered here is Al5754 aluminum, with Young's modulus and Poisson's ratio equal to $70{,}000$ MPa and 0.33, respectively. The associated hardening parameters, according to the Swift isotropic hardening law, and damage parameters are summarized in Table 1 (see [8]).

Table 1: Hardening and damage parameters for Al5754

ε_0	k [MPa]	n	f_0	s_N	ε_N	f_N	f_{cr}	δ_{GTN}	q_1	q_2	q_3
0.00173	309.1	0.177	0.001	0.1	0.32	0.034	0.00284	7	1.5	1.0	2.15

4.1.1 Effect of damage parameters

The effect of damage parameters on the ductility limit predictions for the Al5754

aluminum alloy is analyzed here. A relatively large number of damage parameters are involved in the GTN model; for conciseness, attention is focused on the initial void volume fraction f_0 and the nucleation parameter f_N.

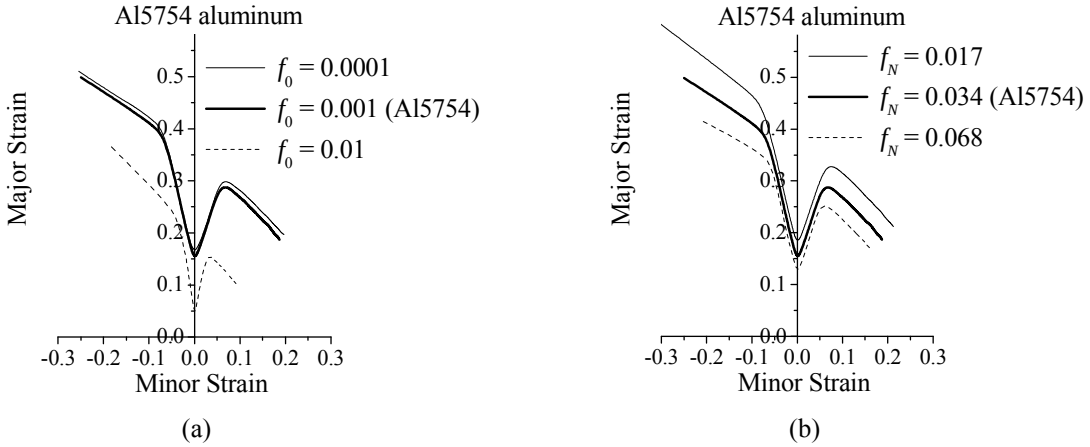

Figure 1: Effect of the initial void volume fraction f_0 (a), and the nucleation parameter f_N (b) on the ductility limit predictions for Al5754 aluminum

Figure 1 shows the impact of varying one damage parameter at a time on the prediction of the ductility limits for Al5754 aluminum. Concerning the effect of the initial void volume fraction f_0 (Figure 1(a)), large values for this parameter (e.g., $f_0 = 0.01$) imply that the material has already entered the coalescence stage, which dramatically lowers the predicted ductility limits. However, for very small values for parameter f_0, the ductility limit predictions are only slightly affected, which suggests that at such low void volume fraction levels, void growth is not the predominant mechanism for damage evolution. For the nucleation parameter f_N, the predicted ductility limits are lowered as this parameter increases. This trend is consistent with the physical meaning of this parameter (volume fraction of void-nucleating particles), as larger values for the latter tend to precipitate damage, thus promoting early plastic flow localization (see Eq. (6)).

4.1.2 Effect of the hardening exponent n

The impact of the hardening exponent n, associated with the Swift law, on the ductility limit predictions is analyzed here for the Al5754 aluminum material. Figure 2 shows the predicted limit strains obtained with different hardening exponents n for the dense matrix material. These results reveal that the effect of the hardening exponent n on the ductility limit predictions is much smaller than that observed for damage parameters (see the previous section). Similar results are observed when varying the k and ε_0 Swift hardening parameters, and are not reported here for conciseness. However, a more perceptible effect is found near the plane-strain tension (PST) loading path (see Figure 2).

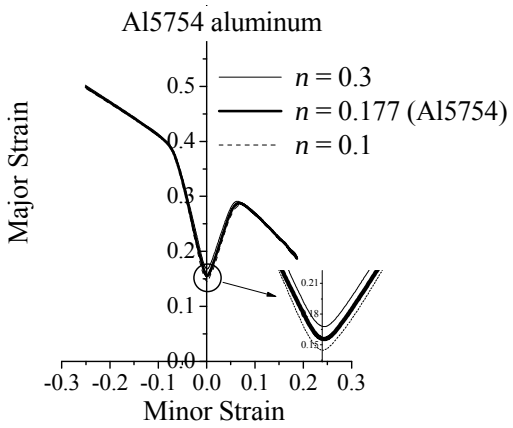

Figure 2: Effect of the hardening exponent n, associated with the Swift law, on the ductility limit predictions for Al5754 aluminum with strain-controlled nucleation

Similar trends have been observed in [9], where the GTN model was used with strain-controlled nucleation and coupled with the bifurcation theory. Indeed, in such a modeling approach, strain localization is mainly controlled by damage-induced softening, as shown in Figure 3(a) for the uniaxial tensile (UT) strain path, where it can be seen that flow localization occurs at strongly negative hardening moduli. Moreover, the evolution of void volume fraction based on strain-controlled nucleation for this particular loading path (UT) is shown to be insensitive to the strain hardening of the dense matrix material (see Figure 3(b)).

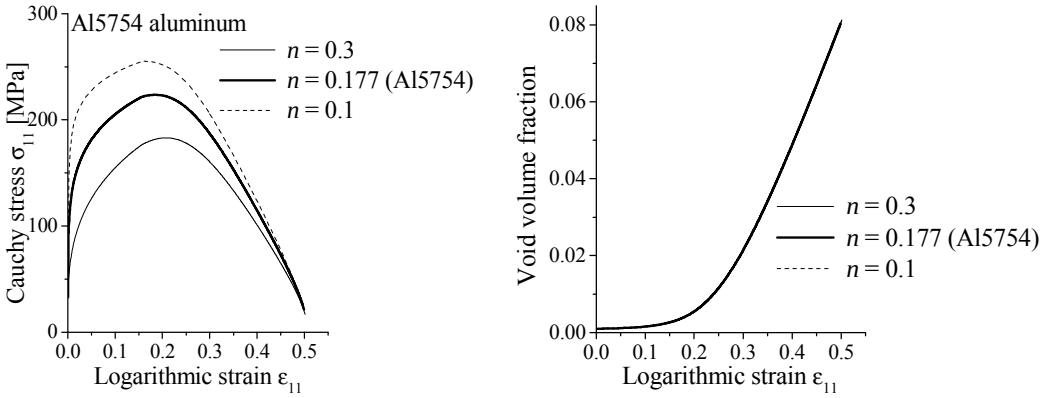

Figure 3: Effect of the hardening exponent n on: (a) the Cauchy stress−strain curve, and (b) void volume fraction, until localization along the uniaxial tensile strain path

4.2 Calibration of the GTN q-parameters

The previous results have shown limitations of the GTN model, with strain-controlled nucleation, in accounting for the effect of strain hardening on the porosity evolution. To overcome such limitations, Faleskog et al. [10] suggested calibrating the GTN q-parameters in order to include the effect of strain hardening on void growth. Tables 2 and 3 summarize

the calibrated q-parameters and the damage parameters for a steel material with yield strength ratio $\sigma_0/E = 0.004$ (see [10]). The isotropic hardening model used in the simulations is based on a hardening power law (see [10]).

Table 2: Calibrated q-parameters

q-parameter	$n = 0.025$	$n = 0.05$	$n = 0.10$
q_1	1.74	1.48	1.29
q_2	1.013	1.013	0.982

Table 3: Damage parameters for the GTN model

Material	f_0	s_N	ε_N	f_N	f_{cr}	δ_{GTN}
Steel	0.001	0.1	0.3	0.05	0.04	5

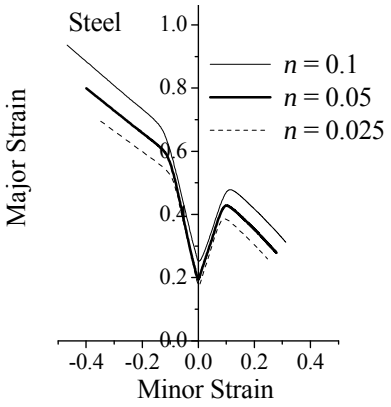

Figure 4: Effect of the hardening exponent n on the prediction of ductility limits using the calibrated q-parameters

Figure 4 shows the effect of the hardening exponent n of the power law on the prediction of ductility limits for the studied steel material based on the calibration of the q-parameters and strain-controlled nucleation model. The predicted ductility limits clearly show sensitivity to strain hardening for all strain paths, thanks to the use of micromechanics-based calibrated q-parameters.

4.3 Stress-controlled nucleation model

The effect of strain hardening on the ductility limits is investigated in this section using the GTN model with stress-controlled nucleation. The associated material parameters corresponding to a steel material are summarized in Table 4. The Ludwig power law is used in the simulations for the modeling of isotropic hardening for the dense matrix material.

Table 4: Hardening and damage parameters for the studied steel material

σ_0 [MPa]	k [MPa]	f_0	s_N	σ_N [MPa]	f_N	f_{cr}	δ_{GTN}	q_1	q_2	q_3
150	800	0.001	0.1	1000	0.05	0.04	10	1.5	1.0	2.15

Figure 5 illustrates the effect of the hardening exponent n on the prediction of limit strains for the studied steel material. It is clearly shown that the consideration of non-normality in the GTN model, due to stress-controlled nucleation, allows for a significant effect of strain hardening on the limit strains. Indeed, the predicted limit strains increase as the hardening exponent n increases, which is consistent with the literature findings (see, e.g., [11]). The effect of the hardening exponent n on the evolution of the Cauchy stress and the void volume fraction until localization for the UT strain path is shown in Figure 6. It can be seen that, in contrast to the case of strain-controlled nucleation (see Figure 3(b)), the evolution of void volume fraction is significantly affected by the hardening exponent n, which allows accounting for strain hardening effects on strain localization. Moreover, the Cauchy stress evolution reveals that the hardening modulus at localization is not strongly negative, as compared to that obtained in the case of strain-controlled nucleation. This is caused by the non-normality of the plastic flow, which plays a destabilizing role in the localization bifurcation analysis.

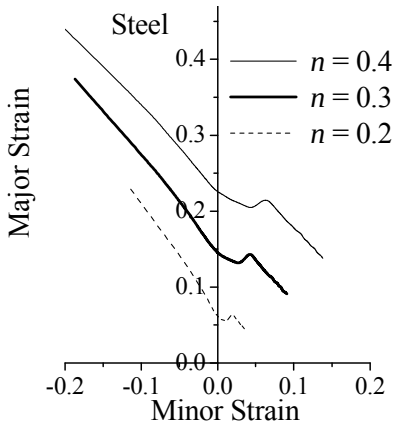

Figure 5: Effect of the hardening exponent n on the prediction of ductility limits for the studied steel material with stress-controlled nucleation

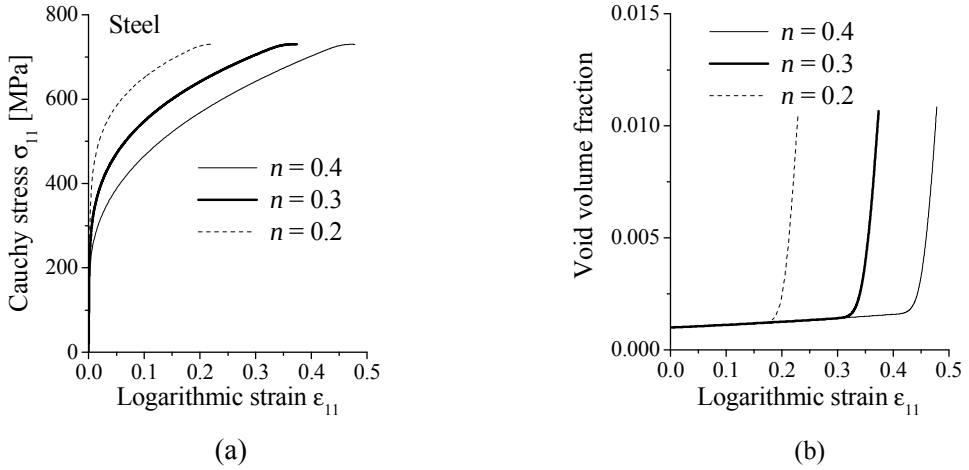

Figure 6: Effect of the hardening exponent n on: (a) the Cauchy stress−strain curve, and (b) void volume fraction, until localization along the UT strain path, in the case of stress-controlled nucleation

12 CONCLUSIONS

In this work, The GTN ductile damage model has been coupled with bifurcation theory to predict the occurrence of strain localization for metallic materials. The resulting approach has been implemented into the finite element software ABAQUS/standard in the framework of large plastic strains and a fully three-dimensional formulation. Ductility limits of metallic materials are then predicted using the proposed approach. A parametric study with respect to damage and hardening parameters has been conducted in order to determine the most influential parameters on strain localization. The analysis showed that the damage parameters have a significant impact on the predicted ductility limits. With regard to hardening, it is shown that the choice of void nucleation mechanism has an important influence on the sensitivity of the predicted ductility limits to strain hardening. Indeed, in the case of strain-controlled nucleation, the predicted limit strains were found almost insensitive to strain hardening for most strain paths, while a significant influence was observed in the case of stress-controlled nucleation. The latter leads to non-normality in the plastic flow rule, which plays a destabilizing role that promotes early strain localization. This work also discussed the use of a micromechanics-based calibration for the GTN q-parameters in the case of strain-controlled nucleation, which is shown to allow accounting for hardening effects on strain localization predictions.

REFERENCES

[1] Keeler, S. and Backofen, W.A. Plastic instability and fracture in sheets stretched over rigid punches. *ASM Trans. Quart.* (1963) **56**:25-48.

[2] Tvergaard, V. and Needleman, A. Analysis of the cup-cone fracture in a round tensile bar. *Acta Metallurgica* (1984) **32**:157-169.

[3] Rudnicki, J.W. and Rice, J.R. Conditions for the localization of deformation in pressure sensitive dilatant materials. *Journal of the Mechanics and Physics of Solids* (1975) **23**:371-394.

[4] Rice, J.R. The localization of plastic deformation. *Theorical and Applied Mechanics*. Koiter ed., 207-227, (1976).
[5] Chu, C. and Needleman, A. Void nucleation effects in biaxially stretched sheets. *Journal of Engineering Materials and Technology* (1980) **102**:249-256.
[6] Abed-Meraim, F., Balan, T. and Altmeyer, G. Investigation and comparative analysis of plastic instability criteria: application to forming limit diagrams. *International Journal of Advanced Manufacturing Technology* (2014) **71**:1247-1262.
[7] Ben Bettaieb, M. and Abed-Meraim, F. Investigation of localized necking in substrate-supported metal layers: Comparison of bifurcation and imperfection analyses. *International Journal of Plasticity* (2015) **65**:168-190.
[8] Brunet, M., Mguil, S. and Morestin, F. Analytical and experimental studies of necking in sheet metal forming processes. *Journal of Materials Processing Technology* (1998) **80-81**:40-46.
[9] Mansouri, L.Z., Chalal, H. and Abed-Meraim, F. Ductility limit prediction using a GTN damage model coupled with localization bifurcation analysis. *Mechanics of Materials* (2014) **76**:64-92.
[10] Faleskog, J., Gao, X. and Shih, C.F. Cell model for nonlinear fracture analysis – I. Micromechanics calibration. *International Journal of Fracture* (1998) **89**:355-373.
[11] Doghri, I. and Billardon, R. Investigation of localization due to damage in elasto-plastic materials. *Mechanics of Materials* (1995) **19**:129-149.

XIV International Conference on Computational Plasticity. Fundamentals and Applications
COMPLAS XIV
E. Oñate, D.R.J. Owen, D. Peric & M. Chiumenti (Eds)

TWO LEVEL HOMOGENIZATION OF FLOWS IN DEFORMING DOUBLE POROSITY MEDIA: BIOT-DARCY-BRINKMAN MODEL

Eduard Rohan*, Vladimír Lukeš*, Jana Turjanicová* and Robert Cimrman†

* European Centre of Excellence, NTIS – New Technologies for Information Society Faculty of Applied Sciences, University of West Bohemia, Univerzitní 8, 30614 Pilsen, Czech Republic
rohan@kme.zcu.cz

† New Technologies Research Centre, University of West Bohemia, Univerzitní 8, 30614 Pilsen, Czech Republic cimrman3@ntc.zcu.cz

Key words: Biot model, Homogenization, Double-porosity media, Poroelasticity, Darcy flow, Stokes flow, Brinkman model

Abstract. We present the two-level homogenization of the flow in a deformable double-porous structure described at two characteristic scales: the higher level porosity associated with the mesoscopic structure is constituted by channels in an elastic skeleton which is made of a microporous material. The macroscopic model is derived by the asymptotic analysis of the viscous flow in the heterogeneous structure characterized by two small parameters. The first level upscaling yields a Biot continuum model coupled with the Stokes flow. The second step of the homogenization leads to a macroscopic flow model which attains the form of the Darcy-Brinkman flow model coupled with the deformation of the poroelastic continuum involving the effective parameters given by the microscopic and the mesoscopic porosity features.

1 INTRODUCTION

The double porosity materials consist of two very distinct porous systems so that their interaction has a strong influence on the fluid transfer and other mechanical properties. In general, the primary and the dual porosities can be distinguished. These two systems characterized by very different pore sizes are arranged hierarchically, one is embedded in the other. In the present study, we consider the fluid-structure interaction problem in the double porosity medium. To respect the skeleton poroelasticity, we extend the model of the hierarchical flow in a rigid double porosity medium described in [8]. The two-level homogenization by the periodic unfolding method was applied to upscale the Stokes flow in a rigid micro-porosity and, consequently, to upscale the Darcy-Stokes system relevant to the mesoscopic medium. The macroscopic flow was described by a Darcy-Brinkman system of equations governing macroscopic fields of pressure and flow velocity. The model

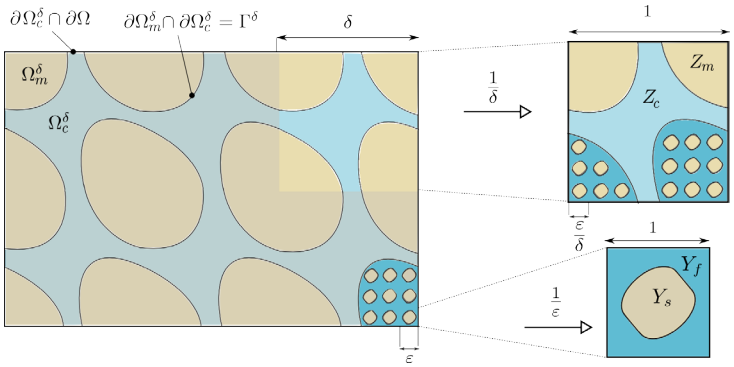

Figure 1: Hierarchical porous structure parameterized by ε, the characteristic size of the microporosity, and by δ which describes the size of the mesoscopic heterogeneities.

derived in this conference paper follows also the hierarchic upscaling procedure described in [7], where a static problem was considered. In [6] we modified the model of a hierarchical poroelastic material by including the Darcy flow in the microporosity. Here we consider a reiterated homogenization of the Stokes flow problem with a strong contrast in the fluid viscosity between the micro- and meso-pores. The 1st level homogenization leads to the Biot model associated with the microporosity whereby interface conditions between the Darcy and Stokes flows are obtained. The 2nd level upscaling of the mesoscopic fractured medium then follows: the mesoscopic model is constituted by the Biot model governing the microporosity and by the Stokes flow model of the fractures. In the paper we present the local problems for characteristic responses; using their solutions the homogenized coefficients of the meso- and macro-models are computed. Numerical illustration is included to illustrate the model response.

2 A MODEL OF FLOW IN DEFORMING HIERARCHICAL POROUS MATERIAL

In this section, we introduce the fluid-structure interaction problem in the pores of the fractured microporous medium. This model is then analyzed using the two level homogenization.

2.1 Geometry and scales

The double porous structure is characterized by two small parameters, ε and δ, which are related to two characteristic scales; denoting by L a macroscopic characteristic length, we have:

- $\ell_{\rm mes} = \delta L$, the mesoscopic characteristic length, and
- $\ell_{\rm mic} = \varepsilon \ell_{\rm mes}$, the microscopic characteristic length.

The hierarchical porous material occupying open bounded domain $\Omega \subset \mathbb{R}^3$ is characterized by two scales related to two small parameters ε and δ, see Fig. 1. At the mesoscopic

scale the periodic structure is formed by channels represented by domain Ω_c^δ occupied by fluid. The domain $\Omega_m^\delta = \Omega \setminus \Omega_c^\delta$ is constituted by a microporous material consisting of the solid and fluid parts. In particular, domain $\Omega_p^{\varepsilon,\delta} \subset \Omega_m^\delta$ represents micro pores occupied by fluid, whereas $\Omega_s^{\varepsilon,\delta} = \Omega_m^\delta \setminus \Omega_p^{\varepsilon,\delta}$ is the skeleton.

The above domain decomposition is summarized, as follows:

$$\begin{aligned} \Omega &= \Omega_m^\delta \cup \Omega_c^\delta \cup \Gamma^\delta \ , \\ \text{solid} \quad \Omega_s^{\varepsilon\delta} &\subset \Omega_m^\delta \ , \\ \text{microporosity} \quad \Omega_p^{\varepsilon\delta} &= \Omega_m^\delta \setminus \Omega_s^{\varepsilon\delta} \ , \\ \text{fluid} \quad \Omega_f^{\varepsilon\delta} &= \Omega_p^{\varepsilon\delta} \cup \Omega_c^\delta \cup \Gamma^\delta \ , \end{aligned} \tag{2.1}$$

Moreover $\overline{\Omega_s^{\varepsilon\delta}} \cap \Gamma^\delta = \emptyset$, thus, the mesoscopic "fictitious" interface is situated in the fluid part.

In the rest of the paper, to simplify the notation, we drop the superscripts ε and δ.

2.2 Problem formulation

The solid skeleton Ω_s is occupied by an elastic material described with the elasticity tensor $\mathbb{D} = (D_{ijkl})$ satisfying the usual symmetries. We consider a viscous incompressible fluid saturating the micro- and the mesoscopic pores, see (2.1). Following the works [2], cf. [8], dealing with models of the rigid double porous media, the viscosity $\eta^{\varepsilon,\delta}$ is given by piece-wise constant function according the micropore size ε:

$$\eta^{\varepsilon,\delta} = \begin{cases} \varepsilon^2 \bar{\eta} & \text{in} \quad \Omega_p^{\varepsilon,\delta} \ , \\ \eta & \text{in} \quad \Omega_c^\delta \ . \end{cases} \tag{2.2}$$

This scaling of the viscosity in micropores is the standard consequence of the non-slip boundary condition for the flow velocity on the pore wall, cf. [4].

The problem imposed in Ω at the microlevel is constituted by the following equations and boundary and interface conditions governing the displacement $\boldsymbol{u}$ of the solid and the fluid pressure and velocity fields $(\boldsymbol{v}^f, p)$:

$$\begin{aligned} -\nabla \cdot \mathbb{D}\boldsymbol{e}(\boldsymbol{u}) &= \boldsymbol{f}^s \quad \text{in } \Omega_s \ , \\ \boldsymbol{n} \cdot \mathbb{D}\boldsymbol{e}(\boldsymbol{u}) &= \boldsymbol{n} \cdot \boldsymbol{\sigma}^f \quad \text{on } \Gamma_{\text{fs}} \ , \\ \boldsymbol{n} \cdot \mathbb{D}\boldsymbol{e}(\boldsymbol{u}) &= \boldsymbol{g}^s \quad \text{on } \partial_\sigma \Omega_s \ , \\ \boldsymbol{u} &= \boldsymbol{0} \quad \text{on } \partial_u \Omega_s \ , \end{aligned} \tag{2.3}$$

$$\begin{aligned} -\nabla \cdot (2\eta \boldsymbol{e}(\boldsymbol{v}^f) - p\boldsymbol{I}) &= \boldsymbol{f}^f \quad \text{in } \Omega_f \ , \\ \nabla \cdot \boldsymbol{v}^f &= 0 \quad \text{in } \Omega_f \ , \\ \boldsymbol{v}^f &= \dot{\boldsymbol{u}} \quad \text{on } \Gamma_{\text{fs}} \ , \\ \boldsymbol{w} &= \bar{\boldsymbol{w}} \quad \text{on } \partial_{\text{ext}} \Omega_f \ , \end{aligned} \tag{2.4}$$

where $\boldsymbol{e}(\boldsymbol{u})$ is the small strain tensor, $\boldsymbol{\sigma}^f$ is the fluid stress, $\boldsymbol{f}$ is the volume force, $\boldsymbol{g}^s$ is the surface traction stresses acting on the solid part; the exterior part $\partial_{\rm ext}\Omega_s$ of the solid splits into two disjoint parts, $\partial_{\rm ext}\Omega_s = \partial_\sigma\Omega_s \cup \partial_u\Omega_s$.

Above, to introduce the relative fluid velocity $\boldsymbol{w} = \boldsymbol{v}^f - \dot{\tilde{\boldsymbol{u}}}$ in the fluid-saturated pores $\Omega_f^{\varepsilon\delta}$, we define a displacement extension $\tilde{\boldsymbol{u}}$ in Ω such that $\tilde{\boldsymbol{u}} \equiv \boldsymbol{u}$ in Ω_s.

To introduce the weak formulation of the fluid-structure interaction problem, we use spaces of admissible and test displacements and relative fluid velocities,

$$\begin{aligned} \boldsymbol{V}_0 &= \{\boldsymbol{v} \in \mathbf{H}^1(\Omega_s) |\ \boldsymbol{v} = \boldsymbol{0} \text{ on } \partial_u\Omega_s\} \\ \boldsymbol{W}_0 &= \{\boldsymbol{v} \in \mathbf{H}^1(\Omega_f) |\ \boldsymbol{v} = \boldsymbol{0} \text{ on } \partial\Omega_f\}\ , \qquad \boldsymbol{W}_{\bar{\boldsymbol{v}}} = \boldsymbol{W}_0 + \bar{\boldsymbol{w}}\ , \end{aligned} \tag{2.5}$$

where $\bar{\boldsymbol{w}}$ is extended from $\partial_{\rm ext}\Omega_f$ to Ω_f. By $\mathbf{H}^1(\Omega)$ we denote the the standard Sobolev space $\boldsymbol{W}^{1,2}(\Omega)$ of vector-valued functions.

The weak formulation of problem (2.3)-(2.4) reads, as follows: For any time instant $t > 0$, find $(\boldsymbol{u}(t,\cdot), \boldsymbol{w}(t,\cdot), p(t,\cdot)) \in \boldsymbol{V}_0 \times \boldsymbol{W}_{\bar{\boldsymbol{v}}} \times H^1(\Omega_f))$, such that

$$\begin{aligned} &\int_{\Omega_s} \mathbb{D}\boldsymbol{e}(\boldsymbol{u}) : \boldsymbol{e}(\boldsymbol{v}) - \int_\Gamma \boldsymbol{n}\cdot\boldsymbol{\sigma}^f\cdot\boldsymbol{v} = \int_{\partial_\sigma\Omega_s} \boldsymbol{g}^s\cdot\boldsymbol{v} + \int_{\Omega_s} \boldsymbol{f}^s\cdot\boldsymbol{v}, \quad \boldsymbol{v}\in\boldsymbol{V}_0\ , \\ &\int_{\Omega_f} 2\eta\boldsymbol{e}(\boldsymbol{w} + \dot{\tilde{\boldsymbol{u}}}) : \boldsymbol{e}(\boldsymbol{z}) + \int_{\Omega_f} \boldsymbol{z}\cdot\nabla p = \int_{\Omega_f} \boldsymbol{f}^f\cdot\boldsymbol{z}, \quad \boldsymbol{z}\in\boldsymbol{W}_0\ , \\ &\int_{\Omega_f} q\nabla\cdot(\boldsymbol{w} + \dot{\tilde{\boldsymbol{u}}}) = 0\ , \quad \forall q \in L^2(\Omega_f)\ . \end{aligned} \tag{2.6}$$

We recall that all functions and parameters involved in (2.6) depend on the two small parameters ε and δ. Passing to the limit with microstructure sized associated with $\varepsilon \to 0$ give rise to the mesoscopic model reported in Section 3. The second level homogenization associated with with parameter $\delta \to 0$ leads to the macroscopic problem described in Section 4.

3 MESOSCOPIC MODEL – THE FIRST LEVEL UPSCALING

The porous medium situated in Ω_m is generated as a periodic lattice by repeating the representative volume element (RVE) occupying domain $Y^\varepsilon = \varepsilon Y$. The zoomed cell $Y = \Pi_{i=1}^3]0, \bar{y}_i[\subset \mathbb{R}^3$ splits into the solid part occupying domain Y_s and the complementary fluid part Y_f, thus

$$Y = Y_s \cup Y_f \cup \Gamma_Y\ , \quad Y_s = Y \setminus Y_m\ , \quad \Gamma_Y = \overline{Y_s} \cap \overline{Y_f}\ . \tag{3.1}$$

For a given scale $\varepsilon > 0$, $\ell_i = \varepsilon\bar{y}_i$ is the characteristic size associated with the i-th coordinate direction, whereby also $\varepsilon \approx \ell_i/L$ for a given macroscopic characteristic length L.

3.1 Local problems and homogenized mesoscopic poroelastic coefficients

For any $D \subset Y$, $⨍_D = \frac{1}{|Y|}\int_D$; the analogical notation is employed for any $A \subset Z$, thus $⨍_A = \frac{1}{|Z|}\int_A$. Further, for any $D \subset Y$, $\mathbf{H}^1_\#(D)$ is the Sobolev space $\boldsymbol{W}^{1,2}(Y) = \mathbf{H}^1(Y)$ of

vector-valued Y-periodic functions (indicated by the subscript #). We define the usual elasticity bilinear form,

$$a_s\left(\boldsymbol{w},\, \boldsymbol{v}\right) = \fint_{Y_s} \left(\mathbb{D}\boldsymbol{e}_y(\boldsymbol{w})\right) : \boldsymbol{e}_y(\boldsymbol{v}) \;,$$

where $\boldsymbol{e}_y(\boldsymbol{w}) = 1/2(\nabla_y \boldsymbol{w} + (\nabla_y \boldsymbol{w})^T)$ is the strain tensor associated with the displacement field $\boldsymbol{w}$.

The local microstructural response is obtained by solving the following decoupled problems:

- Find $\boldsymbol{\omega}^{ij} \in \mathbf{H}^1_{\#}(Y_s)$ for any $i, j = 1, 2, 3$ satisfying

$$a_s\left(\boldsymbol{\omega}^{ij} + \boldsymbol{\Pi}^{ij},\, \boldsymbol{v}\right) = 0 \;, \quad \forall \boldsymbol{v} \in \mathbf{H}^1_{\#}(Y_s) \;. \tag{3.2}$$

- Find $\boldsymbol{\omega}^P \in \mathbf{H}^1_{\#}(Y_s)$ satisfying

$$a_s\left(\boldsymbol{\omega}^P,\, \boldsymbol{v}\right) = \fint_{\Gamma_Y} \boldsymbol{v} \cdot \boldsymbol{n}^{[\mathrm{m}]} \,\mathrm{dS}_y \;, \quad \forall \boldsymbol{v} \in \mathbf{H}^1_{\#}(Y_s) \;. \tag{3.3}$$

- Find $(\boldsymbol{\psi}^i, \pi^i) \in \mathbf{H}^1_{\#}(Y_f) \times L^2(Y_f)$ for $i = 1, 2, 3$ such that

$$\begin{aligned} \int_{Y_f} \nabla_y \boldsymbol{\psi}^k : \nabla_y \boldsymbol{v} - \int_{Y_f} \pi^k \nabla \cdot \boldsymbol{v} = \int_{Y_f} v_k \;, \quad \forall \boldsymbol{v} \in \mathbf{H}^1_{\#}(Y_f) \;, \\ \int_{Y_f} q \nabla_y \cdot \boldsymbol{\psi}^k = 0 \;, \quad \forall q \in L^2(Y_f) \;. \end{aligned} \tag{3.4}$$

Using the characteristic responses (3.2)–(3.4) obtained at the microscopic scale the homogenized coefficients, describing the effective properties of the deformable porous medium, are given by the following expressions:

$$\begin{gathered} A_{ijkl} = a_s\left(\boldsymbol{\omega}^{ij} + \boldsymbol{\Pi}^{ij},\, \boldsymbol{\omega}^{kl} + \boldsymbol{\Pi}^{kl}\right) \;, \quad \hat{B}_{ij} = -\fint_{Y_s} \mathrm{div}_y \boldsymbol{\omega}^{ij} = a_s\left(\boldsymbol{\omega}^P,\, \boldsymbol{\Pi}^{ij}\right) \;, \\ M = a_s\left(\boldsymbol{\omega}^P,\, \boldsymbol{\omega}^P\right) = \fint_{\Gamma_Y} \boldsymbol{\omega}^P \cdot \boldsymbol{n} \,\mathrm{dS}_y \;, \quad K_{ij} = \bar{\eta}^{-1} \fint_{Y_f} \psi^j_i = \bar{\eta}^{-1} \fint_{Y_f} \nabla_y \boldsymbol{\psi}^i : \nabla_y \boldsymbol{\psi}^i \;. \end{gathered} \tag{3.5}$$

Obviously, the tensors $\mathbb{A} = (A_{ijkl})$, $\hat{\boldsymbol{B}} = (\hat{B}_{ij})$ and $\boldsymbol{K} = (K_{ij})$ are symmetric, $\mathbb{A}$ adheres all the symmetries of $\mathbb{D}$; moreover, $\mathbb{A}$ is positive definite and $M > 0$. The hydraulic permeability $\boldsymbol{K}$ is positive semi-definite in general, although it is positive definite whenever the channels intersect all faces of ∂Y and Y_f is connected. Using the fluid compressibility γ and the volume fraction $\phi_f = |Y_f|/|Y|$, we define

$$\boldsymbol{B} := \hat{\boldsymbol{B}} + \phi_f \boldsymbol{I} \;. \tag{3.6}$$

3.2 Mesoscopic problem

The first level homogenization $\varepsilon \to 0$ of the model (2.6) yields the mesoscopic problem governing the fluid redistribution between the deforming microporous material and the mesoscopic channels. The mesoscopic model describes the coupled Darcy and Stokes flows in the deforming porous fractured medium whose properties are constituted by the Biot poroelastic model. The weak formulation of the mesoscopic problem involves the following functional spaces: $\boldsymbol{W}_c = \{\boldsymbol{w} \in \mathbf{H}^1(\Omega_c) |\, \boldsymbol{w} = 0 \text{ on } \partial_{\rm ext}\Omega_c\}$, $\boldsymbol{V}_m = \{\boldsymbol{u} \in \mathbf{H}^1(\Omega_m) |\, \boldsymbol{u} = 0 \text{ on } \partial_u\Omega_m\}$ and $Q_m = H^1(\Omega_m)$. The porous structure is fixed on a part of the boundary $\partial_u\Omega_m \subset \partial\Omega_m \cap \partial\Omega$.

Weak formulation. Find $(\boldsymbol{u}, \boldsymbol{w}, p_m, p_c)(t,\cdot) \in \boldsymbol{V}_m \times [\boldsymbol{W}_c + \bar{\boldsymbol{v}}] \times H^1(\Omega_m) \times L^2(\Omega_c)$ such that

$$
\begin{aligned}
&\int_{\Omega_m} (\mathbb{A}\boldsymbol{e}(\boldsymbol{u}) - p_m\boldsymbol{B}) : \boldsymbol{e}(\boldsymbol{v}) - \int_\Gamma p_m \boldsymbol{n}^{[\mathrm{c}]} \cdot \boldsymbol{v} = \int_{\partial_{\rm ext}\Omega_m} \bar{\phi}_s \boldsymbol{g} \cdot \boldsymbol{v} + \int_{\Omega_s} \phi_s \boldsymbol{f}^s \cdot \boldsymbol{v}, \quad \boldsymbol{v} \in \boldsymbol{V}_m\,,\\
&\int_{\Omega_m} \nabla q_m \cdot \boldsymbol{K}(\nabla p_m - \boldsymbol{f}^f) + \int_{\Omega_m} q_m \boldsymbol{B} : \boldsymbol{e}(\dot{\boldsymbol{u}}) + \int_{\Omega_m} M\dot{p}_m q_m - \int_\Gamma q_m \boldsymbol{w} \cdot \boldsymbol{n}^{[\mathrm{c}]}\\
&\quad = \int_{\partial_{\rm ext}\Omega_m} q_m \phi_f (\dot{\boldsymbol{u}} - \boldsymbol{v}^f) \cdot \boldsymbol{n}\,, \quad \forall q_m \in Q_m\,,\\
&\int_{\Omega_c} 2\eta \boldsymbol{e}(\boldsymbol{w} + \dot{\tilde{\boldsymbol{u}}}) : \boldsymbol{e}(\boldsymbol{\vartheta}) - \int_{\Omega_c} p_c \nabla \cdot \boldsymbol{\vartheta} + \int_\Gamma p_m \boldsymbol{n}^{[\mathrm{c}]} \cdot \boldsymbol{\vartheta} = \int_{\Omega_c} \boldsymbol{f}^f \cdot \boldsymbol{\vartheta}, \quad \boldsymbol{\vartheta} \in \boldsymbol{W}_c\,,\\
&\int_{\Omega_c} q_c \nabla \cdot (\boldsymbol{w} + \dot{\tilde{\boldsymbol{u}}}) = 0\,, \quad \forall q_c \in L^2(\Omega_f)\,.
\end{aligned}
\tag{3.7}
$$

The r.h.s. integral in $(3.7)_2$ expresses the relative outflow form the matrix part, *i.e.* $-\bar{w}_n = -\bar{\boldsymbol{w}} \cdot \boldsymbol{n} = -\boldsymbol{n} \cdot (\boldsymbol{v}^f - \dot{\boldsymbol{u}})$, which is prescribed by the boundary condition. As the byproduct of the first level homogenization, we obtain the following interface conditions on Γ,

$$
\begin{aligned}
\boldsymbol{n}^{[\mathrm{c}]} \cdot (\boldsymbol{w}|_{\Omega_c} - \boldsymbol{w}|_{\Omega_m}) &= 0\,,\\
p_c - p_m &= 2\eta \boldsymbol{e}(\boldsymbol{w}|_{\Omega_c}) : \boldsymbol{n}^{[\mathrm{c}]} \otimes \boldsymbol{n}^{[\mathrm{c}]}\,,\\
\boldsymbol{t} \cdot \partial_n \boldsymbol{w}|_{\Omega_c} + \boldsymbol{n} \cdot \partial_t \boldsymbol{w}|_{\Omega_c} &= 0\,,
\end{aligned}
\tag{3.8}
$$

where $\partial_n = \boldsymbol{n} \cdot \nabla$ and $\partial_t = \boldsymbol{t} \cdot \nabla$ with $\boldsymbol{t}$ being a unit vector in the tangential plane of Γ, *i.e.* $\boldsymbol{n} \cdot \boldsymbol{t} = 0$. It is worth noting that the 3rd condition in (3.8) corresponds to the free-slip condition, in contrast with the Beavers-Joseph-Saffmann condition derived also by the homogenization on a flat interface between the two flows, see e.g. [3], cf. [5].

Problem (3.7) is then subject of the second level homogenization which gives rise the macroscopic problem.

4 MACROSCOPIC MODEL – THE SECOND LEVEL UPSCALING

The mesoscopic heterogeneous structure is generated as a periodic lattice using the mesoscopic cell decomposed into the "microporous" matrix and the mesoscopic channels,

$Z = Z_m \cup Z_c \cup \Gamma_Z$, which are separated by the interface Γ_Z. The global domain Ω generated by δZ as a periodic lattice is decomposed into the corresponding parts, $\Omega = \Omega_m^\delta \cup \Omega_c^\delta \cup \Gamma^\delta$. We recall that the interface Γ_Z^δ of real-sized cell part $\delta Z_m = Z_m^\delta$ is "immersed" in the fluid; this is is the assumption involved in the 1st level homogenization.

The second level homogenization associated with the asymptotic analysis $\delta \to 0$ leads to the following local problems governing the local characteristic responses which constitute the macroscopic effective parameters of the double porosity medium.

4.1 Local problems and homogenized macroscopic coefficients

The following bilinear forms are employed:

$$a_m(\boldsymbol{u},\,\boldsymbol{v}) = \fint_{Z_m} \mathbb{A}\boldsymbol{e}_z(\boldsymbol{u}) : \boldsymbol{e}_z(\boldsymbol{v})\,, \quad b_m(p,\,\boldsymbol{v}) = \fint_{Z_m} p\boldsymbol{B} : \boldsymbol{e}_z(\boldsymbol{v})\,,$$
$$c_m(p,\,q) = \fint_{Z_m} \nabla_z q \cdot \boldsymbol{K}\nabla_z p\,, \quad d_c(\boldsymbol{w},\,\boldsymbol{\vartheta}) = 2\eta \fint_{Z_c} \boldsymbol{e}_z(\boldsymbol{w}) : \boldsymbol{e}_z(\boldsymbol{\vartheta})\,,$$
$$\langle u,\,w\rangle_{Z_c} = \fint_{Z_c} uw\,.$$

To compute the homogenized macroscopic coefficients, the mesoscopic problems for characteristic responses must be solved. The following four decoupled local problems in the matrix are defined: Find $\boldsymbol{\omega}^{ij}, \boldsymbol{\omega}^P \in \mathbf{H}^1_\#(Z_m)/\mathbb{R}^3$, and $\pi^k, \varphi^k \in H^1_\#(Z_m)$ such that,

$$\begin{aligned}
a_m\left(\boldsymbol{\omega}^{ij},\,\boldsymbol{v}\right) &= -a_m\left(\boldsymbol{\Pi}^{ij},\,\boldsymbol{v}\right) \quad \forall \boldsymbol{v} \in \mathbf{H}^1_\#(Z_m)\,,\\
a_m\left(\boldsymbol{\omega}^{P},\,\boldsymbol{v}\right) &= b_m(1,\,\boldsymbol{v}) - \fint_{\Gamma_Z} \boldsymbol{n}^{[\mathrm{m}]} \cdot \boldsymbol{v} \quad \forall \boldsymbol{v} \in \mathbf{H}^1_\#(Z_m)\,,\\
c_m\left(\pi^k,\,q\right) &= -c_m(z_k,\,q) \quad \forall q \in H^1_\#(Z_m)\,,\\
c_m\left(\varphi^k,\,q\right) &= -\fint_{\Gamma_Z} q n_k^{[\mathrm{m}]} \quad \forall q \in H^1_\#(Z_m)\,.
\end{aligned} \tag{4.1}$$

Moreover, three mesoscopic problems for characteristic responses in the channels must be solved:

1. Find $(\boldsymbol{\psi}^{ij}, \hat{\pi}^{ij}) \in \mathbf{H}^1_\#(Z_c)/\mathbb{R}^3 \times L^2(Z_c)$, such that,

$$\begin{aligned}
d_c\left(\boldsymbol{\psi}^{ij},\,\boldsymbol{\vartheta}\right) - \left\langle \hat{\pi}^{ij},\,\nabla_z\cdot\boldsymbol{\vartheta}\right\rangle_{Z_c} &= -d_c\left(\boldsymbol{\Pi}^{ij},\,\boldsymbol{\vartheta}\right)\,,\\
\left\langle \nabla_z\cdot\boldsymbol{\psi}^{ij},\,q\right\rangle_{Z_c} &= -\left\langle \nabla_z\cdot\boldsymbol{\Pi}^{ij},\,q\right\rangle_{Z_c}\,,
\end{aligned} \tag{4.2}$$

   for all $(\boldsymbol{\vartheta}, q) \in \mathbf{H}^1_\#(Z_c) \times L^2(Z_c)$.

2. Find $(\boldsymbol{\psi}^{P}, \hat{\pi}^{P}) \in \mathbf{H}^1_\#(Z_c)/\mathbb{R}^3 \times L^2(Z_c)$, such that,

$$\begin{aligned}
d_c\left(\boldsymbol{\psi}^{P},\,\boldsymbol{\vartheta}\right) - \left\langle \hat{\pi}^{P},\,\nabla_z\cdot\boldsymbol{\vartheta}\right\rangle_{Z_c} &= -\fint_{\Gamma_Z} \boldsymbol{\vartheta}\cdot\boldsymbol{n}^{[\mathrm{c}]} - d_c\left(\tilde{\boldsymbol{\omega}}^{P},\,\boldsymbol{\vartheta}\right)\,,\\
\left\langle \nabla_z\cdot\boldsymbol{\psi}^{P},\,q\right\rangle_{Z_c} &= 0\,,
\end{aligned} \tag{4.3}$$

   for all $(\boldsymbol{\vartheta}, q) \in \mathbf{H}^1_\#(Z_c) \times L^2(Z_c)$.

4.2 Homogenized coefficients

In the following expression, we employ function $\tilde{\boldsymbol{\psi}}^{ij} = \boldsymbol{\psi}^{ij} - \tilde{\boldsymbol{\omega}}^{ij}$. The following homogenized coefficients are involved in the macroscopic problem introduced below. They are expressed using the characteristic responses of local problems (4.1), (4.2) and (4.3).

$$\begin{aligned}
\mathcal{A}_{ijkl} &= a_m\left(\boldsymbol{\Pi}^{kl} + \boldsymbol{\omega}^{kl},\, \boldsymbol{\Pi}^{ij} + \boldsymbol{\omega}^{ij}\right)\,,\\
\mathcal{B}_{ij} &= \phi_m \boldsymbol{B}_{ij} - a_m\left(\boldsymbol{\omega}^{P},\, \boldsymbol{\Pi}^{ij}\right)\,,\\
\mathcal{H}_{ij} &= -\fint_{Z_c} \varphi^j n_i^{[\mathrm{m}]} = c_m\left(\varphi^i,\, \varphi^j\right)\,,\\
\mathcal{Q}^*_{ij} &= \fint_{\Gamma_Z} \pi^j n_i^{[\mathrm{c}]}\,.
\end{aligned} \tag{4.4}$$

$$\begin{aligned}
\mathcal{C}_{ij} &= \phi_m \boldsymbol{B}_{ij} + b_m\left(1,\, \boldsymbol{\omega}^{ij}\right) - \fint_{\Gamma_Z} \boldsymbol{n}^{[\mathrm{c}]}\cdot\tilde{\boldsymbol{\psi}}^{ij}\,,\\
\mathcal{K}_{ij} &= c_m\left(z_j + \pi^j,\, z_i + \pi^i\right)\,,\\
\mathcal{Q}_{ij} &= c_m\left(z_i,\, \varphi^j\right) = \fint_{\Gamma_Z} \pi^i n_j^{[\mathrm{m}]}\,,\\
\mathcal{M} &= \phi_m M + a_m\left(\boldsymbol{\omega}^{P},\, \boldsymbol{\omega}^{P}\right)\,,
\end{aligned} \tag{4.5}$$

$$\begin{aligned}
\mathcal{S}_{ijkl} &= d_c\left(\boldsymbol{\Pi}^{ij} + \boldsymbol{\psi}^{ij},\, \boldsymbol{\Pi}^{kl} + \boldsymbol{\psi}^{kl}\right)\,,\\
\mathcal{F}_{ij} &= \phi_c\delta_{ij} + d_c\left(\boldsymbol{\psi}^{P},\, \boldsymbol{\Pi}^{ij}\right) - \fint_{Z_c} \hat{\pi}^P \nabla_z\cdot\boldsymbol{\Pi}^{ij}\,,\\
\mathcal{E}_{ij} &= d_c\left(\tilde{\boldsymbol{\omega}}^{P},\, \boldsymbol{\Pi}^{ij}\right)\,,
\end{aligned} \tag{4.6}$$

The following relationships hold,

$$\mathcal{Q}_{ij} = -\mathcal{Q}^*_{ji}\,,\quad \mathcal{C}_{ij} = \mathcal{B}_{ij} + \phi_c\delta_{ij}\,, \tag{4.7}$$

and we introduce

$$\mathcal{P}_{ij} = \phi_c\delta_{ij} - \mathcal{Q}_{ij}\,,\quad \mathcal{P}^*_{ij} = \phi_c\delta_{ij} + \mathcal{Q}^*_{ij}\,, \tag{4.8}$$

Except of coefficients $\mathcal{Q}_{ij}$ and $\mathcal{P}_{ij}$, thereby also $\mathcal{Q}^*_{ij}$ and $\mathcal{P}^*_{ij}$, all other coefficients are symmetric tensors, *i.e.* $a_{ij} = a_{ji}$. Moreover $\mathcal{S}_{ijkl} = \mathcal{S}_{klij}$.

4.3 Macroscopic problem

The second level homogenization leads to the following macroscopic problem: Find $(\boldsymbol{u}^0, \boldsymbol{w}^0, p^0) \in \boldsymbol{V}_\Omega \times (\boldsymbol{W}_\Omega + \bar{\boldsymbol{w}}) \times H^1(\Omega)$, such that

$$\begin{aligned}
&\int_\Omega \big(\boldsymbol{\mathcal{A}}\boldsymbol{e}_x(\boldsymbol{u}^0) - p^0\boldsymbol{\mathcal{B}}\big) : \boldsymbol{e}_x(\boldsymbol{v}^0) - \int_\Omega \boldsymbol{v}^0 \cdot \boldsymbol{\mathcal{Q}}^*(\nabla_x p^0 - \boldsymbol{f}^f) - \int_\Omega \boldsymbol{v}^0 \cdot \boldsymbol{\mathcal{H}}\boldsymbol{w}^0 \\
&= \int_{\partial_\sigma\Omega} (\phi_m - \bar{\phi}_m) p^0 \boldsymbol{n} \cdot \boldsymbol{v}^0 - \int_\Omega p^0 \boldsymbol{v}^0 \cdot \nabla\phi_m + \int_\Omega \phi_m\phi_s \boldsymbol{f}^s \cdot \boldsymbol{v}^0 + \int_{\partial\Omega} \bar{\phi}_m\bar{\phi}_s \boldsymbol{g} \cdot \boldsymbol{v}^0 \,, \\
&\int_\Omega q^0 \boldsymbol{\mathcal{C}} : \boldsymbol{e}_x(\dot{\boldsymbol{u}}^0) + \int_\Omega \nabla_x q^0 \cdot \big(\boldsymbol{\mathcal{K}}(\nabla_x p^0 - \boldsymbol{f}^f) - \boldsymbol{\mathcal{P}}\boldsymbol{w}^0\big) + \int_\Omega q^0 \mathcal{M}\dot{p}^0 = -\int_{\partial_w\Omega} q^0 \boldsymbol{n} \cdot \bar{\boldsymbol{w}} \\
&\int_\Omega \boldsymbol{e}_x(\boldsymbol{\vartheta}^0) : \big(\boldsymbol{\mathcal{S}}\boldsymbol{e}_x(\boldsymbol{w}^0 + \dot{\boldsymbol{u}}^0) + \boldsymbol{\mathcal{E}}\dot{p}^0 + \boldsymbol{\mathcal{F}}p^0\big) \\
&+ \int_\Omega \boldsymbol{\vartheta}^0 \big(\boldsymbol{\mathcal{H}}\boldsymbol{w}^0 + \boldsymbol{\mathcal{P}}^*(\nabla_x p^0 - \boldsymbol{f}^f)\big) = \int_{\partial_p\Omega} \bar{\phi}_c \bar{p}^0 \boldsymbol{n} \cdot \boldsymbol{\vartheta}^0 \,,
\end{aligned} \tag{4.9}$$

for all $(\boldsymbol{v}^0, q^0, \boldsymbol{\theta}^0) \in \boldsymbol{V}_\Omega \times \boldsymbol{W}_\Omega \times H^1_\#(\Omega)$. By $\boldsymbol{V}_\Omega \subset \mathbf{H}^1(\Omega)$ we denote the space of admissible macroscopic displacements $\boldsymbol{u}^0$ vanishing on $\partial_u\Omega$, whereby the space $\boldsymbol{W}_\Omega \subset \mathbf{H}^1(\Omega)$ contains velocities vanishing on entire $\partial\Omega$, see the boundary conditions in the initial formulation (2.3)-(2.4).

With the assumptions on the medium periodic structure, *i.e.* $\nabla\phi_m = 0$, and for the usual case $\phi_m = \bar{\phi}_m$, the first two integrals involving p^0 at the r.h.s. of (4.9) vanish. For a special case $\bar{\phi}_m = 1$, further symmetries can be observed, since $\phi_c = 1 - \phi_m$; in particular, the first two r.h.s. integrals are replaced by

$$-\int_\Omega p^0 \phi_c \nabla \cdot \boldsymbol{w}^0 - \int_\Omega \nabla p^0 \cdot \boldsymbol{w}^0 \,,$$

which give rise the following substitutions in eq. $(4.9)_1$:

$$\boldsymbol{\mathcal{B}} := \boldsymbol{\mathcal{C}} \,, \quad \text{and } \boldsymbol{\mathcal{Q}}^* := \boldsymbol{\mathcal{P}}^* \,. \tag{4.10}$$

5 NUMERICAL ILLUSTRATION

In following part the results of numerical simulation illustrating the hierarchical three-scale model proposed above are presented. The computation of effective coefficients can be split into a few steps:

1. Find correctors on the microscale $\boldsymbol{\omega}^{ij}, \boldsymbol{\omega}^P, \boldsymbol{\psi}^i, \pi^i$ as solutions of autonomous problems (3.2)-(3.4) on the cubic periodic cell Y.

2. Compute effective coefficients $\mathbb{A}, \boldsymbol{B}, M$ and $\boldsymbol{K}$ given by (3.5) relevant on the mesoscopic level.

3. Find the mesoscale correctors $\boldsymbol{\omega}^{ij}, \boldsymbol{\omega}^P, \pi^k, \varphi^k, \boldsymbol{\psi}^{ij}, \hat{\pi}^{ij}, \boldsymbol{\psi}^P$ and $\hat{\pi}^P$ as solutions of (4.1), (4.2) and (4.3) on the cubic periodic cell Z.

4. Compute effective coefficients $\boldsymbol{\mathcal{A}}, \boldsymbol{\mathcal{B}}, \boldsymbol{\mathcal{C}}, \boldsymbol{\mathcal{E}}, \boldsymbol{\mathcal{F}}, \boldsymbol{\mathcal{H}}, \boldsymbol{\mathcal{K}}, \mathcal{M}, \boldsymbol{\mathcal{P}}, \boldsymbol{\mathcal{Q}}$ and $\boldsymbol{\mathcal{S}}$ introduced in (4.4), (4.5) and (4.6).

Obtained effective coefficients relevant to the macroscopic scale are then used in simple macroscopic problem.

The macroscopic model and all the autonomous problems at the meso- and microscopic levels were implemented in *SfePy* software [1] which allows for multiscale simulations using the FE method. The macroscopic fields $\boldsymbol{w}^0$ $\boldsymbol{u}^0$ were approximated using the Lagrangian elements Q2 and for macroscopic pressure field p^0 the Q1 elements were used.

The solution of macroscopic problem is illustrated on the simple specimen shaped as a block $(10.0 \times 3.4 \times 3.4)$m with material properties given by effective coefficients obtained through the two-level upscaling from the mesoscopic level. The mesoscopic structure is represented by a periodic cubic cell Z consisting of the microporous matrix Z_m and the fluid-filled channel Z_c, see Section 4. The characteristic size of the real-sized cell Z^δ is $\delta = 10^{-1}$. Viscosity of the fluid in the channel is taken as $\eta = 10^{-3} Nsm^{-2}$. The microporosity is represented by the channel Y_f in the cubic cell Y. Fluid viscosity at this level is rescaled according to (2.2), thus $\bar{\eta} = \varepsilon^{-2}\eta$. The elasticity parameters of the solid matrix are as follows: the Young's modulus $E = 3\,\mathrm{GPa}$ and the Poisson's ratio $\nu = 0.34$.

The geometry representations of the micro-, meso- and the macroscopic level structure are shown in Fig. 2 where the split of the boundary $\partial\Omega$ is illustrated, showing the two segments $\Gamma_{in} \subset \partial\Omega$, and $\Gamma_{out} \subset \partial\Omega$. In the context of (4.9), $\partial\Omega \equiv \partial_w\Omega$ whereas $\Gamma_{out} \equiv \partial_p\Omega$.

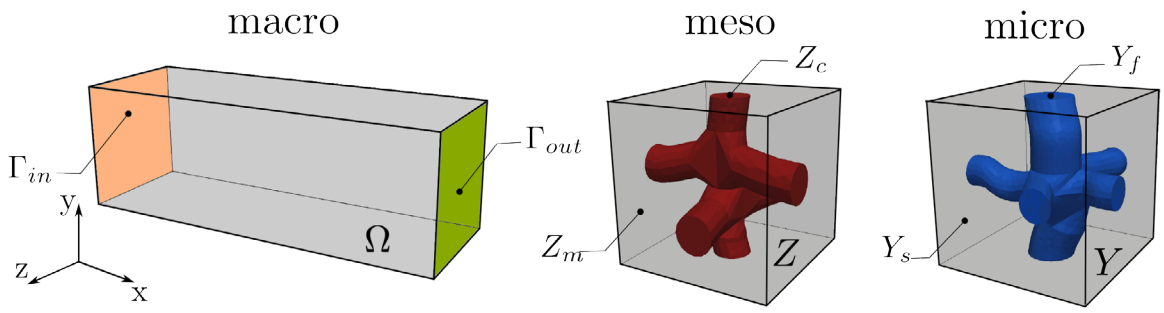

Figure 2: Left: Macroscopic geometry, definition of boundaries Γ_{in}, Γ_{out}; Middle: Mesoscopic geometry consisting of fluid (Z_c) and porous matrix (Z_m), definition of point C; Right: Microscopic geometry constituted by fluid part Y_f and solid Y_s.

In order to illustrate macroscopic behavior of deforming double porosity specimen defined by (4.9), the following boundary conditions are considered:

$$
\begin{aligned}
\boldsymbol{w}^0 &= \bar{\boldsymbol{w}}^0 = -\boldsymbol{n}\bar{w}^0 \text{ on } \Gamma_{in},\\
\boldsymbol{w}^0 &= 0.8\bar{\boldsymbol{w}}^0 = \boldsymbol{n}0.8\bar{w}^0 \text{ on } \Gamma_{out},\\
\boldsymbol{w}^0 &= \boldsymbol{0} \text{ on } \partial\Omega \setminus (\Gamma_{in} \cup \Gamma_{out}).\\
p^0 &= 0 \text{ on } \Gamma_{out},\\
\boldsymbol{u}^0 &= \boldsymbol{0} \text{ on } \Gamma_{in},
\end{aligned}
$$

The seepage velocity $\bar{w}^0$ captures a parabolic profile along the cross-section Γ_{out} and/or Γ_{in}, such that $\bar{w}^0 = 0$ at the edges $\partial\Gamma_{out}$ and/or $\partial\Gamma_{in}$. For simplicity, volume forces and surface tractions are omitted, thus $\boldsymbol{f}^f = 0$, $\boldsymbol{f}^s = 0$ and $\boldsymbol{g}^s = 0$. Results of the numerical simulation at the macroscopic level are shown in Fig. 3, where displacement $\mathbf{u}^0$, velocity $\mathbf{w}^0$ and pressure p^0 fields are displayed.

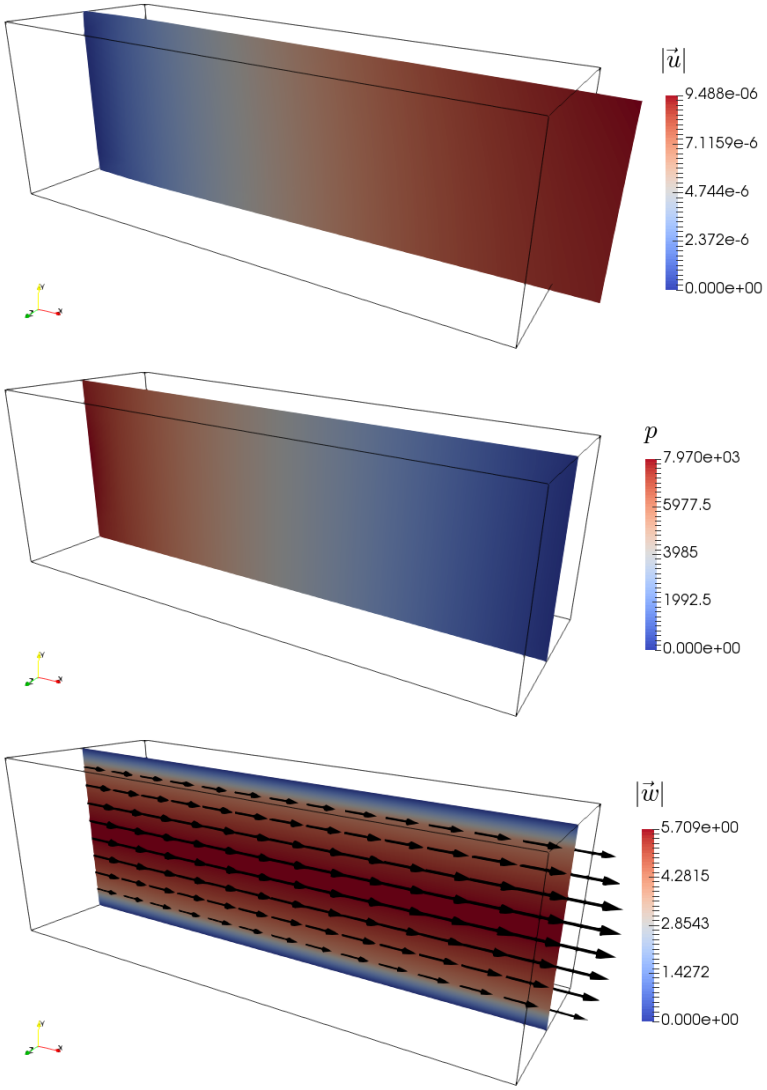

Figure 3: Macroscopic fields: Top: local magnitudes of the displacement $|\boldsymbol{u}_0|$, deformed structure displayed. Middle: pressure p_0; Bottom: magnitude of relative fluid velocity $\boldsymbol{w}_0$.

6 CONCLUSION

In the reported work we propose a new model describing viscous flows in the homogenized double porous deformable medium in terms of coupled Darcy and Brinkman type equations; the phenomenon of deformation introducing the Biot poroelastic coefficients

into the meso- and macroscopic formulations presents the major novelty of the work when compared with our paper [8]. We studied the two-level homogenization of Stokes flows in the microporous material which is drained into the mesoscopic pores. In the proposed model, the mesoscopic pores are much larger than the viscous boundary effects at the interface. When each of the porosities is a connected domain, the flow in both is described by two fields, $\boldsymbol{w}^0$ and p^0, for which boundary conditions must be specified independently. The macroscopic model is not fully symmetric as the result of the fluid-structure interaction. As a future work, we intend to validate the macroscopic model using the direct simulations of a heterogeneous structure at the mesoscopic level.

Acknowledgment This research is supported by project GACR 16-03823S and in part by project GACR 13-00863S of the Scientific Foundation of the Czech Republic. Jana Turjanicová is grateful to the project LO 1506 of the Czech Ministry of Education, Youth and Sports.

REFERENCES

[1] Cimrman, R. SfePy - write your own FE application. In Pierre de Buyl and Nelle Varoquaux, editors, *Proceedings of the 6th European Conference on Python in Science (EuroSciPy 2013)*, pages 65–70, 2014.

[2] Cioranescu, D., Damlamian, A. Griso, G. and et al. The Stokes problem in perforated domains by the periodic unfolding method. new trends in continuum mechanics. *Theta Series in Advanced Mathematics*, 3:67–80, 2005.

[3] Marciniak-Czochra, A. and Mikelic, A. Effective pressure interface law for transport phenomena between an unconfined fluid and a porous medium using homogenization. *SIAM, Multiscale Modeling and Simulation*, 10(2):285–305, 2012.

[4] Hornung, U. *Homogenization and porous media*, Interdisciplinary Applied Mathematics, Springer, Vol. 6 (1997).

[5] Iliev, O., Mikelic, A. and Popov, P. On upscaling certain flows in deformable porous media. *SIAM, Multiscale Model. Simul.* (2008) **7**:93–123.

[6] Rohan, E. and Cimrman, R. Hierarchical numerical modelling of nested poroelastic media. In *Proc. of the 11th Int. Conf. on Comput. Structures Technology*, B.H.V. Topping (ed.), CivilComp Press, Scotland, (2012).

[7] Rohan, E., Naili, S. and Lemaire, T. Double porosity in fluid-saturated elastic media: deriving effective parameters by hierarchical homogenization of static problem. *Continuum Mech. Thermodyn.* (2016) **28**:1263–1293.

[8] Rohan, E., Turjanicová, J. and Lukeš, V. A Darcy-Brinkman model of flow in double porous media – two-level homogenization and computational modelling. *To appear in Comp. & Structures*, (2017).

XIV International Conference on Computational Plasticity. Fundamentals and Applications
COMPLAS XIV
E. Oñate, D.R.J. Owen, D. Peric & M. Chiumenti (Eds)

ANALYSIS OF DAMAGE AND FRACTURE FORMULATIONS IN COLD EXTRUSION

ALEXANDER SCHOWTJAK*, TILL CLAUSMEYER* AND A. ERMAN TEKKAYA*

*Institute of Forming Technology and Lightweight Components (IUL)
Department of Mechanical Engineering, Technical University Dortmund
Baroper Str. 303, 44227 Dortmund, Germany
e-mail: Alexander.Schowtjak@iul.tu-dortmund.de, web page: http://www.iul.eu

Key words: Forming Processes, Finite Element Method, Plasticity, Damage, Fracture, Parameter Identification

Abstract. In forming processes, components generally undergo large deformations. This induces the evolution of damage, which can influence material and product properties. To capture these effects, a continuum damage mechanics (CDM) model, based on the work of Lemaitre [8] and Soyarslan [13, 14] as well as different fracture criteria according to Cockcroft and Latham [2], Freudenthal [4] and Oyane [10] are implemented and investigated. While the CDM theory considers the evolution of damage and the associated softening, fracture criteria do not affect the results of the mechanical finite element (FE) analysis. However, a coupling is generally possible via element deletion, but material softening cannot be depicted in the simulation. Tensile tests with notched specimens are performed in order to obtain the material parameters associated with these models by inverse parameter identification processes. The optimized set of parameters is finally applied to the damage and fracture models used for the FE simulations of a cold extrusion process, which are investigated in terms of damage evolution and material failure. It is demonstrated that the CDM model predicts the evolution of damage observed for different process parameters in cold extrusion quantitatively. The prediction of the failure by the fracture criteria does not agree well with the experiments.

1 INTRODUCTION

In forming processes, the material used to produce components generally undergo large deformations. For metals, this implies large plastic strains and damage, which has a significant effect on the material, and thus, product properties. The depiction of damage in FE-simulations is therefore necessary.

On the microscopic scale, damage occurs at inhomogenities such as inclusions or grain boundaries. During deformation, damage develops as a result of nucleation, growth and coalescence of voids. Excessive growth of these voids finally leads to macroscopic cracks,

and thus, failure of the component. The mere existence of damage, however, does not necessarily imply failure of the part, as Tekkaya et al. point out in [16].

The prediction of damage and fracture with finite element (FE) simulations requires the definition of a constitutive damage model to properly depict the physical behavior. McVeigh et al. [9], Saanouni et al. [12] and Soyarslan et al. [13] investigated cold extrusion processes by predicting central bursting in FE analyses with the use of continuum damage mechanics (CDM) theory. McVeigh et al. implemented a combined Drucker-Prager/HLC-type yield surface based on a micromechanical cell modeling technique. Soyarslan et al. performed investigations based on a Lemaitre-type damage model with fictitious material parameters, while Saanouni et al. used parameters which were identified based solely on uniaxial tensile tests. As an alternative to CDM, damage, which may ultimately lead to fracture, can be accounted for by so-called fracture criteria, which predict fracture in terms of the accumulation of certain stress states. Chen et al. [1] investigated cold extrusion processes with those fracture criteria.

The goal of this work is the analysis of a cold extrusion process for 16MnCr5 in terms of damage and the comparison of different damage and fracture formulations. The material and model parameters associated with the constitutive damage model and the fracture criteria are determined by an inverse parameter identification process for notched tensile tests. Since no macroscopic cracks occur for the experimental setups of the cold extrusion processes investigated in this work, the predictions for damage are validated by comparison with scanning electron microscopy images of voids.

2 FRACTURE AND DAMAGE MODELING

In general, the prediction of damage with fracture criteria is based on very little information about the material and stress states, resulting in a low effort for the computation and the implementation. These criteria can be either used coupled or uncoupled to the FE analysis. While softening effects cannot be conducted, the criteria can be coupled to the simulation via element deletion. In this case, the interaction arises trough changes in stiffness. Although such failure criteria give an estimation of the damage, they do not cover any other effects that micro-cracks might have. Damage can decrease the elasticity modulus, the yield stress, the hardness, the ultrasonic waves velocity, the density or increase the electrical resistance. Constitutive models are capable of covering those effects, since the evolution of damage can be modelled more accurately. However, the computational cost compared to the fracture criteria is higher.

2.1 Fracture Criteria

Various fracture criteria exist to predict failure in forming processes. Most of them can be written as the integral of a function of the stress state expressed in terms of the Cauchy stress $f(\boldsymbol{\sigma})$ over the plastic equivalent strain α with the failure strain α_f as the upper boundary, i.e.

$$C = \int_0^{\alpha_\mathrm{f}} f(\boldsymbol{\sigma})\, d\alpha \ . \tag{1}$$

The variable C can be interpreted as the critical value when failure occurs and therefore is a material parameter.

The established models of Freudenthal, Cockcroft and Latham and Oyane are implemented in this work and explained in the following.

According to Freudenthal [4], the critical parameter at fracture

$$C_{\mathrm{F}} = \int_0^{\alpha_{\mathrm{f}}} \sigma_{\mathrm{eq}} \, d\alpha \ , \tag{2}$$

is a measure for the absorbed energy per unit volume, where σ_{eq} denotes the equivalent stress. This model does not consider the effect of high tensile stresses or hydrostatic stress states explicitly.

Cockcroft and Latham [2] postulated that fracture is triggered by the maximum principle tensile stress instead of the generalized stress. Therefore, the critical material dependent value at fracture

$$C_{\mathrm{CL}} = \int_0^{\alpha_{\mathrm{f}}} \langle \sigma_{\mathrm{p},1} \rangle \, d\alpha \tag{3}$$

is defined as the integral over the largest positive principal stress. The first principal stress is denoted by $\sigma_{\mathrm{p},1}$, where $\sigma_{\mathrm{p},i}$ represents the i-th principal stress, with $\sigma_{\mathrm{p},1} \geq \sigma_{\mathrm{p},2} \geq \sigma_{\mathrm{p},3}$. The expression $\langle \bullet \rangle$ represents the Macaulay brackets, i.e. $\langle \bullet \rangle = 0, \quad \forall \bullet < 0$ and $\langle \bullet \rangle = \bullet, \quad \forall \bullet \geq 0$. This criterion does not consider the influence of hydrostatic stresses explicitly.

Oyane et al. [10] consider a void growth model. They postulate

$$C_{\mathrm{O}} = \int_0^{\alpha_{\mathrm{f}}} \left[1 + \frac{1}{a_0} \frac{\sigma_{\mathrm{h}}}{\sigma_{\mathrm{eq}}} \right] d\alpha \tag{4}$$

to be the criterion for fracture, where $\sigma_{\mathrm{h}} = \frac{1}{3} \mathrm{tr}(\boldsymbol{\sigma})$ denotes the hydrostatic stress. The parameter a_0 can be adapted inside reasonable limits for a better correlation of numerical and experimental results. It is connected with the volumetric strain and can be derived by experiments with two different stress states, as explained in [10].

2.2 Continuum Damage Model

An elasto-plastic material model coupled with damage is selected for this article. It is based on the work of Lemaitre, see [8], with modifications following the implementation of Soyarslan et al. [13, 14]. All simulations in this work are performed with the commercial FE software Abaqus. In the following, the constitutive model is introduced as it is implemented in the framework of the Fortran-based user subroutines for finite strains. It is formulated in terms of the rate of the Mandel stresses and logarithmic stretches.

To define damage, the variable D, with $D \in [0,1]$, is introduced, which describes the surface density of mechanical defects. The stresses acting on the resisting area are called effective stresses, with $\tilde{\bullet} = \bullet/[1-D]$, where $\bullet$ can be any stress measure.

The deformation gradient

$$\boldsymbol{F} = \boldsymbol{F}^{\mathrm{e}} \cdot \boldsymbol{F}^{\mathrm{p}} \tag{5}$$

is decomposed multiplicatively into elastic and plastic parts, $\boldsymbol{F}^{\mathrm{e}}$ and $\boldsymbol{F}^{\mathrm{p}}$, respectively, see [7]. Using the polar decomposition theorem, the deformation gradient can be written as

$$\boldsymbol{F} = \boldsymbol{R} \cdot \boldsymbol{U} = \boldsymbol{V} \cdot \boldsymbol{R} \ , \tag{6}$$

where $\boldsymbol{R}$ is an orthogonal rotation tensor and $\boldsymbol{U}$ and $\boldsymbol{V}$ are symmetric deformation tensors, representing the stretches, as explained in [3]. The logarithmic stretches

$$\ln(\boldsymbol{U}) = \ln(\boldsymbol{U}^{\mathrm{e}}) + \ln(\boldsymbol{U}^{\mathrm{p}}) \tag{7}$$

can be decomposed additively into the elastic $\ln(\boldsymbol{U}^{\mathrm{e}})$ and plastic $\ln(\boldsymbol{U}^{\mathrm{p}})$ part. The rate of the elastic logarithmic strecth $\overline{\ln(\dot{\boldsymbol{U}}^{\mathrm{e}})}$ can be approximated as

$$\overline{\ln(\dot{\boldsymbol{U}}^{\mathrm{e}})} = \boldsymbol{R}^{\mathrm{e}^T} \cdot \boldsymbol{D} \cdot \boldsymbol{R}^{\mathrm{e}} - \boldsymbol{D}^{\mathrm{p}} \tag{8}$$

for small elastic strains ($|\boldsymbol{U}^{\mathrm{e}}| \ll 1$). Assuming that the plastic spin $\boldsymbol{W}^{\mathrm{p}} = \mathrm{skw}(\boldsymbol{L}^{\mathrm{p}}) \approx \boldsymbol{0}$ in terms of the plastic part of the velocity gradient $\boldsymbol{L}^{\mathrm{p}} = \dot{\boldsymbol{F}}^{\mathrm{p}} \cdot \boldsymbol{F}^{p-1}$ can be neglected, one obtains

$$\dot{\boldsymbol{R}}^{\mathrm{e}} = \boldsymbol{W} \cdot \boldsymbol{R}^{\mathrm{e}} - \boldsymbol{R}^{\mathrm{e}} \cdot \boldsymbol{W}^{\mathrm{p}} \tag{9}$$

for the elastic rotation. With this at hand, the rate of the effective Mandel stresses is defined as

$$\dot{\tilde{\boldsymbol{M}}} = \lambda_0 \, \mathrm{tr}(\overline{\ln(\dot{\boldsymbol{U}}^{\mathrm{e}})}) \, \boldsymbol{I} + 2 \, \mu_0 \, \overline{\ln(\dot{\boldsymbol{U}}^{\mathrm{e}})} \ , \tag{10}$$

where the Mandel stresses are related to Cauchy stresses via

$$\boldsymbol{\sigma} = \frac{\boldsymbol{R}^{\mathrm{e}} \cdot \boldsymbol{M} \cdot \boldsymbol{R}^{\mathrm{e}^T}}{\det(\boldsymbol{F})} \ . \tag{11}$$

The damage associated driving force, also referred to as energy density release rate

$$Y = \frac{1+\nu}{2\,E} \left[\langle \tilde{\boldsymbol{M}} \rangle^{+} : \langle \tilde{\boldsymbol{M}} \rangle^{+} + h \, \langle \tilde{\boldsymbol{M}} \rangle^{-} : \langle \tilde{\boldsymbol{M}} \rangle^{-} \right] - \frac{\nu}{2\,E} \left[\left\langle \mathrm{tr}(\tilde{\boldsymbol{M}}) \right\rangle^{2} + h \, \langle \mathrm{tr}(-\tilde{\boldsymbol{M}}) \rangle^{2} \right] \tag{12}$$

is defined as proposed by Soyarslan et al. [13, 14]. The variable h was introduced by Lemaitre as a material-dependent parameter associated with closing micro-defects. In the latter definition of the damage related driving force, the crack-closure effect is not taken into account. Here, h controls the delayed void growth under compressional loading.

The hardening law is chosen to be of a Swift-type, see [15], which defines the yield stress as

$$q = A \, [\alpha_0 + \alpha]^n \ , \tag{13}$$

where A, α_0 and n are material parameters. The yield function is defined as

$$\Phi^{\mathrm{y}}(\boldsymbol{M}, q, D) = \tilde{M}_{\mathrm{eq}} - q \ , \tag{14}$$

with $\tilde{M}_{\mathrm{eq}} = \sqrt{(\tilde{\boldsymbol{M}} : \mathbb{H} : \tilde{\boldsymbol{M}})}$, where $\mathbb{H}$ is the the so-called Hill-operator [5]. With this at hand, the plastic part of the deformation rate can be derived as

$$\boldsymbol{D}^{\mathrm{p}} = \dot{\lambda} \frac{\partial \Phi}{\partial \boldsymbol{M}} = \dot{\lambda} \frac{1}{1-D} \frac{\mathbb{H} : \tilde{\boldsymbol{M}}}{\tilde{\boldsymbol{M}}_{\mathrm{eq}}} \ , \tag{15}$$

where $\dot{\lambda}$ represents the plastic multiplier. The evolution of damage is given via the relation

$$\dot{D} = \dot{\lambda} \left\langle \frac{Y - Y_0}{S} \right\rangle^{\kappa} \frac{1}{[1-D]^{\beta}} \ , \tag{16}$$

where κ, S, Y_0 and β are material parameters.

3 Parameter Identification Process

Material models and fracture criteria used for the simulation of forming processes are generally based on a variety of material and model parameters. For the mathematical modeling of complex material behaviours, adapting the model parameters is essential for the accurate prediction of the material response. While some parameters like the Young's modulus and the Poisson's ratio can be computed directly, others can not. A common approach is an inverse parameter identification process. The aim of the inverse problem of parameter identification is to minimize the deviation between the experimental data and the data obtained by numerical simulations using an optimal set of parameters, under the consideration of mathematical and physical constraints.

To this end, a simulation of the experimental setup has to be performed multiple times, where the material parameters are iteratively updated, until the numerical and experimental results match as best as possible. Mathematically speaking, the optimal parameter set is defined by the minimization problem of the form

$$\min_{\boldsymbol{\kappa}} \left(f(\boldsymbol{\kappa}) \right), \ \forall \, \boldsymbol{\kappa} \in \boldsymbol{K}, \ \text{with } \boldsymbol{K} = \{ \boldsymbol{\kappa} \,|\, \boldsymbol{h}(\boldsymbol{\kappa}) = \boldsymbol{0}, \ \boldsymbol{g}(\boldsymbol{\kappa}) \leq 0 \} \ . \tag{17}$$

where $f(\boldsymbol{\kappa})$ is the objective or error function. It depends on the parameter set $\boldsymbol{\kappa}$ which underlies equality $\boldsymbol{h}$ and inequality constraints $\boldsymbol{g}$.

While the simulations of the experiments are performed with Abaqus, the algorithm for the parameter identification process is implemented in Python, making use of the provided optimization library. Since the minimization algorithms do not necessarily find global minima, all parameter identification processes have been performed with various initial guesses for the starting parameter vectors and different optimization algorithms, i.e. zero-order and gradient-based methods as well as evolutionary algorithms.

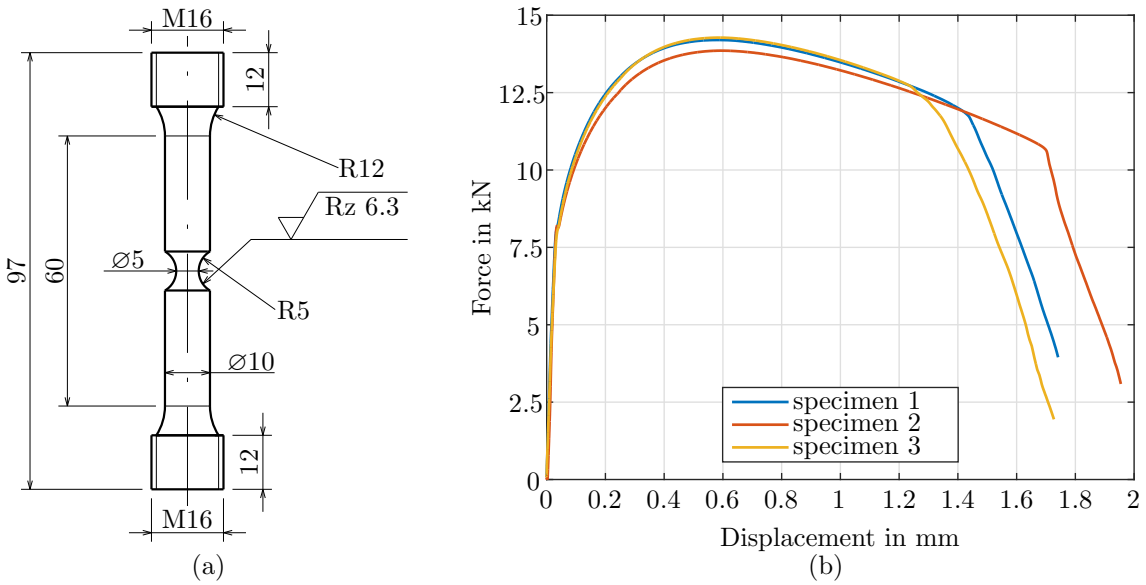

Figure 1: Engineering drawing of the specimen (a) and load displacement curves obtained from the experiments (b).

In general, it is possible to compare any values of the simulation with the experimental data. In this work, the optimization procedure is always applied to the full body response, i.e. the load displacement curve. To this end, the objective function is defined as

$$f(\boldsymbol{\kappa}) := \sqrt{\sum_{i=1}^{n_{\mathrm{sp}}} \left[\boldsymbol{w}(i) \ \left[\boldsymbol{f}^{\mathrm{sim}}(\boldsymbol{\kappa}, i) - \boldsymbol{f}^{\mathrm{exp}}(i)\right]\right]^2} \,, \tag{18}$$

which is a least-square-like error function, where i denotes the summation index, with $i \in n_{\mathrm{sp}}$ and n_{sp} represents the number of sample points. It measures the difference between the numerically and experimentally obtained reaction forces $\boldsymbol{f}^{\mathrm{exp}}$ and $\boldsymbol{f}^{\mathrm{sim}}$, respectively, weighted by $\boldsymbol{w}$.

To this end, experiments have to be carried out in order to generate data for comparison to the simulation results. Notched tensile tests are performed to induce a localization of the deformation and to impose an inhomogeneous stress field throughout the entire experiment. The resulting load displacement curves, as depicted in Figure 1(b), show variations in curvature, as well as differences in the point of crack initiation and failure. Since the response of specimen 1 yields an average behaviour, the following parameter identification processes are performed with respect to its associated experimental data.

Since isotropy is considered, the parameters associated with the Hill operator are chosen as $r_0 = r_{45} = r_{90} = 1$. The elastic properties, i.e. the Young's modulus and the Poisson's ratio, are determined analytically as $E = 210000$ MPa and $\nu = 0.3$, see [11].

Table 1: Identified parameters for elasto-plastic continuum model in conjunction with fracture criteria.

A	9.332	$\cdot 10^{2}$	MPa
α_0	1.196	$\cdot 10^{-3}$	
n	1.575	$\cdot 10^{-1}$	
C_{CL}	5.912	$\cdot 10^{2}$	MPa
C_{F}	4.069	$\cdot 10^{2}$	MPa
C_{O}	9.859	$\cdot 10^{-1}$	

Table 2: Identified parameters for fully coupled continuum model.

A	1.043	$\cdot 10^{3}$	MPa
α_0	5.630	$\cdot 10^{-3}$	
n	2.095	$\cdot 10^{-1}$	
κ	3.087	$\cdot 10^{0}$	
S	3.226	$\cdot 10^{0}$	MPa
Y_0	3.710	$\cdot 10^{-2}$	MPa
β	1.989	$\cdot 10^{1}$	
D_{crit}	4.607	$\cdot 10^{-1}$	

3.1 FE-Model for the Notched Tensile Test

The FE-model including the geometry, the mesh and the boundary conditions of the notched tensile test is shown in Figure 2(a). Axisymmetry, as well as symmetry with respect to the horizontal plane is considered. The geometry is discretized with 230 four-noded, axisymmetric, quadrilateral elements with reduced integration (type CAX4R) and an edge length of 4.3 mm. The load is applied linearly over time as displacement boundary conditions on the thread. In the experiment, the displacements were tracked with an extensometer, with its sensors positioned 20 mm above and below the plane of horizontal symmetry, as indicated in Figure 2(a). The displacements are evaluated at a node at the same exact position to reproduce the load displacement curve correctly.

For the depiction of cracks in FE analyses, element deletion is used. To this end, the parameter D_{crit} is introduced as a threshold value to trigger the removal of elements. The simulations are performed with Abaqus/Explicit.

3.2 Identification of Plasticity Parameters

In this section, a parameter identification is performed for elasto-plasticity with Swift-type hardening, as introduced in Section 2.2. To this end, the error in the load displacement curves in the elasto-plastic area, which is the region before the crack starts to develop, is minimized.

The associated load displacement curve is depicted in Figure 2(b). The numerical results for the optimized parameter set, as shown in Table 1, are in good agreement with the experimental data.

3.3 Parameter Identification for the Fracture Criteria

In the following, an identification of the parameters for the fracture criteria, i.e. $C_{\mathrm{F}}, C_{\mathrm{CL}}$ and C_{O}, as shown in eqs. (3) to (4), is carried out. These constants are used as threshold values for material failure and therefore trigger element deletion. The fracture criteria are used in conjunction with a Swift-type hardening model with the optimized parameter set identified in the previous section.

Performing the test, the specimen fully fails immediately after crack initiation. Since there is no material softening, an excessive amount of elastic energy is released upon

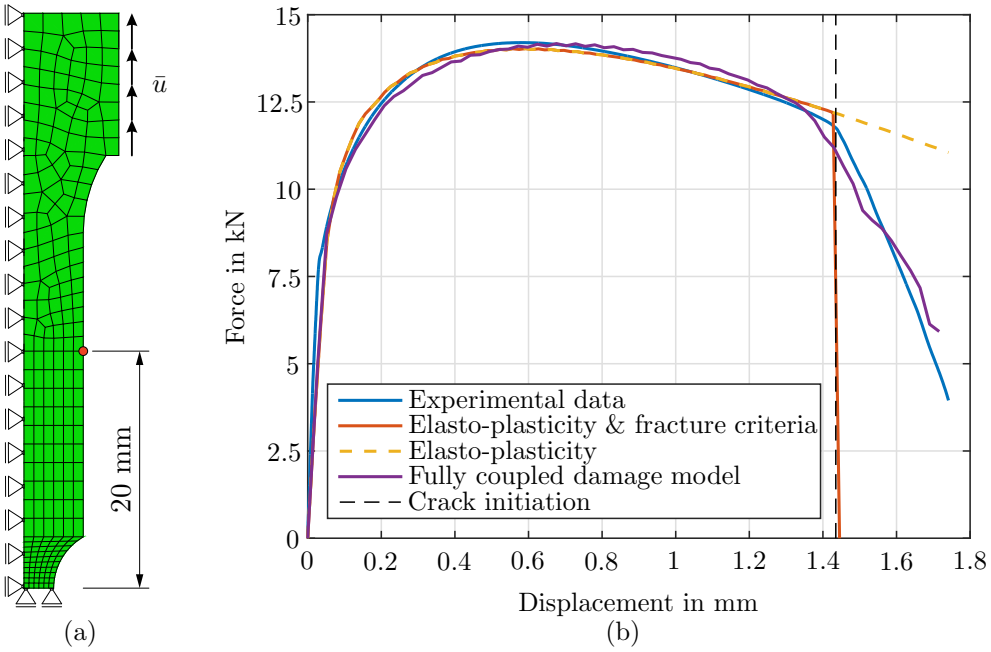

Figure 2: Illustration of the FE-model of the notched tensile test (a). The node, where the displacement is recorded for the load displacement curves, is marked by the red dot. The load displacement curves of the experiment and the simulations (b) are performed with optimized parameter sets.

failure, resulting in unrealistic large vibrations. The resulting oscillations in reaction forces are removed for visualization purposes. Since the time discretization is identical for all simulations, the resulting load displacement curves are identical for all fracture criteria, as depicted in Figure 2(b). The identified threshold values are shown in Table 1.

3.4 Parameter Identification for the Continuum Damage Model

In this section, a parameter identification process for the continuum damage model is performed. In general, various options exist to realize this. One way is the identification of only the damage related parameters, based on the optimized plasticity, as done in Section 3.2. The load displacement curve does not hold any information about the initiation of the damaging process, because the decrease in the reaction force does not necessarily has to be damage induced and can be caused solely by cross section reduction of the specimen. Thus, the optimization of the plasticity and damage associated parameters simultaneously could be another possible way for performing the parameter identification process. This implies, that the damage evolution can start at basically any point.

Here, the latter approach is implemented, because it is more reasonable that the damage evolution is a steady process, that most likely occurs before the crack initiation on macroscopic scale. Since the stress state is purely tensional, the parameter h has no influence on the results and has to be obtained from different experiments. To this end, h

is set to zero.

The resulting load displacement curve is depicted in Figure 2(b). The numerical data is associated with the optimized parameter set in Table 2. While the specimen fails immediately after crack initiation using the fracture criteria, a developing crack can be observed for the continuum damage model.

4 SIMULATION AND ANALYSIS OF COLD EXTRUSION PROCESSES

In the following, the simulation of a cold extrusion process is presented, based on the parameter sets identified in the previous sections.

Simulations are performed for two experimental setups with different extrusion strains, i.e. $\varphi_1 = 0.5$ and $\varphi_2 = 1.0$. The extrusion strain φ is defined as $\varphi = \ln(A_0/A_1)$, where A_0 and A_1 represent the cross sections before and after the extrusion, respectively. The initial workpiece diameter is $D_0 = 30$ mm. A friction coefficient of $\mu = 0.04$ between workpiece and die is used. The shoulder opening angle of the die is defined as $\alpha^* = 45°$, the transition radii are set to 3 mm and an undercut is used. For the sake of saving computational time, axisymmetry is considered for the FE model. The billet is discretized with 4260 four-noded, axisymmetric, quadrilateral elements with reduced integration (type CAX4R) with an edge length of 4.3 mm. The die is modeled as a linear-elastic solid with a Young's modulus of $E_{\text{die}} = 210000$ MPa and a Poisson's ratio of $\nu_{\text{die}} = 0.3$. The parameter sets identified in the previous sections are used. The workpiece is pushed trough the die by a constant velocity of 6.1 mm/s over 7.1 s of process time.

Figure 4 depicts the damage distribution for the continuum damage model for the two experimental setups. It can be observed that the maximum damage appears beneath the surface of the billet. The level of damage for the smaller extrusion strain φ_1 is higher on the central axis compared to φ_2, which is also observed in the experiments, as seen in Figure 4.

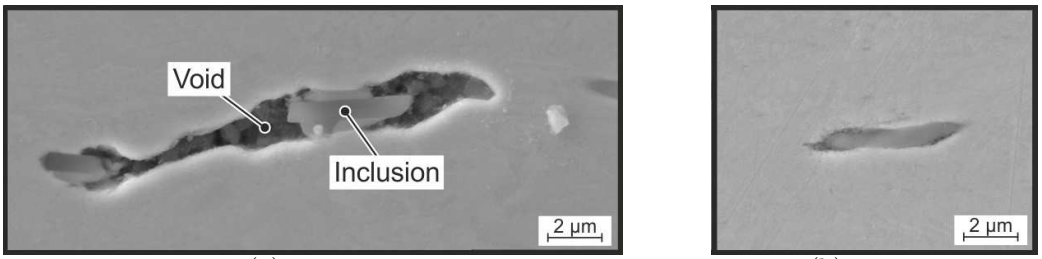

(a) $\varphi = 0.5$ (b) $\varphi = 1.0$

Figure 3: SEM micrographs of 16MnCr5 for extrusion strains of $\varphi = 0.5$ (a) and $\varphi = 1.0$ (b). Taken from [16].

The contour plots of damage for the fracture criteria are shown in Figure 5. Here, damage is defined by the actual value of the associated damage criterion $C_\bullet$ divided by the critical value $C_{\bullet,\text{crit}}$ identified in Section 3.3. Comparing all contour plots for φ_1, they show significant variations in values and distribution. While the maximum damage in the stationary region is 1.5 %, and therefore, rather low, the maximum damage for the criteria

of Cockcroft-Latham, Freudenthal and Oyane is 42 %, 292 % and 51 %, respectively. Using the criteria of Cockcroft-Latham and Oyane, most damage occurs in the center, while the criterion of Freudenthal predicts the highest damage beneath the surface.

Isik et al. investigated damage in terms of void volume fraction experimentally. It was shown that the damage in the dual phase steel DP600 was below 1 % for equivalent plastic strains of up to 0.8. Since 15MnCr6 shows a similar mechanical behavior to DP600, the results of the CDM model seem reasonable, while the damage predicted by the fracture criteria is significantly overestimated.

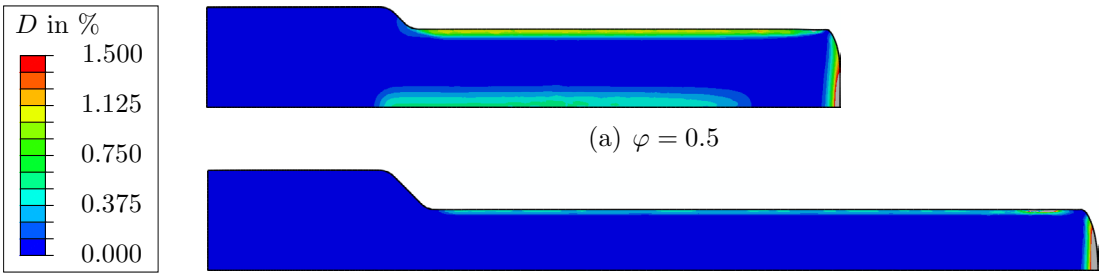

(a) $\varphi = 0.5$

(b) $\varphi = 1.0$

Figure 4: Contour plot of damage D distribution for cold extrusion for extrusion strains of $\varphi = 0.5$ (a) and $\varphi = 0.1$ (b) with the use of the continuum damage model.

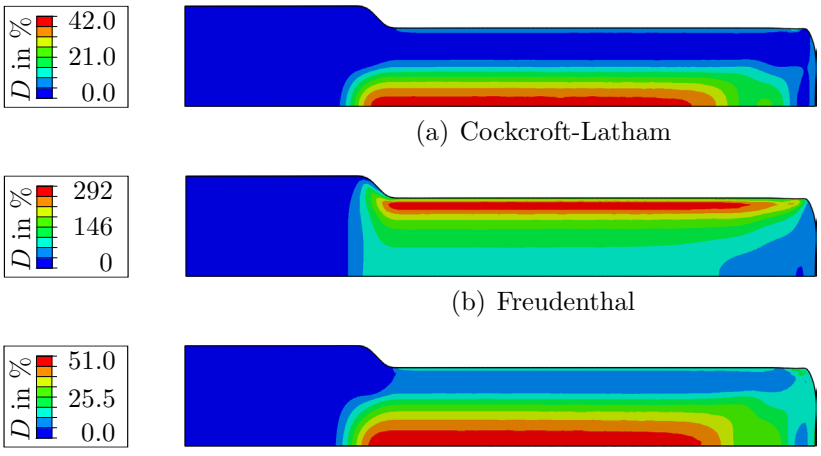

(a) Cockcroft-Latham

(b) Freudenthal

(c) Oyane

Figure 5: Contour plot of damage D distribution for the fracture criteria of Cockcroft-Latham (a), Freudenthal (b) and Oyane (c) for the cold extrusion process with φ_1. The damage value is defined by the actual value of the criterion, divided by the critical value identified in Section 3.3.

5 CONCLUSION

From the simulation results it can be concluded that the use of the presented fracture criteria is very limited and only reasonable in certain cases. In this work, the coupling

between the fracture criteria and the stresses is not implemented, so the effect of damage induced softening cannot be captured explicitly, leading to an overestimated stiffness. Fracture criteria depend on a single stress-dependent function and cannot distinguish between different damage mechanisms, which may lead to errors. Cracks can be depicted by coupling those fracture criteria to an element deletion criterion. Removing undamaged elements, however, is associated with the removal of energy and mass, which may influence the physical behavior. A fine discretization would diminish this effect, but is related to increasing computational effort.

A CDM model generally yields a better prediction of the damage, up to the point of fracture. Elasticity is coupled to the damage evolution and therefore the effect of damage induced softening can be captured. Here, the removal of elements with damaged material is not as significant as for the fracture criteria due to the decrease in stiffness. The CDM model presented in this work can be adapted to the problem more accurately, since the evolution of damage is controlled by several parameters. While the fracture criteria only depend on a single stress dependent function, the constitutive damage model can distinguish between different stress states.

ACKNOWLEDGEMENT

Funding of project S01 within the Collaborative Research Centre CRC/Transregio 188 "Damage-controlled forming processes" by the German Research Foundation (DFG) is highly acknowledged.

REFERENCES

[1] D.C. Chen, S.K. Syu, C.H. Wu, S.K. Lin, Investigation into cold extrusion of aluminum billets using three-dimensional finite element method, Journal of Materials Processing Technology 192-193, pp. 188-193, 2007.

[2] M.G. Cockcroft, D.J. Latham. Ductility and the Workability of Metals, Journal of the Institute of Metals, 96, pp. 33-39, 1968.

[3] F. Dunne, N. Petrinic. Introduction to computational plasticity, Oxford: Oxford University Press, 2005.

[4] A.M. Freudenthal. The inelastic behaviour of engineering materials and structures, Wiley, New York, 1950.

[5] R. Hill. A theory of the yielding and plastic flow of anisotropic metals. Proceedings of the Royal Society of London, 1948.

[6] K. Isik, G. Gerstein, T. Clausmeyer, F. Nürnberger, A.E. Tekkaya, H.J. Maier, Evaluation of Void Nucleation and Development during Plastic Deformation of Dual-Phase Steel DP600. Steel research int. 87, No. 9999, 2016.

[7] E. Lee. Elastic-Plastic Deformation at Finite Strains. ASME. J. Appl. Mech 36(1):1-6, 1969.

[8] J. Lemaitre, R. Desmorat. Engineering Damage Mechanics. Springer, 2005.

[9] C. McVeigh, W.K. Liu. Prediction of central bursting during axisymmetric cold extrusion of a metal alloy containing particles, International Journal of Solids and Structures 43, pp. 3087-3105, 2006.

[10] M. Oyane, T. Sato, K. Okimoto. Criteria for ductile fracture and their applications, Journal of Mechanical Working Technology 4, pp. 65-81, 1980.

[11] F. Richter. The 100 Steels Programme (https://www.tugraz.at/fileadmin/user_upload/Institute/IEP/Thermophysics_Group/Files/Staehle-Richter.pdf).

[12] K. Saanouni, J.F. Mariage, A. Cherouat, P. Lestriez. Numerical prediction of discontinuous central bursting in axissymmetric forward extrusion by continuum damage mechanics, Computers and Structures 82, pp. 2309-2332, 2004.

[13] C. Soyarslan, A.E. Tekkaya. U. Akyuz, Application of Continuum Damage Mechanics in discontinuous crack formation: Forward extrusion chevron predictions, ZAMM - Journal of Applied Mathematics and Mechanics, Volume 88, Issue 6, pp. 436-453. WILEY-VHC, 2008.

[14] C. Soyarslan, A.E. Tekkaya. Finite deformation plasticity coupled with isotropic damage: Formulation in principal axes and applications, Finite Elements in Analysis and Design archive, Volume 46, Issue 8, pp. 668-683, 2010.

[15] H. W. Swift. Plastic instability under plane stress. Journal of the Mechanics and Physics of Solids 1, pp. 1-18, 1952.

[16] A.E. Tekkaya, N. Ben Khalifa, O. Hering, R. Meya, S. Myslicki, F. Walther. Forming-induced damage and its effects on product properties, CIRP Annals Manufacturing Technology, accepted for publication 2017.

EFFECT OF TAPER ANGLE ON PROCESSING LOAD IN FORWARD EXTRUSION

K. KONISHI*, T. MATSUNO†, S. MAYUMI†, Y. TANIGUCHI# AND S. ENOKI#

* Faculty of Advanced Engineering
National Institute of Technology, Nara College
22 Yata, Yamatokoriyama, Nara, 639-1080 Japan
e-mail: a0833@stdmail.nara-k.ac.jp

† SAKAMURA INDUSTRIES, INC.
6-11-18 Hishie, Higashiosaka, Osaka, 578-0984 Japan

Department of Mechanical Engineering
National Institute of Technology, Nara College
22 Yata, Yamatokoriyama, Nara, 639-1080 Japan
e-mail: shinichi_enoki@mua.biglobe.ne.jp , taniguchi@mech.nara-k.ac.jp

Key words: Forward extrusion, Friction coefficient, Contact pressure, Plastic strain, Strain rate, Processing load.

Abstract. There is actuality that forward extrusion processing is difficult when taper angle of die is less than 2°. Aim of this study is to reveal the reason why the forward extrusion processing is difficult in the case of 2°. To know the reason, we simulated forming processes with two-dimensional axisymmetric models under the same processing conditions. Each of two-dimensional axisymmetric model has different taper angles. Processing conditions are same reduction rate in area and taper angles from 25° to 2°. As a result, the smaller the taper angle, the bigger the processing load. To investigate the reason, we compared with contact pressure distributions in these angles. And then, it was revealed that the smaller the taper angle, the bigger the contact pressure distribution at the upper of taper section. When the contact pressure is large, it seems that friction force and the processing load become big. From the above, in the case of 2°, processing load is large. Therefore, depending on the machine, it is difficult to process the blank.

1 INTRODUCTION

In production site, there is actuality that forward extrusion processing is difficult when taper angle of die is less than 2°. In the forward extrusion, engineers have decided the taper angle of die along their experiences. Aim of this study is to reveal the reason why the forward extrusion processing is difficult in the case of 2°. To know the reason, we simulated forming processes with two-dimensional axisymmetric models under the same processing conditions. Each of two-dimensional axisymmetric model has different taper angles. Processing conditions are same reduction rate in area and taper angles from 25° to 2°. In this paper, the formability of forward extrusion is investigated by deformation pattern, contact pressure, load

value, plastic strain and strain rate.

2 ANALYSIS PROCEDURE AND METHOD

We used Simufact forming 13.0 (MSC Software Corporation) for analysis and made two-dimensional axisymmetric models of die with the taper angle of 2°,4°, 6°, 8°, 10°, 15°, 20° and 25°. Figure 1 shows two-dimensional axisymmetric models of die we made. Extrusion die used in this work having reduction factor of 10:5 (Inlet diameter: Outlet diameter).Therefore, reduction rate in area is 0.25. The work piece data used S45C with the dimension of 10mm, 60mm and 80mm in length and 10mm diameter. In the case of 2°, work piece length is 80mm, because amount of work piece for filling the tapered portion is insufficient. For perform analysis under the same conditions, in the case of 6° and 15°, work piece length is 80mm. In the case of less than 10°, work piece length is 60mm. On the other hand, In the case of more than 20°, work piece length is 10mm. Material property in database of Simufact formig was used for workpiece. Punch speed is 200mm/s. To observe the effect of friction, coulomb friction and shear friction are 0.1 and 0.3. From the above conditions, we performed analysis and investigated formability.

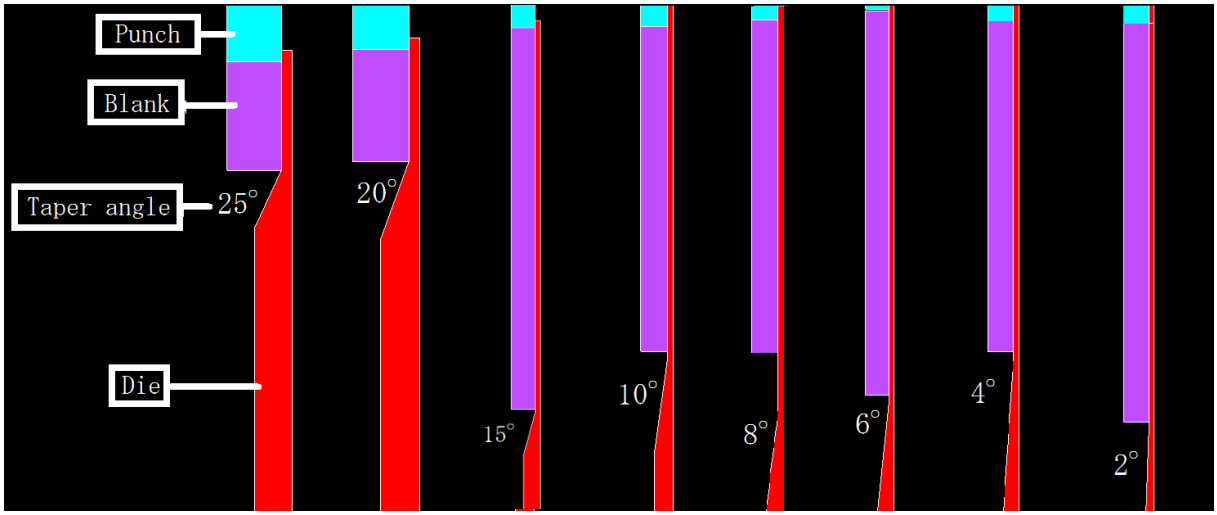

Figure1 Analysis model in a variety of taper angle

3 RESULTS AND DISCUSSION

3.1 Investigation by deformation pattern

Analysis of forward extrusion was conducted to observe the deformation pattern near outlet part. Figure 2 shows difference of deformation pattern between 2° and 25°. This difference shows following two factors. The one case of less than 8°, the center of work piece was flowed out immediately after flowing through the taper section, because it seems that effect of friction is more dominant than more than 10°. The other case of more than 10°, circumstance part of work piece was flowed out, because it seems that effect of material flow

is more dominant than less than 8°. From the above, deformation pattern of work piece attribute to friction.

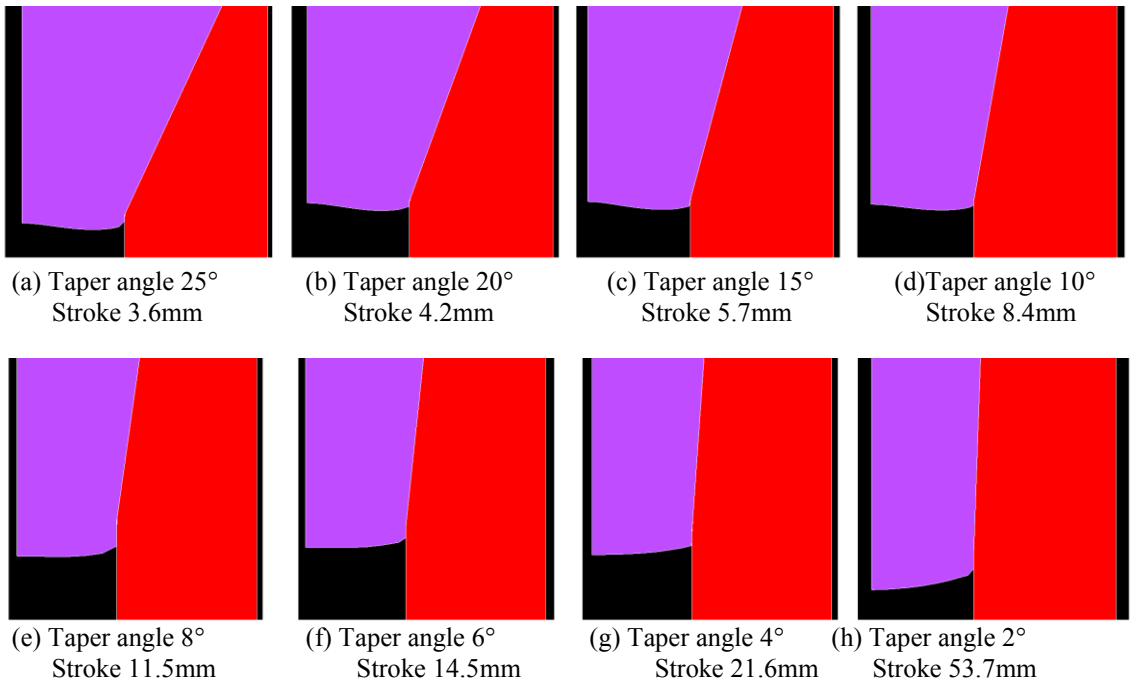

(a) Taper angle 25° Stroke 3.6mm
(b) Taper angle 20° Stroke 4.2mm
(c) Taper angle 15° Stroke 5.7mm
(d)Taper angle 10° Stroke 8.4mm
(e) Taper angle 8° Stroke 11.5mm
(f) Taper angle 6° Stroke 14.5mm
(g) Taper angle 4° Stroke 21.6mm
(h) Taper angle 2° Stroke 53.7mm

Figure2 Difference of deformation pattern in different taper angle

3.2 Effect of deformation pattern and load value by friction

To investigate the effect of friction, analysis was conducted with different friction coefficient value. When both Coulomb friction and shear friction are 0.1, it is expressed as f=0.1. When both Coulomb friction and shear friction are 0.3, it is expressed as f=0.3. Figure 3 shows the comparison between when friction coefficient is 0.1 and when it is 0.3. We compare deformation pattern in case of both 6° and 15° because they have difference of deformation pattern.

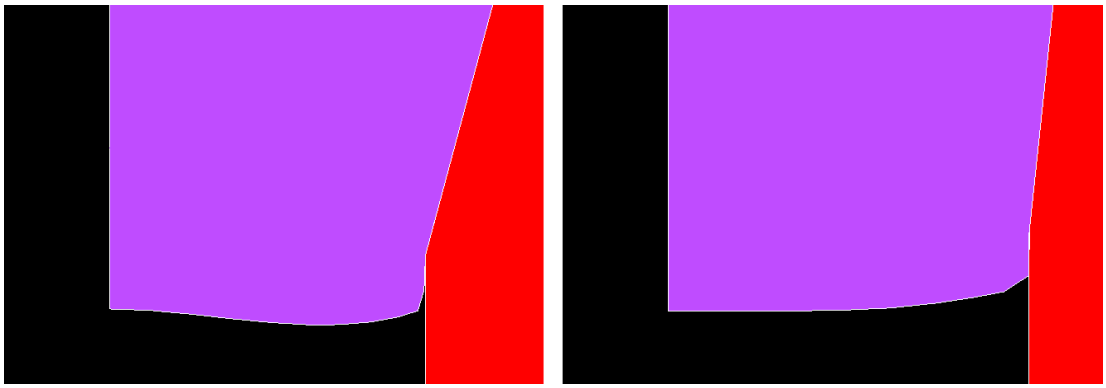

(a) Coulomb friction 0.1
Shear friction 0.1
Taper angle 15°

(b) Coulomb friction 0.1
Shear friction 0.1
Taper angle 6°

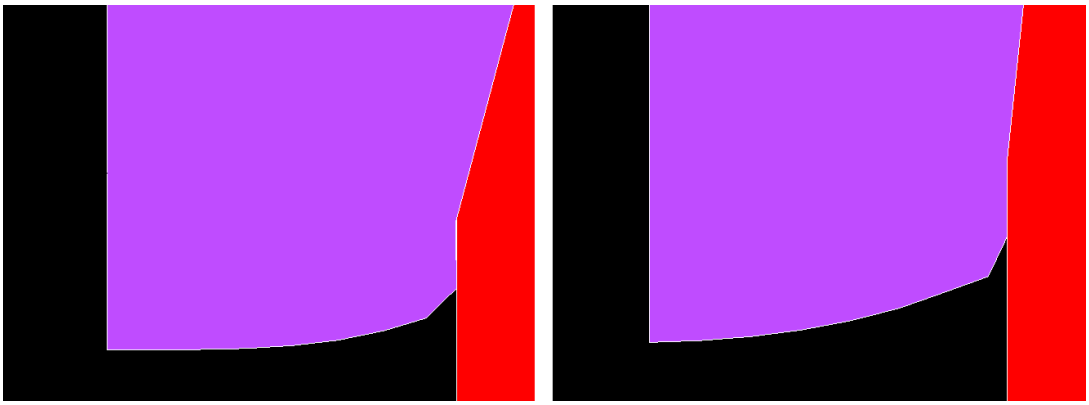

(c) Coulomb friction 0.3
Shear friction 0.3
Taper angle 15°

(d) Coulomb friction 0.3
Shear friction 0.3
Taper angle 6°

Figure 3 Effect of friction on deformation pattern

Figure 3 shows deformation pattern in case of changing friction coefficient. As a result, the bigger friction coefficient, the bigger center flow amount because it seems that deformation pattern is affected by friction coefficient. From the above, it may be suspected that friction coefficient affect processing load value. Therefore, we investigated contact pressure under the same condition at the time of passing through the taper section. Figure 4 shows contact pressure under the same case. To compare at each location, Table 1 Shows contact pressurein case of 2°, 6° and 15°.

Table 1 Contact pressure occurred between work piece and die

	Contact puressure [MPa]		Contact puressure [MPa]		Contact puressure [MPa]	
	Taper angle 15°		Taper angle 6°		Taper angle 2°	
	f=0.1	f=0.3	f=0.1	f=0.3	f=0.1	f=0.3
A Near the punch	1400	3000	1500	3600	1550	6400
B Just before inflow	700	1200	1000	2200	2000	5200
C Immediately after inflow	1800	2200	2000	3000	3100	6300
D After processing	1000	1100	900	1000	800	900

Figure 4 shows that, there was no difference in contact pressure distribution by difference in taper angle when friction in the case of f=0.1. However, the bigger the friction coefficient, the bigger the contact pressure distribution at the upper of taper. From the above, due to work hardening in the vicinity of the outlet part, the material flow becomes worse. As a result, the extrusion load was increased. Therefore, processing load value required for machining increases. As can be seen from the Table 1, contact pressure is big when the taper angle is small and the frictional coefficient is large. This is because, compression deformation occurs before the material flows into the taper section by hardening in the vicinity of the outlet part

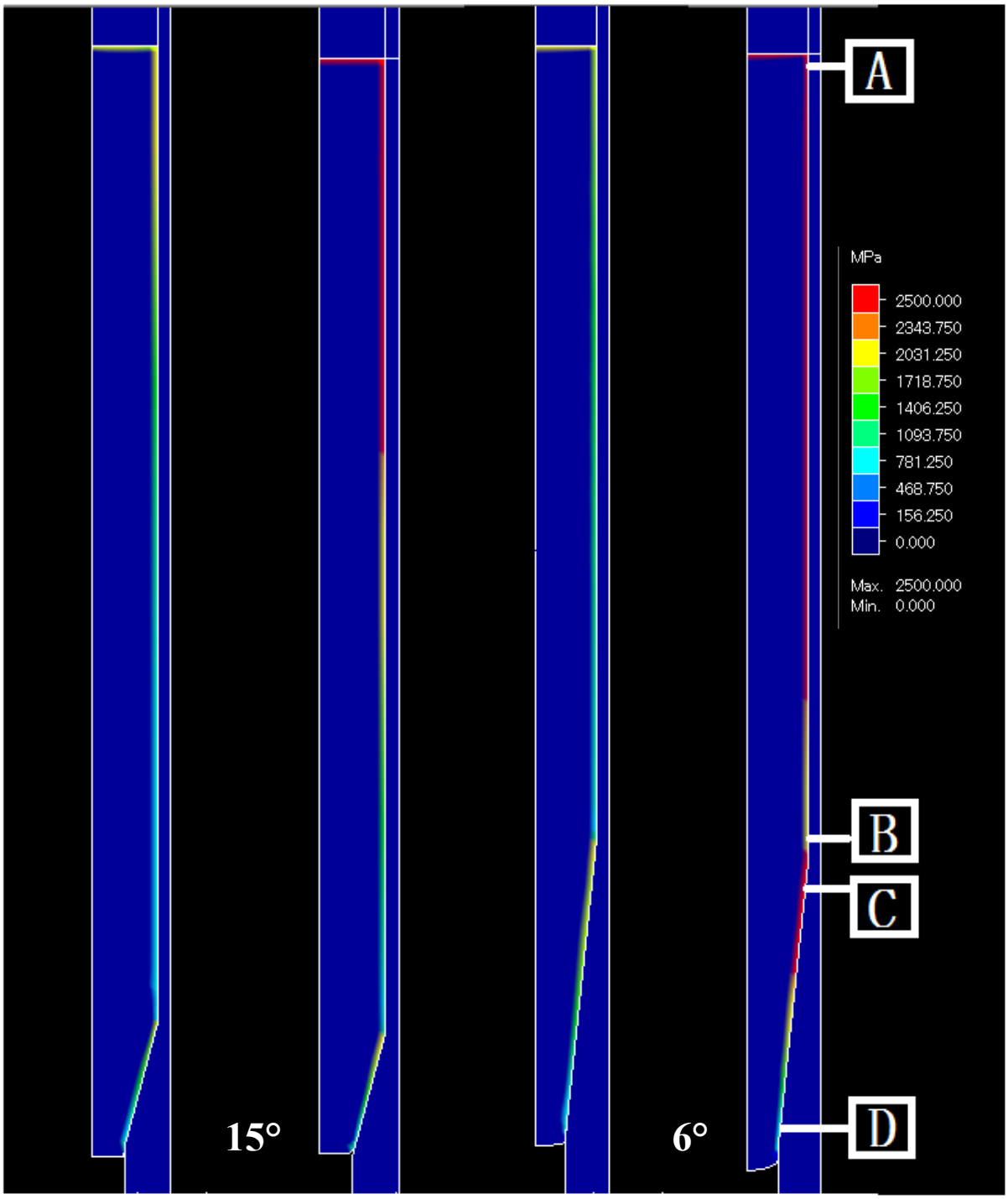

(a) f=0.1 Taper angle 15° (b) f=0.3 Taper angle 15° (c) f=0.1 Taper angle 6° (d) f=0.3 Taper angle 6°

Figure 4 Difference of contact pressure

and friction will occur on the inner wall surface of the die. Therefore, to clarify the causal relation between the contact pressure and the processing load, processing load is shown Figure 5.

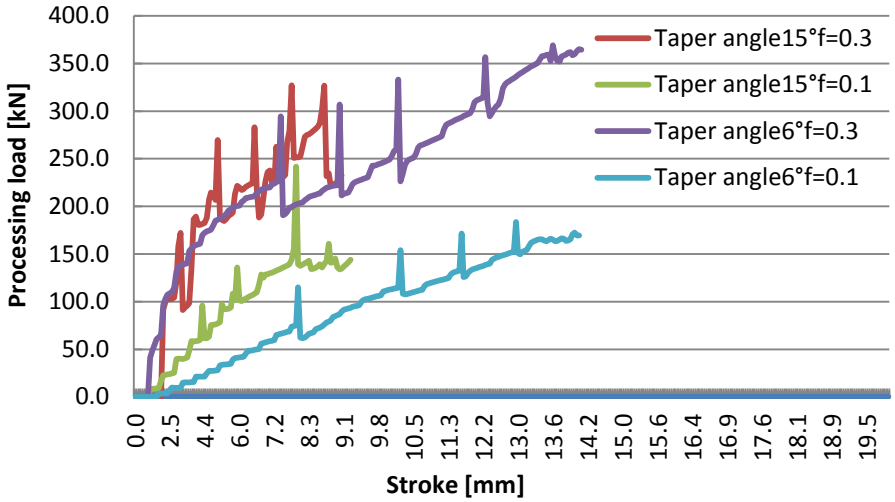

Figure 5 Difference of processing load

In the case of f=0.1, interval in the processing load value between 15 ° and 6 ° is 15 kN. Also, in the case of f=0.3, interval in the processing load value between 15 ° and 6 ° is 80 kN. When the taper angle is 6 ° and friction coefficient is 0.3, the contact pressure is big as compared with the case of 15 °. Therefore, it seems that processing load is increased by influence of friction increasing when taper angle is small. Therefore, as the processing load value vibrates, fatigue fracture punch and die can occur. In addition, we analysed processing load value in the case of 2°. Figure 6 shows processing load value in the case of 2°. Result of analysis, necessary processing load is 220 kN when f=0.1. Also, necessary processing load is 524 kN when f=0.3. The necessary processing load is the biggest when taper angle is 2° in each taper angle. Therefore, there is a possibility of causing die cracking, since the processing load to be used is large.

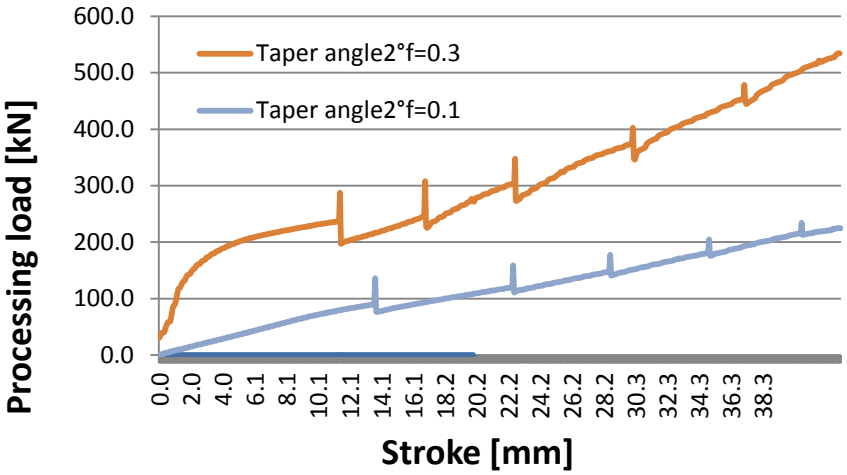

Figure 6 Processing load in the case of 2°

3.3 Investigation by plastic strain

It has been reported that deformation resistance which increases due to work hardening and the work hardening has velocity dependence.[5] In addition, the faster the strain rate, the bigger the work hardening, but deformation resistance becomes smaller. Therefore, the reason why the processing load increases as the taper angle becomes smaller is considered to be in work hardening due to plastic strain. Figure 7 shows results of analysis of plastic strain.

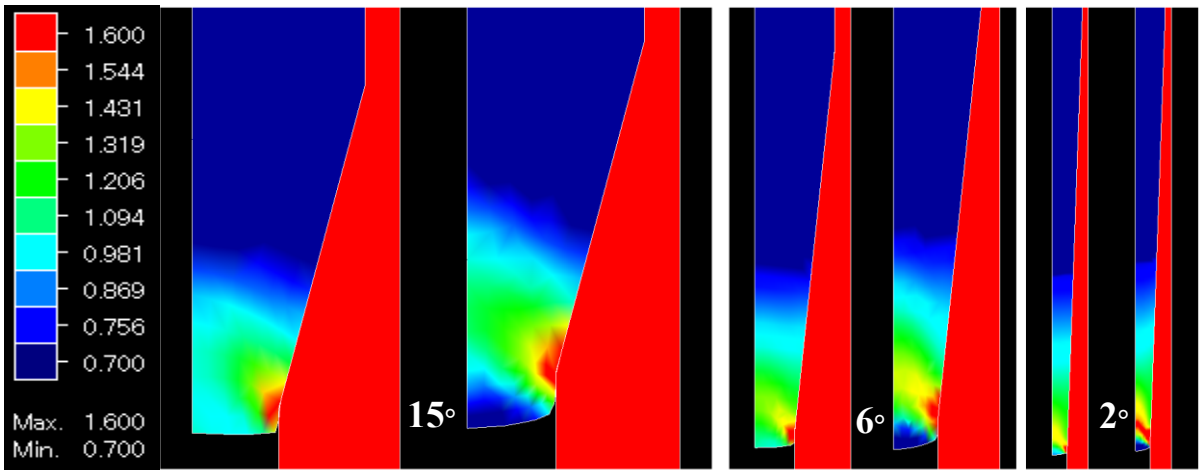

(a) f=0.1 (b) f=0.3 (c) f=0.1 (d) f=0.3 (e)f=0.1 (f)f=0.3

Taper angle 15° Taper angle 6° Taper angle 2°

Figure 7 Difference of plastic strain distribution in friction coefficient

Figure 7 shows plastic strain has occurred in the tapered portion, and deformation resistance is increased by work hardening. It has been reported that the deformation resistance rapidly increases when the plastic strain is bigger than 0.7, but this tendency does not appear when the strain rate is 10^2 s^{-1} or more. [6] Therefore, it is considered that deformation resistance is occurred in the portion where the strain rate is small and plastic strain is big. In order to investigate the extent of work hardening, we analyzed strain rate. Figure 8 shows that when the taper angles are 15 ° and 6 °, the strain rate becomes big around the outlet section. Also, it has been reported that the hardness increases as the strain rate increases during compression processing. It can be seen that when the taper angles are 15 ° and 6 °, the hardness after extrusion is bigger than in the case of 2°. It has been reported that as the strain rate increases, the deformation resistance decreases[6]. the processing load becomes bigger as compared with processing at 15 ° and 6 ° when the taper angle is 2 °. This is due to the effect of friction between inside of the die and the work piece and increase deformation resistance with small strain rate.

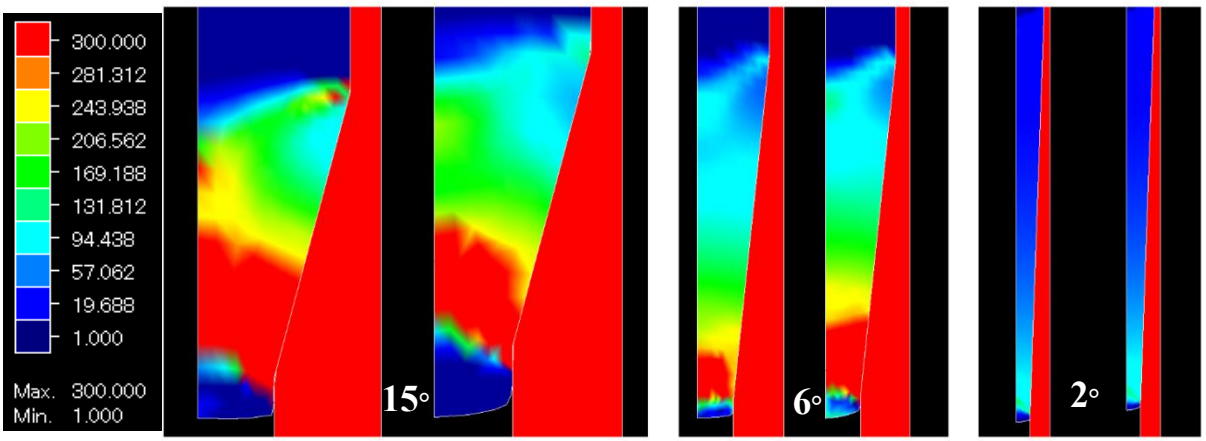

(a) f=0.1 (b) f=0.3 (c) f=0.1 (d) f=0.3 (e) f=0.1 (f) f=0.3
Taper angle 15° Taper angle 6° Taper angle 2°

Figure 8 Strain rate in each angle

4 CONCLUSIONS

In forward extrusion processing, we analyzed the taper angle from 25 ° to 2 °. As a result, the smaller the taper angle, the bigger the processing load. Also the bigger friction coefficient, the bigger deformation resistance. For this reason, plastic strain has occurred in the tapered portion, and deformation resistance is increased by work hardening due to this, and friction by contact pressure increases deformation resistance. From the above, processing load causes cracking of the mold due to increase of processing load. It was revealed that processing is difficult when the taper angle is 2 ° or less.

REFERENCES

[1] Isao KUBOKI, Kazuya YOSHIDA, “Two-dimensions Modeling Analyses of Hot Forming Process to Watch Case in titanium Alloy”, The Horological Institute of Japan, Vol. 42, No. 2 (1998), pp.1-10 (in Japanese).

[2] Hideki KAKIMOTO, Taku NAGATA, Touji TAKAHARA, Youichi TAKAHASHI, Takanori MORI, “Analysis of crankshaft forging process by 3-D FEM”, The Japan Society of Mechanical Engineers Proc. of 2003 annual meeting (1), pp.467-468 (in Japanese).

[3] Zhigang WANG, Shinobu KOMIYAMA, Yuichi YAMAOKA, Development of Extrusion with Bulge Deformation Type Tribotest for Evaluating Lubricant Coating Performance in Cold Forging, Journal of the JSTP vol. 51 no. 597 (2010) pp. 953-957 (in Japanese).

[4] Jayaseelan.V, Kalaichelvan.K, Vijay ananth.S, Lubrication Effect on Friction Factor of AA6063 in Forward Extrusion Process, Procedia Engineering 97 (2014) 166-171.

[5] Manabuu KIUCHI, Tomohiro HOSHINO, Shigeo IIJIMA, Study on Non-Axisymmetric Backward Extrusion・2, University of Tokyo production technology laboratory research news, Vol. 40, No. 4, (1998) pp. 8-11 (in Japanese).

[6] Tomokazu MASUDA, Takehiro TUCHIDA, Masamichi CHIBA, Effect of strain rate on deformation resistance in cold forging steels, KOBE STEEL ENGINEERING REPORTS, Vol. 61, No. 1, (2011), pp. 52-56 (in Japanese).

XIV International Conference on Computational Plasticity. Fundamentals and Applications
COMPLAS XIV
E. Oñate, D.R.J. Owen, D. Peric & M. Chiumenti (Eds)

IDENTIFICATION OF INELASTIC PARAMETERS OF THE 304 STAINLESS STEEL USING MULTI-OBJECTIVE TECHNIQUES

M. VAZ JR. AND M. TOMIYAMA

Department of Mechanical Engineering
State University of Santa Catarina (UDESC)
Campus Universitário Prof. Avelino Marcante, 89219-710 Joinville, Brazil
e-mail: miguel.vaz@udesc.br, masahiro.tomiyama@udesc.br

Key words: Parameter Identification, 304 stainless steel, optimization

Abstract. This work addresses identification of inelastic parameters based on an optimization method using a multi-objective technique. The problem consists in determining the best set of parameters which approximate three different tensile tests. The tensile tests use cylindrical specimens of different dimensions manufactured according to the American ASTM E 8M and Brazilian ABNT NBR ISO 6892 technical standards. A tensile load is applied up to macroscopic failure. The objective functions for each tensile test/specimen is computed and a global error measure is determined within the optimization scheme. The Nelder-Mead simplex algorithm is used as the optimization tool. The proposed identification strategy was able to determine the best set of material parameters which approximate all tensile tests up to macroscopic failure.

1 INTRODUCTION

A proper set of material parameters is one of the most important aspects for a successful simulation of metal forming processes. The present work discusses techniques to obtaining constitutive parameters based on a multi-objective optimization method for the 304 stainless steel. In order to ensure greater generality, the identification strategy is applied simultaneously to tensile tests using specimens of different sizes, defined by the American ASTM E 8M [1] and Brazilian ABNT NBR ISO 6892 [2] standards. The parameter identification method is based on optimization and can approximate the material response up to macroscopic failure with greater accuracy. Noticeably, after the maximum load, the stress state becomes triaxial and the classical calibration techniques cannot be applied.

Identification of elasto-plastic parameters using optimization techniques has long been used in the literature. In the last ten years, many identification strategies have been proposed based on optimization techniques. Most authors agree that the non-linearity of the direct problem (elastoplasticity at finite strains) and the yield curve itself can cause

difficulties in finding the global optimum. A final verdict of best method is temerarious and, so far, the best strategy has proved to be problem dependent. For the sake of objectivity, the reader is referred to Vaz Jr. et al. [3, 4] and references therein for further insights on the application of optimizations techniques to identification of inelastic parameters.

2 PARAMETER IDENTIFICATION AND THE OPTIMIZATION PROBLEM

Parameter identification is a class of inverse problems which determines material or system parameters from a known response. The present problem is formulated using unconstrained optimization and accounts for experimental data obtained from three different tensile tests. Therefore, the multi-objective problem is formulated as

$$\begin{array}{lll} \text{Minimise} & g(\boldsymbol{p}) = \sum_{s=1}^{n_s} \lambda_s g_s(\boldsymbol{p}) & \boldsymbol{p} \in R^{n_d} \\ \text{Such that} & p_i^{\inf} \leq p_i \leq p_i^{\sup} & i = 1, \ldots, n_d \end{array} , \tag{1}$$

where $g(\boldsymbol{p})$ is the objective function (global fitness) of the multi-objective problem, $\boldsymbol{p} = [p_1 \;\; p_2 \;\; \cdots \;\; p_i \;\; \cdots \;\; p_{n_d}]^T$ is the design vector containing n_d material parameters p_i, and $p_i^{\sup}$ and $p_i^{\inf}$ are lateral constraints. The global fitness, $g(\boldsymbol{p})$, comprises contributions from n_s individual problems, so that λ_s is the weight function ($\sum_{s=1}^{n_s} \lambda_s = 1$), and $g_s(\boldsymbol{p})$ is the individual and represents a quadratic relative error measure between the experimental, R_s^{Exp}, and corresponding computed forming load, $R\left(\boldsymbol{p}\right)_s^{Num}$, of a mechanical test "$s$",

$$g_s\left(\boldsymbol{p}\right) = \sqrt{\frac{1}{N_s} \sum_{j=1}^{N_s} \xi_{s,j} \left(\frac{R_{s,j}^{Exp} - R\left(\boldsymbol{p}\right)_{s,j}^{Num}}{R_{s,j}^{Exp}} \right)^2} , \tag{2}$$

in which N_s is the number of experimental points and ξ_s ($0 \leq \xi_{s,j} \leq 1$) is the weight curve of each individual set of experimental data.

The optimization technique adopted in this work uses the gradient-free downhill simplex method, also known as Nelder-Mead algorithm (NM) [5]. The technique defines a regular polytope of $n_d + 1$ vertices (in a n_d dimensional design space), which moves towards the optimum by replacing the worst vertex by a new one selected along a search line. The Nelder-Mead algorithm contains three basic elements: (i) creation of the initial simplex from an initial estimate; (ii) search along a given direction and formation of a new polytope by replacing the worst vertex after the following possible operations: reflexion, expansion, or contraction; and (iii) shrinkage of the polytope towards the best vertex. The reader if referred to References [4, 6, 7] for further insights on the algorithm used in this work.

The Nelder-Mead method has already been used in identification of material constitutive parameters. For instance, Banabic et al. [8] applied to identification of inelastic parameters based on biaxial tensile tests, and Pannier et al. [9] used to find elastic-plastic

constitutive parameters based on the Virtual Fields Method associated to tensile tests. Further details on the application of the NM scheme to mechanical problems are given in Luersen and Le Riche [10]. Noticeably, the authors have already investigated application of the NM scheme for both classical von Mises [4, 6] and damaged materials [7].

3 NUMERICAL RESULTS AND DISCUSSIONS

The identification procedure is based on tensile tests of cylindrical specimens prepared according to the American ASTM E 8M [1] and Brazilian ABNT NBR ISO 6892 [2] technical standards. It is used extensometers with initial gauge length $l_0 = 25$ mm or $l_0 = 50$ mm according to the specimen with maximum crosshead speed 3 mm/min. The specimens used in this work are illustrated in Figure 1 and referred as follows:

- *ASTM #1:* initial gauge length $l_0 = 25$ mm and diameter $d_0 = 6.0$ mm,
- *ASTM #2:* initial gauge length $l_0 = 50$ mm and diameter $d_0 = 12.54$ mm,
- *NBR #3:* initial gauge length $l_0 = 50$ mm and diameter $d_0 = 10.0$ mm,

(a) Specimen *ASTM #1*: $l_0 = 25$ mm, $d_0 = 6$ mm.

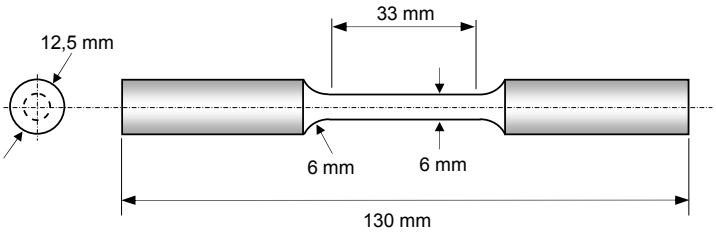

(b) Specimen *ASTM #2*: $l_0 = 50$ mm, $d_0 = 12.54$ mm.

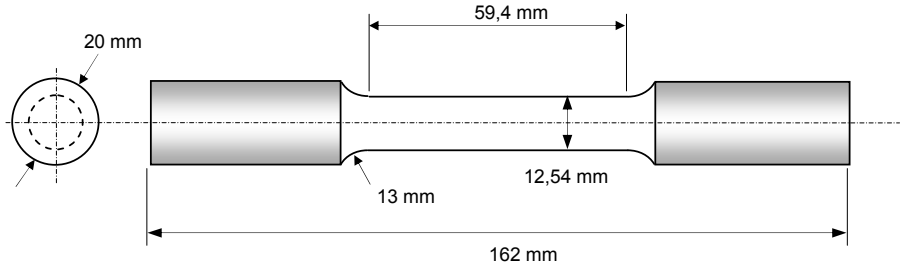

(c) Specimen *NBR #3*: $l_0 = 50$ mm, $d_0 = 10$ mm.

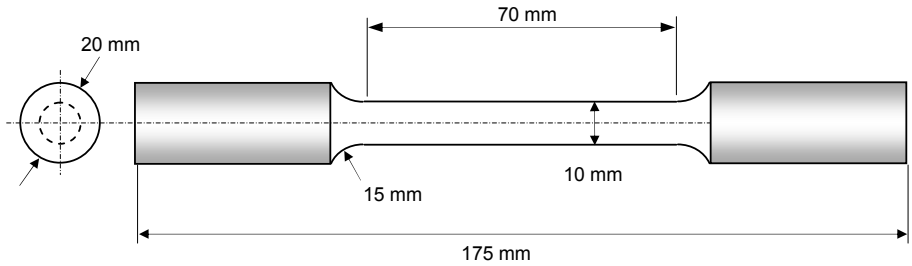

Figure 1: Specimen geometry for ASTM and ABNT-NBR standards.

The finite element mesh used for specimen *ASTM #2* is presented in Figure 2. The geometrical model considers axisymmetry around the rotation axis $Z - Z'$ and symmetry about the $R - R'$ axis, making possible to model only 1/4 of the specimen. It was adopted a structured, eight-noded quadrilateral finite element mesh with 200 elements and 661 nodes with progressive refinement towards the specimen $R - R'$ axis. The meshes used for *ASTM #1* e *NBR #3* specimens were geometrically proportional to *ASTM #2* with identical element topology.

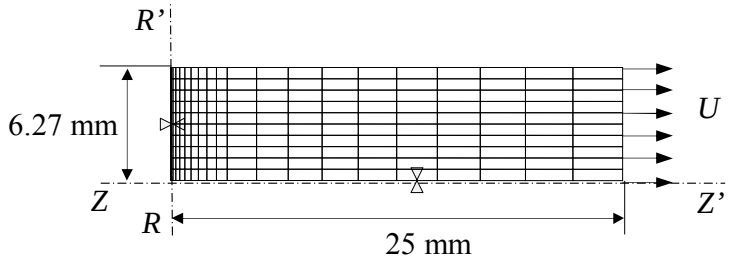

Figure 2: Finite element mesh for the *ASTM #2* specimen.

It is important to highlight that, contrary to the classical calibration procedures, the objective of the present identification process is to determine the material parameters up to macroscopic failure of the specimens. This strategy accounts for larger plastic deformations, making possible to use the material parameters in metal forming processes which present equally large plastic strains. Therefore, instead of using the well-known Swift's [11] equation, this work adopts Voce's [12] modified hardening equation to model isotropic hardening, as

$$\sigma_Y = \sigma_0 + \zeta r + (\sigma_\infty - \sigma_0)\left[1 - \exp\left(-\delta r\right)\right] \ , \tag{3}$$

where σ_0 is the initial yield stress, σ_∞ is the saturation stress, and ζ and δ are the exponential and linear hardening parameters, respectively, so that the parameters to be determined are $\{\boldsymbol{p}\} = \{\sigma_0 \ , \ \sigma_\infty \ , \ \zeta \ , \ \delta\}$.

3.1 The identification process

This section summarises an investigation on convergence aspects of the optimization problem. An initial assessment indicates that the individual (each specimen) and global (combining all specimens) optimization problems are convex, making possible to use the Nelder-Mead optimization scheme. The control parameters for the NM algorithm used in the simulations are $\rho = 1, \gamma = 2, \beta = 0,5$ e $\sigma = 0,5$, whereas the initial estimate and lateral constraints are presented in Table 1.

One can define three basic identification problems according to individual tensile tests. In Case (A) identification is performed taking into account *only* the experimental curve for specimen *ASTM #1*. Cases (B) and (C) are solved in similar fashion, accounting for only experimental curves for specimens *ASTM #2* and *NBR #3*, respectively. Therefore,

Table 1: Lateral constraints and initial estimate.

Parameter p_i	**Lower limit** $p_i^{\inf}$	**Upper limit** $p_i^{\sup}$	**Initial estimate** p_i^0
σ_0 [MPa]	200	800	500
σ_∞ [MPa]	400	1200	800
ζ [MPa]	300	1200	750
δ	0	50	25

identification based on experimental data for specimens *ASTM #1*, *ASTM #2* and *NBR #3* are solved for the following sets of weight parameters, λ_s: Case (A) $\lambda_1^{(A)} = 1.0$ and $\lambda_2^{(A)} = \lambda_3^{(A)} = 0.0$, Case (B) $\lambda_2^{(B)} = 1.0$ and $\lambda_1^{(B)} = \lambda_3^{(B)} = 0.0$, and Case (C) $\lambda_3^{(C)} = 1.0$ and $\lambda_1^{(C)} = \lambda_2^{(C)} = 0.0$.

In addition to the aforementioned cases, in Case (D), identification is also performed assuming that each tensile test imposes the same effect in obtaining the material parameters, i.e. the global objective function, $g(\boldsymbol{p})$, is computed using weights $\lambda_1^{(D)} = \lambda_2^{(D)} = \lambda_3^{(D)} = 1/3$.

Figure 3 shows evolution of the convergence index, $\phi^{(k)} = [g(\boldsymbol{p})_{n_d+1}^{(k)} - g(\boldsymbol{p})_1^{(k)}]/[g(\boldsymbol{p})_{n_d+1}^{(0)} - g(\boldsymbol{p})_1^{(0)}]$, which represents the relative difference between the worst and best vertices of the polytope with respect to the initial simplex. In this work, convergence is assumed for $\phi^{(k)} \leq 10^{-9}$. It can be observed that evolution of the identification process is similar for Cases (A), (B) and (C) and somewhat faster for the equally balanced identification problem, Case (D).

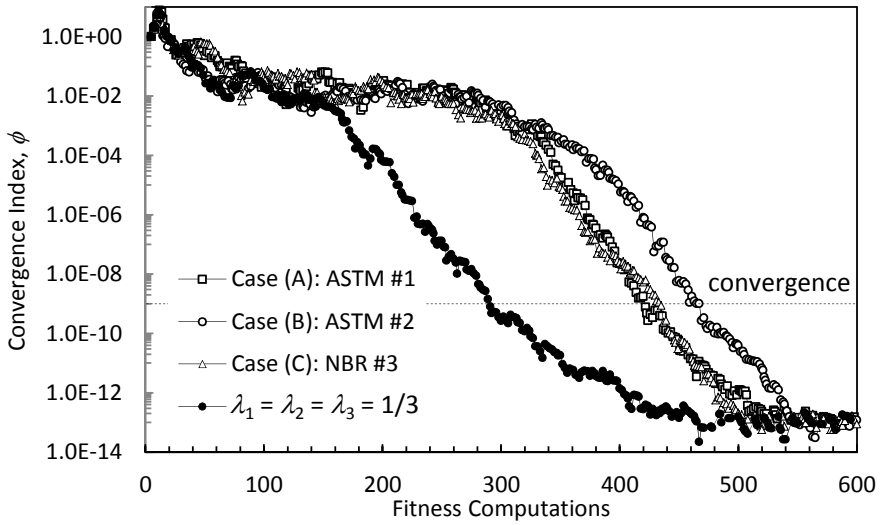

Figure 3: Convergence evolution of the optimization problem.

The Nelder-Mead algorithm requires an initial estimate, from which the initial simplex is constructed. Therefore, the tolerance to changes of the initial estimate yet able to achieve success must also be evaluated. In this case, in addition to the mean values

Table 2: Initial estimates, p_i^0, and final parameters for $\lambda_1 = \lambda_2 = \lambda_3 = 1/3$.

Test	σ_0 [MPa]	σ_∞ [MPa]	ζ [MPa]	δ	**Success?**
Mean	500.00	800.00	750.00	25.0000	Yes
1	200.00	400.40	1084.09	5.0203	Yes
2	638.21	812.33	879.40	0.7273	**No**
3	301.86	1013.47	947.91	7.1787	Yes
4	496.42	1039.51	621.66	6.1902	Yes
5	313.91	614.02	789.68	35.7311	Yes
6	507.68	555.84	696.61	36.4500	Yes
7	509.39	497.26	937.77	19.5037	Yes
8	382.30	504.89	1186.05	27.9432	Yes
9	738.71	766.36	940.71	4.2220	Yes
11	520.93	695.71	958.31	17.6329	Yes
Final Parameters	*399.68*	*686.16*	*878.30*	*9.9677*	

(shown in the last column of Table 1), ten random initial estimates located within the search space are also used. This test was performed for uniform weight parameters ($\lambda_1 = \lambda_2 = \lambda_3 = 1/3$). Table 2 presents the initial estimates, a success indication and final parameters. The simulations show that only one set of initial parameters was not able to obtain the expected results. The reason probably lies on the small value of parameter δ assumed as initial estimate.

3.2 The loading process

The experimental and numerical load curves are shown in Figure 4, from which the three well-known regions can be distinguished: (a) elastic loading, (b) load increase owing to hardening and (c) load decrease due to reduction of the specimen cross-section area. The transition between (b) and (c) is indicated by the maximum load (also known as instability point). Table 3 presents the individual weights, λ_s, and corresponding material parameters for Cases (A)−(D). Case (D) considers that each individual tensile test contributes equally to determine the inelastic parameters.

Table 3: Individual weights, λ_s, and material parameters, $\boldsymbol{p}$.

Case	ASTM #1 $\lambda_1^{(\cdot)}$	ASTM #2 $\lambda_2^{(\cdot)}$	NBR #3 $\lambda_3^{(\cdot)}$	σ_0 [MPa]	σ_∞ [MPa]	ζ [MPa]	δ
(A)	1.0	0.0	0.0	405.89	839.36	714.47	5.3900
(B)	0.0	1.0	0.0	421.45	991.70	372.92	4.6021
(C)	0.0	0.0	1.0	409.16	878.59	597.24	5.1941
(D)	1/3	1/3	1/3	399.68	686.15	878.31	9.9684

Identification for Case (A) requires minimization of the global objective function, $g(\boldsymbol{p})$,

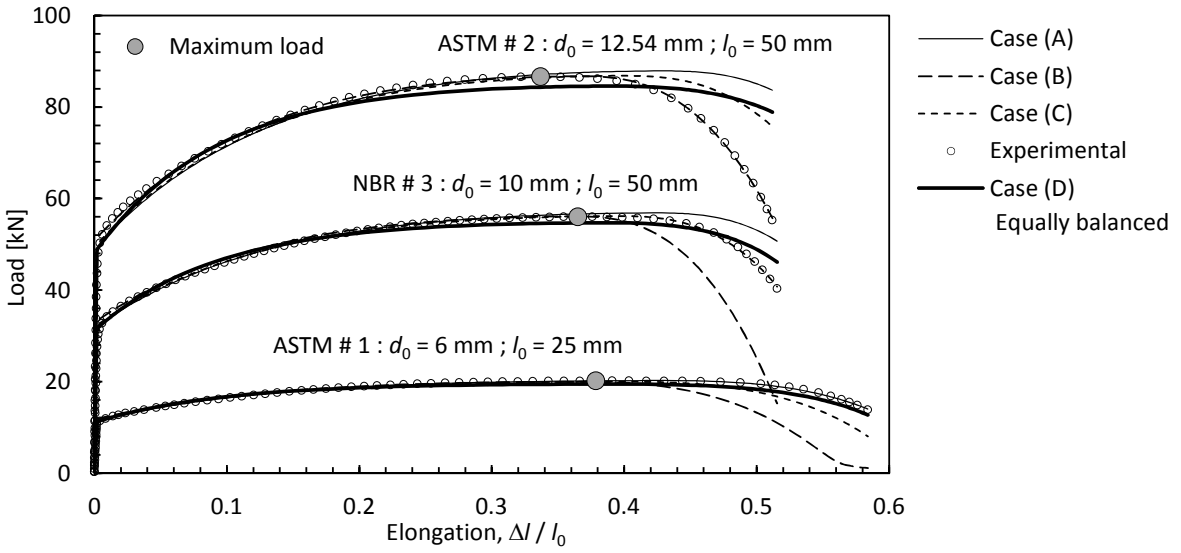

Figure 4: Load curves for tensile tests based on specimens ASTM #1, ASTM #2, and NBR #3.

computed using only the experimental data of specimen ASTM #1 ($\lambda_1^{(A)} = 1.0$, $\lambda_2^{(A)} = \lambda_3^{(A)} = 0.0$). Therefore, the numerical loading curve presents the minimum possible error for specimen ASTM #1, measured by the individual fitness $g_1^{(A)}(\boldsymbol{p}) = 7.2273 \times 10^{-3}$ (the numerical curve visually matches the corresponding experimental data). However, some discrepancies are found when using set (A) of material parameters to simulate tensile tests for ASTM #2 and NBR #3 specimens (the corresponding individual fitness $g_2^{(A)}(\boldsymbol{p}) = 1.4112 \times 10^{-1}$ and $g_3^{(A)}(\boldsymbol{p}) = 5.9591 \times 10^{-2}$).

A similar assessment is also performed for tensile tests of ASTM #1, ASTM #2 and NBR #3 specimens using data sets (B) and (C) of Table 3. Table 4 shows that identification for the corresponding data set yields also very small individual fitness, $g_2^{(B)}(\boldsymbol{p}) = 7.9852 \times 10^{-3}$ and $g_3^{(C)}(\boldsymbol{p}) = 7.9447 \times 10^{-3}$. Nevertheless, as discussed in the previous paragraph, cross-simulations give rise to substantially large individual errors, $g_1^{(B)}$, $g_3^{(B)}$, $g_1^{(C)}$ and $g_2^{(C)}$.

The material data and individual fitness obtained for for Case (D) ($\lambda_1^{(D)} = \lambda_2^{(D)} = \lambda_3^{(D)} = 1/3$) are also presented in Tables 3 and 4. In this case, the numerical curves for ASTM #1, ASTM #2 and NBR #3 specimens present also some differences, especially after the maximum load is reached (see the thick solid line in Figure 4).

The best set of material parameters is not obvious from visual assessment of Figure 4. Furthermore, the differences of the weight parameters, λ_s, for Cases (A)−(D) also preclude use of the global objective function, $g(\boldsymbol{p}) = \sum_{s=1}^{n_s} \lambda_s g_s(\boldsymbol{p})$, to determine the best set of parameters. Therefore, a global index, $G^{(\cdot)}(\boldsymbol{p})$, consisting the mean ratio between the individual fitness and the corresponding minimum value, $g_s^{(\cdot)}/g_s^{min}$, is evaluated as

$$G^{(\cdot)}(\boldsymbol{p}) = \frac{1}{3}\sum_{s=1}^{3} g_s^{(\cdot)}/g_s^{min} \ . \tag{4}$$

Table 4: Individual, $g_s^{(\cdot)}(\boldsymbol{p})$, and relative, $g_s^{(\cdot)}/g_s^{min}$ $^{(*)}$, fitness for Cases (A)−(D).

Case	**Specimen** ASTM#1 $g_1^{(\cdot)}(\boldsymbol{p})$	ASTM#2 $g_2^{(\cdot)}(\boldsymbol{p})$	NBR#3 $g_3^{(\cdot)}(\boldsymbol{p})$	$g_1^{(\cdot)}/g_1^{min}$	$g_2^{(\cdot)}/g_2^{min}$	$g_3^{(\cdot)}/g_3^{min}$	$G^{(\cdot)}(\boldsymbol{p})$
(A)	*7.2273E-03*	1.4112E-01	5.9591E-02	1	17.6721	7.5008	8.7243
(B)	2.9773E-01	*7.9852E-03*	1.5886E-01	41.1946	1	19.9964	20.7303
(C)	1.0617E-01	1.0171E-01	*7.9447E-03*	14.6897	12.7378	1	9.47.58
(D)	3.7466E-02	1.1179E-01	3.1782E-02	5.1839	13.9991	4.0004	7.7278

$^{(*)}$ The minimum individual fitness are $g_1^{min} = g_1^{(A)}$, $g_2^{min} = g_2^{(B)}$ and $g_3^{min} = g_3^{(C)}$.

Table 4 indicates that, based on the global index, Case (D) yields the best numerical approximation to the experimental data of all three tensile tests ($G^{(D)} = 7.7278$). It means that, in average, the error for an individual tensile test is approximately 7.7278 times the minimum possible individual fitness. On the other hand, Case (B) provides the worst set of material parameters with a global index $G^{(B)} = 20.7303$, owing to the excessive load decrease after the maximum load when simulating tensile tests for ASTM #1 and NBR #3 specimens, as shown by the dashed lines in Figure 4.

4 FINAL REMARKS

Hardening parameters for the AISI 304 stainless steel were determined based on three tensile tests using specimens defined by the American ASTM E 8M ($l_0 = 25$ mm, $d_0 = 6.0$ mm, and $l_0 = 50$ mm, $d_0 = 12.54$ mm) [1] and Brazilian ABNT NBR ISO 6892 ($l_0 = 50$ mm, $d_0 = 10.0$ mm) [2] technical standards. The tensile tests were carried out up to macroscopic failure aiming at determining inelastic parameters associated with large plastic strains. The non-uniformity of the stress state after the maximum load precluded application of the classical calibration techniques. Therefore, the identification process used optimization schemes based upon a multi-objective strategy. The global objective function used a weighted combination of individual fitness computed for each tensile test/specimen. The simulations have shown that the size of the specimen plays an important role in the identification problem, thereby requiring a careful balance between effects of individual tensile test/specimen. In the present work, an equally balanced global fitness provided the best approximations for all specimens. However, some differences were observed after the maximum load.

Acknowledgements

The author acknowledges the financial support provided by the Brazilian funding agency CNPq - (National Council for Scientific and Technological Development), grant number 303412/2016-0.

REFERENCES

[1] ASTM - E 8M-86a. Tensile testing of metallic materials. ASTM, Philadelphia (2002).

[2] ABNT NBR ISO 6892. Metallic materials - Tensile testing at ambient temperature. ABNT, Rio de Janeiro (2002).

[3] Vaz Jr. M., Cardoso, E.L., Stahlschmidt, J. Particle swarm optimization and identification of inelastic material parameters *Eng. Comp.* (2013) **30**:936–960.

[4] Vaz Jr. M., Cardoso, E.L., Muñoz-Rojas, P.A., Carniel, T.A., Luersen, M.A., Tomiyama, M., da Silva, J.O., Stahlschmidt, J. and Trentin, R.G. Identification of constitutive parameters - optimization strategies and applications. *Mat.-wiss. u. Werkstofftech.* (2015) **46**:477-491.

[5] Nelder, J.A. and Mead, R. A simplex method for function minimization. *The Comput. Journal* (1965) **7**:308–313.

[6] Vaz Jr., M., Luersen, M. A., Muñoz-Rojas, P. A., and Trentin, R. G. Identification of inelastic parameters based on deep drawing forming operations using a global-local hybrid Particle Swarm approach. *C. R. Mecanique* (2016) **344**:319–334.

[7] Vaz Jr., M., Muñoz-Rojas, P. A., Cardoso, E. L., and Tomiyama, M. Considerations on parameter identification and material response for Gurson-type and Lemaitre-type constitutive models. *Int. J. Mech Sci.* (2016) **106**:254–265.

[8] Banabic D., Kuwabara T., Balan T., Comsa D.S. and Julean D. Non-quadratic yield criterion for orthotropic sheet metals under plane-stress conditions. *Int. J. Mech. Sci.* (2003) **45**:797–811.

[9] Pannier Y., Avril S., Rotinat R. and Pierron F. Identification of elasto-plastic constitutive parameters from statically undetermined tests using the Virtual Fields Method. *Exp. Mech.* (2006) **46**:735–755.

[10] Luersen, M.A. and Le Riche, R. Globalized Nelder-Mead method for engineering optimization. *Comput. & Struct.* (2004) **82**:2251–2260.

[11] Swift, B.H. Plastic instability under plane stress. *J. Mech. Phys. Solids* (1952) **1**:1–18.

[12] Voce, E. The relationship between stress and strain for homogeneous deformation. *J. Inst. Metals* (1948) **74**:537–562.

XIV International Conference on Computational Plasticity. Fundamentals and Applications
COMPLAS XIV
E. Oñate, D.R.J. Owen, D. Peric & M. Chiumenti (Eds)

REDUCTION OF THE MESH SIZE INFLUENCE ON THE RESULTS OF A LAGRANGIAN FINITE ELEMENT MACHINING MODEL

François DUCOBU, Edouard RIVIERE-LORPHEVRE and Enrico FILIPPI

University of Mons (UMONS), Faculty of Engineering (FPMs),
Machine Design and Production Engineering Lab
20 Place du Parc, B-7000 Mons, Belgium
e-mail: Francois.Ducobu@umons.ac.be, web page: http://http://www.geniemeca.fpms.ac.be/

Key words: Damage, Finite Element, Orthogonal Cutting, Mesh Dependence, Titanium Alloy Ti6Al4V

Abstract. Mesh dependence of the results of a finite element model are well known in many fields such as in structural design. This problem is however not much addressed in the literature for machining modelling although it is crucial for the quality of the results and the predictive aspect of the model. In this work, an orthogonal cutting model of the titanium alloy Ti6Al4V is exploited. The model formulation is Lagrangian and a damage criterion with eroding elements is used. A strong sensitivity of the results to the size of the elements is observed and the results do not converge when the size of the mesh decreases. To address this issue, a non-local damage criterion that reduces the mesh dependence of the results is introduced. The results show a strong decrease of their dependence to the size of the mesh. The recommendation is to use elements length that is not too far from the size of the grains of the material to avoid a dramatic increase of the computing time for very small elements and the absence of converged results for too large elements.

1 INTRODUCTION

The problem of mesh dependence of the results of a finite element model of machining is not much addressed in the literature. It is however crucial for the quality of the results and the predictive aspect of the model. Some works were identied on this subject in the literature, and particularly when segmented (also called saw-toothed) chips are formed. Karpat [1] observed that a decrease of the elements length decreases the width of the adiabatic shear band. Zhang et al. [2, 3] worked with four different elements sizes and studied their influence on the modelled cutting force. Larger elements lead to a cutting force value lower than the experimental value. Hortig ans Svendsen [4] noticed that a decrease in the elements length leads to a decrease of the adiabatic shear band width and a lower value of the cutting force. It is important to note that this last result is in contradiction of what Karpat [1] observed. Ambati and Yuan [5] concluded that the

cutting force is not dependent on the mesh density. They also observed that the width of the adiabatic shear band decreases with the size of the elements and that the chip becomes segmented although it was continuous for larger elements.

This literature review shows that a mesh dependence of the results can be highlighted but all the conclusions do not go in the same direction, and particularly for the cutting force. In this paper, an orthogonal cutting model of the titanium alloy Ti6Al4V is used to highlight and then reduce the influence of the mesh on the results when a segmented chip is formed.

2 FINITE ELEMENT MODEL PRESENTATION

The finite element model has previously been introduced by Ducobu et al. [6] to form realistic segmented Ti6Al4V chips, with the major difference that in this study damage properties are given to the whole workpiece. Its main characteristics are that it is a Lagrangian orthogonal cutting model developed with Abaqus. It is composed of a fixed workpiece and a tool moving horizontally at the cutting speed (Figure 1). The machined material, Ti6Al4V, is described by the TANH constitutive model [7], a modified Johnson-Cook material constitutive model [8] taking the strain softening into account. The cutting speed is 75 m/min and the uncut chip thickness is 0.28 mm. The tool has a rake angle of 15°, a clearance angle of 2° and a cutting edge radius of 20 µm. These cutting conditions experimentally lead to the formation of a segmented chip [9].

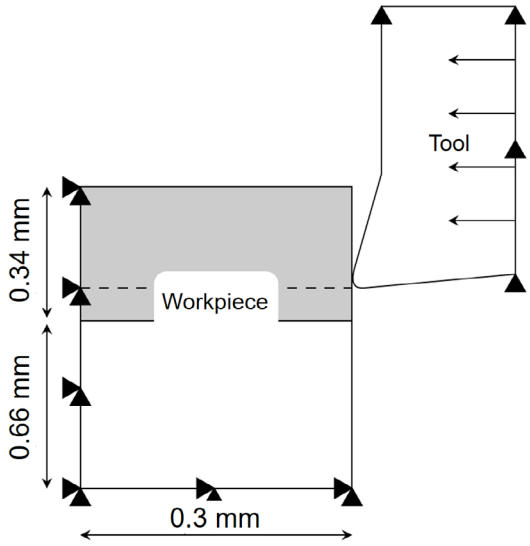

Figure 1: Configuration and boundary conditions of the model

With a Lagrangian formulation, a damage criterion has to be introduced to allow the chip to come off the workpiece. The adopted criterion is the temperature dependent tensile failure of Ti6Al4V [10, 11]. To limit the number of elements of the model and the computation time, only the first segment of the chip is modelled. This allows to consider a rather short workpiece (Figure 1). The size of the square elements ranges from 1 µm to

10 µm with a step of 1 µm. As shown in Figure 2, the computation time, with one Intel CPU at 3 GHz, increases much when the mesh density increases. For 84 µs of simulation time, the computation time is close to 500 h for a mesh of 1 µm while it is less than 5 minutes for a mesh of 10 µm.

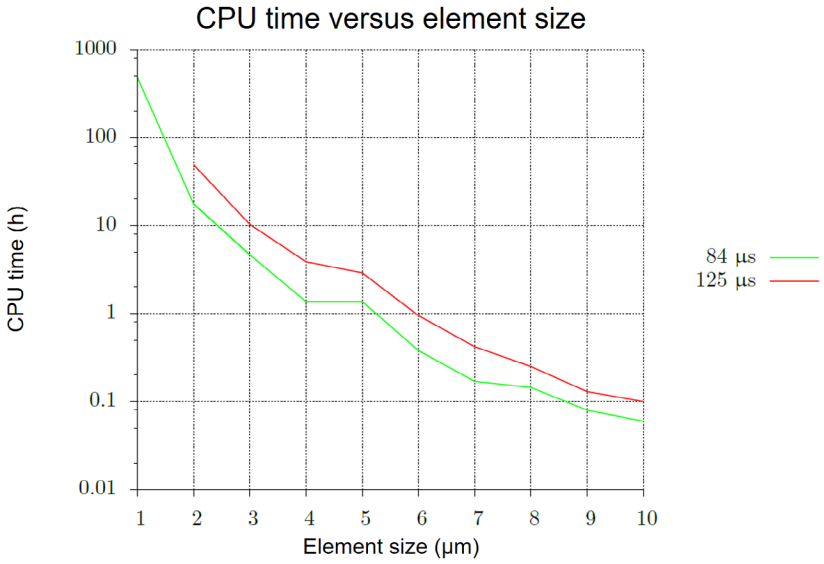

Figure 2: Evolution of the computation time with the mesh density (125 µs corresponds to the formation of the first segment, 84 µs is the maximum simulation time computed for 1 µm due to the very long computation time for that mesh size)

3 RESULTS FOR DIFFERENT MESH DENSITIES

Figure 3 presents the chip morphology for the 10 different meshes. They are globally close, except at 1 µm: a fracture propagates inside the primary shear zone very quickly (within 1 µs, the output frequency of the results) and a second fracture appears in the whole segment to cut it in two parts. When the mesh is 2 µm, the crack propagates quickly in the primary shear zone as well, but not in all of it and it takes longer than at 1 µm. Secondary fracture in the segment is also present at 2 µm and 3 µm. For all the meshes, the fracture propagates inside the primary shear zone, from the free surface of the chip to the tool radius.

As shown by Figure 4, the width of the adiabatic shear band decreases with the length of the elements. It is composed of 3-4 elements that are highly sheared. The decrease of the elements length leads to elements that are sooner highly sheared in the primary shear zone (the simulation time in Figure 4 decreases when the size of the elements decreases), which involves a quicker increase of the temperature.

The cutting and feed forces are presented in Figure 5 for the 10 meshes, together with the experimental reference of Sun et al. [9]. From 5 µm to 10 µm, the evolution and the values of the cutting force are close. Under 5 µm, the value of the first peak is reached sooner and its magnitude decreases. The fall of the cutting force is more abrupt (the

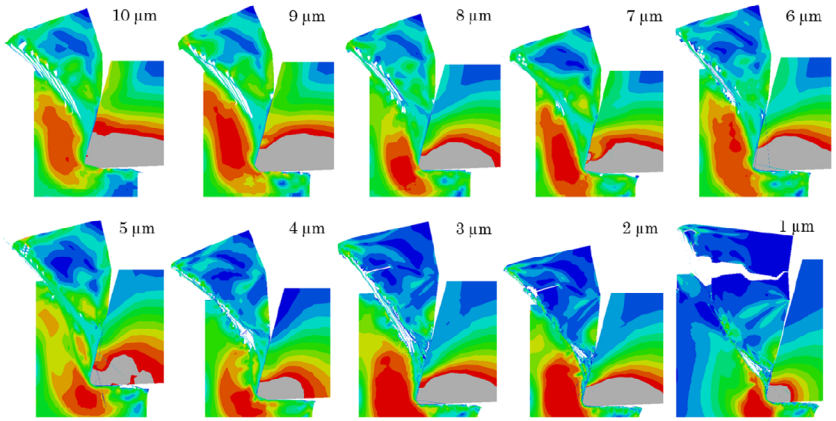

Figure 3: Chip morphology for different mesh densities (after 84 µs for elements of 1 µm and 125 µs from elements of 2 µm to elements of 10 µm)

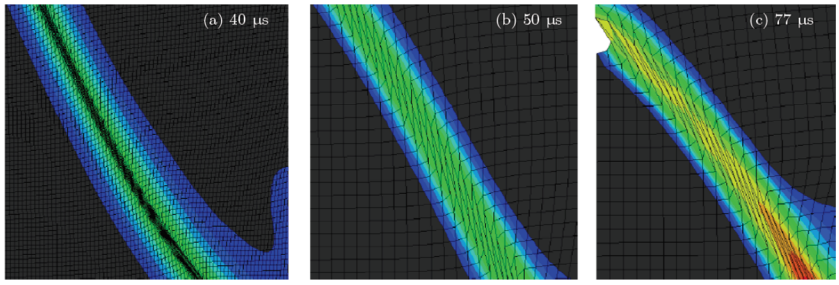

Figure 4: Width of the adiabatic shear band for an elements size of (a) 1 µm, (b) 5 µm and (c) 10 µm

width of the peak is smaller) and of a higher intensity (the minimal value is lower and it is reached sooner). This is due to the higher deformation of the elements and a higher temperature inducing a lower material strength. The fall is quicker and has a higher intensity because the fracture propagates quickly and is longer. For the feed force, it is the contrary (the force decreases when the elements length increases) but still with a significant mesh sensitivity.

In conclusions, the results do not converge when the mesh density increases, contrary to the expectations. The results remain close when the elements size is larger than 5 µm but then, if the elements size continues to decrease, they start to significantly diverge. This is particularly remarkable for the cutting force.

4 INTRODUCTION OF THE NON-LOCAL DAMAGE CRITERION

A significant mesh sensitivity of the results has been observed. This is mainly due to the introduction of damage and the softening of the material [12]. This leads to a strong localization inside the adiabatic shear band. To decrease this mesh sensitivity of the results, several methods can be found in the literature in other fields than metal cutting [12, 13]. Most of them consist of non-local methods that introduce an internal length. This internal length should be linked to the microstructure of the material (the

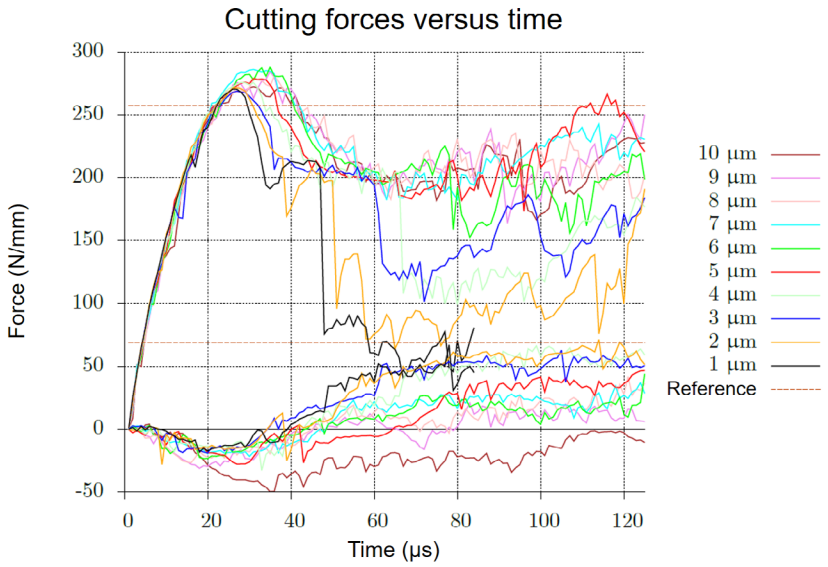

Figure 5: Cutting forces for the different mesh densities (experimental reference: Sun et al. [9])

grain size of Ti6Al4V is close to 5 µm) [12].

In Abaqus, the Johnson-Cook damage model, with initiation and propagation of damage, should allow to decrease the mesh dependence of the results once the damage initiation criterion has been reached in an element. This criterion has already been used in modelling of machining [14–16] and is composed of two steps (Figure 6 (a)). In the first step, the initiation of damage is computed in each element by

$$\omega = \sum \frac{\Delta\varepsilon}{\varepsilon_{D=0}} \tag{1}$$

With $\Delta\varepsilon$ the increment of equivalent plastic strain, $\varepsilon_{D=0}$ the equivalent plastic strain when damage is initiated ($\omega = 1$). It is computed by the Johnson-Cook damage model [17]

$$\begin{aligned} \varepsilon_{D=0} \quad = \quad & \left[D_1 + D_2 \ \exp\left(D_3 \ \sigma^*\right)\right] \left[1 + D_4 \ \ln \frac{\dot{\varepsilon}}{\dot{\varepsilon}_0}\right] \\ & \left[1 - D_5 \left(\frac{T - T_{room}}{T_{melt} - T_{room}}\right)\right] \end{aligned} \tag{2}$$

Where $\sigma^* = \frac{\sigma_m}{\sigma}$ is the stress triaxiality, σ_m is the mean stress and σ is the equivalent Von Mises stress. Variables D_1 to D_5 are model parameters and the other variables have the same meaning as for the Johnson-Cook material constitutive model: $\dot{\varepsilon}$ is the plastic strain rate, $\dot{\varepsilon}_0$ is the reference plastic strain rate, T_{room} is the room temperature and T_{melt} is the melting temperature.

After the initiation criterion has been reached, the damage propagates in a second step. The reduction of the mesh dependence to localization during damage evolution is carried out by introducing the fracture energy during crack propagation [18], G_f. It represents the stress-displacement relation rather than the stress-strain relation:

$$G_f = \int_{\varepsilon_{D=0}}^{\varepsilon_{D=1}} L_c \, \sigma \, \mathrm{d}\varepsilon = \int_0^{u_{D=1}} \sigma \, \mathrm{d}u \tag{3}$$

With L_c the element characteristic length and u the equivalent displacement. Before the onset of damage, $u = 0$ and after, $u = L_c \, \varepsilon$. In this model, the element characteristic length is the square root of the element surface [19]. The evolution of damage, D, is exponential:

$$D = 1 - \exp\left(- \int_0^{u_{D=1}} \frac{\sigma}{G_f} \, \mathrm{d}u \right) \tag{4}$$

When damage is initiated, D is equal to 0 and $\omega = 1$. At material failure, $D = 1$. When this second step is reached in an element, it is deleted which allows the chip to come off the workpiece and the crack can propagate.

Figure 6 compares schematically the behaviour of the material with the non-local damage criterion (a) and with the TANH constitutive model (b). In both cases, the objective is the same: taking into account the strain softening phenomenon that contributes to form a segmented chip.

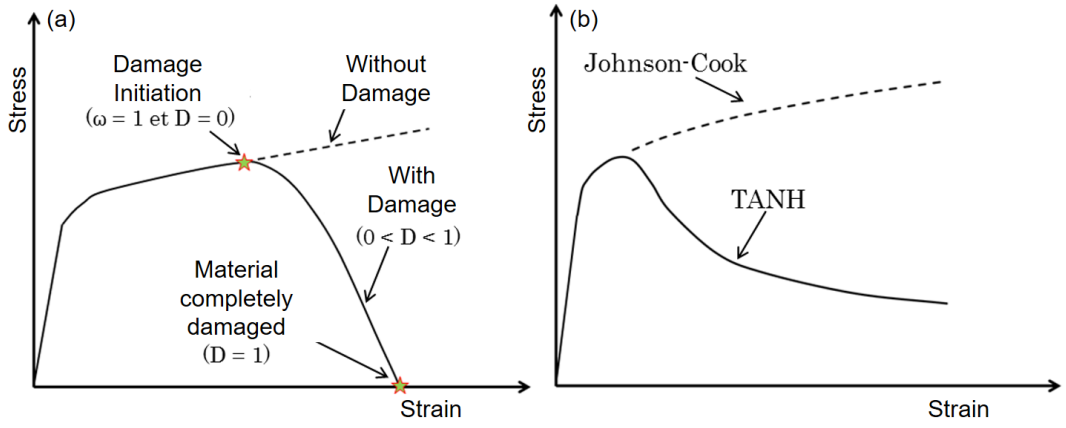

Figure 6: Behaviour of a material (a) with and without damage with the Johnson-Cook model, (b) without damage and the Johnson-Cook and TANH models

5 RESULTS WITH THE IMPROVED DAMAGE CRITERION

The chip morphology for the 10 meshes is presented in Figure 7. All the chips look similar. No damage localization, nor secondary crack are observed. A noticeable improvement is therefore brought. However, for 1 µm, some highly deformed elements are not deleted, which terminates prematurely the computation. The results for the width of the adiabatic shear band are improved as well. From 1 µm to 6 µm, its width remains constant and the number of elements inside of it grows as expected. Longer elements are too large to describe it.

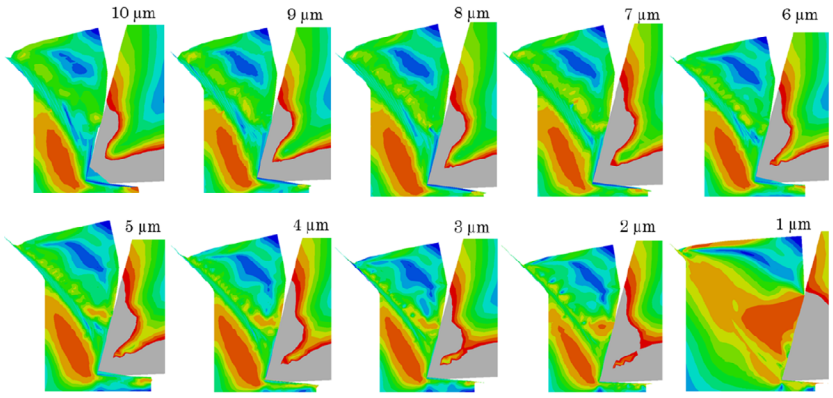

Figure 7: Chip morphology for different mesh densities after 125 µs (except 64 µs for 1 µm) with the non-local damage criterion

In Figure 8, it is seen that the cutting force has similar evolution and values for all the mesh densities up to 100 µs. Indeed, the initial effort rise is identical and the maximal value is reached at the same time. Only the 10 µm mesh has different values and high variations, which shows that the elements are too large. A similar observation is carried out for the feed force. The only difference is that the difference between the meshes begins at around 80 µs. In both cases, elements smaller than 4 µm lead to high forces variations after 100 µs.

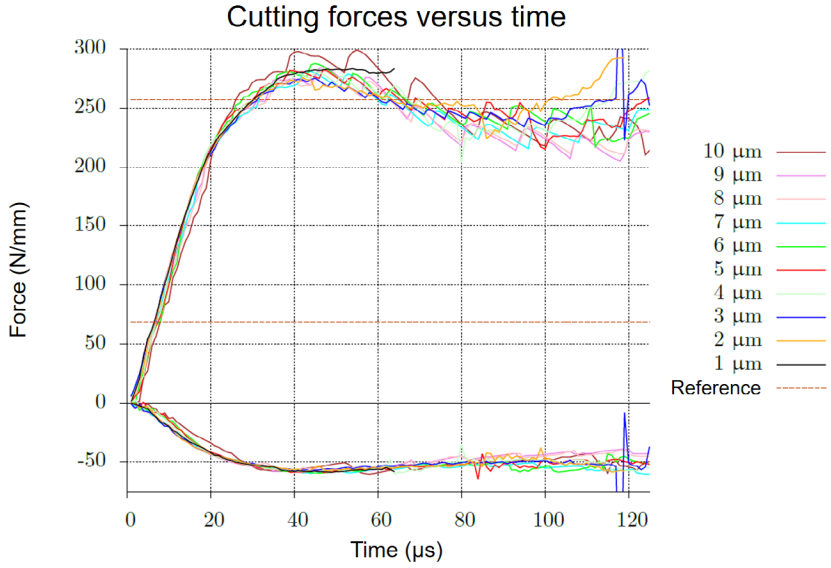

Figure 8: Cutting forces for the different mesh densities (experimental reference: Sun et al. [9]) with the non-local damage criterion

From the chip morphology results, the size of the elements should not be larger than 6 µm and small elements of 1 µm lead to highly deformed elements that are not deleted. For the forces, elements of 10 µm are too large and elements smaller to 4 µm should

not be used. In the end, although the mesh sensitivity is reduced, it has not completely disappeared and an element length of 5 µm would lead to good results in terms of chip morphology and cutting force.

6 CONCLUSIONS

A strong dependence of the results to the mesh density has been observed for the initial model with a local damage criterion. The reduction of this dependence has been carried out by introducing a non-local damage criterion based on the Johnson-Cook damage model. The results showed that localization of damage is reduced and that the sensitivity of the cutting forces to the mesh is significantly reduced. Some highly deformed elements that do not delete are however encountered, which can end prematurely the computation. An elements length of 5 µm is recommended, which is close to the grains size of the machined material.

REFERENCES

[1] Y. Karpat : Temperature dependent flow softening of titanium alloy Ti6Al4V: An investigation using finite element simulation of machining. *Journal of Materials Processing Technology*, 211:737–749, 2011.

[2] Y. Zhang, T. Mabrouki, D. Nelias et Y. Gong : FE-model for titanium alloy (Ti-6Al-4V) cutting based on the identification of limiting shear stress at tool-chip interface. *International Journal of Material Forming*, 4:11–23, 2011.

[3] Y.C. Zhang, T. Mabrouki, D.Nelias et Y.D.Gong : Chip formation in orthogonal cutting considering interface limiting shear stress and damage evolution based on fracture energy approach. *Finite Elements in Analysis and Design*, 47:850–863, 2011.

[4] C. Hortig et B. Svendsen : Simulation of chip formation during high-speed cutting. *Journal of Materials Processing Technology*, 186:66–76, 2007.

[5] R. Ambati et H. Yuan : FEM mesh-dependence in cutting process simulations. *International Journal of Advanced Manufacturing Technology*, 53:313–323, 2011.

[6] F. Ducobu, P.-J. Arrazola, E. Rivière-Lorphèvre et E. Filippi : Comparison of several behaviour laws intended to produce a realistic Ti6Al4V chip by finite elements modelling. *Key Engineering Materials*, 651–653:1197–1203, 2015.

[7] M. Calamaz, D. Coupard et F. Girot : A new material model for 2D numerical simulation of serrated chip formation when machining titanium alloy Ti-6Al-4V. *International Journal of Machine Tools and Manufacture*, 48:275–288, 2008.

[8] G.R. Johnson et W.H. Cook : A constitutive model and data for metals subjected to large strains, high strain rates and high temperatures. *Proceedings of the Seventh*

International Symposium on Ballistics, The Hague, The Netherlands, pages 541–547, 1983.

[9] S. Sun, M. Brandt et M.S. Dargusch : Characteristics of cutting forces and chip formation in machining of titanium alloys. *International Journal of Machine Tools and Manufacture*, 49:561–568, 2009.

[10] S. Lampman : Wrought titanium and titanium alloys, properties and selection: Nonferrous alloys and special-purpose materials. *ASM Handbook, ASM International*, 2:592–633, 1990.

[11] F. Ducobu, E. Rivière-Lorphèvre et E. Filippi : Material constitutive model and chip separation criterion influence on the modeling of Ti6Al4V machining with experimental validation in strictly orthogonal cutting condition. *International Journal of Mechanical Sciences*, 107:136–149, 2016.

[12] R.H.J. Peerlings, W.A.M. Brekelmans, R. de Borst et M.G.D. Geers : Gradient-enhanced damage modelling of fatigue failure. *Proceedings of the European Conference on ComputationalMechanics*, 1999.

[13] R. de Borst, M.G.D. Geers, R.H.J. Peerlings et A. Benallal : Some remarks on gradient and nonlocal damage theories. *Damage Mechanics in Engineering Materials*, 1998.

[14] T. Mabrouki, L. Deshayes, R. Ivester, J.-F. Rigal et K. Jurrens : Material modeling and experimental study of serrated chip morphology. *Proceedings of 7th CIRP International Workshop on Modeling of Machining Operations*, pages 53–66, 2004.

[15] T. Mabrouki et J.-F. Rigal : A contribution to a qualitative understanding of thermo-mechanical effects during chip formation in hard turning. *Journal of Materials Processing Technology*, 176:214–221, 2006.

[16] T. Mabrouki, F. Girardin, M. Asad et J.-F. Rigal : Numerical and experimental study of dry cutting for an aeronautic aluminium alloy (A2024-T351). *International Journal of Machine Tools and Manufacture*, 48:1187–1197, 2008.

[17] G.R. Johnson : Strength and fracture characteristics of a titanium alloy (.06ai, .04v) subjected to various strains, strain rates, temperatures and pressures. Rapport technique, NSWC TR 86-144, Dahlgren, VA, 1985.

[18] A. Hillerborg, M. Moder et P.E. Petersson : Analysis of crack formation and crack growth in concrete by means off racture mechanics and finite elements. *Cement and Concrete Research*, 6:773–782, 1976.

[19] H.K.S. : *Abaqus Analysis User's Manual, Version 6.14*. Dassault Systèmes, 2014.

XIV International Conference on Computational Plasticity. Fundamentals and Applications
COMPLAS XIV
E. Oñate, D.R.J. Owen, D. Peric & M. Chiumenti (Eds)

A VARIATIONAL GROWTH APPROACH TO TOPOLOGY OPTIMIZATION

JUNKER P. *, JANTOS D. R.† and HACKL K.†

* Institute of Continuum Mechanics
Ruhr-Universität Bochum
Universitätsstraße 150, 44801 Bochum, Germany
e-mail: philipp.junker@rub.de

†Institute of Mechanics of Materials
Ruhr-Universität Bochum
Universitätsstraße 150, 44801 Bochum, Germany
e-mail: dustin.jantos@rub.de

Key words: Topology Optimization, Variational Growth, Regularization

Abstract. In this contribution we present an overview of our work on a novel approach to topology optimization based on growth processes [1, 2, 3]. A compliance parameter to describe the spatial distribution of mass is introduced. It serves as an internal variable for which an associated evolution equation is derived using Hamilton's principle. The well-known problem of checkerboarding is faced with energy regularization techniques. Numerical examples are given for demonstration purposes.

1 INTRODUCTION

The objective of topology optimization is to find the topology of a mechanical structure that possess maximum stiffness at minimum weight for given boundary conditions. The topology of a structure can be described by the spatial distribution of mass density within a design space Ω which is subject the boundary conditions i.e. loading and supports. The spatial distribution of mass density serves as indicator function for areas where material and no material (i.e. void) is located. We introduce a continuous interpolation between full material and void for the spatial distribution of density mass as $\rho(\boldsymbol{x}) \in [0,1] \; \forall \; \boldsymbol{x} \in \Omega$. With a non-linear interpolation for the material stiffness (or compliance), intermediate densities $\rho \in \,]0,1[$ can be penalized to provide solution containing only full material ($\rho = 1$) and void ($\rho = 0$). This principle is similar to the well-known SIMP (**S**olid **I**sotropic **M**aterial with **P**enalization) method [5]. According to Bendsøe [5], the problem of topology optimization for a linear-elastic material then reads

$$\min_{\mathbb{E} \in \mathcal{E}_{\text{ad}}} \min_{\boldsymbol{\sigma} \in \mathcal{S}} \left\{ \frac{1}{2} \int_{\Omega} \boldsymbol{\sigma} : \mathbb{C}(\boldsymbol{x}) : \boldsymbol{\sigma} \; \mathrm{d}V \right\} \tag{1}$$

$$\text{with} \qquad \mathcal{S} = \{ \boldsymbol{\sigma} \mid \nabla \cdot \boldsymbol{\sigma} + \boldsymbol{b} = \boldsymbol{0} \text{ in } \Omega, \; \boldsymbol{\sigma} \cdot \boldsymbol{n} = \boldsymbol{t} \text{ on } \partial_{\sigma} \Omega \}$$

where $\boldsymbol{\sigma}$ are the stresses, $\boldsymbol{b}$ are the body forces, and $\boldsymbol{t}$ are the given external tractions that act on the boundary $\partial_\sigma\Omega$. The interpolated material compliance is given by $\mathbb{C}(\boldsymbol{x}) = (\rho(\boldsymbol{x})\mathbb{E}_0)^{-1}$ with the full material stiffness $\mathbb{E}_0$. The set of admissible stiffness tensors $\mathcal{E}_{\text{ad}}$ can be defined in various ways, see [5].

In the proposed approach, we do not solve the problem of topology optimization in a strict way as demanded by Eq. (1). In contrast, we interpret that subject as a problem of optimized and *localized* growth of material. For this purpose, we introduce a compliance parameter (i.e. the inverse of the mass density ρ) which is the additional unknown at the material point (= integration point) level. The governing equations are determined using fundamental principles of thermodynamics which minimize the Gibbs energy. To account for a dissipative behavior, we apply Hamilton's principle. In this way, we are able to determine an evolution equation for the spatial distribution of density mass, which can be evaluated in an iterative update process within a solitary finite element environment like it is common in (microstructural) material modeling e.g. phase transformations, damage, and plasticity.

The evolution equation describes the pseudo-time dependent and local material growth for the current loading conditions. It hence predicts for each structure volume the single topology exhibiting maximum stiffness, depending on the time history. Surely, a completely filled design space Ω possesses per se maximum stiffness (which is equivalent to minimum compliance); however, it is not optimal regarding that only a minimum of mass shall be used. It is thus necessary to constraint the volume structure by either prescribe the total structure volume or model the continuous growth of the structure. In our work, we model the structure growth with two different approaches. Firstly, we introduce evolution equations with a visco-plastic ansatz providing a yield surface for the structure growth: the local density $\rho(\boldsymbol{x})$ only increases in areas where the stresses $\boldsymbol{\sigma}$ are higher than a specific threshold. Secondly, we combine a viscous ansatz for the evolution equation with a Lagrange multiplier which allows us to directly control the structure volume within time. With the *Lagrange shift* approach we define a special growth function which depends only on one parameter, but results in natural growth behavior.

An well-known phenomenon in SIMP-like approachs is the so called checkerboarding which become visible in the form of oscillating mass distributions (see Figure 1): spatial points that possess mass are directly neighbored to spatial points that are mass-free. This numerical artifact produces results that depend on the finite element mesh used for mathematical discretization and repeats (locally at the smallest discretization level) in a periodic manner. In the case of SIMP approaches, this phenomenon is present if tri-linear shape functions are used. In our case, comparable problems are observed which result from a non-convex Helmholtz free energy which is necessary to penalize the gray solution. We solve this problem with two different energy regularization approaches: on the one hand, we penalize the gradient of the spatial distribution of mass by introducing a field function which is coupled to the local compliance parameter. Penalizing the gradient of the field function thus penalizes also the spatial gradient of the compliance parameter. On the other hand, we directly penalize the gradient of the spatial distribution of mass. To condense the resulting field equation again to an evolution equation which can be evaluated *locally*,

we employ special shape functions for the balance equation of the compliance parameter using a discontinuous Galerkin approach.

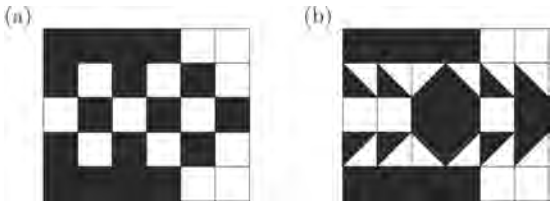

Figure 1: Schematic plot [2] of the usual inter-element checkerboarding (a) for approaches where the spatial distribution of mass is discretized element-wise, and (b) of the intra-element checkerboarding which was observed for our approach with the density field discretized within the integration points of each finite element. Whereas for "regular" checkerboarding entire elements are fluctuating between mass and no mass, mass fluctuates between zero and one *within* elements for the intra-element checkerboarding.

2 VARIATIONAL MODEL

2.1 Hamilton's principle

The Hamilton principle for dissipative continua reads

$$\delta\mathcal{G} + \int_\Omega \frac{\partial \mathcal{D}}{\partial \dot{\chi}} \delta\chi \, \mathrm{d}V + \delta\mathcal{P} = 0 \tag{2}$$

where $\mathcal{G}$ is the Gibbs energy, $\mathcal{D}$ is the dissipation function, χ is a internal variable to describe the spatial distribution of mass, and the functional $\mathcal{P}$ accounts for the problem-specific constraints. For linear elastic materials the Gibbs energy can be defined as

$$\mathcal{G} = \int_\Omega \Psi \, \mathrm{d}V - \int_\Omega \boldsymbol{b} \cdot \boldsymbol{u} \, \mathrm{d}V - \int_{\partial\Omega} \boldsymbol{t} \cdot \boldsymbol{u} \, \mathrm{d}A \tag{3}$$

with the Helmholtz energy

$$\Psi = \Psi_\mathrm{m} + \Psi_\mathrm{r} = \frac{1}{2} \int_\Omega \boldsymbol{\sigma} : \mathbb{C}(\boldsymbol{x}) : \boldsymbol{\sigma} \, \mathrm{d}V + \Psi_\mathrm{r} \tag{4}$$

composed of the part for the regularization Ψ_r and the mechanical part Ψ_m containing the constitutive law with $\boldsymbol{\sigma} = (\mathbb{C}^{-1}(\boldsymbol{x})) : \boldsymbol{\varepsilon}$ and the strains $\boldsymbol{\varepsilon} = \frac{1}{2}(\nabla\boldsymbol{u} + \boldsymbol{u}\nabla)$ containing the displacement field $\boldsymbol{u}$. As we can see here, by minimizing the Gibbs energy $\mathcal{G}$ we also find the minimum of the Helmholtz energy which solves the minimization problem in Eq. (1). We introduce the compliance parameter $\chi(\boldsymbol{x}) \in [0, 1]$ as internal variable to describe the spatial distribution of mass with $\chi = 0 \rightarrow$ full material and $\chi = 1 \rightarrow$ void. As stated before, we apply a non-linear interpolation for the material compliance penalizing intermediate solutions $\chi \in]0, 1[$

$$\mathbb{C}(\chi) = \chi^2 \, \mathbb{C}_\mathrm{void} + (1 - \chi^2)\mathbb{C}_0 \tag{5}$$

For numerical reasons, the material stiffness of the void material cannot be zero. Thus, the material compliance of the void $\mathbb{C}_\mathrm{void}$ must be finite but much larger than the full

material compliance $\mathbb{C}_0$. We introduce the small but non-zero numerical parameter κ and define $\mathbb{C}_{\text{void}} = \frac{1}{\kappa}\,\mathbb{C}_0$ which yields

$$\mathbb{C}(\chi) = f(\chi)\mathbb{C}_0 \quad \Leftrightarrow \quad \mathbb{E}(\chi) = \frac{1}{f(\chi)}\mathbb{E}_0 \tag{6}$$

with the interpolation function $f(\chi)$, which is the inverse of our density function $\rho(\boldsymbol{x})$ (due to numerical reasons the domain for the density function becomes $\rho(\boldsymbol{x}) \in [\kappa, 1]$).

$$f(\chi) = \frac{1}{\rho(\chi)} = 1 + \left(\frac{1}{\kappa} - 1\right)\chi^2 \tag{7}$$

We define the constraint functional $\mathcal{P}$ as

$$\mathcal{P} := \int_\Omega \gamma\,\chi \;\mathrm{d}V \tag{8}$$

with the Kuhn-Tucker parameter γ which constrains the interval of the internal variable $\chi \in [0, 1]$. The Dissipation function $\mathcal{D}$ and the regularization part of the Helmholtz energy Ψ_r vary for the different approaches and will be presented in the following section.

The Gibbs energy constitutes as functional depending on the displacement field $\boldsymbol{u}(\boldsymbol{x})$ and the spatial distribution of the internal variables $\chi(\boldsymbol{x})$, which are also the unknowns for the optimization problem. Thus, the variation in Eq. (2) has to be performed for $\boldsymbol{u}$ and χ which can be evaluated independently. The variation with respect to the displacement field $\boldsymbol{u}$ yields the well-known the balance of linear momentum in its weak form

$$\delta_{\boldsymbol{u}}\mathcal{G} = \int_\Omega \frac{\partial \Psi_\mathrm{m}}{\partial \boldsymbol{\varepsilon}} : \delta\boldsymbol{\varepsilon} \;\mathrm{d}V - \int_\Omega \boldsymbol{b}\cdot\delta\boldsymbol{u} \;\mathrm{d}V - \int_{\partial\Omega} \boldsymbol{t}\cdot\delta\boldsymbol{u} \;\mathrm{d}A = 0 \qquad \forall\,\delta\boldsymbol{u} \tag{9}$$

which can be solved with a common finite element method. The variation with respect to the internal variable χ yields the evolution equation for the compliance parameter in the form $\dot{\chi} = \mathrm{func}(\boldsymbol{\sigma}, \boldsymbol{\varepsilon}, \chi, ...)$. With the results from the finite element method, the evolution equation can be evaluated in an explicit manner after each iteration step i as

$$\chi^{(i+1)} = \chi^{(i)} + \Delta t \dot{\chi}(\boldsymbol{\sigma}^{(i)}) \tag{10}$$

which closes the system of equations to solve the optimization problem. The whole procedure can be incorporated in a Newton-Raphson iteration as done in e.g. damage and plasticity modeling. The actual form of the evolution equation vary for the different approaches shown in the following sections. However, all approaches share the same (mechanical) driving force

$$p_\chi := -\frac{\partial \Psi_\mathrm{m}}{\partial \chi} = -\frac{1}{2}\,\boldsymbol{\sigma} : f'(\chi)\mathbb{C}_0 : \boldsymbol{\sigma} \tag{11}$$

2.2 Regularization of a field function

In our first appraoch [1], we chose a dissipation function $\mathcal{D}$ which yields an evolution equation of elasto-viscoplatic type, as

$$\mathcal{D} = r_1|\dot{\chi}| + r_2\,\frac{\dot{\chi}^2}{2} \quad \Rightarrow \quad \frac{\partial \mathcal{D}}{\partial \dot{\chi}} = r_1\,\partial|\dot{\chi}| + r_2\,\dot{\chi} \tag{12}$$

with the subdifferential $\partial|\dot{\chi}|$ reading

$$\partial|\dot{\chi}| = \begin{cases} \{|\dot{\chi}| \leq 1\} & \text{for } \dot{\chi} = 0 \\ \dfrac{\dot{\chi}}{|\dot{\chi}|} & \text{else} \end{cases} \tag{13}$$

We apply the method of gradient-enhanced free energy for the regularization.The energy Ψ_r contains two term: the first one couples the local information carried by χ to a field function $\varphi(\boldsymbol{x})$. The second term penalizes "large" gradients of φ. We define the regularization part of the Helmholtz energy Ψ_r as

$$\Psi_\mathrm{r} = \frac{\alpha}{2}|\nabla\varphi|^2 + \frac{\beta}{2}(\varphi - \chi)^2 \tag{14}$$

Since χ is coupled to φ, penalization of the gradient of φ also influences the gradient of χ: "large" gradients of χ will be penalized. Because the oscillating pattern of checkerboarding possess "large" gradients of χ, checkerboarding is energetically less favorable and will be suppressed. The slip between the compliance parameter and the field function holds the advantage that local evolution and the far-field behavior of χ can be controlled individually so that the width of the transition zone can be adjusted. This advantage is accompanied by the drawback of a highly increased numerical effort due to the increased number of nodal unknowns.

The variation of Eq. (2) with respect to the internal variable χ yields the evolution equation

$$\dot{\chi} = \frac{1}{r_2}\big[|p_\chi + \beta(\varphi - \chi)| - r_1\big]_+ \,\mathrm{sgn}(p_\chi + \beta(\varphi - \chi)) \tag{15}$$

where $\big[x\big]_+ := (x + |x|)/2$ implies that only positive values are taken into account to ensure structure growth. The the sgn-function reads

$$\mathrm{sgn}p = \begin{cases} 1 & \text{for } p > 0 \\ -1 & \text{for } p < 0 \\ \{\tilde{p} \leq 1\} & \text{for } p = 0 \end{cases} \tag{16}$$

In addition, we have to calculate the variation of Eq. (2) with respect to the field function φ, which yields

$$\int_\Omega \beta\ (\varphi - \chi)\ \delta\varphi\ \mathrm{d}V + \int_\Omega \alpha\ \nabla\varphi\ \nabla\delta\varphi\ \mathrm{d}V = 0 \tag{17}$$

Eqs. (17) and (9) can be solved with the finite element method where the field function φ can be discretized with common shape-functions and becomes an additional nodal unknown (besides the 3 degrees of freedom of the displacement field) for the Newton-Raphson scheme.

2.3 Regularization by direct gradient penalization

In our second approach [2], we penalize the gradient of the internal variable χ directly without introducing a field function φ by applying the energy

$$\Psi_{\mathrm{r}} = \frac{\alpha}{2}|\nabla\chi|^2 \tag{18}$$

The variation of the Gibbs energy with respect to the internal variable χ yields a condition similar to Eq. (17). Instead of using this equation to add the internal variable χ as additional nodal degree of freedom as done for φ, we approximate the gradient of the internal variable with a discontinous Galerkin approach. The tri-linear discontinuous shape functions $\boldsymbol{N}_\chi$ discretize values for the internal variable within the Gauß (integration) points of the finite element mesh. Thus, the gradient of the internal variable will be evaluated *within* each finite element. As shown in Figure 1, checkerboarding occurs in an intra-element way in our approach. Therefore we do not need any penalization of the gradient "over element borders" to suppress checkerboarding. We apply the same dissipation function $\mathcal{D}$ given in Eq. (12) and find the evolution equation

$$\dot{\chi} = \frac{1}{r_2}\left[|p - \overline{\Delta\chi}| - r_1\right]_+ \ \mathrm{sgn}\left[p - \overline{\Delta\chi}\right] \tag{19}$$

with

$$\overline{\Delta\chi_i} := \frac{1}{|\Omega_{\mathrm{e}}|}\left(\int_{\Omega_{\mathrm{e}}} \alpha\,(\nabla\boldsymbol{N}_\chi)^T \cdot (\nabla\boldsymbol{N}_\chi \cdot \tilde{\boldsymbol{\chi}})\ \mathrm{d}V\right)_i \tag{20}$$

where the index refers to a local evaluation at the Gauß (integration) points in each element ($\boldsymbol{x}_{\mathrm{GP},i,\mathrm{e}}$) with volume $|\Omega_{\mathrm{e}}|$. Except for the integral in $\overline{\Delta\chi_i}$, equation (14) can be completely evaluated locally at the Gauß (integration) points as done in e.g. plasticity: the internal variable χ can be evaluated locally without monolithically solution for the whole finite element mesh. The quantity $\overline{\Delta\chi_i}$ is the only one which also depends on other $\chi_k, k \neq i$: the compliance parameters enter $\nabla\boldsymbol{N}_\chi\cdot\tilde{\boldsymbol{\chi}}$ for all Gauß (integration) points in the single element in which χ_i is located. Hence, $\overline{\Delta\chi_i}$ is a measure for the gradient within each element and thus ensures the gradient-penalization which regularizes the Gibbs energy and suppresses the intra-element checkerboarding.

2.4 Controlled growth

In [3], we introduce a Lagrange multiplier to directly control the structure volume within the iteration process. The Lagrange multiplier prevents the trivial solution and therefore the plasticity part in the Dissipation function is not needed anymore. We define

$$\mathcal{D} = r_2\,\frac{\dot{\chi}^2}{2} \tag{21}$$

and the constraint for controlled growth

$$g(\chi) = \frac{1}{|\Omega|}\int_\Omega \rho(\chi)\ \mathrm{d}V - \varrho(t) = \frac{1}{|\Omega|}\int_\Omega \frac{1}{f(\chi)}\ \mathrm{d}V - \varrho(t) \stackrel{!}{=} 0 \tag{22}$$

where $\varrho(t)$ denotes a prescribed growth function. To incorporate this constraint, we have to expand the constraint functional $\mathcal{P}$ as

$$\mathcal{P} := g(\chi) + \int_\Omega \gamma\, \chi \, \mathrm{d}V \tag{23}$$

We apply the regularization scheme including the discontinuous Galerkin approach given in the previous section. The final evolution equation reads

$$\dot{\chi} = \frac{1}{r_2} \left[\frac{\lambda}{|\Omega|} \frac{f'(\chi)}{f(\chi)^2} + p_\chi - \frac{\overline{\Delta\chi}}{|\Omega_\mathrm{e}|} \right] \tag{24}$$

with the Lagrange multiplier

$$\lambda = |\Omega| \, \frac{\displaystyle\int_\Omega \left(-p_\chi + \frac{\overline{\Delta\chi}}{|\Omega|_\mathrm{e}} \right) \frac{f'(\chi)}{f(\chi)^2} \, \mathrm{d}V - r_2 \, |\Omega| \, \dot{\varrho}(t)}{\displaystyle\int_\Omega \left(\frac{f'(\chi)}{f(\chi)^2} \right)^2 \mathrm{d}V} \tag{25}$$

Any arbitrary growth (discretized) function $\varrho(t^{(i)})$ can be inserted into the Lagrange multiplier in Eq. (25) as

$$\dot{\varrho}\left(t^{(i+1)}\right) = \frac{|\Omega| \; \varrho\left(t^{(i+1)}\right) - \displaystyle\int_\Omega \rho(\chi) \, \mathrm{d}V}{\Delta t} \tag{26}$$

For the growth function, we introduced the *Lagrange shift* approach with

$$\varrho(t) := \frac{1 - \lambda_\mathrm{S}}{V_\Omega} \int_\Omega \frac{1}{f\left(\chi(t)\right)} \, \mathrm{d}V \bigg|_{\lambda=0} \tag{27}$$

where $0 < \lambda_\mathrm{S} < 1$ is a numerical parameter. For the Lagrange multiplier follows

$$\lambda = \lambda_\mathrm{S} \; V_\Omega \, \frac{\displaystyle\int_\Omega \left(-p_\chi + \frac{\overline{\Delta\chi}}{V_\mathrm{e}} + \gamma \right) \frac{f'(\chi)}{f(\chi)^2} \, \mathrm{d}V}{\displaystyle\int_\Omega \left(\frac{f'(\chi)}{f(\chi)^2} \right)^2 \mathrm{d}V} \tag{28}$$

The parameter λ_S shifts the model behavior between two "extreme cases": if $\lambda_\mathrm{S} = 1$, there is no growth and the model preserves the structure volume. Choosing $\lambda_\mathrm{S} = 0$ would lead to a model without any restrictions for the structure growth which would obviously result in the trivial solution since the density would increase simultaneously in the entire design space. The *Lagrange shift* approach is numerically quite stable and leads to natural growth behavior. The benefit of the *Lagrange shift* approach is that only one bounded parameter $\lambda_\mathrm{S} \in]0, 1[$ must be chosen to define the growth function. If the solution for a given structure volume is desired, the growth function can be switched according to Eq. (26) (with $\varrho\left(t^{(i+1)}\right) = \text{const.}$ as the target volume) as soon as the structure volume exceeds the given target volume.

3 NUMERICAL RESULTS

Let us now present some numerical results for the three different approaches. Our first example is a simply supported beam given in Figure 2. The essential process of the evolution of the structure is similar for all approaches given in [1, 2, 3]. Figure 2 shows the results for the model given in [3] representative for all models. The model given in [3] differs from the other models in one point: this model allows us to hold the structure volume constant for additional iteration steps, in which the structure is further optimized so that the structural stiffness ($\mathcal{S} = 1/\hat{\boldsymbol{f}} \cdot \hat{\boldsymbol{u}}$) is increased for the same structure volume (see Figure 3). In contrast, the results from the other two approaches are just snapshots for structures with the respective volume structure while the model leads to a continuous growth towards the trivial solution of a structure volume that equals the design space. A comparison of the final results from all approaches for a structure volume $\varrho = 45.65\%$ are given in Figure 3 and 3. The difference between Firgure 3 and 3 is the fineness of the finite element mesh to show the mesh-independence of our models.

As a second example, we introduce a three-dimensional bending problem. The boundary conditions and final results for each model are given in Figure 3.

4 CONCLUSIONS

We presented a novel approach to topology optimization based on the thermodynamic principles known from variational material modeling. The numerical results of all approaches showed overall fine, smooth and reasonable structures, although relatively coarse meshes were used. Checkerboarding was suppressed by energy regularization with two different approaches. The regularization by aid of a field function in [1] holds the advantage that the transition zone between material and void phase can be controlled independently from the actual regularization. This is not possible with the direct gradient penalization of the internal variable in [2]. However, the approach in [2] does not need to introduce additional nodal degrees of freedom by using a discontinuous Galerkin discretization for the internal variable. This reduces the calculation effort remarkably ($\approx 10\%$ of [1]). In [3], we added a way to directly control the structure mass by aid of a Lagrange multiplier which allows us mimic natural growth and find further optimized structures for given structure volumes. The *Lagrange shift* approach led to easy-to-handle and numerically stable growth.

The usage of a variational approach based on thermodynamic principles holds the advantage that the general experience and research results in material modeling (e.g. from phase transformation and plasticity modeling) can be accounted for the development of topology optimization approaches. For example, additional design characteristics for the structure (e.g. the material orientation for anisotropic materials [4]) can be incorporated as additional design variables. Due to the growth-based approaches we are using a close link also to biological systems seems feasible and will be subject of future investigations.

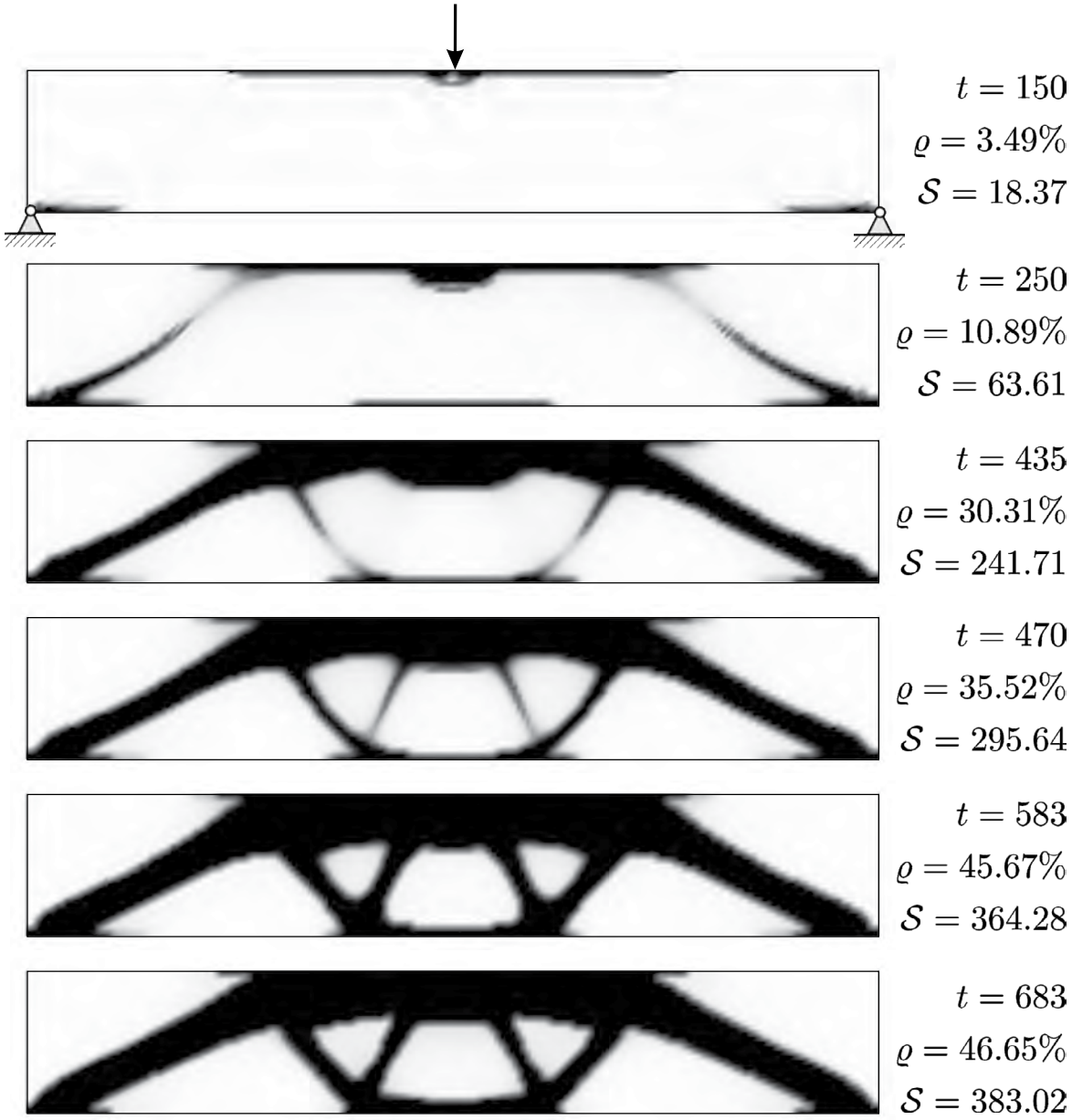

Figure 2: Resulting structural evolution from the model given in 2.4. As soon as the structure volume of $\varrho = 45.65\%$ is reached, the structure volume is held constant for additional 100 iteration steps according to Eq. (26)

REFERENCES

[1] Junker, P. and Hackl, K. *A variational growth approach to topology optimization.* Structural and Multidisciplinary Optimization, Vol. 300,p. 780-801, (2015).

[2] Junker, P. and Hackl, K. *A discontinuous phase field approach to variational topology optimization.* Structural and Multidisciplinary Optimization, Vol. 52, pp. 293-304,

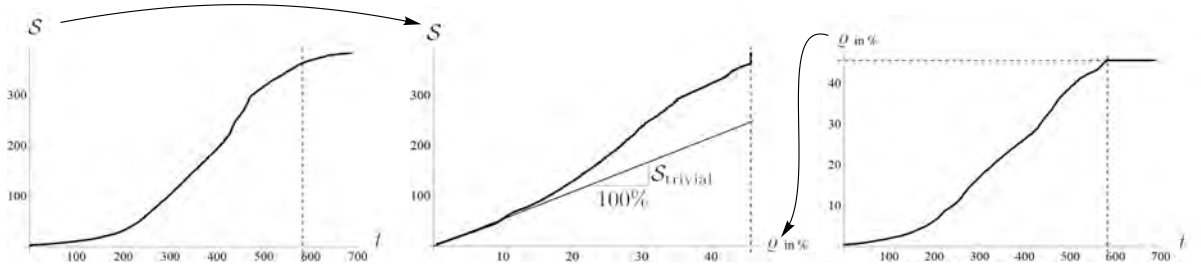

Figure 3: Structure stiffness $\mathcal{S}$ within simulation process, structure stiffness with respect to structure volume ϱ, and structure volume $\mathcal{S}$ within simulation process (from the left hand to the right hand side). The dashed gray lines mark the iteration step $t = 582$ and the structure volume $\varrho = 45.65\%$ which is held constant at this value for iteration steps $t > 582$. The line in the upper right picture shows the linear interpolation of the Stiffness for the trivial solution $\mathcal{S}_{\text{trivial}} = \mathcal{S}(\chi(\boldsymbol{x}) = 0)\ \forall\ \boldsymbol{x} \in \Omega$ over the structure volume ϱ.

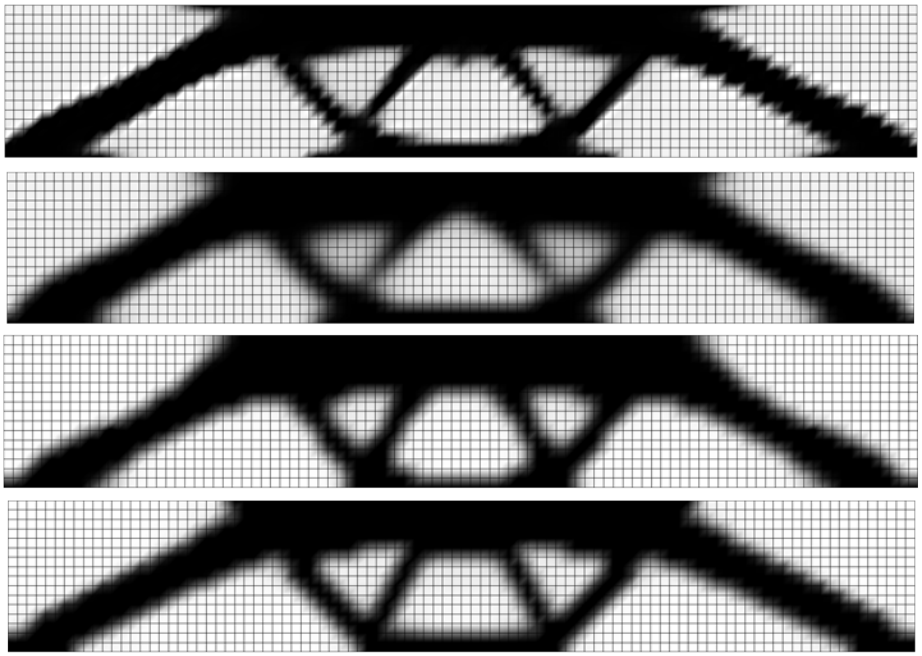

Figure 4: Results for a mesh with $144 \times 96 \times 1$ cubic elements on 3298 nodes from top to bottom: model in [1] (Section 2.2), model in [2] (Section 2.3), model in [3] (Section 2.4) as soon as $\varrho = 45.65\%$ and after additional 100 iteration steps.

(2015).

[3] Jantos, D. R. and Junker, P. and Hackl, K. *An evolutionary topology optimization approach with variationally controlled growth*. Computer Methods in Applied Mechanics and Engineering, Vol. 300,p. 780-801, (2016).

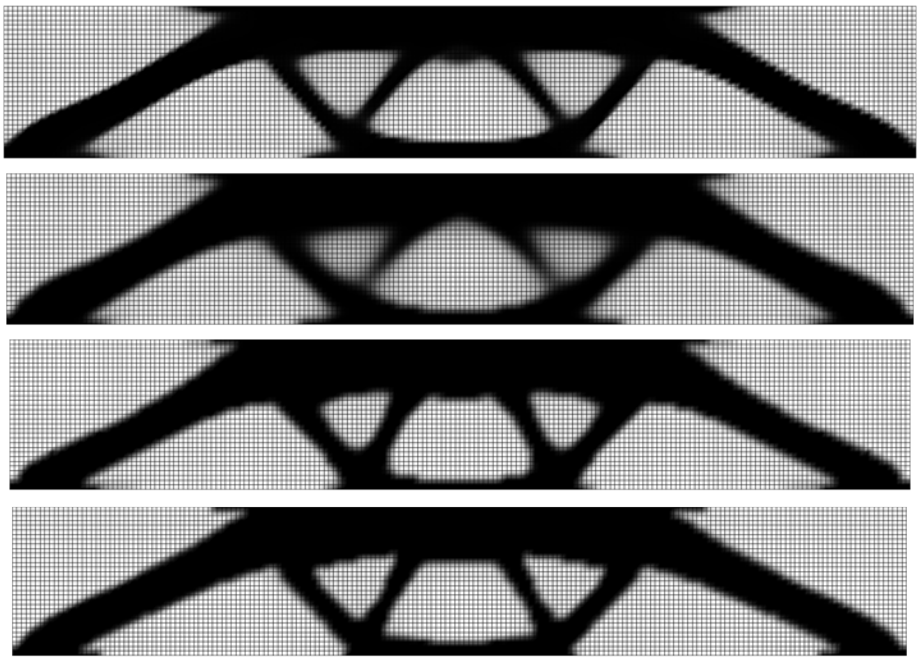

Figure 5: Results for a mesh with $192 \times 32 \times 1$ cubic elements on 12738 nodes from top to bottom: model in [1] (Section 2.2), model in [2] (Section 2.3), model in [3] (Section 2.4) as soon as $\varrho = 45.65\%$ and after additional 100 iteration steps.

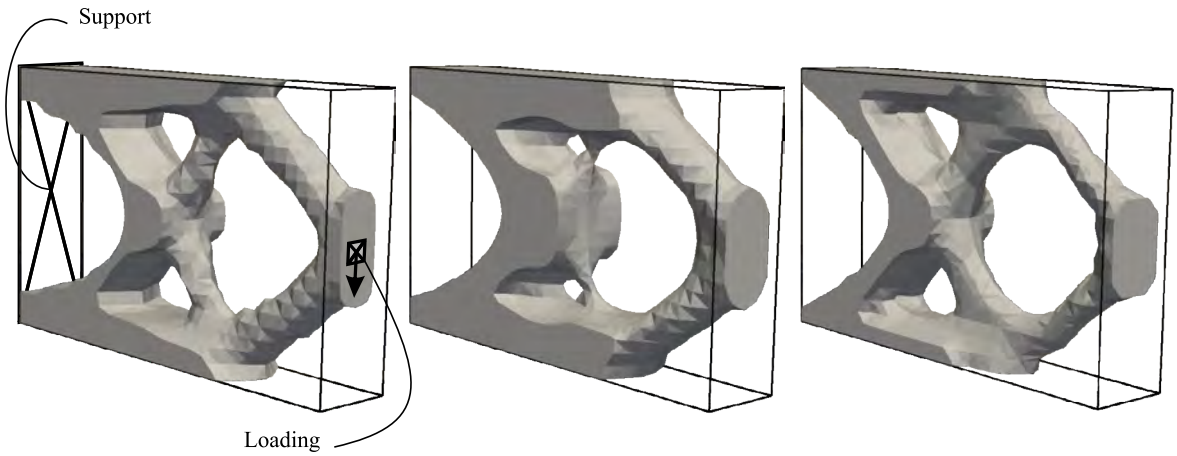

Figure 6: From left to right: Boundary conditions, results for the model in [1] (Section 2.2), model in [2] (Section 2.3), and model in [3] (Section 2.4). Discretization: $32 \times 20 \times 6$ cubic elements on 4851 node. Structure volume: $\varrho = 30\%$.

[4] Jantos, D. R. and Junker, P. and Hackl, K. *Optimized growth and reorientation of anisotropic material based on evolution equations*. Submitted

[5] Bendsøe, M. P. and Sigmund, O *Topology optimization: theory, methods and appli-*

cations. Springer (2003).

XIV International Conference on Computational Plasticity. Fundamentals and Applications
COMPLAS XIV
E. Oñate, D.R.J. Owen, D. Peric & M. Chiumenti (Eds)

BAYESIAN PARAMETER IDENTIFICATION IN PLASTICITY

Ehsan Adeli*, Bojana Rosić*, Hermann G. Matthies* and Sven Reinstädler†

* Institute of Scientific Computing
Technische Universität Braunschweig
Braunschweig, Germany
e-mail: wire@tu-bs.de, web page: http://www.wire.de/

† Institute of Structural Analysis
Technische Universität Braunschweig
Braunschweig, Germany
e-mail: statik@tu-bs.de, web page: http://www.wire.de/

Key words: Viscoplastic Model, Uncertainty Quantification, Probabilistic Inverse Approach, Polynomial Chaos

Abstract. To evaluate the cyclic behaviour under different loading conditions using the kinematic and isotropic hardening theory of steel a Chaboche visco-plastic material model is employed. The parameters of a constitutive model are usually identified by minimization of the distance between model response and experimental data. However, measurement errors and differences in the specimens lead to deviations in the determined parameters. In this article the Choboche model is used and a stochastic simulation technique is applied to generate artificial data which exhibit the same stochastic behaviour as experimental data. Then the model parameters are identified by applying a variaty of Bayes's theorem. Identified parameters are compared with the true parameters in the simulation and the efficiency of the identification method is discussed.

1 Introduction

In order to predict the behaviour of loaded metallic materials, constitutive models are applied, which present a mathematical frame for the description of elastic and inelastic deformation. Miller, Krempl, Korhonen, Aubertin, Chan and Bodner models can be addressed as such well-known constitutive models for isotropic materials [1, 2, 3, 4, 5]. In 1983, Chaboche [6, 7] put forward what has become known as the unified Chaboche viscoplasticity constitutive model, which has been widely accepted.

All inelastic constitutive models contain parameters which have to be identified for a given material from experiments. In the literature only few investigations can be found, dealing with identification problems using stochastic approaches. Klosowski and Mleczek have applied the least-squares method in the Marquardt-Levenberg variant to estimate

the parameters of an inelastic model [8]. Gong et al. have also used some modification of the least-squares method to identify the parameters [9]. Harth and Lehn identified the model parameters of a model by employing some generated artificial data instead of experimental data using stochastic technique [10]. A similar study by Harth and Lehn has been done for other constitutive models like Lindholm and Chan [11].

In this paper, a viscoplastic model of Chaboche is studied. The model contains five material parameters which have to be determined from experimental data. It should be noted that virtual data are employed instead of real experimental data. In addition, a cyclic tension-compression test is applied in order to extract the virtual data.

Section 3 explains how to propagate the uncertainty in the model. Probabilistic model is reformulated from the deterministic model and once the forward model is provided, the model parameters are updated using a stochastic approach.

In section 4 the desired parameters are identified from the measured data. In fact, the parameters which have been considered as uncertain parameters are updated and their uncertainties are narrowed using Bayesian techniques. The results are thoroughly studied and the identified parameters as well as the corresponding model responses are analysed. Finally the prediction of the models is then compared with the measured data.

2 Model problem

The mathematical description of metals under cyclic loading beyond the yield limit that includes the viscoplastic material behaviour as well as the characterization of compulsatory isotropic-kinematic hardening is here given in terms of a modified Chaboche model introduced by [12]. As we consider classical infinitesimal material behaviour, we assume an additive strain decomposition. The material behaviour is described for the elastic part by isotropic homogeneous elasticity, and for visco-plasticity the dissipation potential is given by

$$\phi(\sigma) = \frac{k}{n+1}\left\langle \frac{\sigma_{eq} - \sigma_y}{k} \right\rangle^{n+1} = \frac{k}{n+1}\left\langle \frac{\sigma_{ex}}{k} \right\rangle^{n+1}. \tag{1}$$

with $\langle\cdot\rangle = \max(0, x)$. Here σ_{eq} is the equivalent stress which reads

$$\sigma_{eq} = \sqrt{\frac{3}{2} tr((\sigma - \chi)_D . (\sigma - \chi)_D)} \tag{2}$$

in which χ is the kinematic hardening which is defined later. $\sigma_{ex} = \sigma_{eq} - \sigma_y$ in equation 1 is the over-stress and σ_y is the yield stress. In addition, k and n in equation 1 are material parameters. The partial derivative of the dissipation potential ϕ with respect to σ leads to the equation for the inelastic strain rate

$$\dot{\epsilon}_{vp} = \frac{\partial \phi}{\partial \sigma} = \left\langle \frac{\sigma_{ex}}{k} \right\rangle^{n} \frac{\partial \sigma_{ex}}{\partial \sigma} \tag{3}$$

It should be pointed out that the over-stress σ_{ex} is the second invariant of the deviatoric stress tensor and reads the equation below.

$$\sigma_{ex} = \sigma_{eq} - \sigma_y - R = \sqrt{\frac{3}{2} tr((\sigma - \chi)_D . (\sigma - \chi)_D)} - \sigma_y - R \tag{4}$$

in which R is the isotropic hardening which is introduced in the following. The visco-plastic model allows for isotropic and kinematic hardening, which is considered in order to describe different specifications. Assuming $R(t)$ and $\chi(t)$ with $R(0) = 0$ and $\chi(0) = 0$ to describe isotropic and kinematic hardening respectively, these two are parametrised according to

$$\dot{R} = b_R(H_R - R)\dot{p} \tag{5}$$

and

$$\dot{\chi} = b_\chi(\frac{2}{3} H_\chi \frac{\partial \sigma_{eq}}{\partial \sigma} - \chi)\dot{p} \tag{6}$$

respectively. It should be mentioned that $\dot{p}$ is the visco-plastic multiplier rate given as:

$$\dot{p} = \left\langle \frac{\sigma_{ex}}{k} \right\rangle^n \tag{7}$$

which describes the rate of accumulated plastic strains. The parameter b_R indicates the speed of stabilization, whereas the value of the parameter H_R is an asymptotic value according to the evolution of the isotropic hardening. Similarly, the parameter b_χ denotes the speed of saturation and the parameter H_χ is the asymptotic value of the kinematic hardening variables. The complete model is stated in Table 1. Note that E represents the Young's modulus.

By gathering all the desired material parameters to identify into the vector $q = [\kappa\ G\ b_R\ b_\chi\ \sigma_y]$, where κ and G are bulk modulus and shear modulus, respectively, the goal is to estimate q given measurement displacement data, i.e.

$$u = Y(q) + \varepsilon \tag{8}$$

in which $Y(q)$ represents the measurement operator and ε the measurement (also possibly the model) error. Being an ill-posed problem, the estimation of q given u is not an easy task and requires regularisation. This can be achieved either in a deterministic or probabilistic setting. Here, the latter one is taken into consideration as further described in the text.

3 Bayesian identification

By acquiring additional (prior) knowledge on the parameter set next to the observation data, the probabilistic approach regularise the problem of estimating q with the help of Bayes's theorem

$$\pi_{q|u}(q|u) \propto L(q)\pi_q(q) \tag{9}$$

in which the likelihood $L(q)$ describes how likely the measurement data are given prior knowledge $\pi_q(q)$. This in turn requires the reformulation of the deterministic model into

Table 1: The constitutive model of Chaboche

Strain $\epsilon(t) = \epsilon_e(t) + \epsilon_{vp}(t)$
Hooke's Law $\sigma(t) = E : \epsilon_e(t)$
Flow Rule $\dot{\epsilon}_{vp}(t) = \langle \frac{\sigma_{eq}(t) - \sigma_y - R(t)}{k} \rangle^n \frac{\partial \sigma_{ex}}{\partial \sigma}$
Hardening $\dot{R} = b_R(H_R - R)\dot{p}$ $\dot{\chi} = b_\chi(\frac{2}{3} H_\chi \frac{\partial \sigma_{eq}}{\partial \sigma} - \chi)\dot{p}$
Initial Conditions $\epsilon_{vp}(0) = 0, \;\; R(0) = 0, \;\; \chi(0) = 0$
Parameters σ_y (Yield Stress) k, n (Flow Rule) b_R, H_R, b_χ, H_χ (Hardening)

the probabilistic one, and hence the propagation of material uncertainties through the model —the so-called forward problem— in order to obtain the likelihood [13].

The main difficulty in using equation 9 lies in computation of the likelihood. Various numerical algorithms can be applied, the most popular example of which are the Markov chain Monte Carlo methods. Being constructed on the fundamentals of the ergodic Markov theory, these methods are characterized by very slow convergence. To avoid this, the approximate method based on Kolmogorov́ definition of conditional expectation as already presented in [14] is considered here.

Let the material parameters q be modelled as random variables on a probability space $S := L_2(\Omega, \mathcal{B}, \mathbb{P})$. Here, Ω denotes the space of elementary events ω, $\mathcal{B}$ is the σ-algebra and $\mathbb{P}$ stands for the probability measure. This alternative formulation of Bayes's rule can be achieved by expressing the conditional probabilities in equation 9 in terms of conditional expectation. Following the mathematical derivation in [15, 16], this approach boils down to a quadratic minimisation problem:

$$q_a(\omega) = P_{Q_{sn}} q_f = \underset{\eta \in Q_{sn}}{\arg\min} \; \|q_f - \eta\|^2_{L_2}, \tag{10}$$

in which $P_{Q_{sn}}$ is the orthogonal projection operator of q_f onto the space of the new

information $Q_{sn} := \mathcal{Q} \otimes S_n$ where the space Q_{sn} is the space of the measurement.

Constraining the space of all functions to the subspace of linear maps, the minimisation problem in equation 10 leads to a unique solution K. Note that the projection is performed over a smaller space than Q_{sn}. An implication of this is that available information is not completely used in the process of updating, introducing an approximation error. This gives an affine approximation of equation 10

$$q_a(\omega) = q_f(\omega) + K(z(\omega) - u_f(\omega)), \tag{11}$$

also known as a linear Bayesian posterior estimate. Here, q_f represents the prior random variable, q_a is the posterior approximation, u_f is the forecasted measurement and K represents the very well-known Kalman gain

$$K := C_{q_f u_f}\big(C_{u_f} + C_\varepsilon\big)^{-1} \tag{12}$$

which can be easily evaluated if the appropriate covariance matrices $C_{q_f u_f}$, C_{u_f} and C_ε are known.

An advantage of equation 11 compared to equation 9 is that the inference in equation 11 is given in terms of RVs instead of conditional densities. Namely, $q_a(\omega)$, $q_f(\omega)$, $z(\omega)$ and $u_f(\omega)$ denote the RVs used to model the posterior, prior, observation, and forecasted observation, respectively.

In this light the linear Bayesian procedure can be reduced to a simple algebraic method. Starting from the functional representation of the prior

$$\hat{q}_f = \sum_\alpha q_f^{(\alpha)} \psi_\alpha(\omega) \tag{13}$$

where ψ_α is the Hermit function. Considering the proxy in equation 13, one may discretise 11 as:

$$Q_a = Q_f + K\big(Z - U_f\big), \tag{14}$$

where $Z \in \mathbb{R}^{L \times Z}$ are the PCE coefficient of the measurement. Here, K in equation 14 is the Kalman gain evaluated in an algebraic way knowing that

$$C_{q_f, u_f} = \sum_{\alpha > 0} \alpha!\; q_f^{(\alpha)} (u_f^{(\alpha)})^T. \tag{15}$$

Note that in the numerical computation $Q_f := [q_f(\omega_1), ..., q_f(\omega_Z)]$ is the PCE coefficient of the prior and $Q_a := [q_a(\omega_1), ..., q_a(\omega_Z)]$ is the PCE coefficient of the posterior with cardinality Z determined by $(L+1)$ RVs and polynomial order p. Here, the number $(L+1)$ subsumes all the RVs describing the prior and the RVs $\{\theta_i\}_{i=1}^L$ used to model the measurement error ε.

Table 2: The model parameters

κ	G	σ_y	n	k	b_R	H_R	b_χ	H_χ
1.66e9	7.69e8	1.7e8	1	1.5e8	50	0.5e8	50	0.5e8

4 Numerical results

The identification of the material constants in the Chaboche unified viscoplasticity model is a reverse process based on virtual data. In case of the Chaboche model the best way of parameters' identification is using the results of the cyclic tests, since more information can be obtained from virtual data rather than creep and relaxation tests, specifically information regarding hardening parameters. The aim of the parameter identification is to find a parameter vector q introduced in the previous section. The bulk modulus (κ), the shear modulus (G), the isotropic hardening coefficient (b_R), the kinematic hardening coefficient (b_χ) and the yield stress (σ_y) are considered as the uncertain parameters of the constitutive model.

Preliminary study is on a regular cube, modelled with one 8 node element, completely restrained on the back face, and with normal traction on the opposite (front) face. The magnitude of the normal traction and a stress in the plane of the front face is plotted in Figure 1. Purple and orange colours represent the stress value in normal and in plane directions, respectively. Considering the parameters listed in Table 2, the related σ-ϵ

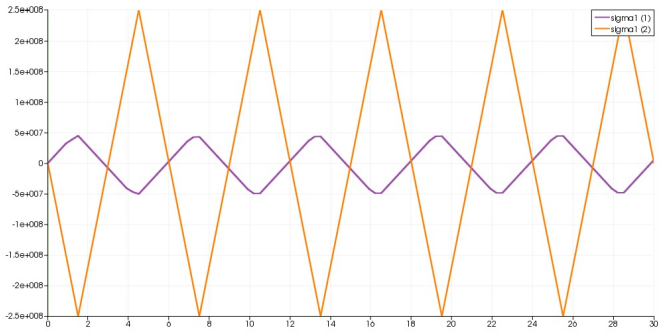

Figure 1: Decomposed applied force on node 6 according to time

hysteretic graph obtained which can be seen in Figure 2.

The displacements of a node on the front surface in normal and in plane directions are observed as the virtual data in this study. Applying stochastic identification and introducing likelihood in such a way that 10 percent of mean values are equal to the variance of the related parameter, the probability density function of prior and posterior of the identified parameters can be seen in Figure 3. From the sharpness of the posterior PDF of κ, G and σ_y, it can be concluded that enough information from virtual data is

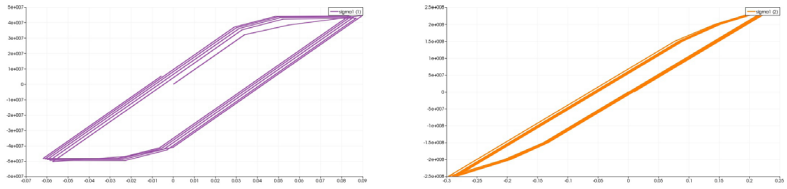

Figure 2: σ-ϵ for node on the front surface in plane and normal directions

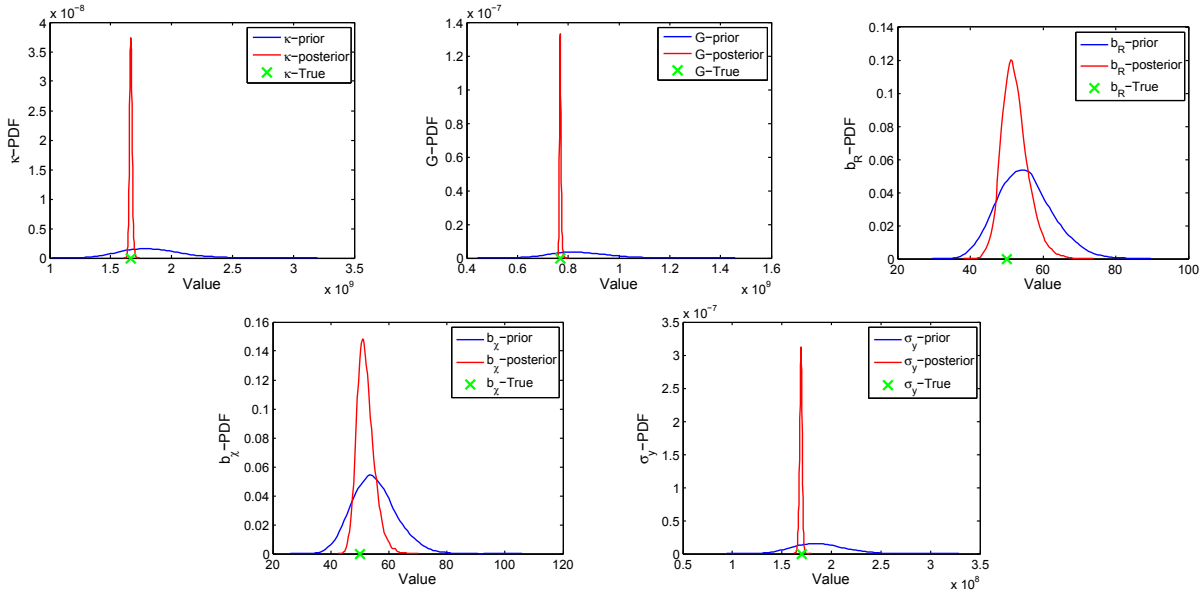

Figure 3: PDF of identified parameters

received and updating the parameters considering their uncertainty is done much easier than the hardening parameters. One reason that can be mentioned is that the process is not always in the states that hardening equations are involved like the elastic states. Therefore less information from the whole simulation can be analysed for estimating the hardening parameters and updating their parameters' uncertainties.

Summarising the results, the true values and the mean and variance of the estimated parameters are compared in Table 3.

5 Summary

Using the stochastic methods explained in section 3 to identify the model parameters of the Choboche model indicates that it is possible to identify the model parameters using Gauss-Markov Kalman filter. The parameters are well estimated and the uncertainty of the parameters is reduced while the probability density function of the parameters are updated during the process. The model is going to be developed by adding a damage model and then the efficiency of the methods used and their developments will also be studied in the near future.

Acknowledgment This work is partially supported by the DFG through GRK 2075.

Table 3: The identified model parameters

Parameters	q_{true}	q_{est}(mean)	q_{est}(standard deviation)
κ	1.66e9	1.66e9	1.13e7
G	7.69e8	7.68e8	3.47e6
b_R	50	52.36	3.71
b_χ	50	52.04	3.01
σ_y	1.7e8	1.69e8	1.35e6

REFERENCES

[1] A. Miller. *An Inelastic Constitutive Model for Monotonic, Cyclic, and Creep Deformation: Part I–Equations Development and Analytical Procedures*. J. Eng. Mater. Technol 98(2), 97-105 (1976).

[2] E. Krempl, J. J. McMahon, and D. Yao. *Viscoplasticity Based on Overstress with a Differential Growth Law for the Equilibrium Stress*. Mechanics of Materials 5, 3548 (1986).

[3] Korhonen, R. K., Laasanen, M. S., Toyras, J., Lappalainen, R., Helminen, H. J., Jurvelin, J. S. *Fibril reinforced poroelastic model predicts specifically mechanical behavior of normal, proteoglycan depleted and collagen degraded articular cartilage*. J Biomech 36, 1373-1379.

[4] Michel Aubertin, Denis E. Gill and Branko Ladanyi. *A unified viscoplastic model for the inelastic flow of alkali halides*. Mechanics of Materials 11 (1991) 63-82.

[5] K.S. Chan a, S.R. Bodner a,l, A.F. Fossum b and D.E. Munson. *A constitutive model for inelastic flow and damage evolution in solids under triaxial compression*. Mechanics of Materials 14 (1992) 1-14.

[6] Chaboche,J. L. and Rousselier, G. *On the plastic and viscoplastic constitutive equations part 1: rules developed with internal variable concept*. J. Press. Vessel Technol., 1983, 105, 153158.

[7] Chaboche, J. L. and Rousselier, G. *On the plastic and viscoplastic constitutive equations part 2: application of internal variable concepts to the 316 stainless steel*. J. Press. Vessel Technol., 1983, 105, 159164.

[8] P. Kłosowski, A. Mleczek. *Parameters' Identification of Perzyna and Chaboche Viscoplastic Models for Aluminum Alloy at Temperature of* $120C$. Engng. Trans. 62, 3, 291305, 2014.

[9] Y. Gong,C. Hyde,W. Sun, and T. Hyde. *Determination of material properties in the Chaboche unified viscoplasticity model*. DOI: 10.1243/14644207JMDA273.

[10] T. Harth and Jürgen Lehn. *Identification of Material Parameters for Inelastic Constitutive Models Using Stochastic Methods*. GAMM-Mitt. 30, No. 2, 409 429 (2007).

[11] K. S. Chan, S. R. Bodner, and U. S. Lindholm. *Phenomenological Modelling of Hardening and Thermal Recovery in Metals*. Journal of Engineering Materials and Technology 110, 18 (1988).

[12] J. Velde. *3D Nonlocal Damage Modeling for Steel Structures under Earthquake Loading*. Department of Architecture, Civil Engineering and Environmental Sciences University of Braunschweig - Institute of Technology (2010).

[13] H. G. Matthies. *Uncertainty Quantification with Stochastic Finite Elements*. DOI: 10.1002/0470091355.ecm071.

[14] H. G. Matthies, E. Zander, B. V. Rosić, A. Litvinenko. *Bayesian Parameter Estimation via Filtering and Functional Approximations*. arXiv:1611.09293v1 [math.NA] 25 Nov 2016.

[15] H. G. Matthies, E. Zander, B. V. Rosić, A. Litvinenko. *Parameter Estimation via Conditional Expectation — A Bayesian Inversion*. arXiv:1606.09440v1 [math.PR] 30 Jun 2016.

[16] H. G. Matthies, E. Zander, B. V. Rosić, A. Litvinenko, Oliver Pajonk. *Inverse Problems in a Bayesian Setting*. DOI: 10.1007/978-3-319-27996-1-10.

[17] S. Ghahramani. *Fundamentals of probability, with stochastic processes*. 3rd ed. New Jersey, USA: Pearson, Prentice Hall, 2005.

XIV International Conference on Computational Plasticity. Fundamentals and Applications
COMPLAS XIV
E. Oñate, D.R.J. Owen, D. Peric & M. Chiumenti (Eds)

SPARSE BAYESIAN POLYNOMIAL CHAOS APPROXIMATIONS OF ELASTO-PLASTIC MATERIAL MODELS

Bojana Rosić and Hermann G. Matthies

Institute of Scientific Computing
Technische Universität Braunschweig
Mühlenpfordstrasse 23, 38106 Braunschweig, Germany
e-mail: bojana.rosic@tu-bs.de

Key words: sparse Bayesian inference, sparse polynomial chaos expansion, uncertainty quantification, spectral Kalman filtering, stochastic elastoplasticity, iterative spectral filter

Abstract. In this paper we studied the uncertainty quantification in a functional approximation form of elastoplastic models parameterised by material uncertainties. The problem of estimating the polynomial chaos coefficients is recast in a linear regression form by taking into consideration the possible sparsity of the solution. Departing from the classical optimisation point of view, we take a slightly different path by solving the problem in a Bayesian manner with the help of new spectral based sparse Kalman filter algorithms.

1 INTRODUCTION

Uncertainty quantification currently becomes the focus of many scientific areas, especially engineering ones, due to the presence of aleatoric and epistemic uncertanties in the models describing for example heterogeneous media, loadings, geometry, etc. Due to the rapid development of experimental devices and massive production of sensors, uncertainty quantification is also extensively used in the process of probabilistic solving of inverse problems, i.e. in the prediction step of the Bayesian inference, for example. However, most of the practically used methods are still based on some kind of sampling either in the process of solving the forward problem or estimation itself. The forward propagation of uncertainty usually employs a large number of determinic software calls. However, real time applications cannot afford this, as the estimation has to be performed under severe time constraints.

The focus of this paper is to show that both stages of Bayesian inference can be resolved in essentially the same manner—by resolving the corresponding inverse problem. Namely, the forward loop of Bayesian inference can be seen as an inverse problem in which the measurement data are given samples. Since the number of samples is usually much smaller than the number of parameters which describe the model response (i.e. random variables or their functional representative — polynomial chaos coefficients), the corresponding problem is ill-posed and thus has to be regularised. This can be done in a Bayesian setting similar to the process of estimation of model parameters given real measurement data. Such an approach turns out to be the generalisation of ℓ_1 and ℓ_2-norm optimisation problems by taking the appropriate priors on the approximation coefficients. However, the sparsity of the solution appearing in the ℓ_1 minimisation in the Bayesian point of view turns out to be computationally difficult, because the distributions in Bayes rule are not conjugate. To resolve this, the sparsity priors are usually assumed in a hierarchical setting such as the normal prior with Gamma distributed hyperparamers used in relevance vector machine approaches [5]. On the other hand, the stochastic search can be also done in a numerical Markov chain Monte Carlo (MCMC) setting [6], however, this can lead to high computational costs. Instead, in this paper the conditional expectation setting of Kolmogorov is used in order to estimate the unknown polynomial chaos coefficients of the solution. The methods were recently developed by the authors and formulated in a purely algebraic setting [1, 3]. Here, the approaches are extended to include the sparsity of the solution.

The paper is organised as follows: in Section 2 the model problem is introduced, Section 3 is discusses its functional approximation. Section 4 presents Bayesian regression, and the new approach is presented in Section 5. Finally, numerical results are depicted in Section 6.

2 MODEL PROBLEM

Let $(\Omega_\theta, \mathcal{B}_\theta, \mathbb{P}_\theta)$ be a probability space, in which Ω_θ denotes the space of all events, $\mathcal{B}_\theta$ is a σ-algebra of subsets of Ω_θ, and $\mathbb{P}_\theta$ is a probability measure. In the presence of material uncertainties, here assumed to have finite variance and belonging to $L_2(\Omega_\theta)$, the elastoplastic material model is described by an uncertain infinitesimal elastoplastic state $w(\omega) := (u(\omega), \boldsymbol{\varepsilon}_p(\omega), \eta(\omega))$ in which u denotes the displacements, $\boldsymbol{\varepsilon}_p$ is the plastic strain, and η is an internal variable. The state satisfies the equilibrium equation $\mathbb{P}_\theta$-almost surely, i.e.:

$$\begin{aligned} -\operatorname{div} \sigma(x,\omega) &= f(x,\omega) \quad \forall x \in \mathcal{G}_t, \\ \sigma(x,\omega) \cdot n(x,\omega) &= \sigma_N(x,\omega) \quad \forall x \in \Gamma_N, \\ u(x,\omega) &= u_0(x,\omega) \quad \forall x \in \Gamma_D, , \end{aligned} \tag{1}$$

with appropriate Dirichlet and Neumann boundary conditions implied on parts Γ_D and Γ_N of the piecewise smooth Lipschitz continuous boundary $\Gamma = \partial\mathcal{G}$ such that $\Gamma_D \subseteq \partial\mathcal{G}$ and $\Gamma_N \subset \partial\mathcal{G}$, respectively. For reasons of simplicity, the last ones are assumed to be deterministic.

The constitutive law for the elastic part is assumed to be of Hooke's type and is described by an uncertain isotropic homogeneous $C(\omega)$ constitutive tensor modelled via bulk $\kappa(\omega)$ and shear $G(\omega)$ moduli taken as independent positive definite lognormally distributed random variables. Finally, the rate of the plastic strain is assumed to follow the associative plastic flow rule $\dot{E}_p(x,\omega) \in N_{\mathscr{K}}(\Sigma(x,\omega))$ in which $N_{\mathscr{K}}(\Sigma(x,\omega))$ is the normal cone on the convex set of addmissible stresses $\mathcal{K}(\omega) = \{\Sigma(\omega) \mid \phi_{\mathcal{K}}(\Sigma(\omega)) \leq 0 \ \mathbb{P}_\theta \text{ a.s.}\}$ described by the von Mises yield function $\phi_{\mathcal{K}}$ with uncertain yield stress $\sigma_y(\omega)$ and the hardening variables $h(\omega)$ as arguments. Here, $E_p := (\boldsymbol{\varepsilon}_p, \eta)$ denotes the generalised plastic strain, and $\Sigma := (\sigma, \chi)$ stands for the generalised stress.

For computational purposes the problem given in Eq. (1) is rewritten on weak form following discussions in [2]. The goal is to estimate the state $w \in H^1(\mathcal{T}, \mathscr{Z})$ with $w(0) = 0$, its dual $w^* \in H^1(\mathcal{T}, \mathscr{Z}^*), w^*(0) = 0$ and $\dot{w} \in \mathscr{K}^\infty$ such that

$$a(w(t), z) + \langle\!\langle \dot{w}(t), z \rangle\!\rangle = \langle\!\langle f, \boldsymbol{z} \rangle\!\rangle \tag{2}$$

for all $z = (v, (\mu, \upsilon)) \in \mathscr{Z}$ and

$$\langle\!\langle \dot{w}, z^* - w^* \rangle\!\rangle \leq 0, \quad \forall z^* \in \mathscr{K} \subset \mathcal{Z}^*. \tag{3}$$

hold a.s. in Ω_θ and a.e. in $\mathcal{T}$. Here, and $\langle\!\langle \cdot, \cdot \rangle\!\rangle$ is the duality pairing given in terms of the mathematical expectation $\mathbb{E}(\langle \cdot, \cdot \rangle) = \int_{\Omega_\theta} \langle \cdot, \cdot \rangle \mathbb{P}_\theta(d\omega)$, and $\langle s_1, s_2 \rangle = \int_{\mathcal{G}} s_1 s_2 dx$. The existence and uniqueness are already studied by authors in [2], and will be not be discussed here. After time (by the implicit Euler) and spatial finite element disretisation, the formulation in Eq. (2)-Eq. (3) reduces to a nonlinear stochastic residual equation to be solved globally for the increment of the displacement $\Delta\boldsymbol{u}_n(\omega)$, and the first order variational inequality which corresponds to the constrained stochastic quadratic convex optimisation problem (the so-called closest point projection scheme) to be solved locally in each integration point of the finite element scheme and the stochastic space for the increments of the strain-like $\Delta\boldsymbol{E}_{pn}$ and the stress like $\Delta\boldsymbol{\Sigma}_n$ variables. These algorithms are very well known in the classical deterministic setting [9], albeit, their extension to the stochastic counterpart is not an easy task, see [2].

In this paper we would like to keep the deterministic algorithms per se, and to use them to estimate the statistics of random variables (fields) $\Delta\boldsymbol{w}_n(\omega)$ and $\Delta\boldsymbol{w}_n^*(\omega)$, i.e. moments

$$\mathbb{E}(\Delta\boldsymbol{w}_n^m) = \int_{\Omega_\theta} (\Delta\boldsymbol{w}_n(\omega))^m \mathbb{P}_\theta(d\omega), \quad \mathbb{E}((\Delta\boldsymbol{w}_n^*)^m) = \int_{\Omega_\theta} (\Delta\boldsymbol{w}_n^*(\omega))^m \mathbb{P}_\theta(d\omega) \tag{4}$$

non-intrusively. This matches with the high-dimensional numerical integration and the Monte Carlo type of algorithms. Due to their slow convergence rates, a large number of evaluation points (i.e. deterministic executions of the finite element code) are needed to achieve the desired accuracy. Therefore, to reduce the computational cost, here we consider the functional approximation algorithms as further described in the text.

3 FUNCTIONAL APPROXIMATION

Instead of integrating the functions $\boldsymbol{y} := \{\Delta \boldsymbol{w}_n, \Delta \boldsymbol{w}_n^*\}$ directly, one may approximate the integrand in Eq. (4) by some known elementary functions, the integration of which is algebraically computable. A typical example is the generalised polynomial chaos expansion

$$y(x,\omega) = \sum_{\alpha \in \mathcal{J}} y^{(\alpha)}(x) \Psi_\alpha(\boldsymbol{\theta}(\omega)) \tag{5}$$

in which Ψ_α are the multi-variate polynomials with the standard random variables $\boldsymbol{\theta}(\omega)$ as arguments, and x denotes the spatial position (i.e. the finite element node for displacements or the Gauss integration point for stress- and strain-like variables). Other kinds of approximation functions can be also used, however this will not be further discussed here. The random variables $\boldsymbol{\theta}(\omega)$ represent the parameterisation of existing uncertanties in model parameters. They are usually taken as independent, uncorrelated random variables of a simpler kind such as normal or uniform random variables corresponding to the Askey scheme as discussed in [10].

Given N samples of $y(x,\omega)$ one may rewrite Eq. (5) as a linear system of equations

$$y(x,\omega_i) = \sum_{\alpha \in \mathcal{J}} y^{(\alpha)}(x) \Psi_\alpha(\boldsymbol{\theta}(\omega_i)), \quad i = 1, ..., N \tag{6}$$

with $y^{(\alpha)}$ being unknown coefficients. Denoting $\boldsymbol{s} := [y(x,\omega_i)] \in \mathbb{R}^N$, $\boldsymbol{\Psi} := [\Psi_\alpha(\theta(\omega_i))] \in \mathbb{R}^{N \times P}$ and $\boldsymbol{v} := [y^{(\alpha)}(x)] \in \mathbb{R}^P$, one may rewrite the previous equation in a matrix-vector form

$$\boldsymbol{s} = \boldsymbol{\Psi} \boldsymbol{v} \tag{7}$$

which is equivalent to the more robust projected version

$$\boldsymbol{d} := \boldsymbol{\Psi}^T \boldsymbol{u} = \boldsymbol{\Psi}^T \boldsymbol{\Psi} \boldsymbol{v} =: \boldsymbol{W} \boldsymbol{v}. \tag{8}$$

The system in the previous equation or in Eq. (7) is quite often depicted as underdetermined, especially when one deals with very expensive solvers, i.e. finely discretised problems, for which $N < P$ with P being the cardinality of the polynomial expansion in Eq. (5). To tackle this problem, different kinds of regularisation

procedures are used in the literature, the most popular among which are the regularised least square (i.e. the Tikhonov regularisation)

$$\boldsymbol{v} = \arg\min \left(\frac{1}{2} \|\boldsymbol{W}\boldsymbol{v} - \boldsymbol{d}\|_2^2 + \frac{\lambda}{2} \|\boldsymbol{v}\|_2^2 \right) \tag{9}$$

and the basis pursuit denoising

$$\boldsymbol{v} = \arg\min \left(\frac{1}{2} \|\boldsymbol{W}\boldsymbol{v} - \boldsymbol{d}\|_2^2 + \frac{\lambda}{2} \|\boldsymbol{v}\|_1 \right) \tag{10}$$

methods, also known as ℓ_2 and ℓ_1 minimisation procedures. These consist of the squared error part used to enforce closeness of $\boldsymbol{v}$ to the data, and the regularisation term enforcing the smoothness of $\boldsymbol{v}$. To balance these two terms, the regularisation parameter λ is used. However, in general the regularisation parameter λ representing the noise variance is known to be an uneducated guess, and it is difficult to find the most optimal value. If $\lambda = 0$ both of problems are equivalent and correspond to the classical least squares procedure. If $\lambda > 0$, then the ℓ_1 minimisation is preferable here compared to the ℓ_2 minimisation as it promotes the sparisty of the solution. On the other hand, in a computational setting the ℓ_2 problem is easier to solve as the solution $\boldsymbol{v}$ is linear in the data $\boldsymbol{b}$ in contrast to the ℓ_1 minimisation. The objective function in Eq. (10) is convex but not differentiable and thus requires special methods such as subgradient methods [8]. In computational practice the problem in Eq. (10) is transformed to the quadratic convex optimisation with linear inequality constraints, which can be solved by interior point methods. On the other hand, in order to be able to recover the sparse solution, the sensing matrix $\boldsymbol{W}$ in Eq. (10) has to satisfy the so-called restricted isometry property [11], which is usually not the case. To ensure this, the principle of random projections [12] is used, such that the $\boldsymbol{d}$ in Eq. (8) is projected onto a basis that consists of random linear combination of basis functions in $\boldsymbol{\Psi}$, i.e. the problem given in Eq. (8) is rewritten to

$$\boldsymbol{b} := \boldsymbol{W}\boldsymbol{d} = \boldsymbol{W}\boldsymbol{\Psi}^T\boldsymbol{\Psi}\boldsymbol{v} = \boldsymbol{A}\boldsymbol{v} \tag{11}$$

in which $\boldsymbol{W}$ denotes the carefully chosen random sensing matrix. This problem will be considered further instead of the one in Eq. (8).

4 BAYESIAN REGRESSION

In this paper the generalisation of the regularisation approach will be considered. The method relies on the probabilistic view of Eq. (8), in which the coefficients are assumed to be unknown, and hence priorly modelled as independent random variables $\boldsymbol{v}_f$ in $(\Omega_\xi, \mathcal{B}_\xi, \mathbb{P}_\xi)$,with the joint probability density function (pdf) given as

$$p_f(\boldsymbol{v}) = \prod_{\alpha \in \mathcal{J}} p(v^{(\alpha)}) \tag{12}$$

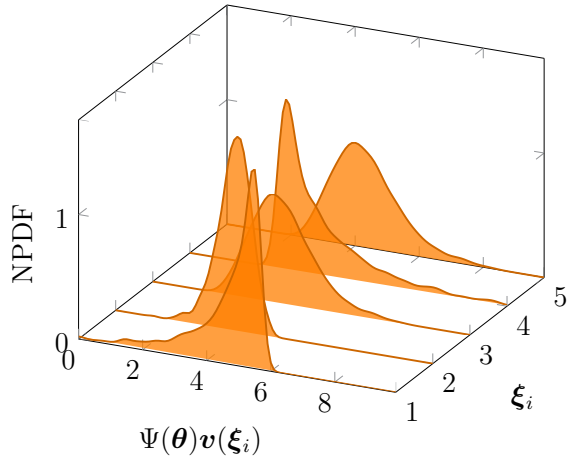

Figure 1: The stochastic version of the polynomial chaos expansion. Each realisation represents the pdf of the expansion given one realisation of the coefficient

with $p(v^{(\alpha)})$ being the pdf of individual parameters. Following this, the linear system in Eq. (8) becomes uncertain and is described by prediction:

$$\boldsymbol{b}_f(\xi) = \boldsymbol{A}\boldsymbol{v}_f(\xi). \tag{13}$$

This can be seen in Fig. 1, in which the schematic representation of the stochastic version of the polynomial chaos expansion from Eq. (8) is depicted.

The pdf of the coefficients can be further updated given data via Bayes's rule

$$\pi(\boldsymbol{v}|\boldsymbol{b}) \sim p(\boldsymbol{b}|\boldsymbol{v})p_f(\boldsymbol{v}) \tag{14}$$

in which $\pi(\boldsymbol{v}|\boldsymbol{b})$ denotes the posterior density, $p(\boldsymbol{b}|\boldsymbol{v})$ corresponds to the likelihood, and $p_f(\boldsymbol{v})$ is the prior. Assuming that the prior is normally distributed

$$p_f(\boldsymbol{v}) \sim \exp\left(-\frac{1}{2}\|\boldsymbol{v}\|_2^2\right) \tag{15}$$

as well as the likelihood, the posterior pdf obtains the form

$$\pi(\boldsymbol{v}|\boldsymbol{b}) \sim \exp\left(-\frac{1}{2}\|\boldsymbol{A}\boldsymbol{v}-\boldsymbol{b}\|_2^2\right)\exp\left(-\frac{1}{2}\|\boldsymbol{v}\|_2^2\right) \tag{16}$$

Its maximum aposteriori (MAP) estimate is the minimiser of the objective function given in Eq. (9). Under the same assumptions, only taking the prior to follow the Laplace distribution

$$p_f(\boldsymbol{v}) \sim \exp\left(-\frac{1}{2}\|\boldsymbol{v}\|_1\right), \tag{17}$$

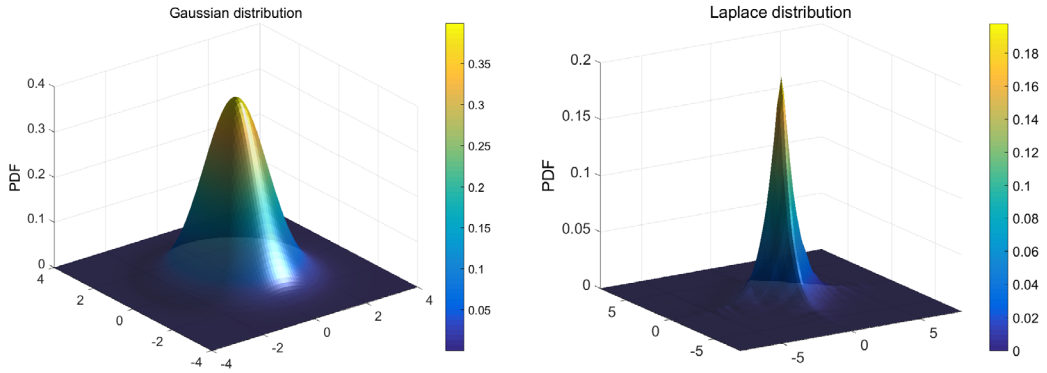

Figure 2: The Gaussian (left) and Laplace (right) probability distributions

one may show that the posterior MAP estimate is the minimiser of the objective function given in Eq. (10).

Similar to the deterministic setting, the process of computing the posterior distribution given the Gaussian prior is easier than in the Laplace case. The reason is that in the former case the prior and the likelihood are conjugate, whereas in the latter case they are not. Hence, the posterior corresponding to the ℓ_1 minimisation cannot be estimated algebraically, but only using some of the sampling based approaches such as the Markov chain Monte Carlo algorithm. To avoid this, one may consider a hierarchical type of prior which mimics the Laplace behaviour, but it is easier to evaluate. Following [5], one may model the polynomial chaos coefficients by normal distribution

$$p(\boldsymbol{v}|\boldsymbol{w}) = \prod_{\alpha} \mathcal{N}(0, w_{\alpha}^{-1}) \tag{18}$$

with zero mean and the precision (inverse variance) $\boldsymbol{w}$ that follows the Gamma distribution. The posterior distribution is then represented as

$$p(\boldsymbol{v}, \boldsymbol{w}|\boldsymbol{y}) \propto p(\boldsymbol{y}|\boldsymbol{v}, \boldsymbol{w}) p(\boldsymbol{v}|\boldsymbol{w}) p(\boldsymbol{w}) \tag{19}$$

and cannot be computed analytically. Therefore, the posterior is re-written as

$$p(\boldsymbol{v}, \boldsymbol{w}|\boldsymbol{y}) = p(\boldsymbol{v}|\boldsymbol{y}, \boldsymbol{w}) p(\boldsymbol{w}|\boldsymbol{y}) \tag{20}$$

in which the first term $p(\boldsymbol{v}|\boldsymbol{y}, \boldsymbol{w})$ follows the normal posterior distribution, whereas the second term is approximated by the delta function at its mode. The latter corresponds to the maximisation of the marginal likelihood as presented in [5]. However, this kind of approach relies on the hierarchical estimation in which the marginalisation over the hyperparameters have to be introduced, which in this paper will be avoided.

5 COMPRESSIVE SENSING SPRECTRAL KALMAN FILTER

To allow for the algebraic evaluation of the posterior, this paper considers a more fundamental Kolmogorov's approach to estimation. The method is based on the definition of the conditional expectation as a projection onto the subspace generated by the σ-algebra of data:

$$\mathbb{E}(\boldsymbol{v}|\boldsymbol{b}) = P_{\sigma(\boldsymbol{b})}\boldsymbol{v} \tag{21}$$

Being an orthogonal projection, the conditional expectation matches the minimum mean square estimate [1, 3]

$$\min \mathbb{E}(\|\boldsymbol{v} - \mathbb{E}(\boldsymbol{v}|\sigma(\boldsymbol{b})\|^2) \tag{22}$$

which according to [1] implies an orthogonal decomposition

$$\boldsymbol{v} = P_{\sigma(\boldsymbol{b})}\boldsymbol{v} + (I - P_{\sigma(\boldsymbol{b})})\boldsymbol{v}. \tag{23}$$

However, as $P_{\sigma(\boldsymbol{b})}\boldsymbol{v}$ is difficult to compute directly, one may further refer to the Doob-Dynkin lemma and search for an optimal map, i.e. a measurable function φ such that

$$\mathbb{E}(\boldsymbol{v}|\sigma(\boldsymbol{b})) = P_{\sigma(\boldsymbol{b})}\boldsymbol{v} = \varphi(\boldsymbol{b})$$

holds. Therefore, Eq. (23) becomes

$$\boldsymbol{v} = \varphi(\boldsymbol{b}) + (\boldsymbol{v} - \varphi(\boldsymbol{b})). \tag{24}$$

The first term is the projection and is altered by data, whereas the remaining orthogonal part stays unchanged, i.e. described by our prior knowledge. This finally leads to the filtering formula:

$$\boldsymbol{v}_a(\xi) = \boldsymbol{v}_f(\xi) + (\varphi(\boldsymbol{b}) - \varphi(\boldsymbol{b}_f(\xi))). \tag{25}$$

Assuming that the optimal map φ is linear, the formula reduces to the so-called Gauss-Markov-Kalman filter

$$\boldsymbol{v}_a(\xi) = \boldsymbol{v}_f(\xi) + \boldsymbol{K}(\boldsymbol{b} - \boldsymbol{b}_f(\xi)), \tag{26}$$

a generalisation of the classical Kalman filter form. For more details please see [1, 3]. Here, the factor $\boldsymbol{K}$ is the Kalman gain

$$\boldsymbol{K} = \mathrm{cov}_{\boldsymbol{v}_f,\boldsymbol{b}_f}(\mathrm{cov}_{\boldsymbol{b}_f} + \mathrm{cov}_{\varepsilon})^{\dagger} \tag{27}$$

with † denoting the pseudo-inverse, and the covariance functions defined as

$$\mathrm{cov}_{q,y} := \mathbb{E}\left((q - \mathbb{E}(q)) \otimes (y - \mathbb{E}(y))\right). \tag{28}$$

The modelling error ε is here introduced as an additional term representing the error of the truncated approximations in Eq. (11).

The linear filter as presented previously will not be optimal in the nonlinear case. To better account for nonlinearity, one may use higher order polynomial approximations as in [1], or turn to the iterative version of Eq. (26). The latter one approximates the nonlinear measurement operator $Y(\boldsymbol{v})$ in $\boldsymbol{b} := Y(\boldsymbol{v}) + \varepsilon$ by [4]

$$Y_\lambda(\boldsymbol{v}) = \boldsymbol{M}(\boldsymbol{v} - \check{\boldsymbol{v}}) + \boldsymbol{a} = M\tilde{\boldsymbol{v}} + \boldsymbol{a} \tag{29}$$

in which $\tilde{\boldsymbol{v}} := \boldsymbol{v} - \check{\boldsymbol{v}}$ (also known as the fluctuating part of the random variable $\boldsymbol{v}$ when $\check{\boldsymbol{v}} := \mathbb{E}(\boldsymbol{v})$) and $\boldsymbol{M}$ is the linear measurement matrix. Then, following [4], one may design the iterative formula:

$$\boldsymbol{v}_a^{(i+1)} \;=\; \boldsymbol{v}_f + \boldsymbol{K}_\lambda^{(i)}(\boldsymbol{b} - \boldsymbol{a}^{(i)} - \boldsymbol{M}^{(i)}(\boldsymbol{v}_f - \check{\boldsymbol{v}}^{(i)}) - \varepsilon). \tag{30}$$

Here, $\boldsymbol{M}^{(i)}$ and $\boldsymbol{a}^{(i)}$ denote either the exact Jacobian and $\boldsymbol{a} := Y(\mathbb{E}(\boldsymbol{v}_f))$, or the inexact Jacobian and $\boldsymbol{a} := \mathbb{E}(Y(\boldsymbol{v}_f))$ in case of an unbiased estimate [4].

The previously described filtering formulas become especially interesting when considered in the functional approximation setting. Instead of sampling, the random variables of interest in Eq. (26) or Eq. (30) can be represented by the polynomial chaos approximations similar to those given in Eq. (5). This leads to the purely deterministic (algebraic) filtering formula:

$$\sum_{\beta\in\mathcal{I}} \boldsymbol{v}_a^{(\beta)}\Gamma_\beta(\xi) = \sum_{\beta\in\mathcal{I}} \boldsymbol{v}_f^{(\beta)}\Gamma_\beta(\xi) + \boldsymbol{K}(\sum_{\beta\in\mathcal{I}} \boldsymbol{b}^{(\beta)}\Gamma_\beta(\xi) - \sum_{\beta\in\mathcal{I}} \boldsymbol{b}_f^{(\beta)}\Gamma_\beta(\xi)) \tag{31}$$

in which Γ denote the polynomials corresponding to the distribution on the polynomial chaos coefficients, and are not necessarily same as Ψ. Note that the first term in the innovation part corresponds to the deterministic measurements, and hence has only non-zero mean. By projecting the formula onto the polynomial basis Γ_β one obtains

$$\mathbf{v}_a = \mathbf{v}_b + \mathbf{K}(\mathbf{b} - \mathbf{b}_f) \tag{32}$$

in which $\mathbf{v}_f := [\boldsymbol{v}_f^{(\beta)}]_{\beta\in\mathcal{I}} = [v_f^{(\alpha,\beta)}]_{\alpha\in\mathcal{J},\beta\in\mathcal{I}}$. Similarly, the Kalman gain $\mathbf{K}$ can be computed using the algebraic expression for the covariance matrix

$$\boldsymbol{C}_{v_f} = \mathbb{E}_\xi((\hat{\boldsymbol{v}}_f - \bar{\boldsymbol{v}}_f) \otimes (\hat{\boldsymbol{v}}_f - \bar{\boldsymbol{v}}_f)) = \sum_{\alpha,\beta\in\mathcal{J}_p} \mathbb{E}_\xi(\Gamma_\alpha\Gamma_\beta)\boldsymbol{v}_f^{(\alpha)} \otimes \boldsymbol{v}_f^{(\beta)} - \bar{\boldsymbol{v}}_f \otimes \bar{\boldsymbol{v}}_f \tag{33}$$

in which $\bar{\boldsymbol{v}}_f := \mathbb{E}_\xi(\boldsymbol{v}_f)$. The last relation can be further rewritten in a matrix form as

$$\boldsymbol{C}_{v_f} = \tilde{\boldsymbol{V}}_f \boldsymbol{\Delta} \tilde{\boldsymbol{V}}_f^T \tag{34}$$

in which $(\boldsymbol{\Delta})_{\alpha\beta} = \mathbb{E}_\xi(\Gamma_\alpha\Gamma_\beta) = \mathrm{diag}(\alpha!)$ and $\tilde{\boldsymbol{V}}_f$ is equal to $\boldsymbol{v}_f := (..., \boldsymbol{v}_f^{(\alpha)}, ...)^T$ without the mean part. In a similar manner one derives algebraic formula for the iterative filter.

The filter in Eq. (32) does not lead to the sparse solution, as only the ℓ_2 minimisation is performed. To allow for the sparsity of the solution, one solves

$$\begin{aligned} \min \quad & \mathbb{E}(\|\boldsymbol{v} - \mathbb{E}(\boldsymbol{v}|\sigma(\boldsymbol{b}))\|^2) \\ \text{such that} \quad & \|\mathbb{E}(\boldsymbol{v}|\sigma(\boldsymbol{b}))\|_1 \leq \epsilon \end{aligned} \tag{35}$$

The inequality in Eq. (35) is nonlinear, and its subgradient can be rewritten as the pseudo-measurement equation

$$\boldsymbol{Z}(\boldsymbol{v}) := H(\boldsymbol{v})\boldsymbol{v} - \epsilon = 0 \tag{36}$$

instead of Eq. (22). Here, $H(\boldsymbol{v}) := \mathrm{sign}(\boldsymbol{v})$, and ϵ is the given tolerance with the covariance $\boldsymbol{C}_\epsilon$ chosen as the regularisation parameter. The computational algorithm consists of a sequential estimation in which the first update is obtained by using the real measurement and Eq. (26), and the second by using the pseudo-one and the iterative formula in Eq. (30).

6 NUMERICAL RESULTS AND CONCLUSIONS

The algorithm as described previously is tested on Cook's membrane benchmark problem in five loading steps (two of which are plastic). The three material parameters (bulk and shear moduli, as well as yield stress) are modelled as independent lognormally distributed random variables, and the response is approximated by Hermite polynomial chaos expansion of fourth order leading to 35 polynomial coefficients. The approximation is computed by using 15 random evaluation points, and its accuracy is tested against the result obtained given 1e4 Monte Carlo simulations. As depicted in Fig. 3, for the last time increment the error in both stress and strain variables is low. Hence, the Bayesian method can catch the sparsity of the solution. However, the error in strain-like variables is slightly higher. The reason lies in the polynomial chaos basis which does not change in time. This can be seen in Fig. 4, where clearly the approximation error increase with time.

According to the previous results, the suggested methods seem to be promissing, and they will be further analysed with respect to the adaptivity of the polynomial chaos scheme.

Acknowledgment: This project is partially funded by DFG.

REFERENCES

[1] H. G. Matthies, E. Zander, B. Rosić and A. Litvinenko. Parameter Estimation via Conditional Expectation: A Bayesian Inversion, *Advanced Modeling and Simulation in Engineering Sciences*, available online, 2016

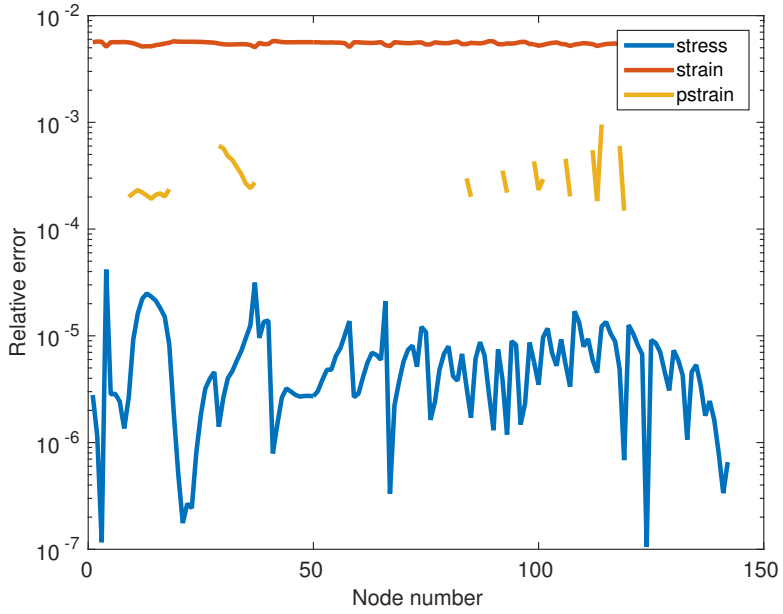

Figure 3: Relative error of approximated solutions across the finite element nodes

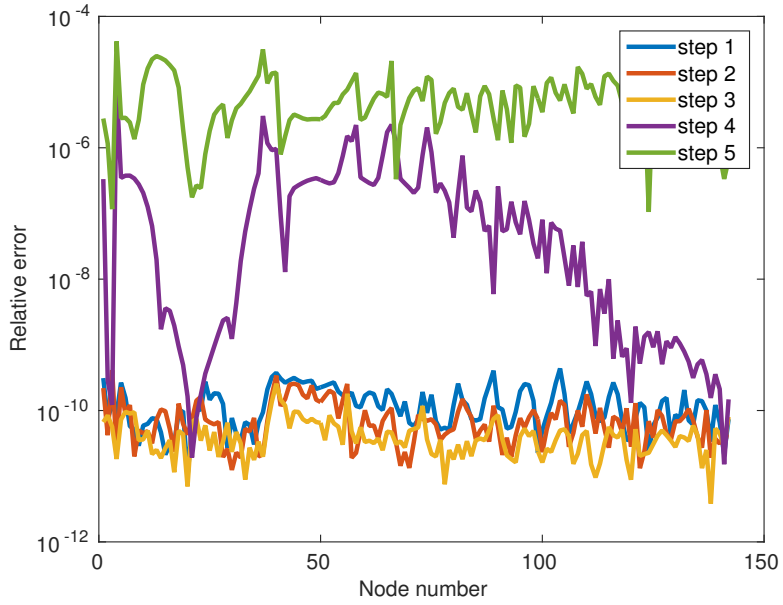

Figure 4: The change of relative error of approximated stress across the finite element nodes and in time

[2] B. Rosić and H. G. Matthies. Variational Theory and Computations in Stochastic Plasticity. *Archives of Computational Methods in Engineering*, 22 (3): 457-509, 2015

[3] B. Rosić, A. Kučerová, J. Sýkora, O. Pajonk, A. Litvinenko and H. G. Matthies. Parameter Identification in a Probabilistic Setting. *Engineering Structures*, 50: 179–196, 2013

[4] B. Rosić. A spectral iterative filter based on conditional expectation for non-linear parameter estimation, submitted, 2017

[5] M. E. Tipping. Sparse Bayesian Learning and the Relevance Vector Machine. *Journal of Machine Learning Research*. 1: 211–244, 2001

[6] X. Chen, Z. Jane Wang, M. J. McKeown. A Bayesian Lasso via reversible-jump MCMC. *Signal Processing*, 91:1920–1932, 2011

[7] K. Koh, S.-J. Kim, and S. Boyd. An Interior-Point Method for Large-Scale l1-Regularized Logistic Regression. *Journal of Machine Learning Research*, 8:1519-1555, 2007.

[8] D. A. Lorenz, M. E. Pfetsch and A. M. Tillmann. Solving Basis Pursuit: Subgradient Algorithm, Heuristic Optimality Check, and Solver Comparison. *ACM Transactions on Mathematical Software*, 41(2), 2015

[9] J. C. Simo and T. R. Hughes. *Computational Inelasticity*. Springer, 1998

[10] D. Xiu and G. Em Karniadakis. The Wiener–Askey Polynomial Chaos for Stochastic Differential Equations. *SIAM J. Sci. Comput.*, 24(2), 619–644, 2002

[11] A. M. Tillmann and M. E. Pfetsch, The Computational Complexity of the Restricted Isometry Property, the Nullspace Property, and Related Concepts in Compressed Sensing," IEEE Trans. Inf. Th., 60(2): 1248–1259 (2014)

[12] D. L. Donoho, Compressed sensing, *IEEE Trans. Information Theory*, vol. 52, no. 4, pp. 1289–1306, Apr. 2006.

XIV International Conference on Computational Plasticity.
Fundamentals and Applications
COMPLAS 2017
E. Oñate, D.R.J. Owen, D. Peric and M. Chiumenti (Eds)

NUMERICAL ANALYSIS OF DESICCATION, SHRINKAGE AND CRACKING IN LOW PLASTICITY CLAYEY SOILS

HECTOR U. LEVATTI*, PERE C. PRAT† & ALBERTO LEDESMA†

* Division of Civil & Building Services Engineering (CBEA), London South Bank University, 103 Borough Road, SE10AA, London, UK
† Dept. of Civil and Environmental Engineering, UPC-BarcelonaTech, Barcelona, Spain

Abstract. This paper presents a numerical study of the desiccation processes of low-plasticity clayey soils that usually result in shrinkage and often in cracking. For the theoretical development of the numerical model, concepts of Unsaturated Soils Mechanics and of classical Strength of Materials are used as a framework for formulating phenomena such as water flow in deformable porous media and cracking. The mathematical formulation of the problem and its implementation in a hydro-mechanical coupled model is presented, in order to simulate fluid flow and cracking in soils, for which the FEM and the node release technique is combined. The code developed has been used to perform several numerical analyses on radial sections of cylindrical soil specimens subjected to a drying process for which experimental laboratory data was available. The objective of these simulations is to determine the mechanisms by which the soil shrinks and cracks during desiccation. The results show the capabilities of the approach to reproduce the main features of the problem, with desiccation, shrinkage, and cracking being reproduced consistently during a desiccation cycle. The model also highlights the key role of the displacement and suction boundary conditions in the development of cracks as a consequence of tensile stress fields. Finally, the model has revealed the necessity of further research in the study of the soil-container and soil-atmosphere interaction in order to reproduce with more accuracy the changes in the main variables.

Key words: cracking, desiccation, shrinkage, flow in deformable porous media, fracture, numerical simulation.

1 INTRODUCTION

The topic of drying cracks in soils has been the object of considerable experimental research, and many significant contributions have been made in recent decades. However, until the development of Unsaturated Soil Mechanics, the problem has not received proper theoretical research taking into account the parameters that govern the behavior of soil in the unsaturated state, mainly suction. Tensile strength, which is suction dependent, and fracture toughness are shown to be also relevant parameters if the initiation and propagation of the cracks have to be studied.

The main variables involved in this problem are the temperature and relative humidity of the environment, but several other factors are involved in the process. In laboratory tests, specimen size, soil-container type of contact, drying rate and specimen's characteristics (such as heterogeneity, anisotropy, imperfections, water content, particle size, tensile strength or fracture toughness) condition how cracking develops. In the field, the soil's fabric, position of

the water table, wind velocity, solar radiation, etc. need also to be considered.

When the soil is dried under laboratory conditions or in an environmental chamber, the first cracks that can be seen on the top surface of the specimen are usually boundary cracks that start at the interface between the soil mass and the container wall. These cracks propagate until the entire soil mass is separated from the wall. During the propagation of this boundary cracks, other cracks may appear in the middle of the specimen. These cracks may initiate at the top or bottom surfaces, or at the middle of the specimen, and propagate simultaneously with the first ones.

Crack formation and propagation in drying soils is a coupled thermo-hydro-mechanical process (not considering the chemical processes that may also take place). However, in the present work and in order to simplify the analysis the thermal component is left out, assuming that the process is isothermal.

The main objective of the numerical analysis is to reproduce the time evolution of the recorded variables (suction, water content, and deformation) during laboratory tests performed in recent years [1, 2] and to estimate the stress evolution before and after the initiation of the cracks. The numerical analysis is carried to simulate the formation and propagation of the first crack, which usually appears at the soil-container interface and initiates from the upper external surface of the specimen and propagates toward the bottom along the interface.

2 NUMERICAL MODEL

The model was formulated assuming that the process of desiccation and cracking take place mainly in unsaturated conditions. In the unsaturated porous medium, the equilibrium equation in terms of the total stresses is:

$$\nabla \cdot (\boldsymbol{\sigma} - u_a \mathbf{1}) + \nabla u_a + \rho \mathbf{g} = \mathbf{0} \tag{1}$$

which is an elliptic partial differential equation where $\boldsymbol{\sigma}(\mathbf{x}, t)$ is the total stress tensor, $(\boldsymbol{\sigma} - u_a \mathbf{1})$ is the net stress tensor, u_a is the air pore pressure, ρ is the average density of the multiphase medium (soil, water and air) and $\mathbf{g}$ is the gravity vector.

The stress-strain relation used in the present model can be written as

$$d\boldsymbol{\sigma} = \mathbf{D}(d\boldsymbol{\varepsilon} - d\boldsymbol{\varepsilon}^s) = \mathbf{D}\left(d\boldsymbol{\varepsilon} + \mathbf{m}\frac{du_w}{3K_t^s}\right) \tag{2}$$

where $d\boldsymbol{\sigma}$ is the increment of the total stress tensor, $\mathbf{D}$ in the elastic tangent stiffness matrix, $d\boldsymbol{\varepsilon}$ and $d\boldsymbol{\varepsilon}^s$ are the total and suction related infinitesimal deformations, u_w is the suction or negative pore water pressure, K_t^s is the suction modulus and $\mathbf{m} = (1 \quad 1 \quad 1 \quad 0 \quad 0 \quad 0)^T$ is the identity tensor in vector form.

The generalized Darcy's law for unsaturated soils, which is the constitutive equation for the flow problem, is written as

$$\mathbf{q} = -\mathbf{K}(S_r) \cdot (\nabla u_w - \rho^w \mathbf{g}) \tag{3}$$

where $\mathbf{q}$ is Darcy's velocity vector; ∇u_w is the porewater pressure gradient; $\mathbf{K}(S_r)$ is the permeability tensor which depends on the saturation degree (S_r); and ρ^w is the water density.

The fluid mass balance equation is

$$\nabla \cdot (\rho^w \mathbf{q}) + \frac{\partial}{\partial t}(\rho^w n S_r) = 0 \tag{4}$$

For the present formulation, it is assumed that the air flow is produced without friction and without phase changes. After the application of the finite element method, the system of partial differential equations (1) that emerges can be written in matrix notation as:

$$\begin{bmatrix} \mathbf{0} & \mathbf{0} \\ \mathbf{0} & \mathbf{H} \end{bmatrix} \begin{bmatrix} \overline{\mathbf{u}} \\ \overline{\mathbf{p}} \end{bmatrix} + \begin{bmatrix} \mathbf{K}_\mathrm{T} & \mathbf{Q}_\mathrm{T} \\ \mathbf{P} & \mathbf{S} \end{bmatrix} \begin{bmatrix} \frac{\partial \overline{\mathbf{u}}}{\partial t} \\ \frac{\partial \overline{\mathbf{p}}}{\partial t} \end{bmatrix} = \begin{bmatrix} \frac{\partial \mathbf{f}^u}{\partial t} \\ \mathbf{f}^p \end{bmatrix} \tag{5}$$

where $\overline{\mathbf{u}}$ is the nodal displacement vector; $\overline{\mathbf{p}}$ is the nodal porewater pressure vector; $\mathbf{H}$ is the diffusion matrix; $\mathbf{K}_T$ is the mechanical stiffness matrix; $\mathbf{S}$ is the storage matrix; $\mathbf{Q}_T$ and $\mathbf{P}$ are coupling matrices between the mechanical and hydraulic problems; and $\mathbf{f}^u$ and $\mathbf{f}^p$ are the external nodal displacement and flow vectors respectively. The Dirichlet boundary conditions of this problem are written in terms of suction and displacements.

3 SIMULATION OF A TEST ON A 80×20 CYLINDRICAL SAMPLE

Several cylindrical specimens of clayey soils were tested at the laboratory to study the problem of desiccation. The sizes of the specimens were 40/80 cm in diameter and 10/20 cm height. The tests were performed in laboratory conditions or in an environmental chamber [3].

The simulation of the desiccation of a 2D radial section (40×20 cm) of an 80×20 cylindrical specimen is presented (Figure 1). This simulation reproduces the initiation and propagation of a crack between the soil and the container on the right lateral edge of the specimen which is typically the first crack to appear in the experiments. The suction boundary condition is applied to the top of the section and the displacement boundary conditions are applied to the right and bottom edges. The left edge of the radial section is the axis of symmetry of the specimen.

The formation of cracks at the soil-container interface is justified by the presence of tensile stresses larger than the tensile strength of the soil, which depends on moisture content. The crack propagates from the top to the bottom of the container. Although the direction of propagation in terms of the maximum principal stress would have to be roughly calculated, vertical propagation was simulated. To simulate crack propagation, the node separation technique has been applied, which modifies the boundary conditions as the tensile strength of the soil is reached. In the numerical simulation, the condition for the first crack was reached during the first day. Although in the laboratory experiments the start of cracking in the 80×20 specimen occurred on day 8, with the 80/40×10 cm specimens the first crack appeared between days 1 and 10. This shows that the variability in the initial cracking time is very large and the repeatability of the tests and cracking start times cannot be guaranteed neither in the laboratory nor in the numerical simulations.

It has been possible to simulate quite accurately the evolution of the moisture content and of shrinkage of the soil due to desiccation. Also, the simulations of the specimen's shrinkage agree quite well with the experimental observations.

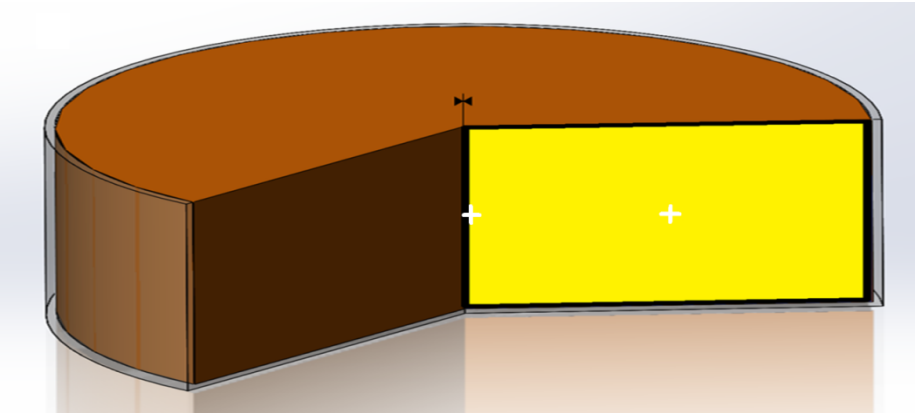

Figure 1 – 80×20 cylindrical specimen with the radial section (40×20 cm, yellow) used in the numerical simulation of the desiccation process. The two reference points are shown with the white crosses.

Although there were some small temperature fluctuations in the laboratory during the experiments, the process can be assumed to be isothermal. The relative humidity during the laboratory tests was maintained around 40% for most of the test. In the simulation, a constant suction equal to 60 MPa has been imposed on the boundary exposed to the atmosphere. This value has allowed the best possible adjustment although it can be considered a somewhat low value compared to what was measured in the laboratory which reached 100 MPa.

Figure 2 shows the evolution of the suction field during the 120 days of the simulation. It is assumed in this case that there is no adherence between the soil and the bottom of the container, although the separation from the container is prevented. Thus, once the crack reaches the bottom of the container there is no possibility that other cracks will form. The propagation of the crack has been fast because the tensile stress conditions rapidly exceeded the tensile strength, which is consistent with the tests.

The tensile strength depends largely on the moisture content of the soil. The following equation, that governs the initiation of the crack [4], has been adopted:

$$\sigma_t = -0.0191w^2 + 0.6874w - 2.88 \tag{6}$$

where σ_t is the tensile strength and w is the moisture content of the soil.

The dimensions of the cracks in the simulations correspond also well with the dimensions obtained in the laboratory. Crack formation and propagation modifies the normal stress field and how it changes with time.

Figure 3 shows the evolution of the moisture content and of suction during the test at the reference points shown in Figure 1.

Table 1 summarizes the parameters used in the simulation. A fairly small permeability is needed, but it does not deviate too far from the usual values for clays.

Table 2 lists the parameters of the water retention curve for the used soil [4] obtained using the van Genuchten function [5]:

$$S_r = \left[1 + \left(\frac{s}{P_0 \cdot f_n}\right)^{\frac{1}{1-\lambda}}\right]^{-\lambda} \qquad f_n = \exp[-\eta(n - n_0)] \tag{7}$$

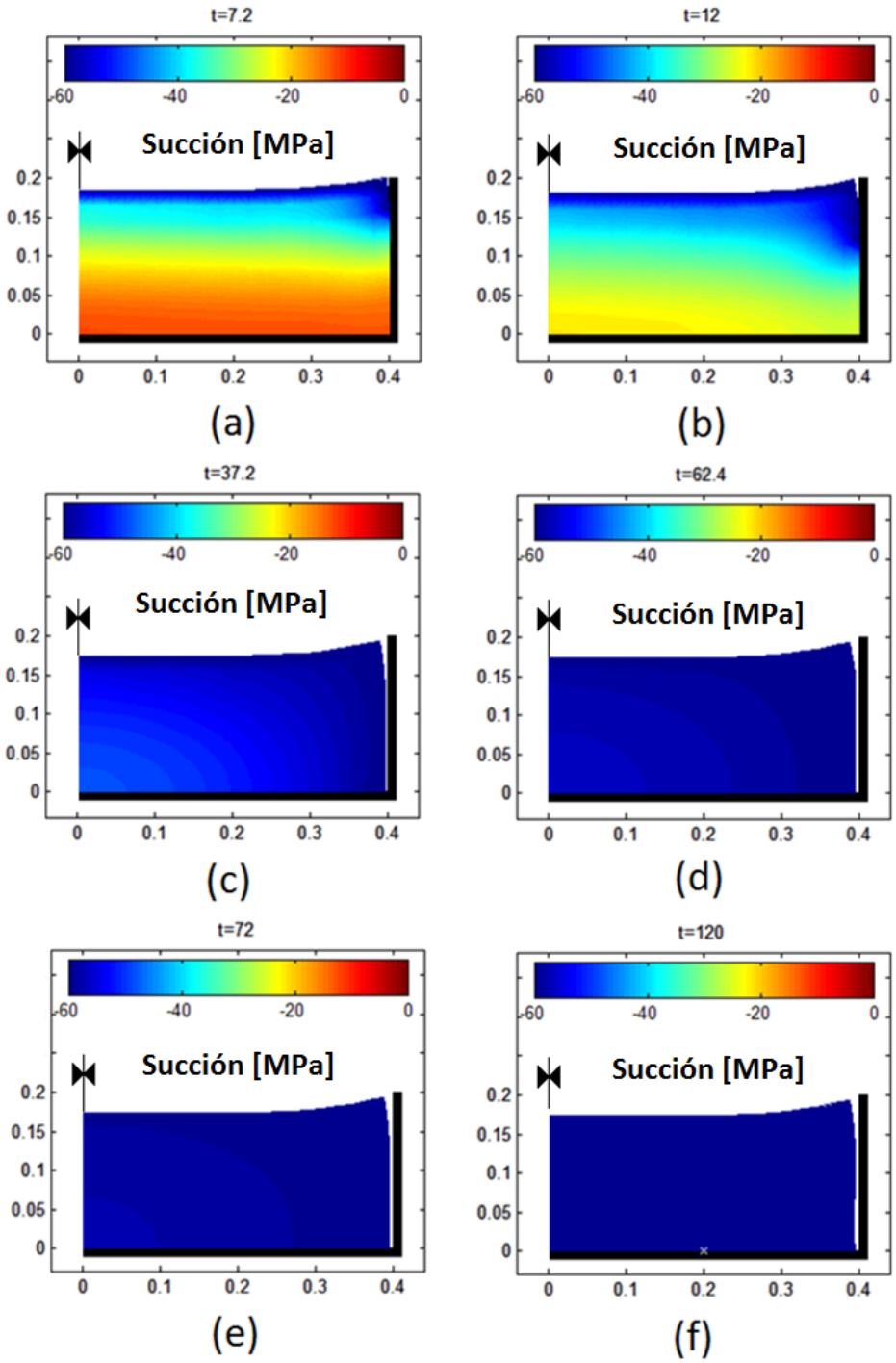

Figure 2 – Evolution of the suction field during drying and propagation of a crack between the soil and the container. Suction an interface crack after a) 7 days of drying; b) 12 days of drying; c) 37 days of drying; d) 62 days of drying; e) 72 days of drying; and f) 120 days of drying.

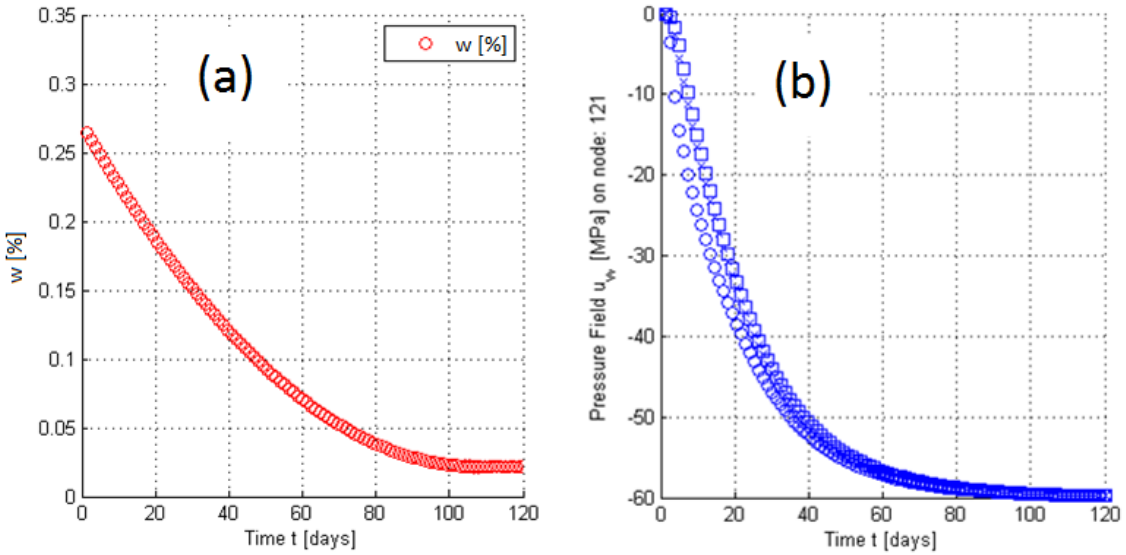

Figure 3 – Simulation of a cracking test: a) change with time of the specimen's moisture content; and b) change of suction at the three reference points in the radial section.

Table 1 – Parameters used in the numerical simulation

Mechanical parameters							
a_1	a_2	a_3	a_4 (MPa)	P_{ref} (MPa)	ν	G (MPa)	σ_c (MPa)
-0.02	-0.0025	-0.000039	0.023	0.1	0.4	$\frac{3K(1-2\nu)}{2(1+\nu)}$	0.0035

Retention curve parameters				Hydraulic parameters			
P_0 (MPa)	λ	n_0		k_0 (m/s)	b	n_0	r
1.05	1.55	0.6		9.27×10^{-10}	25	0.6	3

Table 2 – Parameters of the water retention curve [4]

e	γ_d (kN/m^3)	f_n	λ	n (porosity)
0.87	14.5	0.828	1.524	0.545
0.75	15.5	0.756	1.447	0.527
0.64	16.5	0.485	1.554	0.479
0.55	17.5	0.033	3.052	0.373
0.53	17.7	0.066	2.420	0.380

4 CONCLUSIONS

The behaviour of the numerical model is adequate to simulate the process of desiccation and soil cracking. It has been possible to implement an algorithm capable of triggering crack initiation and of simulating crack propagation using a tensile strength criterion and a node release technique. The hydraulic problem needs special care because of its nonlinearity and because the suction boundary condition generates some instability to the system. The propagation of the cracks introduces still greater instability and requires care to maintain the balance, since imbalances are introduced whenever a node is released. The change in boundary conditions affects the stress field in the vicinity of the crack and these stresses must be redistributed in the soil matrix. In spite of the complications derived from the implementation and the development of the model, it has been demonstrated that it is possible to simulate the drying and cracking process with a relatively simple technique.

In the laboratory experiments, the first crack usually appears at the specimen's boundary (soil/container interface) and propagates from the top surface towards the bottom of the container. This process can be studied numerically in two dimensions, using a radial section.

Laboratory experiments show a great variability in the time of beginning of the first visible crack on the surface, between 1 and 10 days in the tests. Previous research also shows that there is no guarantee that the first crack will always begin at the upper boundary, although this is likely to be the case when adequate boundary conditions are imposed and a minimum of homogeneity is ensured in the specimen. The numerical model has demonstrated the reasons for cracking to start at the edges, because of a state of tensile stresses that the specimen cannot sustain.

The rate of crack propagation is relatively large during the tests. The model allows to propagate the crack in lengths proportional to the length of the edge of the finite element so that in principle it can be adjusted to the measurements made in the laboratory.

The model parameters have been calibrated using all available test information. However, in order to properly calibrate the hydromechanical parameters, simpler tests should be designed on which a smaller number of variables are controlled. On the other hand, due to the natural variability of the phenomenon, it is necessary to perform a large number of tests and conduct a statistical study on the behaviour of some variables, such as the time at which the first crack appears.

ACKNOWLEDGEMENTS

Financial support from research grants BIA2009-08341, awarded by the former Spanish Ministry of Science and Innovation, and BIA2012-36498, awarded by the Spanish Ministry of Economy and Competitiveness (both including FEDER funds, European Commission) is gratefully acknowledged. The first author wishes to thank the support of the ASTUTE Project, College of Engineering at Swansea University.

REFERENCES

[1] H. U. Levatti, "Estudio experimental y análisis numérico de la desecación en suelos arcillosos," Ph.D. Thesis, Dept. of Civil and Environmental Engineering, Division of Geotechnical Engineering and Geosciences, UPC-BarcelonaTech, 2015.

[2] M. R. Lakshmikantha, "Experimental and theoretical analysis of cracking in drying soils," Ph.D. Thesis, Dept. of Civil and Environmental Engineering, Division of Geotechnical Engineering and Geosciences, UPC-BarcelonaTech, 2009.

[3] M. R. Lakshmikantha, P. C. Prat, and A. Ledesma, "Boundary effects in the desiccation of soil layers with controlled environmental conditions," *Geotechnical Testing Journal (submitted - under review),* 2017.

[4] M. Barrera, "Estudio experimental del comportamiento hidro-mecánico de suelos colapsables," Ph.D. Thesis, Dept. of Civil and Environmental Engineering, Division of Geotechnical Engineering and Geosciences, UPC-BarcelonaTech, 2002.

[5] M. T. van Genuchten, "Closed-form equation for predicting the hydraulic conductivity of unsaturated soils," *Soil Science Society of America Journal,* vol. 44, pp. 892-898, 1980.

XIV International Conference on Computational Plasticity. Fundamentals and Applications
COMPLAS 2017
E. Oñate, D.R.J. Owen, D. Peric and M. Chiumenti (Eds)

3D-MESOMECHANICAL ANALYSIS OF EXTERNAL SULFATE ATTACK IN CONCRETE

A. PÉREZ*, C.RIERA*, C.M. LÓPEZ* AND I.CAROL*

* Department of Civil and Environmental Engineering
Universidad Politécnica de Cataluña
Jordi Girona 1, Edif. D2, E-08034 Barcelona, Spain
e-mail:adria.perez@upc.edu, carlos.maria.lopez@upc.edu, ignacio.carol@upc.edu

Key words: External sulfate attack, Concrete degradation, Finite element method, Interface element, Meso-mechanical analysis.

Abstract: The present study focuses on degradation of concrete by external sulfate attack. The numerical model developed by the MECMAT/UPC group, incorporates coupled C-M analysis using a meso-mechanical approach with discrete cracking, using the MEF and zero thickness interface elements with a constitutive law based on nonlinear fracture mechanics concepts. Examples of application are run on 2D and 3D samples, with geometries and FE meshes generated with a code developed also in-house. The numerical analysis is carried out using two independent codes and a "staggered" procedure. The first code performs the mechanical analysis and the second the diffusive/reaction chemical problem. 2D uncoupled and coupled analysis are presented and discussed. Preliminary coupled 3D results are also presented and compared with equivalent 2D results, and the differences are detected and analyzed.

1 INTRODUCTION

External sulfate attack is a chemical-mechanical degradation process that can lead to differential material expansions producing the type of cracking known as concrete "spalling" (figure 1), loss of strength and even the complete disintegration of the material under severe attack conditions. The main conditions that have to be fulfilled are the existence of a medium rich in sulfates, a high permeability (or diffusivity) of the concrete and the presence of a humid environment, which favors the general diffusion of sulfates [1]. Three processes are present in the attack:

1) Transport of sulfate ions through the pore network, mainly controlled by the permeability of the concrete (being the water/cement ratio the key parameter), as well as through the cracking system,

2) chemical reactions between the cement paste components and the sulfate ions (once these ions have entered the material, the type of cement and the content of aluminates will mainly determine the importance of reactions that may occur),

3) expansion phenomena as a consequence of the formation of new crystalline phases.

Figure 1: Cubic mortar specimen under the effects of the external magnesium sulfate attack at 360 days [2]

The presence of sulfates from external sources results in the formation of new phases inside the concrete such as secondary ettringite and gypsum. Most of the experimental evidence has shown that secondary ettringite formation is the major factor involved in expansions [3-5].

The intensity of the attack (or degree of degradation) depends on the quality of the concrete (cement type, w/c ratio, mineral additions or the concrete deterioration before the sulfate attack) and the environmental conditions (concentration, distribution and type of sulfates, humidity, temperature, pH of the solution, combined effect of different degradation processes, etc.). A complete treatment of the problem should involve both chemical and mechanical aspects of sulfate ingress, and its consequences on overall behavior, in order to reliably predict the durability of the concrete structures under sulfate attack.

In recent years, the research group of "Mechanics of Materials" at UPC has developed and consolidated a methodology for the numerical analysis of concrete and other heterogeneous quasi-brittle materials under mechanical and environmental actions, considering the corresponding THMC couplings. In the approach employed, a main focus is on cracking and fracture via a discrete approach using zero-thickness interface elements, which is combined with a meso-level representation of the main aggregate particles. Interface elements are pre-inserted along all lines in the FE mesh, which therefore become potential crack lines, equipped with a traction-separation constitutive model based on principles of non-linear fracture mechanics [6, 7].

This work focuses on the study of the external sulfate attack problem in concrete. First, results of a 2D analysis are presented, and then preliminary results of the extension of the 3D analysis are also presented. The study is an extension of a previous work [8, 9], in which the numerical formulation of the model was developed and some application examples in 2D were also presented. Subsequently, the study was continued in [10, 11] with an extension of the analysis with different size samples in 2D and 3D.

2 DESCRIPTION OF THE DIFUSSION/REACTION MODEL

The model is based in the formulation proposed by Mobasher [12] with the introduction of some improvements [8]. Due to the complexity of the problem, in [12] a simplified point of view of the problem has been considered, in which the external sulfate attack can be analyzed by the diffusion of a single type of ion, the sulfate ions.

It is assumed that the incoming sulfates react first with the portlandite to form gypsum ($C\overline{S}H_2$), and subsequently react with the different phases of non-diffusive calcium aluminates

in the hydrated cement paste, eventually forming secondary ettringite. A further reaction of ettringite formation, not considered in the original model [12], can also be added from the alumina-ferrite phase, resulting in a total of 4 possible reactions shown in expression (1).

$$\begin{aligned} &C_4AH_{13} + 3C\bar{S}H_2 + 14H \rightarrow C_6A\bar{S}_3H_{32} + CH \\ &C_4A\bar{S}H_{12} + 2C\bar{S}H_2 + 16H \rightarrow C_6A\bar{S}_3H_{32} \\ &C_3A + 3C\bar{S}H_2 + 26H \rightarrow C_6A\bar{S}_3H_{32} \\ &3C_4AF + 12C\bar{S}H_2 + xH \rightarrow 4\left(C_6A\bar{S}_3H_{32}\right) + 2\left[(A,F)H_3\right] \end{aligned} \tag{1}$$

While in [12] a grouped reaction is considered to simplify the analysis, in the formulation developed it is possible to treat each of the reactions separately, thus allowing consideration of different kinetics for each individual reaction [8].However, the kinetics of the individual reactions for the formation of ettringite are a priori unknowns, so that it may be convenient to proceed as in [8] where the first three reactions presented in (1) have been grouped, in a unique expression given by:

$$CA + q\bar{S} \rightarrow C_6A\bar{S}_3H_{32} \tag{2}$$

where q is the stoichiometric weighted coefficient of the grouped reaction. Reaction (2), takes place according to the availability of calcium sulfates and aluminates, which is determined in time and space through a second order diffusion-reaction equation for the concentration of sulfates (U [mol/m^3]) plus an equation for the decrease of calcium aluminate:

$$\frac{\partial U}{\partial t} = \frac{\partial}{\partial x}\left(D_U \frac{\partial U}{\partial x}\right) - kUC \tag{3}$$

$$\frac{\partial C}{\partial t} = -k\frac{UC}{q} \tag{4}$$

where C [mol/m^3] is the quantity of calcium aluminate equivalent by the grouping of the reactions (CA in equation (2)), and k is the grouped sulfate reaction rate.

The formulation presented in [12] considers an increase of the chemical diffusion coefficient when microcracking of the concrete occurs, using a damage variable. In the model developed in [8, 9] and used in this work, an improvement is included, considering that the diffusion coefficient decreases as the pores are filled with the precipitated chemicals. On the other hand, the diffusion through the cracks is explicitly considered with the use of the interface elements. In this way, the model used considers the decrease of the diffusivity due to the filling of the pores, simultaneously with an increase of the effective general diffusivity due to cracking phenomena [8, 9]. For this, a variation of the diffusion coefficient has been adopted in terms of a scale function according to the following expressions:

$$D_\Phi\left(\Phi_{cap}\right) = D_0 + \left(D_1 - D_0\right) f\left(\beta_D, \Phi_{cap}\right) \tag{5}$$

$$\text{with } f\left(\beta_D, \Phi_{cap}\right) = \frac{e^{-\beta_D}\xi}{1 + \left(e^{-\beta_D} - 1\right)\xi} \text{ and } \xi = \left(\Phi_{cap}/\Phi_{ini}\right) \tag{6}$$

$$\Phi_{ini} = v_c \cdot \left(\frac{w/c - 0.36\alpha}{w/c + 0.32}\right) \tag{7}$$

$$\Phi_{cap} = \Phi_{ini} - \alpha_s CA_{react} \text{ if } \alpha_s CA_{react} < \Phi_{ini} \text{ (else 0)} \tag{8}$$

where D_0, D_1, are lower and upper reference values, respectively, β_D is a parameter that determines the non linearity of the function, Φ_{ini} is the initial capillary porosity, Φ_{cap} is the updated capillary porosity that takes into account the increase of ettringite, ν_c is the volumetric fraction of cement, *w/c* is the ratio water-cement, α is the hydratation level and α_s y CA_{react} are defined later. Figure 2 shows the variation of the proposed law for β_D = 1.5, which is compared with other formulations of the literature (normalized values of diffusion coefficient and capillary porosity).

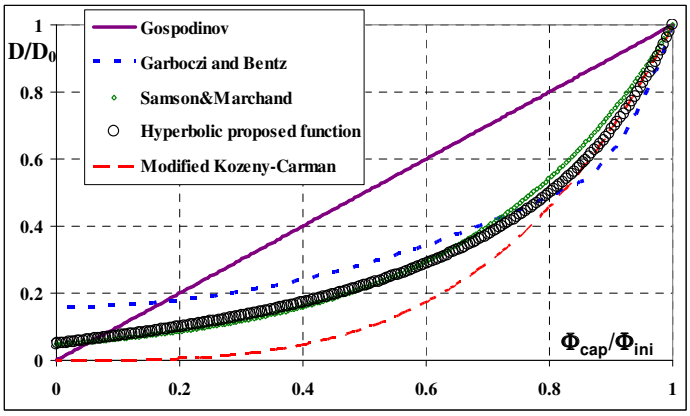

Figure 2: Comparison of the law of variation of the diffusion coefficient proposed in this work [8] with other formulations.

It is assumed that ettringite is the only product of the reactions that produce expansions. The volumetric strain is obtained from the amount of reacted calcium aluminate and the volume change associated therewith. For any of the individual reactions shown above, the volumetric change can be calculated as [12]:

$$\frac{\Delta V_i}{V_i} = \frac{m^{ettr}}{m^i + a_i \cdot m^{gypsum}} - 1 \tag{9}$$

where m^i is the molar volume [m^3/mol] of each chemical species and a_i is the stoichiometric coefficient involved in each reaction. To calculate the total volumetric strain, it is necessary to calculate the amount of reacted alumina phases (CA_{react} in the case of the grouped reaction and C^i_{react} for the extended model). For the complete version of the model, the volumetric deformation is calculated as:

$$\varepsilon_v(t) = \sum_{i=1}^{n} C^i_{react} \frac{\Delta V_i}{V_i} \overline{m}_i - f \cdot \Phi_{ini} \tag{10}$$

$$\overline{m}_i = m_i + a_i \cdot m^{gypsum} \quad \text{and} \quad C^i_{react} = C^i_0 - C^i_{unr} \tag{11}$$

where C_0^i represents the initial concentration of the different alumina phases, C_{unr}^i is the amount of non-reacted aluminates (given by the updated values of the internal values) and *f* is the porosity fraction of the capillary porosity that has to be filled before any expansion occurs.

For the simplified model, an average scheme for the different phases is used again, in which the increase of volume is related to the calcium aluminate reacted by a coefficient α_s. The typical values of *f* found by inverse analysis are in the range of 0.05-0.40 [12]. Additional details of the model and the verification tests can be found in [8, 9].

3 MESOMECHANICAL MODEL

3.1 Geometry and mesh generation

The numerical simulation is based on a meso-structural model in which the largest aggregate particles are represented explicitly, surrounded by a homogeneous matrix representing the average behavior of mortar plus the smaller aggregates. The shape and distribution of the large aggregate particles are randomly generated by a procedure based on the Voronoi-Delaunay theory [13]. In order to capture the main potential crack trajectories, zero-thickness interface elements are inserted a priori of the analysis, along all the aggregate-mortar and some of the mortar-mortar mesh lines.

3.2 Constitutive law for interface elements

The zero-thickness interface elements are equipped with a nonlinear constitutive law based on elasto-plasticity and concepts of fracture mechanics, which is formulated in terms of normal and shear components of the stress on the interface plane and the corresponding relative displacement variables. The initial loading (failure) surface $F = 0$ is given as three-parameter hyperbola (tensile strengthχ, asymptotic cohesion *c* and asymptotic friction angle tanϕ). The evolution of *F* (hardening-softening laws), is based on the internal variable W_{cr} (work spent in fracture processes), with the two material parameters G_F^I and G_F^{IIa} that represent the classical fracture energy in Mode I, plus a second fracture energy for an "asymptotic" Mode IIa under shear and high confinement. A more detailed description of this elasto-plastic constitutive law can be found in the literature [6, 7]. Results of the meso-mechanical model for normal concrete specimens subject to a variety of loading cases in 2D and 3D can also be found elsewhere [7, 8, 14, 15].

3.3 Chemo-Mechanical Coupling

The chemo-mechanical coupling (CM) has been achieved using a "staggered" approach that relates the two independent codes. For each time step, the first code performs the nonlinear diffusion-reaction analysis, and the results in terms of local expansions are imposed in the second code, solving the mechanical problem. The new displacement field obtained from the mechanical problem will modify the diffusion-reaction process due to the cracking, accelerating the sulfate ingress inside the specimen. As a result, this loop must be successively repeated within each time step until a certain tolerance is satisfied. The same FEM mesh is used for both analyses, using zero-thickness interface elements with double-nodes, whose formulation for the diffusion problem is explained in [16].

4 RESULTS

Results of 2D and 3D coupled calculations are presented in which the samples are immersed in a solution of 5% sodium sulfate, corresponding to a concentration of 35.2 mol/m^3. Both the 2D and 3D meshes have a 26% aggregate fraction of the total volume and the same parameters that characterize a CEM I52.5N/SR concrete have been adopted. The parameters of the chemical-reaction problem are: D_1=1.70x10^{-03}, k= 2x10^{-05}(m^3/(mol·day)), q=3, f=0.05, w/c=0.5, α=0.9, D_0/D_1=5x10^{-02}, β_D=1.5, α_s=1.33x10^{-04}, $[C_3A]_{inicial}$=200(mol/m^3). For the mechanical analysis, the aggregate and the mortar are considered linear elastic with parameters: E=70000 MPa (aggregates), E=25000 MPa (mortar) and υ=0.20 (both). For the aggregate-mortar interfaces the parameters are: K_N=K_T=100000 MPa/mm, $tan\phi_0$=0.70, $tan\phi_{res}$=0.40, χ_0=2MPa, c_0=7MPa, G^{I}_{F}=0.03 Nmm, G^{II}_{F}=0.3 Nmm, σ_{dil}=40MPa. For the mortar-mortar interfaces the same parameters are used with the exception of χ_0=4MPa, c_0=14MPa and G^{I}_{F}=0.06 Nmm (and therefore, G^{II}_{F}=0.6 Nmm).

4.1 2D mesh

A mesh of 6 cm side with 4 aggregates per side is used (1720 nodes, 1272 continuous medium elements and 650 zero-thickness inteface elements). It is simulated that the mesh is immersed in a solution of sodium sulfate on the four outer edges (Dirichlet condition). The mechanical calculation is carried out under conditions of plane stress. Figure 3 shows the evolution of sulfate penetration for four different ages, Figure 4 shows the concentrations of precipitated ettringite for those same times and in Figure 5 presents the deformed configuration corresponding to 540 and 740 days.

Figure 3 shows the progressive ingress of sulfates from the edges to the center of the sample. For the last time shown (740 days) sulfates have advanced considerably with values similar to the external concentration in most areas except in the central zone (Fig. 3d).

Figure 4 shows that the ettringite formation front advances towards the center of the sample as time passes. Ettringite precipitation is delayed with respect to the advance of the sulfates, due the reaction rate. Figure 5, shows the deformation of the mesh at 540 and 740 days. In that figure, one can see a perimeter cracking that practically has formed a closed line (spalling) for the last graphical age (740 days).

4.2 3D mesh

In this case, a 4cm side 3D cubic mesh with 28 aggregates is used (35673 nodes, 12749 continuum elements and 18346 zero-thickness interface elements). The specimen (Figure 6) represents a quarter of a pillar, with boundary conditions for the mechanical problem that restrict the movement in the normal direction of all faces in contact with the rest of the pillar material (see Figure 9). For the diffusion problem, unlike the 2D case, a convective boundary condition is applied to these free faces. The reason for applying this condition is that, unlike the 2D mesh and due to its complexity, the 3D mesh has not been refined in the area close to the surfaces in contact with the sulfates, and when applying plain Dirichlet conditions it results in numerical oscillations and negative values of sulfate concentrations, both in the matrix and in the aggregates. In contrast to the 2D case, in 3D there are faces of aggregates that are on the edges of the specimen, and for this reason the code has been modified and the aggregates do not intervene in the diffusion-reaction analysis.

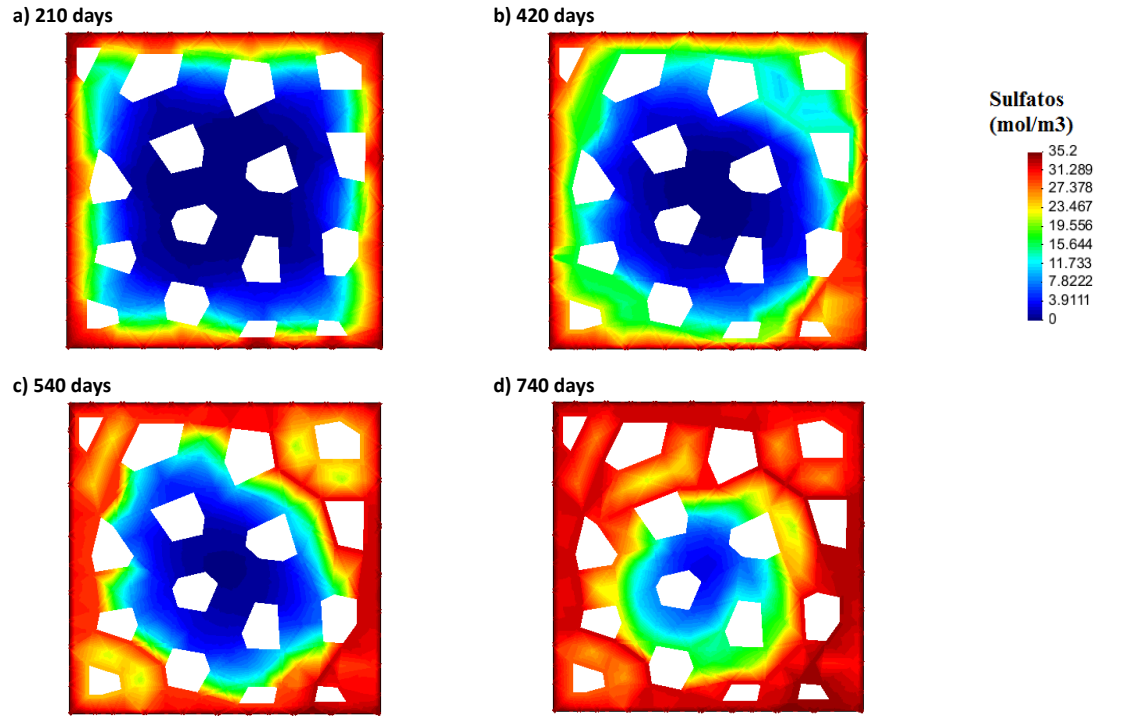

Figure 3: Sulfate progress for the following time values: a) 210 days, b) 420 days, c) 540 days and d) 740 days.

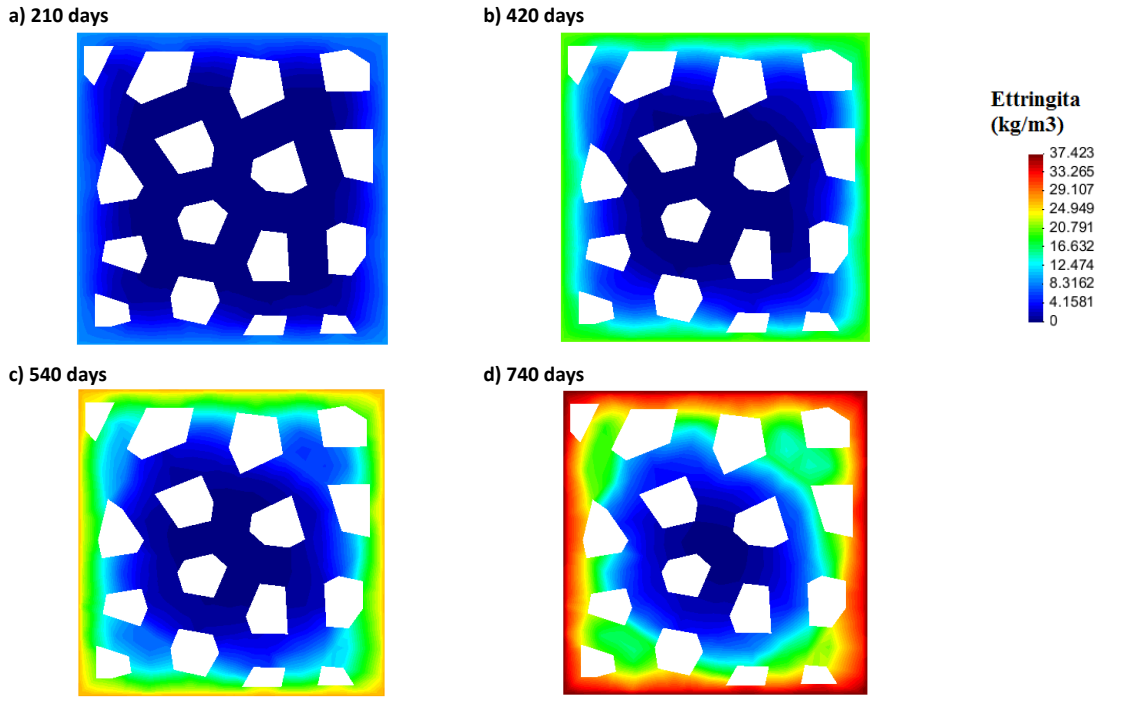

Figure 4: Ettringite precipitation due to the intrusion of the sulfates for the following time values: a) 210 days, b) 420 days, c) 540days and d) 740 days.

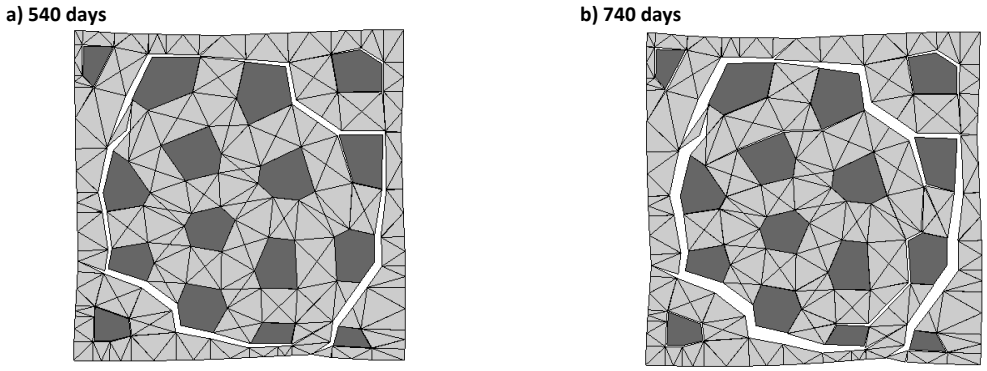

Figure 5: Deformed mesh for the following time values: a) 540 days and b) 740 days (deformation factor x50).

Figure 7 shows the distribution of sulfates and Figure 8 shows the precipitation of ettringite for the ages of 250, 450 and 740 days, from two different perspectives and without representing the aggregates, which allows to appreciate the corresponding penetration towards the interior of the mortar matrix.

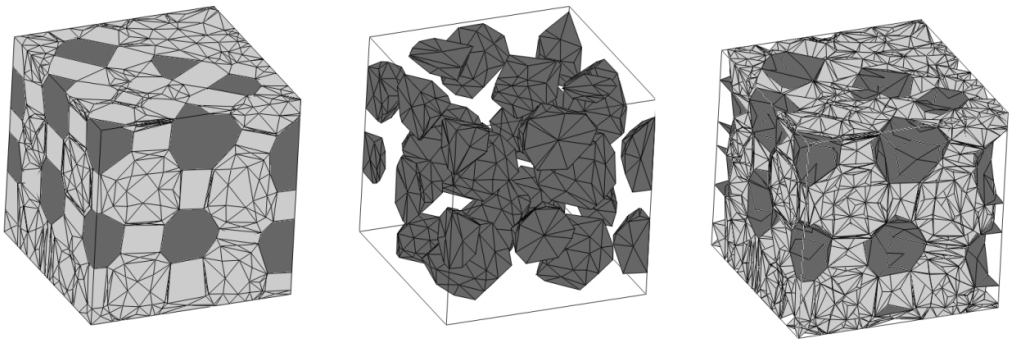

Figure 6: 3D mesh: representation of the mortar and aggregate phases (left), only the aggregates (center) and the two families of interfaces (right): aggregate-mortar (dark gray) and mortar-mortar (gray) interfaces.

As expected, the sulfate penetration front (Fig. 7) and the formation of ettringite (Fig. 8) in the mortar matrix from the two lateral edges towards the center of the sample are observed. However, Figure 7 shows that the sulfate advance occurs in a more attenuated and uniform manner if compared to the 2D results shown in Figure 3. These 3D results seem to be closed to the 2D uncoupled behavior, as shown in Figure 9, where the sulfate advance of the 3D case (right) is compared with the 2D case decoupled (left) at the age of 740 days.

Figure 10 shows the results of the deformation and the work consumed during the cracking process at 740 days. The column on the left shows the results as seen from a top view, and the right column shows them in side-view. Figure 10a clearly shows that at the corner of the faces in contact with the sulfate there is a concentration of volumetric deformations, which results in the formation of fractures. In Figures 10c and 10e it is observed that these fractures are located in vertical planes inclined with respect to the corner. The graphs on the right show that the main planes of fracture propagate vertically along the sample, running in between two rows of aggregates. It is observed that the cracks reach the edges in contact to the sulfates, and

therefore should become preferential paths of penetration and accelerate the deterioration process. However, this effect appears in the 2D analysis but does not occur in the 3D case.

Probably, the anomalous behavior is due to the fact that the convective-type boundary condition generates lower sulfate concentration values at the interface nodes located on the boundaries, resulting in much lower localized inflow *via* open cracks than in the 2D analysis.

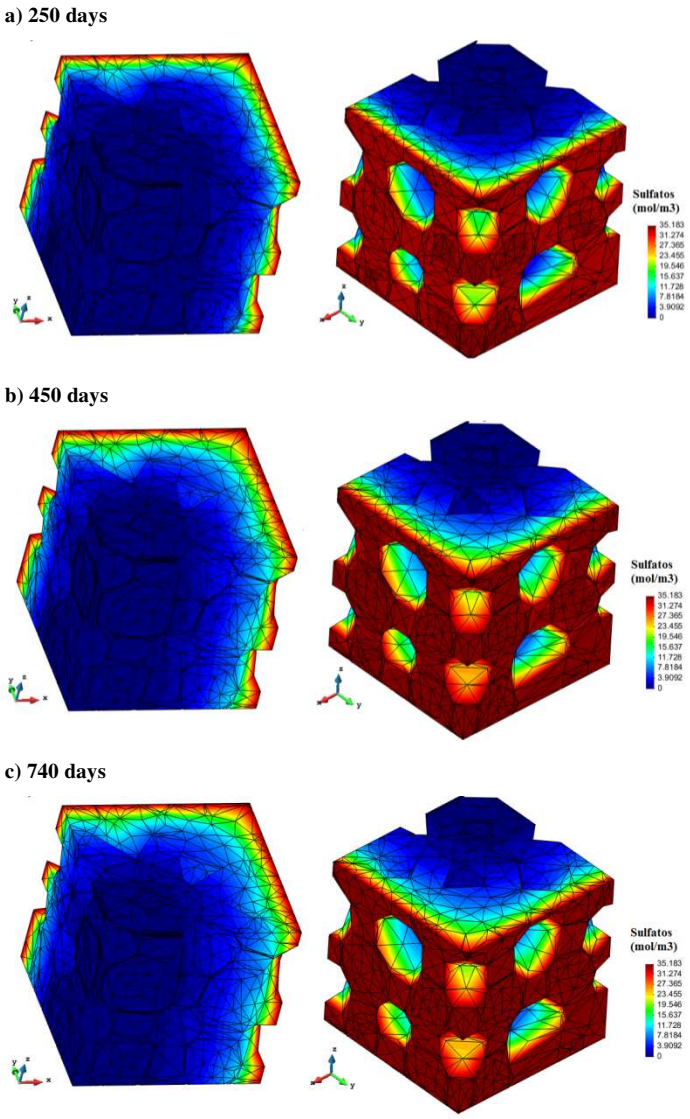

Figure 7: 3D representation of sulfate concentrations for: a) 250 days, b) 450 days and c) 740 days.

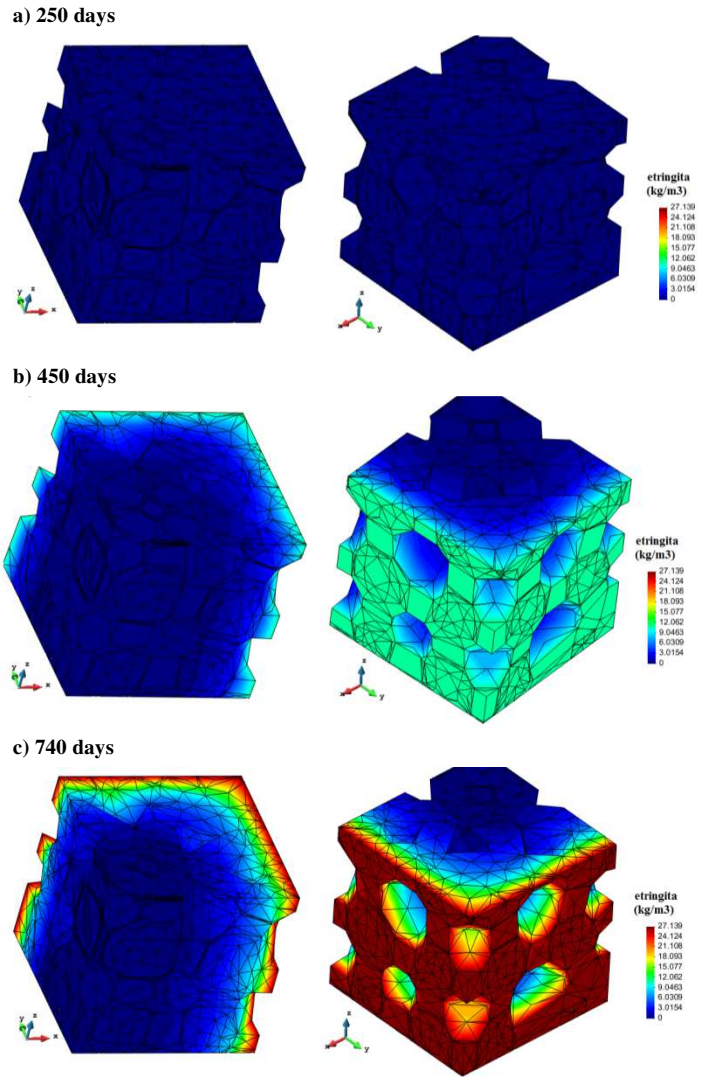

Figure 8: 3D representation of ettringite precipitation for the following time values: a) 250 days, b) 450 days and c) 740 days.

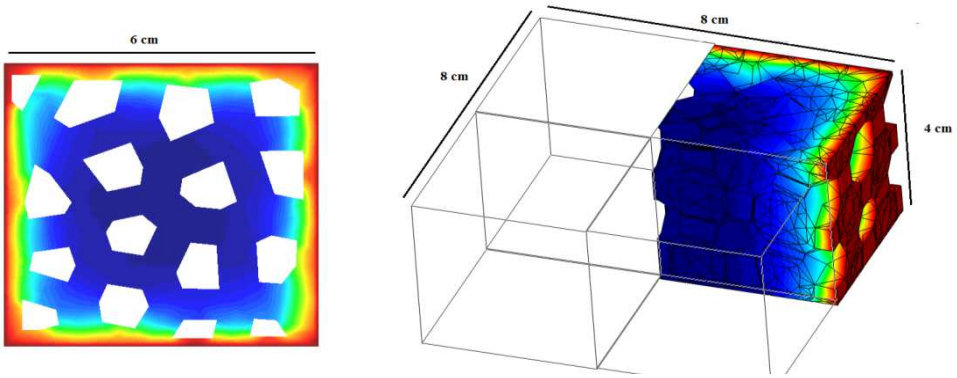

Figure 9: Representation of the sulfate advance front: 2D decoupled (left) and 3D coupled (right) at the age of 740 days.

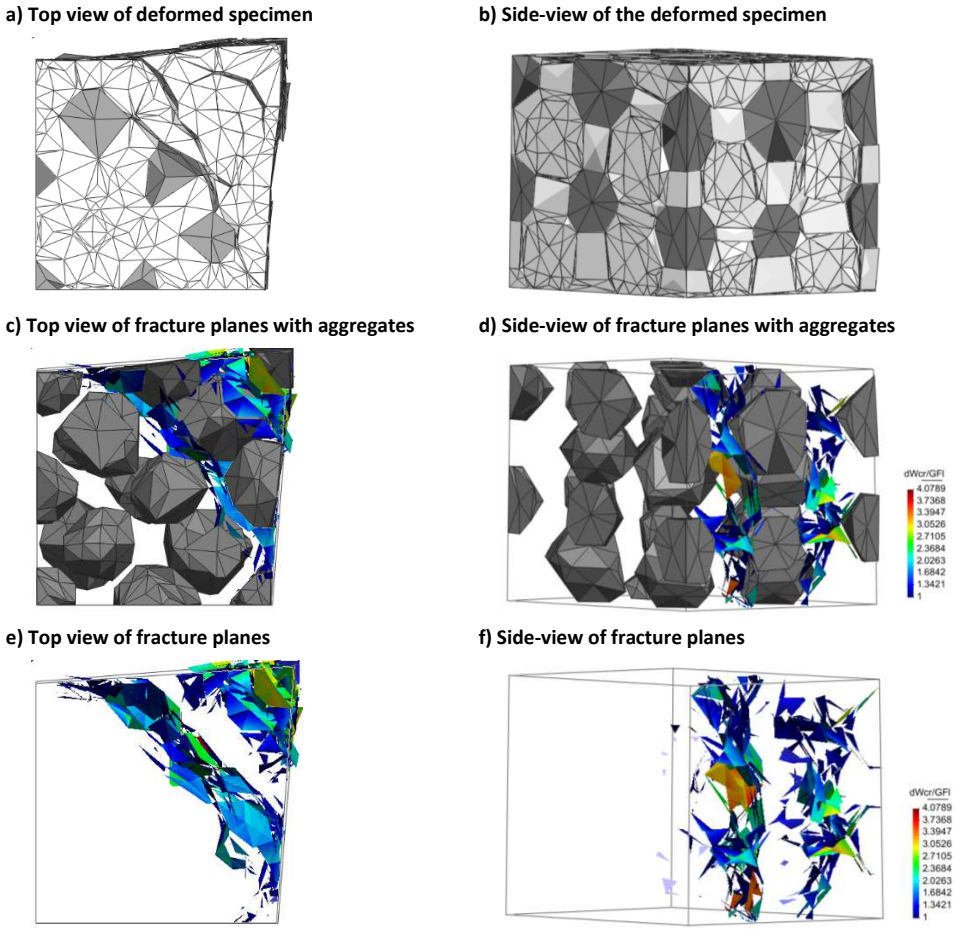

Figure 10: 3D deformed mesh (factor x50) and work dissipated by the fracture process at the age of 740 days.

5 CONCLUDING REMARKS

The 2D coupled results show that the model is able to simulate that, as the interfaces open, creating new channels, the sulfate ingress increases drastically thus forming penetration fronts into the sample. A preliminary 3D coupled analysis has shown that, in terms of depth and penetration of the sulfates and cracking scheme, the results obtained are more similar to those obtained from the 2D uncoupled analysis than to the coupled 2D analysis. In a first interpretation this fact could be explained on the basis of the boundary conditions imposed (of the Newmann-convective type) which were used in order to overcome a lack of mesh refinement near the specimen surface. Current work is oriented to verify this conjecture, and to run the analysis of a more refined 3D cube specimen so that Dirichlet boundary conditions can be applied directly on the specimen surface.

ACKNOWLEDGMENTS

This research is supported by grants BIA2016-76543-R funded by MEC (Madrid), which includes FEDER funds, 2014SGR-1523 from AGAUR-Generalitat de Catalunya (Barcelona) and under a FPU doctoral fellowship (FPU13/02185) from MEC (Madrid) to the first author.

REFERENCES

[1] Collepardi, M. A state-of-the-art review on delayed ettringite attack on concrete. *Cem. Concr. Comp.*, **25**:401-407 (2003).

[2] Lee, S., Hooton, R., Jung, H., Park, D., Choi, C., Effect of limestone filler on the deterioration of mortars and pastes exposed to sulfate solutions at ambient temperature. *Cem. Concr. Res.*, **38**:68-76, (2008).

[3] Brown, P. and Hooton, H., Ettringite and thaumasite formation in laboratory concretes prepared using sul-fate-resisting cements. *Cem. Concr. Comp.*, **24**:361-70 (2002).

[4] Al-Amoudi, O., Attack on plain and blended cements exposed to aggressive sulfate environments. *Cem. Concr. Comp.*, **24**:305-316 (2002).

[5] Irassar, E., Bonavetti, V. and González, M., Micro-structural study of sulfate attack on ordinary and limestone Portland cements at ambient temperature. *Cem. Concr. Res.*, **33**:31-41 (2003).

[6] Carol, I., Prat, P. C., López, C.M. A normal/shear cracking model. Application to discrete crack analysis. *Engng.Mech. ASCE*, **123**:765–773 (1997).

[7] Carol, I., López, C.M. and Roa, O. Micromechanical analysis of quasi-brittle materials using fracture-based interface elements. *Int. J. Num. Meth. Engng*. **52**:193-215 (2001).

[8] Idiart, A., *Coupled analysis of degradation processes in concrete specimens at the meso-level*. Ph.D. Thesis. UPC, Barcelona, (2009).

[9] Idiart, A., López, C.M. and Carol, I. Chemo-mechanical analysis of concrete cracking and degradation due to external sulfate attack: A meso-scale model, *Cem. Concr. Comp.*, **33**:411-423 (2011).

[10] Riera, C. *Advanced Modeling of fracture problems in concrete due to external sulfate attack*. Graduation Thesis for the degree of Geological Engineering, ETSECCPB (School of Civil Engineering)-UPC, Barcelona (in Spanish) (2015).

[11] Riera, C. *3D mesomechanical modeling of external sulphate attack on concrete*. Master Thesis in Geotechnical Engineering, ETSECCPB (School of Civil Engineering)-UPC, Barcelona (in Spanish) (2016).

[12] Tixier, R., Mobasher, B., Modeling of damage in cement-based materials subjected to external sulfate attack. I: Formulation. *J. of Mat. In Civil Engng, ASCE*, **15(4)**:305-313 (2003).

[13] Caballero, A., Carol, I., López C. M. 3D mesomechanical analysis of concrete specimens under biaxial loading. *Fatigue and Fracture Engng. Materials and Structures*, **30**:877-886 (2007).

[14] López C.M., Carol I., Aguado A. Meso-structural study of concrete fracture using interface elements. I: numerical model and tensile behavior. *Materials and Structures*, **41(3)**:583-599 (2008).

[15] López C.M., Carol I., Aguado A. Meso-structural study of concrete fracture using interface element II: compression, biaxial and Brazilian test. *Materials and Structures*, **41(3)**:601-620 (2008).

[16] Segura, J.M., Carol, I., Coupled HM analysis using zero-thickness interface elements with double nodes. Part I: Theoretical model and Part II: Verification and application. *Int. J. Numer. Anal. Meth. Geomech*. **32**:2083–2123, (2008).

XIV International Conference on Computational Plasticity. Fundamentals and Applications
COMPLAS 2017
E. Oñate, D.R.J. Owen, D. Peric and M. Chiumenti (Eds)

HOLISTIC MESOSCALE MODELLING OF CONCRETE – RECENT DEVELOPMENTS

YONG LU AND RONGXIN ZHOU

Institute for Infrastructure and Environment, School of Engineering
University of Edinburgh
The King's Buildings, Edinburgh EH9 3JL, UK
e-mail: yong.lu@ed.ac.uk

Key words: Concrete, heterogeneity, mesoscale model, macroscopic behaviour, interface, numerical simulation

Abstract. Modelling of concrete at the mesoscale is needed in many applications, but developing a realistic mesoscale model for the analysis of concrete behaviour under general loading conditions is challenging. This paper presents an overview of the development of mesoscale modelling of concrete within a finite element framework for both quasi-static and high strain rate applications. A 2D mesoscale model incorporating random aggregates and equivalent interfacial transition zones enables examination into the effects of random aggregate structure and the sub-scale non-homogeneity within the mortar matrix on the macroscopic behaviour of concrete. In applications where multi-axial stresses and confinement effects are significant, such as under high-strain rate loading where the inertial confinement plays an important role, a realistic representation of the multi-axial stress condition becomes necessary, and this requires 3D mesoscale model. Two types of 3D mesoscale concrete model have been developed, namely a pseudo-3D mesoscale model and a full 3D mesoscale model. For the explicit representation of the fracture process, a cohesive-contact approach has been implemented, at present in a 2D mesoscale framework. Illustrative examples are given to demonstrate the performance of the mesoscale models and the results are discussed.

1 INTRODUCTION

The behaviour of concrete has a strong influence by the composition of the concrete mix and the process of damage and fracture within the mortar matrix and at the interfacial transition zone (ITZ). To capture the underlining damage process requires appropriate representation of the material composition and this means a mesoscale model. In fact modelling of concrete at the mesoscale is needed in many applications, for example for investigation into the micro-meso mechanics underlying the macroscopic behaviour of the concrete material, and for realistic simulation of damage evolution in critical regions of concrete structures where complex stress conditions take place.

In standard computational modelling of concrete structures, concrete is typically modelled as homogeneous material with macroscopic material properties. Such an approach is

computationally economical, and can be suited for a wide range of applications. However, the constitutive laws in homogenised models for concrete are derived from the nominal stress-strain response of standard specimens, therefore the applicability of the macroscopic model are generally limited to problems which does not involve drastic spatial variation of the stress and strain within a certain characteristic dimension. For an analysis where finer spatial resolution than the characteristic size of bulk concrete or representative volume element RVE is required, homogenization can no longer be justified. It is clear that the properties of the material would exhibit a much increased scatter as the element size is reduced into the sub-RVE regime [1].

For a conceptual discussion, four levels of spatial discretization may be defined for the purpose of classifying the material descriptions [2], as schematically illustrated in Fig. 2. Spatial discretization at levels I and II may be suitable mainly in quasi-static loading analysis and for relatively large structures, and homogenization is most appropriate for these levels of discretization. On the other hand, for problems such as high strain rate loading, spatial discretization at levels III and IV are commonly used due to the need of capturing the transient stress wave effects. As the discretization refines, the properties of the material within individual elements will tend to vary distinctively, and eventually resembles the variation in a mesoscale framework, i.e. between mortar and aggregates.

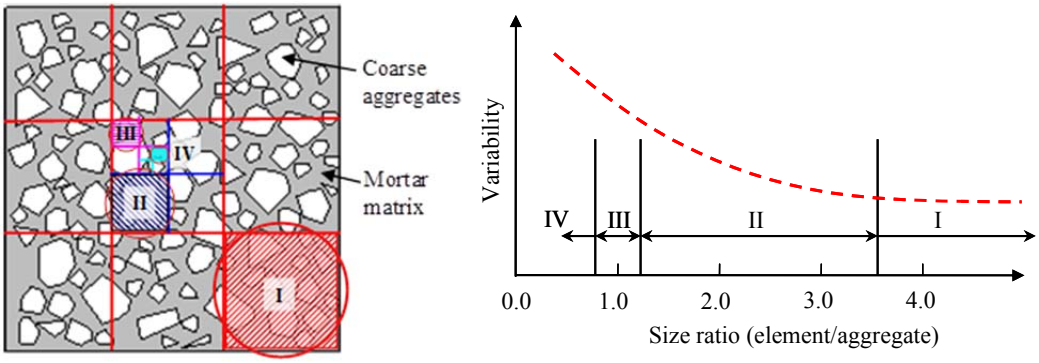

Figure 1: Representative levels of discretization (left) and variability of material properties (right) [2]

Modelling of concrete at the mesoscale has been a subject of much research over the last 3 decades. Three main alternative approaches have been employed, namely lattice models (e.g. [3]), discrete element models (e.g. [4-5]), and continuum based FE models. A main challenge with the lattice models is the difficulty in determining the equivalent model parameters. Similar issues exist in the DEM approach where the interface between aggregates and the mortar matrix, which effectively is continuous, has to be represented through contacts. The determination of the modelling parameters in a continuum based FE model, on the other hand, is relatively more straightforward.

Mesoscale modelling of concrete using a continuum-based finite element framework allows for the multi-phasic continuous nature of concrete to be explicitly represented. The evolving discontinuity due to fracture can be simulated by damage laws of the constituent materials. Most of the early mesoscale models were actually developed in this framework (e.g. [6-8]). However, Generation of the meso-geometry and the FE meshing are the main

challenges. Especially for 3-dimensional (3D) mesoscale models, simplified geometries with spherical or elliptical inclusions are often employed, while alternative methods include the use of regular FE method and create the heterogeneity by joining adjacent elements to form aggregates (e.g. [9]).

A series of studies has been undertaken in recent years by the authors and co-workers in developing a holistic mesoscale modelling framework for general analysis of concrete under a variety of loading conditions. A 2D mesoscale model incorporating random aggregates and equivalent interfacial transition zones enables examination into the effects of random aggregate structure and the sub-scale non-homogeneity within the mortar matrix on the macroscopic behaviour of concrete. In applications where multi-axial stresses and confinement effects are significant, including high-strain rate loading where the inertial confinement plays an important role, a realistic representation of the multi-axial stress condition becomes necessary, and this requires 3D mesoscale model. Two types of 3D mesoscale concrete model have been developed, namely a pseudo-3D mesoscale model and a full 3D mesoscale model. In the latest development, a cohesive-contact approach has been adopted in the description of the ITZ to allow for explicit representation of complex fracture and interaction between fractured surfaces. This approach has been implemented in a 2D mesoscale framework and work is to be carried out to extend this approach to 3D mesoscale analysis.

2 THE GENERAL 2D MESOSCALE MODEL

The creation of a 2D (as well as 3D) mesoscale model for concrete starts with the generation of the random geometric structure encompassing random polygon (or polytope) aggregates following a specified size distribution, e.g., a Fuller curve. A standard take-and-place procedure is employed in which individual aggregates are randomly generated and placed into the space representing the target concrete specimen. Checks are carried out to ensure that aggregates do not overlap and that a minimum gap is preserved between aggregates. Once a target packing density (defined by the volume ratio of the aggregates) is satisfied, the geometric structure creation phase is completed and the geometric data are taken to a mesh generator for meshing. Fig. 2 depicts a sample of the generated mesoscale geometry and the FE mesh for the three individual phases. Note that the ITZ phase here is represented by an equivalent thin layer of solid elements in the model shown.

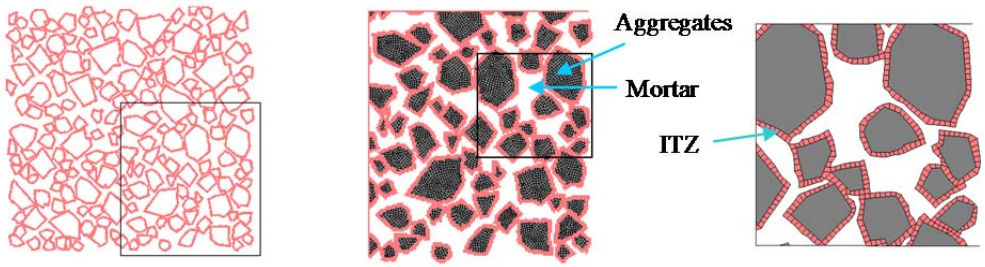

Figure 2: A typical 2D mesoscale model for concrete and FE mesh with equivalent ITZ

The material models for aggregates and mortar matrix can be adapted to represent the

specific properties for these distinctive materials. For quasi-static loading aggregates do not normally fail and so use may be made of elastic material model for aggregates. For mortar matrix a generic geomaterial constitutive model may be appropriate, and in the present study we use the concrete damage model (K&C model [10]) which is available in LS-DYNA, the software utilised to carry out the mesoscale model analysis in the present study.

It is worth noting that further variability of the material properties within each of the three individual phases may be incorporated by a stochastic sampling approach such that each element will acquire a specific property from a target property distribution. Fig. 4 shows a set of simulated cubic compressive stress-strain curves for 30-MPa concrete using the 2D mesoscale model. The variation in the post-peak regime reflects the influence of varying the material properties within each individual phase.

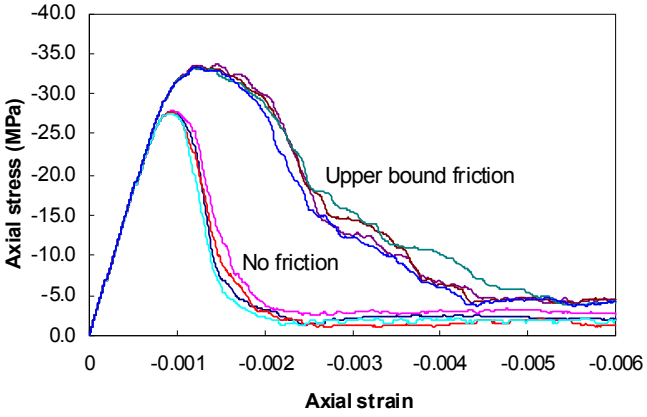

(a) Stress-strain curves: variation in descending branch attributable to random properties within each material

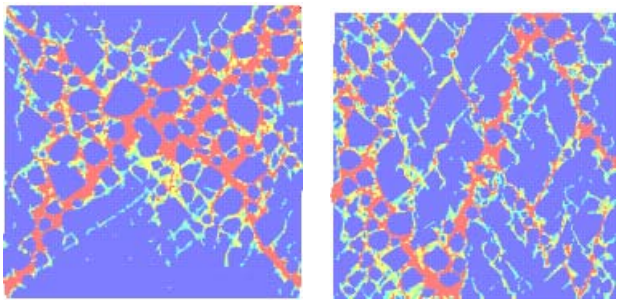

(b) Damage patterns: High friction (left) and Low friction (right)

Figure 3: Computed compressive stress-strain curves for 30-MPa concrete for two levels of loading face frictions and the damage patterns

3 A PSEUDO 3D MESOSCALE MODEL

For concrete under multi-axial stresses, a 3D mesoscale model would be desirable, which however means significantly increased computational cost. As an alternative to a true 3D mesoscale model, a pseudo 3D mesoscale model has been devised. Fig. 4 illustrates such a pseudo 3D mesoscale scheme. The actual mesoscale description is contained in a slice of 2D mesoscale model, in which the mesoscale features are fully represented. The 3D effect is achieved by sandwiching the mesoscale layer between two half-sized homogeneous bodies to complete the whole specimen. The interface between the mesoscale layer and the

homogeneous parts is made to be friction free but fully coupled in the normal direction, so that any incompatibility within the mesoscale plane will have no effect on the mesoscale model part while transmission of the pressure (confining stress) on the mesoscale model is almost fully preserved.

A schematic of the pseudo 3D mesoscale model setup for cylinder and cube specimens is given in Fig. 4(a). Fig. 4(b) shows the effects of the model in creating a realistic 3D stress field for the mesoscopic observations.

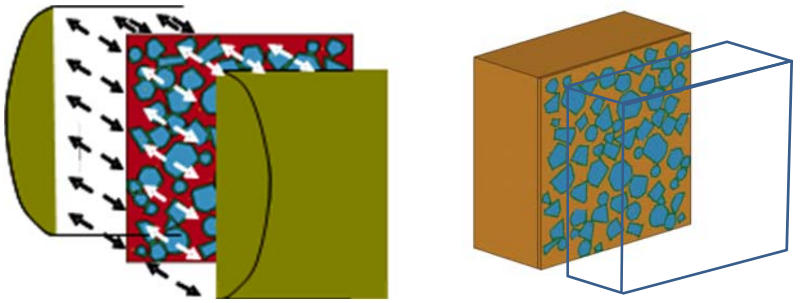

(a) Model setup: cylinder (left) and cube (right) specimens

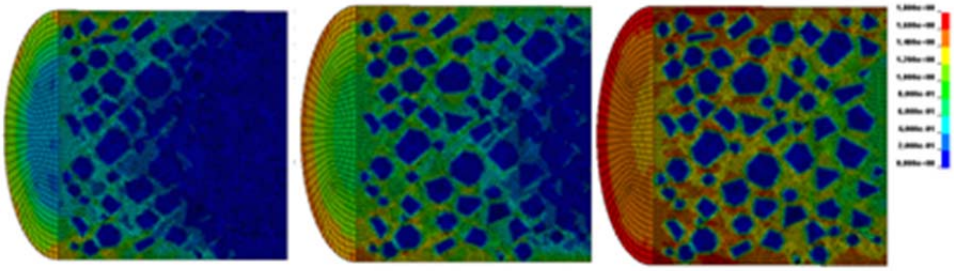

(b) Pseudo 3D cylinder under fast compression: 3D stress field is clearly visible

Figure 4: Pseudo 3D mesoscale models and simulation effects [11]

4 A FULL 3D MESOSCALE MODEL

For a fuller description of the 3D mesoscale structure and the associated 3D effects, especially under high strain rate loading, a true 3D mesoscale model with random polytopes has also been developed. The procedure of creating such a 3D mesoscale model is similar to the 2D mesoscale model, but the complexities in the generation of the random mesoscale geometry increase. In the present scheme, we create the aggregate particles by bounded polyhedrons in convex hulls according to computational geometry. Flaky and elongated aggregates are realised from the regular polytopes by shrinking or elongation operations. In the subsequent ‘place’ process, a pre-selection algorithm is used to identify the existing polytopes that may have a chance to intersect with the one being placed. Subsequent intersection check only needs to be carried out for polytopes whose bounding spheres intersect with that of the current particle. To improve the efficiency of the existing “place” procedure, in the event an aggregate being placed is found to intersect with any aggregates already in place, a translate-and-rotate procedure is employed on the aggregate being placed.

Fig. 5(a) shows a typical 3D mesoscale aggregate structure. The remaining space in the

sample domain is automatically occupied by the mortar matrix, while the interface between the aggregates and the mortar matrix may be treated as the ITZ. It should be mentioned that meshing for a 3D mesoscale model in not a trivial task. Due to randomly shaped aggregates, the meso-structure is highly unstructured. Specific smoothing algorithms such as Octree, advancing front and Delaunay refinement need be involved for meshing unstructured domain. Fig. 5(a) also shows an example of the 3D FE mesh. In the model shown the interface in treated an equivalent thin layer of solid elements surrounding the aggregates.

The 3D mesoscale model can then be subjected to any loading by applying appropriate boundary conditions. Fig. 5(b) shows an example analysis under high rate compression with a nominal strain rate at 50 s^{-1}, The phenomenon of distributed damage and the 3D inertia confinement effect is clearly reproduced in a the 3D mesoscale model.

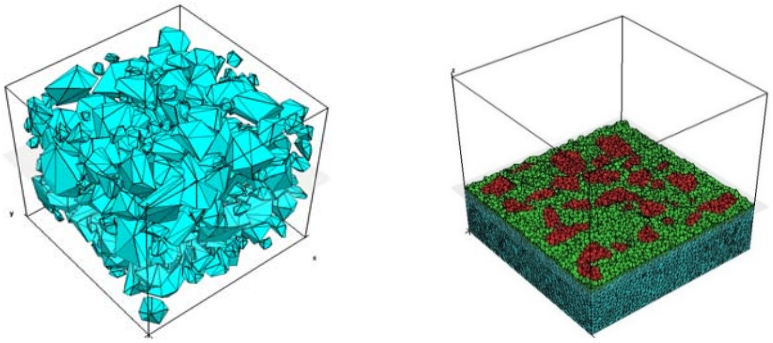

(a) A full 3D mesoscale model: meso-geometry

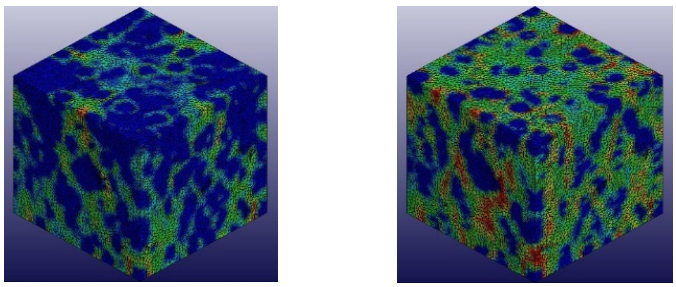

(b) Pseudo 3D cylinder under high rate compression

Figure 5: 3D mesoscale model and example simulation

5 A COHESIVE-CONTACT INTERFACE MODEL FOR THE ITZ

In the above-described mesoscale models, fracture within the material is generally represented by failure of the corresponding solid elements through the constitutive descriptions. Although the effect of fracture can be reproduced to a large extent through the deterioration and loss of strength and stiffness in the elements, the inability of depicting explicitly the discontinuity induced by fractures limits the capability of the model in replicating the fracture evolution, and fracture opening and closure processes.

To tackle this issue a cohesive-contact model has been incorporated in a mesoscale framework. The incorporation of the contact process is to address the problem with the classical cohesive model in which complex stress condition at the interface is often ignored or

treated poorly, resulting in poor performance of the model under general loading other than simple tension or shear ([12]).

Fig. 6 depicts the generation of the zero-thickness interface elements for the ITZ in the mesoscale model, and Fig. 7 shows the simulated stress-strain curves under uniaxial tension and compression using such a mesoscale model. It is clearly observed that, while the new interface model maintains similar effect as the cohesive-only model in a tension condition, significant improvement is achieved under compression. As the interface is always subjected to complex stress conditions in a mesoscale model even though the whole specimen is under a uniaxial loading, the satisfactory performance of the cohesive-contact approach indicates that this approach is effective in practically any interface stress conditions.

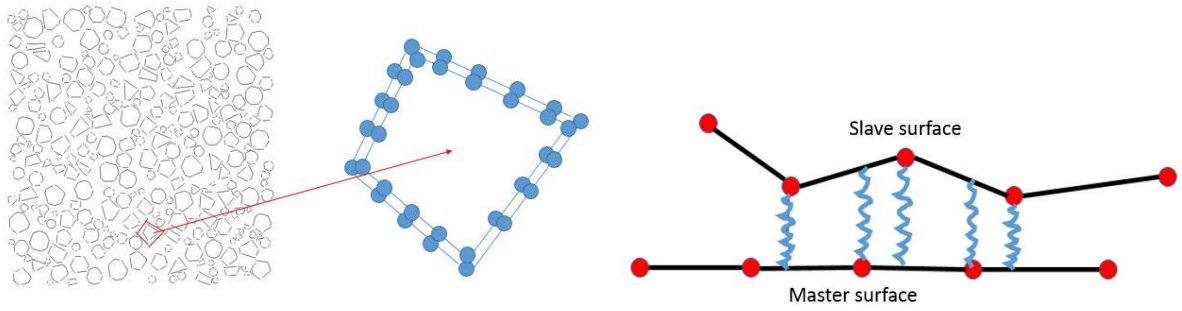

(a) Generation of interface element (b) Incorporation of contact in interface element

Figure 6: Interface elements with cohesive and contact-friction functions

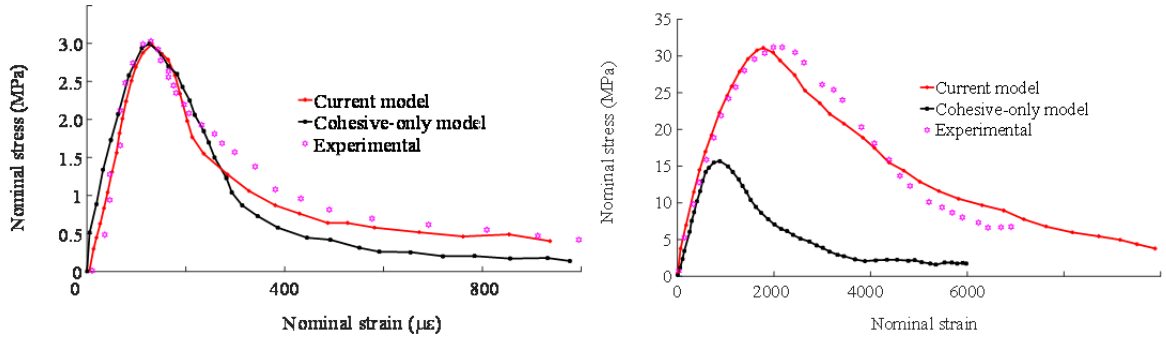

(a) Uniaxial tension (b) Uniaxial compression

Figure 7: Simulation of uniaxial tension and compression with the cohesive-contact mesoscale model

At present the cohesive-contact modelling approach has been implemented in 2D mesoscale models. The extension to general 3D mesoscale will clearly incur significant increase in the computation cost but in principle it is doable.

6 CONCLUSIONS

A series of studies has been undertaking to develop a holistic mesoscale modelling framework for numerical simulation of concrete and concrete-like materials under general loading and stress conditions. The mesoscale model in 2D allows realistic representation of the material composition and is suitable for characterisation of the mesoscopic damage

processes and quantitative simulation of the concrete behaviour under uniaxial and biaxial stress conditions. The incorporation of the cohesive-contact interface for the ITZ enables explicit simulation of the fracture and the induced discontinuity, and therefore allows for direct simulation of complex processes involving discontinuity such as cyclic process of crack opening and closure, as well as shear interlock.

The development of the 3D mesoscale models allows simulation of loadings in which significant pressure (hydrostatic stress) component is involved, such as confined concrete, and concrete under high strain rate compression where lateral inertia confinement is known to play a significant role.

The mesoscale modelling approach can be employed to assist in the material investigation, characterisation, and the analysis of concrete structures in critical regions where the true behaviour of the material has so far been understood on a largely empirical basis.

REFERENCES

[1] Rossi, P., Ulm, F.-J., and Hachi, F. Compressive behavior of concrete: physical mechanisms and modeling. *J Eng. Mechanics* (1997) **122**(11): 1038-1043.

[2] Lu Y. Modelling the dynamic response of concrete with mesoscopic heterogeneity. In *Understanding the Tensile Properties of Concrete* (Ed. J Weerheijm), Chapter 8, Woodhead Publishing, 2013:218-267.

[3] Schlangen, E. and van Mier, J. Simple lattice model for numerical simulation of fracture of concrete materials and structures. *Mater Struct* (1992) **25**: 534-942.

[4] Donzé, F.V., Magnier, S.-A., Daudeville, L., Mariotti, C., and Davenne, L. Numerical study of compressive behavior of concrete at high strain rates. *J. Engineering Mechanics* (1999) **125**(10): 1154-1163.

[5] Azevedo, M. N., Lemos, J.V. and de Almeida, J. R. Influence of aggregate deformation and contact behaviour on discrete particle modelling of fracture of concrete, *Eng Fracture Mech* (2008) **75**(6): 1569-1586.

[6] Wittmann, F.H., Roelfstra, P.E., Sadouki, H. Simulation and analysis of composite structures. *Mater Sci Eng.* (1984) **68**: 239-248.

[7] van Mier, J. G. M., and Vonk, R. A. Fracture of concrete under multiaxial stress - recent developments. Mater. Struct. (1991) **24**(1): 61–65.

[8] Wang, Z.M., Kwan, A.K.H. and Chan, H.C. Mesoscopic study of concrete I: generation of random aggregate structure and finite element mesh. *Comput Struct* (1999) **70**: 533-44.

[9] Wriggers, P. and Moftah, S.O. Mesoscale models for concrete: Homogenisation and damage behaviour. *Finite Elem Anal Des* (2006) **42**: 623-36.

[10] Malvar, L.J. , Crawford, J.E. , Wesevich, J.W. A plasticity concrete material model for Dyna3D, *Int J Impact Eng* (1997) **19**(9/10): 847–73.

[11] Song, Z. and Lu, Y. Mesoscopic analysis of concrete under excessively high strain rate compression and implications on interpretation of test data. *Int J Impact Eng* (2012) **46**:41-55.

[12] Lu, Y. and Tu, Z. Mesoscale modelling of concrete for general FE analysis - Part 2: Numerical investigation under static and dynamic loading conditions. *Struct Eng Mech* (2011) **37**(2): 215-231.

XIV International Conference on Computational Plasticity. Fundamentals and Applications
COMPLAS XIV
E. Oñate, D.R.J. Owen, D. Peric & M. Chiumenti (Eds)

MODELING THE BEHAVIOR OF ELASTIC MATERIALS WITH STOCHASTIC MICROSTRUCTURE

NAGEL J.*, JUNKER P. †

*Department of Mathematics and Computer Science
Eindhoven University of Technology
5612 AZ Eindhoven, Netherlands
e-mail: j.h.nagel@tue.nl

† Institute of Continuum Mechanics
Ruhr-Universität Bochum
Universitätsstraße 150, 44801 Bochum, Germany
e-mail: philipp.junker@rub.de

Key words: Stochastic Material Behavior, Stochastic Series Expansion, Energy Relaxation, Stress Expectation and Variance, Analytical Solution

Abstract. Even in the simple linear elastic range, the material behavior is not deterministic, but fluctuates randomly around some expectation values. The knowledge about this characteristic is obviously trivial from an experimentalist's point of view. However, it is not considered in the vast majority of material models in which "only" deterministic behavior is taken into account.

One very promising approach to the inclusion of stochastic effects in modeling of materials is provided by the Karhunen-Loève expansion. It has been used, for example, in the stochastic finite element method, where it yields results of the desired kind, but unfortunately at drastically increased numerical costs.

This contribution aims to propose a new ansatz that is based on a stochastic series expansion, but at the Gauß point level. Appropriate energy relaxation allows to derive the distribution of a synthesized stress measure, together with explicit formulas for the expectation and variance. The total procedure only needs negligibly more computation effort than a simple elastic calculation. We also present an outlook on how the original approach in [7] can be applied to inelastic materials

1 INTRODUCTION

The real behavior of materials is influenced by many different aspects. Examples are grain size and grain size distributions, dislocations, segregations, crystal orientation, defects, inclusions, and many more. Since these phenomena cannot be predicted for engineering materials, they have to regarded as random. Thus, the respective material

behavior, which is realized e.g. in terms of stress/strain diagrams, shows stochastic fluctuations. For a material prediction with increased accuracy, material models are desired which account for the stochastic properties of materials: a simulation yielding the expectation value of important quantities as elastic constants and stresses along with an error estimate or, to be more precise, along with with the variance would be of major interest.

There exist different strategies to include stochastic information to material modeling. A prominent example is the use of the so-called Chaos Polynomial Expansion and the derived Karhunen-Loève expansion. It has been successfully applied in sensitivity analysis [2], nonlinear random vibration [10] the analysis of human faces [9] and selection and ordering [5]. The key idea is to approximate the stochastic quantities like elastic constants by a broken series expansion while the stochastic dependence is expressed in terms of a stochastic vector $\boldsymbol{\xi} = (\xi_1, \ldots, \xi_{k_{\max}})$ with $k_{\max}$ the maximum number of terms considered. The space-dependent stochastic elastic tensor is thus approximated by

$$\mathbb{E}(\boldsymbol{x}, \boldsymbol{\xi}) = \mathbb{E}_0(\boldsymbol{x}) + \sum_{k=1}^{k_{\max}} \xi_k \, \mathbb{E}_k(\boldsymbol{x}) \tag{1}$$

with the spatial coordinate $\boldsymbol{x}$ and the expectation value $\mathrm{E}[\mathbb{E}(\boldsymbol{x}, \boldsymbol{\xi})] = \mathbb{E}_0(\boldsymbol{x})$ [6]. For scalar random fields, the coefficients in the series are obtained from an eigenvalue decomposition of the covariance operator, see [13] and [1]. An analogous series expansion for the displacements $\boldsymbol{u}$ yields the stochastic finite element method (see e.g. [4, 11, 3]). Here, the expected value $\boldsymbol{u}_0$ together with the series terms $\boldsymbol{u}_k$ are the unknowns in a coupled algebraic equation system. It is obvious that the calculation of both the eigenfunctions $\mathbb{E}_k$ and the vector of unknown displacements $(\boldsymbol{u}_0, \boldsymbol{u}_1, ..., \boldsymbol{u}_{k_{\max}})$ is of high numerical effort compared to the simple elastic simulation. Of course, the benefit of the increased computation time is a stochastic displacement field from which the strains and thus stresses may be derived. The level of accuracy is increased with increasing length of the series expansion, i.e. with higher values for $k_{\max}$ resulting in higher computational costs.

In this contribution, we recall a novel approach for the calculation of stochastic information for the elastic constants and stresses at the Gauß point level, which was presented in [7]. In this approach, also a stochastic series expansion as in (1) is applied. However, since there is no mathematical theory for the the general expansion of tensor-valued fields, we start with a general representation as in (1), where we assume that the ξ_k are independent random variables with

$$\mathrm{E}[\xi] = \mathrm{E}[\xi^3] = 0, \qquad \mathrm{E}[\xi^2] = 1, \tag{2}$$

and the coefficients $\mathbb{E}_k(\boldsymbol{x})$ satisfy the symmetry conditions $\mathbb{E}_{ijkl} = \mathbb{E}_{klij} = \mathbb{E}_{jikl} = \mathbb{E}_{ijlk}$ and such that the expectation and variance

$$\mathrm{E}[\mathbb{E}(\boldsymbol{x}, \boldsymbol{\xi})] = \mathbb{E}_0(\boldsymbol{x}) \quad \text{and} \quad \mathrm{Var}(\mathbb{E}(\boldsymbol{x}, \boldsymbol{\xi})) = \sum_{k=1}^{k_{\max}} \mathbb{E}_k(\boldsymbol{x}) : \mathbb{E}_k(\boldsymbol{x}) \tag{3}$$

are stationary, i.e., they do not depend on the location. This allows to model a wide range of random distributions and is not restricted to Gaussians like in the case of the stochastic

finite elements. Furthermore, it turns out that in the new approach we may choose $k_{\max}$ very large without a substantial increase in the numerical cost. We present the derivation based on [7] and recall several numerical results which compare the analytical solution with Monte Carlo calculations.

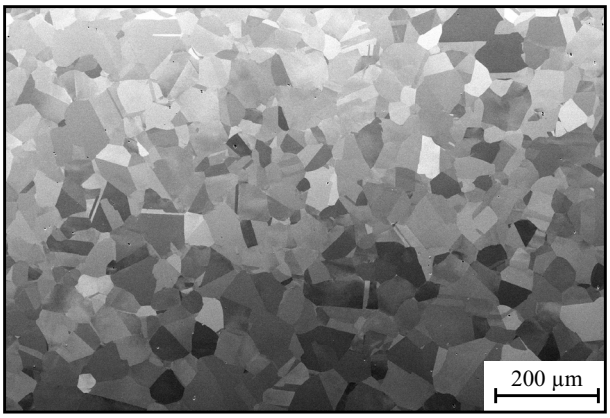

Figure 1: Microstructure in steel. Result of a scanning electron microscopy after [12].

2 THE STOCHASTIC MATERIAL POINT BEHAVIOR

An example for a typical microstructure is presented in Figure 1. Here, steel is investigated by scanning electron microscopy showing very nicely the random areas of different gray level. Each area with constant gray level possesses a constant orientation of the crystallographic lattice and is referred to as grain. Due to orientation, segregation, local defects and others, see also the introduction, the material properties are subjected to stochastic fluctuations even in the elastic regime. Since the same "chaotic" picture is present for different sampling points in a construction part, the local spatial behavior is stochastic even in a homogenized way, i.e. in terms of effective elastic constants and stresses for the entire microstructural domain.

To model this stochastic behavior in a numerically efficient and physically very reasonable manner, basically two homogenized and effective quantities have to be specified

1. a stochastic measure for the elastic constants denoted by $\bar{\mathbb{E}} = \bar{\mathbb{E}}(\boldsymbol{\xi})$ and

2. a stochastic measure for the strains denoted by $\boldsymbol{\varepsilon} = \boldsymbol{\varepsilon}(\boldsymbol{\xi})$

Combining these two measures results in a homogenized and effective but also *stochastic* measure for the stress

$$\boldsymbol{\sigma} = \boldsymbol{\sigma}(\boldsymbol{\xi}) = \bar{\mathbb{E}}(\boldsymbol{\xi}) : \boldsymbol{\varepsilon}(\boldsymbol{\xi}) \tag{4}$$

A subsequent calculation of the expectation and variance of the elastic constants and the stress is then quite feasible.

The previously defined goal is achieved in two steps. In a first step, a stochastic series expansion as described in the previous section is employed to the elastic constants. A

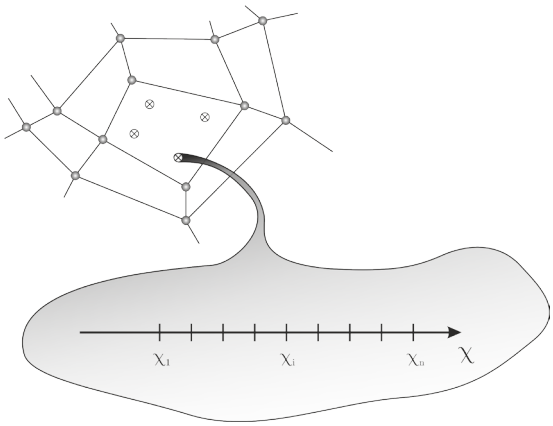

Figure 2: Material point in a finite element setting which is expanded by the microstructural coordinate χ to account for the discretized domains in a real microstructure as shown in 1. Figure 2 after [7].

relaxation of an associated energy yields the desired effective but stochastic measure for the elastic constants. In a second step, a stochastic series expansion is also employed to the strains. Relaxation of the modified energy yield the unknown coefficients of the series expansion for the strains and thus the desired stochastic measure for the effective strains.

2.1 First step: stochastic measure for the effective elastic constants

The material point is defined as the ensemble of grains (or more generally: domains) as exemplary showed in Figure 1. To merge the local behavior in each domain to an effective behavior at the material point level, we introduce a "microstructural coordinate" χ on the domain level, see Figure 2. Here, the domains are presented in a discretized way using the index i. For each discretized microstructural coordinate χ_i – referring to one discrete domain in the real material – varying stochastic elastic constants are present yielding to varying stochastic strains in each domain χ_i.

The elastic constants are expressed in terms of a stochastic series for each domain by

$$\mathbb{E}_i = \mathbb{E}(\chi_i, \xi) = \mathbb{E}_{0,i} + \sum_{k=1}^{k_{\max}} \xi_k \, \mathbb{E}_{k,i} \tag{5}$$

with the assumptions on ξ and $\mathbb{E}_{k,i}$ as outlined in Section 1. For the strains in each domain, we do not make any assumption at this stage nor do we approximate them by a series expansion but leave them completely general. Then, the Helmholtz free energy of each domain is given by

$$\Psi(\chi_i, \xi) = \Psi_i = \frac{1}{2} \boldsymbol{\varepsilon}_i : \mathbb{E}_i : \boldsymbol{\varepsilon}_i. \tag{6}$$

which allows for formulating the associated relaxation problem as

$$\Psi = \inf_{\boldsymbol{\varepsilon}_i} \left\{ \frac{1}{n} \sum_{i=1}^{n} \Psi_i \quad \middle| \quad \frac{1}{n} \sum_{i=1}^{n} \boldsymbol{\varepsilon}_i = \boldsymbol{\varepsilon} \right\}. \tag{7}$$

The parameter n accounts for the number of domains in each material point ensemble. The unknown strains in each domain are computed by the minimization problem

$$\mathcal{L} = \frac{1}{2n} \sum_{i=1}^{n} \boldsymbol{\varepsilon}_i : \left(\mathbb{I} + \sum_{k=1}^{k_{\max}} \xi_k \, \mathbb{E}_{k,i} \right) : \boldsymbol{\varepsilon}_i + \boldsymbol{\sigma} : \left[\boldsymbol{\varepsilon} - \frac{1}{n} \sum_{i=1}^{n} \boldsymbol{\varepsilon}_i \right] \rightarrow \min_{\boldsymbol{\varepsilon}_i, \boldsymbol{\sigma}} \tag{8}$$

in which for simplicity we rescaled the elastic constants such that $\mathbb{E}_{0,i} = \mathbb{I}$. For more details we refer to [7]. The Lagrange parameter $\boldsymbol{\sigma}$ accounts to the constraint that the mean of all strains in the individual grains equals the (given) homogenized strain of the material point ensemble $\boldsymbol{\varepsilon}$. This Lagrange parameter is indeed the stress measure we are looking for. Solving the Lagrange equations yields the homogenized energy $\Psi = 1/n \sum_{i=1}^{n} \Psi_i = 1/2 \boldsymbol{\varepsilon} : \bar{\mathbb{E}} : \boldsymbol{\varepsilon}$ with the effective, *stochastic* elastic constant

$$\bar{\mathbb{E}} = \bar{\mathbb{E}}(\boldsymbol{\xi}) = \left[\frac{1}{n} \sum_{i=1}^{n} \left[\mathbb{I} + \sum_{k=1}^{k_{\max}} \xi_k \mathbb{E}_{k,i} \right]^{-1} \right]^{-1} \tag{9}$$

which is the harmonic mean of the individual elastic constants in the respective domains. The expectation value for the harmonic mean is highly inaccessible. Thus, we approximate it with a Taylor series of order two. This yields

$$\bar{\mathbb{E}} \approx \mathbb{I} + \frac{1}{n} \sum_{i=1}^{n} \sum_{k=1}^{k_{\max}} \xi_k \mathbb{E}_{k,i} - \frac{1}{n} \sum_{i=1}^{n} \left(\sum_{k=1}^{k_{\max}} \xi_k \mathbb{E}_{k,i} \right)^2 + \frac{1}{n^2} \left(\sum_{i=1}^{n} \sum_{k=1}^{k_{\max}} \xi_k \mathbb{E}_{k,i} \right)^2 . \tag{10}$$

2.2 Second step: stochastic measure for the effective strains

The purpose of this second step is the search of an appropriate stochastic measure of the effective strains, i.e. we are seeking for a formulation for $\boldsymbol{\varepsilon} = \boldsymbol{\varepsilon}(\boldsymbol{\xi})$. To this end, we employ the same stochastic series expansion to the strains in each domain $\boldsymbol{\varepsilon}_i$ which we also used for the elastic constants. This means

$$\boldsymbol{\varepsilon}_i = \boldsymbol{\varepsilon}(\chi_i, \xi) = \boldsymbol{\varepsilon}_{0,i} + \sum_{k=1}^{k_{\max}} \xi_k \, \boldsymbol{\varepsilon}_{k,i} \tag{11}$$

with the unknown expectation values in each domain $\boldsymbol{\varepsilon}_{0,i}$ and series coefficients $\boldsymbol{\varepsilon}_{k,i}$. To compute them, we employ a second relaxation approach for the homogenized energy, more precisely

$$\Psi^{\mathrm{E}} = \inf_{\boldsymbol{\varepsilon}_{0,i}, \boldsymbol{\varepsilon}_{k,i}} \left\{ \frac{1}{n} \sum_{i=1}^{n} \Psi_i^{\mathrm{E}} \;\middle|\; \frac{1}{n} \sum_{i=1}^{n} \boldsymbol{\varepsilon}_{0,i} = \boldsymbol{\varepsilon}_0 \right\} \tag{12}$$

The superscript refers to the expectation value of the respective quantities. This procedure is similar to the derivation of the stochastic finite elements and is required to find the (deterministic) series coefficients. More details are given in [7].

The expected homogenized Helmholtz free energy is given by

$$\Psi^{\mathrm{E}} = \frac{1}{n}\sum_{i=1}^{n}\Psi_i^{\mathrm{E}} = \frac{1}{n}\sum_{i=1}^{n}\left(\frac{1}{2}\sum_{k=0}^{k_{\max}}\boldsymbol{\varepsilon}_{k,i} : \mathbb{I} : \boldsymbol{\varepsilon}_{k,i} + \boldsymbol{\varepsilon}_{0,i} : \sum_{k=1}^{k_{\max}}\mathbb{E}_{k,i} : \boldsymbol{\varepsilon}_{k,i}\right), \tag{13}$$

see [7]. Again, the elastic constants are rescaled to yield $\mathbb{E}_{i,0} = \mathbb{I}$. The associated minimization problem reads

$$\frac{\partial \mathcal{L}}{\partial \boldsymbol{\varepsilon}_{0,i}} = \mathbf{0} = \frac{1}{n}\left(\mathbb{I} : \boldsymbol{\varepsilon}_{0,i} + \sum_{k=1}^{k_{\max}}\mathbb{E}_{k,i} : \boldsymbol{\varepsilon}_{k,i}\right) - \frac{1}{n}\hat{\boldsymbol{\sigma}} \tag{14}$$

$$\frac{\partial \mathcal{L}}{\partial \boldsymbol{\varepsilon}_{k,i}} = \mathbf{0} = \frac{1}{n}\left(\mathbb{I} : \boldsymbol{\varepsilon}_{k,i} + \boldsymbol{\varepsilon}_{0,i} : \mathbb{E}_{k,i}\right) \tag{15}$$

$$\frac{\partial \mathcal{L}}{\partial \hat{\boldsymbol{\sigma}}} = \mathbf{0} = \boldsymbol{\varepsilon}_0 - \frac{1}{n}\sum_{i=1}^{n}\boldsymbol{\varepsilon}_{0,i}. \tag{16}$$

with a new Lagrange parameter $\hat{\boldsymbol{\sigma}}$ which, however, is very closely related to $\boldsymbol{\sigma}$. Solving the minimization conditions for the unknown coefficients in the series expansion results finally in the desired formulation for the effective stochastic strain of the homogenized microstructure as

$$\boldsymbol{\varepsilon} = \boldsymbol{\varepsilon}(\boldsymbol{\xi}) = \frac{1}{n}\sum_{i=1}^{n}\boldsymbol{\varepsilon}_i = \frac{1}{n}\sum_{i=1}^{n}\left(\mathbb{I} - \sum_{k=1}^{k_{\max}}\xi_k\mathbb{E}_{k,i}\right) : \boldsymbol{\varepsilon}_0. \tag{17}$$

2.3 Result: stochastic measure of the stress

Combing the results of the previous two subsections result in the desired stochastic measure for the stress of the homogenized material point as

$$\begin{aligned}\boldsymbol{\sigma} &= \boldsymbol{\sigma}(\boldsymbol{\xi}) = \bar{\mathbb{E}}(\boldsymbol{\xi}) : \boldsymbol{\varepsilon}(\boldsymbol{\xi}) \\ &= \left[\mathbb{I} + \frac{1}{n}\sum_{i=1}^{n}\sum_{k=1}^{k_{\max}}\xi_k\mathbb{E}_{k,i} - \frac{1}{n}\sum_{i=1}^{n}\left(\sum_{k=1}^{k_{\max}}\xi_k\mathbb{E}_{k,i}\right)^2 + \frac{1}{n^2}\left(\sum_{i=1}^{n}\sum_{k=1}^{k_{\max}}\xi_k\mathbb{E}_{k,i}\right)^2\right] \\ &\quad : \frac{1}{n}\sum_{i=1}^{n}\left(\mathbb{I} - \sum_{k=1}^{k_{\max}}\xi_k\mathbb{E}_{k,i}\right) : \boldsymbol{\varepsilon}_0\end{aligned} \tag{18}$$

The stochastic information in terms of expectation and variance can now be calculated for both the elastic constants and the strains. For the elastic constants they read

$$\mathrm{E}[\bar{\mathbb{E}}] = \mathbb{E}_{0,1} - \mathbb{E}_{0,1}^{1/2} : \mathbb{V} : \mathbb{E}_{0,1}^{1/2} + \frac{1}{n}\mathbb{E}_{0,1}^{1/2} : \mathbb{C} : \mathbb{E}_{0,1}^{1/2} \tag{19}$$

and

$$\mathrm{Var}(\mathbb{E}_{0,1}^{-1/2} : \bar{\mathbb{E}} : \mathbb{E}_{0,1}^{-1/2}) = \frac{1}{n}\mathbb{C} + \frac{1}{n}\mathbb{C}^{(2)} + o\left(\frac{1}{n}\right), \tag{20}$$

respectively, where here we give the general formula without assuming $\mathbb{E}_{0,1} = \mathbb{I}$ anymore.

For the stress, they are calculated as

$$\mathrm{E}[\boldsymbol{\sigma}] = \mathbb{E}_{0,1}^{1/2} : (\mathbb{I} - \mathbb{V}) : \mathbb{E}_{0,1}^{1/2} : \boldsymbol{\varepsilon}_0. \tag{21}$$

and

$$\mathrm{Var}(\mathbb{E}_{0,1}^{-1/2} : \boldsymbol{\sigma} : \mathbb{E}_{0,1}^{-1/2}) = \frac{1}{n}\boldsymbol{\varepsilon}_0 : \hat{\mathbb{C}}^{(2)} : \boldsymbol{\varepsilon}_0 + \frac{1}{n}\boldsymbol{\varepsilon}_0 : \hat{\mathbb{C}}_{\mathbb{V}} : \boldsymbol{\varepsilon}_0 + o\left(\frac{1}{n}\right). \tag{22}$$

Note that here the variance is calculated as a fourth order tensor as in (3). The following abbreviations have been used

$$\mathbb{V} = \mathrm{E}[\mathbb{X}_1 : \mathbb{X}_1], \tag{23}$$

$$\mathbb{C} = \frac{1}{n}\sum_{i,j=1}^{n} \mathrm{E}[\mathbb{X}_i : \mathbb{X}_j], \tag{24}$$

$$\hat{\mathbb{C}} = \frac{1}{n}\sum_{i,j=1}^{n} \mathrm{E}[\mathbb{X}_i \cdot \mathbb{X}_j], \tag{25}$$

$$\hat{\mathbb{C}}_{\mathbb{V}} = \frac{1}{n}\sum_{i,j=1}^{n} \mathrm{E}[\mathbb{X}_i : \mathbb{V} \cdot \mathbb{V} : \mathbb{X}_j] \tag{26}$$

and

$$\mathbb{C}^{(2)} = \frac{1}{n}\sum_{i,j=1}^{n} (\mathrm{E}[\mathbb{X}_i^2 : \mathbb{X}_j^2] - \mathbb{V} : \mathbb{V}) \tag{27}$$

$$\hat{\mathbb{C}}^{(2)} = \frac{1}{n}\sum_{i,j=1}^{n} \mathrm{E}[\mathbb{X}_i^2 \cdot \mathbb{X}_j^2] - \mathbb{V} \cdot \mathbb{V}) \tag{28}$$

with

$$\mathbb{X}_i = \mathbb{E}_{0,1}^{-1/2} : (\mathbb{E}_i - \mathbb{E}_{0,1}) : \mathbb{E}_{0,1}^{-1/2}. \tag{29}$$

Details can be found in [7]. We emphasize two important consequences of our approach: firstly, the variances and covariances as in (23) to (28) can be estimated from data. Once they are known, one does not need to calculate the coefficients $\mathbb{E}_{k,i}$ in the expansion of the random field. Secondly, this formulation of the results is independent of the number $k_{\max}$ of terms in the expansion. The expansion (1) is important for our derivation of the results, but $k_{\max}$ may be supposed to be very high, thereby allowing for a more general distribution of the random field. Together with the first point, that there is no need to compute the coefficients in the expansion, this implies the results have a much higher precision.

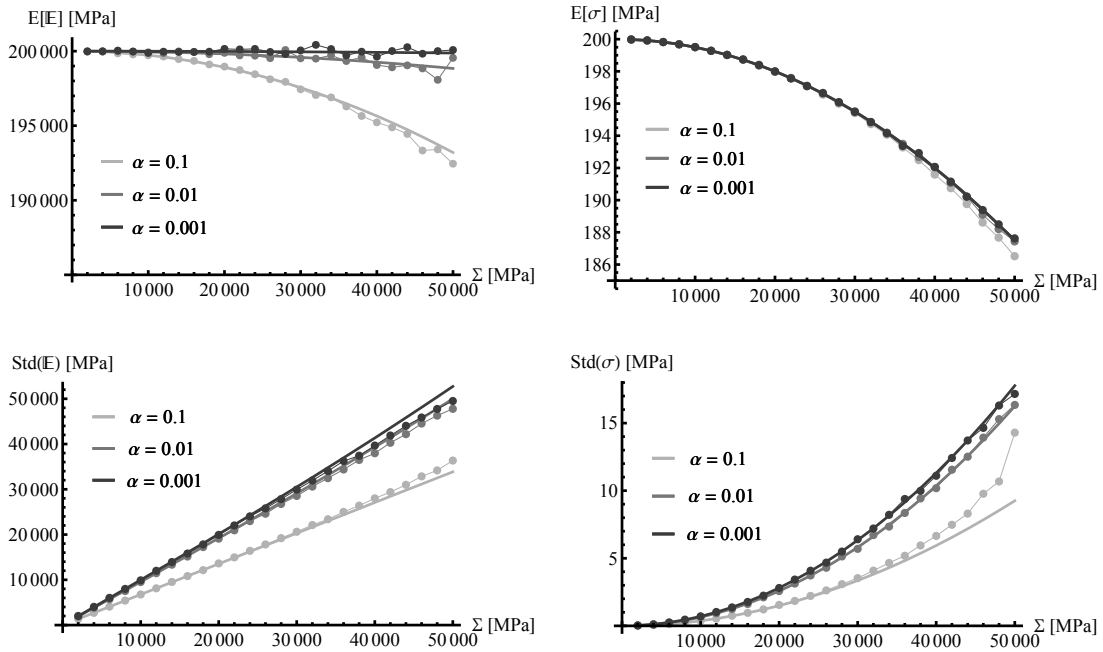

Figure 3: Mean of the stochastic simulation for 20,000 random variables (dots) vs. the analytical values proposed by our model (lines) for Case 1 and varying α. The number of domains is $n = 30$. After [7], Figure 6.

3 NUMERICAL RESULTS

To illustrate our results collected in Section 2.3, we discuss two numerical examples for the case of a one-dimensional stochastic field, which are recalled from [7].

We model two different distributions of $\mathbb{E}_i$, a Gaussian with square-exponential covariance, and a finitely dependent linear combination of uniformly varying random variables.

Case 1: The ξ_k are independent standard Gaussian and the covariance is given by $C(\chi_i, \chi_j) = \Sigma^2 \exp(-\alpha|i-j|^2)$. This is a two-parameter family with variance Σ and α corresponding to the strength of the correlations.

Case 2: The ξ_k are independent and uniform distributed on $[-\sqrt{3}, \sqrt{3}]$. Each $\mathbb{E}_i$ is a homogeneous linear combination of three ξ_k, such that $\mathbb{E}_i$ and $\mathbb{E}_j$ are independent whenever $|i-j| \geq 2$ and $\mathrm{Var}(\mathbb{E}_i) = \Sigma^2$.

In both cases we use an expectation value of $\mathbb{E}_0 = 200'000$ [MPa] and a strain of $\varepsilon_0 = 1 \times 10^{-4}$ [-] and let the standard deviation Σ vary between 2,000 and 50,000. For Case 1, we additionally vary $\alpha = \{0.001, 0.01, 0.1\}$ and we let $n = 30$. The expectation $\mathrm{E}[\bar{\mathbb{E}}]$ and $\mathrm{E}[\sigma]$ and the standard deviation $\mathrm{Std}(\bar{\mathbb{E}}) = \sqrt{\mathrm{Var}(\bar{\mathbb{E}})}$ and $\mathrm{Std}(\sigma) = \sqrt{\mathrm{Var}(\sigma)}$ are calculated for the effective Young's modulus and the stress, respectively, evaluated according to the formulas above. These analytic results are compared with the empirical estimated from a Monte Carlo simulation with 20,000 iterations in Figures 3 and 4.

Several conclusions can be drawn from our results:

1. Our analytical formulas show excellent agreement with the numerical simulations;

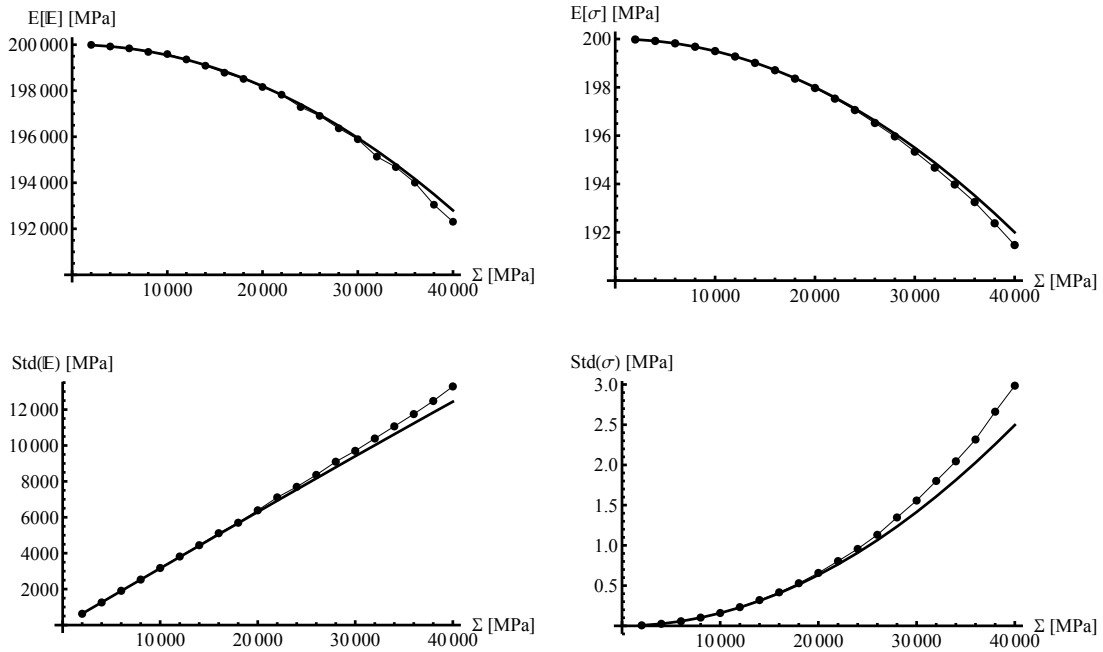

Figure 4: Mean of the stochastic simulation for 20,000 random variables (dots) vs. the analytical values proposed by our model (lines) for Case 2. The number of domains is $n = 30$. After [7], Figure 8.

in particular for small values of the variance.

2. The Gaussian distribution in Case 1, which a priori does not satisfy the ellipticity constraint, also performs well in the numerical comparison.

3. The stochastic stress **cannot** be calculated simply by $\mathbb{E}\,\varepsilon_0$; it decreases quite strongly for all model parameters (n, Σ, α); our equation captures this aspect correctly.

4. The standard deviation of the stress is large for high standard deviations Σ of the Young's modulus (close to 10%); it also **cannot** be concluded solely from the standard deviation Σ without our equations.

We emphasize that our equations can be evaluated basically without any computational effort. In contrast, 20,000 stochastic simulations are necessary in order to receive the same behavior just by averaging the realizations of the stochastic behavior. The effect is even more pronounced for a finite element simulation. Furthermore, the presented model is also much faster than a stochastic finite element framework due to the increased number of nodal unknowns in the latter method. The excellent agreement between simulation and evaluation of our equations, which captures the averaged stochastic behavior very well, proves that our assumptions are very reasonable and even the broken Taylor series produces only negligible errors.

4 OUTLOOK

It is possible to extend the method to the modeling of inelastic materials. We give here a very brief outlook on how this yields a formula for the expected stress measure and refer to the forthcoming paper [8] for the derivation. The strains can be decomposed into the elastic and inelastic parts as $\boldsymbol{\varepsilon}_i = \boldsymbol{\varepsilon}_i^{\mathrm{e}} + \boldsymbol{\varepsilon}_i^{\mathrm{p}}$, and applying the relaxation method in Sections 2.1 and 2.2 to the elastic parts results in

$$\boldsymbol{\varepsilon} - \boldsymbol{\varepsilon}^{\mathrm{p}} = \left[\mathbb{I} - \sum_{k=1}^{k_{\max}} \xi_k \mathbb{E}_0^{-1} : \mathbb{E}_{k,i}\right] : (\boldsymbol{\varepsilon}_0 - \boldsymbol{\varepsilon}_0^{\mathrm{p}}) \tag{30}$$

and $\boldsymbol{\sigma} = \bar{\mathbb{E}} : (\boldsymbol{\varepsilon} - \boldsymbol{\varepsilon}_{\mathrm{p}})$ with $\bar{\mathbb{E}}$ as in (10). It remains to obtain a formula for the inelastic strains, which can be done by employing the Hamilton principle in its form for absent gradients of $\boldsymbol{\varepsilon}_{\mathrm{p}}$ reading

$$\mathcal{L} = \dot{\Psi}^{\mathrm{E}} + \Delta^{\mathrm{E}} + \mathrm{cons} \to \underset{\dot{\boldsymbol{\varepsilon}}_0^{\mathrm{p}}, \dot{\boldsymbol{\varepsilon}}_k^{\mathrm{p}}}{\mathrm{stat}}, \tag{31}$$

where $\Delta = r\dot{\boldsymbol{\varepsilon}}^{\mathrm{p}} : \dot{\boldsymbol{\varepsilon}}^{\mathrm{p}}$ is a dissipation function homogeneous of order two. This results in the differential equation

$$\dot{\boldsymbol{\varepsilon}}_0^{\mathrm{p}} = r^{-1}\mathrm{dev}\left[\mathbb{E}_{0,1}^{1/2} : (\mathbb{I} - \mathbb{V}) : \mathbb{E}_{0,1}^{1/2} : (\boldsymbol{\varepsilon}_0 - \boldsymbol{\varepsilon}_0^{\mathrm{p}})\right] \tag{32}$$

for $\boldsymbol{\varepsilon}_0^{\mathrm{p}}$. Solving this equation allows then to compute the expected stress as in formula (21). Figure 5 shows a comparison of this analytic formula with the estimation obtained from a Monte-Carlo simulation.

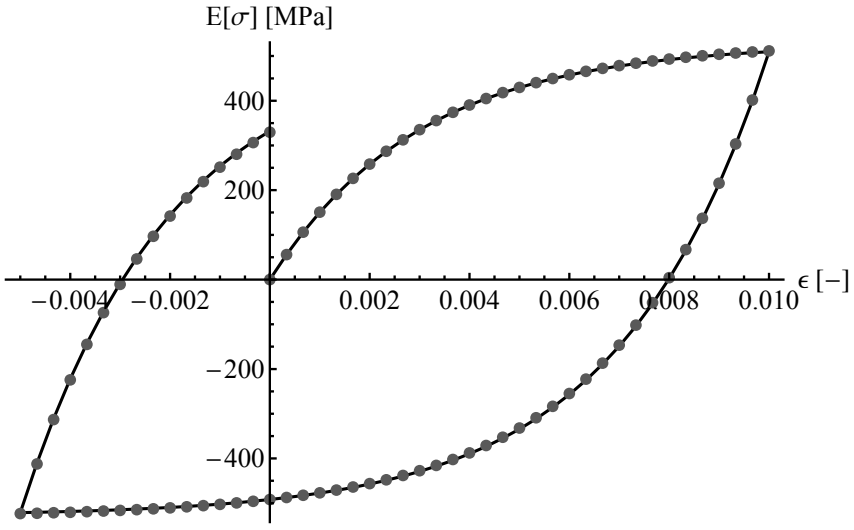

Figure 5: Mean of the stochastic simulation for 2,000 random variables (dots) vs. the analytical values proposed by our model (lines) in the viscous material for Case 1. The number of domains is $n = 30$.

5 CONCLUSIONS

The inclusion of stochastic information in modeling of materials is highly appreciated since construction parts are increasingly being designed at the edge of the sustainability. The stochastic fluctuations of material properties have a strong impact on the respective material behavior during operation. In this contribution, we propose a novel approach that is based on a stochastic field at the material point which is physically motivated. In a first step, we applied a stochastic expansion to the elastic constants and performed a homogenization over the material point. This results in a stress measure, which includes a stochastic effective elastic constant that depends on the harmonic mean of the elastic constants in each domain. In a second step, we employed the same stochastic expansion as for the elastic constants for the strains at the microlevel. The relaxation of the expected Helmholtz free energy yielded then the stochastic coefficients of the strain expansion. Double contraction of the stochastic elastic constants and the stochastic strains gives the appropriate stress measure. Using these formulas for the stress measure, we were able to calculate the expectation and variance. For this computation, only the knowledge of covariances of the elastic constants needs to be given so that the stress as well as its expectation and variance can be calculated in a closed form. For an implementation into a finite element routine, only "modified" elastic constants have to be used.

REFERENCES

[1] Alexanderian, A., A brief note on the Karhunen-Loève expansion, *arXiv preprint*, (2015).

[2] Crestaux, T. and Le Maître, O. and Martinez, J. Polynomial chaos expansion for sensitivity analysis. *Reliability Engineering & System Safety* (2009) **37**:3323–3341.

[3] Dasgupta, G., Stochastic shape functions and stochastic strain–displacement matrix for a stochastic finite element stiffness matrix, *Acta Mechanica*, (2008) **195**:379–395.

[4] Frauenfelder, P., Schwab, C. and Todor, R., Finite elements for elliptic problems with stochastic coefficients, *Computer methods in applied mechanics and engineering*, (2005) **194**:205–228.

[5] Fukunaga, K. and Koontz, W., Application of the Karhunen-Loeve expansion to feature selection and ordering, *IEEE Transactions on Computers*, (1970) **19**:311–318.

[6] Ghanem, R. and Spanos, P., *Stochastic finite elements: a spectral approach*, Courier Corporation, (2003).

[7] Junker, P. and Nagel, J., A relaxation approach to modeling the stochastic behavior of elastic materials. *In review.*

[8] Junker, P. and Nagel, J., A relaxation approach to modeling the stochastic behavior of inelastic materials. *In preparation.*

[9] Kirby, M. and Sirovich, L., Application of the Karhunen-Loeve procedure for the characterization of human faces, *IEEE Transactions on Pattern analysis and Machine intelligence*, (1990) **12**:103–108.

[10] Li, R. and Ghanem, R., Polynomial chaos expansion for sensitivity analysis. *Reliability Engineering & System Safety*, (2009) **13**:125–136.

[11] Matthies, H. and Keese, A., Galerkin methods for linear and nonlinear elliptic stochastic partial differential equations, *Computer Methods in Applied Mechanics and Engineering*, (2005) **194**:1295–1331.

[12] Nabiran N., Berns H. and Rieder S., High interstitial stainless austenitic steel: As cast vs. esr and hot worked. *Super-High Strength Steels*, Oct. 17.-20. 2010, Italy.

[13] Spanos, P. and Ghanem, R., Stochastic finite element expansion for random media, *Journal of engineering mechanics*, (1989) **115**:1035–1053.

XIV International Conference on Computational Plasticity. Fundamentals and Applications
COMPLAS XIV
E. Oñate, D.R.J. Owen, D. Peric & M. Chiumenti (Eds)

A CONTINUUM MODEL ACCOUNTING FOR THE EFFECT OF THE INITIAL AND EVOLVING MICROSTRUCTURE ON THE EVOLUTION OF DYNAMIC RECRYSTALLIZATION

HARM KOOIKER[†*], EMIN S. PERDAHCIOĞLU[†] AND TON VAN DEN BOOGAARD[†]

[†] Department of Nonlinear Solid Mechanics
University of Twente
Drienerlolaan 5, 7522 NB Enschede, the Netherlands

[*]Philips Consumer Lifestyle
Amstelplein 2, 1096 BC, Amsterdam
e-mail: harm.kooiker@philips.com

Key words: Dynamic Recrystallization, Grain Size, Microstructure, Constitutive Modeling

Abstract. Laser assisted forming is a process which is increasingly being adopted by the industry. Application of heat by a laser to austenitic stainless steel (ASS) sheet provides *local* control over formability and strength of the material. The hot forming behavior of ASS is characterized by significant dynamic recovery and dynamic recrystallization. These two processes lead to a softening stress-strain response and have a significant impact on the microstructure of the material. Most of the research performed on hot forming of ASS focuses on dynamic recrystallization and then specifically on the behavior of the annealed state, consisting of relatively large equiaxed austenite grains. However, in industry it is common to use cold rolled ASS sheet which is a mixture of austenite and martensite. Application of a laser heat treatment to the cold rolled grades of ASS induces a so-called 'reverse' transformation of martensite to austenite which, depending on the exact time-temperature combinations, leads to an austenite grain size in the range of nano- to micrometer. It is known from experiments that the effect of initial grain size on dynamic recrystallization is significant, especially on the initial stages of recrystallization. Therefore any continuum model capable of describing hot forming of cold rolled ASS should include the effect of the initial grain size.

In this work a physically based continuum model for dynamic recrystallization is presented which accounts for the effect of the initial *and* evolving grain size on the evolution of dynamic recrystallization. It is shown that the initial grain size can be accounted for by incorporating its effect on the availability of preferred nucleation sites, i.e. grain edges. The new model is compared to experimental results and it is shown that the model correctly predicts accelerated recrystallization with decrease in grain size and that

there is a weak dependence of the dynamically recrystallized grain size on the initial grain size. Furthermore predicted recrystallized grain sizes are in good agreement with the experimentally measured values.

1 INTRODUCTION

Metastable austenitic stainless steels (ASS) are widely used in industry due to their excellent corrosion resistance and formability. When designing products from ASS a designer must adhere to the current trade-off between hardness and ductility, where high hardness is usually required for product performance and ductility is required for make-ability, the latter limiting the attainable functional hardness of the product. Recently, there is an increased focus on laser assisted forming of ASS to enable local control of strength and formability. During this high temperature forming of ASS, dynamic recovery and dynamic recrystallization takes place leading to significant stress softening and a steady state stress lower than the peak stress [1, 2].

In industry it is common to use cold-rolled grades of ASS to achieve the desired overall functional hardness. The cold rolled grades are a mixture of austenite and martensite due to the mechanically induced transformation during rolling. When they are exposed to a heat treatment, such as during laser assisted forming, the martensite can revert back to finely grained austenite [3–5]. Numerous experimental results show that the initial grain size has a significant effect on the onset and progression of recrystallization [1,6,7] because of the dependence of potential nucleation sites on the grain size [8]. Another important observation is the weak to non-existent dependence of the steady state grain size on the initial grain size where it is found that deformation conditions are leading.

To be able to design optimal and safe products and first-time-right processes, it is imperative to have accurate quantitative models with which the process *and* product performance can be predicted up-front. The functional strength of a laser assisted forming zone *after* forming (and cooling down) is dependent on the grain size evolution during the transient hot forming process. Therefore a proper continuum mechanical description of the hot forming behavior of ASS should be able to account for the effect of initial *and* evolving grain size.

In [9] the authors have presented a physically based continuum model to predict the hot forming behavior of austenitic stainless steel at a range of high temperatures and strain rates. In this paper this model is adapted to be able to predict the effect of initial *and* evolution of austenitic grain size on the dynamic recrystallization and stress-softening behavior. The adapted model is fitted to the experimental results of Wahabi et al. [7] and it is shown that it is capable of accounting for the effect of initial grain size on the progression of dynamic recrystallization and that there is a good match between the predicted and reported grain sizes.

2 MODELING OF HOT FORMING

In this section, for sake of clarity, the complete model is highlighted, however the novelty of the current work lies in the treatment of the effect of grain size on the *recrystallization* behavior. To model the hot forming behavior of austenitic stainless steel we employ the Bergström equation [10] and assume that the behavior can be modeled by properly accounting for the effect of several mechanisms on one internal variable, i.e. the average density of immobile dislocations (henceforth dislocation density). The mechanisms included in this work are dynamic recovery, dynamic recrystallization (and the effect of grain size on this behavior) and grain boundary strengthening.

$$\sigma_y = \sigma_i + \sigma_w + \frac{k_d}{\sqrt{D}} \tag{1}$$

In which σ_i and σ_w is the frictional stress and work hardening stress respectively and $\frac{k_d}{\sqrt{D}}$ represents the Hall-Petch effect accounting for grain boundary strengthening. The Taylor equation is now employed for the relation between work-hardening and dislocation density.

$$\sigma_w = \alpha \mu b M \sqrt{\rho} \tag{2}$$

Dynamic recrystallization is modeled by incorporating it as a time-dependent factor in the Bergström work hardening equation.

$$d\rho = (h\sqrt{\rho} - f\rho)d\varepsilon - \frac{dR}{dt}(\rho - \rho_0)dt \tag{3}$$

Here $h\sqrt{\rho}$ describes the hardening by immobilization of dislocations and is inversely proportional to the mean free path of dislocations, f describes the annihilation and remobilization of immobile dislocations by dynamic recovery and $\frac{dR}{dt}$ is the time dependent dynamic recrystallization term.

In previous research, it was shown that annealed austenitic stainless steel tends to form subgrains after some deformation and that this significantly affects the mean free path [11]. In order to be able to accommodate this changing mean free path the following evolution equation for the hardening parameter is adopted [12]:

$$\frac{dh}{d\varepsilon} = \frac{K}{\sqrt{\rho}}(h_s - h) \tag{4}$$

Where K describes the rate at which the substructure is formed and h_s is the saturation value of the hardening parameter.

2.1 Dynamic recrystallization and the effect of grain size

Discontinuous dynamic recrystallization is a process governed by nucleation and growth. During dynamic recrystallization new grains nucleate and consume highly dislocated grains replacing it with new grains of relatively low dislocation density. As the hot deformation process proceeds the new grains can harden to the point where they themselves

can be consumed by yet new grains. The continuous nucleation and growth process leads to a distribution of recrystallizing grains continuously replacing the concurrently hardening material. At the steady state stress there is a balance between new nucleation, growth of previously nucleated grains and impingement of grains that thus cannot grow further and therefore the distribution will remain constant, see Figure 1. Note that this does not mean that recrystallization is finished. It means that the recrystallization *rate* at the steady state is constant and therefore the recrystallized fraction can exceed 100%. In [9] it was shown that it is possible to accurately describe the effect of recrystallization on the stress–strain behavior by modeling the volume consumption of an assembly of N grains of average diameter $\bar{D}_r$ as a representative of the volume consumption of the distribution of recrystallizing grains.

$$\frac{dR}{dt} = \pi N \bar{D_r}^2 \bar{v} + \frac{1}{6}\pi \frac{dN}{dt} \bar{D_r}^3 \tag{5}$$

Where N is the amount of recrystallizing grains of average size $\bar{D}_r$ and $\bar{v}$ is the grain boundary migration speed. To complete this model a relation is needed to describe the evolution of the average grain size and the amount of recrystallizing grains of this average size, i.e. $\frac{d\bar{D}_r}{dt}$ and $\frac{dN}{dt}$ respectively. The novelty of the current work lies in the definition of these two evolution laws by incorporating the effect of grain size.

To include the effect of grain size on recrystallization it is proposed to couple the net nucleation of grains *and* growth of the average grain size to the availability of preferred nucleation sites like grain junctions, edges or surfaces. Though it is likely that more than one type of nucleation site will be(come) active throughout a hot deformation process, here it is assumed that recrystallization can be described by properly modeling the dominant nucleation site, i.e. grain edge. Note that *net* nucleation means that it represents both new nucleation and impingement, i.e. at the steady state there is a constant distribution and thus no net nucleation.

Available edge length

The availability of grain edges for net nucleation is determined by comparing the currently occupied grain edge L_{oc} to the available grain edge L_{av}. The available grain edge depends on the current grain size of the material, i.e. D_a which, depending on the extent of recrystallization, is a mix of the initial grains and recrystallizing grains $\bar{D}_r$, see Eq. 11. The amount of grain edge available for nucleation is determined by assuming that a representative volume is filled homogeneously by cubes of size D_a. It is clear that a cube is a simplification of the actual grain shape, however it is expected that the functional dependence of the explicit relations derived below will be similar for other grain shapes. The cube-approach has the distinct advantage of being easy to visualize. Every cube of size D_a has 12 edges and every edge is shared by 4 neighbors, therefore the amount of edge per unit volume can be described by:

$$L_{av} = (12/4) D_a N_{max} = 3 D_a \left(\frac{1}{D_a} \right)^3 \tag{6}$$

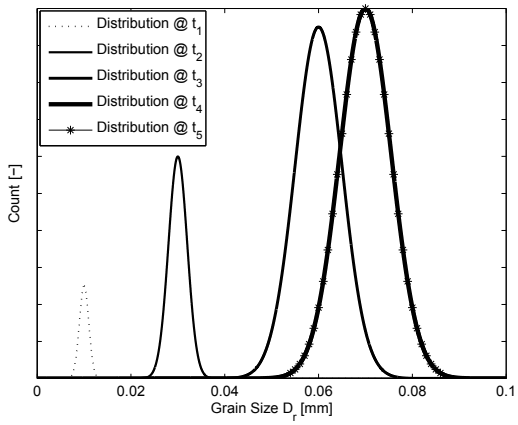

Figure 1: Change of the distribution of recrystallizing grains ($t_1 < t_2 < t_3 < t_4 < t_5$), at the steady state the distribution is constant (compare t_4 and t_5), i.e. nucleation and impingement cancel and the average of the grain size remains constant

Occupied edge length

To determine the occupation of grain edge by the assembly of recrystallizing grains it is important to account for the relative size of the recrystallizing grains $\bar{D}_r$ versus the current average grain size D_a. For average recrystallizing grain sizes above $\frac{1}{2}D_a$ the occupied grain edge is simply the amount of D_a grains encompassed by $\bar{D}_r$ grains times the grain edge of a D_a-grain ($3D_a$). For grain sizes smaller than $\frac{1}{2}D_a$ the occupied grain edge length is determined by looking at the amount of $\bar{D}_r$-grains that can fit on the perimeter of a D_a-grain. A D_a grain has 12 edges and 8 corners, every edge can house $(\frac{D_a}{\bar{D}_r} - 2)$ grains. This leads to the following conditional relation for the *average* occupied edge length:

$$L_{oc} = \begin{cases} \dfrac{3ND_a}{8 + 12(\frac{D_a}{\bar{D}_r} - 2)}, & \text{if } \bar{D}_r \leq .5D_a \\ 3ND_a\left(\frac{\bar{D}_r}{D_a}\right)^3, & \text{if } \bar{D}_r > .5D_a \end{cases} \tag{7}$$

This relation converges to the appropriate edge consumption for $\bar{D}_r << D_a$ being $\frac{1}{4}\bar{D}_r$ and to $\frac{3}{4}\bar{D}_r$ for $\bar{D}_r = 0.5D_a$.

Note that this type of nucleation and growth dependence makes it possible to describe the necklacing behavior seen in many experiments [7, 13–15] and which has a significant effect on the recrystallization evolution. The principle of necklacing is explained in 2D in Figure 2(a-b) and shown in a micrograph in Figure 2(c). If the recrystallizing grain size is small compared to the average size of the grains $\bar{D}_r << D_a$ a necklace of small grains will be formed along the grain edge. The interior of the large grains can only be recrystallized *after* they are reached by subsequent necklaces and grain edge becomes locally available. From a recrystallization viewpoint necklacing serves to delay the peak of recrystallization due to the fact that initially, depending on the ratio $\bar{D}_r$ and D_a, only a small portion of the volume *can* be recrystallized.

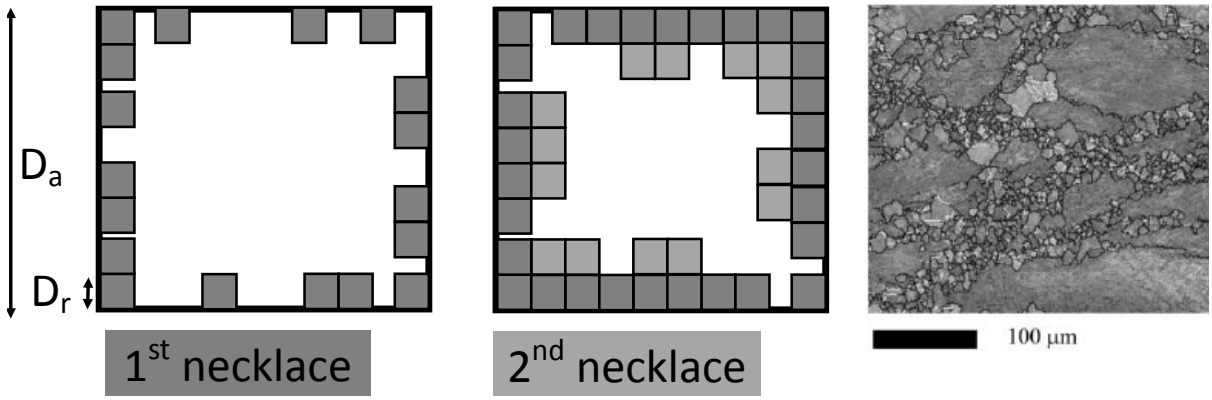

Figure 2: Explanation of a necklacing recrystallization sequence in *one* D_a-grain with a corresponding micrograph [7] displaying the phenomenon in the 92 µm experiments modeled in this paper

The derived formulations for the available and occupied edge length can now be implemented into the evolution equations for the average recrystallizing grain size $\frac{d\bar{D}_r}{dt}$ and number of recrystallizing grains $\frac{dN}{dt}$.

Average size of recrystallizing grains

The average size of the assembly of recrystallizing grains is determined by three mechanisms: nucleation, growth and impingement. Nucleation proportionally lowers the average size of the recrystallizing grains towards the size of the nuclei ($\bar{D_{r_0}}$). Growth enlarges the average size of the assembly with the average grain boundary migration speed $\bar{v}$. However growth cannot continue unbounded, i.e. growth stops when the occupied edge length equals the available edge length.

$$\frac{d\bar{D}_r}{dt} = 2\bar{v}\Big(1 - \frac{L_{oc}}{L_{av}}\Big) - (\bar{D}_r - \bar{D_{r_0}})\frac{1}{N}\frac{dN}{dt} \tag{8}$$

The term $\left(1 - \frac{L_{oc}}{L_{av}}\right)$ represents the lack of growth space for the growing grains. It is implicitly assumed that they remain equiaxed and do not bulge into the interior of the grain. This is in line with the frequently reported equiaxed recrystallization structures found in experiments [16]. The grain boundary migration speed is derived from the pressure on the boundary P and the grain boundary mobility m [8].

$$\bar{v} = mP = m\frac{1}{2}\mu b^2\rho \tag{9}$$

Table 1: Material, chosen and optimized parameters

α	0.5	$\bar{D}_{r0}$	$1 \cdot 10^{-3}$ mm	f	7.3	m	$9.9 \cdot 10^{-5}$ mm^4/Js
μ	$4.6 \cdot 10^4$ N/mm^2	ρ_0	$2.0 \cdot 10^4$ mm^{-2}	K	$1.6 \cdot 10^5$ mm^{-1}		
b	$2.8 \cdot 10^{-7}$ mm	h_0	$1.5 \cdot 10^6$ mm^{-1}	k_d	1.2 N/mm$^{3/2}$		
M	3	h_s	$5.2 \cdot 10^4$ mm^{-1}	c_n	$2.5 \cdot 10^5$ (Nm)$^{-1}$		

Number of recrystallizing grains

The nucleation of new grains into the assembly of grains of average size $\bar{D}_r$ depends on the available driving force P and availability of nucleation sites $\left(1 - \frac{L_{oc}}{L_{av}}\right)$.

$$\frac{dN}{dt} = c_n\Big(1 - \frac{L_{oc}}{L_{av}}\Big)P = c_n\Big(1 - \frac{L_{oc}}{L_{av}}\Big)P \tag{10}$$

Where c_n is the proportionality between the driving force and nucleation rate. The last equation that is needed is a relation between the change in the average size, the size of the recrystallizing grains and the ongoing recrystallization, i.e. when the materials recrystallizes the old (*initial*) grains of size D_0 are replaced by new grains of size $\bar{D}_r$. It is assumed that D_a is completely represented by $\bar{D}_r$ when the entire material has been recrystallized i.e. $R > 1$.

$$D_a = D_0\Big(1 - F(R)\Big) + D_r F(R) \tag{11}$$

Here F is a sigmoid function which, depending on R, ranges from zero to one, representing the smooth transition from D_0 to $\bar{D}_r$ from $R = 0$ to $R \geq 1$.

3 RESULTS

The proposed model is fitted to the data presented by Wahabi et al. who performed hot compression experiments on highly pure austenitic stainless steel of varying initial grain size (10, 24 and 92 µm). The material can be considered a model material for commercially available AISI-304 in regards to nickel and chrome content, but has a very low amount of interstitial elements. The experiments that were modeled were performed at 850°C and a strain rate of 0.001 s^{-1}. The model has in total 13 parameters of which 8 were fitted, 4 are material parameters and one was selected (respectively α, μ, b, M and the nucleus size $\bar{D}_{r0}$). The fitting was done by least squares optimization and the set of best fitting parameters is presented in Table 1. The results of the model are presented in Figure 3. Note that the entire recrystallization behavior is represented by only two parameters, the grain boundary mobility m and the nucleation proportionality c_n.

4 DISCUSSION AND CONCLUSION

The experiments of Wahabi et al. depicted in Figure 3(a) show that the smaller grain size materials display a pronounced softening whereas the large grain material does not

show softening. In the same graph, the results of the model are in very good agreement with the experimental results. Clearly the observed softening, and its grain size dependence, can be described by using only two parameters for recrystallization supplemented with the proposed explicit relations for edge availability and occupation. For the larger grain material (92 µm) the stress–strain curve seems hardly affected by recrystallization, although the micrograph in Figure 2(c) made after the experiment does show a significant amount of small recrystallized grains arranged in necklace formation along the perimeter of large grains. Figure 3(b) and 3(c) show that the model closely matches this observation with the prediction of a significant amount of small recrystallizing grains, yet without having much effect on the stress–strain response. In Figure 3(c) the evolution of the amount of grains for the largest grain size (92 µm) displays a plateau, indicating that the occupied grain edge equals the available grain edge, i.e. a necklace of small grains has formed. Figure 3(b) depicts the evolution of both the average recrystallized grain size $\bar{D}_r$ and the average grain size D_a. Here it can be seen that the average grain size of the smaller grain material (10 and 24 µm initial size) is equal to the recrystallized grain size resulting in an equiaxed grain morphology of grains of average size $\bar{D}_r$.

The model inherently predicts the lack of dependence of the steady state grain size on the initial grain size [7,17,18] which is a widely reported feature of discontinuous dynamic recrystallization. In Figure 3(b) it can be seen that the smaller grain sizes (10 and 24 µm) have more or less converged to the same grain size. The larger initial grain size has a smaller recrystallized grain size, this is due to the fact that the recrystallization is not yet at the steady state. Lastly there is a good match between the recrystallized grain sizes reported by Wahabi et al. and the one predicted by the proposed model. Wahabi measured the recrystallized grain size for the 10, 24 and 92 µm initial grain size experiments to be approximately 5.2, 5 and 3.2 µm, the model is in good agreement with predicted grain sizes of respectively 5.2, 4.9 and 1.9 µm.

In short a physically based model was presented that is able to describe the effect of grain size on the recrystallization behavior. The model predicts not only the effect of recrystallization on the stress–strain response, but also correctly predicts other important microstructural features like recrystallized grain size and morphology aspects like necklacing.

REFERENCES

[1] Sakai, T. and Jonas, J.J, Dynamic Recrystallization: Mechanical and Microstructural considerations, *Acta metall.* Vol. 32 No. 2 (1984) 189-209.

[2] Luton, M.J. and Sellars, C.N. Dynamic recrystallization in nickel and nickel-iron alloys during high temperature deformation, *Acta Metallurgica* Vol 17 (1969) 1033-43.

[3] Misra, R.D.K., Nayak, R.D.K., Mali, S.A., Shah, J.S., Somani, M.C. and Karjalainen, L.P. Microstructure and Deformation Behavior of Phase-Reversion-Induced

Nanograined/Ultrafine-Grained Austenitic Stainless Steel, *Metallurgical and Materials Transactions A*, Vol. 40A (2009) 2498

[4] M.C. Somani, P. Juntunen, L.P. Karjalainen, R.D.K. Misra, A. Kyröläinen, Enhanced Mechanical Properties through Reversion in Metastable Austenitic Stainless Steels, *Metallurgical and Materials Transactions A*, Vol. 40A (2009) 729

[5] Di Schino, A., Barteri, M. and Kenny, J.M Development of ultra fine grain structure by martensitic reversion in stainless steel, *Journal of Materials Science Letters* Vol. 21 (2002) 751-753

[6] Ohadi, D., Parsa, M.H. and Mirzadeh H., Development of dynamic recrystallization maps based on the initial grain size, *Materials Science & Engineering A*, Vol. 565 (2013) 90-95

[7] Wahabi, M. El., Gavard, L., Montheillet, F., Cabrera, J.M. and Prado, J.M. Effect of initial grain size on dynamic recrystallization in high purity austenitic stainless steels, *Acta Materialia*, Vol. 53 (2005) 4605-4612

[8] Humphreys, F.J. and Hatherly, M. *Recrystallization and Related Annealing Phenomena*, second edition, Elsevier Ltd., 2004.

[9] Kooiker, H., Perdahcıoğlu, E.S. and van den Boogaard, A.H. A physically based continuum model for the effect of dynamic recrystallization on the stress–strain response of austenitic stainless steels, submitted

[10] Bergström, Y. 2010, A theory for the temperature and strain-rate dependences of dislocation re-mobilisation, (URL http://www.plastic-deformation.com/paper3.pdf)

[11] Angella, G., Donnini, R., Maldini, M. and Ripamonti, D. Combination between Voce formalism and improved Kocks-Mecking approach to model small strains of flow curves at high temperatures, *Materials Science and Engineering A* 594 (2013) 381-8.

[12] Kooiker, H., Perdahcıoğlu, E.S. and van den Boogaard, A.H. Constitutive modeling of hot forming of austenitic stainless steel 316LN by accounting for recrystallization in the dislocation evolution, *Journal of Physics: Conference Series* Vol. 734 Part B (2016).

[13] Sakai, T., Belyakov, A., Kaibyshev, R., Miura, H. and Jonas, J.J. Dynamic and post-dynamic recrystallization under hot, cold and severe plastic deformation conditions, *Progress in Materials Science*, Vol. 60 (2014) 130-207

[14] Hoseini Asli, A. and Zarei-Hanzaki, A. Dynamic Recrystallization Behavior of a Fe-Cr-Ni Super-Austenitic Stainless Steel, *J. Mater. Sci. Technol.* Vol. 25 No. 5 (2009) 603-606

[15] Tikhonova, M., Dolzhenko, P., Kaibyshev, R. and Belyakov, A. Grain Boundary Assemblies in Dynamically-Recrystallized Austenitic Stainless Steels, *Metals* (2016)

[16] Doherty, R.D., Hughes, D.A., Humphreys, F.J., Jonas, J.J., Juul Jensen, D., Kassner, M.E., King, W.E., McNelley, T.R., McQueen, H.J. and Rollet A.D., Current issues in recrystallization: a review, *Materials Science and Engineering* A 238 (1997) 219-74.

[17] Takigawa, Y., Honda, M., Uesughi, T. and Higashi, K. Effect of Initial Grain Size on Dynamically Recrystallized Grain Size in AZ31 Magnesium Alloy, *Materials Transactions*, Vol. 49 No. 9 (2008) 1979-1982

[18] Zhao, D. and Chaudbury, P.K. Effect of starting grain size on as-deformed microstructure in high temperature deformation of alloy 718, *The minerals, Metals & Materials Society*, (1994) 303-313

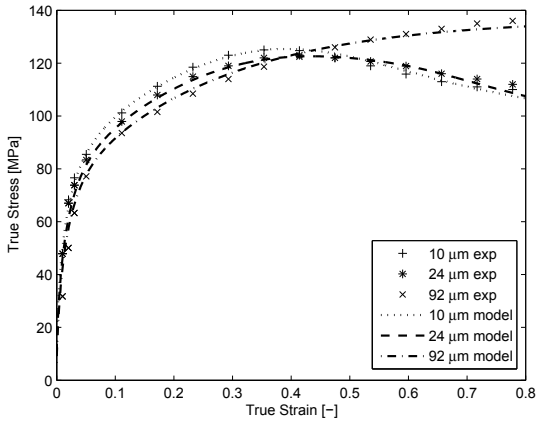

(a) Stress–strain response, experimental and simulation

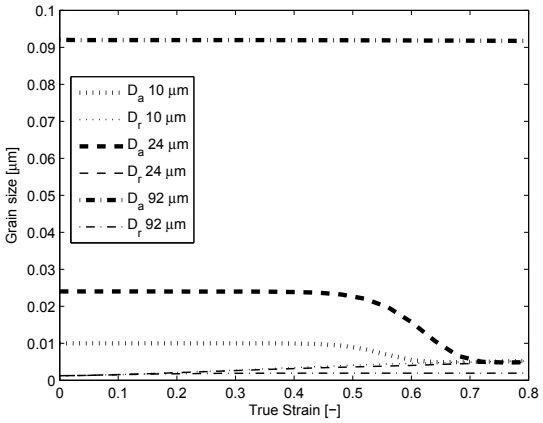

(b) Simulation of the evolution of the recrystallized grain size $\bar{D}_r$ and overall grain size D_a

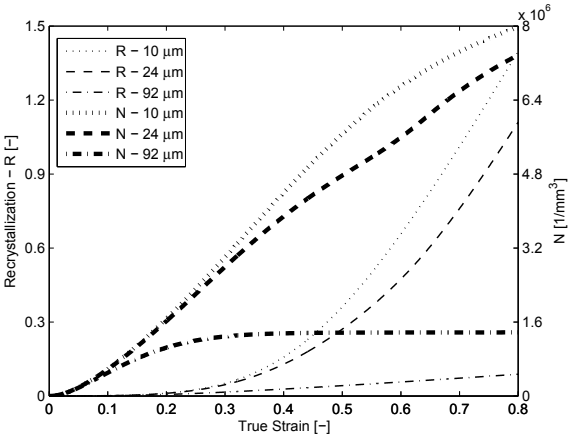

(c) Simulation of the evolution of the recrystallization and number of actively recrystallizing grains

Figure 3: Selected experimental and model results for initial grain sizes 10, 24 and 92 µm

A NEW CREEP MODEL DIRECTLY USING TABULATED TEST DATA AND IMPLEMENTED IN ANSYS

KANG SHEN, WILHELM J.H. RUST

Hochschule Hannover –University of Applied Sciences und Arts
Faculty II department of Mechanical Engineering
Ricklinger Stadtweg 120 30459 Hannover, Germany
E-mail: kang.shen@hs-hannover.de, wilhelm.rust@hs-hannover.de

Keywords: creep, material model, tabulated test data, ANSYS.

Abstract. Nowadays plastics are increasingly used in highly stressed structures in all kinds of constructions. The time dependency, the so-called viscosity, is a crucial part of the material behavior of plastics. A typical form of viscosity is creep. Creep is the increase of deformation under constant load. In the FE-simulation creep behavior is usually described by creep law functions. The commercial software provide many creep law functions depending on time, stress, strain, temperature and multiple material parameters. To run a creep simulation, the user must define all the parameters which requires a certain effort. Curve-fitting procedures might be of help, the results, however, often are not precise enough. For these reasons, we introduce our new creep model doing the similar job as the creep law functions but being able to directly use the tabulated data of the creep tests without curve-fitting procedures. In this paper, we use the model to create a 3D stress-creep strain-time surface based on the tabulated data like isochronous curves, which is represented by bicubically blended Coons patches to provide a good convergence due to their differentiability. This creep model supports strain hardening, which shows more realistic behavior when the load changes significantly during the simulated process.

1 INTRODUCTION

Numerous plastics show a combined material behavior like elastic, plastic and viscous one. The viscosity of plastics strongly depends on the loading rate, the loading duration and the temperature [1, 2]. Ignoring the viscosity of plastics like creep can lead to a severe failure of construction based on simulation [3]. Creep describes the increase of the deformation with time under a mechanical stress [4].

The simulation of creep behavior is based on the creep test data. The creep is directly measured from the creep and relaxation test. Creep curve provides a dependence of creep strain on time, relaxation curve provides a dependence of stress on time while creep strain can indirectly be determined. The isochronous curves are concluded from those two types of curve [5]. The isochronous curve gives a stress-strain relation at the identical time point.

Another well-established curve for creep is the creep modulus curve. The creep modulus is the quotient of the stress and total strain, thus showing a combination of creep and elastic behavior over time. Considering Young's modulus as constant there is a direct relation to creep strain.

Besides of stress and time creep behavior of plastics also depends on temperature. Conventional creep models usually describe the temperature dependency using the Arrhenius equation showing exponentially growing creep rates with respect to the inverse of the temperature [6]. Modelling temperature dependency in this way shows limited accuracy. On the other hand creep rate indeed varies nonlinearly with the temperature. Thus, the alternative, linearly interpolating all creep parameters might better match the material behavior for the given temperatures but lacks in between.

2 MOTIVATION

Numerous creep models proposed creep law functions defining creep behavior. For those functions several more or less abstract, not directly measurable material parameters must be specified. The difficulty is to determine the parameters as accurate for general application. Often one creep curve for a single stress can be fitted accurately. The other dependencies, those of temperature and stress, then show larger errors if - which is often the case - the curves for different stress levels are not similar in the mathematical sense, i.e. not scalable. Furthermore, it has to be emphasized that usual creep models give functions not for creep strain but for strain rate. Curve fitting requires either the solution of the differential equation given in this way or the determination of strain rates from measured strain which can be difficult due to either a small number of sampling points or oscillations in the measured curves if the number of sampling points is larger. The study of [7] indicate that general curve fitting functions could create insufficiently accurate or even wrong parameters and mislead the simulation. As a consequence the user has a larger effort to determine creep parameters and will even though finally not be satisfied.

Furthermore, due to numeric (time integration scheme) creep rate models can be subject to larger initial errors, e.g. for the power function of time with negative exponent, even if the analytical use of the parameters show good accordance with tests. The latter is the reason why the authors avoid rate formulations but use incremental ones as shown below.

Despite the right selection of creep model and define its parameter, the material behavior of a creep model can also differ from the test data[8,9]. The reason for that is the fact that constant material parameters compromise the accuracy with multiple loads and temperatures. With the compromise the material behavior in simulation is only accurate in a limited range [10].

In this work, we focus our attention on the construction of a creep model with direct use of tabulated test data from the creep test. The tabulated data here are e.g. the creep-time curve, isochronous curve and creep modulus curve. This creep model works without parameter identification and the curve fitting function. Instead of the parameters it uses a three-dimensional surface to find the proper creep state for calculation. For a good differentiability and a decent extensionality, we decided to use bicubical Coons patches (also named bicubically blended Coons patches) for the surface construction.

3 CONVENTIONAL CREEP MODEL

Numerous conventional creep models describe the creep behavior using strain rate formulation in a creep equation like:

$$\dot{\varepsilon}^{cr} = f(\sigma, t, \varepsilon, T) \tag{1}$$

It shows that the creep strain rate depends on stress, time (or creep strain) and temperature. The dependencies of time and strain are normally not modelled within the same creep equation. As example, a creep equation of direct time dependency (also called time hardening) is defined as

$$\dot{\varepsilon}^{cr} = C_1 \sigma^{c_2} t^{c_3} \cdot e^{-\frac{c_4}{T}} \tag{2}$$

whereas an example for indirect time dependency (strain-hardening), which show better accuracy if the stress significantly changes (or creep process is interrupted) during the simulation, reads

$$\dot{\varepsilon}^{cr} = C_1 \sigma^{c_2} (\varepsilon^{cr})^{c_3} \cdot e^{-\frac{c_4}{T}} \tag{3}$$

where the $C_1 \dots C_4$ are the material parameter. These parameters are fitted to the creep test data for a number of stress, time (or creep strain) and temperature points. The creep strain rate for a single curve may be accurate. However, the parameter identification goes easily wrong considering multiple stress levels at different time point. The reason is that the stress, time and creep strain have a complex relation. Furthermore, defining the material parameter for indirect time dependency is harder than for the direct way, since the creep strain rate depends on the creep strain which makes the solution of the differential equation more difficult.

4 SURFACE CONSTRUCTION

In our new creep model, we need a three-dimensional surface to describe the creep strain depending on time and stress.[1] The new creep model uses three types of creep test data for the users' convenience. The creep test data can be the creep-time curve, isochronous curve and creep modulus curve.

The creep curve uses stress as curve parameter and describes the increase of creep strain with time. The isochronous curve connects stress-strain points at the same time level and is not a directly measured curve. These curves describe the strain-stress-time relation. Since the creep strain is our primary variable, the surface should be

$$\varepsilon^{cr} = f_{cp}(\sigma, t) \tag{4}$$

To create the surface with the given curves as tabulated data, we need to construct the curves in both σ- and t-directions first. The curve requires to smoothly cross all the data points in one direction due to accuracy and differentiability. Thus, the cubic spline is used to create the curve. The advantage to build the cubic spline is that the spline exactly meets selected data points, avoid an unnecessary oscillation and provide C^2-continuity. The spline for creep strain and time uses the logarithmic timeline due to rapid change of the creep strain at the beginning.

The surface is based on cubic splines as boundary curves. It should fit the splines and be smooth perpendicular to the edges. For this purpose, we use the bicubical Coons patches. The Coons patches use the boundary curves to generate surfaces [12, 13]. A bicubical Coons patch combines four edges from splines and the surface interpolation with the cubic Hermite Interpolation. We define the Hermite functions with cubical Bézier form as:

[1]The temperature effect is discussed in section 6.

$$\begin{aligned} B_0^3(\sigma) &= (1-\sigma)^3 \\ B_1^3(\sigma) &= 3\sigma(1-\sigma)^2 \\ B_2^3(\sigma) &= 3\sigma^2(1-\sigma) \\ B_3^3(\sigma) &= \sigma^3 \end{aligned} \tag{5}$$

So that Hermite function for $\sigma \in [a,b]$ is:

$$\begin{aligned} H_0^3(\sigma) &= B_0^3(\sigma) + B_1^3(\sigma) \\ H_1^3(\sigma) &= \frac{1}{3}(b-a)B_1^3(\sigma) \\ H_2^3(\sigma) &= -\frac{1}{3}(b-a)B_2^3(\sigma) \\ H_3^3(\sigma) &= B_2^3(\sigma) + B_3^3(\sigma) \end{aligned} \tag{6}$$

From the cubical spline, the positional data is available for Coons patch, the four splines are:

$$f(a,t), f(b,t), f(\sigma,c), f(\sigma,d) \tag{7}$$

which $\sigma \in [a,b],\ t \in [c,d]$. For purpose of continuity, first derivative information for both σ- and t-direction is desired but not given. The two patches, which share the same edge in σ- or t-direction, must have the same derivative in t- resp. σ-direction of the edge. Therefore, the derivative is defined through a linear interpolation from two ends of the edge. Hence, there are four derivatives for each boundary:

$$\frac{\partial f(a,t)}{\partial \sigma}, \frac{\partial f(b,t)}{\partial \sigma}, \frac{\partial f(\sigma,c)}{\partial t}, \frac{\partial f(\sigma,d)}{\partial t} \tag{8}$$

Through four boundary curves and their derivatives two ruled surfaces are defined:

$$\begin{aligned} hc(\sigma,t) &= H_0^3(\sigma)\cdot f(a,t) + H_1^3(\sigma)\cdot\frac{\partial f(a,t)}{\partial \sigma} + H_2^3(\sigma)\cdot\frac{\partial f(b,t)}{\partial \sigma} + H_3^3(\sigma)\cdot f(b,t) \\ hd(\sigma,t) &= H_0^3(t)\cdot f(\sigma,c) + H_1^3(t)\cdot\frac{\partial f(\sigma,c)}{\partial t} + H_2^3(y)\cdot\frac{\partial f(\sigma,d)}{\partial t} + H_3^3(t)\cdot f(\sigma,d) \end{aligned} \tag{9}$$

The interpolated surface $hc(\sigma,t)$ is ruled by the splines $f(a,t), f(b,t)$ in t-direction for $\sigma \in [a,b]$ and $hd(\sigma,t)$ is ruled by the splines $f(\sigma,c), f(\sigma,d)$ in σ-direction for $t \in [c,d]$.Thus, we need $hc(\sigma,t)$ to fix its course in t-direction and change its course in σ-direction like $hd(\sigma,t)$. In this case, a new surface is used to achieve this goal. We define a surface with the corner data for the interpolation:

$$hcd(\sigma,t) = \begin{pmatrix} H_0^3(\sigma) & H_1^3(\sigma) & H_2^3(\sigma) & H_3^3(\sigma) \end{pmatrix} \cdot \begin{pmatrix} f(a,c) & \frac{\partial f(a,c)}{\partial t} & \frac{\partial f(a,d)}{\partial t} & f(a,d) \\ \frac{\partial f(a,c)}{\partial \sigma} & 0 & 0 & \frac{\partial f(a,d)}{\partial \sigma} \\ \frac{\partial f(b,c)}{\partial \sigma} & 0 & 0 & \frac{\partial f(b,d)}{\partial \sigma} \\ f(b,c) & \frac{\partial f(b,c)}{\partial t} & \frac{\partial f(b,d)}{\partial t} & f(b,d) \end{pmatrix} \cdot \begin{pmatrix} H_0^3(t) \\ H_1^3(t) \\ H_2^3(t) \\ H_3^3(t) \end{pmatrix} \tag{10}$$

The bicubical Coons Patch is defined as:

$$hg(\sigma,t) = hc(\sigma,t) + hd(\sigma,t) - hcd(\sigma,t) \tag{11}$$

The surface we construct for isochronous curves with the Coons patches is shown in Figure *1*.

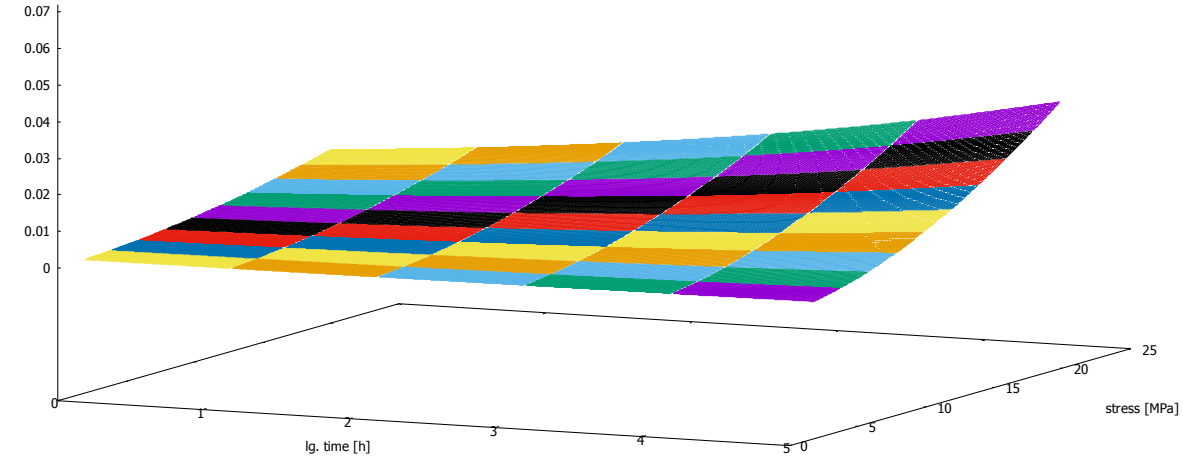

(a) $\mathrm{T} = 23°\mathrm{C}, \mathrm{t} = 1{\sim}10^5\mathrm{h}, \sigma_{\mathrm{eqv}} = 2{\sim}20\mathrm{MPa}$

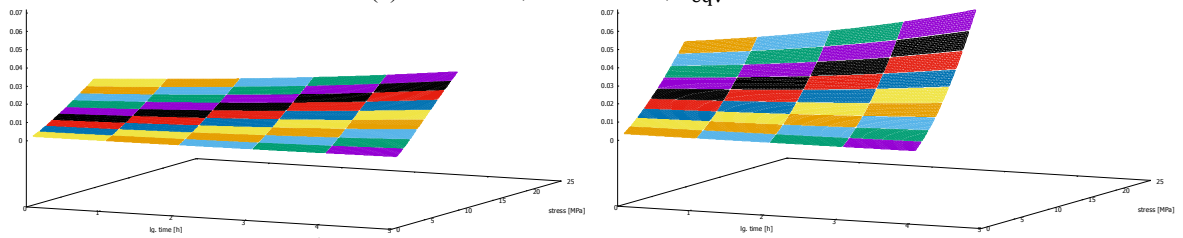

(b) $\mathrm{T} = 60°\mathrm{C}, \mathrm{t} = 1{\sim}10^5\mathrm{h}, \sigma_{\mathrm{eqv}} = 1{\sim}100\mathrm{MPa}$ (c)$\mathrm{T} = 100°\mathrm{C}, \mathrm{t} = 1 - 10^4\mathrm{h}, \sigma_{\mathrm{eqv}} = 1{\sim}10\mathrm{MPa}$

Figure 1 creep strain with logarithmic time and loads for Ultradur B 2550

The entire surface consists of multiple Coons patches. The cross points in the surface are the data points from the database. With this surface, the creep strain can be interpolated for one specific couple of time and stress.

5 NEW CREEP MODEL WITH CREEP STRAIN FORMULATION

In our new creep model, we use the incremental creep strain formulation instead of rate formulation. Since the creep strain $\varepsilon^{cr} \to 0$ at the time $t \to 0$, the creep process can start from time $t = 0$ without the numerical problem even if the strain rate tends to infinity in a rate formulation. We create a surface from the creep curve, isochronous curve as a creep strain function of time and stress. Therefore, the incremental creep strain formulation for direct time dependency is

$$\Delta\varepsilon^{cr} = f_{cp}(\sigma, t + \Delta t) - f_{cp}(\sigma, t) \tag{12}$$

Since the surface of creep strain is defined as a three-dimensional function f_{cp}, the creep strain increment is interpolated using the stress σ, the time t and the time increment Δt. The term $f_{cp}(\sigma, t)$ is equal to the creep strain ε_0^{cr} from the last converged state.

To model indirect time dependency, we must determine the point of the surface where the same creep strain ε_0^{cr} is valid, but now for the actual stress σ_{i+1}. Since the data form triples of strain, stress and time, the time is the only differing quantity and thus is no longer the real time. Hence, the time of this point is called pseudo-time ξ (at point a in Figure 2). The surface f_{cp}

describes the creep strain depending on time and stress. The inverse function, time as a function of stress and strain is not given. To solve for the pseudo-time ξ, we use a Newton-Raphson scheme for the equation

$$h(\sigma_{i+1}, \xi) = f_{cp}(\sigma_{i+1}, \xi) - \varepsilon_0^{cr} = 0 \tag{13}$$

Then we obtain the creep strain ε^{cr} after time increment Δt at point b in Figure 2. The difference of point a and b is the creep increment $\Delta\varepsilon^{cr}$.[2]

$$\Delta\varepsilon^{cr}(\sigma_{i+1}, \xi + \Delta t) = f_{cp}(\sigma_{i+1}, \xi + \Delta t) - \varepsilon_0^{cr} \tag{14}$$

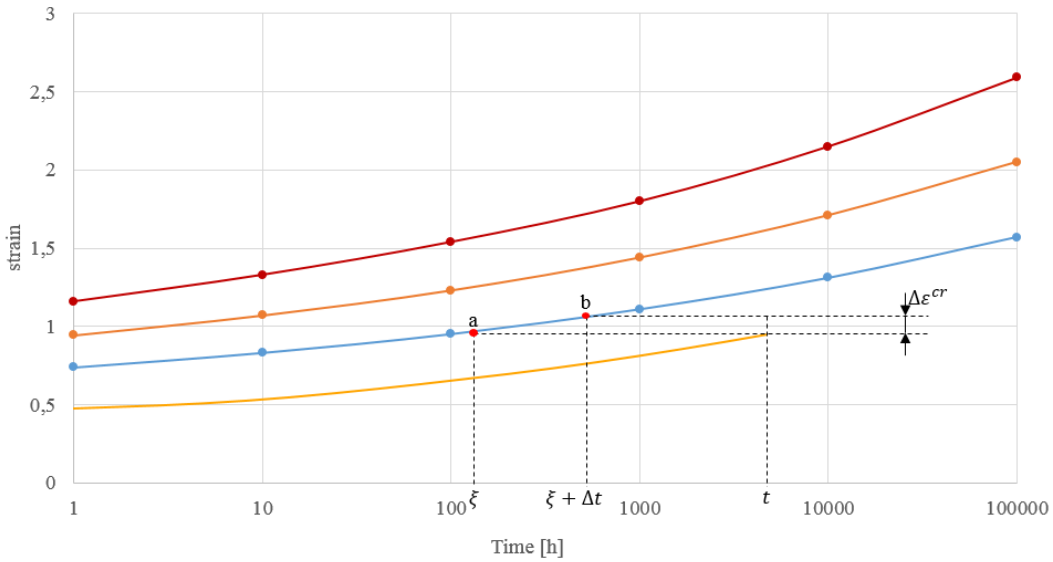

Figure 2 creep curve with search process

Alternatively we can also create a surface from the creep modulus curve which uses the creep modulus depending on time and stress. In this case, the creep modulus is depending variable, so the surface is

$$E^{cr} = f_{cp}(\sigma, t) \tag{15}$$

The creep modulus is defined as the quotient of stress and total strain. The pseudo-time now is the time point where the same creep modulus applies as in the converged state but for the new stress. It is determined by a Newton-Raphson scheme for

$$h(\sigma_{i+1}, \xi) = f_{cp}(\sigma_{i+1}, \xi) - E_0^{cr} = 0 \tag{16}$$

where E_0^{cr} is the creep modulus from last converged state. The E_0^{cr} is calculated using the creep strain as:

$$E_0^{cr} = \frac{\sigma_i}{\varepsilon_{cr}(t_i) + \varepsilon_{el}} \tag{17}$$

As a result, the creep modulus for the time $\xi + \Delta t$ is

$$E^{cr} = f_{cp}(\sigma_{i+1}, \xi + \Delta t) \tag{18}$$

[2] Further discussion for pseudo-time and stress out of the surface, see ([14])

To use the same local iteration of creep strain formulation (Figure 3), we convert creep modulus to creep strain

$$\Delta\varepsilon_{cr}(\sigma_{i+1}, t+\Delta t) = \frac{\sigma_{i+1}}{E_{cr}(\sigma_{i+1}, \xi+\Delta t)} - \frac{\sigma_{i+1}}{E} - \varepsilon_0^{cr} \tag{19}$$

where the first term is the new total strain and the second one the new elastic strain. Its partial derivative with respect to σ is

$$\frac{\partial\Delta\varepsilon_{cr}(\sigma_{i+1}, t+\Delta t)}{\partial\sigma} = \frac{\partial}{\partial\sigma}\left(\frac{\sigma_{i+1}}{E_{cr}(\sigma_{i+1}, \xi+\Delta t)}\right) - \frac{1}{E} = \frac{1}{E_{cr}} - \frac{\sigma}{{E_{cr}}^2}\frac{\partial E_{cr}}{\partial\sigma} - \frac{1}{E} \tag{20}$$

and with respect to t :

$$\frac{\partial\Delta\varepsilon_{cr}(\sigma_{eqv,i+1}, t+\Delta t)}{\partial t} = -\frac{\sigma}{{E_{cr}}^2}\frac{\partial E_{cr}}{\partial t} \tag{21}$$

Thus, all three types of test data curves are united by the incremental creep strain formulation. With the creep strain increment, the three-dimensional creep state is defined

$$\Delta\boldsymbol{\varepsilon}^{cr} = \Delta\varepsilon^{cr} \cdot \frac{\partial Q}{\partial\boldsymbol{\sigma}} \tag{22}$$

where Q is plastic potential. This equation is adopted from the flow rule of plastic material, where the plastic multiplier is replaced by the creep strain increment in this case. Like in plastics, we use the flow rule associated with the yield condition F after von Mises. There is no threshold like the yield stress, thus creep is always present if there is non-zero equivalent stress.

After the $\Delta\boldsymbol{\varepsilon}^{cr}$ is determined, the current stress state is

$$\boldsymbol{\sigma} = \boldsymbol{E}\left(\boldsymbol{\varepsilon}^{tot} - \boldsymbol{\varepsilon}^{cr}(\mathrm{t_i}) - \Delta\boldsymbol{\varepsilon}^{cr}\left(\xi+\Delta t, \sigma_{eqv}(\boldsymbol{\sigma})\right)\right) \tag{23}$$

where $\boldsymbol{E}$ is the elasticity matrix, $\boldsymbol{\varepsilon}^{tot}$ is total strain for this step. The stress state changes with the creep increment updates. The equivalent stress is defined after von Mises. In equation (23), stress tensor $\boldsymbol{\sigma}$ is defined implicitly. Therefore, a local iteration with Newton-Raphson method should take place

$$g = \Delta\varepsilon^{cr} - \Delta\varepsilon^{cr}\left(\sigma_{eqv}(\boldsymbol{\sigma}), \xi+\Delta t\right) - \varepsilon_{eqv}^{cr}(t_i) = 0 \tag{24}$$

The derivative of g is

$$\frac{\partial g}{\partial\Delta\varepsilon^{cr}} = 1 + \frac{\partial\Delta\varepsilon^{cr}}{\partial\sigma_{eqv}}\left(\frac{\partial Q}{\partial\boldsymbol{\sigma}}\right)^T \boldsymbol{E}\frac{\partial Q}{\partial\boldsymbol{\sigma}} - \frac{\partial\Delta\varepsilon^{cr}}{\partial\varepsilon^{cr}} \tag{25}$$

For each iteration, the creep increment and its derivative is determined using the surface of Coons patches. The process for the creep increment calculation is shown in Figure 3

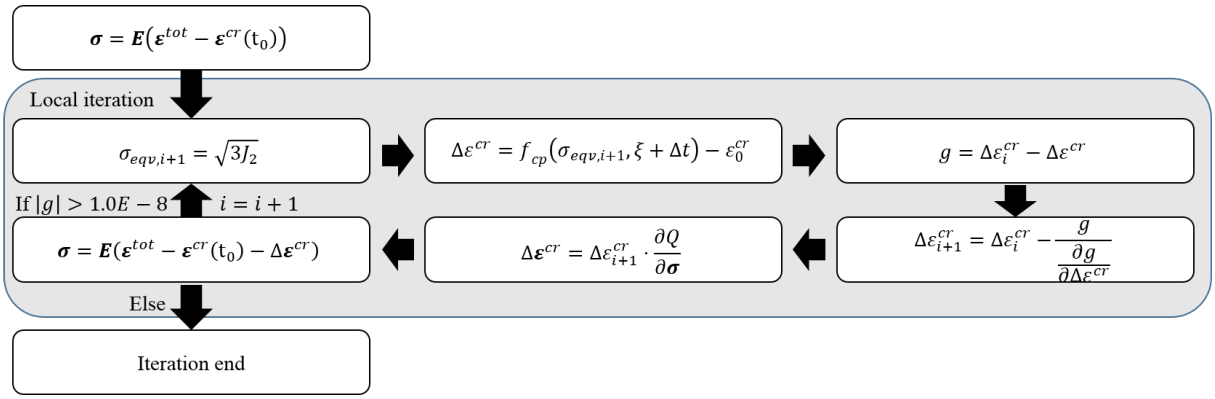

Figure 3 flow chart for local iteration

Once the creep increment is determined and the local iteration is converged, the consistent tangent is requested from the global iteration. The total differential of the stress is:

$$d\boldsymbol{\sigma} = \boldsymbol{E}\left(d\boldsymbol{\varepsilon}^{tot} - \frac{\partial Q}{\partial \boldsymbol{\sigma}}\mathrm{d}\Delta\varepsilon^{cr} - \Delta\varepsilon^{cr}\frac{\partial^2 Q}{\partial \boldsymbol{\sigma}^2}d\boldsymbol{\sigma}\right) \tag{26}$$

The total differential of the creep increment is:

$$\mathrm{d}\Delta\varepsilon^{cr} = \frac{\partial \Delta\varepsilon^{cr}}{\partial \sigma_{eqv}}\frac{\partial Q}{\partial \boldsymbol{\sigma}}d\boldsymbol{\sigma} + \frac{\partial \Delta\varepsilon^{cr}}{\partial \varepsilon^{cr}}\mathrm{d}\Delta\varepsilon^{cr} \tag{27}$$

Together with equation (26) and (27) a linear system of equations of order n+1 with n columns at the right hand side is obtained:

$$\begin{pmatrix} \mathbf{1} + \Delta\varepsilon^{cr}\boldsymbol{E}\frac{\partial^2 Q}{\partial \boldsymbol{\sigma}^2} & \boldsymbol{E}\frac{\partial Q}{\partial \boldsymbol{\sigma}} \\ \frac{\partial \Delta\varepsilon^{cr}}{\partial \sigma_{eqv}}\left(\frac{\partial Q}{\partial \boldsymbol{\sigma}}\right)^T & \frac{\partial \Delta\varepsilon^{cr}}{\partial \varepsilon^{cr}} + 1 \end{pmatrix} \begin{pmatrix} d\boldsymbol{\sigma} \\ \mathrm{d}\Delta\varepsilon^{cr} \end{pmatrix} = \begin{pmatrix} \boldsymbol{E} \\ 0 \end{pmatrix} d\boldsymbol{\varepsilon}^{tot} \tag{28}$$

where n is the number of strain components. The first n rows of the solution form the consistent tangent $\frac{d\boldsymbol{\sigma}}{d\boldsymbol{\varepsilon}^{tot}}$.

6 TEMPERATURE EFFECT

In conventional creep models the Arrhenius equation is often used to characterize the temperature effect.

$$\dot{\varepsilon^{cr}} = f(\sigma, t, \varepsilon) \cdot e^{-\frac{c}{T}} \tag{29}$$

The constant c is the quotient of activation energy and universal gas constant R. However, the constant c is not a measurable parameter during a creep test. The normal way to determine this parameter is using a curve fitting or solving the equation for selected data points. For the MaterialPBT-GB30 (Ultradur B 4300 K6[3]), we obtain the creep data like:

[3] Creep data from [11], the isochronous curves is interpolated using Coons patches. The original data was measured form different load classes. In order to explain the temperature effect without other disruption, a constant load is assumed.

Table 1: Temperature-creep relation for PBT-GB30

$T\ [K]$	ε^{cr}	c
296,15	2,26E-04	
313,15	2,78E-03	1,37E+04
333,15	5,44E-03	3,51E+03
363,15	6,25E-03	5,61E+02
393,15	8,87E-03	1,67E+03
413,15	1,43E-02	3,89E+03

for $\sigma = 5\ \mathrm{MPa}, \mathrm{t} = 10\mathrm{h}$. Hence the parameter c can be determined from two data points in the Table 1:

$$c_i = \frac{ln\frac{\dot{\varepsilon}_i^{cr}}{\dot{\varepsilon}_{i+1}^{cr}}}{\frac{1}{T_{i+1}} - \frac{1}{T_i}} \tag{30}$$

Using this parameter c for the temperature outside of these two data points causes an error (Figure 4).

A linear interpolation for parameter c can improve the behavior (Figure 4) but does not solve the problem that the creep curves for different temperatures can show different shape.

The new model for this creep strain-temperature relation uses the Coons patches (Figure 5). Once the stress and the time are set, we obtain the creep strain ε^{cr} from the surface of Coons patch as interpolated points. A cubical spline connects interpolated points and creates a creep strain-temperature function. Thus, the creep strain could be determined from a specific temperature within the spline. This solution creates a smooth creep strain-temperature curve (Figure 4). Since temperature is a given value during the simulation no derivative with respect to it is requested. Thus, lower order piecewise interpolation is possible. It might be the more accurate the more temperature points are available from test data. For a smaller number of temperatures spline interpolation is preferable.

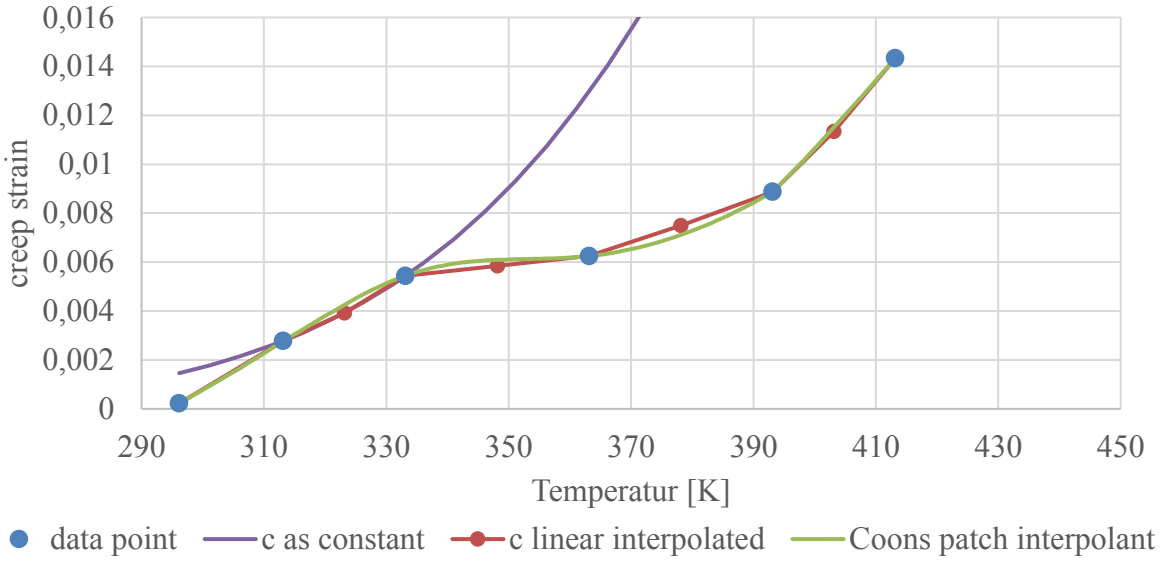

Figure 4 Creep strain-temperature relation using interpolation

If the temperature changes during the test, this interpolation takes place in every step. If the simulation takes place at a specific constant temperature but not matching a test temperature we first process the creep strain-temperature function for the corner points and create a new surface for creep strain-stress-time relation at this temperature before the simulation starts.

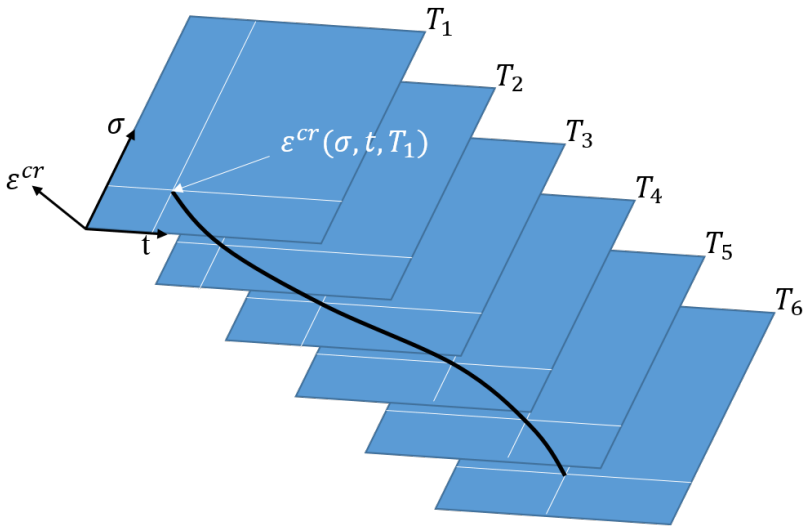

Figure 5 new model illustration for interpolation of the temperature effect

5 RESULTS

Figure 6 shows the results of this new creep model. To compute these results, a solid element with 8 nodes is used. The curve "00iso" uses the isochronous curve and the curve"00cm" uses the creep modulus curve. Both curves start the creep at $t = 0\ h$. They match the data point exactly. The maximum difference between the two curves amounts to 1.12%.

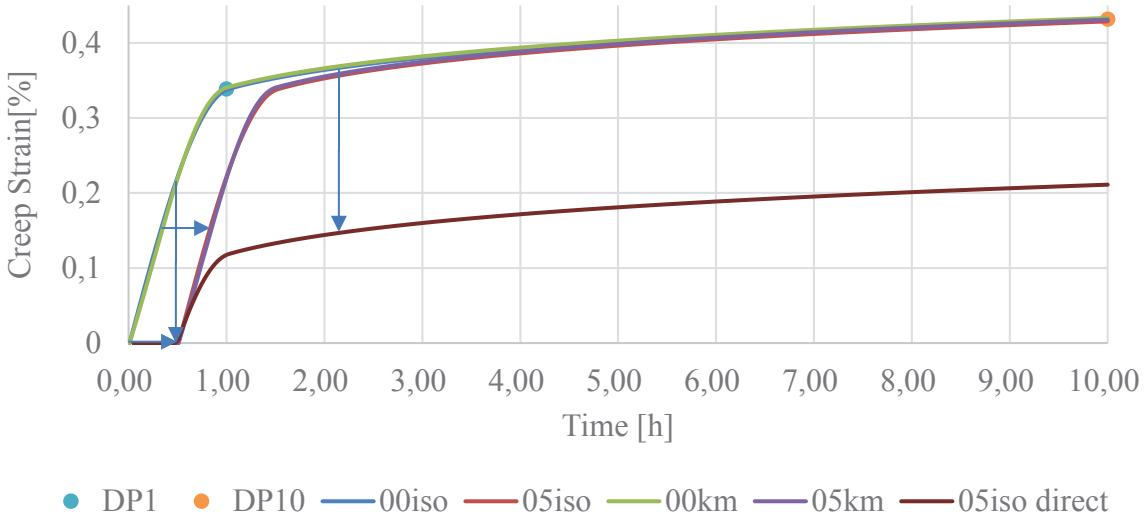

Figure 6 creep curve using the new model in compare with data points

The other two results (05iso and 05cm) start the creep calculation after 30min with indirect time dependency. Until then the creep strain keeps zero. After 30 minutes, they start with the

same curve as“00iso” and “00cm”. This result shows that the indirect time dependency work properly. For the direct time dependency the curve “05iso direct” is considering the creep process as already done for 30 minutes, so it starts with the range of the curve “00iso” beginning at the same time point. Thus, this creep model works as it should be.

We implement this creep model into the commercial software ANSYS. Figure 7 shows two examples for the use of the creep model. First model is a tensile specimen. One side of the specimen is fixed, on the other side a tensile load of 10 MPa is applied. As we expect, the creep strain concentrate on the reduced cross section. The second model is a plate with a hole in it. We apply the same boundary conditions to this model. In this model, we observe the creep concentration and the gradient of the creep strain.

These results show that the new creep model works properly with a complex geometry and multiple elements. It provides also a convergence like other creep models. The huge advantage of this new creep model is that:

- Only tabulated creep test data are used as input data
- No material parameters, are required, i.e. no curve fitting must take place
- The surface of Coons patches meets every data point.

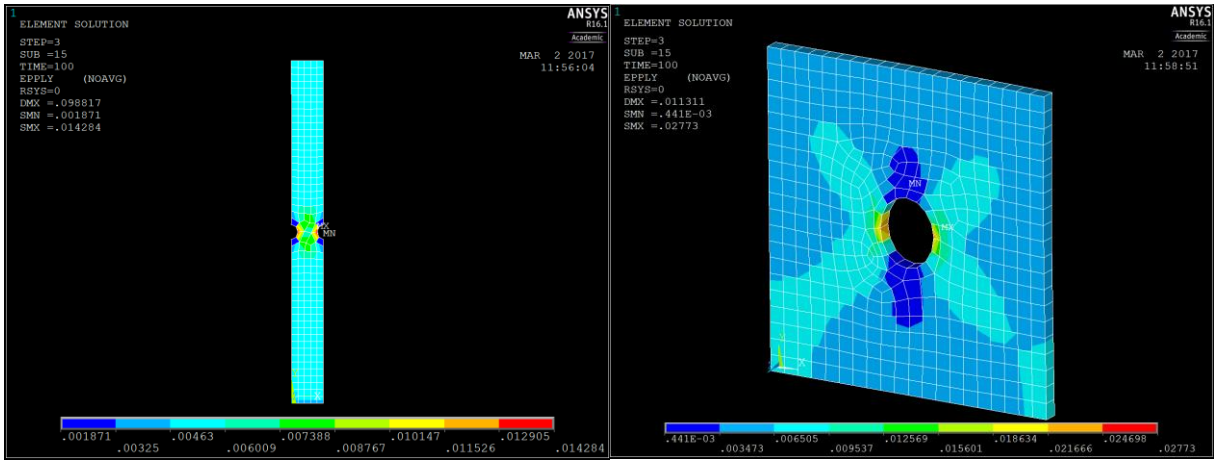

Figure 7 two examples: a tensile specimen and a plate with hole

REFERENCES

[1] L. C. Brinson and T. S. Gates, “Effects of physical aging on long term creep of polymers and polymer matrix composites,” *International Journal of Solids and Structures*, vol. 32, no. 6-7, pp. 827–846, 1995.

[2] C. Marais and G. Villoutreix, “Analysis and modeling of the creep behavior of the thermostable PMR-15 polyimide,” *J. Appl. Polym. Sci.*, vol. 69, no. 10, pp. 1983–1991, 1998.

[3] M. Ezrin, *Plastics failure guide: Cause and prevention,* 2nd ed. Munich: Hanser, 2013.

[4] W. Rust, *Non-Linear Finite-Elemente Analysis in Structural Mechanics,* Cham/Heidelberg: Springer, 2015.

[5] M. Stommel, M. Stojek, and W. Korte, *FEM zur Berechnung von Kunststoff- und Elastomerbauteilen*. München: Hanser Carl, 2011.

[6] I. SAS IP, *Ansys Help*, 2016.

[7] F. Vogt, *Simulation von Kriechgesetzen*, student project, Hochschule Hannover, 2016.

[8] M. J. Dropik, D. H. Johnson, and D. E. Roth, “Developing an ANSYS creep model for polypropylene from experimental data,” in *Proceedings of International ANSYS Conference*, 2002.
[9] Y. S. Kim and D. R. Metzger, “A finite element study of friction effect in four-point bending creep test,” in *ASME 2003 Pressure Vessels and Piping Conference*, 2003, pp. 99–107.
[10] T. Pulngern *et al.,* “Effect of temperature on mechanical properties and creep responses for wood/PVC composites,” *Construction and Building Materials*, vol. 111, pp. 191–198, 2016.
[11] M-Base Engineering + Software GmbH, *CAMPUS® Plastics Material Database.* [Online] Available: http://www.campusplastics.com/campus/.
[12] G. Farin, *Curves and surfaces for CAGD: A practical guide,* 5th ed. San Francisco, Calif.: Morgan Kaufmann Publ, 2006.
[13] S. A. Coons, “Surfaces for computer-aided design of space forms,” DTIC Document, 1967.
[14] Wilhelm J.H. Rust, Kang Shen, “Ein Kriechmodell für ANSYS unter direkter Verwendung von Versuchsdaten”,*Proceedings of 34. CADFEM ANSYS Simulation Conference*, 2016.

XIV International Conference on Computational Plasticity. Fundamentals and Applications
COMPLAS 2017
E. Oñate, D.R.J. Owen, D. Peric and M. Chiumenti (Eds)

CONTINUUM DAMAGE MECHANICS MODEL AS AN INSTRUMENT FOR DEVELOPMENT OF DESIGN RULES FOR STEEL STRUCTURES IN SEISMIC AFFECTED ZONES

B. HOPPE*, Y. DI*, D. NOVOKSHANOV*, S. MÜNSTERMANN*

* Department of Ferrous Metallurgy (IEHK)
RWTH Aachen University
Intzestrasse 1, 52072 Aachen, Germany
e-mail: barbara.hoppe@iehk.rwth-aachen.de, www.iehk.rwth-aachen.de

Key words: Coupled Damage Mechanics Model, ULCF, HSLA Steel, Toughness Properties.

1 INTRODUCTION

Modern HSLA steels show a superior profile in mechanical properties as they have a high yield strength as well as excellent toughness properties. Nevertheless, HSLA steels are still only rarely used for steels constructions despite their excellent property balance of strength and toughness. This rare application is due to the fact that there are no reliable quantitative methods to predict damage initiation in HSLA steels components; hence, there is not yet a conclusive limit state analysis for components. One criterion of such a limit state analysis should be a consideration how steels components react under external loading influence like cyclic loading with large strain amplitudes as they occur during seismic events. Conventional, well established fracture mechanics approaches are unfit for the description of phenomenological occurrences under ULCF loading since they do not consider the ongoing kinematic hardening conditions and the J-integral is not applicable for cyclic loading conditions with large plastic strain amplitudes.

Thus, the material properties to consider are toughness and stiffness. To get a better understanding of their influence and relationship onto each other an examination through a coupled damage mechanics approach might be helpful. Over the years scientists developed many different approaches to encounter this issue. A macroscopic approach was proposed by Gurson [8] and led to a family of similar models. Another strategy was chosen by the limit strain concept most famously encountered by Bai and Wierzbicki [3]. Later on then modified with Lode-angle consideration by Lian et al. [1], the so called modified Bai – Wierzbicki (MBW) model. Also, there have been many different propositions made to encounter the issue of cyclic loading. Most known would be the model introduced by Armstrong and Frederick [2] with its non-linear kinematic hardening law. Other more advanced models came from Chaboche [6] or also, the two yield surface approach by Yoshida and Uemori [5].

As previously discussed, damage mechanics approaches are able to give a limit state analysis because of a local strain approach. Nevertheless, as it becomes obvious from the previous state of the art representation, some modifications need to be done to a general damage mechanics approach Such an approach was done in this paper. The modified Bai-Wierzbicki

model as provided by Lian [1] is a coupled damage model that has proven to give good results for state limit analysis for modern steels under monotonic load. Since it is assumed that the onset of damage is not different under monotonic or cyclic loading, in the frame of this work, the MBW model was used as foundation for the model regarding damage initiation and evolution. Armstrong-Frederick provided a good plasticity model to depict material behaviour cyclic loading conditions. It was used to replace the plasticity core of the MBW model. The damage evolution also considers an effective strain concept.
For the experimental part of this work, the focus lies on the ductile damage crack criterion based on the model by Lian and the parameter calibration to find the damage initiation locus. In a following step a possibility for a toughness criterion is proposed based on nominal damage initiation curves.

2 COUPLED DAMAGE MECHANICS MODEL FOR ULCF

There hereby presented plasticity model consists of a plasticity core based on the Armstrong-Frederick model [2] with a non-linear kinematic hardening law to depict the hardening and softening effects during cyclic loading and a ductile crack initiation criterion with a corresponding damage evolution law following the modified Bai-Wierzbicki model proposed by Lian [1].

2.1 Plasticity core based on Armstrong-Frederick model

The plasticity model chosen to depict mechanic effects that occur under cyclic loading conditions such as the Bauschinger effect is the Armstrong-Frederick model [2]. The aim is to reproduce local stress and strain features of the material in detail. In equation (1) the equation to describe the von Mises yield surface can be seen. In the genuine Armstrong- Frederick model the size of the yield surface was considered to be constant. In this version of the model this condition was relaxed by the term $\mathrm{k}^2(\varepsilon_\mathrm{q})$.

$$F = \frac{1}{2}(\boldsymbol{s}-\boldsymbol{a})\cdot(\boldsymbol{s}-\boldsymbol{a}) - \frac{k^2(\varepsilon_q)}{3} = 0 \tag{1}$$

The yield surface can now change in size depending on the amount of equivalent plastic strain. Therefore, the hardening of the material can consequently be considered as mixed isotropic-kinematic.

$$\dot{\boldsymbol{a}} = C(\varepsilon_{qpl})\dot{\boldsymbol{\varepsilon}}^{\boldsymbol{p}} - \gamma\boldsymbol{a}\dot{\varepsilon}_q \tag{2}$$

The kinematic hardening part of the model is expressed in form of a backstress tensor $\mathbf{a}$ that contains a ‘recall’-term. The according backstress evolution law can be seen in equation (2). This rule is taken from the original Armstrong-Frederick model [2] and directs the movement of the yield surface through the principal stress space. The parameters C and γ are material parameters which can be obtained from cyclic test data.

2.2 Ductile crack imitation criterion and corresponding damage evolution law

During seismic events such as earthquakes the material impacting load can be characterized as ultra-low cyclic fatigue conditions, whereas the material can undergo only a few loading cycles with large plastic strains until it fails. It is therefore crucial to have an

accurate description of the damage initiation conditions and a damage evolution law that can reproduce the ongoing softening of the material in a precise manner. To represent these effects, damage is coupled to the plasticity model. The result is a hybrid plasticity and damage model based on the approach by Lian [1]. It is assumed the material shows pure plastic behavior before damage initiation. When damage initiates the material undergoes damage induced softening. To consider loading conditions under cyclic loading an amount of equivalent plastic strain is considered to initiate as well as advance ductile damage which is called an effective damage concept. Concurrently, the influence of the third invariant of the deviatoric stress tensor and the stress triaxiality is considered too at damage initiation and included into the description if the damage initiation locus. As damage emerges through the material it is assumed that the material eventually separates when it reaches a critical amount. Figure 1 schematically depicts the stress-strain behavior of the material with the above described hybrid plasticity-damage model.

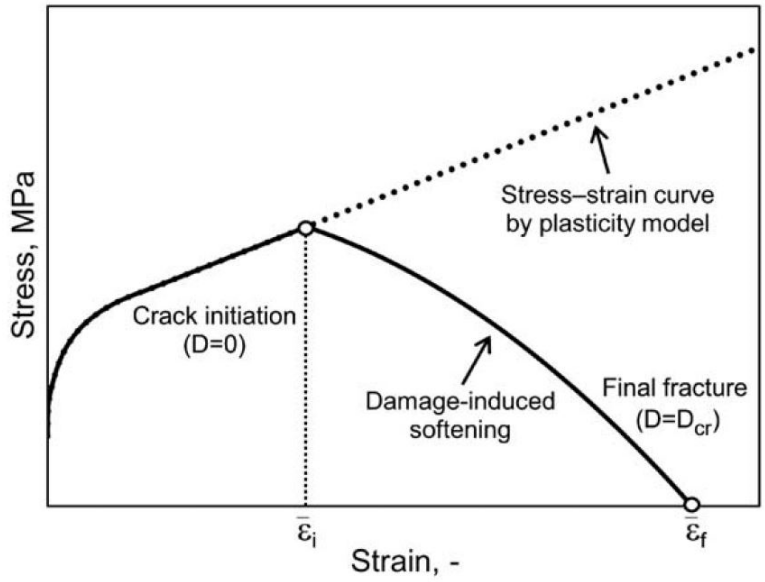

Figure 1: Schematic illustration of the stress-strain behavior with the hybrid plasticity and damage model [1]

It has been shown in many works that hydrostatic pressure and fracture strain correlate [9-11]. As hydrostatic pressure increases, fracture strain decreases. Especially, Bai and Wierzbicki investigated in their work the influence of the equivalent plastic strain on fracture. Whereat, they found a dependence of the equivalent plastic strain on the stress triaxiality and the lode angle which can be expressed in the third invariant of the deviatoric stress tensor. In Figure 2 a representation of both stress triaxiality and lode angle can be seen in principal stress space. Different lode angles and stress triaxialities can be achieved by a variation of testing specimens as it is shown in Figure 3. The result is a three dimensional fracture locus depending on equivalent strain, stress triaxiality and lode angle.

Additionally, resulting from the investigations of Lian [1] on the onset of damage, a three dimensional damage initiation locus which is also depending on equivalent strain, stress triaxiality and lode angle is employed. Its mathematical representation can be found in

Equation (3). Here, the parameters C_1, C_2, C_3 and C_4 are material parameters which can be identified through a variation of small scale tests with different geometries.

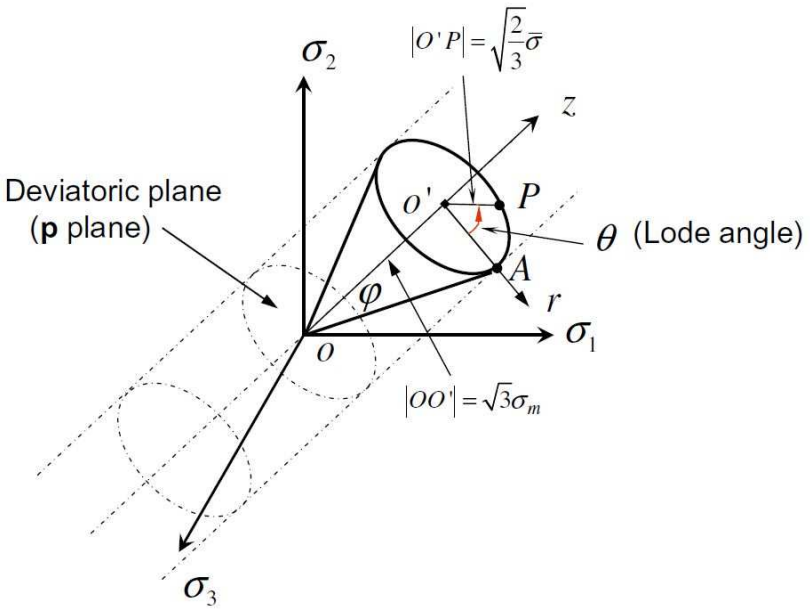

Figure 2: Geometric representation of a stress state in the mean stress space [3]

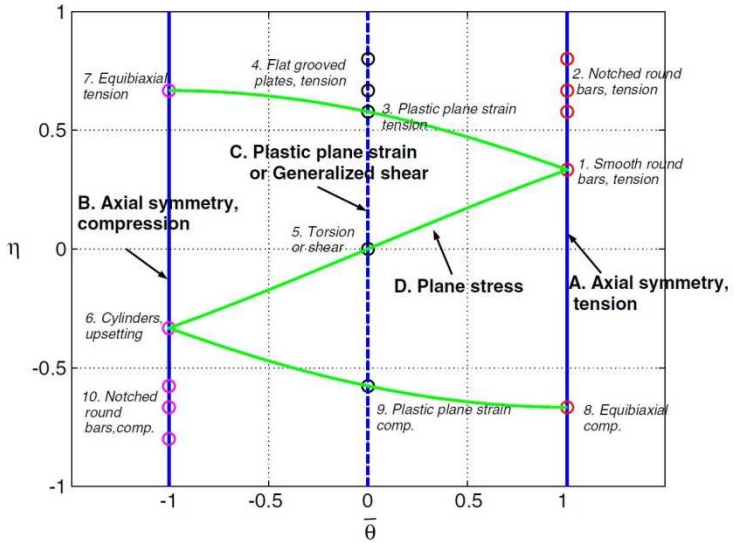

Figure 3: Representation of initial stress state [3]

Stress triaxiality η and lode angle parameter $\bar{\theta}$ can be obtained through Equations (4), repectively, (5).

$$\overline{\varepsilon}_i = (C_1 e^{-C_2\eta} - C_3 e^{-C_4\eta})\overline{\theta}^2 + C_3 e^{-C_4\eta} \tag{3}$$

$$\eta = \frac{\sigma_m}{\overline{\sigma}} \tag{4}$$

$$\overline{\theta} = 1 - \frac{60}{\pi} = 1 - \frac{2}{\pi} arccos\left(\frac{\frac{27}{2} det([S])^{\frac{1}{3}}}{\overline{\sigma}}\right)^3 \tag{5}$$

Finally, an internal variable D is introduced to couple the ongoing damage induced material softening to the constitutive equations. Therefore the following damage evolution law is employed:

$$D_j = \begin{cases} 0; & \overline{\varepsilon}_{eff,j} \leq \overline{\varepsilon}_i \\ D_{j-1} + \frac{\sigma_{y0}}{G_f} \cdot \Delta\varepsilon_j \cdot \left(1 - e^{-m\cdot(D_{j-1}+0.1)}\right); & \overline{\varepsilon}_{eff,j} \geq \overline{\varepsilon}_i \wedge \overline{\varepsilon}_j < \varepsilon_f \wedge \eta_j > \eta_c \wedge m \neq 0 \\ D_{j-1} + \frac{\sigma_{y0}}{G_f} \cdot \Delta\varepsilon_j & \overline{\varepsilon}_{eff,j} \geq \overline{\varepsilon}_i \wedge \overline{\varepsilon}_j < \varepsilon_f \wedge \eta_j > \eta_c \wedge m = 0 \\ D_{cr}; & \overline{\varepsilon}_j = \varepsilon_f \end{cases} \tag{6}$$

It is assumed, to consider the cyclic loading conditions that an effective equivalent plastic strain ε_{eff} has to be reached in order to accumulate damage. This assumption is further formulated in Equations (7) and is based on the effective strain concept introduced by Ohata and Toyoda [4].

$$\Delta\varepsilon_{eff} = (1 - e^{-m\cdot\varepsilon_{eff}}) \cdot \Delta\varepsilon \tag{7}$$

Furthermore, the parameter G_f represents the dissipated energy for the crack opening at a unit area and the stress σ_{y0} equates the stress at damage initiation. Fracture occurs when a critical amount of damage D_{cr} is reached.

3 MATERIALS

In the following paragraph the investigated steel grades are characterized. The selected steel grades S500MC, S700, S355 with different toughness levels (T1) and (T2) were chosen to determine the damage initiation locus.

3.1 Chemical Composition

All presented steel grades were also micro alloyed. The chemical compositions (Table 1) were obtained by spectroscopic analysis.

Table 1: Chemical composition of the steel grades (in %)

	C	Si	Mn	P
S500MC	0.02	0.21	1.57	0.008

3.2 Microstructure

The microstructural analysis has been achieved by LOM. The microstructural composition can be found in Table 2. The corresponding pictures are shown in Figure 4.

Table 2: Microstructure analysis of the steel grades (in %)

Steel grade	Bainite	Pearlite	Ferrite
S500MC	100%	--	--

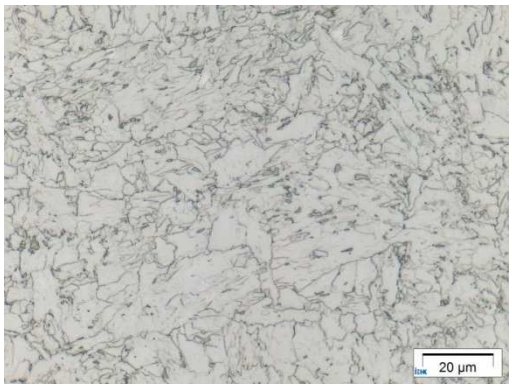

Figure 4: Microstructural configuration of (a) S500MC

3.3 Mechanical properties

Figure 5 shows the strength properties of the investigated steel grades. They have been achieved through tensile tests at room temperature. The extrapolation was done according to the Ludwik expression.

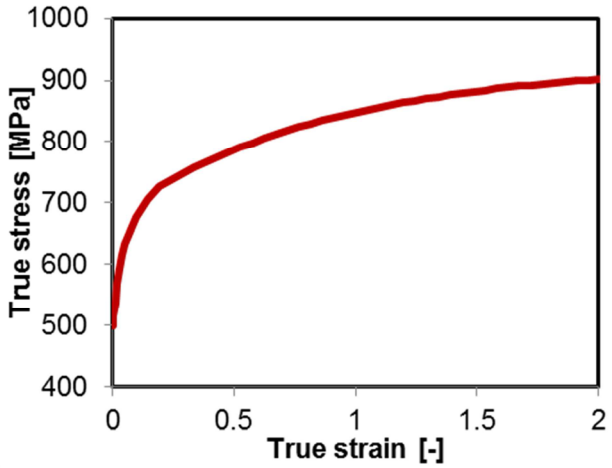

Figure 5: Flow curves of the selected steels S500MC

To consider temperature and strain rate effects on material behavior, equations (8) and (9) were employed and regarded for the materials' yield strength based on the approach by

Münstermann et al. [7]. The material parameters C_1^T, C_2^T and C_3^T to considers the temperature effect were obtained by tensile test at varying temperatures and are listed in Table 3.

$$f(T) = C_1^T \cdot \exp(C_2^T \cdot T) + C_3^T \tag{8}$$

Table 3: Calibrated parameters for temperature effect

	C_1^T	C_2^T	C_3^T
S500	0.0198	-0.018	0.983

The material parameter from Equation (9) $C_1^{\dot{\varepsilon}}$ and $C_2^{\dot{\varepsilon}}$ were obtained from high speed tensile tests and are listed in Table 4.

$$f(\dot{\varepsilon}) = C_1^{\dot{\varepsilon}} \cdot ln\dot{\varepsilon}^{p} + C_2^{\dot{\varepsilon}} \tag{9}$$

Table 4: Calibrated parameters for strain rate effect

	$C_1^{\dot{\varepsilon}}$	$C_2^{\dot{\varepsilon}}$
S500	0.0023	1.0173

4 DETERMINATION OF DAMAGE INITIATION LOCUS

In order to obtain a toughness based safety assessment for a steel grade the determination the damage initiation locus (DIL) is crucial. The DIL indicates the beginning of the damage induced softening. The material specific DIL was obtained by calibrating the material parameters from Equation (3). Moreover, Equation (10) gives the critical damage variable D_{crit} before material failure and therefore the damage crack locus (DCL).

$$D_{crit} = \left(C_1^{crit} e^{-C_2^{crit}\eta} - C_3^{crit} e^{-C_4^{crit}\eta}\right)\overline{\theta} + C_3^{crit} e^{-C_4^{crit}\eta} + C_5^{crit} \tag{10}$$

The parameters were calibrated on a variation of small scale samples with different geometries, consequently, specimens with various stress states. The critical equivalent strain is estimated through the direct current potential drop (DCPD) method and later on then verified by metallographic investigations. For simulation Abaqus/Standard is used.

4.1 S500

For the construction steel S500, tensile tests with DCPD were conducted on notched round bar samples with different notch radii, on plane strain samples with different radii and on shear samples. According to the experimental results with DCPD method, the DIL can be determined, as shown Figure 6 (a).The tensile tests are simulated by Abaqus. The parameters D_3, G_f, and C_1^{crit} - C_5^{crit} are iteratively calibrated until the simulated force-displacement curves fit the experimental results, as shown exemplarily in Figure 7 for (a) a round bar

sample and (c) a shear sample. Accordingly the DCL of S500 is constructed and shown in Figure 6 (b). The calibrated parameter set for S500 is summarized in Table 5. To validate the calibrated parameters, those parameters are used in the simulation of Charpy test at room temperature. Figure 7 (b) shows the simulated force-displace curve of the Charpy test which corresponds to the experimental result.

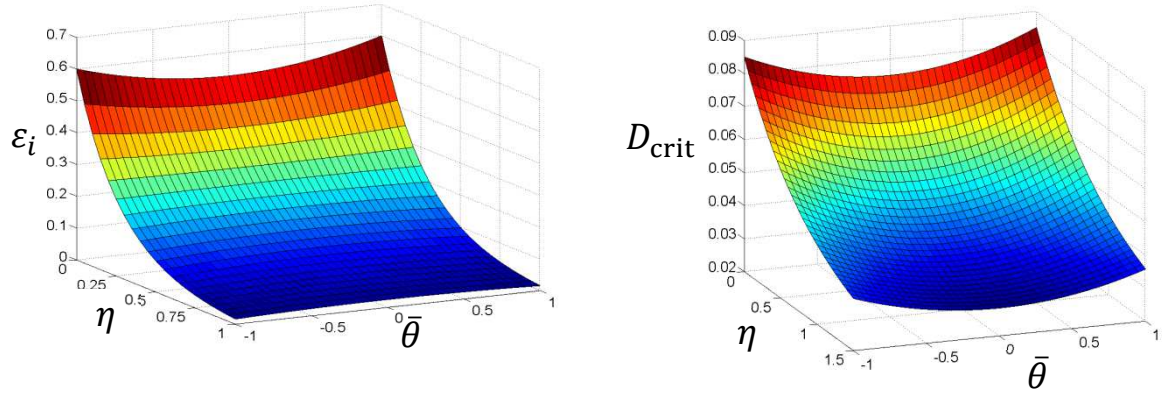

(a) (b)

Figure 6: (a) DIL of S500 (b) DCL of S500

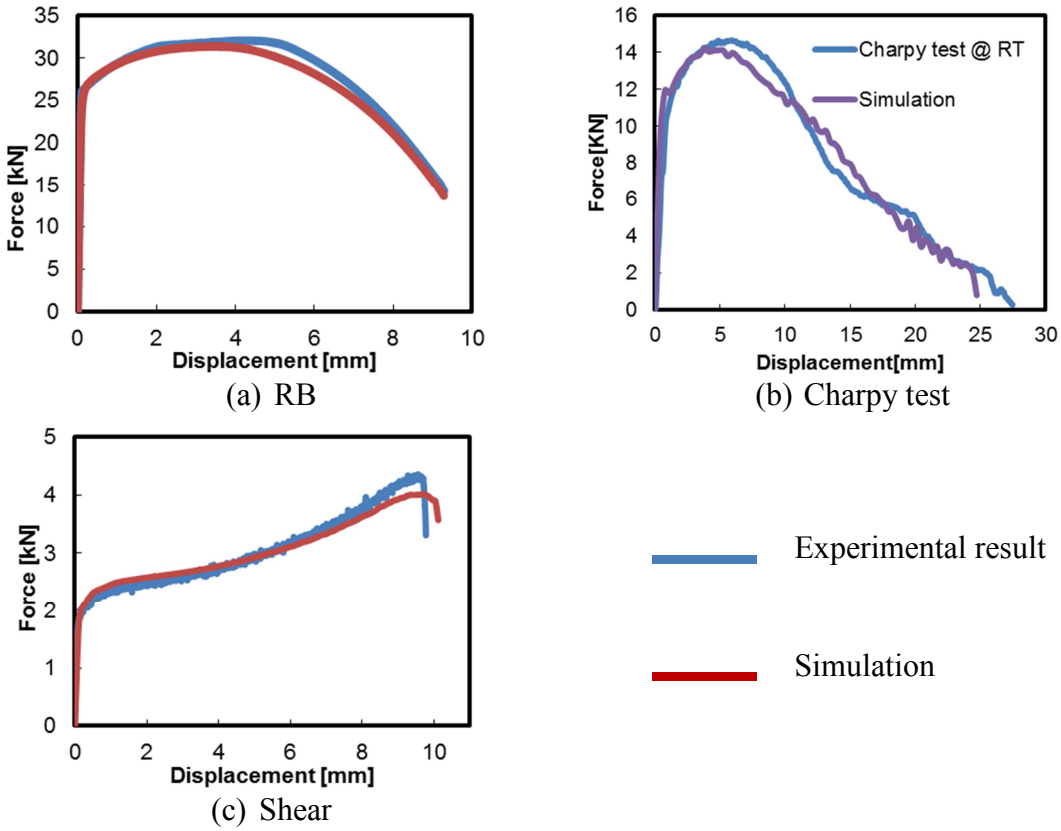

(a) RB (b) Charpy test

(c) Shear

Figure 7: Force-displacement curves from tensile tests, Charpy tests and simulations (S500)

Table 5: Calibrated parameter set for S500

DIL				Damage evolution
C_1	C_2	C_3	C_4	G_f
0.6	3.644	0.5262	3.062	10000
DCL				
C_1^{crit}	C_2^{crit}	C_3^{crit}	C_4^{crit}	C_5^{crit}
0.06	0.895	0.05	1.415	0.025

5 DETERMINATION OF NOMINAL DUCTILE CRACK INITIAION LOCUS

The derivation of nominal ductile crack initiation loci stands on the nominal material properties, namely the nominal upper shelf toughness. To eliminate the chance of brittle fracture of steel components under operation, it is assumed that above 0 °C the steel toughness should be at upper shelf. According to EN 10025 [12], the required minimum impact energies corresponding the investigated steel grades are listed in Table 7.

Table 7: Minimum impact energy (longitudinal) according to delivery standard

Selected steel grade	Corresponding standard	20 °C	0 °C	-10 °C	-20 °C
S500ML	EN10025-4	63 J	55 J	51 J	47 J
S700	EN10025-6	--	50 J	--	40 J

To acquire the corresponding nominal upper shelf toughness, Wallin´s [13] approach is adapted. After Wallin, the Charpy transition curve of can be mathematically obtained from an exponential function as shown in Equation (13). The parameter C_{TC} controls the steepness of the transition curve.

$$C_{TC} \approx 34°C + \frac{\sigma_y}{35.1MPa} - \frac{C_{V-US}}{14.3J} \tag{13}$$

Through the Charpy impact energy the nominal ductile crack initiation loci is determined. The calibrated parameter sets are applied to Charpy test simulations. The computed impact energy as well as the load-deflection curve are compared to the experimental results at room temperature. Consequently, the DILs were fitted in order to match the computed impact energy to the previously determined nominal upper shelf toughness.

5.1 S500MC

By the multiplication of the factor for DIL and DCL, the computed Charpy impact energies are tailored to different target values. Figure 10**Fehler! Verweisquelle konnte nicht gefunden werden.** shows the obtained force-displacement curves and the corresponding nominal DIL for the target Charpy impact energies. Table 8 summarized the nominal DIL parameters for S500.

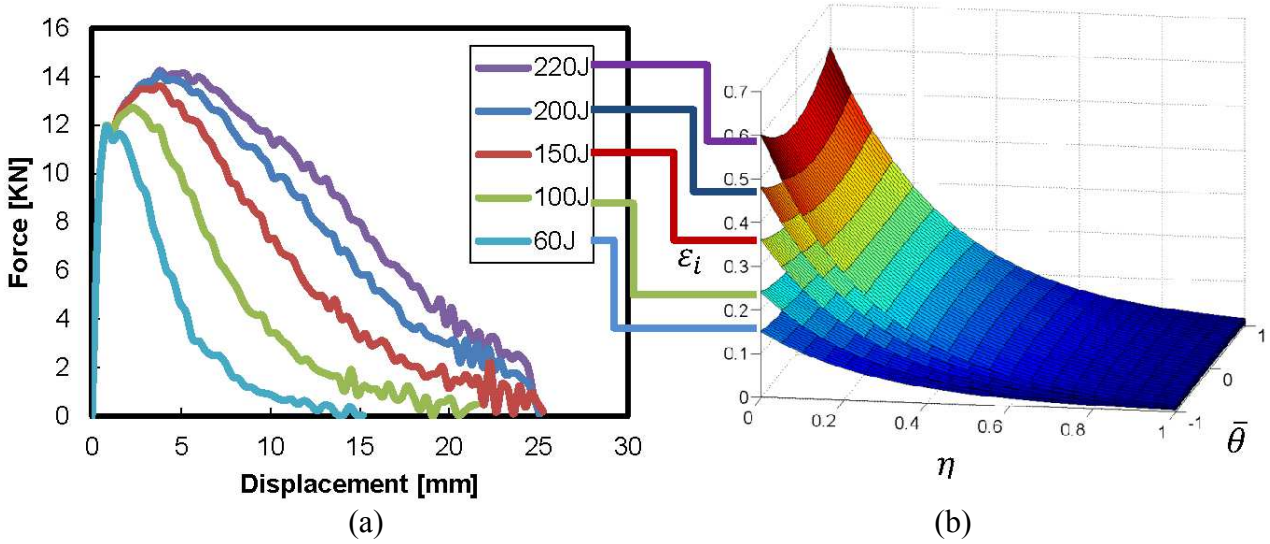

Figure 10: (a) Simulated force-displacement curves of Charpy tests with (b) varied DIL (S500)

Table 8: Nominal DIL for S500

Nominal Charpy impact energy	C_1	C_2	C_3	C_4
200 J	0.48	3.644	0.42096	3.062
150 J	0.36	3.644	0.31572	3.062
100 J	0.24	3.644	0.21048	3.062
60 J	0.144	3.644	0.13155	3.062

6 CONCLUSIONS

In the frame of this work, a coupled damage mechanics model for ULCF loading conditions was presented. It is based on the damage mechanics model by Lian and the plasticity model presented by Armstrong and Ferderick. Hereby, the focus was set on the determination of a crack initiation criterion and the following damage evolution restricted by an effective strain concept. This method was the applied to the construction steel S500. The damage initiation locus and the critical damage locus were obtained. Furthermore, a new criterion based on nominal toughness values was introduced to enable a prediction of the load capacity of the material according to the variation of toughness properties.

REFERENCES

[1] J. Lian, M. Sharaf, F. Archie und S. Münstermann, „A hybrid approach for modelling of plasticity and failure behaviour of advanced high strength sheets,“ *International Journal of Damage Mechanics,* Nr. Vol. 22 (2), pp. 188-218, 2012.

[2] P. Armstrong und C. Frederick, „A mathematical representation of the multiaxial Bauschinger effect,“ 1966.

[3] Y. Bai und T. Wierzbicki, „A new model of metal plasticity and fracture with pressure and Lode dependence," *International Journal of Plasticity,* Bd. 24, pp. 1071 - 1096, 2008.

[4] M. Ohata und M. Toyoda, „Damage concept for evalutating ductile cracking of steel structure subjected to large-scale cyclic straining," *Science and Technology of Advanced Materials,* Bd. 5, pp. 241-249, 2004.

[5] F. Yoshida und T. Uemori, „A model of large-strain cyclic plasticity describing the Bauschinger effect and workhardening stagnation," *International Journal of Plasticity,* Bd. 18, pp. 661 - 686, 2002.

[6] J. L. Chaboche, „On some modifications of kinematic hardening to improve the description of ratchetting effects," *Internatinal Journal of Plasticity,* Bd. 7, Nr. 7, pp. 661-678, 1991.

[7] S. Münstermann, C. Schruff, J. Lian, B. Dobereiner, V. Brinnel und B. Wu, „Predicting lower bound damage curves for high-strength low-alloy steels," *Fatigue & Fracture Eingineering Materials & Structures,* Bd. 36, pp. 779-794, 2013.

[8] A. L. Gurson, „Continuum Theory of Ductile Rupture by Void Nucleation and Growth: Part I—Yield Criteria and Flow Rules for Porous Ductile Media," *Journal of Engineering Materials and Technology,* Bd. 99, Nr. 1, pp. 2-14, 1977.

[9] G. Johnson und W. Cook, „Fracture characteristics of three metals subjected to various strains, strain rates, temperatures and pressures," *Engineering Fracture Mechanics,* Bd. 21, Nr. 1, pp. 31-48, 1985.

[10] J. Hancock und A. Mackenzie, „On the mechanisms of ductile failure in high-strength steels subjected to multi-axial stress-states," *Journal of the Mechanics and Physics of Solids,* Bd. 24, Nr. 2-3, pp. 147-160, 1976.

[11] F. McClintock, „A criterion of ductile fracture by the growth of holes," *Journal of Applied Mechanics,* Bd. 35, pp. 363-371, 1968.

[12] *EN 10025-2011: Hot rolled products of structural steels,* 2011.

[13] K. Wallin, Fracture Toughness of Engineering Materials: Estimation and Application, Warrington: EMAS Publishing, 2011.

XIV International Conference on Computational Plasticity. Fundamentals and Applications
COMPLAS XIV
E. Oñate, D.R.J. Owen, D. Peric & M. Chiumenti (Eds)

A COMPARISON OF TWO FRAMEWORKS FOR KINEMATIC HARDENING IN HYPERELASTO-PLASTICITY

Knut A. Meyer*, Magnus Ekh

Department of Applied Mechanics, Division of Material and Computational Mechanics,
Chalmers University of Technology, 412 96 Gothenburg, Sweden
e-mail*: knut.andreas.meyer@chalmers.se, web page: http://www.chalmers.se/

Key words: Hyperelasto-plasticity, Finite strains, Kinematic hardening

Abstract. In this work we compare two frameworks for thermodynamically consistent hyperelasto-plasticity with kinematic hardening. The first was formulated by Dettmer and Reese (2004), inspired by Lion (2000), and has been used to model sheet metal forming. The second, formulated by Wallin et al. (2003), has been used to model large shear strains and cyclic ratcheting behavior of pearlitic steel (Johansson et al. 2006). In this paper we show that these frameworks can result in equivalent models for certain choices of free energies. Furthermore, it is shown that the choices of free energy found in the literature only result in minor differences. These differences are discussed theoretically and investigated numerically.

1 INTRODUCTION

Large strains in metals during room temperature occur in many technical applications, often during manufacturing, such as sheet metal forming. Some components are also subjected to large strains during service, for example in the surface layer of railway rails and wheels (see e.g. [1, 2]). Experiments have shown that the Bauchinger effect, often modeled with kinematic hardening, is pronounced in many metals. Kinematic hardening can be modeled with different thermodynamically consistent hyperelasto-plastic frameworks found in the literature, and two of them are considered here. The first framework is based on rheological models with an Armstrong-Frederick (AF) type of kinematic hardening, and was proposed by Lion [3] and further developed by Dettmer and Reese [4]. The second framework, introduced by Wallin et al. [5], also features an AF type of kinematic hardening, and has been used to model the Swift effect [6] and large deformations in railway applications [7, 8]. In this paper we compare these frameworks, both theoretically and numerically.

2 DESCRIPTION OF FRAMEWORKS

In this section, the modeling frameworks are presented in terms of their assumed kinematics and thermodynamics. The common parts are presented in Subsections 2.1 and 2.2, followed by a description of how the frameworks differ in Subsections 2.3 and 2.4. Three specific models are defined in Subsections 2.5 and 2.6, which are compared in the numerical examples in Section 3. For the clarity of the presentation, only linear kinematic hardening is considered in the current section. In Section 4 we investigate nonlinear kinematic hardening, e.g. of Armstrong-Frederick type.

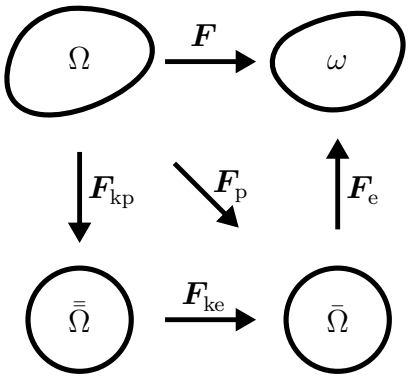

Figure 1: Configurations and deformation gradients

2.1 Kinematics and notations

Figure 1 shows the different configurations used in both [4] and [5]. Dettmer and Reese [4] introduce the inelastic plastic deformation gradient $\boldsymbol{F}_{\mathrm{kp}}$ connecting the fictitious kinematic configuration $\bar{\bar{\Omega}}$ to the initial configuration Ω. This connection is not introduced in Wallin et al. [5], but otherwise the same configurations and remaining deformation gradients are present in both frameworks.

Tensors on the current configuration ω are denoted with lower case letters and no bars, e.g. $\boldsymbol{b}$. Tensors on the intermediate $\bar{\Omega}$ and kinematic $\bar{\bar{\Omega}}$ configurations are denoted by one bar, e.g. $\bar{\boldsymbol{C}}_{\mathrm{e}}$, and two bars, e.g. $\bar{\bar{\boldsymbol{C}}}_{\mathrm{ke}}$, respectively. The following decompositions of the deformation gradients and definitions of the deformation tensors will be used:

$$\begin{aligned} \boldsymbol{F} &= \boldsymbol{F}_{\mathrm{e}}\boldsymbol{F}_{\mathrm{p}} & \bar{\boldsymbol{C}}_{\mathrm{e}} &= \boldsymbol{F}_{\mathrm{e}}^{\mathrm{t}}\boldsymbol{F}_{\mathrm{e}} & \boldsymbol{c}_{\mathrm{e}} &= \boldsymbol{F}_{\mathrm{e}}^{-\mathrm{t}}\boldsymbol{F}_{\mathrm{e}}^{-1} = \boldsymbol{b}_{\mathrm{e}}^{-1} \\ \boldsymbol{F}_{\mathrm{p}} &= \boldsymbol{F}_{\mathrm{ke}}\boldsymbol{F}_{\mathrm{kp}} & \bar{\bar{\boldsymbol{C}}}_{\mathrm{ke}} &= \boldsymbol{F}_{\mathrm{ke}}^{\mathrm{t}}\boldsymbol{F}_{\mathrm{ke}} & \bar{\boldsymbol{c}}_{\mathrm{ke}} &= \boldsymbol{F}_{\mathrm{ke}}^{-\mathrm{t}}\boldsymbol{F}_{\mathrm{ke}}^{-1} = \bar{\boldsymbol{b}}_{\mathrm{ke}}^{-1} \end{aligned} \tag{1}$$

The velocity gradients on the intermediate and kinematic configurations are defined as

$$\bar{\boldsymbol{L}}_{\mathrm{p}} = \dot{\boldsymbol{F}}_{\mathrm{p}}\boldsymbol{F}_{\mathrm{p}}^{-1} \tag{2}$$

$$\bar{\boldsymbol{L}}_{\mathrm{ke}} = \dot{\boldsymbol{F}}_{\mathrm{ke}}\boldsymbol{F}_{\mathrm{ke}}^{-1} \tag{3}$$

$$\bar{\bar{\boldsymbol{L}}}_{\mathrm{kp}} = \dot{\boldsymbol{F}}_{\mathrm{kp}}\boldsymbol{F}_{\mathrm{kp}}^{-1} \tag{4}$$

and hence the velocity gradient $\boldsymbol{l}$ on the current configuration can be written as

$$\boldsymbol{l} = \dot{\boldsymbol{F}}\boldsymbol{F}^{-1} = \dot{\boldsymbol{F}}_{\mathrm{e}}\boldsymbol{F}_{\mathrm{e}}^{-1} + \boldsymbol{F}_{\mathrm{e}}\bar{\boldsymbol{L}}_{\mathrm{p}}\boldsymbol{F}_{\mathrm{e}}^{-1} \tag{5}$$

2.2 Thermodynamics

The free energy Ψ is introduced with the additive split according to

$$\Psi = \Psi_{\mathrm{e}}\left(\bar{\boldsymbol{C}}_{\mathrm{e}}\right) + \Psi_{\mathrm{kin}}\left(\boldsymbol{F}_{\mathrm{ke}}\right) \tag{6}$$

whereby the dissipation inequality (see e.g. Simo (1998) [9]) becomes

$$D = \boldsymbol{\tau} : \boldsymbol{l} - \dot{\Psi} = \boldsymbol{\tau} : \boldsymbol{l} - \frac{\partial \Psi_{\mathrm{e}}}{\partial \bar{\boldsymbol{C}}_{\mathrm{e}}}\dot{\bar{\boldsymbol{C}}}_{\mathrm{e}} - \frac{\partial \Psi_{\mathrm{kin}}}{\partial \boldsymbol{F}_{\mathrm{ke}}} : \dot{\boldsymbol{F}}_{\mathrm{ke}} \geq 0 \tag{7}$$

where $\boldsymbol{\tau}$ is the Kirchhoff stress. Using the requirement of zero dissipation during elastic loading and Equation (5), the reduced dissipation inequality becomes

$$D = \bar{\boldsymbol{M}} : \bar{\boldsymbol{L}}_{\mathrm{p}} - \left(\frac{\partial \Psi_{\mathrm{kin}}}{\partial \boldsymbol{F}_{\mathrm{ke}}}\boldsymbol{F}_{\mathrm{ke}}^{\mathrm{t}}\right) : \bar{\boldsymbol{L}}_{\mathrm{ke}} \tag{8}$$

where the Mandel stress $\bar{\boldsymbol{M}}$ is defined as

$$\bar{\boldsymbol{M}} = 2\bar{\boldsymbol{C}}_{\mathrm{e}}\frac{\partial \Psi_{\mathrm{e}}}{\partial \bar{\boldsymbol{C}}_{\mathrm{e}}} \tag{9}$$

In a standard fashion, we adopt an associative evolution of the plastic deformation gradient in this paper:

$$\bar{\boldsymbol{L}}_{\mathrm{p}} = \dot{\lambda}\frac{\partial \Phi}{\partial \bar{\boldsymbol{M}}} \tag{10}$$

where the functional dependence of the yield function $\Phi \leq 0$ will be specified later. Up until this point the two frameworks are identical. We first describe the framework by Dettmer and Reese [4], before proceeding with the framework by Wallin et al. [5].

2.3 1st framework [4]

In the first framework proposed by Lion [3] and further developed by Dettmer and Reese [4], the plastic deformation gradient $\boldsymbol{F}_{\mathrm{p}}$ is multiplicatively decomposed into an elastic part $\boldsymbol{F}_{\mathrm{ke}}$ and a plastic part $\boldsymbol{F}_{\mathrm{kp}}$. The physical motivation is that $\boldsymbol{F}_{\mathrm{ke}}$ represents local elastic deformations on the microscale caused by dislocations and $\boldsymbol{F}_{\mathrm{kp}}$ represents irreversible displacements in the slip systems. The assumption is that development of $\boldsymbol{F}_{\mathrm{ke}}$ results in linear kinematic hardening and the development of $\boldsymbol{F}_{\mathrm{kp}}$ reduces $\boldsymbol{F}_{\mathrm{ke}}$, hence causing saturation (dynamic recovery) of the kinematic hardening. This is illustrated using a rheological model by Lion [3]. The multiplicative split of $\boldsymbol{F}_{\mathrm{p}}$ results in the following additive split of the plastic velocity gradient $\bar{\boldsymbol{L}}_{\mathrm{p}}$

$$\bar{\boldsymbol{L}}_{\mathrm{p}} = \bar{\boldsymbol{L}}_{\mathrm{ke}} + \boldsymbol{F}_{\mathrm{ke}}\bar{\bar{\boldsymbol{L}}}_{\mathrm{kp}}\boldsymbol{F}_{\mathrm{ke}}^{-1} \tag{11}$$

For the case of purely linear hardening ($\boldsymbol{F}_{\mathrm{kp}} = \boldsymbol{I}$), the reduced dissipation, Equation (8), can be written as

$$D = \left(\bar{\boldsymbol{M}} - {}^{1}\bar{\boldsymbol{M}}_{\mathrm{k}}\right) : \bar{\boldsymbol{L}}_{\mathrm{p}} \tag{12}$$

where the kinematic hardening stress of Mandel type (also denoted back-stress) is defined as

$${}^{1}\bar{\boldsymbol{M}}_{\mathrm{k}} = \frac{\partial \Psi_{\mathrm{kin}}}{\partial \boldsymbol{F}_{\mathrm{ke}}} \boldsymbol{F}_{\mathrm{ke}}^{\mathrm{t}} \tag{13}$$

This motivates that the driving force for plastic flow is $\bar{\boldsymbol{M}} - {}^{1}\bar{\boldsymbol{M}}_{\mathrm{k}}$ and thereby a yield criterion expressed as $\Phi(\bar{\boldsymbol{M}} - {}^{1}\bar{\boldsymbol{M}}_{\mathrm{k}})$.

2.4 2nd framework [5]

In the second framework, proposed by Wallin et al. [5], the deformation gradient $\boldsymbol{F}_{\mathrm{ke}}^{-1}$ is introduced to model the deformation of the crystal lattice, due to the residual micro stresses responsible for the Bauchinger effect. From this deformation gradient the kinematic hardening stress of Mandel type is defined as

$${}^{2}\bar{\boldsymbol{M}}_{\mathrm{k}} = -\frac{\partial \Psi_{\mathrm{kin}}}{\partial \boldsymbol{F}_{\mathrm{ke}}} \boldsymbol{F}_{\mathrm{ke}}^{\mathrm{t}} \tag{14}$$

which yields that the reduced dissipation inequality (8) is

$$D = \bar{\boldsymbol{M}} : \bar{\boldsymbol{L}}_{\mathrm{p}} + {}^{2}\bar{\boldsymbol{M}}_{\mathrm{k}} : \bar{\boldsymbol{L}}_{\mathrm{ke}} \tag{15}$$

Using the standard interpretation of ${}^{2}\bar{\boldsymbol{M}}_{\mathrm{k}}$ as a back-stress that reduces the driving force for plasticity, motivates the yield function $\Phi(\bar{\boldsymbol{M}} - {}^{2}\bar{\boldsymbol{M}}_{\mathrm{k}})$. This gives, by the postulate of maximum dissipation, the kinematic relation

$$\bar{\boldsymbol{L}}_{\mathrm{p}} = -\bar{\boldsymbol{L}}_{\mathrm{ke}} \tag{16}$$

and the same reduced dissipation inequality as in Equation (12) is obtained:

$$D = \left(\bar{\boldsymbol{M}} - {}^{2}\bar{\boldsymbol{M}}_{\mathrm{k}}\right) : \bar{\boldsymbol{L}}_{\mathrm{p}} \tag{17}$$

2.5 Specific formats for free energy

The elastic and kinematic free energies (with the third invariant $I_{3\bullet} = \det(\bullet)$) proposed by Vladimirov et al [10] are

$${}^{\mathrm{A}}\Psi_{\mathrm{e}} = \frac{1}{2} G \left(\mathrm{tr}(\bar{\boldsymbol{C}}_{\mathrm{e}}) - 3 - \ln\left(I_{3\mathrm{C}_{\mathrm{e}}}\right)\right) + \frac{\Lambda}{4}\left(I_{3\mathrm{C}_{\mathrm{e}}} - 1 - \ln\left(I_{3\mathrm{C}_{\mathrm{e}}}\right)\right) \tag{18}$$

$${}^{\mathrm{A}}\Psi_{\mathrm{kin}} = \frac{1}{2} H_{\mathrm{kin}} \left(\mathrm{tr}(\bar{\bar{\boldsymbol{C}}}_{\mathrm{ke}}) - 3 - \ln\left(I_{3\mathrm{C}_{\mathrm{ke}}}\right)\right) \tag{19}$$

The part of the elastic free energy, corresponding to Lamé's second parameter Λ, is thus not included in the kinematic free energy.

A similar split is introduced in [5], but the free energy in that work is decomposed into an isochoric and a volumetric part. The formulation for the volumetric part is not the same in [5] and [7, 8], and here we use the formulation from [7, 8]. This difference only affects the bulk elastic response and the influence on the numerical results studied in this paper is therefore negligible.

$$ {}^{\mathrm{B}}\Psi_{\mathrm{e}} = \frac{1}{2}G\left(\mathrm{tr}\left(I_{3\mathrm{C_e}}^{-1/3}\bar{\boldsymbol{C}}_{\mathrm{e}}\right) - 3\right) + \frac{1}{2}K\left(I_{3\mathrm{C_e}}^{1/2} - 1\right)^2 \tag{20} $$

$$ {}^{\mathrm{B}}\Psi_{\mathrm{kin}} = \frac{1}{2}H_{\mathrm{kin}}\left(\mathrm{tr}\left(I_{3\mathrm{c_{ke}}}^{-1/3}\bar{\boldsymbol{c}}_{\mathrm{ke}}\right) - 3\right) \tag{21} $$

From the discussion so far, there seem to be several differences between the frameworks: (1) the definition of the Mandel back-stress (${}^{1}\bar{\boldsymbol{M}}_{\mathrm{k}}$ or ${}^{2}\bar{\boldsymbol{M}}_{\mathrm{k}}$), (2) the variable of which the kinematic free energy depends on ($\bar{\bar{\boldsymbol{C}}}_{\mathrm{ke}}$ or $\bar{\boldsymbol{c}}_{\mathrm{ke}}$) and (3) what part of the elastic free energy formulation that is used to formulate the kinematic free energy. The third of these can be investigated by taking the format of free energy from the second framework, but using the definitions and variables from the first framework to obtain model C:

$$ {}^{\mathrm{C}}\Psi_{\mathrm{e}} = {}^{\mathrm{B}}\Psi_{\mathrm{e}} \tag{22} $$

$$ {}^{\mathrm{C}}\Psi_{\mathrm{kin}} = \frac{1}{2}H_{\mathrm{kin}}\left(\mathrm{tr}\left(I_{3\mathrm{C_{ke}}}^{-1/3}\bar{\bar{\boldsymbol{C}}}_{\mathrm{ke}}\right) - 3\right) \tag{23} $$

2.6 Stresses for each model

We have now described both frameworks, the first by Dettmer and Reese [4] and the second by Wallin et al. [5]. By letting Ψ_{kin} depend on $\bar{\bar{\boldsymbol{C}}}_{\mathrm{ke}}$ or $\bar{\boldsymbol{c}}_{\mathrm{ke}}$ we can use (13) and (14), respectively, to obtain the Mandel back-stresses for the two frameworks:

$$ {}^{1}\bar{\boldsymbol{M}}_{\mathrm{k}} = \left(\frac{\partial\Psi_{\mathrm{kin}}}{\partial\bar{\bar{\boldsymbol{C}}}_{\mathrm{ke}}} : \frac{\partial\bar{\bar{\boldsymbol{C}}}_{\mathrm{ke}}}{\partial\boldsymbol{F}_{\mathrm{ke}}}\right)\boldsymbol{F}_{\mathrm{ke}}^{\mathrm{t}} = 2\boldsymbol{F}_{\mathrm{ke}}\left(\frac{\partial\Psi_{\mathrm{kin}}}{\partial\bar{\bar{\boldsymbol{C}}}_{\mathrm{ke}}}\right)\boldsymbol{F}_{\mathrm{ke}}^{\mathrm{t}} \tag{24} $$

$$ {}^{2}\bar{\boldsymbol{M}}_{\mathrm{k}} = -\left(\frac{\partial\Psi_{\mathrm{kin}}}{\partial\bar{\boldsymbol{c}}_{\mathrm{ke}}} : \frac{\partial\bar{\boldsymbol{c}}_{\mathrm{ke}}}{\partial\boldsymbol{F}_{\mathrm{ke}}}\right)\boldsymbol{F}_{\mathrm{ke}}^{\mathrm{t}} = 2\bar{\boldsymbol{c}}_{\mathrm{ke}}\frac{\partial\Psi_{\mathrm{kin}}}{\partial\bar{\boldsymbol{c}}_{\mathrm{ke}}} \tag{25} $$

The Mandel stresses for model A, ${}^{\mathrm{A}}\bar{\boldsymbol{M}}$ and ${}^{\mathrm{A}}\bar{\boldsymbol{M}}_{\mathrm{k}}$, are found using Equations (9) and (24) with the free energies in Equations (18) and (19):

$$ {}^{\mathrm{A}}\bar{\boldsymbol{M}} = G(\bar{\boldsymbol{C}}_{\mathrm{e}} - \boldsymbol{I}) + \frac{\Lambda}{2}(I_{3\mathrm{C_e}} - 1)\boldsymbol{I}, \qquad {}^{\mathrm{A}}\bar{\boldsymbol{M}}_{\mathrm{k}} = H_{\mathrm{kin}}\left(\bar{\boldsymbol{b}}_{\mathrm{ke}} - \boldsymbol{I}\right) \tag{26} $$

The stresses for model B, ${}^{\mathrm{B}}\bar{\boldsymbol{M}}$ and ${}^{\mathrm{B}}\bar{\boldsymbol{M}}_{\mathrm{k}}$, are given by using Equations (9) and (25) with the free energies in Equations (20) and (21):

$$ {}^{\mathrm{B}}\bar{\boldsymbol{M}} = GI_{3\mathrm{C_e}}^{-1/3}\bar{\boldsymbol{C}}_{\mathrm{e}}^{\mathrm{dev}} + K(I_{3\mathrm{C_e}} - I_{3\mathrm{C_e}}^{1/2})\boldsymbol{I}, \qquad {}^{\mathrm{B}}\bar{\boldsymbol{M}}_{\mathrm{k}} = H_{\mathrm{kin}}I_{\mathrm{c_{ke}}}^{-1/3}\bar{\boldsymbol{c}}_{\mathrm{ke}}^{\mathrm{dev}} \tag{27} $$

For model C, we use the first framework, i.e. the stresses ${}^{\mathrm{C}}\bar{\boldsymbol{M}}$ and ${}^{\mathrm{C}}\bar{\boldsymbol{M}}_{\mathrm{k}}$ are given by using Equations (9) and (24), but with the free energies in Equations (22) and (23). We further note that $I_{3\mathrm{C}_{\mathrm{ke}}} = I_{3\mathrm{b}_{\mathrm{ke}}}$ and $\mathrm{tr}(\bar{\boldsymbol{C}}_{\mathrm{ke}}) = \mathrm{tr}(\bar{\boldsymbol{b}}_{\mathrm{ke}})$, which leads to:

$$ {}^{\mathrm{C}}\bar{\boldsymbol{M}} = {}^{\mathrm{B}}\bar{\boldsymbol{M}} \qquad {}^{\mathrm{C}}\bar{\boldsymbol{M}}_{\mathrm{k}} = H_{\mathrm{kin}} I_{\mathrm{b}_{\mathrm{ke}}}^{-1/3} \bar{\boldsymbol{b}}_{\mathrm{ke}}^{\mathrm{dev}} \tag{28} $$

If ${}^{\mathrm{B}}\bar{\boldsymbol{c}}_{\mathrm{ke}} = {}^{\mathrm{C}}\bar{\boldsymbol{b}}_{\mathrm{ke}}$ then clearly model B and C are equivalent. Assuming that is the case for some point in time, we also have ${}^{\mathrm{B}}\bar{\boldsymbol{L}}_{\mathrm{p}} = {}^{\mathrm{C}}\bar{\boldsymbol{L}}_{\mathrm{p}} = \bar{\boldsymbol{L}}_{\mathrm{p}}$. Since model B is using the second framework, and model C is using the first, we also have $-{}^{\mathrm{B}}\bar{\boldsymbol{L}}_{\mathrm{ke}} = {}^{\mathrm{C}}\bar{\boldsymbol{L}}_{\mathrm{ke}} = \bar{\boldsymbol{L}}_{\mathrm{p}}$, hence

$$ {}^{\mathrm{B}}\dot{\bar{\boldsymbol{c}}}_{\mathrm{ke}} = -\left({}^{\mathrm{B}}\bar{\boldsymbol{L}}_{\mathrm{ke}}^{\mathrm{t}}\, {}^{\mathrm{B}}\bar{\boldsymbol{c}}_{\mathrm{ke}} + {}^{\mathrm{B}}\bar{\boldsymbol{c}}_{\mathrm{ke}}\, {}^{\mathrm{B}}\bar{\boldsymbol{L}}_{\mathrm{ke}} \right) = \bar{\boldsymbol{L}}_{\mathrm{p}}^{\mathrm{t}}\, {}^{\mathrm{B}}\bar{\boldsymbol{c}}_{\mathrm{ke}} + {}^{\mathrm{B}}\bar{\boldsymbol{c}}_{\mathrm{ke}} \bar{\boldsymbol{L}}_{\mathrm{p}} \tag{29} $$

$$ {}^{\mathrm{C}}\dot{\bar{\boldsymbol{b}}}_{\mathrm{ke}} = \left({}^{\mathrm{C}}\bar{\boldsymbol{L}}_{\mathrm{ke}}\, {}^{\mathrm{C}}\bar{\boldsymbol{b}}_{\mathrm{ke}} + {}^{\mathrm{C}}\bar{\boldsymbol{b}}_{\mathrm{ke}}\, {}^{\mathrm{C}}\bar{\boldsymbol{L}}_{\mathrm{ke}}^{\mathrm{t}} \right) = \bar{\boldsymbol{L}}_{\mathrm{p}}\, {}^{\mathrm{C}}\bar{\boldsymbol{b}}_{\mathrm{ke}} + {}^{\mathrm{C}}\bar{\boldsymbol{b}}_{\mathrm{ke}} \bar{\boldsymbol{L}}_{\mathrm{p}}^{\mathrm{t}} \tag{30} $$

As ${}^{\mathrm{B}}\bar{\boldsymbol{c}}_{\mathrm{ke}} = {}^{\mathrm{C}}\bar{\boldsymbol{b}}_{\mathrm{ke}} = \boldsymbol{I}$ initially, the statement ${}^{\mathrm{B}}\bar{\boldsymbol{c}}_{\mathrm{ke}} = {}^{\mathrm{C}}\bar{\boldsymbol{b}}_{\mathrm{ke}}$ is true for all points in time under the assumption that $\bar{\boldsymbol{L}}_{\mathrm{p}}$ is symmetric. If the free energy is isotropic, the Mandel stresses $\bar{\boldsymbol{M}}$ and $\bar{\boldsymbol{M}}_{\mathrm{k}}$ are symmetric, and hence $\bar{\boldsymbol{L}}_{\mathrm{p}}$ becomes symmetric for the associative choice of $\bar{\boldsymbol{L}}_{\mathrm{p}}$ in Equation (10). This leads to the conclusion that model B and C are equivalent, which is verified numerically later. Furthermore, this proof leads to the interesting conclusion that the frameworks can give exactly the same model with proper choices of free energy. The possibility to formulate an unsymmetric $\bar{\boldsymbol{L}}_{\mathrm{p}}$ for isotropy is discussed in e.g. Wallin et al. [5] and Wallin and Ristinmaa [6], but is not investigated in this paper.

3 NUMERICAL RESULTS

In this section we evaluate the response of the material models for uniaxial loading and simple shear loading. The models are implemented using a standard Backward Euler integration scheme, for which Vladimirov et al. [10] noted that the accuracy suffers at large time steps. To avoid these accuracy problems, approximately $4 \cdot 10^4$ and $5 \cdot 10^4$ load steps are used for the uniaxial and simple shear loading, respectively.

The von Mises effective stress is used to define the yield function Φ according to

$$ \Phi = \sqrt{\frac{3}{2}} \sqrt{\mathrm{dev}\left(\bar{\boldsymbol{M}}^{\mathrm{t}} - \bar{\boldsymbol{M}}_{\mathrm{k}}^{\mathrm{t}}\right) : \mathrm{dev}\left(\bar{\boldsymbol{M}} - \bar{\boldsymbol{M}}_{\mathrm{k}}\right)} - Y_0 = f\left(\bar{\boldsymbol{M}} - \bar{\boldsymbol{M}}_{\mathrm{k}}\right) - Y_0 \leq 0 \tag{31} $$

whereby the evolution of the plastic deformation gradient in (10) becomes

$$ \bar{\boldsymbol{L}}_{\mathrm{p}} = \dot{\lambda} \frac{3}{2} \frac{\mathrm{dev}\left(\bar{\boldsymbol{M}}^{\mathrm{t}} - \bar{\boldsymbol{M}}_{\mathrm{k}}^{\mathrm{t}}\right)}{f\left(\bar{\boldsymbol{M}} - \bar{\boldsymbol{M}}_{\mathrm{k}}\right)} \tag{32} $$

From this it follows that the plastic deformation is isochoric: By time differentiation of $\det\left(\boldsymbol{F}_{\mathrm{p}}\right)$ and using (2)

$$ \frac{\partial}{\partial t} \det\left(\boldsymbol{F}_{\mathrm{p}}\right) = \det\left(\boldsymbol{F}_{\mathrm{p}}\right) \boldsymbol{F}_{\mathrm{p}}^{-\mathrm{t}} : \left(\bar{\boldsymbol{L}}_{\mathrm{p}} \boldsymbol{F}_{\mathrm{p}}\right) = \det\left(\boldsymbol{F}_{\mathrm{p}}\right) \mathrm{tr}\left(\bar{\boldsymbol{L}}_{\mathrm{p}}\right) = 0 \tag{33} $$

hence, $\det\left(\boldsymbol{F}_{\mathrm{p}}\right) = 1$.

The following material parameters: $G = 81\,\mathrm{GPa}$, $K = 174\,\mathrm{GPa}$, $\Lambda = K - 2G/3$, $Y_0 = 100\,\mathrm{MPa}$ and $H_{\mathrm{kin}} = 1000\,\mathrm{MPa}$, are used in the numerical examples in Figure 2.

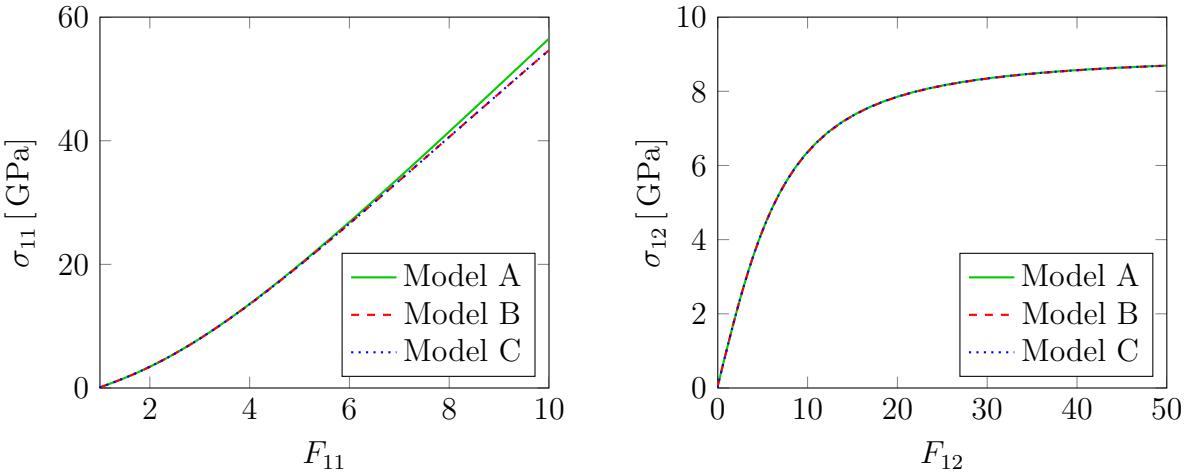

(a) Uniaxial response

(b) Simple shear response

Figure 2: Numerical results

We first consider uniaxial stress in Figure 2a, by letting the normal deformation gradient F_{11} increase from 1 to 10 while keeping the Cauchy stresses $\sigma_{22} = \sigma_{33} = 0$ ($\boldsymbol{\sigma} = \boldsymbol{\tau}/I_{3\mathrm{F}}$). As previously shown theoretically, model B and C give the same response. Model A gives a somewhat stiffer response at large deformations, due to the different choice of free energy.

In the case of simple shear loading, Figure 2b shows that the response of all the models coincide. While this is expected for model B and C, the fact that model A and C coincide is explained with simple shear being an isochoric process ($I_{3\mathrm{F}} = I_{3\mathrm{F_p}} = 1 \Rightarrow I_{3\mathrm{F_e}} = 1$)

The results in Figure 2 show negligible differences between the different formulations of free energy. From a theoretical point of view, one could argue that the deviatoric dependence of the back-stress is more correct, based on the experimental evidence of volume preservation for metal plasticity.

4 ARMSTRONG-FREDERICK SATURATION

Linear kinematic hardening was considered in Section 2, for which Dettmer and Reese [4] set $\boldsymbol{F}_{\mathrm{kp}} = \boldsymbol{I}$, yielding the reduced dissipation inequality in Equation (12). If the general case with an evolving $\boldsymbol{F}_{\mathrm{kp}}$ is considered, the reduced dissipation inequality, using Equation (11), becomes

$$D = \left(\bar{\boldsymbol{M}} - {}^{1}\bar{\boldsymbol{M}}_{\mathrm{k}}\right) : \bar{\boldsymbol{L}}_{\mathrm{p}} + {}^{1}\bar{\boldsymbol{M}}_{\mathrm{k}} : \left(\boldsymbol{F}_{\mathrm{ke}}\bar{\bar{\boldsymbol{L}}}_{\mathrm{kp}}\boldsymbol{F}_{\mathrm{ke}}^{-1}\right) \tag{34}$$

From this the kinematic stress of Mandel type on the kinematic configuration ${}^{1}\bar{\bar{\boldsymbol{M}}}_{\mathrm{k}}$ is defined as

$${}^{1}\bar{\bar{\boldsymbol{M}}}_{\mathrm{k}} = \boldsymbol{F}_{\mathrm{ke}}^{\mathrm{t}}\,{}^{1}\bar{\boldsymbol{M}}_{\mathrm{k}}\boldsymbol{F}_{\mathrm{ke}}^{-\mathrm{t}} \tag{35}$$

Saturation is motivated by the rheological model, setting the evolution on $\bar{\bar{\boldsymbol{L}}}_{\mathrm{kp}}^{\mathrm{sym}}$. As the Mandel stresses in [4] are symmetric, this can be written as

$$\bar{\bar{\boldsymbol{L}}}_{\mathrm{kp}} = \dot{\lambda}\frac{{}^{1}\bar{\bar{\boldsymbol{M}}}_{\mathrm{k}}^{\mathrm{t}}}{b_{\infty}} \tag{36}$$

where b_{∞} is a material parameter controlling the kinematic saturation. Equation (11) and (35) then yield

$$\bar{\boldsymbol{L}}_{\mathrm{ke}} = \bar{\boldsymbol{L}}_{\mathrm{p}} - \dot{\lambda}\frac{{}^{1}\bar{\boldsymbol{M}}_{\mathrm{k}}^{\mathrm{t}}}{b_{\infty}} \tag{37}$$

This Equation can be compared with Wallin et al. [5], who use a modified potential Φ_{kin}^{*} to obtain

$$\bar{\boldsymbol{L}}_{\mathrm{ke}} = \dot{\lambda}\frac{\partial\Phi_{\mathrm{kin}}^{*}}{\partial\left({}^{2}\bar{\boldsymbol{M}}_{\mathrm{k}}\right)} = -\bar{\boldsymbol{L}}_{\mathrm{p}} + \dot{\lambda}\frac{{}^{2}\bar{\boldsymbol{M}}_{\mathrm{k}}^{\mathrm{t}}}{b_{\infty}} \tag{38}$$

$\bar{\boldsymbol{L}}_{\mathrm{ke}}$ will be symmetric if a modified yield potential Φ_{kin}^{*} exists and we have, as before, symmetric Mandel stresses. This is the case for the considered model with Armstrong-Frederick type of non-linear kinematic saturation. $\bar{\boldsymbol{L}}_{\mathrm{ke}}$ is also symmetric in the work by Zhu et al. [11], where the first framework was extended to include nonlinear kinematic hardening of Ohno-Wang type. When $\bar{\boldsymbol{L}}_{\mathrm{ke}}$ is symmetric, the same arguments as before relating to Equations (29) and (30) hold true. Hence, for appropriate free energies the two frameworks give the same model also for nonlinear kinematic hardening.

5 CONCLUDING REMARKS

We have shown that the two different frameworks, introduced by [4] and [5], can give equivalent models for isotropic free energies. The major difference between the models used for the different frameworks is the kinematic free energy. To obtain the same model, the same structure of the kinematic free energy must be used, but with a different variable ($\bar{\bar{\boldsymbol{C}}}_{\mathrm{ke}}$ or $\bar{\boldsymbol{c}}_{\mathrm{ke}}$). The numerical results confirm these theoretical findings. They further show that the difference between the formulations of free energy has a negligible effect on the material response up to a stretch of 5 for uniaxial loading, and no effect during simple shear.

6 ACKNOWLEDGMENTS

This work has been partly financed within the European Horizon 2020 Joint Technology Initiative Shift2Rail through contract no. 730841. The use of AceGen [12] has been very effective in speeding up the implementation of the material models.

REFERENCES

[1] F. A. M Alwahdi, A. Kapoor, and F. J. Franklin. "Subsurface microstructural analysis and mechanical properties of pearlitic rail steels in service". In: *Wear* 302.1-2 (2013), pp. 1453–1460. DOI: 10.1016/j.wear.2012.12.058.

[2] K. Cvetkovski and J. Ahlström. "Characterisation of plastic deformation and thermal softening of the surface layer of railway passenger wheel treads". In: *Wear* 300.1-2 (2013), pp. 200–204. DOI: 10.1016/j.wear.2013.01.094.

[3] A. Lion. "Constitutive modelling in finite thermoviscoplasticity: a physical approach based on nonlinear rheological models". In: *International Journal of Plasticity* 16.5 (2000), pp. 469–494. DOI: 10.1016/S0749-6419(99)00038-8.

[4] W. Dettmer and S. Reese. "On the theoretical and numerical modelling of Armstrong-Frederick kinematic hardening in the finite strain regime". In: *Computer Methods in Applied Mechanics and Engineering* 193.1 (2004), pp. 87–116. DOI: 10.1016/j.cma.2003.09.005.

[5] M. Wallin, M. Ristinmaa, and N. S. Ottosen. "Kinematic hardening in large strain plasticity". In: *European Journal of Mechanics - A/Solids* 22.3 (2003), pp. 341–356. DOI: 10.1016/S0997-7538(03)00026-3.

[6] M. Wallin and M. Ristinmaa. "Deformation gradient based kinematic hardening model". In: *International Journal of Plasticity* 21.10 (2005), pp. 2025–2050. DOI: 10.1016/j.ijplas.2005.01.007.

[7] G. Johansson, J. Ahlström, and M. Ekh. "Parameter identification and modeling of large ratcheting strains in carbon steel". In: *Computers and Structures* 84.15-16 (2006), pp. 1002–1011. DOI: 10.1016/j.compstruc.2006.02.016.

[8] N. Larijani, G. Johansson, and M. Ekh. "Hybrid micro-macromechanical modeling of anisotropy evolution in pearlitic steel". In: *European Journal of Mechanics - A/Solids* 38 (Mar. 2013), pp. 38–47. DOI: 10.1016/j.euromechsol.2012.09.011.

[9] J. C. Simo. "A Framework For Finite Strain Based on Maximum plastic dissipation and the multiplicative decomposition: Part I. Continuum formulation". In: *Computer Methods in Applied Mechanics and Engineering* 66 (1988), pp. 199–219.

[10] I. N. Vladimirov, M. P. Pietryga, and S. Reese. "On the modelling of non-linear kinematic hardening at finite strains with application to springback - Comparison of time integration algorithms". In: *International Journal for Numerical Methods in Engineering* 75.1 (July 2008), pp. 1–28. DOI: 10.1002/nme.2234.

[11] Y. Zhu et al. "An extended cyclic plasticity model at finite deformations describing the Bauschinger effect and ratchetting behavior". In: *13th International Conference on Fracture 2013, ICF 2013* 5 (2013), pp. 1–11.

[12] J. Korelc. "Multi-language and Multi-environment Generation of Nonlinear Finite Element Codes". In: *Engineering with Computers* 18.4 (Nov. 2002), pp. 312–327. DOI: 10.1007/s003660200028.

XIV International Conference on Computational Plasticity. Fundamentals and Applications
COMPLAS XIV
E. Oñate, D.R.J. Owen, D. Peric & M. Chiumenti (Eds)

EXPLICIT FINITE ELEMENT IMPLEMENTATION OF A SHAPE MEMORY ALLOY CONSTITUTIVE MODEL AND ASSOCIATED ANALYSES

G. Scalet[°,*], E. Boatti[†], M. Ferraro[§], V. Mercuri[°], D.J. Hartl[^] and F. Auricchio[°]

[°] Dipartimento di Ingegneria Civile e Architettura
Università di Pavia
Via Ferrata 3, 27100 Pavia, Italy
e-mail: giulia.scalet@unipv.it/ valentina.mercuri01@universitadipavia.it / auricchio@unipv.it

[†]John A. Paulson School of Engineering and Applied Sciences
Harvard University
Cambridge, MA 02138, USA
e-mail: eboatti@seas.harvard.edu

[§]Institute of Bioengineering
École Polytechnique Fédérale de Lausanne, EPFL
BM 5125 Lausanne 1015, Switzerland
e-mail: mauro.ferraro@epfl.ch

[^]Department of Aerospace Engineering
Texas A&M University
College Station, TX 77843-3409, USA
e-mail: darren.hartl@tamu.edu

Key words: Shape memory alloys, Pseudoelasticity, Shape memory effect, Explicit integration, Constitutive modeling

Abstract. Shape memory alloys (SMA) represent an important class of smart metallic materials employed in various innovative applications thanks to their unique thermomechanical behavior. Since the 1980s, several SMA constitutive models have been proposed and implemented into both commercial and academic finite element analysis software tools. Such models have demonstrated their reliability and robustness in the design and optimization of a wide variety of SMA-based components. However, most models are implemented using implicit integration schemes, thus limiting their applicability in highly nonlinear analyses. The objective of this work is to present a novel explicit integration scheme for the numerical implementation of the three-dimensional Souza-Auricchio model, a phenomenological model able to reproduce the primary SMA responses (i.e., pseudoelasticity and shape memory effect). The model constitutive equations are formulated by adopting the continuum thermodynamic theory with internal variables, following a plasticity-like approach. An elastic predictor-inelastic corrector scheme is here used to

solve the time-discrete non-linear constitutive equations in the explicit framework. The proposed algorithm is investigated through several benchmark boundary-value problems of increasing complexity, considering both pseudoelastic and shape memory response in quasi-static conditions; a comparison with an implicit integration scheme is also performed. Such numerical tests demonstrate the ability of the algorithm to reproduce key material behaviors with effectiveness and robustness. Particularly, the analysis of SMA cables demonstrates the effectiveness of the explicit algorithm to solve complex problems involving widespread nonlinear contact, which prevent the convergence of the implicit scheme. Details such as mass-scaling options are also discussed.

1 INTRODUCTION

In the last three decades the utilization of shape memory alloys (SMA) has evolved from academic and niche applications to the mass production of a wide variety of industrial components. The great commercial success of SMA is due to two unique mechanical properties: pseudoelasticity and shape memory effect. These features have enabled a wide range of commercial applications, e.g., biomedical devices, civil engineering components, and mechanical systems [1]. Several efforts have been made during the past years to propose reliable constitutive models for SMA to be incorporated in numerical analysis tools, which can be generally categorized as microscopic, macroscopic, or micro-macro (see, e.g., [2, 3] for a review). This paper focuses on macroscopic ones, widely employed because of their simple numerical implementation and reduced cost of calculation.

Most of the phenomenological models available in the literature are implemented in an implicit time integration framework, with only few recent contributions utilizing an explicit alternative [4, 5, 6]. As well known, the employment of explicit methods becomes truly enabling in cases where complexity makes implicit algorithms impractical, such as in high-speed/non-linear dynamic analyses or in fully coupled thermo-mechanical dynamic analyses, which characterize several SMA applications.

The present paper aims to improve the current state-of-the-art regarding explicit implementation of SMA models within the general-purpose commercial Finite Element Analysis (FEA) solver Abaqus by proposing an explicit integration scheme for the three-dimensional phenomenological model presented in [7, 8], and defined in the following as the *Souza-Auricchio model*. This model has been chosen because of its extremely simple solution scheme and its ability in describing both of pseudoelastic and shape memory behaviors. In fact, it represents an improvement over the Auricchio-Taylor-Lubliner [9] model, which is currently available as built-in subroutine in Abaqus but it is not able to reproduce the zero-stress shape memory effect.

The present study provides a detailed description of the explicit integration scheme for the Souza-Auricchio model and an in-depth investigation of the corresponding algorithm. The constitutive and algorithmic framework is tested via the simulation of two complex three-dimensional boundary-value problems and compared to the implicit scheme as proposed in [8]. The first one assesses thermally-induced actuation problems through the

study of a SMA micro-gripper for micro-parts manipulation; while the pseudoelastic effect is investigated through a SMA cable segment, where widespread frictional contact among twisted SMA wires can be exploited for applications in civil and seismic engineering.

2 Souza-Auricchio model: time-continuous formulation

The present section briefly reviews the time-continuous formulation of the Souza-Auricchio model. The reader is referred to [7, 8] for further details.

The control variables are the total strain $\boldsymbol{\varepsilon}$ and the absolute temperature T, while the internal variable is transformation strain $\boldsymbol{e^{tr}}$. The Helmoltz free energy function is expressed as follows:

$$\Psi = \frac{1}{2}\,\kappa\,\theta^2 + G\,\|\boldsymbol{e} - \boldsymbol{e^{tr}}\|^2 + \tau_M\,\|\boldsymbol{e^{tr}}\| + \frac{1}{2}\,h\,\|\boldsymbol{e^{tr}}\|^2 + \mathcal{I}_{\varepsilon_L}(\boldsymbol{e^{tr}})\ . \tag{1}$$

Here, θ and $\boldsymbol{e}$ are the volumetric and deviatoric part of $\boldsymbol{\varepsilon}$, respectively; $\tau_M = \beta\langle T - T^*\rangle$, where β is a positive parameter and T^* is a reference temperature; κ and G are the bulk and shear modulus, respectively; h defines the phase transformation hardening. The indicator function

$$\mathcal{I}_{\varepsilon_L}(\boldsymbol{e}^{tr}) = \begin{cases} 0 & \text{if } \|\boldsymbol{e}^{tr}\| \le \varepsilon_L \\ +\infty & \text{otherwise} \end{cases} \tag{2}$$

is introduced to satisfy the transformation strain constraint $\|\boldsymbol{e}^{tr}\| \le \varepsilon_L$.

The constitutive equations are found to be:

$$\begin{aligned} \boldsymbol{s} &= \frac{\partial \Psi}{\partial \boldsymbol{e}} = 2G(\boldsymbol{e} - \boldsymbol{e}^{tr})\ , \\ \boldsymbol{X} &= -\frac{\partial \Psi}{\partial \boldsymbol{e}^{tr}} = \boldsymbol{s} - \tau_M \frac{\boldsymbol{e}^{tr}}{\|\boldsymbol{e}^{tr}\|} - h\boldsymbol{e}^{tr} - \gamma \frac{\boldsymbol{e}^{tr}}{\|\boldsymbol{e}^{tr}\|}\ , \end{aligned} \tag{3}$$

where $\boldsymbol{s}$ is the deviatoric part of $\boldsymbol{\sigma}$ and $\boldsymbol{X}$ is the thermodynamic force associated to $\boldsymbol{e}^{tr}$. The variable γ results from the subdifferential $\partial\mathcal{I}_{\varepsilon_L}(\boldsymbol{e}^{tr})$ and it is defined as follows:

$$\gamma = \begin{cases} 0 & \text{if } \|\boldsymbol{e}^{tr}\| < \varepsilon_L \\ \ge 0 & \text{if } \|\boldsymbol{e}^{tr}\| = \varepsilon_L \end{cases}\ , \tag{4}$$

with $\partial\mathcal{I}_{\varepsilon_L}(\boldsymbol{e}^{tr}) = \gamma \boldsymbol{e}^{tr}/\|\boldsymbol{e}^{tr}\|$.

To describe phase transformation and inelasticity evolution, a classical Mises-type limit function is introduced in the following form:

$$F = \|\boldsymbol{X}\| - R_Y\ , \tag{5}$$

where R_Y is a positive material parameter.

The evolution equation for the internal variable takes the form:

$$\dot{\boldsymbol{e}}^{tr} = \dot{\lambda}\frac{\partial F}{\partial \boldsymbol{X}} = \dot{\lambda}\frac{\boldsymbol{X}}{\|\boldsymbol{X}\|}\ , \tag{6}$$

where $\dot{\lambda}$ is the non-negative consistency parameter. The model is then completed by the classical Kuhn-Tucker conditions:

$$\dot{\lambda} \geq 0, \quad F \leq 0, \quad \dot{\lambda} F = 0 \, . \tag{7}$$

3 Souza-Auricchio model: time-discrete formulation

We now focus on the algorithmic treatment of the continuum model equations in an explicit framework. In the following we use subscript n for the variables at previous time t_n and we drop subscript *n+1* for the variables at current time t_{n+1}. We make use of a forward Euler scheme foor the evolution equation (6), as follow:

$$\boldsymbol{e}^{tr} = \boldsymbol{e}^{tr}_n + \Delta\lambda \frac{\boldsymbol{X}_n}{\|\boldsymbol{X}_n\|} \, , \tag{8}$$

where $\Delta\lambda = \int_{t_n}^{t_{n+1}} \dot{\lambda} \;\; dt$. The proposed algorithm is provided in Table 1. An elastic predictor/inelastic corrector scheme is adopted to compute the variables at the current time t_{n+1} based on the quantities at the previous time t_n: if the trial state is admissible, the step is elastic; otherwise, the step is inelastic and the transformation strain must be updated through the time-discrete evolution equation (8). We compute the inelastic increment (referred to as the *first phase transformation* or *PT1 step* in Table 1) to evaluate the consistency parameter $\Delta\lambda$. We derive the needed relation for $\Delta\lambda$ by enforcing the consistency condition $F(\Delta\lambda) = 0$. The consistency parameter $\Delta\lambda = \Delta\lambda_{PT1}$ is explicitly derived by applying a single iteration of the Newton-Raphson scheme to the consistency condition, as follows:

$$\Delta\lambda_{PT1} = \Delta\lambda^{(0)} + \delta\Delta\lambda^{(0)} = \Delta\lambda^{(0)} - \left(\left. \frac{dF}{d\Delta\lambda} \right|^{(0)} \right)^{-1} F^{(0)} \, , \tag{9}$$

where we consider:

$$\begin{cases} \Delta\lambda^{(0)} = \Delta\lambda_{TR} = 0 \\ F^{(0)} = F_{TR} \\ \left. \dfrac{dF}{d\Delta\lambda} \right|^{(0)} = \left. \dfrac{dF}{d\Delta\lambda} \right|_{TR} \end{cases} \, . \tag{10}$$

The derivative $dF/d\Delta\lambda$ is therefore computed as:

$$\left. \frac{dF}{d\Delta\lambda} \right|_{TR} = \frac{\boldsymbol{X}_{TR}}{\|\boldsymbol{X}_{TR}\|} : \left\{ -(2G+h)\mathbb{I} - \frac{\tau_M}{\|\boldsymbol{e}^{tr}_{TR}\|} \left[\mathbb{I} - \frac{\boldsymbol{e}^{tr}_{TR} \otimes \boldsymbol{e}^{tr}_{TR}}{\|\boldsymbol{e}^{tr}_{TR}\|} \right] \right\} : \frac{\boldsymbol{X}_{TR}}{\|\boldsymbol{X}_{TR}\|} \, , \tag{11}$$

where $\mathbb{I}$ is the fourth order identity tensor. Then, we can derive the transformation strain, as follows:

$$\boldsymbol{e}^{tr}_{PT1} = \boldsymbol{e}^{tr}_n + \Delta\lambda_{PT1} \frac{\boldsymbol{X}_{TR}}{\|\boldsymbol{X}_{TR}\|} \, . \tag{12}$$

After the inelastic step is performed, a check is made on the transformation strain constraint. If the constraint is not satisfied, a further inelastic step (referred to as the *second phase transformation* or *PT2 step* in Table 1) is performed, where the transformation strain $\boldsymbol{e}^{tr} = \boldsymbol{e}^{tr}_{PT2}$ is calculated starting from the PT1 step solution, as follow:

$$\boldsymbol{e}^{tr}_{PT2} = \varepsilon_L \frac{\boldsymbol{e}^{tr}_{PT1}}{\|\boldsymbol{e}^{tr}_{PT1}\|} \, . \tag{13}$$

Such an approximation allows for a simplified calculation and reduced number of functional evaluations for each time increment, but small increments are required. From Eqs (5) and (6) we obtain:

$$\boldsymbol{X} = R_Y \frac{\boldsymbol{e}^{tr} - \boldsymbol{e}^{tr}_n}{\overline{\|\boldsymbol{e}^{tr} - \boldsymbol{e}^{tr}_n\|}} \, . \tag{14}$$

Combining Eqs (13), (14) and $(3)_2$, we obtain the following relation:

$$R_Y \frac{\boldsymbol{e}^{tr}_{PT2} - \boldsymbol{e}^{tr}_n}{\overline{\|\boldsymbol{e}^{tr}_{PT2} - \boldsymbol{e}^{tr}_n\|}} - 2G\left(\boldsymbol{e} - \boldsymbol{e}^{tr}_{PT2}\right) + \tau_M \frac{\boldsymbol{e}^{tr}_{PT2}}{\|\boldsymbol{e}^{tr}_{PT2}\|} + h\boldsymbol{e}^{tr}_{PT2} + \gamma_{PT2} \frac{\boldsymbol{e}^{tr}_{PT2}}{\|\boldsymbol{e}^{tr}_{PT2}\|} = 0 \, , \tag{15}$$

from which we derive the saturation coefficient $\gamma = \gamma_{PT2}$:

$$\gamma_{PT2} = \left(-R_Y \frac{\boldsymbol{e}^{tr}_{PT2} - \boldsymbol{e}^{tr}_n}{\overline{\|\boldsymbol{e}^{tr}_{PT2} - \boldsymbol{e}^{tr}_n\|}} + 2G\left(\boldsymbol{e} - \boldsymbol{e}^{tr}_{PT2}\right) - \tau_M - h\boldsymbol{e}^{tr}_{PT2} \right) : \frac{\boldsymbol{e}^{tr}_{PT2}}{\|\boldsymbol{e}^{tr}_{PT2}\|} \, . \tag{16}$$

where $\overline{\|\boldsymbol{e}^{tr} - \boldsymbol{e}^{tr}_n\|}$ is the regularized expression. The proposed algorithm is simple to implement. Compared to [6], our procedure does not include a convergence criterion to determine $\Delta\lambda_{PT1}$, thus making it truly explicit, compatible with the global explicit scheme, and allowing a low computational cost per increment. Similarly, the computation of γ_{PT2} is straightforward, contrary to the method of [6], which proposed a linearization and then an iterative procedure for the PT2 step. Finally, unlike the implicit scheme, the explicit algorithm does not require the often expensive computation of a tangent matrix, consistent or otherwise.

4 Numerical simulations

We now test the performance of the proposed algorithm, which is implemented within Abaqus/Explicit through a VUMAT user subroutine. A comparison with the implicit scheme, implemented within Abaqus/Standard through a UMAT user subroutine, is provided [8]. In particular, we use the package AceGen of the symbolic software Mathematica to generate the numerical subroutines for Abaqus. All bodies considered are discretized into first-order hexahedral elements with full and reduced integration, respectively, for the implicit and explicit method. Since the explicit method is here used to solve quasi-static problems, we employ the method of mass scaling to reduce the simulation runtime. To avoid inflation of the mass and oscillations during the quasi-static solution, we carefully check that the kinetic energy was below 5-10% of the internal energy. In all numerical studies we adopt the material parameters reported in Table 2.

Table 1: Explicit algorithm proposed for the Souza-Auricchio model.

Given quantities: $\boldsymbol{\varepsilon}, T, \boldsymbol{e}_n^{tr}, \Delta\lambda_n, \gamma_n$

Compute trial state:

$\Delta\lambda_{TR} = 0$; $\boldsymbol{e}_{TR}^{tr} = \boldsymbol{e}_n^{tr}$; $\gamma_{TR} = 0$

$\boldsymbol{s}_{TR} = 2G\left(\boldsymbol{e} - \boldsymbol{e}_{TR}^{tr}\right)$

$\boldsymbol{X}_{TR} = \boldsymbol{s}_{TR} - \tau_M \dfrac{\boldsymbol{e}_{TR}^{tr}}{\|\boldsymbol{e}_{TR}^{tr}\|} - h\boldsymbol{e}_{TR}^{tr}$

$F_{TR} = \|\boldsymbol{X}_{TR}\| - R_Y$

IF $F_{TR} \leq tol$ THEN

Elastic step:

$\Delta\lambda = \Delta\lambda_{TR}$; $\boldsymbol{e}^{tr} = \boldsymbol{e}_{TR}^{tr}$; $\gamma = \gamma_{TR}$; $\boldsymbol{s} = \boldsymbol{s}_{TR}$; $\boldsymbol{X} = \boldsymbol{X}_{TR}$

ELSE

Inelastic step:

Compute $\Delta\lambda_{PT1}$ via Eq. (9)

$\boldsymbol{e}_{PT1}^{tr} = \boldsymbol{e}_n^{tr} + \Delta\lambda_{PT1} \dfrac{\boldsymbol{X}_{TR}}{\|\boldsymbol{X}_{TR}\|}$

IF $\|\boldsymbol{e}_{PT1}^{tr}\| \leq \varepsilon_L$ THEN

$\Delta\lambda = \Delta\lambda_{PT1}$; $\boldsymbol{e}^{tr} = \boldsymbol{e}_{PT1}^{tr}$; $\gamma = \gamma_{TR}$

$\boldsymbol{s} = 2G\left(\boldsymbol{e} - \boldsymbol{e}^{tr}\right)$

$\boldsymbol{X} = \boldsymbol{s} - \tau_M \dfrac{\boldsymbol{e}^{tr}}{\|\boldsymbol{e}^{tr}\|} - h\boldsymbol{e}^{tr}$

ELSE

Saturation step:

$\boldsymbol{e}^{tr} = \boldsymbol{e}_{PT2}^{tr} = \varepsilon_L \dfrac{\boldsymbol{e}_{PT1}^{tr}}{\|\boldsymbol{e}_{PT1}^{tr}\|}$

Compute $\gamma = \gamma_{PT2}$ via Eq. (16)

$\boldsymbol{s} = 2G\left(\boldsymbol{e} - \boldsymbol{e}^{tr}\right)$

$\boldsymbol{X} = \boldsymbol{s} - \left(\tau_M + \gamma\right) \dfrac{\boldsymbol{e}^{tr}}{\|\boldsymbol{e}^{tr}\|} - h\boldsymbol{e}^{tr}$

END IF

END IF

Table 2: Adopted material parameters for the Souza-Auricchio model (taken from [10]).

Description	Symbol	Value	Unit
Young's modulus	E	53,000	MPa
Poisson's ratio	ν	0.33	-
Stress-strain slope during transformation	h	1,000	MPa
Maximum axial transformation strain	ε_L	0.056	-
Reference temperature	T^*	243	K
Term related to $\tau_M = \beta(T - T^*)^+$	β	6.1	MPa/K
Elastic domain radius in the deviatoric stress space	R_Y	100	MPa

4.1 Actuation of a micro-gripper

The adopted geometry for the SMA micro-gripper is shown in Figure 1 which reports the adopted reference mesh, consisting of 14, 376 elements and 24, 417 nodes.

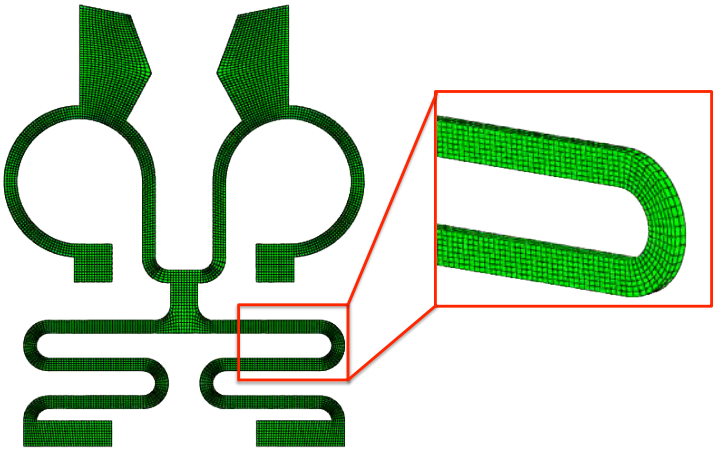

Figure 1: SMA micro-gripper: mesh and initial geometry.

The micro-gripper operates via a complex antagonistic actuation cycle, as shown in Figure 2. The gripper is divided in two actuation units: the upper part, actually devoted to the action of gripping, is referred to as the *rotational stage*; the lower part, which stretches and contracts, is referred to as the *linear stage*. The four small quadrilateral features in Figure 2 are referred to as *tabs*. During the full working cycle, the tabs of the *linear stage* are fully constrained (steps A-C of Figure 2). At the beginning of the actuation cycle, the gripper is at low temperature. In step A, a displacement v of 2.5 mm is applied to the region connecting the two stages, and the linear stage is stretched. During step B, the tabs of the *rotational stage* are fully constrained and the linear stage is heated; it thus tends to recover its original configuration and contracts (the direction is indicated by the black arrow in step B). The contraction of the linear stage combined with the full constraint on the four tabs produces the gripping action (clockwise rotation of the rotational part in step B). Finally, during step C, the linear stage is cooled down, and

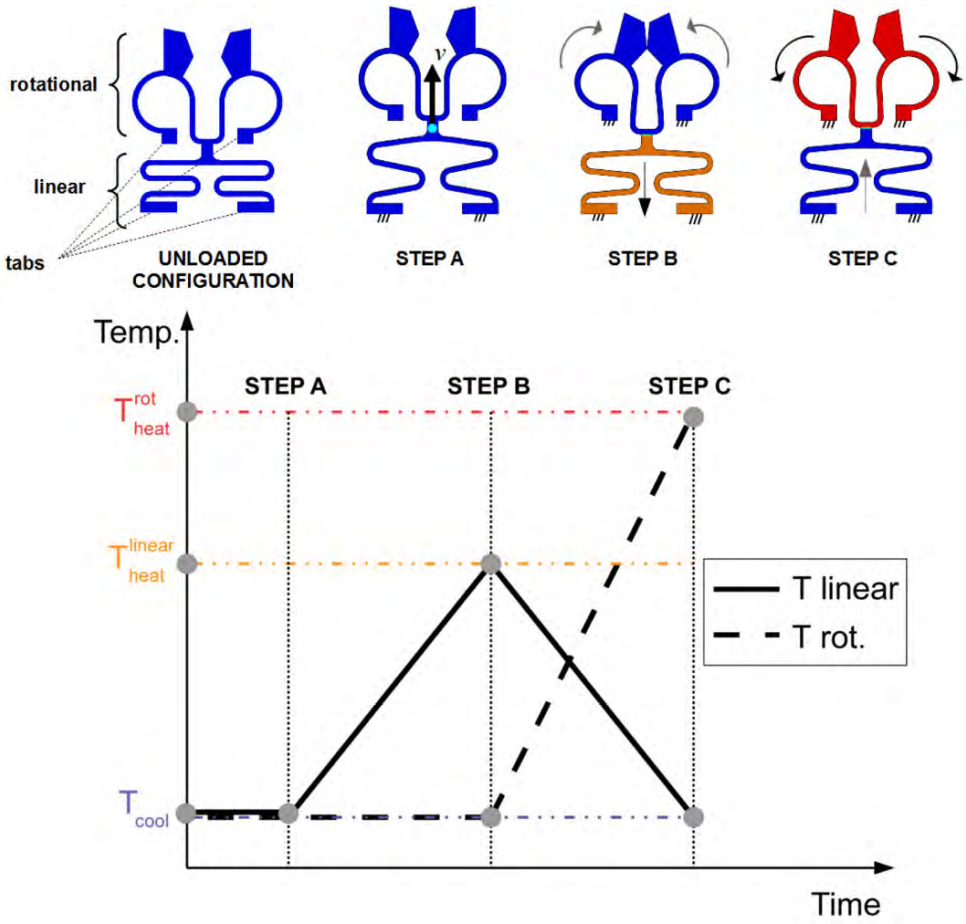

Figure 2: SMA micro-gripper: (above) working principle; (below) trends of the temperature T over time. T *linear* is the temperature history for the linear stage, while T *rot* is the temperature history for the rotational stage.

the rotational stage is heated; it thus recovers its initial shape, reaching the open position (anti-clockwise rotation in step C). As the rotational stage moves, it forces the linear stage to stretch (the direction is indicated by the grey arrow in step C). Figure 3 shows the deformed state of the micro-gripper and contour plots of the transformation strain norm at steps B and C for both implicit and explicit analyses. Since a different element integration type has been used in the implicit and explicit analyses, it can be noted that some difference exists between the two deformed shapes at state B; moreover, some very small concentrations of transformation strain are observable in the highly curved regions of the micro-gripper in the case of the implicit analysis results.

In the explicit analysis, the stable time increment evaluated by Abaqus at the beginning of the analysis is $9.64 \cdot 10^{-9}$ s. Mass scaling is here applied in such a way that the minimum stable time increment (and the used time increment) can be set to 10^{-8} s. During the implicit analysis, the time increment is set to 10^{-2} s.

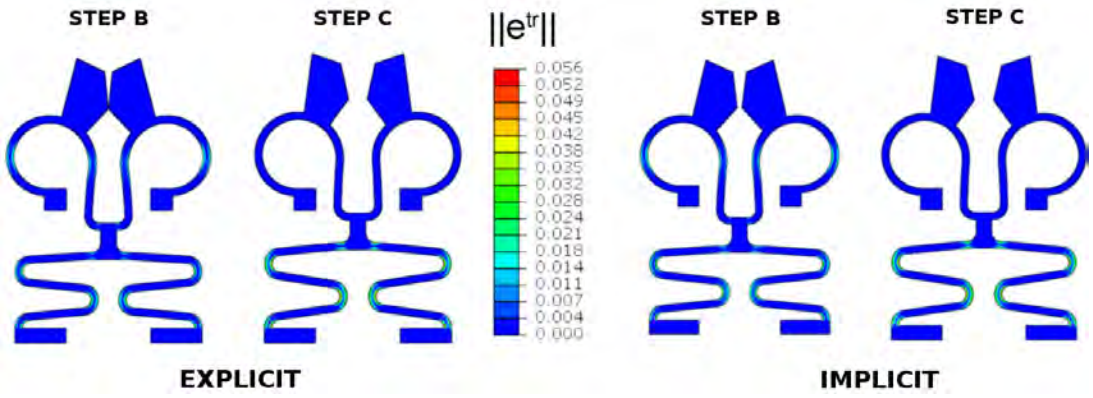

Figure 3: SMA micro-gripper: deformed shape of the gripper for implicit and explicit analyses at steps B and C of Figure 2. The contour plot of the transformation strain norm is displayed.

4.2 Pseudoelastic SMA cable

We analyze a structural cable model consisting of SMA wire assemblies as used in the development of a vibration absorber. The model considers a three layer straight cable segment having a total diameter of 30 mm. The relatively simple cable is composed by a central straight wire (core) and two layers helically wrapped around the core. The adopted discretization is reported in Figure 4 and consists of $323,158$ solid brick elements and $416,357$ nodes.

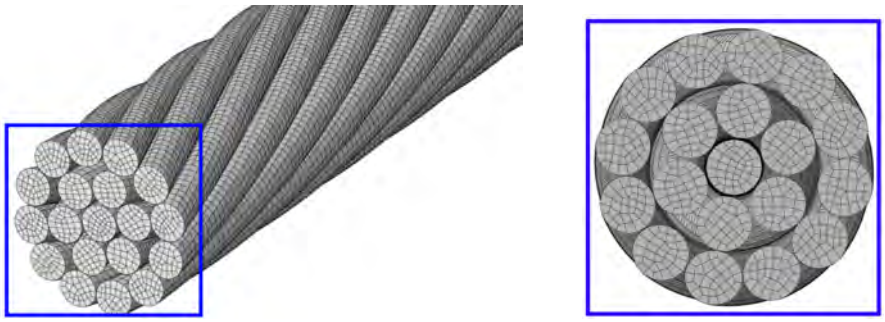

Figure 4: SMA cable: adopted mesh.

Following [11], our goal is to describe a hysteretic load-displacement cycle in the transverse direction Y preceded by a pretension phase along the longitudinal direction Z (Figure 5a-b). Contacts between the many wires exist and must be taken into account. To do so, a penalty formulation with Coulomb model is employed using a friction coefficient equal to 0.5. In this complex contact, the implicit iterative solver encounters a highly non-linear response and it attempts increasingly small time increments to solve the equilibrium equations, without achieving equilibrium and convergence. Therefore, a natural alternative to solve such problems is via an explicit approach. The stable time increment, evaluated by Abaqus at the beginning of the analysis, is $1.12 \cdot 10^{-8}$ s. Mass scaling is applied considering a fixed time increment of 10^{-7} s. The kinetic energy, despite some

oscillations, remains negligible, validating the appropriateness of the mass scaling for a hypothesis of quasi-static conditions. Figure 5c presents the hysteretic load displacement

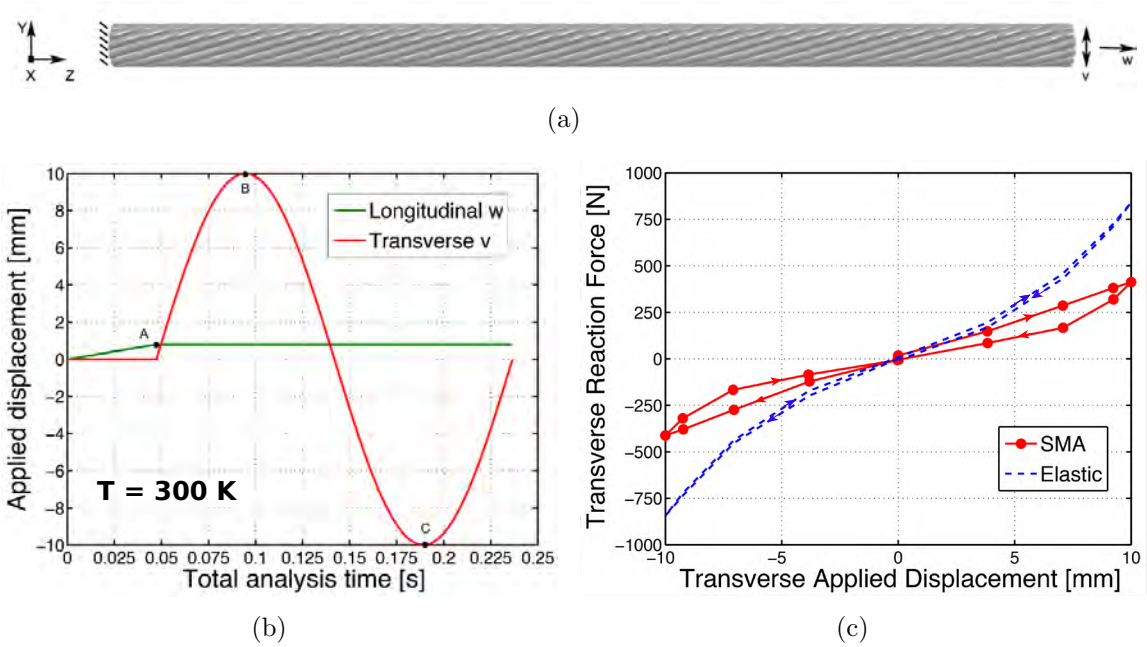

Figure 5: SMA cable: (a) applied boundary conditions; (b) loading history in terms of displacements. A total of 0.2364336 time units are used; (c) transverse force-displacement diagram.

relationship evaluated at the free end of the cable. A comparison with the curve obtained for an elastic cable with the same elastic properties is also provided. The responses are clearly different and evidence the hysteretic area obtained by using the SMA cable, which correspond to a gain in term of dissipatiton. Figure 6 shows the contour plot of the Von Mises stress evaluated at the mid section of the cable during pretension (a), maximum displacement (b), and minimum displacement (c) loading stages. Figure 7 shows the contour plot of the norm of the transformation strain at instant B of Figure 5. The figure clearly highlights that phase transformation is taking place: the transformation is complete close to the section where the load is applied and it is partial in most part of the core of the cable.

5 CONCLUSIONS

The present paper has proposed a novel implementation of the three-dimensional phenomenological Souza-Auricchio model using an explicit framework. A comparison of output results with the implicit integration scheme has also been made whenever possible. The explicit implementation has successfully simulated the quasi-static response of the considered devices. Particularly, the analysis of SMA cable has demonstrated the effectiveness of the explicit algorithm to solve complex problems involving widespread nonlinear contact. The results show the potential of the proposed computational framework to provide a virtual engineering tool for design, simulation, and optimization of SMA devices.

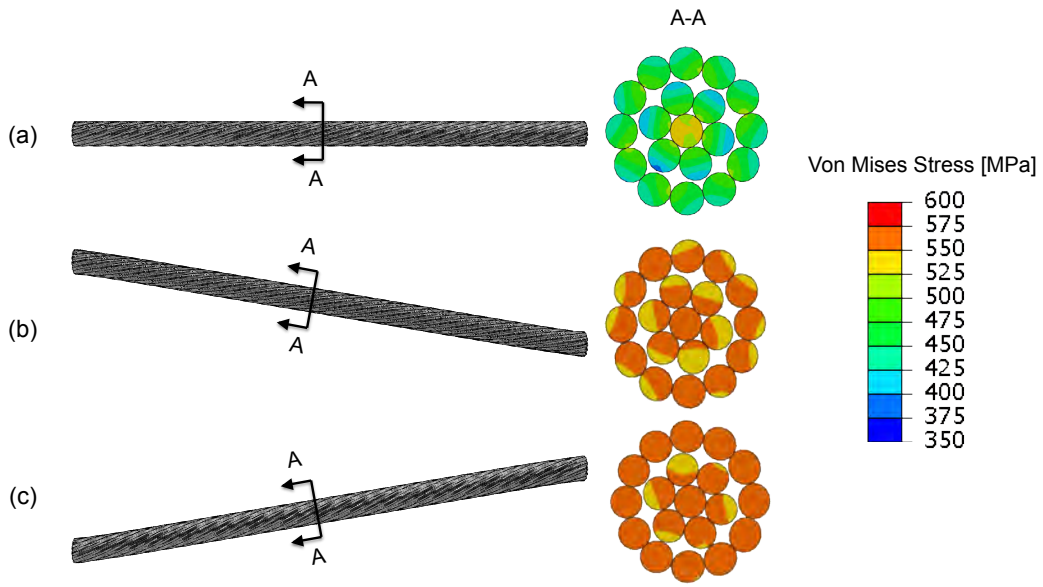

Figure 6: SMA cable: contour plot of the Von Mises stress at istants A, B, and C of Figure 5.

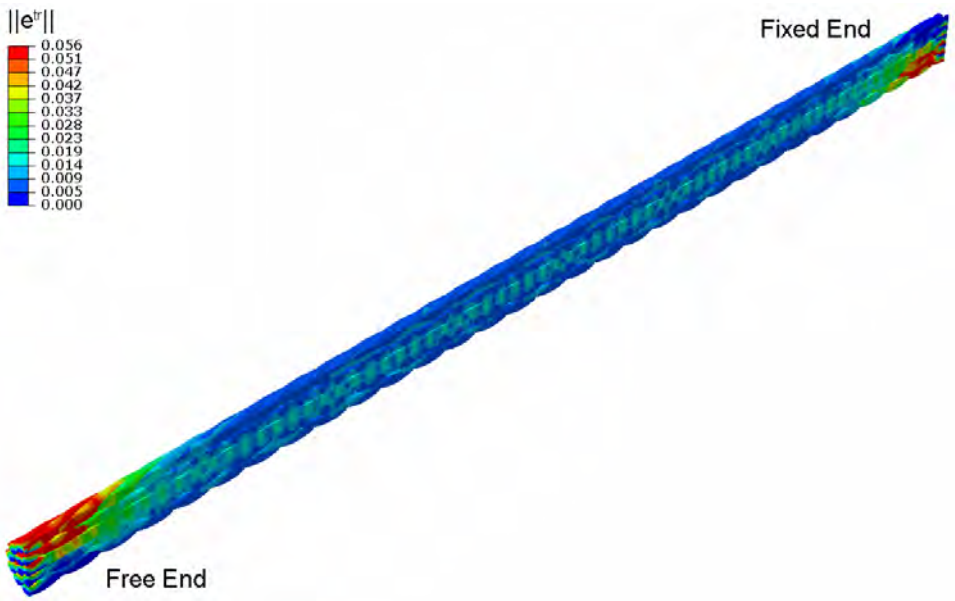

Figure 7: SMA cable: contour plot of the transformation strain norm at instant B of Figure 5.

Additionally, since SMA modeling techniques are continuously evolving, understanding the nature, advantages, and disadvantages of both implicit and explicit methods is helpful in choosing the right algorithm for the problem under investigation. Future developments will use the proposed explicit algorithm for high-speed dynamic simulations which are

widely exploited in SMA-based seismic or impact applications.

REFERENCES

[1] Jani, J., Leary, M., Subic, A. and Gibson, M. A review of shape memory alloy research, applications and opportunities. *Mater Design.* (2014) **56**: 1078-1131.

[2] Cisse, C., Zaki, W. and Zineb, T.B. A review of constitutive models and modeling techniques for shape memory alloys. *Int. J. Plasticity.* (2016) **76**: 244-284.

[3] Khandelwal, A. and Buravalla., V. Models for shape memory alloy behavior: An overview of modeling approaches. *Int. J. Struct. Changes Solids.* (2009) **1**: 111-148.

[4] Scalet, G., Auricchio, F. and Hartl, D. Efficiency and effectiveness of implicit and explicit approaches for the analysis of shape-memory alloy bodies. *J. Intel. Mat. Syst. Str* (2015) **27**: 384-402.

[5] Stebner, A. and Brinson, L. Explicit finite element implementation of an improved three dimensional constitutive model for shape memory alloys. *Comput. Method. App. M.* (2013) **257**: 17-35.

[6] Jähne, R., *Multiaxial mechanical characterization and constitutive modeling of superelastic sheets for solid-state hinges.* Ph.D. thesis, ETH Zurich (2012).

[7] Souza, A., Mamiya, E. and Zouain, N. Three-dimensional model for solids undergoing stress-induced phase transformations. *Eur. J. Mech. A/Solids.* (1998) **17**: 789-806.

[8] Auricchio, F. and Petrini, L. A three-dimensional model describing stress-temperature induced solid phase transformations: solution algorithm and boundary value problems. *Int. J. Numer. Meth. Eng.* (2004) **61**: 807-836.

[9] Auricchio, F. and R. L. Taylor R. L. Shape-memory alloys: Modelling and numerical simulation of the finite-strain superelastic behavior. *Comput. Method. App. M.* (1997) **143**: 175-194.

[10] Auricchio, F., Morganti, S. and Reali, A. SMA numerical modeling versus experimental results. *Proc. Europ. Symp. on Martensitic Transformations* ESOMAT (2009): 1-6.

[11] Carboni, B., Lacarbonara, W. and Auricchio, F. Hysteresis of multiconfiguration assemblies of nitinol and steel strands: Experiments and phenomenological identification. *J. Eng. Mech.* (2014) **141**: 04014135.

XIV International Conference on Computational Plasticity. Fundamentals and Applications
COMPLAS XIV
E. Oñate, D.R.J. Owen, D. Peric & M. Chiumenti (Eds)

HARDENING AND NON-ASSOCIATED FLOW NURBS PLASTICITY

WILLIAM M. COOMBS*

* School of Engineering & Computing Sciences,
Durham University,
Lower Mountjoy, South Road, Durham, DH1 3LE, UK.
e-mail: w.m.coombs@dur.ac.uk, web page: www.dur.ac.uk

Key words: Computational plasticity, NURBS, non-associated flow, stress integration

Abstract. In numerical analysis the failure of engineering materials is controlled through specifying yield envelopes (or surfaces) that bound the allowable stress in the material. Simple examples include the prismatic von Mises (circle) and Tresca (hexagon) yield surfaces. However, each surface is distinct and requires a specific equation describing the shape of the surface to be formulated in each case. These equations impact on the numerical implementation (specifically relating to stress integration) of the models and therefore a separate algorithm must be constructed for each model. Recently a framework was proposed that allows any isotropic yield surface to be represented by a NURBS surface and the constitutive model formulated using the name numerical algorithm.

This paper presents, for the first time, an extension to this framework to allow both hardening (expansion/contraction of the surfaces) and a non-associated plastic flow rule. As with previous work on NURBS plasticity, the constitutive framework is combined with an implicit backward-Euler-type stress integration algorithm. The numerical performance of the algorithm is demonstrated using both material point investigations and boundary value simulations.

1 INTRODUCTION

Robust and efficient constitutive models are at the heart of every boundary value stress analysis problem, providing the essential link between stress and strain for the material that they represent. Elasto-plasticity is one class of inelastic material behaviour that allows these models to predict yield and capture post-yield behaviour. Central to these models is the concept of a yield surface that provides the boundary between elastic (inside the surface) and elasto-plastic behaviour (on the surface). However, such models are typically developed in rate form, providing a rate relationship between stress and stain that conflicts with an incremental boundary value solver, such as the finite element method. These boundary value solvers work with finite steps of stress and strain and therefore the rate-form constitutive relationships must be integrated. Typically the form of the yield

surface impacts on the stress integration algorithm with specific details change within the numerics (and code) for each implemented yield surface. This issue was overcome by the paper of Coombs et al. [1] for yield surfaces that are fixed in stress space, known as perfect plasticity. It allowed any smooth isotropic yield surface to be modelled without changing the numerical algorithm or underlying code by using non-uniform rational basis spline (NURBS) surfaces to represent the yield envelope. This paper extends that work to allow for isotropic expansion/contraction of the yield surface and for the evolution of plastic strains to be decoupled from the normal to the yield surface (that is, allowing a non-associated flow rule).

Here we follow the approach of Coombs et al. [1] and adopt an implicit stress integration algorithm coupled with a plasticity formulation that expresses the yield envelope as a NURBS surface. The key extensions that we allow here are for: (i) the yield surface to expand (hardening) or contract (softening) under plastic straining and (ii) decoupling the flow direction from the spatial gradient of the surface. This is achieved by allowing the position of the control points to be a function of inelastic straining and for the flow direction to be approximated by a separate NURBS basis. This extends the NURBS plasticity framework to include materials where the yield stress is a function of the history of plastic straining that the body has experienced and to those materials where an associated flow rule is not appropriate (such as geotechnical materials where an associated flow rule overestimates the volumetric dilation).

The layout of the paper is as follows, Section 2 provides the theoretical framework for hardening non-associated flow NURBS-based plasticity. Section 3 briefly explains the numerical implementation of the model and Section 4 provides some numerical examples. Finally, conclusions are drawn in Section 5.

2 NURBS PLASTICITY

This section provides the essential equations required to define an isotropically hardening NURBS surface and include it within a non-associated flow plasticity framework. For more detailed information on the construction of NURBS-based surfaces see the work of Piegl and Wayne [7] and the paper of Coombs et al. [1] for the particular case of perfect plasticity yield envelopes.

A general NURBS surface can be expressed in Haigh-Westergaard (H-W) coordinates as

$$S_k(\eta,\zeta) = \frac{\xi}{\sqrt{3}}\begin{Bmatrix} 1 \\ 1 \\ 1 \end{Bmatrix} + \sqrt{\frac{2}{3}}\rho \begin{Bmatrix} \sin(\theta + 2\pi/3) \\ \sin(\theta) \\ \sin(\theta - 2\pi/3) \end{Bmatrix}, \tag{1}$$

where the hydrostatic position ξ, radial coordinate ρ and Lode angle θ are dependent on the values at the control points and the local position on the NURBS surface, η and ζ

$$\xi(\eta,\zeta) = \sum_{i=0}^{n}\sum_{j=0}^{m} R_{i,j}(\eta,\zeta)\Xi_{i,j}, \qquad \rho(\eta,\zeta) = \sum_{i=0}^{n}\sum_{j=0}^{m} R_{i,j}(\eta,\zeta)P_{i,j} \tag{2}$$

and

$$\theta(\eta,\zeta) = \sum_{i=0}^{n}\sum_{j=0}^{m} R_{i,j}(\eta,\zeta)\Theta_{i,j}. \tag{3}$$

$\Xi_{i,j}$, $P_{i,j}$ and $\Theta_{i,j}$ are the control point values of the Haigh-Westergaard coordinates. The NURBS basis functions are given by

$$R_{i,j}(\xi,\eta) = \frac{N_{i,p}(\xi)N_{j,q}(\eta)w_{i,j}}{\sum_{k=0}^{n}\sum_{l=0}^{m} N_{k,p}(\xi)N_{l,q}(\eta)w_{k,l}}. \tag{4}$$

$N_{i,p}$ and $N_{j,q}$ are the p^{th} and q^{th}-degree B-spline basis functions (see [2, 7], amongst others), η and ζ are the local positions within the two Knot vectors that describe the surface and $w_{i,j}$ are the weights associated with the control points. In the work of [1] the control points were defined in Cartesian coordinates, however in this paper we change to using H-W coordinates to allow for the extension to non-associated flow.

2.1 NURBS-based yield envelopes

Starting from the equation for a NURBS surface (1), a NURBS-based yield envelope [1] can be expressed as

$$f = \Big(\sigma_i - S_i(\eta,\zeta,\varepsilon_i^{\mathrm{p}})\Big)(S_{,\sigma})_i = 0, \tag{5}$$

where $(S_{,\sigma})_i$ is the surface outward normal (that is, the partial derivative of S with respect to stress), $\varepsilon_i^{\mathrm{p}}$ is the principal plastic strain state and σ_i the principal stress state. The yield surface separates stress space into two regions: an elastic region where $f < 0$ and an inadmissible region where $f > 0$. The boundary between these two regions ($f = 0$) is used to define material failure and points on this surface will undergo elasto-plastic deformation. The outward normal to the yield envelope can be obtained through the cross product of the two local derivatives

$$(S_{,\sigma})_i = (S_{,\zeta} \times S_{,\eta})_i = \epsilon_{ijk}(S_{,\zeta})_j(S_{,\eta})_k, \tag{6}$$

where ϵ_{ijk} is the Levi-Civita tensor[1]. $S_{,\eta}$ and $S_{,\zeta}$ are the derivatives of the NURBS surface with respect to the local coordinates η or ζ.

2.2 Non-associated flow

In the case of non-associated flow the evolution of plastic strains is decoupled from the spatial gradient of the yield envelope. The plastic strains evolve according to

$$\dot{\varepsilon}_i^{\mathrm{p}} = \dot{\gamma}(g_{,\sigma})_i, \tag{7}$$

[1] $\epsilon_{ijk} = 0$ if $i = j$, $j = k$ or $k = i$, $\epsilon_{ijk} = 1$ for even permutations of i, j and k and $\epsilon_{ijk} = -1$ for odd permutations of i, j and k.

where $\dot{\gamma}$ is the scalar plastic multiplier (or consistency parameter) and $(g_{,\sigma})_i$ is the gradient of the plastic potential surface. This plastic multiplier must satisfy the Kuhn-Tucker-Karush consistency conditions

$$f(\sigma_i, \varepsilon_i^{\mathrm{p}}) \leq 0, \qquad \dot{\gamma} \geq 0 \qquad \text{and} \qquad f(\sigma_i, \varepsilon_i^{\mathrm{p}})\dot{\gamma} = 0. \tag{8}$$

These conditions enforce that the material must either be on the yield surface undergoing elasto-plastic deformation ($f = 0$ and $\dot{\gamma} \geq 0$) or inside the yield surface with purely elastic behaviour ($f \leq 0$ and $\dot{\gamma} = 0$).

In this NURBS plasticity approach the gradient of the plastic potential surface is given by

$$(g_{,\sigma})_i = \lambda_g \left\{ \begin{array}{c} 1 \\ 1 \\ 1 \end{array} \right\} + \sqrt{2} \left\{ \begin{array}{l} \sin(\theta_g + 2\pi/3) \\ \sin(\theta_g) \\ \sin(\theta_g - 2\pi/3) \end{array} \right\}, \tag{9}$$

where λ_g is the volumetric to devitaoric ratio of the plastic flow direction and θ_g is the Lode angle of the plastic flow direction. λ_g and θ_g are dependent on the corresponding control point values, $\Lambda_{i,j}^g$ and $\Theta_{i,j}^g$, and the local position on the NURBS surface through

$$\lambda_g(\eta, \zeta) = \sum_{i=0}^{n} \sum_{j=0}^{m} R_{i,j}^g(\eta, \zeta)\Lambda_{i,j}^g \qquad \text{and} \qquad \theta_g(\eta, \zeta) = \sum_{i=0}^{n} \sum_{j=0}^{m} R_{i,j}^g(\eta, \zeta)\Theta_{i,j}^g. \tag{10}$$

The NURBS basis functions $R_{i,j}^g(\eta, \zeta)$ are calculated in the same way as (4).

2.3 Isotropic hardening

Introducing hardening into the NURBS yield surfaces results in a yield surface that is dependent on the level of inelastic straining at a material point. This is included within the NURBS plasticity framework by allowing the control points to evolve with plastic straining, that is

$$\Xi = h(\varepsilon_i^{\mathrm{p}})\Xi^0 \qquad \text{and} \qquad P = h(\varepsilon_i^{\mathrm{p}})P^0 \tag{11}$$

where the superscript $(\cdot)^0$ denotes the original control point coordinates and $h(\varepsilon_i^{\mathrm{p}})$ controls the evolution of the control points. For linear isotropic hardening we can assume

$$h(\varepsilon_i^{\mathrm{p}}) = 1 + \alpha \; || \int_0^t \dot{\varepsilon}_i^{\mathrm{p}} dt \; ||, \tag{12}$$

where α is a material constant controlling the hardening ($\alpha > 0$) or softening ($\alpha < 0$) rate and perfect plasticity is obtained with $\alpha = 0$. We can approximate the isotropic hardening function to provide an incremental function of the form

$$h(\Delta\varepsilon_i^{\mathrm{p}}) = h_n + \alpha||\Delta\varepsilon_i^{\mathrm{p}}||, \tag{13}$$

where $h_n = h\big((\varepsilon_n^{\mathrm{p}})_i\big)$ is the value of the hardening function from the previously converged state and it is assumed that initially, $h_0 = 1$.

2.4 Stress integration

In this work we use an implicit elastic predictor, plastic corrector scheme [11], where the elastic trial stress is given by

$$\sigma_i^t = \sigma_i^n + \Delta\sigma_i, \qquad \text{where} \qquad \Delta\sigma_i = D_{ij}^{\mathrm{e}}\Delta\varepsilon_j \qquad \text{and} \qquad \sigma_i^n = D_{ij}^{\mathrm{e}}(\varepsilon_n^{\mathrm{e}})_j. \tag{14}$$

$(\varepsilon_n^{\mathrm{e}})_j$ and σ_i^n are the elastic strain and stress state from the previous load (or time) step in the global solution algorithm, $\Delta\varepsilon_i$ is the strain increment associated with the global boundary value displacement and D_{ij}^{e} contains the principal components of the linear elastic stiffness matrix.

If the trial elastic stress state exceeds the yield envelope ($f > 0$) then it must be corrected back onto the yield surface using a plastic stress increment, that is

$$\sigma_i^r = \sigma_i^t - \Delta\sigma_i^{\mathrm{p}}, \qquad \text{where} \qquad \Delta\sigma_i^{\mathrm{p}} = D_{ij}^{\mathrm{e}}\Delta\varepsilon_j^{\mathrm{p}}, \tag{15}$$

σ_i^r is the *returned* stress state on the yield surface and $\Delta\epsilon_j^{\mathrm{p}}$ is the plastic strain increment obtained from the incremental form of (7). Once this correction has been applied the updated elastic strain can be obtained from

$$(\varepsilon_{n+1}^{\mathrm{e}})_i = (\varepsilon_n^{\mathrm{e}})_i + \Delta\varepsilon_i - \Delta\varepsilon_i^{\mathrm{p}}, \tag{16}$$

and the updated hardening parameter, h, from (13).

3 NUMERICAL IMPLEMENTATION

Consistent with the perfect plasticity implementation of Coombs et al. [1], here we use a coarse initial subdivision algorithm to provide the initial starting point for a backward Euler (bE) implicit stress integration process. This is to provide an initial estimate for the local positions within the Knot vectors, η and ζ in (5) that act as the primary unknowns in the closest point projection (CPP) problem (in addition to the updated hardening parameter). However, despite this process being referred to as a CPP, the return stress is not generally the closest point geometrically in standard stress space.

In this paper we make use of energy-mapped space [3] to convert this CPP minimisation into a problem of finding the point on the yield envelope that the normal to the plastic potential surface passes through when intersecting with a trial point outside of the surface. Once the closest point solution in energy-mapped stress space has been found, the solution can be transformed back to conventional stress space. For a NURBS yield surface we only need to map the control point coordinates, (Ξ, P, Θ), and flow directions, $(g_{,\sigma})_i$, into energy-mapped space, the rest of the NURBS information remains unchanged.

As with the algorithm for associated flow perfect plasticity, the stress return path for bE procedure described in this paper starts and remains in the yield envelope and thereby satisfies the consistency conditions not only at the final state but also during the stress updating algorithm.

4 NUMERICAL ANALYSIS

This section presents both material point and boundary value simulations for the isotropically hardening/softening von Mises plasticity model represented and integrated in the NURBS plasticity framework. The yield surface can be expressed as

$$f = \rho - h\rho_y = 0, \tag{17}$$

where the deviatoric stress is $\rho = \sqrt{2J_2}$ with $J_2 = \frac{1}{2}s_{ij}s_{ji}$ and $s_{ij} = \sigma_{ij} - \frac{1}{3}\sigma_{kk}\delta_{ij}$, ρ_y is the yield stress of the material and defines the radius of the von Mises cylinder.

4.1 Material point investigations

The stress integration errors for a von Mises yield surface with $E = 200$Pa, $\nu = 0.2$, $\rho_y = 1$Pa and $\alpha = 10$ (hardening) using the NURBS integration procedure are shown in Figure 1. The stress state is initially located on the shear meridian in the $\sigma_{zz} > \sigma_{yy} > \sigma_{xx}$ sextant of stress space. This point is then subjected to a stress increment that will take the trial stress state outside of the yield envelope into one of the three sextants shown in Figure 1. The space of trial states was explored for $\rho_t/\rho_y \in [1, 6]$ and the errors associated with the trial state shown on the right of Figure 1. The normalised error measure used is

$$\text{error} = \frac{||\{\sigma_{\text{NURBS}}\} - \{\sigma_e\}||}{||\sigma_e||}, \tag{18}$$

where $\{\sigma_{\text{NURBS}}\}$ is the stress return location associated with the NURBS model and $\{\sigma_e\}$ is the exact stress return [5].

Although errors of over 20% are present in the model, exactly the same level of errors are observed in the von Mises yield surface integrated with a conventional bE stress integration procedure. As expected with any predictor-correction stress integration algorithm, the error increases as the tangential proportion of the stress increment increases. The errors are almost identical to those reported by Coombs et al. [1] for the perfect plasticity yield surface.

Figure 2 (i) shows the converged hardening parameter value for the same range of trial stress states as analysed in Figure 1. As expected, the value of the hardening parameter is only dependent on the magnitude of the plastic strain increment, or equivalently, the radial distance that the trial state is from the yield surface. Figure 2 (ii) gives the normalised error in the hardening parameter, the distribution of the error is similar to the stress errors shown in Figure 1 as the error in the stress increment will be proportional to the error in the return stress.

4.2 Plane strain double notched plate

Here we present the analysis of the plane strain stretching of a double-notched plate. The problem was initially presented by Nagtegaal *et al.* [6] for small strain plasticity to demonstrate the spurious response of standard finite-elements and was subsequently re-analysed in a number of papers, including [1, 4, 8, 9]. The plate had a Young's modulus

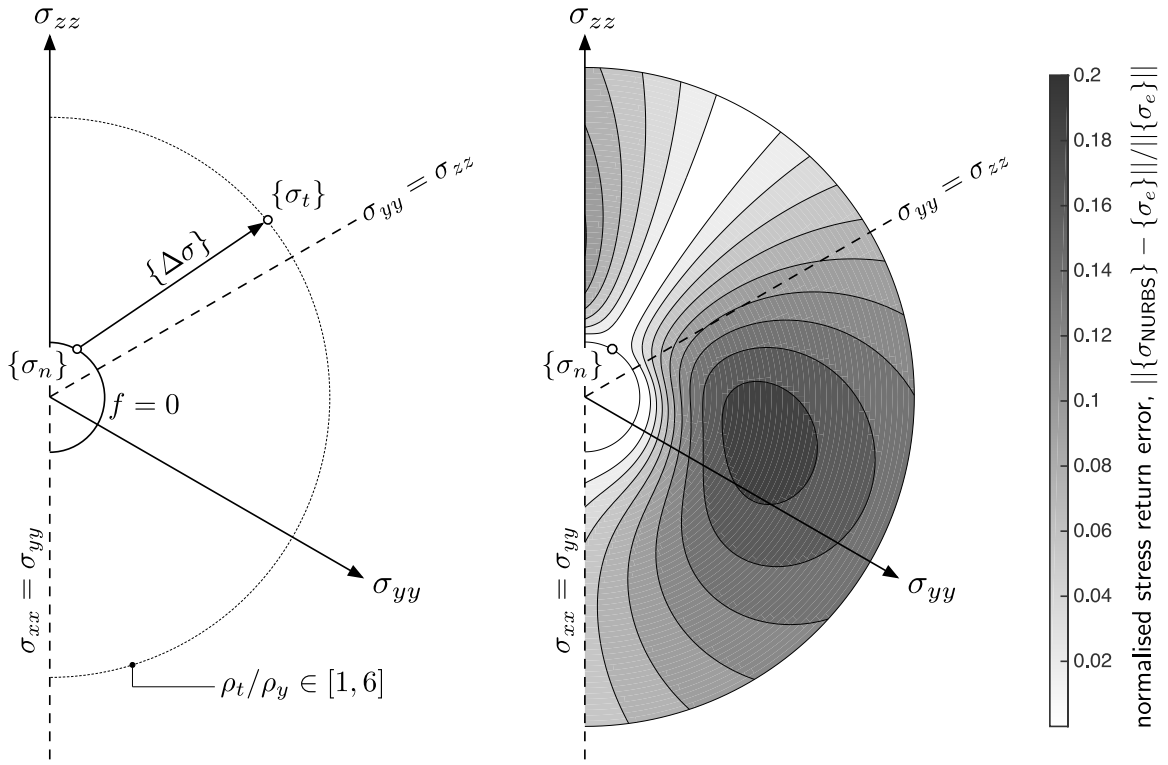

Figure 1: Stress return error analysis for an isotropically hardening von Mises NURBS yield envelope.

of 206.9GPa, Poisson's ratio of 0.29 and was modelled using an isotropically hardening von Mises yield surface with associated flow with an initial yield stress of $\rho_y = 0.45$GPa.

Nagtegaal *et al.* [6] provided the small strain analytical limit load for the case of perfect plasticity ($\alpha = 0$), controlled by the stress at the notch $\sigma_{\text{lim}} \approx 2.97\rho_y$. The specimen had a total height and width of 30mm and 10mm respectively, with a 2mm unit linking ligament at mid height. For this geometry the small strain perfect plasticity limit load is $f^{\text{lim}} \approx 2.673$kN. Due to symmetry, only one quarter of the specimen was initially discretised using 75 plane strain eight-noded elements with reduced four-point integration, as shown in Figure 3. A displacement of 0.2mm was applied in 20 equal displacement-controlled increments.

Figure 3 shows three different model responses for two finite element discretisations. The three cases are where $\alpha = 1$ (hardening or expansion of the yield surface, black dashed line), $\alpha = 0$ (perfect plasticity, fine black line) and $\alpha = -1$ (softening or contraction of the yield surface, thick grey line). As the mesh is refined the perfect plasticity response approaches the analytical limit load. As expected the hardening and softening responses predict force versus displacement responses above and below the perfect plasticity response, respectively.

The global normalised residual out of balance force

$$\bar{f}^{\text{oobf}} = \frac{||\{f^{\text{ext}}\} - \{f^{\text{int}}\}||}{||\{f^{\text{ext}}\}||}, \tag{19}$$

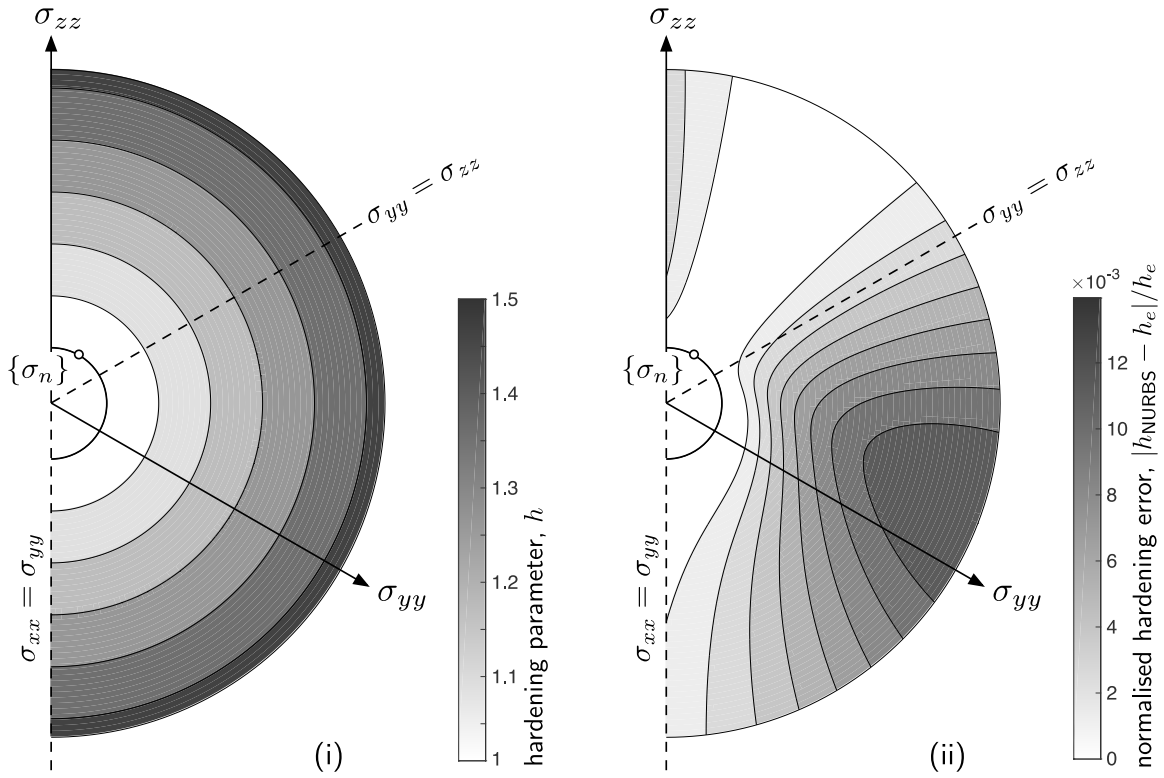

Figure 2: (i) stress return hardening parameter values and (ii) errors for an isotropically hardening von Mises NURBS yield envelope.

is given in Table 1 for each of the global Newton iterations for four loadsteps of the 75 element simulation with a softening yield surface with $\alpha = -1$. The tolerance on the residual was set to 1×10^{-8}. All of the loadsteps converged in five iterations, or less, with the final iterations within each loadstep approaching a quadratic convergence rate, demonstrating the correct implementation of the algorithmic consistent tangent [10] for the constitutive model, including the case of material softening. For this case by the end of the simulation the minimum size of the yield surface had reduced to 78% of the original.

Table 1: Plane strain notched plate convergence for the NURBS implementation of the von Mises yield surface with linear isotropic softening ($\alpha = -1$) with 75 elements (1×1mm element size).

	loadstep			
NR iteration	2	3	10	20
1	8.953×10^{-2}	2.502×10^{-1}	2.392×10^{-2}	1.553×10^{-3}
2	6.891×10^{-3}	6.605×10^{-2}	9.518×10^{-4}	8.705×10^{-5}
3	4.050×10^{-5}	2.205×10^{-3}	1.278×10^{-6}	8.828×10^{-9}
4	1.435×10^{-9}	6.933×10^{-6}	1.270×10^{-12}	-
5	-	6.474×10^{-11}	-	-

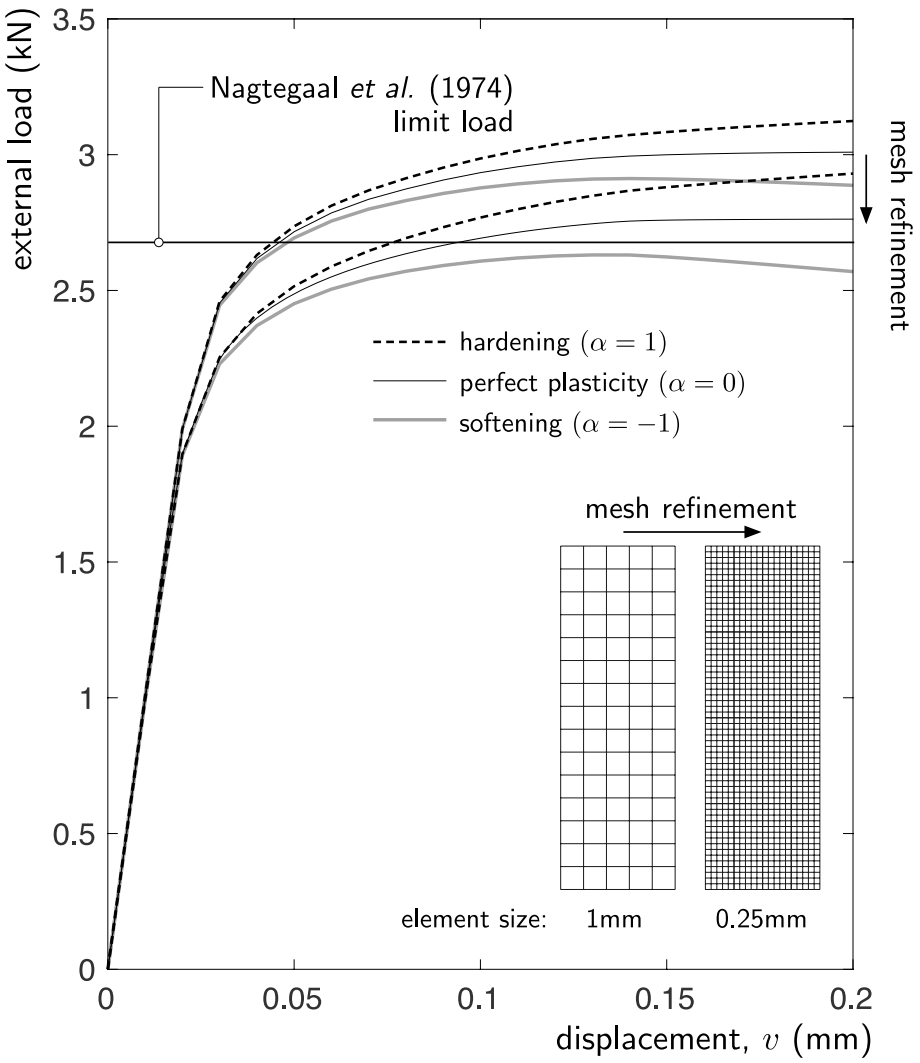

Figure 3: Double notched plate with NURBS-based von Mises plasticity with hardening, perfect plasticity and softening responses.

5 CONCLUSIONS

This paper extends the NURBS plasticity framework of Coombs et al. [1] to allow: (i) the yield surface to expand (hardening) or contract (softening) under plastic straining and (ii) decoupling the flow direction from the spatial gradient of the surface. This is achieved by allowing the position of the control points to be a function of inelastic straining and for the flow direction to be approximated by a separate NURBS basis. The formulation has been validated at both a material point level and in bounadry value simulations.

References

[1] W. M. Coombs, O. A. Petit, and Y. Ghaffari Motlagh. NURBS plasticity: Yield surface representation and implicit stress integration for isotropic inelasticity. *Comput. Meth. Appl. Mech. Eng.*, 304:342 – 358, 2016.

[2] J. A. Cottrell, T. J. R. Hughes, and Y. Bazilevs. *Isogeometric Analysis: Toward Integration of CAD and FEA*. Wiley, New York, 2009.

[3] R. S. Crouch, H. Askes, and T. Li. Analytical CPP in energy-mapped stress space: application to a modified Drucker-Prager yield surface. *Comput. Methods Appl. Mech. Eng.*, 198(5-8):853–859, 2009.

[4] E. A. de Souza Neto, D. Perić, M. Dutko, and D. R. J. Owen. Design of simple low order finite elements for large strain analysis of nearly incompressible solids. *Int. J. Solids Struct.*, 33(20-22):3277–3296, 1996.

[5] A. Kossa and L. Szabó. Exact integration of the von Mises elastoplasticity model with combined linear isotropic-kinematic hardening. *International Journal of Plasticity*, 25(6):1083–1106, 2009.

[6] J. C. Nagtegaal, D. M. Parks, and J. R. Rice. On numerically accurate finite element solutions in the fully plastic range. *Comput. Meth. Appl. Mech. Eng.*, 4:153–177, 1974.

[7] L. Piegl and W. Tiller. *The NURBS book*. Springer Science & Business Media, 2012.

[8] J. C. Simo. Associative coupled thermoplasticity at finite strains: Formulation, numerical analysis and implementation. *Comput. Meth. Appl. Mech. Eng.*, 98(1): 41–104, 1992.

[9] J. C. Simo and M. S. Rifai. A class of mixed assumed strain methods and the method of incompatible modes. *Int. J. Numer. Meth. Engng.*, 29(8):1595–1638, 1990.

[10] J. C. Simo and R. L. Taylor. Consistent tangent operators for rate-independent elastoplasticity. *Comput. Meth. Appl. Mech. Eng.*, 48(1):101–118, 1985.

[11] M. Wilkins. Calculation of elastic-plastic flow. In S. Fernback and M. Rotenberg, editors, *Methods of Computational Physics*, volume 3, 1964.

XIV International Conference on Computational Plasticity. Fundamentals and Applications
COMPLAS XIV
E. Oñate, D.R.J. Owen, D. Peric & M. Chiumenti (Eds)

IDENTIFICATION OF NONLINEAR KINEMATIC HARDENING PARAMETERS FOR SHEET METAL FROM BIAXIAL LOADING TESTS

B. SÖHNGEN* AND K. WILLNER*

*Institute of Applied Mechanics
Friedrich-Alexander-Universität Erlangen-Nürnberg
Egerlandstr. 5, 91058 Erlangen, Germany
e-mail: benjamin.soehngen@fau.de, kai.willner@fau.de
web page: www.ltm.fau.de

Key words: Kinematic Hardening, Anisotropic Plasticity, Parameter Identification, Biaxial Loading, Sheet Metal

Abstract. In this work an anisotropic material model at finite strains with nonlinear mixed (isotropic and kinematic) hardening is used for the identification of the hardening parameters of sheet steel. The algorithmic system is thereby reduced to a single equation return mapping. For the identification, a cruciform specimen is loaded biaxially in an alternating shear test to provoke the kinematic hardening behavior and prevent the sheet from buckling. The material parameters are found through an optimization strategy by comparing the deformation field from the experiment to that from a finite element (FE) simulation. The resulting cost function is minimized by means of a gradient-based method.

1 INTRODUCTION

Minimizing production costs and overall weight of products is a major goal for manufacturers in the 21st century. In the context of sheet metals an ongoing development is the incorporation of functional elements through bulk forming operations by means of the technology of sheet-bulk metal forming [1]. Here, both sheet and bulk forming is applied to thin sheets to generate complex shape elements and reduce waste.

The accurate rendering of forming processes by the finite element method (FEM) requires suitable material models and proper identification of therein specified parameters. This can be a challenging task as the ever-increasing complexity of the constitutive models demand for appropriate identification methods by simultaneously decreasing experimental effort.

In this contribution a material law capable of describing elasto-plastic material behavior utilizing a Hill-type yield function in combination with a mixed hardening law is used to identify parameters for the dual-phase steel DP600.

2 MATERIAL MODEL

2.1 Notation

In this work, scalar quantities are represented by lower case letters $a, b, \ldots$. Boldfaced characters $\boldsymbol{A}, \boldsymbol{B}, \ldots$ denote second-order tensors; in particular $\boldsymbol{I}$ denotes the second-order identity tensor $\boldsymbol{A} \cdot \boldsymbol{I} = \boldsymbol{A}$. Fourth- and sixth-order tensors are defined by calligraphic symbols $\mathcal{A}, \mathcal{B}, \ldots$. The dyadic product between two second-order tensors yield a tensor of fourth-order $\mathcal{C} = \boldsymbol{A} \otimes \boldsymbol{B}$ and can be expressed in index notation as $C_{ijkl} = A_{ij} B_{kl}$. The fourth-order tensor $\mathcal{C}$ is a linear map from $\boldsymbol{A}$ to $\boldsymbol{B}$ which is given as $\boldsymbol{B} = \mathcal{C} : \boldsymbol{A}$ in this work (accordingly for sixth-order tensors). The fourth-order symmetric identity tensor is defined through the Kronecker delta as $I^{\mathrm{sym}} = \frac{1}{2}(\delta_{ik}\delta_{jl} + \delta_{jk}\delta_{il})$ and has the property that it projects a symmetric tensor on itself $\boldsymbol{A}^{\mathrm{sym}} = \mathcal{I}^{\mathrm{sym}} : \boldsymbol{A}^{\mathrm{sym}}$ for any symmetric second-order tensor $\boldsymbol{A}^{\mathrm{sym}} = \frac{1}{2}(\boldsymbol{A} + \boldsymbol{A}^{\mathsf{T}})$. The Euclidean norm of a second-order tensor is defined as $||\boldsymbol{A}|| = \sqrt{\boldsymbol{A} : \boldsymbol{A}}$ where the double dot product reads $a = \boldsymbol{A} : \boldsymbol{B} = A_{ij} B_{ij}$.

2.2 Model formulation

The formulation of large strain plasticity is based on the algorithm presented by Miehe and Lambrecht [2]. It consists of the calculation of stresses and elasticity moduli with regard to a Seth-Hill strain tensor. For the application to elasto-plasticity, the algorithm can be interpreted as a pre- and postprecessing of the stresses and elasto-plastic material tangent originating from a "small strain" algorithm based on the Hencky (logarithmic) strain tensor

$$\boldsymbol{E}^0 = \frac{1}{2} \ln \boldsymbol{C} \,, \tag{1}$$

where $\boldsymbol{C} = \boldsymbol{F}^{\mathsf{T}} \boldsymbol{F}$ denotes the right Cauchy-Green tensor, as shown by Miehe, Apel, et al. [3]. Referring to $\boldsymbol{T}$ as the work-conjugate stress measure to the logarithmic strain $\boldsymbol{E}^0$ and $\mathcal{C}^{\mathrm{ep}}$ as the consistent material tangent, the transformation to the Lagrangian stress and module is performed by

$$\boldsymbol{S} = \boldsymbol{T} : \mathcal{P} \quad \text{and} \quad \mathcal{C}_{\mathrm{L}}^{\mathrm{ep}} = \mathcal{P}^{\mathsf{T}} : \mathcal{C}^{\mathrm{ep}} : \mathcal{P} + \boldsymbol{T} : \mathcal{L} \tag{2}$$

via the fourth and sixth-order projection tensors $\mathcal{P}$ and $\mathcal{L}$ that are defined as

$$\mathcal{P} = 2 \frac{\partial \boldsymbol{E}^0}{\partial \boldsymbol{C}} \quad \text{and} \quad \mathcal{L} = 4 \frac{\partial^2 \boldsymbol{E}^0}{\partial \boldsymbol{C} \partial \boldsymbol{C}} \,. \tag{3}$$

The first and second derivative of the logarithmic strain tensor can be obtained by usage of a spectral decomposition of the right Cauchy-Green tensor and subsequent differentiation of the eigenvalues and -vectors w.r.t. $\boldsymbol{C}$, as shown in [2].

The model regards nonlinear isotropic and kinematic hardening as well as Hill-type anisotropic plasticity. The yield function therefore reads

$$\Phi = ||\boldsymbol{\xi}||_{\mathcal{H}} - \sqrt{\frac{2}{3}} \, \sigma_{\mathrm{Y}} \tag{4}$$

where the tensor norm $||\boldsymbol{\xi}||_{\mathcal{H}}$ is given by

$$||\boldsymbol{\xi}||_{\mathcal{H}} = \left|\left|\boldsymbol{\xi}^{\mathsf{T}} : \mathcal{H} : \boldsymbol{\xi}\right|\right| \tag{5}$$

with the relative stress tensor $\boldsymbol{\xi}$ being defined by the stress tensor $\boldsymbol{T}$ and the backstress tensor $\boldsymbol{B}$

$$\boldsymbol{\xi} = \boldsymbol{T} - \boldsymbol{B}\,. \tag{6}$$

The anisotropic plasticity is modeled by the fourth-order HILL tensor $\mathcal{H}$ which shows minor (as well as major) symmetry properties and can therefore be represented in a contracted notation. Besides the popular VOIGT notation there are others that show certain advantages over the former. The main disadvantages of VOIGT's notation are the different representation of (symmetric) second-order tensors for stress- and strain-like quantities (coefficient of 2 for shear strain) and that certain tensor operations will not be transferred to the reduced notation. E.g. the scalar product between two symmetric second-order tensors or the tensor product between a fourth- and a second-order tensor do not yield the same result in VOIGT notation, $\boldsymbol{A} : \boldsymbol{B} \neq {}^{\mathrm{V}}\boldsymbol{A} \cdot {}^{\mathrm{V}}\boldsymbol{B}$ and $\mathcal{A} : \boldsymbol{B} \neq {}^{\mathrm{V}}\mathcal{A} \cdot {}^{\mathrm{V}}\boldsymbol{B}$, but using the representation according to MANDEL, $\boldsymbol{A} : \boldsymbol{B} = {}^{\mathrm{M}}\boldsymbol{A} \cdot {}^{\mathrm{M}}\boldsymbol{B}$ and $\mathcal{A} : \boldsymbol{B} = {}^{\mathrm{M}}\mathcal{A} \cdot {}^{\mathrm{M}}\boldsymbol{B}$. With the choice of MANDEL notation the HILL tensor can be displayed as

$${}^{\mathrm{M}}\mathcal{H} = \frac{1}{3}\begin{bmatrix} a_2+a_3 & -a_3 & -a_2 & 0 & 0 & 0 \\ -a_3 & a_1+a_3 & -a_1 & 0 & 0 & 0 \\ -a_2 & -a_1 & a_2+a_1 & 0 & 0 & 0 \\ 0 & 0 & 0 & 2\cdot{}^3\!/_2\, a_6 & 0 & 0 \\ 0 & 0 & 0 & 0 & 2\cdot{}^3\!/_2\, a_5 & 0 \\ 0 & 0 & 0 & 0 & 0 & 2\cdot{}^3\!/_2\, a_4 \end{bmatrix} \tag{7}$$

with the anisotropy parameters a_i which are based on the HILL parameters h_i

$$\begin{aligned} a_1 &= \frac{1}{h_2^2} + \frac{1}{h_3^2} - \frac{1}{h_1^2} \quad a_2 = \frac{1}{h_3^2} + \frac{1}{h_1^2} - \frac{1}{h_2^2} \quad a_3 = \frac{1}{h_1^2} + \frac{1}{h_2^2} - \frac{1}{h_3^2} \\ a_4 &= \frac{1}{h_6^2} \qquad\qquad a_5 = \frac{1}{h_5^2} \qquad\qquad a_6 = \frac{1}{h_4^2}\,. \end{aligned} \tag{8}$$

Remark The tensor $\mathcal{P}$ has the property $\mathcal{P} : \boldsymbol{I} = \boldsymbol{0}$ of a deviatoric projection tensor [3] and specifically for $h_i = 1$ reduces to the deviatoric identity tensor $\mathcal{I}^{\mathrm{dev}} = \mathcal{I}^{\mathrm{sym}} - \frac{1}{3}\boldsymbol{I} \otimes \boldsymbol{I}$ which yields the classical J_2-plasticity for the tensor norm, $\sqrt{3/2}\,||\boldsymbol{\xi}||_{\mathcal{H}|_{h_i=1}} = \sqrt{3\,\mathrm{J}_2(\boldsymbol{\xi})} = \sqrt{3/2}\,||\mathrm{dev}(\boldsymbol{\xi})||$.

Considering isotropic hardening, the yield stress in equation (4) is represented by the exponential law according to HOCKETT and SHERBY [4],

$$\sigma_{\mathrm{Y}}(\bar{\varepsilon}^{\mathrm{pl}}) = \sigma_\infty + [\sigma_0 - \sigma_\infty] \exp\left(a\,\bar{\varepsilon}^{\mathrm{pl}\,b}\right)\,, \tag{9}$$

where σ_0 and σ_∞ are stress-like quantities and a and b describe the curvature of the yield stress. As the algorithm is not limited to this formulation, other well known hardening laws like the ones from LUDWIK, VOCE or SWIFT could be used as well.

The shift of the yield surface in stress space is considered by ARMSTRONG and FREDERICK [5] nonlinear kinematic hardening through the evolution of the backstress by

$$\dot{\boldsymbol{B}} = \dot{\gamma}\left[k_1 \boldsymbol{N} - k_2 \boldsymbol{B}\right] , \tag{10}$$

with the material parameter k_1 representing the kinematic hardening modulus and k_2 the rate of saturation. For usage in a finite element code the evolution law is discretized in time by an implicit Euler scheme, resulting in

$$\boldsymbol{B}_{n+1} = \frac{1}{\Delta\gamma_{n+1} + k_2}\left[k_1 \boldsymbol{N}_{n+1} + \Delta\gamma_{n+1}\boldsymbol{B}_n\right] . \tag{11}$$

Declaring the flow rule to be of an associative type, the flow vector reads $\boldsymbol{N} = {}^{\partial\Phi}/_{\partial\boldsymbol{T}}$ and the evolution of the plastic strain tensor is defined through

$$\dot{\boldsymbol{E}}^{\mathrm{pl}} = \dot{\gamma}\boldsymbol{N} , \quad \text{resp.} \quad \boldsymbol{E}^{\mathrm{pl}}_{n+1} = \boldsymbol{E}^{\mathrm{pl}}_{n} + \Delta\gamma_{n+1}\boldsymbol{N}_{n+1} \tag{12}$$

2.3 Single equation return-mapping

Using a radial return-mapping algorithm (see e.g. [6]) and starting off with the trial stress as

$$\widetilde{\boldsymbol{T}}_{n+1} = \mathcal{C}^{\mathrm{el}} : \widetilde{\boldsymbol{E}}^{\mathrm{el}}_{n+1} = \mathcal{C}^{\mathrm{el}} : \left[\boldsymbol{E}_{n+1} - \boldsymbol{E}^{\mathrm{pl}}_{n}\right] , \tag{13}$$

where $\widetilde{[\cdot]}$ indicates a trial value, the updated stress then reads

$$\boldsymbol{T}_{n+1} = \widetilde{\boldsymbol{T}}_{n+1} - \Delta\gamma_{n+1}\, \mathcal{C}^{\mathrm{el}} : \boldsymbol{N}_{n+1} . \tag{14}$$

Combining equation (14) with equation (11) into the relative stress gives

$$\begin{aligned} \boldsymbol{\xi}_{n+1} &= \boldsymbol{T}_{n+1} - \boldsymbol{B}_{n+1} \\ &= \widehat{\boldsymbol{\xi}}_{n+1} - \frac{\Delta\gamma_{n+1}}{\left|\left|\boldsymbol{\xi}_{n+1}\right|\right|_{\mathcal{H}}}\, \mathcal{B}_{n+1} : \mathcal{H} : \boldsymbol{\xi}_{n+1} , \end{aligned} \tag{15}$$

where the definitions for the stress tensor $\widehat{\boldsymbol{\xi}}_{n+1}$ and the fourth-order tensor $\mathcal{B}_{n+1}$,

$$\widehat{\boldsymbol{\xi}}_{n+1} = \widetilde{\boldsymbol{T}}_{n+1} - \frac{1}{1 + k_2\,\Delta\gamma_{n+1}}\boldsymbol{B}_n \quad \text{and} \quad \mathcal{B}_{n+1} = \mathcal{C}^{\mathrm{el}} + \frac{k_1}{1 + k_2\,\Delta\gamma_{n+1}}\,\mathcal{I}^{\mathrm{sym}} \tag{16}$$

are introduced. Since in the converged step $\Phi = 0$ and thus $||\boldsymbol{\xi}||_{\mathcal{H}} = \sqrt{{}^{2}/_{3}}\,\sigma_{\mathrm{Y}}$ holds, equation (15) can be rewritten as

$$\boldsymbol{\xi}_{n+1} = \left[\mathcal{I}^{\mathrm{sym}} + \frac{\Delta\gamma_{n+1}}{\sqrt{\frac{2}{3}}\,\sigma_{\mathrm{Y}}}\mathcal{B}_{n+1} : \mathcal{H}\right]^{-1} : \widehat{\boldsymbol{\xi}}_{n+1} = \left[\mathcal{A}_{n+1}\right]^{-1} : \widehat{\boldsymbol{\xi}}_{n+1} , \tag{17}$$

hence being solely a function of the unknown plastic multiplier $\Delta\gamma$. By substitution into the definition of the yield function (equation (4)) a scalar equation with only one

unknown is derived. To solve the (nonlinear) equation for $\Delta\gamma$ a NEWTON-RAPHSON scheme is applied, giving

$$\Delta\gamma^{k+1} = \Delta\gamma^{k} - \left[\frac{\partial \Phi}{\partial\, \Delta\gamma}\bigg|_{\Delta\gamma^k} \right]^{-1} \Phi^{k}\,, \tag{18}$$

with k the iteration counter. The derivative of the yield function w.r.t. the plastic multiplier can be displayed after straightforward usage of the chain rule as

$$\begin{aligned} \frac{\partial \Phi}{\partial\, \Delta\gamma} = \boldsymbol{N}_{n+1} : \left[\mathcal{A}_{n+1}\right]^{-1} : \Bigg\{ k_2 \kappa_{n+1}^2 \boldsymbol{B}_n - \Bigg\{ \left[\frac{1}{\sqrt{2/3}\ \sigma_\mathrm{Y}} - \frac{\eta_{n+1}}{\sigma_\mathrm{Y}} \frac{\partial \sigma_\mathrm{Y}}{\partial\, \Delta\gamma} \right] \mathcal{B}_{n+1} \\ - \eta_{n+1} k_1 k_2 \kappa_{n+1}^2\, \mathcal{I}^{\mathrm{sym}} \Bigg\} : \mathcal{P} : \boldsymbol{\xi}_{n+1} \Bigg\} - \sqrt{\frac{2}{3}} \frac{\partial \sigma_\mathrm{Y}}{\partial\, \Delta\gamma}\,, \end{aligned} \tag{19}$$

with the auxiliary variables

$$\kappa = \frac{1}{1 + k_2\, \Delta\gamma} \quad \text{and} \quad \eta = \frac{\Delta\gamma}{\sqrt{2/3}\, \sigma_\mathrm{Y}}\,. \tag{20}$$

2.4 Consistent elasto-plastic tangent modulus

In the algorithmic implementation, the related tangent modulus plays the major role for achieving (quadratic) convergence in the Newton-Raphson iteration for the global equilibrium. It enters the calculation of the overall stiffness and needs to be *consistent* with the algorithm for stress calculation, hence the name of a consistent elasto-plastic tangent modulus. To develop the algorithmic tangent the system of equations (equations (4), (11), (12), (14) and (15)) is linearized, giving

$$\left.\begin{aligned} \mathrm{d}\boldsymbol{\xi} &= \mathrm{d}\boldsymbol{T} - \mathrm{d}\boldsymbol{B} \\ \mathrm{d}\boldsymbol{T} &= \mathcal{C}^{\mathrm{el}} : \left[\mathrm{d}\boldsymbol{E} - \mathrm{d}\boldsymbol{E}^{\mathrm{pl}}\right] \\ \mathrm{d}\boldsymbol{B} &= \kappa \left[\left[k_1 \boldsymbol{N} - k_2 \boldsymbol{B}\right] \mathrm{d}\, \Delta\gamma + k_1\, \Delta\gamma \tfrac{\partial \boldsymbol{N}}{\partial \boldsymbol{\xi}} : \mathrm{d}\boldsymbol{\xi} \right] \\ \mathrm{d}\boldsymbol{E}^{\mathrm{pl}} &= \Delta\gamma \tfrac{\partial \boldsymbol{N}}{\partial \boldsymbol{\xi}} : \mathrm{d}\boldsymbol{\xi} + \boldsymbol{N}\, \mathrm{d}\, \Delta\gamma \\ \mathrm{d}\Phi &= \tfrac{1}{\|\boldsymbol{\xi}\|_{\mathcal{H}}} \mathcal{H} : \boldsymbol{\xi} : \mathrm{d}\boldsymbol{\xi} - \sqrt{\tfrac{2}{3}} \tfrac{\partial \sigma_\mathrm{Y}}{\partial\, \Delta\gamma}\, \mathrm{d}\, \Delta\gamma = 0\,. \end{aligned}\right\} \tag{21}$$

Solving the linearized system for $\mathrm{d}\boldsymbol{T}/\,\mathrm{d}\boldsymbol{E}$ leads to the desired tangent operator

$$\mathcal{C}^{\mathrm{ep}} = \frac{\mathrm{d}\boldsymbol{T}}{\mathrm{d}\boldsymbol{E}} = \mathcal{C}_1 : \left[\left[\mathcal{C}^{\mathrm{el}}\right]^{-1} : \mathcal{C}_1 + \mathcal{C}_2 \right]^{-1} \tag{22}$$

with the fourth-order auxiliary tensors

$$\mathcal{C}_1 = -\sqrt{\frac{2}{3}} k_1 \kappa\, \Delta\gamma \frac{\partial \sigma_\mathrm{Y}}{\partial \Delta\gamma} \frac{\partial \boldsymbol{N}}{\partial \boldsymbol{\xi}} + k_2 \kappa \boldsymbol{B} \otimes \boldsymbol{N} - k_1 \kappa \boldsymbol{N} \otimes \boldsymbol{N} - \sqrt{\frac{2}{3}} \frac{\partial \sigma_\mathrm{Y}}{\partial \Delta\gamma}\, \mathcal{I}^{\mathrm{sym}} \tag{23}$$

$$\mathcal{C}_2 = -\sqrt{\frac{2}{3}} \frac{\partial \sigma_\mathrm{Y}}{\partial \Delta\gamma}\, \Delta\gamma \frac{\partial \boldsymbol{N}}{\partial \boldsymbol{\xi}} - \boldsymbol{N} \otimes \boldsymbol{N}\,. \tag{24}$$

It should be noted that the consistent tangent modulus is calculated at the end of the stress update, hence all quantities are evaluated at the updated state and the index $[\cdot]_{n+1}$ has been suppressed to improve readability.

The continuum tangent modulus is defined by the rate relation

$$\dot{\boldsymbol{T}} = \mathcal{C}_{\mathrm{c}}^{\mathrm{ep}} : \dot{\boldsymbol{E}} = \mathcal{C}^{\mathrm{el}} : \left[\dot{\boldsymbol{E}} - \dot{\boldsymbol{E}}^{\mathrm{pl}}\right] , \tag{25}$$

where $[\cdot]_{\mathrm{c}}$ denotes the *continuum* operator. Under usage of the consistency condition $\dot{\Phi} = 0$ an expression for the rate of the backstress can be derived as

$$\dot{\boldsymbol{B}} = \frac{[k_1 \boldsymbol{N} - k_2 \boldsymbol{B}] : \boldsymbol{N}}{\frac{2}{3}\frac{\partial \sigma_{\mathrm{Y}}}{\partial \bar{\varepsilon}^{\mathrm{pl}}} + [k_1 \boldsymbol{N} - k_2 \boldsymbol{B}] : \boldsymbol{N}} \dot{\boldsymbol{T}} , \tag{26}$$

which - inserted back into equation (25) along with the consistency condition and the rate of the plastic strain tensor (equation (12)) - yields the continuum tangent operator as

$$\mathcal{C}_{\mathrm{c}}^{\mathrm{ep}} = \frac{\dot{\boldsymbol{T}}}{\dot{\boldsymbol{E}}} = \left[\left[\mathcal{C}^{\mathrm{el}}\right]^{-1} + \frac{1}{\frac{2}{3}\frac{\partial \sigma_{\mathrm{Y}}}{\partial \bar{\varepsilon}^{\mathrm{pl}}} + [k_1 \boldsymbol{N} - k_2 \boldsymbol{B}] : \boldsymbol{N}} \boldsymbol{N} \otimes \boldsymbol{N} \right]^{-1} . \tag{27}$$

Calculating the limit case $\Delta\gamma \to 0$ for the consistent tangent operator leads, after some rearrangement and by using $\frac{\partial \sigma_{\mathrm{Y}}}{\partial \bar{\varepsilon}^{\mathrm{pl}}} = \sqrt{\frac{2}{3}}\frac{\partial \sigma_{\mathrm{Y}}}{\partial \Delta\gamma}$, to the continuum tangent operator as expected, $\lim_{\Delta\gamma \to 0} \mathcal{C}^{\mathrm{ep}} = \mathcal{C}_{\mathrm{c}}^{\mathrm{ep}}$. It is emphasized that although the chosen plasticity model is associative, the kinematic hardening law is of a non-associative type. This leads to a non-symmetric elasto-plastic tangent modulus that needs to be taken into consideration when solving the global equilibrium, as the overall stiffness matrix loses its symmetry as well and therefore needs a solver that can handle non-symmetric systems. The loss of symmetry thereby only refers to the major symmetry of $\mathcal{C}^{\mathrm{ep}}$, leading to a non-symmetric representation in MANDEL notation ${}^{\mathrm{M}}\mathcal{C}^{\mathrm{ep}} \neq [{}^{\mathrm{M}}\mathcal{C}^{\mathrm{ep}}]^{\mathsf{T}}$. The algorithmic equations are listed in table 1 for convenience.

Remark As already mentioned above, all equations can be represented in some compressed notation. Every fourth-order tensor shows at least minor symmetry and by making use of e.g. MANDEL representation, the calculation time on local Gauss point level can be reduced substantially.

3 PARAMETER IDENTIFICATION

The experimental investigation is carried out on a biaxial testing machine with four electro-mechanical actuators of which the two of each axis are operated in master/slave control to keep the specimen centered and inhibit rigid body motion. To prevent buckling, the loading along the two axes is applied in an alternating fashion rather than by pure tension/compression. Therefore, the applied force is equal in amount but opposite in direction, resulting in an alternating shear loading.

Table 1: Single-equation return-mapping algorithm

- Geometric preprocessing: $\boldsymbol{C} = \boldsymbol{F}^{\mathsf{T}}\boldsymbol{F}$, $\quad \boldsymbol{E}^{0}_{n+1} = \frac{1}{2}\ln(\boldsymbol{C})$
- Plasticity algorithm:
  - Trial stress: $\widetilde{\boldsymbol{T}}_{n+1} = \mathcal{C}^{\mathrm{el}} : \left[\boldsymbol{E}_{n+1} - \boldsymbol{E}^{\mathrm{pl}}_{n}\right]$
  - Evaluate yield function: $\Phi = \|\widetilde{\boldsymbol{\xi}}_{n+1}\|_{\mathcal{H}} - \sqrt{\frac{2}{3}}\,\sigma_{\mathrm{Y}}(\bar{\varepsilon}^{\mathrm{pl}}_{n})$, $\quad \widetilde{\boldsymbol{\xi}}_{n+1} = \widetilde{\boldsymbol{T}}_{n+1} - \boldsymbol{B}_{n}$

    if $\Phi \leq 0.0\mathrm{d}0$ **then**
    `// Elastic step`
    Set: $\boldsymbol{T}_{n+1} = \widetilde{\boldsymbol{T}}_{n+1}$, $\quad \boldsymbol{B}_{n+1} = \boldsymbol{B}_{n}$, $\quad \mathcal{C}^{\mathrm{ep}}_{n+1} = \mathcal{C}^{\mathrm{el}}$
    else
    `// Plastic step`
    Set: $k = 0$, $\quad \Delta\gamma^{0}_{n+1} = 0.0\mathrm{d}0$, $\quad \boldsymbol{\xi}^{0}_{n+1} = \widetilde{\boldsymbol{\xi}}_{n+1}$, $\quad \varepsilon_{\mathrm{tol}} = 1.0\mathrm{d}{-8}$
    while $|\Phi^{k}| > \varepsilon_{\mathrm{tol}}$ **do**
    $\left.\frac{\partial\Phi}{\partial\,\Delta\gamma}\right|^{k} = \left.\frac{\partial\Phi}{\partial\,\Delta\gamma}\right|_{\Delta\gamma^{k}}$
    $\Delta\gamma^{k+1}_{n+1} = \Delta\gamma^{k}_{n+1} - \left[\left.\frac{\partial\Phi}{\partial\,\Delta\gamma}\right|^{k}\right]^{-1}\Phi^{k}$
    $\widehat{\boldsymbol{\xi}}^{\,k+1} = \widetilde{\boldsymbol{T}}_{n+1} - \kappa^{k+1}\boldsymbol{B}_{n}$, $\quad \boldsymbol{\xi}^{k+1}_{n+1} = [\mathcal{A}]^{-1} : \widehat{\boldsymbol{\xi}}^{\,k+1}$
    $\bar{\varepsilon}^{\mathrm{pl}\,k+1}_{\;\;n+1} = \bar{\varepsilon}^{\mathrm{pl}}_{n} + \sqrt{\frac{2}{3}}\,\Delta\gamma^{k+1}_{n+1}$, $\quad \sigma^{k+1}_{\mathrm{Y}} = \sigma_{\mathrm{Y}}(\bar{\varepsilon}^{\mathrm{pl}\,k+1}_{\;\;n+1})$
    $\Phi^{k+1} = \left|\left|\boldsymbol{\xi}^{k+1}_{n+1}\right|\right|_{\mathcal{H}} - \sqrt{\frac{2}{3}}\,\sigma^{k+1}_{\mathrm{Y}}$
    $k = k + 1$
    end while
    $\boldsymbol{B}_{n+1} = \kappa_{n+1}\left[k_{1}\boldsymbol{N}_{n+1} + \Delta\gamma_{n+1}\boldsymbol{B}_{n}\right]$, $\quad \boldsymbol{T}_{n+1} = \boldsymbol{\xi}_{n+1} + \boldsymbol{B}_{n+1}$
    $\mathcal{C}^{\mathrm{ep}}_{n+1}$ from equations (22) to (24)
    end if
- Geometric postprocessing: $\boldsymbol{S} = \boldsymbol{T} : \mathcal{P}$, $\quad \mathcal{C}^{\mathrm{ep}}_{\mathrm{L}} = \mathcal{P}^{\mathsf{T}} : \mathcal{C}^{\mathrm{ep}} : \mathcal{P} + \boldsymbol{T} : \mathcal{L}$

3.1 Experimental and numerical setup

The considered material is a DP600 sheet steel with 2 mm thickness. In the experimental investigation a cruciform specimen with the dimensions depicted in figure 1 is used. To obtain the deformation field a speckle pattern which is captured with a stereo camera setup is applied to the surface of the specimen. The captured images are subsequently analyzed with the digital image correlation (DIC) software ARAMIS to generate the displacements. For the numerical computation a FE-mesh consisting of 3080 eight-noded 3D continuum elements (two in thickness direction) with linear shape functions is used. Assuming a uniform load distribution generated by the clamping, the respective edge nodes are coupled through nodal ties and the measured forces are taken as boundary conditions. To assess the residual of experimental and numerical displacements only a subset of the FE nodes are considered. These optimization nodes are shown in figure 2 along with the

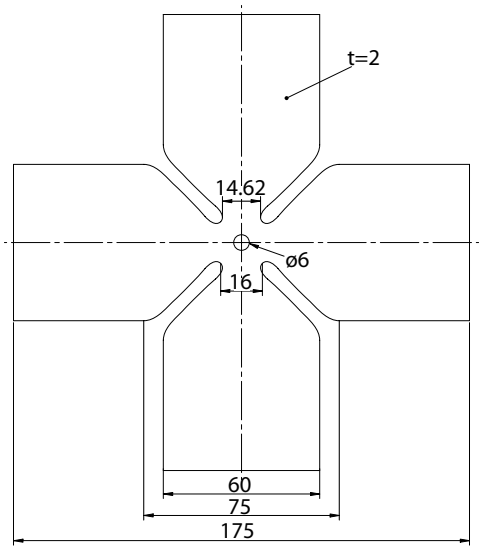

Figure 1: Dimensions of the cruciform specimen in mm

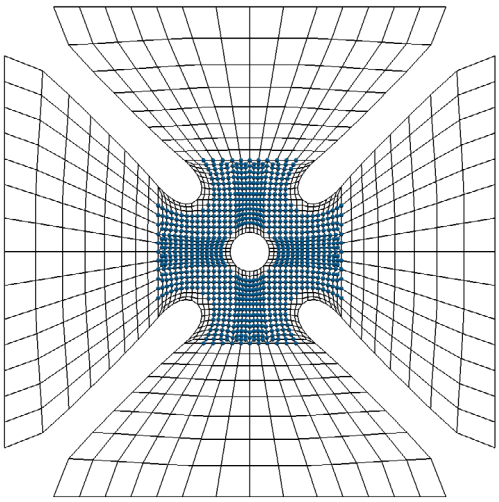

Figure 2: Finite element mesh of specimen (dots mark optimization nodes)

discretization.

To encourage the heterogeneity of the deformation state a bore of 6 mm in diameter is introduced at the center of the specimen, resulting in various strain states. In figure 3 major vs. minor strain is plotted for the optimization nodes along with the strain states for uniaxial compression ($\varepsilon_1 = -0.5\varepsilon_2$), pure shear ($\varepsilon_1 = -\varepsilon_2$), uniaxial tension ($\varepsilon_1 = -2\varepsilon_2$), plane strain ($\varepsilon_2 = 0$) and equi-biaxial tension ($\varepsilon_1 = \varepsilon_2$). Though the specimen exhibits mainly pure shear as expected it can be seen that also other strain states are induced.

The afore-mentioned alternating shear loading of the specimen is depicted in figure 4. Starting off with the initial unloaded configuration the speckle patterns for the three peak loading values ($|F_{\mathrm{x/y}}| = 8\,\mathrm{kN}$, $|F_{\mathrm{x/y}}| = 9\,\mathrm{kN}$ and $|F_{\mathrm{x/y}}| = 10\,\mathrm{kN}$) are shown. The deformation state can be judged by the elliptic deformation of the originally circular bore in the middle. For the loading a linear force rate of $|\dot{F}_{\mathrm{x/y}}| = 100\,\mathrm{N/s}$ is chosen.

3.2 Inverse Identification

The identification process is based on a comparison of the displacements obtained from experiment and FE simulation. The minimization function can be formulated as

$$\min_{\boldsymbol{\alpha}} f(\boldsymbol{\alpha}) = \min_{\boldsymbol{\alpha}} \frac{1}{2} \left|\left| \boldsymbol{x}_{\mathrm{Sim}}(\boldsymbol{\alpha}) - \boldsymbol{P}\boldsymbol{x}_{\mathrm{Exp}} \right|\right|_2^2 , \tag{28}$$

with $\boldsymbol{x}_{\mathrm{Sim}}$ denoting the nodal displacements from the FE-calculation and $\boldsymbol{x}_{\mathrm{Exp}}$ the displacements coming from the experimental full-field measurement. As the discretization of the numerical analysis and that of the image correlation do in general not coincide, the operator $\boldsymbol{P}$ is used to map the experimentally obtained deformation values on the nodal positions of the FE-mesh. The discretization introduced by DIC is thereby about ten times finer than that of the FE-mesh, hence the possible error derived from interpolation should be marginal. The vector $\boldsymbol{\alpha}$ contains the parameters to be optimized, in the

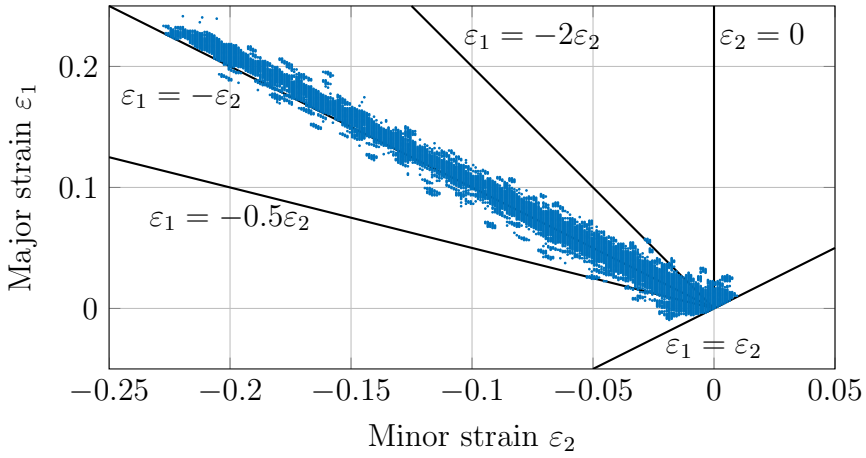

Figure 3: Distribution of major vs. minor strain in the specimen during loading

present case it consists of the four parameters describing the mixed hardening behavior, $\boldsymbol{\alpha} = [\sigma_0, \sigma_\infty, k_1, k_2]^\mathsf{T}$. As a remark, the identification of the mixed hardening parameters demand a strategy where both phenomena are considered simultaneously. The parameters for isotropic hardening may not be taken from e.g. a uniaxial tensile test.

To minimize the cost function $f(\boldsymbol{\alpha})$, an appropriate optimization algorithm has to be chosen. In general, one distinguishes between gradient-based and gradient-free methods, the latter having the advantage of not needing derivatives of the minimization functions. Nevertheless, in the context of material parameter identification, experience shows that gradient-based approaches should be chosen over gradient-free methods. Not only having an increased rate of convergence by nature, the amount of function evaluations can be significantly lower, despite using a finite difference scheme to approximate the gradient, see as well e.g. [7]. The application of a finite difference procedure to evaluate the sensitivity of the cost function w.r.t. the design parameters $\boldsymbol{\alpha}$ seems a necessary evil. An attempt to an analytical derivation for elasto-plastic material behaviour was made by Cooreman et al. [8]. The derivation however is simplified substantially and only applicable to isotropic plasticity with a strictly homogeneous strain field (simple tensile test). Moreover, the sensitivity of every node has to be calculated in an iterative manner, leading to the question about performance gain over finite differences, which keeps unanswered.

A well-suited and in the area of parameter optimization widely used (see e.g. [9]) algorithm is the Levenberg-Marquardt method. It shows quadratic convergence (see e.g. [10]) and is used with a forward finite differences scheme in this work. The minimum of the cost function is assumed to be found once either the relative step size of the design parameters or of the objective function itself reaches a threshold of 1.0d−6. The parameters for the anisotropy of the yield surface h_i for the considered material have been identified in [11] and are listed in table 2. For that identification the same cruciform specimen geometry was loaded with equi-biaxial tension. In the elastic region the material is assumed to behave isotropically with an elastic modulus of $E = 210\,000\,\mathrm{MPa}$ and a Poisson's ratio of $\nu = 0.3$. The optimization of the mixed hardening parameters is

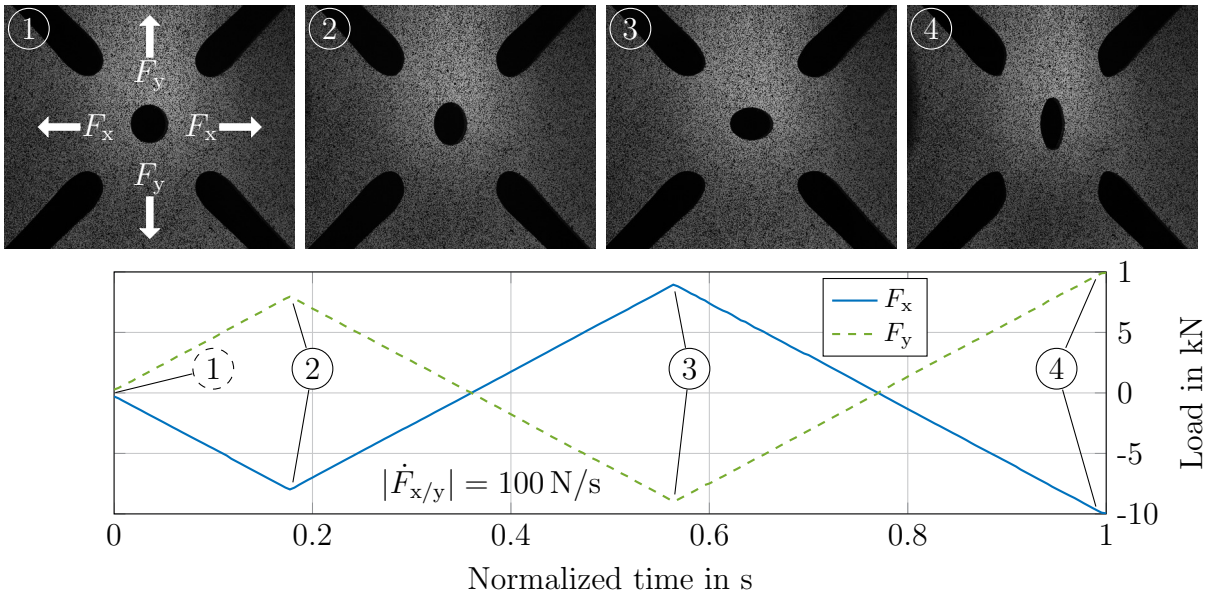

Figure 4: Specimen at four different stages of loading: (1) initial unloaded configuration, (2) $|F_{x/y}| = 8\,\mathrm{kN}$, (3) $|F_{x/y}| = 9\,\mathrm{kN}$, (4) $|F_{x/y}| = 10\,\mathrm{kN}$

Table 2: Hill parameters for DP600 [11]

h_1	h_2	h_3	h_4	h_5	h_6
0.9759	1.0039	0.9714	1.0571	1.0000	1.0000

based on three different initial values sets that are given in table 3 along with the mean and standard deviation (SD) of the three optimization runs. Observing a relative SD of

Table 3: Initial and identified parameters of the mixed hardening formulation for DP600

	σ_0 in MPa	σ_∞ in MPa	k_1	k_2
Set 1	350	1500	1000	10
Set 2	350	1500	5000	100
Set 3	400	3000	1000	100
Mean of optimization	263.2	821.7	17 434.9	174.1
SD	3.3d−2	2.9d−2	9.0d0	5.5d−2

5.0d−4 and less confirms the significance of the mean values and hence the global nature of the minimum. To fulfill the above- mentioned convergence criteria the Levenberg-Marquardt optimization of the three sets needs between 14 (Set 2) and 25 (Set 3) iterations. Thereby, the number of iterations refer to the optimization algorithm itself and does not represent the total number of FE simulations which is greater due to the

evaluation of the finite differences. In figure 5 the isotropic hardening function for the initial values and the mean of the identified parameters is plotted vs. the equivalent plastic strain ($\bar{\varepsilon}^{\mathrm{pl}} = \int_0^t \dot{\gamma}\,\mathrm{d}t$). The evolution of the backstress in loading direction w.r.t. $\bar{\varepsilon}^{\mathrm{pl}}$ is depicted in figure 6. As can be seen the kinematic hardening modulus k_1 leads to an initially steep incline while the parameter k_2 causes the increase in backstress to saturate with advancing plastic strain for the identified parameters.

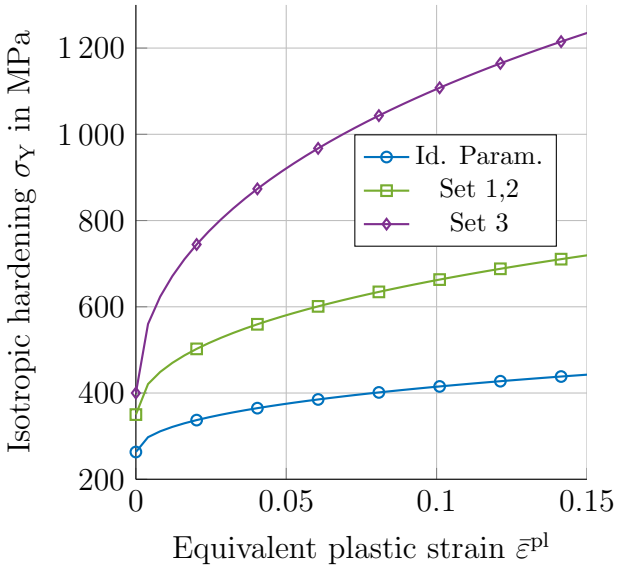

Figure 5: Evolution of isotropic hardening w.r.t. the equivalent plastic strain

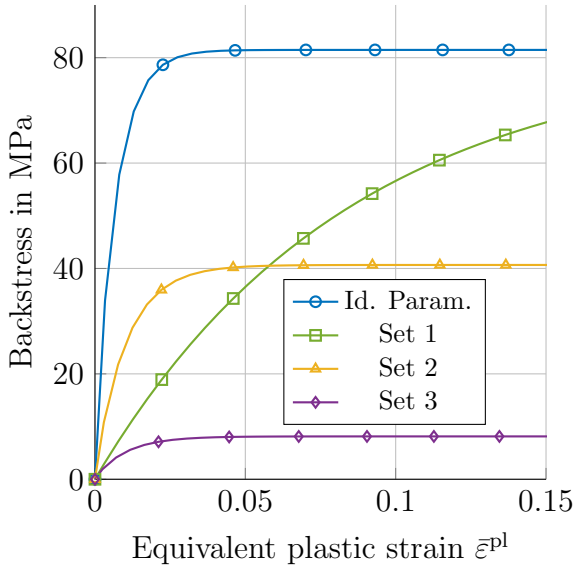

Figure 6: Evolution of backstress in loading direction w.r.t. the equivalent plastic strain

4 CONCLUSION AND OUTLOOK

In this contribution a single equation return mapping algorithm for large strain anisotropic plasticity with isotropic and kinematic hardening is presented. The identification of the mixed hardening parameters for the dual-phase steel DP600 with a Levenberg-Marquardt approach is performed on a cruciform specimen, which is loaded in an alternating shear test on a biaxial testing machine. To assure the obtained minimum of the cost function to be of a global nature, the optimization is run with three distinct initial values sets, whereby all lead to similar material parameters with only small deviations. The material model is written in Fortran and can be used (with rather minor adjustments) in commercial FE-packages like Marc or Abaqus through the provided user subroutines hypela2 and UMAT, respectively.

To further enhance the identification of material parameters with the proposed method, uncertainties in the experimental investigation will be considered in a next step. This includes in particular the determination of the deformation field through digital image correlation where the uncertainty in dependence of the deformation state can be included in the minimization function by weighting factors.

Acknowledgments. This work is supported by the German Research Foundation (DFG) within the Transregional Collaborative Research Centre TCRC 73: "Manufacturing of complex functional components with variants by using a new sheet metal forming process - Sheet-Bulk Metal Forming" (`www.tr-73.de`).

REFERENCES

[1] Merklein, M., Allwood, J., Behrens, B.-A., Brosius, A., Hagenah, H., Kuzman, K., Mori, K., Tekkaya, A., and Weckenmann, A. Bulk forming of sheet metal. *CIRP Annals-Manufacturing Technology* 61.2 (2012), pp. 725–745.

[2] Miehe, C. and Lambrecht, M. Algorithms for computation of stresses and elasticity moduli in terms of Seth-Hill's family of generalized strain tensors. *Communications in Numerical Methods in Engineering* 17.5 (2001), pp. 337–353.

[3] Miehe, C., Apel, N., and Lambrecht, M. Anisotropic additive plasticity in the logarithmic strain space: modular kinematic formulation and implementation based on incremental minimization principles for standard materials. *Computer Methods in Applied Mechanics and Engineering* 191.47-48 (2002), pp. 5383–5425.

[4] Hockett, J. E. and Sherby, O. D. Large strain deformation of polycrystalline metals at low homologous temperatures. *Journal of the Mechanics and Physics of Solids* 23.2 (1975), pp. 87–98.

[5] Armstrong, P. J. and Frederick, C. O. *A mathematical representation of the multiaxial Bauschinger effect*. Tech. rep. Reproduced as article in Mater. High Temp, 24, 1-26 (2007). GEGB Rep. RD/B/N 731, 1966.

[6] De Souza Neto, E. A., Owen, D. R. J., and Periae, D. *Computational Methods for Plasticity: Theory and Applications*. Chichester: Wiley, 2008.

[7] Schmaltz, S. and Willner, K. Material modelling and parameter identification for sheet-bulk metal forming. *COMPLAS 2013*. Barcelona, 2013, pp. 39–50.

[8] Cooreman, S., Lecompte, D., Sol, H., Vantomme, J., and Debruyne, D. Elasto-plastic material parameter identification by inverse methods: Calculation of the sensitivity matrix. *International Journal of Solids and Structures* 44.13 (2007), pp. 4329–4341.

[9] Chaparro, B., Thuillier, S., Menezes, L., Manach, P. Y., and Fernandes, J. V. Material parameters identification: Gradient-based, genetic and hybrid optimization algorithms. *Computational Materials Science* 44.2 (2008), pp. 339–346.

[10] Nocedal, J. and Wright, S. *Numerical Optimization*. New York: Springer, 2006.

[11] Landkammer, P., Söhngen, B., Steinmann, P., and Willner, K. On gradient-based optimization strategies for inverse problems in metal forming. *GAMM-Mitteilungen* (in press).

XIV International Conference on Computational Plasticity. Fundamentals and Applications
COMPLAS XIV
E. Oñate, D.R.J. Owen, D. Peric & M. Chiumenti (Eds)

MODELS OF NONLINEAR KINEMATIC HARDENING BASED ON DIFFERENT VERSIONS OF RATE-INDEPENDENT MAXWELL FLUID

ALEXEY V. SHUTOV[*] [†]

[*] Novosibirsk State University
Pirogova 2, 630090 Novosibirsk, Russia

[†]Lavrentyev Institute of Hydrodynamics
Pr. Lavrenyeva 15, 630090 Novosibirsk, Russia
e-mail: alexey.v.shutov@gmail.com, web page: http://sites.google.com/site/materialmodeling

Key words: Finite Strain Plasticity, Kinematic Hardening, Classification, w-invariance, Rate-independent Maxwell

Abstract. Different models of finite strain plasticity with a nonlinear kinematic hardening are analyzed in a systematic way. All the models are based on a certain formulation of a rate-independent Maxwell fluid, which is used to render the evolution of backstresses. The properties of each material model are determined by the underlying formulation of the Maxwell fluid. The analyzed approaches include the multiplicative hyperelasto-plasticity, additive hypoelasto-plasticity and the use of generalized strain measures. The models are compared with respect to different classification criteria, such as the objectivity, thermodynamic consistency, pure volumetric-isochoric split, shear stress oscillation, exact integrability, and w-invariance.

1 INTRODUCTION

As is well known, a correct numerical analysis of residual stresses and springback is possible only if the material model accounts for the nonlinear kinematic hardening. Nowadays, there is a big variety of phenomenological approaches to the nonlinear kinematic hardening and different formulations may be available for the same approach. Even more, some new approaches are occasionally developed, which are effectively equivalent to the already existing ones. Thus, there is a need for a unifying classification study. Here, some of the basic approaches are compared in a qualitative way, using a set of classification criteria. These criteria include the objectivity (frame invariance), thermodynamic consistency, pure split of the stress response into volumetric and isochoric parts, stress oscillation under simple shear, integrability of the elastic formulation, and w-invariance. We discuss the hyperelasto-plasticity based on the multiplicative split of the deformation gradient, hypoelasto-plasticity based on the additive split of the strain rate tensor

with different corotational and non-corotational stress rates, and a model employing the structure of the small-strain plasticity in combination with a generalized strain measure.

Second- and fourth-rank tensors in $\mathbb{R}^3$ are denoted by bold symbols. The trace, transposition, inverse of transposed, determinant, and Frobenius norm are denoted respectively by $\mathrm{tr}(\cdot)$, $(\cdot)^{\mathrm{T}}$, $(\cdot)^{\text{-T}}$, $\det(\cdot)$. The deviatoric part, symmetric part, and scalar product of two second-rank tensors are defined through

$$\mathbf{Y}^{\mathrm{D}} := \mathbf{Y} - \frac{1}{3}\mathrm{tr}(\mathbf{Y})\ \mathbf{1}, \quad \mathrm{sym}(\mathbf{Y}) := \frac{1}{2}(\mathbf{Y} + \mathbf{Y}^{\mathrm{T}}), \quad \mathbf{A} : \mathbf{B}\ := \mathrm{tr}(\mathbf{A}^{\mathrm{T}}\ \mathbf{B}). \tag{1}$$

Here, $\mathbf{1}$ stands for the identity tensor. The Frobenius norm and the unimodular part are defined as follows

$$\|\mathbf{Y}\| := \sqrt{\mathbf{Y} : \mathbf{Y}} = \sqrt{\mathrm{tr}(\mathbf{Y}^{\mathrm{T}}\ \mathbf{Y})}, \quad \overline{\mathbf{Y}} := (\det(\mathbf{Y}))^{-1/3}\ \mathbf{Y}. \tag{2}$$

2 SMALL STRAIN CASE

Let us consider a small-strain model of an elasto-plastic material with a nonlinear kinematic hardening. The overall infinitesimal strain tensor $\boldsymbol{\varepsilon}$ is decomposed additively into the inelastic (plastic) strain $\boldsymbol{\varepsilon}_{\mathrm{i}}$ and the elastic strain $\boldsymbol{\varepsilon}_{\mathrm{e}}$. The inelastic strain, in turn, is decomposed into the dissipative part $\boldsymbol{\varepsilon}_{\mathrm{ii}}$ and the conservative part $\boldsymbol{\varepsilon}_{\mathrm{ie}}$

$$\boldsymbol{\varepsilon} = \boldsymbol{\varepsilon}_{\mathrm{i}} + \boldsymbol{\varepsilon}_{\mathrm{e}}, \quad \boldsymbol{\varepsilon}_{\mathrm{i}} = \boldsymbol{\varepsilon}_{\mathrm{ii}} + \boldsymbol{\varepsilon}_{\mathrm{ie}}. \tag{3}$$

The Helmholz free energy per unit mass is a sum of the elastic part ψ_{el} and the part ψ_{kin}, related to the kinematic hardening:

$$\psi = \psi(\boldsymbol{\varepsilon}_{\mathrm{e}}, \boldsymbol{\varepsilon}_{\mathrm{ie}}) = \psi_{\mathrm{el}}(\boldsymbol{\varepsilon}_{\mathrm{e}}) + \psi_{\mathrm{kin}}(\boldsymbol{\varepsilon}_{\mathrm{ie}}), \tag{4}$$

$$\rho\psi_{\mathrm{el}}(\boldsymbol{\varepsilon}_{\mathrm{e}}) = \frac{k}{2}(\mathrm{tr}\boldsymbol{\varepsilon}_{\mathrm{e}})^2 + \mu\boldsymbol{\varepsilon}_{\mathrm{e}}^{\mathrm{D}} : \boldsymbol{\varepsilon}_{\mathrm{e}}^{\mathrm{D}}, \quad \rho\psi_{\mathrm{kin}}(\boldsymbol{\varepsilon}_{\mathrm{ie}}) = \frac{c}{2}\boldsymbol{\varepsilon}_{\mathrm{ie}}^{\mathrm{D}} : \boldsymbol{\varepsilon}_{\mathrm{ie}}^{\mathrm{D}}, \tag{5}$$

where ρ is the mass density, k and μ are the elastic constants, and c is the bulk modulus of the substructure. The stress tensor $\boldsymbol{\sigma}$ and the backstress tensor $\mathbf{x}$ are evaluated through

$$\boldsymbol{\sigma} = \rho\frac{\partial\psi_{\mathrm{el}}(\boldsymbol{\varepsilon}_{\mathrm{e}})}{\partial\boldsymbol{\varepsilon}_{\mathrm{e}}}, \quad \mathbf{x} = \rho\frac{\partial\psi_{\mathrm{kin}}(\boldsymbol{\varepsilon}_{\mathrm{ie}})}{\partial\boldsymbol{\varepsilon}_{\mathrm{ie}}}, \tag{6}$$

$$\boldsymbol{\sigma} = k\ \mathrm{tr}(\boldsymbol{\varepsilon}_{\mathrm{e}})\mathbf{1} + 2\mu\ \boldsymbol{\varepsilon}_{\mathrm{e}}^{\mathrm{D}}, \quad \mathbf{x} = c\ \boldsymbol{\varepsilon}_{\mathrm{ie}}^{\mathrm{D}}. \tag{7}$$

Let $K \geq 0$ be the initial uniaxial yield stress of the material. Neglecting the isotropic hardening, the yield function f is then defined by

$$f := \|(\boldsymbol{\sigma} - \mathbf{x})^{\mathrm{D}}\| - \sqrt{\frac{2}{3}}K. \tag{8}$$

The flow rule governing the evolution of $\boldsymbol{\varepsilon}_{\mathrm{i}}$ is given by

$$\dot{\boldsymbol{\varepsilon}}_{\mathrm{i}} = \lambda_{\mathrm{i}}\frac{(\boldsymbol{\sigma} - \mathbf{x})^{\mathrm{D}}}{\|(\boldsymbol{\sigma} - \mathbf{x})^{\mathrm{D}}\|}, \quad \lambda_{\mathrm{i}} \geq 0,\ f \leq 0,\ \lambda_{\mathrm{i}}f = 0. \tag{9}$$

The nonlinear kinematic hardening of Armstrong-Frederick type is described by the rule

$$\dot{\boldsymbol{\varepsilon}}_{\mathrm{ii}} = \lambda_{\mathrm{i}} \; \varkappa \; \mathbf{x}, \tag{10}$$

where $\varkappa \geq 0$ is a material parameter. Taking $(3)_2$ and $(7)_2$ into account, this equation is equivalent to

$$\dot{\mathbf{x}} = c \; \dot{\boldsymbol{\varepsilon}}_{\mathrm{i}} - c \; \lambda_{\mathrm{i}} \; \varkappa \; \mathbf{x}. \tag{11}$$

This structure corresponds to a small-strain version of a rate-independent Maxwell fluid. It is commonly employed to model the evolution of backstresses $\mathbf{x}$ in a hardening/dynamic recovery format. Depending on the formulation, the initial conditions can be set in terms of $\boldsymbol{\sigma}$ and $\mathbf{x}$, or, alternatively, in terms of $\boldsymbol{\varepsilon}_{\mathrm{i}}$ and $\boldsymbol{\varepsilon}_{\mathrm{ii}}$.

This material model is thermodynamically consistent and objective. In the following, its finite strain extensions are analyzed. The crucial part of any extension is how the rate-independent Maxwell equation (11) is modified to the geometrically nonlinear case.

3 PRINCIPLES OF CONSTITUTIVE MECHANICS

Along with the general constitutive restrictions, like objectivity and thermodynamic consistency, some more specific principles will be considered in the presented study.

3.1 W-invariance

In the case of metal plasticity, it is reasonable to consider the following property (cf. [16]). Let $\mathbf{F}$ be the deformation gradient which maps the local reference configuration $\tilde{\mathcal{K}}$ to the current configuration $\mathcal{K}$. For a simple material with initial conditions, the current Kirchhoff stress tensor $\mathbf{S}$ is a function of the local history of $\mathbf{F}$ and a set of initial conditions $\mathcal{Z}_0$:

$$\mathbf{S}(t) = \underset{t_0 \leq t' \leq t}{\mathbf{S}} \big(\mathbf{F}(t'), \mathcal{Z}_0 \big). \tag{12}$$

Next, let $\mathbf{F}_0$ be a second-rank tensor, such that $\det(\mathbf{F}_0) = 1$. Let $\widetilde{\mathcal{K}}^{\mathrm{new}} := \mathbf{F}_0 \widetilde{\mathcal{K}}$ be a new reference configuration. The corresponding new deformation gradient (also known as the relative deformation gradient) is given by

$$\mathbf{F}^{\mathrm{new}}(t) := \mathbf{F}(t) \; \mathbf{F}_0^{-1}. \tag{13}$$

The model (12) is weakly invariant under the transformation (13) if there is

$$\mathcal{Z}_0^{\mathrm{new}} = \mathcal{Z}_0^{\mathrm{new}}(\mathcal{Z}_0, \mathbf{F}_0), \tag{14}$$

such that the material model predicts the same Kirchhoff stresses:

$$\underset{t_0 \leq t' \leq t}{\mathbf{S}} \big(\mathbf{F}(t'), \mathcal{Z}_0 \big) = \underset{t_0 \leq t' \leq t}{\mathbf{S}} \big(\mathbf{F}^{\mathrm{new}}(t'), \mathcal{Z}_0^{\mathrm{new}} \big). \tag{15}$$

If the model (12) is invariant under arbitrary isochoric changes of the reference configuration, we say that it is *weakly invariant* or, shortly, *w-invariant* (cf. [16]). Similar to the classical (strong) invariance, the w-invariance represents a certain symmetry of the constitutive equations. Just as any other symmetry, w-invariance provides insights into the structure of the underlying constitutive equations.

3.2 Pure volumetric-isochoric split

Again, consider the model (12). Let $\overline{\mathbf{F}}(t) := \det(\mathbf{F}(t))^{-1/3}\ \mathbf{F}(t)$ be the isochoric (unimodular) part of the deformation gradient $\mathbf{F}(t)$. We say that (12) exhibits a pure volumetric-isochoric split (v-i split) with elastic volume changes, if

i:
$$\mathrm{tr}\Big(\underset{t_0\le t'\le t}{\mathbf{S}}\Big(\overline{\mathbf{F}}(t'),\mathcal{Z}_0\Big)\Big)\equiv 0,\ \text{whenever}\ \ \mathrm{tr}\ \mathbf{S}|_{t=t_0}=0;$$

ii: there is $\mathcal{Z}_0^{dev}=\mathcal{Z}_0^{dev}(\mathcal{Z}_0)$ such that
$$\Big(\underset{t_0\le t'\le t}{\mathbf{S}}\big(\mathbf{F}(t'),\mathcal{Z}_0\big)\Big)^{\mathrm{D}}\equiv\underset{t_0\le t'\le t}{\mathbf{S}}\big(\overline{\mathbf{F}}(t'),\mathcal{Z}_0^{dev}\big);$$

iii: $\mathrm{tr}\big(\mathbf{S}(t)\big)$ is a function of the instant value $\det\big(\mathbf{F}(t)\big)$.

The most crucial part here is the condition i. Indeed, consider, for example, a model where the initial conditions are formulated with respect to the Kirchhoff stresses: $\mathcal{Z}_0=\{\mathbf{S}|_{t=t_0}\}$. If the property i is satisfied for a certain model, then the properties ii and iii can be enforced by putting

$$\underset{t_0\le t'\le t}{\mathbf{S}}\big(\mathbf{F}(t'),\mathbf{S}|_{t=t_0}\big):=\underset{t_0\le t'\le t}{\mathbf{S}}\big(\overline{\mathbf{F}}(t'),(\mathbf{S}|_{t=t_0})^{\mathrm{D}}\big)+p\big(\det(\mathbf{F}(t))\big)\mathbf{1},\tag{16}$$

where $p=\frac{1}{3}\mathrm{tr}\ \mathbf{S}$ is a suitable function of the current $\det\mathbf{F}$.

Note that a certain volumetric-isochoric split is satisfied by the small strain model presented in the previous section. Therefore, it is natural to expect the v-i split in the finite strain context as well.

4 GENERALIZATIONS TO FINITE STRAINS

4.1 Hyperelasto-plasticity with a nested multiplicative split

We discuss here a special case of a multiplicative viscoplasticity, which was proposed in [17]. First, consider a multiplicative split of the deformation gradient $\mathbf{F}$ into the inelastic (plastic) part $\mathbf{F}_{\mathrm{i}}$ and the elastic part $\mathbf{F}_{\mathrm{e}}$. Next, basing on the seminal idea of Lion [8], the inelastic part $\mathbf{F}_{\mathrm{i}}$ is decomposed into the dissipative part $\mathbf{F}_{\mathrm{ii}}$ and the conservative (energetic) part $\mathbf{F}_{\mathrm{ie}}$:
$$\mathbf{F}=\mathbf{F}_{\mathrm{e}}\mathbf{F}_{\mathrm{i}},\quad \mathbf{F}_{\mathrm{i}}=\mathbf{F}_{\mathrm{ie}}\mathbf{F}_{\mathrm{ii}}.\tag{17}$$
Note that the kinematic relations (3) are restored from (17) in the small strain case.

The right Cauchy-Green tensor (RCGT) $\mathbf{C}$, the inelastic RCGT $\mathbf{C}_{\mathrm{i}}$, and the inelastic RCGT of substructure $\mathbf{C}_{\mathrm{ii}}$ are defined through
$$\mathbf{C}:=\mathbf{F}^{\mathrm{T}}\mathbf{F},\quad \mathbf{C}_{\mathrm{i}}:=\mathbf{F}_{\mathrm{i}}^{\mathrm{T}}\mathbf{F}_{\mathrm{i}},\quad \mathbf{C}_{\mathrm{ii}}:=\mathbf{F}_{\mathrm{ii}}^{\mathrm{T}}\mathbf{F}_{\mathrm{ii}}.\tag{18}$$

Analogously to (4), the free energy per unit mass is represented in the form
$$\psi=\psi_{\mathrm{el}}(\mathbf{C}\mathbf{C}_{\mathrm{i}}{}^{-1})+\psi_{\mathrm{kin}}(\mathbf{C}_{\mathrm{i}}\mathbf{C}_{\mathrm{ii}}{}^{-1}),\tag{19}$$

where $\psi_{\mathrm{el}}(\cdot)$ and $\psi_{\mathrm{kin}}(\cdot)$ are isotropic functions. To be definite, neo-Hookean assumptions are used for the deviatoric part of the free energy

$$\rho_{\mathrm{R}}\psi_{\mathrm{el}} = \rho_{\mathrm{R}}\psi_{\mathrm{vol}}(\det(\mathbf{C}\mathbf{C}_{\mathrm{i}}^{-1})) + \frac{\mu}{2}\big(\mathrm{tr}\overline{\mathbf{C}\mathbf{C}_{\mathrm{i}}^{-1}} - 3\big), \quad \rho_{\mathrm{R}}\psi_{\mathrm{kin}} = \frac{c}{4}\big(\mathrm{tr}\overline{\mathbf{C}_{\mathrm{i}}\mathbf{C}_{\mathrm{ii}}^{-1}} - 3\big), \tag{20}$$

where $\rho_{\mathrm{R}} > 0$ is the mass density in the reference configuration, μ and c have the same meaning as in the small strain case. We do not specify the volumetric part ψ_{vol}, since it is irrelevant for the current study. The second Piola-Kirchhoff stress $\tilde{\mathbf{T}}$ and the backstress $\tilde{\mathbf{X}}$, both operating on $\tilde{\mathcal{K}}$, are computed through

$$\tilde{\mathbf{T}} = 2\rho_{\mathrm{R}}\frac{\partial\psi_{\mathrm{el}}(\mathbf{C}\mathbf{C}_{\mathrm{i}}^{-1})}{\partial\mathbf{C}}\Big|_{\mathbf{C}_{\mathrm{i}}=\mathrm{const}}, \quad \tilde{\mathbf{X}} = 2\rho_{\mathrm{R}}\frac{\partial\psi_{\mathrm{kin}}(\mathbf{C}_{\mathrm{i}}\mathbf{C}_{\mathrm{ii}}^{-1})}{\partial\mathbf{C}_{\mathrm{i}}}\Big|_{\mathbf{C}_{\mathrm{ii}}=\mathrm{const}}. \tag{21}$$

Using (20) we arrive at

$$\tilde{\mathbf{T}} = p(\det(\mathbf{C}))\ \mathbf{C}^{-1} + \mu\ \mathbf{C}^{-1}(\overline{\mathbf{C}}\mathbf{C}_{\mathrm{i}}^{-1})^{\mathrm{D}},\ p\in\mathbb{R}, \quad \tilde{\mathbf{X}} = \frac{c}{2}\ \mathbf{C}_{\mathrm{i}}^{-1}(\mathbf{C}_{\mathrm{i}}\mathbf{C}_{\mathrm{ii}}^{-1})^{\mathrm{D}}. \tag{22}$$

The norm of the driving force $\mathfrak{F}$ and the yield function f are defined through

$$\mathfrak{F} := \sqrt{\mathrm{tr}\big[\big(\mathbf{C}\tilde{\mathbf{T}} - \mathbf{C}_{\mathrm{i}}\tilde{\mathbf{X}}\big)^{\mathrm{D}}\big]^2}, \quad f := \mathfrak{F} - \sqrt{\frac{2}{3}}K. \tag{23}$$

The inelastic flow is described by the following system of constitutive equations

$$\dot{\mathbf{C}}_{\mathrm{i}} = 2\frac{\lambda_{\mathrm{i}}}{\mathfrak{F}}\big(\mathbf{C}\tilde{\mathbf{T}} - \mathbf{C}_{\mathrm{i}}\tilde{\mathbf{X}}\big)^{\mathrm{D}}\mathbf{C}_{\mathrm{i}}, \quad \dot{\mathbf{C}}_{\mathrm{ii}} = 2\lambda_{\mathrm{i}}\varkappa(\mathbf{C}_{\mathrm{i}}\tilde{\mathbf{X}})^{\mathrm{D}}\mathbf{C}_{\mathrm{ii}}, \tag{24}$$

$$\lambda_{\mathrm{i}} \geq 0,\ f \leq 0,\ \lambda_{\mathrm{i}} f = 0. \tag{25}$$

Finally, the initial conditions are formulated in terms of $\mathbf{C}_{\mathrm{i}}$ and $\mathbf{C}_{\mathrm{ii}}$.

This material model is thermodynamically consistent (cf. [17]) and objective. As shown in [20], the material model is w-invariant. Since the evolution of internal variables $\mathbf{C}_{\mathrm{i}}$ and $\mathbf{C}_{\mathrm{ii}}$ depends on $\bar{\mathbf{C}}$, this model exhibits the pure v-i split. Within the elastic range, the stress response is hyperelastic. The model is free from any spurious oscillations of shear stresses under monotonic simple shear. As shown in [22], the w-invariance allows one to build an efficient numerical procedure (one-equation integrator) for this model. Various extensions of this model are presented, among others, in [19, 21, 23, 18]. An alternative derivation of the model was presented in [5]. The practical application of the w-invariance of this model is discussed in [20, 14].

4.2 Logarithmic strain with the small strain structure

Another popular approach to the finite strain elasto-plasticity adopts the structure of the geometrically linear theory (3) – (11) (cf. [12, 9, 15]). Let $\mathbf{H}$ be the Lagrangian logarithmic strain (Hencky strain)

$$\mathbf{H}(t) := \frac{1}{2}\ln(\mathbf{C}(t)). \tag{26}$$

The infinitesimal strain tensor which appears in the geometrically linear theory, is replaced now by the logarithmic strain: $\boldsymbol{\varepsilon}(t) := \mathbf{H}(t)$. Let $\boldsymbol{\sigma}(t)$ be the stress tensor, computed by the small strain theory as a response to $\boldsymbol{\varepsilon}(t)$. In the finite strain case, $\boldsymbol{\sigma}$ is understood as a Lagrangian stress measure which is power conjugate to the logarithmic strain $\mathbf{H}$:

$$\boldsymbol{\sigma} : \dot{\mathbf{H}} = \widetilde{\mathbf{T}} : \left(\frac{1}{2}\dot{\mathbf{C}}\right) \quad \text{for all} \quad \dot{\mathbf{C}} \in Sym. \tag{27}$$

Using this identity, we obtain the following formula for the second Piola-Kirchhoff $\widetilde{\mathbf{T}}$

$$\widetilde{\mathbf{T}} = \frac{\partial \ln(\mathbf{C})}{\partial \mathbf{C}} : \boldsymbol{\sigma}. \tag{28}$$

The resulting finite strain model is objective. Since the small-strain model (3) – (11) is thermodynamically consistent, so is its finite-strain counterpart. The model is free from the shear stress oscillations (cf. Section 5). The stress response in the elastic domain is hyperelastic. The model exhibits a pure v-i split. Efficient and robust numerical procedures are available for this approach. Unfortunately, this model is not w-invariant (this can be shown using a procedure, presented in [16]). Since the constitutive equations depend on the choice of the reference configuration, one needs to specify exactly, which configuration is used as a reference.

4.3 Hypoelasto-plasticity with an additive split

Another major modelling framework is based on a nested additive split of the strain rate tensor, used in combination with hypoelastic relations (cf. [10, 11]). Let $\mathbf{L} := \dot{\mathbf{F}}\mathbf{F}^{-1}$ be the velocity gradient. Its symmetric part, called the strain rate $\mathbf{D} := \mathrm{sym}(\mathbf{L})$, is decomposed into the inelastic (plastic) part $\mathbf{D}_\mathrm{i}$ and the elastic part $\mathbf{D}_\mathrm{e}$. The inelastic part itself is decomposed into the dissipative part $\mathbf{D}_\mathrm{ii}$ and the conservative part $\mathbf{D}_\mathrm{e}$

$$\mathbf{D} = \mathbf{D}_\mathrm{e} + \mathbf{D}_\mathrm{i}, \quad \mathbf{D}_\mathrm{i} = \mathbf{D}_\mathrm{ii} + \mathbf{D}_\mathrm{ie}. \tag{29}$$

These relations can be seen as a generalization of (3). Let $\mathbf{S}$ and $\mathbf{X}$ be the Kirchhoff stress and the backstress, respectively, both operating on the current configuration $\mathcal{K}$. Denote by $\overset{\circ}{\mathbf{Y}}$ an objective time derivative of a second-rank tnesor $\mathbf{Y}$. As a generalization of (7), we consider the following hypoelastic relations

$$\overset{\circ}{\mathbf{S}} = k\ \mathrm{tr}(\mathbf{D}_\mathrm{e})\mathbf{1} + 2\mu\mathbf{D}_\mathrm{e}^\mathrm{D}, \quad \overset{\circ}{\mathbf{X}} = c\mathbf{D}_\mathrm{ie}, \tag{30}$$

where k, μ, and c were already introduced in (7). These equations corresponds to the grade-zero hypoelasticity. Next, the yield function is postulated in the form (cf. (8))

$$f := \|(\mathbf{S} - \mathbf{X})^\mathrm{D}\| - \sqrt{2/3}K, \tag{31}$$

where $K > 0$ is the initial uniaxial yield stress. The inelastic flow is governed by (cf. (9) and (10))

$$\mathbf{D}_\mathrm{i} = \lambda_\mathrm{i} \frac{(\mathbf{S} - \mathbf{X})^\mathrm{D}}{\|(\mathbf{S} - \mathbf{X})^\mathrm{D}\|}, \quad \mathbf{D}_\mathrm{ii} = \lambda_\mathrm{i}\ \varkappa\ \mathbf{X}, \tag{32}$$

$$f \leq 0,\ \lambda_{\mathrm{i}} \geq 0,\ f\lambda_{\mathrm{i}} = 0. \tag{33}$$

The initial conditions are imposed on the Kirchhoff stresses $\mathbf{S}$ and the backstress $\mathbf{X}$.

Different models can be build by using different objective stress rates which appears in (30). Some authors apply the so-called *yield stationarity criterion*, which was proposed by Prager in [13]. For the models, where the yield function f is a general isotropic function of $\mathbf{S}$ and $\mathbf{X}$, the yield stationarity requires that $f = const$ whenever $\overset{\circ}{\mathbf{S}} = \overset{\circ}{\mathbf{X}} = \mathbf{0}$. As shown in [26], the yield stationarity implies that the objective rates $\overset{\circ}{\mathbf{S}}$ and $\overset{\circ}{\mathbf{X}}$ must be corotational rates of the same type. In other words, the yield stationarity implies

$$\overset{\circ}{\mathbf{S}} = \dot{\mathbf{S}} + \mathbf{S}\boldsymbol{\Omega} - \boldsymbol{\Omega}\mathbf{S}, \quad \overset{\circ}{\mathbf{X}} = \dot{\mathbf{X}} + \mathbf{X}\boldsymbol{\Omega} - \boldsymbol{\Omega}\mathbf{X}, \quad \boldsymbol{\Omega} \in \mathrm{Skew}. \tag{34}$$

Here, Skew stands for the set of skew-symmetric tensors, the skew-symmetric operator $\boldsymbol{\Omega}$ is referred to as a spin tensor, superimposed dot stands for the material time derivative. There are infinitely many ways of defining the spin tensor $\boldsymbol{\Omega}$ [25, 7, 3]. Clearly, the properties of the resulting material model depend on the specific choice of the spin $\boldsymbol{\Omega}$. In particular, we have the following theorem (cf. [16]):

Theorem. *Constitutive relations* (29)—(34) *are w-invariant if and only if the spin tensor* $\boldsymbol{\Omega}$ *does not depend on the choice of the reference configuration.*

Let us consider some of the commonly used spins.

Zaremba-Jaumann rate. Fot the Zaremba-Jaumann rate (also known as the Zaremba-Jaumann-Noll rate), we put

$$\boldsymbol{\Omega}^{ZJ} := \mathbf{W} = \mathrm{skew}(\mathbf{L}), \quad \overset{\circ}{\mathbf{Y}}{}^{ZJ} := \dot{\mathbf{Y}} + \mathbf{Y}\boldsymbol{\Omega}^{ZJ} - \boldsymbol{\Omega}^{ZJ}\mathbf{Y}. \tag{35}$$

Note that the continuum spin $\mathbf{W} = \mathrm{skew}(\mathbf{L})$ does not depend on the choice of the reference configuration. Therefore, the corresponding system of equations is w-invariant. One major drawback of this approach is that the stress response exhibits non-physical oscillations under the simple shear: The shear stress oscillates like $\sin(\gamma)$, where γ is the shear strain. These oscillations may lead to absurd results in case of kinematic hardening, although the elastic strains may remain small (cf. Section 5). Another drawback is that the material response fails to become hyperelastic in case of a frozen inelastic flow (when $\lambda_{\mathrm{i}} = 0$).

Green-Naghdi rate. In order to define the Green-Naghdi rate (also known as the Green-Naghdi-Dienes rate, Green-McInnis rate or polar rate) we consider the polar decomposition of the deformation gradient: $\mathbf{F} = \mathbf{RU} = \mathbf{VR}$. Then we put

$$\boldsymbol{\Omega}^{GN} := \dot{\mathbf{R}}\mathbf{R}^{\mathrm{T}} \in \mathrm{Skew}, \quad \overset{\circ}{\mathbf{Y}}{}^{GN} := \dot{\mathbf{Y}} + \mathbf{Y}\boldsymbol{\Omega}^{GN} - \boldsymbol{\Omega}^{GN}\mathbf{Y}. \tag{36}$$

Unfortunately, the spin $\boldsymbol{\Omega}^{GN}$ depends on the choice of the reference configuration [6, 16]. Thus, the corresponding system of equations is not w-invariant. On the other hand, such a model is free from spurious shear oscillations (see Section 5). Just as in the previous case, the corresponding material model fails to provide a hyperelastic response even for a frozen inelastic flow.

Logarithmic rate. Let $\mathbf{V}$ be the left stretch tensor ($\mathbf{V} := \sqrt{\mathbf{F}\mathbf{F}^{\mathrm{T}}}$). The logarithmic stress rate is given by

$$\overset{\circ}{\mathbf{S}}{}^{\log} := \dot{\mathbf{S}} + \mathbf{S}\boldsymbol{\Omega}^{\log} - \boldsymbol{\Omega}^{\log}\mathbf{S}, \tag{37}$$

where the logarithmic spin $\boldsymbol{\Omega}^{\log} = \boldsymbol{\Omega}^{\log}(\mathbf{V}, \mathbf{L})$ is uniquely defined by the relation (cf. [24, 27])

$$\mathbf{D} = (\ln \overset{\circ}{\mathbf{V}})^{\log}. \tag{38}$$

The following statement was proved in [2]: Dealing with grade-zero hypoelasticity with corotational rates and constant elastic stiffness, the logarithmic stress rate *is the only choice* which allows one to build integrable stress-strain relations in the elastic range. For that reason, the logarithmic rate enjoys a privileged position among all the corotational rates. As was shown in [16], the spin $\boldsymbol{\Omega}^{\log}$ depends on the choice of the reference configuration. Therefore, the corresponding material model is not w-invariant. In the purely elastic case, the stress response reduces to a special type of hyperelasticity, where the strain energy function is given by a quadratic function of the Hencky strain. This elastic potential is known to produce absurd results for large elastic strains.

In a summary, it is *impossible* to build a material model of type (29)–(33), which would combine the yield stationarity, w-invariance and exact integrability of the elastic part. On the other hand, a positive feature of the corotational spin (34) is that the corresponding models always exhibit the pure v-i split. Now, in an attempt to build a model, which would be objective, w-invariant, and exactly integrable in the elastic domain, we proceed to non-corotational rates.

Covariant Oldroyd rate. The covariant Oldroyd rate (also known as the lower Oldroyd rate or the Cotter-Rivlin rate) of a Eulerian tensor $\mathbf{Y}$ is defined by

$$\mathfrak{O}_{covar}(\mathbf{Y}) := \dot{\mathbf{Y}} + \mathbf{L}^{\mathrm{T}}\ \mathbf{Y} + \mathbf{Y}\ \mathbf{L}. \tag{39}$$

A material model of type (29)–(33), based on this stress rate, is objective and w-invariant. One remarkable property of this rate is that for the Almansi strain $\mathbf{A}$ we have

$$\mathfrak{O}_{covar}(\mathbf{A}) = \mathbf{D}, \quad \text{where } \mathbf{A} := \frac{1}{2}(\mathbf{1} - \mathbf{F}^{-\mathrm{T}}\mathbf{F}^{-1}). \tag{40}$$

Thus, the stress response is exactly integrable whenever $\lambda_{\mathrm{i}} = 0$. Unfortunately, the corresponding model does not exhibit the pure v-i split: Even if the prescribed strain rate $\mathbf{D}$ is trace-free and the initial stresses are deviatoric, the natural condition $\mathrm{tr}\mathbf{S} = \mathrm{tr}\mathbf{X} = 0$ is violated. Nevertheless, although Prager's yield stationarity condition is violated by this model, the model allows one to obtain plausible results (see Section 5).

The corresponding rate-independent Maxwell fluid is a scleronomous version of the covaraint Maxwell model (cf. [4]).

Deviatorized covariant Oldroyd rate. In an attempt to enforce the pure v-i split we consider a deviatorized covariant Oldroyd rate as follows

$$\mathfrak{O}^{dev}_{covar}(\mathbf{Y}) := \mathfrak{O}_{covar}(\mathbf{Y}) - \frac{2}{3}(\mathbf{Y} : \mathbf{D})\mathbf{1} = \dot{\mathbf{Y}} + \mathbf{L}^{\mathrm{T}}\ \mathbf{Y} + \mathbf{Y}\ \mathbf{L} - \frac{2}{3}(\mathbf{Y} : \mathbf{D})\mathbf{1}. \tag{41}$$

The corresponding material model is objective and w-invaraint; the pure v-i split holds true. According to the available analytical solutions (cf. [1]), the stress rate (41) produces an oscillatory response to the monotonic simple shear even in the purely elastic case. The

shear stress oscillates like $\sin(\sqrt{\frac{2}{3}}\gamma)$, where γ is the shear strain. Thus, the oscillation frequency is slightly lower than in the case of the Zaremba-Jaumann stress rate. In general, this model should not be used if the elastic strains in the corresponding rate-independent Maxwell body exceed a certain limit (see Section 5).

Contravariant Oldroyd rate. The contravariant Oldroyd rate (upper Oldroyd rate) is defined as,

$$\mathfrak{O}_{contravar}(\mathbf{Y}) := \dot{\mathbf{Y}} - \mathbf{L}\mathbf{Y} - \mathbf{Y}\mathbf{L}^{\mathrm{T}}. \tag{42}$$

The corresponding material model is objective and w-invariant. The contravariant rate of the Finger tensor $\mathbf{a}$ is related to the strain rate in the following way:

$$\mathfrak{O}_{contravar}(\mathbf{a}) = -\mathbf{D}, \quad \text{where } \mathbf{a} := \frac{1}{2}(\mathbf{1} - \mathbf{F}\mathbf{F}^{\mathrm{T}}). \tag{43}$$

Thus, this stress rate allows one to obtain exactly integrable response in the elastic range. Unfortunately, just as for the covariant rate, the corresponding material model does not exhibit the pure v-i split. Although the model violates Prager's yield stationarity, it allows one to obtain a reasonable stress response, even dealing with linear and nonlinear kinematic hardening (see Section 5). The underlying Maxwell fluid is a scleronomous version of the contravaraint Maxwell model (cf. [4]).

Deviatorized contravariant Oldroyd rate. In order to enforce the pure v-i split, we consider now a deviatorized variant of the contravariant Oldroyd rate

$$\mathfrak{O}^{dev}_{contravar}(\mathbf{Y}) := \mathfrak{O}_{contravar}(\mathbf{Y}) + \frac{2}{3}(\mathbf{Y} : \mathbf{D})\mathbf{1} = \dot{\mathbf{Y}} - \mathbf{L}\mathbf{Y} - \mathbf{Y}\mathbf{L}^{\mathrm{T}} + \frac{2}{3}(\mathbf{Y} : \mathbf{D})\mathbf{1}. \tag{44}$$

The resulting system of constitutive equations is objective and w-invaraint; the pure v-i split is satisfied. An analytical solution is available for the simple shear (cf. [1]); the solution says that the stresses oscillate like $\sin(\sqrt{\frac{2}{3}}\gamma)$, where γ is the shear strain. Just as its covariant counterpart, this model should not be implemented if the elastic strains in the rate-independent Maxwell body exceed a certain limit (see Section 5).

5 NUMERICAL RESULTS

Let us simulate a stress response under the non-monotonic simple shear

$$\mathbf{F}(t) = \mathbf{1} + \gamma(t)\mathbf{e}_x \otimes \mathbf{e}_y, \quad \gamma(t) = \min(5t, 10 - 5t), \quad t \in [0, 2]. \tag{45}$$

The following material parameters are used (all quantities are non-dimensional): $K = 1$, $\mu = 10$, $c = 0.5$, $\varkappa = 0.5$. Since the simple shear is isochoric, the bulk modulus k is irrelevant. Since the elastic strains accumulated in the rate-independent Maxwell fluid are large, second-order effects like the stress oscillation and Poynting/Swift effect are clearly visible (see Figure 1). Plausible results are predicted by the multiplicative model (Section 4.1) and the hypoelasto-plasticity with logarithmic rate (Section 4.3). Unrealistic shear stresses are observed for oscillating models (Zaremba-Jaumann, deviatorized contravariant and covariant Oldroyd); the small-strain-structure-model with the logarithmic strain (Section 4.2) exhibits very strong isotropic softening, caused by the model kinematics.

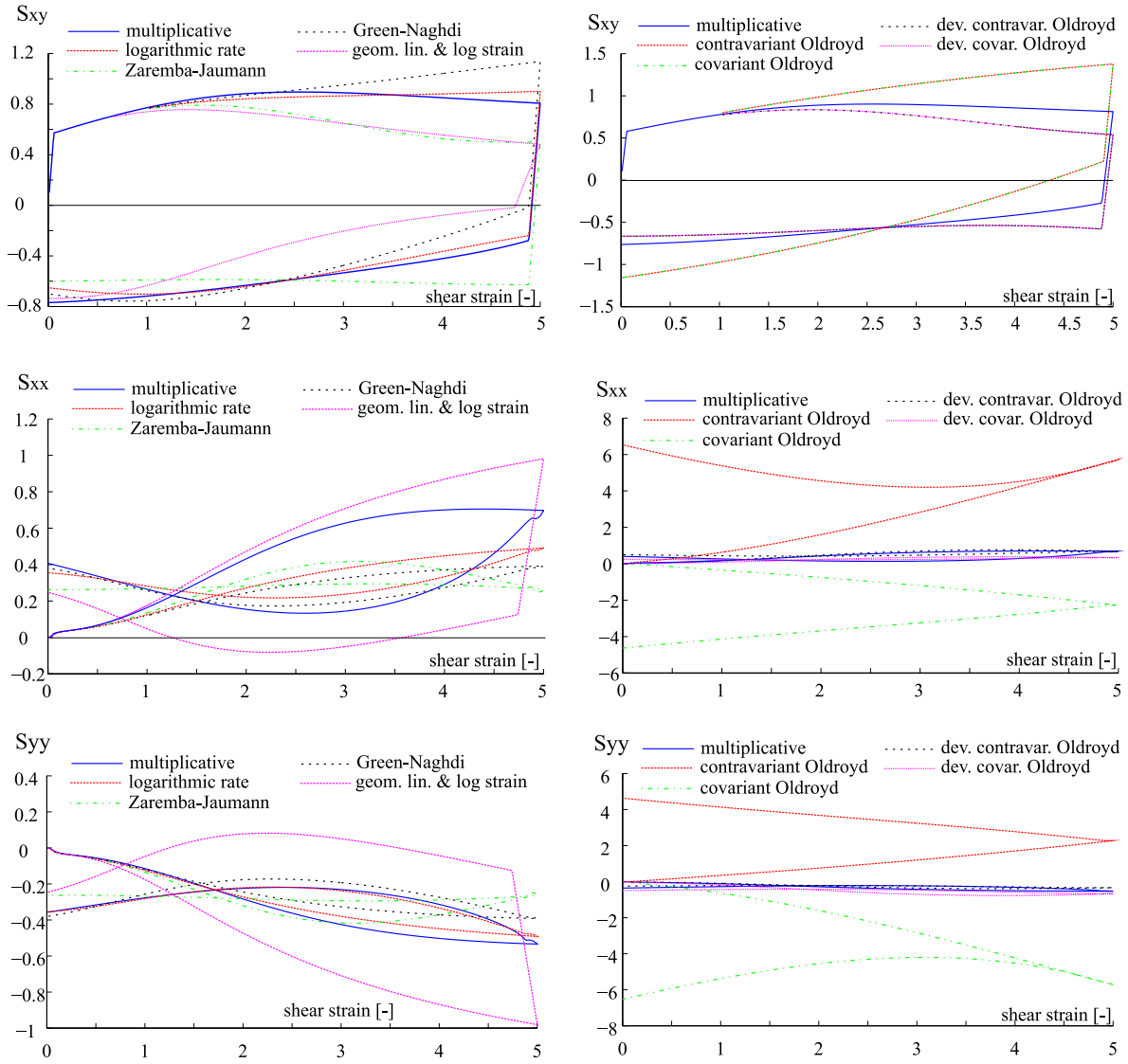

Figure 1: Simulations results for non-monotonic simple shear using different material models

6 CONCLUSIONS

Nine different models of finite strain plasticity with the nonlinear kinematic hardening are analyzed in a qualitative way, using a number of criteria. The model based on the multiplicative split (Section 4.1) is the only model which combines objectivity, thermodynamic consistency, w-invariance, and the pure v-i split.

Acknowledgement: The research was supported by the Russian Science Foundation (project number 15-11-20013).

REFERENCES

[1] Alturi S.N. On constitutive relations at finite strain: hypo-elasticity and elasto-plasticity with isotropic or kinematic hardening, *Comput. Methods Appl. Mech. En-*

grg. (1984) **43**: 137–171.

[2] Bruhns, O.T., Xiao, H. and Meyers, A. Self-consistent Eulerian rate type elasto-plasticity models based upon the logarithmic stress rate. *Int. J. Plast.* (1999) **15**: 479–520.

[3] Hashiguchi, K. and Yamakawa, Y. *Introduction to Finite Strain Theory for Continuum Elasto-Plasticity*. John Wiley & Sons (2012).

[4] Haupt, P. and Lion, A. On finite linear viscoelasticity of incompressible isotropic materials. *Acta Mech.* (2002) **159**: 87–124.

[5] Kießling, R., Landgraf, R., Scherzer, R. and Ihlemann, J. Introducing the concept of directly connected rheological elements by reviewing rheological models at large strains. *Int. J. Solids Struct.* (2016) **97-98**: 650–667.

[6] Korobeynikov, S.N. Objective tensor rates and applications in formulation of hyper-elastic relations. *Journal of Elasticity* (2008) **93**(2): 105–140.

[7] Korobeynikov, S.N. Families of continuous spin tensors and applications in continuum mechanics. *Acta Mech.* (2011) **216**: 301–332.

[8] Lion, A. Constitutive modelling in finite thermoviscoplasticity: a physical approach based on nonlinear rheological elements. *Int. J. Plast.* (2000) **16**: 469–494.

[9] Miehe, C., Apel, N. and Lambrecht, M. Anisotropic additive plasticity in the logarithmic strain space: modular kinematic formulation and implementation based on incremental minimization principles for standard materials. *Comput. Methods Appl. Mech. Engrg.* (2002) **191**: 5383–5425.

[10] Neale, K.W. Phenomenological constitutive laws in finite plasticity. *Solid Mech. Arch.* (1981) **6**: 79–128.

[11] Nemat-Nasser, S. On finite deformation elastoplasticity. *Int. J. Solids Struct.* (1982) **18**: 857–872.

[12] Papadopoulus, P. and Lu, J. A general framework for the numerical solution of problems in finite elasto-plasticity. *Comput. Methods Appl. Mech. Engrg.* (1998) **159**: 1–18.

[13] Prager, W. An elementary discussion of definitions of stress rate. *Quart. Appl. Math.* (1960) **18**: 403–407.

[14] Scherzer, R., Silbermann, C.B., Landgraf, R. and Ihlemann, J. FE-simulation of the Presta joining process for assembled camshafts modelling of the joining process. *IOP Conf. Series: Materials Science and Engineering* (2017) **181** 012030 doi:10.1088/1757-899X/181/1/012030

[15] Schröder, J., Gruttmann, F. and Löblein, J. A simple orthotropic finite elasto-plasticity model based on generalized stress-strain measures. *Computational Mechanics* (2002) **30**: 48–64.

[16] Shutov, A.V. and Ihlemann, J. Analysis of some basic approaches to finite strain elasto-plasticity in view of reference change. *Int. J. Plast.* (2014) **63**: 183–197.

[17] Shutov, A.V. and Kreißig, R. Finite strain viscoplasticity with nonlinear kinematic hardening: Phenomenological modeling and time integration. *Comput. Methods Appl. Mech. Engrg.* (2008) **197**: 2015–2029.

[18] Shutov, A.V., Larichkin, A. Yu. and Shutov, A.V. Modelling of cyclic creep in the finite strain range using a nested split of the deformation gradient. *Z. Angew. Math. Mech.* (2017) DOI 10.1002/zamm.201600286 .

[19] Shutov, A.V., Panhans, S. and Kreißig, R. A phenomenological model of finite strain viscoplasticity with distortionalhardening. *Z. Angew. Math. Mech.*, (2011) **91**(8): 653–680.

[20] Shutov, A. V., Pfeiffer, S. and Ihlemann, J. On the simulation of multi-stage forming processes: invariance under change of the reference configuration. *Mat.-wiss. u. Werkstofftech.* (2012) **43**(7): 617–625.

[21] Shutov, A.V., Silbermann, C.B. and Ihlemann, J. Ductile damage model for metal forming simulations including refined description of void nucleation. *Int. J. Plast.* (2015) **71**: 195–217.

[22] Shutov, A.V. Efficient implicit integration for finite-strain viscoplasticity with a nested multiplicative split. *Comput. Methods Appl. Mech. Engrg.* (2016) **306**(1): 151–174.

[23] Silbermann, C.B., Shutov, A.V. and Ihlemann, J. Modeling the evolution of dislocation populations under non-proportional loading. *Int. J. Plast.* (2014) **55**: 58–79.

[24] Xiao, H., Bruhns, O.T. and Meyers, A. Logarithmic strain, logarithmic spin and logarithmic rate. *Acta Mech.* (1997) **124**: 89–105.

[25] Xiao, H., Bruhns, O.T. and Meyers, A. On objective corotational rates and their defining spin tensors. *Int. J. Solids Struct.* (1998) **35**(30): 4001–4014.

[26] Xiao, H., Bruhns, O. T.and Meyers, A. The choice of objective rates in finite elasto-plasticity: General results on the uniqueness of the logarithmic rate. *Proc. Roy. Soc. London A* (2000) **456**, 1865–1882.

[27] Zhilin, P.A., Altenbach, H., Ivanova, E.A. and Krivtsov, A.M. Material Strain Tensor, in *Generalized Continua as Models for Materials* (2013) 321–331.

XIV International Conference on Computational Plasticity. Fundamentals and Applications
COMPLAS XIV
E. Oñate, D.R.J. Owen, D. Peric & M. Chiumenti (Eds)

NUMERICAL INTEGRATION OF THE INCREMENTALLY NON-LINEAR, ZERO ELASTIC RANGE, BOUNDING SURFACE PLASTICITY MODEL FOR SAND

A. L. Petalas *, **Y. F. Dafalias**†

* Department of Civil and Enviromental Engineering, University of California, Davis, USA
e-mail: alpetalas@ucdavis.edu

†Department of Civil and Enviromental Engineering, University of California, Davis, USA
and Department of Mechanics, Faculty of Applied Mathematical and Physical Sciences,
National Technical University of Athens, Greece
e-mail: jfdafalias@ucdavis.edu

Key words: constitutive equations, computational plasticity, implicit integration, bounding surface plasticity, zero elastic range

Abstract. SANISAND-Z is a recently developed plasticity model for sands with zero purely elastic range in stress space within the framework of Bounding Surface (BS) plasticity. As a consequence of zero elastic range the plastic strain increment direction, and consequently the elastic-plastic moduli fourth order tensor depends on the direction of the stress increment, rendering the model incrementally non-linear and intrinsically implicit. An iterative algorithm based on the Backward Euler method is presented to solve the non-linear system of ordinary differential equations. A non-traditional consistency condition based on the plastic multiplier is introduced as a core element of the system. A thorough analysis of the stability and accuracy of the algorithm is presented based on error estimation. The proposed integration scheme allows the use of SANISAND-Z framework in Finite Element Analysis.

1 INTRODUCTION

The idea of zero elastic range in plasticity theory was first presented by Dafalias [1] and the physical motivation was the effort to simulate the response of artificial graphite, a material which exhibits zero purely elastic range in loading and unloading [2].

In the zero elastic range bounding surface (BS) plasticity the yield surface shrinks to zero, the surface degenerates to the current stress point and the BS determines the loading direction and plastic modulus. The "image" point on the BS, at which the plastic strain rate direction is defined, is the intersection of a line along the stress increment direction with the BS. Thus, the plastic strain increment direction and consequently the fourth order elastic-plastic moduli fourth order tensor depends on the stress increment direction, rendering the model incrementally non-linear.

The numerical consequence of this type of formulation is that the model is intrinsically implicit. To solve incrementally the elasto-plastic constitutive equations, and compute the stress increment based on a given strain increment, the stress increment direction has to be specified. An iterative numerical integration scheme is proposed in this work.

2 SANISAND-Z: The model

The Sanisand-Z model developed by Dafalias and Taiebat [3] is based on the zero elastic range BS plasticity framework and the two surface formulation for sands which was presented by Manzari and Dafalias [4], Dafalias and Manzari [5] and Taiebat and Dafalias [6]. A brief discussion for the model's formulation is presented in this section, and for more details and illustrations the reader is referred to [3].

The hypoelastic moduli, K and G, are defined as functions of the isotropic stress p and the current void ratio e by:

$$G = G_0 p_{at} \frac{(2.97 - e)^2}{1 + e} \left(\frac{p}{p_{at}} \right)^{1/2} \tag{1}$$

$$K = \frac{2(1 + \nu)}{3(1 - 2\nu)} G \tag{2}$$

where p_{at} is the atmospheric pressure, ν is the poisson's ratio and G_0 a material constant.

The bounding surface (BS) and the dilatancy surface (DS) are lode angle independent and given by:

$$F^b = (\boldsymbol{r}^b : \boldsymbol{r}^b)^{1/2} - \sqrt{\frac{2}{3}} M^b = 0; \quad M^b = exp(-n^b \psi) \tag{3}$$

$$F^d = (\boldsymbol{r}^d : \boldsymbol{r}^d)^{1/2} - \sqrt{\frac{2}{3}} M^d = 0; \quad M^d = exp(-n^d \psi) \tag{4}$$

where $\boldsymbol{r} = \boldsymbol{s}/p$ is the deviatoric stress ratio tensor, n^d and n^b are material constants, and ψ is the soil state parameter [7].

The "image" point on the BS is the intersection of a line along the stress increment direction and the circular BS:

$$\boldsymbol{r}^b = \boldsymbol{r} + b\boldsymbol{\nu}; \quad b = -\boldsymbol{r} : \boldsymbol{\nu} + \left[(\boldsymbol{r} : \boldsymbol{\nu})^2 + (2/3)(M^b)^2 - \boldsymbol{r} : \boldsymbol{r} \right]^{1/2} \tag{5}$$

where $\boldsymbol{\nu}$ is a unit norm deviatoric tensor along the stress increment direction on the deviatoric plane, and b is the distance of the current stress point to the BS along the direction of the stress increment.

The loading direction is defined at the "image" point by:

$$\boldsymbol{n} = \frac{\partial F^b}{\partial \boldsymbol{r}^b} = \frac{\boldsymbol{r}^b}{|\boldsymbol{r}^b|} \tag{6}$$

Based on the loading direction the "image" point on the DS surface is given by:

$$\boldsymbol{r}^d = \sqrt{\frac{2}{3}} M^d \boldsymbol{n} \tag{7}$$

For the plastic strain rate direction $\boldsymbol{R}$= $\boldsymbol{R'}$+(1/3)D$\boldsymbol{I}$ we need to determine the Dilatancy (D) and the deviatoric plastic strain rate direction ($\boldsymbol{R'}$). The dilatancy is given in Dafalias and Manzari [5] by:

$$D = A_d(\boldsymbol{r}^d - \boldsymbol{r}) : \boldsymbol{n} \tag{8}$$

Assuming a non-associative flow rule in the deviatoric plane the deviatoric plastic strain rate direction is given by:

$$\boldsymbol{R'} = B\boldsymbol{n} - C(\boldsymbol{n}^2 - \frac{1}{3}\boldsymbol{I}); \quad B = 1 + \frac{2}{3}\frac{1-c}{c} g(\theta) cos3\theta; \quad C = 3\sqrt{\frac{3}{2}}\frac{1-c}{c} g(\theta) \tag{9}$$

where θ is the lode angle and $g(\theta)$ is a non-linear function of the lode angle [5].

The plastic modulus is defined by:

$$K_p = \frac{2}{3} ph \frac{(\boldsymbol{r}^b - \boldsymbol{r}) : \boldsymbol{n}}{(\boldsymbol{r} - \boldsymbol{r_{in}}) : \boldsymbol{n}} \tag{10}$$

where $h = G_0 h_0 (1-e)(p/p_{at})^{-0.5}$, with h_0 a material constant.

Finally, the plastic multiplier (or loading index) is given by:

$$L = \frac{1}{K_p} \boldsymbol{n} : p\dot{\boldsymbol{r}} = \frac{2G\boldsymbol{n} : \dot{\boldsymbol{e}} - K(\boldsymbol{n} : \boldsymbol{r})\dot{\epsilon}_\nu}{K_p + 2G(\boldsymbol{n} : \boldsymbol{R'}) - KD(\boldsymbol{n} : \boldsymbol{r})} \tag{11}$$

With all the plasticity formulation ingredients one can solve based on a given strain increment for the stress increment:

$$\dot{\boldsymbol{\sigma}} = 2G\dot{\boldsymbol{e}} + K\dot{\epsilon}_v \boldsymbol{I} - \langle L \rangle (2G\boldsymbol{R'} + KD\boldsymbol{I}) \tag{12}$$

3 IMPLICIT INTEGRATION

A fully implicit integration scheme is being used to integrate the rate equations outlined in the previous section. The backward Euler method together with a Damped Newton's Method is used to solve the non-linear system of ordinary differential equations. In the zero elastic range model there is no yield surface, and the enforcement of the classical consistency condition cannot be used in the iterative process.

De Borst and Heeres [8] used the definition of the plastic multiplier (L) as the replacement of the classical consistency condition for a generalized plasticity model without an explicit yield surface. Following this concept the plastic multiplier which is defined in Eq. (11) is used as the consistency parameter for the system of non-linear equations.

The stress increment tensor ($\boldsymbol{d\sigma}$) defined in Eq. 12 (notice that $\boldsymbol{d\sigma}$=$\dot{\boldsymbol{\sigma}}dt$) is decomposed into it's isotropic (dp) and deviatoric part ($\boldsymbol{ds}$). The independent variables of the system are defined in the following vector of unknowns:

$$\boldsymbol{U} = [\boldsymbol{ds}, dp, L] \tag{13}$$

The residual vector for the three unknowns is defined as follows:

$$\boldsymbol{R} = [\boldsymbol{R_1}, R_2, R_3] \tag{14}$$

In each iteration the algorithm solves the following linearized system:

$$\left(\frac{\partial \boldsymbol{R}}{\partial \boldsymbol{U}}\right)^{(k)} \delta \boldsymbol{U}^{(k)} = -\boldsymbol{R}^{(k)} \tag{15}$$

Finally, the updated variables are calculated by:

$$\boldsymbol{U}^{(k+1)} = \boldsymbol{U}^{(k)} + \lambda \delta \boldsymbol{U}^{(k)} \tag{16}$$

where λ is the damping parameter which takes values smaller than 1 when the error does not decrease monotonically. The first trial guess assumes elastic stress and L=0.

4 NUMERICAL EXAMPLE-VERIFICATION

A numerical example is used in order to verify the numerical integration scheme. The material constants for the model are summarized in Table 1. The total strain increment which is applied and the initial stress state are given bellow:

Table 1: Sanisand-Z model parameters [3] for the numerical example

Model Constant	Symbol	Value
Elasticity	G_0	125
	ν	0.05
Critical State	M_c	1.25
	M_c	1.25
	c	0.712
	e_0	0.934
	λ	0.019
	ξ	0.7
Plastic Modulus	h_0	15
	c_h	0.
	n^b	1.25
Dilatancy	A_0	0.704
	n^d	2.1

$$\dot{\epsilon} = \begin{bmatrix} 0.01 & 0 & 0 \\ 0 & -0.006 & 0 \\ 0 & 0 & -0.006 \end{bmatrix}; \quad \sigma^0 = \begin{bmatrix} 100 & 0 & 0 \\ 0 & 100 & 0 \\ 0 & 0 & 100 \end{bmatrix} \tag{17}$$

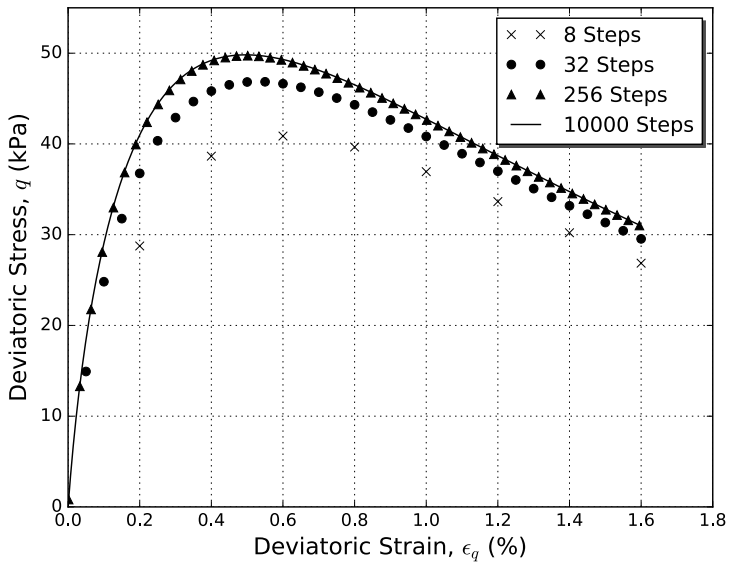

Figure 1: Stress and strain reliationship. Solution using different number of steps.

The total strain increment is applied incrementally in steps. The stress path begins from the stress state which is given by Equation (17.b) and the strain controlled test is done with the strain increment given by Equation (17.a). In Figure 1 the deviatoric stress (q) is plotted against the deviatoric strain (ϵ_q). The solution which is obtained after the application of 10000 steps is called the "accurate" solution since we lack the exact solution for this non-linear elatsto-plastic problem, and 10000 steps are enough to ensure that the solution is the converged one. We observe that the algorithm converges fast to the "accurate" solution. Moreover, even with a small number of steps (8) the integration is stable and sufficiently accurate. In Figure 2 the simulated stress path is presented. The accuracy of the algorithm is quickly improved as we move from the 8 step application towards higher number of steps.

In order to quantify the accuracy of the proposed algorithm, we compute the relative error of the computed stress for 10 simulations with different strain increment step sizes. h is the discretization parameter and the number of steps are calculated by $steps$=2^h (h=3,4,5...12). Each discretization parameter h defines a norm of the strain increment tensor per step which is computed as follows:

$$||\dot{\boldsymbol{\epsilon}}_{\boldsymbol{n}}|| = \frac{||\dot{\boldsymbol{\epsilon}}||}{2^h} \tag{18}$$

The relative error in a given strain level is computed as follows [9]:

$$\delta^r = \frac{\sqrt{\boldsymbol{\sigma} - \boldsymbol{\sigma}^*}}{\sqrt{\boldsymbol{\sigma}^* : \boldsymbol{\sigma}^*}} \tag{19}$$

where σ^* is the stress computed after the application of 10000 steps (the "accurate" solution). The relative error is computed for each strain level at the end of an aplied

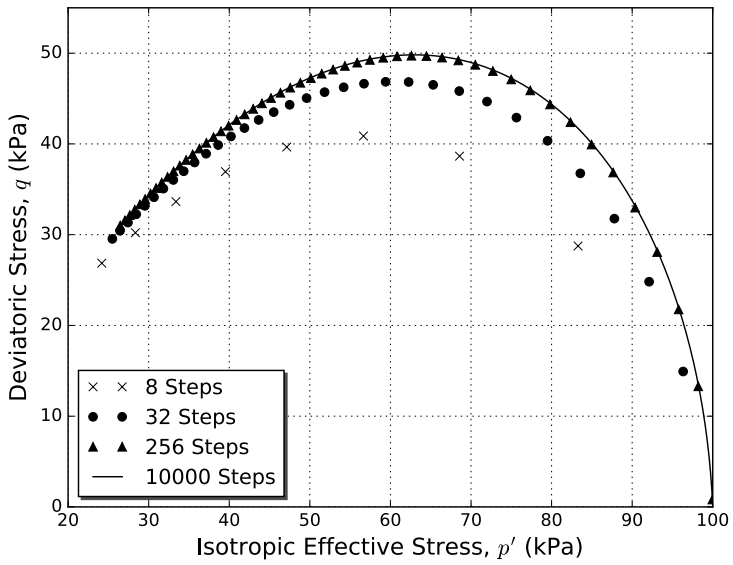

Figure 2: Stress path in the p'-q space. Solution using different number of steps.

strain increment (end of a step). We form an error vector $\boldsymbol{E}$ which has all the values of the errors computed at the end of each step. The size of this vector equals the number of steps applied for each of the simulations.

Three norms of the vector $\boldsymbol{E}$ are computed (L^1, L^2, L^∞) in order to have an error estimation for the whole numerical simulation. The three norms are defined as follows:

$$|\boldsymbol{E}|_{L1} = \sum_{r=1}^{k} |E_k| \tag{20}$$

$$|\boldsymbol{E}|_{L2} = \sqrt{\sum_{r=1}^{k} |E_k|^2} \tag{21}$$

$$|\boldsymbol{E}|_{L\infty} = \max_i |E_i| \tag{22}$$

The error estimation for the numerical test is presented in Figure 3. We observe that the error goes to zero as the strain increment per step approaches very small values for all three norms. The order of accuracy is presented in Figure 4 which depicts the rate that the error minimizes. We observe that the error minimizes linearly, when the strain increment is very small, since the order of accuracy (n) is 0.6 for the larger strain increment per step and above 1 for the smaller strain increments. This verifies that the numerical integration works accurately since the design order of accuracy of the Backward Euler method is 1 when small integration steps are being used. The Newton method shows super-linear convergence when the solution is highly non-linear and quadratic when the solution shows less non-linearity.

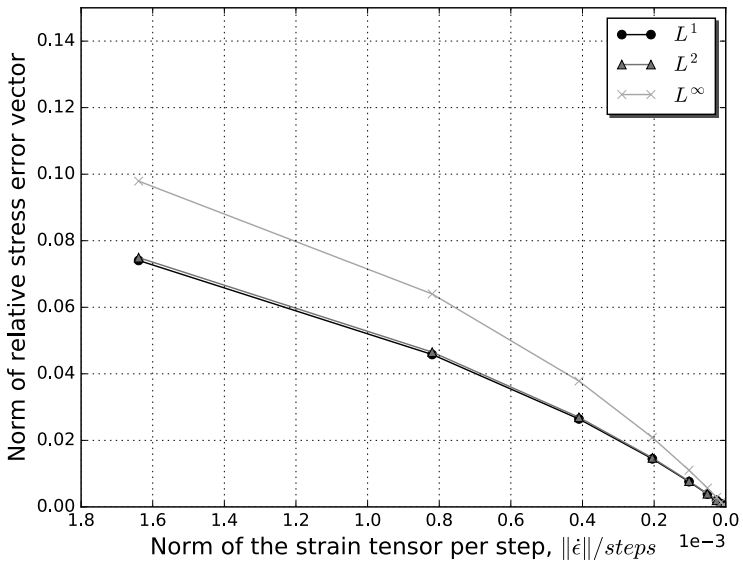

Figure 3: Relative stress error for different applied strain increments per step.

5 CONCLUSSIONS

The proposed integration scheme allow the use of the incrementally non-linear model SANISAND-Z in Finite Element Analysis. The zero elastic range bounding surface plasticity is intrinsically implicit and a iterative algorithm is needed. The system of non-linear equations solved by a Backward Euler integration scheme with Damped Newton's Method. The integration method shows 1^{st} order accuracy for small strain increments per step. The Newton's algorithm shows super-linear convergence in the strain levels where the solution is highly non-linear, and quadratic convergence in steps when the solution is less non-linear.

6 Acknowledgments

The research leading to these results has received funding from the European Research Council under the European Union's Seventh Framework Program (FP7/2007-2013) / ERC IDEAS Grant Agreement n 290963 (SOMEF).

REFERENCES

[1] Dafalias, Y.F. On cyclic and anisotropic plasticity. Ph.D. Thesis. *Department of Civil Engineering, University of California, Berkeley, CA, USA.* (1975).

[2] Dafalias, Y.F. and Popov, E. P. Cyclic loading for materials with a vanishing elastic region. *Nuclear Engineering and Design* (1977) **41**:293–302.

[3] Dafalias, Y.F. and Taiebat, M. SANISAND-Z: Zero Elastic Range Sand Plasticity Model. *Géotechnique* (2017) **66**:999–1013.

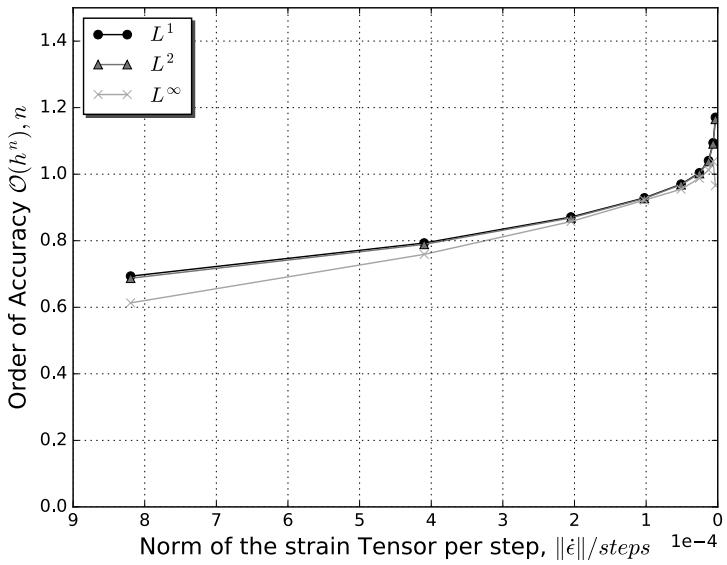

Figure 4: Order of accuracy for different applied strain increments per step.

[4] Manzari, M. T. and Dafalias, Y.F. A two-surface critical plasticity model for sand. *Géotechnique* (1997) **47**:255–272.

[5] Dafalias, Y.F. and Manzari, M. T. Simple Plasticity Sand Model Accounting for Fabric Effects *Géotechnique* (2004) **130**:622–634.

[6] Taiebat, M. and Dafalias, Y.F. SANISAND: Simple anisotropic plasticity model. *International Journal for Numerical and Analytical Methods in Geomechanics* (2008) **32**:915–948.

[7] Been, K., and Jefferies, M. G. A state parameter for sands. *Géotechnique* (1985) **35**:99–112.

[8] de Borst, R. and Heeres, O. M. A unified approach to the implicit integration of standard, non-standard and viscous plasticity models. *International Journal for Numerical and Analytical Methods in Geomechanics* (2002) **26**:1059–1070.

[9] Simo, J. C. and Hughes, T. J. R. *Computational Inelasticity.* Springer-Verlag, New York, (1998).

XIV International Conference on Computational Plasticity. Fundamentals and Applications
COMPLAS XIV
E. Oñate, D.R.J. Owen, D. Peric & M. Chiumenti (Eds)

NUMERICAL MODELING OF STRAIN RATE HARDENING EFFECTS ON VISCOPLASTIC BEHAVIOR OF METALLIC MATERIALS

TIAGO DOS SANTOS[⋆], PEDRO A. R. ROSA[†], SAMIR MAGHOUS[‡], AND RODRIGO ROSSI[♮]

[⋆]Departamento de Engenharia Mecânica
Universidade Federal de Santa Maria
Santa Maria, RS, Brazil - 97105-900.
e-mail: tsantos.mec@gmail.com

[†]Instituto de Engenharia Mecânica
Instituto Superior Técnico, Universidade de Lisboa
Lisboa, Portugal - 1049-001.
e-mail: pedro.rosa@tecnico.ulisboa.pt

[‡]Departamento de Engenharia Civil
Universidade Federal do Rio Grande do Sul
Porto Alegre, RS, Brazil - 90040-020.
e-mail: rrossi@ufrgs.br

[♮]Departamento de Engenharia Mecânica
Universidade Federal do Rio Grande do Sul
Porto Alegre, RS, Brazil - 90046-902.
e-mail: rrossi@ufrgs.br

Key words: High strain rate effects, Finite strain, Elastic-viscoplastic material, Numerical algorithms, Finite elements.

Abstract. The main goal of the present work is to provide a finite strain elastic-viscoplastic framework to numerically account for strain, strain rate hardening, and viscous effects in cold deformation of metallic materials. The aim is to provide a simple and robust numerical framework capable of modeling the main macroscopic behavior associated with high strain rate plastic deformation of metals. In order to account for strain rate hardening effects at finite strains, the hardening rule involves a rate dependent saturation hardening, and it accounts for linear hardening prevailing at latter deformation stages. The numerical formulation, finite element implementation, and constitutive modeling capabilities are assessed by means of decremental strain rate testing and constant strain rate loading followed by stress relaxation. The numerical results have demonstrated the overall framework can be an efficient numerical tool for simulation of plastic deformation processes where strain rate history effects have to be accounted for.

1 Introduction

High strain rates and large strains are present in several engineering applications of polycrystalline metallic materials, such as manufacturing (e.g. high speed forming and machining of metals), machine tools design, analysis of structural crashworthiness in the automotive and aerospace industries, terminal ballistics research for safety and military activities, among several others. Modeling of these applications requires large scale simulations and adequate constitutive predictions.

To properly predict high strain rate straining of metals, a constitutive framework should account for deformation and loading history effects. For example, the hardening response of FCC metals is strongly rate-dependent at high velocity conditions [1, 2, 3, 4, 5]. In summary, a high strain rate model has to comply with adequate constitutive features accounting for the main plastic effects on the flow stress and material hardening responses. However, while incorporating suitable constitutive capabilities, a constitutive model to be employed in large scale engineering computations has to be simple enough to be experimentally and numerically "attractive". From a constitutive point of view, physically-based models employing macroscopic [6, 7, 8, 9] or microscopic frameworks [10, 11, 12] allow for a detailed description of both material behavior and its current state, thus providing an appropriate framework for capturing loading-history effects. However, in contrast physically-based models require complex optimization algorithms and large computational efforts to find associated model constants, see for instance comments provided in references [8, 13]. In addition, due to formulation complexity, physically-based approaches are less numerically efficient than phenomenological procedures, thus requiring more computational time and efforts in numerical simulation of large scale problems. Concerning the formulation simplicity, the lower number of material parameters and of experiments to identify them, many researchers [14, 15, 16, 17] have proposed semi-physical constitutive models, once a detailed physical description increase the model complexity and the number of constants to be adjusted.

In large scale simulations, accurate, efficient, and robust numerical tools are mandatory in order to guarantee appropriate predictions and to save computational time. In a global standpoint, the finite element (FE) method has proved to be a suitable tool in solving nonlinear initial boundary value problems [18, 19]. The whole numerical framework must integrate the set of nonlinear constitutive equations into a FE context, requiring the fulfillment of two main tasks at the material level: (i) the update of stress and state variables from a given strain increment, and (ii) the calculation of consistent tangent modulus to be used in the global implicit FE scheme, thus preserving quadratic convergence rate of *Newton*-type solution algorithms [18, 19]. Aiming at accomplishing these tasks and improving the computational efficiency, several viscoplastic implicit integration algorithms for large strain problems have been proposed [20, 21, 22, 23]. Mostly of the large strain formulations are based on the well-known multiplicative decomposition of the deformation gradient [24, 25], and generally associated algorithmic formulations preserves material objectivity.

Aiming at contributing to the constant search for models combining both constitu-

tive adequacy and computational efficiency, the present work has the goal of providing a simple and efficient numerical framework capable of modeling the main macroscopic behavior associated with high strain rate plastic deformation of metals at room temperature. The work concerns numerical formulation and simulations where advantage is taken of a constitutive model previously presented [26], which proved to be suitable for this task. Adopting a simplified semi-physical approach allows to maintain the corresponding computational efficiency associated with phenomenological models [27, 28, 29, 30] while incorporating adequate constitutive capabilities, such as strain rate history effects, in simulations where high velocity plastic features have to be taken into account.

The present constitutive formulation adopts a *von Mises* plasticity employing a strain-rate-history-dependent isotropic hardening, whose evolution equations follow the viscoplastic framework of *Perzyna* [31, 27], in which the inelastic evolution is given in terms of an *overstress* function. Specifically, the isotropic hardening is taken into account by a single scalar internal variable, which can be interpreted as an effective microstructural feature [15, 26]. The stress hardening variable is composed by two main contributions, namely A_1 and A_2. The first is associated with dislocations storage, and its evolution is based on physical aspects as dislocation generation and annihilation mechanisms. The second contribution, A_2, is linked to geometric hardening mechanisms associated with deformation Stage IV, in which the hardening is mainly induced by granular misorientations. It is worth mentioning that a formulation following an overstress description needs an explicit definition of the strain rate, and it presents some constitutive differences compared to other viscoplastic contexts as the consistency model [32, 33]. For example, concerning the overstress description, plastic deformation increase during unloading while overstress function has a nonzero value [22, 13]. However, within the present approach this constitutive distinction is not so relevant once it is intended to monotonic loading, thus justifying the employment of an overstress formulation, as well as a pure isotropic hardening. From an overall point of view, the elastic-viscoplastic model presented in [26] is embedded into a finite strain framework, which adopts a total *Lagrangian* description and employ the classical multiplicative decomposition of the deformation gradient into its viscoplastic and elastic parts. An isotropic material is considered, whose constitutive formulation is given in terms of the logarithmic deformation measure and the rotated *Kirchhoff* stress. The elastic response is assumed to be linear and given by the *Hencky* hyperelastic model. The numerical approach follows ideas presented in references [34, 21], where a standard elastic predictor-plastic corrector algorithm is employed. However, to incorporate rate dependent hardening features, additional incremental equations arise within the return mapping step. Seeking for computational efficiency, an analytical consistent tangent operator is obtained from linearization of the return mapping equations.

The work is organized as follows. Section 2 presents an overview of the constitutive model adopted [26]. In this section, the global boundary value problem in its strong and weak form is stated. From linearization of weak formulation the continuum material tangent modulus is identified. Section 4 outlines the local incremental constitutive formulation, recalling the well-known elastic predictor-plastic corrector algorithm. Also, the consistent tangent modulus is given in a closed-form. In the sequel, with the aim of show-

ing the model constitutive capabilities, and highlighting the main macroscopic material behavior associated with loading history effects, a numerical decremental strain rate test and a constant strain rate loading followed by stress relaxation testing are performed in Sec. 5, employing the model parameters obtained in [26] for an annealed OFHC copper. Numerical results are compared with experimental data available in the literature [3, 35]. Furthermore, as a non-homogeneous deformation example, a billet upsetting is simulated. Convergence analyzes, considering both frictionless and frictional billet upsetting cases, are also performed. Our conclusions and comments are given in Sec. 6. Tangent terms required into return mapping algorithm are given in A and the analytical consistent tangent modulus is derived in B.

2 Overview of constitutive model

We adopt the classical multiplicative[1] decomposition of the deformation gradient [24, 36]

$$\boldsymbol{F} = \boldsymbol{F}^e \boldsymbol{F}^{vp}, \tag{1}$$

where $\boldsymbol{F} = \frac{\partial \boldsymbol{\varphi}(\boldsymbol{X},t)}{\partial \boldsymbol{X}}$, $\boldsymbol{\varphi}$ being the displacement function which maps an initial point $\boldsymbol{X} \in \Omega_0$ onto a current one $\boldsymbol{x} \in \Omega$ at time t, such that $\boldsymbol{x} = \boldsymbol{\varphi}(\boldsymbol{X}, t)$. Terms $\boldsymbol{F}^e$ and $\boldsymbol{F}^{vp}$ are the elastic and viscoplastic part of $\boldsymbol{F}$. By adopting decomposition (1), the specific *Helmholtz* free-energy can be split [37],

$$\psi = \psi^e(\boldsymbol{E}^e) + \psi^{vp}(\alpha), \tag{2}$$

into its elastic ψ^e and inelastic ψ^{vp} parts. Tensor $\boldsymbol{E}^e = \ln(\boldsymbol{U}^e)$ is the *Hencky* elastic strain with $\boldsymbol{U}^{e^2} = (\boldsymbol{F}^e)^T \boldsymbol{F}^e$ and $\boldsymbol{F}^e = \boldsymbol{F}\boldsymbol{F}^{vp^{-1}}$. A single internal variable α is assumed to describe irreversible material behavior (see for instance references [38, 39, 40, 37]). In this work we assume standard quadratic forms

$$\psi^e = \frac{1}{2}\boldsymbol{E}^e : \mathbb{D}^e : \boldsymbol{E}^e \;\text{ and }\; \psi^{vp} = \frac{1}{2}H\alpha^2, \tag{3}$$

where $\mathbb{D}^e$ is a symmetric positive-definite forth-order elastic tensor and $H \geq 0$ is the hardening modulus. Furthermore, isotropic elasticity is considered in subsequent analysis:

$$\mathbb{D}^e = 2\mu\mathbb{I} + \left(\kappa - \frac{2}{3}\mu\right)\boldsymbol{I} \otimes \boldsymbol{I}, \tag{4}$$

where $\mathbb{I}$, $\boldsymbol{I}$, μ and κ are the fourth-order and the second-order identity tensors, the shear and bulk modulus, respectively. Components of $\mathbb{I}$ are $I_{ijkl} = \frac{1}{2}(\delta_{ik}\delta_{jl} + \delta_{il}\delta_{jk})$ with δ_{ij} denoting the *Kronecker*'s symbol.

Thermodynamic forces must obey the constitutive relations

$$\bar{\boldsymbol{\tau}} = \rho_0 \frac{\partial \psi^e}{\partial \boldsymbol{E}^e} = \mathbb{D}^e : \boldsymbol{E}^e \;\text{ and }\; A = \rho_0 \frac{\partial \psi^{vp}}{\partial \alpha} = H\alpha, \tag{5}$$

[1] Along this work single contractions between second-order tensors are omitted, i.e., $\boldsymbol{S} \cdot \boldsymbol{T} = \boldsymbol{S}\boldsymbol{T}$, in components $(\boldsymbol{S}\boldsymbol{T})_{ij} = S_{ik}T_{kj}$.

where $\bar{\boldsymbol{\tau}}$ is the rotated *Kirchhoff* stress [34]. The latter is related to the *Kirchhoff* stress tensor $\boldsymbol{\tau}$ by means of the right rotation tensor $\boldsymbol{R} = \boldsymbol{F}\boldsymbol{U}^{-1}$ with $\boldsymbol{U}^2 = \boldsymbol{F}^T\boldsymbol{F}$, such that $\bar{\boldsymbol{\tau}} = \boldsymbol{R}^T\boldsymbol{\tau}\boldsymbol{R}$. It is recalled that $\boldsymbol{\tau}$ and the *Cauchy* stress tensor $\boldsymbol{\sigma}$ are related through $\boldsymbol{\tau} = J\boldsymbol{\sigma}$ with $J = \det(\boldsymbol{F})$. Parameter A stands for the isotropic hardening associated with α. For sake of simplicity, in what follows we adopt a *von Mises* yield criterion together with an isotropic hardening A

$$f(\bar{\boldsymbol{\tau}}, A) = \left\|\bar{\boldsymbol{\tau}}^D\right\| - \sqrt{\frac{2}{3}}(\sigma_y + A), \tag{6}$$

where $\left\|\bar{\boldsymbol{\tau}}^D\right\| = \sqrt{\bar{\tau}_{ij}^D\bar{\tau}_{ij}^D}$, $\bar{\boldsymbol{\tau}}^D = \bar{\boldsymbol{\tau}} - \frac{1}{3}\mathrm{tr}(\bar{\boldsymbol{\tau}})\boldsymbol{I}$ is the deviatoric part of $\bar{\boldsymbol{\tau}}$ and σ_y is the initial yield stress.

2.1 Evolution equations

The viscoplastic strain rate $\bar{\boldsymbol{D}}^{vp} = \mathrm{sym}\left(\dot{\boldsymbol{F}}^{vp}\boldsymbol{F}^{vp^{-1}}\right)$ is given by the evolution equation[2]

$$\bar{\boldsymbol{D}}^{vp} = \dot{\lambda}\frac{\partial f}{\partial \bar{\boldsymbol{\tau}}} \tag{7}$$

where the viscoplastic multiplier $\dot{\lambda}$ expresses as [31, 27]

$$\dot{\lambda} = \frac{1}{\vartheta}\Theta(\langle f\rangle, A). \tag{8}$$

In the above equality, operator $\langle x\rangle \equiv \frac{1}{2}(x + |x|)$ denotes the *Macaulay* brackets, $\vartheta \geq 0$ is the material viscosity parameter and $\Theta \geq 0$ is the *overstress* function which should be convex with relation to both f and A. Hardening variable A is given by

$$A = A_1 + cA_\infty\epsilon, \tag{9}$$

where $c \geq 0$ is a material parameter, A_∞ is the saturation work hardening, A_1 is associated with hardening induced by dislocation storage and its arrangement in dislocation cells, and term $cA_\infty\epsilon$ is related to geometric hardening due to cellular and granular misorientations. Evolution of first term is given by

$$\dot{A}_1 = H_1\left(1 - \frac{A_1}{A_\infty}\right)\dot{\epsilon}, \tag{10}$$

where H_1 is the hardening rate and

$$\dot{\epsilon} = \sqrt{\frac{2}{3}}\left\|\bar{\boldsymbol{D}}^{vp}\right\| \geq 0 \tag{11}$$

[2]Under the hypothesis of inelastic isotropy, without loss in generality, a irrotational viscoplastic flow may be assumed [21, 41]: $\bar{\boldsymbol{W}}^{vp} = \mathrm{skew}\left(\dot{\boldsymbol{F}}^{vp}\boldsymbol{F}^{vp^{-1}}\right) = \boldsymbol{0}$.

is the accumulated viscoplastic strain rate. Assuming constant value for $\dot{\epsilon}$, evolution equation (10) is directly integrated leading to a *Voce* hardening law [42],

$$\frac{A_1 - A_\infty}{A_{1_i} - A_\infty} = \exp\left[-\delta\left(\epsilon - \epsilon_i\right)\right]. \tag{12}$$

Parameters A_{1_i} and ϵ_i stand for the initial values of A_1 and ϵ, respectively, and $\delta = \frac{H_1}{A_\infty}$. In the present formulation we assume the ratio $\delta = \frac{H_1}{A_\infty}$ as constant, and a rate dependence will be assigned to A_∞. Combination of Eqs. (9) and (12) yields

$$A = A_i + A_\infty c\left(\epsilon - \epsilon_i\right) + \left[A_\infty\left(1 + c\epsilon_i\right) - A_i\right]\left\{1 - \exp\left[-\delta\left(\epsilon - \epsilon_i\right)\right]\right\}, \tag{13}$$

where A_i is the initial value of A. Considering that $A_i = \epsilon_i = 0$, Eq. (13) reduces to

$$A = A_\infty\left[1 + c\epsilon - \exp\left(-\delta\epsilon\right)\right], \tag{14}$$

which is a modified *Voce* hardening law. Hardening equation (13), obtained based upon the assumption of constant rate $\dot{\epsilon}$, is usefull to be employed within numerical algorithms in which inelastic strain rate is assumed within each increment. Now, Eq. (14) is intended to monotonic loading applications starting from a non-deformed state.

The following *a priori* rate-dependent form is postulated for A_∞, see reference [26]:

$$A_\infty = \left[1 - \beta\left(\dot{\epsilon}\right)\right] A_\infty^{lwr} + \beta\left(\dot{\epsilon}\right) A_\infty^{up}, \tag{15}$$

where A_∞^{lwr} is the *quasi*-static value of A_∞ measured at a lower reference rate $\dot{\epsilon}_{lwr} \ll 1$ and A_∞^{up} is the value associated with upper reference strain rate $\dot{\epsilon}_{up} \gg 1$. Function β is given by

$$\beta\left(\dot{\epsilon}\right) = \left(\frac{\dot{\epsilon} - \dot{\epsilon}_{lwr}}{\dot{\epsilon}_{up} - \dot{\epsilon}_{lwr}}\right)^{\xi}, \tag{16}$$

which obviously satisfies $\beta\left(\dot{\epsilon}_{lwr}\right) = 0$ and $\beta\left(\dot{\epsilon}_{up}\right) = 1$, scalar $\xi > 0$ is a material constant.

In the present work, a viscoplastic constitutive function $\Theta\left(\langle f\rangle, A\right)$ based on that proposed in [28] is adopted,

$$\vartheta\dot{\lambda} = \Theta\left(\langle f\rangle, A\right) = \left(\frac{\langle f\rangle + R}{R}\right)^m - 1. \tag{17}$$

For $f \geq 0$, the inverse of Θ with respect to $\dot{\lambda}$ and f reads

$$f = \Theta^{-1}\left(\dot{\lambda}, A\right) = R\left[\left(1 + \vartheta\dot{\lambda}\right)^{\frac{1}{m}} - 1\right], \tag{18}$$

where $\frac{1}{m}$ is the rate sensitivity parameter and $R\left(A\right)$ is a characteristic size of the yield locus, which is expressed as

$$R\left(A\right) = \sqrt{\frac{2}{3}}\left(\sigma_y + A\right) \tag{19}$$

in the case of *von Mises* yield criterion (6).

3 Incremental formulation and finite element implementation

Let Ω_0 be the initial configuration of a body with boundary $\partial\Omega_0$ and particles labeled $\boldsymbol{X} \in \Omega_0$. An ordinary loading is defined by a prescribed body force $\bar{\boldsymbol{b}}$ in Ω_0, a prescribed surface traction $\bar{\boldsymbol{t}}$ acting on Γ_0^t and a displacement $\bar{\boldsymbol{u}}$ prescribed on Γ_0^u, with $\partial\Omega_0 = \Gamma_0^t \cup \Gamma_0^u$ and $\Gamma_0^t \cap \Gamma_0^u = \emptyset$. Deformed body is defined by the current configuration Ω with boundary $\partial\Omega$ and particles $\boldsymbol{x} \in \Omega$, being the displacement field given by $\boldsymbol{u} = \boldsymbol{x} - \boldsymbol{X}$. The mechanical problem in its strong form, disregarding inertia effects, can be stated as follows: Find $\boldsymbol{u}$ such that

$$\left\{ \begin{array}{rcl} \mathrm{div}\boldsymbol{P} + \bar{\boldsymbol{b}} & = & \boldsymbol{0} \text{ on } \Omega_0 \\ \boldsymbol{P}\boldsymbol{m} & = & \bar{\boldsymbol{t}} \text{ on } \Gamma_0^t \\ \boldsymbol{u} & = & \bar{\boldsymbol{u}} \text{ on } \Gamma_0^u \end{array} \right. , \tag{20}$$

where $\boldsymbol{P} = \boldsymbol{\tau}\boldsymbol{F}^{-T}$ is the first *Piola-Kirchhoff* stress tensor and $\boldsymbol{m}$ is the unit outward normal vector at $\boldsymbol{X} \in \partial\Omega_0$. Based on strong form given by Eqs. (20), the weak formulation, employing the virtual work principle, consists of finding $\boldsymbol{u}$ satisfying

$$\mathscr{R}\left(\boldsymbol{u}, \hat{\boldsymbol{u}}\right) = \int_{\Omega_0} \boldsymbol{P}\left(\boldsymbol{u}\right) : \nabla_{\boldsymbol{X}} \hat{\boldsymbol{u}} dV - \int_{\Omega_0} \rho_0 \bar{\boldsymbol{b}} \cdot \hat{\boldsymbol{u}} dV - \int_{\Gamma_0^t} \bar{\boldsymbol{t}} \cdot \hat{\boldsymbol{u}} dA = 0, \tag{21}$$

$\forall \hat{\boldsymbol{u}} \in \mathscr{W}_p^1\left(\Omega_0\right)$, where $\nabla_{\boldsymbol{X}}\left(\cdot\right)$ denotes the material derivative of field $\left(\cdot\right)$ and $\hat{\boldsymbol{u}}$ is the virtual displacement vector field.

3.1 Linearized incremental Boundary Value Problem

The incremental strategy adopted herein consists of subdividing the whole time interval of interest $\mathscr{I}$ into $N > 0$ subintervals $(t_n, t_{n+1}]$: $\mathscr{I} = \bigcup_{n=1}^{N} (t_n, t_{n+1}]$. Adopting an implicit solution scheme, for a time subinterval $(t_n, t_{n+1}]$ Eq. (21) have to be satisfied at t_{n+1}, and the increment associated with a given quantity $\left(\cdot\right)$ is given by $\Delta\left(\cdot\right) := \left(\cdot\right)_{n+1} - \left(\cdot\right)_n$, being $\left(\cdot\right)_{n+1}$ and $\left(\cdot\right)_n$ the values at instants t_{n+1} and t_n, respectively. Following this incremental strategy, the internal variables $\boldsymbol{\alpha}_n\left(\boldsymbol{X}\right)$, the displacement $\boldsymbol{u}_n\left(\boldsymbol{X}\right)$, as well as the stress $\boldsymbol{P}_n\left(\boldsymbol{X}\right)$ fields are assumed to be known at the initial time instant t_n and to comply with Eq. (21). The incremental equilibrium problem corresponding to a time subinterval $(t_n, t_{n+1}]$ consists therefore of finding the current displacement field $\boldsymbol{u}_{n+1}\left(\boldsymbol{X}\right) \in \mathcal{K}_{n+1}$, satisfying

$$\mathscr{R}\left(\boldsymbol{u}_{n+1}, \hat{\boldsymbol{u}}\right) = \int_{\Omega_0} \boldsymbol{P}_{n+1} : \nabla_{\boldsymbol{X}} \hat{\boldsymbol{u}} dV - \int_{\Omega_0} \rho_0 \bar{\boldsymbol{b}}_{n+1} \cdot \hat{\boldsymbol{u}} dV - \int_{\Gamma_0^t} \bar{\boldsymbol{t}}_{n+1} \cdot \hat{\boldsymbol{u}} dA = 0, \ \ \forall \hat{\boldsymbol{u}} \in \mathscr{W}_p^1\left(\Omega_0\right), \tag{22}$$

where $\mathcal{K}_{n+1}$ is the set of kinematically admissible displacements at t_{n+1}. Within the present numerical framework, the local integration algorithm provides an incremental stress function $\bar{\boldsymbol{P}}$ given in terms of $\boldsymbol{F}_{n+1}$ and $\boldsymbol{\alpha}_n$ [19]: $\boldsymbol{P}_{n+1} = \bar{\boldsymbol{P}}\left(\boldsymbol{F}_{n+1}, \boldsymbol{\alpha}_n\right)$.

Solving Eq. (22) by means of an iterative procedure, such as the Newton-Raphson method, at iteration $k+1$ one has to determine a displacement increment $\Delta\boldsymbol{u}_{n+1}^{k+1}$ satisfying condition

$$\mathscr{R}\left(\boldsymbol{u}_{n+1}^{k+1}, \hat{\boldsymbol{u}}\right) = \mathscr{R}\left(\boldsymbol{u}_{n+1}^{k} + \Delta\boldsymbol{u}_{n+1}^{k+1}, \hat{\boldsymbol{u}}\right) = 0, \ \ \forall \hat{\boldsymbol{u}} \in \mathscr{W}_p^1\left(\Omega_0\right), \tag{23}$$

where $\boldsymbol{u}_{n+1}^{k+1} = \boldsymbol{u}_{n+1}^{k} + \Delta\boldsymbol{u}_{n+1}^{k+1}$ is the approximated iterative solution. Expanding $\mathscr{R}\left(\boldsymbol{u}_{n+1}^{k+1}, \hat{\boldsymbol{u}}\right)$ according to a *Taylor* series around $\boldsymbol{u}_{n+1}^{k}$, keeping only the first-order term, yields

$$D\mathscr{R}\left(\boldsymbol{u}_{n+1}^{k}, \hat{\boldsymbol{u}}\right)\left[\Delta\boldsymbol{u}_{n+1}^{k+1}\right] = -\mathscr{R}\left(\boldsymbol{u}_{n+1}^{k}, \hat{\boldsymbol{u}}\right), \quad \forall\hat{\boldsymbol{u}} \in \mathscr{W}_{p}^{1}\left(\Omega_0\right). \tag{24}$$

Term $D\mathscr{R}\left(\boldsymbol{u}_{n+1}^{k}, \hat{\boldsymbol{u}}\right)\left[\Delta\boldsymbol{u}_{n+1}^{k+1}\right]$ stands for the directional derivative of $\mathscr{R}$ at $\boldsymbol{u}_{n+1}^{k}$ in the direction of increment $\Delta\boldsymbol{u}_{n+1}^{k+1}$. The formal definition of this derivative is: $D\mathscr{R}\left(\boldsymbol{u}, \hat{\boldsymbol{u}}\right)\left[\Delta\boldsymbol{u}\right] = \frac{d}{d\epsilon}\mathscr{R}\left(\boldsymbol{u} + \epsilon\Delta\boldsymbol{u}, \hat{\boldsymbol{u}}\right)\big|_{\epsilon=0}$ [43, 19, 18]. Accordingly, the linearized virtual work equation at an instant t_{n+1} and iteration $k+1$ becomes [19]:

$$\int_{\Omega_0} \mathbb{M}_{n+1}^{k} : \nabla_{\boldsymbol{X}}\left(\Delta\boldsymbol{u}_{n+1}^{k+1}\right) : \nabla_{\boldsymbol{X}}\hat{\boldsymbol{u}} dV = -\mathscr{R}\left(\boldsymbol{u}_{n+1}^{k}, \hat{\boldsymbol{u}}\right), \quad \forall\hat{\boldsymbol{u}} \in \mathscr{W}_{p}^{1}\left(\Omega_0\right). \tag{25}$$

where term

$$\mathbb{M}_{n+1}^{k} \coloneqq \left.\frac{d\boldsymbol{P}}{d\boldsymbol{F}}\right|_{\boldsymbol{u}_{n+1}^{k}} \tag{26}$$

is the consistent tangent modulus calculated in terms of displacement $\boldsymbol{u}_{n+1}^{k}$. An explicit expression for $\mathbb{M}_{n+1}$ is going to be derived latter. Equation (25) has to be solved in terms of increment $\Delta\boldsymbol{u}_{n+1}^{k}$, which then provides the next iterative displacement $\boldsymbol{u}_{n+1}^{k+1} \leftarrow \boldsymbol{u}_{n+1}^{k} + \Delta\boldsymbol{u}_{n+1}^{k+1}$. Knowing the new incremental displacement, a new residual $\mathscr{R}\left(\boldsymbol{u}_{n+1}^{k+1}, \hat{\boldsymbol{u}}\right)$ is therefore computed and compared with a tolerance e_{tol}. The iterative procedure is repeated until condition $\mathscr{R}\left(\boldsymbol{u}_{n+1}^{k+1}, \hat{\boldsymbol{u}}\right) < e_{tol}$ is satisfied.

3.2 Finite element discretization

Using the finite element method to solve Eq. (25), continuum domain Ω_0 is then approximately represented by a finite number $n_e > 0$ of non-overlapping elements $\Omega_0^{(e)}$ connected by their boundary nodes: $\Omega_0 \approx {}^{h}\Omega_0 = \bigcup_{e=1}^{n_e} \Omega_0^{(e)}$. Furthermore, both displacement $\boldsymbol{u}$ and virtual displacement $\hat{\boldsymbol{u}}$ fields are approximated by their finite element counterparts:

$$\Delta^{h}\boldsymbol{u}_{n+1}^{k}\left(\boldsymbol{X}\right) = \mathbf{N}^{g}\left(\boldsymbol{X}\right)\Delta\mathbf{u}_{n+1}^{k} \;\text{ and }\; {}^{h}\hat{\boldsymbol{u}}\left(\boldsymbol{X}\right) = \mathbf{N}^{g}\left(\boldsymbol{X}\right)\hat{\mathbf{u}}, \tag{27}$$

where $\mathbf{N}^{g}$ is the global interpolation matrix, $\mathbf{u}_{n+1}^{k}$ and $\hat{\mathbf{u}}$ are the nodal displacement and virtual displacement global vectors, respectively. Gradients are approximate by: $\nabla_{\boldsymbol{X}}\boldsymbol{u}\left(\boldsymbol{X}\right) \approx \mathbf{G}^{g}\left(\boldsymbol{X}\right)\mathbf{u}$, where is the appropriate gradient of interpolation matrix $\mathbf{N}^{g}$. The stress tensor $\boldsymbol{P}$ is also replaced by a corresponding stress vector field $\mathbf{P}$. Accordingly, finite element counterpart of Eq. (25) is

$$\left(\mathbf{K}_T\right)_{n+1}^{k}\Delta\mathbf{u}_{n+1}^{k} = -R\left(\mathbf{u}_{n+1}^{k}\right), \tag{28}$$

in which $R\left(\mathbf{u}_{n+1}^{k}\right) = \left(\mathbf{f}_{int}\right)_{n+1}^{k} - \left(\mathbf{f}_{ext}\right)_{n+1}$ is the residual at iteration k. Then, the nodal displacement increment at an iteration $k+1$ and instant $t+1$ is computed by

$$\Delta\mathbf{u}_{n+1}^{k+1} = -\left[\left(\mathbf{K}_T\right)_{n+1}^{k}\right]^{-1}\left[\left(\mathbf{f}_{int}\right)_{n+1}^{k} - \left(\mathbf{f}_{ext}\right)_{n+1}\right]. \tag{29}$$

Internal $\mathbf{f}_{int}$ and external $\mathbf{f}_{ext}$ global force vectors at t_{n+1} for an iteration $k+1$ are given respectively as:

$$(\mathbf{f}_{int})_{n+1}^{k} = \int_{{}^{h}\Omega_0} (\mathbf{G}^{g})^{T} \mathbf{P}_{n+1}^{k} dV, \tag{30}$$

$$(\mathbf{f}_{ext})_{n+1} = \int_{{}^{h}\Omega_0} (\mathbf{N}^{g})^{T} \bar{\boldsymbol{b}}_{n+1} dV + \int_{{}^{h}\Gamma_0^{t}} (\mathbf{N}^{g})^{T} \bar{\boldsymbol{t}}_{n+1} dA. \tag{31}$$

Furthermore, the global stiffness tangent matrix $\mathbf{K}_T$ at t_{n+1} and iteration $k+1$ is computed according to

$$(\mathbf{K}_T)_{n+1}^{k} = \int_{{}^{h}\Omega_0} (\mathbf{G}^{g})^{T} \mathbf{M}_{n+1}^{k} \mathbf{G}^{g} dV, \tag{32}$$

where $\mathbf{M}_{n+1}^{k}$ is the matrix counterpart of the tangent modulus $\mathbb{M}_{n+1}^{k}$ defined in Eq. (26).

4 Local integration and consistent tangent modulus computation

To update the stress field $\boldsymbol{P} = \boldsymbol{P}(\boldsymbol{F}(\boldsymbol{u}))$ at each iterative step and to compute the consistent tangent modulus $\mathbb{M}$, local constitutive equations have to be integrated. For this purpose we first start by recalling the basic elements of elastic predictor-plastic corrector algorithm.

4.1 Elastic prediction and plastic correction

In the elastic prediction step, the elastic formal condition

$$\dot{\boldsymbol{F}}^{vp} = \mathbf{0} \ \text{ and } \ \dot{\alpha} = 0 \tag{33}$$

and its incremental counterpart

$$\boldsymbol{F}_{n+1}^{vp^{trial}} = \boldsymbol{F}_{n}^{vp} \ \text{ and } \ \alpha_{n+1}^{trial} = \alpha_n \tag{34}$$

hold. From these conditions, the *trial elastic state* is defined in terms of elastic deformation gradient and elastic logarithmic strain measure,

$$\boldsymbol{F}_{n+1}^{e^{trial}} = \boldsymbol{F}_{n+1} \left(\boldsymbol{F}_{n+1}^{vp^{trial}} \right)^{-1} \quad \rightarrow \quad \boldsymbol{E}_{n+1}^{e^{trial}} = \frac{1}{2} \ln \left(\boldsymbol{C}_{n+1}^{e^{trial}} \right), \tag{35}$$

with $\boldsymbol{C}_{n+1}^{e^{trial}} = \left(\boldsymbol{F}_{n+1}^{e^{trial}} \right)^{T} \boldsymbol{F}_{n+1}^{e^{trial}}$. Tensor $\boldsymbol{E}_{n+1}^{e^{trial}}$ being given, the trial-rotated *Kirchhoff* stress tensor is computed using Eq. (4): $\bar{\boldsymbol{\tau}}_{n+1}^{trial} = \bar{\boldsymbol{\tau}}_{n+1}^{trial} \left(\boldsymbol{E}_{n+1}^{e^{trial}} \right)$.

The plastic correction is required when $f\left(\bar{\boldsymbol{\tau}}_{n+1}^{trial}, A_{n+1}^{trial}\right) > 0$. The procedure adopted to perform the plastic correction refers to the return mapping algorithms, which is extensively explored in the literature. In this work, an exponential mapping is employed (see references [34, 21]). The discretization of the plastic flow $\dot{\boldsymbol{F}}^{vp} = \bar{\boldsymbol{D}}^{vp} \boldsymbol{F}^{vp}$, together with its approximation based on a backward exponential mapping, leads to

$$\boldsymbol{F}_{n+1}^{vp} = \exp\left(\Delta\lambda \boldsymbol{N}_{\bar{\boldsymbol{\tau}}_{n+1}}\right) \boldsymbol{F}_{n}^{vp}. \tag{36}$$

where $\boldsymbol{N}_{\bar{\boldsymbol{\tau}}_{n+1}} = \frac{\partial f_{n+1}}{\partial \bar{\boldsymbol{\tau}}_{n+1}} = \frac{\bar{\boldsymbol{\tau}}^D_{n+1}}{\left\|\bar{\boldsymbol{\tau}}^D_{n+1}\right\|}$. Moreover, after some manipulations Eq. (36) reduces to [34, 21]

$$\boldsymbol{E}^e_{n+1} = \boldsymbol{E}^{e^{trial}}_{n+1} - \Delta\lambda \boldsymbol{N}_{\bar{\boldsymbol{\tau}}_{n+1}}. \tag{37}$$

When the constitutive formulation is restricted to elastic and inelastic isotropy, equivalence of Eqs. (36) and (37) is exact. Otherwise, that passage is an approximation based on moderately small elastic deformation with a second-order error on elastic strains. These conditions are needed in order to obtain the relation $\boldsymbol{R}^e_{n+1} = \boldsymbol{R}^{e^{trial}}_{n+1}$, where $\boldsymbol{R}^e = \boldsymbol{F}^e \boldsymbol{U}^{e^{-1}}$ is the elastic right rotation tensor with $\boldsymbol{U}^{e^2} = \boldsymbol{F}^{e^T} \boldsymbol{F}^e$ [34, 21].

The evolution of the accumulated viscoplastic strain ϵ, introduced in Eq. (11), is approximated based on a backward *Euler* method

$$\epsilon_{n+1} = \epsilon_n + \sqrt{\frac{2}{3}}\Delta\lambda, \tag{38}$$

in which the incremental viscoplastic multiplier $\Delta\lambda$ must satisfy

$$f\left(\bar{\boldsymbol{\tau}}_{n+1}, A_{n+1}\right) = \bar{\Theta}^{-1}\left(\Delta\lambda, A_{n+1}\right), \tag{39}$$

where $\bar{\Theta}^{-1}$ is the inverse function of $\bar{\Theta}$ in terms of f_{n+1} and $\Delta\lambda$. Function $\bar{\Theta}$ is the algorithmic version of Θ given in Eq. (17).

To compute the evolution of hardening variable A from Eq. (10) together with Eq. (9), we assume that the rate $\dot{\epsilon} \approx \frac{\epsilon_{n+1}-\epsilon_n}{\Delta t}$ is constant within time step $(t_n, t_{n+1}]$. Then, Eq. (13) can be used considering t_n as the initial state and t_{n+1} as the current state, leading to

$$A_{n+1} = A_n + A_{\infty_{n+1}} c\left(\epsilon_{n+1} - \epsilon_n\right) + \left[A_{\infty_{n+1}}\left(1 + c\epsilon_n\right) - A_n\right]\left\{1 - \exp\left[-\delta\left(\epsilon_{n+1} - \epsilon_n\right)\right]\right\}, \tag{40}$$

where by virtue of Eq. (15)

$$A_{\infty_{n+1}} = \left(1 - \beta_{n+1}\right) A^{lwr}_{\infty} + \beta_{n+1} A^{up}_{\infty}, \tag{41}$$

with (see Eq. (16))

$$\beta_{n+1} = \left[\frac{1}{\Delta t}\left(\frac{\epsilon_{n+1} - \epsilon_n - \Delta t \dot{\epsilon}_{lwr}}{\dot{\epsilon}_{up} - \dot{\epsilon}_{lwr}}\right)\right]^{\xi}. \tag{42}$$

The return mapping algorithm consists therefore in determining the solution to nonlinear system of equations (37)-(42) with respect to the set of unknowns $\left\{\boldsymbol{E}^e_{n+1}, \epsilon_{n+1}, \Delta\lambda, A_{n+1}, A_{\infty_{n+1}}, \beta_{n+1}\right\}$. However, equality $\boldsymbol{N}_{\bar{\boldsymbol{\tau}}_{n+1}} = \boldsymbol{N}_{\bar{\boldsymbol{\tau}}^{trial}_{n+1}}$ can be established in the context of *von Mises* criterion stated in Eq. (6). Equations (37)-(38) thus reduce to the single scalar equation:

$$\left\|\bar{\boldsymbol{\tau}}^{D^{trial}}_{n+1}\right\| - \Delta\lambda 2\mu - \sqrt{\frac{2}{3}}\left(\sigma_y + A_{n+1}\right) = \bar{\Theta}^{-1}\left(\Delta\lambda, A_{n+1}\right), \tag{43}$$

with unknowns $\Delta\lambda$ and A_{n+1}. Furthermore, inserting Eq. (38) into Eq. (40) yields

$$A_{n+1} = A_n + A_{\infty_{n+1}} c\sqrt{\frac{2}{3}}\Delta\lambda + \left[A_{\infty_{n+1}}\left(1 + c\epsilon_n\right) - A_n\right]\left[1 - \exp\left(-\delta\sqrt{\frac{2}{3}}\Delta\lambda\right)\right], \quad (44)$$

while substituting Eqs. (38) and (42) into Eq. (41) gives

$$A_{\infty_{n+1}} = A_\infty^{lwr} + \left[\frac{1}{\Delta t}\left(\frac{\sqrt{\frac{2}{3}}\Delta\lambda - \Delta t\dot{\epsilon}_{lwr}}{\dot{\epsilon}_{up} - \dot{\epsilon}_{lwr}}\right)\right]^{\xi}\left(A_\infty^{up} - A_\infty^{lwr}\right). \quad (45)$$

Then, the reduced return mapping algorithm consists in solving Eqs. (43)-(45) with respect to $\Delta\lambda$, A_{n+1} and $A_{\infty_{n+1}}$. Derivatives of Eqs. (43)-(45) with respect to unknowns $\left\{\Delta\lambda, A_{n+1}, A_{\infty_{n+1}}\right\}$, required into nonlinear problem solution, are given in A.

4.2 Consistent tangent modulus

Consistent tangent modulus introduced in Eq. (26) can be given in components according to

$$M_{ijkl_{n+1}} = \left(\frac{\partial\tau_{ip}}{\partial F_{kl}}F_{jp}^{-1} - \tau_{ip}F_{jk}^{-1}F_{lp}^{-1}\right)_{n+1}. \quad (46)$$

Computation of $\mathbb{M}_{n+1}$ requires the derivative calculation of $\boldsymbol{\tau}$ with respect to $\boldsymbol{F}$ at t_{n+1}. However, expressing $\boldsymbol{\tau}$ as a function of the rotated *Kirchhoff* stress tensor $\bar{\boldsymbol{\tau}}$ provides an alternative way to compute this derivative,

$$\tilde{\mathbb{D}}_{n+1} = \frac{\partial\bar{\boldsymbol{\tau}}_{n+1}}{\partial\boldsymbol{F}_{n+1}} = \mathbb{D}_{n+1} : \mathbb{P}_{n+1} : \mathbb{Q}_{n+1}, \quad (47)$$

since $\bar{\boldsymbol{\tau}}_{n+1}$ is a function of input variables $\boldsymbol{E}_{n+1}^{e^{trial}}$ and α_n. In the above equation, $\mathbb{D}_{n+1} = \frac{\partial\bar{\boldsymbol{\tau}}_{n+1}}{\partial\boldsymbol{E}_{n+1}^{e^{trial}}}$, $\mathbb{P}_{n+1} = \frac{\partial\boldsymbol{E}_{n+1}^{e^{trial}}}{\partial\boldsymbol{C}_{n+1}^{e^{trial}}}$ and $\mathbb{Q}_{n+1} = \frac{\partial\boldsymbol{C}_{n+1}^{e^{trial}}}{\partial\boldsymbol{F}_{n+1}}$. Observing that $\boldsymbol{C}_{n+1}^{e^{trial}} = \left(\boldsymbol{F}_{n+1}^{e^{trial}}\right)^T\boldsymbol{F}_{n+1}^{e^{trial}}$, the components of the fourth-order tensor $\mathbb{Q}_{n+1}$ read

$$Q_{ijkl_{n+1}} = F_{li_n}^{vp^{-1}}F_{kj_{n+1}}^{e^{trial}} + F_{ki_{n+1}}^{e^{trial}}F_{lj_n}^{vp^{-1}}. \quad (48)$$

The fourth-order tensor $\mathbb{P}_{n+1}$ is computed as

$$\mathbb{P}_{n+1} = \frac{\partial}{\partial\boldsymbol{C}_{n+1}^{e^{trial}}}\ln\left(\boldsymbol{U}_{n+1}^{e^{trial}}\right) = \frac{1}{2}\frac{\partial}{\partial\boldsymbol{C}_{n+1}^{e^{trial}}}\ln\left(\boldsymbol{C}_{n+1}^{e^{trial}}\right). \quad (49)$$

The terms $\mathbb{P}_{n+1}$ and $\mathbb{Q}_{n+1}$ are geometrical quantities related to finite strains while the tangent operator $\mathbb{D}_{n+1}$ is the unique term of $\tilde{\mathbb{D}}_{n+1}$ that depends on material response. In the elastic range, $\mathbb{D}_{n+1}$ turns to be coincident with the elastic stiffness $\mathbb{D}^e$, while it becomes the elastic-viscoplastic tangent operator

$$\mathbb{D}_{n+1}^{vp} = \frac{\partial\bar{\boldsymbol{\tau}}_{n+1}}{\partial\boldsymbol{E}_{n+1}^{e^{trial}}} \quad (50)$$

in the inelastic range. Evaluation of $\mathbb{D}^{vp}_{n+1}$ is obtained from linearization of Eqs. (37), (39), (45) and (44), what yields (see B)

$$\mathbb{D}^{vp}_{n+1} = \frac{\partial \bar{\boldsymbol{\tau}}_{n+1}}{\partial \boldsymbol{E}^{e^{trial}}_{n+1}} = \left(\mathbb{D}^{e^{-1}} + \Delta\lambda \frac{\partial \boldsymbol{N}_{\bar{\boldsymbol{\tau}}_{n+1}}}{\partial \bar{\boldsymbol{\tau}}_{n+1}} + \frac{1}{\chi} \boldsymbol{N}_{\bar{\boldsymbol{\tau}}_{n+1}} \otimes \boldsymbol{N}_{\bar{\boldsymbol{\tau}}_{n+1}} \right)^{-1}, \tag{51}$$

where

$$N_{A_{n+1}} = \frac{\partial f_{n+1}}{\partial A_{n+1}}, \tag{52}$$

$$\chi = \left[\frac{\partial \bar{\Theta}^{-1}}{\partial \Delta\lambda} + \left(\frac{\partial \bar{\Theta}^{-1}}{\partial A_{n+1}} - N_{A_{n+1}} \right) \Lambda \right], \tag{53}$$

$$\begin{aligned} \Lambda \;=\; & \left[(1 + c\epsilon_n)(1 - \varphi) + c\sqrt{\frac{2}{3}}\Delta\lambda \right] \omega + \ldots \\ & \ldots + \sqrt{\frac{2}{3}} \left\{ \delta \left[A_{\infty_{n+1}} (1 + c\epsilon_n) - A_n \right] \varphi + A_{\infty_{n+1}} c \right\}, \end{aligned} \tag{54}$$

$$\omega = \sqrt{\frac{2}{3}} \frac{\xi}{\Delta t} \left(\frac{A^{up}_{\infty} - A^{lwr}_{\infty}}{\dot{\epsilon}_{up} - \dot{\epsilon}_{lwr}} \right) \left[\frac{1}{\Delta t} \left(\frac{\sqrt{\frac{2}{3}}\Delta\lambda - \Delta t \dot{\epsilon}_{lwr}}{\dot{\epsilon}_{up} - \dot{\epsilon}_{lwr}} \right) \right]^{\xi - 1}, \tag{55}$$

$$\varphi = \exp\left(-\delta \sqrt{\frac{2}{3}} \Delta\lambda \right). \tag{56}$$

5 Numerical results and discussion

Aiming to assess the capabilities of the present constitutive model in accounting for strain hardening, strain rate hardening and viscous effects, the numerical procedure described in Section 4 is first applied to analyze the local material response subjected to uniaxial tension/compression loading. The latter is described by prescribing the value of axial strain E_{11} and associated strain rate $\bar{D}_{11}$. The material is elastic-viscoplastic and the corresponding material parameters to be used are given in Tab. 1. These parameters were obtained in a previous work [26] considering experimental data for an annealed OFHC copper available in the literature [3, 7, 35]. Classical relationships relate the *Young* modulus E and *Poisson* ratio ν appearing in Tab. 1 with elastic coefficients μ and κ of Eq. (4) through $\mu = \frac{E}{2(1+\nu)}$ and $\kappa = \frac{E}{3(1-2\nu)}$. We emphasize that the elastic part of strain is expected to be infinitesimal since the ratio $\frac{\sigma_y + A}{E}$ is very small when compared to unity. Furthermore, it should be kept in mind that the *Perić* viscoplastic function is considered throughout the paper, see Eqs. (17)-(19).

Table 1: Material properties and model parameters associated with annealed OFHC copper [26].

E [GPa]	ν [–]	σ_y [MPa]	δ [–]	c [–]	A_∞^{lwr} [MPa]	A_∞^{up} [MPa]	$\dot{\epsilon}_{lwr}$ [s^{-1}]	$\dot{\epsilon}_{up}$ [s^{-1}]	ξ [–]	ϑ [s]	m [–]
112	0.33	35	6.46	0.42	233	420	10^{-4}	10^4	3.16	1.2×10^3	105

5.1 Decremental strain rate test

Strain rate hardening (or strain rate history) effects can be demonstrated from decremental strain rate testing. In this case, the material is subjected to a monotonic loading with a given initial strain rate $\bar{D}_{11_1}$ which is then abruptly decreased to a value $\bar{D}_{11_2}$. The phenomenon is evidenced when the decremental response is compared to those obtained during a monotonic loading under a constant strain rate $\bar{D}_{11} = \bar{D}_{11_2}$ during overall deformation process. For this purpose the present analysis will include two load conditions (employed in experiments of [3]):

- Q.S.: *quasi*-static test. Material is subjected to a total strain equal to 92% imposed very slowly with $\bar{D}_{11} = 4 \times 10^{-4}\,\mathrm{s}^{-1}$;
- D.T.: decremental strain rate test. Material is subjected to at a high strain rate of $\bar{D}_{11_1} = 6 \times 10^3\,\mathrm{s}^{-1}$ until a partial strain of 32% is reached, then the strain rate is abruptly changed to a lower value $\bar{D}_{11_2} = 4 \times 10^{-4}\,\mathrm{s}^{-1}$ while strain reaches 79%.

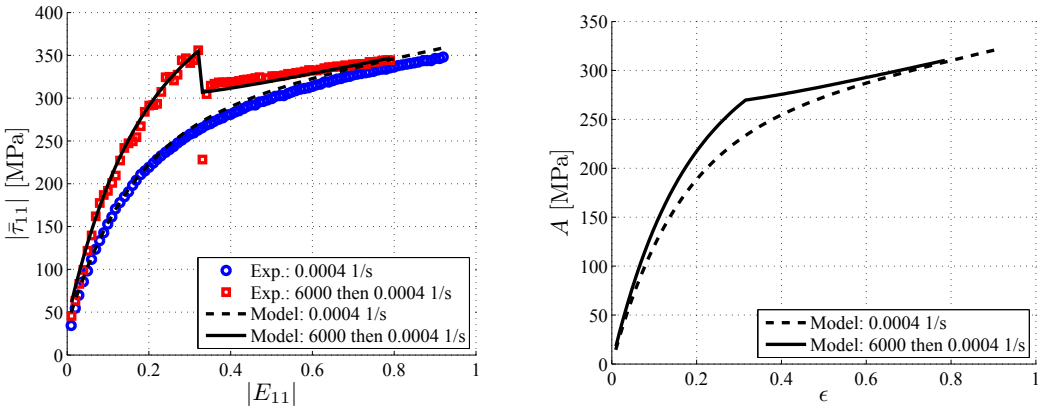

(a) (b)

Figure 1: Decremental strain rate test results: (a) Model-predicted stress-strain curves compared with experimental data of [3]; (b) Stress hardening vs. accumulated viscoplastic strain curves.

Numerical analyzes were performed considering a local convergence tolerance equal to 10^{-6}, 92 time steps[3] for *Q.S.* simulation and 78 for *D.T.* case. The numerical results are depicted in Figs. 1(a) and (b) showing the effects of strain rate history on the material response. Figure 1(a) shows the stress-strain curves for *Q.S.* and *D.T.* results are

[3]Numbers of time steps are equal to number of experimental points.

compared with experiments of [3], where a good agreement between predicted and experimental data is observed. When the strain rate changes abruptly from $\bar{D}_{11_1} = 6 \times 10^3\,\mathrm{s}^{-1}$ to $\bar{D}_{11_2} = 4 \times 10^{-4}\,\mathrm{s}^{-1}$, an abrupt change in flow stress is observed. It is due to instantaneous strain rate sensitivity related to viscous mechanisms, while no jump is observed in hardening response as illustrated by Fig. 1(b). This behavior feature could be expected, since parameter A is related to current microstructural configuration, which does not undergo an instantaneous change by abruptly shifting strain rate (see reference [1]). Moreover, *Q.S.* curves should only be recovered asymptotically by both stress and hardening responses of *D.T.* simulation. This is attributed to the fact that the flow stress does not depend only on instantaneous values of strain rate, but also on strain rate history. In other words, a higher previous strain rate induces a larger hardening when compared to a lower strain rate imposed during the whole deformation process, what can be physically related to the rate-dependence of dislocation storage [1, 2, 44, 45]. This rate-sensitivity is captured by the present model through the rate dependence attributed to saturation hardening A_∞ (see Eq. (15)).

5.2 Rate-dependence and stress relaxation

The current material strength induced by previous deformation history can also be characterized from stress relaxation testing, where the obtained equilibrium state reflects the current microstructural configuration. Thereby, the strain rate history effects on material state can be evaluated by varying the loading strain rate preceding stress relaxation, and thus observing the associated equilibrium stress states that are reached asymptotically. A constitutive model capable of accounting for strain rate history effects should theoretically be able to predict the distinct equilibrium stress states reached after different previous loading strain rates. For this purpose, numerical simulations of stress relaxation tests are undertaken using the proposed elastic-viscoplastic formulation.

Table 2: Loading strain rates of stress relaxation testing.

	Q.S.	case *R1*	case *R2*	case *R3*
$\bar{D}_{11}$ [s^{-1}]	4×10^{-4}	10^3	6×10^3	9×10^3

The numerical analyzes are carried out prescribing a total strain equal to 100% at different strain rates (see Tab. 2) and then keeping it constant along time. The material properties are those given in Tab. 1. All analyzes were performed considering 200 time steps and a local convergence tolerance equal to 10^{-6}. The stress-strain curves obtained for loading and stress relaxation simulations are shown in Fig. 2(a). In this figure, cases *Q.S.*, *R2* and *R3* are compared with experiments showing a good agreement. As expected, the flow stress is an increasing function of strain rate. This effect could readily be predicted by a conventional viscoplastic model that accounts only for instantaneous rate-sensitivity. However, the proposed constitutive model is also capable to predict the hardening rate-sensitivity, since the hardening A should be a direct consequence of the

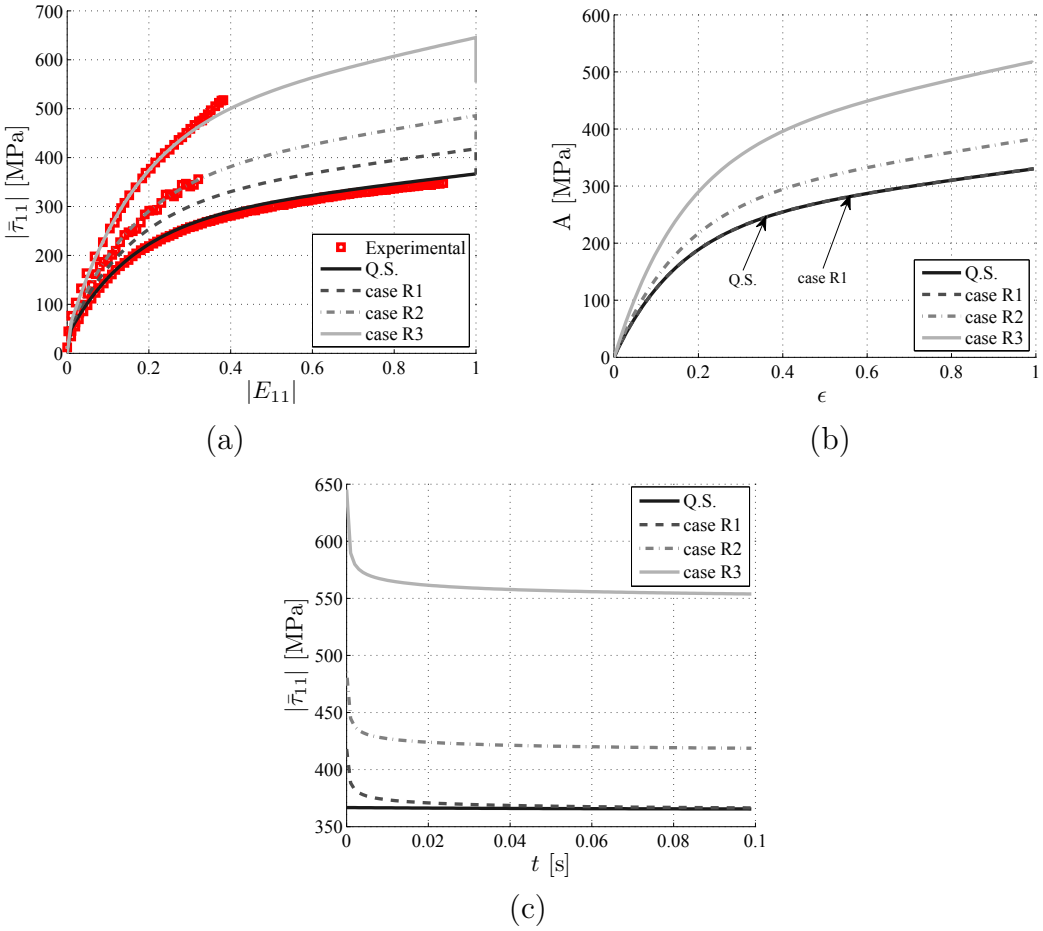

Figure 2: (a) Strain rate effects on stress-strain curves: comparison of model prediction and experiments of [3] (*Q.S.* and *R2*) and of [35] (*R3*); (b) Strain rate history effect on hardening curves; (c) Strain rate history effect on stress relaxation.

current microstructure, which in turn is affected by the whole plastic strain and strain rate history and not only by their current values.

In the proposed model, the hardening variable A increases with rate $\dot{\epsilon}$, as emphasized in Fig. 2(b). But, the strain rate influence on hardening becomes significant only for strain rates greater than $10^3\,\mathrm{s}^{-1}$. That is, up to a strain rate of $10^3\,\mathrm{s}^{-1}$ (cases *Q.S.* and *R1*) hardening responses are practically overwritten and for strain rates exceeding $10^3\,\mathrm{s}^{-1}$ (cases *R2* and *R3*) the effect of previous strain rate history upon A becomes significant. The rate dependence of hardening variable A can also be clearly evidenced in Fig. 2(c), where the relaxation response tends toward an asymptotic equilibrium stress state, which is given by the non-viscous stress $(\sigma_y + A)$ associated with each previous loading strain rate. In this figure, we observe that *R1* curve reaches the *Q.S.* response asymptotically, what demonstrates that the difference between cases *Q.S.* and *R1* observed in Fig. 2(a) is mainly due to viscous effects. On the other hand, the equilibrium stress state $(\sigma_y + A)$ is significantly increased by strain rate for values exceeding $10^3\,\mathrm{s}^{-1}$. Note that the reference

time $t = 0$ in Fig. 2(c) corresponds to the instant at which the stress relaxation starts.

5.3 Billet upsetting simulation

In order to evaluate the whole numerical framework (local constitutive integration and finite element solution), a billet upsetting simulation is carried out in the sequel. Numerical results are compared with analytical solution, which was derived in work [26] for uniaxial compression test,

$$|\bar{\tau}_{11}| = (\sigma_y + A)\left(1 + \sqrt{\frac{3}{2}}\vartheta\dot{\epsilon}\right)^{\frac{1}{m}}, \tag{57}$$

where $|\bar{\tau}_{11}|$ is the absolute value of axial rotated *Kirchhoff* stress. The analyzes aim to demonstrate the strain rate effects on plastic fields of a non-homogeneous deformation process. Furthermore, to assess numerical efficiency and robustness convergence studies are performed. Convergence criterion is the number of iterations (n_{iter}) to reach the admissible error given by $\|\boldsymbol{r}_{n+1}\|_{\infty}^{adm} = 10^{-6}$. The residue vector is the classical one used into finite element framework, $\boldsymbol{r} = \boldsymbol{f}^{ext} - \boldsymbol{f}^{int}$, in which $\boldsymbol{f}^{ext}$ and $\boldsymbol{f}^{int}$ are the external and internal finite element force vectors, respectively.

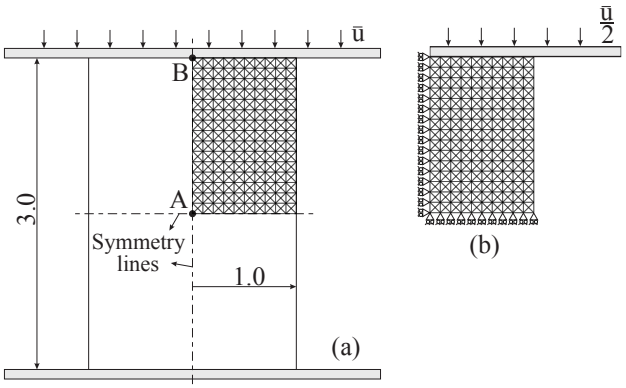

Figure 3: (a) Axisymmetric billet upsetting model (dimensions are in mm); (b) Finite element mesh and boundary conditions for a quarter of workpiece.

Figure 3 schematically presents the axisymmetric model considered for analysis, where upper and lower gray regions represent rigid platens. Finite element discretization consists of 600 quadratic triangular elements (1251 nodes). Material parameters are also those of Tab. 1. The contact formulation is based on *Signorini* condition and friction is modeled by regularized *Coulomb* model with a friction coefficient of $f_c = 0.1$ and regularization parameter $\epsilon_T = 10^{-4}$. The *Augmented Lagrangian* algorithm [46, 47] is employed to impose the contact, and penalty parameter associated with the impenetrability condition is set as $\epsilon_v = 10^{-7}$. The main focus of the present simulation is to analyze the structural response in frictional compression test. However, the simulation with $f_c = 0$ shall also be performed and corresponding predictions compared to analytical results derived for

frictionless case. Starting from $\bar{u}\,(t=0)=0$, the prescribed displacement takes the form [26]:

$$\bar{u}\,(t) = l_0\,[1-\exp\,(Kt)]\,, \tag{58}$$

which would correspond in a frictionless problem to a homogeneous axial strain rate of $-\bar{D}_{11} = K > 0$. In Eq. (58) $l_0 = 3\,\text{mm}$ is the specimen initial length. A total prescribed displacement $\bar{u}_{total} = 1.0\,\text{mm}$ is applied and maintained in 100 equal time steps (50 for loading stage and 50 for stress relaxation phase). Considering different values of K according to Tab. 2, the loading process is defined as follows:

$$\bar{u}\,(t) = \begin{cases} l_0\,[1-\exp\,(Kt)] & 0 \le t \le T \\ \bar{u}_{total} & T \le t < \infty \end{cases}\,, \tag{59}$$

with $\bar{u}_{total} = l_0\,[1-\exp\,(KT)]$ being the total prescribed displacement reached at an instant $t = T$. For $t \ge T$, the applied displacement is maintained constant along time in order to investigate the structural response during stress relaxation test. Considering the friction case, the prescribed displacement $\bar{u}_{total} = 1.0\,\text{mm}$ induces a non-homogeneous strain field in the specimen whose maximum magnitude is in all cases lower than 55%. The limitation to this strain level has been deliberately adopted to avoid numerical difficulties, thus focusing on the constitutive effects of numerical modeling. For example, the present numerical strategy does not prevent volumetric locking, and in this case it expected that for strains higher than 0.55 this numerical issue can become significant.

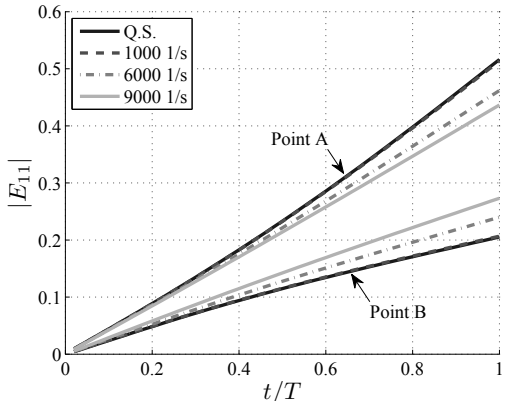

Figure 4: Influence of loading rate parameter K on axial strain of point A and point B (friction cases).

As mentioned early, friction conditions along loaded faces induce a heterogeneous strain field in the specimen. This aspect will be characterized considering two distinct points A and B of the discretized workpiece, see Fig. 3(a). The loading rate influence on axial strain history of points A and B is shown in Fig. 4, that is, the influence of loading rate parameter K on axial strain response vs. normalized time $\frac{t}{T}$. Due to friction effects, point B undergoes smaller strains than point A, since this phenomenon restricts the radial displacement at platen/specimen interface. However, increasing K leads to a decrease in axial strain of point A, while it induces an increase in axial strain of B.

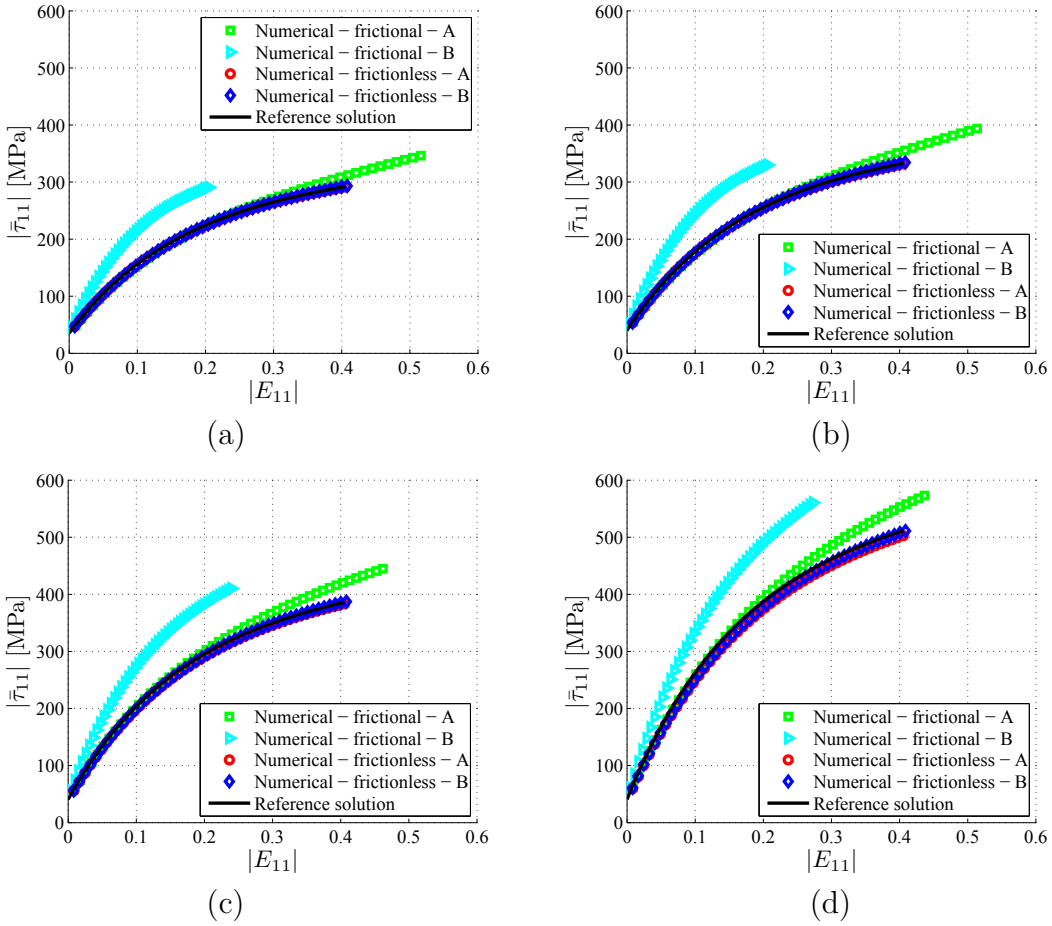

Figure 5: Axial stress vs. strain curves: (a) *Quasi*-static case, $K = 4 \times 10^{-4}\,\mathrm{s}^{-1}$; (b) $K = 10^{3}\,\mathrm{s}^{-1}$; (c) $K = 6 \times 10^{3}\,\mathrm{s}^{-1}$; (d) $K = 9 \times 10^{3}\,\mathrm{s}^{-1}$.

Figures 5(a)-(d) display, for different values of K, the axial rotated *Kirchhoff* stress vs. strain curves of points A and B. In addition to results obtained from numerical simulations of frictional compression test, these figures also show the numerical predictions for frictionless situation as well as for the rigid-viscoplastic analytical solution given in Eq. (57). Note that frictionless numerical predictions are very close to analytical reference solution. In friction case, the response of point A remains close to that obtained in frictionless compression (reference situation) until a strain of about 20%. Beyond this strain level, the response in friction case begins to deviate from this reference situation. In contrast, due to confined strain state, stress triaxiality appears in vicinity of point B right after the loading process has started, leading to lower strain and higher stress levels than at point A.

Comparisons for different values of K of axial rotated *Kirchhoff* stress vs. logarithmic strain curves are shown in Figs. 6(a) and (b) for frictional compression test. This comparisons indicate that increasing the value of K induces higher absolute stress levels in the specimen. However, the maximum strain level decreases with K at point A, while it

exhibits opposite trend at point B.

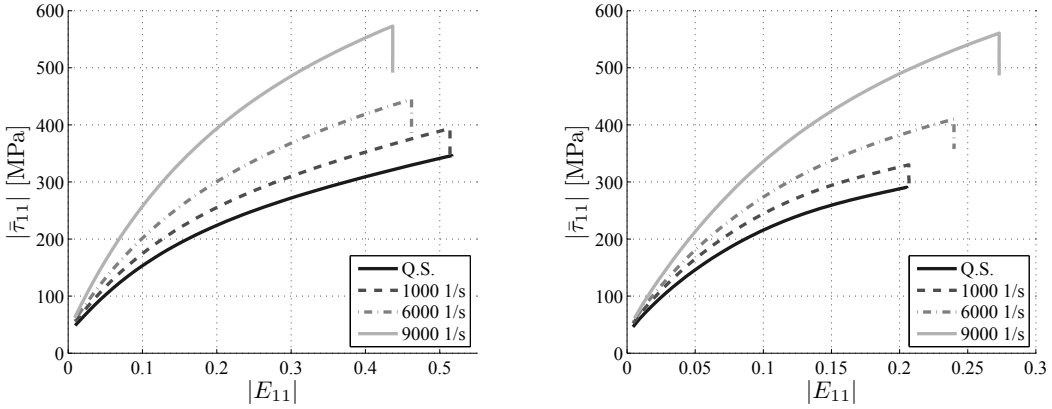

Figure 6: Influence of loading rate parameter K on axial stress vs. strain curves (friction cases): (a) Point A; (b) Point B.

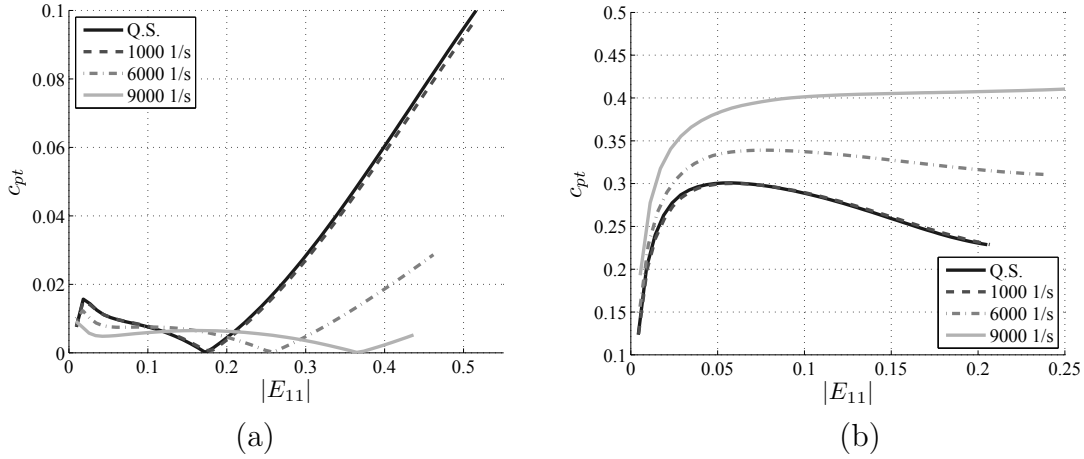

Figure 7: Influence of loading rate parameter K on pressure transmission coefficient $c_{pt} = \frac{\bar{\tau}_{22}}{\bar{\tau}_{11}}$ vs. strain curves (friction cases): (a) Point A; (b) Point B.

Stress triaxiality effects are illustrated in Figs. 7(a) and 7(b), where the pressure transmission coefficients[4] $c_{pt} = \frac{\bar{\tau}_{22}}{\bar{\tau}_{11}}$ at points A and B are plotted against the axial strain. Scalars $\bar{\tau}_{11}$ and $\bar{\tau}_{22}$ refer to axial and radial rotated *Kirchhoff* stresses, respectively. In accordance with observations related to Figs. 5, it is first observed that ratio c_{pt} at point A remains very small for strain lower than 20%, and then increases continuously with the strain level (Fig. 7(a)). In contrast, ratio c_{pt} at point B increases rapidly with strain in the small range (until $\approx 5\%$), followed by a moderate decreasing with strain level (Fig. 7(b)).

[4]It is worth to recall that in an axisymmetric deformation the value $c_{pt} = 0$ indicates an axial stress

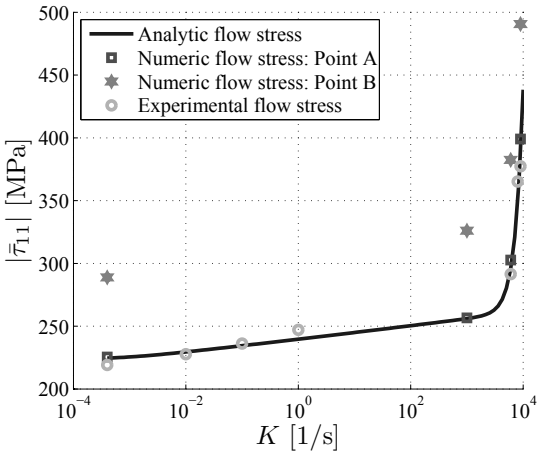

Figure 8: Influence of loading rate parameter K on flow stress of Point A and Point B, for a given absolute strain of 0.2 (friction cases). Analytical solution is taken from Eq. (57), considering a frictionless rigid-viscoplastic case. Experimental data were taken from references [3, 7, 35] considering an annealed OFHC copper (see also reference [26]).

Concerning the strain rate sensitivity, in Fig. 8 the influence of loading rate parameter K on flow stress response can be realized, considering a given absolute strain level of 0.2. In this figure an upturn in the rate sensitivity is observed for values of K greater than $10^3\,\mathrm{s}^{-1}$. As discussed by some authors (see for instance [48, 8, 26]) this sudden upturn behavior is a result of the strain rate hardening observed e.g. in FCC metals as copper and aluminum. Notice that the stress response of point A is very close to the frictionless rigid-viscoplastic analytical solution given in Eq. (57) and to the experimental data related to annealed OFHC copper, see [3, 7, 35]. However, in contrast to point A, due to confined strain state and then to higher stress triaxiality, point B presents a higher absolute stress level for the same given total strain of 0.2.

The overall behavior of structure may be characterized by means of the evolution of resultant vertical force applied to specimen with respect to prescribed displacement. Figures 9(a)-(d) show the results obtained from numerical simulations as well as analytical solution for frictionless compression obtained from stress solution of Eq. (57)

$$|f_1| = \frac{V_0}{l}\,|\bar{\tau}_{11}|\,, \tag{60}$$

where $|f_1|$ is the resultant applied force, V_0 is the initial volume and l is the current length of workpiece. The numerical frictionless results are very close to analytical reference solutions. However, slight effects of friction are observed as prescribed displacement is increasing. It is emphasized that the whole results should be interpreted keeping in mind that the considered value of friction coefficient is rather small ($f_c = 0.1$). Regarding the influence of strain rate parameter K, Figs. 10(a) and (b) corroborate, as expected, that higher forces are needed to impose a given displacement when the loading rate K increases.

state and $c_{pt} = 1$ a hydrostatic stress state.

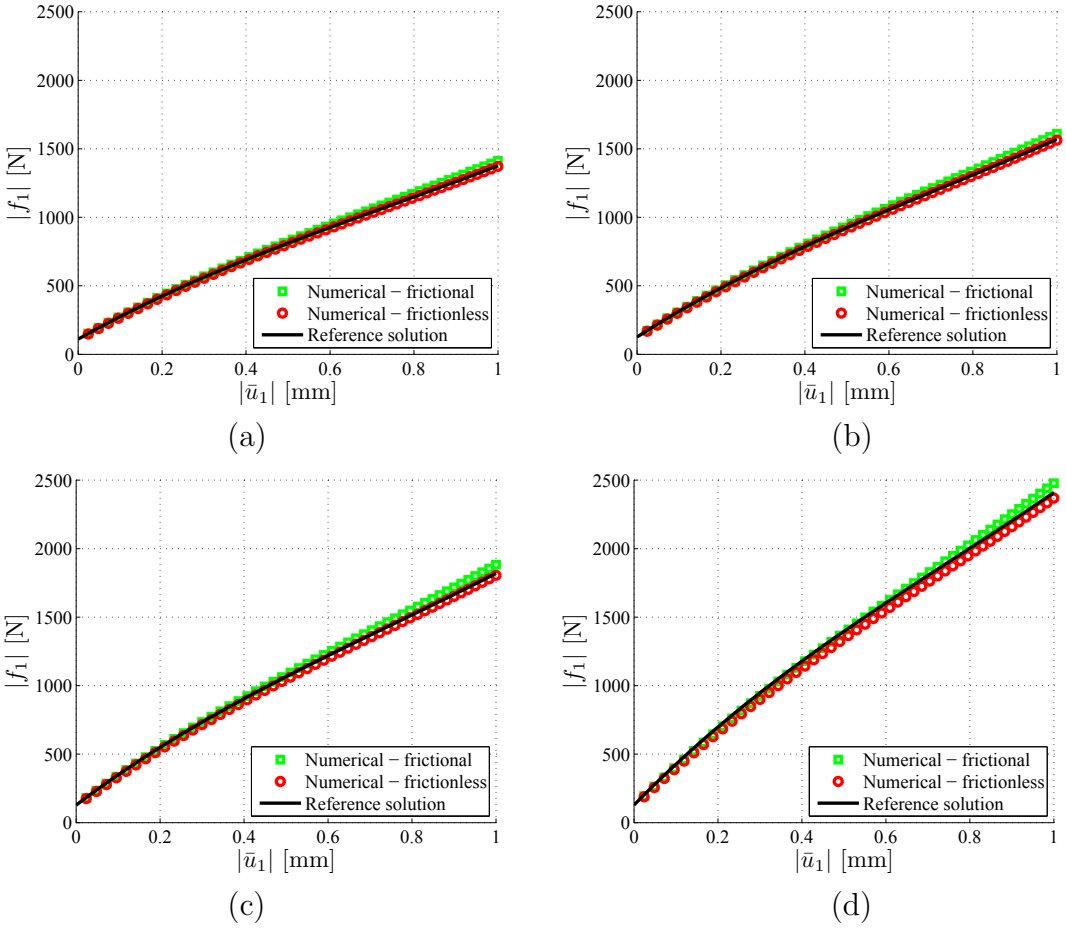

Figure 9: Applied force vs. applied displacement curves: (a) *Quasi*-static case, $K = 4 \times 10^{-4}\,\mathrm{s}^{-1}$; (b) $K = 10^3\,\mathrm{s}^{-1}$; (c) $K = 6 \times 10^3\,\mathrm{s}^{-1}$; (d) $K = 9 \times 10^3\,\mathrm{s}^{-1}$. Notice that the reference solution is for rigid-viscoplastic case, see Eq. (57), while the FE solution is for elastic-viscoplastic one.

The capability of the proposed constitutive model to capture the effects of strain rate on stress response has been illustrated in Figs. 6, which indicate that axial stress-strain curves are significantly affected by the value of imposed loading rate K. At strain rates until $10^3\,\mathrm{s}^{-1}$ the rate dependence is mainly due to viscous effects, and for strain rates exceeding $10^3\,\mathrm{s}^{-1}$ proposed model accounts for the dependence of hardening with respect to strain rate (see for instance [26]). The effects of strain rate on the material hardening response are clearly evidenced in Figs. 11(a) and (b) in frictional compression test with $f_c = 0.1$. These figures emphasize how increasing the value of K induces, for a given accumulated viscoplastic strain, a larger material hardening. However, note that the curves related to cases *Q.S.* and $K = 10^3\,\mathrm{s}^{-1}$ are practically overwritten, what clearly shows that for strain rates $< 10^3\,\mathrm{s}^{-1}$ the proposed model predicts a small strain rate influence on hardening response.

The analysis performed during loading phase ($t \leq T$) suggests that, due to rate sensitivity of material hardening, significant effects of strain rate on flow stress rise when

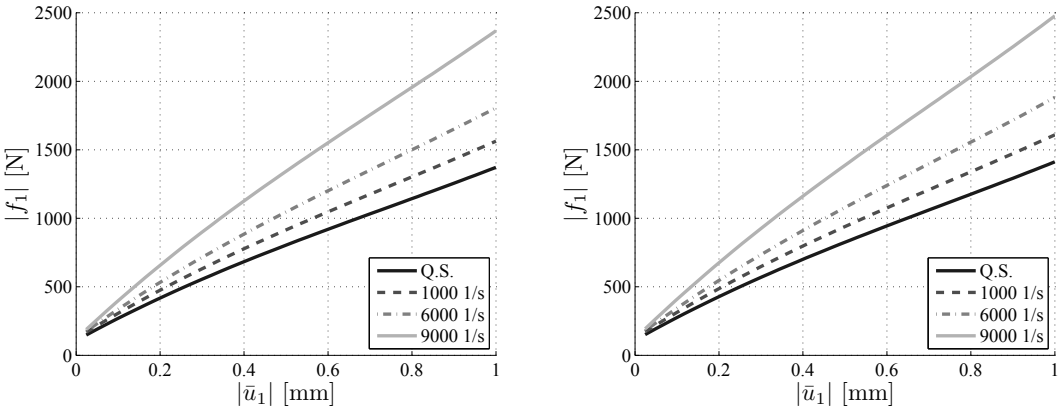

Figure 10: Influence of loading rate parameter K on applied force vs. applied displacement curves: (a) Frictionless; (b) Frictional cases.

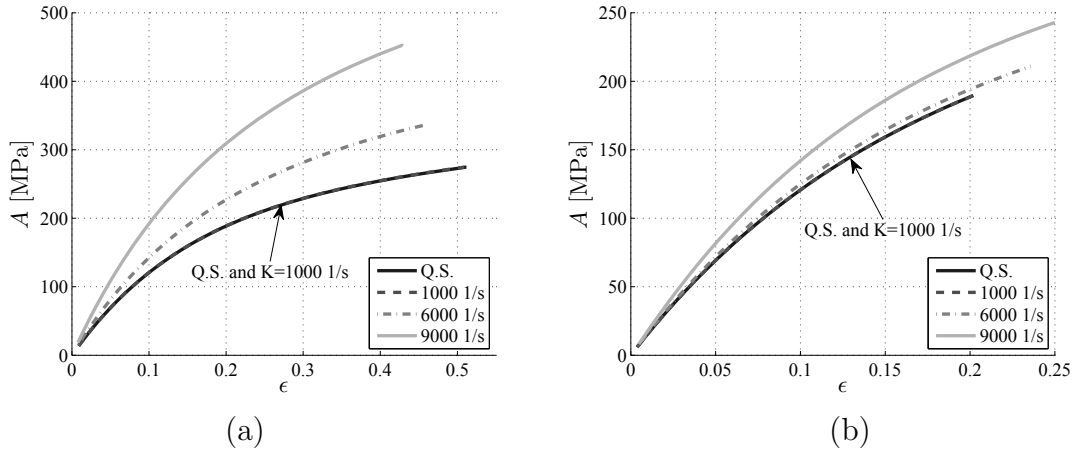

Figure 11: Influence of loading rate parameter K on stress hardening vs. accumulated viscoplastic strain (friction cases): (a) Point A; (b) Point B.

$K > 10^3\,\mathrm{s}^{-1}$. This feature is also corroborated in the relaxation phase imposed to specimen. Figures 12(a) and (b) present the stress relaxation curves of points A and B, i.e., evolution of axial rotated *Kirchhoff* stress vs. time t. It is observed from these figures that the equilibrium stress state (asymptotic stress state) reached after relaxation process is generally sensitive to strain rate history. However, since equilibrium stress quantity is a direct consequence of material hardening, as commented early, the strain rate influence on relaxed state becomes significant only for loading rates $K > 10^3\,\mathrm{s}^{-1}$. Consequently, the case with $K = 10^3\,\mathrm{s}^{-1}$ tends asymptotically to the *Q.S.* curve. The reference time $t = 0$ in Fig. 12 corresponds to instant (T) at which the stress relaxation starts.

An alternative way to illustrate the strain rate history effects on specimen response consists of visualizing the contours of *von Mises* equivalent stress, as displayed in Figs. 13(a)-(d). Two particular instants are considered for each value of K, namely at the

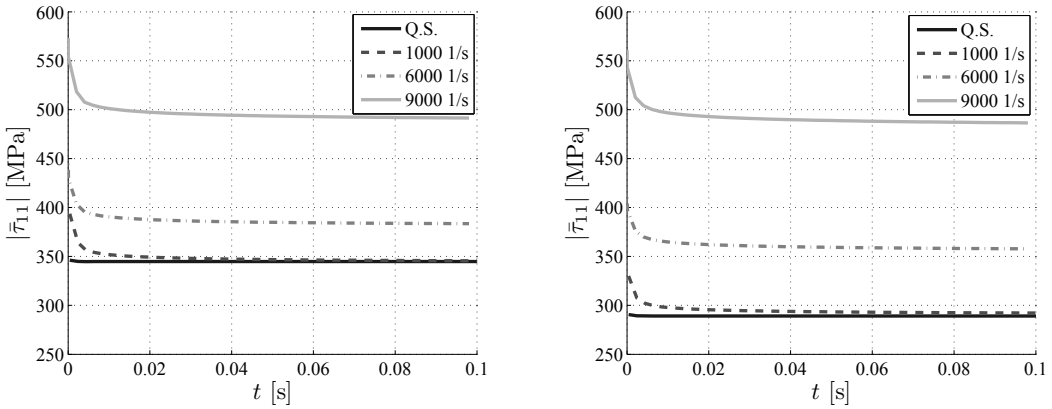

Figure 12: Influence of loading rate parameter K on stress relaxation (friction cases): (a) Point A; (b) Point B.

onset of stress relaxation ($t = T$) and at the relaxed state. Once again, these figures confirm the existence of a value of loading rate beyond which strain rate history effects prove significant. As expected, no noticeable change is observed between the "before relaxation" and "after relaxation" states for the *quasi*-static case. In contrast, significant changes between the "before relaxation" and "after relaxation" states are observed for the high strain rate cases ($K \geq 10^3\,\mathrm{s}^{-1}$), what is due to instantaneous viscous effects. Furthermore, comparison of all "after relaxation" states indicates that the $K = 10^3\,\mathrm{s}^{-1}$ case relaxes to a state close to the *quasi*-static one. On the other hand, higher values of K leads to higher absolute values of equilibrium stress fields.

The performance of numerical procedure is assessed by means of convergence analyzes in both *quasi*-static and high strain rate ($K = 9 \times 10^3\,\mathrm{s}^{-1}$) cases. The results are summarized in Tab. 3 for $\frac{t}{T} \in \{0.02, 0.2, 0.5, 1.0\}$ considering frictionless ($f_c = 0$) and frictional ($f_c = 0.1$) compression. In this table term AL_i stands for the number of iterations to reach convergence in the *Augmented Lagrangian* algorithm employed to solve contact problem [46, 47] and n_{iter} for the number of iterations to reach finite element equilibrium ($\|\boldsymbol{r}_{n+1}\|_\infty \leq 10^{-6}$). The end of loading phase ($t = T$) in *Q.S.* case correspond to the higher required iterations for numerical convergence ($n_{iter} = 15$). Table 3 also indicates that convergence is enhanced with higher loading rate K.

Convergence curves are displayed in Figs. 14(a) and (b) for simulations considering smooth and frictional contact in the *quasi*-static and high strain rate ($K = 9 \times 10^3\,\mathrm{s}^{-1}$) cases. Two particular instants were examined, namely $\frac{t}{T} = 0.02$ and $\frac{t}{T} = 1.0$. Figure 14(a) shows that there is no significant difference between the *quasi*-static and high strain rate cases for frictionless compression simulations. On the other hand, it is observed in Fig. 14(b) that the convergence is significantly improved when imposing a higher strain rate in the case of frictional compression test. As a matter of fact, the number of iterations for convergence drops from 50 to 5 at instant $\frac{t}{T} = 1.0$ and iteration $AL_i = 2$ of *Augmented Lagrangian* algorithm. Furthermore, as can be seen in Tab. 3, the *Augmented Lagrangian* algorithm took 3 steps to converge in the *quasi*-static frictional problem. The *quasi*-static

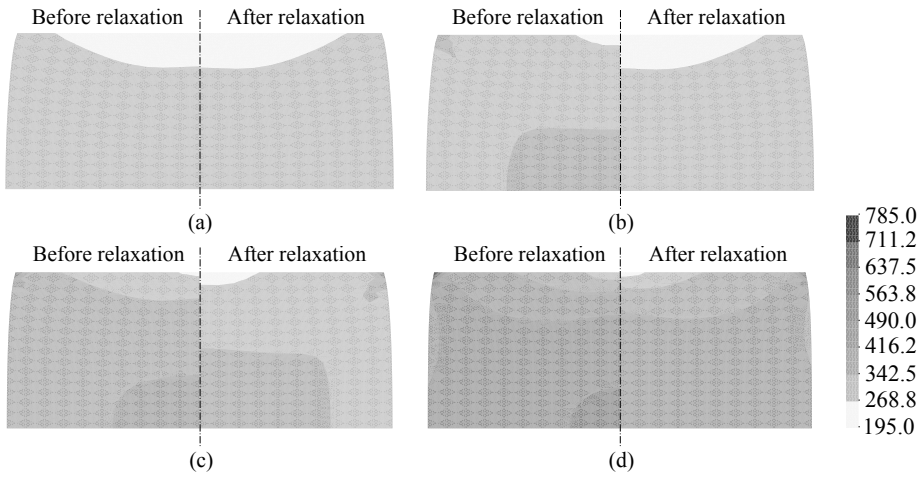

Figure 13: Contours of *von Mises* equivalent stress [MPa], before stress relaxation ($t = T$) and after stress relaxation: (a) *Quasi*-static case, $K = 4 \times 10^{-4}\,\mathrm{s}^{-1}$; (b) $K = 10^{3}\,\mathrm{s}^{-1}$; (c) $K = 6 \times 10^{3}\,\mathrm{s}^{-1}$; (d) $K = 9 \times 10^{3}\,\mathrm{s}^{-1}$.

simulation has a worse global convergence because, in addition to the trial elastic state being far from the current solution, in this case a higher time increment Δt is obtained, what can give an ill-conditioned tangent operator $\mathbb{D}^{vp}$. See for instance Eqs. (51)-(55), as well as Eqs. (70) and (71).

Table 3: Number of iterations required for convergence of frictional contact algorithm.

$\frac{t}{T}$ - (step number)	AL_i	*Quasi*-static		$K = 9 \times 10^{3}\,\mathrm{s}^{-1}$	
		n_{iter}		n_{iter}	
		$f_c = 0$	$f_c = 0.1$	$f_c = 0$	$f_c = 0.1$
0.02 - (1)	1	15	25	11	15
	2	11	17	8	11
0.2 - (10)	1	6	9	7	7
	2	5	9	5	6
0.5 - (25)	1	6	8	6	7
	2	5	9	4	5
1.0 - (50)	1	6	42	6	7
	2	4	50	4	5
	3	–	29	–	–

6 Conclusions

A finite strain elastic-viscoplastic numerical framework was developed and implemented into the FE context. The overall approach is intended to simulate high velocity plastic deformation processes in which loading history effects have to be considered. The main goal was to provide an adequate and computationally efficient numerical tool for high strain

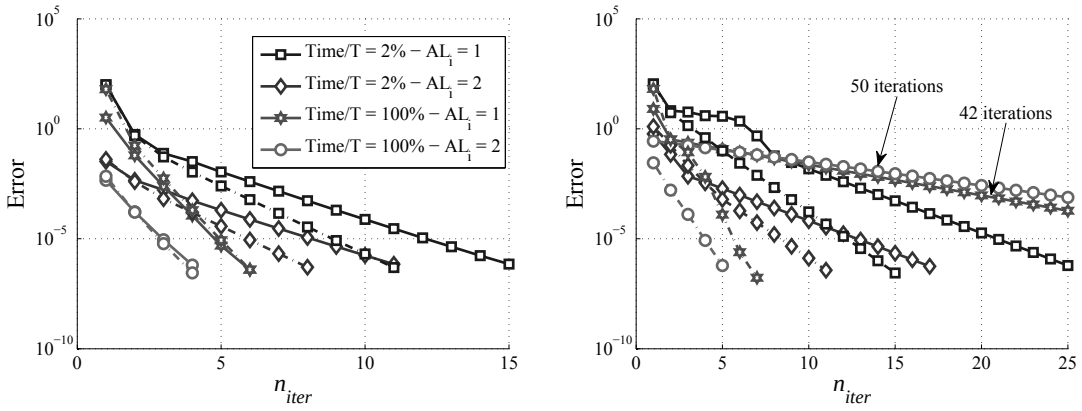

Figure 14: Convergence curves for *quasi*-static (solid lines) and high strain rate $\left(K = 9 \times 10^3\,\mathrm{s}^{-1}\right)$ (dash-doted lines) cases: (a) Frictionless compression; (b) Frictional compression.

rate straining of metals. The accuracy of constitutive modeling and related numerical procedure was assessed by means of homogeneous decremental strain rate and constant strain rate loading followed by stress relaxation testing, and global analysis consisting of a billet upsetting considering friction contact conditions. The loading process in the latter analysis is also defined by an initial constant loading rate stage followed by a stress relaxation phase. All these analysis have demonstrated the capabilities of the constitutive and numerical modeling to properly capture the main features of strain rate history effects on material and structural response of elastic-viscoplastic media. The algorithm convergence analyzes emphasized the good performance and robustness of numerical procedure. The numerical results obtained in this paper contribute to the understanding of high strain rate processes while encouraging for future developments in high strain rate material modeling.

Acknowledgements

The author Tiago dos Santos wishes to acknowledge the doctoral scholarship support of *CAPES*, Coordenação de Aperfeiçoamento de Pessoal de Nível Superior of Brazil. Process number BEX 7023/15-4. The author Rodrigo Rossi wishes to acknowledge the support of *CNPq*, Conselho Nacional de Desenvolvimento Científico e Tecnológico of Brazil. Grant number 304044/2015-6.

REFERENCES

[1] Klepaczko, J. Thermally activated flow and strain rate history effects for some polycrystalline f.c.c. metals. *Mater. Sci. Engng.* (1975) **18**:121–135.

[2] Chiem, C. and Duffy, J. Strain rate history effects and observations of dislocation substructure in aluminum single crystals following dynamic deformation. *Mater. Sci. Engng.* (1983) **57**:233–247.

[3] Tanner, A.B. and McDowell, D.L. Deformation, temperature and strain rate sequence experiments on OFHC Cu. *Int. J. Plast.* (1999) **15**:375–399.

[4] Huang, F. and Tao, N. Effects of strain rate and deformation temperature on microstructures and hardness in plastically deformed pure aluminum. *J. Mater. Sci. Tech.* (2011) **27**:1–7.

[5] Luo, Z., Zhang, H., Hansen, N. and Lu, K. Quantification of the microstructures of high purity nickel subjected to dynamic plastic deformation. *Acta Mater.* (2012) **60**:1322–1333.

[6] Follansbee, P. and Kocks, U. A constitutive description of the deformation of copper based on the use of the mechanical threshold stress as an internal state variable. *Acta Metall.* (1988) **36**:81–93.

[7] Nemat-Nasser, S. and Li, Y. Flow stress of f.c.c. polycrystals with application to OFHC Cu. *Acta Mater.* (1998) **46**:565–577.

[8] Gao, C. and Zhang, L. Constitutive modelling of plasticity of fcc metals under extremely high strain rates. *Int. J. Plast.* (2012) **32-33**:121–133.

[9] Rodríguez-Martínez, J., Rodríguez-Millán, M., Rusinek, A. and Arias A. A dislocation-based constitutive description for modeling the behavior of FCC metals within wide ranges of strain rate and temperature. *Mech. Mater.* (2011) **43**:901–912.

[10] Nemat-Nasser, S., Ni, L. and Okinaka, T. A constitutive model for fcc crystals with application to polycrystalline OFHC copper. *Mech. Mater.* (1998) **30**:325–341.

[11] Lebensohn, R. and Tomé, C. A self-consistent anisotropic approach for the simulation of plastic deformation and texture development of polycrystals: Application to zirconium alloys. *Acta Metall. Mater.* (1993) **41**:2611–2624.

[12] Roters, F., Eisenlohr, P., Hantcherli, L., Tjahjanto, D., Bieler, T. and Raabe, D. Overview of constitutive laws, kinematics, homogenization and multiscale methods in crystal plasticity finite-element modeling: Theory, experiments, applications. *Acta Mater.* (2010) **58**:1152–1211.

[13] Rusinek, A. and Jankowiak, T. *Constitutive Relations under Impact Loadings: Experiments, Theoretical and Numerical Aspects*, chap. Dynamic Behavior of Materials. Constitutive Relations and Applications. Springer Vienna: Vienna, (2014) 87–135.

[14] Bodner., S.R. and Rubin, M.B. Modeling of hardening at very high strain rates. *J. Appl. Phys.* (1994) **76**:2742–2747.

[15] Molinari, A. and Ravichandran, G. Constitutive modeling of high-strain-rate deformation in metals based on the evolution of an effective microstructural length. *Mech. Mater.* (2005) **37**:737–752.

[16] Durrenberger, L., Molinari, A. and Rusinek, A. Internal variable modeling of the high strain-rate behavior of metals with applications to multiphase steels. *Mater. Sci. Engng. A-Struct.* (2008) **478**:297–304.

[17] Rodríguez-Martínez, J., Rusinek, A. and Klepaczko, J. Constitutive relation for steels approximating quasi-static and intermediate strain rates at large deformations. *Mech. Res. Commun.* (2009) **36**:419–427.

[18] Simo, J.C. and Hughes, T.J.R. *Computational Inelasticity*. Interdisciplinary applied mathematics: Mechanics and materials, Springer, (1998).

[19] de Souza Neto, E.A, Perić, D. and Owen, D.R.J. *Computational Methods for Plasticity: Theory and Applications*. John Wiley & Sons, (2008).

[20] Lush, A., Weber, G. and Anand, L. An implicit time-integration procedure for a set of internal variable constitutive equations for isotropic elasto-viscoplasticity. *Int. J. Plast.* (1989) **5**:521–549.

[21] Weber, G. and Anand, L. Finite deformation constitutive equations and a time integration procedure for isotropic, hyperelastic-viscoplastic solids. *Comput. Meth. Appl. Mech. Engng.* (1990) **79**:173–202.

[22] Zaera, R. and Fernández-Sáez, J. An implicit consistent algorithm for the integration of thermoviscoplastic constitutive equations in adiabatic conditions and finite deformations. *Int. J. Solids Struct.* (2006) **43**:1594–1612.

[23] Mourad, H., Bronkhorst, C., Addessio, F., Cady, C., Brown, D., Chen, S., Gray III, G.T. Incrementally objective implicit integration of hypoelastic-viscoplastic constitutive equations based on the mechanical threshold strength model. *Comput. Mech.* (2014) **53**:941–955.

[24] Lee, E.H. Elastic-plastic deformation at finite strains. *J. Appl. Mech.* (1969) **36**:1–6.

[25] Mandel, J. *Plasticité classique et viscoplasticité: course held at the Department of Mechanics of Solids, September-October, 1971*. Courses and lectures - International Centre for Mechanical Sciences, Springer-Verlag, (1972).

[26] dos Santos, T., Rosa, P.A., Maghous, S. and Rossi, R. A simplified approach to high strain rate effects in cold deformation of polycrystalline FCC metals: Constitutive formulation and model calibration. *Int. J. Plast.* (2016) **82**:76–96.

[27] Perzyna P. Thermodynamic theory of viscoplasticity. Elsevier, (1971) 313–354.

[28] Perić D. On a class of constitutive equations in viscoplasticity: Formulation and computational issues. *Int. J. Num. Meth. Engng.* (1993) **36**:1365–1393.

[29] Ristinmaa, M. and Ottosen, N.S. Viscoplasticity based on an additive split of the conjugated forces. *Eur. J. Mech. A-Solids.* (1998) **17**:207–235.

[30] Alfano, G., Angelis, F.D. and Rosati, L. General solution procedures in elasto/viscoplasticity. *Comput. Meth. Appl. Mech. Engng.* (2001) **190**:5123–5147.

[31] Perzyna, P. Fundamental problems in viscoplasticity. Elsevier, (1966) 243–377.

[32] Wang, W.M., Sluys, L.J. and de Borst, R. Viscoplasticity for instabilities due to strain softening and strain-rate softening. *Int. J. Num. Meth. Engng.* (1997) **40**:3839–3864.

[33] Ristinmaa, M. and Ottosen, N.S. Consequences of dynamic yield surface in viscoplasticity. *Int. J. Solids Struct.* (2000) **37**:4601–4622.

[34] Eterovic, A.L. and Bathe, K.J. A hyperelastic-based large strain elasto-plastic constitutive formulation with combined isotropic-kinematic hardening using the logarithmic stress and strain measures. *Int. J. Num. Meth. Engng.* (1990) **30**:1099–1114.

[35] Jordan, J., Siviour, C., Sunny, G., Bramlette, C. and Spowart, J. Strain rate-dependant mechanical properties of OFHC copper. *J. Mater. Sci.* (2013) **48**:7134–7141.

[36] Mandel, J. Equations constitutives et directeurs dans les milieux plastiques et viscoplastiques. *Int. J. Solids Struct.* (1973) **9**:725–740.

[37] Lubliner, J. A maximum-dissipation principle in generalized plasticity. *Acta Mech.* (1984) **52**:225–237.

[38] Coleman, B.D. and Gurtin, M.E. Thermodynamics with Internal State Variables. *Rep. Prog. Phys.* (1967) **47**:597–613.

[39] Rice J. Inelastic constitutive relations for solids: An internal-variable theory and its application to metal plasticity. *J. Mech. Phys. Solids.* (1971) **19**:433–455.

[40] Lubliner, J. On the thermodynamic foundations of non-linear solid mechanics. *Int. J. Nonlinear Mech.* (1972) **7**:237–254.

[41] Gurtin, M., Fried, E. and Anand, L. *The Mechanics and Thermodynamics of Continua*. The Mechanics and Thermodynamics of Continua, Cambridge University Press, (2010).

[42] Voce, E. The relationship between stress and strain for homogeneous deformation. *J. Inst. Metals.* (1948) **74**:537–562.

[43] Bonet, J. and Wood, R. *Nonlinear Continuum Mechanics for Finite Element Analysis*. Cambridge University Press, (1997).

[44] Klepaczko, J. and Chiem, C. On rate sensitivity of f.c.c. metals, instantaneous rate sensitivity and rate sensitivity of strain hardening. *J. Mech. Phys. Solids.* (1986) **34**:29–54.

[45] Rashid, M.M., Gray, G.T. and Nemat-Nasser, S. Heterogeneous deformations in copper single crystals at high and low strain rates. *Philos. Mag. A.* (1992) **65**:707–735.

[46] Rossi, R., Alves, M.K. and Al-Qureshi, H.A. A total lagrangian framework for simulation of powder compaction process based on a smooth three-surface cap model and a mesh-free method. *Int. J. Num. Meth. Engng.* (2008) **75**:1457–1491.

[47] Rossi, R., Alves, M.K. and Al-Qureshi, H.A. An element-free galerkin method for metal forming simulations. *Engng. Comput.: Int. J. Comput. Aided Engng.* (2009) **26**:327–346.

[48] Follansbee, P.S. High strain rate deformation of FCC metals and alloys. *Metallurgical Applications of Shock-Wave and High-Strain Rate Phenomena*, Murr LE, Staudhammer KP, , Meyers MA (eds.). Marcel Dekker Inc.: New York, (1986) 451–479.

A Tangent quantities for return mapping algorithm

The return mapping algorithm is used to solve the nonlinear equations (43), (44) and (45), making use of an iterative procedure, such as the *Newton-Raphson* algorithm. In this context, some tangent quantities have to be evaluated. The system of nonlinear linear equations to be solved can be set as

$$f_1 = \left\| \bar{\boldsymbol{\tau}}^{D^{trial}}_{n+1} \right\| - \Delta\lambda 2\mu - \sqrt{\frac{2}{3}} \left(\sigma_y + A_{n+1}\right) - \bar{\Theta}^{-1}\left(\Delta\lambda, A_{n+1}\right) = 0, \tag{61}$$

$$f_2 = A_{n+1} - A_n - A_{\infty_{n+1}} c\sqrt{\frac{2}{3}}\Delta\lambda - \left[A_{\infty_{n+1}}\left(1 + c\epsilon_n\right) - A_n\right]\left[1 - \exp\left(-\delta\sqrt{\frac{2}{3}}\Delta\lambda\right)\right] = 0, \tag{62}$$

$$f_3 = A_{\infty_{n+1}} - A^{lwr}_{\infty} - \left[\frac{1}{\Delta t}\left(\frac{\sqrt{\frac{2}{3}}\Delta\lambda - \Delta t\dot{\epsilon}_{lwr}}{\dot{\epsilon}_{up} - \dot{\epsilon}_{lwr}}\right)\right]^{\xi}\left(A^{up}_{\infty} - A^{lwr}_{\infty}\right) = 0, \tag{63}$$

where involved unknowns are $\left\{\Delta\lambda, A_{n+1}, A_{\infty_{n+1}}\right\}$. Accordingly, the tangent terms are defined by

$$\frac{\partial f_1}{\partial\Delta\lambda} = -2\mu - \frac{\partial\bar{\Theta}^{-1}}{\partial\Delta\lambda}, \tag{64}$$

$$\frac{\partial f_2}{\partial\Delta\lambda} = -\sqrt{\frac{2}{3}}A_{\infty_{n+1}}c - \sqrt{\frac{2}{3}}\delta\left[A_{\infty_{n+1}}\left(1 + c\epsilon_n\right) - A_n\right]\exp\left(-\delta\sqrt{\frac{2}{3}}\Delta\lambda\right), \tag{65}$$

$$\frac{\partial f_3}{\partial\Delta\lambda} = -\sqrt{\frac{2}{3}}\frac{\xi}{\Delta t}\left[\frac{1}{\Delta t}\left(\frac{\sqrt{\frac{2}{3}}\Delta\lambda - \Delta t\dot{\epsilon}_{lwr}}{\dot{\epsilon}_{up} - \dot{\epsilon}_{lwr}}\right)\right]^{\xi-1}\left(\frac{A^{up}_{\infty} - A^{lwr}_{\infty}}{\dot{\epsilon}_{up} - \dot{\epsilon}_{lwr}}\right), \tag{66}$$

$$\frac{\partial f_1}{\partial A_{n+1}} = -\sqrt{\frac{2}{3}} - \frac{\partial \bar{\Theta}^{-1}}{\partial A_{n+1}}, \tag{67}$$

$$\frac{\partial f_2}{\partial A_{n+1}} = 1, \quad \frac{\partial f_3}{\partial A_{n+1}} = 0, \quad \frac{\partial f_1}{\partial A_{\infty_{n+1}}} = 0, \quad \frac{\partial f_3}{\partial A_{\infty_{n+1}}} = 1, \tag{68}$$

$$\frac{\partial f_2}{\partial A_{\infty_{n+1}}} = -c\sqrt{\frac{2}{3}}\Delta\lambda - (1 + c\epsilon_n)\left[1 - \exp\left(-\delta\sqrt{\frac{2}{3}}\Delta\lambda\right)\right]. \tag{69}$$

From Eq. (18) we have the derivatives

$$\frac{\partial \bar{\Theta}^{-1}}{\partial \Delta\lambda} = \sqrt{\frac{2}{3}}\left(\sigma_y + A_{n+1}\right)\frac{1}{m}\frac{\vartheta}{\Delta t}\left(1 + \vartheta\frac{\Delta\lambda}{\Delta t}\right)^{\frac{1}{m}-1}, \tag{70}$$

$$\frac{\partial \bar{\Theta}^{-1}}{\partial A_{n+1}} = \sqrt{\frac{2}{3}}\left[\left(1 + \vartheta\frac{\Delta\lambda}{\Delta t}\right)^{\frac{1}{m}} - 1\right]. \tag{71}$$

B Analytical consistent tangent operator

Evaluation of $\mathbb{D}^{vp}_{n+1}$ is obtained from linearization of Eqs. (37), (39), (45) and (44),

$$d\boldsymbol{E}^{e}_{n+1} + d\left(\Delta\lambda\right)\boldsymbol{N}_{\bar{\boldsymbol{\tau}}_{n+1}} + \Delta\lambda\frac{\partial \boldsymbol{N}_{\bar{\boldsymbol{\tau}}_{n+1}}}{\partial \bar{\boldsymbol{\tau}}_{n+1}} : d\bar{\boldsymbol{\tau}}_{n+1} = d\boldsymbol{E}^{e^{trial}}_{n+1} \tag{72}$$

$$\boldsymbol{N}_{\bar{\boldsymbol{\tau}}_{n+1}} : d\bar{\boldsymbol{\tau}}_{n+1} + N_{A_{n+1}} dA_{n+1} = \frac{\partial \bar{\Theta}^{-1}}{\partial \Delta\lambda} d\left(\Delta\lambda\right) + \frac{\partial \bar{\Theta}^{-1}}{\partial A_{n+1}} dA_{n+1} \tag{73}$$

$$\begin{aligned} dA_{n+1} \;=\; & \left[\left(1 + c\epsilon_n\right)\left(1 - \varphi\right) + c\sqrt{\frac{2}{3}}\Delta\lambda\right] dA_{\infty_{n+1}} + \ldots \\ & \ldots + \sqrt{\frac{2}{3}}\left\{\delta\left[A_{\infty_{n+1}}\left(1 + c\epsilon_n\right) - A_n\right]\varphi + A_{\infty_{n+1}} c\right\} d\left(\Delta\lambda\right) \end{aligned} \tag{74}$$

$$dA_{\infty_{n+1}} = \omega d\left(\Delta\lambda\right) \tag{75}$$

where

$$\frac{\partial \boldsymbol{N}_{\bar{\boldsymbol{\tau}}_{n+1}}}{\partial \bar{\boldsymbol{\tau}}_{n+1}} = \frac{1}{\left\|\bar{\boldsymbol{\tau}}^{D}_{n+1}\right\|}\left(\mathbb{I} - \frac{1}{3}\boldsymbol{I}\otimes\boldsymbol{I} - \boldsymbol{N}_{\bar{\boldsymbol{\tau}}_{n+1}}\otimes\boldsymbol{N}_{\bar{\boldsymbol{\tau}}_{n+1}}\right), \tag{76}$$

$$N_{A_{n+1}} = \frac{\partial f_{n+1}}{\partial A_{n+1}} = -\sqrt{\frac{2}{3}}, \tag{77}$$

$$\varphi = \exp\left(-\delta\sqrt{\frac{2}{3}}\Delta\lambda\right), \tag{78}$$

and

$$\omega = \sqrt{\frac{2}{3}}\frac{\xi}{\Delta t}\left(\frac{A^{up}_{\infty} - A^{lwr}_{\infty}}{\dot{\epsilon}_{up} - \dot{\epsilon}_{lwr}}\right)\left[\frac{1}{\Delta t}\left(\frac{\sqrt{\frac{2}{3}}\Delta\lambda - \Delta t\dot{\epsilon}_{lwr}}{\dot{\epsilon}_{up} - \dot{\epsilon}_{lwr}}\right)\right]^{\xi-1}. \tag{79}$$

Combining Eqs. (74) and (75) reads to

$$dA_{n+1} = \Lambda d\left(\Delta\lambda\right), \tag{80}$$

where

$$\begin{aligned}\Lambda \;=\; & \left[\left(1+c\epsilon_n\right)\left(1-\varphi\right)+c\sqrt{\frac{2}{3}}\Delta\lambda\right]\omega+\ldots \\ & \ldots+\sqrt{\frac{2}{3}}\left\{\delta\left[A_{\infty_{n+1}}\left(1+c\epsilon_n\right)-A_n\right]\varphi+A_{\infty_{n+1}}c\right\}.\end{aligned} \tag{81}$$

Inserting Eq. (80) into Eq. (73) yields

$$\boldsymbol{N}_{\bar{\boldsymbol{\tau}}_{n+1}} : d\bar{\boldsymbol{\tau}}_{n+1} = \left[\frac{\partial\bar{\Theta}^{-1}}{\partial\Delta\lambda}+\left(\frac{\partial\bar{\Theta}^{-1}}{\partial A_{n+1}}-N_{A_{n+1}}\right)\Lambda\right] d\left(\Delta\lambda\right)$$

$$d\left(\Delta\lambda\right) = \frac{1}{\chi}\boldsymbol{N}_{\bar{\boldsymbol{\tau}}_{n+1}} : d\bar{\boldsymbol{\tau}}_{n+1}, \tag{82}$$

where

$$\chi = \left[\frac{\partial\bar{\Theta}^{-1}}{\partial\Delta\lambda}+\left(\frac{\partial\bar{\Theta}^{-1}}{\partial A_{n+1}}-N_{A_{n+1}}\right)\Lambda\right]. \tag{83}$$

Substitution of Eq. (82) in Eq. (72) provides

$$d\boldsymbol{E}^{e}_{n+1}+\left(\frac{1}{\chi}\boldsymbol{N}_{\bar{\boldsymbol{\tau}}_{n+1}} : d\bar{\boldsymbol{\tau}}_{n+1}\right)\boldsymbol{N}_{\bar{\boldsymbol{\tau}}_{n+1}}+\Delta\lambda\frac{\partial\boldsymbol{N}_{\bar{\boldsymbol{\tau}}_{n+1}}}{\partial\bar{\boldsymbol{\tau}}_{n+1}} : d\bar{\boldsymbol{\tau}}_{n+1} = d\boldsymbol{E}^{e^{trial}}_{n+1}. \tag{84}$$

Observing that $\left(\boldsymbol{A}\otimes\boldsymbol{G}\right):\boldsymbol{K}=\left(\boldsymbol{G}:\boldsymbol{K}\right)\boldsymbol{A}$, the above equation writes

$$d\boldsymbol{E}^{e}_{n+1}+\frac{1}{\chi}\left(\boldsymbol{N}_{\bar{\boldsymbol{\tau}}_{n+1}}\otimes\boldsymbol{N}_{\bar{\boldsymbol{\tau}}_{n+1}}\right) : d\bar{\boldsymbol{\tau}}_{n+1}+\Delta\lambda\frac{\partial\boldsymbol{N}_{\bar{\boldsymbol{\tau}}_{n+1}}}{\partial\bar{\boldsymbol{\tau}}_{n+1}} : d\bar{\boldsymbol{\tau}}_{n+1} = d\boldsymbol{E}^{e^{trial}}_{n+1}, \tag{85}$$

and from the elastic relationship $d\boldsymbol{E}^{e}_{n+1}=\mathbb{D}^{e^{-1}} : d\bar{\boldsymbol{\tau}}_{n+1}$ Eq. (85) can be rearranged as

$$\left(\mathbb{D}^{e^{-1}}+\Delta\lambda\frac{\partial\boldsymbol{N}_{\bar{\boldsymbol{\tau}}_{n+1}}}{\partial\bar{\boldsymbol{\tau}}_{n+1}}\right) : d\bar{\boldsymbol{\tau}}_{n+1}+\frac{1}{\chi}\left(\boldsymbol{N}_{\bar{\boldsymbol{\tau}}_{n+1}}\otimes\boldsymbol{N}_{\bar{\boldsymbol{\tau}}_{n+1}}\right) : d\bar{\boldsymbol{\tau}}_{n+1} = d\boldsymbol{E}^{e^{trial}}_{n+1}, \tag{86}$$

leading finally to

$$\mathbb{D}^{vp}_{n+1} = \frac{\partial\bar{\boldsymbol{\tau}}_{n+1}}{\partial\boldsymbol{E}^{e^{trial}}_{n+1}} = \left(\mathbb{D}^{e^{-1}}+\Delta\lambda\frac{\partial\boldsymbol{N}_{\bar{\boldsymbol{\tau}}_{n+1}}}{\partial\bar{\boldsymbol{\tau}}_{n+1}}+\frac{1}{\chi}\boldsymbol{N}_{\bar{\boldsymbol{\tau}}_{n+1}}\otimes\boldsymbol{N}_{\bar{\boldsymbol{\tau}}_{n+1}}\right)^{-1}. \tag{87}$$

XIV International Conference on Computational Plasticity. Fundamentals and Applications
COMPLAS 2017
E. Oñate, D.R.J. Owen, D. Peric and M. Chiumenti (Eds)

PLASTIC DILATION RATE CHARACTERISTIC OF CONCRETE CONFINED WITH STEEL TUBE

BAMBANG PISCESA*, MARIO M. ATTARD* AND ALI K. SAMANI†

* School of Civil Engineering and Environmental
University of New South Wales
Kensington, Sydney NSW 2051, Australia
e-mail: bambang.piscesa@unsw.edu.au and m.attard@unsw.edu.au

† School of Civil Engineering and Information Technology
Federation University
Ballarat, VIC 3350, Australia
email: a.khajehsamani@federation.edu.au

Keywords: Plastic dilation rate, concrete-filled-steel-tube, external confinement.

Abstract. The use of external confining devices to confine concrete has become widely used. One of the purposes is to gain additional concrete strength and ductility. Although there are many types of external confining devices, in this paper, the attention is limited to the use of the steel tube as an external confining device. One of the main objectives of this research is to study the plastic dilation rate behavior of concrete-filled-steel-tube (CFST) columns. The experimental data for the plastic dilation rate is extracted, and compared with the authors concrete plasticity model. In the authors' previous research, the calibration of the plastic dilation rate model was based on confined concrete tested under both active and passive confinement using FRP wraps. Since the behavior of the steel tube and the FRP materials are different, the author's plastic dilation rate model needs to be re-evaluated for CFST columns. Comparisons of the extracted experimental plastic dilation rates with the model prediction for CFST specimens with normal strength concrete show good agreement and requires no adjustment in the formulation. However, for a specimen with 80 MPa concrete, the proposed formulation shows slightly lower plastic dilation rates. More experimental data for CFST using high strength concretes is required for further investigation. For the sake of completeness, the overall response of two CFST specimens is also evaluated using an in-house three-dimensional non-linear finite element analysis (3D-NLFEA) using the author's proposed plasticity formulation for confined concrete.

1 INTRODUCTION

The use of external confining devices to confine concrete is widely used. The external confining device is defined as any material other than concrete (such as FRP or steel tube) which has a mechanism to provide a kinematic lateral restraint [1] for the confined material. One of the purposes is to gain additional concrete strength and ductility. The kinematic lateral restraint is related to the lateral modulus (E_L) of the external confining devices. The lateral

modulus (E_L) of the confining device can be computed by solving the compatibility equation between the external confining device and the concrete core. By using E_L, the effectiveness of the confinement can be measured. For an external confining device made of a material with a simple stress-strain relationship, such as FRP wrap, the lateral modulus E_L can be assumed to be constant throughout the loading. However, for a concrete-filled-steel-tube (CFST) the lateral modulus E_L keeps changing once the steel yields.

Recently, the authors proposed a constitutive plasticity model [2, 3] for confined concrete. In this model, the flow rule is a function of the plastic dilation rate of the confined concrete. The plastic dilation rate (β) was defined as the ratio of the lateral to axial plastic strains ($\beta = \varepsilon^{p}_{lat} / \varepsilon^{p}_{axial}$). The plastic dilation rate formulation itself is a function of the confining pressures of the concrete core and lateral modulus (E_L) of the external confining device. The proposed plastic dilation rate model was calibrated using the experimental data from both active and passive confinement. However, for the passive confinement, the calibration of the plastic dilation rate was solely based on the FRP confined concrete [2], and therefore, further validation of the proposed model with different types of the external confining devices needs to be carried out.

In this paper, the model of [2, 3] is validated for cases where the steel tube is used as the external confining device. The focus is to obtain the plastic dilation rate behavior of the concrete-filled-steel-tube (CFST). The steel tube material has a different behavior in comparison to FRP material. The FRP material has a linear elastic behavior up to failure and is considered an orthotropic material. Usually, the axial load carrying capacity of the FRP tube is sufficiently small and thus neglected in the analysis. In contrast, the steel tube material is considered as an isotropic material and obeys a J2 plasticity model with zero hardening modulus. When the CFST column is axially loaded, due to the higher elastic modulus in comparison with the concrete material, the steel tube yields first before the concrete core reaches its peak stress capacity. Further, at the state where the steel tube is yielding, the axial stress is much higher than the stress in the other directions which may complicate the measurement of the lateral modulus, as well as the confining pressures to the concrete core. Hence, investigating the plastic dilation rate characteristic for CFST is a challenge.

To maintain clarity in the discussion, the sections in this paper are organized by firstly presenting a short introduction showing the main objective of the paper followed by the study on the plastic dilation rate behavior for CFST. In the second section, previous studies on the plastic dilation rate behavior for FRP confined concrete and then the plastic dilation rate behavior for the CFST are discussed. It will be shown that despite the different constitutive behavior between the FRP confined concrete and CFST, the authors' plastic dilation rate formulation is sufficiently accurate and adaptable. In the third section, numerical modeling to investigate the performance of the authors' plasticity model is presented by using a three-dimensional non-linear finite element analysis (3D-NLFEA) developed by the authors [4]. Finally, conclusions are drawn, and some future research suggested.

2 PLASTIC DILATION RATE BEHAVIOR OF CFST

The plastic dilation rate from any experiment is evaluated by observing the changes of the plastic strain both in the lateral and axial direction. However, from the experiments, mostly, only the axial force, axial strain and circumferential strain are obtained. Hence, to get the plastic

dilation rate from the experiments, the raw data needs to be further processed. During the extraction process, some assumptions are made, and it is important to note that different assumptions may lead to a different value for the plastic dilation rate. The plastic dilation rate itself is highly sensitive to the increment of the selected data points from the experiment. The smaller the increment, the distortion of the plastic dilation rate becomes more pronounced. Due to this sensitivity, obtaining the data from available experiments in the literature requires a special filtering, unless, the experiments have complete data sets including the computed confining pressure and the axial stress within the concrete core.

To extract the confining pressure from the experiments, it is required computing the stress in the radial direction which is equal to the confining pressure of the concrete core. In the case of FRP confined concrete, because the FRP material is always elastic up to the fracturing point, the computation of the confining pressure is obtained by multiplying the lateral strain with the lateral modulus of the FRP confining device. Further, for FRP confined concrete, the axial stress in the FRP material can be neglected. These material assumptions simplify the data extraction for the plastic dilation rate. However, for an external confining devices with a yield point such as a steel-tube, computing the confining pressure must conform to the stress-strain relation of the J2 material. Generally, during the loading, initially before the steel starts to yield, the axial stress in the steel tube is higher than the stresses in other directions. Once the steel yields, the axial stress in the steel tube reduces and the stresses in other directions increase.

Before looking further at the plastic dilation rate behavior for CFST columns, it is important to understand the plastic dilation rate behavior for FRP confined concrete. Figure 1 shows the plastic dilation rate behavior for FRP confined concrete extracted from experiments. A method to extract the plastic dilation rate for FRP confined concrete is explained in [2]. The expression of the plastic dilation rate formulation at peak stress in [2] is written here as:

$$\beta = \beta_0 + \left(\beta_{\text{core}} - \beta_0\right)\tanh\left(a_4\left(\frac{f_{\text{r}}}{f_{\text{c}}^{'}}\right)^{b_4}\right) \tag{1}$$

in the above, β_0 is the uniaxial plastic dilation rate at the peak stress, β_{core} is the upper limit of the plastic core compaction, a_4 and b_4 are the calibrated parameters. Samani and Attard [5] suggested a value for β_0 of -2.5. The upper limit of the plastic core compaction (β_{core}) is calibrated with the experimental data for FRP confined concrete and is a function of both the confining pressure (f_{r}) and the lateral modulus (E_{L}) of the external confining devices. However, the value for β_{core} should not be less than the elastic Poisson's ratio of the external confining devices (μ_{Ext}). The expression for β_{core} is:

$$\beta_{\text{core}} = -0.5 + 0.0275\Phi \le -\mu_{\text{Ext}} \qquad \Phi = \sqrt{\frac{f_{\text{r}}}{f_{\text{c}}^{'}}\frac{E_{\text{L}}}{f_{\text{c}}^{'}}} \tag{2}$$

in the above, f_{c} is the uniaxial concrete compressive strength. In [2], the calibration of the parameters a_4 and b_4 uses a genetic optimization algorithm, and the expressions for both parameters are:

$$a_4 = 2.5 + 0.25\sqrt{\frac{E_{\text{L}}}{f_{\text{c}}^{'}}} \quad b_4 = 0.0915\sqrt{f_{\text{c}}}\exp\left[-0.0192\Phi\left\langle f_{\text{c}}^{'} - 73\right\rangle\right] \quad \Phi = \sqrt{\frac{f_{\text{r}}}{f_{\text{c}}^{'}}\frac{E_{\text{L}}}{f_{\text{c}}^{'}}} \tag{3}$$

In Eqn.(3), the presence of the McCauley bracket is because of the variation of the plastic dilation rate for high strength concrete. To implement the plastic dilation rate formulation in

the flow rule, a method involving the plastic dilation rate control parameter (α_{p0}) in the flow rule is used in [2]. Further a scaling function is introduced for the smooth transition of the plastic dilation rate from the beginning of plastic flow up to the peak stress. At the start of plastic flow, the plastic dilation rate is equal to zero and at the peak stress, the plastic dilation rate is equal to Eqn.(1).

In Figure 1, there are two regions of the plastic dilation rate. The first region is where the increment of the plastic volumetric strain is in compaction ($|\beta| < 0.5$) and the second region is where the increment of the plastic volumetric strain is in dilation ($|\beta| > 0.5$). The predicted plastic dilation rates in Figure 1 are generated using the expression from Eqn. (1). The predictions represent different stiffness of the external confining devices and their effect on the plastic dilation rate behavior of FRP confined concrete. Note that the observed value of the plastic dilation rate, which is shown in Figure 1, shows the peak plastic dilation rate. For actively confined concrete (E_L = 0 MPa), the plastic dilation rate asymptotes to a value of -0.5. As the E_L increases, the plastic dilation rate shifts to the plastic volumetric compaction region. This phenomenon occurs for FRP confined concrete with sufficiently high stiffness [6, 7].

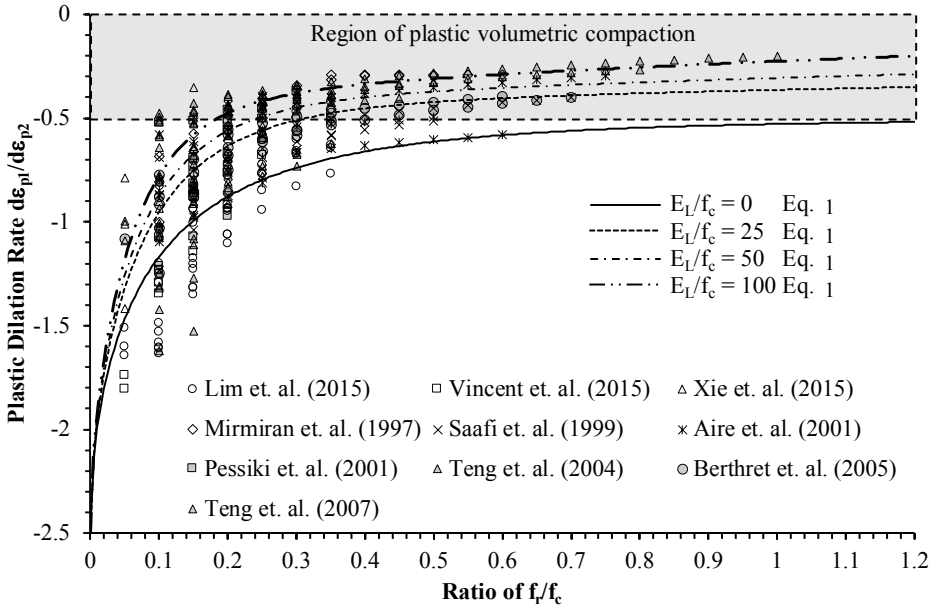

Figure 1 Plastic dilation rate behavior for FRP confined concrete [2]

Figure 2 shows the development of the plastic dilation rate for FRP confined concrete with different ply tested by [8] with ID 01-09. In Figure 2, the prediction of the plastic dilation rate using Eqn.(1) and also using the complete stress-strain curve for FRP confined concrete via the constitutive driver are presented. By looking at the complete development of the plastic dilation rate from the analysis, at the initial plastic flow, the value of the plastic dilation rate starts from zero and goes up to a value of -0.5. this region is called the initial plastic compaction. It is also worth mentioning that a flow rule that always dilates such as in [9, 10], will never be able to capture initial plastic compaction. After passing the initial plastic compaction region, the plastic dilation rate keeps increasing until reaching the peak plastic dilation ratio and continues to

follow the path of the peak plastic dilation rate as shown in Figure 2. Note, in the experiments, the plastic dilation rate also starts from zero. In Figure 2, however, the experimental plastic dilation rate is plotted once the minimum secant dilation rate is found in the experiment (see [2]) and therefore the plastic dilation rate from the zero point up to the minimum plastic dilation rate is not shown.

For CFST, it is expected that the plastic dilation rate after the steel tube yields should be almost equal to that of actively confined concrete ($E_L = 0$). After the steel yields, the confining pressure increases, the value for the initial lateral modulus will be small. The experiments carried out in [11] are examined and are used in this study. The work in [11] provides a complete data set which can be used for evaluating the plastic dilation rate for CFST. The axial stress in the concrete and the confining pressure is extracted, and Hook's law is used to compute the axial and lateral elastic strains. The axial and lateral plastic strains are further computed by subtracting the elastic strains from the total strains. The plastic dilation rate is obtained by computing the ratio of the lateral to axial plastic strains.

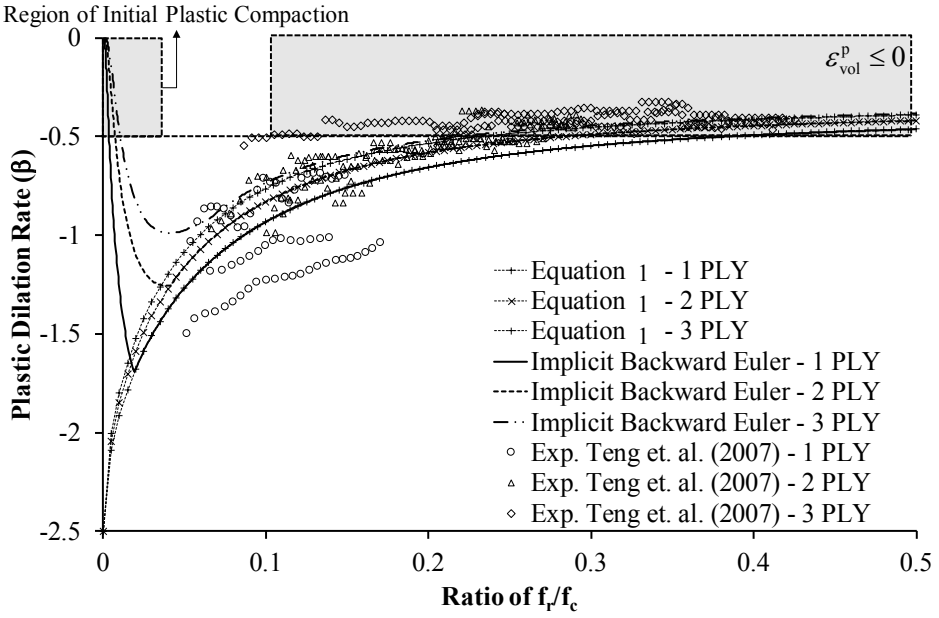

Figure 2 Comparison of the plastic dilation rate formulation with the constitutive driver and the experiments [2]

Figure 3 shows the plastic dilation rate behavior for CFST specimens taken from [11] are selected for investigation. Two specimens with normal strength concrete (NSC) and one specimen with high strength concrete (HSC) are selected. In Figure 3, the plastic dilation rates are plotted as a function of axial strain. In Figure 3, the peak plastic dilation rate are generated using Eqn. (1) with two different values of the lateral modulus. One with zero lateral modulus, which in Figure 3 is represented as the active model and the other with the lateral modulus calculated from the experiments and is represented as the passive model. Note, for zero confining pressure (uniaxial case) or when the confining pressure is tensile, the plastic dilation rate at the peak stress is equal to β_0 which is equal to -2.5. Hence, in Figure 3, at the initial loading stage, where the confining pressure is in tension (see [11]), the peak plastic dilation rate is equal to -2.5.

The plastic dilation rate from all the specimens starts at zero plastic dilation rate which clearly identifies the initial plastic volumetric compaction for CFST specimens. As the loading increases, the absolute value of the plastic dilation rate also increases up to the maximum value. For NSC, it is difficult to distinguish between the maximum and the minimum values of the plastic dilation rate once the steel tube yields. However, for the HSC specimen, we can easily distinguish between the maximum and the minimum values of the plastic dilation rate. The maximum absolute plastic dilation rate for the 80 MPa concrete occurs at an axial strain of about -0.0025 and as the loading increases, the plastic dilation rate drops to a value of -1.2. Notice that there is a small increase in the plastic dilation rate throughout the loading for HSC while for NSC, the plastic dilation rate is almost constant.

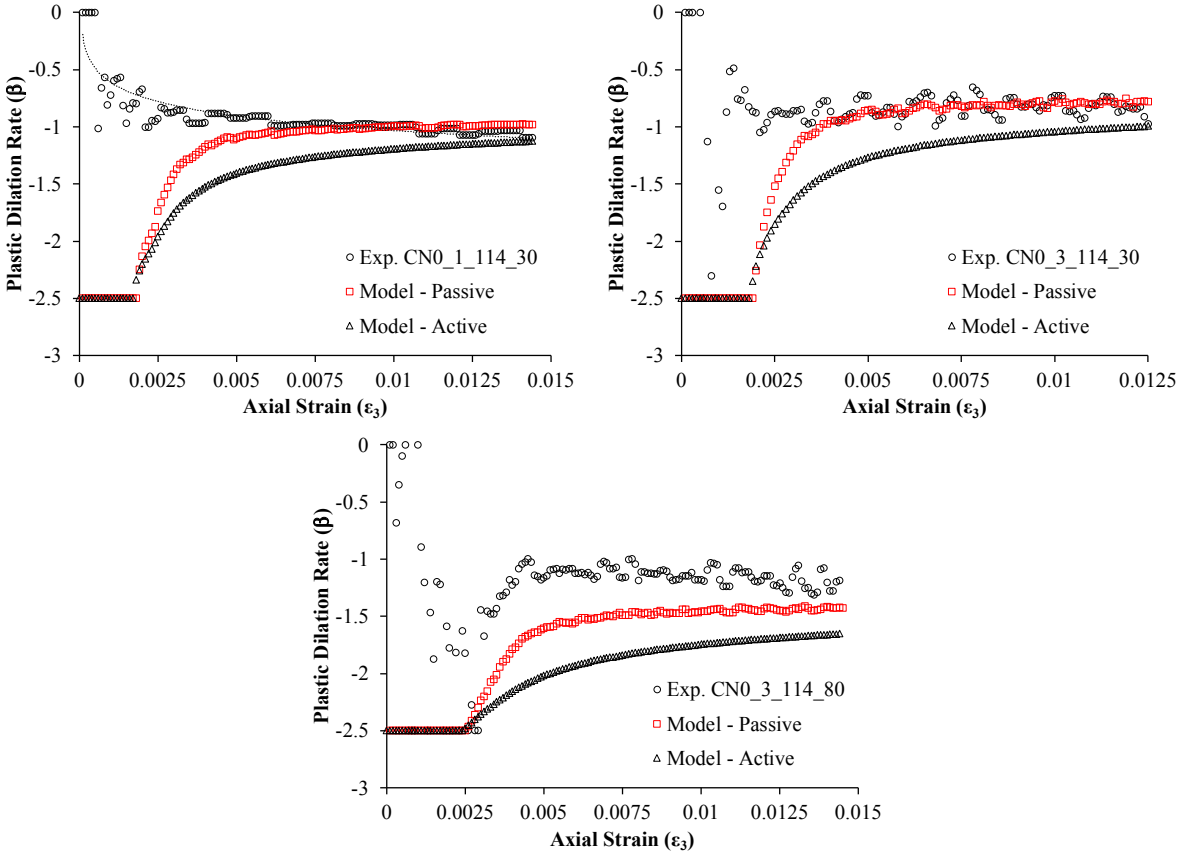

Figure 3 Plastic dilation rate behavior for CFST specimens

For normal strength concrete, the prediction of the plastic dilation rate for CFST is excellent. The model for passively confined concrete can capture the plastic dilation rate behavior of CFST while the actively confined concrete model has a higher plastic dilation rate. From both the experiments and the model prediction, the plastic dilation rate is almost constant after the CFST yields. However, the almost constant plastic dilation rate does not mean that the confining pressure is constant. The confining pressure is still increasing but the lateral modulus decreases which means the effectiveness of the external confining device is also decreasing. This finding is important and the model can explain this behavior clearly. A model without a clear definition between active and passive modes cannot identify this difference and although these models

may provide good predictions, they lack the explanation of what is happening in the experiments.

For high strength concrete, the prediction of the plastic dilation rate is lower in absolute terms than the experiments. When evaluating the experimental data for FRP confined concrete, there is a term inside the McCauley bracket Eqn.(3) to cater for the test results available for HSC which were from one source and had a compressive strength of 73 MPa. The term has a purpose to accelerate the increase in the plastic dilation rate for high strength concrete. It is therefore important to investigate more HSC experimental results and re-evaluate Eqn.(3). Further, for a CFST specimen, the yielding of the steel tube lowered the value of the lateral modulus, and thus the limit of plastic dilation rate as shown in Eqn.(2) remain untouched.

3 MODELLING AND DISCUSSION

This section presents two finite element models for CFST short column specimen using an in-house three-dimensional non-linear finite element analysis (3DNLFEA) program. 3DNLFEA is an in-house program developed by the authors which focuses on non-linear analysis for reinforced concrete structures. 3DNLFEA is now under heavy development focusing on parallel computation and the use of Graphical Processing Unit (GPU) to improve the computational performance. The pre- and post-processor use SALOME [12] and ParaView [13, 14], respectively. In solving the global equilibrium equations in the non-linear finite element analysis, the initial elastic stiffness method combined with a process modification [15] (acceleration technique) are used in the analysis. The constitutive model for concrete and steel materials are based on the plasticity model developed by the authors [2, 3] and a J2 plasticity with zero hardening modulus, respectively. The 2nd order effects are considered using an updated Lagrangian formulation.

Two experiments from Lai and Ho [11] are selected for comparisons. The first and the second specimen have an annotation of CN0_4_139_100 and CN0_8_168_120, respectively. The first term of the annotation which is "CN0" shows that the specimen is a pure CFST column with no additional external confining devices provided. The second term shows the thickness of the steel tube in mm. The outer diameter (mm) is shown in the third term and the uniaxial concrete compressive strength (MPa) is shown in the fourth term. The height of the CN0_4_139_100 and CN0_8_168_120 specimens are 420 mm and 330 mm, respectively. The CN0_4_139_100 and CN0_8_168_120 specimens are constructed with 1,953 and 1,944 hexahedral elements, respectively. Both ends of the CFST column are fixed. The loading in the analysis is controlled using a displacement control applied at the top end of the specimen.

Figure 4 and Figure 5 shows the meshed elements, Von-Mises stresses, the hardening parameter and the lateral modulus for the CN0_4_139_100 and CN0_8_168_120 specimens, respectively. The output data was evaluated at the final load step. The Von-Mises stress distribution in concrete for both specimens is similar despite the different ratio of the height over diameter (l/d) of the specimen (see Figures 1b and 2b). Since both ends of the specimens were fixed, the localization during softening occurs at the mid-height of the specimen. From Figures 4c and 5c, the hardening parameter (k), which is a measure of cumulative plastic volumetric strain, has the highest value at the mid height. As for the lateral modulus, theoretically, if there are no increases in the confining pressure, the value of the lateral modulus should be zero. However, the values of the lateral modulus shown in Figures 4d and 5d are not

zero which explains that even under softening, the confining pressure is still increasing.

Figure 6 and Figure 7 show the comparison of the axial force versus the axial strain between the 3DNLFEA and the experimental results. Note that in Figures 6 and 7, the input data for the 3DNLFEA is shown below the specimen ID. For example, in Figure 6, the first line below the specimen ID identifies the actual concrete compressive strength in MPa (F104.5), the Young's Modulus of the concrete in GPa (E34.5) and the concrete uniaxial axial peak strain at the peak stress (EPS0.0038). The second line below the specimen ID shows the actual yield stress of the steel tube in MPa (S361), the Poisson's ratio of the steel tube (P0.29), the Young's Modulus of the steel tube in GPa (E205) and the thickness of the steel tube in mm (T7.82).

From the comparisons, the overall predicted responses for both specimens are in good agreement. The prediction of the peak axial load for CN0_4_139_100 is slightly higher than the experiment and the traced softening response is steeper than the experiment. However, the predicted residual stress, where the axial load is almost like a plateau, is in good agreement with the experiments. For the CN0_8_168_120 specimen, the predicted peak stress and peak strain are excellent. The softening response is excellent up to some degree, however, as the specimen softens further, the predicted axial load carrying capacity is higher than the experiment.

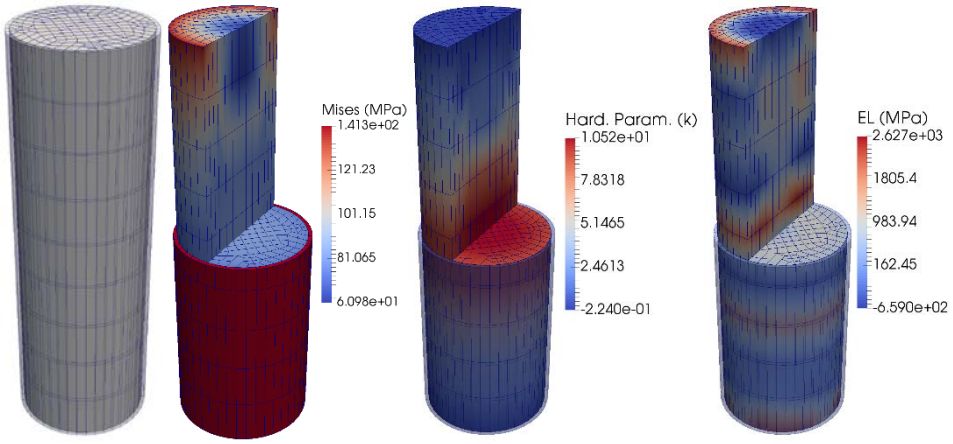

(a) (b) (c) (d)

Figure 4 (a) 3D Model of CN0_4_139_100 specimen (b) Von-Mises Stress (c) Hardening parameter (d) Lateral Modulus parameter (E_L)

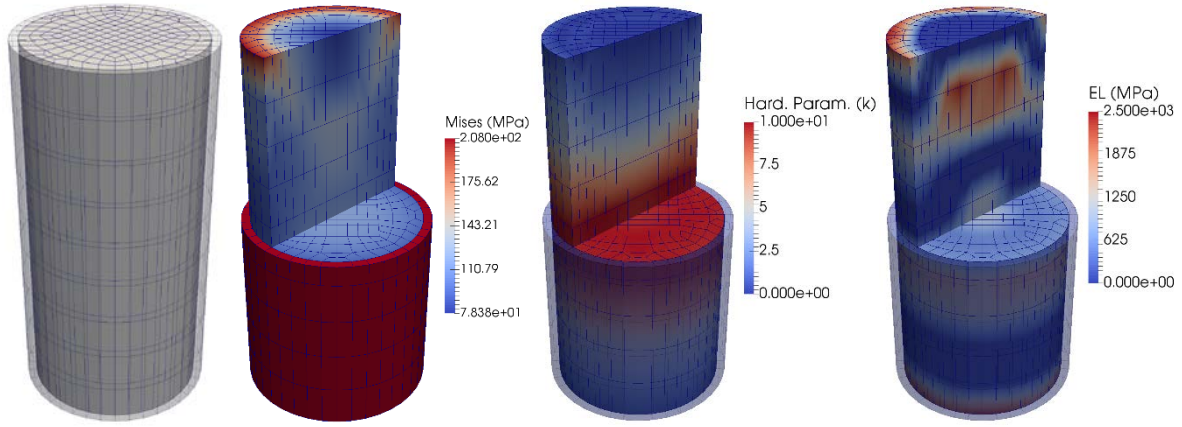

(a) (b) (c) (d)

Figure 5 (a) 3D Model of CN0_8_168_120 specimen (b) Von-Mises Stress (c) Hardening parameter (d) Lateral Modulus parameter (E_L)

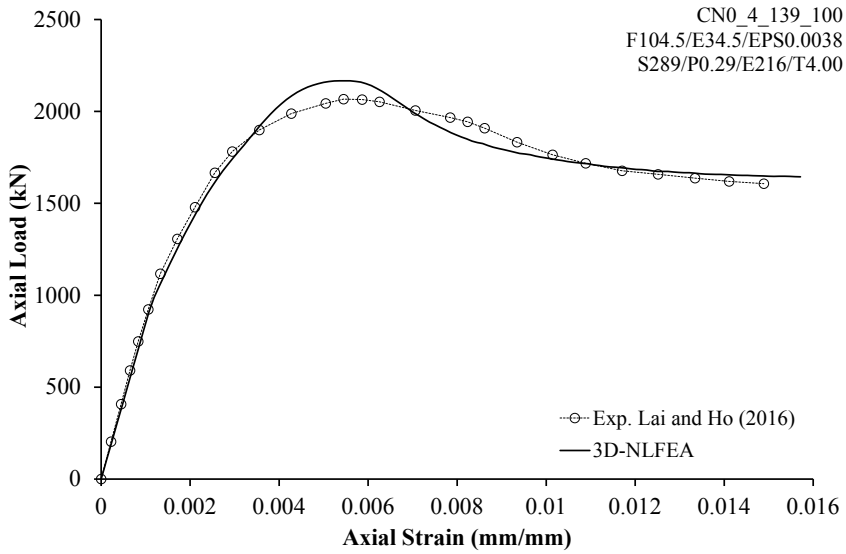

Figure 6 Comparison between 3DNLFEA and CN0_4_139_100 experimental result

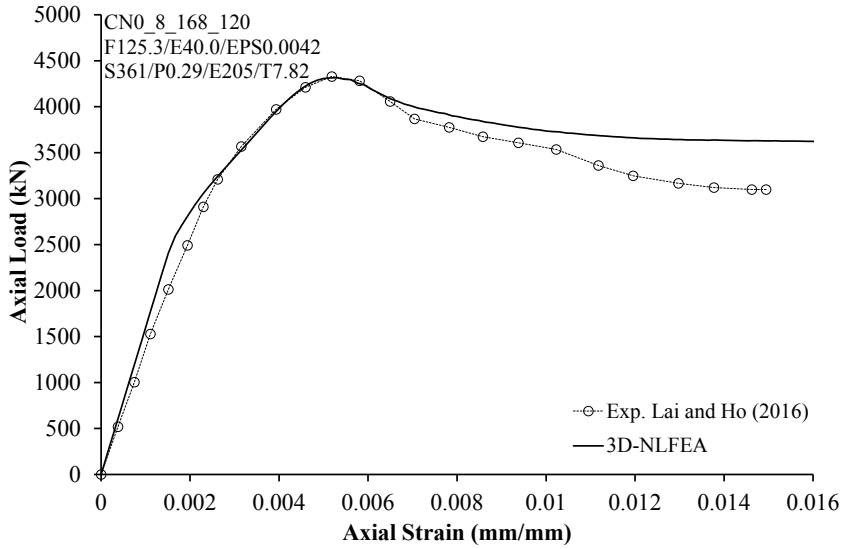

Figure 7 Comparison between 3DNLFEA and CN0_8_168_120 experimental result

4 CONCLUSIONS

This paper investigates the plastic dilation rate behavior of CFST columns. The experimentally extracted plastic dilation rates are compared with the plastic dilation rate formulation proposed by the authors. The comparison of the plastic dilation rate shows good agreement despite slightly higher prediction for high strength concrete. For a concrete-filled-steel-tube (CFST) specimen, once the steel tube yields, the value of the lateral modulus drops and thus the limit of the plastic dilation rate [2] remains untouched. Further, it was found that for normal strength concrete, the plastic dilation rate after the steel tube yields is almost constant. However, this did not mean that the confining pressure is constant. The confining pressure increases, but the lateral modulus reduces and produces an almost constant plastic dilation rate. Although the plastic dilation formulation was initially developed using data from FRP confined concrete, the formulation is also valid for CFST specimens. To further verify the developed plasticity constitutive model, comparisons between the CFST experiments from the literature with the non-linear finite element analysis (3D-NLFEA) were also presented. The comparisons between the model and the experiments were excellent with sufficiently high accuracy prediction of the peak axial load and peak axial strain. Further work will concentrate on obtaining more experimental data for high strength concretes.

REFERENCES

[1] S. Pantazopoulou, "Role of expansion on mechanical behavior of concrete," *Journal of structural engineering,* vol. 121, pp. 1795-1805, 1995.

[2] B. Piscesa, M. M. Attard, and A. K. Samani, "A lateral strain plasticity model for FRP confined concrete," *Composite Structures,* vol. 158, pp. 160-174, 2016.

[3] B. Piscesa, M. Attard, A. Samani, and S. Tangaramvong, "Plasticity Constitutive Model for Stress-Strain Relationship of Confined Concrete," *ACI Structural Journal,* vol. 114, p. 361, 2017.

[4] B. Piscesa, M. M. Attard, and A. K. Samani, "Three-dimensional Finite Element Analysis of Circular Reinforced Concrete Column Confined with FRP using Plasticity Model," *Procedia Engineering,* vol. 171, pp. 847-856, 2017.
[5] A. K. Samani and M. M. Attard, "Lateral Strain Model for Concrete under Compression," *ACI Structural Journal,* vol. 111, 2014.
[6] A. Mirmiran and M. Shahawy, "Dilation characteristics of confined concrete," *Mechanics of Cohesive-frictional Materials,* vol. 2, pp. 237-249, 1997.
[7] S. Tastani, I. Balafas, A. Dervisis, and S. Pantazopoulou, "Effect of core compaction on deformation capacity of FRP-jacketed concrete columns," *Construction and Building Materials,* vol. 47, pp. 1078-1092, 2013.
[8] T. Jiang and J. Teng, "Analysis-oriented stress–strain models for FRP–confined concrete," *Engineering Structures,* vol. 29, pp. 2968-2986, 2007.
[9] V. K. Papanikolaou and A. J. Kappos, "Confinement-sensitive plasticity constitutive model for concrete in triaxial compression," *International Journal of Solids and Structures,* vol. 44, pp. 7021-7048, 2007.
[10] J. Bao, X. Long, K. H. Tan, and C. K. Lee, "A new generalized Drucker–Prager flow rule for concrete under compression," *Engineering Structures,* vol. 56, pp. 2076-2082, 2013.
[11] M. Lai and J. Ho, "A theoretical axial stress-strain model for circular concrete-filled-steel-tube columns," *Engineering Structures,* vol. 125, pp. 124-143, 2016.
[12] CEA/DEN, EDF_R&D, and OPEN_CASCADE, "SALOME - The Open Source Integration Platform for Numerical Simulation. http://www.salome-platform.org/," Ver. 7.8.0 ed, 2016.
[13] J. Ahrens, B. Geveci, C. Law, C. Hansen, and C. Johnson, "36-ParaView: An End-User Tool for Large-Data Visualization," *The Visualization Handbook,* p. 717, 2005.
[14] U. Ayachit, "The paraview guide: a parallel visualization application," 2015.
[15] R. Lawther, "Modification of iterative processes for improved convergence characteristics," *International Journal for Numerical Methods in Engineering,* vol. 15, pp. 1149-1159, 1980.

XIV International Conference on Computational Plasticity: Fundamentals and Applications
COMPLAS 2017
E. Oñate, D.R.J. Owen, D. Peric and M. Chiumenti (Eds)

VISCO-PLASTIC CHABOCHE MODEL FOR NICKEL-BASED ALLOYS UNDER ANISOTHERMAL CYCLIC LOADING

HÉLÈNE MORCH[*], LAURENT DUCHÊNE[*] AND ANNE-MARIE HABRAKEN[*†]

[*] Dpt ArGEnCo, MS²F-MSM
University of Liège
Allée de la Découverte 9, 4000 Liège, Belgium
e-mail: helene.morch@ulg.ac.be; l.duchene@ulg.ac.be; anne.habraken@ulg.ac.be
http://www.uee.ulg.ac.be/cms/c_2672632/fr/mecanique-des-solides-et-des-materiaux-msm

[†] Fund for Scientific Research (FRS-FNRS)
www.fnrs.be

Key words: Constitutive modeling, Nickel-based superalloys, Cyclic plasticity, Thermo-mechanical modeling

Summary: The mechanical behavior of visco-plastic materials such as nickel-based alloys is highly dependent on temperature. Some characteristics such as viscosity, hardening, static recovery, dynamic recovery have more or less influence on the overall behavior depending on the considered temperature. The unified constitutive model developed by Chaboche [1] is very efficient in representing this complexity as it is very adaptable and can contain many features. A basic Chaboche model contains a viscosity law and one or several hardening equations. Within these hardening equations, it is possible to add several features that will represent the complex behavior of the material.

The aim of this study is to understand the role of the different parameters and the influence of the different features in an advanced Chaboche model adapted to cyclic anisothermal loading. This specific model was also developed in [2],[3]. However, part of this study is based on particular cases where different features of the model are analyzed [4]–[6].

1 INTRODUCTION

The use of nickel-based superalloys at high temperature requires advanced visco-plastic models to accurately represent the material behavior. The Chaboche model is very efficient for representing complex behavior as it can include various features such as isotropic hardening, kinematic hardening, static recovery, or thermo-mechanical behavior. The drawback of this type of model is the number of parameters. Indeed, a high level of accuracy of the model requires a high number of parameters. As a consequence, the determination of these parameters can be an arduous task. To facilitate this important step in the completion of the model, a sensitivity study can provide valuable information. The sensitivity analysis reveals which tests are more relevant for the determination of each parameter, but also how the parameters can impact the model and what physical meaning they have.

2 VISCO-PLASTIC MODELING

The visco-plastic model used in this study is a Chaboche-type constitutive model as developed in Ahmed, 2013 [2] for superalloy Haynes 230 at high temperture. This model, described hereafter, was implemented in the 3D finite element code Lagamine [7] developed at the University of Liège. For simplification, the model is described here as a 1D model, since only uniaxial tests are used in this study.

2.1 Visco-plasticity

The mechanical strain can be decomposed in an elastic contribution and a visco-plastic contribution:

$$\varepsilon = \varepsilon^e + \varepsilon^{vp} \tag{1}$$

The elastic strain and the stress are related through Hooke's law, where E is the Young's modulus:

$$\sigma = E\varepsilon^e \tag{2}$$

The yield locus is defined by the von-Mises criterion, with X the back-stress, σ_0 the initial yield strength, and R the isotropic hardening variable:

$$f = |\sigma - X| - \sigma_0 - R \tag{3}$$

The viscosity is modeled through Norton's equation (equation (4)), with viscous parameters n and K.

$$\dot{p} = |\dot{\varepsilon}^{vp}| = \langle\frac{f}{K}\rangle^n \tag{4}$$

$$where\ \langle x\rangle = \begin{cases} x\ if\ x \geq 0 \\ 0\ if\ x < 0 \end{cases}$$

2.2 Hardening equations

The evolution of the isotropic variable R, described by equation (5) depends on the plastic strain rate $\dot{p}$ and on two parameters b and Q. b can be understood as the rate at which variable R will reach its saturation value Q.

$$\dot{R} = b(Q - R)\dot{p} \tag{5}$$

The back-stress X is composed of one or several back stresses X_i. Each of these X_i obeys a non linear kinematic hardening rule defined through an Armstrong-Frederick equation [8]. Following the work of Yaguchi et al., 2002 [4], [5] a state variable Y_i can be added in the equation in order to model the evolution of the mean stress and a temperature-dependency term is used for anisothermal modeling. The variable Y_i is controlled by parameters $\alpha_{b,i}$ and $Y_{st,i}$, both positive. The equation of a back stress X_i therefore consists of 4 terms:

- strain hardening, controlled by parameter C_i;
- dynamic recovery, controlled by parameter γ_i;
- static recovery, controlled by parameters b_i and r_i;
- temperature rate, with the influence of parameter C_i.

$$X = \sum_{i=1}^{n} X_i$$
$$\dot{X}_i = C_i \dot{\varepsilon}^{vp} - \gamma_i (X_i - Y_i)\dot{p} - b_i \, |X_i|^{r_i} X_i + \frac{1}{C_i}\frac{\partial C_i}{\partial T}\dot{T} X_i \quad (6)$$
$$with \; \dot{Y}_i = -\alpha_{b,i}\left(Y_{st,i}\frac{X_i}{|X_i|} + Y_i\right)|X_i|^{r_i}$$

Cyclic hardening is represented by the evolution of the dynamic recovery parameter γ_i. The rate of evolution of this parameter is controlled by the plastic strain rate $\dot{p}$ and a parameter D_{γ_i}. The parameter γ_i evolves towards a saturation value γ_i^0 which depends on the radius of the strain memory surface q. The strain memory surface g_M is defined by equation (8), where $H(x)$ is the Heaviside step function.

$$\dot{\gamma}_i = D_{\gamma_i}(\gamma_i^0 - \gamma_i)\dot{p}$$
$$with \; \gamma_i^0 = a_{\gamma_i} + b_{\gamma_i} e^{-c_{\gamma_i} q} \quad (7)$$

$$g_M(\varepsilon^{vp} - \zeta) = |\varepsilon^{vp} - \zeta| - q$$
$$\dot{\zeta} = (1 - \eta) H(g_M)\dot{p} \quad (8)$$
$$\dot{q} = \eta \, H(g_M)\dot{p}$$

2.3 Influence of the maximum temperature

In the case of anisothermal cyclic loading on Haynes 230, experiments show that the maximum temperature of the cycle has an influence on the overall behavior of the material [2]. This is modeled by a variation of the Young's modulus, expressed as a weighted average of the initial Young's modulus at temperature T and the Young's modulus at maximum temperature T_{max}:

$$E = f_E E + (1 - f_E) E_{T_{max}}$$
$$\dot{f}_E = b_E (f_E^S - f_E)\dot{p} \quad (9)$$

The weighted average factor f_E represents the weight of the initial Young's modulus. A small value of f_E corresponds to a significant influence of the maximum temperature. f_E evolves at a rate b_E towards a saturated value f_E^S.

3 METHOD

The sensitivity study was conducted using reference sets of parameters available in the literature. These sets of parameters came from models that did not contain as many features as the model hereinbefore presented. However, using different sub-models allowed to study the sensitivity of the model to each of the parameters.

3.1 Numerical tests

The sensitivity study was conducted numerically on each parameter by performing a cyclic test and modifying one parameter at a time. Different sets of reference parameters were used to perform the simulations. Table 1 summarizes the reference articles used depending on the tested parameters.

Table 1 : Reference articles used to obtain parameters

Parameter studied	Set of reference parameters used
$K, n, b, Q, C_1, C_2, \gamma_1, \gamma_2$	Zhan and Tong, 2007 [6]
$b_1, r_1, \alpha_{b,1}, Y_{st,1}, D_{\gamma_1}, a_{\gamma_1}, b_{\gamma_1}, c_{\gamma_1}, \eta$	Yaguchi et al., 2002a [4]
b_E, f_E^s	Yaguchi et al., 2002b [5]

The first model used [6] is an isothermal model describing the behavior of Alloy X at 650°C with two back-stresses for kinematic hardening, where no static recovery effect is taken into account. To study the influence of static recovery, variable Y, and cyclic hardening, a different model was used [4]. The latter describes the behavior of IN738LC at 850°C. Kinematic hardening is modeled using only one back-stress, with an internal variable Y. The influence of parameters b_E and f_E^s was tested on an anisothermal model [5] identical to [4].

It is to be noted that no reference was available for parameters $D_{\gamma_1}, a_{\gamma_1}, b_{\gamma_1}, c_{\gamma_1}, \eta, b_E$ and f_E^s, therefore, a reference value was determined for each of these parameters through trial and error, to obtain results that seemed coherent with the experimental data available (although the parameters were not determined to fit experimental curves). These reference values are summarized in Table 2.

Table 2 : Reference parameters

D_{γ_1}	a_{γ_1}	b_{γ_1}	c_{γ_1}	η	b_E	f_E^s
10	300	100	10	0.2	1000	0.2

The sensitivity of the model on the different parameters was tested on two strain-controlled cyclic tests. A schematic representation of one period of the cyclic tests is given in Figure 1 (a). Anisothermal tests (Figure 1 (b)) were used to evaluate the sensitivity of the model to parameters b_E and f_E^s. For both Test 1 and Test 2, the strain amplitude is $\Delta\varepsilon = 2\%$. The strain rates $\dot{\varepsilon}$ and hold times t_H of Test 1 and 2 are respectively {0.1%/s, 20s} and {0.001%/s, 1000s}. Each of these tests were performed for 50 cycles, which is enough for the stress-strain hysteresis loop to reach its saturation value using the reference parameters.

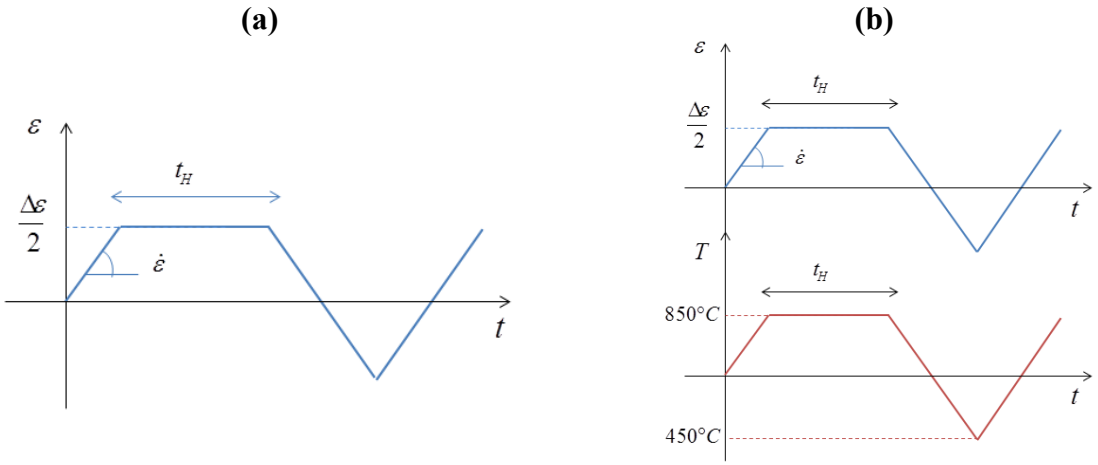

Figure 1: (a) Strain-controlled isothermal test; (b) Strain-controlled anisothermal test

3.2 Sensitivity criteria

Different criteria F_i were used to determine the sensitivity of the model to the different parameters:

- F_1: The tensile stress before the first hold time (equivalent to the stress at the end of a tensile test);
- F_2: The amount of stress relaxation during the first hold time (equivalent to a relaxation test);
- F_3: The stress amplitude $\sigma_{amp} = \frac{\sigma_{min}+\sigma_{max}}{2}$ at the 50th cycle;
- F_4: The mean stress $\sigma_{mean} = \frac{\sigma_{max}-\sigma_{min}}{2}$ at the 50th cycle.

The mean stress and the stress amplitude were also used as criteria to study the sensitivity over the cycles.

For each criterion F_i, the sensitivity to a parameter P is expressed as $\frac{\partial F_i}{\partial P}$. The criterion F_i is computed for three values of the parameter P and the sensitivity $\frac{\partial F_i}{\partial P}$ is calculated as the slope of the $F_i(P)$ line obtained from a linear regression.

4 RESULTS

4.1 Viscous parameters K, n

The viscous parameters K and n represent the relation between the stress and the strain rate. Figure 2 shows the sensitivity of criteria F_1, F_2, F_3 and F_4. Both parameters have an influence on the tensile stress (F_1) and on the stabilized stress amplitude (F_3). The stress relaxation is also influenced by these viscous parameters but to a smaller extent.

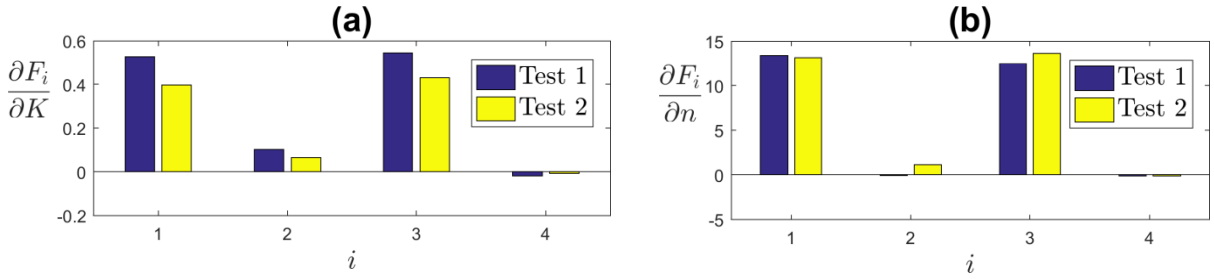

Figure 2: (a) Sensitivity to the drag stress K; (b) Sensitivity to the viscous exponent n

4.2 Isotropic hardening parameters b, Q

The isotropic hardening parameters b and Q control the growth of the yield surface. Knowing this, it is predictable that these parameters will influence mostly the tensile stress and the stress amplitude. Figure 3 shows that these parameters influence mainly the stress amplitude over the cycles, with b reaching a peak around the 10th cycle, where the stress amplitude starts to stabilize. The small sensitivity of the tensile stress to these isotropic hardening parameters is due to the test itself, which only reaches a 1% strain, therefore not allowing isotropic hardening to fully develop. In practise, a tensile test to rupture would show as much sensitivity to isotropic hardening as the cyclic tests that were performed here.

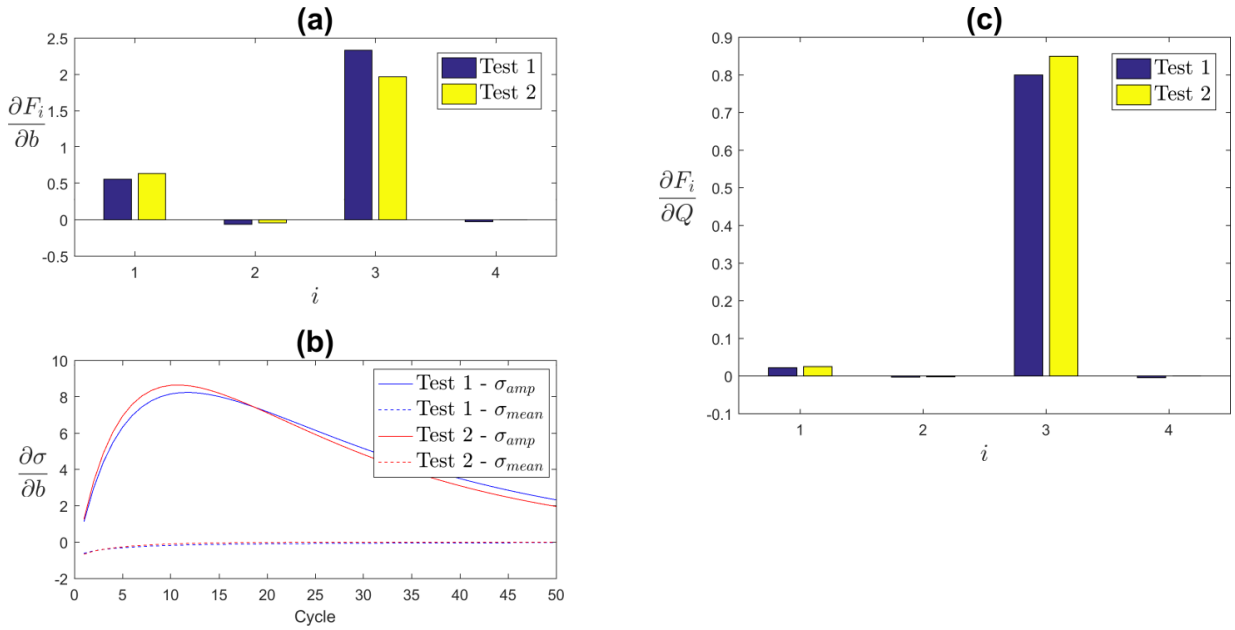

Figure 3 - (a) Sensitivity to parameter b; (b) Stress amplitude and mean stress sensitivity to b over cycles; (c) Sensitivity to parameter Q

4.3 Kinematic hardening parameters C_i

Kinematic hardening is characterized by a change in the position of the yield surface. As for isotropic hardening, the parameters controlling kinematic hardening influence the tensile stress and the stress amplitude, as seen in Figure 4. As shown in Tong et al. [9], the use of two parameters C_1 and C_2 allows the description of a transient region with a fast growing back-stress X_1 and a steady-state behaviour once X_1 has reached its stabilized value, with back-stress X_2 growing at a quasi-steady pace. The parameters C_1 and C_2 also have an influence on the shape of the hysteresis loop, and more particularly on its curvature in the visco-platic domain.

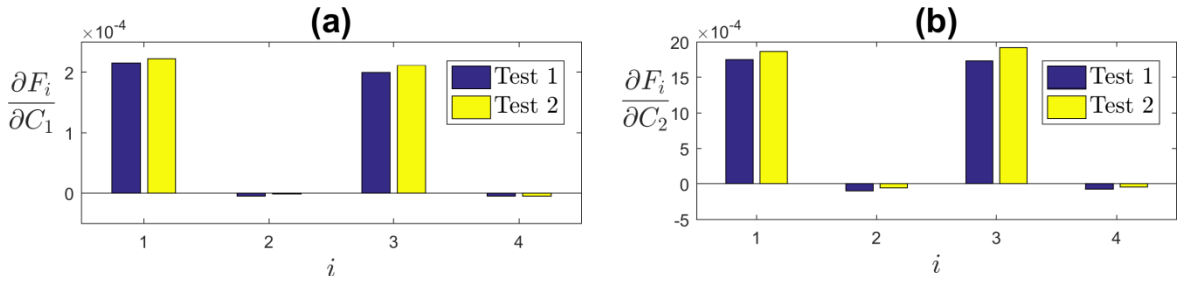

Figure 4 - (a) Sensitivity to parameter C_1; (b) Sensitivity to parameter C_2

4.4 Dynamic recovery parameters γ_i

The dynamic recovery parameters γ_1 and γ_2 have the opposite effect of C_1 and C_2. Figure 5 shows that F_1 and F_3 show a negative sensitivity to both γ_1 and γ_2, which means an increase

in γ_i will lead to a decrease in F_j. Similarly to the kinematic hardening parameters, γ_1 and γ_2 also have an effect on the curvature of the hysteresis loop.

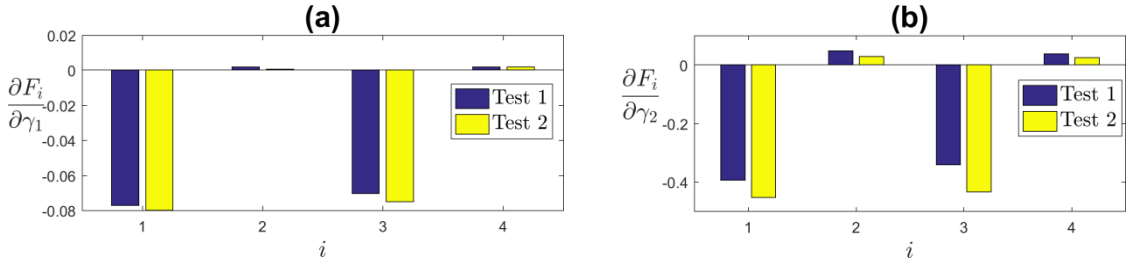

Figure 5 - (a) Sensitivity to parameter γ_1; (b) Sensitivity to parameter γ_2

4.5 Static recovery parameters b_i, r_i

To study the influence of the static recovery parameters, the internal variable Y was not taken into account. Indeed, parameter r_i is used both in the static recovery term of the back-stress evolution and in the evolution of internal variable Y - equation (6). Figure 6 shows the sensitivity to static recovery parameters b_1, r_1 without considering the effect of r_1 on Y. It is apparent that Test 2, which is slower and has longer hold times than Test 1, is much more impacted by the variation of these parameters. This is an expected result considering static recovery is a phenomenon that takes place at a constant strain. The influence is maximal on the stress relaxation (criterion F_2), but also appears on the other criteria. This can be explained by equation (6): a higher value of b_1 or r_1 will lead to a greater decrease in the back-stress X_1, therefore lowering the tensile stress and stress amplitude.

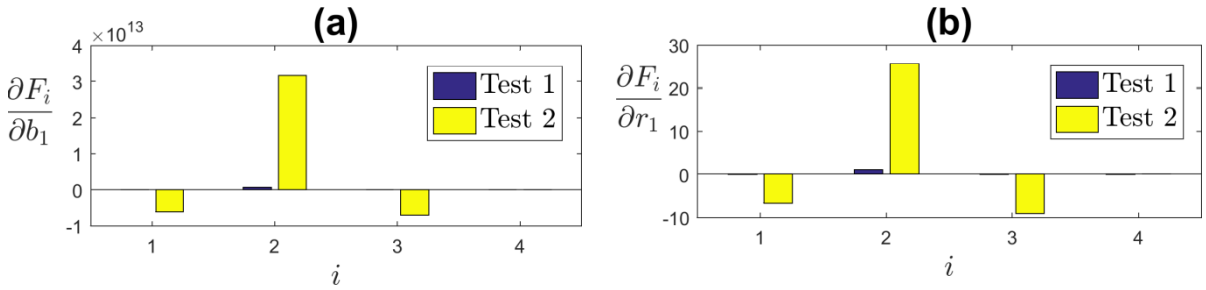

Figure 6 - (a) Sensitivity to b_1; (b) Sensitivity to r_1 (without considering the internal variable Y)

4.6 Mean stress evolution parameters $\alpha_{b,i}$, $Y_{st,i}$, r_i

The internal variable Y_1 that controls the evolution of the mean stress over cycles is calculated using three parameters $\alpha_{b,1}$, $Y_{st,1}$, r_1. Figure 7 (a) represents the sensitivity to parameter $\alpha_{b,1}$.

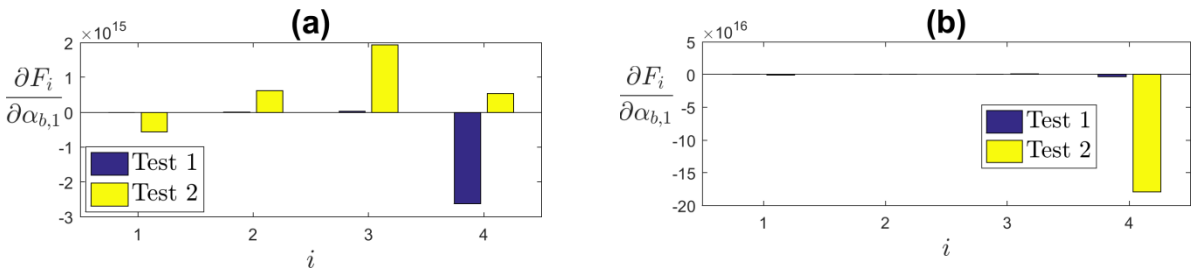

Figure 7 - (a) Sensitivity to $\alpha_{b,1}$; (b) Sensitivity to modified $\alpha_{b,1}$

The sensitivity computed with Test 1 seems coherent: the parameter influences only the mean stress. However, sensitivities computed with Test 2 give rather unexpected results, and show a bigger influence on the stress amplitude than on the mean stress. The reason for this can be found by considering the evolution of variable Y_1 over time, described by equation (6). The variable Y_1 varies within $-Y_{st,1}$ and $+Y_{st,1}$. Therefore, according to (6), $\dot{Y}_1$ is positive when $X_1 > 0$ and negative when $X_1 < 0$ unless Y_1 has reached its upper bound or lower bound. During a cycle, if $\alpha_{b,1}$ is small enough, Y_1 decreases slowly while $X_1 > 0$ (tensile deformation), and then increases when $X_1 < 0$ (compressive deformation). The time spent in compressive deformation is much smaller than in tension, therefore, the variable Y_1 globally decreases over cycles. However, if $\alpha_{b,1}$ is too big compared to the frequency of the test, the variable Y_1 reaches its upper and lower bound during the first cycle. This is an unwanted effect because Y_1 will assume positive values, meaning the mean stress can increase over cycles, which is physically incoherent.

As a result, in order to represent the mean stress evolution properly, $\alpha_{b,1}$ should be chosen accordingly to the frequency of the cyclic test. Particularly, the value of $\alpha_{b,1}$ should be bigger for bigger frequencies. Figure 7 (b) shows the sensitivity to $\alpha_{b,1}$, using $\alpha_{b,1} = 0.01 * \alpha_{b,1}$ for Test 2. It appears clearly that $\alpha_{b,1}$ then only influences the mean stress.

The influence of parameters $Y_{st,1}$ and r_1 is tested using the modified value of $\alpha_{b,1}$ for Test 2. The results are shown in Figure 8. $Y_{st,1}$ has an influence on the mean stress, as expected. r_1 has an influence on both stress relaxation and mean stress since this parameter is used both for the variable Y_1 and for the static recovery term in the equation of the back-stress.

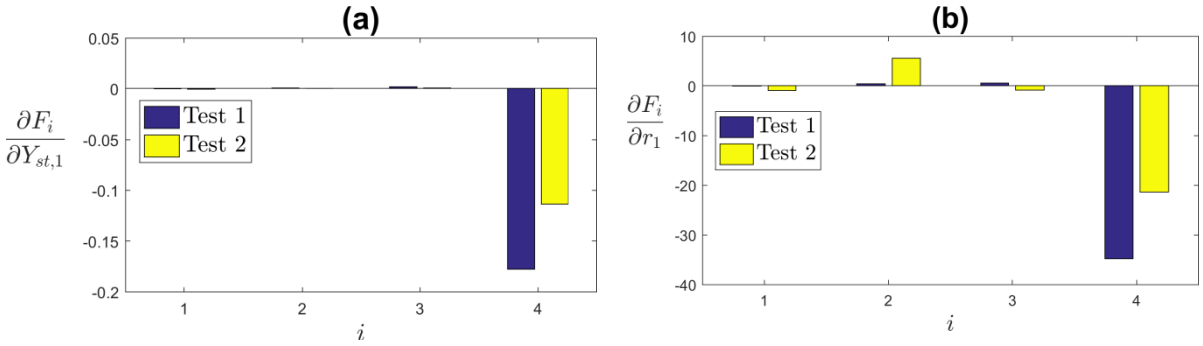

Figure 8 - (a) Sensitivity to $Y_{st,1}$; (b) Sensitivity to r_1

4.7 Cyclic hardening parameters $D_{\gamma_i}, a_{\gamma_i}, b_{\gamma_i}, c_{\gamma_i}, \eta$

Cyclic hardening is described using five parameters that impact the value of parameter γ_i over the cycles. Parameters D_{γ_i} and η control respectively the rate of cyclic hardening and the rate of growth of the plastic strain memorization surface. Figure 9 (a) and (b) show the sensitivity of the stress amplitude and mean stress to D_{γ_1} and η. In both cases, the sensitivity grows to a peak value, and then decreases towards 0 as the values of γ_1 (for D_{γ_1}) and q (for η) stabilize. $a_{\gamma_i}, b_{\gamma_i}$ and c_{γ_i} control the stabilized value of γ_i. Therefore, it is expected that these parameters only influence the stabilized value of the stress amplitude, as seen in Figure 9. Parameters a_{γ_i} and b_{γ_i} have a negative influence while c_{γ_i} has a positive influence on the stress amplitude. These parameters also have a small influence on the mean stress, which can be explained by the fact that the evolution law of Y_1 depends on the back-stress X_1, which is itself dependent on γ_1. The sensitivity observed for Test 2 on the mean stress should however not be taken into account, as it is the result of the inadequacy of $\alpha_{b,1}$ mentioned in the previous paragraph.

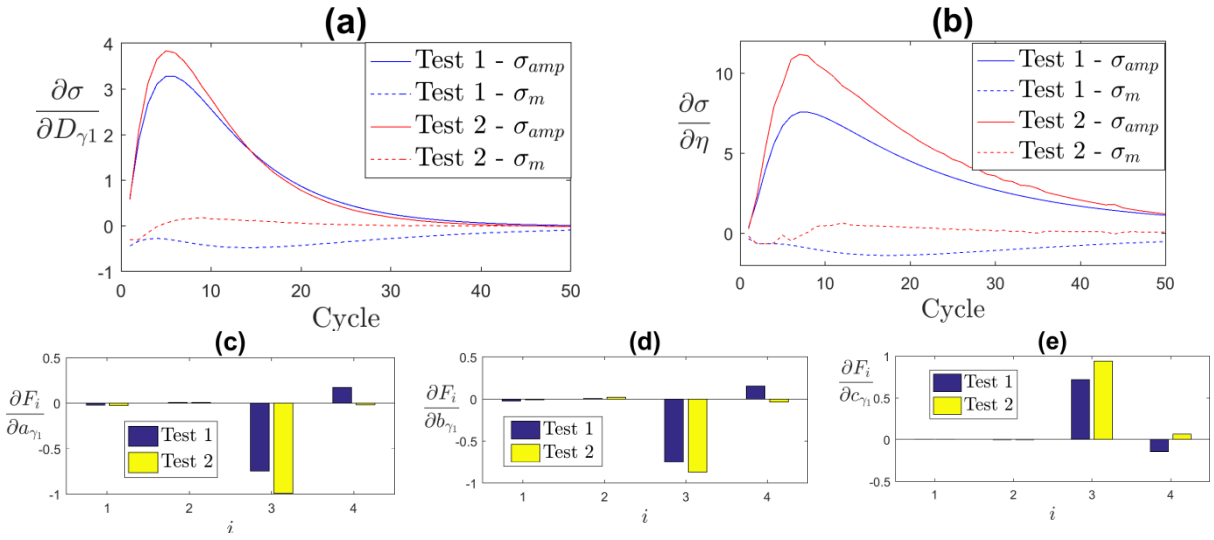

Figure 9 - (a) Cyclic sensitivity to D_{γ_1}; (b) Cyclic sensitivity to η; (c) Sensitivity to a_{γ_1}; (d) Sensitivity to b_{γ_1}; (e) Sensitivity to c_{γ_1}

4.8 Maximum temperature parameters b_E, f_E^S

Parameters b_E and f_E^S, that represent the influence of the maximum temperature, do not have a visible and clear influence on the criteria used previously. Figure 10 shows the stabilized hysteresis loop of Test 1 for three values of f_E^S. Small values of f_E^S - i.e. substantial influence of the maximum temperature - lead to a decrease in the slope of the stress-strain curve in the small temperature domain (corresponding to compression strain). This is an expected result considering that the Young's modulus, which partly controls the slope of the stress-strain curve, decreases with temperature.

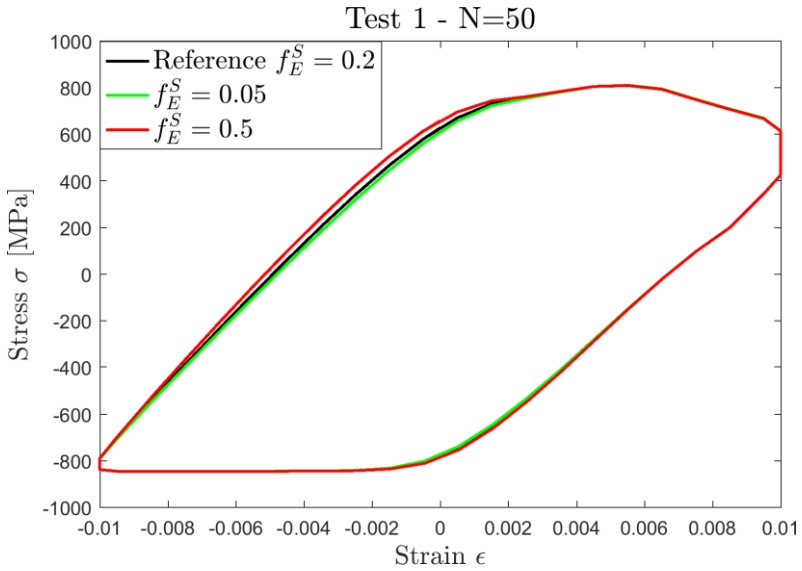

Figure 10 - Influence of parameter f_E^S on the stabilized hysteresis loop

The influence of b_E is difficult to show, as b_E represents the rate at which the slope decreases over time. Ahmed, 2013 [2] suggests that b_E should be chosen to make f_E evolve at a quick rate, so that the saturation value f_E^S is reached for a cumulative plastic strain p of approximately 0.2% for Haynes 230.

5 CONCLUSION

Based on numerical tests, the sensitivity of the model to each of its parameters was determined based on various criteria. The results of this sensitivity study were analyzed to narrow down the number and type of tests necessary for the determination of each parameter. The study shows that tensile tests, relaxation tests, and cyclic tests are necessary for the determination of the parameters of this model. A special attention should be given to parameter $\alpha_{b,1}$ for the representation of the mean stress evolution. Indeed, the sensitivity study revealed that this parameter must be chosen with consideration to the frequency of the test simulated. Particularly, low-frequency cyclic tests should be modeled with a small value of $\alpha_{b,1}$.

Further work needs to be made to determine a dependency law between $\alpha_{b,1}$ and the test frequency, based on experimental tests. The sensitivity study can also serve as a basis to establish a method for the determination of the parameters.

ACKNOWLEDGEMENTS

The authors acknowledge the Interuniversity Attraction Poles Program - Belgian State – Belgian Science Policy (P6-24). A.M. Habraken and L. Duchêne acknowledge the Belgian Fund for Scientific Research FRS-FNRS for its support.

REFERENCES

[1] J. L. Chaboche, "A review of some plasticity and viscoplasticity constitutive theories," *Int. J. Plast.*, vol. 24, no. 10, pp. 1642–1693, 2008.

[2] R. Ahmed, "Constitutive Modeling for Very High Temperature Thermo-Mechanical Fatigue Responses," North Carolina State University, 2013.

[3] R. Ahmed, M. Menon, and T. Hassan, "Constitutive Model Development for Thermo-Mechanical Fatigue Response Simulation of Haynes 230," in *Proceedings of the ASME 2012 Pressure Vessels & Piping Conference*, 2012, pp. 171–179.

[4] M. Yaguchi, M. Yamamoto, and T. Ogata, "A viscoplastic constitutive model for nickel-base superalloy, part 1: Kinematic hardening rule of anisotropic dynamic recovery," *Int. J. Plast.*, vol. 18, no. 8, pp. 1083–1109, 2002.

[5] M. Yaguchi, M. Yamamoto, and T. Ogata, "A viscoplastic constitutive model for nickel-base superalloy, part 2: Modeling under anisothermal conditions," *Int. J. Plast.*, vol. 18, no. 8, pp. 1111–1131, 2002.

[6] Z. L. Zhan and J. Tong, "A study of cyclic plasticity and viscoplasticity in a new nickel-based superalloy using unified constitutive equations. Part II: Simulation of cyclic stress relaxation," *Mech. Mater.*, vol. 39, no. 1, pp. 73–80, 2007.

[7] "Lagamine code, http://www.uee.ulg.ac.be/cms/c_2383455/en/lagamine." .

[8] P. J. Armstrong and C. O. Frederick, "A Mathematical Representation of the Multi Axial Bauschinger Effect," CEGB Report RD/B/N 731,Central Electricity Generating Board, 1966.

[9] J. Tong, Z. L. Zhan, and B. Vermeulen, "Modelling of cyclic plasticity and viscoplasticity of a nickel-based alloy using Chaboche constitutive equations," *Int. J. Fatigue*, vol. 26, no. 8, pp. 829–837, 2004.

XIV International Conference on Computational Plasticity. Fundamentals and Applications
COMPLAS 2017
E. Oñate, D.R.J. Owen, D. Peric and M. Chiumenti (Eds)

PERFORMANCE EVALUATION OF A PULSATILE VENTRICULAR ASSIST DEVICE UNDER NON PHYSIOLOGIC PUMPING FREQUENCIES BY MEANS FEM AND 2D APPROACH.

EXEQUIEL R. FRÍES [1] AND JOSÉ DI PAOLO [2]

[1,2] Grupo Biomecánica Computacional (GBC)
Universidad Nacional de Entre Ríos (UNER)
Ruta Prov. 11, km 10, 3100 Oro Verde, Entre Ríos, Argentina
[2] Facultad Regional Santa Fe - Universidad Tecnológica Nacional (FRSF-UTN)
Lavaisse 610, 3000 Santa Fe, Pcia. Santa Fe, Argentina
e-mail: efries@ingenieria.uner.edu.ar,
e-mail: jdipaolo@ingenieria.uner.edu.ar,
web page: http://ingenieria.uner.edu.ar/grupos/biomecanica_computacional/

Key words: Ventricular assist device, blood damage, platelet activation, pulsatile flow.

Abstract. A ventricular assist device (VAD) is a blood pump that works in parallel with heart. It is used as a mechanical assistance for patients that suffer cardiac insufficiency: as a therapy, as a bridge to transplant or to extend life. The blood flow simulation into VAD is of great interest for the design and evaluation, mainly before building the prototypes. In previous works, by means of blood flow simulation, was evaluated a new concept of implantable VAD consisting on a pump with a double effect piston, driven without contact and four active valves. In this work, the flow into VAD is analyzed for four frequencies values: 1.05, 2.10, 3.15 and 4.20 Hz. The former is the physiologic frequency, the second allows the basal flow rate (5 l/min), while the others are higher in order to assure an increase in flow rates. The analysis is carried out comparing variables as velocity and pressure distribution into VAD and evaluating blood damage due to acting shear stress over cells. The blood flow simulation is performed on a 2D simplified geometry using COMSOL Multiphysics software to resolve Navier-Stokes and continuity equations, assuming blood as a Newtonian incompressible fluid. The blood damage is evaluated by means of platelet activation state index and a cumulative damage model. The global variables as flow rate, force and power to impel fluid, are shown in agreement with theoretical predictions. The risk of blood damage raises for higher frequencies, however, the predictions shown that the VAD analyzed is comparable and best to other VAD and mechanical heart valves.

1 INTRODUCTION

Heart failure (HF) affects heart avoiding the accomplishment of its function; this is currently one of the greater pandemics in the world [1], mainly in the occidental world. People suffer HF can be assisted with different treatments, mainly when the pathology is in advanced stages. A possible one for patients with HF is the mechanical circulatory assistance (MCA), which has been accepted as a therapeutic option, as a bridge to heart transplant or in cases where this is not possible; even more when the number of people affected by HF increases and the number of donors for a heart transplant (HT) relatively diminishes. However, HT is the more accepted option by the medical community [2].

Ventricular assist devices are pumps that are placed in parallel to the heart, usually pumping blood from the left ventricle into the aorta (LVAD). Implantables VAD are given more attention because they can be fully implanted and allow long-term care (from months to some years), as well as to improve the quality of life because they allow patients to do simple daily activities. A VAD is a therapeutic option to be used as a definitive solution, as a bridge to HT or, in some cases, as a treatment to recover the normal function of the damaged heart.

In previous works [3, 4, 5], using a numerical simulation of blood flow, a new concept of VAD was analyzed in a simplified way. This is a double-acting pump with a non-contact and external driven piston (i.e. electromagnetically) and four active valves. In this work, the flow in the same device for four operating frequencies *(f)* (1.05, 2.10, 3.15 and 4.20 Hz) by comparing the fields of velocity and pressure and the applied power, is studied. In addition, blood damage caused by the shear forces for $f=2.10$ *Hz* and $f=4.20$ *Hz* are compared. Blood flow is simulated into a simplified two-dimensional (2D) geometry using the COMSOL Multiphysics software, solving the Navier-Stokes and continuity equations, assuming blood as an incompressible and Newtonian fluid. Blood damage is assessed by calculating the platelet activation state (PAS) using a cumulative damage model [6, 7].

2 METODOLOGY

2.1 Description of the simulated VAD

Starting from the concept of a simple design volumetric pump and taking into account the functional VAD's characteristics, a two-dimensional (2D) approach is made. This approach involves the simulation of blood flow to investigate its possible damage. The simplified VAD geometry is presented in Figure 1; it has a piston, two chambers, right and left (LC and RC), input and exit ducts, two inlet valves (Vi) and two output valves (Vo). Piston without contact would demand high electromagnetic technology to be driven. The 2D geometry is selected to acquire preliminary knowledge using standard computational resources, as a guide for further investigation with more realistic geometries.

The double effect piston is assumed with periodical movement, in each run, piston pumps blood from one chamber and suctions it in the other, while two valves are open and two others are closed. The movement of each valve depends only of an actuator that controls the closing and reopening speed. The actuators move valves normally to flow in the input and exit conduits, they open and close in a few milliseconds assuming no secondary effects as rebound or vibration. The simulation of valves opening and closing, is done using moving meshes, with appropriate functions that allow a valve to be in synchronism with the piston movement,

as is described in a previous work [5].

Figure 1 shows a Cartesian two-dimensional simplified diagram of VAD, where the piston is moving to the left, pumping blood from the left chamber to the outlet (red region), while the right chamber receives blood from the input (blue region). In this case, the upper Vi and lower Vo are closed to assure net flow rate. When the piston reaches the left end, the lower Vi and the upper Vo quickly close and the upper Vi and the lower Vo quickly open. The piston starts moving to the right, pumping blood from the CD to the exit and suction it from the inlet to the IC.

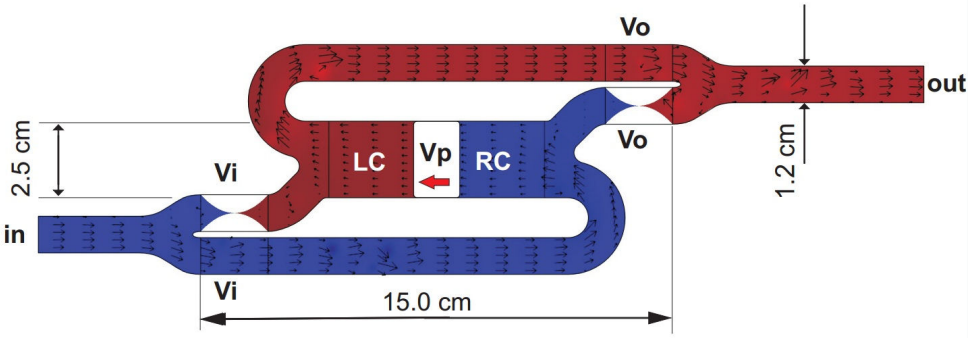

Figure 1: Description of VAD with input (in) and output (out) regions, the piston is moving to the left. There are some representative dimensions.

2.2 The model of blood flow

As was said, numerical simulations of blood flow are made in a simplified 2D plane geometry. Considering blood as an incompressible and Newtonian fluid [8], the Navier-Stokes and continuity equations with the governing law of motion for piston and valves movements, are solved using an appropriate coordinate mapping as described in the next section.

2.2.1 Moving domain and mesh deformation:

Equation 1 and 2 represent a simple harmonic motion (Xp), which is appropriate for this kind of pump, where $A=2.0\ cm$ is the amplitude in each chamber, Vp is the harmonic velocity of piston and f is the frequency of movement; the parameter of interest in this work. The movement of each valves, is implemented with ad hoc functions that avoid the collapse of the elements [3, 5]. This motion produces a deformation of the flow domain and to trace it, an Arbitrary Langrangian-Eulerian (ALE) deformable mesh technique is implemented [10] [9].

$$Xp = A \sin(2\pi f) \tag{1}$$

$$Vp = 2\pi f A \cos(2\pi f) \tag{2}$$

2.2.2 Boundary conditions for blood flow

On fixed and moving solid surfaces, no-slip boundary conditions are considered. Thus, $\boldsymbol{v}=0$ on the chamber and ducts walls, $\boldsymbol{v}=Vp$ on the piston wall and $\boldsymbol{v}=Vvalve$ on the valves boundaries are imposed [5]. On the input and output sections, reference pressures are imposed: $Pin = 0$

and *Pout* =13.3 kPa (~ 100 mmHg), which approaches the mean aortic pressure. Furthermore, constant values are assumed for the viscosity and blood density: 1.060×10^3 kg/m^3 and 3.5×10^{-3} Pa·s, respectively [3, 10, 7].

2.2.3 Numerical simulation

The 2D geometry is divided with a mesh of Ne (see table 1) triangular elements P3-P2 kind, whose size varies according to each adopted *f*. The maximum and minimum dimensions of elements where taken according to a suitable refinement test. The maximum time step is reduced as *f* increases. Table 1 shows these parameters for each of four simulations. The simulated time intervals are 1.2 s for 1.05 Hz, 1.0 s for 2.10 Hz, 0.5 s for 3.15 Hz and 0.5 s for 4.20 Hz. The simulation time interval is selected to complete at least one operating cycle to do possible the computation and comparison of blood damage.

The system of equations is solved simultaneously through a monolithic scheme. In order to start the simulation, a higher viscosity is used while all variables are initialized with zeros. Although the initial higher viscosity quickly descends to the assumed value, in all the simulations the first half-cycle is not considered for the analysis.

Table 1: Parameters for each simulation.

Frequency *f* [Hz]	1.05	2.10	3.15	4.20
Simulated time period [s]	1.20	1.00	0.50	0.50
Maximum time step [s]	1×10^{-3}	5×10^{-4}	4×10^{-4}	2×10^{-4}
Maximum element size [m]	5×10^{-3}	5×10^{-3}	5×10^{-3}	2.5×10^{-3}
Total number of elements Ne ($\times 10^3$)	206	206	206	376

2.3 Global variables calculation

Since the DAV is a volumetric pump, the output flow is obtained by integrating the normal component of the velocity (v_x) in the output section as defined in equation 3. The pumping force and the pumping power are determined by equation 4 and 5, respectively. It should be noted that the area integral for the force, becomes line integral over the contour of the piston for the 2D geometry, where $t_x(\boldsymbol{n}, t)$ is the vector of tension *x* component over piston surface.

$$q(t) = \iint v_x(t)\, dy \tag{3}$$

$$Fx(t) = \oint t_x(\boldsymbol{n}, t)\ dl \tag{4}$$

$$Pwr(t) = Fx(t) * Vp \tag{5}$$

2.4 Model of blood damage

The platelet activation phenomenon modeling is a complex task. If considering only physical aspects, platelet activation state (*PAS*) can be predicted using a model based on the rate at which the shear stress is applied. This model should consider, also, the history of shear stress acting on the cells. Thus, in this work the model proposed by Nobili *et al.*[7] is adopted. For its application, the path of a set of PLs drifting in the flow domain must be known. For that purpose, it is supposed that PLs moves massless-like virtual particles and their pathes are computed by integration of velocity field. Then, the equivalent shear stress (τ) is evaluated for each PL (particle) path by equation 6 proposed by De Tulio *et al.*, [11]. Finally, the shear stress history is used in equation 7 to evaluate the PAS_n, that is the PAS for the *n*-PL, where the constants *a, b* and *C* are extracted from Nobili *et al.* [7]. A global quantity *PASmean* can be computed as the average of all PAS_n by means of equation 8, over a set of PLs released at the same time in a given region. In this work, four groups, each one composed for a set of N= 20 particles representing the PLs, are released. Four groups are considered for simulation, two groups corresponding to 2.10 Hz (one for each chamber) and, in the same way, two groups corresponding to 4.20 Hz, see table 2.

$$\tau = \frac{1}{2}\sqrt{\left(2\mu\frac{\partial u}{\partial x} - 2\mu\frac{\partial v}{\partial y}\right)^2 + 4\left[\mu\left(\frac{\partial u}{\partial y} + \frac{\partial v}{\partial x}\right)\right]^2} \tag{6}$$

$$PAS_n = \sum_{i=1}^{N} C\ a\left[\sum_{j=1}^{i}(\tau(t_j)^{\frac{b}{a}}\Delta t_j + D_o)\right]^{a-1} \tau(t_i)^{b/a}\Delta t_i \tag{7}$$

$$PASmean = \frac{1}{N}\sum_{n=1}^{N} PAS_n \tag{8}$$

Table 2: PLs groups for blood damage evaluation.

Groups	1	2	3	4
N - Number of Pls	20	20	20	20
Time initial [ms]	150 ms	150 ms	100 ms	100 ms
Frecuency [Hz]	2.10	2.10	4.20	4.20
Chamber	LC	RC	LC	RC
Initial position	Vi in LC	Vi in RC	Vi in LC	Vi in RC

The model used to evaluate the *PASmean* is the most used by the reserchers' community and is the most cited in literature [6, 7, 10, 5, 12]. It predicts the platelet activation because of shear stress from physiological or artificial source. This cumulative damage model is adapted to represent experimental situations of pulsating shear stress, in this case the model works

appropriately as described by Nobili *et al.*[7]. However, there are situations of high shear stress in which the model can not properly represent the sensitization of PL [12].
It is important to note that numerical simulation of platelet activation is an open study field and there is not an optimal model for all situations of blood flow (natural or artificial). The model used in this study was modified by Sheriff et al. (2013), incorporating new parameters to better represent blood damage in many flow situations. However, these researchers have pointed out model limitations to represent certain in vitro results due to the power law description (see equation 7).

3 RESULT

3.1 Flow rate and velocity

Figure 2 shows the output flow rate generated by the VAD operating at different frequencies. This flow rate is composed by: the flow rate pumps by the piston whose shape is a "sinusoidal rectified" function; the overflow rate induced for the closing of a respective valve (positive peak) and a backflow rate induced for the opening of the counterpart valve (negative peak). This flow rate is obtained integrating as is indicated by equation 3. On the other hand, in figure 3 is presented a comparison between the ideal flow rate for a cycle (without differential flow rates because valves), represented by the blue line, versus the average flow obtained in each simulation, indicated by red dots.

Figure 4 depicts the magnitude of velocity field when the piston moves to the left at the maximum speed, in the four images the scale is the same (0 to 3 m/s). When the operating *f* raises, the speed at certain points is greater, as happens at the valve gaps.

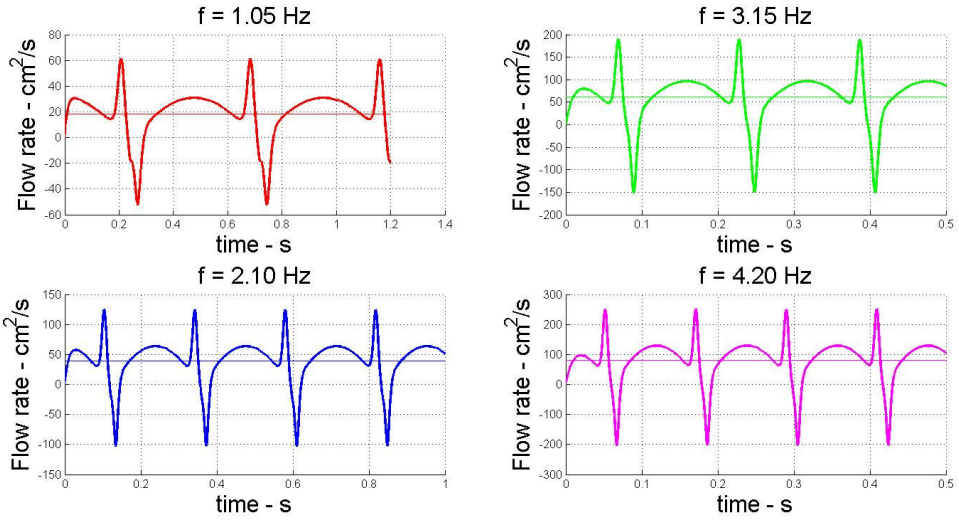

Figure 2: Flow rate for each frequency. The horizontal line indicates the average flow rate.

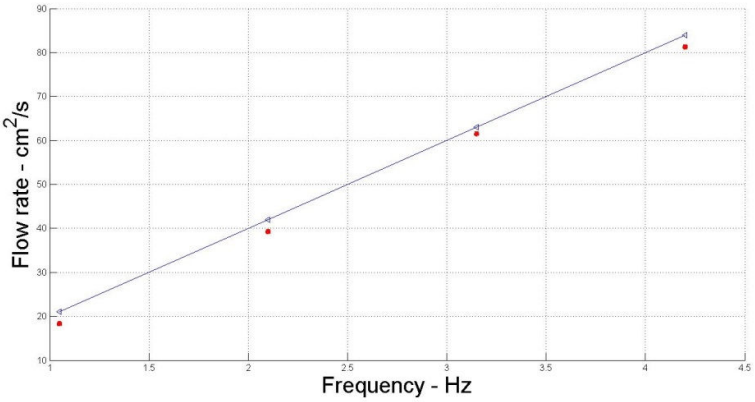

Figure 3: Average flow rate for each operating frequency (in red). The blue line indicates the ideal flow rate.

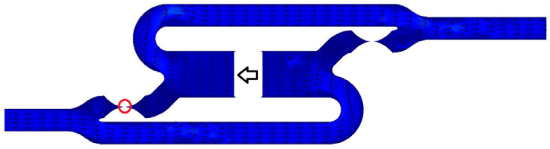

a) f = 1.05 Hz
Time in 0.476 s; Vp = 0.13 m/s and $Vmax$ = 1.69 m/s

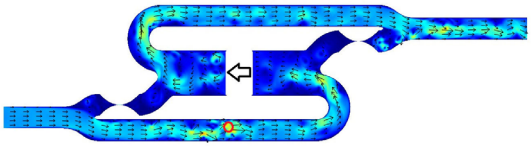

c) f = 3.15 Hz
Time in 0.476 s; Vp = 0.39 m/s and $Vmax$ = 2.2 m/s

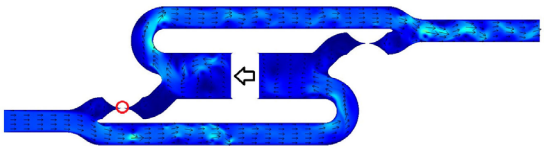

b) f = 2.10 Hz
Time in 0.358 s; Vp = 0.27 m/s and $Vmax$ = 1.72 m/s

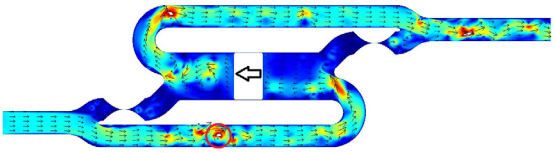

d) f = 4.20 Hz
Time in 0.358 s; Vp = 0.52 m/s and $Vmax$ = 3.4 m/s

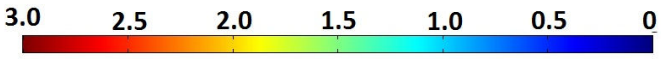

Figure 4: Velocity field module for the instant when the piston moves at the maximum speed to the left. The maximum velocity is indicated with a red circle, in the location of valve gaps for a) and b), and into the input branch for c) and d).

3.2 Pressure

Figure 5 shows the pressure distribution in LC, very close to the edge of the piston. It is observed that the mean pressure in each half-cycle is equal to the inlet pressure (0 Pa) or the

outlet pressure ($1.3x10^4$ Pa). As frequency rises, the time derivative of pressure, raises too. In addition, the pressure peaks generated by the valves closing and opening are relatively higher because the closing and opening speed increases with frequency.

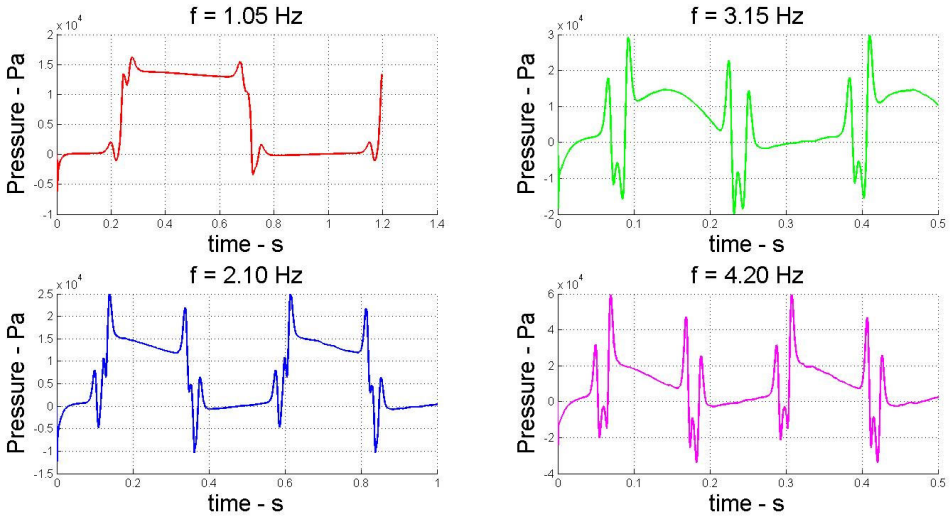

Figure 5: Pressure into the left chamber for each operating frequency.

3.3 Force and Power

The *Fx(t)* required to drive the fluid over time, is obtained by equation 4 and is presented in figure 6 for the frequencies analyzed. As the *f* increases, the time derivative of *Fx* is strongly modified. The instantaneous pumping power (*Pwr(t)*) is depicted in figure 7, where the average power for a cycle is indicated by a line for each frequency.

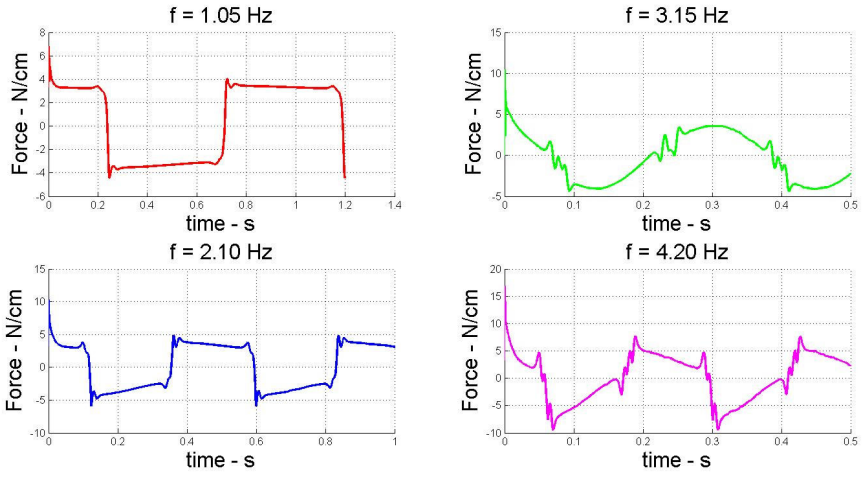

Figure 6: Force on fluid for each operating frequency.

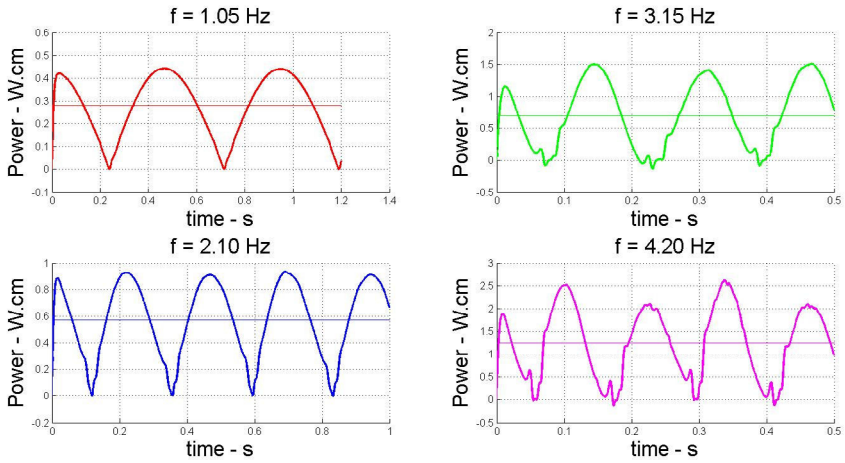

Figure 7: Power on fluid for each operating frequency.

3.4 Platelet paths and PAS mean

The platelet trajectories in the blood flow are of the kind of those show in Fig. 8, the trajectories in dashed line correspond to PLs for the DAV operating at 2.1 Hz released at LC (group 1) and released at RC (group 2) for red and blue color respectively. While the trajectories in continuous line correspond to PLs for the DAV operating at 4.2 Hz, released at LC (group 3) and released at RC (group 4) for red and blue color respectively.

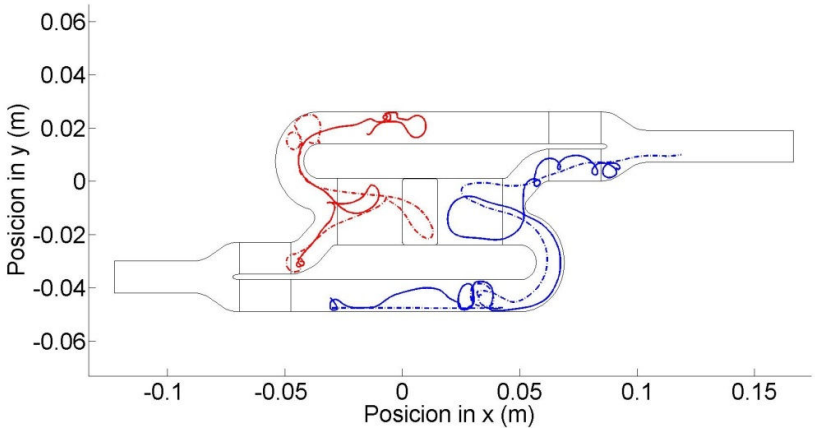

Figure 8: Some PLs paths correspond to examples of: group 1 (2.1 Hz) released at LC (red dashed line), group 2 (2.1 Hz) released at RC (blue dashed line), group 3 (4.2 Hz) released at LC (red solid line) and group 4 (4.2 Hz) released at RC (blue solid line). The *y* dimension has been shifted to better comprehension.

The calculated shear stress as indicated in equation 6 varies over time along of a PL path. Figure 9 shows the variation of the shear stress as a function of time, for the same trajectories presented in figure 8. It may be observed that the highest stress reaches 4.1 Pa for the

trajectory of group 4. When evaluated the *PASn* by equation 7 in these trajectories, the functions that are depicted in figure 10 are obtained.

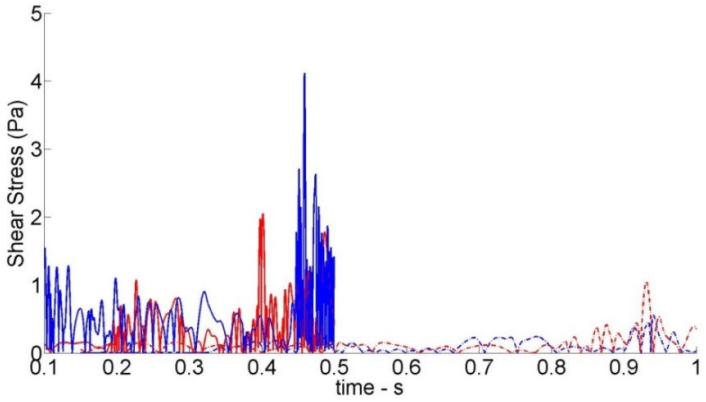

Figure 9: Shears stress for the PL paths corresponding to examples of figure 8.

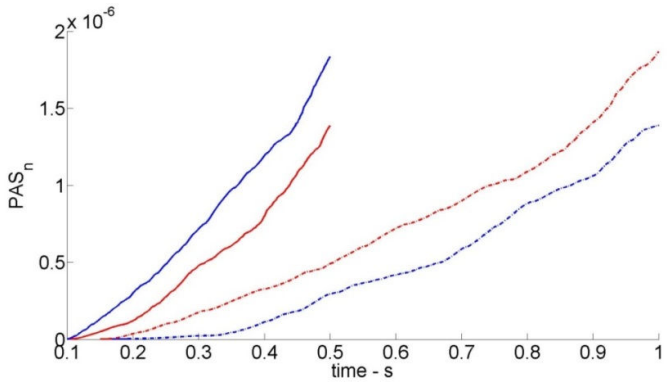

Figure 10: PAS_n for each path of the figure 8. Group 1: red dashed line, group 2: blue dashed line, group 3:red solid line and group 4: blue solid line.

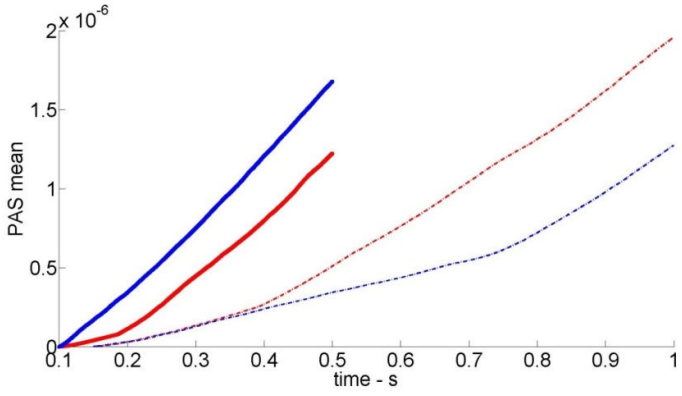

Figure 11: *PASmean* for the four groups. Group 1 (2.1 Hz) released at LC (red dashed line), group 2 (2.1 Hz) released at RC (blue dashed line), group 3 (4.2 Hz) released at LC (red solid line) and group 4 (4.2 Hz) released at RC (blue solid line).

Figure 11 shows the all *PASmeans* obtained. Groups 1 and 2 have practically the same slope of growth at the end of curves, which is 2.85×10^{-6} 1/s, while group 3 has a slope of 3.65×10^{-6} 1/s and group 4, 3.35×10^{-6} 1/s. These high slopes for group 3 and 4, imply a greater possibility of blood damage.

4 DISCUSSION

Fig. 3 shows that the VAD output flow rate is proportional to the frequency and is smaller than theoretical flow rate prediction. This occurs as a consequence of differential flow rate induced for the valve closing and reopening and losses for the piston-chamber wall clearance. Some unexpected results are obtained in the simulation of blood flow, those are the maximum velocities that appear inside the flow when driven frequencies are high (see fig. 4 c and d). This fact may be explained because the *Re* number has values of 900, 1900, 2800 to 3700 at the input and output conduits, for the four simulated frequencies. Thus, the laminar model in these cases of high frequencies may be inappropriate due to possible local turbulence, this may be resolved with more refined discretization and best computational resources.

As the piston movement *f* increases, higher velocities are developed within the flow, which leads to an increase in the shear stress on blood involving an increasing risk of blood damage. This fact can be verified by comparing the shear stresses for the simulation corresponding to $f = 2.10$ Hz (groups 1 and 2) versus the simulation corresponding to $f = 4.20$ Hz (groups 3 and 4), for practically the same number of cycles. Figure 9 shows the shear stresses are higher for groups 3 and 4, and it happens with faster variations in time (more abrupt peaks), in certain way, this is explained by the tortuous trajectories followed by particles (see figure 8).

In Figure 2, it can be seen that the output flow rate as the frequency rises, has instantaneous higher peaks (positives and negatives) due to the valve closing and reopening, that derive in pumping efficiency loss and increasing possibility of blood damage. On the other hand, figure 5 shows that pressure peaks increase more than twice; the positive peak generated by the Vo closure, goes from 2.5×10^{4} Pa for $f = 2.10$ Hz to 6.0×10^{4} Pa for $f = 4.20$ Hz, while the negative peak generated by the Vi opening goes from -1.0×10^{4} Pa for $f = 2.10$ Hz to -3.0×10^{4} Pa for $f = 4.20$ Hz. This high reduction of suction pressure may promote blood damage by flow cavitation, as is discussed in a previous work [1, 2, 6].

When the *PASmean* results, from 2.85×10^{-6} 1/s to 3.35×10^{-6} 1/s for group 4, are compared, all of these values are lower than the results obtained by Morbiducci et al. [10] (6.0×10^{-6} 1/s) by a simulation of 350 ms period of time for a mechanical cardiac valve (MHV). Therefore, even in the case of elevated frequency, VAD could cause less blood damage than an MHV.

It is important to note that predictions in this work, must be compared with predictions of future research. The need of a 3D realistic geometry arises, so as to make the model better for active valves and the piston driven without contact. A higher computational cost must be assumed.

5 CONCLUSION

A ventricular assist device consisting in a driven piston without contact and four active valves, pumping at four different frequencies: 1.05, 2.10, 3.15 and 4.20 Hz, considering a

simplified plane 2D geometry and laminar flow conditions,was simulated. Global variables as output flow rate, force and power applied to the flow have practically linear dependence behavior with the driven frequency parameter.

The results obtained show that, the emerging blood damage due to flow conditions, as velocities, pressures and acting shear stress, are far from the risk values. In this sense, the mean platelet activation state prediction, could be of the same order of magnitude, and smaller than which evaluated over mechanical heart valves and other pulsatile devices.

It is important to emphasize that predictions must be corroborated by future researches, considering a 3D realistic geometry, and a flow model adapted to conditions of transition or turbulent flow, for high frequency pumping. However, the predictions communicated in this paper may be taken as preliminary to conduct new computational simulation or experimental analysis.

REFERENCES

[1] Ho K.K.L., Pinsky J.L., Kannel W.B., Levy D. The Epidemiology of Heart Failure: The Framingham Study. JACC Vol. 22. Nº 4 (Supplement A), October 1993:6A-13A.

[2] McCarthy P.M. *Mechanical Assist Devices*. Volume 16, Issue 3, May 2001 Page 177.

[3] Di Paolo, J., Insfrán, J., Fríes, E.R., Berli, M.B., Campana, D.M. and Ubal, S. A preliminary simulation for the development of an implantable pulsatile blood pump, *Advances in biomechanics and applications*, 1, 127-14, (2014).

[4] Fríes, E.R., Berli, M.B., Campana, D.M., Ubal, S., and Di Paolo, J., Computer simulation of the blood flow in a planar configuration for a pulsatile ventricular assist device. *IFMBE Proceedings* (2015) 49: 892-895.

[5] Fríes E.R., Berli, M.B., Campana, D.M., Ubal S. and Di Paolo, J. Computer simulation of platelet activation in a pulsatile ventricular assist device, through finite elements and a simplified geometry, *Latin American Applied Research (LAAR)*, in press.

[6] Alemu, Y. and Bluestein, D. Flow-induced Platelet Activation and Damage Accumulation in a Mechanical Heart Valve: Numerical Studies, *Artificial Organs* (2007) 31(9):677–688.

[7] Nobili, M., Sheriff, J., Morbiducci, U.et al., Platelet Activation Due to Hemodynamic Shear Stresses: Damage Accumulation Model and Comparison to In Vitro Measurements". *ASAIO Journal*, 54(1):64–72, (2008).

[8] Fraser, K., Taskin, M., Griffith, B. et al. The use of computational fluid dynamics in the development of ventricular assist devices. *Medical Engineering & Physics*, (2010) 33:263–280.

[9] Donea, J., Huerta, A., Ponthot, J., y Ferran, R. *Encyclopedia of Computational Mechanics, Chapter 14: Arbitrary Lagrangian–Eulerian Methods*. Edited by Erwin Stein, Ren´e de Borst and Thomas J.R. Hughes. Volume 1: Fundamentals. (2004) John Wiley & Sons, Ltd. ISBN: 0-470-84699.

[10] Morbiducci, U., Ponzini, R., Nobili M. et al., Blood damage safety of prosthetic heart valves. Shear-induced platelet activation and local flow dynamics: A fluid–structure interaction approach. *Journal of Biomechanics*, 42:1952–1960, (2009).

[11] De Tullio, D., Cristallo, A., Balaras, E., et al. Direct numerical simulation of the pulsatile flow through an aortic bileaflet mechanical heart valve. *J. Fluid Mech* (2009) 622:259–290.

[12] Sheriff, J., Silva Soares, J. S., Xenos, M., Jesty J. and Bluestein, D. Evaluation of Shear-Induced Platelet Activation Models Under Constant and Dynamic Shear Stress Loading Conditions Relevant to Devices. *Ann Biomed Eng* (2013) **41**(6):1279–1296.

XIV International Conference on Computational Plasticity. Fundamentals and Applications
COMPLAS 2017
E. Oñate, D.R.J. Owen, D. Peric and M. Chiumenti (Eds)

ANALYSIS OF PRE-TENSIONED STRUCTURES BY MEANS OF A CONSTITUTIVE SERIAL-PARALLEL RULE OF MIXTURES

L. G. BARBU[*], C. ESCUDERO[†], A. CORNEJO[†], X. MARTINEZ[†], S. OLLER[†] AND A. H. BARBAT[†]

[*, †]International Center for Numerical Methods in Engineering (CIMNE)
Universidad Politécnica de Cataluña
Campus Norte UPC, 08034 Barcelona, Spain
e-mail: lgratiela@cimne.upc.edu

Key words: Pre-stressed concrete, Rule of mixtures, Composites, FEM.

Abstract. The main purpose of this paper is to develop a reliable method based on a three-dimensional (3D) finite-element (FE) model to simulate the constitutive behaviour of reinforced concrete structures strengthened with post-tensioned tendons. A 3D FE model was used, where the nonlinear material behaviour and geometrical analysis based on incremental–iterative load methods were adopted. The pre-tensioned concrete is modelled as a composite material whose behaviour is described with the serial-parallel rule of mixtures (S/P RoM) [1-3]. The effective pre-tensioning stress was applied as an initial strain imposition in the steel material used to model the tendons. The methodology is valid for both straight and curvilinear steel tendons. Examples of both cases will be shown. Validation by comparison with the analytic solution is done for the case of a concrete beam with a straight pre-tensioned steel tendon embedded. Other examples are also included.

1 INTRODUCTION AND STATE OF THE ART

Pre-stressing a structure consists in introducing a system of forces previously to the action of the external loads, with the objective of achieving an equilibrium state without tensions or cracking. In order to carry out a pre-stressing system it is mandatory to use some high performance materials in terms of the concrete and the steel used in the pre-stressing tendons. One of the main advantages of the pre-stressing system is the reduction of the material needed in order to build a certain structure due to the increase of the efficiency of the concrete, whose behaviour is better in compression. The already mentioned pre-compression of the concrete induced by the steel tendons can reduce or even remove the cracks at short and long term, enhancing the durability and impermeability of the material.

One of the most commonly used methods to simulate the pre-stressed system (for straight and parabolic shaped tendons) consists in adding concentrated loads at the anchoring zones and an ascending distributed load that represents the effect of the curvature of the tendon along its path [4]. The mentioned method is simple and straightforward but is limited to simple geometries in which the equivalent uniform effect of the pre-stressing can be computed analytically. A more sophisticated method consists in simulating the continuum by means of

finite elements (tetrahedral and hexahedral in general) and artificially add biarticulated elements connecting pairs of nodes that create the effect of the post tensioned tendons [5]. The previous method achieves satisfactory results but, implicitly, the mesh is conditioned by the path of the tendons whose trajectory has to connect nodes of the finite element mesh. This conditioning can be challenging when meshing. In addition, the sliding between the steel tendon and the concrete cannot be added as occurs in real cases.

The formulation shown in this article requires only a finite element mesh of any type and any spatial discretization. In this case the steel tendons are taken into account in a constitutive way, which means that the active steel is a component of the composite material of each finite element of the mesh that coincides with (is intersected by) the path of the tendon. This implies that the stress and strain state at each integration point is computed from the participation of each component inside the influence zone of that integration point. This global participation results of imposing the equilibrium and/or compatibility between the simple materials at each point, by means of a formulation called Serial-Parallel Rule of Mixtures. Applying the mentioned theory one can assume that each material behaves following its own constitutive law (elasticity, damage, plasticity, viscoelasticity, etc.). The same formulation takes into account all the materials in order to obtain the behaviour of the composite. Finally, the pre-stressing is introduced as an initial imposed strain in the active steel which is going to be partially compensated by the concrete. Next, the displacement field is updated until a global convergence of forces is achieved.

2 CONSTITUTIVE MODELLING OF PRE-STRESSED REINFORCED CONCRETE WITH THE SERIAL-PARALLEL RULE OF MIXTURES

The serial/parallel mixing theory (S/P RoM) is based on the definition of two different compatibility equations between the strain and stress states of the composite constituent materials: it defines an iso-strain condition on the parallel direction, usually the fiber direction, and it defines an iso-stress condition on the serial direction, usually the remaining directions. Using these compatibility equations in a composite made of matrix and fiber, if the matrix structural capacity is lost due to excessive shear stresses, the iso-stress condition also reduces the shear capacity of fiber, and consequently the composite serial strength is also reduced.

For this reason, it is necessary to define, and split, the serial and parallel parts of the strain and stress tensors. This is done with two complementary fourth order projector tensors, one corresponding to the serial direction (P_S) and the other to the parallel direction (P_P). These tensors are defined from the fibre axial direction in the composite. Thus,

$$\varepsilon = \varepsilon_P + \varepsilon_S \quad \text{with} \quad \varepsilon_P = P_P : \varepsilon \quad \text{and} \quad \varepsilon_S = P_S : \varepsilon \tag{1}$$

where,

$$P_S = I - P_P ; \; P_P = N_P \otimes N_P \text{ and } N_P = e_1 \otimes e_1 \tag{2}$$

Being e_1 , the director vector that determines the parallel behaviour (fibre direction), and I the identity. The stress state may be split analogously, finding its parallel and serial parts using also the 4th order tensors P_P and P_S :

$$\sigma = \sigma_P + \sigma_S \text{ with } \sigma_P = P_P : \sigma \text{ and } \sigma_S = P_S : \sigma \tag{3}$$

3.1 Hypothesis for the numerical modelling

The numerical model developed to take into account this strain-stress state is based on the following hypothesis:

1. The composite is composed by only two components: fibre and matrix
2. Component materials have the same strain in parallel (fibre) direction.
3. Component materials have the same stress in serial direction.
4. Composite material response is in direct relation with the volume fractions of compounding materials.
5. Homogeneous distribution of phases is considered in the composite.
6. Perfect bounding between components is also considered.

3.2 Constitutive equations of component materials

Each composite component material is computed with its own constitutive equation. However, as in this paper the materials will be modelled with a damage formulation, the description of the formulation is done considering the particular case of isotropic damage. So, the stresses in matrix and fibre materials are obtained using:

$$\begin{aligned} {}^{m}\sigma &= (1-{}^{m}d)\cdot {}^{m}C : {}^{m}\varepsilon \\ {}^{f}\sigma &= (1-{}^{f}d)\cdot {}^{f}C : {}^{f}\varepsilon \end{aligned} \tag{4}$$

being ${}^{m}C$ and ${}^{f}C$ the matrix and fibre stiffness tensors, respectively. These equations can be rewritten taking into account the serial and parallel split of strain and stress tensors (equations (1) and (3)), obtaining:

$$\begin{bmatrix} {}^{i}\sigma_P \\ {}^{i}\sigma_S \end{bmatrix} = (1-{}^{i}d)\cdot \begin{bmatrix} {}^{i}C_{PP} & {}^{i}C_{PS} \\ {}^{i}C_{SP} & {}^{i}C_{SS} \end{bmatrix} : \begin{bmatrix} {}^{i}\varepsilon_P \\ {}^{i}\varepsilon_S \end{bmatrix} \tag{5}$$

where

$$\begin{aligned} {}^{i}C_{PP} &= P_P : {}^{i}C : P_P & {}^{i}C_{PS} &= P_P : {}^{i}C : P_S \\ {}^{i}C_{SP} &= P_S : {}^{i}C : P_P & {}^{i}C_{SS} &= P_S : {}^{i}C : P_S \end{aligned} \quad \text{with } i = m, f \tag{6}$$

3.3 Equilibrium and compatibility equations

The equations that define the stress equilibrium and establish the stain compatibility between components arise from the analysis of the hypotheses previously exposed,

Parallel behaviour:
$$\begin{aligned} {}^{c}\varepsilon_P &= {}^{f}\varepsilon_P = {}^{m}\varepsilon_P \\ {}^{c}\sigma_P &= {}^{f}k \cdot {}^{f}\sigma_P + {}^{m}k \cdot {}^{m}\sigma_P \end{aligned} \tag{7}$$

Serial behaviour:
$$\begin{aligned} {}^{c}\varepsilon_S &= {}^{f}k \cdot {}^{f}\varepsilon_S + {}^{m}k \cdot {}^{m}\varepsilon_S \\ {}^{c}\sigma_S &= {}^{f}\sigma_S = {}^{m}\sigma_S \end{aligned} \tag{8}$$

where superscripts c , m and f stand for composite, matrix and fibre, respectively and ${}^{i}k$ corresponds to the volume fraction coefficient of each constituent in the composite.

3.4 Serial/parallel rule of mixtures algorithm

The known variable that enters the algorithm is the strain state ${}^{c}\varepsilon$ of the composite material at time $t+\Delta t$. From this variable, the serial/parallel rule of mixtures algorithm has to find the strain and stress state of each component that fulfils the equilibrium, the compatibility and the constitutive equations and the evolution of the internal variables. The first thing done by the algorithm is to split the strain tensor into its parallel and its serial parts, in order to compute the strain state in the matrix and the fiber. The parallel strain component is, according to equation (7), the same for both materials and for the composite. On the other hand, the serial strain component requires a prediction of the strains expected in one of the composite components. If this prediction is done for the matrix, the increment of its serial strains can be computed as

$$\left[{}^{m}\Delta\varepsilon_S\right]^{0} = A : \left[{}^{f}C_{SS} : {}^{c}\Delta\varepsilon_S + {}^{f}k \cdot \left({}^{f}C_{SP} - {}^{m}C_{SP}\right) {}^{c}\Delta\varepsilon_P\right] \tag{9}$$

with $A = \left[{}^{m}k \cdot {}^{f}C_{SS} + {}^{f}k \cdot {}^{m}C_{SS}\right]^{-1}$ and ${}^{m}\Delta\varepsilon_S = {}^{t+\Delta t}\left[{}^{c}\varepsilon_S\right] - {}^{t}\left[{}^{c}\varepsilon_S\right]$.

The initial prediction of matrix serial strains, proposed by Rastellini [1] and described in equation (9), is obtained considering that the distribution of the total strain, in its parallel and serial parts, is done in function of the composite tangent stiffness obtained in previous time step. With the prediction of the matrix serial strains, the fibre serial strains can be computed, in the iteration step *n*, according to equation (8),

$${}^{t+\Delta t}\left[{}^{f}\Delta\varepsilon_S\right]^{n} = \frac{1}{{}^{f}k}\,{}^{t+\Delta t}\left[{}^{c}\varepsilon_S\right] - \frac{{}^{m}k}{{}^{f}k}\,{}^{t+\Delta t}\left[{}^{m}\varepsilon_S\right]^{n} \tag{10}$$

where ${}^{t+\Delta t}\left[{}^{m}\varepsilon_S\right]^{n} = {}^{t}\left[{}^{m}\varepsilon_S\right] + \left[{}^{m}\Delta\varepsilon_S\right]^{n}$.

Regrouping again the serial and parallel components of the strain tensor (equation (3)), the constitutive equations can be applied to the predicted strains to obtain the stress tensor for both materials and the update of their internal variables. Fibre and matrix are modelled, each one, with their own constitutive law. If both materials are described with an additive plasticity formulation, the stress vector for each one is obtained using equation (4). The stresses obtained must fulfil the following equation:

$$[\Delta\sigma_S]^n = {}^{t+\Delta t}[{}^m\sigma_S]^n - {}^{t+\Delta t}[{}^f\sigma_S]^n \leq toler \tag{11}$$

If the residual stress is smaller than the tolerance, the computed strains and stresses are considered to be correct and the structural calculation can continue. However, if equation (11) is not fulfilled, the initial prediction of the matrix strain tensor has to be corrected. This correction is performed using a Newton-Raphson scheme, in which the update is made using the Jacobian of the residual forces. It is obtained deriving the residue function with respect to the unknown. According to Rastellini [1], the expression for the Jacobian is given as follows:

$$J = [{}^mC^t_{SS}]^n + \frac{{}^mk}{{}^fk} \cdot [{}^fC^t_{SS}]^n \tag{12}$$

and, the correction of the matrix serial strains becomes

$${}^{t+\Delta t}[{}^m\varepsilon_S]^{n+1} = {}^{t+\Delta t}[{}^m\varepsilon_S]^n - J^{-1} : [\Delta\sigma_S]^n \tag{13}$$

To obtain quadratic convergence in the S/P mixing theory, the Jacobian must be obtained using the tangent constitutive tensors for the fibres and the matrix. Depending on the constitutive equation defined for each material, the constitutive tensor cannot be obtained analytically. Thus, in order to obtain a reliable algorithm, the expression of the tangent tensor is obtained numerically with the procedure shown in Martinez et al. [1][3].

3.5 Peculiarities of the imposed strain loading

The theoretical frame developed in the previous sections suffices to represent the behaviour of reinforced concrete as a composite material composed by concrete and passive steel. In order to take into account the case of the active steel, both for the pre and the post-tensioned case, it is necessary to rewrite the compatibility condition of the S/P RoM.

Specifically, it is necessary to break the perfect adherence between the two components: active steel and concrete.

6. Relative movement between the components is allowed if and only if an imposed strain condition exists over one of them.

Therefore, loss of adherence is allowed only in the presence of the imposed strain loading, a peculiar load due to the fact that it is applied only on a component of the composite material. This implies that its contribution is not quantified in the external forces vector and it is an auto balanced load.

Equations (7) must therefore be rewritten taking into account the imposition of an initial strain for the fiber in order to represent the pre-stressing or post-tensioning of the active steel. In the first iteration of the increment when the pre-stressing strain is to be applied, the fiber strain in the parallel direction is fixed to the desired pre-stress value. Based on the serial fiber strains (obtained with eq. (10)) and the parallel ones (eq. (14)) the fiber strain tensor is computed and, depending on the desired fiber constitutive model, the stress tensor is obtained.

The resolution algorithm of the S/P RoM equilibrates the serial components at each integration point and with the integrated stresses the internal forces vector is assembled. At this point in the problem resolution, the parallel component of the fiber stresses has yet to be balanced. Its effect is quantified in the system of equations in the residual forces computed at the end of the first global iteration of the problem.

$$\begin{aligned} incr = 1; iter = 1; \quad & {}^{m}\varepsilon_P = {}^{c}\varepsilon_P \\ & {}^{f}\varepsilon_P = \varepsilon_{imp} \\ incr \geq 1; iter > 1; \quad & {}^{m}\varepsilon_P = {}^{c}\varepsilon_P \\ & {}^{f}\varepsilon_P = {}^{c}\varepsilon_P + \varepsilon_{imp} \end{aligned} \tag{14}$$

These residual forces are then used to correct the nodal displacements and consequently the strains at the integration points. In the second global iteration of the problem, the parallel component of the strains at layer level that is the input of the S/P RoM is equal to the matrix strain needed to accommodate the imposed fiber strain.

Therefore, in the first global iteration the active steel has its parallel strain component fixed at the level of strain associated to the desired pre-stressing force, while in the second iteration the fiber strain is balanced by the resulting compression in the concrete.

3 VALIDATION OF THE FORMULATION

In this section some examples of application of the formulation shown in this article are presented. The two fist examples are compared with the expected analytical solution since their geometry is sufficiently simple to be solved. In the third example, a more complex problem has been analysed, so in this case the solution cannot be compared with any analytical expression.

3.1 Pre-stressed beam with a straight tendon

In this example, the behaviour of a 7 m length and 1 m quadrangular beam is analysed. Aligned with the center of gravity of the beam there is a linear steel tendon whose area, A_s, is equal to 0.04 m^2 which means that the participation with respect to the concrete is 4%. The geometry of the specimen can be appreciated in the Fig 1a. The self-weight has been neglected in order to focus on the pre-stressing effect. In addition, one edge of the beam is free and the other one is clamped.

The geometry shown in the Fig. 1a has been meshed with linear hexahedral finite elements obtaining the finite element mesh depicted in the Fig. 1b. The pre-stressed tendon has been stressed up to 1176 Mpa, corresponding to a strain, ε_s, equal to 0.0056. The Young's modulus of the steel has been considered to be 210000 MPa whereas the concrete modulus is equal to 35000 Mpa.

The axial force in the steel tendon can be computed using the equation (15). On the other hand, the elastic shortening of the concrete can be obtained by means of the equation (16). Finally, the longitudinal displacement of the whole beam due to the pre-stressing load can be calculated using the equation (17). The finite elements intersected by the tendon can be seen in

the Fig. 1c. Those elements, which have a certain participation of active steel, will have an imposed strain loading condition, simulating the effect of the pre-stressing.

$$N_t = A_s\,\sigma_t = 4.704 \cdot 10^7\ N \tag{15}$$

$$\Delta\varepsilon = -\frac{N_t}{E_c A_c + E_s A_s} = -1{,}12 \cdot 10^{-3} \tag{16}$$

$$\delta_{long} = \Delta\varepsilon \cdot L = -7{,}840 \cdot 10^{-3}\ m \tag{17}$$

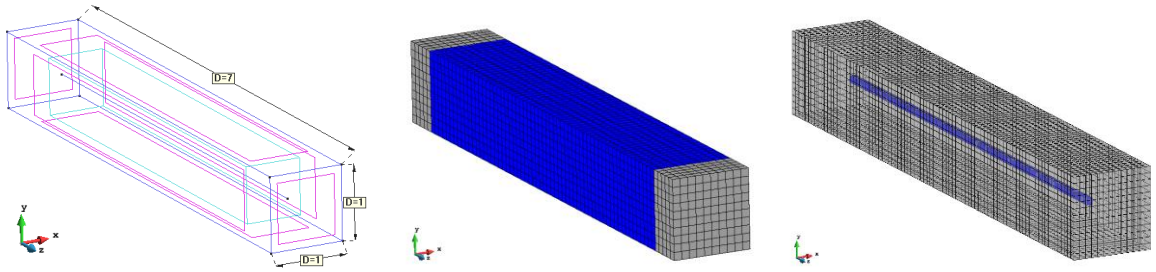

Figure 1. a) Geometry of the beam; b) Finite element mesh (7000 elements); c) Elements intersected by the steel tendon

Carrying out the calculation with the finite element code PLCd [6-9], one can obtain the displacement field shown in the Fig. 2. As can be seen in the previous figure, the maximum shortening of the beam has a value of $7.83 \cdot 10^{-3}$ m whereas the analytical solution is $7.84 \cdot 10^{-3}$ m. This result shows the high precision of the formulation.

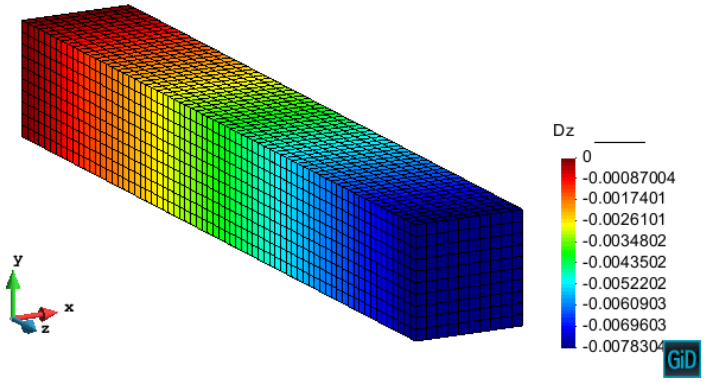

Figure 2. Displacement field as resulting from the pre-stressing

3.2 Pre-stressed beam with a curvilinear tendon

In this case, a 10 m length and 1 m height beam has been simulated. In order to increase the complexity of the pre-stressing system, the steel tendon has a parabolic shaped curve, as is commonly used in pre-stressed beams. The geometry is shown in the Fig 3 and the local axes of the active steel can be seen in the Fig. 4a. Each colour in the Fig. 4b represents a different composite material in terms of steel participation as well as its direction since the slope of the

tendon is not constant. The steel tendon has been pre-stressed with a force, P, equal to 5000 kN and has an area of 0.005 m^2. One can easily notice that the stress in the tendon is 1000 Mpa. The concrete used in the simulation has a Young's modulus, E_c, equal to 35875 Mpa.

The finite element mesh depicted in the Fig. 4a consists of 1288 linear hexahedra. In the same figure one can see the different composite materials existent inside the beam.

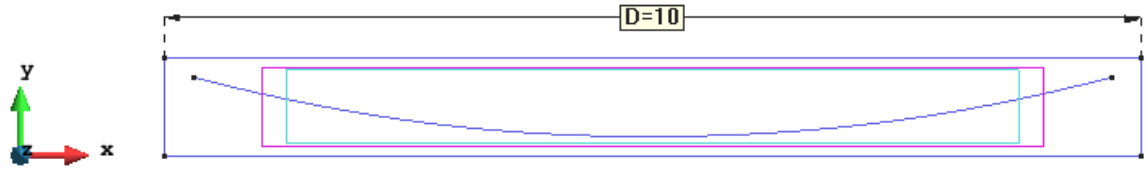

Figure 3. Geometry of the beam and of the steel tendon

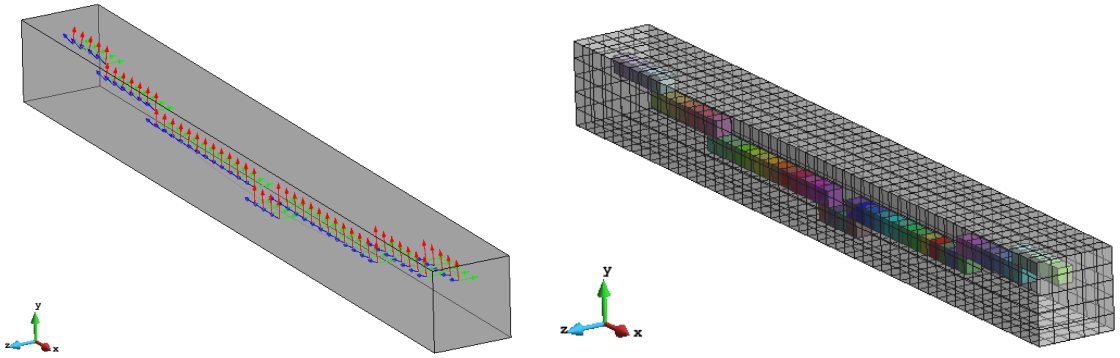

Figure 4. a) Local axes of the tendon on the finite elements; b) Finite element mesh used

In order to compute the analytical vertical displacement, one must simplify the structural system as can be seen in the Figs. 5 and 6. In the Fig. 6 one can appreciate the equivalent load system that simulates the effect of the pre-stressing force. In this case, the steel tendon has been substituted with two concentrated loads in the anchoring zone and, due to the eccentricity in the anchoring zone, two bending moments. The parabolic shape is represented by a uniformly distributed load whose value is obtained with the equation (18).

$$\eta = \frac{8P(e_1 + e_2)}{L^2} = 240\,\frac{kN}{m} \tag{18}$$

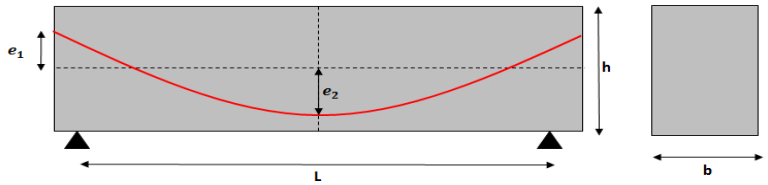

Figure 5. Schematic representation of the beam

By means of tables and the superposition hypothesis, one can obtain the analytical expression of the maximum vertical displacement of the beam (18). It is important to notice that the tables, in general, omit the effect of the shear strain as well as the elastic shortening of the concrete.

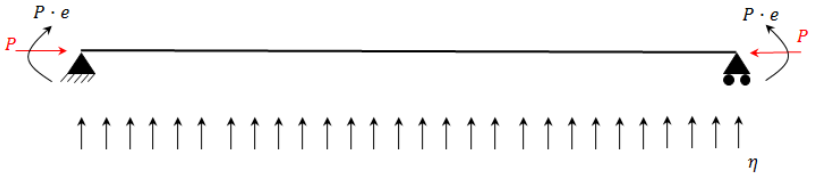

Figure 6. Structural scheme of the beam with one curvilinear tendon

$$\delta = \frac{5\eta L^4}{384 E_h I} - \frac{3P\cos(\phi) e_1 L^2}{24 E_h I} = 4.38 \text{ mm} \tag{19}$$

where E_h corresponds to the Young's modulus of the homogenized section, I is the inertia of the section and ϕ is the slope of the tendon in the anchoring zone.

Using the in-house finite element code PLCd, one can obtain the displacement field depicted in the Fig. 7 with a maximum vertical displacement equal to 4.60 mm. Comparing the expected results with the simulated ones, the difference between them assuming that the analytical is exact, which is not entirely correct, is about a 5%. Additionally, the stress field for each simple material can be seen in the Figs. 8 and 9. As indicated in the previous figures, the pre-stressing system induces a bending state in the structure that causes tension on the superior fibre and compression on the lower fibre which compensates the effect of the self-weight. The stress field of the steel oscillates between the 900-1000 Mpa as has been indicated in the previous paragraphs. The mentioned variation is caused by the elastic shortening of the concrete.

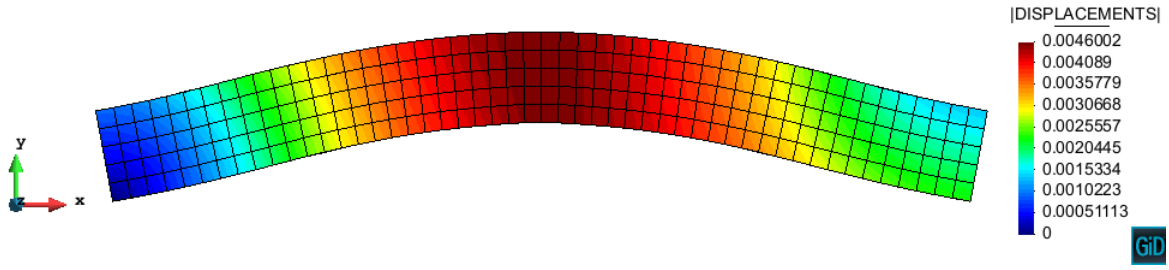

Figure 7. Displacement field obtained with PLCd

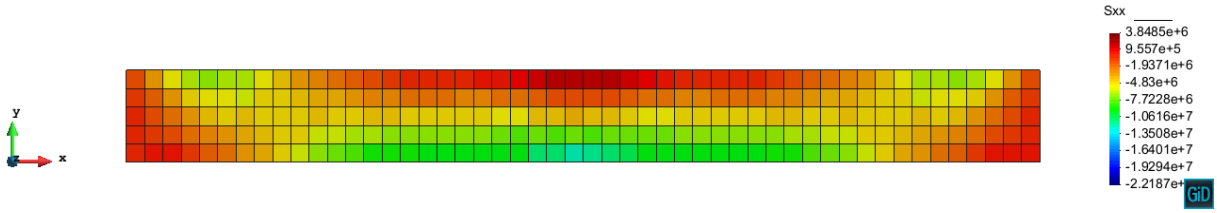

Figure 8. Longitudinal stresses S_{xx} in the concrete

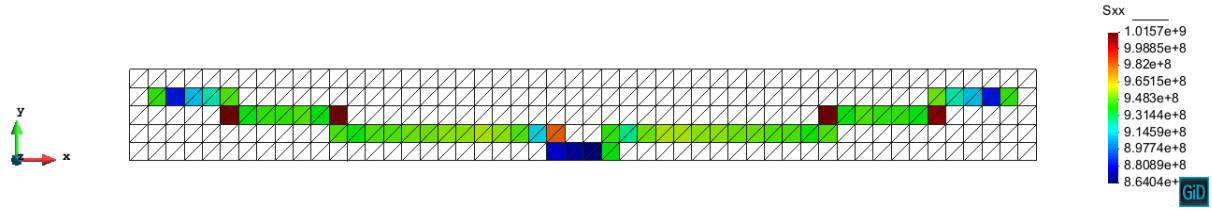

Figure 9. Longitudinal stresses S_{xx} in the active steel

3.3 Concrete ring reinforced with pre-stressed tendons

In order to analyse a more complex geometry, a three-dimensional model of a 10 m height and 1.15 m thickness concrete ring is shown. The structure is stiffened with 3 buttresses (spaced 120º) and reinforced with 3 steel tendons whose anchoring zone coincides with the position of the buttresses. In Fig. 10 the geometry of the analysed structure is depicted, as well as the finite element mesh that consists of 69324 linear hexahedra elements.

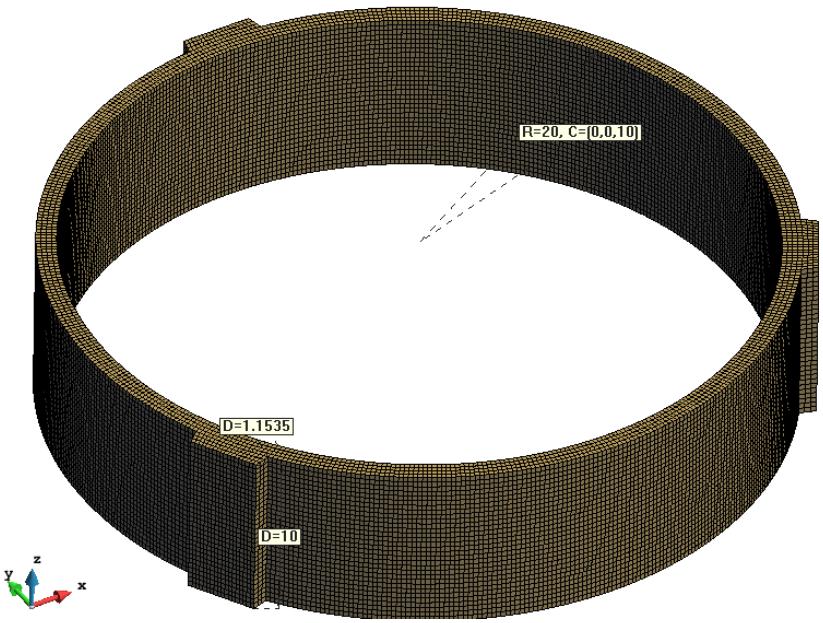

Figure 10. Geometry and finite element mesh of the ring

In Fig. 11a the trajectory of the three steel tendons can be seen. In the same figure one can notice that each tendon covers 240º of the annular section. Those tendons have a diameter of 0.082 m and have been pre-stressed with an imposed strain of 0.0062. The corresponding stress in each tendon is 1302 Mpa.

As explained in previous paragraphs, the finite elements intersected by the linear elements (tendons) have a certain participation of active steel inside the composite material as well as a certain orientation of it. The mentioned orientation (local axes) of the steel can be analysed in the Fig. 11b for each tendon.

The results of the numerical simulation are depicted in the Figs. 12 and 13. As expected, the central part of the ring experiences a deformation inwards. This tendency is smoother near the buttresses where the stiffness is greater, as expected.

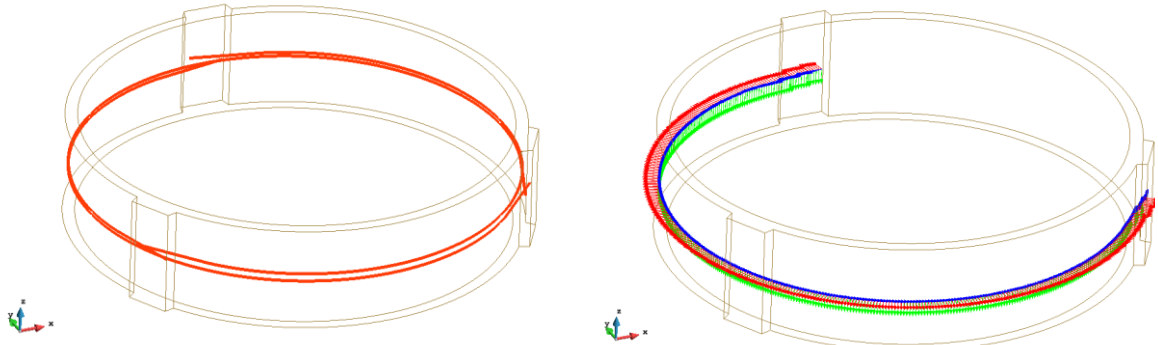

Figure 11. a) Schematic trajectory of the steel tendons; b) Local axes of the finite elements intersected by the tendon

The Figs. 13a and 13b represent a horizontal cut of the ring in the x-y plane showing the stress state in the two composite components, steel and concrete. The mentioned cut coincides with the path of one of the tendons so, in this case, one can appreciate the local effect of that tendon.

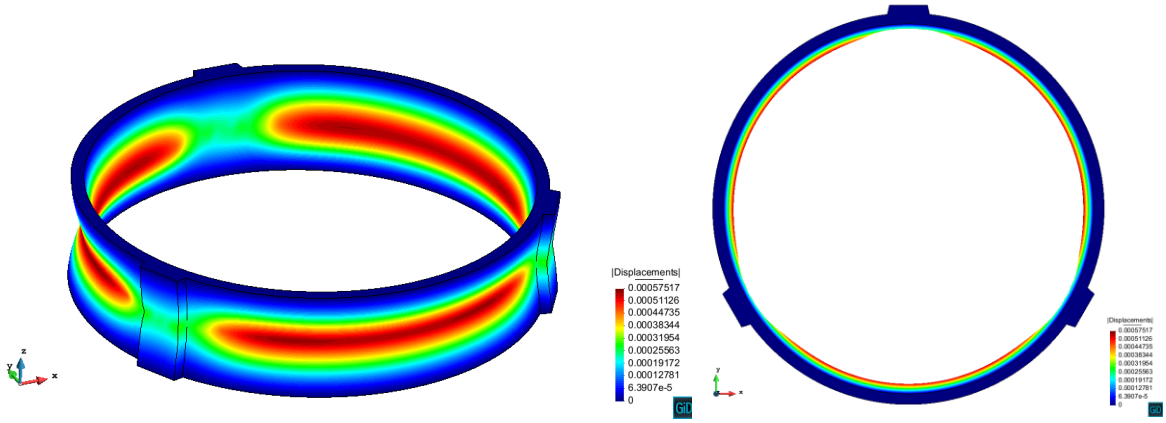

Figure 12. Displacement field in m on the deformed shape of the geometry (100x)

In the Fig. 13a, the concrete is fully compressed except for the anchoring zone where, in general, a large quantity of passive reinforcement is placed to compensate this effect that would lead to the cracking of the concrete.

On the other hand, in Fig. 13b, one can observe that the steel tendon is completely tensioned. It is important to note that the stress along the tendon is not constant, being minimum in the mid-point of it.

4 CONCLUSIONS

As has been shown in the previous paragraphs, the current formulation is capable of simulating the effect of the pre-stressed system in arbitrary geometries and obtains coherent results with a reduced error in comparison with the most used methods to deal with similar problems. That said, one can conclude that the formulation presented in this article represents a powerful tool when dealing with complex geometries or sophisticated constitutive models of composite materials.

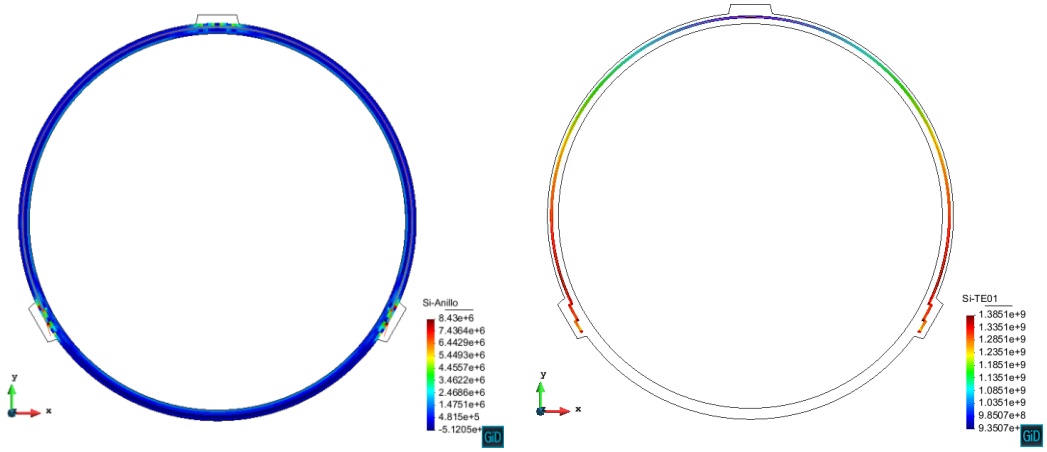

Figure 13. a) Stress field S_1 in the concrete; b) Stress field S_1 in the active steel

REFERENCIAS

[1] Rastellni, F., Oller, S., Salomon, O., Oñate, E.: Composite materials non-linear modelling for long fibre reinforced laminates: Continuum basis, computational aspects and validations. *Computers and Structures* (2008) **86**(9), 879-896.

[2] Martinez, X., Oller, S., Rastellini, F. and Barbat, A. A numerical procedure simulating RC structures reinforced with FRP using the serial/parallel mixing theory, *Computers and Structures*, (2008) **86**(15-16):1604-18.

[3] Martinez, X., Oller, S., Rastellini, F. *Análisis no-lineal de materiales compuestos mediante la teoría de mezclas serie-paralelo*. Omnia Publisher, 2014. Capítulo 10 - p. 237-260. Libro: Aplicaciones avanzadas de los materiales compuestos en la obra civil y la edificación, (http://dx.doi.org/10.3926/oms.209)

[4] Rezaie, F., Famam, S.M. Fracture mechanics analysis of pre-stressed concrete sleepers via investigating crack initiation length. *Engineering Failure Analysis* 58 (2015) 267–280.

[5] Shokoohfar, A., Rahai, A. Nonlinear analysis of pre-stressed concrete containment vessel (PCCV) using the damage plasticity model. *Nuclear Engineering and Design* 298 (2016) 41–50.

[6] PLCd Manual. Non-linear thermo-mechanic finite element code oriented to PhD student education. Code developed at CIMNE; 1991–to present. URL: <http://www.cimne.com/plcd>.

[7] Barbu, L.G., Oller, S., Martinez, X. and Barbat, A. High cycle fatigue simulation: A new stepwise load-advancing strategy, *Engineering Structures* (2015) 97: 118-129, http://dx.doi.org/10.1016/j.engstruct.2015.04.012.

[8] Barbu, L.G., Martinez, X., Oller, S. and Barbat, A.H. Validation on large scale tests of a new hardening-softening law for the Barcelona plastic damage model, *Int. J. Fat*. 2015; 81:213-226.

[9] Martinez, X., Oller, S., Barbu, L., Barbat, A. and De Jesus, A.M.P., 2015. Analysis of ultra-low cycle fatigue problems with the Barcelona plastic damage model and a new isotropic hardening law, *Int. J. Fatigue*, 73, pp 132-142.

XIV International Conference on Computational Plasticity. Fundamentals and Applications
COMPLAS 2017
E. Oñate, D.R.J. Owen, D. Peric and M. Chiumenti (Eds)

COMPUTATIONAL ANALYSIS OF PROJECTILE IMPACT RESISTANCE ON ALUMINIUM (A356) CURVILINEAR SURFACE REINFORCED WITH CARBON NANOTUBES (CNTS) FOR APPLICATIONS IN SYSTEMS OF PROTECTION

SUÁREZ GUERRERO G.*, MARTÍNEZ TEJADA H.V. † AND VALENCIA GARCÍA M. F. +

* Grupo de Investigación en Matemática (GMAT)
Universidad Pontificia Bolivariana
Circular 1era #70-01, 05004 Medellín, Colombia
gustavo.suarez@upb.edu.co, www.upb.edu.co

† Grupo de Investigación sobre Nuevos Materiales (GINUMA)
Universidad Pontificia Bolivariana
Circular 1era #70-01, 05004 Medellín, Colombia
gustavo.suarez@upb.edu.co, www.upb.edu.co

+ Grupo de Materiales Alternativos y Procesos Automáticos (MAPA)
Escuela de Ingeniería
Km2+200 vía Aeropuerto J.M.C., 055428 Envigado, Colombia
marco.valencia@eia.edu.co, www.eia.edu.co

Key words: Computational Tests, A356/CNTs Composite, Ballistic Impact Energy, Johnson-Cook's Model.

Abstract. Computational tests for ballistic impact energy absorption were developed on A356/CNTs composite material with the goal of estimating the improvement of the material's mechanical properties by the contribution of the CNTs [1]. For the implementation of computational tests on the material exposed to projectile impact, A356/CNTs was configured by means of generalized Hooke's model for anisotropic materials [1] and Johnson-Cook's model was used to determine material failure and propagation of energy [2]. A curvilinear surface (semi-spheres on a plaque) with an area of 23x23 cm and thickness of 12 mm was elaborated to represent the composite material. The impact on surface was done with a 9 mm projectile and the surface was developed with 4.5 mm radium semi-spheres. It was used a 0.3% of nanotube insertions on the composite total volume. The results indicated the plaque stopped the impact without drilling. Incidence of damage to wearer, as well as possibility of composite material improvement and the diffusion/dispersion analysis on the curvilinear surface was also done.

1 INTRODUCTION

A curvilinear plaque was elaborated in order to determine the behaviour of the surface when subjected to impact dynamic force. Semi-spheres of 4.5 mms de radium were designed

on the surface since this geometric shape provides greater resistance to the material. The materials' properties values used during ballistic computational tests for A356/CNTs composite with a material type A356 and for CNTs were given a stiffness module of 1.81e12 Pa and a Poisson ratio of 0.45 [3, 4, 5]. During computational tests, finite elements analysis (FEA) was used to study the behavior of A356/CNTs composite.

A mesh was elaborated in order to determine the behavior of the surface when subjected to impact dynamic force. Solid elements were used to develop the mesh. NOM-166-SCFI-2005 was the main guideline for the development of simulations and the determination of ballistics-specific characteristics [13].

2 MATHEMATICAL MODELING

For the implementation of computational tests on the material exposed to projectile impact, A356/CNTs was configured by means of generalized Hooke's model for anisotropic materials [7, 8] and Johnson-Cook's model was used to determine material failure and propagation of energy [7, 8]. In Hooke's model, composite density was calculated from mass proportions [7, 8, 9, 10, 11]:

$$\rho_c = \frac{1}{\frac{m_{AL}}{\rho_{AL}} + \frac{m_{NTC}}{\rho_{NTC}} + \frac{V_V}{\rho_C}} \tag{1}$$

m_{NTC}, m_{AL} are the mass proportions of the constituent and Vc is the proportion in void volume. Johnson-Cook's Constitutive Model describes the relationship between stress, strain, strain rate and visco-elastic material temperature [8, 9, 10, 11].

This model is appropriate in a situation where strain rate varies between $10^2 s^{-1}$ and $10^6 s^{-1}$ and temperature varies according to plastic deformation caused by thermal softening. Stress flux model is represented as in (8) [8, 9]:

$$\sigma = (A + B\varepsilon^n)(1 + C\ln\dot{\varepsilon}^*)(1 - T^{*m}) \tag{2}$$

In (2) T is the system temperature, $\dot{\varepsilon}^*$ is the velocity of equivalent plastic deformation, ε is the equivalent plastic deformation, A is the initial cadence stress (MPa), B is the hardening module, n is the strain hardening exponent, C is the strain-rate dependent coefficient and m is the thermal softening coefficient.

The materials' properties values used during diffusion process and ballistic computational tests for A356/CNTs composite with a material type A356 and for CNTs were given a stiffness module of 1.8×1012 and a Poisson ratio of 0.45 [9,10,11].

The fracture model is combined with the criteria of Cockcroft and Latham where the element is eroded when $D = 1$, is described as [8, 9, 10, 11]:

$$D = \frac{1}{W_{cr}} \int_0^{\varepsilon eq} max(\sigma_1, 0) d_{\varepsilon eq} \tag{3}$$

Where: $\sigma_1$main maximum stress, W_{cr} total plastic work.

3 COMPUTATIONAL MODELING

A curvilinear plaque with an area of 23x23 cm and and thickness of 12 mm was elaborated to represent the composite material, fig.1.

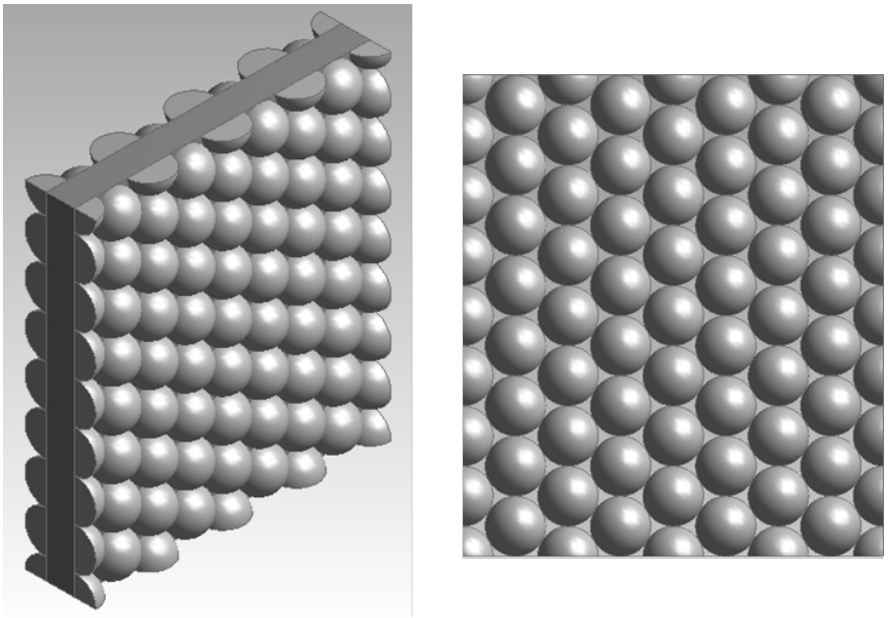

Figure 1. Three-dimensional plate with semi-spheres and core (test panel).

A Parabellum 9mm caliber projectile was selected to perform the tests. Based on international standards for shielding and ballistic testing [13, 14, 15], criteria and reference data for computational tests were determined. Projectile velocity of 436 m/s ± 9.1 m/s, dimensions and geometric characteristics were selected as show the fig. 2.

Figure 2. Parabellum 9mm-caliber projectile.

The system of the plate and the projectile is presented, fig. 3.

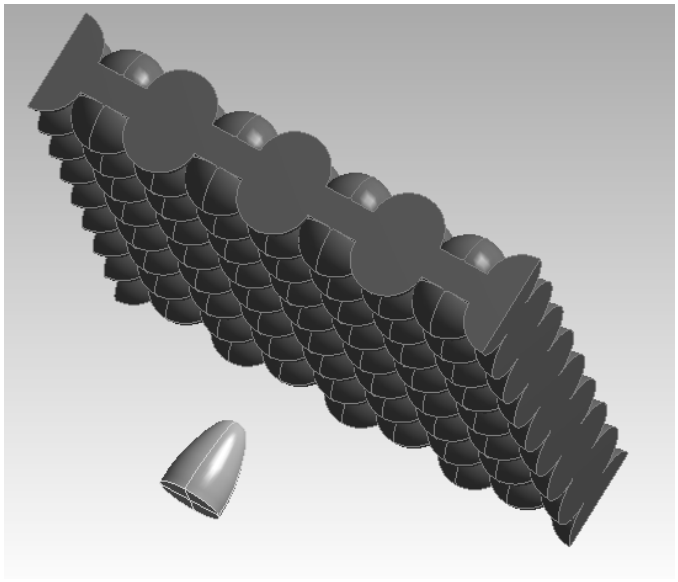

Figure 3. Plate-projectile system for the development of impact tests

4 NUMERICAL MODELING

During computational tests, finite elements analysis (FEA) was used to study the behavior of A356/CNTs composite. A mesh was elaborated in order to determine the behavior of the plaque when subjected to dynamic impact energy. 3D elements of 20 nodes were used to develop the mesh, fig. 4.

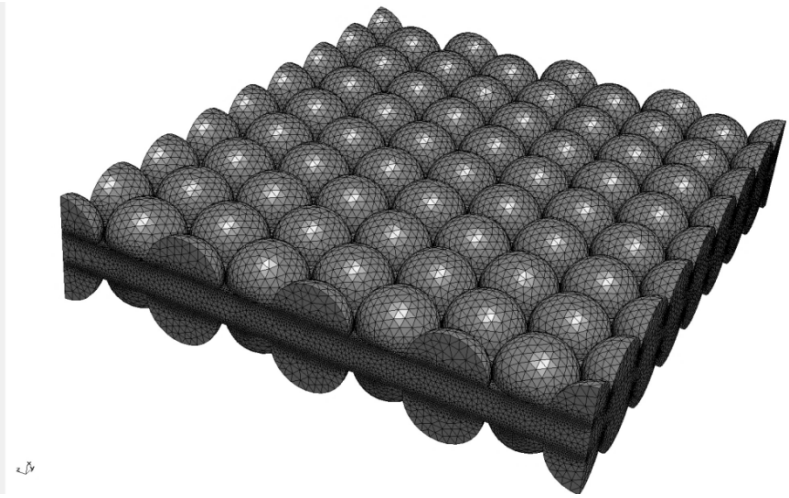

Figure 4. Meshed of the 3D curvilinear plate by means of solid elements.

In the same way, another numerical mesh for the 9 mm-caliber projectile was elaborated. This projectile impacted the curvilinear plaque, fig. 5.

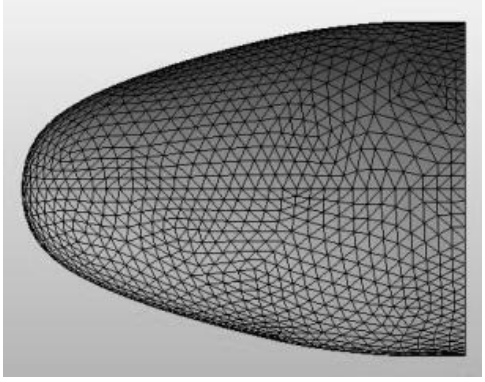

Figure 5. Meshed of the 9 mm-caliber brass projectile.

5 RESULTS

Mechanical tests performed on the impact-subjected A356/CNTs composites indicated that reinforcement material favor the composite's mechanical properties, achieving energy dissipation-absorption and effectively stopping the projectile trajectory.

Results were validated by means experimental tests where the surface was impacted by a Parabellum projectile. Results of the simulations and of the experiments tests were similaires. In general, the results showed the composite exhibited kinetic energy dissipation modes and a capacity to diminish impact damage, fig 6 and fig. 7.

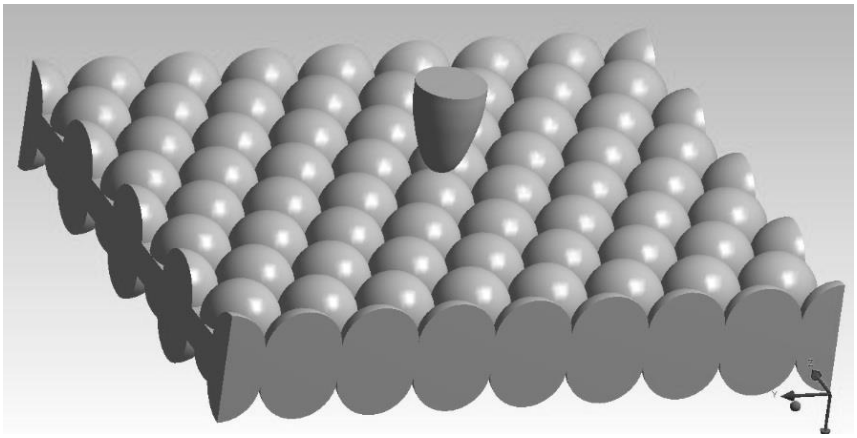

Figura 6. Initial position of projectile and panel A356 before impact.

.

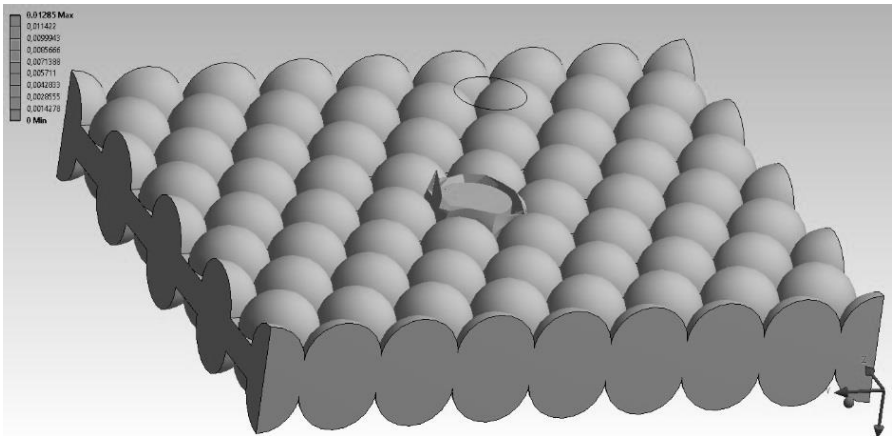

Figure 7. Penetration of the projectile in the impact without perforation.

6 CONCLUSIONS

- Several simulations were executed on an A356/CNTs plaque subjected to dynamic impact load until the perforated surface didn't pass the security limit defined by NOM-166-SCFI-2005 guidelines. Simulations considered a solid projectile in order to grant the design a higher safety factor.
- The most favorable result was achieved using a plaque made of semi-spheres.
- This research offers insight on how perforation of composite materials subjected to ballistic impact is generated. Incidence of damage to wearer, as well as possibility of reinforcement improvement and diffusion/dispersion of CNTS in A356 is also discussed.

REFERENCES

[1] K. Chang, R. A. Scott and G. S. Springer. , "Environmental effects on composite materials", *J. of composite materials*, Vol. 18, Sept. (1984). 464-477.

[2] D Fernández., "Desarrollo de una nueva herramienta basada en redes neuronales para el diseño de protecciones ligeras cerámica-metal frente a impacto de alta velocidad", *Tesis Doctoral*, Ed Carlos III de Madrid, (2007).

[3] Z. Y. Liu, S. J. Xu, B. L. Xiao, P. Xue, W. G. Wang, and Z. Y. Ma, "Effect of ball-milling time on mechanical properties of carbon nanotubes reinforced aluminum matrix composites", Compos. *Part A Appl. Sci. Manuf.*, (2012). vol. 43, no. 12, 2161–2168.

[4] Esawi A M K, Morsi K, Sayed A, Abdel Gawad A and Borah P. Fabrication and properties of dispersed carbon nanotube–aluminum composites *J. Mat. Sc. and Eng.* (2009) A **508** 167.

[5] Javadi A H, Mirdamadi Sh, Faghihisani M A, Shakhesi S and Soltani R. Fabrication of well-dispersed, multiwalled carbon nano- tubes-reinforced aluminum matrix composites *J. New Carbon Materials* (2012). **27(3)** 161.

[6] Cleary P. W. Elastoplastic deformation during projectile–wall collision *J. Applied Mathematical Modelling* (2010). **34(2)** 266–283.

[7] Chang F K, Scott R A and Springer G S. Failure strength of nonlinearly elastic composite laminates containing a pin loaded hole, *J. of Composite Materials*, (1984). 18(5) 464.

[8] Fernandez D. A new tool based on artificial neural networks for the design of lightweight ceramic–metal armour against high-velocity impact of solids *Int. J. of Solids and Structures.* (2008) 45 63-69.

[9] Raguraman M and Deb A. Accurate prediction of proyectile residual velocity for impact on sigle multilayered steel and aluminum plates *9th Int. LS-Dyna User Conf. Centre for Product Design and Manufacturing* Bangalore. (2016). 2-48.

[10] Pignetti J A. METALMEN (http://www.metalmensales.com/aluminum.html) St. Long Island City NY 11106. (2016).

[11] Z Y Liu, Xu S J, Xiao B L, Xue P, Wang W G and Ma Z Y. Effect of ball-milling time on mechanical properties of carbon nanotubes reinforced aluminum matrix composites *Compos. Part A Appl. Sci. Manuf.* (2012). **43(129)** 2161.

[12] Burden R L and Faires D J.*Numerical Analysis. NINTH* (Boston: PWS-Kent Publishing Company). (2011).

[13] Norma Oficial Mexicana NOM-166-SCFI-2005 *Seguridad al usuario-Chalecos antibalas-especificaciones y métodos de prueba* (Mexico: Secretaria de Economía Dirección Nacional de Normas) 23-V-2005.

[14] Duvenbeck A, Hanke S, Weidtmann B and Wucher A. A molecular dynamics investigation of kinetic electron emission from silver surfaces under varying angle of projectile impact *J. Nuclear Instruments and Methods in Physics Research Section B: Beam Interactions with Materials and Atoms* (2011). **269(14)** 1661.

[15] Johnson B C, Bowling T J and Melosh H J. Jetting during vertical impacts of spherical projectiles *J. Icarus*. (2014). **238** 13.

XIV International Conference on Computational Plasticity. Fundamentals and Applications
COMPLAS 2017
E. Oñate, D.R.J. Owen, D. Peric and M. Chiumenti (Eds)

A CONTACT PROBLEM APLICATION FOR THE LOCAL BEHAVIOUR OF SOIL PILE INTERACTION

Borana Kullolli*, Henning Stutz†, Jeffrey Bronsert* Paola Dutto* and Matthias Baeßler*

* Bundesanstalt für Materialforschung und Prüfung (BAM)
Unter den Eichen 87, 12205 Berlin
e-mail: borana.kullolli@bam.de web: www.bam.de

† Marine and Land Geomechanics / Geotechnics
Institute of Geo-science Kiel University
Ludewig-Meyn-Str. 10 24118 Kiel

Key words: numerical modeling, contact problem, soil-structure interaction

Abstract: In geotechnical engineering, the main parameter for the performance of structures such as reinforced walls or deep foundations is often the shaft bearing capacity. In numerical analysis, important advancements have been made on studying the behavior of the soil and the retaining structures separately.

The performance of many geotechnical foundation systems depends on the shear behavior at the soil structure interface. For deep foundations, the main component that affects friction is the horizontal earth pressure. When a pile is getting axially loaded, the soil grain network at the interface, starts to move and rearrange. In conditions of axial cyclic loading a contractive behavior of soil can generally be observed as in [1] and [2]. This can be explained by the progressive densification and relaxation of the soil under cyclic shear at the soil pile interface, as well as the local refinement of the grain distribution by grain breakage and rearrangements. As the soil contracts and decreases in volume, the normal stress around the pile surface decreases and the soil pile friction degrades. This can lead to failure of the whole geotechnical foundation system.

The purpose of the work presented in this paper is to analyze locally (at the element level) the contact behavior of a soil-pile contact problem. Therefore, a 2D shear test is modeled using the Finite Element Method. The formulation of a 4 nodded zero-thickness interface element of Beer [3] is chosen with a linear interpolation function. Four constitutive contact models adapted for contact problems have been implemented. The simple Mohr-Coulomb [4] and Clough and Duncan [5] models were chosen initially, due to the ease of implementation and few number of parameters needed. After, more complicated models in the framework of elasto-plasticity such as: Lashkari [6] and Mortara [7] were implemented for the first time into the finite element code of the shear test problem. They include other phenomena such as: relative density of soil, the stress level and sand dilatancy. From the results the relation

between shear displacement and shear stress has been deduced. Finally, a discussion of the advantages and the drawbacks during computation of each model is given at the end.

1 INTRODUCTION

In the last century, the number of geotechnical structures has increased significantly. Structures as: reinforced embankments, anchors and deep foundations (offshore and onshore) are becoming more and more present and sophisticated in the civil engineering domain. One of the main parameters of these elements is the shaft bearing capacity [8]. A significant component of the shaft bearing capacity is the shear resistance.

Important advancements have been made on modelling the behavior of the soil and the retaining structures (pile, wall, anchors) separately. The zone in which the soil is attached to a structure is called the interface or contact zone. Many issues and questions arise when it comes to the contact zone between soil and geotechnical element (ex: deep foundation).

The major used numerical technique for modelling the contact behavior in geotechnical engineering is the zero-thickness interface element (e.g. Beer [9] and Goodman [3]). The contact element itself, according to the current deformation and loading, can govern four different states: stick, slip, de-bonding (gap opening) and re-bonding.

The shear behavior of this contact zone is complex due to the composition of materials with a very high stiffness (structure) and in comparison, a very low stiffness (soil). A lot of different experimental studies have indicated the importance of this narrow zone for the global load displacement behavior of geotechnical structures (e.g. for piles [10] and [11]). The before mentioned importance is modelled since a long time using elastoplastic models as the simple Mohr-Coulomb model [4] or more recent elasto-plastic models e.g. Lashkari [6] and Liu [12]. Beside the classical elasto-plastic, generalized plasticity models Liu [13] or hypoplastic models by Stutz et al [14] and [15] exist.

In this paper, the focus was given to the local behavior at the contact zone. An implementation of four different contact constitutive models, two of them for the first time, into a zero-thickness interface element implementation is shown. Because advanced models are seldom implemented into finite-element codes and used for pile-soil interaction analysis. This issue is overcome into this publication. To demonstrate the implementation, a direct interface shear test is modelled using the finite element method. By the results of this direct interface shear test it is shown that the models can be implemented into zero-thickness interface elements even if they have different formulations than the mechanical model used by Goodman [9].

2 CONSTITUTIVE MODELS FOR CONTACT PROBLEMS

When it comes to soil modelling many different constitutive models have been used the theories of elasto-plasticity, hyper-elasticity, hypo-plasticity, generalized plasticity. The majority of this constitutive frameworks have been used for modelling of the interface behavior. All constitutive models treated in the paper are in the framework of elasto-plasticity. The properties and parameters of each model are given in the following subsections.

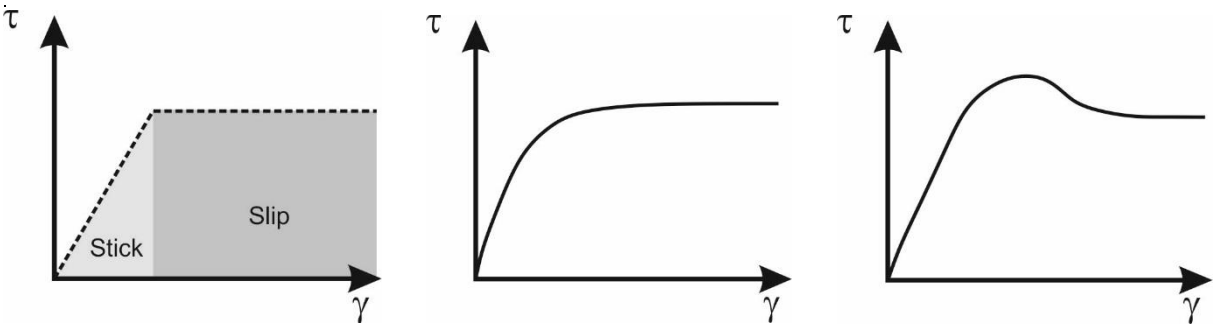

a) **b)** **c)**

Figure 1: Shear stress vs. shear strain relation for a) Mohr-Coulomb, b) Hyperbolic, c) Mortara and Lashkari

2.1 Mohr-Coulomb model

Mohr-Coulomb model was introduced in 1821 by [4] and since then, further improvement or adaptations for different problems have been made. The formulation of the Mohr-Coulomb model for zero-thickness interface models from [16] is used. As it is a linear-elastic perfectly-plastic model (Figure 1a), after the elastic stress limit is exceed no additional shear stresses are possible. The yield function f is defined as:

$$f = |\tau| + \sigma_n \tan\varphi - c \qquad (1)$$

Where τ is the shear stress, σ_n is normal stress, φ is friction angle at interface, and c the cohesion. Vanlangen [4] uses in his model non-associated plasticity. Therefore, the plastic potential g is defined as:

$$g = |\tau| + \sigma_n \tan\psi \qquad (2)$$

Where ψ is the dilatation angle. The incremental constitutive relation is obtained as:

$$\dot{t} = D^{ep}\dot{u^e} \qquad D^{ep} = D^e - \frac{\alpha}{d} D^e \frac{\partial g}{\partial \sigma_n}\frac{\partial f^T}{\sigma_n} D^e \qquad (3)$$

Where $\dot{t}$ denotes the rate of traction vector, $D^{ep}$is the elasto-plastic matrix, α indicates plasticity if (α =1) or elastic conditions (α =0).

4.2 Hyperbolic model

Clough and Duncan [5] use the nonlinear elasticity model (Figure 1b) from the nonlinear soil model of [4]. To model the non-linear hardening behavior of the interface zone in a Goodman [9] type element. The hyperbola is approximated using some shear test data. The empirical derived equation for the interface behavior is:

$$\tau = \frac{u_s}{a_r + b_r \cdot u_s} \qquad (4)$$

Here, τ is the shear stress, a_r, b_r= fitting parameters of hyperbola, u_s = the interface shear displacement.

The model is based on empirical equation converted by linearization to estimate the hyperbolic parameters. Then the straight lines are fitted to the experimental data at the points where the values of shear stress are 70% - 90% of the maximum values.

The shear stiffness depends on normal stress and it is updated at every loop increment.

$$K_s = K_I \gamma_w \left(\frac{\sigma_n}{p_a}\right)^{nHY} \left(1 - \frac{R_f \tau}{\sigma_n \tan \varphi}\right)^2 \quad (5)$$

The shear stress is then calculated as $\tau = K_s * u_s$ and the normal stress σ_n is constant in this model formulation.

4.3 Lashkari model

Here the elasto-plastic model (Figure 1c) according to Lashkari [6] is introduced. The constitutive model relates stress rate vector $[\dot{\sigma}]$ to the velocity vector $[\dot{\Delta}]$ under monotonic shearing. In addition, the model is state dependent and considers the state parameter from Been and Jeffries [17]. By this the parameter calibration is unique for a soil and can be modified to its different states (e.g. loose or dense).

The stress vector $[\sigma]$ and the relative displacement vector $[\Delta]$ are defined as:

$$[\sigma] = \begin{bmatrix} \tau \\ \sigma_n \end{bmatrix} \quad ; \quad [\Delta] = \begin{bmatrix} u \\ v \end{bmatrix} \quad ; \quad [\dot{\Delta}] = [\dot{\Delta}]^e + [\dot{\Delta}]^p \quad (6)$$

Where u, v are the normal and shear displacement respectively. The relative velocity vector is composed out of the elastic and plastic component. For the elastic branch of the velocity vector, the following relation is adapted:

$$[\dot{\sigma}] = \frac{1}{t}[D]^e [\dot{\Delta}]^e \quad (7)$$

Here *t* represents the thickness and $[D]^e$ is the elastic material matrix. An important parameter is the stress ratio $\eta = \frac{\sigma_n}{\tau}$. It is the main component of model for the yielding plasticity. In case the stress ratio is constant, the behavior remains elastic.

The yield function f is defined as:

$$f = \tau - \eta \sigma_n \quad (8)$$

Finally, the elasto-plastic matrix is given as below:

$$[D]^{ep} = [D]^e - \frac{[D]^e \{R\} \{n\}^T [D]^e}{K_p + \{n\}^T [D]^e \{R\}} \quad (9)$$

Here, $\{n\}$ denotes the yield direction vector, $\{R\}$ is the direction of plastic velocity vector and K_p represents the hardening modulus. For additional details of the model it is referred to Lashkari [6].

4.4 Mortara Model

The elasto-plastic model (Figure 1c) proposed by [7] is an interface constitutive model, which is based on mathematical plasticity formulations. The main advantage of this model is

that can be calibrated with CNL tests, and simulate both Constant Normal Load (CNL) and Constant Normal Stiffness (CNS) boundary conditions in good agreement. In the elasto-plastic theory the stress and strain relation would be:

$$[\dot{\sigma}] = [D]^{ep}[\dot{\varepsilon}] \tag{10}$$

The expression for $[D]^{ep}$ is given as:

$$[D]^{ep} = [D]^{e} - \frac{[D]^{e} m_M}{H + n^T [D]^{e} m_M} \tag{11}$$

The component terms of $[D]^{ep}$ are:

$$[D]^{e} = \begin{bmatrix} K_s^e & 0 \\ 0 & K_n^e \end{bmatrix} \qquad m_M = \begin{bmatrix} \frac{\partial g}{\partial \tau} \\ \frac{\partial g}{\partial \sigma_n} \end{bmatrix} \qquad n = \begin{bmatrix} \frac{\partial f}{\partial \tau} \\ \frac{\partial f}{\partial \sigma_n} \end{bmatrix} \qquad H = -\frac{\partial f}{\partial u_x^p} \tag{12}$$

Where $[D]^e$ is the elastic matrix, K_s^e and K_n^e are the elastic shear and normal stiffness, m_M is the gradient of plastic potential, n is the gradient of plastic surface and H is the hardening modulus. The plastic function of the model was deriving assuming as hardening parameter the normalized shear relative displacement $[\dot{w}_n] = \frac{[\dot{w}^p]}{[w_p^p]}$.

The $\dot{w}^p$ is the time derivative of the plastic shear relative displacement and w_p^p is the shear relative displacement corresponding to the maximum value of the stress ratio. The plastic yield function is given by the expression below:

$$f = \tau - \alpha_M \sigma_n^{\beta M} = 0 \tag{13}$$

Where α_M is the current value of the hardening rule. More details of the model can be found in [18] and [19].The plastic potential is given as g is given as:

$$g = \tau - \frac{b}{1+a}\sigma_n \left[1 + a\left(\frac{\sigma_n}{\sigma_c}\right) - \frac{1+a}{a}\right] = 0 \tag{14}$$

Where σ_c is the critical stress. The parameters a and b are the slope and the intercept of the flow rule to the stress ratio η.

3 CONTACT ELEMENT DESCRIPTION

Beside the constitutive models that are necessary, the numerical simulation technique for the discontinuity at the contact is also important. Here, we use the zero-thickness interface , beside this the thin-layer element formulation from Desai [20] and the Mortara [7] method can be used. For the shear test modeled numerically in this paper, the zero thickness element of [9] , was used. It has 4 nodes and 8 displacement degrees of freedoms in total. The formulation is derived based on two relative displacements of the continuum element on both sides of the interface. One displacement component is the normal, and the other one is the tangential component to the interface.

Starting from the energy equation and minimizing with respect to nodal point displacements, the element stiffness for the four-nodal point element is indicated in Figure 2.

As the element has zero thickness, the nodes 1,4 and 2,3 have identical coordinates at the beginning of the simulation.

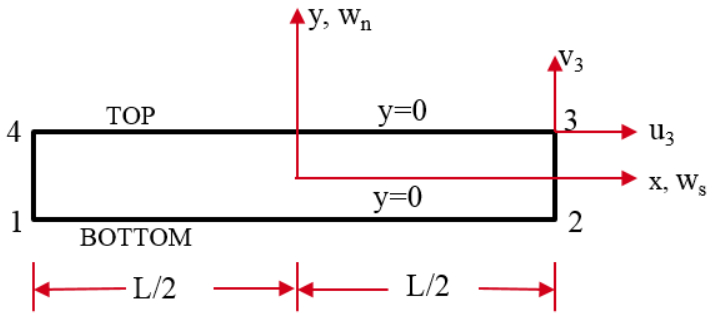

Figure 2: Zero thickness contact element geometry [9]

The vector $[\boldsymbol{u}]$ contains all nodal displacements in the local coordinate system, where u refers to horizontal displacement and v to vertical displacement. Indexes 1,2,3,4 refer to the node number.

$$[\boldsymbol{u}] = [u1\ v1\ u2\ v2\ u3\ v3\ u4\ v4] \tag{15}$$

The vector of relative displacements $\{w\}$ is defined as:

$$\{w\} = \begin{Bmatrix} w_s \\ w_n \end{Bmatrix} = \begin{Bmatrix} u_t - u_b \\ v_t - v_b \end{Bmatrix} \tag{16}$$

Where w_s, w_n are tangential and normal relative displacements. u, v are the displacements along x and y axis and t, b= top/bottom segment of the interface. Displacements u, v can be approximated by using standard linear Gaussian interpolation functions $N1, N2$:

$$N1 = \frac{1}{2} - \frac{x}{l} \qquad N2 = \frac{1}{2} + \frac{x}{l} \tag{17}$$

$$\begin{matrix} u_t \\ v_t \end{matrix} = \begin{bmatrix} -N1 & 0 & -N2 & 0 & 0 & 0 & 0 & 0 \\ 0 & -N1 & 0 & -N2 & 0 & 0 & 0 & 0 \end{bmatrix} [\boldsymbol{u}] \tag{18}$$

$$\begin{matrix} u_b \\ v_b \end{matrix} = \begin{bmatrix} 0 & 0 & 0 & 0 & N1 & 0 & N2 & 0 \\ 0 & 0 & 0 & 0 & 0 & N1 & 0 & N2 \end{bmatrix} [\boldsymbol{u}] \tag{19}$$

The strain displacement matrix $[B]$ is given as:

$$[B] = \begin{bmatrix} -N1 & 0 & -N2 & 0 & N1 & 0 & N2 & 0 \\ 0 & -N1 & 0 & -N2 & 0 & N1 & 0 & N2 \end{bmatrix} \tag{20}$$

The strain energy U can be calculated as:

$$U = \frac{1}{2}[u]^T \int_{-l/2}^{l/2} [B]^T [D^e][I][B]\, dx \tag{21}$$

From the Eq. (21) the stiffness matrix K can be calculated:

$$K = \int_0^l [B]^T [D^e][I][B]\, dx \tag{22}$$

The strain matrix:

$$\varepsilon = [B]\,[u] \tag{23}$$

The assumption of Goodman et al. [9] is to have a continuous displacement field that leads to a continuous stress field through the length l. For an elastic behavior, the stress as obtained:

$$\sigma = [D^e]\,[\varepsilon] \tag{24}$$

In the group of zero thickness family can be found more advanced contact elements which take in consideration more complicated phenomena. Cerfontaine et al [21] proposed a 3D hydro-mechanical coupled element. The element belongs to the zero-thickness formulation and the contact constraint is ensured by the penalty method. Fluid flow is discredited through a three-node scheme, discrediting the inner flow by additional nodes. The element can reproduce stick, slip, bonding, de-bonding degrees of freedom. Stutz et al [22] proposed an extended zero thickness element which reproduces the gap opening for cohesive soils. The interface element consists in a 16-node element with an isoparametric formulation.

4 NUMERICAL MODEL

4.1 Direct shear test model description

In order to study the local soil-pile interface behavior, a direct shear test was modeled numerically. The problem was treated with a 2D plane strain model. The model consists of two different domains: soil (upper part) and solid (lower part) as shown in Figure 3.

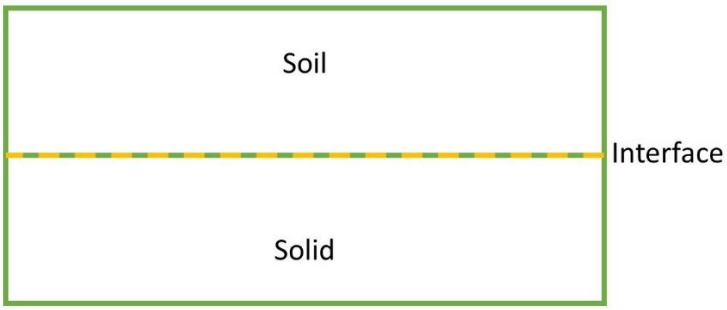

Figure 3: Shear test geometry

On the structure/solid block, zero displacement both in vertical and horizontal direction were imposed (Figure 4). The normal pressure p_n =100kPa was imposed on top of the soil part and a shear displacement u_s =1 cm was imposed on the left side. The continuum behavior of the solid and the soil domain are considered purely elastic. In this study only the non-linear behavior of the contact zone is studied. The dimensions of each block are 25cm x 5 cm. The model has in total 20 elements. Each block is divided in 8 quadrilateral elements with 4 nodes and the contact area has 4 zero thickness elements as in [3] also with 4 nodes.

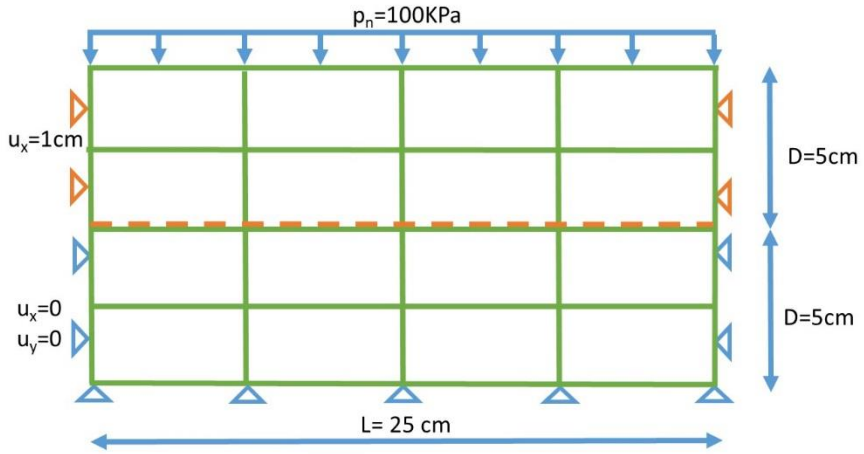

Figure 4: Shear test dimensions and boundary conditions

4.2 Results and discussion

For each constitutive model the relation between shear stress and shear strain is plotted in Figure 5. Even though the continuum material properties and boundary conditions remained the same, different interface models lead to different stress-displacement results. The parameters for each model can be found in the Apendix A.

The Mohr-Coulomb contact model is advantageous in terms of computational effort, and it has only four parameters to consider. Being a bilinear model, has the disadvantage that once it reaches the maximal stress limit, no other additional stress is captured. The general behavior of this model does not include advances for softening and hardening behavior.

The hyperbolic model is very sensitive to any change of parameters. The displacement increment needs to be very small and having consequently many time steps.

The model from Lashkari [6] model involves 11 parameters . It does not converge until the end, but it is possible reach the peak value. The problem starts to appear when the softening behaviour should appear.

Mortara's model [7] converges until the last step and it reproduces well hardening and softening behavior. The only drawback is the high number of parameters (15).

The comparison of all different implementation is not the aim of the paper, however it is shown that the implementation of advanced interface models is possible and successful. However differences in the achieved accuracy and computional robustness are obvious. A

comparison of values can not be done due to the differences parameter sets which was used in the simulations. The global behaviour of shear test under normal pressure loading and shear displacements is given in Figure 6 using Mortara model. The global behaviour of the direct interface test simulation in terms of shear stress deformed shape is presented in Figure 6 and shows the expected results.

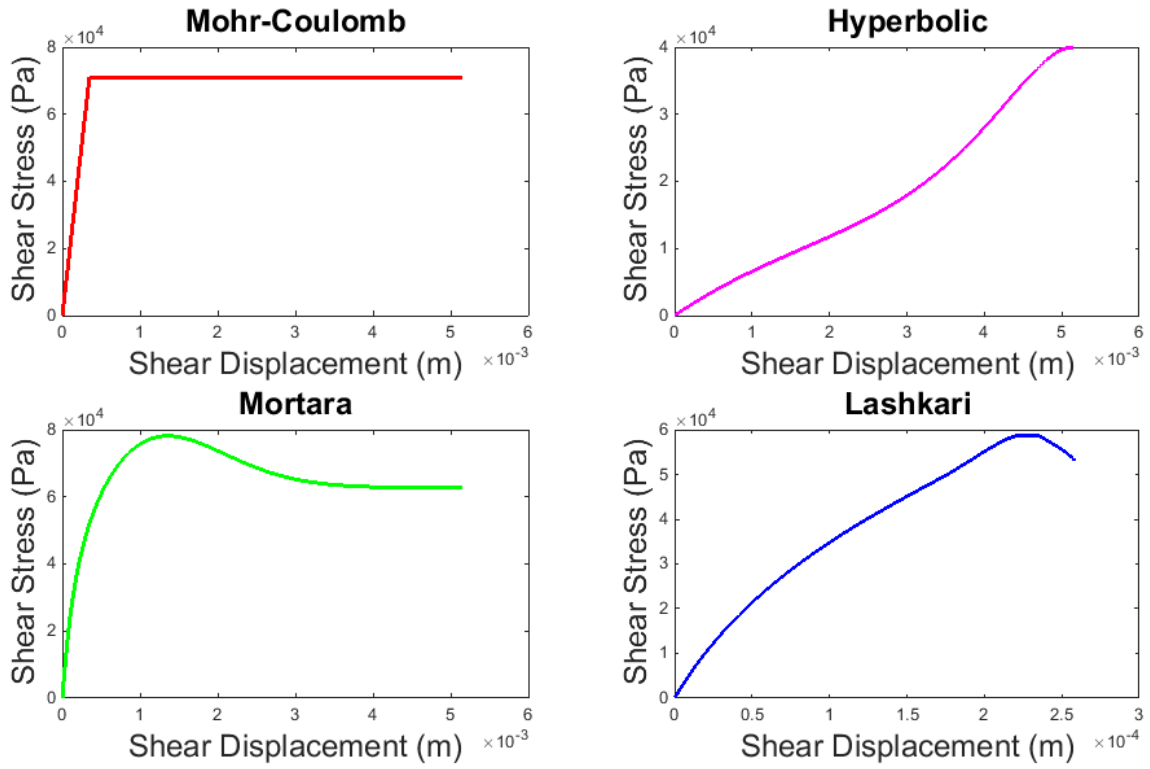

[21]

Figure 5: Results from the numerical model for each constitutive model

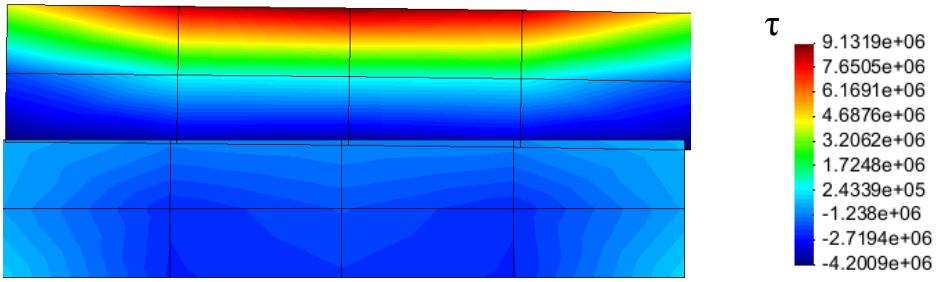

Figure 6: Gid post-process results

5 CONCLUSIONS

- Contact elements are an important tool to study the behavior of shaft friction. Along with an adequate constitutive model, they are able model numerically the phenomena that are important in the contact area between soil and pile.
- Preliminary results on monotonic loading showed that Mortara's model produces reasonable results compared to the other model. Nevertheless, the high number of parameters makes it challenging to use the model for different soils.
- The study of the different models helps to identify issues and challenges for future work about the implementation and usage of the different models. In addition, this helps for model improvement and development of the models.

REFERENCES

[1] Boulon M, Foray P. Physical and numerical simulation of lateral shaft friction along offshore piles in sand. Proc 3rd International Conference on Numerical methods in offshore piling, Nantes, France1986. p. 127-47.
[2] Dejong JT, White DJ, Randolph MF. Microscale observation and modeling of soil-structure interface behavior using particle image velocimetry. Soils and Foundations. 2006;46:15-28 DOI: 10.1002/nme.1620210402.
[3] Beer G. An isoparametric joint/interface element for finite element analysis. International journal for numerical methods in engineering. 1985;21:585-600 DOI: 10.1002/nme.1620210402.
[4] de Coulomb CA. Théorie des machines simples: en ayant égard au frottement de leurs parties et à la roideur des cordages: Bachelier; 1821.
[5] Duncan J, Clough G. Finite element analysis of retaining wall behaviour. Journal of Geotechnical Engineering, ASCE. 1971;97:232-40
[6] Lashkari A. Prediction of the shaft resistance of nondisplacement piles in sand. International Journal for numerical and analytical methods in geomechanics. 2013;37:904-31
[7] Mortara G. An elastoplastic modelling sand structure interface behaviour under monotonic and cyclic loading [PhD]2003.
[8] Jardine R, Standing J. Pile load testing performed for HSE cyclic loading study at Dunkirk, France: Health and Safety Executive; 2000.
[9] Goodman RE, Taylor RL, Brekke TL. A model for the mechanics of jointed rocks. Journal of Soil Mechanics & Foundations Div. 1968
[10] Lehane BM, White DJ. Lateral stress changes and shaft friction for model displacement piles in sand. Canadian Geotechnical Journal. 2005;42:1039-52 DOI: 10.1139/T05-023.
[11] Tehrani F, Han F, Salgado R, Prezzi M, Tovar R, Castro A. Effect of surface roughness on the shaft resistance of non-displacement piles embedded in sand. Géotechnique. 2016;2:1-15 DOI: 10.1680/jgeot.15.P.007
[12] Liu H, Song E, Ling HI. Constitutive modeling of soil-structure interface through the concept of critical state soil mechanics. Mechanics Research Communications. 2006;33:515-31 DOI: 10.1016/j.mechrescom.2006.01.002.

[13] Liu J, Zou D, Kong X. A three-dimensional state-dependent model of soil–structure interface for monotonic and cyclic loadings. Computers and Geotechnics. 2014;61:166-77 DOI: 10.1016/j.compgeo.2014.05.012.
[14] Stutz H, Mašín D. Hypoplastic interface models for fine-grained soils. International Journal for numerical and analytical methods in geomechanics. 2017;41:284-303 DOI: 10.1002/nag.2561.
[15] Stutz H, Mašín D, Wuttke F. Enhancement of a hypoplastic model for granular soil–structure interface behaviour. Acta Geotechnica. 2016;11:1249-61 DOI: 10.1007/s11440-016-0440-1.
[16] Vanlangen H. Numerical analysis of soil-structure interaction. 1991
[17] Been K, Jefferies MG. A state parameter for sands. Géotechnique1985. p. 99-112.
[18] Ghionna VN, Mortara G. An elastoplastic model for sand–structure interface behaviour. Géotechnique. 2002;52:41-50 DOI:10.1680/geot.2002.52.1.41.
[19] Mortara G. An elastoplastic model for sand-structure interface behaviour under monotonic and cyclic loading: Ph. D. Thesis. Technical University of Torino; 2001.
[20] Desai C, Zaman M, Lightner J, Siriwardane H. Thin-layer element for interfaces and joints. International Journal for numerical and analytical methods in geomechanics. 1984;8:19-43
[21] Cerfontaine B, Dieudonné A-C, Radu J-P, Collin F, Charlier R. 3D zero-thickness coupled interface finite element: formulation and application. Computers and Geotechnics. 2015;69:124-40 DOI: 10.1016/j.compgeo.2015.04.016.
[22] Stutz H, Wuttke F, Benz T. Extended zero-thickness interface element for accurate soil–pile interaction modelling. Numerical Methods in Geotechnical Engineering. 2014:283 DOI: 10.1201/b17017-52

APENDIX A

Mohr-Coulomb			
Parameter	***Definition***	***Unit***	***Value***
E	Young Modulus	MPa	60
υ	Poisson ratio	-	0.35
φ	Interface friction angle	-	35
c	Cohesion	*KPa*	1

Hyperbolic			
Parameter	***Definition***	***Unit***	***Value***
γ_w	Unit weight of water	N/m^3	10000
K_I	Dimensionless stiffness number	-	70000
n_{HY}	Stiffness exponent	-	0.75
R_f	Failure ratio	-	0.92
φ	Interface friction angle	^{o}	35

Mortara			
Parameter	***Definition***	***Unit***	***Value***
K_{s0}^{e}	Elastic tangential stiffness	MPa	500e6
K_{n0}^{e}	Elastic Normal stiffness	MPa	585e6
A_0	Initial dilatancy constant	-	11
A_{1L}	Intermediate dilatancy constant	-	0.85
h_0	Plastic hardening modulus constant	-	0.35
M_L	Critical stress ratio	-	0.638
e_0	Initial void ratio	-	1.01
λ_L	Critical state line location in e-lnσ_n	-	0.09
n^b	Influence of interface state on peak stress ratio	-	1.15
n^d	Influence of state on phase transformation	-	0.73
t	thickness	m	0.003

Lashkari			
Parameter	***Definition***	***Unit***	***Value***
K_n^e	Elastic normal stiffness	Pa/m	1.0e10
C_k	Ratio between normal and shear stiffness	-	1
α_p	Maximum value of hardening value	$PA^{1-\beta M}$	2.68
α_c	Asymptotic value of the hardening function	$PA^{1-\beta M}$	2.15
ξ_M	ω_p paramater	PA^{-1}	3.68e-9
ζ	ω_p paramater	m	7.26e-5
μ_M	d_{max} paramater	PA^{-1}	2.171e-7
υ_d	d_{max} paramater	-	0.24
ρ_M	Ratio between stress ratios for d=0 for hardening or softening condition	-	0.550
β_M	Exponent of plastic functions	-	0.9
ω	Hardening model parameter	-	235.6
ψ	Hardening model parameter	-	0.16

XIV International Conference on Computational Plasticity. Fundamentals and Applications
COMPLAS 2017
E. Oñate, D.R.J. Owen, D. Peric and M. Chiumenti (Eds)

CONTACT MESH AND PENALTY METHOD APPROACHES APPLIED TO A SEVERE CONTACT PROBLEM

OLIVEIRA, S. A. G.*, FELICE-NETO, F. R. † AND WEYLER, R.§

*† FEMEC-CIMNE Classroom - School of Mechanical Engineering - Federal University of Uberlândia - Campus Santa Mônica -Caixa Postal 593 - CEP 38400-902 - Uberlândia - MG - Brasil
* sgoulart@ufu.br; † fabioraf@hotmail.com
§ E.T.S. Enginyeria Aeronáutica i Industrial Technical University of Catalonia (UPC), Edifici TR45 (ETSEIAT), Terrassa, Spain
weyler@upc.edu

Keywords: Explicit FEM, Contact, Contact Mesh, Severe Contact

Abstract. This work aims to propose a comparison between the well known penalty method and the contact mesh approach in an Explicit Finite Element Method applied to a severe contact simulation. The contact mesh links the probable contact regions and minimizes the potential error. In this approach, the algorithm shrinks the whole model in the same proportion, searches for the nodes which will probably start contact in the next iterations, creates the contact mesh and transfers the conditions when the distance would be enough to start the contact without the shrinkage. After the simulation finishes, the whole model returns to its normal size to correct visualization. In order to test the method efficiency and guarantee a reliable comparison, a microindentation experiment that represents a severe contact problem was simulated using explicit integration for both contact approaches. As results, both methods showed similar good results when compared to experimental tests for large deformations and to observe the overall behavior. In the case of small deformations and to observe the local behavior of small contact areas, the penalty method presents instabilities variations that are close in size to the real deformations, different from the contact mesh approach, which shows smooth transition between the mesh nodes, similar to the experimental results.

1 INTRODUCTION

Numerical Methods are often used to solve mathematical problems which describe physical phenomena, when they have several variables or even does not have analytical solution. A heavily widespread numerical method is the Finite Element Method (FEM), which provides an approximate solution to differential equations that usually represent physical phenomena, such as continuum mechanics and fluid mechanics [1, 2, 3].

The contact method most used in FEM commercial programs is the Penalty Method, in which is used a force to avoid the penetration of volumes. Its calculation considers geometrical and space conditions (such as body shape and penetration gap), other variables (material properties and process parameters) and a penalty constant to multiply the penetration, which is chosen by the user. A small value for the penalty could violate the contact condition (allow penetration) and a big value could destabilize the simulation. This method achieves good results for macro sized problems, like stamping process, but for micro and nano sized process, like microindentation tests, the error can be greater than the tolerances for a correct analysis. Another problem is the penalty constant given by the user, which is highly non-linear and dependent on the user experience. [4]

Another method to deal with the contact problem is the Lagrange Method, which establishes a minimization with boundary conditions, creating a Lagrangian function. This function relates the objective function to the problem restrictions and is ensured by the Kuhn-Tucker conditions [5]. Based on the Lagrange and Penalty Method the Augmented Lagrange Method can be also postulated, using both the penalty factor and the Lagrange multipliers, but in this case the Lagrange multipliers are updated each step and a finite penalty factor guarantee the convergence. This method is stable but it must iterate each step, which is a problem for explicit methods. [6]

A relatively new approach on the contact problem is the contact domain approach, or contact mesh, which creates a mesh linking the nodes that will possibly begin contact from one surface to another, with a single layer of elements. This mesh is responsible for predicting the contact and reduces the error, by virtually shrinking the elements and transmitting the conditions from one surface to another.

Thus, this work aims to compare the mesh approach method and the penalty method, both in Explicit FEM time integration codes. The first approach (contact mesh) was simulated using the COMFORM software, which is an academic algorithm, developed by the Polytechnic University of Catalunya (UPC) in partnership with other institutes [7]. The second contact approach (penalty method) was simulated using the STAMPACK® software, developed by QUANTECH ATZ, an explicit FEM commercial algorithm, focused on mechanical forming processes. The severe contact problem chosen to simulate were a microindentation problem in a copper specimen, with maximum penetration depth not superior to 3 μm.

2 CONTACT MESH APPROACH

According to Oliver et al. [8], the contact domain is a fictive intermediate region, with the same dimension as the contacting bodies, connecting the potential contact surfaces of those bodies. This leads to a purely displacement problem, because the contact function is now based on the dimensionless measure of the normal and tangential gaps. Therefore, the difference between this method and the node-to-node or segment-to-segment strategy lays on the interpretation of the contact domain. In the classical methods, the contact conditions are formulated due to a projection of the contact surface or point (slave contact surface) onto the other contact surface (master contact surface), as shown in Fig. 1 (a). Considering that, the contact problem is a subdomain, with lower dimension. On the other hand, the contact mesh

establishes patches, connecting the potential contact surfaces, in other words, an intermediate domain with the same dimension as the bodies in contact, Fig. 1 (b) [9,10,11]. In order to connect the potential contact surfaces, the patches created must not overlap, it must be a unique layer and it converge to the contact domain as the number of vertices increases. As shown on Fig. 2, the contact patches can be designed in multiples ways. In our study, we used only tetrahedral linear-linear shaped patches due to the best results in the contact formulation, according to Oliver et al. [8]

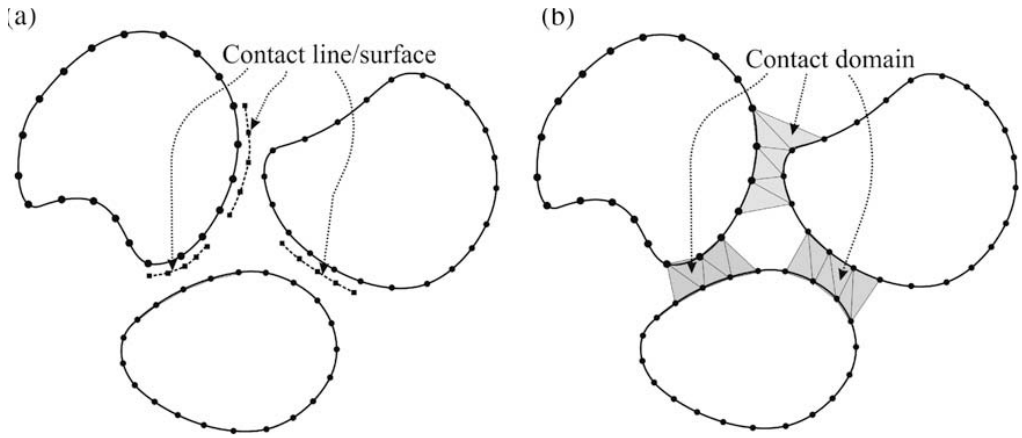

Fig. 1. Imposition of contact constraints in: (a) Classical Methods; (b) Contact Domain Method. (Adapted from [8])

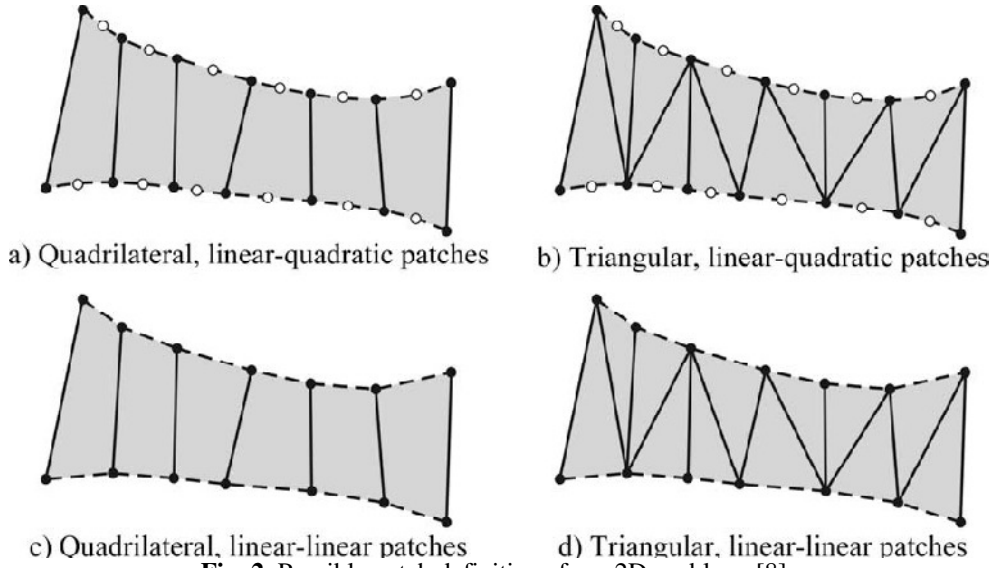

Fig. 2. Possible patch definitions for a 2D problem. [8]

It is important to note that the creation of a contact mesh is independent of the master/slave relation, it means that it doesn't matter which body will be considered as master or slave in the contact pair. The determination of the contact mesh, i.e., which points of each contact pair will be connected and when the mesh will be created is defined by an active strategy, following 4 steps: i. the process starts with a FEM meshed pair of bodies, where the element

chosen doesn't affect the contact approach (Fig. 3 (a)); ii. the interior nodes are removed and the boundaries are shrunk (Fig. 3 (b)); iii. the contact mesh is created, linking both bodies in the probable contact areas (Fig. 3 (c)); iv. The original boundary and mesh are retrieved (Fig. 3.6 (d)). [10]

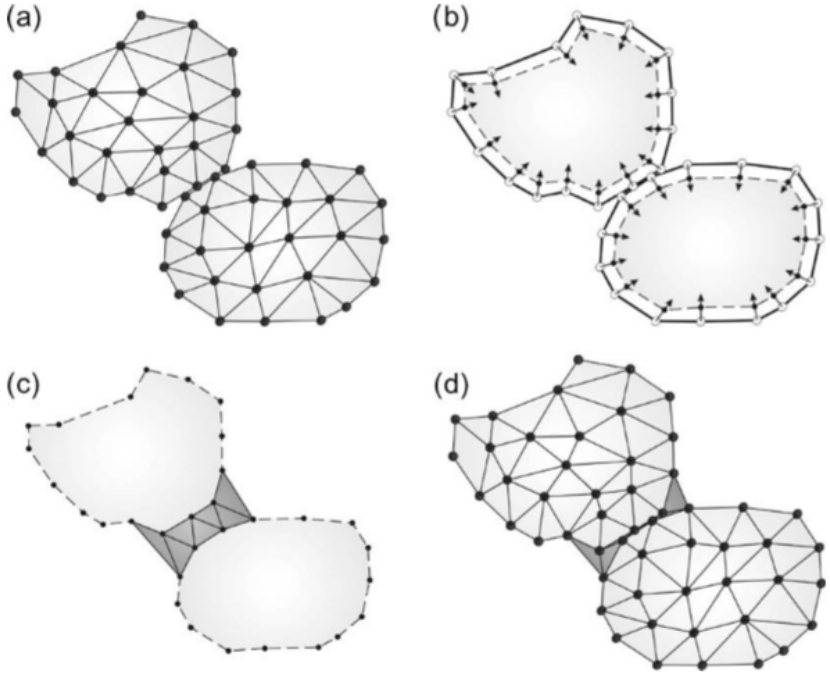

Fig. 3. Generating of the contact mesh: (a) Original Mesh; (b) Removal of internal nodes and shrinkage; (c) Creation of the contact mesh; (d) Original boundary and mesh retrieved.[10]

3 MICROINDENTATION TEST

A microindentation test consists in an experimental method in which the specimen is pressed by a known shaped indenter, with controlled load and displacement. Analyzing the load, displacement and also the indentation mark, it is possible to calculate the bulk or multi-layered materials properties. It is also possible to characterize the multi-layered material adhesion between layers and analyze other phenomena, such as the pile-up and sink-in. A microindentation experiment can be simulated as if the plastic deformations are greater when compared to elastic ones, enough to neglect the elastic part of the total deformations in the material formulation. Considering that, the formulation respected the big plastic deformation continuum mechanics theory, in which the process was considered purely mechanic, because in a quasistatic process, velocities are sufficiently low to neglect any heat or heat transfer. [12, 13, 14, 15]

The microindentation test performs a deformation in the specimen under the tool and that causes deformation in the mark´ surroundings. If the material experience hardening when it undergoes plastic deformation, the surroundings will go up, forming the pile up. On the other hand, if the specimen undergoes annealing during the plastic deformation, the surroundings go down, performing a sink in phenomena. Both the pile up and the sink in are represented by the Fig.4. [16, 17, 18]

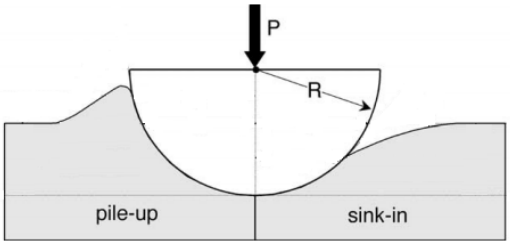

Fig. 4. Pile up and sink in phenomena. (Adapted from [18])

In order to validate and compare the simulations, experimental results from Da Silva [19] were used. Figure 5 shows the Force vs. Depth experimental curve for a maximum force of 5 N. Figure 6 shows the laser interferometry of the indented surface after the microindentation. Finally, Fig. 7 shows the roughness profile of the indented surface, emphasizing the pile up phenomena.

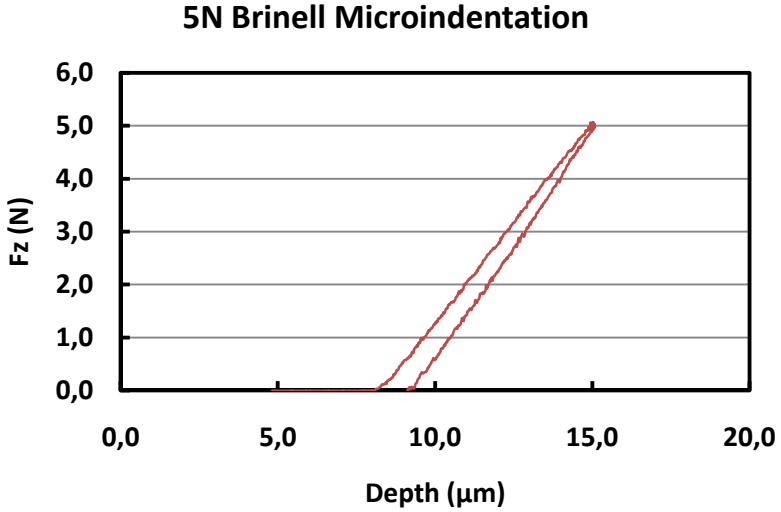

Fig.5. 5N Brinell Microindentation Force vs. Depth curve [19]

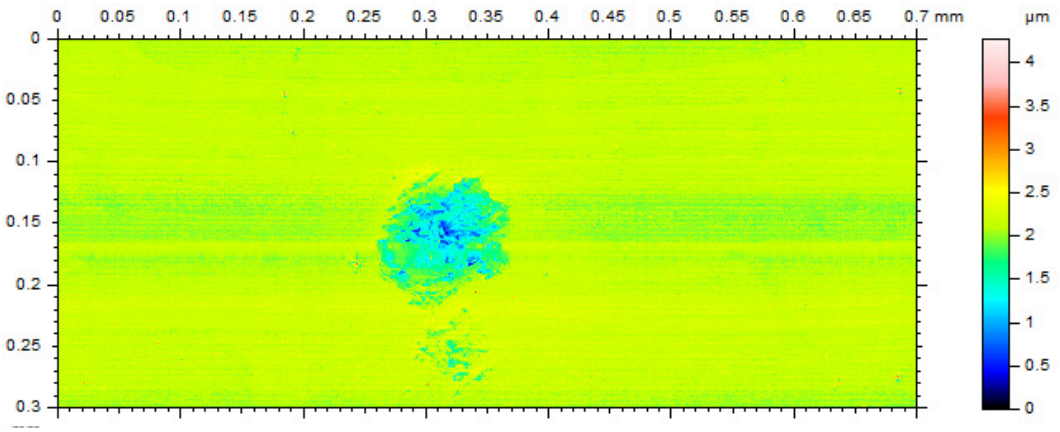

Fig. 6. Laser Interferometry of the 5N Brinell microindentation [19]

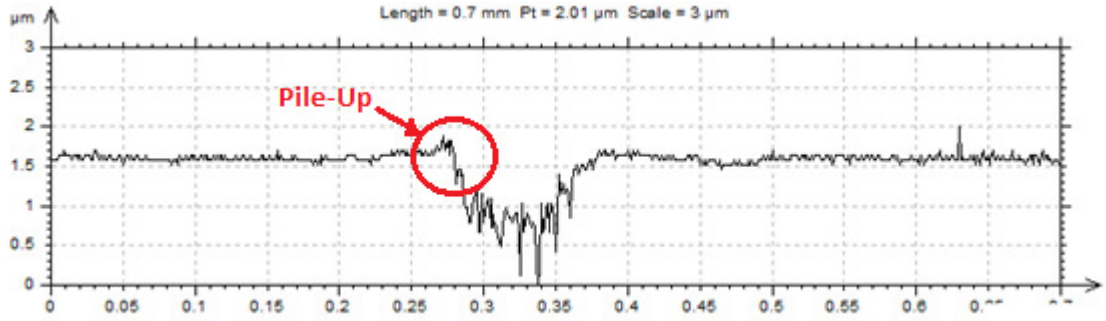

Fig. 7. 5N Brinell microindentation roughness profile. [19]

4 MATERIALS AND METHODS

In order to guarantee reliable results, both simulations used the same model, developed in the GiD software, which is a pre and post process platform. The model was constituted by a sphere shaped indenter with 2.5 mm diameter and a copper specimen (designed with 0.7 x 0.7 x 1.4 mm). To decrease simulation time, the model was a quarter of the whole model, i.e., XZ and XY plans symmetry. The geometry was scale in 10^3 and the total time used was $1.6\ x\ 10^{-4}$. For the indenter in COMFORM, a hard material (tool steel) with elastic properties shown in table 1, was used. For STAMPACK, the indenter was considered a rigid body, and because of that, the indenter was reduced to a surface only.

Table 1. Microindentation Simulation Indenter properties.

	Value	Unity
Young Modulus (E)	210	GPa
Poisson's ratio (ν)	0.3	-
Density (ρ)	7850.0	Kg/m³

For the copper specimen, the same properties for both programs were used, from FELICE-NETO [7], which constitutes table 2.

Table 2 Copper specimen properties**.**

	Value
Young Modulus (E)	117 GPa
Yielding Stress (σ_y)	110.83 MPa
Poisson's ratio (ν)	0.3
Density (ρ)	8960.0 kg/m³
Hardening modulus (k)	446.2088 MPa
Hardening exponent (n)	0.2797

The boundary conditions created for this model consists in the restriction of displacement of the bottom surface specimen nodes, in the axis X, Y and Z. The symmetry surfaces, XZ and YZ, had the Y displacement and X displacement equals to zero respectively, to guarantee the model symmetry.

The displacement imposed to the indenter is 3 μm (indentation depth) and shows 4 stages: i. In the first stage the displacement is in a short range, just to approximate the indenter to the copper specimen. The simulation did not start with the bodies in touch, because of several convergence problems found; ii. In the second stage the displacement is increased slowly to guarantee the algorithm convergence, until it comes to the maximum Z axis Displacement; iii. In the third stage the displacement is constant, to be sure that there are no dynamic effect or numerical disturbance, which would make the specimen surface point to move even with the indenter stopped; iv. The fourth stage is the unloading, which can be fast and is really important because the specimen material will undergo a spring-back (elastic deformation recuperation) that will enable the comparison between the final stage of the simulation with experimental specimen surface topography, measured with a Laser Interferometry.

The two codes have different algorithms, which forbid some mesh properties. Considering that the meshes were created differently. For COMFORM the mesh created is constituted by tetrahedral elements in both bodies (indenter and specimen). The global element size for the unstructured mesh is 0.09. This size was chosen considering the minimum deformation expected in the copper specimen, i.e., the mesh must be small enough to perform the shape of the indentation mark left on the copper specimen surface. The indenter has the global element size for the bottom surface and the global size multiplied by a factor of 10, totalizing 1142 nodes and 5750 elements. For the specimen, the top surface has the global element size (0.09) and the bottom surface has the global element size multiplied by a factor of 100, totalizing 2636 nodes and 22847 elements. Fig.8 (a) represents the mesh created for the whole model. On the other hand, the STAMPACK mesh is constituted by triangular elements for the indenter (surface) and hexahedral elements for the indenter (volume). The indenter has 783 nodes and 1539 elements and the specimen has 13002 nodes and 100000 elements, as shown in Fig. 8 (b).

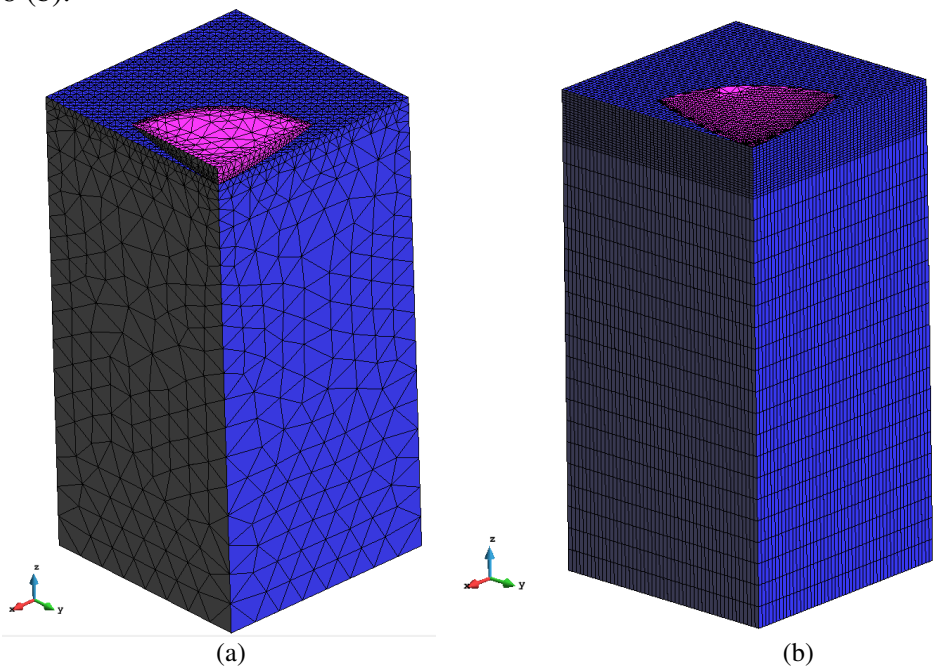

Fig. 8. Mesh of the FEM Microindentation model.(a) COMFORM. (b) STAMPACK

5 RESULTS AND DISCUSSION

After simulating in COMFORM and STAMPACK, the nodal Z displacement results were obtained for the indentation depth profile, for the nodes marked in the Fig.9. Considering that the two models had different meshes, the analyzed nodes positions had a minimum position variation, as shown in table 3.

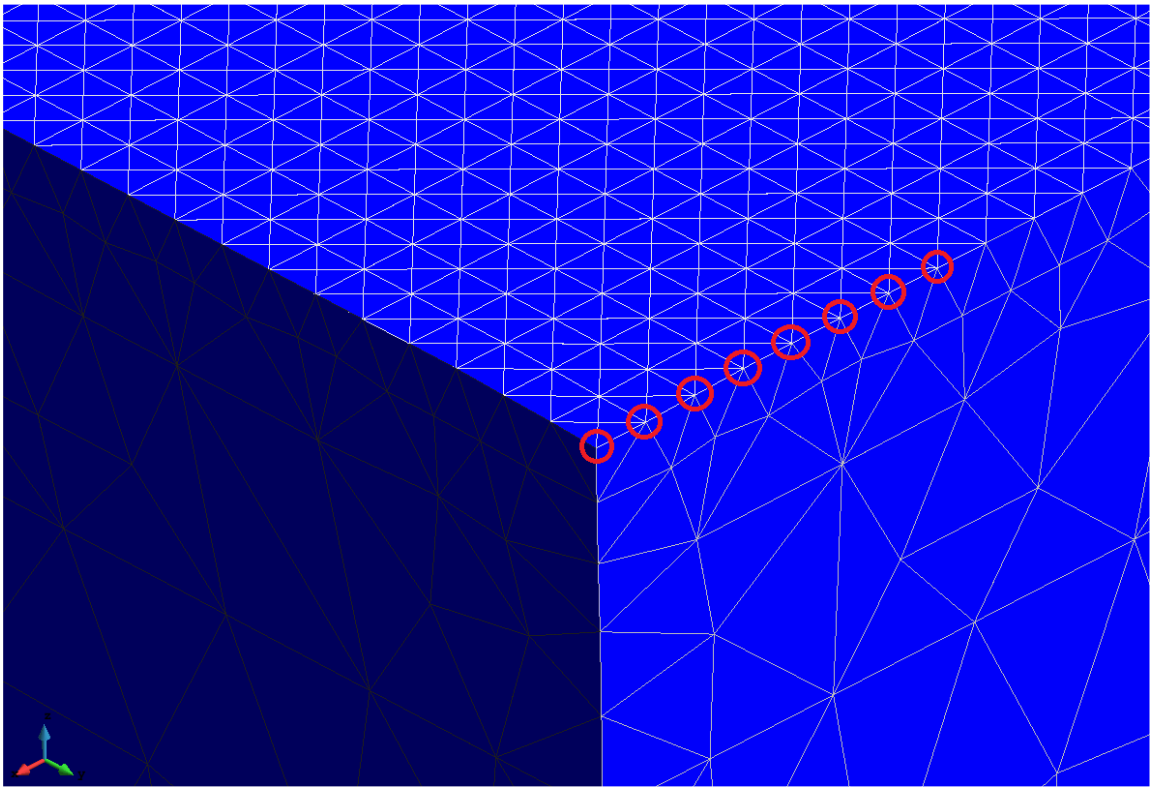

Fig. 9. Nodes taken in the surface, X axis, to analyze the microindentation Z displacement profile.

Table 3. Analyzed nodes position

Node	(X,Y) position COMFORM	(X,Y) position STAMPACK
1	(0.0,0.31805)	(0.0,0.31805)
2	(0.02331,0.31805)	(0.01396,0.31805)
3	(0.04662,0.31805)	(0.02793,0.31805)
4	(0.06992,0.31805)	(0.04195,0.31805)
5	(0.09312,0.31805)	(0.05599,0.31805)
6	(0.11675,0.31805)	(0.06997,0.31805)
7	(0.14052,0.31805)	(0.08410,0.31805)
8	(0.16519,0.31805)	(0.09864,0.31805)

The Z axis Displacement vs. the X axis position for both simulations (Fig.10) shows a smoother result transition for the contact mesh approach (COMFORM) when compared to the penalty method approach (STAMPACK) result.

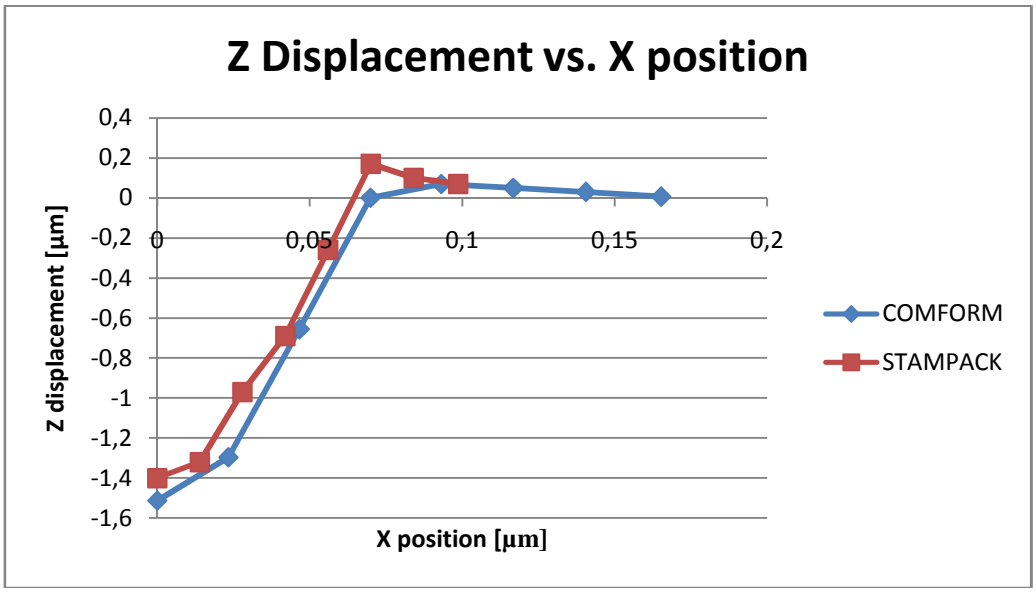

Fig.10. Z axis Displacement vs. the X axis position for both simulations.

Figures 11 and 12 show the Z displacement distribution for the contact mesh and penalty method approaches respectively. The difference in the distribution along the surface indicates instability due to the contact development. For a macro sized contact, this instability probably would not represent great result divergence, but for micro sized analysis the contact gap error introduced by the penalty method could lead to considerable errors.

6 CONCLUSIONS

- First, it is important to emphasize that both simulations used similar models with different meshes due to limitations in the software used, not the contact method. This shows that the contact mesh approach can be as versatile as the penalty method, which is the most used in FEM algorithms.
- Comparing the indentation depth results, the contact mesh approach shows smoother transition between nodes, which possibly lead to more reliable results for severe contact problems.
- Comparing the simulation results to the experimental results from Da Silva [19], it is reasonable to infer that the contact mesh approach obtained more accurate results when compared to the penalty method approach. The maximum experimental indentation depth is ~1.5 µm, which is closer to 1.5132 µm from the contact mesh approach than from 1.4000 µm from the penalty method.

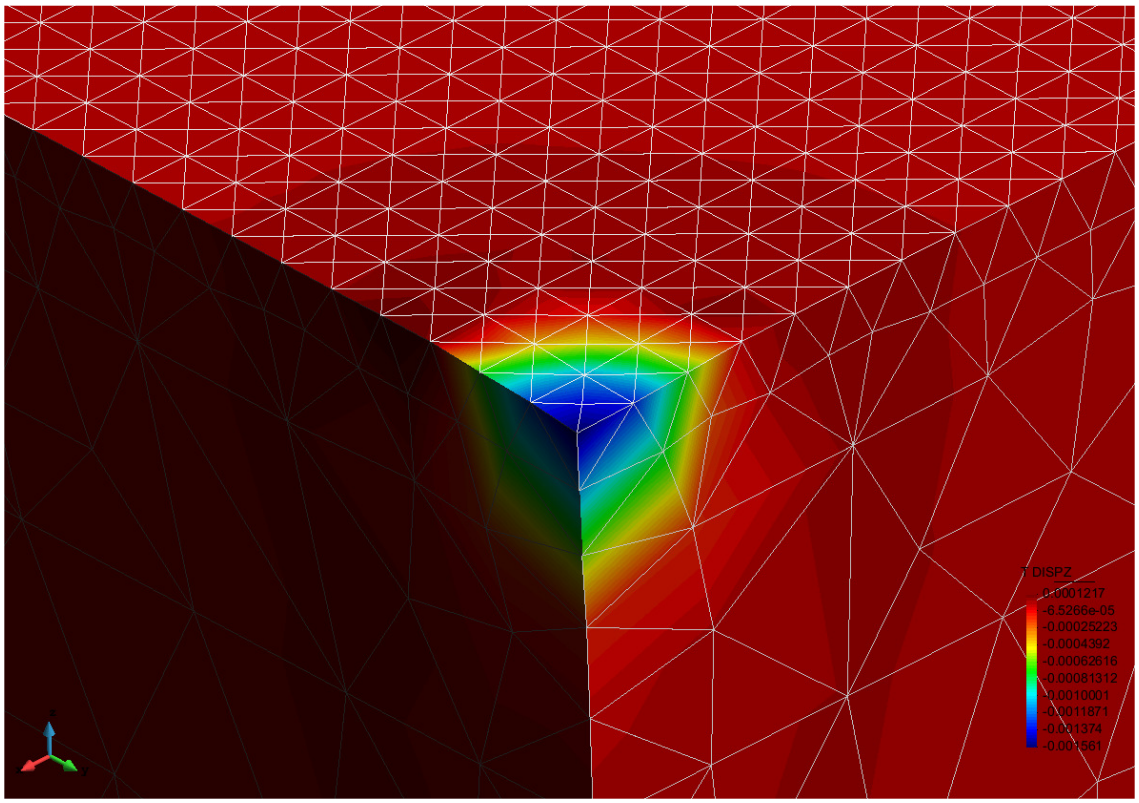

Fig. 11. Z Displacement for the Contact Mesh Approach

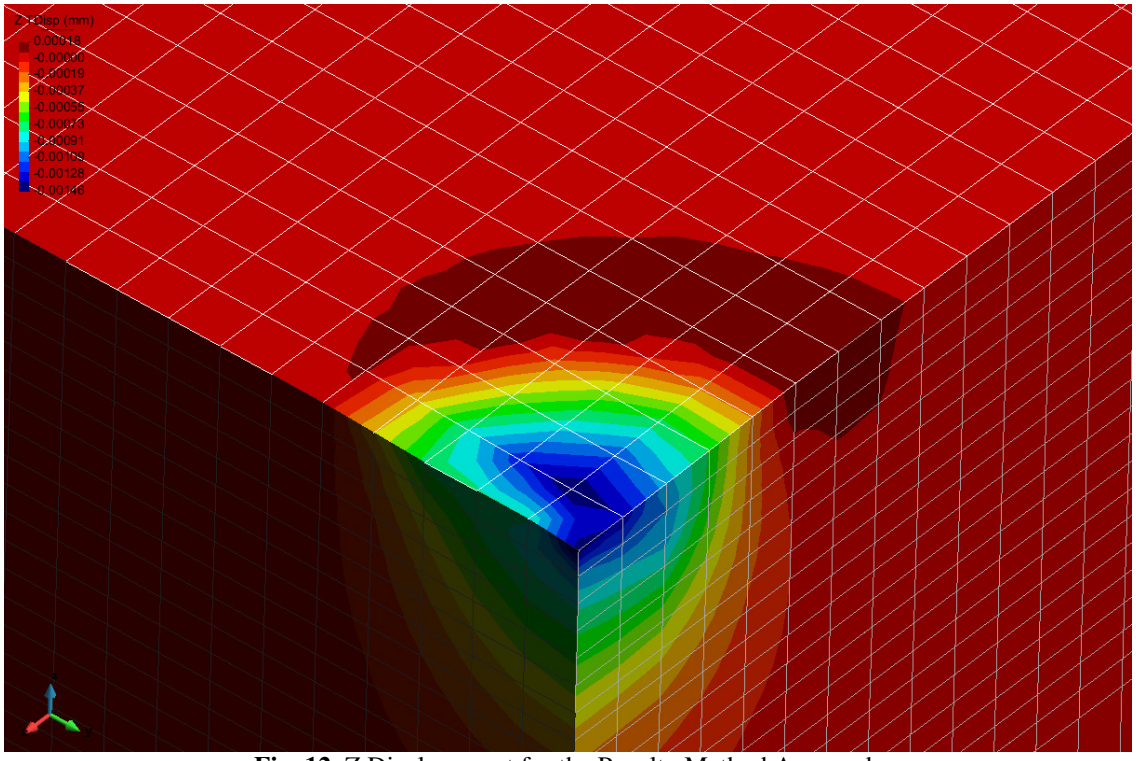

Fig. 12. Z Displacement for the Penalty Method Approach

7 ACKNOWLEDGEMENTS

The authors would like to thank Capes/Proex, CNPq, and FAPEMIG for financial support. They are also thankful to Red de Aulas CIMNE and QUANTECH ATZ

REFERENCES

[1] ZIENKIEWICZ, O.C., *The Finite Element Method*, 3rd edition, McGraw-Hill BookCo.,1991.

[2] BARKANOV, E., *Introduction To The Finite Element Method*, Institute of Materials and Structures , Faculty of Civil Engineering, Riga Technical University, 2001.

[3] DESAI, C.S., ABEL, J.F., *INTRODUCTION TO THE FINITE ELEMENT METHOD*, Van Nostrand, 1972.

[4] SILVA, P.S. da., *Análise Do Uso De Escalas Nas Simulações De Processos De Estampagem*. 100f. Dissertação de Mestrado, Faculdade de EngenhariaMecânica, Universidade Federal de Uberlândia, Uberlândia, 2016.

[5] SIMO, J. C., LAURSEN, T. A., *An Augmented Lagrangian Treatment Of Contact Problems Involving Friction*, Computers & Structures, Vol. 42, No. 1, pp 97-116, 1992.

[6] BERTSEKAS, D.P., *Nonlinear Programming*, Massachusetts Institute of Technology, second edition, Athena Scientific, Belmont, Massachusetts, 1995.

[7] FELICE-NETO, F.R., *Contact Mesh Approach in Explicit Finite Element Method: An Application to a Severe Contact Problem*, PhD thesis, Federal University of Uberlândia, Brazil, 2016.

[8] OLIVER, J., HARTMANN, S., CANTE, J.C., WEYLER, R., HERNANDEZ, J.A., *A Contact Domain Method For Large Deformation Frictional Contact Problems. Part i: Theoretical Basis*, Computational Methods Applied to Engineering, 198, pg 2591-2606, Elsevier, 2009.

[9] HARTMANN, S, OLIVER, J., WEYLER, R., CANTE, J.C., HERNANDEZ, J.A., *A Contact Domain Method For Large Deformation Frictionless Problem. Part 2: Numerical Aspects*, Computational Methods Applied to Engineering, 198, pg 2607-2631, Elsevier, 2009.

[10] HARTMANN, S,WEYLER, R.,OLIVER, J.,CANTE, J.C.,HERNANDEZ, J.A., *A 3d Frictionless Contact Domain Method For Large Deformation Problems*, Computer Modeling in Engineering & Science (CMES), vol. 55, no. 3, pp.211-269, Tech Science Press, 2010.

[11] WEYLER, R., *Simulación Numérica De Procesos De Compactación Y Extrusión De Materiales Pulverulentos - Aplicación A La Pulvimetalurgia Industrial*, Tesis doctoral, Universitat Politécnica de Catalunya, Barcelona, 2000.

[12] GU, Y., NAKAMURA, T., PRCHLIK, L., SAMPATH, S., WALLACE, J., *Micro-Indentation And Inverse Analysis To Characterize Elastic-Plastic Graded Materials*, Materials Science and Engineering, Elsevier, 2003.

[13] CHEN, R., YANG, F., LIAW, P.K., FAN, G., CHOO, H., *Microindentation Of A Zr57ti5cu20ni8al10 Bulk Metallic Glass*, Special Issue on Bulk Metallic Glasses – Selected Papers from the Fifth International Conference on Bulk Metallic Glasses (BMGV), Materials Transactions, vol. 48, No. 7, pp. 1743 to 1747, The Japan Institute of Metals, 2007.

[14] HOLMBERG, K, MATTHEWS, A, *COATINGSTRIBOLOGY – Properties, Mechanisms, Techniques And Applications In Surface Engineering*, Second Edition, Tribology and Interface Engineering Series, vol. 56, Elsevier, 2009.

[15] RUTHERFORD, K. L.; HUTCHINGS, I. M. *A Micro-Abrasive Wear Test, With Particular Application To Coated Systems, Surface And Coatings Technology*, volume 79, pp 231-239, 1996.

[16] LEE, Y.H., HAHN, J.H., NAHM, S.H., JANG, J.I., KWON, D., *Investigations On Indentation Size Effects Using A Pile-Up Corrected Hardness*, Journal of Physics D: Applied Physics, volume 41, number 7, 2008.

[17] TALJAT, B., PHARR, G. M., *Development Of Pile-Up During Spherical Indentation Of Elastic-Plastic Solids*, International Journal of Solids and Structures, Elsevier, 2004.

[18] TALJAT, B., ZACHARIA, T., PHARR, G. M., *Pile-Up Behaviour Of Spherical Indentations In Engineering Materials*, MRS Procedings, Volume 522, 2011.

[19] DA SILVA, W. M., *Simulação Do Desgaste Abrasivo Via Iterações Múltiplas*, Tese de Doutorado, 177f., Programa de Pós Graduação em Engenharia Mecânica, Universidade Federal de Uberlândia, Uberlandia, 2008.

XIV International Conference on Computational Plasticity. Fundamentals and Applications
COMPLAS XIV
E. Oñate, D.R.J. Owen, D. Peric & M. Chiumenti (Eds)

AVOIDING FRACTURE INSTABILITY IN WEDGE SPLITTING TESTS BY MEANS OF NUMERICAL SIMULATIONS

J. LIAUDAT*, D. GAROLERA*, A. MARTÍNEZ*, I. CAROL*, M.R. LAKSHMIKANTHA† AND J. ALVARELLOS†

* ETSECCPB (School of Civil Engineering-Barcelona)
UPC (Technical University of Catalonia)
E-08034 Barcelona
e-mail: joaquin.liaudat@upc.edu, daniel.garolera@upc.edu,ariadna.martinez.e@upc.edu, ignacio.carol@upc.edu

†CTR-Repsol, 28935 Móstoles (Madrid)
e-mail: m.lakshmikantha@repsol.com, jose.alvarellos@repsol.com

Key words: Rock, WST, Fracture Mechanics, FEM, Interface Elements

Abstract. In this paper, unstable fracture propagation obtained in a in-house performed experimental Wedge Splitting Test (WST) is simulated by means of the FEM and fracture-based zero-thickness interface elements. In order to obtain a specimen geometry suitable for a stable WST without modifying the remaining significant parameters of the test (machine stiffness and control parameter), additional simulations were performed varying the length of the specimen notch, until a load-COD (Crack Opening Displacement) curve without snap-back was obtained. Finally, a new experimental WST with the modified geometry was carried out leading to a stable load-COD curve. In the simulations, elastic continuum elements were used to represent the rock, the steel loading plates and the testing machine compliance via an "equivalent spring", whereas interface elements were used for the notch and along the potential crack path. The interface elements representing the notch were equipped with linear elastic constitutive law, with very low elastic stiffness K_n and K_t so that they do not oppose any significant resistance to opening. For the interface elements along the fracture path, an elastoplastic constitutive model with fracture energy-based evolution laws was used.

1 INTRODUCTION

The Wedge Splitting Test (WST) is a method to generate fracture propagation in quasi-brittle materials in order to determine fracture mechanics parameters in mode I, such as the fracture toughness (K_{IC}) for the linear theory, or the specific fracture energy (G_f^I) for the linear or also non-linear theory [1, 2]. In any case, it is essential that the propagation of the fracture occurs in a stable manner. A WST is stable if no sudden

drop of the the applied load follows the peak. that is, a stable WST shows an overall load-COD (Crack Opening Displacement) diagram with a descending branch after peak load is reached [1]. The stability of the fracture propagation depends on the interaction between of the control parameter chosen (displacement of the testing machine actuator or COD), the stiffness of the testing machine, the specimen stiffness and geometry, as well as the material properties.

In this paper, experimental results from an unstable WST are simulated via a Finite Element model in order to interpret the reasons of the unstable propagation of the fracture, and to explore possible solutions for avoiding it in following tests. Afterwards, based on the conclusions reached in the first analysis, a new WST test was performed in which the specimen geometry was slightly modified. As result, stable WST was obtained, proving the effectiveness of the proposed procedure.

2 WST EXPERIMENTAL SET-UP

2.1 Principles

The method uses cylindrical or prismatic specimens in which a notch has been cut in order to prefigure the cracking path. A pair of steel loading plates equipped with roller bearings is glued to both sides of the notch mouth, and lateral opening displacement of the rollers is imposed through a wedge moving vertically down in order to create a crack. A scheme of the test setup and a free body diagram of forces on the wedge are shown in Fig. 1, taken from Ref. [3]. The horizontal force applied to the specimen (P_H) is calculated by means of Eq. (1), where P_V is the vertical load applied, θ is the wedge angle and μ is the coefficient of friction between wedge and roller.

$$P_H = \frac{1 - \mu \tan\theta}{2(\mu + \tan\theta)} P_V \tag{1}$$

If the fracture process is stable, the specific fracture energy of the material G_f^I can be obtained from the $P_H - COD$ response of the specimen using Eq. (2), where A_l is the surface of the ligament area ($A_l = L \cdot D$, in Fig. 2).

$$G_f^I = \frac{1}{A_l} \int_0^{+\infty} P_H \; dCOD \tag{2}$$

The displacement of the wedge is imposed by means of a testing machine with a closed-loop control, which can be controlled in two different ways: (1) by fixing the vertical displacement rate of the machine actuator, or (2) by fixing a COD rate. According with Brühwiler and Wittmann [1], the stability of the fracture process in each case depends on fulfilling the following generic conditions:

$$\text{Actuator control}: \; l_{ch} > K \cdot L_c \cdot (k_s/k_M + 1) \tag{3}$$

$$\text{COD control}: \; l_{ch} > K \cdot L_c \tag{4}$$

where $l_{ch} (= E \cdot G_f^I / f_t^2)$ is the characteristic length of the material (E is the elastic modulus, f_t is the tensile strength), K is a constant depending on the specimen geometry, L_c is the

cantilever length, k_s is the specimen stiffness, and k_M is the testing machine (including the WST device) stiffness.

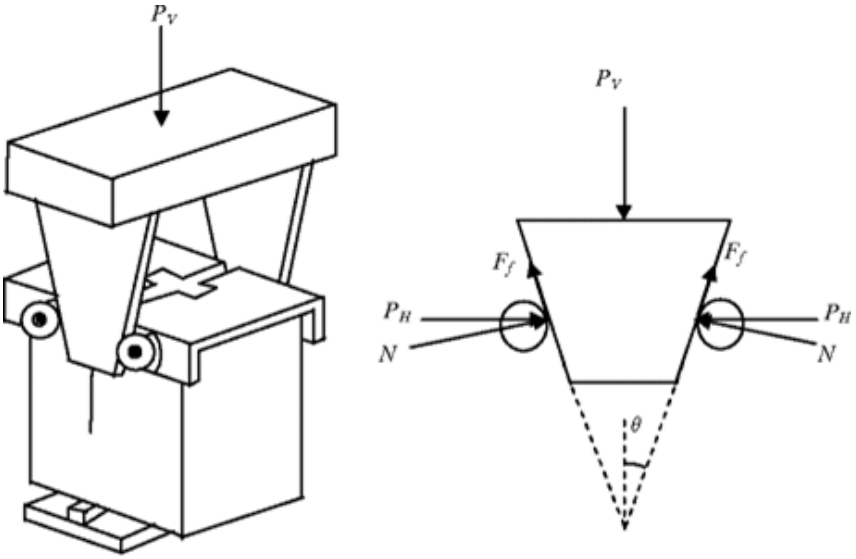

Figure 1: Details of the Wedge Splitting Test (WST) set up: test setup of the WST specimen (left), and free body diagram of forces (right). Taken from Ref. [3].

In this paper, results of two experimental WST performed on core samples from the same source are presented. In both cases, the WST were performed controlling the actuator displacement. In the first test, an unstable fracture was obtained. In order to avoid this in the following test, the specimen stiffness k_s was reduced according to the procedure described in Sec. 4.

2.2 Apparatus

A WST device similar to the one illustrated in Fig. 1 was placed in a "ELE Digital Tritest 100 testing machine" (loading capacity 500 kN). As mentioned above, the test were performed controlling displacement rate of the actuator. The vertical load was measured using a load cell UtilCell 610 (nominal load 25 kN, linearity error $< \pm 0.25\%$ F.S.) with signal conditioning amplifiers Krenel CEL/M010. The COD was measured with two LVDT sensors RDP GT2500 (± 2.5 mm, linearity error $< \pm 0.1\%$ F.S.), with signal conditioning amplifiers RDP S7AC. The LVDTs were placed in the axis of the horizontal splitting force, one on each side of the specimen (COD1 on side 1, COD2 on side 2). The experimental COD informed in Sec. 4 is the average of these two measurements. Finally, the data from the sensors was acquire through a ELE Automatic Data Acquisition unit.

2.3 Specimens

The experimental WSTs were performed on a calcareous rock from a deep perforation core of 100 mm diameter. No physical properties of this rock were known at the moment of performing the WST. In order to prepare the specimens for the WSTs, two consecutive

sections of 100 mm length were cut from the perforation core. Then, a groove and a notch were cut in each specimen according to the geometry and dimensions indicated in Fig. 2, where L is the ligament length and D the ligament depth. In order to force a straight crack propagation path, a 5 mm-deep groove was cut on both sides of the specimen, on the circular surfaces perpendicular to its axis (see perspective view in Fig. 2).

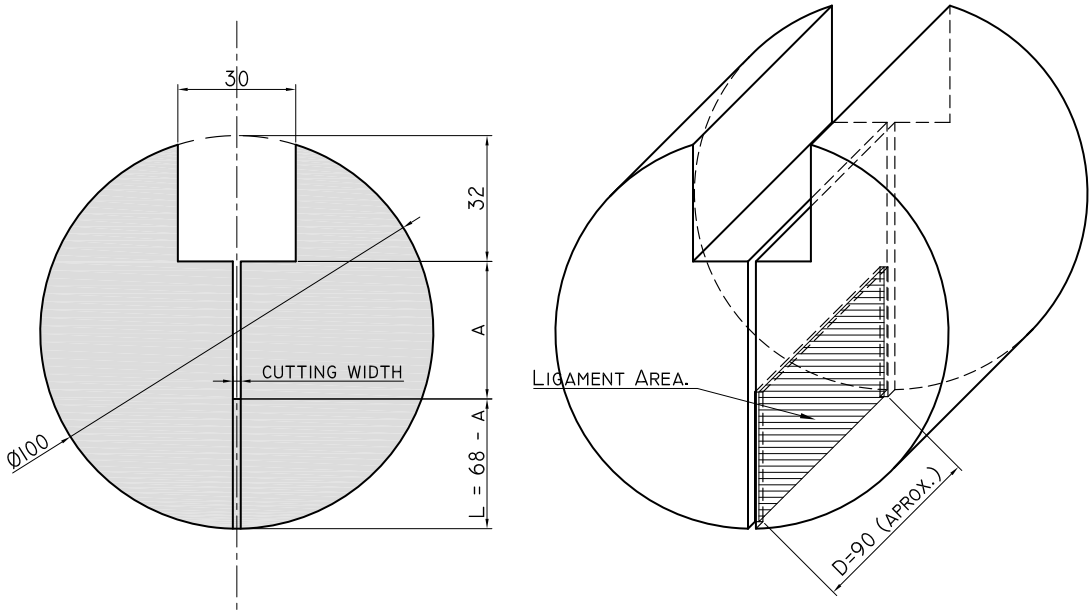

Figure 2: Dimensions of the WST specimen. Taken from Ref. [5].

The ligament length is given generically as L in Fig. 2 since it is the geometry parameter to be determined in Sec. 4 in order to avoid fracture instability. Note that by reducing L one can reduce the specimen stiffness (k_s) and, eventually, make stable an originally unstable test configuration by fulfilling the relationship stated in Eq. (3). On the other hand, the ligament area must be large enough to be representative of the macroscopic material behavior.

3 NUMERICAL MODELLING OF THE WST

The model geometry and the FE mesh used are presented in Fig. 3, where grey elements represent the rock, blue elements represent the steel loading plates and magenta elements represent an "equivalent spring" on behalf of the machine compliance. The notch (green line) and the fracture path (red line) on the rock were represented by zero-thickness interface elements.

The lower roller support was simulated by restricting the vertical displacement of the lowest nodes. The horizontal displacements imposed on the roller bearings by the testing machine were simulated by imposing horizontal displacements of same values and opposite sign, on the equivalent springs.

For continuum elements (rock, plates and equivalent spring), isotropic linear elastic materials were assumed. The interface elements representing the notch were equipped with a linear elastic constitutive law and very low elastic stiffness K_n and K_t, so that they do not oppose any significant resistance to opening. The constitutive model used for the interface elements along the fracture path was the elastoplastic constitutive model with fracture energy-based evolution laws described in detail in Ref. [4].

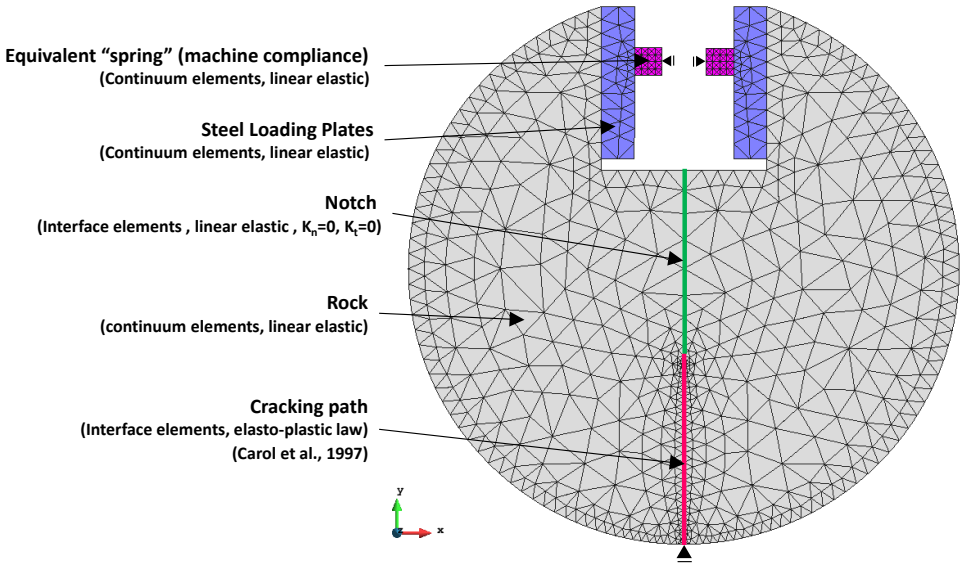

Figure 3: FE mesh and boundary conditions.

The stiffness of the 5×5 mm equivalent spring has been calibrated in a previous work [5], resulting in a elastic modulus $E = 700$ MPa with a Poisson's coefficient of ν =0. For the steel loading plates, conventional values of $E = 200$ GPa and $\nu = 0.30$ were adopted.

No mechanical properties of the rock were known at the moment of performing the WST and no additional tests, such compression tests, were performed. Therefore, the mechanical parameters used int he simulations had to be obtained by fitting the experimental WST curves presented in the next Section.

4 NUMERICAL AND EXPERIMENTAL RESULTS

4.1 Specimen 1 - Unstable fracture

The $P_H - COD$ curve obtained from the first tested specimen (Specimen 1) is plotted in gray in Fig. 4. This specimen, with a ligament length of $L = 34.5$ mm and a ligament depth of $D = 90$ mm, developed an unstable fracture propagation as it can be inferred from the abrupt load drop in the $P_H - COD$ curve after peak. This behavior suggests that the stiffness relation between the testing machine and the specimen was not high enough to guarantee a stable fracture process. For the following specimen, not being possible to increase the stiffness of the machine, it was decided to reduce the stiffness of the specimen by reducing the length of the ligament (L).

In order to illustrate the beneficial effect of reducing L on the fracture stability, Fig. 4 shows some $P_H - COD$ of curves obtained from the simulations performed with tentative mechanical parameters of the rock for different L values, together with the experimental results. The red curve, corresponding to a ligament length equal to the one of Specimen 1, exhibits a snapback behavior, which explains the unstable load drop of the experimental curve. As the ligament length is reduced, the snapback is reduced until it completely disappears.The results suggested that a ligament length of about 20 mm would assure a stable fracture process.

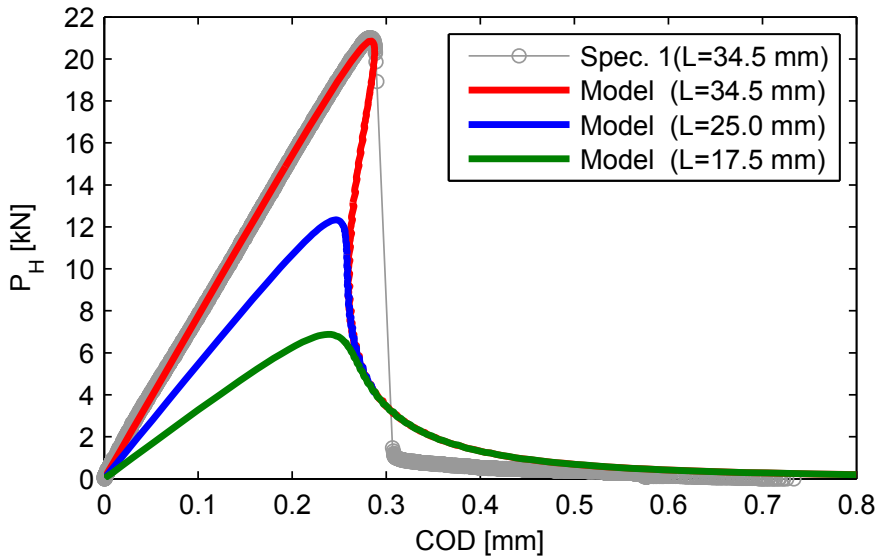

Figure 4: $P_H - COD$ curve from experimental WST of Specimen 1 and from model simulations performed with different ligament lengths L. All the curves are normalized to a specimen depth of 1000 mm.

4.2 Specimen 2 - Stable fracture

Specimen 2 was tested with a ligament length of 19.5 mm. As predicted, the $P_H - COD$ curve obtained (Fig. 5) indicates a stable fracture process. The specific fracture energy (G_f^I) measured was 52.9 N/m.

Finally, the experimental WST on Specimen 2 was numerically simulated using the measured value of G_f^I. The tensile strength (f_t) and the elastic modulus of the rock (E) were adjusted by trial and error to 10 MPa and 45 GPa, respectively, in order to fit the experimental $P_H - COD$ curve, as it is shown in Fig. 5.

5 CONCLUDING REMARKS

- Numerical modelling of experimental WST has helped to interpret failed results and to solve the underlying problems. Additionally, it has allowed to indirectly estimate other mechanical parameters of the rock (E, f_t) besides the specific fracture energy.

- More WST are needed in order to assess the statistical reliability of the measured G_f^I value reported.
- Standard uniaxial and triaxial tests would be also desirable in order to verify the values estimated from retrofitting of numerical simulations.

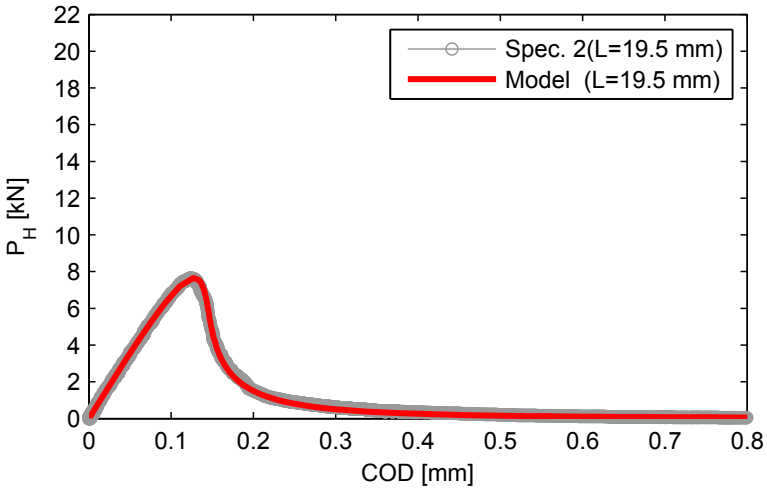

Figure 5: $P_H - COD$ curves from rock specimens obtained experimentally and from numerical simulation. Results are normalized to a specimen depth of 1000 mm.

ACKNOWLEDGEMENT

This work was partially supported by research grant BIA2016-76543-R from MEC (Madrid), which includes European FEDER funds and by AGAUR / Generalitat de Catalunya (Barcelona) through project 2014SGR-1523. The support from REPSOL for this research is also gratefully acknowledged. The third author also acknowledges AGAUR for her FI doctoral fellowship.

REFERENCES

[1] Brühwiler, E. and Wittmann, F. The wedge splitting test, a new method of performing stable fracture mechanics tests. *Engineering Fracture Mechanics* (1990) **35**(1):117–125.

[2] Saouma, V., Broz, J., Brühwiler, E. and Boggs, H. Effect of aggregate and specimen size on fracture properties of dam concrete. *J. Mater. Civ. Eng.* (1991)(3):204–218.

[3] Kumar, S. and Barai, S.V., *Concrete fracture models and applications*. Springer Science & Business Media (2011).

[4] Carol, I., Prat, P. and López, C.M., Normal/Shear Cracking Model: Application to Discrete Crack Analysis. *Journal of Engineering Mechanics* (1997) **123**(8):765–773.

[5] Liaudat, J., Garolera, D., Martínez, A., Carol, I., Lakshmikantha, M.R. and Alvarellos, J. Numerical modelling of the Wedge Splitting Test in rock specimens, using fracture-based zero-thickness interface elements. In: Oñate E., Owen D.R.J., Peric D., Chiumeti M. (eds), *XIII International Conference on Computational Plasticity - Fundamentals and Applications*. CIMNE, Barcelona (2015), pp 974-981.

XIV International Conference on Computational Plasticity. Fundamentals and Applications
COMPLAS 2017
E. Oñate, D.R.J. Owen, D. Peric and M. Chiumenti (Eds)

BOUNDED RATE DAMAGE PLASTIC MODEL FOR CONCRETE FAILURE UNDER IMPULSIVE LOADINGS

DANIEL GUILBAUD[*a,b]

* a DEN-Service d'études mécaniques et thermiques (SEMT), CEA, Université Paris-Saclay,
F-91191, Gif-sur-Yvette, France
* b IMSIA, EDF, CEA, CNRS, ENSTA Paris Tech, Université Paris Saclay,
828 Boulevard des Maréchaux, 91762 Palaiseau Cedex, France
e-mail: daniel.guilbaud@cea.fr

Key words: Concrete, Damage, Bounded rate, Mesh objectivity.

1 INTRODUCTION

This paper deals with the objective prediction of cracks in concrete structures within the framework of a local constitutive model. To reach this goal, it is necessary to overcome mesh dependency due to the softening of concrete. The constitutive law for concrete is an isotropic damage plastic model already described in [1]. The model has been introduced in EUROPLEXUS, a general finite element explicit code for fast transient analysis. The Hilleborg method used to maintain constant fracture energy regardless of element size is not able to deal with mesh-induced directional bias. In some cases, this leads to wrong failure mechanisms of the structure and to false ultimate load. Non-local models by their implicit nature are not adapted to explicit code and adversely affect its performance. This is the reason why the bounded rate concept presented in [2] has been introduced in the model. From a physical point of view, the basic idea is that the damage rate is finite because the cracking velocity is not instantaneous and from a mathematical point of view it was demonstrated in [2] that the problem remains well posed as long as damage rate is bounded and the damage not too close to 1.

After a short theoretical overview of the model, numerical implementation and calibration procedure are succinctly described, and then comparisons with tests are presented.

2 THEORETICAL OVERVIEW

The DPDC model belongs to the wide family of phenomenological concrete models. It is an isotropic damage plastic model for concrete failure. The plastic part is based on stress of the undamaged state of the material (named effective stress) and the damage part is based on total strains. The behaviour of concrete is elastic until the yield surface is reached. The initial damage threshold surface is identical to the shear yield surface. This kind of concrete model is widely used because plasticity and damage are simply coupled and it mathematically leads to

a well posed problem. Furthermore, calibration procedure of parameters is relatively easy to deal with.

Experiments show an increase of concrete strength as strain rate increases, both in tension and in compression. In the model described here, this phenomenon is taken into account as follows: plasticity is replaced by viscoplasticity to allow stress state to lie outside the yield surface and damage rate is bounded to produce a viscous regularization.

1.1 Elasto-viscoplastic formulation

The elasto-viscoplastic formulation is an extension of the commonly used Duvaut-Lions model described in [3]. Simo postulated that the elasto-viscoplastic strain rate is given by:

$$\dot{\varepsilon}^{vp} = C^{-1} : \frac{1}{\eta}\left(\sigma^{vp} - \sigma^{ep}\right) \tag{1}$$

where he introduced η called the "fluidity parameter" (physically, η is a time constant which could be related to crack propagation). σ^{ep} is the elastoplastic stress and σ^{vp} the elasto-viscoplastic stress, and C the Hooke's tensor. The viscoplastic stress rate:

$$\dot{\sigma}^{vp} = C : \left(\dot{\varepsilon} - \dot{\varepsilon}^{vp}\right) = C : \dot{\varepsilon} - \frac{1}{\eta}\left(\sigma^{vp} - \sigma^{ep}\right)$$

is replaced by the first order accurate formulae thanks to an Euler backward scheme:

$$\frac{\Delta\sigma^{vp}_{n+1} - \Delta\sigma^{vp}_{n}}{\Delta t} = C : \frac{\Delta\varepsilon}{\Delta t} - \frac{1}{\eta}\left(\sigma^{vp}_{n+1} - \sigma^{ep}_{n+1}\right) \tag{2}$$

where Δt is the current time step.

From which we finally obtain:

$$\sigma^{vp}_{n+1} = \frac{\sigma^{vp}_{n} + C : \Delta\varepsilon + \frac{\Delta t}{\eta}\sigma^{ep}_{n+1}}{1 + \frac{\Delta t}{\eta}} = \frac{\eta\sigma^{vp}_{trial} + \Delta t\sigma^{ep}_{n+1}}{\eta + \Delta t} \tag{3}$$

Then, the next step is to provide a fit between the fluidity coefficient η and the strain rate. The fluidity coefficient η varies with strain rate according to the generic expression below:

$$\eta = \eta_{0i}(\hat{\dot{\varepsilon}} / \dot{\varepsilon}_{0i})^{-n_i} \tag{4}$$

where n_i, η_{0i}, $\dot{\varepsilon}_{0i}$ are input parameters and $\hat{\dot{\varepsilon}}$ is a measure of the strain rate defined as follows:

$$\hat{\dot{\varepsilon}} = Max(\dot{\varepsilon}^{d}, \dot{\varepsilon}_{V} / 3) \tag{5}$$

where :

$$\dot{\varepsilon}^{d} = \frac{\varepsilon^{d}_{n+1} - \varepsilon^{d}_{n}}{\Delta t}$$

$$\dot{\varepsilon}_V = (tr\Delta\varepsilon)/\Delta t$$

with $\varepsilon_i^d = \sqrt{\frac{1}{2}\left[\left(\varepsilon_{xx}-\varepsilon_{yy}\right)^2+\left(\varepsilon_{yy}-\varepsilon_{zz}\right)^2+\left(\varepsilon_{zz}-\varepsilon_{xx}\right)^2+6(\varepsilon_{xy}^2+\varepsilon_{yz}^2+\varepsilon_{xz}^2)\right]_i}$ $\quad i\in[n,n+1]$

ε_i^d is a measure of the deviatoric strain rate and $\dot{\varepsilon}_V$ is the volumetric strain rate, the latter being introduced to have a strain rate in tri-tension.

Two distinct fluidity parameters are used: these are the fluidity parameters in uniaxial tensile stress η_t and uniaxial compressive stress η_c. η_t and η_c are defined according to equation (4), but with different input parameters for each.

$$\eta_t = \eta_{0t}\left(\dot{\hat{\varepsilon}}/\dot{\hat{\varepsilon}}_0\right)^{-n_t} \quad \eta_c = \eta_{0c}\left(\dot{\hat{\varepsilon}}/\dot{\hat{\varepsilon}}_0\right)^{-n_c} \tag{6a&b}$$

In both cases, $\dot{\hat{\varepsilon}}_0$ is chosen equal to 1 s^{-1}. Default values of the four parameters: η_{0t}, η_{0c}, n_t and n_c have to be identified on experimental correlations of Dynamic Increased Factors.

For triaxial stress cases, the fluidity parameter η used in equation (3) is interpolated between tensile and compressive fluidity parameters as a function of the viscoplastic stress triaxiality $T_x^{vp} = J_1/\sqrt{3J_2}$ as follows:

$$\eta = (1-H(T_x^{vp}))\left[\eta_t + \min(1,\langle -T_x^{vp}\rangle)(\eta_c-\eta_t)\right] + H(T_x^{vp})\eta_t \tag{7}$$

when $-1 < T_x^{vp} < 0$. $\langle X\rangle = X \; if \; X>0, else \; 0$ is the Macaulay brackets and H is the Heaviside function.

1.2 The bounded rate model

The bounded rate model is described in [2]. From a physical point of view, the basic idea is that the damage rate is finite because the cracking process is not instantaneous (the crack velocity is finite) and from a mathematical point of view it was demonstrated that the problem remains well posed as long as damage rate is bounded and the damage is not too close to 1.

The damage rate $\dot{d}$ is asymptotically bounded thanks to the following expression:

$$\dot{d} = \dot{d}_\infty\left(1-e^{-b\langle d^s-d\rangle}\right) \tag{8}$$

where: $\dot{d}_\infty$ stands for the maximum damage rate, d^s is the static damage i.e. calculated without rate effect, d is the damage and b is a parameter.

When the argument of the exponential term is much smaller than one, the damage rate can be approximated by:

$$\dot{d} \simeq b\dot{d}_\infty\langle d^s-d\rangle = \frac{\langle d^s-d\rangle}{\mu} \tag{9}$$

This formula is that provided by simple delay damage model; see for example [4]. Expression (9) shows that the product $b\dot{d}_\infty$ is the inverse of a time constant μ. As shown by parametrical studies, it was important to maintain this product constant so b is replaced by μ that turns to be the new parameter of the model.

Implementation of the model is easy. First, the time derivative of (8) is calculated and expressed as follow:

$$\ddot{d} = b(\dot{d}_s - \dot{d})(\dot{d}_\infty - \dot{d})$$

Then, as in viscoplasticity, an Euler backward scheme leads to the first order accurate formulae:

$$\frac{\dot{d}_{n+1} - \dot{d}_n}{\Delta t} = b(\dot{d}^s_{n+1} - \dot{d}_{n+1})(\dot{d}_\infty - \dot{d}_{n+1}) \tag{10}$$

So, it remains to solve the second order equation:

$$\dot{d}^2_{n+1} - \left(\dot{d}_\infty + \dot{d}^s_{n+1} + \frac{1}{b\Delta t}\right)\dot{d}_{n+1} + \dot{d}^s_{n+1}\dot{d}_\infty + \frac{\dot{d}_n}{b\Delta t} = 0$$

from which the solution gives an explicit expression of damage rate at each time increment:

$$\dot{d}_{n+1} = \frac{1}{2}\left((\dot{d}_\infty + \dot{d}^s_{n+1} + \frac{1}{b\Delta t}) - \sqrt{(\dot{d}_\infty + \dot{d}^s_{n+1} + \frac{1}{b\Delta t})^2 - 4(\dot{d}^s_{n+1}\dot{d}_\infty + \frac{\dot{d}_n}{b\Delta t})}\right) \tag{11}$$

Damage at time step $n+1$ is finally obtained by integrating the damage rate over the time step:

$$d_{n+1} = d_n + \dot{d}_{n+1}\Delta t \tag{12}$$

Brittle damage accumulation law is given by the linear law:

$$d^s(\tau) = d_{max}A^{bs}(\tau - \tau_0) \; for \; \tau \le \tau_{\max} \mid A^{bs}(\tau_{\max} - \tau_0) \le 1 \tag{13}$$

Brittle fracture energy is equal to the area under the stress-displacement curve after reaching the strength in tension and that gives the value of the shape parameter A^{bs}:

$$A^{bs} = \frac{\tau_0 L_{ch}}{2G^b_f} \tag{14}$$

where L_{ch} is the 'crack band width' of the integration domain also called the concrete characteristic length. Thanks to an equivalent interpretation due to [5], this parameter is the ratio of the specific energy per unit of volume g^b_f dissipated during the deformation to the fracture energy per unit of area G^b_f:

$$L_{ch} = G^b_f / g^b_f \tag{15}$$

Within this model, damage is no longer localized in a single element but is spread over the concrete characteristic length. In [6], authors proposed to choose L_{ch} within the range $\left[3D_{agg}, 5D_{agg}\right]$ where D_{agg} is the maximum aggregate size. Nevertheless, there is no consensus on this subject. For example, in [7], when studying calibration of concrete model on three sizes of concrete beams, the author obtained the better fit with a much larger value (x3). So, L_{ch} is a parameter of the model to be calibrated such as μ and $\dot{d}_{\infty}$.

With increasing deformation rate, damage is spread out over a larger band than L_{ch}. Of course, the size of the mesh should be such that several elements are inside the band in order to have an adapted discretization (see Figure 3). Conversely, with decreasing deformation rate, damage is localized on a narrow band. Therefore a very fine mesh is required to avoid mesh dependency and, in practice, if the strain rate is too low, the bounded rate model is ineffective to regularize. Indeed, parametric studies have shown that regularization is obtained only when the following condition: $\dot{d}^s > \dot{d}_{\infty}$ is fulfilled.

To avoid introducing a new parameter, μ could be taken as the fluidity parameter η which is consistent with the definition of the shifted damage threshold (eq. 9). The fluidity parameter η is nevertheless not constant but as it varies more slowly than damage, the previous implementation of the model is still relevant.

3 EVALUATION TESTS

After a single element test used to check the implementation of the bounded rate model within the DPDC constitutive law, two other tests are presented: the first one is an indirect tension test and the second a three-point bending test on an impacted notched beam.

3.1 Single element test

A cubic element is loaded in uniaxial tension along the z axis with a constant strain rate $\dot{\varepsilon}_{zz}$ = 100 s^{-1}. Default parameters values are used for the bounded rate model: L_{ch} = 0.01 m and $\dot{d}_{\infty} = 10^4$ s^{-1}. The element length of the cube is L = 0.001 m, one tenth of L_{ch}.

For this simple case, the initial damage threshold and the current thresholds read:

$$\tau_0^b = \left[\sqrt{E}\varepsilon_{\max}^{princ}\right]_{\text{when the shear failure is reached at } t=t_p \text{ and } \varepsilon_{\max}^{princ}>0} = \sqrt{E}\dot{\varepsilon}_{zz}t_p$$

$$\tau^b = \sqrt{E}\varepsilon_{max}^{princ} = \sqrt{E}\dot{\varepsilon}_{zz}t$$

Then, the static damage is given by equations (13) and (14):

$$d^s(\tau) = d_{max}A^{bs}(\tau-\tau_0) = \frac{\tau_0 L_{ch}}{2G_f^b}\sqrt{E}\dot{\varepsilon}_{zz}(t-t_p) = \frac{f'_t L_{ch}}{2G_f^b}\dot{\varepsilon}_{zz}(t-t_p) \; for \; t > t_p$$

from which the static damage rate is deduced: $\dot{d}^s(\tau) = \frac{f'_t L_{ch}}{2G_f^b}\dot{\varepsilon}_{zz}$. The numerical application

gives: $\dot{d}^s(\tau) = 2.64\ 10^4\ s^{-1}$ in agreement with the calculation as can be verified on Figure 1 showing static and dynamic damage. The third parameter: $\mu = \eta$ affects the nonlinear part of the dynamic damage evolution (until the maximum damage rate is reached).

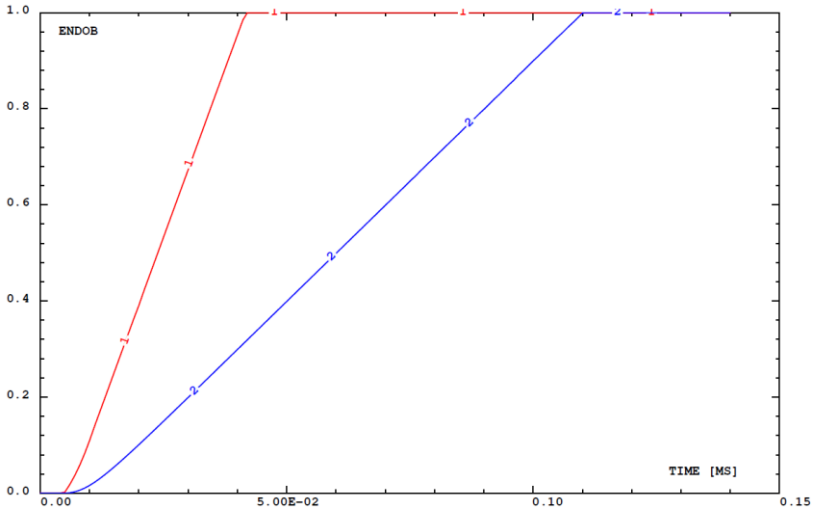

Figure 1: Static damage (in red) and dynamic damage (in blue) for tension loading at a strain rate $\dot{\varepsilon}_{zz}$ = 100 s^{-1}.

Stress time histories σ_{zz}(t) within the bounded rate model are plotted on Figure 2. It can be seen that the transition between hardening and softening is smooth which is favorable to avoid localization.

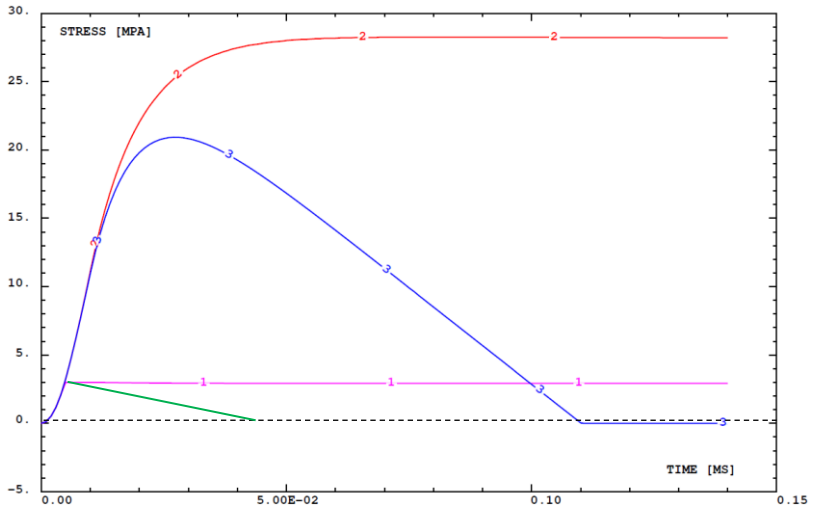

Figure 2: Stress time histories for a tension test at a strain rate $\dot{\varepsilon}_{zz}$ = 100 s^{-1}.
(Plastic stress is colored in pink, viscoplastic stress in red, final stress in blue and final static stress in green.)

3.2 Dynamic Brazilian test

The test in tension is a Brazilian one in which a vertical compressive load is applied diametrically to a cylindrical specimen by mean of two thin strip bearings between the sample and the steel plates. The cylinder is 7 cm high and 7 cm in diameter (B = 7 cm, D = 7 cm). The mean element size is 1.25 mm. The characteristic data used for concrete are: E_c = 26.4 GPa, ν_c = 0.2, ρ_c = 2400 kg/m^3, f'_c = 30 MPa and $Dagg$ = 1.0 cm. All others parameters are default values given by the DPDC model, so f'_t = 3 MPa, L_{ch} = 1 cm and $\dot{d}_\infty = 10^4$ s^{-1}.

The bearings are modelled with an elastic material whose elastic properties are the same as the concrete. Perfect bond is assumed between the bearings and the specimen. The bottom steel plate is blocked and the upper one moved downward with a speed of 20 cm/s.

To study mesh bias, the mesh is not aligned with the crack, but is rotated by about thirty degrees counter-clockwise.

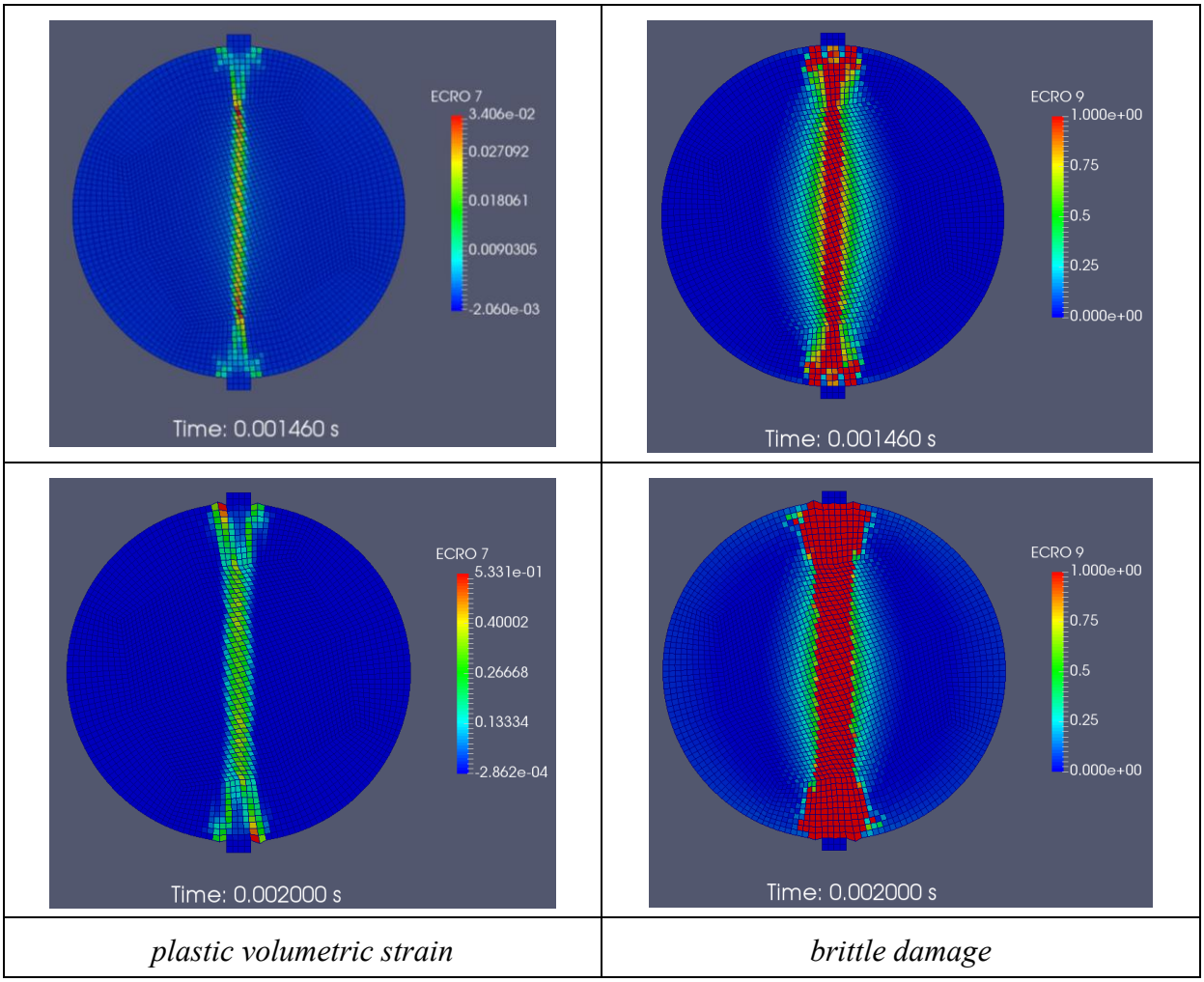

Figure 3: Damage patterns for the Brazilian test.

The plastic volumetric strain which is a good marker of cracks, and the brittle damage are plotted on Figure 3. It can be seen that both are vertical so no mesh bias is noticeable.

The first instant is the one for which damage reached one along the entire vertical plane. Damage is not localized but varies smoothly within a vertical band. At the end of the simulation, this is no longer true, because the complete damaged zone (where d^b =1, in red on Figure 3) has gained ground on the intermediate damaged zone. Simultaneously, the crack width has increased.

Vertical force time history and equivalent tension stress versus vertical displacement of bearings are drawn on Figure 4. The tensile stress decreases toward zero without any artificial rebound. The simulation gives σ_t = 5.2 MPa and the dynamic increase factor is *DIF* = 1.73 in reasonable agreement with the tabulated values.

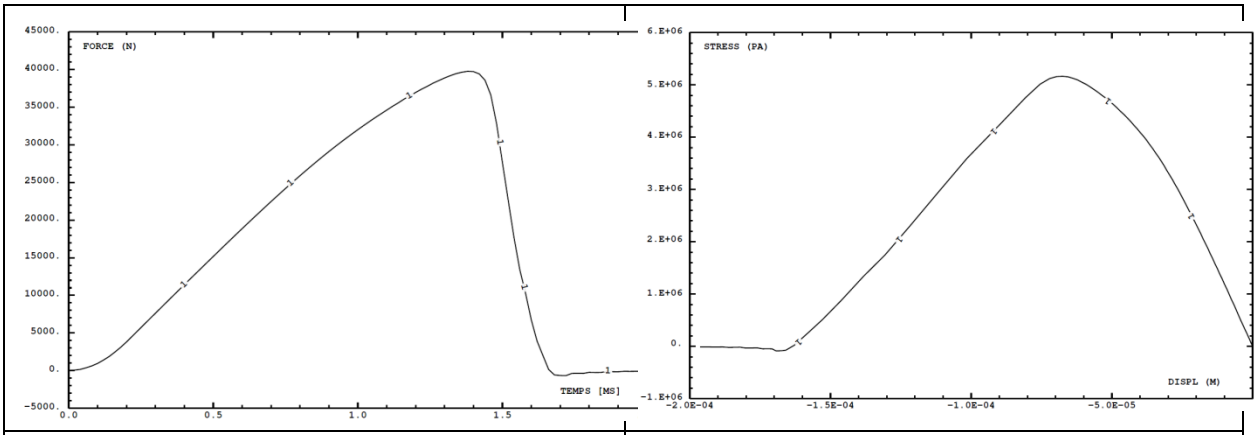

Vertical force time history | *Equivalent tension stress versus displacement*

Figure 4: Strengths obtained with the bounded rate model.

3.3 Dynamic three-point bending tests on notched beams

Zhang's results about the fracture behavior of high-strength concrete at a wide range of loading rates are used to test the bounded rate model [8]. Dynamic tests were performed with a drop-weight impact machine.

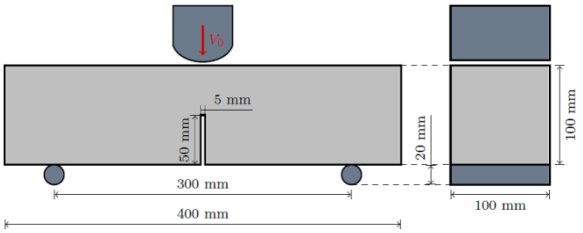

Figure 5: Geometry of specimen.

Three-point bending tests on notched beams were carried out as sketched on Figure 5 where the dimensions of the tested beam are given. The mass of the hammer is 120.6 kg.

Mechanical properties of concrete and steel for the hammer and the support rollers are gathered in Table 1 and Table 2 respectively. Here, the following values have been used: L_{ch} = 1 cm (the maximum size of aggregates is 1.2 cm) and $\dot{d}_{\infty}$ = 2 10^3 s^{-1}. These low values have been chosen to favor regularization and to fit with the highest velocity of the hammer.

Table 1: Mechanical properties of the high-strength concrete.

ρ (kg/m^3)	E (GPa)	ν	f_c (MPa)	f_t (MPa)	G_f (J/m^2)
2400.	43.3	0.18	105.	6.3	148.

Table 2: Mechanical properties of steel.

E (GPa)	ν
200	0.33

3.3.1 Mesh objectivity

Three element sizes are used for the meshes: L = 5 mm, L = 1.66 mm and L = 1 mm. Furthermore, to study mesh bias, the region of the mesh where the crack develops is not aligned with the crack, but is rotated by about thirty or seventy degrees clockwise. In these last cases, the element size is L = 1.66 mm.

Brittle damage and plastic volumetric strain obtained with the various meshes when the initial velocity of the hammer is V_{0ham} = 1.76 m/s are shown on Figure 6. In all cases, the brittle damage zone is almost the same whatever the size of the mesh and its orientation relative to the crack. Nevertheless, the plastic volumetric strain reveals two parallel cracks which is surprising. As the bifurcation occurs at the notch root, an area of stress concentration, the bounded rate model is suspected to be not suitable for zones of strong stress gradient.

Reaction force time histories and internal energy time histories are plotted on Figure 7. The results are not identical but the discrepancies introduced by the meshes seem reasonable.

3.3.1 Comparison with the experiments

Reaction forces are plotted against loading point displacement of the notched beams for the two highest velocities of the hammer (see Figure 8). Due to the fit, the agreement for the test with the highest velocity is good, but the agreement is lost for the other tests.

The maximum of reaction forces and the apparent fracture energies are gathered in Table 3. It can be verified that the accuracy of the results decreases with the loading rate. Consequently, a single set of coefficient $\dot{d}_{\infty}$ seems not able to reproduce strain rate effect.

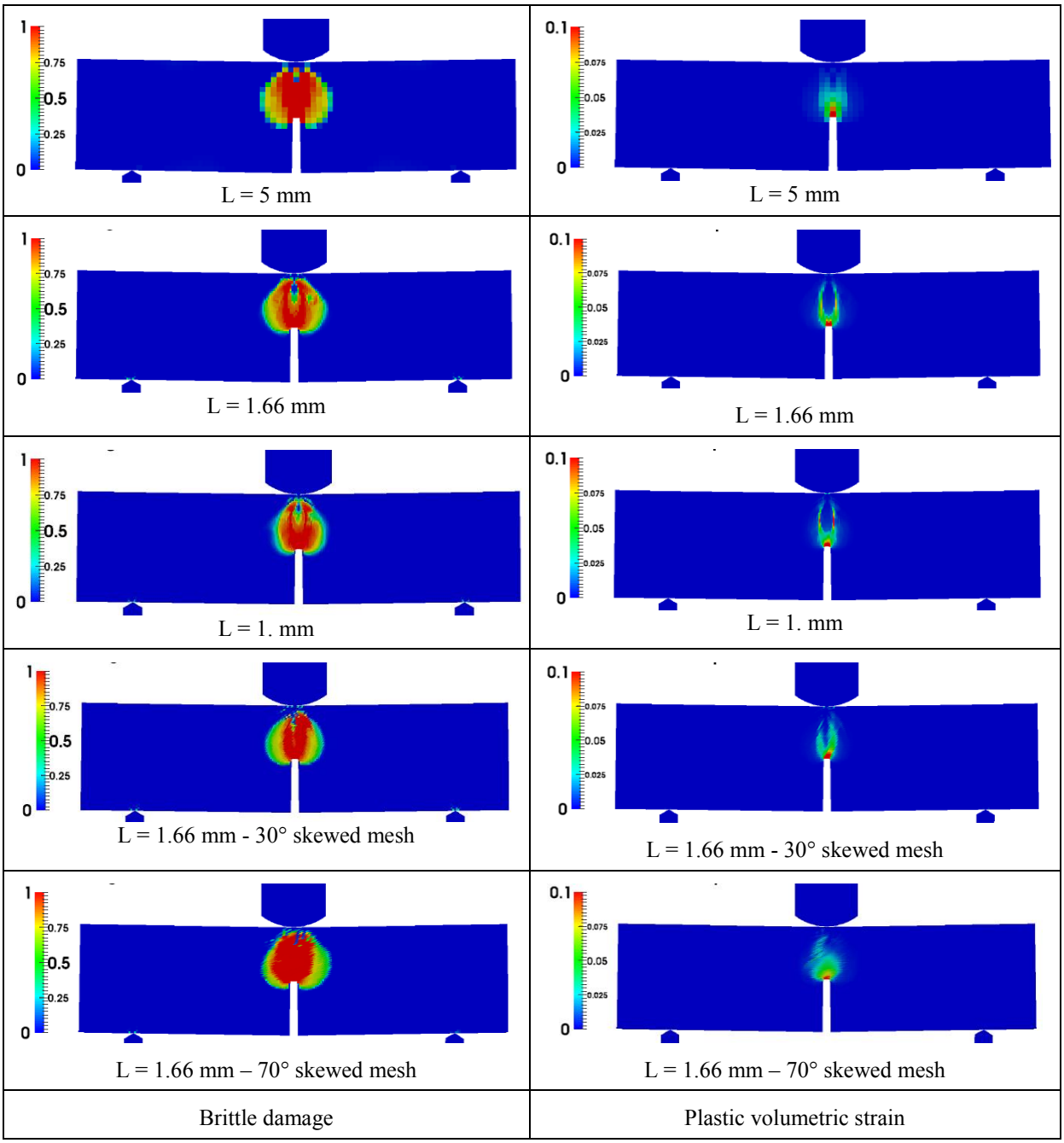

Figure 6: Damage patterns of the impacted notched beam – V_{0ham} = 1.76 m/s.

Table 3: Comparison between experiments and model.

V_{0ham} (m/s)	0.88	1.76	2.64		V_{0ham} (m/s)	0.88	1.76	2.64
Max. of reaction force (kN) - test	21.9	34.7	38.0		G_f (J) -test	6.0	16.8	33.6
Max. of reaction force (kN)- model	17.9	28.4	34.5		G_f (J) -model	6.9	18.4	32.4

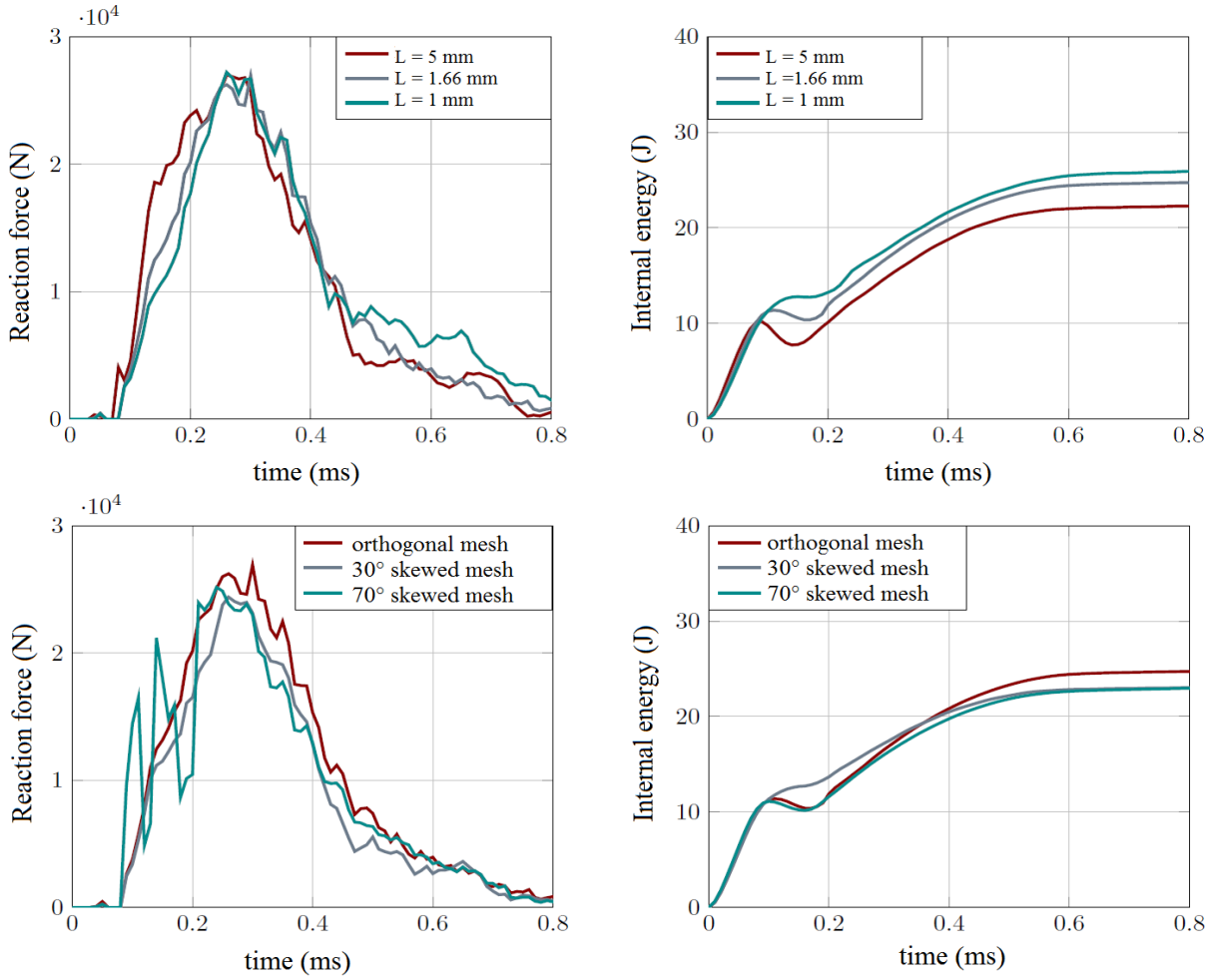

Figure 7: Reaction force and internal energy of the impacted notched beam – V_{0ham} = 1.76 m/s.

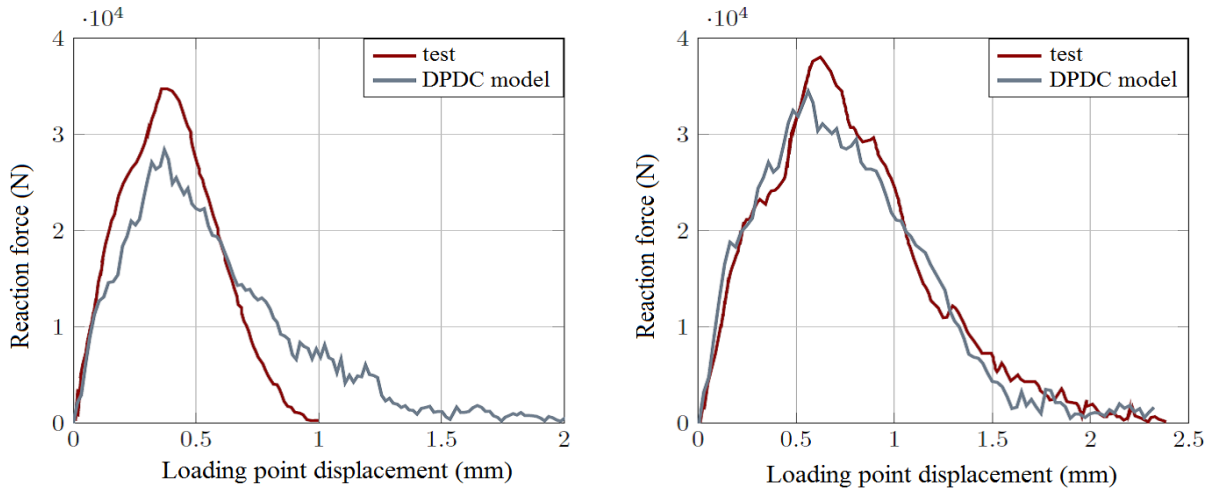

Figure 8: Reaction forces versus loading point displacement (left: V_{0ham} = 1.76 m/s, right: V_{0ham} = 2.64 m/s).

4 CONCLUSIONS

The model is very easy to implement because it leads to an explicit expression of the rate of damage at each time increment.

The new model has been verified on skewed mesh (relatively to crack) and compared to experimental results of the literature: an impacted notched beam [8] loaded at relatively moderate rates ($\simeq$ 1 m/s). It was shown that the bounded rate model regularizes deformations when the strain rate is larger than 1 s^{-1} and the mesh size about 1 mm. In that case, damaged zones are almost mesh-independent in size and orientation. Nevertheless, crack pattern revealed by the plastic volumetric strain is not satisfactory because it does not match with a single crack. So, the bounded rate model is suspected to be not suitable for zone of strong stress gradient such as notch tip.

Furthermore, calibration on these experiments has not led to a universal set of coefficients yet. So, a large amount of investigation remains to be done to broaden the loading rate range, to precise the lower bound rate that maintains regularization for a given mesh size, and to find a formulation with a single set of parameters.

REFERENCES

[1] D. Guilbaud, Damage plastic model for concrete failure under impulsive loadings, COMPLAS XIII (2015).
[2] O. Allix, The bounded rate concept: A framework to deal with objective failure predictions in dynamic within a local constitutive model, International Journal of Damage Mechanics 0(0), pp. 1-21, (2012).
[3] J.C. Simo, J.G. Kennedy, S. Govindjee, Non-smooth multisurface plasticity and visco-plasticity, loading / unloading conditions and numerical algorithms, Int. J. for Numerical Methods in Engineering, Vol. 26, pp. 2161-2185, (1988).
[4] A. Genikomsou, M. A. Polak , Finite element analysis of punching shear of concrete slabs using damaged plasticity model in ABAQUS, Engineering Structures 98, pp. 38-48, (2015).
[5] J. Oliver, A consistent characteristic length for smeared cracking models, Int. J. for Numerical Methods in Engineering, vol. 28, pp. 461-474, (1989).
[6] Z.P. Bazant and G. Pijaudier-Cabot, Measurement of the characteristic length of non-local continuum, J. of Engineering Mechanics, ASCE, Vol. 115, pp.755-767, (1989).
[7] Dubé J.F., Identification des paramètres d'un modèle de comportement pour les structures en béton, Mémoire d'Habilitation à Diriger les Recherches, Université de Montpellier II, (2005).
[8] X. Zhang, G. Ruiz, R. Yu and M. Tarifa, Fracture behavior of high-strength concrete at a wide range of loading rates, International Journal of Impact Engineering, 36(10-11), pp. 1204-1209, (2009).

XIV International Conference on Computational Plasticity. Fundamentals and Applications
COMPLAS XIV
E. Oñate, D.R.J. Owen, D. Peric & M. Chiumenti (Eds)

DUCTILE FRACTURE SIMULATIONS USING A MULTI-SURFACE COUPLED DAMAGE-PLASTICITY MODEL

D. REDDI† AND S. M. KERALAVARMA

Department of Aerospace Engineering
Indian Institute of Technology Madras, Chennai 600036, India
†e-mail: dheereshreddi@gmail.com

Key words: Ductile Fracture, Void Growth, Void Coalescence, Shear Failure

Abstract. In this paper, an isotropic porous metal plasticity model accounting for both void growth by diffuse plastic deformation and void 'coalescence' by localization of plastic flow in the inter-void ligaments is presented. Predictions for the effective stress-strain response, evolution of damage and the strains to failure are obtained by integrating the model numerically under triaxial proportional loading conditions. The model predictions are compared with results from micromechanical finite element simulations of the average response of voided unit cells under similar loading conditions. It is shown that the model predictions for the failure strains as a function of the loading path are in good qualitative agreement with the results of the cell model simulations.

1 INTRODUCTION

Fracture of ductile materials is usually preceded by the localization of plasticity in a failure process zone such as a diffuse neck or a shear band. Material separation occurs by the growth and coalescence of micro-voids inside the process zone that initiate from second phase particles or inclusions [1]. Both the condition for the onset of plastic instabilities and the rate of crack growth within the localization zone are strongly influenced by the local state of stress. Void growth by diffuse plastic flow around the voids depends on the relative magnitude of the hydrostatic stress, while void coalescence occurs due to plastic collapse of the ligament separating neighboring voids, which depends on the ligament thickness and stress components in the transverse plane of the ligament. Denoting the stress state via two commonly used non-dimensional parameters, the stress triaxiality, T, defined as the ratio of the mean and Von Mises effective stresses and the Lode parameter, L, proportional to the determinant of the deviatoric stress, void growth by diffuse plastic flow depends only on T, while void coalescence in general depends on both T and L. Predictive modeling of ductile fracture therefore requires a physics-based plasticity model that not only accounts for the effect of the loading path on the damage growth rates, but also the condition for the onset of void coalescence and consequent rapid softening due to transitions in the deformation mode at the micro-scale.

Micromechanics-based plasticity models have been developed since the late 60's to predict the evolution of plastic strains and damage in a porous ductile material in the pre-coalescence phase [2, 3]. The Gurson model [3] in particular has been successfully used to predict several experimental features of ductile fracture [4–6] using a heuristic criterion for the onset of coalescence proposed by Tvergaard and Needleman [4]. In the Gurson-Tvergaard-Needleman (GTN) model, void coalescence is assumed to initiate once the porosity reaches a critical value. When the critical porosity is exceeded, the damage growth rate is accelerated to simulate the rapid material degradation as observed in finite element simulations of void growth using the unit cell model. However, a major limitation of the above phenomenological approach is that both the critical porosity for the onset of coalescence and the form of the post-coalescence damage evolution law are calibrated based on cell model simulations using a limited set of loading paths; mainly axisymmetric loadings. Importantly, predictions for the ductility obtained using the GTN model under proportional loading conditions depend only on the stress triaxiality T and are independent of the Lode parameter L.

While the major influence of the stress triaxiality parameter on the ductility has been understood for a long time, both experimentally [7] and computationally [8], the importance of the Lode parameter has only been appreciated recently, with the publication of experimental data that appears to suggest that the ductility under low triaxiality loading (typically $T < 1$) depends on the Lode parameter with significantly lower ductilities predicted under shear dominated loadings compared to axisymmetric loadings at higher triaxialities [9, 10]. Subsequently, several authors have investigated further the effect of the Lode parameter on the strains to the onset of void coalescence at the micro-scale using three-dimensional cell model simulations of void growth under combined axisymmetric and shear loading [11–13]. A significant reduction in ductility has been consistently observed in these simulations under shear dominated loadings. These results clearly establish that the critical porosity criterion in the GTN model needs to be replaced with a stress-based criterion that includes the observed effect of the Lode parameter L on the onset of coalescence, since the value of L allows to distinguish between axisymmetric and shear dominated loadings at the same triaxiality.

In the past few years, several authors have attempted to develop such models by extending the Thomason [14] model for void coalescence by internal necking to account for coalescence under combined tension and shear [15–17]. Most recently, Keralavarma [18] proposed a multi-surface plasticity model for void growth and coalescence in an isotropic material by combining the Gurson [3] void growth model with the void coalescence model of Keralavarma and Chockalingam [17], appropriately extended to account for arbitrary orientations of the coalescence band. The objective of this paper is to examine predictions for the material's intrinsic ductility as a function of the applied loading path predicted by the above multi-surface model under proportional loading conditions, and to compare the predicted trends with those observed in recent cell model simulations under combined tension and shear [11–13]. A brief summary of the model is presented in section 2, followed by comparison of the model predictions with two-dimensional axisymmetric cell model simulations and predictions from the GTN model in section 3.1. Finally, predictions for the variation of the material's ductility under general proportional loadings as a function

of the loading path parameters T and L are presented and discussed in section 3.2.

2 MULTI-SURFACE POROUS PLASTICITY MODEL

Consider an elasto-plastic Von Mises material containing a random distribution of equiaxed voids at the micro-scale. Assuming a dilute volume fraction of voids with porosity $f \ll 1$, the yield stress of a macroscopic material element may be predicted using the Gurson [3] yield criterion

$$\mathcal{F}^G(\boldsymbol{\Sigma}) \equiv \frac{\Sigma_{\text{eq}}^2}{\bar{\sigma}^2} + 2qf\cosh\left(\frac{3}{2}\frac{\Sigma_{\text{m}}}{\bar{\sigma}}\right) - 1 - (qf)^2 = 0 \tag{1}$$

where $\boldsymbol{\Sigma}$ is the macroscopic stress tensor, $\Sigma_{\text{m}} = \frac{1}{3}\text{tr}(\boldsymbol{\Sigma})$ and $\Sigma_{\text{eq}} = \sqrt{\frac{3}{2}\boldsymbol{\Sigma}^{'} : \boldsymbol{\Sigma}^{'}}$ are the mean and Von Mises equivalent stresses respectively, $\boldsymbol{\Sigma}^{'}$ is the deviatoric stress, $\bar{\sigma}$ is the flow stress of the matrix material and q is a heuristic parameter introduced by Tvergaard [19]. Capital symbol $\boldsymbol{\Sigma}$ is used for the stress to emphasize the fact that $\boldsymbol{\Sigma}$ is the average stress tensor over a porous representative volume element (RVE) Ω; i.e. $\boldsymbol{\sigma} = \langle\boldsymbol{\sigma}\rangle_\Omega$ where $\boldsymbol{\sigma}$ is the Cauchy stress. The above yield function can be formally derived using limit analysis by assuming that plastic flow occurs in the entire RVE during yielding.

However, at finite values of the porosity, an RVE can also yield by localized plastic flow (coalescence) in a narrow band encompassing the ligaments connecting neighboring voids and band width equal to the void diameter. For a given orientation of the localization (or coalescence) band identified by the unit normal vector $\underline{n}$, Keralavarma and Chockalingam [17] derived the following yield function

$$\mathcal{F}^C(\boldsymbol{\Sigma}, \underline{n}) \equiv 3\frac{\Sigma_{\text{sh}}^2}{\bar{\sigma}^2} + 2f_b\cosh\left(\frac{\Sigma_{\text{n}}}{\Sigma^{\text{c}}}\right) - 1 - f_b^2 = 0 \tag{2}$$

where $\Sigma_{\text{n}} = \underline{n}\cdot\boldsymbol{\Sigma}\underline{n}$ and $\Sigma_{\text{sh}} = \sqrt{\underline{n}\cdot\boldsymbol{\Sigma}^2\underline{n} - \Sigma_{\text{n}}^2}$ are respectively the normal and shear stresses on the coalescence plane, $f_b = f^{2/3}$ and Σ^{c} is a critical stress given by

$$\Sigma^{\text{c}} = \bar{\sigma}\sqrt{\frac{6}{5}}\left[\sqrt{b^2+1} - \sqrt{b^2+f_b^2} + b\ln\left(\frac{b+\sqrt{b^2+f_b^2}}{f_b(b+\sqrt{b^2+1})}\right)\right]\left(\log\frac{1}{f_b}\right)^{-1} \tag{3}$$

with the parameter b given by

$$b = \sqrt{\frac{1}{3} + \frac{5}{288}\left(1 + \frac{1}{f_b} - 5f_b + 3f_b^2\right)} \tag{4}$$

Σ^{c} is a positive definite function of f_b that tends to infinity in the limit $f_b \to 0^+$, so that at dilute porosities, the yield surface defined by (2) falls outside the Gurson yield surface (1) for most loading paths. However for finite values of f (typically $f > \sim 0.01$), the yield stress predicted by the coalescence criterion can be lower than the Gurson value for several loading paths in stress space.

In a statistically isotropic material, the inter-void ligament dimensions are approximately the same along any material direction. Therefore, according to limit analysis

theory, coalescence occurs along the direction $\underline{n}$ that yields the smallest value of the yield stress or, equivalently, maximizes the coalescence yield function $\mathcal{F}^C$ in (2). Thus, the coalescence criterion for an isotropic material is written as

$$\mathcal{F}^{C^{\text{iso}}}(\boldsymbol{\Sigma}) \equiv \max_{\underline{n}} \mathcal{F}^C(\boldsymbol{\Sigma}, \underline{n}) = 0 \tag{5}$$

Performing the above maximization leads to the result that coalescence occurs either on one of the principal stress planes or on a non-principal plane $\underline{n}$ on which the normal stress Σ_{n} satisfies the following equation (see [18])

$$2\Sigma_{\text{n}} - \frac{2}{3}\frac{\bar{\sigma}^2}{\Sigma^c} f_b \sinh\left(\frac{\Sigma_{\text{n}}}{\Sigma^{\text{c}}}\right) = \Sigma_1 + \Sigma_2 \tag{6}$$

where Σ_1 and Σ_2 are two unequal principal stresses. Solving the above equation for every unequal pair of principal stresses yields the normal stresses on planes where shear assisted coalescence can occur, and the corresponding shear stress is found from the equation

$$\Sigma_{\text{sh}}^2 = \left(\frac{\Sigma_1 - \Sigma_2}{2}\right)^2 - \left[\Sigma_{\text{n}} - \left(\frac{\Sigma_1 + \Sigma_2}{2}\right)\right]^2 \tag{7}$$

The value of the isotropic coalescence function $\mathcal{F}^{C^{\text{iso}}}$ then corresponds to the maximum value of $\mathcal{F}^C$ over all $(\Sigma_{\text{m}}, \Sigma_{\text{sh}})$ pairs obtained above, and coalescence occurs when $\mathcal{F}^{C^{\text{iso}}} \geq 0$. Finally, combining the Gurson and the isotropic coalescence models using the same multi-surface approach, Keralavarma [18] proposed the following for the effective yield criterion for a porous isotropic material accounting for both void growth and coalescence

$$\mathcal{F}(\boldsymbol{\Sigma}) \equiv \max\left\{\mathcal{F}^G(\boldsymbol{\Sigma}), \mathcal{F}^{C^{\text{iso}}}(\boldsymbol{\Sigma})\right\} = 0 \tag{8}$$

The macroscopic plastic strain rate, $\mathbf{D}^p$, is obtained from the yield function via the normality property, which yields

$$\mathbf{D}^p = \dot{\lambda}\mathbf{N}, \qquad \mathbf{N} = \frac{\partial \mathcal{F}}{\partial \boldsymbol{\Sigma}} \tag{9}$$

where $\dot{\lambda}$ is the plastic multiplier and the direction of plastic flow $\mathbf{N}$ depends on the active yield surface, $\mathcal{F} = \mathcal{F}^G$ or $\mathcal{F}^C$. We have

$$\mathbf{N} = \begin{cases} 3\dfrac{\boldsymbol{\Sigma}'}{\bar{\sigma}^2} + q\dfrac{f}{\bar{\sigma}}\sinh\left(\dfrac{3}{2}\dfrac{\Sigma_{\text{m}}}{\bar{\sigma}}\right)\mathbf{I}, & \mathcal{F} = \mathcal{F}^G \\ \dfrac{3}{\bar{\sigma}^2}[\underline{n}\otimes\boldsymbol{\Sigma}\underline{n} + \boldsymbol{\Sigma}\underline{n}\otimes\underline{n} - 2\Sigma_{\text{n}}\underline{n}\otimes\underline{n}] + \dfrac{2f_b}{\Sigma^{\text{c}}}\sinh\left(\dfrac{\Sigma_{\text{n}}}{\Sigma^{\text{c}}}\right)\underline{n}\otimes\underline{n}, & \mathcal{F} = \mathcal{F}^C(\underline{n}) \end{cases} \tag{10}$$

The evolution of porosity follows from plastic incompressibility of the matrix, which yields

$$\frac{\dot{f}}{1-f} = \text{tr}(\mathbf{D}^p) = \begin{cases} \dot{\lambda}\dfrac{3f}{\bar{\sigma}}\sinh\left(\dfrac{3}{2}\dfrac{\Sigma_{\text{m}}}{\bar{\sigma}}\right), & \mathcal{F} = \mathcal{F}^G \\ \dot{\lambda}\dfrac{2f_b}{\Sigma^{\text{c}}}\sinh\left(\dfrac{\Sigma_{\text{n}}}{\Sigma^{\text{c}}}\right), & \mathcal{F} = \mathcal{F}^C(\underline{n}) \end{cases} \tag{11}$$

Strain hardening in the matrix is accounted for by making the matrix yield stress a function of the plastic strain as $\bar{\sigma} = \bar{\sigma}(\epsilon^p_{\text{eq}})$, where ϵ^p_{eq} is an average measure of the equivalent plastic strain in the matrix material, whose evolution is obtained from the equivalence of the plastic power at the macro- and micro-scales; i.e.

$$\boldsymbol{\Sigma} : \mathbf{D}^p = (1-f)\bar{\sigma}(\epsilon^p_{\text{eq}})\dot{\epsilon^p_{\text{eq}}} \tag{12}$$

In this paper, a power-law relationship between ϵ^p_{eq} and $\bar{\sigma}$ is assumed, of the form

$$\bar{\sigma} = \sigma_0 \left(1 + \frac{\epsilon^p_{\text{eq}}}{\epsilon_0}\right)^n \tag{13}$$

where σ_0 is the initial yield stress, ϵ_0 is a reference strain and n is the strain hardening exponent.

In the following section, rate equations (9)–(12) are integrated along radial loading paths in stress space characterized by constant values of the loading path parameters, the triaxiality T and the Lode parameter L, to obtain the evolution of the equivalent stress and porosity as a function of the equivalent plastic strain ϵ^p_{eq}. T and L are related to the invariants of the stress tensor as

$$T = \frac{\Sigma_{\text{m}}}{\Sigma_{\text{eq}}}, \qquad L = -\frac{27}{2}\frac{\det(\boldsymbol{\Sigma}')}{\Sigma^3_{\text{eq}}} \tag{14}$$

T is a measure of the magnitude of the hydrostatic stress relative to the deviatoric stresses, while the value of L allows to distinguish between different states of stress for the same T. L is bounded between -1 and +1, with $L = -1$ for axisymmetric loadings with a major axial stress, $L = 0$ for pure shear with superposed hydrostatic stress and $L = +1$ for axisymmetric loading with major radial stresses.

3 RESULTS

3.1 Comparison with axisymmetric cell model simulations

The heuristic parameters in the classical GTN model, namely the Tvergaard parameter q and the critical porosity for the onset of coalescence, f_c, are usually calibrated by comparison with cell model simulations under axisymmetric loading conditions (e.g. see [8,19]). In the latter, the average response of a transversely isotropic distribution of voids in an elastic-plastic matrix is simulated using finite element analysis of a two-dimensional RVE subjected to proportional axisymmetric loading, as shown in Fig.1. A periodic distribution of voids in the plane of analysis is assumed so that, exploiting the symmetries of the geometry and the applied loading, the average response of the unit cell shown using dashed lines in Fig.1(a) can be obtained from analysis of the quarter cell shown in Fig.1(b), subject to symmetry boundary conditions on the inner boundaries (edges that intersect the voids) and periodicity condition on the outer boundaries. The unit cell is loaded in such a way that the ratio of the principal stresses in the axial and radial directions, or equivalently the triaxiality T, remains constant during the deformation. The major stress is applied in the axial direction, so that the Lode parameter $L = -1$ in all the simulations

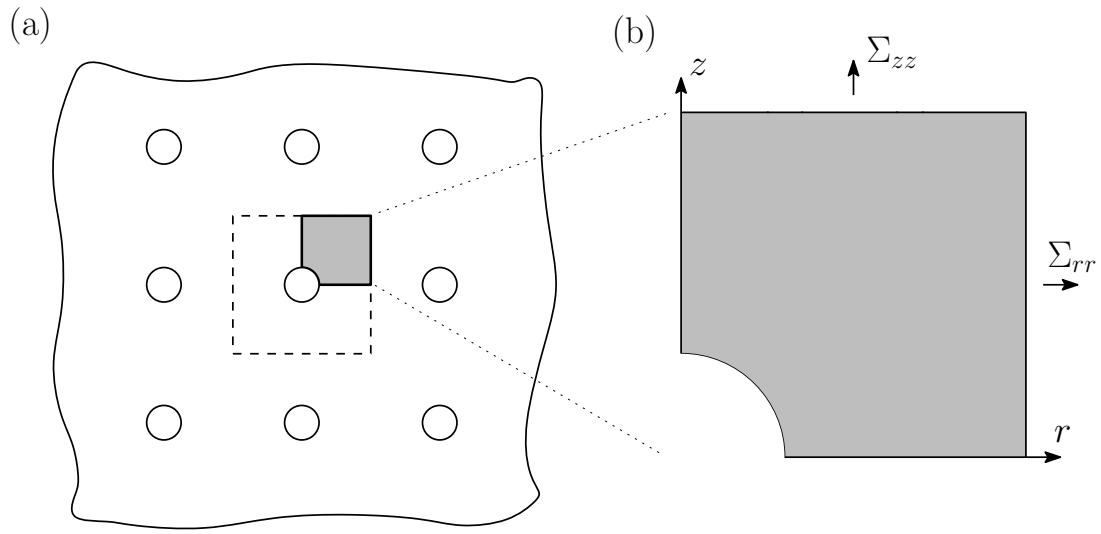

Figure 1: (a) Schematic of a transversely isotropic porous material containing a periodic distribution of voids in the plane of analysis, (b) one quarter of a periodic unit cell used in the finite element analysis.

presented here. Further details of the axisymmetric cell model simulations can be found in [8].

Fig.2 shows the response of periodic unit cells of the type shown in Fig.1(b) made of an elasto-plastic Von Mises material with power law hardening. The void shape is assumed to be initially spherical with a volume fraction $f = 0.001$. The values of the material properties assumed are Young's modulus $E = 210$ GPa, Poisson ratio $\nu = 0.3$, initial yield stress $\sigma_0 = 420$ MPa, hardening exponent $n = 0.1$ and reference strain $\epsilon_0 = 0.002$; see Eq.(13). Fig.2(a) shows the equivalent stress-strain response of the unit cell (solid black lines) for axisymmetric loadings with $L = -1$ and four different values of the triaxiality $T = 2/3, 1, 3/2$ and 2. The equivalent stress and strains are defined as

$$\Sigma_{\text{eq}} = |\Sigma_{zz} - \Sigma_{rr}|, \quad E_{\text{eq}} = \frac{2}{3}|E_{zz} - E_{rr}| \tag{15}$$

where $\boldsymbol{\Sigma} = \langle \boldsymbol{\sigma} \rangle_\Omega$ is the average Cauchy stress and E_{rr} and E_{zz} are the logarithmic strains in the radial and axial directions of the cell respectively. The corresponding evolution of the porosity f as a function of equivalent strain is shown in Fig.2(b). The simulations are terminated at the onset of coalescence (indicated by the $\times$ symbol), when the deformation localizes into the transverse ligament between the voids, which also coincides with the unit cell switching to a uniaxial mode of deformation along the z direction.

The figure also shows predictions of the effective stress-strain response and damage growth obtained from the the multi-surface plasticity model summarized in the previous section (blue dashed lines) and the GTN model (red dotted lines). In the pre-coalescence regime, the GTN model is identical to the multi-surface model, since the yield surface coincides with the Gurson yield surface, i.e. $\mathcal{F} = \mathcal{F}^G$, and the state evolution equations are identical. However, the criterion for the onset of coalescence is different for the two models. In the GTN model, coalescence occurs when the porosity reaches a critical value f_c, while coalescence occurs in the multi-surface model when $\mathcal{F}^G \leq \mathcal{F}^{C^{\text{iso}}} = 0$; see section 2. In both

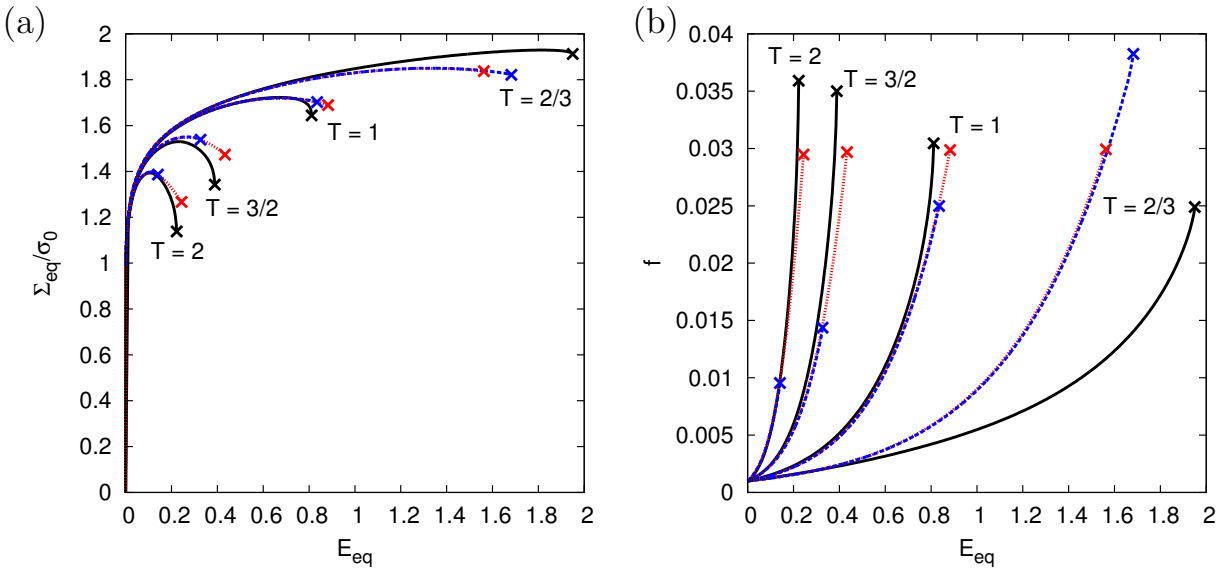

Figure 2: Comparison of the effective response of two dimensional porous unit cells shown in Fig.1 subjected to axisymmetric proportional loading with $L = -1$ and various values of T (solid lines). Predictions from the GTN (dotted lines) and multi-surface (dashed lines) porous plasticity models are also shown. (a) Equivalent stress vs. strain and (b) porosity vs. equivalent strain.

cases, the simulations are terminated when the onset of coalescence is detected. The values of the GTN model parameters are adopted from [8] with $q = 1.25$ and $f_c = 0.03$. The same value of the Tvergaard parameter q is also used in the simulations using the multi-surface model. Further, the coalescence yield function of Eq.(2) is heuristically modified in the spirit of Tvergaard's modification of the original Gurson model to redefine the effective porosity parameter as $f_b = q_b f^{2/3}$, where $q_b = q^{2/3}$ is assumed in the present calculations.

Comparison of the model predictions with the cell model simulations in Fig.2 shows that both the GTN and the multi-surface models provide reasonable predictions for the strains to the onset of coalescence. However, neither model is satisfactory for predicting the correct trends for the porosity at the onset of coalescence, which appears to increase with T in the cell model simulations, while the multi-surface model predicts the opposite trend. Nevertheless, it is significant that the multi-surface model can capture the correct trends for the ductility in the axisymmetric simulations, without use of the heuristic f_c parameter, because the coalescence criterion in the multi-surface model depends on both the triaxiality T and the Lode parameter L, unlike the GTN model, which depends only on T. Hence, the stress state dependence of the ductility can now be examined under general triaxial loading conditions, as is done in the next section, and compared with the trends reported in the recent literature.

3.2 Loading path dependence of the ductility

Fig.3 shows the effective stress strain response predicted by the multi-surface model under triaxial radial loading with $T = 1$ and several values of the Lode parameter L. Unlike in Fig.2, the post-coalescence response of the material is also included in Fig.3. Notice that the effective stress-strain response depends on the Lode parameter unlike the

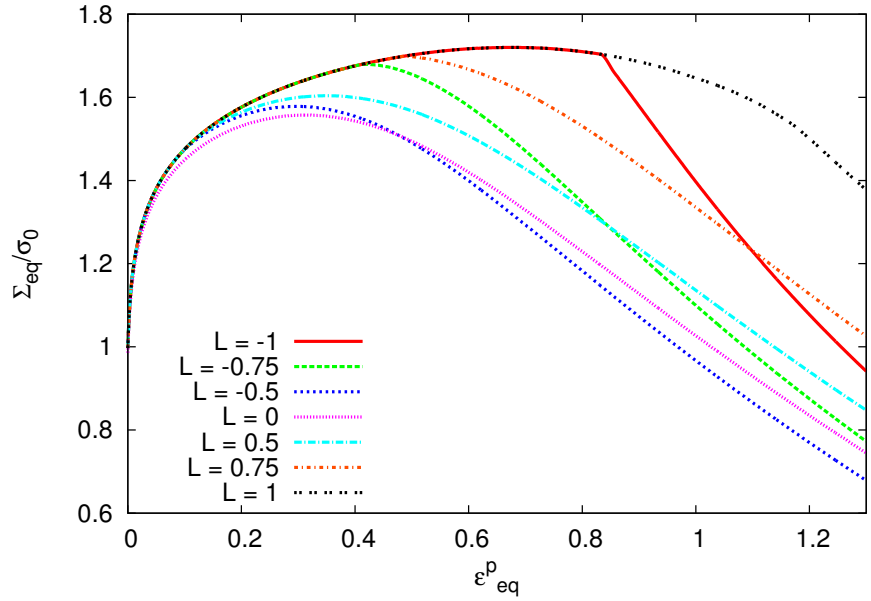

Figure 3: Equivalent stress vs. strain response predicted by the multi-surface plasticity model under triaxial proportional stressing with $T = 1$ and various values of L.

GTN model, whose predictions essentially collapse into a single curve (not shown). The onset of coalescence is visible as a sharp change in the slope of the stress-strain curve in some of the simulations for large $|L|$. However, for shear dominated loadings ($|L|$ near zero), coalescence tends to occur early and without a sharp change is the slope of the stress-strain curve. Also, the material undergoes significant stable plastic flow and strain hardening *after* the onset of coalescence, so that the strain to the onset of coalescence is not an accurate measure of the 'intrinsic' ductility of the material. It is more reasonable in such cases to adopt the plastic strain corresponding to the maximum in the stress-strain curve as the material's ductility. For the present study, we thus adopt the following measure of the 'failure strain' ϵ^p_f of the material

$$\epsilon^p_f = \max\left\{\epsilon^p_{\text{ult}}, \epsilon^p_{\text{coal}}\right\} \tag{16}$$

where ϵ^p_{ult} and ϵ^p_{coal} are the equivalent plastic strains corresponding to the ultimate stress and the onset of coalescence respectively.

The results in Fig.3 show that the strain to failure under proportional stressing ϵ^p_f, as defined above, predicted by the multi-surface model shows a non-monotonic trend with respect to L at fixed T, and the minimum ductility is predicted for shear dominated stress states near $L = 0$. The Lode parameter dependence of the ductility is further illustrated in Fig.4(a). The figure plots the strain to failure ϵ^p_f as a function of L for several representative values of T. Notice that the predicted curves have an approximately convex shape, except for a region near $L = 0$ where slight concavity is observed. The ductility minimum occurs for shear dominated stress states with small negative values of L. Further, ϵ^p_f also shows a dependence on the sign of L (equivalently the sign of the determinant of the deviatoric stress), with relatively higher ductilities predicted for

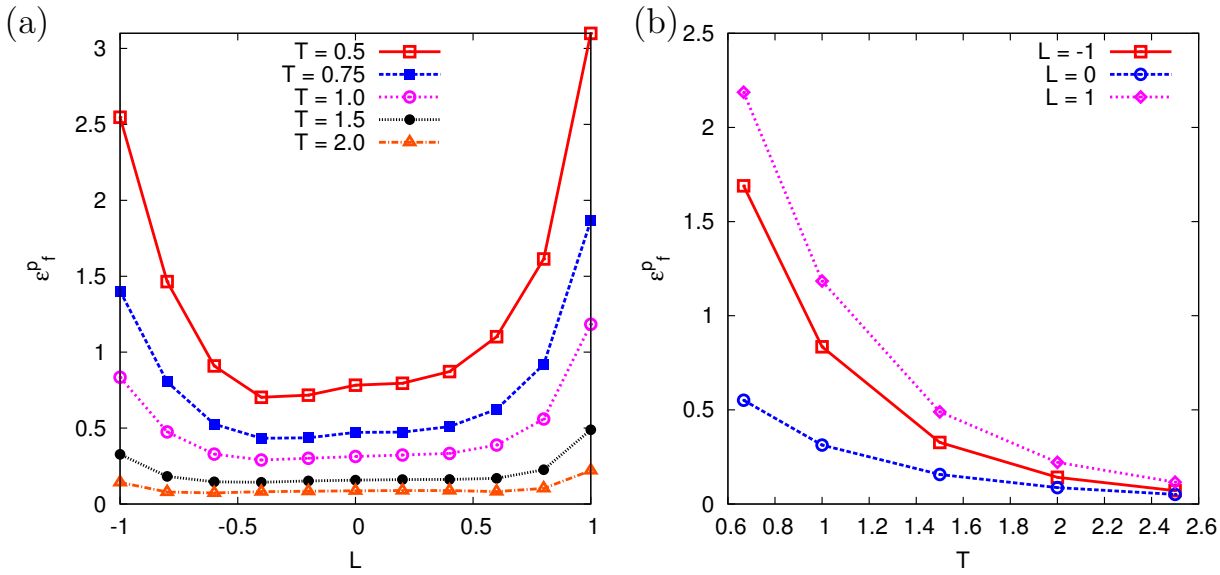

Figure 4: Variation of the strain to failure ϵ_f^p under proportional loading as a function of: (a) the Lode parameter L for various values of T and (b) the triaxiality T for various values of L.

positive values of L. In contrast, the triaxiality dependence of the ductility in Fig.4(a) exhibits a monotonic trend as expected, with lower failure strains predicted towards higher values of T. The triaxiality dependence of the ductility is also illustrated in Fig.4(b), which plots ϵ_f^p as a function of T for several values of L. The shapes of these curves are in accordance with predictions from classical porous plasticity models, except for the significant dependence on L.

Recently, several authors have performed cell model simulations in the spirit of section 3.1, using three dimensional unit cells subjected to periodic boundary conditions and combined tensile and shear loads to simulate proportional stressing for arbitrary values of T and L [11–13]. They report predictions for the strains to the onset of coalescence in remarkable qualitative agreement with the predictions from the multi-surface model in Fig.4. In particular, the shape of the ϵ_f^p vs. L and ϵ_f^p vs. T curves and the dependence of the failure strains on the sign of L are in qualitative agreement with the above cell model simulations, which indicates that the mechanisms of coalescence assumed in the multi-surface model are fundamentally correct. It remains to perform a quantitative comparison and calibration of the model against three dimensional unit cell simulations, with possibly introduction of additional heuristics to correct for some of the discrepancies observed in Fig.2. The results of such a study will be reported in a future publication.

4 CONCLUSION

Conclusions from the above study are summarized below.

- It is shown that a multi-surface porous plasticity model [18], combining the Gurson model with a void coalescence model accounting for arbitrary orientations of the coalescence band and the effect of the loading path on the coalescence stress, can predict the triaxiality and Lode parameter dependence of the ductility observed in

three dimensional cell model simulations [11–13].

- Quantitative comparison with axisymmetric cell model simulations shows that the strains to coalescence predicted by the multi-surface model are in reasonable agreement with the simulations, although the results for the porosity at the onset of coalescence are significantly different.

REFERENCES

[1] A. Pineau, A. A. Benzerga, and T. Pardoen. Failure of metals I: Brittle and ductile fracture. *Acta Mater.*, 107:424–483, 2016.

[2] J. R. Rice and D. M. Tracey. On the enlargement of voids in triaxial stress fields. *J. Mech. Phys. Solids*, 17:201–217, 1969.

[3] A. L. Gurson. Continuum Theory of Ductile Rupture by Void Nucleation and Growth: Part I– Yield Criteria and Flow Rules for Porous Ductile Media. *J. Eng. Mat. Tech.*, 99:2–15, 1977.

[4] V. Tvergaard and A. Needleman. Analysis of the cup–cone fracture in a round tensile bar. *Acta Metall.*, 32:157–169, 1984.

[5] A. Needleman and V. Tvergaard. An analysis of ductile rupture in notched bars. *J. Mech. Phys. Solids*, 32:461–490, 1984.

[6] J. Besson, D. Steglich, and W. Brocks. Modeling of plane strain ductile rupture. *Int. J. Plasticity*, 19:1517–1541, 2003.

[7] J. W. Hancock and D. K. Brown. On the role of strain and stress state in ductile failure. *J. Mech. Phys. Solids*, 31:1–24, 1983.

[8] J. Koplik and A. Needleman. Void growth and coalescence in porous plastic solids. *Int. J. Solids Struct.*, 24(8):835–853, 1988.

[9] Y. Bao and T. Wierzbicki. On fracture locus in the equivalent strain and stress triaxiality space. *Int. J. of Mech. Sci.*, 46(81):81–98, 2004.

[10] I. Barsoum and J. Faleskog. Rupture mechanisms in combined tension and shear-Experiments. *Int. J. Solids Struct.*, 44:1768–1786, 2007.

[11] I. Barsoum and J. Faleskog. Micromechanical analysis on the influence of the lode parameter on void growth and coalescence. *Int. J. Solids Struct.*, 48(6):925–938, 2011.

[12] Matthieu Dunand and Dirk Mohr. Effect of lode parameter on plastic flow localization after proportional loading at low stress triaxialities. *J. Mech. Phys. Solids*, 66:133–153, 2014.

[13] C. Tekoğlu, J. W. Hutchinson, and T. Pardoen. On localization and void coalescence as a precursor to ductile fracture. *Philosophical Transactions of the Royal Society of London A: Mathematical, Physical and Engineering Sciences*, 373:20140121, 2015.

[14] P. F. Thomason. A three–dimensional model for ductile fracture by the growth and coalescence of microvoids. *Acta Metallurgica*, 33(6):1087–1095, 1985.

[15] C. Tekoglu, J.-B. Leblond, and T. Pardoen. A criterion for the onset of void coalescence under combined tension and shear. *J. Mech. Phys. Solids*, 60:1363–1381, 2012.

[16] M. E. Torki, A. A. Benzerga, and J.-B. Leblond. On void coalescence under combined tension and shear. *J. App. Mech.*, 82:071005, 2015.

[17] S. M. Keralavarma and S. Chockalingam. A criterion for void coalescence in anisotropic ductile materials. *Int. J. Plasticity*, 82:159–176, 2016.

[18] S. M. Keralavarma. A multi-surface plasticity model for ductile fracture simulations. *J. Mech. Phys. Solids*, 103:100–120, 2017.

[19] V. Tvergaard. On localization in ductile materials containing spherical voids. *Int. J. Frac.*, 18:237–252, 1982.

XIV International Conference on Computational Plasticity. Fundamentals and Applications
COMPLAS 2017
E. Oñate, D.R.J. Owen, D. Peric and M. Chiumenti (Eds)

EXPERIMENTAL AND NUMERICAL ANALYSIS OF A HELICAL SPRING FAILURE

GORAN VUKELIC*, MARINO BRCIC†, DARKO PASTORCIC‡

* Department of Marine Engineering and Ship Power Systems, Faculty of Maritime Studies
University of Rijeka
Studentska 2, 51000 Rijeka, Croatia
E-mail: gvukelic@pfri.hr, web page: www.pfri.uniri.hr

† Department of Engineering Mechanics, Faculty of Engineering,
University of Rijeka
Vukovarska 58, 51000 Rijeka, Croatia
Email: mbrcic@riteh.hr, Web page: www.riteh.uniri.hr

‡ Maritime Department
University of Zadar
M. Pavlinovica 1, 23000 Zadar, Croatia
Email: darko.pastorcic@zd.t-com.hr, Web page: www.unizd.hr

Key words: helical spring, failure, fracture, fatigue.

Abstract. Results of experimental and numerical analysis of a broken motor vehicle helical spring are presented in this paper. Location of the fracture is on a first active coil of the spring. Experimental part of the research employed optical microscopy that revealed fractured surface microstructure and allowed for detection of inclusions. Corroded fracture surface limited scanning electron microscopy examination (SEM). Nevertheless, corrosion pits on the edge of the spring wire which served as crack initiation points could be detected by SEM along with radiating ridges left by the fracture front that propagated to the opposite edge of the wire. Optical emission spectrometer with glow discharge source sample stimulation was used to determine material chemical composition that is adequate to spring steel 61SiCr7. Additionally, hardness test was performed and obtained value was used to derive maximum tensile strength of the steel. Experimentally collected data served as input for numerical analysis of helical spring. Finite element analysis of a helical spring model was performed. Stress distribution was determined and fatigue life of the undamaged helical spring predicted. Results were compared with those obtained analytical. Causes of failure are outlined assessing the results of the performed experimental and numerical analysis. Insufficient corrosion protection and excessive contact between the coils caused damage that developed from initial crack to final fracture of the spring. Results obtained by this research are valuable in understanding fracture behavior of helical spring mounted in suspension system of various motor vehicles. Given the presented results, further improvements of spring design can be made in order to reduce failures.

1 INTRODUCTION

Helical springs are used in the construction of motor vehicles suspension system as one of the primary elastic members connecting the wheel and the vehicle chassis. Absorption and subsequent release of external loads from uneven road surfaces comes in a form of elastic energy so, if designed properly, springs tend to return to their initial form when unloaded.

To assure proper design, engineers can, among others, benefit from failure analysis of broken springs. Springs fail mostly because of the local stress raisers that come in a form of a material surface roughness, inclusions and deficient microstructure. Causes of common spring failures along with spring material characteristics, manufacturing of springs and their fundamental stress distribution are outlined in the work of Prawoto et al. [1]. Dealing with the failure of motor vehicle coil springs, some of the recent work includes failure analysis of shock absorption helical spring in a motorcycle [2] where insufficient shot peening and embrittlement induced from electroplating were recognized and, based on this, a process optimization was proposed to reach the standard service life. Experimental investigation of a prematurely failed passenger car coil spring discovered that it was caused by inherent material defects coupled with deficient processing [3]. Experimental procedures employed on a fractured torsion springs mounted on an electric-powered vehicle determined that the fractures initiated due to electric arc damage [4]. Besides experimental failure analysis, numerical approach is also employed to gain thorough insight into the mechanical behaviour of failed component. Stress analysis, fatigue life calculations and failure simulations are fairly easy performed using finite element analysis [5]. Causes of compression helical spring fracture were analysed by employing experimental methods while numerical methods served to determine contact points between the spring coils from which crack originated [6].

Additionally, it is also important to understand the behaviour of spring material in order to improve performance of springs. Some of the recent work on this topic includes a comprehensive overview of fatigue behaviour of spring steels DIN 17223C and 55Si7 coupled with mathematical models of adequate da/dN diagrams [7]. Ductility of Si-Cr spring steel is improved by refining grain boundary carbides using thermomechanical treatment [8]. Empirical corrosion fatigue life prediction models are developed based on a study of a crack initiation and growth behaviour in Si-Mn spring steel [9]. Basic spring material behaviour can be significantly improved by treatments like heating, quenching and tempering [10]. Also, microshot peening can be successfully employed to improve fatigue life of spring steel [11]. Proper surface treatment of coil spring steels needs to be employed in order to avoid surface defects that can become predominant origin of spring steel failures under very high cycle fatigue [12].

Research of springs is ongoing as new design and spring materials coupled with harsh service conditions give reason for continuous improvement. Failure analysis of fractured springs serves as a valuable tool for design improvement. This paper presents results of experimental and numerical analysis of a broken motor vehicle helical spring. Results can be taken as a reference in further improvement of helical springs, especially having in mind that local car dealership confirmed that there has been a noticeable amount of failures on that particular spring design.

2 EXPERIMENTAL ANALYSIS

2.1 Visual and microscope examination

Helical spring mounted on a front suspension of a passenger car fractured after 145.000 km and 7 years of service. Fracture occurred at the transition point from the lower bearing coil to the first upper coil. Geometry and dimensions of helical spring extracted from the car are shown in Fig. 1.

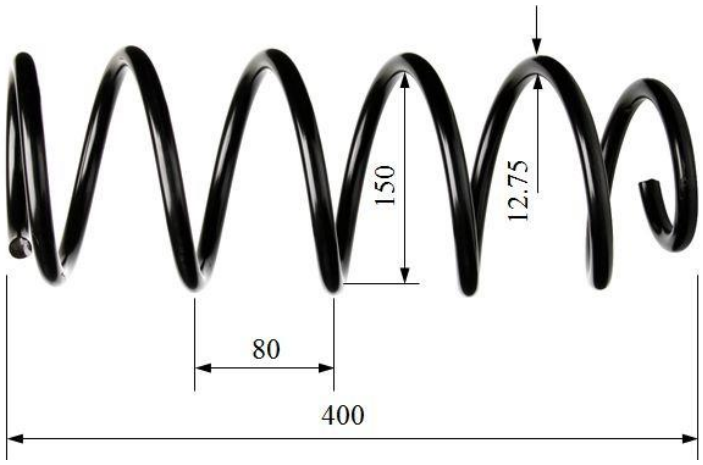

Figure 1: Helical spring dimensions (in mm)

In order to perform experimental analysis, specimens were cut from fractured helical spring, Fig. 2. Fracture surface is oriented at 45º to the wire centerline which is typical for torsional fatigue failure under cyclic loading. Protective layer of polymer-based paint is damaged around the fracture surface. Damage can be contributed to the contact of bearing and first active coil.

Figure 2: Specimens extracted from failed coil spring

Heavily corroded outer surface of the wire is exposed in Fig. 3 and there is a layer of rust on the fracture surface, also, Fig 4. Thicker and darker semicircular part of the rust layer marks portion of the surface where crack formed gradually and was exposed to corrosive environment for a longer period of time before the final failure occured. Rest of the fracture surface is covered in lighter layer of rust and marks a portion of surface where accelerated crack propagation happened.

Figure 3: Heavily corroded wire surface

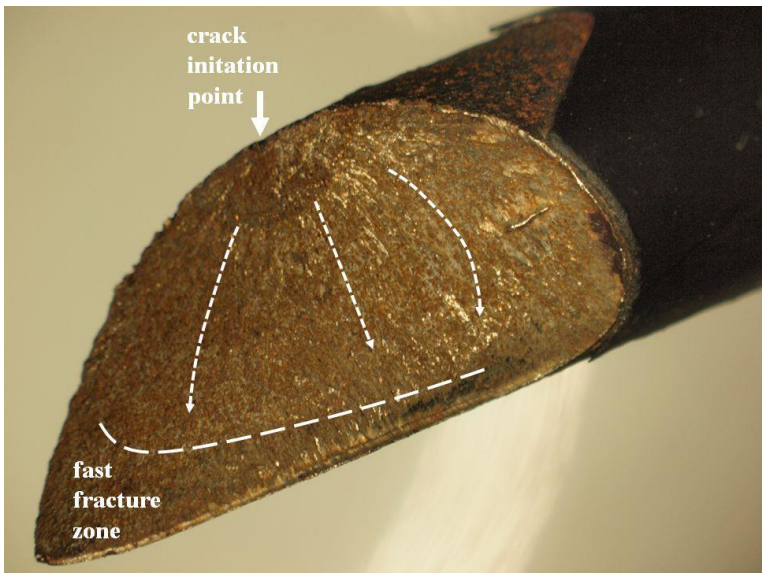

Figure 4: Fracture surface

Corrosion pits can be observed at the point where the protective layer of paint was damaged. Fracture originated from one of this pits and continued propagation towards opposite end

leaving radiating ridges behind and suggesting fatigue failure caused by cyclic loading from the vehicle. At the side opposite of the crack initiation point, fast fracture area can be observed corresponding to the final stage of failure.

Specimens of a failed helical spring were examined using optical and scanning electron microscope. Optical microscopy was performed using Olympus SZX10 stereo microscope and investigation of the fracture surface was concentrated on the area of probable crack initiation point, Fig. 5.

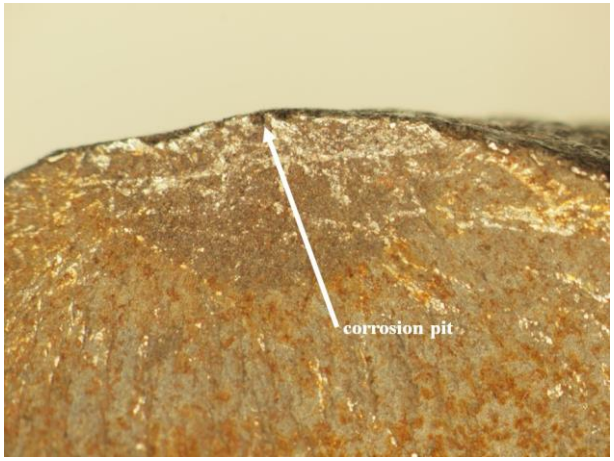

Figure 5: Corrosion pit serving as crack initiation point

Corrosion pits can be observed at the edge of the fracture surface where the protective paint layer is damaged. Main pit served as crack initiation point from which crack propagated towards opposite edge of the wire causing final failure.

Crack initiation area, obtained by FEI Quanta 250 scanning electron microscope (SEM) under suitable magnification, is shown in Fig. 6.

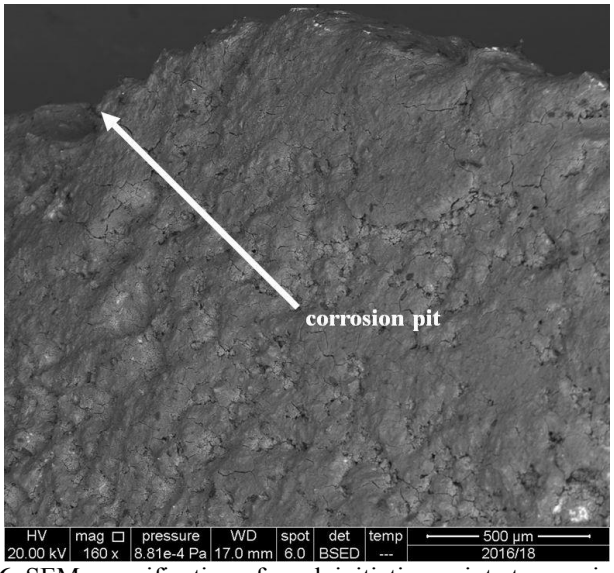

Figure 6: SEM magnification of crack initiation point at corrosion pit

SEM analysis was difficult to perform because the fracture surface was damaged by corrosion. Examination of the fracture surface at 80x magnification revealed a heavily oxidized and corroded surface which obscured fracture surface details. Although an attempt was made to remove the corrosion layer using aggressive cleaning agent, corrosion products could still be seen on SEM images.

2.2 Material

Glow discharge spectrometer (GDS) LECO GDS500A was used to determine chemical composition of spring material, Tab. 1.

Table 1: Chemical composition of spring material (wt%).

C	Mn	Si	P	S	Mo	Ni	Cr	V	W	Cu
0.612	0.698	1.78	0.018	0.0165	0.0133	0.107	0.598	0.0139	0.0565	0.147
Al	Ti	Co	Nb	Pb	Sn	As	Sb	Zr	Rest	
0.0036	0.0134	0.0497	0.0704	0.0029	0.146	0.0213	0,003	0.0087	95.6	

Comparing it to standard materials used in spring manufacturing, composition is adequate to chromium-silicon steel 61SiCr7. This spring steel is typically used in production of light and heavy motor vehicle leaf springs and coil springs, safety valve springs, shock absorbers, instrument springs, friction plates, etc. If compared to EN 10089-2002 standard, percentage of manganese in tested steel is just below the standard range (0.7-1 %), while chromium exceeds the maximum standard value (0.2-0.45 %). Standard maximum tensile strength of steel 61SiCr7 is 1850 MPa.

Using Struers hardness tester Duramin-2 hardness test was performed. Mean hardness value is 590 HV (Vickers hardness number) and it can be used to derive maximum tensile strength of the tested material [13]:

$$\sigma_{TS} = 3.2HV = 1888 \text{ MPa}. \quad (1)$$

3 NUMERICAL ANALYSIS

Common failure analysis usually constitutes only of experimental metallurgical analysis in order to establish the causes of failure. Since the failed structures are often subjected to tensile overload, excessive creep or localized fatigue damage, mechanics of the failure should also be considered, e.g. stress analyses, fatigue life analyses and simulations of failure process. Finite element (FE) analysis represents cost and time effective tool for determining the causes of failure and this numerically obtained results complement the ones obtained experimentally providing broader insight into the failure of structures.

According to geometry in Fig. 1, simplified 3D FE model of helical spring was built in Ansys. A model without any crack was analyzed first, in order to determine stress range, contact point between the coils and fatigue life of undamaged spring. A load of 4000 N was applied on top coil and nodes on bottom coil were restrained from motion. Load was estimated as a quarter of total car weight plus average passenger weight. Material behavior was modelled according to available experimental data for 61SiCr7 spring steel [14]. In accordance with the previously

derived value of maximum tensile strength, data for 61SiCr7 spring steel annealed at 425ºC were taken along with results of fatigue tests and S-N curves needed for proper numerical model.

Shear stress distribution in the considered helical spring is presented in Fig. 7.

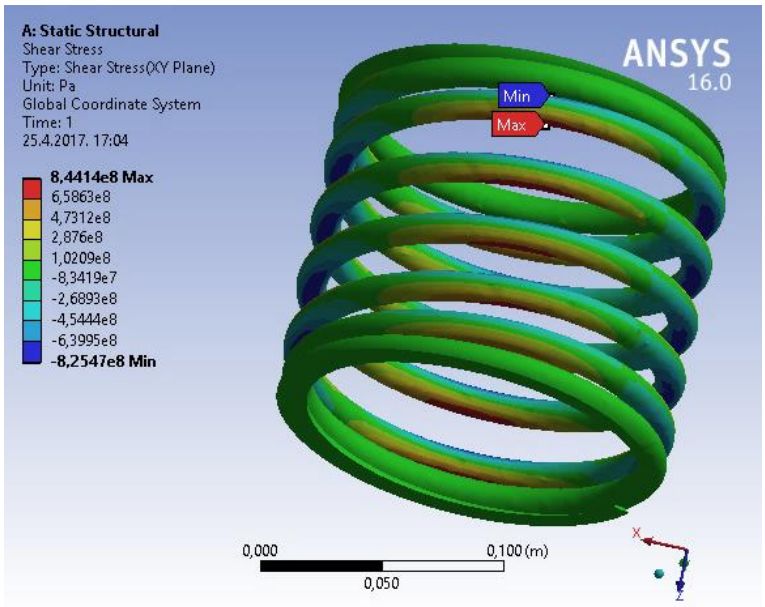

Figure 7: Shear stress distribution

It can be noted that the maximum value of stress is numerically predicted just at the point where actual fracture occurred. During service, dynamic loads and shocks resulted in contact between the bearing coil and the first active coil. As a result of repeated contact and impact between the coils, the contact surfaces were gradually worn out leading to crack occurrence and fracture. FE model was built to simulate frictionless contact behavior between the mentioned coils.

In order to validate FE model, numerically obtained values of shear are compared to ones calculated analytically. The maximum stress in the spring wire, occurring on the inner surface, can be calculated as [15]:

$$\tau_{\max} = K_W \frac{8FD}{\pi d^3}, \tag{2}$$

where F is the load, D outer diameter of the spring, d wire diameter and K_W is a Wahl's coefficient:

$$K_W = \frac{4C-1}{4C-4} + \frac{0.615}{C}, \tag{3}$$

while C is a spring index:

$$C = \frac{D}{d}. \tag{4}$$

According to Eq. 2, maximum shear stress in considered helical spring is 827.4 MPa which can be correlated to 844.1 MPa obtained numerically.

Also, in order to numerically predict fatigue life of helical spring, fatigue analysis is performed and results are presented in Fig. 8.

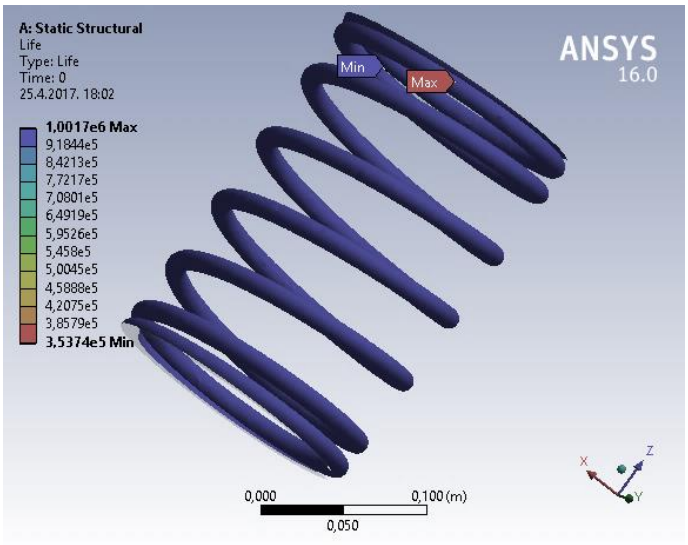

Figure 8: Fatigue life

In order to get more accurate results, loads coming from road irregularities are considered, also. Passing of the vehicle on irregular road surfaces generates oscillation of the vehicle mass with a consequent increase of the load. Final load is a combination of several factors, e.g. vehicle mass, travelling speed, type of suspension, road irregularities, etc. Quarter car model (QCM) [16] can be used to study the interaction between vehicle and road profile. Also, classification of road profiles according to ISO 8608 [17] has to be considered. The use of ISO 8608 presumes that a specific road has equal statistical properties along an examined section. In this work, ISO A-B road profile was chosen along with 70 km/h vehicle speed. A Matlab code was written [18] to calculate the behavior of a vehicle according to road irregularities and further to estimate the effect on helical spring fatigue life. Fig. 9 shows non-constant amplitude load used in the analysis.

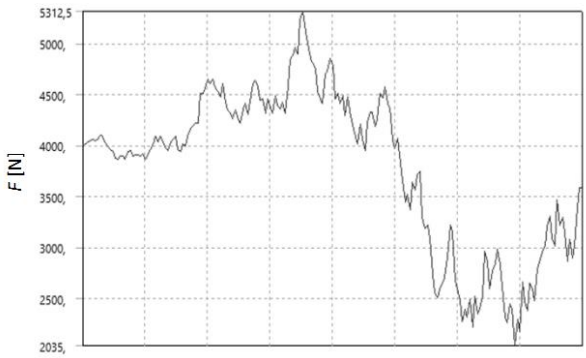

Figure 9: Non-constant amplitude load

Fig. 10 has shear stress distribution in the considered helical spring with load from road irregularities added and Fig. 11 predicted fatigue life.

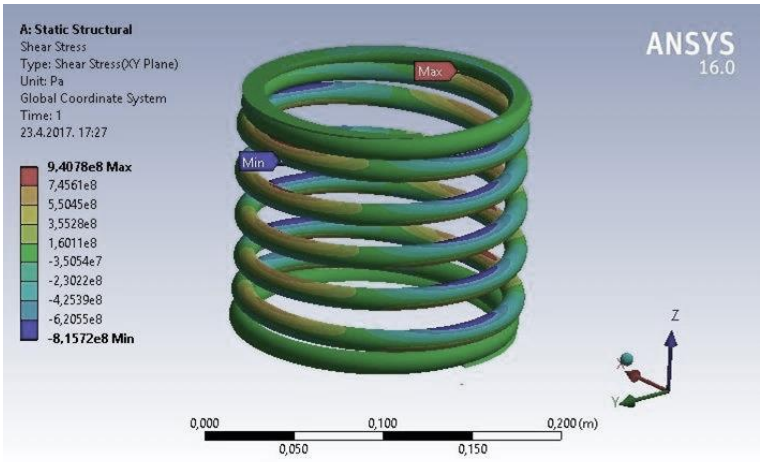

Figure 10: Shear stress distribution with road irregularities load accounted

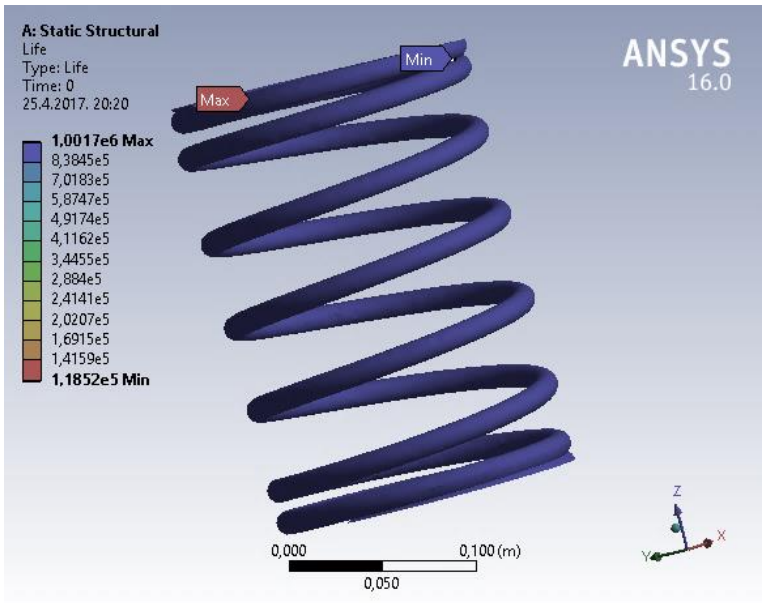

Figure 11: Fatigue life with road irregularities load accounted

5 DISCUSSION

Visual examination of failed helical spring revealed that the protective layer of paint was mechanically damaged at the contact point between the lower bearing coil and first adjacent active coil. Therefore, wire surface was exposed to corrosive environment allowing the formation of corrosion pits. These pits served as crack initiation points influenced by cyclic loading from the vehicle travelling on the road irregularities. Primary fracture zone that was exposed to corrosion for a longer period of time can be observed on the fracture surface. Crack

front propagated towards opposite edge of the wire leaving radiating ridges behind. Finally, fast fracture zone can be observed near the opposite edge of the spring wire, marking the final stage of failure.

Experimental analysis revealed that spring was made of 61SiCr7, a spring steel with somewhat elevated content of silicone and chromium. Chromium at steels tends to increase tensile strength, hardness, toughness, resistance to wear and corrosion [19], while silicon is used as a deoxidizer in the manufacture of steel and it slightly increases tensile strength and can help in increasing the toughness and hardness levels. However, special attention must be taken to ensure that paint layer remains undamaged in order to protect spring against exposure to corrosive environment.

Optical and scanning electron microscopy examination revealed damage to the wire surface caused by continuous contact between the coils. Heavily oxidized and corroded fracture surface limited SEM examination so deeper insight could not be performed.

Performed finite element analysis served to determine stress distribution along the spring, contact point between the coils and fatigue life of undamaged spring. Comparing results of numerically predicted and analytically calculated maximum stress level, it can be noted that FE model successfully represents real helical spring. In order to obtain accurate fatigue life, load on helical spring is modelled first just as a quarter of average vehicle weight, then additionally with load from road irregularities. Difference in fatigue is significant suggesting that load from road irregularities should also be included in vehicle helical spring calculation.

6 CONCLUSION

Results of the research presented in this paper gave insight into the causes of motor vehicle helical spring failure. Failed spring was examined experimentally; visual observation, determination of chemical composition, hardness testing, optical and scanning electron microscope analysis were employed. Additionally, FE analysis was performed to determine stress ranges, contact points between the coils and fatigue life.

Experimental results suggest a corrosion fatigue failure. Protective layer of paint was damaged which introduced corrosion pits on the surface of the wire. Corrosion pits served as crack initiation points that grew under the influence of cycling loading causing the final fracture. Radiating ridges on the fracture surface show the path of crack advancement.

Finite element analysis was employed to determine stress levels in helical coil spring along with numerical estimation of fatigue life. Obtained results are valuable in understanding fracture behavior of helical spring as a part of motor vehicle suspension system. Further improvements of spring design are possible in order to reduce potential failures.

7 ACKNOWLEDGEMENT

This work has been financially supported in part by University of Rijeka under the project 13.07.2.2.04. The materials and data in this publication have been obtained through the support of the International Association of Maritime Universities (IAMU) and The Nippon Foundation in Japan.

REFERENCES

[1] Prawoto, Y., Ikeda, M., Manville, S.K. and Nishikawa, A. Design and failure modes of automotive suspension springs. *Eng. Fail. Anal.* (2008) **15**(8):1155-1174.

[2] Bo-Chao, L. and Zhen-Guo, Y. Failure Analysis of Shock Absorption Spring in Motorcycle. *J. Fail. Anal. Prev.* (2016) **16**(3):337-345.

[3] Das, S.K., Mukhopadhyay, N.K., Ravi Kumar, B. and Bhattacharya, D.K. Failure analysis of a passenger car coil spring. *Eng. Fail. Anal.* (2007) **14**(1):158-163.

[4] Maciejewski, J. and Akyuz, B. Spring Fatigue Fractures Due to Microstructural Changes in Service. *J. Fail. Anal. Prev.* (2014) **14**(2):148-151.

[5] Prawoto, Y. Quantitative Failure Analysis Using a Simple Finite Element Approach. *J. Fail. Anal. Prev.* (2010) **10**(1):8-10.

[6] Zhu, Y., Wang, Y. and Huang, Y. Failure analysis of a helical compression spring for a heavy vehicle's suspension system. *Case Studies Eng. Fail. Anal.* (2014) **2**(2):169-173.

[7] Angelova, D., Yordanova, R., Lazarova, T. and Yankova, S. On Fatigue Behavior of Two Spring Steels. Part I: Wöhler Curves and Fractured Surfaces. *Proc. Mat. Sci.* (2014) **3**:1453-1458.

[8] Barani, A., Ponge, D. and Raabe, D. Refinement of grain boundary carbides in a Si-Cr spring steel by thermomechanical treatment. *Mat. Sci. Eng. A* (2006) **426**(1-2):194-201.

[9] Murtaza, G. and Akid, R. Empirical corrosion fatigue life prediction models of a high strength steel. *Eng. Fract. Mech.* (2000) **67**(5):461-474.

[10] Fragoudakis, R., Karditsas, S., Savaidis, G. and Michailidis, N. The Effect of Heat and Surface Treatment on the Fatigue Behaviour of 56SiCr7 Spring Steel. *Proc. Eng.* (2014) **74**:309-312.

[11] Harada, Y., Tanaka, S., Itoh, M. and Nakatani, M. Effect of Microshot Peening on Fatigue Life of Spring Steel SUP9. *Proc. Eng.* (2014) **81**:1493-1498.

[12] Li, W., Sakai, T., Wakita, M. and Mimura, S. Influence of microstructure and surface defect on very high cycle fatigue properties of clean spring steel. *Int. J. Fatig.* (2014) **60**:48-56.

[13] Boyer, H.E. and Gall, T.L. *Metals handbook*. American Society for Materials. (1985).

[14] Weber, B., Montero, C., Bergamo, S., Rennert, R., Wünsche, A., Budano, S. and Aranguren, I. *Load spectrum lightening of fatigue tests data for time reduction of design validation – Speedfat*. European Commission Research Fund for Coal and Steel. (2010).

[15] Shigley, J. E. and Mischke, C. R. *A textbook of Mechanical Engineering Design*. McGraw Hill, VI ed. (2005).

[16] Jazar, R.N. *Vehicle Dynamics: Theory and Application.* Springer. (2008).

[17] ISO 8608:2016 *Mechanical vibration - Road surface profiles*. International Organization for Standardization. (2016).

[18] Rill, G. *Road Vehicle Dynamics: Fundamentals and Modeling*. CRC Press. (2011).

[19] Vukelic, G. and Brnic, J. Predicted Fracture Behavior of Shaft Steels with Improved Corrosion Resistance. *Metals*. (2016) **6**(2):40.

XIV International Conference on Computational Plasticity. Fundamentals and Applications
COMPLAS XIV
E. Oñate, D.R.J. Owen, D. Peric & M. Chiumenti (Eds)

MULTI-FIELD MODELLING AND SIMULATION OF LARGE DEFORMATION DUCTILE FRACTURE

M. DITTMANN*, C. HESCH*, J. SCHULTE*, F. ALDAKHEEL† AND M. FRANKE#

* Chair of Computational Mechanics
University of Siegen
Paul-Bonatz-Straße 9-11, 57068 Siegen, Germany
e-mail: maik.dittmann@uni-siegen.de, christian.hesch@uni-siegen.de,
web page: https://www.mb.uni-siegen.de/nm

† Institute of Applied Mechanics
University of Stuttgart
Pfaffenwaldring 7, 70569 Stuttgart, Germany
e-mail: fadi.aldakheel@mechbau.uni-stuttgart.de,
web page: http://www.mechbau.uni-stuttgart.de/ls1

Institute of Mechanics
Karlsruhe Institute of Technology
Otto-Ammann-Platz 9, 76131 Karlsruhe, Germany
e-mail: marlon.franke@kit.edu
web page: https://www.ifm.kit.edu

Key words: Ductile Fracture, Large Deformation, Phase-field, Contact mechanics

Abstract. In the present contribution we focus on a phase-field approach to ductile fracture applied to large deformation contact problems. Phase-field approaches to fracture allow for an efficient numerical investigation of complex three-dimensional fracture problems, as they arise in contact and impact situations. To account for large deformations the underlying formulation is based on a multiplicative decomposition of the deformation gradient into an elastic and plastic part. Moreover, we make use of a fourth-order crack regularization combined with gradient plasticity. Eventually, a demonstrative example shows the capability of the proposed framework.

1 INTRODUCTION

The numerical investigation of fracture using phase-field approaches has gained increasing attention in the last decade, see Miehe et al. [1] and Kuhn and Müller [2]. In contrast to the costly and complex computational modeling of sharp cracks, the formulation in this works is based on the introduction of a diffusive interface, see also Weinberg and Hesch [3] for a detailed investigation on Allen-Cahn type as well as Cahn-Hilliard type equations.

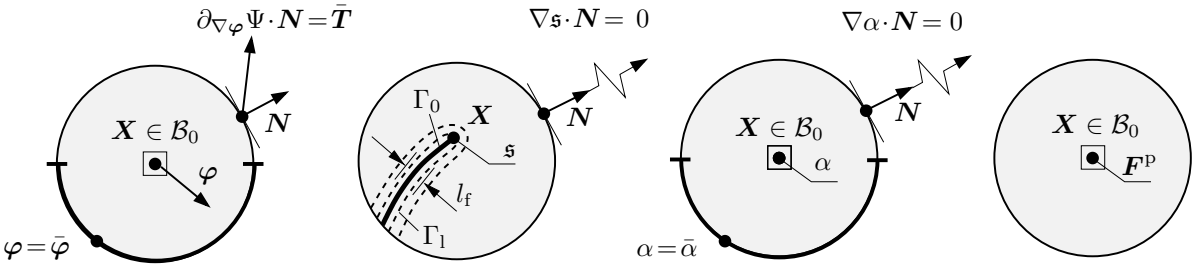

Figure 1: Primary fields of inelastic deformable solids coupled with phase field fracture.

The assumption that the material fails locally upon the attainment of a specific fracture energy as introduced by Francfort and Marigo [4] and Bourdin et al. [5], allows to formulate a variational statement for brittle fracture, see e.g. Karma et al. [6]. An extension to large deformations relying on a multiplicative decomposition of the deformation gradient into a compressive and a tensile part along with a structure preserving time integration scheme is given in Hesch and Weinberg [7], whereas adaptations to ductile fracture have recently proposed in e.g. Aldakheel [8], Miehe et al. [9] and Borden et al. [10]. The formulations introduced therein are able to predict fracture in ductile solids which undergoes large elastic and/or plastic deformations. In addition, the application of a phase-field fracture approach to contact and impact problems was recently proposed in Hesch et al. [11] and Dittmann et al. [12].

The purpose of the present contribution is to introduce a framework for the simulation of ductile fracture within large deformation contact and impact situations. Therefore, we combine a nonlinear elastoplastic formulation based on a multiplicative decomposition of the deformation gradient with a fourth order phase-field formulation and gradient plasticity. Eventually, we apply the proposed approach along with a frictional mortar contact formulation and demonstrate the capability on a representative example.

2 GOVERNING EQUATIONS

Let $\mathcal{B}_0 \subset \mathbb{R}^n$ with $n \in \{2,3\}$ be the reference configuration of the body of interest. The proposed multi-field approach to phase-field-type crack propagation in inelastic deformable solids is described by the following primary fields of the coupled problem:

- The *deformation map* $\boldsymbol{\varphi}$ which maps at time $t \in \mathcal{T}$ points $\boldsymbol{X} \in \mathcal{B}_0$ of the reference configuration $\mathcal{B}_0$ onto points $\boldsymbol{x} \in \mathcal{B}_t$ of the current configuration $\mathcal{B}_t$

$$\boldsymbol{\varphi}(\boldsymbol{X}) : \mathcal{B}_0 \times \mathcal{T} \to \mathbb{R}^n \quad \text{with} \quad \boldsymbol{x} = \boldsymbol{\varphi}(\boldsymbol{X}, t) \tag{1}$$

  as depicted in Figure 1a. The material deformation gradient is defined by $\boldsymbol{F} := \nabla\boldsymbol{\varphi}(\boldsymbol{X})$ with $J := \det[\boldsymbol{F}] > 0$.

- The *crack phase-field* $\mathfrak{s}$ is interpreted as an auxiliary variable that approximates the sharp crack topology. It defines a regularized crack surface functional $\Gamma_l(\mathfrak{s})$ that

converges in the limit $l_\mathrm{f} \to 0$ to the sharp crack surface Γ_0

$$\mathfrak{s}(\boldsymbol{X},t) : \mathcal{B}_0 \times \mathcal{T} \to \mathbb{R}, \quad \text{with} \quad \mathfrak{s} \in [0,1] \quad \text{and} \quad \dot{\mathfrak{s}} \geq 0 \tag{2}$$

as indicated in Figure 1b, where the value $\mathfrak{s}(\boldsymbol{X},t) = 0$ refers to the unbroken and $\mathfrak{s}(\boldsymbol{X},t) = 1$ to the fully broken state of the material. The crack growth creates a new internal boundary $\Gamma_0^{\mathrm{cr}}(t) \subset \mathbb{R}^{n-1}$ based on energetic criterion. Here, the total energy within the sharp crack interface E^{cr} is approximated based on a crack surface density function γ resulting with a regularized crack interface as

$$\int_{\Gamma_0^{\mathrm{cr}}} g_\mathrm{c} \, \mathrm{d}\Gamma \approx \int_{\mathcal{B}_0} g_\mathrm{c} \gamma \, \mathrm{d}V \quad \text{with} \quad \gamma(\mathfrak{s}, \nabla\mathfrak{s}, \Delta\mathfrak{s}) = \frac{1}{4l_\mathrm{f}}\mathfrak{s}^2 + \frac{l_\mathrm{f}}{2}\nabla\mathfrak{s}\cdot\nabla\mathfrak{s} + \frac{l_\mathrm{f}^3}{4}(\Delta\mathfrak{s})^2 \tag{3}$$

g_c is the Griffith-type critical energy release rate and l_f is the fracture length scale.

- The long-range micro-motion field α denoted as the global hardening variable

$$\alpha(\boldsymbol{X},t) : \mathcal{B}_0 \times \mathcal{T} \to \mathbb{R} \quad \text{with} \quad \alpha = \bar{\alpha} \text{ on } \partial\mathcal{B}_0^{\alpha_\mathrm{d}} \quad \text{and} \quad \nabla\alpha \cdot \boldsymbol{N} = 0 \text{ on } \partial\mathcal{B}^{\alpha_\mathrm{n}} \tag{4}$$

illustrated in Figure 1c, where the gradient $\nabla\alpha(\boldsymbol{X},t)$ is governed by a *plastic length scale* l_p that accounts for nonlocal hardening effects. Following the recent work Miehe et al. [14], the fracture length scale is $l_\mathrm{f} \leq l_\mathrm{p}$ to ensures that the damage zones of ductile fracture are inside of plastic zones.

- The short range micro-motion field $\boldsymbol{F}^\mathrm{p}$ denoted as the plastic deformation map

$$\boldsymbol{F}^\mathrm{p}(\boldsymbol{X},t) : \mathcal{B}_0 \times \mathcal{T} \to \mathbb{R}^{n\times n}, \quad \det[\boldsymbol{F}^\mathrm{p}] = 1, \tag{5}$$

is locally defined and not constrained by boundary conditions, see Figure 1d.

The subsequent constitutive approach to phase-field ductile fracture focuses on the set

$$\mathfrak{C} := \{\nabla\boldsymbol{\varphi}, \boldsymbol{F}^\mathrm{p}, \alpha, \nabla\alpha, \mathfrak{s}, \nabla\mathfrak{s}, \Delta\mathfrak{s}\} \ , \tag{6}$$

2.1 Evolution of the Regularized Crack Surface Topology

Following the recent work of Miehe et al. [9], the rate of the work needed to create a diffusive fracture topology is driven by constitutive functions, postulating a global evolution equation of regularized crack surface

$$\dot{E}^{\mathrm{cr}} = \int_{\mathcal{B}_0} g_\mathrm{c} \, \delta_\mathfrak{s}\widehat{\gamma}(\mathfrak{s}, \nabla\mathfrak{s}, \Delta\mathfrak{s}) \, \dot{\mathfrak{s}} \, \mathrm{d}V = \int_{\mathcal{B}_0} \Big[\mathcal{H} - \mathcal{R}\Big] \, \dot{\mathfrak{s}} \, \mathrm{d}V \tag{7}$$

Here, $\mathcal{H}$ is the crack driving force defined in (27) and $\mathcal{R} = \eta_\mathrm{f} \, \dot{\mathfrak{s}}$ is a viscous crack resistance, where $\eta_\mathrm{f} \geq 0$ is a material parameter which characterize viscosity of the crack propagation. The functional derivative of the crack density function is defined as

$$\delta_\mathfrak{s}\widehat{\gamma}(\mathfrak{s}, \nabla\mathfrak{s}, \Delta\mathfrak{s}) := \partial_\mathfrak{s}\widehat{\gamma} - \mathrm{Div}[\partial_{\nabla\mathfrak{s}}\widehat{\gamma}] + \Delta[\partial_{\Delta\mathfrak{s}}\widehat{\gamma}] \ . \tag{8}$$

Then equation (7) gives the crack phase field evolution as a generalized Ginzburg-Landau-type structure

$$\eta_{\mathrm{f}}\,\dot{\mathfrak{s}} = \mathcal{H} - g_{\mathrm{c}}\left[\frac{1}{2l_{\mathrm{f}}}\,\mathfrak{s} - l_{\mathrm{f}}\Delta\mathfrak{s} + \frac{l_{\mathrm{f}}^3}{2}\,\Delta\Delta\mathfrak{s}\right] , \tag{9}$$

along with the Neumann-type boundary conditions

$$\nabla(l_{\mathrm{f}}^2\Delta\mathfrak{s} - \mathfrak{s})\cdot\boldsymbol{N} = 0 \text{ on } \partial\mathcal{B}_0^{\mathfrak{s}_{\mathrm{n}}} \quad \text{and} \quad \Delta\mathfrak{s}\cdot\boldsymbol{N} = 0 \text{ on } \partial\mathcal{B}_0^{\mathfrak{s}_{\mathrm{n}}} , \tag{10}$$

where the expression $\Delta\Delta\mathfrak{s} = \mathrm{Div}[\mathrm{Div}[\nabla^2\mathfrak{s}]]$ is the Bi-Laplacian of the crack phase field. Based on thermodynamical arguments, we demand irreversible crack evolution $\dot{E}^{\mathrm{cr}} \geq 0$, as discussed in the work of Miehe et al. [1, 9]. This global irreversibility constraint of crack evolution is satisfied by ensuring a positive evolution of the crack phase field as

$$\dot{\mathfrak{s}} = \frac{1}{\eta_{\mathrm{f}}}\left\langle\, \mathcal{H} - g_{\mathrm{c}}\left[\frac{1}{2l_{\mathrm{f}}}\,\mathfrak{s} - l_{\mathrm{f}}\Delta\mathfrak{s} + \frac{l_{\mathrm{f}}^3}{2}\,\Delta\Delta\mathfrak{s}\right] \right\rangle \geq 0 , \tag{11}$$

where $\langle x\rangle := (x + |x|)/2$ is the McAuley bracket.

2.2 Coupling Gradient Plasticity to Gradient Damage Mechanics

In large strain context, the deformation gradient is given by a multiplicative decomposition into elastic and plastic parts $\boldsymbol{F} = \boldsymbol{F}^{\mathrm{e}}\boldsymbol{F}^{\mathrm{p}}$. Then, an elastic deformation measure is the *contra-variant Eulerian elastic Finger tensor* $\boldsymbol{b}^{\mathrm{e}} = \boldsymbol{F}^{\mathrm{e}}(\boldsymbol{F}^{\mathrm{e}})^{\mathrm{T}}$ that provides the definition

$$\boldsymbol{b}^{\mathrm{e}} = \boldsymbol{F}(\boldsymbol{C}^{\mathrm{p}})^{-1}\boldsymbol{F}^{\mathrm{T}} \quad \text{with} \quad \boldsymbol{C}^{\mathrm{p}} = (\boldsymbol{F}^{\mathrm{p}})^{\mathrm{T}}\boldsymbol{F}^{\mathrm{p}} . \tag{12}$$

The kinematic basis for a decoupling of the constitutive response into volumetric elastic and isochoric elastic-plastic contributions is

$$\boldsymbol{b}^{\mathrm{e}} = J^{2/3}\bar{\boldsymbol{b}}^{\mathrm{e}} \tag{13}$$

which defines the volumetric and isochoric parts

$$J = \det[\boldsymbol{F}] = \det[\boldsymbol{F}^{\mathrm{e}}\boldsymbol{F}^{\mathrm{p}}] = \det[\boldsymbol{F}^{\mathrm{e}}] = J^{\mathrm{e}} \quad \text{and} \quad \bar{\boldsymbol{b}}^{\mathrm{e}} = J^{-2/3}\boldsymbol{F}(\boldsymbol{C}^{\mathrm{p}})^{-1}\boldsymbol{F}^{\mathrm{T}} . \tag{14}$$

The storage energy function $\widehat{\Psi}$ is assumed to depend on the array $\mathfrak{C}$ of constitutive state variables introduced in (6) as

$$\widehat{\Psi}(\mathfrak{C}) = \widehat{\Psi}^{\mathrm{e}}(\boldsymbol{b}^{\mathrm{e}};\mathfrak{s}) + \widehat{\Psi}^{\mathrm{p}}(\alpha,\nabla\alpha) . \tag{15}$$

Here, the phase field $\mathfrak{s}$ enters the constitutive functions as a generalized internal variable. However, it is considered as a geometric property that models a regularized crack surface. The elastic contributions are given by

$$\begin{aligned}\widehat{\Psi}^{\mathrm{e}} &= g_{\mathrm{vol}}(\mathfrak{s})\widehat{\Psi}^{\mathrm{e}}_{\mathrm{vol}}(J) + g_{\mathrm{dev}}(\mathfrak{s})\widehat{\Psi}^{\mathrm{e}}_{\mathrm{dev}}(\bar{\boldsymbol{b}}^{\mathrm{e}}) \\ &= \frac{\kappa}{2}g_{\mathrm{vol}}(\mathfrak{s})(J-1)^2 + \frac{\mu}{2}g_{\mathrm{dev}}(\mathfrak{s})(\mathrm{tr}[\bar{\boldsymbol{b}}^{\mathrm{e}}] - 3)\end{aligned} \tag{16}$$

in terms of the volumetric and isochoric degradation functions defined as

$$g_{\mathrm{vol}}(\mathfrak{s}) = \begin{cases} g(\mathfrak{s}) & J > 1 \\ 1 & J \leq 1 \end{cases} \quad \text{and} \quad g_{\mathrm{dev}}(\mathfrak{s}) = g(\mathfrak{s}), \tag{17}$$

where $g(\mathfrak{s}) = a_{\mathrm{g}}((1-\mathfrak{s})^3 - (1-\mathfrak{s})^2) - 2(1-\mathfrak{s})^3 + 3(1-\mathfrak{s})^2$ with $a_{\mathrm{g}} \geq 0$. Next, we introduce the constitutive relation related to the Kirchhoff stress as

$$\boldsymbol{\tau} = 2\frac{\partial \widehat{\Psi}^{\mathrm{e}}}{\partial \boldsymbol{b}^{\mathrm{e}}}\boldsymbol{b}^{\mathrm{e}} = \boldsymbol{\tau}_{\mathrm{vol}} + \boldsymbol{\tau}_{\mathrm{dev}} \tag{18}$$

with the volumetric and isochoric stress parts defined as

$$\boldsymbol{\tau}_{\mathrm{vol}} = \kappa g_{\mathrm{vol}}(\mathfrak{s})(J^2 - J)\boldsymbol{I} \quad \text{and} \quad \boldsymbol{\tau}_{\mathrm{dev}} = \mu g_{\mathrm{dev}}(\mathfrak{s})\mathrm{dev}[\bar{\boldsymbol{b}}^{\mathrm{e}}]. \tag{19}$$

The plastic contribution is decomposed into local and gradient parts. For the modeling of length scale effects in isotropic gradient plasticity, we focus on the equivalent plastic strain α and its gradient $\nabla\alpha$. It is assumed to have the form

$$\widehat{\Psi}^{\mathrm{p}}(\alpha, \nabla\alpha) = \int_0^{\alpha} \widehat{y}(\tilde{\alpha})\,\mathrm{d}\tilde{\alpha} + y_0\frac{l_p^2}{2}\|\nabla\alpha\|^2, \tag{20}$$

where $l_p \geq 0$ is a plastic length scale related to a strain-gradient hardening effect. $\widehat{y}(\alpha)$ is an isotropic local hardening function obtained form homogeneous experiments. We use in what follows the saturation-type function

$$\widehat{y}(\alpha) = y_0 + (y_\infty - y_0)(1 - \exp[-\eta\alpha]) + h\alpha \tag{21}$$

widely used in metal plasticity, in terms of the four material parameters $y_0 > 0$, $y_\infty \geq y_0$, $\eta > 0$ and $h \geq 0$, where the initial yield stress y_0 determines the threshold of the effective elastic response. Next, we define the dissipation energy *locally* as the difference of the external stress power and the evolution of the energy storage, by the standard Clausius-Planck inequality

$$\mathcal{D} = \boldsymbol{\tau} : \boldsymbol{d} - \frac{\mathrm{d}}{\mathrm{d}t}\widehat{\Psi}^{\mathrm{e}} \geq 0, \tag{22}$$

where the rate of the deformation tensor $\boldsymbol{d}$ is the symmetric part of the spatial velocity gradient $\boldsymbol{l} = \dot{\boldsymbol{F}}\boldsymbol{F}^{-1}$. Moreover, the rate of change of the energy storage reads

$$\frac{\mathrm{d}}{\mathrm{d}t}\widehat{\Psi}^{\mathrm{e}} = \frac{\partial \widehat{\Psi}^{\mathrm{e}}}{\partial \boldsymbol{b}^{\mathrm{e}}} : \dot{\boldsymbol{b}}^{\mathrm{e}} + \frac{\partial \widehat{\Psi}^{\mathrm{e}}}{\partial \mathfrak{s}}\dot{\mathfrak{s}}, \tag{23}$$

the evolution of the elastic storage energy function can be expressed in terms of the material time derivative

$$\dot{\boldsymbol{b}}^{\mathrm{e}} = \boldsymbol{l}\boldsymbol{b}^{\mathrm{e}} + \boldsymbol{b}^{\mathrm{e}}\boldsymbol{l}^{\mathrm{T}} + \boldsymbol{F}(\dot{\boldsymbol{C}}^{\mathrm{p}})^{-1}\boldsymbol{F}^{\mathrm{T}}, \quad \dot{\boldsymbol{C}}^{\mathrm{p}} = (\dot{\boldsymbol{F}}^{\mathrm{p}})^{\mathrm{T}}\boldsymbol{F}^{\mathrm{p}} + (\boldsymbol{F}^{\mathrm{p}})^{\mathrm{T}}\dot{\boldsymbol{F}}^{\mathrm{p}}. \tag{24}$$

In case of isotropy, the skew-symmetric part of the spatial velocity gradient vanishes, i.e. $\boldsymbol{l} = \boldsymbol{d}$, and $\partial_{\boldsymbol{b}^{\mathrm{e}}} \widehat{\Psi}^{\mathrm{e}}$ commutes with $\boldsymbol{b}^{\mathrm{e}}$ such that the first term in (23) can be written as

$$\begin{aligned} \frac{\partial \widehat{\Psi}^{\mathrm{e}}}{\partial \boldsymbol{b}^{\mathrm{e}}} : \dot{\boldsymbol{b}}^{\mathrm{e}} &= \left[\frac{\partial \widehat{\Psi}^{\mathrm{e}}}{\partial \boldsymbol{b}^{\mathrm{e}}} \boldsymbol{b}^{\mathrm{e}}\right] : \boldsymbol{d} + \left[\boldsymbol{b}^{\mathrm{e}} \frac{\partial \widehat{\Psi}^{\mathrm{e}}}{\partial \boldsymbol{b}^{\mathrm{e}}}\right] : \boldsymbol{d} + \left[\frac{\partial \widehat{\Psi}^{e}}{\partial \boldsymbol{b}^{\mathrm{e}}} \boldsymbol{b}^{\mathrm{e}}\right] : [\boldsymbol{F}(\dot{\boldsymbol{C}}^{\mathrm{p}})^{-1} \boldsymbol{F}^{\mathrm{T}} (\boldsymbol{b}^{\mathrm{e}})^{-1}] \\ &= \left[2 \frac{\partial \widehat{\Psi}^{\mathrm{e}}}{\partial \boldsymbol{b}^{\mathrm{e}}} \boldsymbol{b}^{\mathrm{e}}\right] : [\boldsymbol{d} - \boldsymbol{d}^{\mathrm{p}}], \end{aligned} \tag{25}$$

where $\boldsymbol{d}^{\mathrm{p}} = -\frac{1}{2} \boldsymbol{F}(\dot{\boldsymbol{C}}^{\mathrm{p}})^{-1} \boldsymbol{F}^{\mathrm{T}} (\boldsymbol{b}^{\mathrm{e}})^{-1}$ is the Eulerian plastic rate of deformation tensor. With the Kirchoff stress we obtain the dissipation in the more explicit form

$$\mathcal{D} = \boldsymbol{\tau} : \boldsymbol{d}^{\mathrm{p}} + \mathcal{H} \dot{\mathfrak{s}}. \tag{26}$$

Therein, the former terms represent the plastic part of dissipation and the latter term is the fracture part of dissipation. Here, we introduced per definition the energetic driving force for the fracture phase-field $\mathcal{H}$ as

$$\mathcal{H} = -\partial_{\mathfrak{s}} \widehat{\Psi}^{\mathrm{e}}. \tag{27}$$

Regarding to the plastic material behavior, we postulate a von Mises type plastic yield function as

$$\widehat{\Phi}^{\mathrm{p}}(\boldsymbol{\tau}, r^{\mathrm{p}}) = \|\boldsymbol{\tau}_{\mathrm{dev}}\| - \sqrt{\frac{2}{3}} r^{\mathrm{p}} \tag{28}$$

in terms of the dissipative resistance force r^{p} dual to the hardening variable α defined by the variational derivative of $\widehat{\Psi}^{\mathrm{p}}$ by α as

$$r^{\mathrm{p}} := \delta_{\alpha} \widehat{\Psi}^{\mathrm{p}} = \partial_{\alpha} \widehat{\Psi}^{\mathrm{p}} - \mathrm{Div}[\partial_{\nabla \alpha} \widehat{\Psi}^{\mathrm{p}}] \tag{29}$$

reflecting the characteristics of the gradient-extended plasticity model under consideration. A plastic Lagrange multiplier λ^{p} can introduced to enforce the Karush-Kuhn-Tucker conditions

$$\lambda^{\mathrm{p}} \geq 0, \quad \widehat{\Phi}^{\mathrm{p}} \leq 0, \quad \lambda^{\mathrm{p}} \widehat{\Phi}^{\mathrm{p}} = 0. \tag{30}$$

An extended dissipation potential can now be defined for the constrained optimization problem based on the concept of maximum dissipation

$$\widehat{V}(\dot{\mathfrak{C}}) = \underbrace{\sup_{\boldsymbol{\tau}, r^{\mathrm{p}}}}_{\boldsymbol{\tau}, r^{\mathrm{p}}} \underbrace{\sup_{\lambda^{\mathrm{p}}}}_{\lambda^{\mathrm{p}}} \left[\boldsymbol{\tau} : \boldsymbol{d}^{\mathrm{p}} - r^{\mathrm{p}} \dot{\alpha} - \lambda^{\mathrm{p}} \widehat{\Phi}^{\mathrm{p}}(\boldsymbol{\tau}, r^{\mathrm{p}})\right], \tag{31}$$

where the Lagrange parameter λ^{p} control the non-smooth evolution of the plasticity. This allows us to define the associated plastic evolution equations as follows

$$\boldsymbol{d}^{\mathrm{p}} = \lambda^{\mathrm{p}} \frac{\partial \widehat{\Phi}^{\mathrm{p}}}{\partial \boldsymbol{\tau}} = \lambda^{\mathrm{p}} \boldsymbol{n} \quad \text{and} \quad \dot{\alpha} = -\lambda^{\mathrm{p}} \frac{\partial \widehat{\Phi}^{\mathrm{p}}}{\partial r^{\mathrm{p}}}, \tag{32}$$

along with the loading-unloading condition introduced in (30). The evolution of the plastic deformation can be reformulated as

$$(\dot{\boldsymbol{C}}^{\mathrm{p}})^{-1} = -2\lambda^{\mathrm{p}} \boldsymbol{F}^{-1} \boldsymbol{n} \boldsymbol{b}^{\mathrm{e}} \boldsymbol{F}^{-\mathrm{T}} \tag{33}$$

To calculate the Lagrange multiplier, a penalty regularization can be utilized as follows

$$\lambda^{\mathrm{p}} = \frac{3}{2\eta_p} \left\langle \widehat{\Phi}^{\mathrm{p}}(\boldsymbol{\tau}, r^{\mathrm{p}}) \right\rangle \geq 0, \tag{34}$$

such that we obtain

$$\widehat{V}(\dot{\mathfrak{C}}) = \underbrace{\sup_{\boldsymbol{\tau}, r^{\mathrm{p}}}}_{} \left[\boldsymbol{\tau} : \boldsymbol{d}^{\mathrm{p}} - r^{\mathrm{p}} \dot{\alpha} - \frac{3}{4\eta_{\mathrm{p}}} \left\langle \widehat{\Phi}^{\mathrm{p}}(\boldsymbol{\tau}, r^{\mathrm{p}}) \right\rangle^2 \right] . \tag{35}$$

This approach can be interpreted physically as a viscous regularization function. η_{p} is an additional material parameter which characterize viscosity of the plastic deformation.

The time integration of the plastic evolution equations is performed by a backward Euler scheme that leads to the construction of a return-mapping algorithm (see e.g. Simo and Hughes [13]) which is outlined in the following. For each time interval $[t_n, t_{n+1}]$ we assume the state at time t_n and the time step size $\Delta t = t_{n+1} - t_n$ are known. Furthermore we assume a trial state based on a purely elastic deformation and obtain the following trial variables

$$\begin{aligned} \boldsymbol{b}^{\mathrm{e}}_{\mathrm{tr}} &= \boldsymbol{F}_{n+1} (\boldsymbol{C}^{\mathrm{p}})^{-1}_{n} \boldsymbol{F}^{\mathrm{T}}_{n+1} \,, \\ \boldsymbol{\tau}_{\mathrm{dev,tr}} &= \mu g_{\mathrm{dev}}(\mathfrak{s}) \mathrm{dev}[\bar{\boldsymbol{b}}^{\mathrm{e}}_{\mathrm{tr}}] \,, \\ \boldsymbol{n}_{\mathrm{tr}} &= \frac{\boldsymbol{\tau}_{\mathrm{dev,tr}}}{\|\boldsymbol{\tau}_{\mathrm{dev,tr}}\|} \,, \\ \widehat{\Phi}^{p}_{\mathrm{tr}} &= \|\boldsymbol{\tau}_{\mathrm{dev,tr}}\| - \sqrt{\frac{2}{3}} r^{\mathrm{p}}_{n} \,, \end{aligned} \tag{36}$$

where $(\bullet)_n$, $(\bullet)_{n+1}$ and $(\bullet)_{\mathrm{tr}}$ denote the value of a given physical quantity for the respective state. A simplified time integration of (33) with the backward Euler scheme leads to

$$(\boldsymbol{C}^{\mathrm{p}}_{n+1})^{-1} = (\boldsymbol{C}^{\mathrm{p}}_{n})^{-1} - \frac{2}{3} \Delta t \lambda^{\mathrm{p}}_{n+1} \mathrm{tr}[\boldsymbol{b}^{\mathrm{e}}_{\mathrm{tr}}] \boldsymbol{F}^{-1}_{n+1} \boldsymbol{n}_{\mathrm{tr}} \boldsymbol{F}^{-\mathrm{T}}_{n+1} \tag{37}$$

supplemented by

$$\alpha_{n+1} = \alpha_n + \sqrt{\frac{2}{3}} \Delta t \lambda^{\mathrm{p}}_{n+1}. \tag{38}$$

If $\widehat{\Phi}^{\mathrm{p}}_{\mathrm{tr}} \leq 0$, then the process is purely elastic and the elastic trial state is the solution, i.e $\lambda^{\mathrm{p}}_{n+1} = 0$. If, on the other hand $\widehat{\Phi}^{\mathrm{p}}_{\mathrm{tr}} > 0$, then the trial state is not admissible and a plastic correction is needed.

$$\lambda^{\mathrm{p}}_{n+1} = \frac{3}{2\eta_{\mathrm{p}}} \left\langle \widehat{\Phi}^{\mathrm{p}}_{n+1} \right\rangle = \frac{3}{2\eta_{\mathrm{p}}} \left\langle \|\boldsymbol{\tau}_{\mathrm{dev},n+1}\| - \sqrt{\frac{2}{3}} r^{\mathrm{p}}_{n+1} \right\rangle \tag{39}$$

Because of the simplifications regarding the time integration of $\boldsymbol{C}^{\mathrm{p}}$ in (37), the incompressibility of the plastic deformation is not preserved. As a correction, we apply the return-map update only onto the deviatoric part of $\boldsymbol{C}^{\mathrm{p}}$ and make additionally use of the constraint $\det(\bar{\boldsymbol{b}}^{\mathrm{e}}_{n+1}) = 1$, see Borden et al. [10] for more details.

2.3 Contact formulation

Assuming that multiple bodies i are in contact, the boundary of the mechanical field is subdivided into Dirichlet, Neumann and contact boundaries

$$\partial\mathcal{B}_0^{(i),\varphi} \cup \partial\mathcal{B}_0^{(i),\sigma} \cup \partial\mathcal{B}_0^{(i),\mathrm{c}} = \partial\mathcal{B}_0^{(i)}. \tag{40}$$

Note that the actual contact surface $\partial\mathcal{B}_0^{(i),\mathrm{c}}$ does not interfere with the phase-field or hardening-field boundary, which is in contrast to, e.g. a thermal boundary of a thermo-mechanical problem which establishes an energy transfer across the contact zone, see e.g. Dittmann et al. [15]. Taking the local linear momentum balance across the contact interface into account, the contact contributions to the total virtual work of a two body contact problem can be written as

$$G_{\mathrm{c}} = \int\limits_{\partial\mathcal{B}_0^{(1),\mathrm{c}}} \boldsymbol{t}^{(1)} \cdot (\delta\boldsymbol{\varphi}^{(1)} - \delta\boldsymbol{\varphi}^{(2)})\, \mathrm{d}A, \tag{41}$$

where $\boldsymbol{t}^{(1)}$ denote the Piola tractions related to the surface $\partial\mathcal{B}_0^{(1),\mathrm{c}}$. Next, we decompose the contact tractions in normal and tangential components as

$$\boldsymbol{t}^{(1)} = t_{\mathrm{N}}\boldsymbol{\nu} + \boldsymbol{t}_{\mathrm{T}}, \quad \boldsymbol{t}_{\mathrm{T}} \cdot \boldsymbol{\nu} = 0, \quad \boldsymbol{t}_{\mathrm{T}} = t_{\mathrm{T},\alpha}\boldsymbol{a}^{\alpha}. \tag{42}$$

Here, $\boldsymbol{\nu}$ denotes the current outward normal vector on $\partial\mathcal{B}_0^{(1),\mathrm{c}}$ and $\boldsymbol{a}^{\alpha}$, $\alpha \in [1,2]$ the contravariant tangential basis vectors. For convenience, we introduce the gap functions in normal and tangential directions

$$g_{\mathrm{N}} = \boldsymbol{\nu} \cdot (\boldsymbol{\varphi}^{(1)} - \boldsymbol{\varphi}^{(2)}), \quad \boldsymbol{g}_{\mathrm{T}} = (\boldsymbol{I} - \boldsymbol{\nu} \otimes \boldsymbol{\nu}) \cdot (\boldsymbol{\varphi}^{(1)} - \boldsymbol{\varphi}^{(2)}). \tag{43}$$

The normal contact conditions are given in the form of Karush Kuhn-Tucker (KKT) conditions via

$$g_{\mathrm{N}} \leq 0, \quad t_{\mathrm{N}} \geq 0, \quad t_{\mathrm{N}} g_{\mathrm{N}} = 0, \tag{44}$$

which are the classical complementary condition for contact problems. Furthermore, we postulate that the frictional response is prescribed by Coulomb's friction law, given as follows

$$\hat{\phi}_{\mathrm{c}} := \|\boldsymbol{t}_{\mathrm{T}}\| - \mu|t_{\mathrm{N}}| \leq 0, \quad \dot{\zeta} \geq 0, \quad \hat{\phi}_{\mathrm{c}}\dot{\zeta} = 0, \quad \mathscr{L}\boldsymbol{t}_{\mathrm{T}} = \epsilon_{\mathrm{T}} \left(\dot{\boldsymbol{g}}_{\mathrm{T}} - \dot{\zeta} \frac{\boldsymbol{t}_{\mathrm{T}}}{\|\boldsymbol{t}_{\mathrm{T}}\|} \right). \tag{45}$$

The last equation makes use of the Lie derivative $\mathscr{L}\boldsymbol{t}_{\mathrm{T}} = \dot{t}_{\mathrm{T},\alpha}\boldsymbol{a}^{\alpha}$ of the frictional tractions and aligns them to the tangential velocity $\dot{\boldsymbol{g}}_{\mathrm{T}}$ with respect to the tangential penalty parameter ϵ_{T}. Note that the penalization of the stick condition implies an additive split of the tangential gap into a reversible (elastic) part $\boldsymbol{g}_{\mathrm{T}}^{\mathrm{e}}$ and an irreversible (inelastic) part $\boldsymbol{g}_{\mathrm{T}}^{\mathrm{s}}$. Moreover, μ denotes the coefficient of friction and $\dot{\zeta}$ a consistency parameter in analogy to the plastic multiplier in plasticity, where $\dot{\zeta} = 0$ represents stick and $\dot{\zeta} > 0$ slip.

To demonstrate thermodynamical consistency, we introduce a local energy density function $\Psi_{\mathrm{c}} := \Psi_{\mathrm{c}}(\boldsymbol{\varphi})$ and substitute again $\delta\boldsymbol{\varphi} = \dot{\boldsymbol{\varphi}}$. The global power balance across the interface reads now

$$\int\limits_{\partial\mathcal{B}_0^{(1),\mathrm{c}}} \dot{\Psi}_{\mathrm{c}} \, \mathrm{d}V = \int\limits_{\partial\mathcal{B}_0^{(1),\mathrm{c}}} t_{\mathrm{N}}\dot{g}_{\mathrm{N}} + \boldsymbol{t}_{\mathrm{T}} \cdot (\dot{\boldsymbol{g}}_{\mathrm{T}}^{\mathrm{e}} + \dot{\boldsymbol{g}}_{\mathrm{T}}^{\mathrm{s}}) \, \mathrm{d}V. \tag{46}$$

Enforcing (44) exactly and assuming that the elastic part of the tangential gap is small enough to be neglected, the global frictional dissipation is given by

$$D_c = \int\limits_{\partial\mathcal{B}_0^{(1),\mathrm{c}}} \boldsymbol{t}_{\mathrm{T}} \cdot \dot{\boldsymbol{g}}_{\mathrm{T}}^{\mathrm{s}} \, \mathrm{d}V. \tag{47}$$

Along with the dissipation of energy due to plastic deformation D^{p} and fracture D^{f}, the total dissipation is given by $D = D^{\mathrm{p}} + D^{\mathrm{f}} + D^{\mathrm{c}}$. This total dissipation D represents the amount of energy transferred into the thermal field, which we did not consider here.

To determine the Coulomb frictional traction a return map strategy together with the Euler backward scheme is applied. In particular on the basis of a trial state for the frictional tractions (for more details see Hesch et al. [11]) the slip function given by $(45)_1$ is evaluated and the frictional tractions are computed with

$$\boldsymbol{t}_{\mathrm{T},n+1} = \begin{cases} \boldsymbol{t}_{\mathrm{T},n+1}^{\mathrm{trial}}, & \text{if} \quad \hat{\phi}_{\mathrm{c},n+1} \leq 0, \\ \mu |t_{\mathrm{N},n,n+1}| \frac{\boldsymbol{t}_{\mathrm{T},n+1}^{\mathrm{trial}}}{\|\boldsymbol{t}_{\mathrm{T},n+1}^{\mathrm{trial}}\|}, & \text{elseif} \quad \hat{\phi}_{\mathrm{c},n+1} > 0. \end{cases} \tag{48}$$

For the spatial discretization of the contact boundaries the variational consistent mortar method is applied. See Hesch et al. [11] for more details on the mortar method.

2.4 Weak formulation

The resulting variational formulation and the constitutive contact laws for the coupled phase-field approach to ductile fracture are summarized in Table 1. Note that the Macaulay bracket for the crack phase field in (11) and the plastic multiplier in (34) are evaluated by inserting the local variables χ_{p} in (50) and χ_{f} in (51).

3 NUMERICAL EXAMPLE

Finally, we present a demonstrative example for the considered ductile fracture and contact formulation, cf. Hesch et al. [11] and Dittmann [12]. In particular, we consider a deformable block to be in contact with an elastic plate, see Figure 2 for the initial configuration. The plate is clamped on the right hand side, whereas the upper surface of the block is moved downwards with a constant increment size of $\Delta u = 0.15 \times 10^{-3}$m. Moreover, the plate of size 0.3m $\times$ 0.2m $\times$ 0.02m is discretized by $13 \times 19 \times 2$ quadratic B-spline based finite elements and block is of size 0.04m $\times$ 0.04m $\times$ 0.04m is discretized by $5 \times 5 \times 5$ quadratic B-spline elements. The center point of the block is placed 0.265m away form the clamping in longitudinal direction. For both bodies, we assume that the

Table 1: Variational formulation of the coupled contact problem

1) Mechanical field

$$\sum_i \int_{\mathcal{B}_0^{(i)}} \boldsymbol{P}^{(i)} : \nabla \delta\boldsymbol{\varphi}^{(i)} - \delta\boldsymbol{\varphi}^{(i)} \cdot \boldsymbol{B}^{(i)} \, \mathrm{d}V - \sum_i \int_{\partial\mathcal{B}_0^{(i),T}} \delta\boldsymbol{\varphi}^{(i)} \cdot \bar{\boldsymbol{T}}^{(i)} \, \mathrm{d}A + \int_{\partial\mathcal{B}_0^{(1),c}} (t_\mathrm{N} \delta g_\mathrm{N} + \boldsymbol{t}_\mathrm{T} \cdot \delta \boldsymbol{g}_\mathrm{T}) \, \mathrm{d}A = 0 \tag{49}$$

2) Hardening Field

$$\int_{\mathcal{B}_0^{(i)}} \eta_\mathrm{p} \delta\alpha^{(i)} \dot{\alpha}^{(i)} + \chi_\mathrm{p} \delta\alpha^{(i)} \left(\hat{y}^{(i)} - \sqrt{\frac{3}{2}} \|\boldsymbol{\tau}_\mathrm{dev}^{(i)}\| \right) + \chi_\mathrm{p} y_0 l_\mathrm{p}^2 \nabla\delta\alpha^{(i)} \cdot \nabla\alpha^{(i)} \, \mathrm{d}V = 0 \tag{50}$$

3) Phase-field

$$\int_{\mathcal{B}_0^{(i)}} \eta_f \delta\mathfrak{s}^{(i)} \dot{\mathfrak{s}}^{(i)} - \chi_\mathrm{f} \delta\mathfrak{s}^{(i)} \left(\mathcal{H}^{(i)} - \frac{g_\mathrm{c}}{2 l_\mathrm{f}} \mathfrak{s}^{(i)} \right) + \chi_\mathrm{f} g_\mathrm{c} l_\mathrm{f} \nabla\delta\mathfrak{s}^{(i)} \cdot \nabla\mathfrak{s}^{(i)} + \frac{\chi_\mathrm{f} g_\mathrm{c} l_\mathrm{f}^3}{2} \Delta\delta\mathfrak{s}^{(i)} \, \Delta\mathfrak{s}^{(i)} \, \mathrm{d}V = 0 \tag{51}$$

4) Interface conditions

- Normal contact

$$g_\mathrm{N} \geq 0, \qquad t_\mathrm{N} \leq 0, \qquad t_\mathrm{N} g_\mathrm{N} = 0 \tag{52}$$

- Tangential contact

$$\hat{\phi}_\mathrm{c} = \|\boldsymbol{t}_\mathrm{T}\| - \mu_\mathrm{c} |t_\mathrm{N}| \leq 0, \qquad \dot{\zeta} \geq 0, \qquad \hat{\phi}_\mathrm{c} \dot{\zeta} = 0, \qquad \dot{\boldsymbol{g}}_\mathrm{T} = \dot{\zeta} \frac{\boldsymbol{t}_\mathrm{T}}{\|\boldsymbol{t}_\mathrm{T}\|} \tag{53}$$

constitutive behavior is governed by the Neo-Hookean material law defined in (16). The material parameters of the plate correspond to an aluminum-like material and take the values $\mu = 26.455\mathrm{GPa}$ and $\kappa = 72.917\mathrm{GPa}$ supplemented by an initial yield stress of $y_0 = 95\mathrm{MPa}$ and an ultimate yield stress of $y_\infty = 110\mathrm{MPa}$. The parameters of the block are given by $\mu = 35\mathrm{MPa}$ and $\kappa = 333\mathrm{MPa}$, which correspond to a synthetic substance with Young's modulus of $E = 100\mathrm{MPa}$ and a Poisson ratio of $\nu = 0.45$. In addition, the phase-field parameters of the plate are specified as $g_\mathrm{c} = 150\mathrm{kJ/m^2}$, $l = 15.79 \times 10^{-3}\mathrm{m}$ and $a_\mathrm{g} = 2$, whereas the saturation exponent for hardening is chosen as $\eta = 25.4$.

Eventually, the phase-field as well as hardening field is depicted in Figure 3. As expected, the plate will ripped out of the clamping and plastic deformation occurs in this region of the plate.

4 CONCLUSIONS

In this paper, mortar contact formulations are adapted to the field of coupled gradient plasticity and gradient damage mechanics. The underlying formulation based on a multiplicative elastoplastic decomposition of the deformation gradient allows for the nu-

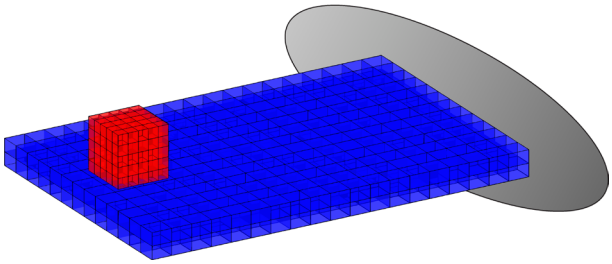

Figure 2: Bending contact fracture problem: Reference configuration.

merical treatment of large deformation problems, whereas a phase-field approach enables the prediction of complex three-dimensional fracture patterns in ductile solids. The resulting numerical framework is able to investigate ductile crack propagation within large deformation contact and impact problems. Eventually, the capability of the approach is demonstrated via a representative example.

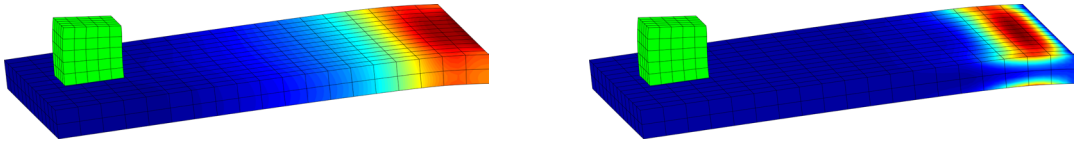

Figure 3: Bending contact fracture problem: Phase-field (left) and hardening field (right) after 113 quasi-static time steps.

ACKNOWLEDGEMENTS

Support for this research was provided by the Deutsche Forschungsgemeinschaft (DFG) under grant HE5943/6-1 and HE5943/8-1. The author C. Hesch gratefully acknowledge support by the DFG in the framework of the Priority Programme „Reliable Simulation Techniques in Solid Mechanics. Development of Non-standard Discretization Methods, Mechanical and Mathematical Analysis“ (SPP 1748) under project HE5943/5-1.

REFERENCES

[1] Miehe, C., Hofacker, M. and Welschinger, F. A phase field model for rate-independent crack propagation: Robust algorithmic implementation based on operator splits. *Comput. Methods Appl. Mech. Engrg.* (2010) 199:2765–2778.

[2] Kuhn, C. and Müller, R. A continuum phase field model for fracture. *Engineering Fracture Mechanics* (2010) 77:3625–3634.

[3] Weinberg, K. and Hesch, C. A high-order finite-deformation phase-field approach to fracture. *Continuum Mech. Thermodyn.* (2015) doi: 10.1007/s00161-015-0440-7.

[4] Francfort, G.A. and Marigo, J.J. Revisiting brittle fracture as an energy minimization problem. *Journal of the Mechanics and Physics of Solids* (1998) 46:1319-1342.

[5] Bourdin, B., Francfort, G.A. and Marigo, J.J. The variational approach to fracture. *Journal of Elasticity* (2008) 9:5–148.

[6] Karma, A., Kessler, D.A., Levine, H. Phase-field model of mode III dynamic fracture. *Physical Review Letters* (2001) 92:8704.045501.

[7] Hesch, C. and Weinberg, K. Thermodynamically consistent algorithms for a finite-deformation phase-field approach to fracture. *Int. J. Numer. Meth. Engng.* (2014) 99:906–924.

[8] Aldakheel, F. *Mechanics of Nonlocal Dissipative Solids: Gradient Plasticity and Phase Field Modeling of Ductile Fracture*. PhD thesis (2016) http://dx.doi.org/10.18419/opus-8803.

[9] Miehe, C. and Hofacker, M. and Schänzel, L.-M. and Aldakheel, F., Phase field modeling of fracture in multi-physics problems. Part II. Coupled brittle-to-ductile failure criteria and crack propagation in thermo-elastic-plastic solids. *Computer Methods in Applied Mechanics and Engineering* (2015) 294:486–522.

[10] Borden, J.M., Hughes, T.J.R., Landis, C.M, Anvari, A. and Lee, I.J., A phase-field formulation for fracture in ductile materials: Finite deformation balance law derivation, plastic degradation, and stress triaxiality effects. *Comput. Methods Appl. Mech. Engrg.* (2016) 312:130–166.

[11] Hesch, C., Franke, M., Dittmann, M. and Temizer, İ. Hierarchical NURBS and a higher-order phase-field approach to fracture for finite-deformation contact problems. *Computer Methods in Applied Mechanics and Engineering* (2016) 301:242–258.

[12] Dittmann, M. *Isogeometric analysis and hierarchical refinement for multi-field contact problems*. PhD thesis (2017) doi: 10.5445/KSP/1000063914.

[13] Simo, J.C. and Hughes, T.J.R.,*Computational Inelasticity* (1998), Springer Verlag.

[14] Miehe, C. and Kienle, D. and Aldakheel, F. and Teichtmeiter, S.,Phase field modeling of fracture in porous plasticity: A variational gradient-extended Eulerian framework the macroscopic analysis of ductile failure. *Computer Methods in Applied Mechanics and Engineering* (2016) 312:3–50.

[15] Dittmann, M., Franke, M., Temizer, İ and Hesch, C. Isogeometric Analysis and thermomechanical Mortar contact problems. *Computer Methods in Applied Mechanics and Engineering* (2014) 274:192–212.

XIV International Conference on Computational Plasticity. Fundamentals and Applications
COMPLAS XIV
E. Oñate, D.R.J. Owen, D. Peric & M. Chiumenti (Eds)

LATTICE MODEL FOR FAILURE BASED ON EMBEDDED STRONG DISCONTINUITIES IN DYNAMIC FRAMEWORK

Mijo Nikolic*, Jakov Cesic†, Adnan Ibrahimbegovic†† and Zeljana Nikolic†

* University of Split
Faculty of Civil Engineering, Architecture and Geodesy
Matice hrvatske 15, 21000 Split, Croatia
e-mail: mijo.nikolic@gradst.hr

†University of Split
Faculty of Civil Engineering, Architecture and Geodesy
Matice hrvatske 15, 21000 Split, Croatia

††Chair for Computational Mechanics
UT Compiègne/Sorbonne Universités
Laboratoire Roberval de Mécanique
Centre de Recherches Royallieu, 60200 Compiègne, France

Key words: localized failure, lattice model, embedded strong discontinuities, dynamics

Abstract. Identifying the failure of materials and structures is still a challenging task and there is no unique approach or model to tackle this problem. Complexities that arise in failure modelling are numerous, starting from mesh dependency for softening to various numerical difficulties and instabilities, tracking algorithms, multiple cracking with crack interactions etc. Failure in the dynamic framework is even more challenging bringing inertial effects, crack branching etc. In this paper, lattice model for dynamic failure is presented. The final goal is to simulate crack initiation and propagation in 2D brittle and quasi-brittle structures exposed to dynamic environment. The strength of the lattice models is in their successful representation of failure mechanisms. The presented model is based on a triangular lattice of Timoshenko beams which act as cohesive links between the Voronoi cells used to compute beam cross sections. The embedded strong discontinuities in axial and transversal beam directions serve for representation of failure mechanisms in modes I and II, while mass and inertial effects are included into lattice network.

1 INTRODUCTION

Modeling of failure mechanisms and fracture are still challenging topics and are important for many applications. The main difficulties arise from non-smooth solution character and one needs to deal with discontinuities in displacement (or strain) fields [1]. Among different approaches to tackle fracture and failure mechanisms, lattice element models are a class of discrete models which have been widely used to simulate failure in terms

of localized crack initiation or propagation [2]. Moreover, it is possible to account for heterogeneities in material structure, multiple crack propagation, crack coalescence with respect to heterogeneities. This is suitable for failure of heterogeneous materials, such as rocks or concrete, but the approach can also be used to simulate the failure of structures or solids. The main idea is to use spatial beam elements, which are geometrically built using Delaunay triangulation inside the domain of interest. The Delaunay edges in triangulation can be converted into lattice elements representing cohesive links between the Voronoi cells which are dual to Delaunay triangulation (Figure 1.a). Such Voronoi cells represent units of material in the domain, while lattice elements are here Timoshenko beams. Each beam in domain has its own geometrical properties; namely cross section is extracted from common area between the two neighboring Voronoi cells (Figure 1.b). In order to represent failure of single cohesive link between the Voronoi cells, we enhance the Timoshenko beams with embedded strong discontinuities, which provide jump in the displacement fields [1]. Introduction of embedded strong discontinuity into beams axial direction is related to mode I opening, while mode II is related to discontinuity in transversal direction. Such model for quasi-static crack propagation is given in [3, 4, 5]. The focus in this work is to enhance the existing formulation and to give the framework for dynamic crack propagation. Notable papers which deal with dynamic crack propagation where displacement fields are enriched to provide non-smooth discontinuous solutions with XFEM (Extended Finite Element Method) are [6, 7], or with embedded strong discontinuities in solid elements [8]. Lattice model with Reissner's beams as lattice elements for dynamic crack propagation is given in [9]. The outline is as follows. Section 2 explains the numerical model for crack propagation in dynamic environment. Section 3 provides representative numerical simulation. Conclusions are given at the end of paper.

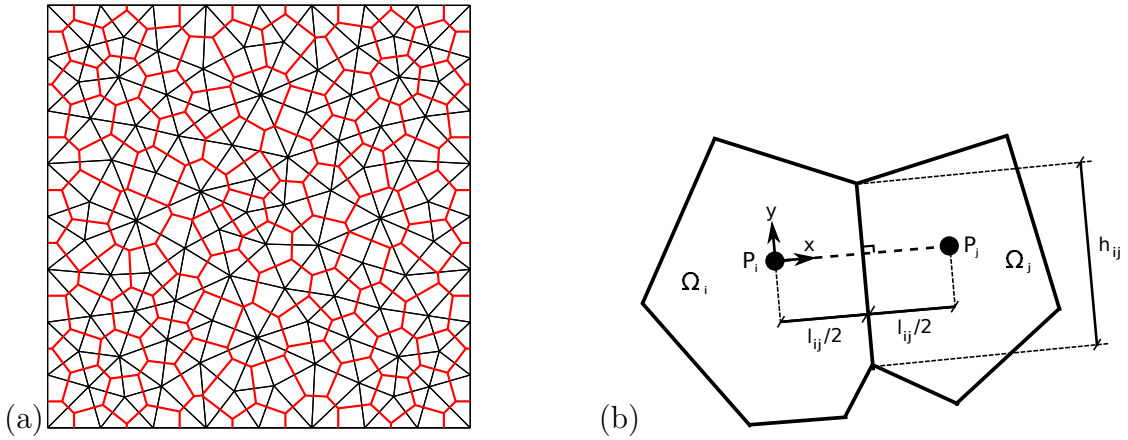

Figure 1: (a) Structure of discrete lattice model with Voronoi cells as units of heterogeneous material and cohesive links between them (b) two neighbouring Voronoi cells

2 NUMERICAL MODEL

As already indicated above, model is assembled from Voronoi cells which are kept together by Timoshenko beams as cohesive links. Failure of Timoshenko beams occur when certain threshold is reached. Furthermore, plasticity softening regime is triggered together with activation of embedded discontinuities in axial and transversal direction of beams. The strains for standard Timoshenko beams of length l_e and cross section A are

$$\boldsymbol{\epsilon}(x) = \begin{bmatrix} \epsilon(x) = \frac{du}{dx} \\ \gamma(x) = \frac{dv}{dx} - \theta \\ \kappa(x) = \frac{d\theta}{dx} \end{bmatrix} \tag{1}$$

Standard kinematics is enhanced with additional degrees of freedom in the element interior multiplied by Dirac function. Thus, enhanced beam element with standard and additional degrees of freedom is constructed (Figure 2.) The non-regular strain field can be written

$$\boldsymbol{\epsilon}(x) = \overline{\boldsymbol{\epsilon}}(x) + \boldsymbol{\alpha}\delta_{x_c} = \begin{bmatrix} \overline{\epsilon}(x) \\ \overline{\gamma}(x) \\ \overline{\kappa}(x) \end{bmatrix} + \begin{bmatrix} \alpha_u \\ \alpha_v \\ 0 \end{bmatrix} \delta_{x_c} \tag{2}$$

Finite element interpolation for beam element with interpolation functions $\{N_1(x) = 1 - \frac{x}{l_e},\ N_2(x) = \frac{x}{l_e}\}$ and their derivatives $\{B_1^d(x) = -\frac{1}{l_e},\ B_2^d(x) = \frac{1}{l_e}\}$ produces enhanced strain field which can be written in matrix form

$$\boldsymbol{\epsilon} = \mathbf{B}\mathbf{d} + \mathbf{G}\boldsymbol{\alpha}, \tag{3}$$

where $\mathbf{B}$ is a strain displacement matrix and matrix $\mathbf{G}$ contains interpolation function G for discontinuity (Figure 2).

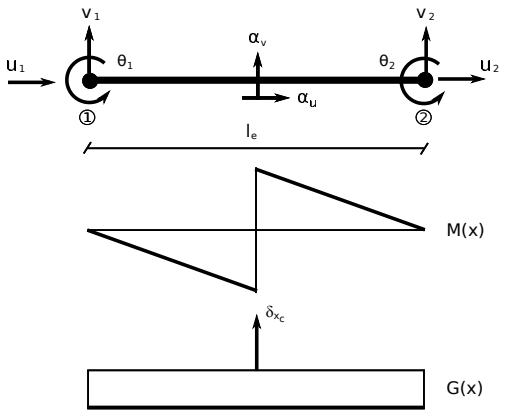

Figure 2: Enhanced Timoshenko beam element with standard and additional degrees of freedom. M and G are interpolation functions for discontinuity

Such enhancement of strain field produces the localized failure of cohesive links between Voronoi cells (Figure 3.) Virtual strain field can be written with the same interpolations

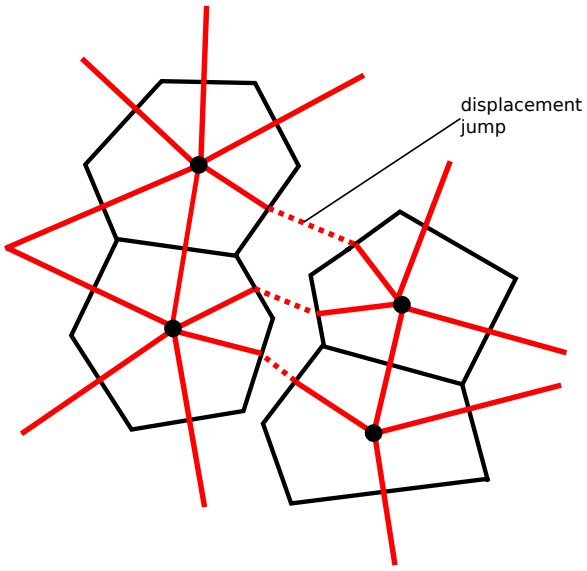

Figure 3: Localized failure of cohesive links when threshold is reached and discontinuity is activated

as the real strain field resulting with enhanced virtual work with G^{int} as internal work

$$G^{int} = \int_{l_e} (\mathbf{B}\delta\mathbf{d})^T \boldsymbol{\sigma} dx + \underbrace{\int_{l_e} \delta\boldsymbol{\alpha}^T (\overline{\mathbf{G}} + \delta_{x_c}) \boldsymbol{\sigma} dx.}_{\text{h(e)=0}} \tag{4}$$

Standard internal force vector and the local residual vector due to discontinuity are obtained from enhanced virtual work

$$\begin{aligned} \mathbf{F}^{int} &= \textstyle\int_0^{l_e} \mathbf{B}^{d,T} \boldsymbol{\sigma} dx \\ \mathbf{h}^{(e)} &= \textstyle\int_0^{l_e} (\overline{\mathbf{G}} + \delta_{x_c}) \boldsymbol{\sigma} dx. \end{aligned} \tag{5}$$

Vector of internal forces can be obtained through the regular part of the enhanced local function

$$\mathbf{t} = -\int_0^{l_e} \overline{\mathbf{G}} \boldsymbol{\sigma} dx, \quad \mathbf{t} = (t_u, t_v, 0)^T \tag{6}$$

Softening plasticity law is implemented in computation of traction forces, while the internal variables are obtained with local return mapping algorithm for softening. Reader is referred to [1, 2, 3, 4] for more details. Linearization of enhanced virtual work and local character of embedded discontinuities allow to perform static condensation of stiffness matrix resulting with single element contribution to the FE assembly

$$A_{e=1}^{n_{el}} \left(\widehat{K}_{n+1}^{(e),(i)} \Delta \mathbf{d}_{n+1}^{(e),(i)} \right) = A_{e=1}^{n_{el}} \left(\mathbf{F}^{ext,(e)} - \mathbf{F}^{int,(e),(i-1)} \right) \tag{7}$$

where $\widehat{K}_{n+1}^{(e),(i)}$ is statically condensed stiffness matrix.

The extension of quasi-static system from above (7) towards dynamic regime can be achieved taking into consideration that local problem with embedded strong discontinuities is not directly affected by dynamic effects [8]. Thus, standard finite element procedure for dynamic case results with typical inertial terms based on a global mass matrix

$$M_n a_{n+1}^{(i)} + K_n \Delta d^{(i)} = F_{n+1}^{ext} - F_{n+1}^{(i-1)} \tag{8}$$

where M is a global mass matrix, K global stiffness matrix assembled from statically condensed local matrices due to embedded discontinuities, n and i denote time step and iteration respectively. The velocity-dependent damping is not considered presently. Direct time integration procedure is applied here for the analysis of presented nonlinear dynamic problem, with trapezoidal rule, or yet called the average acceleration method. By applying the trapezoidal rule (e.g. [10]) to the equations of motion, we obtain second order approximation to evolution equations for displacement d and velocity v, which can be written:

$$\begin{array}{ll} \dot{d}(t) = v(t) & \Longrightarrow \; d_{n+1} - d_n = \frac{h}{2}(v_n + v_{n+1}) \\ \dot{v}(t) = a(t) & \Longrightarrow \; v_{n+1} - v_n = \frac{h}{2}(a_n + a_{n+1}) \end{array} \tag{9}$$

Rewriting the result in $(9)_1$ we can obtain the corresponding approximation for the velocity vector in terms of displacement increment:

$$v_{n+1} = -v_n + \frac{2}{h}(d_{n+1} - d_n) \tag{10}$$

Acceleration vector at time t_{n+1} can then be obtained similarly from $(9)_2$ using the same kind of approximation

$$a_{n+1} = -a_n - \frac{4}{h} v_n + \frac{4}{h^2}(d_{n+1} - d_n) \tag{11}$$

Both of these approximations are implicit in the sense that they depend upon the displacement value at time t_{n+1}. If we implement Newton iterative algorithm, we can rewrite equations from (10) and (11) in sense of iterations

$$\begin{array}{l} v_{n+1}^{(i)} = -v_n + \frac{2}{h}(d_{n+1}^{(i-1)} + \Delta d^{(i)} - d_n) \\ a_{n+1}^{(i)} = -a_n - \frac{4}{h} v_n + \frac{4}{h^2}(d_{n+1}^{(i-1)} + \Delta d^{(i)} - d_n) \end{array} \tag{12}$$

We have to solve at each iteration the consistently linearized form of the system, which can be written as

$$[\frac{4}{h^2} M + K_n] d_{n+1}^{(i)} = F_{n+1}^{ext} - F_{n+1}^{(i-1)} - M \underbrace{[-a_n - \frac{4}{h} v_n + \frac{4}{h^2}(d_{n+1}^{(i-1)} - d_n)]}_{a_{n+1}^{(i-1)}} \tag{13}$$

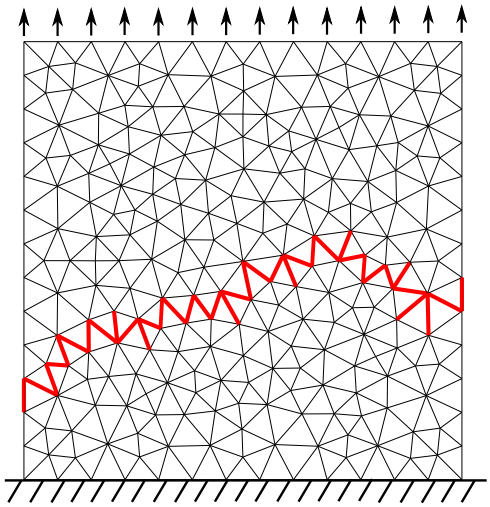

Figure 4: Uniaxial tension test and final failure pattern. Increasing softening elements at the end of simulation are red coloured

3 NUMERICAL SIMULATION

We consider here the uniaxial tension test of specimen from Figure 4. It is a heterogeneous specimen constructed from two phase elements with equal volume fraction randomly distributed throughout the domain, where one phase is strong and the other is weak [3]. The dimensions of the specimen are 10x10 cm, with moduli of elasticity being $7000kN/cm^2$ and $1000kN/cm^2$ for strong and weak phase elements and Poisson ratio 0.2. Weak phase elements are allowed to break, trigering the softening behaviour, with failure threshold for tension failure (mode I) being $0.2kN/cm^2$ and for shear failure (mode II) $0.13kN/cm^2$. Fracture energies for softening behaviour for weak elements are $0.0001kN/cm$ for tension failure case and $0.0005kN/cm$ for shear failure case. The test is conducted with imposed displacement on the upper side of the specimen, while the sum of all reactions is monitored and plotted (Figure 5) providing the macroscopic response of the specimen. Three tests are performed, including quasi-static case and two dynamic cases with differently imposed displacement rates.

It can be noted that specimen is completely broken with macro crack which propagated through the specimen (Figure 5), while in dynamic regime macroscopic curves oscillate around static response due to inertial effects. It is also observed that global softening is triggered in the time step when macro-crack found its way throughout complete specimen (Figure 4).

4 CONCLUSIONS

Lattice element model for localized failure of heterogeneous materials and structures is presented, with its extension towards dynamic regime. The main advantage of the approach is that inertial effects can be considered without changing formulation for stat-

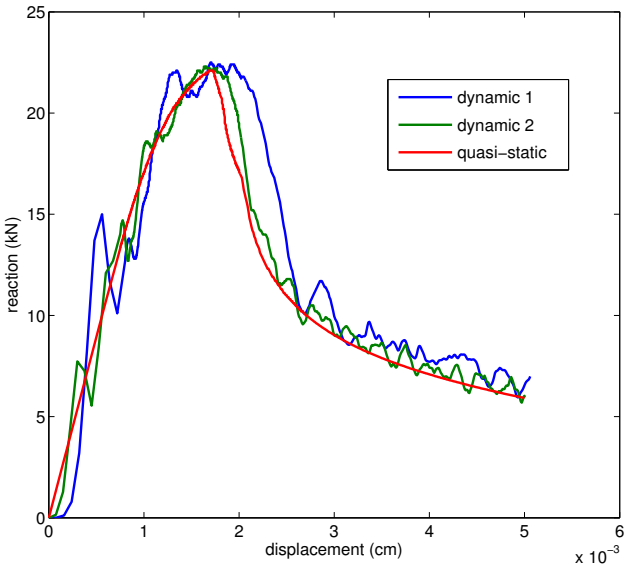

Figure 5: Macroscopic response in uniaxial tension test. Static response versus dynamic1 and dynamic2 (imposed displacement rate is two times higher for dynamic1 than for dynamic2 load)

ically condensed stiffness matrix which arises due to local discontinuous enhancements. Representative numerical simulation is performed comparing the results for static and dynamic analysis.

Acknowledgements

This work has been fully supported by Croatian Science Foundation under the project *Development of numerical models for reinforced-concrete and stone masonry structures under seismic loading based on discrete cracks* (IP-2014-09-2319).

REFERENCES

[1] Ibrahimbegovic, A. *Nonlinear Solid Mechanics: Theoretical Formulations and Finite Element Solution Methods*. Springer, London, (2009).

[2] Nikolic, M., Karavelic, E., Ibrahimbegovic, A. and Miscevic, P. Lattice Element Models and Their Peculiarities. *Arch. Comput. Meth. Eng.* (2017) doi:10.1007/s11831-017-9210-y

[3] Nikolic, M., Ibrahimbegovic, A. and Miscevic, P. Brittle and ductile failure of rocks: Embedded discontinuity approach for representing mode I and mode II failure mechanisms. *Int. J. Num. Meth. Engng.* (2015) **102**:1507–1526.

[4] Nikolic, M. and Ibrahimbegovic, A. Rock mechanics model capable of representing initial heterogeneities and full set of 3D failure mechanisms. *Comput. Methods Appl. Mech. Eng.* (2015) **290**:209-227.

[5] Nikolic, M., Ibrahimbegovic, A. and Miscevic, P. Discrete element model for the analysis of fluid-saturated fractured poro-plastic medium based on sharp crack representation with embedded strong discontinuities. *Comput. Methods Appl. Mech. Eng.* (2016) **298**:407-427.

[6] Rethore, J. Gravouil, A. and Combescure A. An energy-conserving scheme for dynamic crack growth using the eXtended finite element method. *Int. J. Num. Meth. Engng.* (2005) **63**:631-659.

[7] Menouillard, T., Rethore, J., Moes, N., Combescure, A. and Bung, H. Mass lumping strategies for X-FEM explicit dynamics: Application to crack propagation. *Int. J. Num. Meth. Engng.* (2008) **74**:447-474.

[8] Armero, F. and Linder, C. Numerical simulation of dynamic fracture using finite elements with embedded discontinuities. *Int. J. Fract.* (2009) **160**:119-141

[9] Ibrahimbegovic, A. and Delaplace, A. Microscale and mesoscale discrete models for dynamic fracture of structures built of brittle. *Comput. Struct.* (2003) **81**:1255-1265

[10] Bathe, K.J. *Finite Element Procedures*. Klaus-Jurgen Bathe, 2nd edition (2014).

XIV International Conference on Computational Plasticity. Fundamentals and Applications
COMPLAS XIV
E. Oñate, D.R.J. Owen, D. Peric & M. Chiumenti (Eds)

PHENOMENOLOGICAL MODELING OF STRAIN HARDENING, PHASE TRANSFORMATION AND DAMAGE EFFECTS OF TRIP-STEELS

ANDREAS SEUPEL AND MEINHARD KUNA

TU Bergakademie Freiberg
Institute of Mechanics and Fluid Dynamics
Lampadiusstraße 4, 09599 Freiberg, Germany
e-mail: Andreas.Seupel@imfd.tu-freiberg.de, web page: http://www.tu-freiberg.de/

Key words: TRIP-steel, Asymmetric Strain Hardening, Non-local Damage Model

Abstract. In this study, the constitutive modeling of loading state dependent strain hardening and martensite evolution of high alloyed TRIP-steels are addressed, which are experimentally observed comparing uni-axial tension and compression test results. Furthermore, a damage mechanics extension of the model is proposed, which is based on the continuum damage mechanics framework. An implicit gradient based enrichment method is applied to realize a non-local damage formulation. For the implementation into the commercial FEM-software ABAQUS, the analogy between the additional Helmholtz-type equation of implicit gradient enrichment and the already built-in heat conduction equation is used. Finally, the developed model is fitted to experimental data and cell model calculations. A convergence study using the non-local extension is discussed.

1 INTRODUCTION

Metastable austenitic steels exhibit outstanding strain hardening and ductility properties due to a martensitic phase transformation during thermo-mechanical loading. The typical strain hardening behavior and the additional plastic deformations caused by phase transition are often summarized as TRIP-effect (TRansformation Induced Plasticity).

In this paper, we focus on the mechanical behavior of a special TRIP-steel considering its stress state dependent material response. Starting point is the experimental observation of asymmetric strain hardening and martensite evolution under uni-axial tension and compression loading. We propose a model, which comprises both features. Similar effects are extensively discussed in literature (see e. g. [1, 2]).

Furthermore, the description of the material's failure is addressed. Existing local approaches to fracture for TRIP-steels (see [3, 4]) suffer from their well known mesh dependency in finite element computations. Therefore, a continuum damage mechanics model with non-local regularization is also proposed in this paper to include failure into the developed constitutive model of TRIP-steel.

The modeling approaches are successively applied: (i) The plasticity model is fitted to tension and compression experiments conducted for a high alloyed TRIP-steel. (ii) The proposed damage extension of the model is calibrated and tested with help of cell model simulations of TRIP-steel containing micro-voids. (iii) The mentioned regularization method is investigated by means of a convergence study.

Notation hints: Tensors are subsequently introduced. Symbolic notation is used, where scalars are denoted italic A, first order tensors as $\vec{A}$, second order tensors as bold symbols $\boldsymbol{A}$ and fourth order tensor are highlighted calligraphically $\mathcal{A}$. Single and double contraction of tensors are denoted by '$\cdot$' and ':', respectively.

2 PROPOSED MODEL

2.1 Stress-strain relation

Starting with an additive split of the rate of deformation tensor $\boldsymbol{D}$ into an elastic, plastic and a transformation induced part

$$\boldsymbol{D} = \boldsymbol{D}_{\mathrm{el}} + \boldsymbol{D}_{\mathrm{pl}} + \boldsymbol{D}_{\mathrm{tr}}, \tag{1}$$

we assume the following hypo-elastic relation between the Kirchhoff-stress tensor $\hat{\boldsymbol{\tau}}$ and the elastic part of the rate of deformation tensor:

$$(\hat{\boldsymbol{\tau}})^{\circ} = \mathcal{C} : \boldsymbol{D}_{\mathrm{el}}. \tag{2}$$

In the previous and following equations, a hat ($\hat{\cdot}$) highlights an effective (undamaged) value. The objective time derivative of the Kirchhoff-stress tensor is denoted by $(\cdot)^{\circ}$, where the Jaumann-rate is used in what follows. The fourth-order tensor of isotropic, linear elastic stiffness is denoted by $\mathcal{C}$. The relation between the Kirchhoff-stress tensor $\hat{\boldsymbol{\tau}}$ and the Cauchy-(true)-stress tensor $\hat{\boldsymbol{\sigma}}$ reads

$$\hat{\boldsymbol{\tau}} = \det(\boldsymbol{F})\, \hat{\boldsymbol{\sigma}}, \tag{3}$$

with the deformation gradient $\boldsymbol{F}$.

2.2 TRIP-effect: martensite evolution, kinematics and strain hardening

The evolution of strain induced martensite (volume fraction z) is based on the Olson-Cohen-model (see [5])

$$\dot{z} = (1 - z)\, \beta n f_{\mathrm{sb}}^{n-1} \dot{f}_{\mathrm{sb}}, \tag{4}$$

where $\dot{f}_{\mathrm{sb}}$ denotes the volume fraction of shear bands, which act as nucleation sites for martensite. The probability of forming a martensite nucleus at crossing points of shear bands is included in the parameter β, whereas n is a geometrical constant. The shear band volume fraction is assumed to obey the evolution law

$$\dot{f}_{\mathrm{sb}} = \alpha\, (1 - f_{\mathrm{sb}})\, \dot{\varepsilon}_{\mathrm{eq}}. \tag{5}$$

The entire martensite evolution is driven by the plastic deformation (equivalent plastic strain $\varepsilon_{\mathrm{eq}}$). Former studies propose a dependency of the shear band rate α and the probability parameter β on temperature, strain rate and stress state (see e. g. [6]). We focus on the stress state dependency only. The stress state of uni-axial tension and compression loadings can be distinguished by the stress triaxiality h

$$h = \frac{I_1}{3\sqrt{3J_2}} \tag{6}$$

and the Lode-parameter

$$\cos(3\phi) = \frac{3\sqrt{3}}{2}\frac{J_3}{J_2^{\frac{3}{2}}}, \qquad -1 \leq \cos(3\phi) \leq 1. \tag{7}$$

The necessary invariants of the stress tensor $\hat{\boldsymbol{\tau}}$ to calculate the former values are the first invariant of the stress tensor I_1 as well as the second and third invariant of the stress deviator $\hat{\boldsymbol{S}}$, J_2 and J_3, respectively. At this stage of investigation, a primary influence of the stress triaxiality h on martensite formation is considered. The ansatz for the triaxiality dependent parameter α reads:

$$\alpha(\hat{\boldsymbol{\tau}}) = \alpha_0 + \alpha_1 \left(\frac{2}{\pi} \arctan(h\,\alpha_2) + 1 \right). \tag{8}$$

To ensure $\alpha \geq 0$, the restrictions $\alpha_0 \geq 0$ and $\alpha_1 \geq -\frac{\alpha_0}{2}$ apply. An analogous term is used to define $\beta(\hat{\boldsymbol{\tau}})$ with upcoming parameters β_0, β_1 and β_2. Therewith, a triaxiality influence occurs, but the values of α and β are limited for $h \to (-\infty, +\infty)$. An additional term containing the Lode-parameter $\cos(3\phi)$ can be added to delineate further loading states (see [1]).

The martensite evolution leads to additional inelastic deformations on the macroscopic scale (TRIP-strains). Besides deviatoric contributions, also a volume change can be detected. The rate of deformation tensor related to phase transformation is introduced as

$$\boldsymbol{D}_{\mathrm{tr}} = M\boldsymbol{N}\dot{z} + \frac{1}{3}\triangle_{\mathrm{v}}\boldsymbol{\delta}\dot{z}. \tag{9}$$

This postulates, that the transformation strains are proportional to the martensite volume fraction and that the deviatoric part has the direction of the yield normal $\boldsymbol{N}$ associated with the conventional plastic flow. The unity tensor related to the volumetric part is denoted as $\boldsymbol{\delta}$. The amount of shearing and volume change due to martensite evolution is controlled by the parameters M and $\triangle_{\mathrm{v}}$.

The martensite formed during deformation apparently affects the strain hardening behavior (i. e. typical sigmoidal hardening curves). The physical hardening mechanisms resulting from dislocation-martensite interactions are illustrated elsewhere for the considered steel (see [7]). A phenomenological contribution to the isotropic hardening of the material is applied

$$\tau_{\mathrm{m}}(z) = Z_1\left(\exp(Z_2 z) - 1\right), \tag{10}$$

containing two parameters (Z_1, Z_2).

2.3 Elasto-plasticity with asymmetric strain hardening

From multi-axial testing of the considered TRIP-steel, the von Mises yield criterion was found to be appropriate to describe the initial yield stress (see [8]). Therefore, the modeling is based on the yield function

$$y = \tau_{\mathrm{eq}} - R\left(r\right) - \tau_{\mathrm{m}}\left(z\right) - \tau_0 \leq 0, \tag{11}$$

in the framework of rate independent plasticity. Only an isotropic hardening is considered with contributions due to martensite evolution $\tau_{\mathrm{m}}\left(z\right)$ and dislocation based mechanisms $R\left(r\right)$. An asymmetry of the strain hardening between uni-axial tension and compression can be caused by the martensite contribution. Due to the proposed martensite evolution approach, more martensite is formed during tensile loading, i. e. the flow stress should be higher than under compressive loading at comparable strains. But a higher flow stress is experimentally observed during uni-axial compression (see Fig. 1). Therefore, the hardening variable r is defined as follows: Firstly, an associated flow rule for the plastic rate of deformation tensor is utilized

$$\boldsymbol{D}_{\mathrm{pl}} = \dot{\Lambda}\frac{\partial y}{\partial \hat{\boldsymbol{\tau}}} = \dot{\Lambda}\boldsymbol{N} \tag{12}$$

$$\boldsymbol{N} = \frac{3}{2\tau_{\mathrm{eq}}}\hat{\boldsymbol{S}}. \tag{13}$$

One finds an expression for the equivalent plastic strain rate and the relation to the Lagrangian multiplier $\dot{\Lambda}$ in the well known manner:

$$\dot{\varepsilon}_{\mathrm{eq}} = \sqrt{\frac{2}{3}\boldsymbol{D}_{\mathrm{pl}} : \boldsymbol{D}_{\mathrm{pl}}} = \dot{\Lambda}. \tag{14}$$

The hardening variable is now introduced as

$$\dot{r} = \left(1 - G\right)\dot{\varepsilon}_{\mathrm{eq}} \geq 0, \tag{15}$$

where G is assumed to be a function of the Lode-parameter $\cos\left(3\phi\right)$:

$$G\left(\cos\left(3\phi\right)\right) = \frac{B}{2}\left(1 + \cos\left(3\phi\right)\right), \qquad \text{with } 0 \leq B, G < 1. \tag{16}$$

Just the additional parameter B appears. The uni-axial compression test can be seen as reference, because G vanishes. The strain hardening during uni-axial tension can be decreased by finding an appropriate value of $B < 1$. The hardening rule is very flexible, because it can be easily extended by dependencies on z or $\varepsilon_{\mathrm{eq}}$. Considering an effect of the Lode-parameter on strain hardening implies an orientation influence, which has to be clarified in future investigations.

The hardening function is assembled by the case differentiation

$$R = \begin{cases} Hr^q & ,r \leq r_{\mathrm{c}} \\ Hr_{\mathrm{c}}^q + R_\infty\left(1 - \exp\left(-\frac{H\,q\,r_{\mathrm{c}}^{q-1}}{R_\infty}\left(r - r_{\mathrm{c}}\right)\right)\right) & ,\text{else.} \end{cases} \tag{17}$$

with the four parameters H, q, r_c and R_∞. This extends the typical power law for hardening to incorporate a saturation after exceeding a critical value r_c.

The elasto-plastic model for TRIP-steel is completed by the Kuhn-Tucker-conditions

$$\dot{\Lambda} \geq 0, \qquad \dot{\Lambda}\, y = 0, \qquad y \leq 0 \tag{18}$$

and the consistency condition

$$\dot{y} = 0. \tag{19}$$

The derived model equations can be numerically solved by standard methods (see [9]). The finite strain formulation, which is based on an updated Lagrange-method combined with an integration of the hypo-elastic equation, is directly provided by the FEM-software (ABAQUS/standard version 6.14).

2.4 Damage model

Starting point of continuum damage mechanics is the effective stress concept leading to

$$\boldsymbol{\sigma} = (1 - D)\, \hat{\boldsymbol{\sigma}}, \tag{20}$$

where $\boldsymbol{\sigma}$ is the macroscopic stress, $\hat{\boldsymbol{\sigma}}$ is the effective stress acting on the undamaged material and D is an isotropic damage variable with $0 \leq D \leq 1$. The damage variable D is typically considered as ratio of damaged area over net area, whereby also the meaning of a porosity is possible.

Damage evolves until reaching a critical value of $D_\mathrm{c} \ll 1$. We interpret this as the beginning of a void coalescence mechanism leading rapidly to the failure of the material. A phenomenological acceleration of damage is taken into account by introducing the modified damage variable D^*:

$$D^* = \begin{cases} D & , D < D_\mathrm{c} \\ D + \kappa \left(D_\mathrm{c} - D\right)^2 & , \text{else.} \end{cases} \tag{21}$$

The acceleration is driven by $\kappa > 0$. In order to realize a smooth transition to the total failure state, a second modification is used after a critical value near failure D_t^* is reached. An exponential type function

$$D^* = D_\mathrm{max}^* \left(1 - \exp\left[-D_2 \left(D - D_3\right)\right]\right), \qquad D^* > D_\mathrm{t}^* \tag{22}$$

is utilized, where the maximum damage value D_max^* and the transition D_t^* can be chosen (choice: $D_\mathrm{max}^* = 0.9999$, $D_\mathrm{t}^* = 0.8$). The other parameters are determined by demanding smooth differentiability at $D^* = D_\mathrm{t}^*$ considering Eqn. (21) and (22):

$$D_1 = \frac{2 D_\mathrm{c} \kappa - 1 + \sqrt{1 + 4\kappa \left(D_\mathrm{t} - D_\mathrm{c}\right)}}{2\kappa} \tag{23}$$

$$D_2 = \frac{1 + 2\kappa \left(D_1 - D_\mathrm{c}\right)}{D_\mathrm{max}^* - D_\mathrm{t}} \tag{24}$$

$$D_3 = D_1 + \frac{1}{D_2} \ln\left[1 - \frac{D_\mathrm{t}}{D_\mathrm{max}^*}\right]. \tag{25}$$

When damage at a material point attains a value $D^* = 1$, a crack is assumed to be initiated. For technical reasons, we declare the criterion $D^* \geq 0.99$ as initiation point.

Typically, failure of steels originates from nucleation, growth and coalescence of micro-voids. Therefore, the Rice and Tracey model of void growth is taken into account (see [10]). The damage (porosity) evolves as

$$\dot{D} = (1 - D)\, \dot{\varepsilon}_\mathrm{d}, \tag{26}$$

where the damage driving strain rate $\dot{\varepsilon}_\mathrm{d}$ is formulated to yield :

$$\dot{\varepsilon}_\mathrm{d} = \begin{cases} D^* K_1 \exp\left(\frac{h}{h_1}\right) \dot{\varepsilon}_\mathrm{dev} & , h < h_\mathrm{t} \text{ and } D < D_\mathrm{c} \\ D^* K_1 e_\mathrm{smooth}\,(h)\, \dot{\varepsilon}_\mathrm{dev} & , h \geq h_\mathrm{t} \text{ and } D < D_\mathrm{c}. \end{cases} \tag{27}$$

Damage is then a function of stress triaxiality h. A scalar measure of deviatoric deformation $\dot{\varepsilon}_\mathrm{dev}$ is introduced, which combines plastic and TRIP-contributions. Its formulation is discussed subsequently. K_1 and h_1 are adjustable parameters. To avoid numerical problems, the exponential term of the Rice and Tracey model is restricted by determining a cut-off triaxiality h_t. The function e_smooth provides a finite value for $h \to \infty$ and contains one additional parameter h_max (see Appendix).

Results of cell model simulations on porous metals show, that a uni-axial straining state occurs after exceeding the critical damage D_c (see e. g. [4]). Therefore, the damage driving strain rate switches to

$$\dot{\varepsilon}_\mathrm{d} = \frac{3}{2}\dot{\varepsilon}_\mathrm{dev}, \qquad D \geq D_\mathrm{c}. \tag{28}$$

We suggest an approximation of the rate of equivalent inelastic strain $\dot{\varepsilon}_\mathrm{dev}$ by the value calculated from the deviatoric part $\boldsymbol{D}_\mathrm{dev}$ of the whole rate of deformation tensor $\boldsymbol{D}$ as:

$$\dot{\varepsilon}_\mathrm{dev} = \begin{cases} \sqrt{\frac{2}{3}\boldsymbol{D}_\mathrm{dev} : \boldsymbol{D}_\mathrm{dev}} & , \dot{\Lambda} > 0 \\ 0 & , \text{ else.} \end{cases} \tag{29}$$

As a result, after computing the effective stress response, damage can be evaluated separately by integrating Eq. (26). Regarding all modifications, Eq. (20) is rewritten as

$$\boldsymbol{\sigma} = (1 - D^*)\, \hat{\boldsymbol{\sigma}}. \tag{30}$$

2.5 Non-local damage model

An implicit gradient regularization method is used to obtain a non-local spatial average of a damage related variable (see e. g. [11]). The deformation and stress dependent damage driving strain rate $\dot{\varepsilon}_\mathrm{d}$ is chosen to be replaced by its non-local counterpart $\dot{\bar{\varepsilon}}_\mathrm{d}$ in the damage evolution law Eq. (26). This ensures, that a fully damaged state $D^* \to D^*_\mathrm{max}$ can be achieved. The non-local variable is determined by solving the additional field equation of Helmholz-type (∇^2 - Laplacian, $\vec{\nabla}$ - Nabla-operator):

$$\bar{\varepsilon}_\mathrm{d} - L^2 \nabla^2 \bar{\varepsilon}_\mathrm{d} = \varepsilon_\mathrm{d}. \tag{31}$$

The regularization involves an additional internal length parameter L. The boundary conditions are chosen as

$$\vec{\nabla}\bar{\varepsilon}_{\mathrm{d}} \cdot \vec{n} = 0, \tag{32}$$

according to [11] ($\vec{n}$ - normal to current boundary).

At this point, some remarks on possible implementation strategies using the FE-code ABAQUS/standard (version 6.14) should be given. The constitutive law is defined via subroutine UMAT. The similarity between the field equation Eq. (31) and the stationary heat equation can be used to avoid implementing a user defined finite element (subroutine UEL). The temperature degree of freedom changes its meaning to the non-local variable $\bar{\varepsilon}_{\mathrm{d}}$. Firstly, a fully thermal-displacement-coupled simulation step with stationary heat transfer has to be defined. Declaring a 'heat generation' r_{pl} in subroutine HETVAL as

$$r_{\mathrm{pl}} = -\bar{\varepsilon}_{\mathrm{d}} + \varepsilon_{\mathrm{d}} \tag{33}$$

changes the heat equation into the desired Helmholtz-equation. The implementation requires also additional material tangent entries, which can be defined in subroutines UMAT and HETVAL. The internal length is provided by defining the 'conductivity' L^2. For the considered 2D-plane strain-problems in section 3.3 we use quadratic shape functions to approximate the displacements and linear shape functions for the non-local variable. A reduced integration scheme is applied (ABAQUS element CPE8RT).

3 RESULTS AND DISCUSSION

Firstly, the results of fitting the TRIP-steel model to experimental data is discussed. No damage is considered at this stage. The chemical composition of the considered TRIP-steel is given in Tab. 1. The uni-axial tensile and compressive tests were conducted at a low temperature (273.15 K) to generate a high amount of martensite during mechanical loading; the experimental techniques can be found in [12]. For measuring the martensite content, the setup described in [13] was used.

Secondly, the *local* damage model is fitted to cell model simulations of TRIP-steel with micro-voids (porosity=1 %). Cell model simulations of porous metals are well known, general information can be found in [14]. The simple case of an axi-symmetric unit cell is used here. During loading, the stress triaxiality h is held constant. Macroscopic stress-strain curves can be extracted. As material model for the metal matrix, the fitted TRIP-steel model without damage is utilized.

Finally, a convergence study using the *non-local* damage model is presented. The considered 2D boundary value problem of a plate with a hole and some kinematic restrictions are sketched in Fig. 2 (symmetry conditions are applied, plane strain state, displacement controlled).

3.1 Fit to uni-axial experiments

As illustrated in Fig. 1, the stress-strain response as well as the martensite evolution of uni-axial compression and tension tests are captured by the proposed model. Espe-

Table 1: Chemical composition of the investigated 16Cr-7Mn-7Ni TRIP-steel (in mass-%)

Fe	C	Cr	Mn	Ni	Al	Si	Mo	Ti	N
bal.	0.02	15.9	7.1	6.9	0.015	1.16	0.025	0.01	0.08

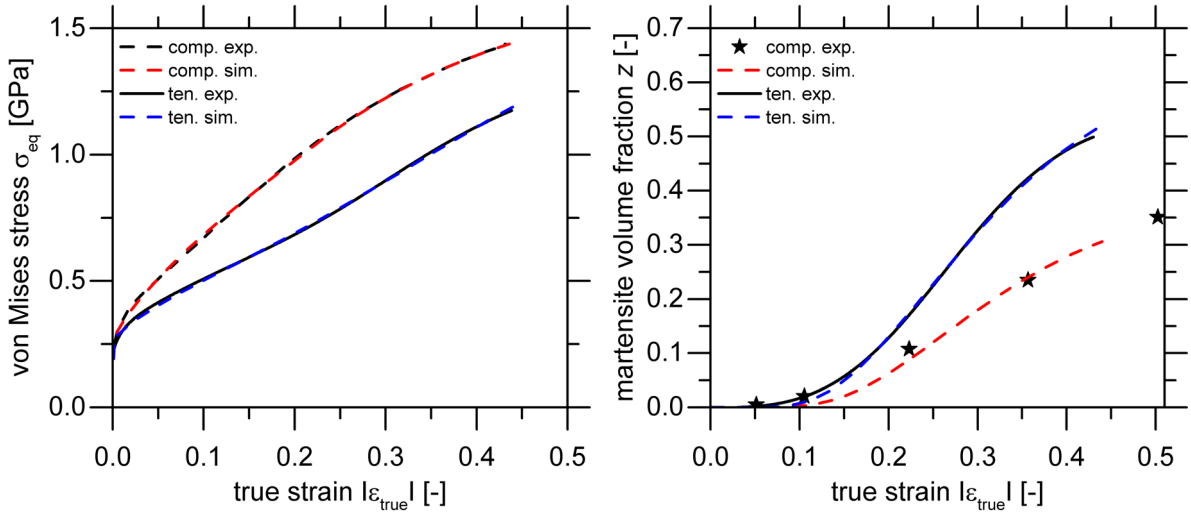

Figure 1: Fitting results of the model (sim.) to uni-axial tension (ten.) and compression (comp.) results (exp.): true stress-strain-curves (lhs) and martensite evolution (rhs)

cially the asymmetric hardening is matched well. During parameter optimization, the martensite evolution parameters can be fitted prior to the hardening parameters.

3.2 Fit to cell model simulation

Prior to the fitting procedure, a convergence study regarding the permissible strain increment during loading was performed. After exceeding D_c, a high sensitivity concerning the strain increment was found. In all upcoming simulations, the possible crossing of D_c is checked during computation at every integration point. The (absolute) biggest component of the strain increment tensor must not exceed 0.001 for $D \geq D_c$.

An initial damage of $D_0 = 0.01$ is applied during the calibration of the damage model to the cell model results. The hardening and martensite evolution parameters are optimized to fit the uni-axial cell model result ($h = 1/3$, see Tab. 2), where damage has a minor influence. Afterwards, the damage parameters K_1, h_1, D_c and κ are calibrated to match the stress-strain behavior of the cell model at higher stress triaxialities (see Tab. 2). According to Fig. 2 (lhs), the qualitative behavior is reasonable. A good agreement is found for $h = 2$, whereas a slight mismatch is visible for $h = 1$ and $h = 3$.

3.3 Numerical example and convergence study

For the convergence study concerning the spatial discretization, the boundary value problem depicted in Fig. 2 (rhs) with the parameter set of Tab. 2 is considered. Five discretization variants are realized, where the ratio of a characteristic element length l_e over

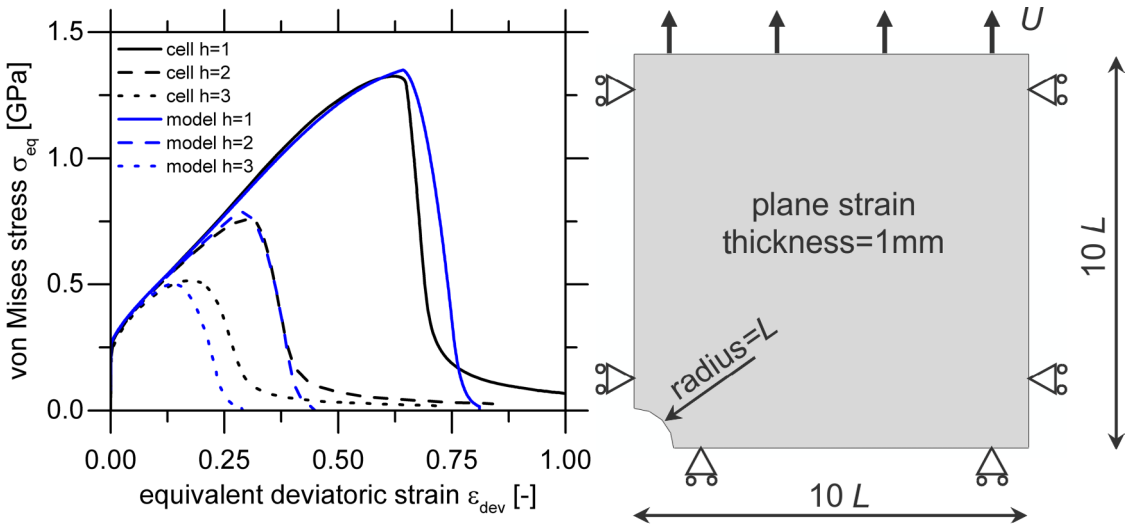

Figure 2: Fitting results of the local damage model to cell model results at three different triaxialities h (equivalent stress - equivalent strain curves of model and cell simulations, lhs) and boundary value problem of the convergence study (plate with hole, rhs)

Table 2: Model and material parameters found from cell model fit (E - Young's modulus, ν - Poisson's ratio, τ_0 - initial yield stress)

E [GPa]	ν [-]	τ_0 [MPa]	H [MPa]	q [-]	r_c [-]	R_∞ [MPa]	Z_1 [MPa]	Z_2 [-]
192	0.24	264.216	2427.952	0.753	0.199	428.93	177.96	1.864
B [-]	M [-]	$\triangle_v$ [-]	α_0 [-]	α_1 [-]	α_2 [-]	β_0 [-]	β_1 [-]	β_2 [-]
0.535	0.12	0.02	0.101	7.006	0.083	0.517	0.272	294.679
n [-]	D_0 [-]	K_1 [-]	h_1 [-]	D_c [-]	κ [-]	h_t [-]	h_{max} [-]	L [mm]
6.037	0.01	1.507	1.21	0.085	30	3	5	0.4

internal length L is systematically varied: $l_e/L = 1/16...1$. Quadrilateral finite elements are utilized; the prescribed edge length is chosen as l_e. The simulation is interrupted, if crack initiation is reached anywhere. Fig. 3 (lhs) shows the global response of the structure for different meshes. A sharp load drop prior to crack growth can be observed. No mesh size dependency exists, where the load drop would clearly occur at different displacements.

The magnified view of the load drop highlights the convergent behavior. The curves for $l_e/L \leq 1/4$ seem to coincide. A quantitative error analysis is performed through defining a relative error

$$\Delta_U = \frac{|U_{ci} - U_{ci,l_e=1/16}|}{U_{ci,l_e=1/16}} \tag{34}$$

of the nominal displacement at crack initiation $U = U_{ci}$ with respect to the finest mesh. Fig. 3 (rhs) reveals that a convergence exists, where the relative error for $l_e/L = 1/4$ is already smaller than 0.1%. This confirms the recommendation to use $l_e/L = 1/4$, which can be found in [11].

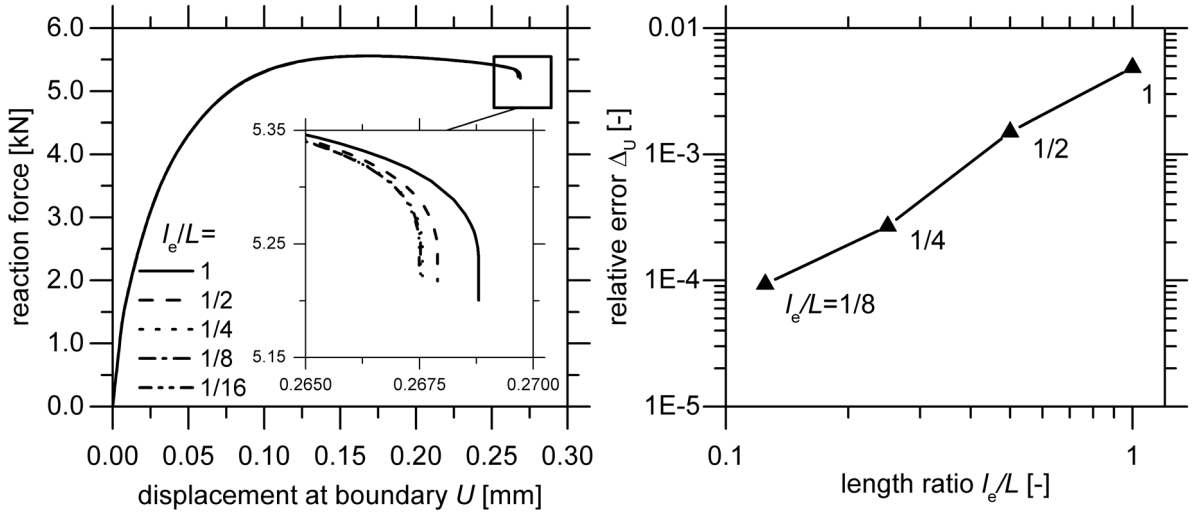

Figure 3: Convergence study results: force-displacement response until crack initiation of different discretization l_e/L (lhs) and relative error analysis of the displacement at crack initiation (rhs)

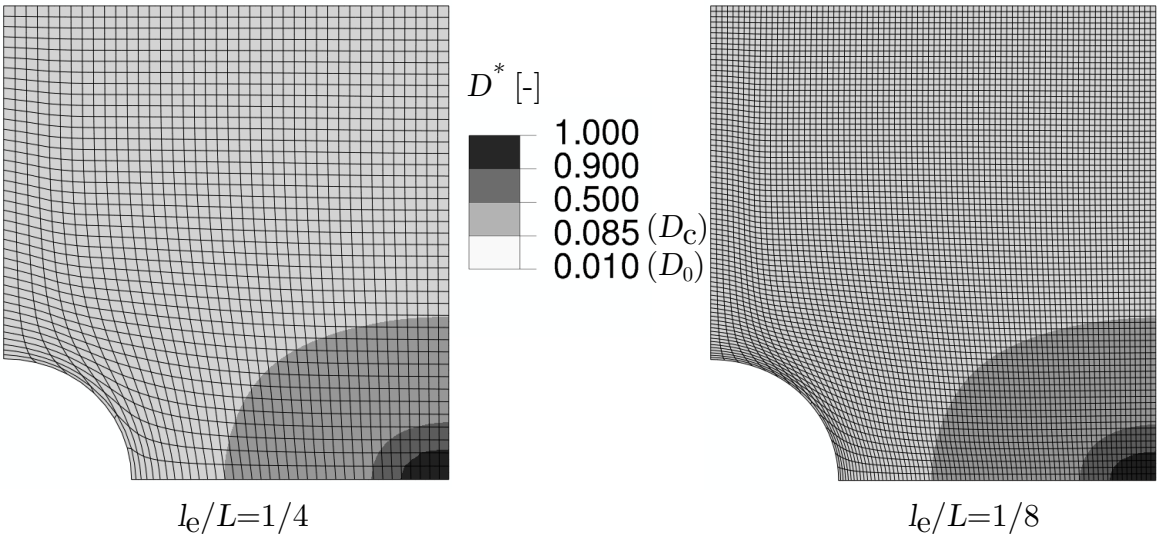

Figure 4: Convergence study results: contour plot of damage D^* at crack initiation point for two meshes $l_\mathrm{e}/L = 1/4$ (lhs) and $l_\mathrm{e}/L = 1/8$ (rhs)

Remark: For the previous convergence study, the change of the damage driving force $\dot{\varepsilon}_\mathrm{d}$ beyond D_c is neglected (see Eq. (28)). We found also mesh independent results for activating this switching, but the convergence behavior was not as 'beautiful' as for the non-switching case.

The local convergence behavior is illustrated by a closer view to the damage distribution at the point of crack initiation (Fig. 4). Two mesh sizes are compared: $l_\mathrm{e}/L = 1/4$ and $l_\mathrm{e}/L = 1/8$. Firstly, the location of damage should be mentioned, which is not directly near the hole, but rather at the right boundary, because higher triaxiality values occur

at this position. Both meshing variants show a qualitatively and quantitatively similar distribution of damage. It can be clearly seen, that the zone of massive damage ($D^* > 0.9$) is spread over some layers of elements, especially for the fine mesh $l_\mathrm{e}/L = 1/8$. No damage localization in single element layers for fine meshes is detected, which indicates the non-local character of the regularized damage model.

4 CONCLUSIONS

A rather simple model to express the asymmetric behavior (strain hardening, martensite evolution) during monotonic, uni-axial tension and compression loading of TRIP-steel is proposed. Experimental data can be fitted well.

A local damage model based on the effective stress concept is applied. Damage evolution is modeled by a modified Rice and Tracey [10] description of void growth. Void coalescence and the linked accelerated damage evolution up to crack initiation are tackled by a phenomenological approach. Cell model predictions of damaged TRIP-steel can be successfully fitted in terms of macroscopic stress-strain curves.

A non-local extension based on a regularization technique is incorporated. A convergence study proves the non-local properties of the proposal.

ACKNOWLEDGMENTS

The authors gratefully acknowledge the German Research Foundation (DFG) for supporting this work carried out in the framework of the Collaborative Research Center 799 (subproject C5). We gratefully acknowledge Ralf Eckner and Michael Hauser (IWT & IEST, TU Bergakademie Freiberg) for providing the experimental data.

APPENDIX

The definition of e_smooth in Eq. (27) should ensure a transition at triaxiality $h = h_\mathrm{t}$ which is smooth differentiable with respect to h. A saturation of the exponential term in Eq. (27) is desired, which starts at $h = h_\mathrm{t}$ and reaches its final value e_max at the prescribed triaxiality parameter h_max:

$$
\begin{aligned}
e_\mathrm{smooth} &= e_\mathrm{max}\left(1 - \exp\left(\frac{e_\mathrm{c}}{h_1\,(e_\mathrm{max} - e_\mathrm{c})}\,(h_\mathrm{t} - h) + \ln\left(\frac{(e_\mathrm{max} - e_\mathrm{c})}{e_\mathrm{max}}\right)\right)\right), \\
e_\mathrm{max} &= \exp\left(h_\mathrm{max}/h_1\right), \\
e_\mathrm{c} &= \exp\left(h_\mathrm{t}/h_1\right).
\end{aligned}
$$

REFERENCES

[1] A. M. Beese and D. Mohr. Anisotropic plasticity model coupled with Lode angle dependent strain-induced transformation kinetics law . *Journal of the Mechanics and Physics of Solids*, 60:1922–1940, 2012.

[2] M. P. Miller and D. L. McDowell. Modeling large strain multiaxial effects in fcc polycrystals. *International Journal of Plasticity*, 12(9):875–902, 1996.

[3] C. Garion, B. Skoczen, and S. Sgobba. Constitutive modelling and identification of parameters of the plastic strain-induced martensitic transformation in 316L stainless steel at cryogenic temperatures . *International Journal of Plasticity*, 22:1234–1264, 2006.

[4] A. Seupel and M. Kuna. Application of a Local Continuum Damage Model to Porous TRIP-Steel. *Applied Mechanics and Materials*, 784:484–491, 2015.

[5] G. B. Olson and M. Cohen. Kinetics of strain-induced martensitic nucleation. *Metallurgical Transactions A*, 6A:791–795, 1975.

[6] T. Iwamoto, T. Tsuta, and Y. Tomita. Investigation on deformation mode dependence of strain-induced martensitic transformation in TRIP steels and modelling of transformation kinetics. *International Journal of Mechanical Sciences*, 40:173–182, 1998.

[7] S. Martin, S. Wolf, S. Decker, L. Krüger, and U. Martin. Deformation Bands in High-Alloy Austenitic 16Cr6Mn6Ni TRIP Steel: Phase Transformation and Its Consequences on Strain Hardening at Room Temperature. *Steel Research International*, 86(10):1187–1196, 2015.

[8] D. Kulawinski, S. Ackermann, A. Seupel, T. Lippmann, S. Henkel, M. Kuna, A. Weidner, and H. Biermann. Deformation and strain hardening behavior of powder metallurgical TRIP steel under quasi-static biaxial-planar loading . *Materials Science & Engineering A*, 642:317–329, 2015.

[9] J. C. Simo and T. J. R. Hughes. *Computational Inelasticity*. Springer, 1998.

[10] J. R. Rice and D. M. Tracey. On the ductile enlargement of voids in triaxial stress fields. *Journal of the Mechanics and Physics of Solids*, 17:201–217, 1969.

[11] T. Linse., G. Hütter, and M. Kuna. Simulation of crack propagation using a gradient-enriched ductile damage model based on dilatational strain. *Engineering Fracture Mechanics*, 95:13–28, 2012.

[12] A. Seupel, R. Eckner, A. Burgold, M. Kuna, and L. Krüger. Experimental characterization and damage modeling of a particle reinforced TWIP-steel matrix composite. *Materials Science & Engineering A*, 662:342–355, 2016.

[13] M. Hauser, M. Wendler, S. Ghosh Chowdhury, A. Weiß, and J. Mola. Quantification of deformation induced a'- martensite in Fe-19Cr-3Mn-4Ni-0.15C- 0.15N austenitic steel by in situ magnetic measurements . *Materials Science and Technology*, 31(12):1473–1478, 2015.

[14] M. Kuna and D. Z. Sun. Three-dimensional cell model analyses of void growth in ductile metals. *International Journal of Fracture*, 81:235–258, 1996.

XIV International Conference on Computational Plasticity. Fundamentals and Applications
COMPLAS XIV
E. Oñate, D.R.J. Owen, D. Peric & M. Chiumenti (Eds)

THE PERFORMANCE AND PREDICTION ABILITY OF ADVANCED APPROACH TO DUCTILE FRACTURE

FRANTIŠEK ŠEBEK, JINDŘICH PETRUŠKA* AND PETR KUBÍK

* Faculty of Mechanical Engineering
Brno University of Technology
Technická 2896/2, 616 69 Brno, Czech Republic
e-mail: petruska@fme.vutbr.cz, web page: http://www.fme.vutbr.cz/

Key words: Rupture, Failure, Weakening, Coupled damage, Continuum Damage Mechanics

Abstract. The present paper deals with the modelling of ductile fracture which is the result of severe plastic deformation under monotonic loading. It can be the result of a crash or accident or introduced intentionally. There is a need of increasing the safety in many fields of industrial sector or transportation. The aluminium alloy 2024-T351 is widely used for studies of ductile fracture. The material was supplied as a cold-rolled plate for this study and examined within a broad range of stress states. First of all, the flow curve was determined using the standard tensile test of smooth cylindrical bar. Then, the tensile tests of variously notched cylindrical bars were conducted to show the pressure dependence. The tensile and torsion tests of notched tube were added in order to document the dependency on the deviatoric stress state. Finally, the compression test of smooth cylinder was executed. Then, deviatoric stress state dependent plasticity and the original ductile fracture hyperbolic criterion were calibrated. The damage accumulation nonlinearity was examined through loading–unloading experiments. The double damage curve approach, inspired by the fatigue life prediction, was revisited and calibrated using the semi-cyclic testing. Finally, the softening effect was studied aiming to couple the damage with plasticity. The performance and prediction ability was verified after the model was completely calibrated and implemented into the Abaqus finite element software. Three different cases of tension were chosen for this comparative purpose. The tension of notched cylindrical and tubular specimens and flat specimen. The ductile fracture criterion coupled with plasticity should provide the slant fracture in the conditions of plane strain due to localization. Nevertheless, it is shown that the proposed approach has still some drawbacks in prediction of the crack propagation.

1 INTRODUCTION

The ductile fracture has been studied using different approaches and for various applications so far [1, 2, 3].

One measure can be the ability to produce a similar mode of cracking [4] and the other perceives the global performance [5, 6]. The ability to describe the plastic behaviour remains one of the cornerstones when concerning the uncoupled ductile fracture criteria [7, 8]. Notwithstanding how well the phenomenological criterion is calibrated, it is crucial what history preceded the crack initiation [9]. Then, there is a transition in the form of partially coupled criteria which brings the important advantage in more realistic crack propagation [10]. Besides the ability to produce the slant fracture, the coupled ductile fracture criteria provide a tool how to put the plasticity and damage together. Apart from the criteria based on Gurson-type model [11], which incorporates the damage directly into the plasticity, the plasticity and damage are computed along each other and influence one another [12]. Then, various possibilities are opened for describing the material behaviour which can be useful in vast area of applications [13, 14, 15].

The purpose of this paper is to design a set of reliable fracture tests and to develop a universal ductile fracture criterion. Aluminium alloy 2024-T351 was chosen for those studies as a suitable candidate [16]. It has been widely used in aerospace industry [17]. The plasticity is another feature of the whole model. It was considered as a non-quadratic one to describe different behaviour at uniaxial tension and plane strain. It is suitable to couple the plasticity with damage to make the approach advanced as much as possible. This can be realized through weakening. The nonlinear damage accumulation is the last important part of the approach. It was shown that it is not suitable to investigate it through the step-wise testing [18], but rather using loading–unloading experiments [8]. The verification of results were conducted on three cases of tension. Tension of notched cylindrical and tubular specimens, covered in calibration and describing the tensile axial symmetry and plane strain tension, and additional test – tension of flat plate.

2 YIELD CRITERION

First of all, the tensile test of smooth cylindrical specimen was conducted. Then, the flow curve was estimated (Fig. 1a). It is very useful to use the approach of Xue [19] who introduced the flow curve of matrix. In our case, this curve (Fig. 1b) was obtained by multiplying the flow stress by correction function ($m = 1$ during plasticity calibration)

$$m = 1 + \bar{\epsilon}^p, \tag{1}$$

where $\bar{\epsilon}^p$ is the equivalent plastic strain. It was revealed that the behaviour of studied aluminium alloy cannot be described by quadratic von Mises plasticity well [20]. Instead, the yield criterion proposed by Kroon and Faleskog [21] was adopted. Yield function is

$$\Phi = \bar{\sigma} - mw\sigma_Y k, \tag{2}$$

where $\bar{\sigma}$ is the equivalent von Mises stress, w is the weakening function ($w = 1$ during plasticity calibration), σ_Y is the yield stress, and k is the yield function correction as

$$k = 1 - \gamma\omega \left(\frac{1 + \omega_0^{\frac{1}{a}}}{\omega^{\frac{1}{a}} + \omega_0^{\frac{1}{a}}} \right)^a, \tag{3}$$

where $\gamma = 0.123$, $\omega_0 = 0.18$ and $a = 4$ are calibrated material constants, so it is close to Tresca yield criterion, and ω is the normalized Lode parameter [22].

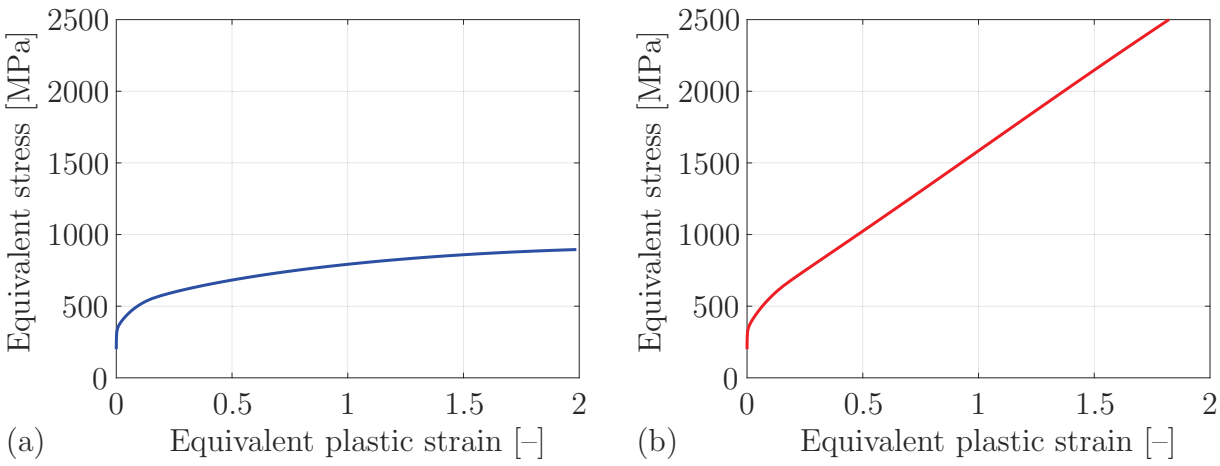

Figure 1: The flow curve: (a) conventional; (b) of matrix material

3 DAMAGE ACCUMULATION

The semi-cyclic testing was used to study the nonlinear damage accumulation. First, the damage parameter can be estimated as [23]

$$D = 1 - \frac{\bar{E}}{E}, \tag{4}$$

where $\bar{E}$ is the actual degraded Young's modulus and E is the virgin Young's modulus.

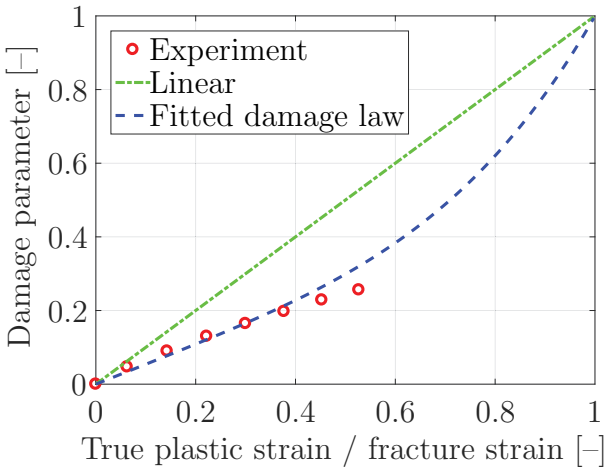

Figure 2: The semi-cyclic testing and fitted nonlinear damage accumulation

Then, the double damage curve approach proposed by Manson and Halford [24] for fatigue was revisited. The damage parameter reads

$$D = \int_0^{\hat{\epsilon}^D} q_1 \frac{\mathrm{d}\bar{\epsilon}^p}{C + \bar{\epsilon}^f} + \int_0^{\hat{\epsilon}^D} q_2(1 - q_1) \left(\frac{\bar{\epsilon}^p}{C + \bar{\epsilon}^f} \right) \frac{\mathrm{d}\bar{\epsilon}^p}{C + \bar{\epsilon}^f}, \tag{5}$$

where $\hat{\epsilon}^D$ is the equivalent plastic strain for a given loading path, q_1, q_2 and C are three material constants and $\bar{\epsilon}^f$ is the fracture envelope.

The two material constants were calibrated using the semi-cyclic experiments (Fig. 2) as $q_1 = 0.54$ and $q_2 = 4$.

4 MATERIAL WEAKENING

The material weakening is realized through the weakening function mentioned earlier

$$w = 1 - D^{\beta}, \tag{6}$$

where β is the weakening exponent. It was calibrated together with constant C to fit the tensile test of smooth cylindrical specimen (Fig. 3) as $\beta = 1.1$ and $C = 0.28$.

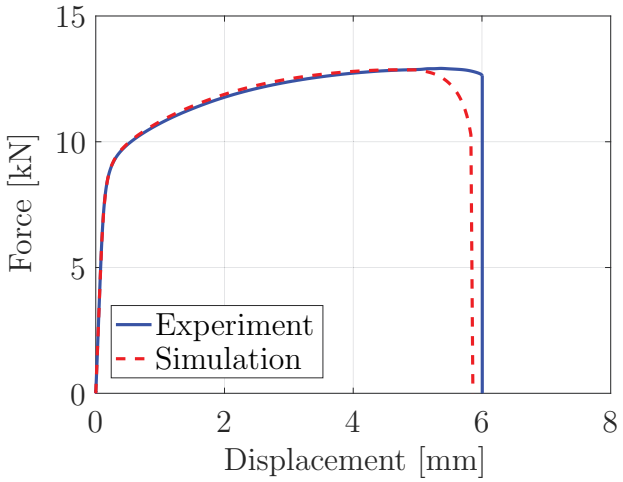

Figure 3: The force–displacement response for calibrated constants β and C

5 DUCTILE FRACTURE CRITERION

Table 1: Calibrated material constants for 2024-T351

G_1	G_2	G_3	G_4	G_5	G_6
-0.178	1.195	1.189	0.104	0.301	0.327

The hyperbolic ductile fracture criterion KHPS2 was proposed. It is based on KHPS criterion [25]. It has the fracture envelope as

$$\bar{\epsilon}^f = \left[\frac{1}{2}\left(\frac{G_4}{\langle\eta+g\rangle} + \frac{G_5}{\langle\eta+g\rangle}\right) - \frac{G_6}{\langle\eta+g\rangle}\right]\xi^2 + \frac{1}{2}\left(\frac{G_4}{\langle\eta+g\rangle} + \frac{G_5}{\langle\eta+g\rangle}\right)\xi + \frac{G_6}{\langle\eta+g\rangle}, \tag{7}$$

where $G_1, \ldots, G_6$ are material constants given in Tab. 1, ξ is the normalized third invariant of the deviatoric stress tensor, η is the stress triaxiality and g is the parabolic cut-off

$$g = \left(G_3 + \frac{G_1 - G_3}{2} - G_2\right)\xi^2 + \frac{G_1 - G_3}{2}\xi + G_2. \tag{8}$$

6 PREDICTION SIMULATIONS

There were chosen three different cases for examination of the performance and prediction ability under tension.

The first is the tension of notched cylindrical specimen. The force–displacement response is predicted slightly higher with also higher displacement at fracture (Fig. 4). The proposed approach predicted the slant fracture in the final stage of cracking, similarly as in the experiment (Fig. 4). Nevertheless, the classical cup and cone fracture was not observed experimentally.

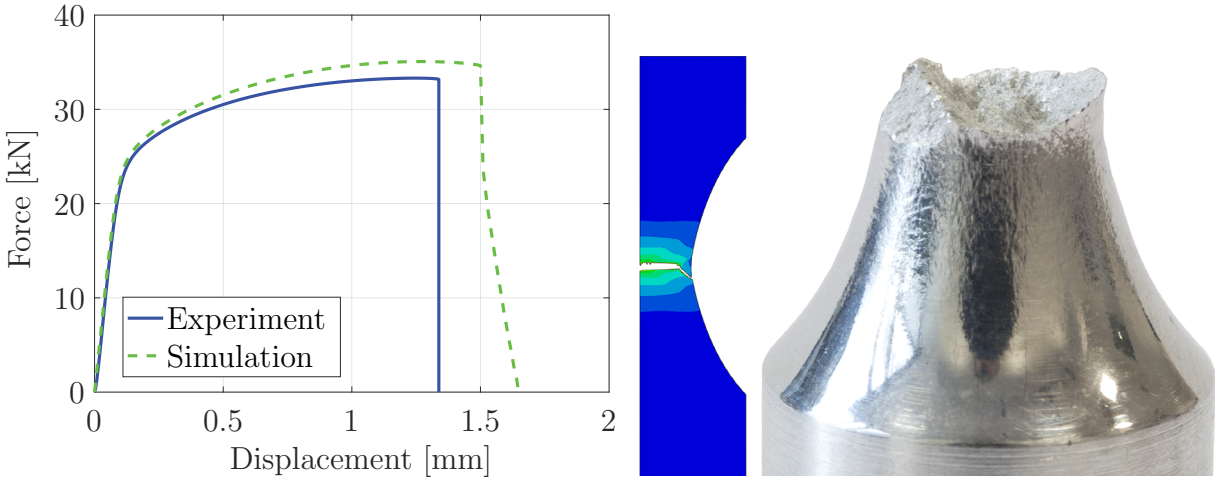

Figure 4: The responses for notched cylindrical specimen and specimens from experiment and simulation

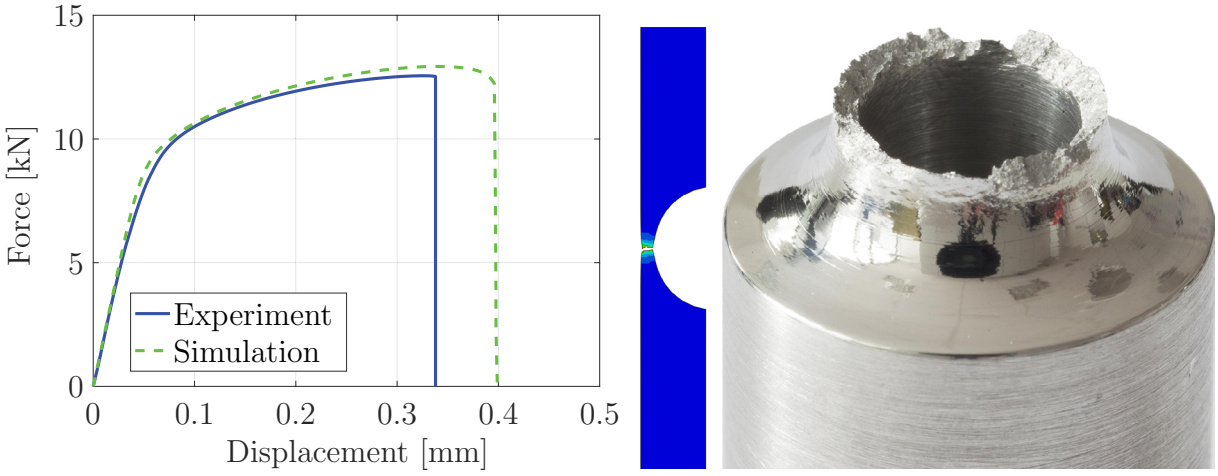

Figure 5: The responses for notched tubular specimen and specimens from experiment and simulation

The second case is the tension of notched tubular specimen. The shape of force–displacement curve is captured very well but the model still predicted higher displacement at fracture (Fig. 5). The slant fracture was not predicted by the model as in the experiment (Fig. 5).

The last simulation is the tension of flat plate. The material behaviour at plane strain or generalized shear was described well the by non-quadratic yield criterion. The material often obeys lower ductility at this region in comparison to uniaxial tension, as tested at previous case. The displacement at fracture is grossly over predicted. On the other hand, the typical slant fracture was formed the same as experimentally observed (Fig. 6).

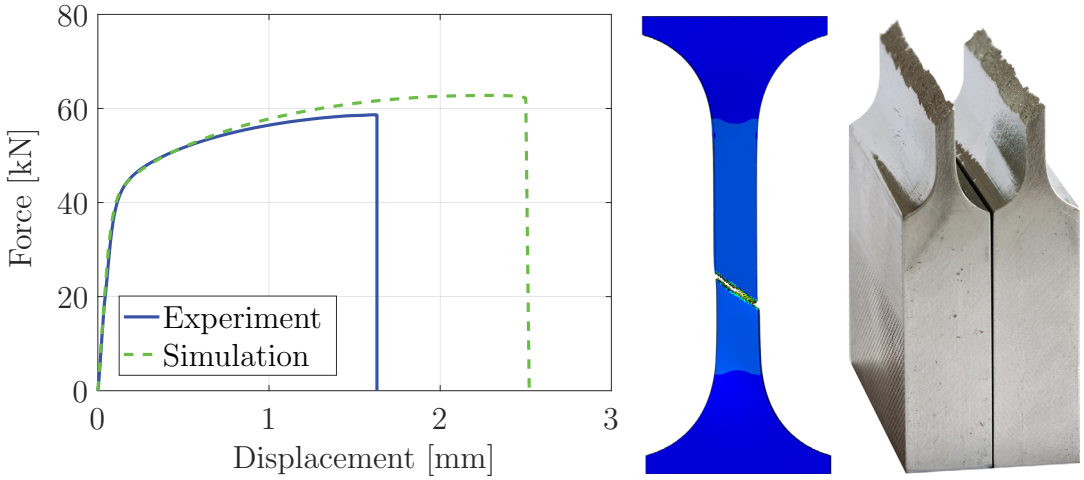

Figure 6: The responses for flat plate specimen and specimens from experiment and simulation

The results suggest that the constant C should be lower, so it would prevent the late cracking. On the other hand, it would deteriorate the force–displacement response of smooth cylindrical specimen (Fig. 3), where the early cracking would occur.

7 CONCLUSIONS

The present paper dealt with ductile fracture. Proposed criterion KHPS2 was calibrated using tensile smooth and notched cylindrical specimens, tensile and torsional notched tube specimens and upsetting cylinder. The damage was coupled with plasticity to form the coupled model in the sense of continuum damage mechanics.

The model was verified under the tensile loading. The force–displacement curves were described well in overall, but there were some drawbacks in over estimating the final fracture. The remarkable difference was observed at plane strain tension. This discrepancy could be attributed to the different stress state. It is expected that the normalized third invariant of deviatoric stress tensor should be zero but it tends to approach unity [21, 26]. Nevertheless, this should also affect the flow behaviour which still seems to be described well contrary to that.

The fracture surfaces were predicted in correspondence with experimental observation, except for the tension of notched tubular specimen. This could by caused by a very small thickness of the specimen wall.

The model should be examined further. It would be also useful to conduct more extensive experimental program and test the aluminium alloy 2024-T351 under more stress states.

8 ACKNOWLEDGEMENT

This work is an output of project NETME CENTRE PLUS (LO1202) created with financial support from the Ministry of Education, Youth and Sports under the "National Sustainability Programme I".

REFERENCES

[1] Dunand, M. and Mohr, D. On the predictive capabilities of the shear modified Gurson and the modified Mohr–Coulomb fracture models over a wide range of stress triaxialities and Lode angles. *J. Mech. Phys. Solids* (2011) **59**:1374–1394.

[2] Törnqvist, R. *Design of crashworthy ship structures*. PhD Thesis, Technical University of Denmark (2003).

[3] Komori, K. Simulation of crack arrest in blanking using the node separation method. *Int. J. Mech. Sci.* (2013) **68**:150–159.

[4] Kubík, P., Šebek, F. and Petruška, J. Ductile fracture criteria in prediction of slant fracture. In *ECCOMAS Congress 2016*, 6699–6710 (2016).

[5] Pack, K., Luo, M. and Wierzbicki, T. Sandia fracture challenge: Blind prediction and full calibration to enhance fracture predictability. *Int. J. Fract.* (2014) **186**:155–175.

[6] Papasidero, J., Doquet, V. and Mohr, D. Ductile fracture of aluminum 2024-T351 under proportional and non-proportional multi-axial loading: Bao–Wierzbicki results revisited. *Int. J. Solids Struct.* (2015) **69–70**:459–474.

[7] Joun, MS., Eom, J.G. and Lee, M.Ch. A new method for acquiring true stress–strain curves over a large range of strains using a tensile test and finite element method. *Mech. Mater.* (2008) **40**:586–593.

[8] Celentano, D.J. and Chaboche, J.-L. Experimental and numerical characterization of damage evolution in steels. *Int. J. Plast.* (2007) **23**:1739–1762.

[9] Beese, A.M., Luo, M., Li, Y., Bai, Y. and Wierzbicki, T. Partially coupled anisotropic fracture model for aluminum sheets. *Eng. Fract. Mech.* (2010) **77**:1128–1152.

[10] Šebek, F., Kubík, P. and Petruška, J. Localization problem of coupled ductile failure models compared to uncoupled ones. In *Engineering Mechanics 2014*, 632–635 (2014).

[11] Türtük, İ.C. and Deliktaş, B. Coupled porous plasticity – Continuum damage mechanics approaches for modelling temperature driven ductile-to-brittle transition fracture in ferritic steels. *Int. J. Plast.* (2016) **77**:246–261.

[12] Šebek, F., Hůlka, J., Kubík, P. and Petruška, J. On the proportionality of damage rule in finite element simulations of the ductile failure. *Adv. Mater. Res.* (2014) **980**:189–193.

[13] Petruška, J., Návrat, T. and Šebek, F. A new model for fast analysis of leveling process. *Adv. Mater. Res.* (2012) **586**:389–393.

[14] Petruška, J., Návrat, T., Šebek, F. and Benešovský, M. Optimal intermeshing of multi roller cross roll straightening machine. *AIP Conf. Proc.* (2016) **1769**:120002-1–120002-4.

[15] Peč, M., Kubík, P., Šebek, F., Návrat, T. and Petruška, J. Modeling of the blast load effects in explicit dynamics. In *Engineering Mechanics 2016*, 442–445 (2016).

[16] Papasidero, J., Doquet, V. and Lepeer, S. Multiscale investigation of ductile fracture mechanisms and strain localization under shear loading in 2024-T351 aluminum alloy and 36NiCrMo16 steel. *Mater. Sci. Eng. A* (2014) **610**:203–219.

[17] Rodríguez-Millán, M., Vaz-Romero, Á and Arias, Á. Failure behavior of 2024-T3 aluminum under tension-torsion conditions. *J. Mech. Sci. Technol.* (2015) **29**:4657–4663.

[18] Šebek, F., Petruška, J. and Kubík, P. The role of loading path in ductile fracture. In *6th International Conference on Structural Engineering, Mechanics and Computation 2016*, 550–555 (2016).

[19] Xue, L. *Ductile fracture modeling - Theory , experimental investigation and numerical verification*. PhD Thesis, Massachusetts Institute of Technology (2007).

[20] Peč, M., Vosynek, P., Šebek, F. and Návrat, T. Implementation of American weld connection standards into finite element computations. *IOP Conf. Ser.: Mater. Sci. Eng.* (2017) **179**:012056-1–012056-7.

[21] Kroon, M. and Faleskog, J. Numerical implementation of a J_2- and J_3-dependent plasticity model based on a spectral decomposition of the stress deviator. *Comput. Mech.* (2013) **52**:1059–1070.

[22] Nahshon, K. and Hutchinson J.W. Modification of the Gurson Model for shear failure. *Eur. J. Mech. A Solids* (2008) **27**:1–17.

[23] Lemaitre, J. Coupled elasto-plasticity and damage constitutive equations. *Comput. Methods Appl. Mech. Engrg.* (1985) **51**:31–49.

[24] Manson, S.S. and Halford, G.R. *Re-examination of cumulative fatigue damage analysis—An engineering perspective.* NASA Technical Memorandum 87325 (1985).

[25] Kubík, P., Šebek, F., Hůlka, J. and Petruška, J. Calibration of ductile fracture criteria at negative stress triaxiality. *Int. J. Mech .Sci.* (2016) **108–109**:90–103.

[26] Šebek, F., Petruška, J. and Kubík, P. Behavior of lode dependent plasticity at plane strain condition and its implication to ductile fracture. *Solid State Phenom.* (2017) **258**:213–216.

XIV International Conference on Computational Plasticity. Fundamentals and Applications
COMPLAS XIV
E. Oñate, D.R.J. Owen, D. Peric & M. Chiumenti (Eds)

UNCOUPLED MATERIAL MODEL OF DUCTILE FRACTURE WITH DIRECTIONAL PLASTICITY

MIROSLAV ŠPANIEL*, TOMÁŠ MAREŠ*, JIŘÍ KUŽELKA*, FRANTIŠEK ŠEBEK † AND JAN DŽUGAN°

*Czech Technical University in Prague (CTU)
Faculty of Mechanical Engineering
Technická 4, 166 07, Prague, Czech Republic
e-mail: miroslav.spaniel@fs.cvut.cz, web page: http://www.ctu.cz

†Brno University of Technology
Faculty of Mechanical Engineering
Technická 2896/2, 616 69 Brno
e-mail: sebek@fme.vutbr.cz - Web page: http://www.fme.vutbr.cz

°Comtes FHT a.s.
Faculty of Mechanical Engineering
Prøumyslová 995, Dobřany 334 41, Czech Republic
e-mail: jdzugan@comtesfht.cz - Web page: http://www.comtesfht.com

Key words: directional distortional hardening, ductile fracture

Abstract. Proposed paper deals with the application of plastic response with directional distortional hardening (DDH) in uncoupled ductile fracture model and comparison of the results with the same ductile fracture model based on isotropic J2 plasticity. The results of simulations have proven not negligible role of model of plasticity and the response of the model with DDH plasticity is closer to reality then the one of the model with isotropic plasticity.

1 INTRODUCTION

Ductile fracture plays not negligible role in industry. For example safety evaluation of vehicles in case of crash, design and optimization of forming processes, limit analysis of steel structures, etc. may be based on computational models of ductile fracture. Ductile fracture is understood as an integrity loss of bodies due to process of material damaging with significant dissipation of strain energy in conditions of monotonic loading. In finite element calculations ductile fracture is usually performed using constitutive models based on progressive damage following plastic straining. Phenomenological material models describing ductile damage in continuum mechanics mostly act as extension of plastic response models. However damage can be represented as directional, scalar damage parameter is introduced in most application. Damage increment is based on plastic strain

increment. Plastic strain increment is usually scaled such a way, that at point of plastic instability (necking) the integral value of damage reaches unity. The dependence of scale factor on actual stress and/or strain state introduces the dependence of damage on loading path. From the point of view of interpretation of real process inside material the ductile damage material models anticipate the damage to occur on the basis of two different mechanisms: 1) Initiation, growing and connecting of micro–cavities that dominates in domains with tri-axial tensional stress. Load carrying cross section is reduced during damage process and finally leads to failure. Based on representative volume with cavity some micro mechanical continuum models were derived (Rice and Tracey, 1969, etc), that proved exactly the dominant role of stress triaxiality for this damage mechanism occurrence. Stress triaxiality is dimensionless parameter based on stress components that expresses contribution of hydrostatic tension in actual stress state. However models based purely on this damage concept exhibit unrealistic response in domains at which pressure and/or shear stress are dominant. 2) Occurence of localized shear strain in plane of maximal shear stress that holds an angle 45° with first principal plane. Lode angle is another dimensionless stress component parameter, that expresses contribution of shear stress in actual stress state. Based on the interconnection between constitutive models of plastic response and constitutive models of ductile damage two basic categories of ductile damage constitutive models can be distinguished: Uncoupled ductile damage models and coupled ductile damage models. Uncoupled models, simply said, separate plastic response and ductile damage. Parameters of plasticity are not influenced by damage. Coupled models modify plastic response in dependence on damage. Coupled models are generally more complex and they are expected to be closer to reality. On the other hand their complexity causes significant calibration costs in comparison to uncoupled models. Easier calibration process is an essential advantage of uncoupled material models. The calibration of plastic response and calibration of ductile damage can be separated. The calibration is distinctly easier if the uncoupled material model is used.

Most used constitutive models of plastic response of metallic materials in engineering computational mechanics are based on Von Mises plastic condition with either isotropic, either kinematic hardening and associative plastic flow rule. In our previous work we have found uncoupled models based on Von Mises plasticity with isotropic hardening acceptable, except for the response of parts with higher stress concentration [1].

This paper deals with the application of model of plastic response with directional distortional hardening (DDH), that allows to control both position and shape of plastic surface in ductile fracture model described above and comparison of the results with the same ductile fracture model based on Von Mises plasticity with isotropic hardening. Calibration experiments using both smooth and notched round bars, small-punch test, and NT tension-torsion specimens made of steel 08CH18N10T had been performed in the past and referred in [1].

2 DUCTILE DAMAGE MODEL

Material models discussed in this paper are based on incremental model of plastic response with Von Mises condition of plasticity and isotropic hardening (further VMI) or

on incremental model of plastic response with directional distortional hardening (further DDH), and phenomenological model of ductile damage according to Bai–Wierzbicki.

2.1 Plastic response models

Both plastic response models DDH and VMI are based on yield condition and flow rule. Yield condition of DDH, resp. VMI is expressed as

$$f_{DDH} = (\mathbf{S} - \alpha) : \mathbf{H} : (\mathbf{S} - \alpha) - k^2 = 0\,, \quad \text{resp.} \quad f_{VMI} = \mathbf{S} : \mathbf{S} - k^2 = 0\,\cdot \tag{1}$$

The deviatoric part $\mathbf{S}$

$$\mathbf{S} = \sigma + p\mathbf{I} \tag{2}$$

of stress tensor, σ is used in yield conditions as the independence of plastic flow onset on hydrostatic pressure is generally accepted for metallic material. Hydrostatic stress, p, is defined by

$$p = -\frac{1}{3}\mathrm{tr}\,(\sigma)\,\cdot \tag{3}$$

Geometric interpretation of yield condition is usually provided in the space of principal deviatoric stresses (three–dimensional space at which the point $[S_1, S_2, S_3]$ represents the deviatoric stress principal components S_1, S_2, and S_3). It is in evidence, that VMI yield condition represents the surface of sphere with center at origin of principal deviatoric stress space and radius of k. DDH yield condition employs the deviatoric back–stress α determining the location of yield surface, k determines the size of yield surface. Fourth order tensor $\mathbf{H}$ represents the distortion of yield surface. Let's note, that if $\mathbf{H}$ equal unity, DDH becomes Von Mises with kinematic hardening. Associative flow rule in form

$$\dot{\varepsilon}^p = \lambda \frac{\partial f}{\partial \sigma} \tag{4}$$

has been adopted in both DDH and VMI models. Detailed description of VMI plastic response model is well known. In this work native implementation provided within Simulia/Abaqus FE code has been used. Theoretical description of DDH can be found in [3]. The implementation according to [2] in form of so called "alpha model" has been provided by our colleagues as user subroutine under Simulia/Abaqus FE code.

2.2 Ductile damage model

Ductile damage model in this work follows the damage mechanics concept with cumulative scalar damage parameter

$$\omega = \int_0^t \frac{\dot{\bar{\varepsilon}}_{pl}\mathrm{d}t}{\bar{\varepsilon}_f\,(\eta,\ \xi)}\,. \tag{5}$$

Plastic strain intensity rate, $\dot{\bar{\varepsilon}}_{pl}$, is defined as

$$\dot{\bar{\varepsilon}}_{pl} = \sqrt{\frac{2}{3}\dot{\varepsilon}_{pl} : \dot{\varepsilon}_{pl}}\,. \tag{6}$$

Fracture locus $\bar{\varepsilon}_f(\eta,\ \xi)$ expresses the dependence of equivalent plastic strain at the instant of onset of fracture on stress state represented by dimensionless parameters–stress triaxiality, η, resp. Lode parameter, ξ. These parameters are defined using second, J_2, resp. third, J_3, invariant of deviatoric stress

$$J_2 = \frac{1}{2}\mathbf{S} : \mathbf{S} = \frac{1}{2}\left(S_1^2 + S_2^2 + S_3^2\right)\,, \quad \text{resp. } J_3 = \det\mathbf{S} = S_1 S_2 S_3\,, \tag{7}$$

and, Von Mises stress, q,

$$q = \sqrt{3J_2}\,. \tag{8}$$

Then stress triaxiality, resp. Lode parameter is defined as

$$\eta = -\frac{p}{q}\,, \quad \text{resp.} \quad \xi = \frac{27}{2}\frac{J_3}{q^3}\,. \tag{9}$$

If we kept constant both stress triaxiality, η_0, and Lode parameter, ξ_0, during whole loading, then fracture occured at instant t_{crit}, when accumulated equivalent plastic strain, $\bar{\varepsilon}_{pl}$ equal $\bar{\varepsilon}_{f0} = \bar{\varepsilon}_f(\eta_0,\ \xi_0)$

$$\bar{\varepsilon}_{pl} = \int_0^{t_{crit}} \dot{\bar{\varepsilon}}_{pl}\mathrm{d}t = \bar{\varepsilon}_f(\eta_0,\ \xi_0)\,, \tag{10}$$

and critical damage, ω_{crit}, at fracture onset has to be, according to (5)

$$\omega_{crit} = \frac{1}{\bar{\varepsilon}_f(\eta_0,\ \xi_0)}\int_0^{t_{crit}} \dot{\bar{\varepsilon}}_{pl}\mathrm{d}t = 1\,. \tag{11}$$

Assuming the damage to be proportional, we utilize (5) to express the damage caused by plastic straining during the loading history from beginning up to time t with both stress triaxiality and Lode parameter varying. Fracture onset occurs when damage reaches critical value

$$\omega = \omega_{crit} = 1\,. \tag{12}$$

Fracture locus suggested by Bai and Wierzbicki in [4] has form

$$\begin{aligned} \bar{\varepsilon}_f(\eta,\xi) &= \left[\frac{1}{2}\left(D_1 e^{-D_2\eta} + D_5 e^{-D_6\eta}\right) - D_3 e^{-D_4\eta}\right]\xi^2 + \\ &+ \frac{1}{2}\left(D_1 e^{-D_2\eta} - D_5 e^{-D_6\eta}\right)\xi + D_3 e^{-D_4\eta}. \end{aligned} \tag{13}$$

Material parameters D_1, D_2, D_3, D_4, D_5, and D_6 have to be determined on the base of experiments. This ductile damage model has been used to extend both VMI and

DDH plastic response model. These extensions are further referred as VMI based Bai–Wierzbicki ductile fracture model (VMIBW), resp. DDH based Bai–Wierzbicki ductile fracture model (DDHBW).

Artificial degradation on the base of Hillerborg's fracture energy is implemented in both VMIBW and DDHBW in order to guarantee sufficient smoothness of fracture process simulation. Instead of immediate removing the stress gradual loss of material stiffness in term of Young modulus, E, driven by parameter of degradation $D \in \langle 0; 1 \rangle$, is employed in material point of FE model since damage reached it's critical value

$$E^* = (1 - D)\, E \cdot \tag{14}$$

3 CALIBRATION

As both VMIBW and DDHBW are uncoupled ductile damage models, the plastic response has been calibrated separately using the same test performed on smooth round bar. Further the calibration of fracture locus will be discussed. Tensile experiments with both smooth and notched round bars using four different notch radii, tension-torsion experiments using NT specimen with five different proportional loading paths, and small punch test have been utilized to calibrate fracture loci for both VMIBW and DDHBW models. Calibration experiments are briefly listed in table 3. Each row in the table

Table 1: Complete portfolio of experiments, that have been used to calibrate both VMIBW and DDHBW.

Smooth, resp. notched round bars, tension					
Label	R [mm]	d [mm]	N	ΔL_f [mm]	Remark
R_0	∞	12	5	14	Smooth bar
R_{15}	15	12	2	8.1	Notched bar
R_7	7	12	2	6.6	Notched bar
R_4	4	12	5	5.7	Notched bar
NT specimens, proportional tension–torsion					
Label	p [mm]	cal. quantity	N	$\Delta L_f or \Delta\varphi_f$ [mm], or [1]	Remark
NT_3	0.000000000	$\Delta\varphi$	2	0.6637	Pure torsion
NT_4	0.000152425	$\Delta\varphi$	2	0.6744	Tension–torsion
NT_5	0.000304851	$\Delta\varphi$	2	0.5681	Tension–torsion
NT_6	0.001278454	ΔL	2	0.8181	Tension–torsion
NT_7	∞	ΔL	2	0.6027	Pure tension
Small punch test					
Label	D_{punch} [mm]	t [mm]	N	Δu_f [mm]	Remark
SP	2.5	0.5	5	2.05	

represents single calibration case. N for all cases means the number of specimens that had been tested within the case. For smooth/notched round bars R means the radius of the notch, d is the diameter of bar cross-section at notch tip. For NT specimens p describes the loading path as the ratio between the extension ΔL and torsion $\Delta\varphi$

$$p = \frac{\Delta L}{\Delta \varphi} \cdot \tag{15}$$

Proportional loading had been performed, so p is kept constant during loading. For small punch test D_{punch} is the diameter of spherical punch, t is thickness of the penny–like specimen. The calibration is based on critical extensions, critical torsions, or critical

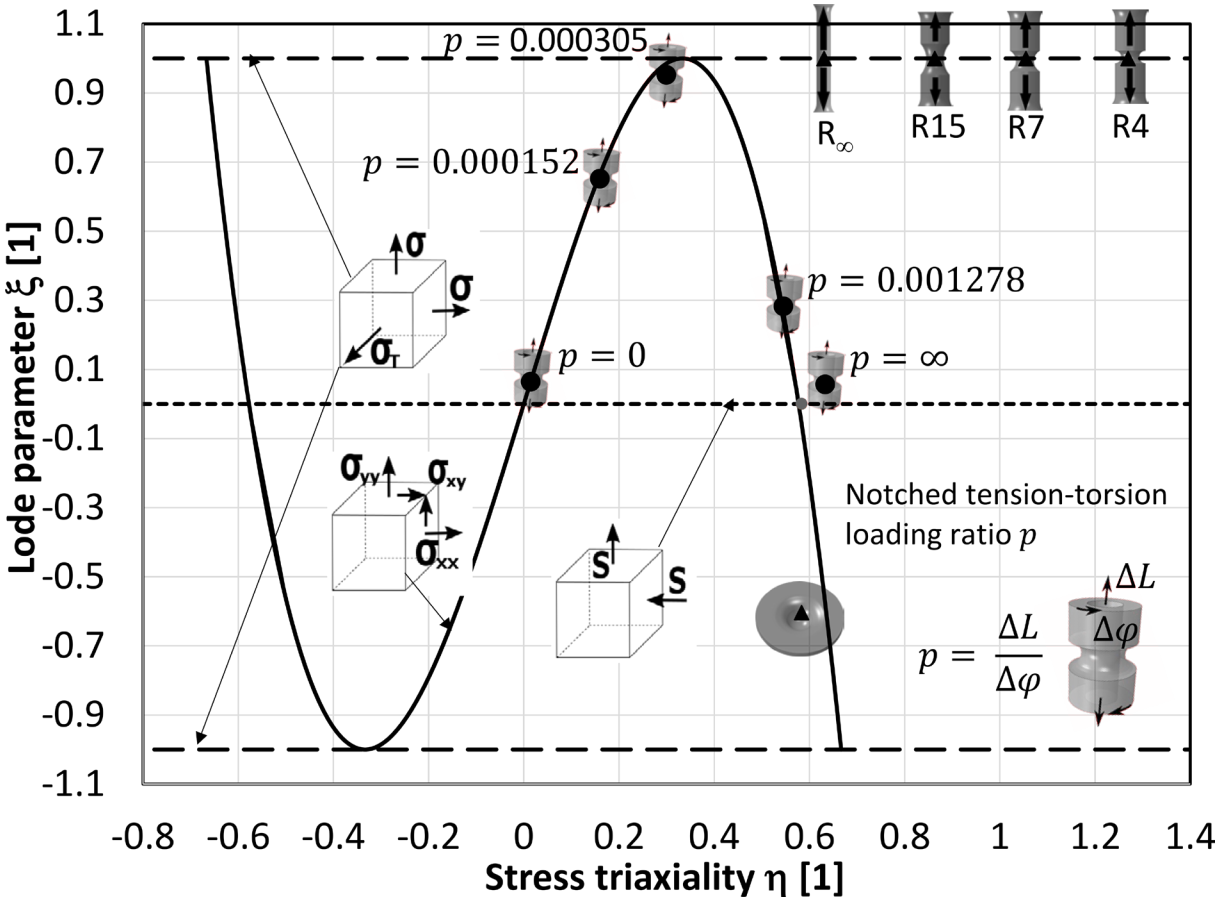

Figure 1: Portfolio of calibration cases.

displacements. For smooth/notched round bars the extension has been measured using extensometer (the fracture of all valid specimens has to occure within the base of extensometer). Critical extension ΔL_f has been determined as average value of extension at fracture onset of all valid specimens. For NT specimens both the extension and the relative torsion has been measured for each specimen. The calibration quantity has been chosen as ΔL or as $\Delta\varphi$ with respect to dominating deformation. Then corresponding critical value ΔL_f or $\Delta\varphi_f$ has been determined as average value of calibration quantity at

fracture onset of all valid specimens as well. For small punch test the punch displacement Δu has been measured. Critical displacement Δu_f has been determined as average value of punch displacements at fracture onset of all valid specimens. Corresponding tensile forces and/or torques have been measured at the same time, so the experimental loading curves can be used to evaluate results of calibration.

Calibration of fracture locus means to determine parameters D_1, D_2, D_3, D_4, D_5, and D_6 of fracture locus (13) providing good approximation of fracture of single specimens. This is usually performed as minimization of target function representing the deviation of FE calculation results and corresponding experiments in average sense over all calibration cases. In this work target function F_ω defined in sense of deviations between critical damage ω_i estimation and it's exact value $\omega_{crit} = 1$ for i^{th} calibration case, averaged over all calibration cases

$$F_\omega = \sqrt[m]{\frac{1}{N}\sum_{i=1}^{N} |1 - \omega_i|^m} \,. \tag{16}$$

ω_i estimation is evaluated by integration up to critical extension, resp. critical torsion, resp. critical displacement

$$\omega_i = \int_0^{\Delta\mathcal{L}_{\mathrm{f,i}}} \frac{\mathrm{d}\bar{\varepsilon}_{pl}}{\bar{\varepsilon}_f\left(\eta,\, \xi\right)} \,, \tag{17}$$

where $\Delta\mathcal{L}_{\mathrm{f,i}} = \Delta L_{f,i}$, resp. $\Delta\mathcal{L}_{\mathrm{f,i}} = \Delta\varphi_{f,i}$, resp. $\Delta\mathcal{L}_{\mathrm{f,i}} = \Delta u_{f,i}$. Let's denote, that initial values of D_1, D_2, D_3, D_4, D_5, and D_6 for minimization of target F_ω have been determined using more conservative approach based on averaging both stress triaxiality and Lode parameter up to critical extension, resp. critical torsion, resp. critical displacement Weighted average values of stress triaxiality for i^{th} calibration case $\eta_{av,i}$ is calculated according to

$$\eta_{av} = \frac{1}{\bar{\varepsilon}_{f,i}} \int_0^{\bar{\varepsilon}_{f,i}} \eta_i\left(\bar{\varepsilon}_{pl}\right) \mathrm{d}\bar{\varepsilon}_{pl} \,, \tag{18}$$

lode parameter weighted average is expressed as

$$\xi_{av} = \frac{1}{\bar{\varepsilon}_{f,i}} \int_0^{\bar{\varepsilon}_{f,i}} \xi_i\left(\bar{\varepsilon}_{pl}\right) \mathrm{d}\bar{\varepsilon}_{pl} \,. \tag{19}$$

The point $[\eta_{av,i},\, \xi_{av,i},\, \bar{\varepsilon}_{f,i}]$ can be determined by this approach for each individual calibration case. Fracture locus should pass these points, so target function

$$F_{av} = \sqrt[m]{\frac{1}{N}\sum_{i=1}^{N} \left|\bar{\varepsilon}_{f,i} - \bar{\varepsilon}_f\left(\eta_{av,i},\, \bar{\theta}_{av,i}\right)\right|^m} \tag{20}$$

can be used. The main disadvantage of this approach is wide range of stress triaxiality η and Lode parameter ξ for some specimen types resulting in non-negligible error due to the averaging of these quantities. On figure 3 single calibration cases are located at stress triaxiality–Lode angle space in sense of average values.

4 RESULTS AND DISCUSSION

Finite element calculation of both VMI and DDH elastic plastic response of all calibration cases have been done. Axisymmetry, resp. cyclic symmetry has been employed in smooth/notched round bars and small punch test FE models, resp. NT FE models to speed up the analyses. Then calibration of fracture loci have been performed. Calibrated parameters are provided in table 4, fracture loci of both VMIBW and DDHBW are plotted in figure reffig:Flocus Finite elements calculations of both VMIBW and DDHBW

Table 2: Fracture locus parameters for both VMIBW and DDHBW.

model	D_1	D_2	D_3	D_4	D_5	D_6
VMIBW	1.14620935	0.92336854	0.52982388	1.3923699	1.84258408	0.62297372
DDHBW	1.24892547	0.77904199	0.6579249	1.4036429	1.61503802	0.7210034

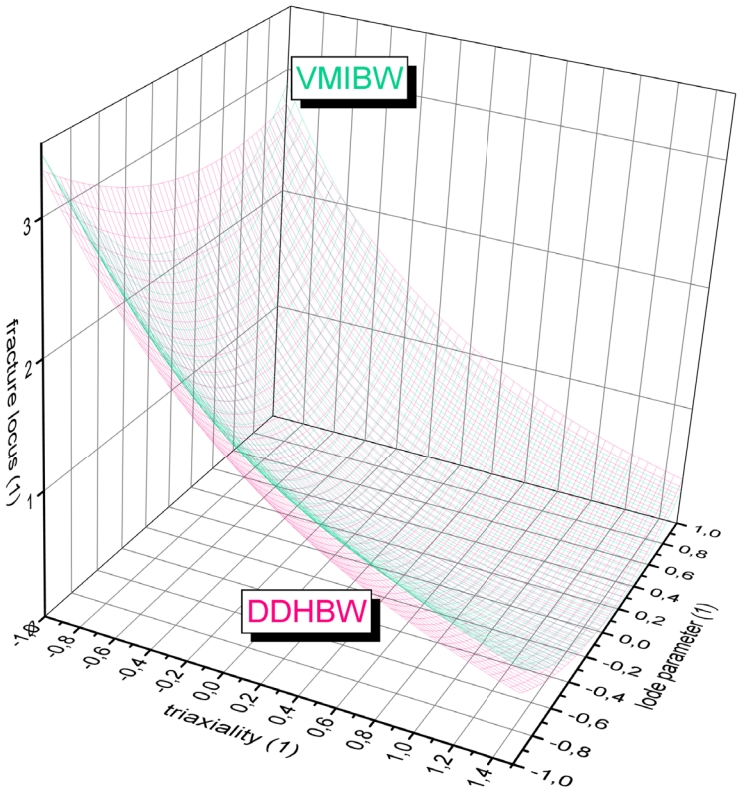

Figure 2: Fracture locus for both VMIBW and DDHBW models

elastic plastic ductile fracture response of selected specimens smooth/notched round bar (including R_1, R_2, that had not been used in calibration) have been done using calibrated fracture loci. The comparison of loading curves $\Delta L - F$ is provided on figures 3, 4, and

5. All these plot show, that DDHBW agreement with experimental data is better than the VMIBW one.

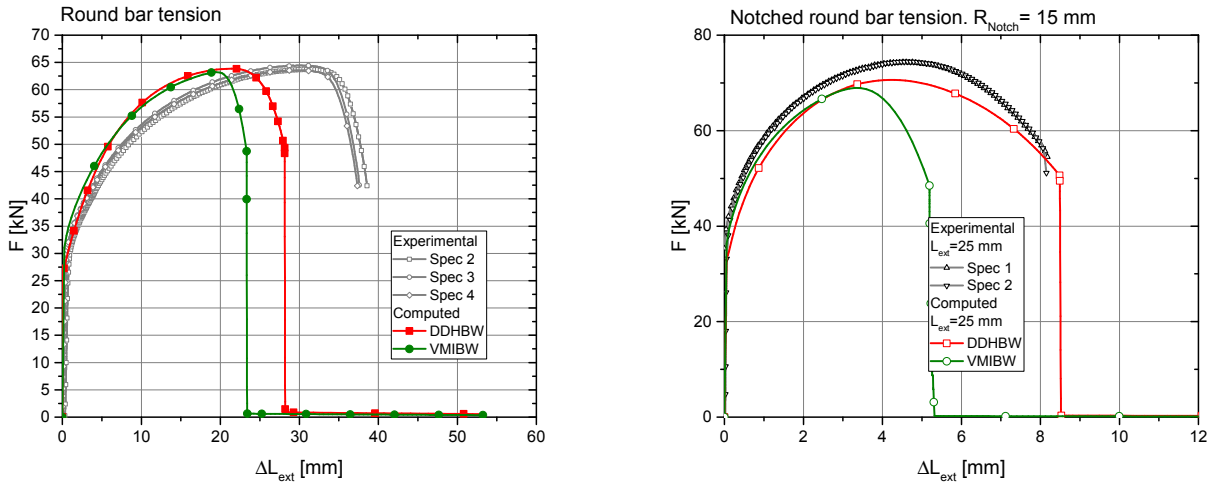

Figure 3: Comparison of experimental loading curves with computed using both VMIBW and DDHBW. Specimens R_0, R_{15}.

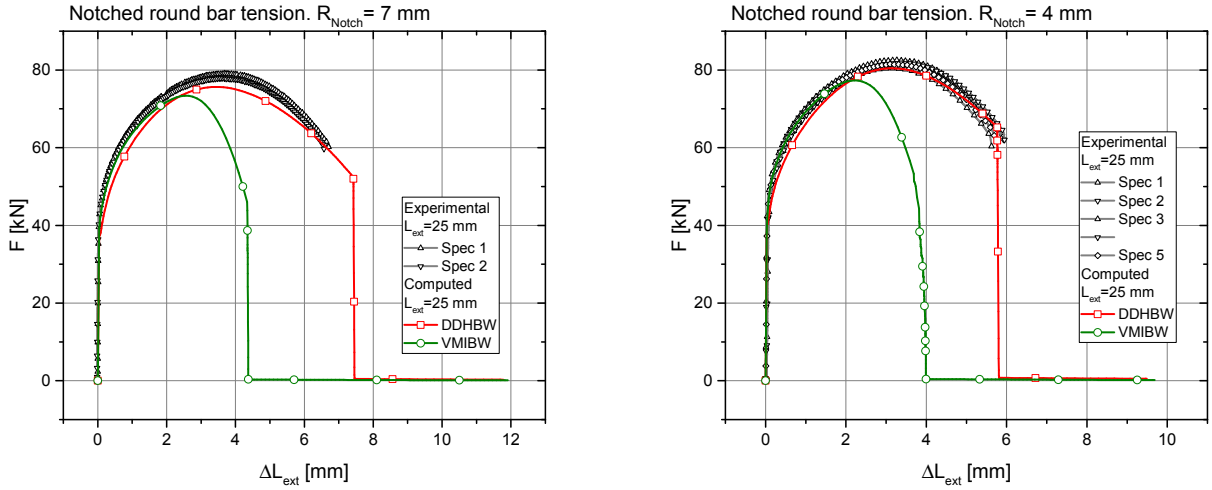

Figure 4: Comparison of experimental loading curves with computed using both VMIBW and DDHBW. Specimens R_7, R_4.

5 CONCLUSIONS

- The results of performed simulations of ductile fracture have proven not negligible role of model of plasticity on the results.
- The results of models with DDHBW elastic plastic ductile fracture model is closer to reality then the results of the model with VMIBW elastic plastic ductile fracture model calibrated with the same portfolio of specimens.

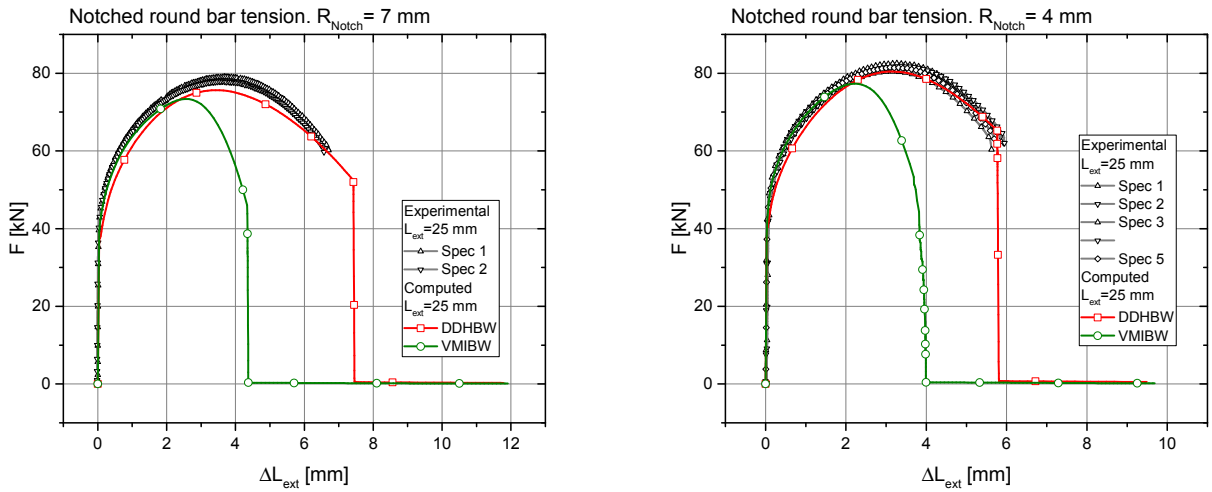

Figure 5: Comparison of experimental loading curves with computed using both VMIBW and DDHBW. Specimens R_2, R_1 had not been used in calibration.

- Using of DDHBW uncoupled ductile fracture model may be an alternative approach to more expensive coupling damage with plasticity if improvement of prediction is needed.

- Further, analyses of more cases, testing of alternative fracture locus formulation with DDH is planed.

6 ACKNOWLEDGMENT

The financial support provided by the Czech Science Foundation (GAČR grant no. 15-20666S) is gratefully acknowledged.

REFERENCES

[1] Španiel, M. Prantl, A. Džugan, J. Røužička, J. and Moravec, M. Calibration of fracture locus in scope of uncoupled elastic-plastic-ductile fracture material models. *Advances in Engineering Software.* (2014) **76**:95-108

[2] Plešek, J. Feigenbaum, H.P. Marek, R. Dafalias, Y.F. Hrubý, Z. and Parma, S. Numerical Implementation of A Model With Directional Distortional Hardening. *Journal of Engineering Mechanics.* (2015) **141, 12**

[3] Feigenbaum, H.P. and Dafalias, Y.F. Directional distortional hardening in metal plasticity within thermodynamics. *International Journal of Solids and Structures.* (2007) **44**:75267542

[4] Bai, Y. and Wierzbicki, T. A new model of metal plasticity and fracture with pressure and lode dependence. *International Journal of Plasticity.* (2008) **24, 6**:10711096

XIV International Conference on Computational Plasticity. Fundamentals and Applications
COMPLAS XIV
E. Oñate, D.R.J. Owen, D. Peric & M. Chiumenti (Eds)

ANALYSIS OF STRAIN LOCALIZATION WITH A NONLOCAL PLASTICITY MODEL

MIGUEL A. MÁNICA*, ANTONIO GENS†, JEAN VAUNAT† AND DANIEL F. RUIZ†

*†Department of Geotechnical Engineering and Geo-sciences
Universitat Politècnica de Catalunya (UPC)
Campus Nord, 08034 Barcelona, Spain
*e-mail: miguel.angel.manica@estudiant.upc.edu

Key words: Strain localization, nonlocal plasticity, plane strain, stiff fine-grained soils

Abstract. In the present paper a nonlocal plasticity model is described, intended to reproduce the mechanical behaviour of stiff fine-grained soils, including the objective simulation of strain localization; the phenomenon of accumulation of deformations in narrow zones in the form of shear bands or fractures. A number of analyses have been performed to assess the developed formulation. Relevant aspects have been addressed such as the thickness of the shear band, its orientation, and the onset of localization in a boundary value problem (BVP). Results provide useful insigths into relevant aspects of the numerical simulation of strain localization.

1 INTRODUCTION

In conventional geotechnical engineering situations stiff fine-grained materials show a quasi-brittle behaviour under deviatoric loading [1]. The resulting strain field is generally non homogeneous and deformations tend to localize into thin zones of intense shearing in the form of fractures or slip surfaces. This phenomenon is known as *strain localization*, observed also in other geomaterials like concrete, rocks or dense sands. The numerical simulation of such phenomenon under the framework of continuum mechanics involves a number of difficulties, as standard formulations tend to deliver non-objective results due to the loss of ellipticity of the governing equation at the onset of localization. This non-objectivity is recognized by a strong dependency of results with the employed mesh; a vanishing energy dissipation and localization into a zone of vanishing volume are obtained by reducing the size of elements. Enriched continuum formulations must be employed, providing the material with an internal length scale, not present in the standard formulation, which tend to prevent the common pathologies arising from the simulation of strain localization.

In this contribution, a nonlocal plasticity model is described, capable of simulating strain localization objectively, without resulting in mesh-dependent results. The model

is intended for the simulation of stiff fine-grained soils. A number of analyses have been performed to assess the developed formulation for the simulation of localized deformation patterns. Relevant aspects have been addressed, such as the thickness of the shear band, its orientation, and the onset of localization in a BVP.

2 MODEL FORMULATION

2.1 Local model

The local model refers to the employed standard elasto-plastic constitutive law, without the enrichment provided by the nonlocal approach. It is based on the simple conceptual scheme depicted in Fig. 1, for the strength of stiff clays under shearing, where the following characteristic pattern is modelled: after reaching the peak, a first rapid reduction of strength is identified, associated with the degradation and breakage of interparticle bonds; then, a more gentle strength reduction is observed, associated with the realignment of clay particles tending towards the residual state, where no further strength reduction occurs. Experimental evidence supporting this conceptual scheme is summarized in [1], as well as a comprehensive review on the hydromechanical behaviour of these materials.

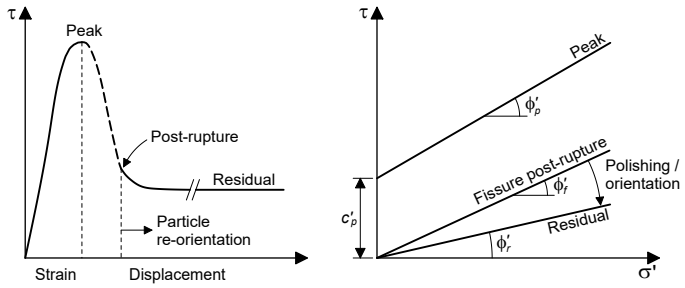

Figure 1: Conceptual scheme for the strength of stiff plastic clays [2]

Inside the yield surface, the response is assumed linear elastic. The employed yield criterion is defined by a hyperbolic approximation of the Mohr-Coulomb envelope, expressed as,

$$F = -\left(c^* + p\tan\phi^*\right) + \sqrt{\frac{J_2}{f(\theta)} + \left(c^* + p_t\tan\phi^*\right)^2} \tag{1}$$

where c^* is the apparent cohesion, ϕ^* is the apparent friction angle, p_t is the isotropic tensile strength, p is the mean stress, J_2 is the second invariant of the deviatoric stress tensor, θ is the Lode's angle, and $f(\theta)$ is a function defining the shape in the octahedral plane. Eq. (1) describes a curved envelope at low mean stresses, with a limited tensile strength, as generally occurs in stiff clayey materials. For high mean stresses, the criterion tends to converge to a linear Mohr-Coulomb envelope, with $\phi = \phi^*$ and $c = c^*$.

Isotropic non-linear hardening/softening was considered in such a way that the main characteristics of the conceptual scheme for the strength of stiff clays (Fig. 1) were incor-

porated. Hardening/softening is driven by the evolution of the strength parameters with plastic strains, characterized by a scalar state variable defined as,

$$\epsilon_{eq}^{p} = \left(\boldsymbol{\epsilon}^{p} : \boldsymbol{\epsilon}^{p}\right)^{1/2} \tag{2}$$

where $\boldsymbol{\epsilon}^{p}$ is the plastic strain tensor. Strength parameters vary in a piecewise manner as shown in Fig. 2.

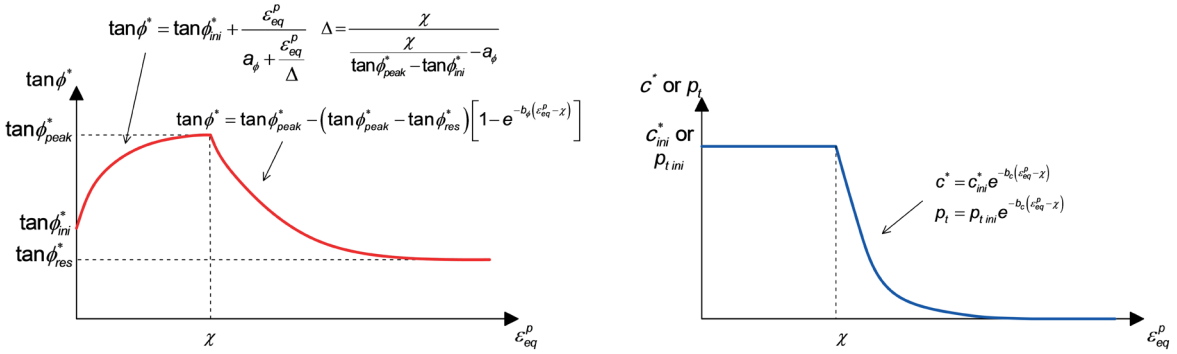

Figure 2: Hardening/softening rules

A non-associated flow rule is adopted. Rather than deriving a specific function for the plastic potential, the flow rule us directly obtained in the following way,

$$\frac{\partial G}{\partial \boldsymbol{\sigma}} = \omega \frac{\partial F}{\partial p}\frac{\partial p}{\partial \boldsymbol{\sigma}} + \frac{\partial F}{\partial J_2}\frac{\partial J_2}{\partial \boldsymbol{\sigma}} + \frac{\partial F}{\partial \theta}\frac{\partial \theta}{\partial \boldsymbol{\sigma}} \tag{3}$$

where G is the plastic potential and ω is a constant that controls the volumetric component of plastic deformations.

Other important features exhibited by these materials are not included here, such as stiffness and strength anisotropy, consolidation processes (i.e. hydromechanical coupling), creep, or yielding under volumetric loading. The main purpose of the present work is the objective simulation of localization under deviatoric loading, and therefore the incorporation of these features within the present approach will be addressed in future work.

2.2 Nonlocal extension

A nonlocal model is one where the behaviour at a material point (or at a Gauss point in a finite element simulation) depends not only on its state, but also on the state of neighbouring points within a certain region. This is accomplished by replacing a given variable by its nonlocal counterpart. If $f(\boldsymbol{x})$ is some local field within a body of volume V, the nonlocal field can be expressed as,

$$\bar{f}(\boldsymbol{x}) = \int_{V} w(\boldsymbol{x}, \boldsymbol{\xi}) f(\boldsymbol{\xi}) \mathrm{d}\boldsymbol{\xi} \tag{4}$$

where $w(\boldsymbol{x}, \boldsymbol{\xi})$ is a weight function controlling the importance of neighbouring points as a function of its position ($\boldsymbol{\xi}$), relative to the position of the actual point ($\boldsymbol{x}$). Typically,

only the distance between them is considered, and a Gaussian function is employed as the weighting function, where the width of the bell-shaped curve implicitly introduces a length scale to the continuum formulation.

Different nonlocal models are obtained depending on which variable (or variables) is considered nonlocal (see [3] for a compenhensive review). Here, we applied the approach given by [4], for the enrichment of the local model described in Section 2.1. The variable assumed nonlocal is the state variable controlling softening (Eq. 2), but using the alternative weight function depicted in Fig. 3. Its main characteristic is that the influence of the actual point is removed, and the highest weight is located at a distance of $0.707l_s$, where l_s controls the width of the symmetrical curves, acting as the internal length scale.

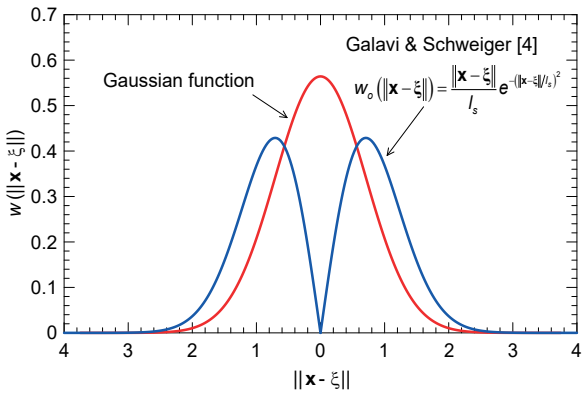

Figure 3: Representation of the weight function from [4]

In the implementation of this approach, the nonlocal state variable is computed only for points in the softening regime, and considering neighbouring points at distances lower than $2l_s$ [4].

3 STRAIN LOCALIZATION ANALYSES

A number of two-dimensional analyses were performed to assess the developed constitutive model for the simulation of localized deformation patters, corresponding to a drained biaxial plane strain test under displacement control. The specimen is 6 cm width and 10 cm height and fixed horizontal displacement were considered at the top and bottom ends, in order to develop a non-homogeneous stress/strain field and favour the onset of localization.

Fig. 4a shows the contours of shear strain ($\epsilon_s = (\epsilon_1 - \epsilon_3)/2$) of three analyses with different meshes and $l_s = 1.0$ cm. Because of the rough boundary conditions, stresses concentrate at the four corners of the model, allowing the simultaneous formation of two X-shaped shear bands. In the three analyses, the same localization pattern and the same width of shear bands were obtained regardless the number of elements. In addition, an almost unique force-displacement curve was obtained (Fig. 4b), demonstrating the ability of the approach to deliver objective results.

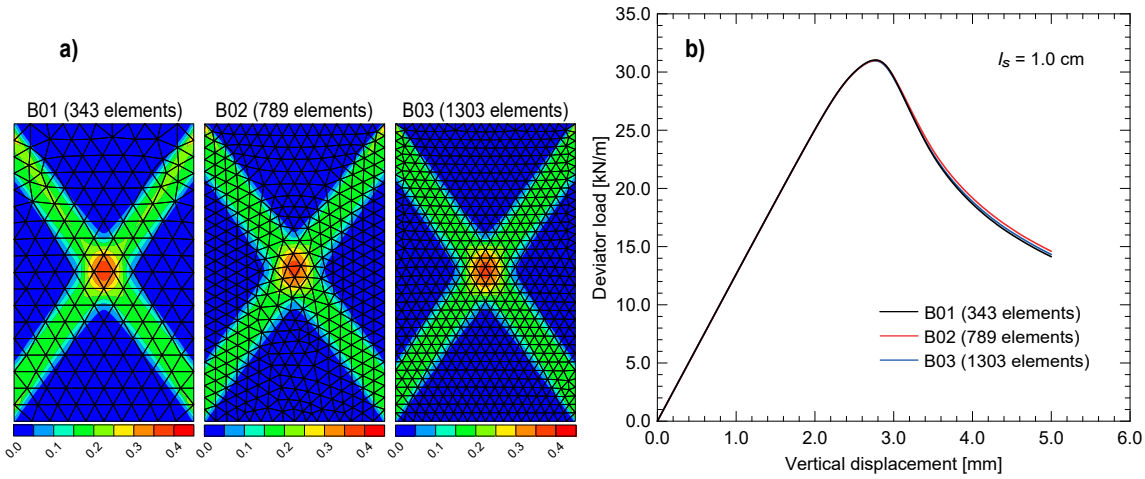

Figure 4: (a) Contours of shear strain and (b) force-displacement curves for different meshes

The effect of l_s on the configuration of shear bands is shown in Fig. 5a. As l_s is decreased, the interaction zone (considered neighbouring Gauss points) is also decreased, and plastic deformations tend to localize in a narrower zone. The width of the numerical shear bands is roughly equal to l_s, as already obtained by [4]. However, a thinner shear band renders a lower energy dissipation, and therefore a more brittle response (Fig. 5b). In the simulation of a given material, the constitutive softening rate can be adjusted to match the desired global force-displacement response for a given l_s; a technique known as *softening scaling* [4].

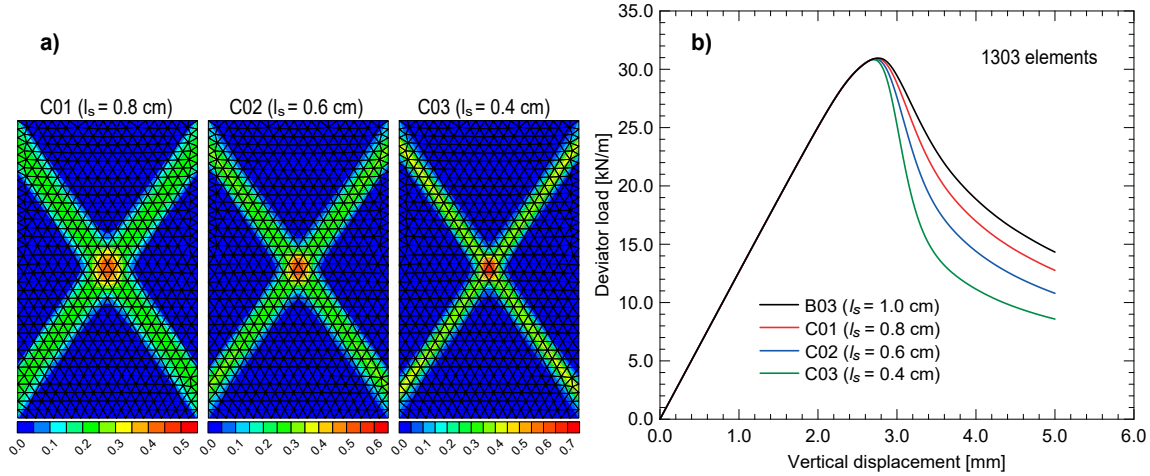

Figure 5: (a) Contours of shear strain and (b) force-displacement curves for different length scale parameters

The onset of localization was identified by the evolution of the second derivative of the shear strain with respect to time, averaged from all Gauss points ($\bar{\epsilon}_s''$), i.e. some sort of global shear strain acceleration. Fig. 6a shows the evolution of this variable during

one of the analysis. A distinct jump is clearly identified, suggested here as the onset of localization of the BVP. This point does not necessarily occurs at the global peak strength, and in this case occurs slightly before it. Its actual location seems to be controlled by the amount of points entering to the softening regime before the peak strength, which in turn is mainly the result of the considered boundary conditions.

Regarding the orientation of shear bands, this problem has been historically bounded by two limits: the upper bound given by Coulomb's theory ($\theta_C = 45° + \phi/2$), and the lower bound given by Roscoe's solution [5] ($\theta_R = 45° + \psi/2$) (ϕ and ψ are the mobilized friction and dilation angles). The theoretical orientation given by these solutions has been computed in one of the analyses, at a point within the shear band, and the results have been compared to the actual inclination obtained from the simulation (Fig. 6b). Coulomb's orientation seems to overestimate the obtained shear band inclination, which appears to coincide with Roscoe's solution at the onset of localization.

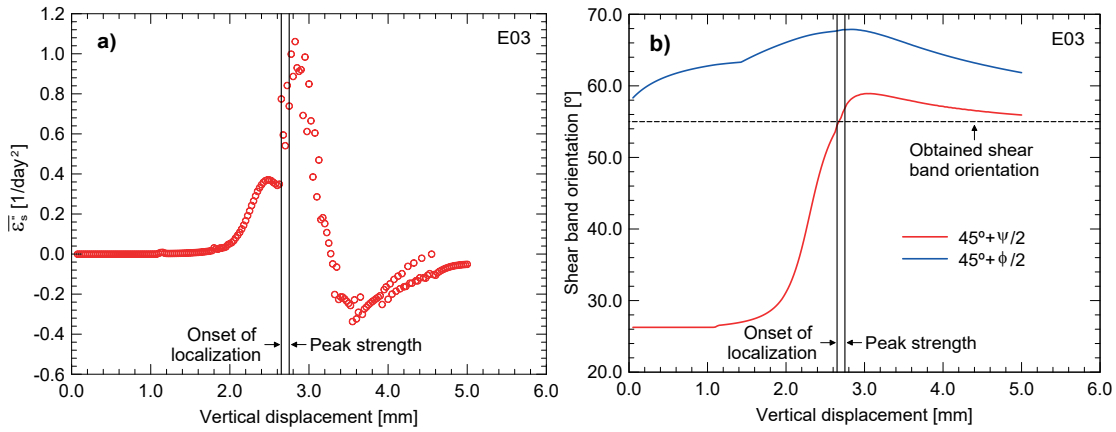

Figure 6: (a) Onset of localization and (b) theoretical and obtained shear band orientations

Since the amount of dilation at the onset of localization seems to control the orientation of the shear band, a given BVP should render a different orientation if the flow rule (Eq. 3) of the constitutive law is modified. The latter is shown in Fig. 7, where the same analysis was performed using different values of ω, controlling the amount of volumetric plastic strains (vertical displacements were normalized with the corresponding value at the onset of localization). As ω is reduced, a smaller ψ is attained at the onset of localization, rendering a gentler inclination of shear bands. Nevertheless, the obtained orientations can again be explained in terms of Roscoe's solution at the onset of localization.

4 CONCLUSIONS

A nonlocal plasticity model has been described, aimed to reproduce the strength characteristics of stiff fine-grained soils, including the objective simulation of strain localization. The selected results presented here, provide useful insights into relevant aspects of the numerical simulation of strain localization, and demonstrate the capability of the approach to simulate localized deformation patterns.

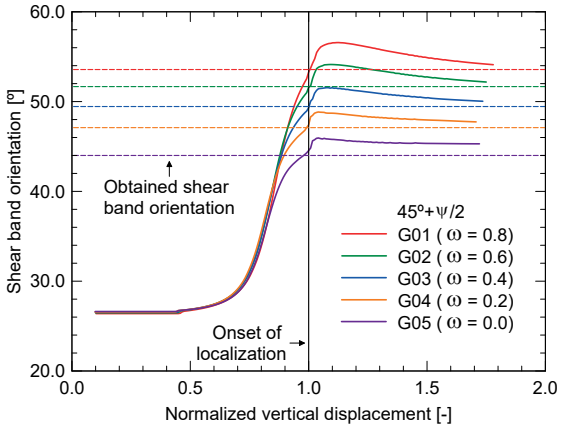

Figure 7: Theoretical and obtained shear band orientations for different flow rules

REFERENCES

[1] A. Gens, "On the hydromechanical behaviour of argillaceous hard soils-weak rocks (Keynote Lecture)," in *Geotechnics of Hard Soils Weak Rocks, Proceedings of the 15th European Conference on Soil Mechanics and Geotechnical Engineering*, vol. 4, (London), pp. 71–118, Thomas Telford, 2011.

[2] R. J. Jardine, A. Gens, D. W. Hight, and M. R. Coop, "Developments in understanding soil behaviour," in *Advances in geotechnical engineering: The Skempton conference* (R. J. Jardine, D. M. Potts, and K. G. Higgins, eds.), pp. 103–206, 2004.

[3] Z. P. Bažant and M. Jirásek, "Nonlocal Integral Formulations of Plasticity and Damage: Survey of Progress," *Journal of Engineering Mechanics*, vol. 128, no. 11, pp. 1119–1149, 2002.

[4] V. Galavi and H. F. Schweiger, "Nonlocal Multilaminate Model for Strain Softening Analysis," *International Journal of Geomechanics*, vol. 10, no. 1, pp. 30–44, 2010.

[5] K. H. Roscoe, "The influence of strains in soil mechanics," *Géotechnique*, vol. 20, no. 2, pp. 129–170, 1970.

XIV International Conference on Computational Plasticity. Fundamentals and Applications
COMPLAS XIV
E. Oñate, D.R.J. Owen, D. Peric & M. Chiumenti (Eds)

COUPLED H-M FRACTURE INTERACTION USING FEM WITH ZERO-THICKNESS INTERFACE ELEMENTS

D. GAROLERA*, J.M. SEGURA†, I. CAROL*, M.R. LAKSHMIKANTHA† AND J. ALVARELLOS†

* Dept. of Civil and Environmental Eng., Div. of Geotechnical Eng.
BarcelonaTech (UPC), Campus Nord UPC, 08034 Barcelona, Spain
e-mail: daniel.garolera(a).upc.edu and ignacio.carol(a)upc.edu

†Repsol Technology Centre
28935 Móstoles (Madrid), Spain

Key words: zero-thickness interface, hydraulic fracture interaction, hydro-mechanic coupling

Abstract. Intensive hydraulic fracturing is a procedure employed for low permeability reservoir stimulation. This technique consists of generating a sequence of regularly spaced parallel fractures (multi-stage fracturing). The generation of a fracture involves the modification of the local stress state, and therefore, in the case of multi-stage fracturing, the propagation of a certain fracture can be affected by the injection sequence, as it has been observed with microseismicity monitoring [1]. This paper describes a study of this technique by means of the Finite Element Method with zero-thickness interface elements for the geo-mechanical modelling of discontinuities [2]. The technique consists in inserting interface elements in between standard elements to allow jumps in the displacement solution fields. For the mechanical problem, their kinematic constitutive variables are relative displacements, and the corresponding static variables are stress tractions. The relationship between variables is controlled via a fracture-based constitutive law with elasto-plastic structure [3]. Concerning the hydraulic problem, the interface formulation includes both the longitudinal flow (with a longitudinal conductivity parameter strongly dependent on the fracture aperture), as well as and the transversal flow across the element [4]. Previous work by the authors focused on the validation of the method, the analysis a single fracture plane problem [5, 6]. In this case the method is extended to allow free propagation of fractures in any direction, by means of inserting interface elements between all continuum elements. The results presented in this paper analyse the effect of material properties, in particular fracture characterization, in the propagation and the effect of different major to minor principal horizontal stress ratio, on the trajectory and interaction of the fractures.

1 INTRODUCTION

Advanced modelling of reservoir geo-mechanics involves the numerical representation of geological discontinuities. In the approach described in this paper, zero-thickness interface elements of the Goodman type [2] are considered for this purpose. Those elements can also be used for representing the fluid flow and the coupled hydro-mechanical problem [7]. The technique consists in inserting interface elements in between standard elements to allow jumps in the solution fields. For the mechanical problem, their kinematic constitutive (strain-type) variables are relative displacements, and the corresponding static (stress-type) variables are stress tractions. The relationship between variables is controlled via a fracture-based constitutive law with elasto-plastic structure [3]. Concerning the hydraulic problem, the interface formulation includes both the longitudinal flow (with a longitudinal conductivity parameter strongly dependent on the fracture aperture, cubic law), as well as and the transversal flow across the element (and an associated localized pressure drop, with the corresponding transversal conductivity parameter).

The study presented in this paper is an extension of recent work presented by the authors [4, 5, 6] which was verified first by comparison to existing analytical and numerical solutions for the propagation of a single hydraulic fracture [8].

2 HYDROMECHANICAL FORMULATION FOR ZERO-THICKNESS INTERFACE ELEMENTS

Present work follows the definition of zero-thickness interface element originally proposed in [9]. The main characteristic of this type of element is that one of its dimensions has collapsed. Therefore the integration is reduced in one order, line integration for 2D and surface integration for 3D. The mid-plane surface is defined via isoparametric interpolation on the basis of the coordinates of the mid-points, or points at mid-distance between each pair of nodes. This interpolation is based on a set of local coordinates ξ, η for the mid-plane surface in 3D, or ξ for the mid-plane line in 2D.

Nodal unknowns are transformed into mid-plane variables which represent variations (jumps or drops) of field variables. Mid-plane variables are expressed in terms of the local orthogonal coordinates system, presented in section 2.1. Then, the HM formulation is shown in section 2.2.

2.1 Zero-thickness variables

The nodal variables in a hydro-mechanical problem include the nodal displacements ($\mathbf{u}_e$) and the nodal fluid pressures ($\mathbf{p}^f{}_e$). The nodal (absolute) displacements are transformed into normal (r_n) and shear (r_{l_1}, r_{l_2}) relative displacements, which have the meaning of displacements jumps across the discontinuity. The other variable, fluid pressure, is transformed into two components, the average pressure ($\bar{p}^f_J$) and the pressure drop ($\check{p}^f_J$), across the discontinuity. A description of these variables and their conjugates is provided in the following paragraphs.

The relative displacement at a mid-plane point (ξ, η) of the discontinuity is denoted

as:

$$\mathbf{r} = \begin{pmatrix} r_n & r_{l_1} & r_{l_2} \end{pmatrix}^{\mathsf{T}} \tag{1}$$

where r_n is the normal component and the $r_{l_{(*)}}$ are the tangential components. These relative displacements and the corresponding stress variables are depicted in Fig. 1.

The relation between relative displacements and nodal displacements is given by the the following expressions:

$$\mathbf{r} = \mathbf{R}\, \mathbf{N}_{\text{J}}^{u}\, \mathbb{T}^{u}\, \mathbf{u}_e = \mathbf{B}_{\text{J}}\, \mathbf{u}_e \tag{2}$$

where $\mathbf{R}$ is the rotation matrix that transforms vector components into local orthogonal axes, $\mathbf{N}_{\text{J}}^{u}$ is matrix of nodal shape functions evaluated at integration position (ξ, η), and $\mathbb{T}^{u}$ is the "transformation" matrix, which generates the difference between bottom and top face of interface element.

Then, the $\mathbf{B}_{\text{J}}$ matrix is defined in analogy to the classical FEM continuum elements.

$$\mathbf{B}_{\text{J}} = \mathbf{R}\, \mathbf{N}_{\text{J}}^{u}\, \mathbb{T}^{u} \tag{3}$$

The matrix of nodal shape functions is defined in Eq. (4), where m is the number of nodes at midplane (which is half of the number of nodes of the interface element n) and d represents the number of mechanical degrees of freedom per node. The operator "$\otimes$" indicates the Kronecker product.

$$\mathbf{N}_{\text{J}}^{u} = \begin{pmatrix} N_1 & N_2 & \cdots & N_m \end{pmatrix} \otimes \mathbf{I}_d \tag{4}$$

The mechanical transformation matrix for the mechanical problem is defined as:

$$\mathbb{T}^{u} = \begin{pmatrix} -\mathbf{I}_m & \mathbf{I}_m \end{pmatrix} \otimes \mathbf{I}_d \tag{5}$$

The conjugate variables to the relative displacements are the stress tractions at the discontinuity mid-plane ($\boldsymbol{\sigma}_{\text{J}}$), which, for a specific point (ξ, η) of that surface, may be expressed as:

$$\boldsymbol{\sigma}_{\text{J}} = \begin{pmatrix} \sigma_n & \tau_{l_1} & \tau_{l_2} \end{pmatrix}^{\mathsf{T}} \tag{6}$$

where σ_n is the normal stress and τ_{l_1} and τ_{l_2} are the tangential components.

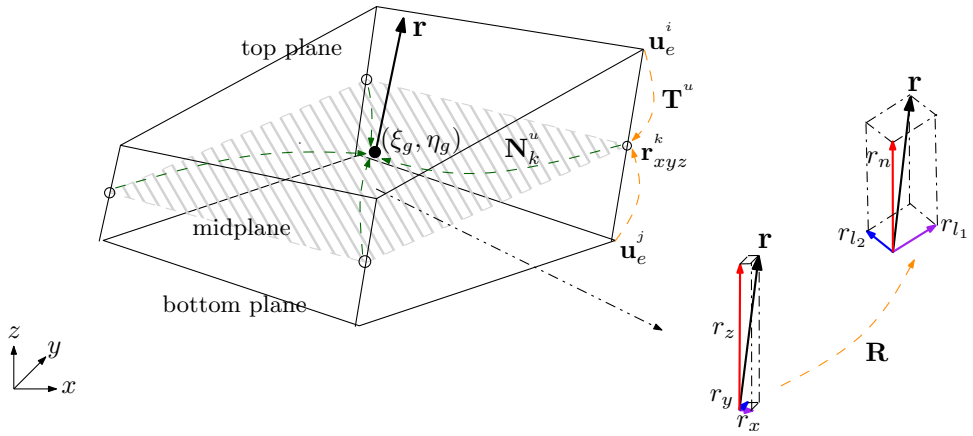

Figure 1: Relative displacements of zero-thickness interface element.

The average fluid pressure ($\bar{p}^f_{\text{J}}$) at a given point (ξ, η) of the discontinuity is obtained as the average between bottom and top fluid pressures and it can be expressed as:

$$\bar{p}^f_{\text{J}} = \mathbf{N}^{p\mathsf{T}}_{\text{J}}\ \mathbb{T}^p_L\ \mathbf{p}^f{}_e \tag{7}$$

$$\mathbf{N}^p_{\text{J}} = \begin{pmatrix} N_1 & N_2 & \cdots & N_m \end{pmatrix} \tag{8}$$

$$\mathbb{T}^p_L = \frac{1}{2}\begin{pmatrix} \mathbf{I}_m & \mathbf{I}_m \end{pmatrix} \tag{9}$$

The fluid pressure drop at the same point is given by the difference between top and bottom fluid pressures at element nodes:

$$\check{p}^f_{\text{J}}\big|_\xi = \mathbf{N}^{p\mathsf{T}}_{\text{J}}\ \mathbb{T}^p_T\ \mathbf{p}^f{}_e \tag{10}$$

$$\mathbb{T}^p_T = \begin{pmatrix} -\mathbf{I}_m & \mathbf{I}_m \end{pmatrix} \tag{11}$$

2.2 Finite element method formulation

This section describes the weak form of the equilibrium/continuity used for the implementation of zero-thickness interface elements. This equations are obtained from the application of Virtual work Principle. and the details can be found in [7]. The notation follows the terminology used in [10]:

$$\int_{\Omega_j} \mathbf{B}_{\text{J}}{}^{\mathsf{T}}\ \boldsymbol{\sigma}'_{\text{J}}\, d\Omega_j + \mathbf{Q}_{\text{J}}\ \mathbf{p}^f{}_e = \mathbf{f}^u_{\text{J}} \tag{12}$$

$$\mathbf{H}_{\text{J}}\ \mathbf{p}^f{}_e + \mathbf{S}_{\text{J}}\frac{\partial\, \mathbf{p}^f{}_e}{\partial t} + \mathbf{Q}_{\text{J}}{}^{\mathsf{T}}\frac{\partial\, \mathbf{u}_e}{\partial t} = \mathbf{f}^p_{\text{J}} \tag{13}$$

in which $\mathbf{Q}_{\text{J}}$ is the coupling matrix, $\mathbf{H}_{\text{J}}$ the diffusion matrix, $\mathbf{S}_{\text{J}}$ the storage matrix, and $\mathbf{f}^u_{\text{J}}$, $\mathbf{f}^p_{\text{J}}$ are the initial force and flow vector, with expressions:

$$\mathbf{Q}_{\text{J}} = \mathbb{T}^{u\mathsf{T}} \left(\int_{\Omega_{\text{J}}} \mathbf{N}^{u\mathsf{T}}_{\text{J}} \, \mathbf{R}^{\mathsf{T}} \, \alpha_{\text{J}} \, \mathbf{m}_{\text{J}} \, \mathbf{N}^p_{\text{J}} \, d\Omega_{\text{J}} \right) \mathbb{T}^p_L \tag{14}$$

$$\mathbf{H}_{\text{J}} = \mathbf{H}^p_{\text{J}_T} + \mathbf{H}^p_{\text{J}_L} = \tag{15}$$

$$= \mathbb{T}^{p\mathsf{T}}_T \left(\int_{\Omega_{\text{J}}} \mathbf{N}^{p\mathsf{T}}_{\text{J}} \, \check{K}_t \, \mathbf{N}^p_{\text{J}} \, d\Omega_{\text{J}} \right) \mathbb{T}^p_T + \mathbb{T}^{p\mathsf{T}}_L \left(\int_{\Omega_{\text{J}}} \left(\frac{\partial \, \mathbf{N}^p_{\text{J}}}{\partial \boldsymbol{x}_{\text{J}}} \right)^{\mathsf{T}} \frac{(-T^f_l)}{\gamma_f} \frac{\partial \, \mathbf{N}^p_{\text{J}}}{\partial \boldsymbol{x}_{\text{J}}} \, d\Omega_{\text{J}} \right) \mathbb{T}^p_L$$

$$\mathbf{S}_{\text{J}} = \mathbb{T}^{p\mathsf{T}}_L \left(\int_{\Omega_{\text{J}}} \mathbf{N}^{p\mathsf{T}}_{\text{J}} \, \frac{1}{M_{\text{J}}} \, \mathbf{N}^p_{\text{J}} \, d\Omega_{\text{J}} \right) \mathbb{T}^p_L \tag{16}$$

$$\mathbf{f}^u_{\text{J}} = \mathbb{T}^{u\mathsf{T}} \int_{\Gamma} \mathbf{N}^{u\mathsf{T}}_{\text{J}} \, \boldsymbol{\sigma}^{'}_0 \, d\Gamma \tag{17}$$

$$\mathbf{f}^p_{\text{J}} = \mathbb{T}^{p\mathsf{T}}_L \int_{\Omega_j} \left(\frac{\partial \, \mathbf{N}^p_{\text{J}}}{\partial \boldsymbol{x}_{\text{J}}} \right)^{\mathsf{T}} \frac{(-T^f_l)}{\gamma_f} \frac{\partial z}{\partial \boldsymbol{x}_{\text{J}}} \, d\Omega_j + \mathbb{T}^{p\mathsf{T}}_L \int_{\Gamma^f_q} \mathbf{N}^{p\mathsf{T}}_{\text{J}} \, \tilde{Q}^{\prime f} \, d\Gamma \tag{18}$$

where α_{J} is the Biot's coefficient, $\mathbf{m}_{\text{J}} = (1 \; 0 \; 0)^{\mathsf{T}}$, $\check{K}_t$ the transversal conductivity, T^f_l the longitudinal transmissivity, γ_f the specific fluid weight, M_{J} the Biot's modulus and $\tilde{Q}^{\prime f}$ the discharge per unit width.

3 STUDY OF FIVE-STAGE HF IN 2D

The study presented in this section is the analysis of multiple interacting hydraulic fractures using an academic example of 5 fracture jobs. The purpose of this study is to show the influence of previous hydraulic fractures on a subsequent fracture.

As said before, the interaction between different fracture jobs is due to the modification of local effective stress field. This variation is caused by the redistribution of stresses due to the fracture propagation and to the variation of fluid pressure after pumping.

The principal factors involved in this modelling are:

- The material properties of the rock (mechanical and fluid properties)
- The production design (spacing between jobs, volume of fluid injected, rate of injection, sequence of jobs, etc.).
- The initial stress state (vertical, horizontal maximum and minimum.)

Table 1: Material properties of continuum.

Parameter		*Value*	*Units*
E	Young's modulus	14400	MPa
ν	Poisson's ratio	0.2	-
K	Hydraulic conductivity	1×10^{-15}	$\mathrm{m\,s^{-1}}$
Ks	Solid compressibility	36000	MPa
α	Biot coef.	1.0	-

3.1 Model description

3.1.1 Geometry

A simplified configuration of five fracture jobs in a horizontal perforation is considered (see Fig. 2). In the current model the domain considered for the numerical analysis is composed of two subdomains (see Fig. 3):

- A *fractured subdomain*, which includes the zone in which the fractures can propagate (Fig. 3b), is discretized with a relatively dense FE mesh in which a network of interfaces is pre-inserted in between most continuum elements (Fig. 3c), with the purpose of allowing for sufficient freedom in the propagation of the fractures without predefined initial directions.

- A *continuum subdomain*, which corresponds to the surrounding domain farer from the fractures themselves, and consists of a layer or continuum elements without interfaces (Fig. 3a). This second subdomain is included in order to ensure the correct application of the boundary conditions (*in situ* stress and initial fluid pressure).

In this model the injection points are distributed along the x-axis (horizontal well) with fixed spacing of 5 m. Finally, as a first (2D) approach, the analysis is performed assuming plane strain conditions. Note that in order to avoid perturbations due to boundary conditions, the external boundary is placed around 200 m away from the interest area. In the fractured subdomain (Fig. 3b) zero-thickness interface elements are introduced between each pair of continuum elements. To ensure compatibility between the two subdomains, elastic interface elements are introduced all along the perimeter between the (outer) continuous and the (inner) fracture subdomains.

3.1.2 Material properties

The material properties used in the simulations are given below. For the continuum elements, an elastic isotropic material is assumed. Regarding the hydraulic behaviour, a practically impervious material is selected. All parameters are displayed in Table 1.

For the mechanical behaviour of the interface elements, normal and shear stiffness are assigned high values. These parameters may be understood as penalty coefficients with high values in order to avoid excessive unrealistic elastic deformations at the interfaces.

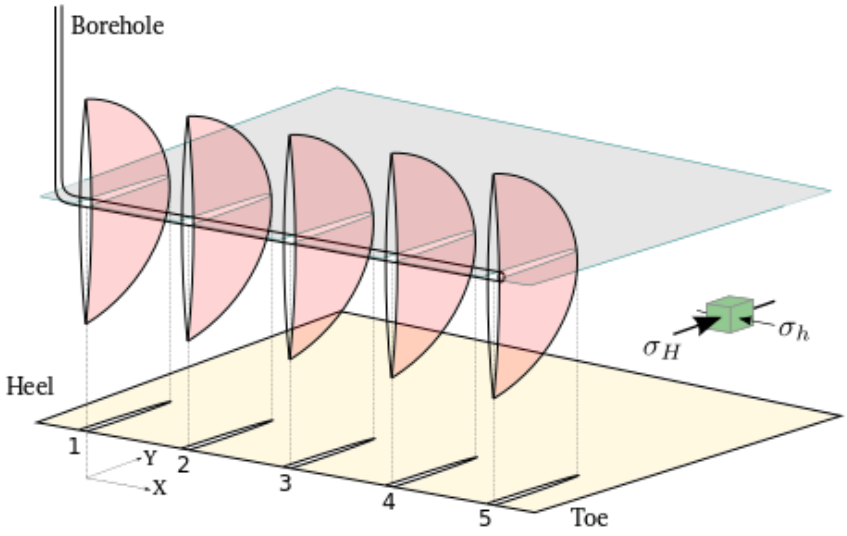

Figure 2: Scheme of 5 fracture job test.

Therefore, in practice the resulting deformation of the fractures can be assumed to represent almost exclusively the inelastic behaviour, that is, crack opening and shear slip.

The constitutive model used for the fractures is the elastoplastic constitutive formulation with fracture energy-based evolution laws described in detail in [3]. Low values of strength (tensile strength and cohesion) are selected in order to simulate existing fractures with very low or practically null cohesion [8]. The hydraulic behaviour of the interface is controlled by the so-called cubic law. The summary of interface parameters is shown in Table 2.

3.1.3 Boundary conditions

The boundary conditions are applied in a sequence of six steps (see Fig. 4):

Step 1: Stress initialization. In this step, a distributed load is applied over the external boundary: 1.0 MPa is imposed in the y-direction (σ_H). For the x-axis three cases are considered: 0.5 MPa, 0.7 MPa and 0.9 MPa (values of σ_h). The difference of principal stresses ensures that the preferential fracture direction is the y-direction (see Fig. 4, first row).

Steps 2-6: Single fracture jobs. A flow rate of $Q = 0.001\,\mathrm{m}^3/\mathrm{s}$ is injected at the injection point during 25 s. This step is repeated starting from job 1 and finishing at job 5 (see Fig. 4, second row)

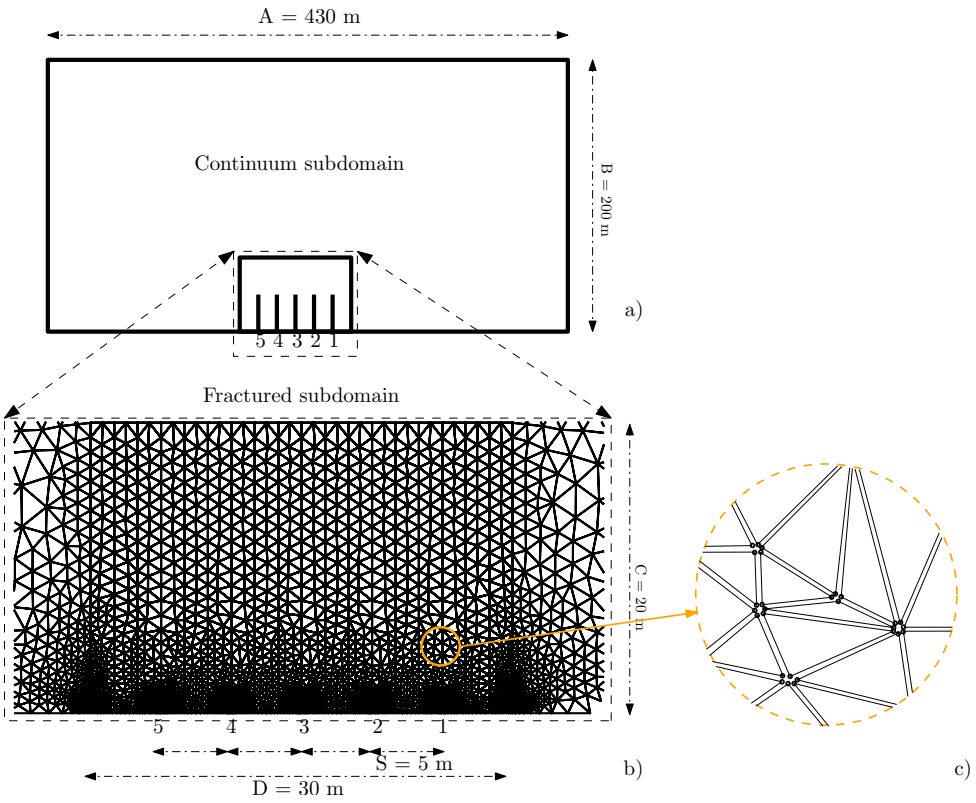

Figure 3: Model geometry for 5 fracture job test; a) full domain; b) fractured subdomain with detail of injection points position; and c) detail of network of interface elements inserted between continuum element. All dimensions are in meters.

3.2 Numerical Results and discussion

As already said, the objective of this study case was to learn about the interaction between subsequent fracturing jobs. The interaction is caused by the modification of the effective stress field during fracture propagation. For this purpose, several computations were performed focusing the interest on the effect of the *in situ* stress anisotropy. In particular, three cases with different ratio between maximum (σ_H) and minimum (σ_h) horizontal stress were run. All calculations assume the same maximum compression applied along the y-axis (on top and bottom limits of the domain), and different levels of minimum compression applied over the x-axis: a high anisotropic case $0.5\sigma_H$, a medium anisotropy case $0.7\sigma_H$ and a low anisotropy case $0.9\sigma_H$.

Figure 5 shows the evolution of fluid pressure at the injection points (crack mouths) along the entire simulation for the low anisotropy case. It is observed that the peak pressure for each injection is higher than the previous one, due to the increment of stress confinement after the previous fracture job. Therefore, the pressure necessary for opening the fracture increases due to the interaction of jobs, that is, the sequential scheme of injections causes a slow but gradual increase of the subsequent injection pressures.

Figure 6 shows the fluid pressure distribution at the end of fith fracture job, for the

Table 2: Material properties of interfaces.

Parameter		*Value*	*Units*
K_n	Normal stiffness	1×10^{-6}	$\mathrm{MPa\,m^{-1}}$
K_{t_1} and K_{t_2}	Tangentials stiffness	1×10^{-6}	$\mathrm{MPa\,m^{-1}}$
χ_0	Tensile strength	0.05	MPa
$\tan(\phi)$	Friction angle	0.2 (11.3°)	
c_0	Cohesion	0.5	MPa
G_f^I	Energy mode I	0.001	MPa m
G_f^{IIa}	Energy mode IIa	0.01	MPa m
T_{l_0}	Ini. Long. transmi.	0.0	$\mathrm{m^2/s}$
K_t^p	Trans. conduc.	1.0	$\mathrm{s^{-1}}$

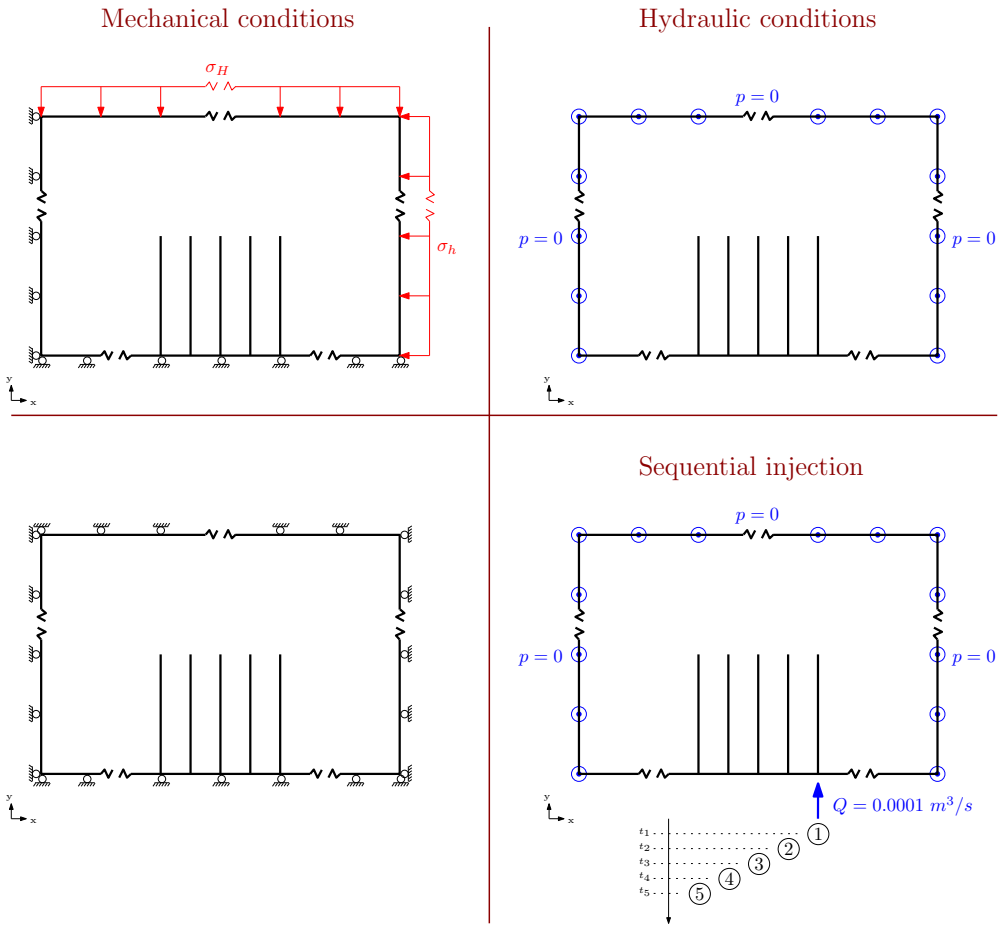

Figure 4: Boundary conditions for mechanical (left column) and flow (right column), for each of all the steps of the analysis (rows) in the two injection sequences considered.

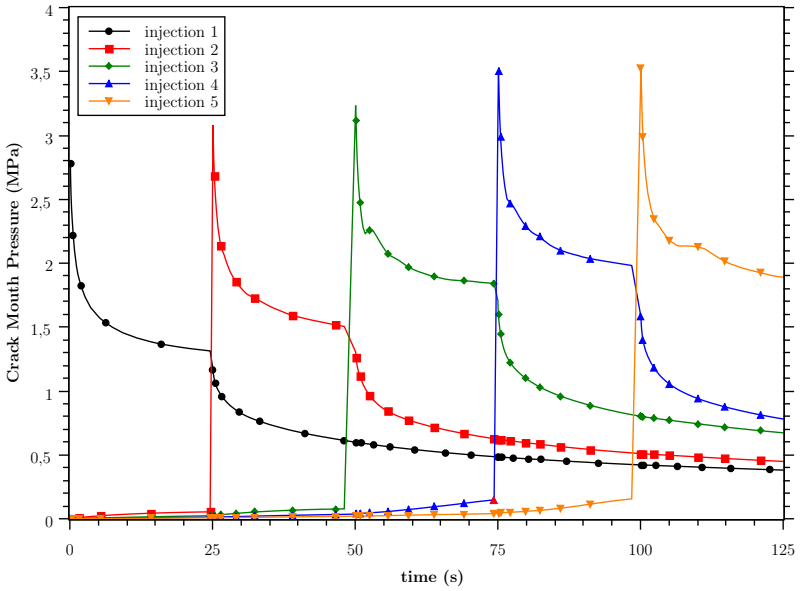

Figure 5: Crack Mouth Pressure evolution after 5 fracture jobs. Case $\sigma_h/\sigma_H = 0.9$

various σ_h/σ_H ratios scenarios. For a given *in situ* stress ratio, a slight interaction between fractures may seem to start appearing already from the second injection, although a clear interaction is not observed until the fifth injection for the high anisotropy case and until the third injection for the low anisotropy case, when the fracture clearly deviates from the initial vertical trajectory.

It is possible that these results may be slightly affected by the mesh layout, although after various tentative calculations these effects seem not to be very significant.

The results demonstrate that fracture interaction is clearly more pronounced as the difference between principal stresses is lower. For instance, the third injection in the case with ratio 0.9 shows a deviation of the last fractures which is not detected for ratios 0.7 and 0.5 until the fifth job and with much lower intensity.

4 CONCLUDING REMARKS

A methodology for 2D analysis of multi-stage hydraulic fracture is presented through the use of zero-thickness interface elements with full HM coupling. In this study an academic example of five fracture jobs in 2D is analysed in order to investigate the interaction between diffents jobs as observed in the field. Among all the variables involved in the interaction between fracture jobs, this paper has focused on the effect of different *in situ* stress states in terms of maximum-to-minimum horizontal stress ratio. The results presented in this paper show a clear interaction between different jobs, with more pronounced effects when the two horizontal stresses tend to be similar.

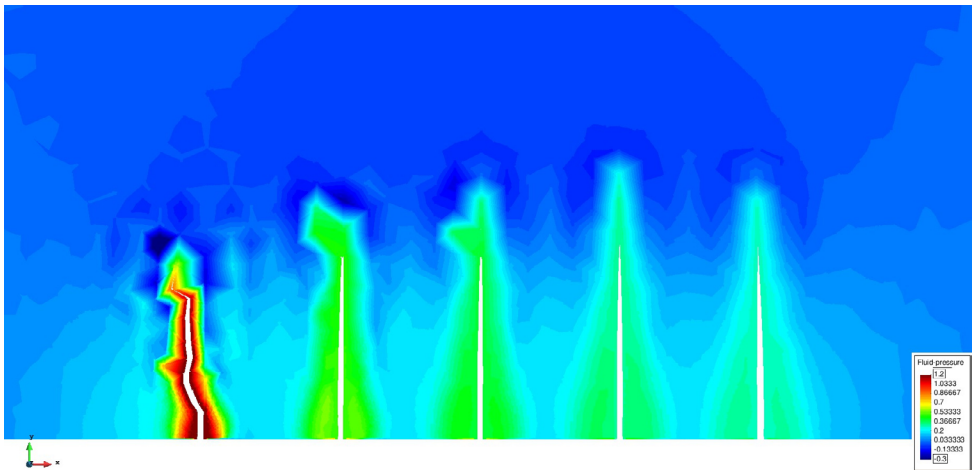

(a) $\sigma_h/\sigma_H = 0.5$

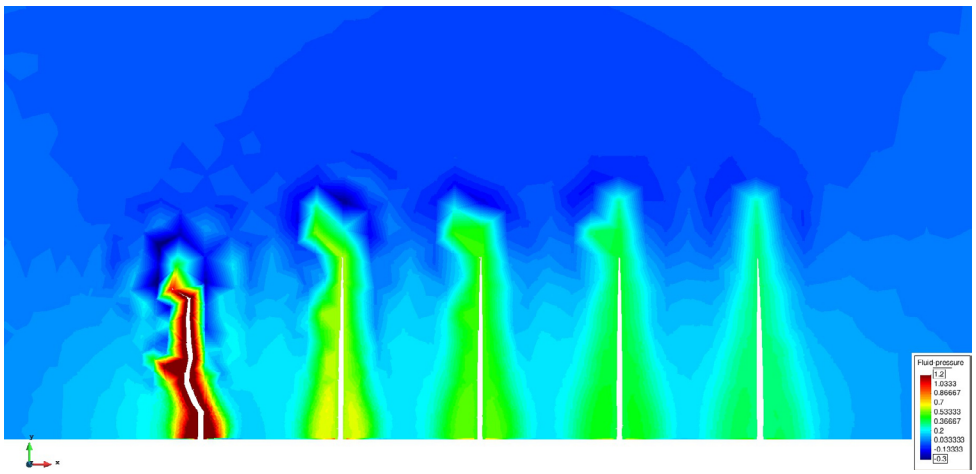

(b) $\sigma_h/\sigma_H = 0.7$

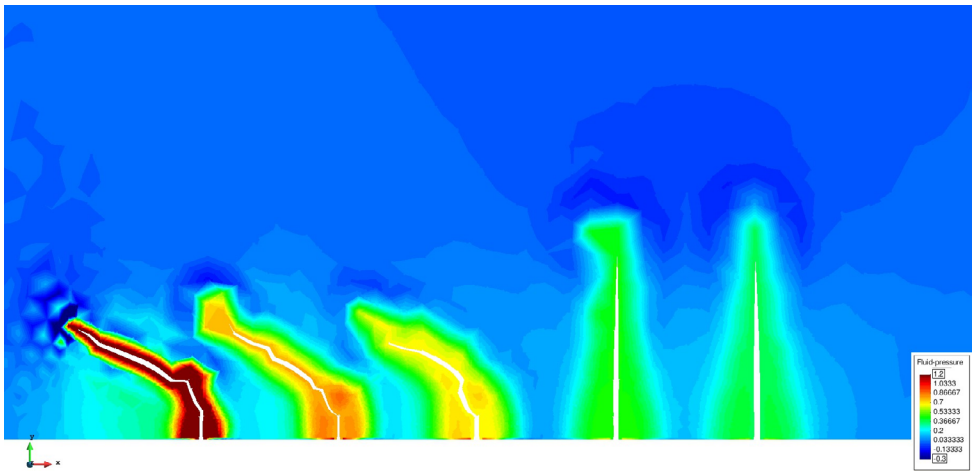

(c) $\sigma_h/\sigma_H = 0.9$

Figure 6: Effect of stress anisotropy on fracture interaction for different stress ratios: a) $\sigma_h/\sigma_H = 0.5$, b) $\sigma_h/\sigma_H = 0.7$ and c) $\sigma_h/\sigma_H = 0.9$. Fluid pressure distribution at time 125s.

5 ACKNOWLEDGEMENTS

The work was partially supported by research grants BIA2016-76543-R from MEC (Madrid), which includes FEDER funds, and 2014SGR-1523 from Generalitat de Catalunya (Barcelona). The support from REPSOL for this research is also greatfully acknowledged.

REFERENCES

[1] J. Daniels, G. Waters, J. Le Calvez, D. Bentley, and J. Lassek. Contacting more of the barnett shale through an integration of real-time microseismic monitoring, petrophysics, and hydraulic fracture design. *SPE-110562-MS*, 2007.

[2] A. Gens, I. Carol, and E. Alonso. A constitutive model for rock joints formulation and numerical implementation. *Computers and Geotechnics*, 9:3–20, 1990.

[3] I. Carol, P. Prat, and C. López. A normal/shear cracking model. application to discrete crack analysis. *ASCE J. Engrg. Mech.*, 123(8):765–773, 1997.

[4] J. M. Segura and I. Carol. Coupled hm analysis using zero-thickness interface elements with double nodes. Part II: Verification and application. *International Journal for Numerical and Analytical Methods in Geomechanics*, 32(18):2103–2123, 2008.

[5] D. Garolera, I. Aliguer, J. Segura, I. Carol, M. Lakshmikantha, and J. Alvarellos. Hydro-mechanical coupling in zero-thickness interface elements, formulation and applications in geomechanics. In *Proceedings of EUROCK 2014*, pages 1379–1384. CRC Press, 2014.

[6] D. Garolera, J. Segura, I. Carol, M. Lakshmikantha, and J. Alvarellos. Hydro-mechanical coupling in zero-thickness interface elements, formulation and applications in geomechanics. In *Proceedings of COMPLAS 2015*, pages 1379–1384. CIMNE, 2015.

[7] J. M. Segura and I. Carol. Coupled hm analysis using zero-thickness interface elements with double nodes. Part I: Theoretical model. *International Journal for Numerical and Analytical Methods in Geomechanics*, 32(18):2083–2101, 2008.

[8] T. J. Boone and A. R. Ingraffea. A numerical procedure for simulation of hydraulically-driven fracture propagation in poroelastic media. *Int. J. for Numer. Analyt. Meth. in Geomechanics*, 14(1):27–47, 1990.

[9] R. E. Goodman, R. L. Taylor, and T. L. Brekke. A model for the mechanics of jointed rock. *Journal of the Soil Mechanics and Foundation Division*, 94:637–659, 1968.

[10] O. Zienkiewicz and R. Taylor. *The finite element method.*, volume I. McGraw Hill, 2000.

XIV International Conference on Computational Plasticity. Fundamentals and Applications
COMPLAS 2017
E. Oñate, D.R.J. Owen, D. Peric and M. Chiumenti (Eds)

DIFFUSION-REACTION MODELLING OF THE DEGRADATION OF OIL-WELL CEMENT EXPOSED TO CARBONATED BRINE

A. MARTÍNEZ, J. LIAUDAT, C. M. LÓPEZ AND I. CAROL

ETSECCPB (School of Civil Engineering)
UPC (Technical University of Catalonia)
E-08034 Barcelona, Spain
e-mail: ariadna.martinez.e@upc.edu, joaquin.liaudat@upc.edu, carlos.maria.lopez@upc.edu, ignacio.carol@upc.edu

Key words: Carbon sequestration, Oil-well cement, CO_2, Carbonic acid, Chemical model, Finite Element Method.

Abstract. The essential aspects of a diffusion-reaction model in development for the degradation process of oil-well cement exposed to carbonated brine are presented in this paper. The formulation consists of two main diffusion/reaction field equations for the concentrations of aqueous calcium and carbon species in the hardened cement paste pore solution, complemented by a number of chemical kinetics and chemical equilibrium equations. The volume fraction distribution of the solid constituents of the hardened cement paste and the reaction products evolve with the progress of the reaction, determining the diffusivity properties of the material. A sensitivity analysis of some parameters of the model is presented to illustrate the capabilities to reproduce realistically some aspects of the degradation process.

1 INTRODUCTION

Geological storage of carbon dioxide (CO_2) is considered a promising solution to the global warming arising from anthropogenic CO_2 emissions, by capturing CO_2 from industrial and energy-related sources, transporting it usually by pipelines and injecting it into suitable deep rock formations [1]. Among other options, the storage of CO_2 in depleted oil and gas reservoirs is distinguished as one of the most favourable options; first, because the oil and gas that originally accumulated in traps did not escape, in some cases for many millions of years, demonstrating the integrity and safety of the storage site, and second, because these structures are well known and significant infrastructures are already in place at those sites. However a major source of concern arises when the security of exhausted oil fields is assessed for CO_2 storage: the presence of abandoned wells that perforate the caprock of the reservoir and which may potentially constitute CO_2 leakage pathways [2]. In particular, attention needs to be paid to the chemical stability of the cementations of those wells in the case they are exposed to carbonic acid formed by CO_2 injections. Since in most cases the construction and sealing of existing wells were not conceived taking into account future CO_2 storage, they were executed using ordinary Portland cement, which is chemically unstable in acid environments [3-8]. In this context, it becomes essential for practitioners the availability of accurate numerical

models in order to assess the long term performance of the cementation of abandoned wells in case of being exposed to new, acidic, environment due to CO_2 injections.

In this paper, a chemical model under development for simulating cement paste degradation when exposed to acidic solutions [9] is summaries together with some examples of applications. In this model the emphasis has been made on capturing the most significant chemical mechanisms that control the kinetics of the cement degradation, while keeping the formulation as simple as possible. In order to illustrate the capability of the model to reproduce realistically some aspects of the degradation process, the model was used to simulate experimental results found in the literature. Additionally, a sensitivity analysis of some model parameters is presented.

2 THE MODEL

2.1 Reaction mechanism considered

The proposed reaction mechanism is schematically summarized in Fig.1, which represents the interfacial zone between the hardened cement paste (HCP) and carbonated brine in the reservoir. The HCP is considered to be composed by four volumetric fractions: portlandite, calcium silicate hydrates (C-S-H), inert cement hydration products, namely aluminate and sulfate compounds, and capillary pores. The HCP pores are assumed to be fully saturated with water with concentrations of alkalis (sodium and potassium) and chlorides resultant from the cement hydration and from the exchange with the surrounding medium. These conditions, as well as the system pressure and temperature, are assumed to remain constant at all times during the reaction. For the sake of simplicity, C-S-H is assumed to have a fixed stoichiometry of $C_{1.7}SH_{3.2}$ (in cement chemistry notation). Then, it is decomposed in two parts, on one hand portlandite and, on the other, low calcium C-S-H, i.e. $C_{1.7}SH_{3.2}$=0.7CH + $CSH_{2.5}$. For all purposes, the portlandite in the C-S-H is treated as the rest of portlandite in the HCP.

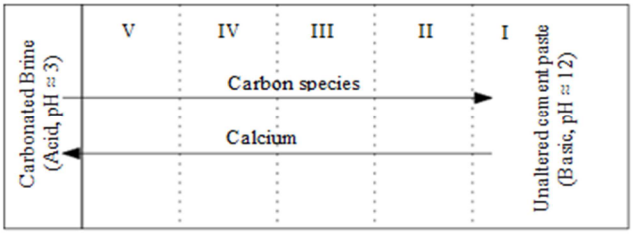

Figure 1: Scheme of the proposed degradation mechanism.

When CO_2 is dissolved in brine, carbonic acid (H_2CO_3) is formed, which is subsequently dissociated into HCO_3^- and CO_3^{2-}. This process is summarized in two Reactions (Eqs. (1) and (2)), where the intermediate formation of H_2CO_3 is omitted. The concentration gradient of carbon species causes a diffusion process from the brine towards the HCP, which is followed by a decrease of the pH of the pore solution in the HCP. As pH lowers, the portlandite in contact with the pore solution (zone II, Fig.1) becomes unstable dissolving into Ca^{2+} (Eq. (3), towards right). While there is portlandite in contact with the pore solution, the pH will remain high, and the predominant species of aqueous carbon will be CO_3^{2-}, which in turn will react

with Ca^{2+} resulting from portlandite dissolution forming calcite ($CaCO_3$) (zone III, Fig.1), as it is indicated in Eq. (4), towards left. If carbon species continue entering, the portlandite will be eventually exhausted. Consequently, the pH will decrease dissolving the calcium present in the $CSH_{2.5}$ (Eq. (5), towards right), and slowing down but not stopping the formation of calcite (zone IV, Fig.1). Additional ingress of carbon species will induce further reduction of the pH, driving calcite dissolution (Eq. (4), towards right), and continuing with the dissolution of the remaining calcium in the $CSH_{2.5}$, leaving only amorphous silicate hydrates, which are assumed to be stable in contact with the carbonated brine (zone V, Fig.1). At this stage, HCP is completely degraded with practically no mechanical strength and with high permeability.

In this processes the evolution of the solid volumetric fractions will determine important variations of the microstructure of the cement paste. In particular, the porosity of the degraded zone II is much higher than that of the unaltered cement paste. In contrast, the precipitation of calcite will reduce the porosity, in some cases, below the original value.

$$\mathrm{CO_{2\,(aq)}} + \mathrm{H_2O} \leftrightarrow \mathrm{HCO_3^-} + \mathrm{H^+} \tag{1}$$

$$\mathrm{HCO_3^-} \leftrightarrow \mathrm{CO_3^{2-}} + \mathrm{H^+} \tag{2}$$

$$\mathrm{Ca(OH)_{2\,(s)}} \leftrightarrow \mathrm{Ca^{2+}} + 2\mathrm{OH^-} \tag{3}$$

$$\mathrm{CaCO_{3\,(s)}} \leftrightarrow \mathrm{Ca^{2+}} + \mathrm{CO_3^-} \tag{4}$$

$$[\mathrm{Ca(OH)_2}][(\mathrm{SiO_2})(\mathrm{H_2O})_{1.5}] \leftrightarrow \mathrm{Ca^{2+}} + 2\mathrm{OH^-} + (\mathrm{SiO_2})(\mathrm{H_2O})_{1.5\,(s)} \tag{5}$$

$$\mathrm{H_2O} \leftrightarrow \mathrm{OH^-} + \mathrm{H^+} \tag{6}$$

2.2 Formulation

Assuming that the diffusion of aqueous species in the pore solution obeys Fick's diffusion law, averaging it in the saturated porous medium and posing the corresponding mass balance equation, the following diffusion-reaction equations for the continuum porous medium are obtained

$$\begin{cases} \dfrac{\partial(\phi c^{ca})}{\partial t} = \boldsymbol{\nabla}(D^{ca}\boldsymbol{\nabla}c^{ca}) + q^{ca} \\ \dfrac{\partial(\phi c^{tc})}{\partial t} = \boldsymbol{\nabla}(D^{tc}\boldsymbol{\nabla}c^{tc}) + q^{tc} \end{cases} \tag{7}$$

where the superscripts *ca* and *tc* indicate calcium and total carbon, respectively; ϕ is the total porosity; c^{β} [mol/m^3] is the concentration of aqueous β-species in the pore solution; D^{β} [m^2/s] is the effective diffusivity of aqueous β-species in the porous medium (assumed isotropic) and q^{β} [mol/(m^3·s)] is the rate of production/consumption of β-species per unit volume of porous medium, which in turn is a function of the concentration of aqueous calcium and total carbon, i.e. $q^{\beta} = q^{\beta}(c^{ca}, c^{ct})$. Finally, $\boldsymbol{\nabla} = [\partial/\partial x \;\; \partial/\partial y]^T$. The variable c^{tc} represents the summation of the molar concentrations of the different carbonic species in pore solution, i.e. $c^{tc}=c^{c0}+c^{c1}+c^{c2}$, where the superscript *c0* stands for $CO_{2(aq)}$, *c1* for HCO_3^- and *c2* for CO_3^{2-}.

Expressions of the production rate of calcium and total carbon are given in Eqs. (8) as functions of the net rate of production of solid species resultant from Reactions (3), (4) and

(5), where Γ^{α} [mol/(m^3·s)] is the reaction rate of solid α-species per unit volume of pore solution and superscripts CH, $C\bar{C}$ and CSH stands for portlandite, calcite and $CSH_{2.5}$.

$$q^{ca} = -\phi\left(\Gamma^{CH} + \Gamma^{C\bar{C}} + \Gamma^{CSH}\right)$$
$$q^{ct} = -\phi\left(\Gamma^{C\bar{C}}\right) \tag{8}$$

The calculation of the sink/source terms q^{β} according to Eqs. (8) requires establishing the kinetic laws for Reactions (3), (4) and (5) in order to obtain the corresponding Γ^{α}. To do so, it is assumed that the driving force of the dissolution/precipitation reaction of reactive solid α-species is (ψ^{α}-1), where ψ^{α} is the dimensionless saturation index of the pore solution with respect to the solid α-species. The saturation indexes are calculated in terms of the activity of the aqueous β-species intervening in the formation of the solid species. Activity and concentrations are related by means of dimensionless factors γ^{β} (activity coefficients), which are calculated using the well-known Davis Equation with the modification on the second term proposed by Samson and Lemaire [10]. In order to determine the concentration of secondary species, additional calculations need to be performed considering the equilibrium equations of the dissociation Reactions (1), (2) and (6), as well as, the electric charge neutrality of the pore solution. In these calculations, the concentration of other species present in the pore solution (such as alkalis or chlorides) but not intervening in Reactions (1) to (6) may be considered.

If $\psi^{\alpha} > 1$ the solution is oversaturated with respect to α-species, consequently, the reaction progresses in the precipitation direction. If $\psi^{\alpha} < 1$, the solution is under-saturated and solid dissolution occurs. If $\psi^{\alpha} = 1$, the solid and the solution are in thermodynamically equilibrium. The resulting kinetic law is formulated for a generic solid α-species in Eq.(9), where k_f^{α} and k_d^{α} [mol/(m^3·s)] are kinetic constants to be fitted and N^{α} [mol/m^3] is the concentration of solid α-species.

$$\Gamma^{\alpha} = \begin{cases} k_f^{\alpha}(\psi^{\alpha} - 1) & if\ \ \psi^{\alpha} \geq 1 \\ k_d^{\alpha}(\psi^{\alpha} - 1) & if\ \ \psi^{\alpha} < 1\ ;\ N^{\alpha} > 0 \\ 0 & if\ \ \psi^{\alpha} < 1\ ;\ N^{\alpha} = 0 \end{cases} \tag{9}$$

The mass balance equation of solid α-species is given by

$$\frac{\partial(\mathcal{U}N^{\alpha})}{\partial t} = \phi\mathcal{U}\Gamma^{\alpha} \tag{10}$$

where $\phi\mathcal{U}$ is the volume of pore solution and $\mathcal{U}$ [m^3] is the total volume of porous medium.

The total volume balance equation is given in Eq. (11), where ω^{α} [m^3/mol] is the apparent molar volume of solid α-species, and $\mathcal{U}^{cp}$[m^3] is the capillary porosity, i.e. the part of material volume that is not occupied by the solid phases and which is assumed to be filled with free water. Additionally, the total volume of pore solution includes also gel water present in gel-like solids such as C-S-H.

$$\mathcal{U} = \mathcal{U}^{cp} + \sum_{\alpha} \omega^{\alpha} M^{\alpha} \tag{11}$$

The effective diffusivity of the β-species in water-saturated HCP (D^{β}) is calculated by means of the analytical formula proposed by Oh and Jang [11] given in Eqs.(12), where D_0^{β} [m^2/s] is the diffusivity of the β-species in bulk water. This equation uses four constant dimensionless parameters which characterize the microstructure of the HCP, namely the capillary porosity (ϕ^{cp}), the percolation threshold (ϕ_c), the normalized diffusivity of the solid phase (D_s^{β}/D_0^{β}) and the percolation exponent (n). In order to introduce the effect of C-S-H dissolution in the reduction of the tortuosity of the pore structure, instead of considering n as constant, an additional expression is introduced (Eq. (13)), where n_i and n_f are the percolation exponents for unaltered and for completely decalcified HCP, respectively, and $\mathcal{U}_i^{CSH}$ is the volume of $CSH_{2.5}$ in the unaltered HCP.

$$\frac{D^{\beta}}{D_0^{\beta}} = \left(m_{\phi} + \sqrt{m_{\phi}^2 + \frac{\phi_c}{1-\phi_c}\left(\frac{D_s^{\beta}}{D_0^{\beta}}\right)^{1/n}} \right)^n \tag{12a}$$

$$m_{\phi} = \frac{1}{2}\left[\left(\frac{D_s^{\beta}}{D_0^{\beta}}\right)^{1/n} + \frac{\phi^{cp}}{1-\phi_c}\left(1 - \left(\frac{D_s^{\beta}}{D_0^{\beta}}\right)^{1/n}\right) - \frac{\phi_c}{1-\phi_c} \right] \tag{12b}$$

$$n(t) = n_i - \left(n_i - n_f\right)\left(1 - \frac{\mathcal{U}^{CSH}(t)}{\mathcal{U}_i^{CSH}}\right) \tag{13}$$

2.3 Numerical implementation

The above-described formulation has been implemented in the Finite Element code DRACFLOW, in-house developed by the group of Mechanics of Materials at UPC (MECMAT/UPC). This code has been previously used to model a number of durability problems in concrete such as drying shrinkage [12], external sulfate attack [13], Alkali-Silica Reaction [14] and high temperatures [15].

3 MODELLING RESULTS

The proposed diffusion-reaction model has been used for simulating one of the laboratory experiments performed by Duguid and Scherer [7] of well cement degradation due to exposure to carbonated brine. Additionally, a sensitivity study of the results to variations of the kinetic constants and to the way of calculating the effective diffusivity of the porous material has been performed.

3.1 The experiment

In their experiment, Duguid and Scherer [7] placed cylindrical cement paste samples (7.5 mm in diameter and 200 mm length, w/c ratio of 0.38) in a reactor with CO_2 saturated brine (0.5M NaCl) at 50 ºC. The samples were cured in 0.5 M NaCl brine at 50 ºC for 12 months. The carbonated brine had pH of 3.7 at 20 ºC and was continuously renovated in order to keep the boundary conditions as constant as possible. The evolution of the degradation front was followed by cutting small samples from the cement paste cylinder in the reactor at different times throughout the experiment. On these samples, visual measurements of depth of advance of different degradation fronts were performed.

3.2 Model geometry and parameters

The cylindrical sample has been simulated as a 1D axisymmetric problem, i.e. only radial diffusion in the sample is considered. The sample radius of 3.75 mm was discretized with 50 equal size linear finite elements. All simulations were performed for a total time of 720 hours (30 days) discretized in increments of 0.2 hours. The total carbon concentration in the carbonated brine surrounding the cement sample was estimated by means of additional calculations, as 46 mmol/L, while the concentration of calcium in the brine was assumed to be zero. Given the extended period of curing, the initial concentrations of alkalis (sodium) and chlorides were assumed homogeneous in the sample and equal to that of the brine, i.e. $c^r = c^{cl} =$ 500 mmol/L. The initial calcium concentration in pore solution is given by the equilibrium concentration of portlandite in contact with 0.5 M NaCl brine at 50 ºC, resulting in 20.95 mmol/L.

The initial concentration of the solid compounds was estimated based on the work of Brouwers [16-17] leading to the following volume fractions: $CSH_{2.5}$= 0.212, CH= 0.214, Inert cement paste= 0.220 and Capillary pores= 0.353. The total porosity (considering gel water) resulted in 0.48.

The saturation product constants considered for Reactions (3), (4) and (5) are K_{sp}^{CH}= 3.236E-06, $K_{sp}^{C\bar{C}}$= 2.007E-09 and K_{sp}^{CSH}= 3.236E-09, for activities in mol/L. The equilibrium constants considered for Reaction (1), (2) and (6) are K_{eq}^{c0}= 5.171E-07, K_{eq}^{c1}= 6.748E-11, and K_{eq}^{w}= 5.352E-14, also for activities in mol/L.

The remaining parameters (kinetic constants and diffusivity parameters) are used in the sensitivity analysis and, therefore, are indicated below for each simulated case.

3.3 Results

3.3.1 Reference case

In order to quantify the rate of progress of the degradation process, Duguid and Scherer [7] visually identified in samples taken from the cement cylinders, rings with different coloration, which were associated with different stages in the degradation process. In particular, a white ring developed in between the interior of the specimen and the practically completely decalcified outer corona. This white layer has been attributed to the presence of calcite. Then, in order to compare the measurements by Duguid and Scherer with our simulation results, the whitish color is related to a certain threshold content of calcite (0.22 m^3/m^3).

In Fig. 2, left, calcite profiles at different exposure times are plotted together. It can be appreciated how the precipitated calcite formed a relatively narrow layer that "moves" towards the interior of the sample. In the same plot, it is also indicated the adopted threshold content of calcite above which the material becomes whitish. From this plot the depths of the inner and outer sides of the whitish layer for each exposure time are obtained and plotted together with the experimental results obtained by Duguid and Scherer in Fig. 2, right. Note that the penetration rates of both the inner and the outer sides of the white layer are well reproduced by the model.

The kinetic constants used in this simulation were: $k_f^{C\bar{C}}$=5.00E-02, $k_d^{C\bar{C}}$=5.00E+02, k_d^{CH}= 1.00E+02, and k_d^{CSH}= 2.00E+01, in all cases expressed in mol/(m^3·s). The parameters used for the calculation of the effective diffusivity with Eqs. (12) and (13) were: n_i= 2.7, n_f=0.1, ϕ_c= 0.18, D_s^β / D_0^β=1.00E-04, D_0^{ct}=3.201E-09 m^2/s, and D_0^{ca}=1.327E-09 m^2/s.

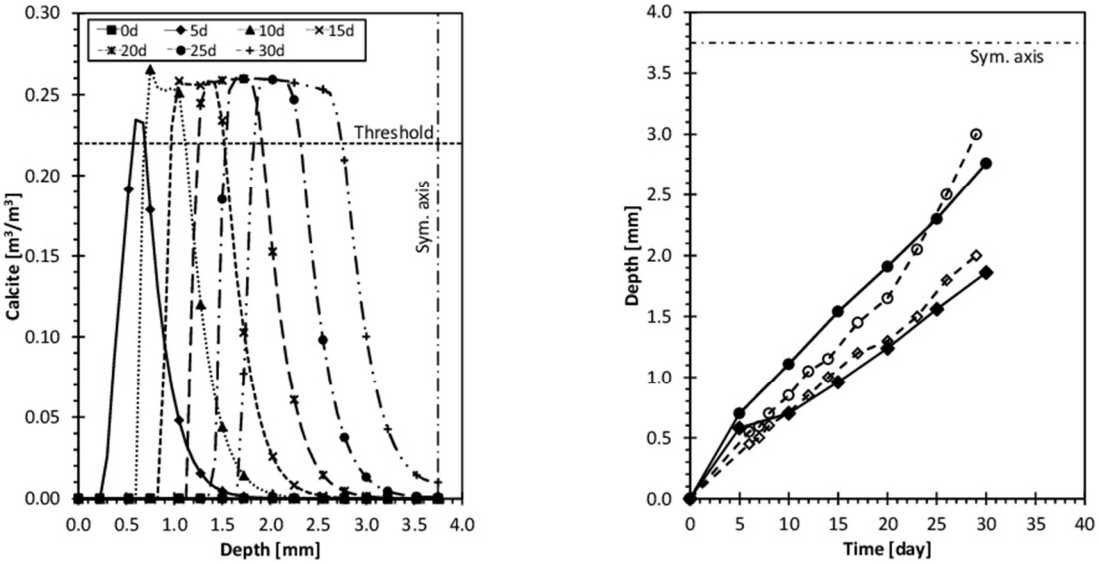

Figure 2: Left, radial profile of calcite volume fraction for different exposure times. Right, experimental and simulated reaction depth versus time. Circles and diamonds indicate the inner and the outer limits of the white layer of the degradation front, respectively. Empty symbols indicate experimental results by Duguid and Scherer [7], while solid symbols indicate simulation results.

3.3.2 Sensitivity analysis

In order to assess the influence of some parameters and modelling assumptions in the simulation results presented in previous Section 3.3.1, additional simulations were performed. In the first analysis, presented in Fig. 3, effective diffusivity was calculated in three different manners: (a) constant througout the simulation; (b) evolving as a function of capillary porosity using Eqs. (12) proposed by Oh and Jang; (c) using the formula proposed by Oh and Jang plus an evolution law, Eq. (13) for the percolation exponent. Note that (c) is the Reference case.

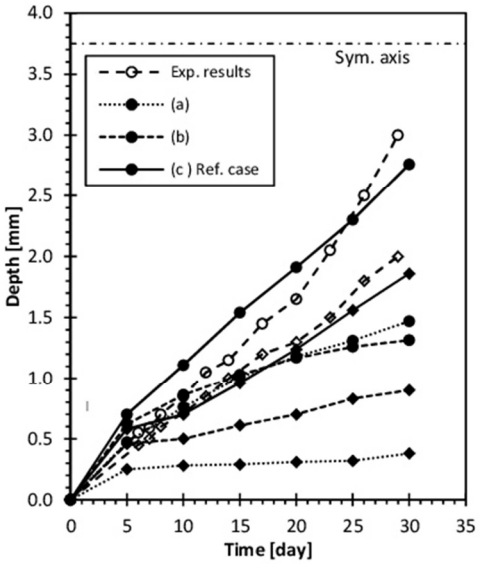

Figure 3: Experimental and simulated reaction depth versus time. The simulation results corresponds to three different maners of considering the effective diffusivity: (a) constant througout the simulation; (b) evolving as a function of capillary porosity using the formula proposed by Oh and Jang [11]; (c) using the formula proposed by Oh and Jang [11] plus an evolution law for the percolation exponent.

The rate of advancement of the reaction fronts obtained with constant diffusivity, case (a), markedly decreases with the penetration depth and clearly diverging from the experimental results. This can be explained by the growing distance to the boundary of the specimen from where the CO_2 is coming. This effect is not as marked in the experimental curves, indicating that it was somehow compensated by other mechanism. One possibility is that the increment of diffusivity due to the degradation of material compensated the greater distance to the boundary. In order to introduce this effect, a first intent was made using the formula proposed by Oh and Jang (case (b) in Fig. 3). As a result, the penetration rate of the outer front increases significantly, but the curve of the inner front remains practically unchanged. It seems that the increment of diffusivity given by the Oh and Jang formula in the degraded material was not high enough to fit the experimental results. Then, a second attempt was made introducing Eq. (13) with the intention of magnifying the effect of cement degradation on the effective diffusivity, resulting in the much better fitting of the curves of case (c).

In a second sensitivity analysis, the influence of the kinetic constants on the results obtained from the Reference case was assessed. To do so, eight additional simulations were performed. In each case, only the value of one kinetic constant was varied with respect to the one used in the Reference case. In Fig. 4, reaction depth-time curves obtained from these additional simulations are plotted together with the experimental curves and with the curves from the Reference case. The values of the corresponding modified kinetics constants are indicated in the legend of the plots.

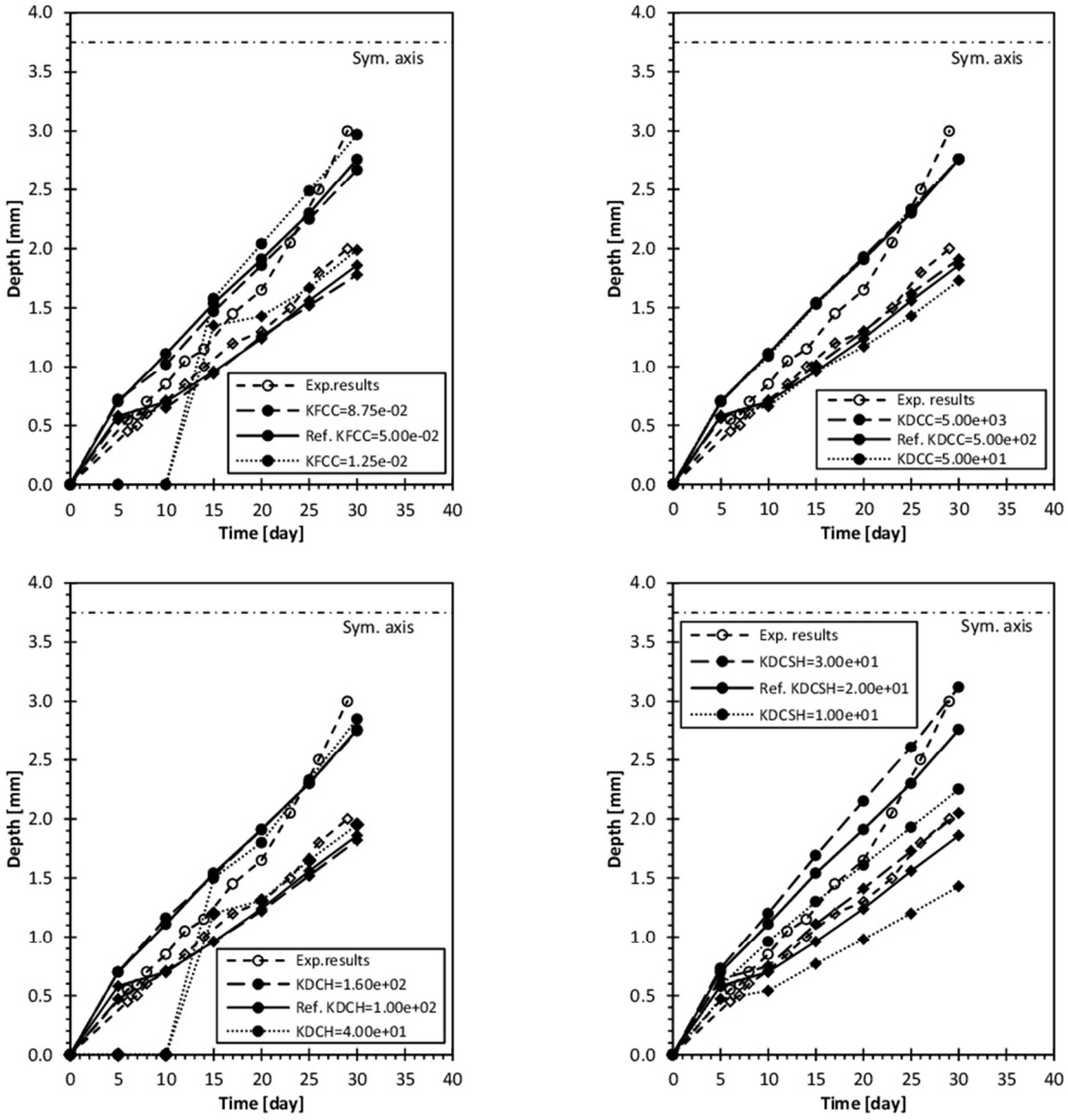

Figure 4: Experimental and simulated reaction depth versus time for the sensivity study of kinetics constants.

In the upper left plot of Fig. 4, the effect of modifying the kinetic constant of calcite formation $k_f^{C\bar{C}}$ has been represented. When $k_f^{C\bar{C}}$ is reduced, the volume of calcite formed in the first 10 days stays below the threshold value. Afterwards, the amount of calcite surpasses the adopted threshold, showing that the rate of advancement of the degradation front has not been reduced with respect to the Reference case, but slightly increased. On the other hand, increasing $k_f^{C\bar{C}}$ leads to practically the same curves as the Reference case. These results indicate that $k_f^{C\bar{C}}$ determines the peak value of the calcite radial profile, and may have also some influence on the advancement rate of the degradation fronts.

In the upper right plot of Fig. 4, the effect of modifying the kinetic constant of calcite dissolution $k_d^{C\bar{C}}$ has been represented. As expected, only the position of the outer degradation front, corresponding to the dissolution of the calcite layer, is affected by $k_d^{C\bar{C}}$. When $k_d^{C\bar{C}}$ is reduced, the dissolution of calcite is delayed and, consequently, the width of the white layer is increased. Inversely, when $k_d^{C\bar{C}}$ is increased, the width of the white layer is reduced.

In the bottom left plot of Fig. 4, the effect of modifying the kinetic constant of portlandite dissolution k_d^{CH} has been represented. As it occurs when k_d^{CH} is reduced the volume of calcite formed in the first 10 days stays below the threshold value. These results indicate that k_d^{CH} determines the peak value of the calcite radial profile but not the advancement of the degradation fronts.

In the bottom right plot of Fig. 4, the effect of modifying the kinetic constant of $CSH_{2.5}$ dissolution k_d^{CSH} has been represented. When k_d^{CSH} is increased both the inner and the outer advancement rates are increased. Inversely, when k_d^{CSH} is decreased both the inner and the outer advancement rates are decreased. This effect is more important for the inner degradation front than for the outer one and, hence, the width of the white layer increases with increasing k_d^{CSH}. The significant influence of k_d^{CSH} in the advancement of the degradation fronts is attributed to the role played by the volume fraction of $CSH_{2.5}$ in the calculation of effective diffusivity (see Eqs. (12) and (13)).

4 CONCLUDING REMARKS

- A general description of quantitative diffusion-reaction model for the simulation of cement paste degradation due to the exposure to carbonated brine has been presented.
- The proposed model seems capable of reproducing the rate of advancement of the degradation fronts.
- In order to fit experimental results, it was essential to introduce the effect of the material decalcification in the evolution of the effective diffusivity of the porous medium.
- A sensitivity analysis indicate that the kinetic constants mainly determine the width of the degradation front, with minor effect on the advancement rate, except for the dissolution kinetic constant of $CSH_{2.5}$ due to its relationship with the manner in which the effective diffusivity is calculated.
- More details of the work presented in this paper can be found in [9].

ACKNOWLEDGMENTS

This research has been supported by MEC (Madrid) through project BIA2016-76543-R which includes European FEDER funds, and by AGAUR/Generalitat de Catalunya (Barcelona) through project 2014SGR-1523. The first author also acknowledges AGAUR (Barcelona) for her FI doctoral fellowship.

REFERENCES

[1] Metz, B., Davidson, O., de Coninck, H., Loos, M., Meyer, L. & Working Group III of the Intergovernmental Panel on Climate Change (IPCC). *Carbon dioxide capture and storage* (2005).

[2] Gasda, S.E., Bachu, S., Celia, M.A. The potential for CO_2 leakage from storage sites in geological media: analysis of well distribution in mature sedimentary basins. *Environmental Geology* (2004) **46**: 6-7.
[3] Kutchko, B.G., Strazisar, B.R., Dzombak, D.A., Lowry, G.V., Thauiow, N. Degradation of well cement by CO_2 under geologic sequestration conditions. *Environmental Science and Technology* (2007) **41**: 4787-4792.
[4] Kutchko, B.G., Strazisar, B.R., Lowry, G.V., Dzombak, D.A., Thauiow, N. Rate of CO_2 Attack on Hydrated Class H Well Cement under Geologic Sequestration Conditions. *Environmental Science and Technology* (2008) **42**: 6237-6242.
[5] Rimmelé, G., Barlet-Gouédard, V., Porcherie, O., Goffé, B., Brunet, F. Heterogeneous porosity distribution in Portland cement exposed to CO_2-rich fluids. *Cement and Concrete Research* (2008) **38**: 1038-1048.
[6] Carey, J.W., Wigand, M., Chipera, S.J., WoldeGabriel, G., Pawar, R., Lichtner, P.C., Wehner, S.C., Raines, M.A., Guthrie, G.D. Analysis and performance of oil well cement with 30 years of CO_2 exposure from SACROC Unit, West Texas, USA. *International Journal of Greenhouse Gas Control* (2007) **1**: 75-85.
[7] Duguid, A., Scherer, G.W. Degradation of oilwell cement due to exposure to carbonated brine. *International Journal of Greenhouse Gas Control* (2010) **4**: 546-560.
[8] Duguid, A., Radonjic, M., Scherer, G.W. Degradation of cement at the reservoir/cement interface from exposure to carbonated brine. *International Journal of Greenhouse Gas Control* (2011) **5**: 1413-1428.
[9] Liaudat, J., Martínez, A., López, C.M., Carol, I. Modelling acid attack of oilwell cement exposed to CO_2 sequestration. *Submitted for publication.*
[10] Samson, E., Lemaire, G. Modeling chemical activity effects in strong ionic solutions. *Computational Materials* (1999) **15**: 285-294.
[11] Oh, B.H., Jang, S.Y. Prediction of diffusivity of concrete based on simple analytic equations. *Cement and Concrete Research* (2004) **34**: 463-480.
[12] Idiart, A.E., López, C.M., Carol, I. Modeling of drying shrinkage of concrete specimens at the meso-level. *Materials and Structures* (2011a) **44**: 415-435.
[13] Idiart, A.E., López, C.M., Carol, I. Chemo-mechanical analysis of concrete cracking and degradation due to external sulfate attack: A meso-scale model. *Cement and Concrete Composites* (2011b) **33**: 411-423.
[14] Liaudat, J., López, C.M., Carol, I. Numerical and Experimental study of ASR in concrete at the meso-level, in Saouma, V., Bolander, J., Landis, E. (Eds.). *The 9th International Conference on Fracture Mechanics of Concrete Structures (FraMCos 9)* (2016).
[15] Rodriguez, M., López, C.M., Carol, I. Modeling of Heat and Mass Transfer Induced by High Temperature in Concrete, in: Oñate, E., Owen, D.R.J., Peric, D., Chiument, M. (Eds). *XIII International Conference on Computational Plasticity. Fundamentals and Applications COMPLAS XIII* (2015) 346-353.
[16] Brouwers, H.J.H. The work of Powers and Brownyard revisited: Part 1. *Cement and Concrete Research* (2004) **34**: 1697-1716.
[17] Brouwers, H.J.H. The work of Powers and Brownyard revisited: Part 2. *Cement and Concrete Research* (2005) **35**: 1922-1936.

XIV International Conference on Computational Plasticity. Fundamentals and Applications
COMPLAS 2017
E. Oñate, D.R.J. Owen, D. Peric and M. Chiumenti (Eds)

FURTHER DEVELOPMENTS IN STRESS INITIALIZATION IN GEOMECHANICS VIA FEM AND A TWO-STEP PROCEDURE INVOLVING AIRY FUNCTIONS

C.R. YBERN[*], I. JAQUÉS[*], I. ALIGUER[*], I. CAROL[*], P.C. PRAT[*], M.R. LAKSHMIKANTHA[†], J.M. SEGURA[†]

[*] ETSECCPB (School of Civil Engineering)
Universitat Politècnica de Catalunya (UPC)
Campus Nord UPC, 08034 Barcelona, Spain
e-mail: ignacio.carol@upc.edu

[†] Repsol Technology Hub
The Woodlands, TX 77381, USA
e-mail: m.lakshmikantha@repsol.com

Key words: *In-situ* stress, initialization stress function, Finite Element Method (FEM), Oil & Gas.

Abstract.

The *in-situ* stress field in rock masses is a key aspect when a numerical analysis of a rock mass is carried out in any area of geo-engineering, such as civil, mining, or Oil & Gas. A method for the numerical generation of the *in-situ* stress state in the FE context, based on Airy stress functions was previously introduced. It involves two steps: 1) an estimate of the stress state at each Gauss point is generated, and 2) global equilibrium is verified and re-balancing nodal forces are applied as needed. In this paper, new developments towards improving the accuracy of the stress proposal are discussed. A real application example has been used to illustrate the results achieved with the new implementation.

1 INTRODUCTION

Geological materials are inevitably subject to an in situ stress field which is crucial for the evaluation of the geomechanical response of the rock mass in a variety of fields of Engineering [1,2]. However, in-situ measurement procedures are complex and expensive, and their accuracy strongly depends of every type of situation. Additionally, although in-situ measurements are certainly essential, stress fields are also subject to some constraints due to physical laws such as equilibrium and limit behaviour of material laws. For this reason, it is nowadays accepted that a sound procedure to reconstruct an accurate picture of the in-situ stress field requires the combination of measurements with numerical calculations [3].

Ideally, the in-situ stress state could be obtained by modelling the complete geological history of the rock mass. However, the realistic analysis of that history would be in general too complex, or the geological history may not be known exactly. This is why the strategy is changed to simply trying to obtain the "current picture" of the stress state in the rock mass, using simplified procedures.

In previous papers [4,5], the authors have discussed the equations to be satisfied by the initial stress field, and have proposed a two-step method to generate in-situ stress states which was based on Airy functions and the Finite Element method. In the first step, a first estimate of the stress state or "guess" at each Gauss point is proposed using vertical stresses due to gravity and horizontal due to the so-called horizontal to vertical stress ratio (K), and in a second step global equilibrium is verified and re-balancing nodal forces are applied as needed.

In this paper, further developments accomplished in this procedure are described, which include a non-linear based redistribution of unbalanced nodal forces and a parametric description of the geometry of the subdomains of interest. As the result of these new developments, the method is now more suitable for more complex geometries and situations, and also these changes are crucial for the extension of the method to 3D problems. The procedure described is illustrated with an example of application to a real reservoir field.

2 GENERATION OF THE INITIAL STRESS PROPOSAL $\boldsymbol{\sigma^{prop}}$ BASED ON STRESS FUNCTIONS

This method is based on the use of the so-called stress functions $\Phi(x, y, z)$, from which the components of the stress tensor are derived as follows:

$$\sigma_{ij} = F_{ij}\{\Phi\}, \tag{1}$$

where F_{ij} is a differential operator and Φ is a scalar function of *x, y* and *z*. In the particular case of two-dimensional analysis, the expression reduces to:

$$\sigma_{xx} = \frac{\partial^2 \phi}{\partial z^2} + \sigma_{xx_0} \tag{2}$$

$$\sigma_{zz} = \frac{\partial^2 \phi}{\partial x^2} - \gamma z + \sigma_{zz_0}$$

$$\sigma_{xz} = \frac{\partial^2 \phi}{\partial x \, \partial z} + \sigma_{xz_0}.$$

and $\Phi(x,z)$ is known as the Airy stress function [6-7]. In our particular case, a third degree polynomial expression with constant coefficients is used as stress function:

$$\Phi(x,z) = \frac{a_1}{6}x^3 + \frac{a_2}{2}x^2 z + \frac{a_3}{2}xz^2 + \frac{a_4}{6}z^3. \tag{3}$$

which leads to linear expressions of stress components in terms of the geometrical coordinates (x,z) and the coefficients a_i, which need to be determined via minimization procedure.

In order to determine the unknown coefficients, the entire domain is decomposed into vertical or sub-vertical strips, that are in turn subdivided into trapezoidal subdomains (Fig. 1-Left).

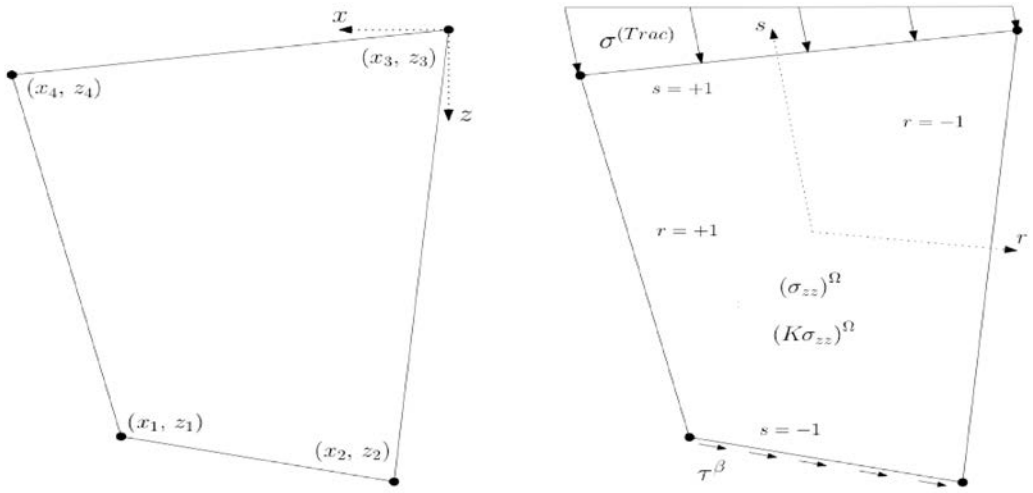

Figure 1 – (Left) Geometric definition of a linear prismatic subdomain and boundaries in the coordinates $(\boldsymbol{x}, \boldsymbol{z})$. (Right) The boundary conditions: $\bar{\sigma}^{(Trac)}$ $\bar{\tau}^{(\beta)}$ and $\bar{\sigma}_{yy}$ in parametrized (r,s) subdomain.

The coordinates (x,z) of each subdomain may be expressed *via* interpolation of the nodal coordinates of the subdomain through linear interpolation functions N_i, i.e. $x = \sum_{i=1}^{4} N_i(r,s)x_i$ and $z = \sum_{i=1}^{4} N_i(r,s)z_i$. This leads to the stress components in the subdomain in terms of the natural coordinates of the subdomain (r,s) as follows:

$$\sigma_{xx} = a_3 \sum_{i=1}^{4} N_i(r,s)x_i + a_4 \sum_{i=1}^{4} N_i(r,s)z_i + \sigma_{xx_0} \tag{4}$$

$$\sigma_{zz} = a_1 \sum_{i=1}^{4} N_i(r,s)x_i + (a_2 - \gamma) \sum_{i=1}^{4} N_i(r,s)z_i + \sigma_{zz_0}$$

$$\sigma_{xz} = -a_2 \sum_{i=1}^{4} N_i(r,s)x_i - a_3 \sum_{i=1}^{4} N_i(r,s)z_i + \sigma_{xz_0}.$$

where the initial stress values $\sigma_{xx_0}, \sigma_{zz_0}, \sigma_{xz_0}$ can be considered as additional subdomain parameters ($a_i,\ i = 5,6,7$) to be included in the minimization procedure.

The subdomains on each vertical strip are considered sequentially from top to bottom. Each subdomain is limited on the top and bottom by edges corresponding to $s = +1$ and $s = -1$ repsectively. Also, left and right edges are given by $r = -1$ and r= $+1$. These edges are plane but not necessarily horizontal, and are subject to the following boundary conditions: 1) The components of traction vector $\left(\bar{\sigma}^{(Trac)}\right)$ on the top edge ($s = +1$) is prescribed as a linear function of *x* and *z*. 2) Vertical stress gradient ($\bar{\sigma}_{zz}$) on entire surface is also prescribed as a linear function of *x* and *z*. 3) The shear intensity $\left(\bar{\tau}^{(\beta)}\right)$ on the bottom edge ($s = -1$) is linked to the amount of normal stress on the same edge. 4) Horizontal stress ($\bar{\sigma}_{xx}$) on entire domain and is related to vertical stress σ_{zz} via K.

According to the boundary conditions imposed on the top and bottom edges and the entire surface of the subdomain (Fig. 1-Right), an objective function $G(a_i)$ is considered for the subdomain that integrates the square difference between: 1) the traction vector components and its prescribed values, 2) the shear stresses and its prescribed values, 3) the horizontal stress component and K times the prescribed vertical stress values, and 4) the vertical stress components and its prescribed values. Considering the derivatives of the objective function with respect to the coefficients a_i, then the stress state that best fits the boundary conditions is defined by the parameters (a_i) that minimize the objective function:

$$\begin{aligned}\frac{\partial \mathrm{G}}{\partial a_i}(a_i) = \frac{\partial}{\partial a_i}\int_{-1}^{+1}\sum_{i=1}^{n}\left(\sigma^{(Trac)} - \bar{\sigma}^{(Trac)}\right)^2 \mathrm{J}^{(s=+1)}dr + \\ + \frac{\partial}{\partial a_i}\int_{-1}^{+1}\left(\tau^{(\beta)} - \bar{\tau}^{(\beta)}\right)^2 \mathrm{J}^{(s=-1)}dr + \\ + \frac{\partial}{\partial a_i}\iint_{-1}^{+1}(\sigma_{xx} - K\bar{\sigma}_{zz})^2 J^{(r,s)}\,drds + \\ + \frac{\partial}{\partial a_i}\iint_{-1}^{+1}(\sigma_{zz} - \bar{\sigma}_{zz})^2 J^{(r,s)}\,drds,\end{aligned} \tag{5}$$

wherein $J^{(\cdot)}$ is the determinant of the Jacobian of the coordinates transformation (global to natural) at the corresponding boundary and n is the number of components of traction vector.

$\sigma^{(Trac)}$, $\tau^{(\beta)}$ are the traction vector and shear stress of the proposed distribution on the top and bottom edges of the subdomain with the corresponding prescribed values $\bar{\sigma}^{(Trac)}$ and $\bar{\tau}^{(\beta)}$. σ_{zz} and σ_{xx} are the corresponding stress components evaluated on entire surface and $\bar{\sigma}_{zz}$ is the vertical stress prescribed nodal value.

3 APPLICATION TO A REAL RESERVOIR CROSS-SECTION

The example of application of the procedure described consists of the real geological 2D cross-section shown in Fig. 2-top.

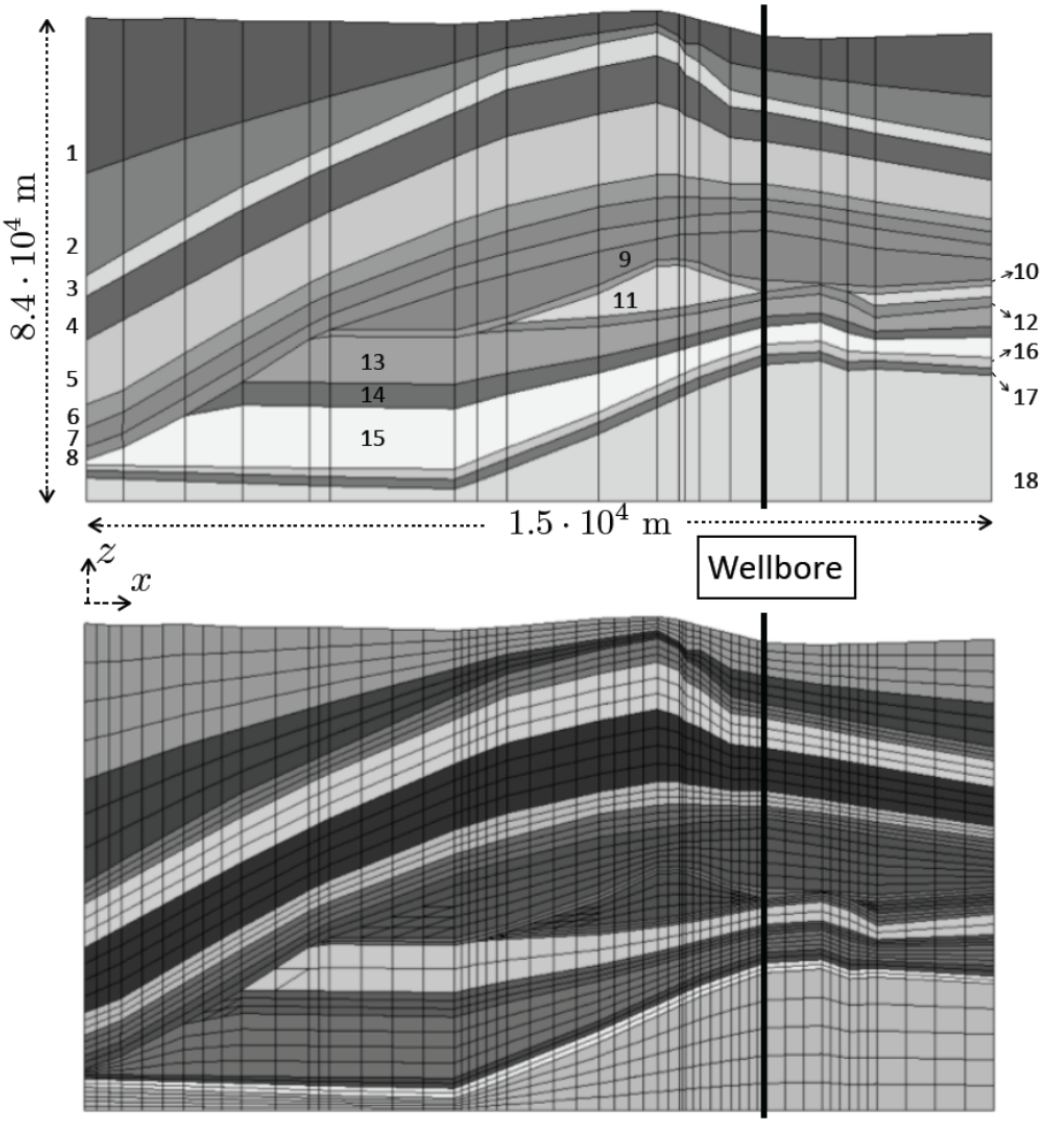

Figure 2 - (Top) Geomechanical model. (Bottom) Finite Element Mesh of the cross-section. The thick vertical line indicates location of a wellbore.

The geometry of the geological formation is very adequate for 2D analysis since all the cross-sections parallel to the one considered have a very similar geometry. Furthermore, the cross-section considered has the advantage of the availability of field measurements from a wellbore. The following data is available: Young's modulus (E), Poisson's ratio (ν), rock density (ρ), fluid pore pressure (P_f), and horizontal-to-vertical stress ratio (K). Table 1 shows these parameters for each layer of the domain (top to bottom).

In order to apply the procedure based on Airy stress functions, the domain is subdivided in a total of 22 vertical stripes, and each of these layers is in turn subdivided into a number of trapezoids by intersection with the 18 geological layers, as also shown in Fig.2-top. Once the geometrical model is established, a FE mesh is generated as depicted in Fig. 2-bottom, with a total of 2899 quadratic elements (2816 quadrangles and 83 triangles), and 8822 nodes.

As previously mentioned, a nonlinear behaviour has been assumed for the rock mass. The use of this type of constitutive behaviour allows the redistribution of excessive and usually unrealistic stress values that typically appear near surface in valleys or other geometries when a pure elastic analysis is carried out. In particular, a simplified elastic perfectly-plastic constitutive law with a hyperbolic Drucker-Prager [8] yield criterion is assumed as follows:

$$F = \sqrt{J_2} - \tan\varphi^f \sqrt{p^2 + \left(\frac{c^f}{\tan\varphi^f} - t_p^f\right)}, \tag{6}$$

where p is the first invariant of the stress tensor, $\sqrt{J_2}$ is the second invariant of the deviatoric tensor, φ^f is the friction angle, c^f is the cohesion and t_p^f is the tensile strength. Also associated plasticity ($F = Q$) has been considered in the present example, as shown in Fig. 3. Values of $c^f = 100\text{kPa}$, $\varphi^f = 30º$ and $t_p^f = 50\text{kPa}$, which are standard in the literature of Rock Mechanics have been used to characterize the non-linear response of the rock mass.

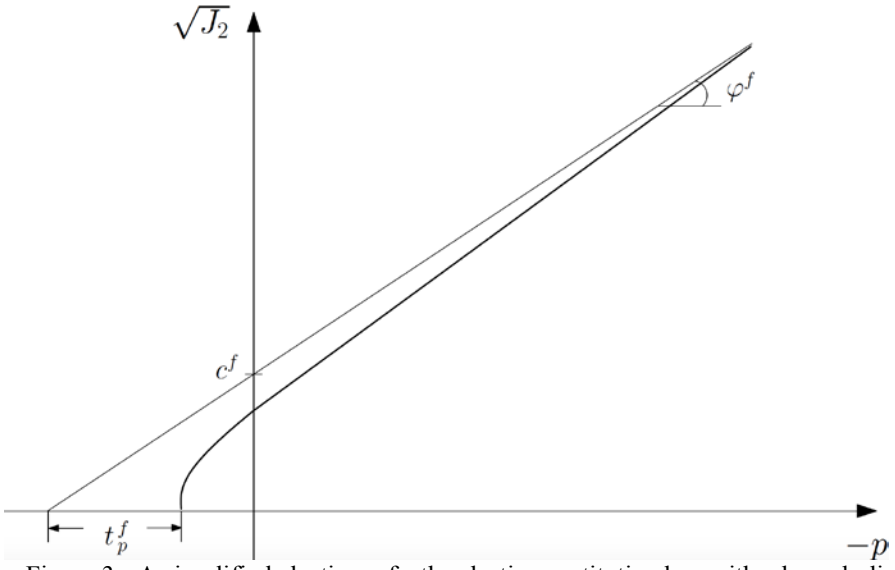

Figure 3 - A simplified elastic perfectly-plastic constitutive law with a hyperbolic Drucker-Prager [8].

Table 1: Values of different parameters used in each layer in the geometry model

Layer	Young (GPa)	Specific weight	Poisson	*K*
1	13.79	24.13	0.224	2.14
2	27.23	25.21	0.23	1.93
3	22.75	25.11	0.227	1.27
4	19.99	24.33	0.22	1.06
5	31.03	25.51	0.235	1.14
6	44.82	25.90	0.235	1.31
7	37.92	24.82	0.24	1.16
8	46.88	25.41	0.25	1.27
9	17.24	24.13	0.233	1.09
10	42.75	25.02	0.25	1.14
11	49.64	25.80	0.253	1.17
12	46.88	25.80	0.22	1.20
13	39.99	25.02	0.244	1.15
14	43.78	25.11	0.245	1.19
15	37.92	25.21	0.24	1.21
16	51.71	25.90	0.25	1.19
17	31.03	25.21	0.245	1.24
18	42.75	25.02	0.25	1.14

The elastic rock properties assigned to each geomechanical unit are listed in Table 1. The results obtained, are presented in Fig. 4 in terms of both total and effective vertical and horizontal stress profiles along the wellbore.

In Fig. 4, dotted-dashed lines represent the stress profiles resulting from the stress proposal based on the Airy functions (step 1 of the procedure). Solid lines represent the equilibrated stress profiles, obtained after the application of the unbalanced nodal forces (step 2). As it can be observed in the figure, the equilibrated stress states exhibit a better agreement with the previous available data along the well (dashed line). Overall, this agreement with available data is remarkable in both horizontal and vertical stress components and the general trend and also local effects are captured. However, vertical stress profile shows a better fit in the upper 3500 m, which is the main area of interest since it corresponds to the reservoir and the overburden.

Since all calculations have been carried out in terms of total stresses, the profiles in terms of effective stresses have been obtained via a post-processing using the available fluid pressure along the wellbore, as shown in Fig.4-bottom.

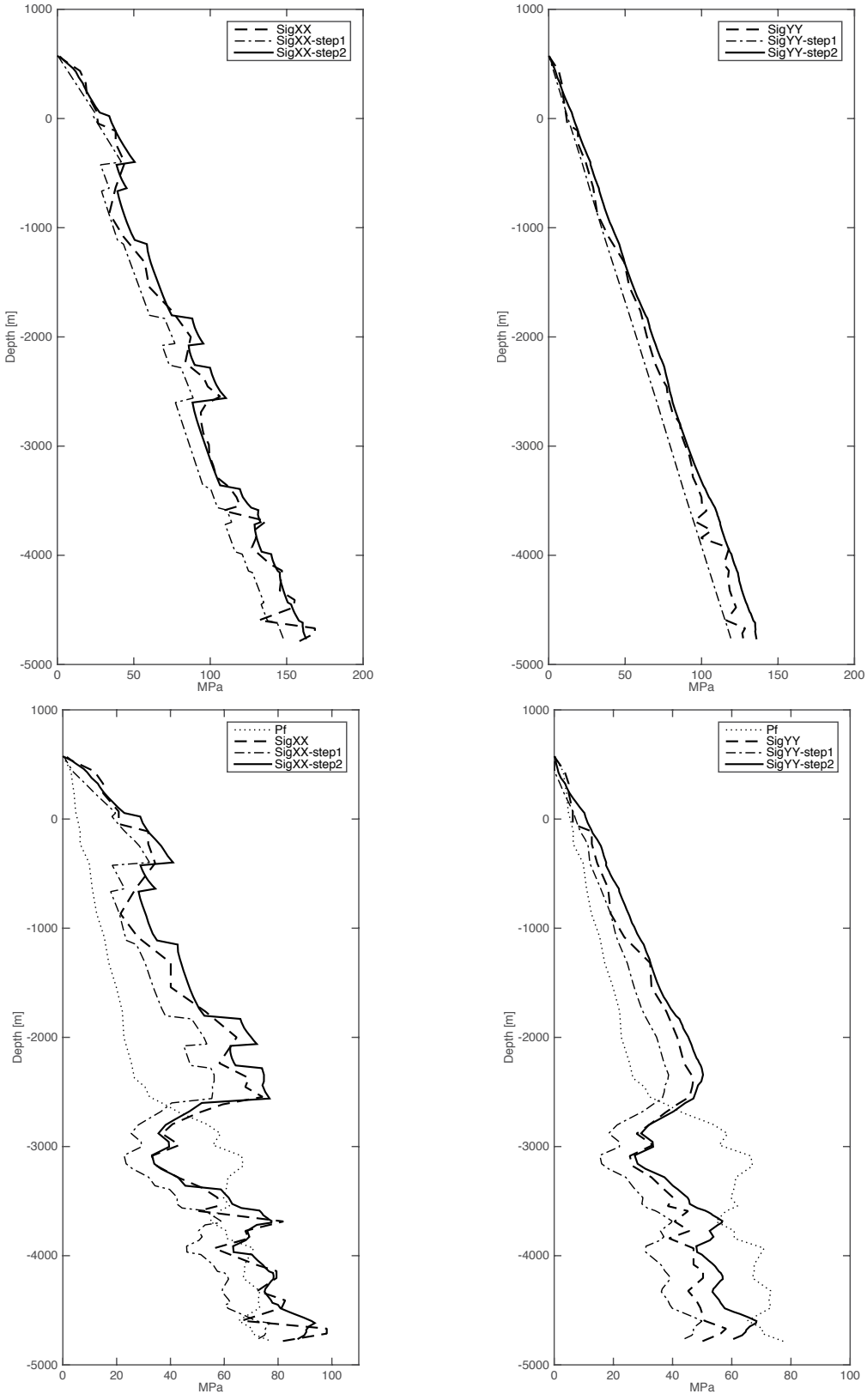

Figure 4 – Comparison of initial stress obtained using two-step procedure with available data: (Top-Left) total horizontal; (Top-Right) total vertical stress; (Bottom-Left); effective horizontal stress; and (Bottom-Right) effective vertical stress. In bottom diagrams dotted line is the available fluid pressure Pf along the wellbore. In all diagrams: continuous line is final initial stress calculated after two-step procedure, dashed line is available data, and dotted-dashed line is intermediate stress obtained in step1 of the procedure.

5 CONCLUDING REMARKS

In the present paper, further developments of the stress initialization technique in geological media described previously in [4-5] have been described. This procedure, based on Airy stress functions, constitutes a step forward with respect the simplest procedure of the fictitious Poission's ratio, widely used in engineering practice. The mentioned improvements include: (1) an isoparametric representation of the subdomains that allow more general geometries, (2) more realistic stress conditions over the subdomain and its boundaries, and (3) the use of non-linear laws in the re-equilibration step, in order to redistribute unrealistically high deviatoric stress that may appear in the stress proposal at specific areas near the surface.

The described procedure has been applied to the stress initialization of a real reservoir cross-section where wellbore measurements were available. The same example was also used in the previous papers, and the results obtained with the new improvements show a better fit of both the stress proposal and the equilibrated stress states.

ACKNOWLEDGEMENTS

The work was partially supported by research grants BIA2016-76543-R from MEC (Madrid), which includes FEDER funds, and 2014SGR-1523 from Generalitat de Catalunya (Barcelona). Support from REPSOL for this research is also gratefully acknowledged. The first author acknowledges his FI doctoral fellowship.received from AGAUR-Generalitat de Catalunya (Barcelona).

REFERENCES

[1] Brown, E.T. and Hoek, E. Trends in relationships between measured in-situ stresses and depth. *International Journal of Rock Mechanics and Mining Sciences & Geomechanics Abstracts* (1978) **15**:211-215.

[2] Fjaer, E., Holt, R. M., Raaen, A. M., Risnes, R. and Horsrud, P. Petroleum related rock mechanics. *Elsevier* (2008) **53**.

[3] Parrish, D.K. and Labreche, D.A. Initializing The Equilibrium Stress state For Stress Analyses In Geomechanics. *The 29th US Symposium on Rock Mechanics (USRMS)* (1988).

[4] Aliguer, I., Carol, I., Prat, P., Ybern, C.R., Lakshmikantha, M.R. and Segura, J.M. Numerical stress initialization in geomechanics via the FEM and a two-step procedure. *COMPLAS XIII: proceedings of the XIII International Conference on Computational Plasticity: fundamentals and applications, CIMNE* (2015) 667-676.

[5] Aliguer, I., Ybern, C.R., Jaqués, I., Carol, I., Prat, P., Lakshmikantha, M.R. and Segura, J.M. Methods for FEM Stress Initialization Based on Stress Functions, and Application to a

Reservoir Cross-Section. *The 50th US Rock Mechanics/Geomechanics Symposium, American Rock Mechanics Association* (2016).

[6] Airy, G.B. On the Strains in the Interior of Beams. *Philosophical Transactions of the Royal Society of London* (1863) **153**:49-79.

[7] Timoshenko, S.P., Goodier, J.N. and Abramson, H.N. Theory of elasticity. *Journal of Applied Mechanics.* (1970) **37**:888.

[8] Drucker, D.C. and Prager, W. Soil mechanics and plastic analysis or limit design. *Quarterly of applied mathematics.* (1952) **10(2)**:157-165.

XIV International Conference on Computational Plasticity. Fundamentals and Applications
COMPLAS 2017
E. Oñate, D.R.J. Owen, D. Peric and M. Chiumenti (Eds)

STABILITY FEM ANALYSIS OF ROCK MASSES MODELING PATTERN OF JOINTS

CARLOS CHÁVEZ[*], LUISA N. EQUIHUA[*] AND FRANCISCO DOMINGUEZ[†]

[*] Facultad de Ingeniería Civil (FIC)
Universidad Michoacana de San Nicolás de Hidalgo (UMSNH)
Francisco J. Mujica S/N, 58030 Morelia, Mexico
cachavez@umich.mx and lequihua@umich.mx, www.umich.mx

[†] Facultad de Físico Matemáticas (FISMAT)
Universidad Michoacana de San Nicolás de Hidalgo (UMSNH)
Francisco J. Mujica S/N, 58030 Morelia, Mexico
dmota@umich.mx, www.umich.mx

Key words: FEM analysis, Rock Masses, Strength Reduction, Joints patterns.

Abstract. In the south of the city of Morelia, Mexico, there is a geological normal fault denominated "La Paloma". It has a height of 180 m and has limited the growth of the city. To improve the connectivity of the city, an urban road is building and it includes the digging of a tunnel that goes through this fault. Due to the presence of an ancient landslide in the exit tunnel, it is imperative to verify the stability of a slope in this zone. The geological structures founded “in situ” make complex the stability analyses, but the used of more realistic representation helps to understand the mechanism of failure. The data collected in geotechnical explorations helped to construct several models for slope stability analysis. Rocks and soils were identified in the interest area. In this way, an elastoplastic Finite Element Analysis (FEA) was carried out to verify the slope stability, considering a strength reduction by a safety factor. Stability was revised in static and seismic conditions. The rock structure is represented by using the Modified Hoek and Brown constitutive model and patterns of the joints with a Mohr-Coulomb constitutive model. The fragments of rock were emulated with joint patterns according to the geologic structure. The slope stability results show a stable slope considering static and pseudo-static FEA analysis. The failure mechanism could be appreciated with the slope stability analysis realized.

1 INTRODUCTION

Behavior of rock mass depends greatly on its origin, discontinuities and of the compressive strength of intact rock. The interaction between discontinuities and the intact rock in the mass, define the stability when the natural equilibrium is disturbed. If a modeling of the rock is closer to the reality, a proper stress-strain analysis can be done and it will be possible to understand the most probable failure mechanism [1].

Elasto-plastic Finite Element Analysis (FEA) is a powerful tool for slope stability analysis for soils and rocks. For rock mass, it is necessary to use joint patterns to have an adequate

representation of real rock configurations. With both components, it is possible to study the slope failure mechanisms and the joint movements that can conduct to the generation of cracks for delimiting the mass of rock that can slide.

In this work, a study of the application of joint or discrete fracture networks to slope stability analysis, in a real case in the zone of an ancient landslide is presented. The zone is located in a populated area into the Morelia city, together with the construction of a tunnel in the zone such it is necessary to verify the stability of the site. With geotechnical information, a stratigraphy with joint patterns is proposed for advanced stability analysis. It was possible to verify the stability and the movement possibilities for the study area.

2 GEOPHISICAL AND GEOTHECNICAL EXPLORATIONS

Indirect methods were the basis for the geotechnical exploration. 15 Vertical Electrical Sounding (VES) with a depth of 250 m in the zone of the tunnel exit portal made by UNAM in 2012 [2] were used to perform the direct exploration. The indirect results show a zone of soil and zone of rock with different qualities. There are low resistivities values in the front of the tunnel and high resistivities in the back of the tunnel, this is an evidence of the location of the "La Paloma Fault" (Figure 1).

Two initial boreholes drilling, with a depth of 40 m, were programmed in the back of tunnel and one Standard Penetration Test (SPT) for soil in the front. The Figure 1 shows the localization of two boreholes. Figure 2 shows the two-borehole logs: the first one (s-1) in the upper part after vegetal layer, there is a stratum of a high plasticity clay mixed with andesite with a mean depth of 10 m, from this depth there is an alternation of andesitic and breccia rock of different thicknesses. The results in the second borehole are the same but with different thicknesses. The rock recovery was between 100 and 25% and the Rock Quality Designation (RQD) between 94 and 0%. It is clear in the stratigraphy that there are zones with rock blocks and zones with broken rock.

A geotechnical profile built with the studies mentioned about and information collected *in situ* is shown in Figure 1. There are four layers: andesite with clay, andesite, breccia and clay. Andesite with clay layer is the product of the weathering of the talus deposit. Andesite has different qualities, in the lowest part of the borehole has RQD of 14.6 and in the upper zone 94%. Breccia has less quality than the andesite and it could be more altered during the drilling. Different RQDs help to select the size of rock blocks for modeling. The transition zone between rock and clay helps to locate "La Paloma Fault". The blue line is at the joint pattern limit of the landslide chosen for the proposed numerical model, which was selected in function of the UNAM studies. In accordance with the stratigraphy and observations in field, there is no clay layer that limits the slip of the rock mass in its natural state.

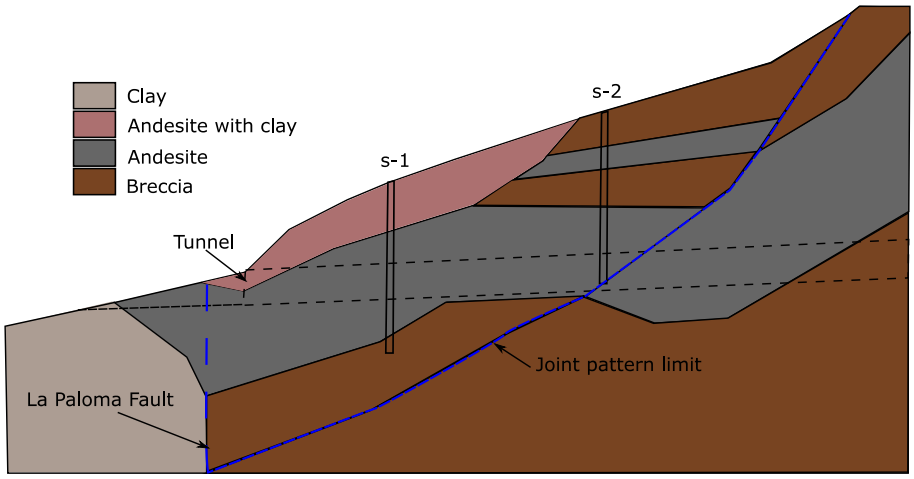

Figure 1: Ancient landslide stratigraphy

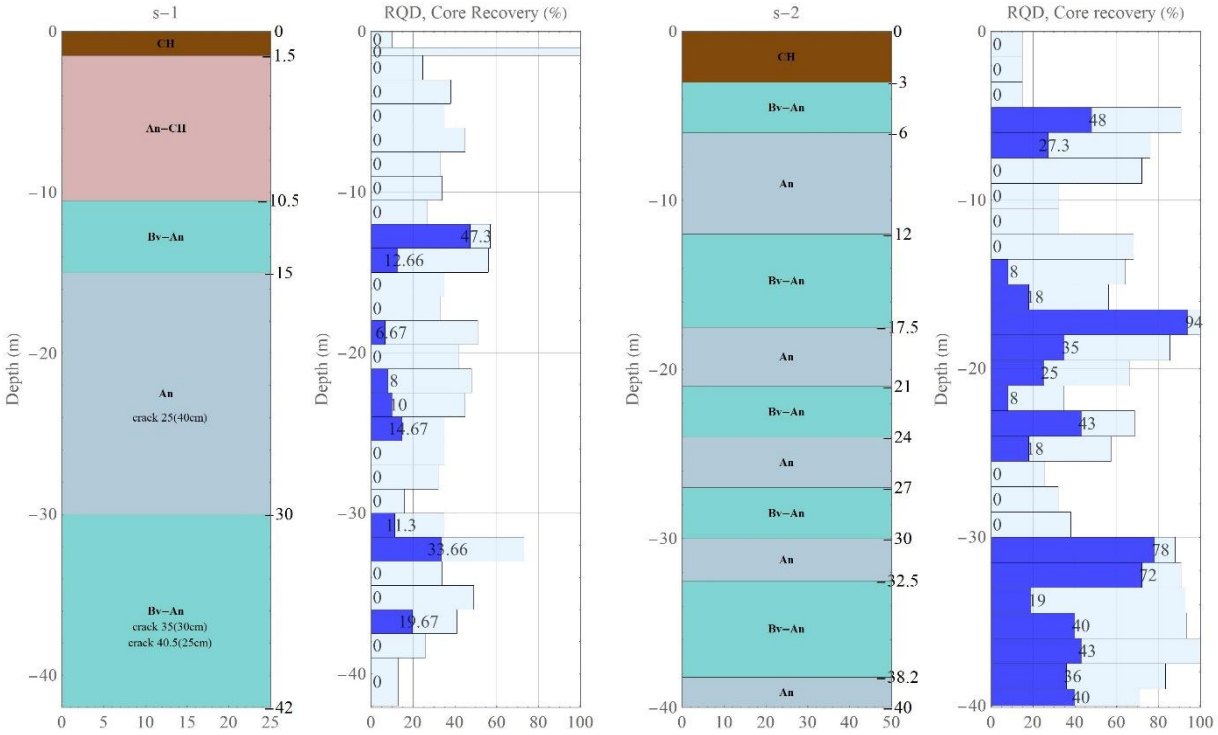

Figure 2: Log of the test boring for boreholes s-1 and s-2.

3 NUMERICAL MODELING

The geometric pattern of discontinuities was defined by the several discontinuities

detected, their orientation, length and the distance between them. Furthermore, physical properties in discontinuities affect the mechanical behavior of the mass as friction, compressive strength, weathering, and filling. In the mass of slipped rock, the fragments are smaller and fragmentation is related to geologic origin of rock.

The rock with discontinuities is modeled with finite elements and joint patterns. The mechanical properties of joints are functions of the physical properties mentioned above. Finite element program RS2 of Rocscience© has the capabilities of performing numerical elastoplastic modeling with joint patterns. Shear Strength Reduction (SSR) technique is applied for performing rock slope stability analysis with Mohr-Coulomb and Hoek y Brown failure criteria.

A volcanic breccia is modeled with a Voronoi joint pattern (Figure 3a). In addition, the andesite has the tendency to be flat and therefore a cross jointed breaking pattern is adopted (Figure 3b). The size of the fragments was approximated according to the core recovery and field observations. The orientation of the rock fragments of andesite is erratic *in situ*, but for the analysis an unfavorable orientation in the movement direction was adopted. Finally, lower left stratum clay was considered continuous. Figure 4 shows the final joint pattern supposed for the slopes stability analysis of the ancient landslide.

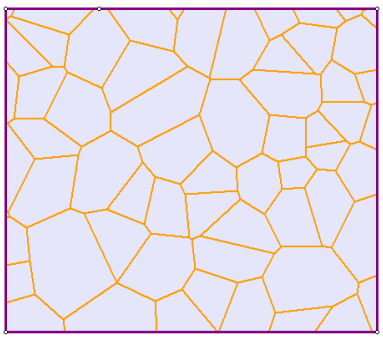

a) Voronoi joint patterns for the breccia

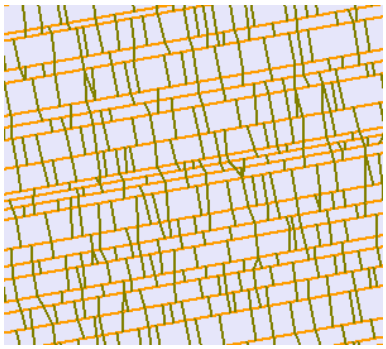

b) Cross jointed pattern for the andesite

Figure 3. Joint patterns employed for the modelling.

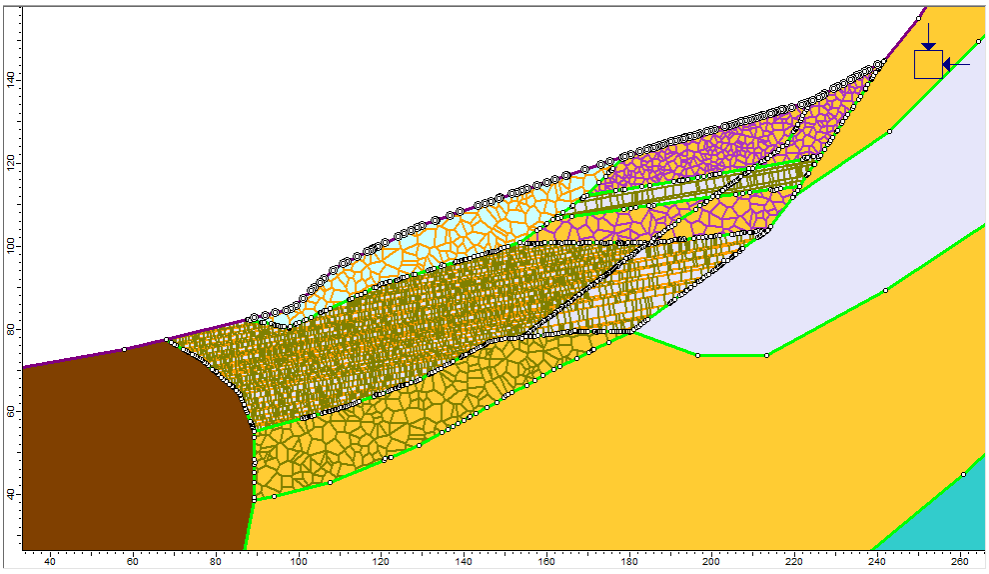

Figure 4. Discretization in RS2® of the domain showing the joint patterns

3.1 Mechanical properties of the rock and soil

Generalized Hoek and Brown Failure criterion [3] for intact rock was used and for the joints Mohr-Coulomb criteria. Hoek and Brown modified a nonlinear failure criterion of brittle intact rock for rock mass. The criterion has factors that reduce mechanical properties of the mass considering the characteristics of the joints in rock mass. Equation (1) defines failure criterion:

$$\sigma_1' = \sigma_3' + \sigma_{ci}\left(m_i \frac{\sigma_3'}{\sigma_{ci}} + s\right)^a \tag{1}$$

Where:

$m_b = m_i\, exp\left(\frac{GSI-100}{28-14D}\right)$, is a reduced value of the intact rock m_i, s and a are constants of the rock mass and are defined by:

$s = m_i\, exp\left(\frac{GSI-100}{9-3D}\right)$ and

$a = \frac{1}{2} + \frac{1}{6}\left(e^{-GSI/15} - e^{-20/3}\right)$

The Geological Strength Index (GSI) relates the geological field observations with the failure envelope, it can be estimated by graph presented by Hoek [3]. D is a parameter related to the degree of disturbance to which rock mass has been subjected to blast damage and stress relaxation. Table 1 present the parameters used for stability analysis of the mass rock.

Table 1. Parameters of the constitutive models of the mass rock.

Material	γ_m (kN/m^3)	σci (MPa)	GSI	mi	E_{RM} (MPa)	Disturbance factor.
Rock with clay	22	67	55	19	26,800	0
Andesite	25	170	75	25	68,000	0
Breccia-Andesite	23	110	70	19	55,000	0

There are two important parameters that control the behavior of intact rock, the compressive strength, and GSI. In the case of the rocks found, andesite is the strongest one and rock with clay the weakest, due to the weathering to which it has been subjected. The GSI parameter represents a geologic structure of the intact rock and surface conditions, andesite has a good surface features, but the rock with clay has a fair surface condition.

Shear strength envelope for clay was estimated with an undisturbed sample obtained just above the rock with clay stratum. A consolidated undrained direct shear test has been carried out. The cohesion was of 29 kPa and the friction angle of 13.6º. Elastic parameters *E*= 15,000 kPa and Poisson ratio of 0.4 are derived also from the laboratory tests.

The crossing discontinuities are the weakest zones of the rock mass and determine its behavior, each material has independent properties. Roughness controls the shear strength of the discontinuities. The Barton and Choubey [4] criterium is used for the estimation of the rock joints strength. Joint Roughness Coefficient (JRC) and other parameters were measured directly from rock core samples of andesite and breccia. RS2® cannot perform the shear strength reduction stability analysis with Barton and Choubey criterium, so Mohr-Coulomb envelope was fitted for the range of normal stresses used. Joint stiffness (normal, *kn*, and shear, *ks*) depends on the infilling material. In the rock with clay case depends on the clay; in the case of the intact rock depends on the andesite and breccia surface roughness and strength. Table 2 shows the properties used for the analysis presented in this work.

Table 2. Parameters of the rock and clay joints

Material	Mohr-Coulomb		kn (kPa/m)	ks
	c (kPa)	ϕ (°)		(kPa/m)
Clay (CU)	29	17	150,000	55,000
Andesite Joint	200	57	5,440,350	2,014,940
Breccia-Andesite Joint	175	53	3,186,990	1,225,770

4 ANALYSIS AND RESULTS

Two cases are considered for the analysis: a static and pseudo-static seismic. The second case due to Morelia city is in a seismic zone, and all the designs are revised under this condition.

SSR technique, in the case or Mohr-Coulomb failure criterion, consists of decreasing the values of c and ϕ original parameters by a safety factor. The result is an increase of the plastic deformations that complicates the numerical convergence. When convergence is not achieved, the safety factor is found [5].

In the case of Modified Hoek and Brown failure criterium, a safety factor divides the equation of the shear failure criterion, to obtain a reduced failure envelope, τ^{red}. Thereafter, a new set of parameters is calculated by modified the reduced envelope to fit the Hoek and Brown criterion. Finally, an elasto-plastic conventional finite element analysis is carried out to check the convergence [6]. The reported safety factor is the minimum value that causes the convergence failure.

Results for the static case are presented in Figure 5, the critical strength reduction factor or safety factor is 2.29. The figure shows the total displacements in meters against Shear Strength Reduction. For the critical safety factor, the largest displacements are in red and the minor ones in blue. It can be deduced that the mechanism of failure is a block with a displacement produced by the low strength of left lower clay. Midzone of the slope moves to the left and a crack is formed at the middle of the slope. The upper part of the movement is reduced but it generates cracks.

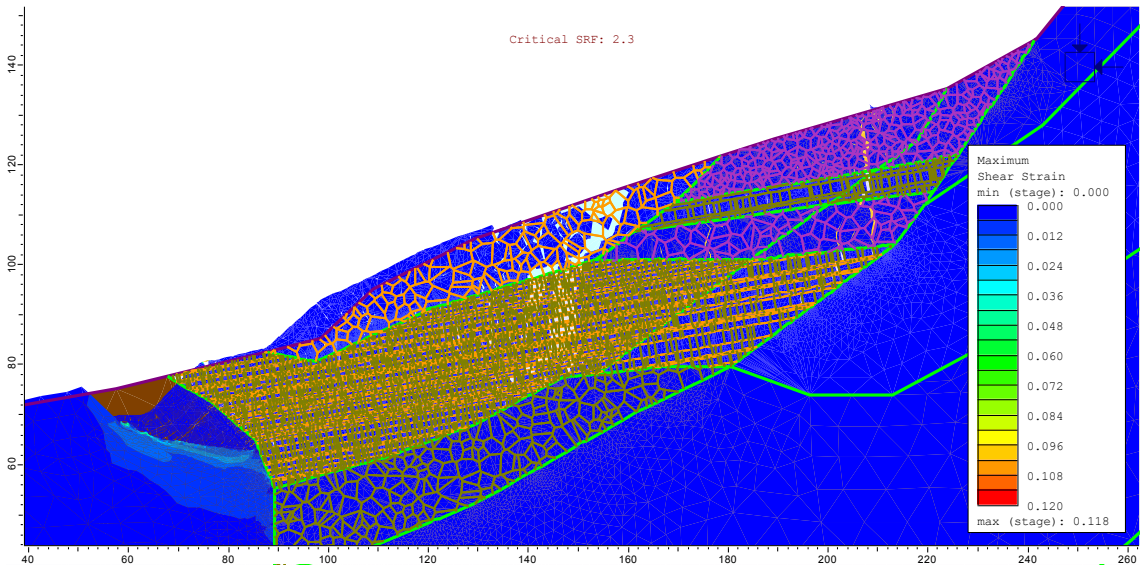

Figure 5. Displacement kinematics for the critical safety factor of the static analysis.

Figure 6 shows the strength reduction factor against the maximum displacement. Red triangles are values that failed to converge, and green ones do converge. Furthermore, the figure shows a very significant change of slope where the displacements are incremented

rapidly. In the zone of the change the critical safety factor can be found. Therefore, this increase of the displacements gives rise to the failure mechanism under the modelized conditions.

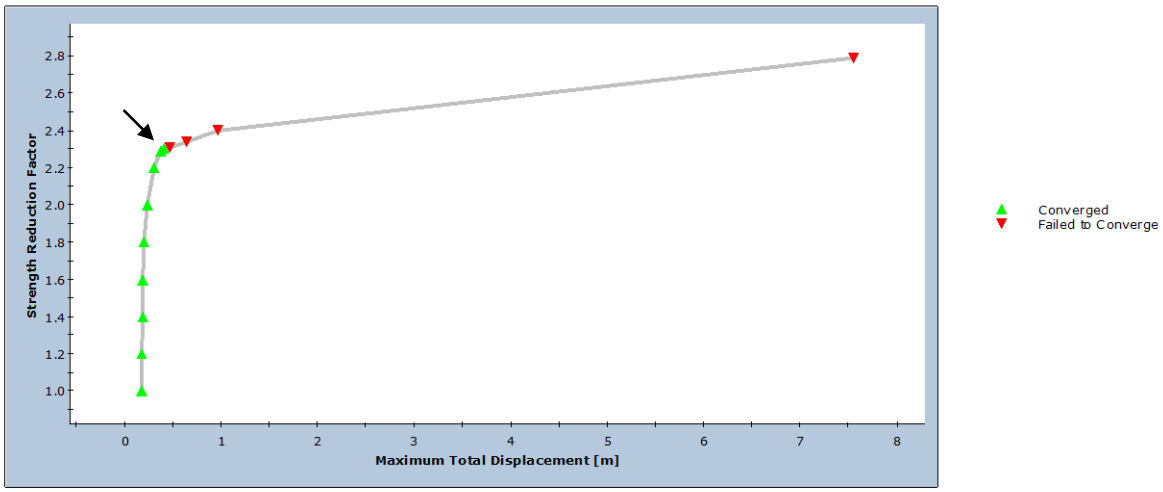

Figure 6. Shear strength reduction versus displacement.

Morelia is located on the central portion of the Mexican volcanic belt. The interaction between the tectonic plates of Rivera, Cocos and North America generates a great number of earthquakes in the region. The displacement between the Cocos and North America plates produces superficial earthquakes, between 15 and 20 km of depth, as in the earthquake of 1985 with magnitude of 8.1 in the coasts of Michoacán, Mexico. An interaction between Cocos and Rivera plates produces earthquakes within the continent, which are less frequent. Cruz in 2015 [7] made a deterministic study to get the seismic coefficient for the design of works of the urban road in the south of Morelia. From the study, it was concluded that the seismic coefficient for pseudo-static slope stability analysis is of 0.145.

For the same previous analysis, a horizontal force proportional was added to the mass and the SSR slope analysis was performed, the results are shown in Figure 7. As consequence, the factor of safety was reduced to 1.24 but it still greater than 1.0. Maximum deformation is incremented from 0.12 to 0.4 meters, so the cracks are more open especially in the middle zone. In general, the mechanism of failure is the same already presented. Increased deformation causes the safety factor to decrease, this is reflected on non-convergence of the calculus. Figure 8 shows a graph of the shear strength reduction *against* maximum displacement. As in the previous analysis, there is a change of slope in the critical strength reduction factor.

A concern of the inhabitants of the zone is the magnitude of the landslide that could be presented. The factor of safety is greater than one so there is not risk of failure. It could exist a risk if the lower clay is removed without an adequate reinforcement. In that case mass of rock could move downward and generate a cracking in the upper zone. It means that rock blocks can stand on their own with certain angles. A physical corroboration of this state was located aside the study zone, were a cut of 20 m height and 70 with degrees was excavated for a

construction of a house and is in stable conditions.

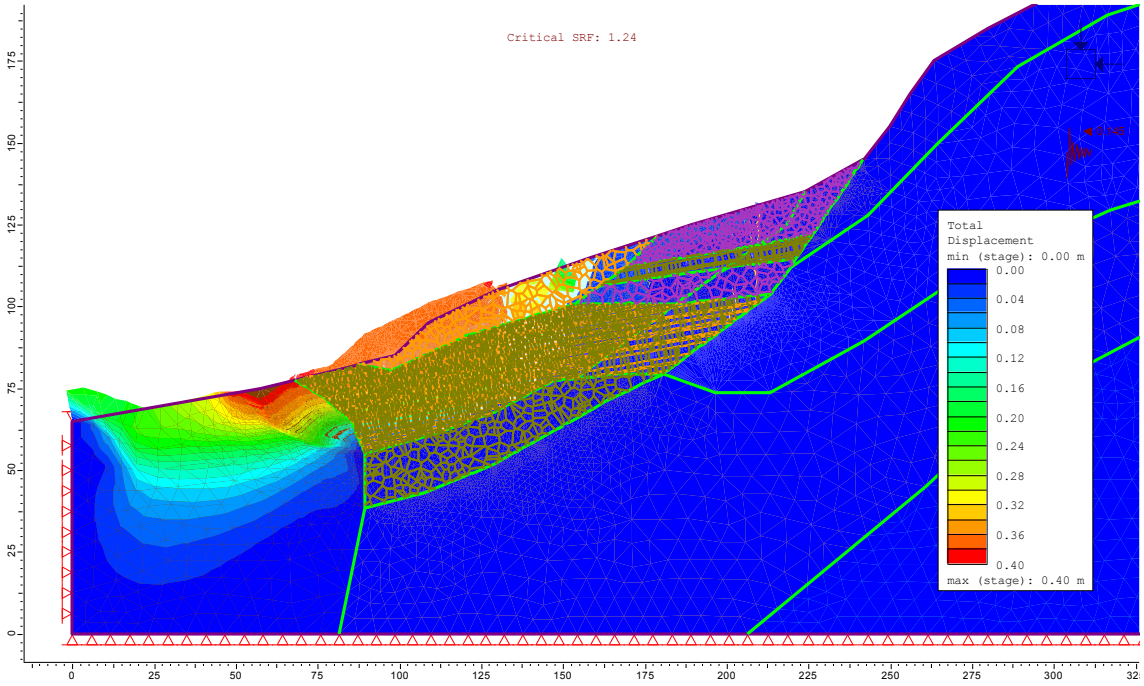

Figure 7. Kinematics displacement of the Pseudo-static analysis obtained from the SSR stability analysis.

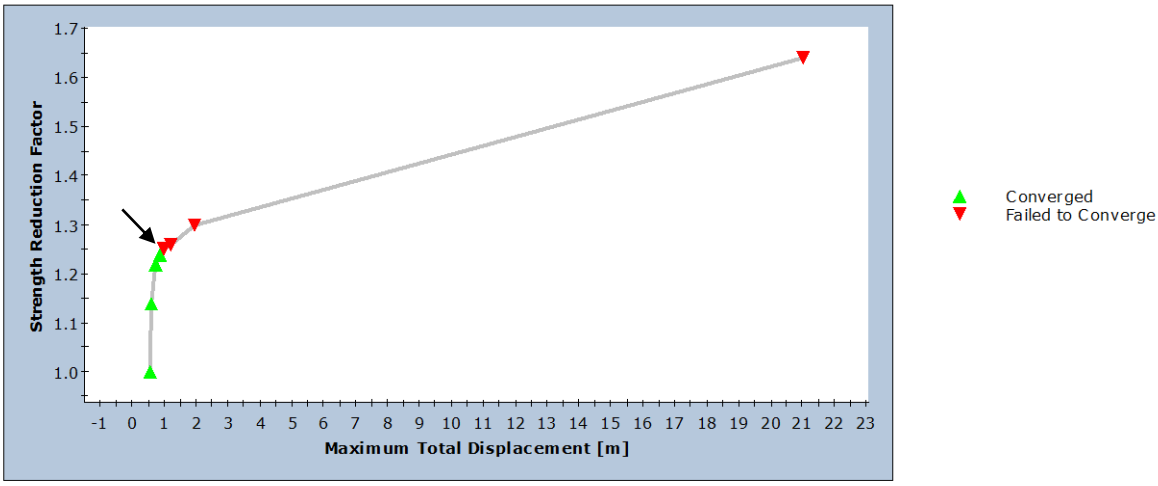

Figure 8. Shear strength reduction versus displacement for pseudo-static analysis.

5 CONCLUSIONS

The use of the finite elements with networks of joints helps to perform a stability analysis of slopes in rock masses more accurately. It is necessary to have field information of the fracturing patterns of the rock, for making a suitable approximation by constructing a dominium with joint networks. With this, it is possible to capture and understand the failure mechanism of rock mass in slope stability analysis in a realistic way. The strength reduction technique within a framework of elasto-plasticity allows to magnify the deformations and failure mechanism emerges in a natural way.

In the case of stability analysis of "La Paloma", antique landslide, it was possible to verify the stability conditions. Factors of safety of 2.3 and 1.24 were derived from static and seismic stability analysis. Two joint patterns were adopted to represent the rock block as observed in the field. Giving to the options available in the RS2®, the Voronoi pattern was selected for breccia and cross jointed for the andesite. This representation is simplified and shows the most unfavorable conditions for stability of the mass rock. For a more accurately representation, more information is needed and can be directly obtained from the tunnel excavation.

More research is required in the use of joint patterns for the analysis of slopes stability. The success depends on adequate pattern representation, geological conditions are complex in this case. Another issue is the constitutive models used for the content between rock, in this work it is used Mohr-Coulomb criterion, but there are some others like Barton and Choubey [4] that can be incorporated in the stress reduction analysis.

REFERENCES

[1] Elmo, Davide, and Doug Stead. "An integrated numerical modelling–discrete fracture network approach applied to the characterization of rock mass strength of naturally fractured pillars." Rock Mechanics and Rock Engineering 43.1 (2010): 3-19.

[2] Universidad Nacional Autónoma de México. Estudio Geológico-Geotécnico del ramal camelinas del Libramiento Sur de Morelia. México, DF., (2012).

[3] Hoek, E., Carranza-Torres, C.T., and Corkum, B. (2002), Hoek-Brown failure criterion – 2002 edition. Proc. North American Rock Mechanics Society meeting in Toronto in July 2002.

[4] Barton, N., and Choubey, V. The shear strength of rock joints in theory and practice. Rock Mechanics and Rock Engineering 10.1 (1977): 1-54.

[5] Abramson, Lee W. Slope stability and stabilization methods. John Wiley & Sons, (2002).

[6] Hammah, R. E., Yacoub, T. E., Corkum, B. C., & Curran, J. H. The shear strength reduction method for the generalized Hoek-Brown criterion. In Alaska Rocks 2005, The 40th US Symposium on Rock Mechanics (USRMS). American Rock Mechanics Association. (2005).

[7] Chávez, C., Arreygue, J. E., Cruz J. I. and Alarcon J. Informe Final de los Estudios Geotécnicos Complementarios al Proyecto Geotécnico del Ramal Camelinas del Libramiento Sur de Morelia. SCT, Mexico, (2015).

XIV International Conference on Computational Plasticity. Fundamentals and Applications
COMPLAS 2017
E. Oñate, D.R.J. Owen, D. Peric and M. Chiumenti (Eds)

CHARACTERIZATION OF EVOLVING PLASTIC ANISOTROPY AND ASYMMETRY OF A RARE-EARTH MAGNESIUM ALLOY SHEET BY MEANS OF A NON-ASSOCIATED FLOW RULE

A. ABEDINI*, C.BUTCHER AND M.J. WORSWICK

* Department of Mechanical and Mechatronics Engineering
University of Waterloo
Waterloo, Ontario, Canada
e-mails: aabedini@uwaterloo.ca, cbutcher@uwaterloo.ca, worswick@lagavulin.uwaterloo.ca
www.formingandimpact.uwaterloo.ca

Key words: Anisotropic Plasticity, Non-associated Flow Rule, Magnesium Alloy

Abstract. The superior ductility of rare-earth magnesium alloys over conventional magnesium sheets makes them promising candidates for light-weight structural alloys. However, these alloys possess severe evolving anisotropy and tension-compression asymmetry as a result of activation of different deformation mechanisms (slip or twinning) that is extremely challenging to model numerically. In this study, the constitutive plastic behaviour of a rare-earth magnesium alloy sheet, ZEK100 (O-temper), was considered at room temperature, under quasi-static conditions. A CPB06 yield criterion for hcp materials was employed along with a non-associated flow rule where the yield function and plastic potential were calibrated at different plastic deformation levels to account for evolving anisotropy in proportional loading. The constitutive model was implemented as a user material subroutine (UMAT) into the commercial finite element package, LS-DYNA, along with an interpolation technique to consider the evolving anisotropy of the material. Finally, predictions of the model were compared with the experimental results in terms of flow stresses and plastic flow directions under various proportional loading conditions and along different test directions. It was shown that the predictions of the model were in good agreement with experimental data.

1 INTRODUCTION

Most commercial alloys used in sheet metal forming and vehicle crashworthiness applications exhibit some degree of orientation-dependent plastic response, and depending on the severity of plastic anisotropy, isotropic yield functions might not be suitable candidates for modelling the behaviour of the materials. To overcome this issue, a large number of anisotropic yield functions have been proposed in the literature with the largest contributions from the Barlat family of yield criteria [1,2] in which linear transformations are applied on the stress tensor to account for anisotropy. However, these models were intended for bcc and fcc cubic materials with slip-dominated deformation mechanisms while magnesium alloys have

an hcp crystal structure. In hcp materials, plastic deformations occur by slip and twinning mechanisms and due to the direction sensitivity of twining mechanisms, strong tension-compression asymmetry is observed in yield loci [3]. In order to account for anisotropy and strength differential effects, Cazacu *et al*. [4] proposed a new yield function (known as the CPB06 yield criterion) based on the linear transformation approach. Later, Plunkett *et al*. [5] showed that the predictions of the CPB06 yield function can be improved if more than one linear transformation is applied on the stress tensor.

Due to texture evolutions during plastic deformation, the shape of the yield surface of magnesium alloys does not remain constant, thus, isotropic hardening models cannot capture the material behaviour accurately. To consider evolving anisotropy, Plunkett *et al*. [5] proposed a piece-wise linear interpolation of the CPB06 yield functions calibrated at different levels of plastic deformation. A similar approach was also adopted by Ghaffari Tari *et al*. [6] for AZ31B magnesium. These models were based on assumption of the associated flow rule (AFR) in which the yield function is also the plastic potential for calculating the plastic strain increments (normality rule). The classical work of Bishop and Hill [7] demonstrated that the AFR holds for metals based on a crystal plasticity model. However, in the last decades, the assumption of the AFR has been challenged by the non-associated flow rule (non-AFR) in which the plastic potential is independent from the yield function [8,9]. Considering materials with severe anisotropy such as magnesium alloys, the non-AFR provides more degrees of flexibility for calibrating yield stresses and r-values. Furthermore, models with the non-AFR enable the possibility that plastic potential and yield functions evolve independently, a feature that is not possible in models based on the AFR. These characteristics make the non-AFR attractive for materials such as ZEK100 with strong evolving anisotropic behaviour.

The objectives of the present work are to investigate and model the anisotropic plastic response of a rare-earth magnesium alloy sheet (ZEK100-O) under quasi-static conditions. To this end, the non-AFR is employed by calibrating yield function and plastic potential at different plastic deformation levels using the CPB06 formulation with two linear stress transformations. The model was implemented into the commercial finite element package, LS-DYNA, along with an interpolation technique to consider the evolving anisotropy of the material. The finite element model comprises a single 3-D element that is subjected to various stress states in different test orientations with respect to the rolling direction. The outcomes of each single-element simulations in terms of flow stresses and r-values are compared to the experimental results of Abedini *et al*. [3] to assess the predictive capabilities of the model.

2 MATERIAL AND EXPERIMENTAL RESULTS

A rare-earth magnesium alloy ZEK100-O rolled sheet with a nominal thickness of 1.55 mm was used in the present study. An extensive experimental investigation into the anisotropy of this same lot of material was performed by Abedini *et al*. [3] and this test data will be utilized in the present paper to develop the constitutive model. Experimental tests in [3] were performed at room temperature, under a quasi-static strain rate of 0.001 s^{-1}. Constitutive plastic behaviour of the material is shown in Figure 1 in terms of stress response and r-values, and it can be seen that the material exhibits significant anisotropy that evolves with deformation. Furthermore, it is apparent from Figure 1(a-c) that ZEK100-O exhibits a

tension-compression asymmetric response which is due to the twinning mechanisms that are more dominant under compression mode [10]. Moreover, the behaviour of the material under shear state (Figure 1e) shows anisotropic trends. It is recently shown in [3,11] that in addition to the asymmetric response in the first and third quadrants of yield loci (tensile and compressive regions), twinning mechanisms activated under shear deformation leads to an additional asymmetry in the second and fourth quadrants for magnesium alloys. The experimental results shown in Figure 1 show the challenging nature of ZEK100-O in terms of modelling and characterization and highlight the need for accurate constitutive plasticity models that are able to capture the evolving anisotropy of the material.

3 PLASTICITY MODEL

In order to consider the anisotropic and asymmetric response of ZEK100-O, the CPB06 phenomenological yield criterion proposed by Cazacu *et al*. [4] was adopted in the present study. In analogy to Plunkett *et al*. [5], two stress transformations were performed to increase the flexibility of the model (denoted as CPB06ex2). The yield function, Φ, is defined as:

$$\Phi = (|\Sigma_1| - k\Sigma_1)^a + (|\Sigma_2| - k\Sigma_2)^a + (|\Sigma_3| - k\Sigma_3)^a + (|\Sigma'_1| - k'\Sigma'_1)^a + (|\Sigma'_2| - k'\Sigma'_2)^a + (|\Sigma'_3| - k'\Sigma'_3)^a \quad (1)$$

where k and k' are material parameters that account for strength differential effects, and a is the exponent of the yield function. Also $\Sigma_{1\text{-}3}$ and $\Sigma'_{1\text{-}3}$ are the principal values of the transformed stress deviators Σ_{ij} and Σ'_{ij} written as:

$$\Sigma_{ij} = C_{ijkl} : S_{kl} \quad \text{and} \quad \Sigma'_{ij} = C'_{ijkl} : S_{kl} \quad (2,3)$$

where S_{kl} and C_{ijkl} are the deviatoric stress tensor and the fourth-order transformation tensor, respectively. The non-associated flow rule was employed in the present study with the same functional form as Eq. (1) to define the plastic potential, Ψ, to which the plastic strain components are normal and their magnitudes are governed by:

$$d\varepsilon_{ij}^p = d\lambda \frac{\partial \Psi}{\partial \sigma_{kl}} \quad (4)$$

where $d\varepsilon_{ij}^p$ is the incremental plastic strain tensor, and $d\lambda$ is the plastic multiplier. The values of coefficients of the transformation tensors and strength differential parameters can be determined from an optimization approach to minimize the errors between the experimental data and the values predicted by the yield function and plastic potential. In the present study, the genetic algorithm (GA) which is a global optimizer available in Matlab® was used to calculate these parameters.

As shown in Figure 1, ZEK100-O exhibits an evolving anisotropic behaviour and therefore, the yield function and plastic potential should be calibrated at different plastic work levels, w_p. To capture the evolution, a piece-wise linear interpolation technique can be used:

$$\Phi = \xi(w^p)\ \Phi_1 + [1-\xi(w^p)]\ \Phi_2 \quad \text{and} \quad \Psi = \xi(w^p)\ \Psi_1 + [1-\xi(w^p)]\ \Psi_2 \tag{5,6}$$

in which Φ_1 (Ψ_1) and Φ_2 (Ψ_2) are the yield function (plastic potential) at the deformation levels associated with the plastic works of w_n^p and w_{n+1}^p, respectively, and $\xi(w_p)$ is calculated by:

$$\xi(w^p) = (w_{n+1}^p - w^p)/(w_{n+1}^p - w_n^p) \tag{7}$$

In terms of the hardening behaviour of the material, a Hockett-Sherby function (Eq. 8) was calibrated to the uniaxial tensile data in the RD (reference direction) up to maximum strain limited by the onset of necking:

$$\bar{\sigma} = 205.59 + 126.60\ [1 - \exp(-1.91(\varepsilon^p)^{0.46})] \tag{8}$$

where $\bar{\sigma}$ is the flow stress and ε^p is the equivalent plastic strain.

The constitutive model described above was implemented as a user material subroutine (UMAT) into the explicit commercial finite element software package, LS-DYNA, using a standard return-mapping algorithm (convex cutting algorithm in Ortiz and Simo [11]). The reader is referred to [8] for the proof of the uniqueness of the stress and strain states as well as the proof of the stability in the non-AFR.

4 RESULTS AND DISCUSSION

To capture the evolving anisotropy of ZEK100-O, nine different plastic work levels for a plastic work range of 2.24 MPa to 22.46 MPa (associated with 1% to 9% equivalent plastic strains in uniaxial tension along the RD) were selected and their corresponding experimental data were used to calibrate yield functions and plastic potentials. Due to brevity, only three levels of plastic deformations (plastic work levels of 2.24 MPa, 14.61 MPa, and 22.46 MPa with anisotropy coefficients presented in Tables 1 and 2) were chosen and their associated yield functions and plastic potentials are shown in Figure 2. It can be seen from Figure 2 that the CPB06ex2 yield function and plastic potential fit the measured data with good accuracy. For the smallest plastic work level of 2.24 MPa which is close to the initial yielding of the material, it can be seen from Figure 2(a) that the material has a clear tension-compression asymmetry with the tension region having larger yield stresses than the compression region. The tension-compression asymmetry of yield loci reduces with deformation due to the high hardening rate in compression offsetting its initially lower yield strength with respect to tension as shown in Figure 2(b) for the plastic work level of 14.61 MPa. At a plastic work level of 22.46 MPa (Figure 2c) the yield stresses in compression have grown larger than in tension which is opposite to that observed for the material at the onset of yielding.

In order to further evaluate the accuracy of the model, a single 3-D brick element under different loading conditions was used to simulate the stress-strain curves and evolution of r-values of the material. Figure 1 compares the predictions of the model with experimental results where it can be seen that the model with the non-AFR is capable of capturing the experimental trends with good accuracy. It should be noted that the FE stress data may exhibit

piece-wide discontinuities due to the inherent nature of the piece-wise linear interpolation approach. This issue may be resolved by better numerical fits (*i.e.* yield functions and plastic potentials with higher flexibility) and increasing the number of calibration levels. Further validations of the model by full-scale FE simulations of structural experiments will be considered in future work.

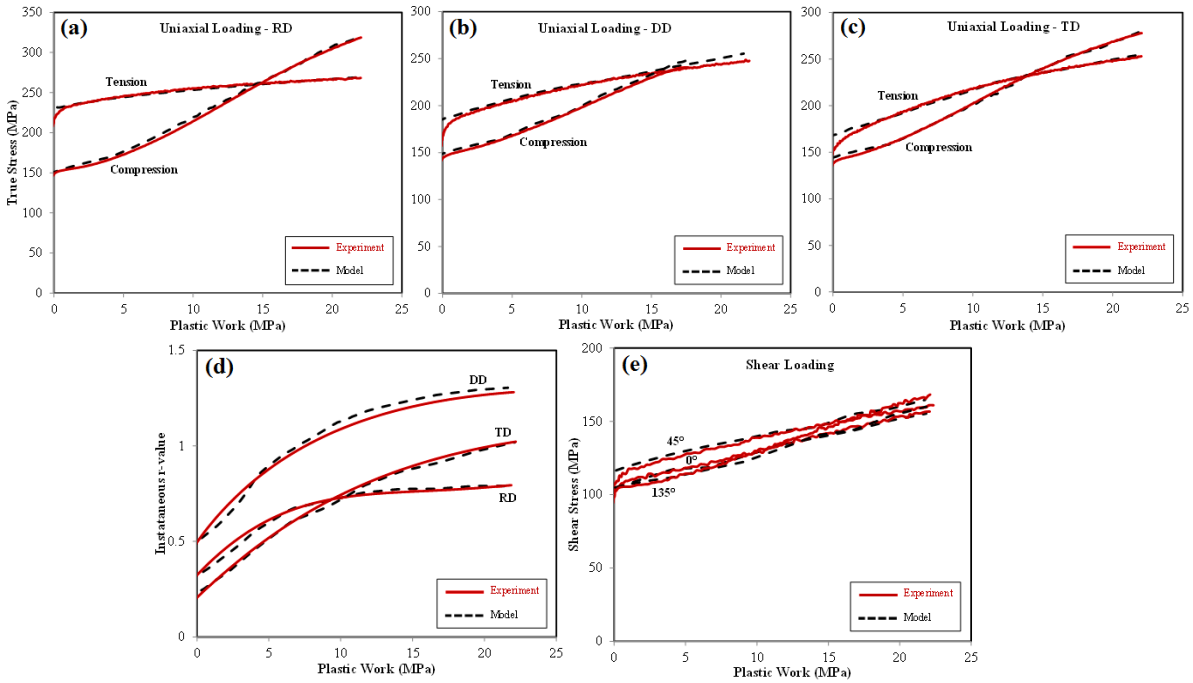

Figure 1: Constitutive plastic behaviour of ZEK100-O in quasi-static conditions. (a-c) show the uniaxial tensile response of the material (d) shows the r-value evolutions, and (e) shows the shear response. All the figures are plotted with respect to the plastic work.

Table 1: Coefficients of the CPB06ex2 yield function.

w_p (MPa)	C_{11}	C_{12}	C_{13}	C_{22}	C_{23}	C_{33}	C_{66}	k	C'_{11}	C'_{12}	C'_{13}	C'_{22}	C'_{23}	C'_{33}	C'_{66}	k'	a
2.24	1.00	1.16	-1.34	-0.73	1.25	-1.34	-2.43	-0.03	1.00	2.67	-0.64	0.66	-0.34	-1.78	1.79	0.21	8.0
14.61	1.00	0.91	-2.06	3.70	-1.05	-2.93	2.80	-0.01	1.00	-2.20	-1.70	-0.11	2.32	-0.04	3.61	-0.02	8.0
22.46	1.00	1.92	1.92	3.11	0.67	-0.41	1.61	-0.13	1.00	-1.20	0.51	-0.20	1.01	-0.76	1.97	0.01	8.0

Table 2: Coefficients of the CPB06ex2 plastic potential.

w_p (MPa)	C_{11}	C_{12}	C_{13}	C_{22}	C_{23}	C_{33}	C_{66}	k	C'_{11}	C'_{12}	C'_{13}	C'_{22}	C'_{23}	C'_{33}	C'_{66}	k'	a
2.24	1.00	-1.02	-0.70	--1.14	-1.02	1.68	2.36	0.0	1.00	-0.97	2.05	0.85	1.89	2.06	2.35	0.0	8.0
14.61	1.00	1.53	1.35	0.72	0.27	1.32	0.32	0.0	1.00	2.49	0.93	1.02	0.92	2.48	1.82	0.0	8.0
22.46	1.00	-0.33	1.57	-1.57	0.76	-0.50	3.01	0.0	1.00	-0.47	-1.87	-1.80	0.97	-0.53	3.05	0.0	8.0

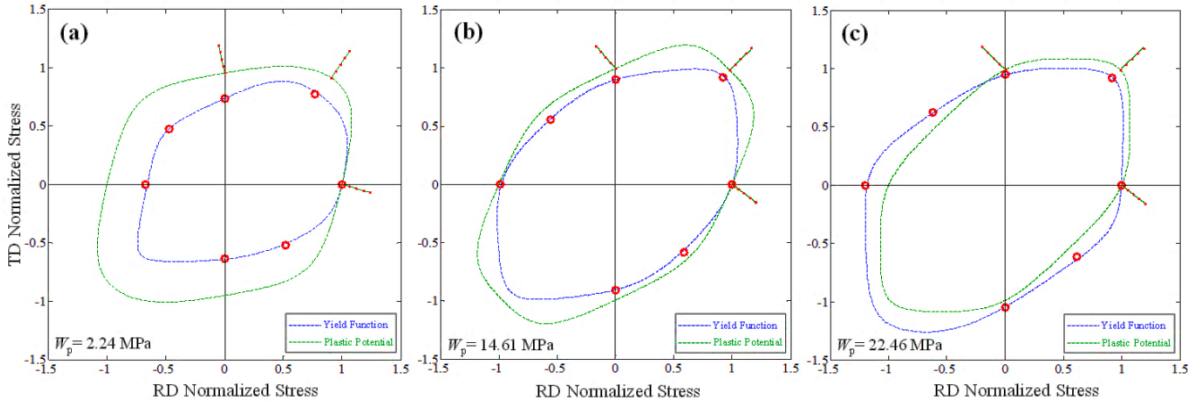

Figure 2: Yield function and plastic potential of ZEK100-O depicted at three different plastic work levels of (a) 2.24 MPa, (b) 14.61 MPa, and (c) 22.46 MPa. Red symbols show the experimental data. The lines normal to plastic potentials show the direction of plastic flow.

5 CONCLUSIONS

The room temperature constitutive plastic behaviour of a rare-earth magnesium alloy sheet, ZEK100-O, was studied under different stress states. It was demonstrated that the material exhibits severe plastic anisotropy that evolves with deformation. It was shown that adopting the non-AFR along with an evolving CPB06 formulation with two linear stress transformations resulted in good agreements between FE predictions and experimental data. The strategy adopted to consider evolution was piece-wise linear interpolations between yield functions and plastic potentials that were calibrated at different plastic work levels.

REFERENCES

[1] F. Barlat, J.C. Brem, J.W. Yoon, K. Chung, R.E. Dick, D.J. Lege, F. Pourboghrat, S.H. Choi, E. Chu, Plane stress yield function for aluminum alloy sheets – part I: theory. *International Journal of Plasticity* (2003) **21**:1009-1039.

[2] F. Barlat, H. Aretz, J.W. Yoon, M.E. Karabin, J.C. Brem, R.E. Dick, Linear transformation-based anisotropic yield functions. *International Journal of Plasticity* (2005) **21**:1009-1039.

[3] A. Abedini, C. Butcher, M.J. Nemcko, S. Kurukuri, M.J. Worswick, Constitutive characterization of a rare-earth magnesium alloy sheet (ZEK100-O) in shear loading: studies of anisotropy and rate sensitivity. *International Journal of Mechanical Sciences* (2017a) **DOI**: 10.1016/j.ijmecsci.2017.04.013.

[4] O. Cazacu, B. Plunkett, F. Barlat, Orthotropic yield criterion for hexagonal closed packed metals. *International Journal of Plasticity* (2006) **21**:1171-1194.

[5] B. Plunkett, O. Cazacu, F. Barlat, Orthotropic yield criteria for description of the anisotropy in tension and compression of sheet metals. *International Journal of Plasticity* (2008) **24**:847-866.

[6] D. Ghaffari Tari, M.J. Worswick, U. Ali, M.A. Gharghouri, Mechanical response of

AZ31B magnesium alloy: Experimental characterization and material modeling considering proportional loading at room temperature. *International Journal of Plasticity* (2014) **55**:247-267.

[7] J.F.W. Bishop, R. Hill, A theory of the plastic distortion of a polycrystalline aggregate under combined stresses. *Philosophical Magazine* (1951) **42**:414-427.

[8] T. B. Stoughton, A non-associated flow rule for sheet metal forming*, International Journal of Plasticity*, 2002, **18**:687-714.

[9] V. Cvitanic, F. Vlak, Z. Lozina, A finite element formulation based on non-associated plasticity for sheet metal forming. *International Journal of Plasticity* (2008) 24:646-687.

[10] S. Kurukuri, M.J. Worswick, A. Bardelcik, R.K. Mishra, J.T. Carter, Constitutive behavior of commercial grade ZEK100 magnesium alloy sheet over a wide range of strain rates. *Metallurgical and Materials Transactions A* (2014) **45**:3321-3337.

[11] A. Abedini, C. Butcher, M.J. Worswick, Fracture characterization of rolled sheet alloys in shear loading: Studies of specimen geometries, anisotropy, and rate sensitivity. *Experimental Mechanics* (2017b) **57**:75-88.

[12] M. Ortiz, J.C. Simo, An analysis of a new class of integration algorithms for elastoplastic constitutive relations, *International Journal for Numerical Methods in Engineering*, 1986, **23**:353-366.

XIV International Conference on Computational Plasticity. Fundamentals and Applications
COMPLAS 2017
E. Oñate, D.R.J. Owen, D. Peric and M. Chiumenti(Eds)

EXPERIMENTAL ANALYSIS AND NUMERICAL SIMULATION OF SINTERED MICRO-FLUIDIC DEVICES

M. SAHLI[*,†], J-C. GELIN[*] AND T. BARRIERE[*]

[*] FEMTO-ST Institute/Applied Mechanics Department, 24 chemin de l'épitaphe, 25000 Besançon, France
e-mail: tbarriere@femto-st.fr, jean-claude.gelin@univ-fcomte.fr

[†] Mechanics Laboratory, Faculty of Engineering Sciences, University Mentouri, 25000 Constantine, Algeria
email: sahlisofiane2@yahoo.fr

Key words: hot embossing, Sintering, Numerical simulation, Constitutive equations, 316L stainless steel powders.

Abstract. This paper investigates the use of numerical simulations to describe solid state diffusion of a sintering stage during a Powder Hot Embossing (PHE) process for micro-fluidic components. Finite element analysis based on a thermo-elasto-viscoplastic model was established to describe the densification process of a PHE stainless steel porous component during sintering. The corresponding parameters such as the bulk viscosity, shearing viscosity and sintering stress are identified from dilatometer experimental data. The numerical analyses, which were performed on a 3D micro-structured component, allowed comparison between the numerical predictions and experimental results of during a sintering stage. This comparison demonstrates that the FE simulation results are in better agreement with the experimental results at high temperatures.

1 INTRODUCTION

The metal hot embossing (MHE) process has become a viable, low cost process for producing parts with complex shapes in short series. MHE combines the shaping efficiency of polymer hot embossing with the capability of powder metallurgy [1-3], which offers many unique advantages in the production of near neat shape micro-structured components. This process is an actually a multi-step process divided into compounding, hot embossing, debinding and sintering components [4-6]. The goal of mixing steps is to form the feedstock for hot embossing by mixing the metallic powders with thermoplastic binders. The binders used in hot embossing are commonly used polymer mixtures, such as polypropylene, a synthetic or natural wax and stearic acid. The resulting mixture is called a feedstock, which is then embossed in a mould to achieve the required shapes. Afterwards, the binder is removed during thermal debinding, and the powder is sintered, yielding the full density necessary to

give the required mechanical properties and geometric size; at the same time, a certain amount of shrinkage occurs (see Fig. 1).

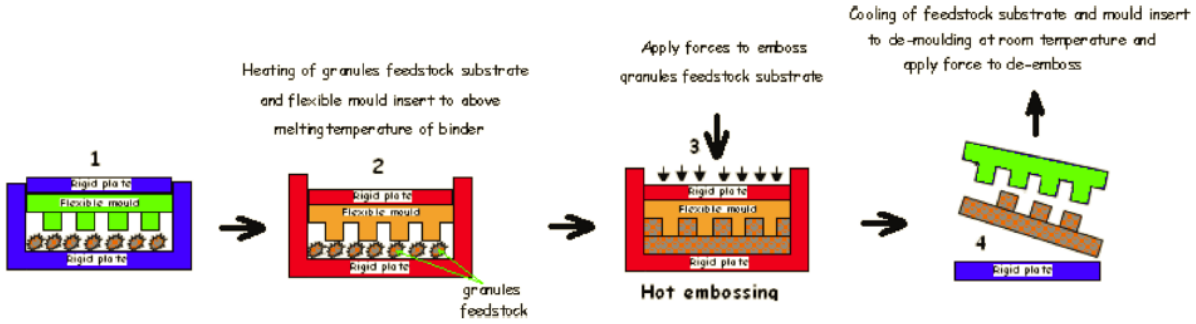

Figure 1: Illustration of the hot embossing process to create micro-devices.

In the MHE process, the metallic components undergo contraction and deformation, leading to challenges in terms of determining the initial structure design of the die mould cavities, the initial size and the processing parameters. Traditionally, in this stage, trials and error methods or empirical formulas have always been applied to control the part shape and dimensional accuracy; however, this has resulted in a high experimental cost and limited control precision. For these reasons,, performing a finite element simulation can be an effective alternative to predict part deformation and estimate anisotropic shrinkages in micro-structured components arising from the MHE process. The first sintering model was developed at the grain scale with only one diffusion mechanism [7]. Then, models improved by coupling several mechanisms and by modifying the geometry of the systems. In addition, the problem can also be solved analytically for simple geometries with a thermo-elastic model [8]. Then, finite element analysis (FEA) is can be used as an effective tool when considering samples with complex geometries and complex boundary conditions [9], or to account for other phenomena such as gravitational effects or a thermal gradient, which induce constrained sintering [10]. The objective of the present work is to predict of anisotropic shrinkages and estimated the dimensional changes of micro-structured components during the sintering step with the FE method. The goal of these simulations is to also provide information regarding the evolution of density variations. In this paper, the material and process sintering parameters are identified from dilatometer experimental datas. The model and the identified material parameters are implemented in a finite element solver to perform the numerical simulation of the sintering step associated to with MHE. Sintering experiments were performed in a batch furnace to verify the numerical model and simulations on 316L stainless steel.

2 CONSTITUTIVE EQUATIONS FOR THE SINTERING PROCESS

Compared with conventional trial and error methods, numerical simulations of sintering using finite element methods can be more effective by minimizing the effects of tooling and processing parameters [11]. The proposed model is based on the assumption that a porous material follows a linear-viscous behavior and behaves according to the continuum theory of sintering [12]. This model is a phenomenological model based on continuum mechanics and uses thermo-elasto-visco-plastic formulations, which are related by the following eq. [13]:

$$\dot{\varepsilon} = \dot{\varepsilon}_e + \dot{\varepsilon}_{th} + \dot{\varepsilon}_{vp} \Rightarrow \dot{\varepsilon} = C_e \dot{\sigma} + \alpha \Delta \dot{T} I + \frac{dev\sigma}{2G_p} + \frac{\sigma_m - \sigma_s}{3K_p} I \quad (1)$$

where εe, εth and εvp are the elastic, thermal and viscoplastic strains rates, respectively, Ce is the elastic compliance matrix, ΔT is the incremental temperature rate, I is the second order identify tensor, α is the thermal expansion coefficient was determined experimentally using a dilatometer, σm = tr(σ)/3 is the trace of the stress tensor, G and K are the shear and bulk viscosity moduli, respectively, and σs is the sintering stress. The variables G, K and σs are material parameters that still need to be determined. The elastic-viscous analogy is used to define the shear and bulk viscosity moduli for sintering materials [14]:

$$G_p = \frac{\eta_p}{2(1+\nu_p)}; \; K_p = \frac{\eta_p}{3(1-2\nu_p)} \quad (2)$$

where ηp and νp are the uniaxial viscosity and viscous Poisson's ratio of a porous material, respectively. Song et al. (2006) derived the following relationship to define the uniaxial viscosity ηp through bending tests in a dilatometer [15]:

$$\eta_p = \frac{1}{\dot{\delta}}\left(\frac{5\rho_0 g L_s^4}{32h^2} + \frac{PL_s^3}{4bh^3}\right) \quad (3)$$

where δ is the deflection rate at the centre of the specimen, ρa is the apparent density, g is gravity, P is the external load, and L_s, b and h are the distance between the two supporting rods and the width and thickness of the specimen [16]. Bordia [16] and Scherer [17] related a phenomenological expression to calculate Poisson's ratio of the sintered material as follows:

$$\nu_p \approx \sqrt{\frac{\rho}{3-2\rho}}; \; \rho = \frac{\rho_0}{(1+\lambda)^3} \quad (4)$$

where ρ is the relative density and λ is the uniaxial shrinkage, which is defined as:

$$\lambda = \frac{L - L_0}{L_0} \quad (5)$$

where L_0 and L are the length of the specimens before and after sintering, respectively. The following equation is used to determine the sintering stress [18]:

$$\sigma_s = Bd^c \quad (6)$$

where B and C are material parameters identified from dilatometry experiments.

Using these proposed constitutive equations, the related material parameters can be determined. The identification algorithm was designed to properly identify of the material parameters B and C used in the sintering stress model to optimise the numerical simulations. The following equation was proposed to calculate the stress during the sintering stage [18]:

$$\frac{\mathrm{dL}}{\mathrm{Ldt}} = \alpha \dot{T} - \frac{\sigma_s}{3K} \quad (7)$$

The proper strategy consists of identifying parameters B and C which determine the numerical shrinkage curve according to Eq. (8), in Matlab®. Therefore, the minimisation algorithm is used to, as best as possible, fit the simulations to the experimental curves by adjusting the physical parameters [18]:

$$\begin{cases} \min G(x) \\ G(x) = \sum_{i=1}^{n} \left| \lambda^{\exp}(T_i, x) - \lambda^{num}(T_i, x) \right|^2 \\ x = [B, C] \end{cases} \quad (8)$$

where λe is the experimental uniaxial shrinkage obtained from the dilatometry tests, λm is the numerical uniaxial shrinkage, F(x) is the mean residual squares of the tolerance, with i = 1,…, n indicating the different sintering temperatures, and x is the set of material parameters that need to be identified.

3 MATERIALS AND EXPERIMENTAL METHODS

3.1 Materials

The powders used to develop the feedstock dedicated to the MHE process are fine 316L stainless steel powders that exhibit excellent mechanical and corrosion properties, as well as biocompatibility. In the present analysis, the stainless steel powders (Osprey® Sandvik, UK) used exhibits a particle size distribution as follows: d10=1.8 µm, d50=3.5 µm and d90=5.0 µm (see Fig. 2a).

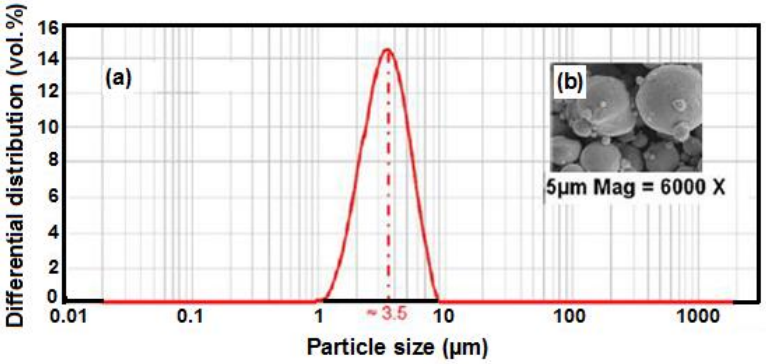

Figure 2: (a) Particle size distribution and (b) SEM micrograph of the 316L stainless steel powder.

Table 1: Characteristics of the 316L stainless steel powders.

Powder size and density						
Powder	Particle shape	D_{10} (µm)	D_{50} (µm)	D_{90} (µm)	Density [g/cm^3]	Tap density [g/cm^3]
Inox 316L	Spherical	1.8	3.4	5.0	7.90	4.50

The binder system used in this study consisted of paraffin wax (PW), polypropylene (PP) and stearic acid (SA), and the highest melting temperature of the binder system measured on a Setaram differential scanning calorimeter (DSC 92) is 160 °C. The composition of the binder, which corresponds to the ratio of PP/PW/SA, is given as the relative fractions 40/55/5. The characteristics of the different binder systems and the raw powders are presented in Tables 1 and 2. Experiments related to the mixing of binders and feedstocks were performed using a twin-screw Brabender® Plastograph EC mixer with a pair of rotor blades. The same

processing conditions were used for each mixture, including a mixing temperature of 180 °C, a mixing time of 30 min and a mixing rotation speed of 30 rpm.

Table 2: Characteristics of the different binder components.

Binders	Density [g/cm^3]	Melting temperature [°C]
Stearic acid (SA)	0.89	70
Paraffin wax (PW)	0.91	60
Polypropylene (PP)	0.90	160

4 FINITE ELEMENT MODELLING OF THE SINTERING PROCESS

4.1 Boundary and initial conditions

A micro-fluidic geometry with the dimension of 70x30x5 mm^3 with and micrometric grounds on the order of 100 µm, is shown in Fig. 3a. The element type and mesh are defined for the geometries as shown in Fig. 3b. We have used anisotropic meshes with the correct mesh concentration that consist of a fine mesh for the micro-fluidic patterns and a coarse mesh for the body of the piece. The anisotropic mesh of micro-fluidic component is composed of 141874 nodes and 92328 C3D8R elements and the densification support used is composed of 1896 nodes and 1170 R3D4 elements. The plate support is assumed to be a rigid body during the simulation, and the micro-fluidic replicas follow thermo-elasto-viscoplastic behaviour.

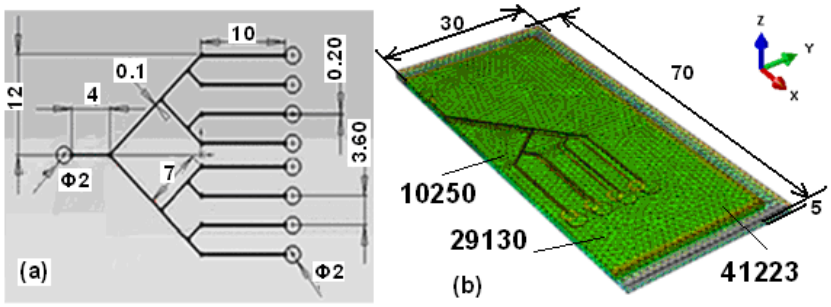

Figure 3: (a) Geometry of micro-fluidic specimens. Dimensions of samples under sintered condition, (b) FE meshes of the micro-fluidic component and the plate support prior to the simultaneous sintering stages.

Based on previous studies, different densification kinetics were retained and corresponds to heating rates of 5 °C/min, 10 °C/min and 15 °C/min to a maximum sintering temperature of 1360 °C. In addition, the «Pressure/Over-closure» contact was selected for the components. For free sintering, Coulomb's frictional law was also used in the simulation [19]. The experiments to determine the frictional coefficient have not yet been performed. However, several values, which range from 0.1 to 0.8, were chosen as the friction coefficient in the numerical simulations. The results of the simulation with the friction coefficient equal to 0.5 are the closes to the experimental results. The density distributions obtained in the hot embossing stage are regarded as the initial conditions of the sintering process with inhomogeneous green density conditions.

Table 4: Changes in the relative density due to sintering at three nodes in the FEM model of the micro-fluidic specimen (see Fig. 6).

Node number	Initial relative density	Final relative density
10250	0.612	0.969
29130	0.618	0.975
41223	0.624	0.976

4.2 Numerical results and discussion

In the powder hot embossing process, segregation occurs between the powders and binders due to their different values of inertia. This induces inhomogeneous density distributions in the green parts. This initial in-homogeneity affects the final dimensions and mechanical properties of the sintered components. The initial and final distribution of relative density after the embossing and sintering stages, respectively obtained by simulation, have been shown in Figure 4. Fig. 4a displays the relative density distribution contour after hot embossing, with its lowest value of 61.20% in the central area and highest value of 62.4% at the outside of the micro-fluidic component. The relative density gap was broadened by ~2% during the hot embossing process, and narrowed after sintering. This finding is observed primarily due to the considerable compression effects of the rubber mould cavities as well as the non-homogeneous loading conditions in terms of the complicated structure.

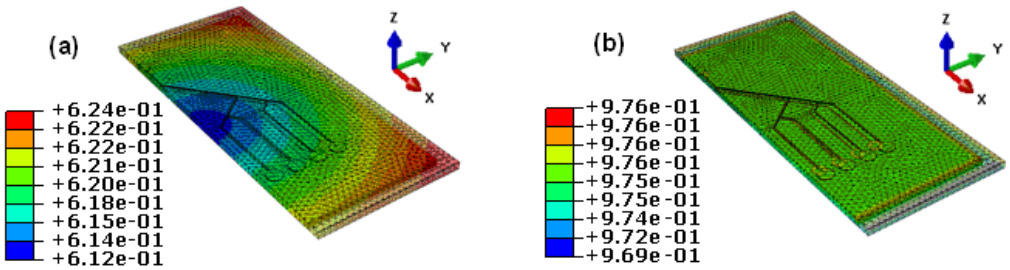

Fig. 4. Final distribution of the relative density in micro-fluidic specimens of 316L stainless steel powders, obtained after the (a) hot embossing process and (b) sintering stage at 1360 °C (solid loading: 60%, heating rate: 15 °C/min, hold time: 120 min).

The influence of the heating rates on the density of the sintered parts is shown in Fig. 5. After the sintering stage, the relative densities are generally homogeneous for most of the simulations, in which the variations have been well controlled within 2%. In addition, the numerical data clearly indicate that the sintering temperature has a significant effect on the sintered density. It was also found that the heating rate only has a significant effect on the sintered density at 1250 °C, which increase the average sintered density from 7.11 g/cm^3 to 7.27 g/cm^3. It can be observed that the final density distribution is still essentially uniform and more homogeneous when the heating rate is equal to 15 °C/min. Generally, all of the sintering variables have a significant effect on the sintered density. The numerical data show that the sintering temperature has the highest influence on the sintered density (64%), followed by the

heating rate (8%), solid loading (4%) and two-factor and three-factor interactions. Other sintering variables, not taken into account in our simulations, also have a significant effect on the sintered density such as the sintering atmosphere and sintering time.

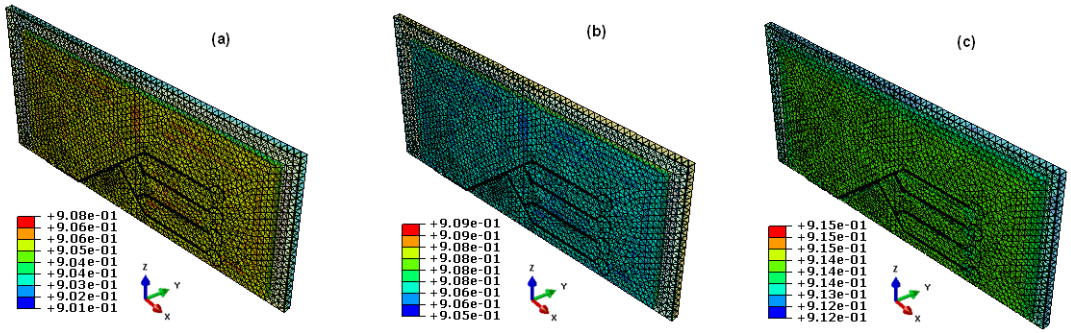

Figure 5: Final relative density of the sintered micro-fluidic components after sintering at 1250°C with a heating rate equal to: (a) 5°C/min, (b) 10°C/min and (c) 15°C/min (solid loading: 60%, hold time: 120 min).

In addition to the relative densities, the shrinkages were also simulated for these micro-fluidic components embossed with different conditions. The heating rate is one of the most important process parameters of sintering processes. It has been observed that the maximum shrinkage rate depends on the heating rates; however, the peaks of the maximum shrinkage rate located in a narrow temperature range. In fact, this narrow range spans merely from 1250 °C to 1360 °C. It is obvious that rapid sintering is favourable for densification; however, fast sintering can induce a crack in the sintered body due to the high thermal or stress gradients. In addition, the final shrinkage decreases with increasing solid loading (see Fig. 6). It can be clearly observed that the shrinkage value was stable and homogeneous, due to the symmetrical geometry. In addition, the shrinkage values increases with increasing heating rate, where it was observed that the shrinkage value was more stable and homogeneous at 15 °C/min.

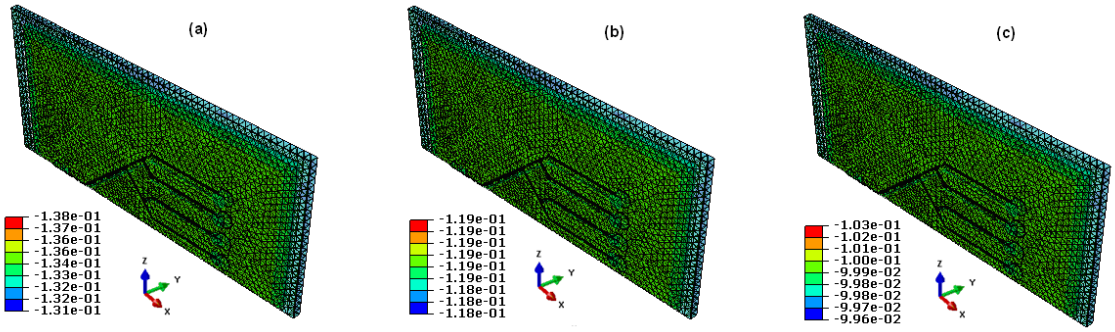

Figure 6: Numerical final shrinkage of the sintered micro-fluidic components after sintering at 1360°C using different solid loading conditions of (a) 60%, (b) 62% and (c) 64% (heating rate: 15°C/min, hold time: 120min).

5 EXPERIMENTAL RESULTS AND DISCUSSION

The microfluidic samples with the PP-based binder have been obtained using hot embossing process, then were subjected to thermal debinding at 500 °C for 1 h and were

subsequently sintered in a high-vacuum furnace at 1360 °C for 2 h. The sintered samples were free of physical defects (see Fig. 7).

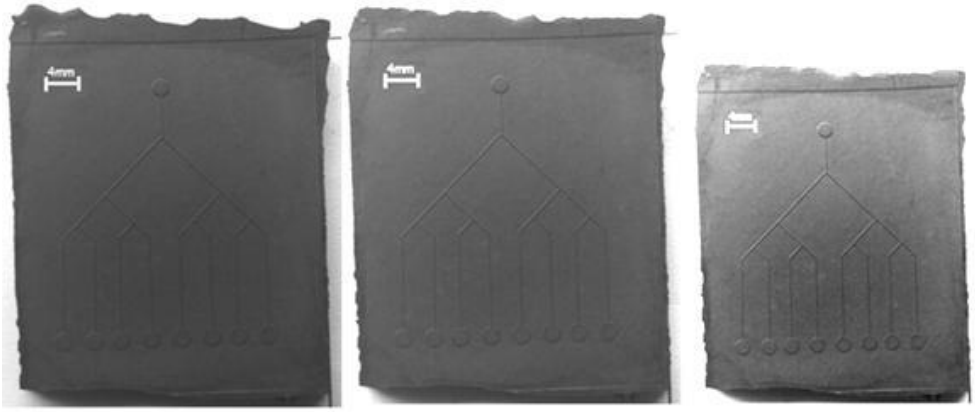

Figure 7: Photographs of the micro-fluidic replicas after the: (a) embossing (b) debinding and (c) sintering steps, which were produced using 316L stainless steel feedstock (with a solid loading of 64%).

The shrinkage values were measured using an Alicona Infinite Focus confocal microscope at twenty chosen points, as shown in Fig. 8. The dimensional changes in the length and width of the micro-structures show similar trends. The shrinkage in the thickness direction is greater than that in the other directions. This same phenomenon has been encountered by other researchers, such as Loh et al. (1996).

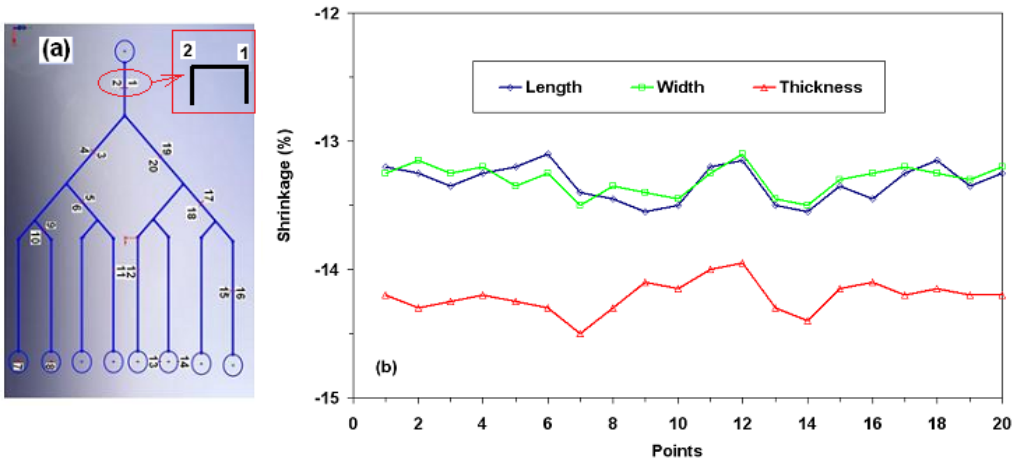

Figure 8: (a) Positions of twenty points chosen to measure the shrinkages of the sintered part (b) shrinkages of the sintered part in different directions, which was measured by an Alicona microscope at the twenty chosen points (solid loading: 60%, heating rate: 15°C/min, sintering temperature: 1360°C).

The dimensions of the micro-fluidic samples are given in Table 5. The relative densities were also determined by the Archimedes water immersion method, and porosity was evaluated using an image analyser device. The theoretical density of stainless steel powder is 7.90 g.cm^{-3}. The sintering temperature had a significant effect on the densification, i.e., the density increased significantly with increasing temperature, as summarized in Fig. 9. The

influence of sintering temperature on the densification of 316L stainless steel is more pronounced; a significant densification was observed when the stainless steel tool became mushy at 1300 °C. The maximum density was obtained when sintering was performed at 1360 °C, which was 98.2% of the theoretical values. The heating rate also has a strong effect on the final density. The porosity is lower and the grains become finer as the heating rate increases.

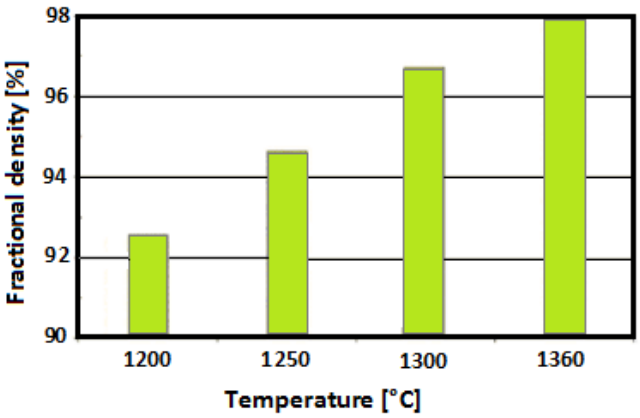

Figure 9: Effect of sintering temperature on the sintered density (dwell time 120min, 15°C/min).

Table 5: Dimensions of the elastomeric mould and micro-sized structures of the micro-fluidic samples.

Micro-sized structure / 316L stainless steel 1360°C - 15°C/min				
		60%	62%	64%
Φ	2	1.72±0.01	1.76±0.01	1.78±0.01
a	5	4.31±0.01	4.41±0.01	4.49±0.01
b	14	12.11±0.01	12.40±0.01	12.53±0.01
c	14	12.15±0.01	12.33±0.01	12.54±0.01
d	4	3.45±0.01	3.53±0.01	3.56±0.01
e	14	12.16±0.01	12.39±0.01	12.55±0.01

6 EXPERIMENTAL VALIDATION

The relative density of the micro-fluidic specimens obtained from the numerical simulations is compared with the experimental values, as shown in Fig. 10. The relative densities are in perfect agreement with the experimental densities, particularly for the sintering cycles with relatively low heating rates. A comparison between the experimental and the simulation results of the shrinkage in three directions (length, width and height) is also shown in Fig. 11. During the sintering stage, the simulated dimensions were in good agreement with the experimental values, with a relative error of less than 3% in both directions. In addition, both the simulated and experimental shrinkages in the height direction were higher than those in the other two directions, which is primarily due to gravity along the height direction. During the sintering process, the relative errors between the simulated and experimental results in the height direction were found to be greater than 5%. This result is

primarily due to the structural anisotropy of the parts processed. This same phenomenon has been encountered by other researchers, such as Loh et al. (1996).

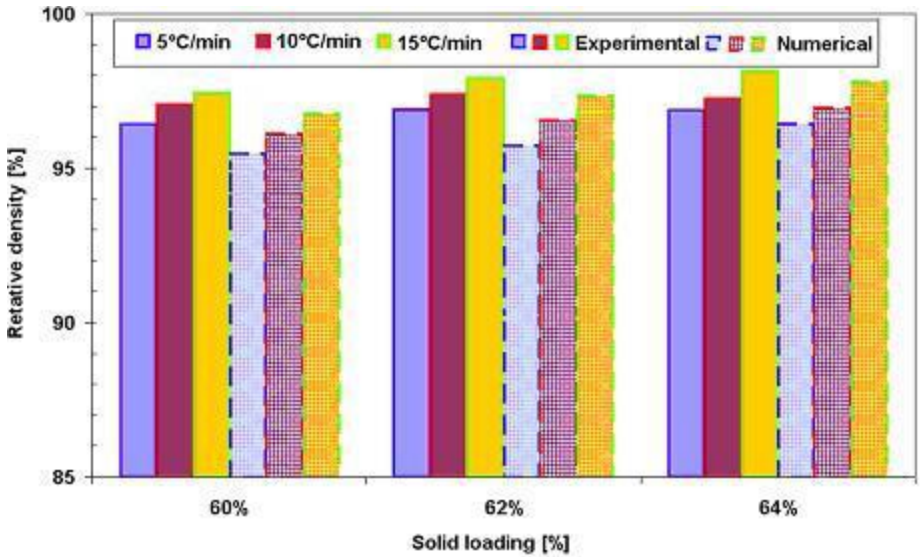

Figure 20: Comparison between the experimental and simulated results of the relative density.

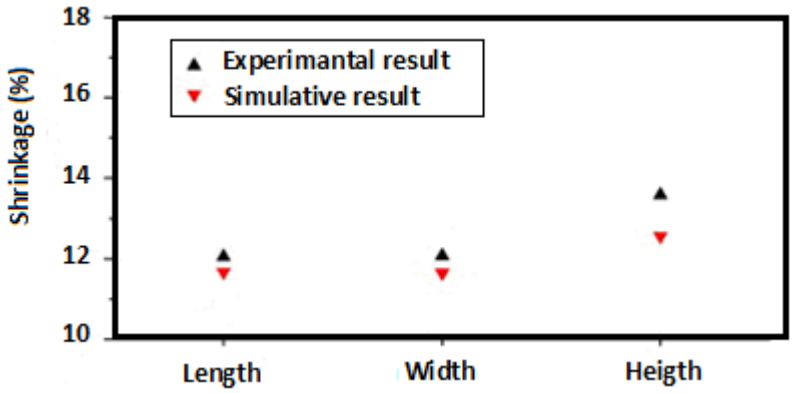

Figure 31: Comparison between the experimental and simulated results of shrinkage in three directions.

7 CONCLUSIONS

A numerical simulation based on a finite element analysis was performed in order to investigate the shrinkage variations and relative density evolutions during a powder hot embossing process. The simulation results are in good agreement with the experimental data, which proves the validity of the physical model and the reliability of the identification and numerical method. The following conclusions can be made:

- The sintering experiments using a dilatometer demonstrate that the sintering parts in 316L stainless steel have the threshold temperatures in the range of 1050 to 1080 °C. In

addition, the rapid sintering is favourable for densification. The maximum shrinkage of 316L stainless steel powders is 14%, at a heating rate of 15 °C/min.

- It can also be observed that the sintering process makes the final density of the sintered bodies essentially uniform, whereas in-homogeneity of the initial density primarily affects uneven shrinkage of the sintered body. In fact, the micro-fluidic components exhibit very small shrinkage after the hot embossing and debinding stages. However, the components exhibit inhomogeneous shrinkage after sintering, which ranges from 11.5% to 14%.

REFERENCES

[1] Santos P. F., Niinomi M., Liu H., Cho K., Nakai M., Itoh Y., Narushima T., Ikeda M., Fabrication of low-cost beta-type Ti–Mn alloys for biomedical applications by metal injection molding process and their mechanical properties, *Journal of the Mechanical Behavior of Biomedical Materials*(2016)**59**:497-507.

[2] Ou H., Sahli M., Gelin J.-C., Barrière T., Experimental analysis and finite element simulation of the co-sintering of bi-material components, *Powder Technology*(2014)**268**:269-278.

[3] Zhao D., Chang K., Ebel T., Qian M., Willumeit R., Yan M., Pyczak F., Microstructure and mechanical behavior of metal injection molded Ti–Nb binary alloys as biomedical material, *Journal of the Mechanical Behavior of Biomedical Materials*(2013)**28**:171-182.

[4] Sahli M., Gelin J.-C., Barriere T., Characterisation and replication of metallic microfluidic devices using three different powders processed by hot embossing, *Powder Technology*(2013)**246**:284-302.

[5] Kurgan N., Effects of sintering atmosphere on microstructure and mechanical property of sintered powder metallurgy stainless steel, *Materials & Design*(2013)**52**:995-998.

[6] Sahli M., Gelin J.-C., Barrière T., Replication of microchannel structures in WC–Co feedstock using elastomeric replica moulds by hot embossing process, *Materials Science and Engineering: C*(2015)**55**:252-266.

[7] Coble R. L., Sintering crystalline solids. I. Intermediate and final state diffusion models, *J. Appl. Phys* (1961)**32**:787-792.

[8] Wakai F., Mechanics of viscous sintering on the micro- and macro-scale, *Acta Mater*(2013)**61**:239-247.

[9] Reiterer M., Kraft T., Janosovits U., Riedel H., Finite element simulation of cold Isostatic pressing and sintering of SiC components. Ceram Int (2004)**30**:177-183.

[10] Bruchon J., Pino-Munoz D., Valdivieso F., Drapier S., Finite element simulation of mass transport during sintering of a granular packing. Part I. Surface and lattice diffusions, *J. American Ceramic Society*(2010)**13**:1-23.

[11] Yu P.C., Li Q.F., Fuh J.Y.H., Li T., Lu L., Two-stage sintering of nano-sized yttria stabilized zirconia process by powder injection moulding, *J. Mater. Process. Technol*(2007)**192**:312-318.

[12] Olevsky E.A., Theory of sintering: from discrete to continuum, *Mater. Sci. Eng*(1998)**23**:41-100.

[13] Gasik M., Zhang B., A constitutive model and FE simulation for the sintering process of powder compacts, *Comput. Mater. Sci*(2000)**18**:93-101.
[14] Bouvard D., McMeeking R.M., Deformation of interparticle necks by diffusion controlled creep. *J. Am. Ceram. Soc*(1996)**79**:666-672.
[15] Song J., Gelin J.C., Barrière T., Liu B., Experiments and numerical modelling of solid state sintering for 316L stainless steel components, *Journal of Materials Processing Technology*(2006)**177**:352-355.
[16] Bordia R.K., Scherer G.W., On constrained sintering. I. Constitutive model for a sintering body, *Acta Mater*(1988)**36**:2393-2397.
[17] Scherer G.W., Sintering inhomogeneous glasses: application to optical waveguides, *J. Non-Cryst. Solids*(1979)**34**:239-256.
[18] Peterson A., Agren J., Constitutive benhavior of WC–Co materials with different grain size sintered under load, *Acta Mater* (2004)**52**:1847-1858.
[19] Olevsky E. A., German R. M., Upadhyaya A., Effect of gravity on dimensional change during sintering- Π shape distortion, *Acta Mater*(2000)**48**:1167-1180.
[20] Loh NH, German RM, Statistical analysis of shrinkage variation for powder injection molding. *J Mater Process Technol*(1996)**59**:278-284.

FORMABILITY EVALUATION OF DOUBLE LAYER CIRCULAR TUBE AS A DEVICE WITH ENERGY ABSORPTION CAPACITY

MASAYA KAWAHARADA*, YUKINORI TANIGUCHI† AND SHINICHI ENOKI†

* Faculty of Advanced Engineering
National Institute of Technology, Nara College
22 Yata, Yamatokoriyama, Nara, 639-1080 Japan
e-mail: a0829@stdmail.nara-k.ac.jp

†Department of Mechanical Engineering
National Institute of Technology, Nara College
22 Yata, Yamatokoriyama, Nara, 639-1080 Japan
e-mail: taniguchi@mech.nara-k.ac.jp, shinichi_enoki@mua.biglobe.ne.jp

Key words: Forward and backward extrusion, Punch speed, Elastic strain, Double layer circular tube, Tightening, Outer layer circular tube

Abstract. Recently, earthquakes frequently occur in Japan. It is desired to promote seismic isolation technology of building. It has been found that newly designed composite material filled with low rigidity material to high rigidity material has significant energy absorbing capacity. However, it must have higher energy absorption capacity in order to respond to a large scale earthquake. Therefore, we have proposed an energy absorbing device with a double layer circular tube as a cell. In previous work, it has been shown that hysteresis occurs and absorbs the energy by friction that is generated between the outer layer and the inner layer. It is effective when inside shape of inner layer is defined as floral pattern. In this study, we considered to form the inner layer circular tube by forward and backward extrusion and to assemble with the outer layer circular tube at the same time. After forming, it is necessary to generate hysteresis around the entire circumference of the circular tube. Ideally, the inner layer circular tube is tightened to the outer layer circular tube. In this research, it was aimed to know the contact state between the outer layer and the inner layer after forming. Therefore, the influence of the presence or absence of the outer layer circular tube on formability was investigated. As a result, there was a tendency for large elastic strain to remain at the contact portion between the circular tubes when the outer layer circular tube was set. This means that the outer layer circular tube hinders elastic recovery of the inner layer circular tube. Therefore, it was confirmed that the inner layer circular tube was tightened by the outer layer circular tube. The same result was obtained when the inner shape of the inner layer circular tube was a flower pattern.

1 INTRODUCTION

Recently, earthquakes frequently occur in Japan. It is desired to promote seismic isolation

technology of building. It has been found that newly designed composite material filled with low rigidity material to high rigidity material has significant energy absorbing capacity[1]. However, it must have higher energy absorption capacity in order to respond to a large scale earthquake. Therefore, we have proposed an energy absorbing device with a double layer circular tube as a cell[2]. In previous work, it has been shown that hysteresis occurs and absorbs the energy by friction that is generated between the outer layer and the inner layer[3]. It is effective when inside shape of inner layer is defined as floral pattern. In this study, we considered to form the inner layer circular tube by forward and backward extrusion and to assemble with the outer layer circular tube at the same time. After forming, it is necessary to generate hysteresis around the entire circumference of the circular tube. Ideally, the inner layer circular tube is tightened to the outer layer circular tube. In this research, it was aimed to know the contact state between the outer layer and the inner layer after forming. Therefore, the influence of the presence or absence of the outer layer circular tube on formability was investigated.

2 ANALAYSIS CONDITIONS

In this study, as a method of forming a double layer circular tube, an outer layer circular tube of carbon steel was placed in a die, a cylindrical blank of aluminum was placed inside the outer layer circular tube, and the inner layer circular tube was formed by cold forging. We thought of we can assemble the inner layer circula tube and the outer layer circular tube at the same time as forming the inner layer. About the model shown in Figure 1, the formability of the double layer circular tube by forward and backward extrusion was investigated. Figure 1 shows the analytical model in the presence and absence of an outer layer circular tube. Figure 2A shows the model in which an outer layer circular tube exists. Figure 2B shows the model without an outer layer circular tube. In addition, a case where the inner surface shape of the inner layer circular tube as shown in Figure 3 is circular and a case where the inner surface shape of the inner layer circular tube is a flower shape as shown in Figure 4 were analyzed, and we studied the case that the punch speed is 10 [mm/s], 30 [mm/s] and 50 [mm/s]. For the circular tube, as shown in Table 1, an outer layer circular tube having an outer diameter of ϕ 28.6 [mm/s] and an inner diameter of ϕ 26.2 [mm/s] and a cylindrical blank (inner layer circular tube) of ϕ 26.2 [mm/s] were used. We used A1100(JIS H 4100) for the inner layer circular tube and STKM11A(JIS G 3445) for the outer layer circular tube. Since it is impossible to punch through to the end, the stroke was set so that the wall thickness of 2 [mm] remains after forming.

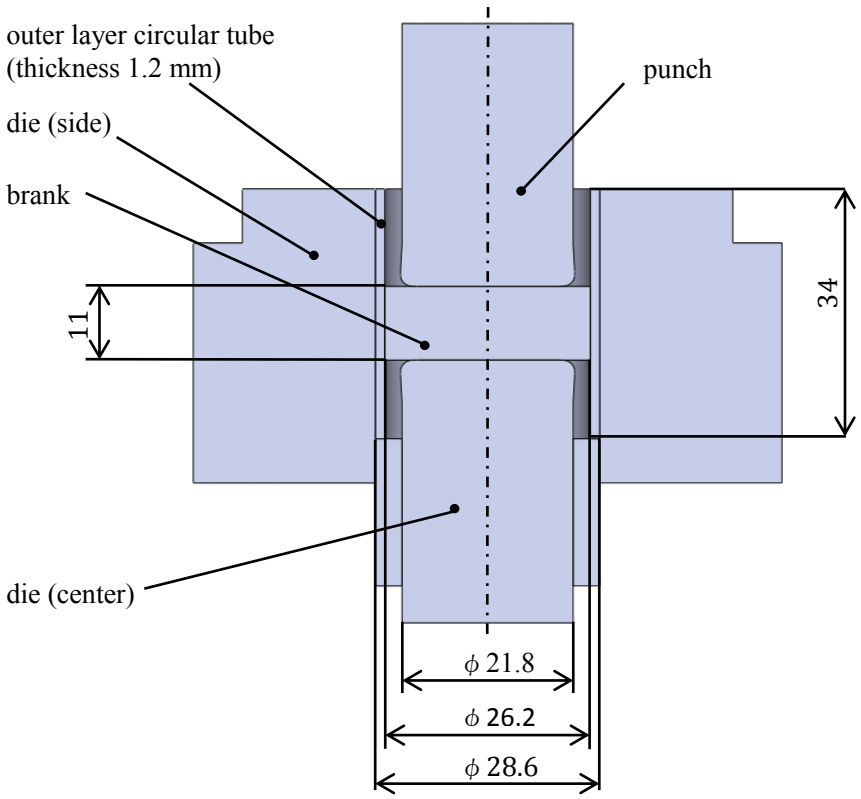

Figure 1: Model of double layer circular tube

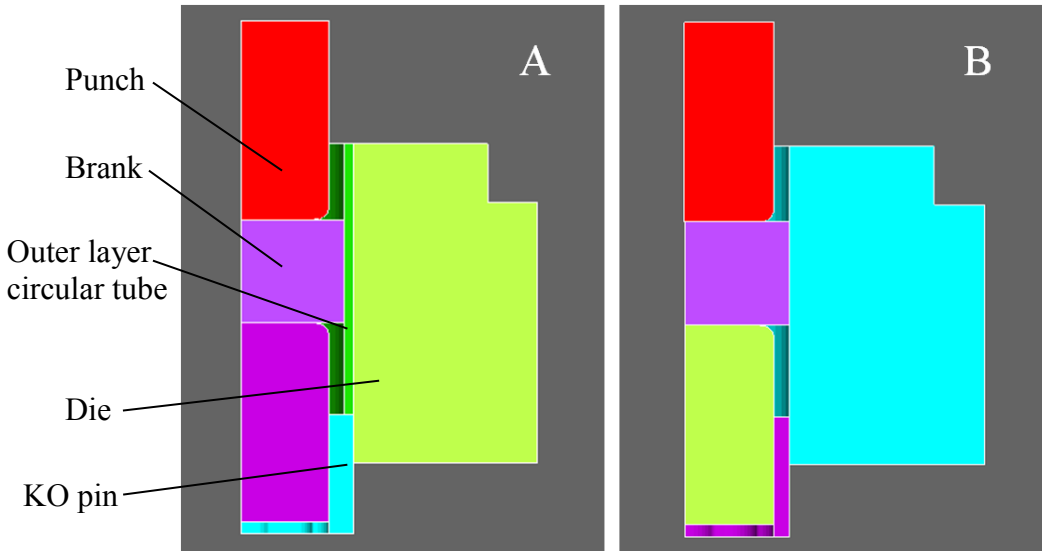

(A) There is an outer layer circular tube (B) There is no outer layer circular tube

Figure 2: Differences in analysis conditions (Axisymmetric model)

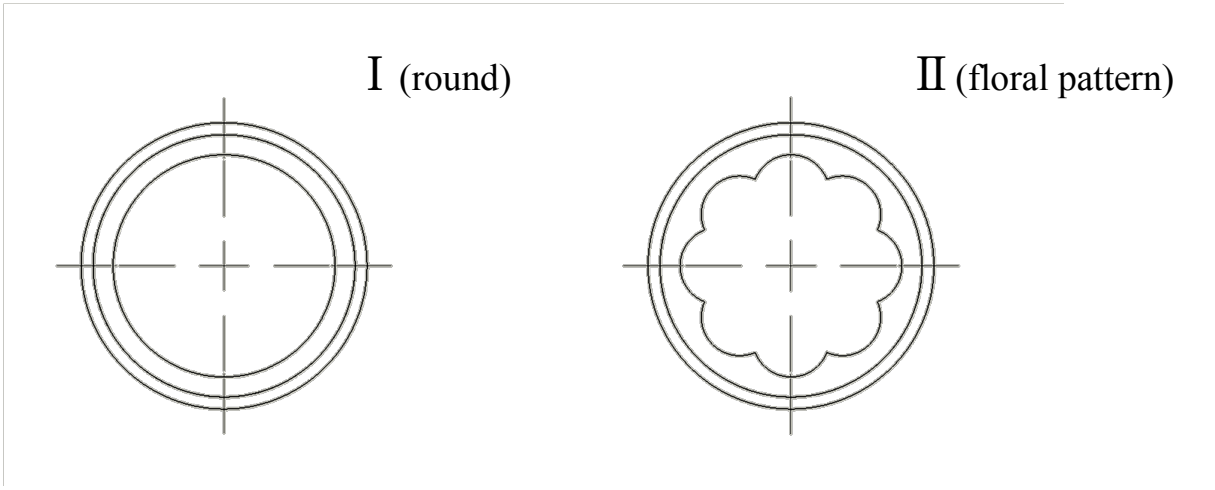

Figure 3: Inner shape of inner layer circular tube

Table 1: Dimension and material of circular tube

	Outside diameter [mm]	Inside diameter [mm]	Length [mm]	Material
Cylindrical blank (floral pattern)	ϕ 26.2		11.5 (13.0)	A1100 (JIS H 4100)
Outer layer circular tube	ϕ 28.6	ϕ 26.2	34	STKM11A (JIS G 3445)

3 RESULTS AND DISCUSSION

Figures 4 and 5 show the results of analysis of the equivalent elastic strain after the punching and die removal at the end, with the Forward and backward extrusion at the punch speed of 10 [mm/s]. Figure 4 shows the results when the inner shape of the inner layer circular tube is circular, Figure 5 shows the result when the inner shape of the inner layer circular tube is a floral pattern. Figure 4(a) and Figure 5(c) show the results when the outer layer circular tube is present, and (b) and (d) are the results without the outer layer circular tube. Comparing Figure 4 (a) and (b), (a) has equivalent elastic strain in the position where the inner layer circular tube and the outer layer circular tube are in contact. On the other hand, in the case of (b), there are many parts where the equivalent elastic strain is close to zero. From this, it can be seen that in Figure 4 (a) the outer layer circular tube impedes elastic recovery of the inner layer circular tube, so that the outer layer circular tube is tightening the inner layer circular tube. Next, when comparing the case of the floral pattern shown in Figure 5, there are some differences in the strain distribution, but in the case of Figure 5(c) elastic strain remains at the contact part between the circular tubes, the same result as in the case of a round was obtained.

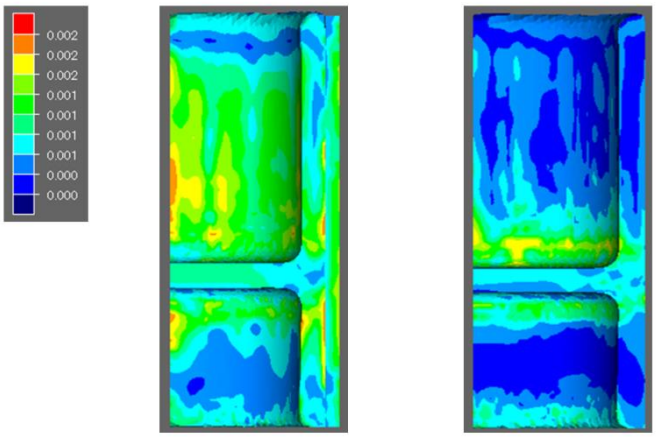

(a) There is an outer layer circular tube

(b) There is no outer layer circular tube

Figure 4: Difference in equivalent elastic strain due to the presence or absence of outer layer circular tube (Round)

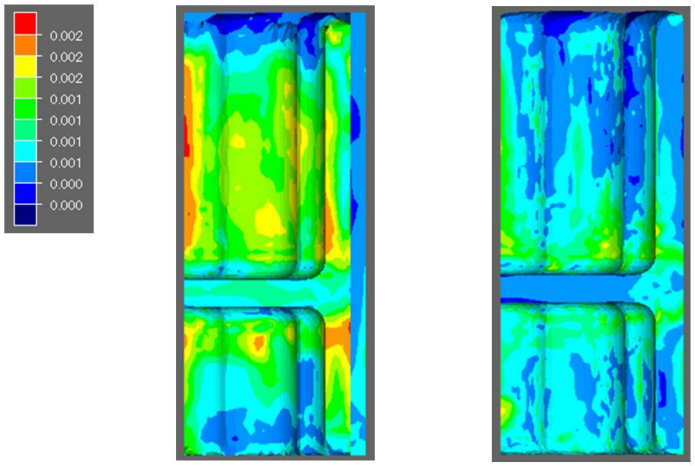

(c) There is an outer layer circular tube

(d) There is no outer layer circular tube

Figure 5: Difference in equivalent elastic strain due to the presence or absence of outer layer circular tube (floral pattern)

Also, as a result of examining the influence of the punch speed on the formability of the two layer circular tube, the results shown in Figure 6 and Figure 7 below were obtained. Figure 6 and Figure 7 are the analysis results of the equivalent elastic strain for punch speeds of 10 [mm/s] and 50 [mm/s]. Figure 6 shows the result of the inner surface shape of the inner layer circular tube being circular, and Figure 7 shows the result of the inner shape of the inner layer circular tube being a floral pattern. Figure 6 (a) and Figure 7 (c) show the results of the punch speed of 10 [mm/s]. Figure 6 (b) and Figure 7 (d) show the results of the punch speed

of 50 [mm/s]. From Figure 6 and Figure 7 it can be seen that there are parts where equivalent elastic strain remains at the contact part between the inner layer circular tube and the outer layer circular tube respectively. As a result of comparing the equivalent elastic strain, the range of equivalent elastic strain corresponding to the outer circumference of the inner layer circular tube is wider in Figure 6 with higher punch speed. For this reason, I think that fast punching speed is good with regard to tightening. The same result was obtained for Figure 7 which is the case of the floral pattern.

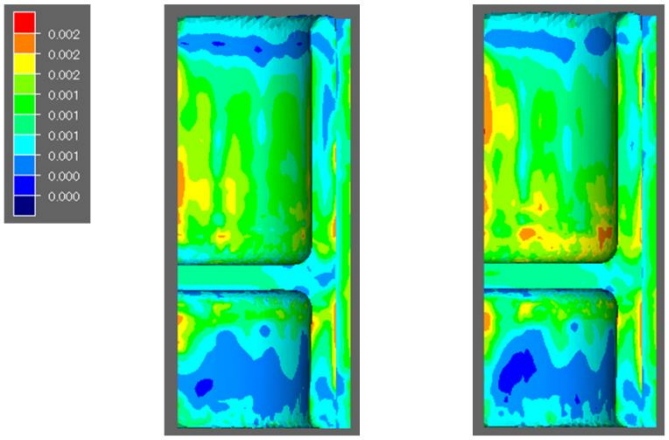

(a) Punch speed 10 mm/s (b) Punch speed 50 mm/s

Figure 6: Difference in equivalent elastic strain due to punch speed (Round)

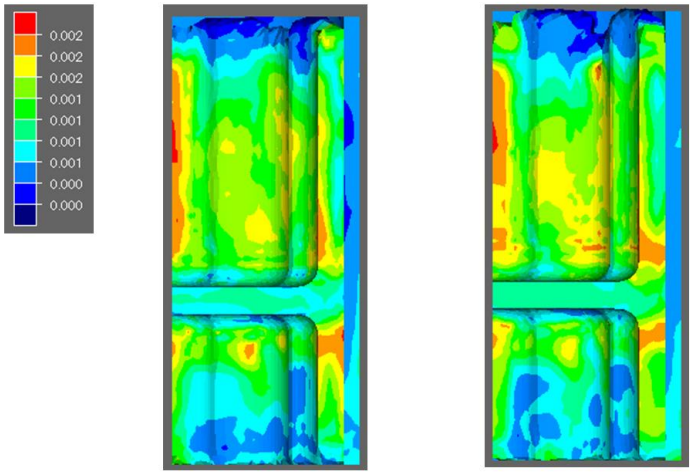

(c) Punch speed 10 mm/s (d) Punch speed 50 mm/s

Figure 7: Difference in equivalent elastic strain due to punch speed (floral pattern)

4 CONCLUSION

As a result of comparing the differences in the corresponding elastic strain due to the presence or absence of the outer layer circular tube, the value of the corresponding elastic strain at the contact portion between the outer layer and the inner layer was almost zero when there was no outer layer circular tube. On the other hand, when there was an outer layer circular tube, the result that the equivalent elastic strain easily remained in the contact part between the circular tubes was obtained. Therefore, it can be seen that the outer layer circular tube is tightening the inner layer circular tube. Those with high punch speeds make it easier for equivalent elastic strain to remain corresponding to the outer periphery of the inner layer circular tube. In terms of tightening, it is better for the punch speed to be faster. A similar tendency was also observed when the inner shape of the inner layer circular tube was a floral pattern.

ACKNOWLEDGMENT

This work was supported by the AMADA Foundation Grant Number AF-2014030.

REFERENCES

[1] Ota et al. “Material design of a biomimetic composite material used for a wooden building joint structure”, Design and Nature V, WIT Transactions on Ecology and the Environment Vol.138(2010), pp.329-337.

[2] Nomura et al. “Design condition of a sustainable two-layer circular tube with absorbing energy capacity”, Computational Methods and Experimental Measurements XVI, WIT Transactions on Modelling and Simulation Vol.55(2013), pp.103-114.

[3] Nomura et al. “Study on hysteresis in sustainable two-layer circular tube under a lateral compression load”, WASET International Journal of Mechanical, Aerospace, Industrial and Mechatronics Engineering, Vol.8, No.12(2014), pp.1885-1889.

XIV International Conference on Computational Plasticity. Fundamentals and Applications
COMPLAS 2017
E. Oñate, D.R.J. Owen, D. Peric and M. Chiumenti (Eds)

MODELLING OF SELF-PIERCING RIVETING WITH ALE, CEL AND SPH BASED ON ABAQUS/EXPLICIT

SATOSHI ISHIKAWA*, HIROSHI AIHARA†

* IDAJ Co., Ltd.
7-1-1 Onogara-dori, Kobe-shi, Hyogo, 651-0088, Japan
e-mail: ishikawa.satoshis@cimne.upc.edu, www.idajco.jp

† IDAJ Co., Ltd.
2-2-1-1 Minatomira, Nishi-ku, Yokohama-shi, Kanagawa, 220-8137, Japan
e-mail: aihara.hiroshi@idaj.co.jp

Key words: Self-piercing riveting, Bonding, Plastic forming, ALE, CEL, SPH.

Abstract. SPR (Self-piercing riveting) is a cold forming process that is used to fasten together two or more sheets of different materials mechanically with a rivet. Also SPR emulates the results and quality of spot welding without many of the risks, such as toxic fumes, sparks and noise. Thus circumstanced, this technique is widely used on the various filed especially within automobile industry. SPR, in particular, is excellent for lightweight manufacturing and for precise working while dramatically reducing cost and production time. The process deformation depends on the sheet size, shape of die, material flow, stiffness, etc. Also material deformation in both of rivet and workpiece sheets is tremendous large, for instance thinning, necking, shear and penetration. Therefore it is very hard to analyze this forming process with FEM which uses normal stress element formulation due to the collapse. On the other hand, Abaqus/Explicit has superb analysis methods, for example ALE, CEL and SPH[1]. This paper investigates several Abaqus/Explicit modeling techniques for simulating and optimizing SPR process. In addition, the effectiveness of these analysis methods was discussed and compared for evaluating SPR process forming in order to achieve an optimal die, material properties and suitability of deformations.

1 INTRODUCTION

For a long time, several joining technologies have been developed for automotive manufacturers to perform weight and cost reduction goals. Among these, SPR is identified with an effective and possible method for uniting some dissimilar panels, for instance aluminum parts and steel parts. SPR is essentially a cold forming operation. A semi-tubular rivet is engaged into two or more sheets of material that are supported on a die and a holder. The rivet pierces the upper sheet and is flared into the bottom sheet, thus mechanical forming interlocks between the two sheets as shown in Figure 1[2]. Also SPR emulates the results and quality of spot welding without many of the risks, such as toxic fumes, sparks and noise. Thus circumstanced, this technique is widely used on the various fields especially within automobile industry. SPR, in particular, is superb for lightweight manufacturing and for precise working while dramatically reducing cost and production time. The process

deformation depends on the sheet size, shape of die, material flow, stiffness, etc. Also material deformation in both of rivet and workpiece sheets is tremendous large, for instance thinning, distortion, shear and penetration. Since it is important for the automotive design engineers to understand the mechanical behavior of different SPR joints, furthermore, to incorporate these joint properties in the early design stage using computer aided engineering and design tools.

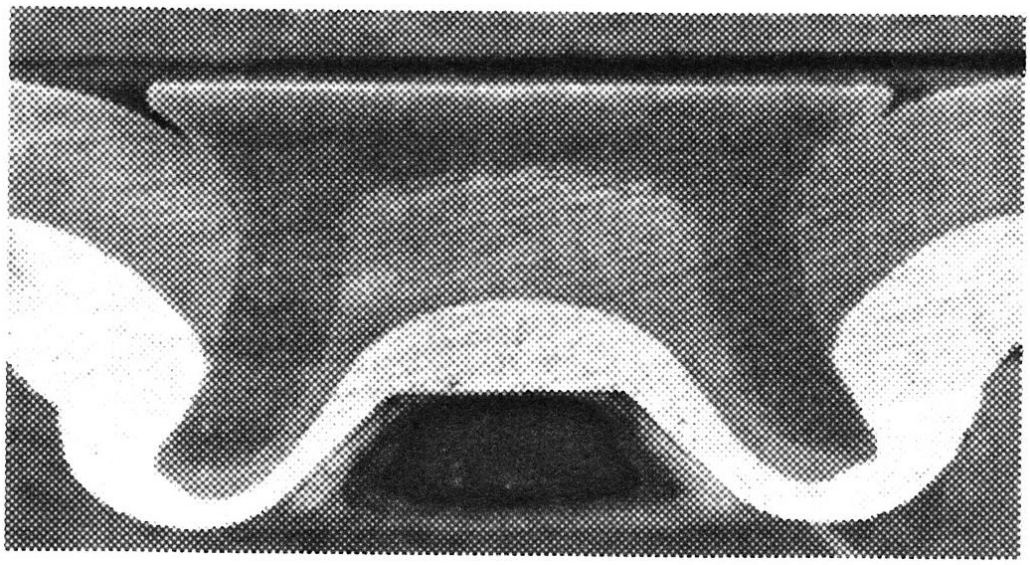

Figure 1: Cross section for experimental SPR forming of 1.4mm SPFC440 (upper sheet) and 1.5mm Aluminum (lower sheet)

2 MODEL DESCRITION

A target axisymmetric section in this research is shown in Figure 2(a). This model consists of six parts of which shapes are conventional design of SPR. Two deformable sheets were put between a rigid holder and a die. Lower sheet was assumed as an aluminum material, and upper sheet was SPFC (Steel Plate Formability Cold). In this paper, we examined three dissimilar flow materials of SPFC for upper sheet. The later three digits of SPFC in the Figure 2(b) mean a minimum tensile strength. Figure 2(b) shows all flow stress curves of all materials, SPFC980 has the largest tensile strength, while aluminum is the most ductile metal. Rivet which was assumed to be a Boron material was placed on the upper sheet and thrusted below by a punch. ALE model was analyzed on this axisymmetric condition, while CEL and SPH were analyzed with 3D models based on this axisymmetric cross section and material condition. Following sections explain each modeling.

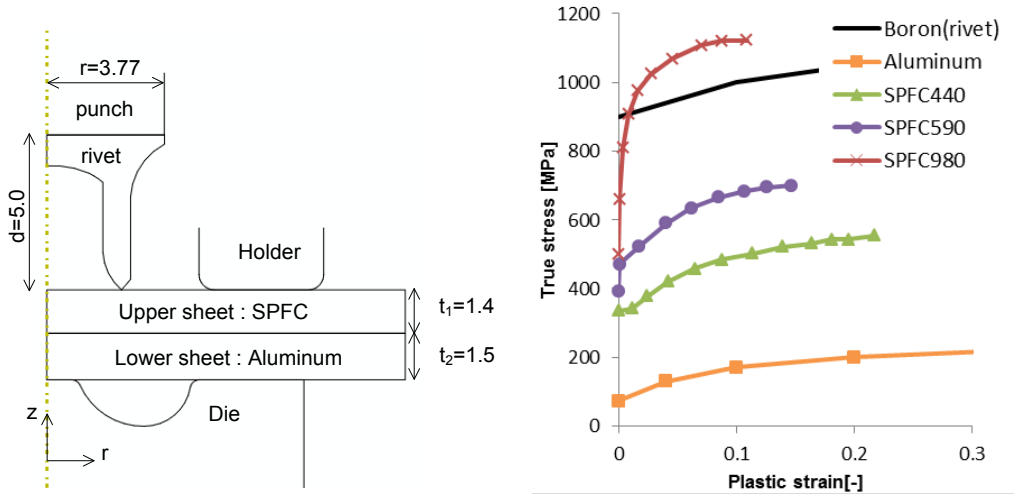

Figure 2: (a) Axisymmetric section; (b) Material flow

2.1 Modeling of ALE

Figure 3(a) shows an axisymmetric ALE model. The element type used in deformable parts such as a rivet and two sheets was CAX4R, while the element type of RAX2 was used in rigid body such as die, holder and punch. Both mesh size of upper and lower sheets was 0.2mm at cross section. The mesh size of rivet was also the same manner. CONTACT PAIR conditions were applied to each contact surface. The velocity of punch was 5mm/s in the minus Y global direction, also one second was taken at the total phenomenon time. ADAPTIVE MESH criteria were applied on the parts of upper and lower sheet, since it was expected that the element of both sheet suffered large shear deformation.

2.2 Modeling of CEL

The modeling of CEL is shown in Figure 3(b). CEL function has to be analyzed only three-dimensional field, therefore this model was comprised of wedge shape of ten degrees. The domain necessary for analysis was occupied in Euler elements EC3D8R with enough space as shown in white mesh. Also discrete field was set for upper sheet with green space by using the volume fraction tool in Abaqus/CAE. In this study, Euler mesh size was adopted 0.1mm at cross section. While two parts of rivet and lower sheet were performed with normal stress element C3D8R of which mesh size at cross section was 0.2mm. Punch speed and phenomenon time were as same as ALE model. To keep wedge shape, local cylindrical hoop boundary condition was applied on the lateral faces on the model.

2.3 Modeling of SPH

The last model in this study was SPH method. This model was also made in wedge style as same as CEL model. Figure 3(c) shows the dummy SPH model which was made with normal solid element C3D8 within the upper sheet space. After it was output as for Abaqus input file, PC3D elements were rewritten by manual operation with an element number same as a node number constituting C3D8. Figure 3(d) shows essential PC3D elements which were located

on the nodal position of constructed dummy solid elements. By using this method, we could handle proper hoop boundary condition at PC3D elements to hold wedge shape. Of course, Abaqus has the methodology that can convert from Lagrangian finite elements to SPH particles. But this conversion technique was not easy to manage appropriate local boundary conditions on the elements on the symmetric face, because SPH is only available with GENERAL CONTACT and the large number of PC3D elements was unnecessary generated.

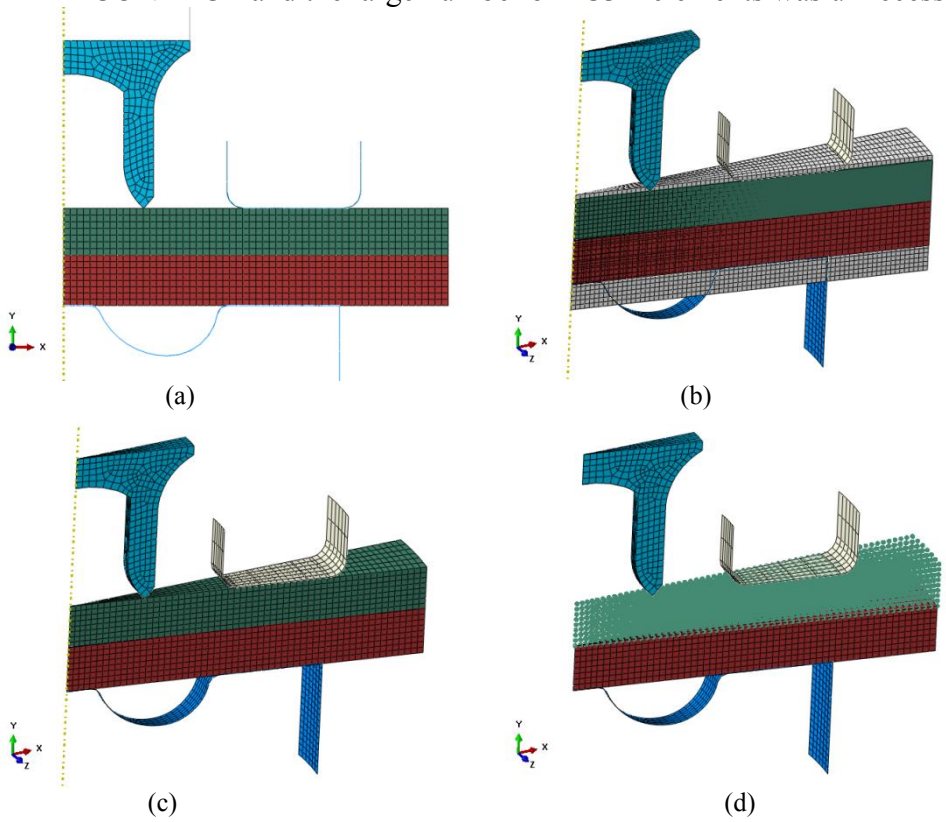

Figure 3: (a) ALE Modeling; (b) CEL Modeling; (c) dummy SPH Model; (d) Essential SPH Modeling

3 RESULTS

3.1 Results

Figure 4 shows the force-displacement responses of the punch for all analyses. The legend is analysis method plus the number of hardness of SPFC. The results of CEL were the largest in three methods among all SPFC materials, while the results of ALE were the smallest.

All deformation plots are shown in Figure 5 to 7. Figures of left column show the contour plots of Mises stress, the other right column figures show the result of Equivalent plastic strain. As the hardness of upper sheet became higher, the axial distortion of the rivet grew large and the rivet was not flared naturally as shown in Figure 7. While the rivet was flared in two sheets and this deformation caused interlock in case of SPFC440 as of Figure 5 (g) (h). These analysis results were not too far from the truth. In addition, deformation figures indicated that PC3D elements on the symmetry boundary area held the fixed condition of the

hoop direction by our modeling method.

Although ALE revealed clear deformation shape of each sheets due to adaptive meshing function, it could not analyze completely in all SPFC specimens because of the element distortion at the center area on aluminum lower sheet (see Figure (a) (b)). And it could not be seen the separation of upper sheet in ALE method.

Similarly, CEL could not express a separation state as shown in Figure (c), and it took tremendous CPU time as shown in Table 1 in the next section 3.2. Furthermore, the lower sheet suffered severe distortion without adaptive meshing.

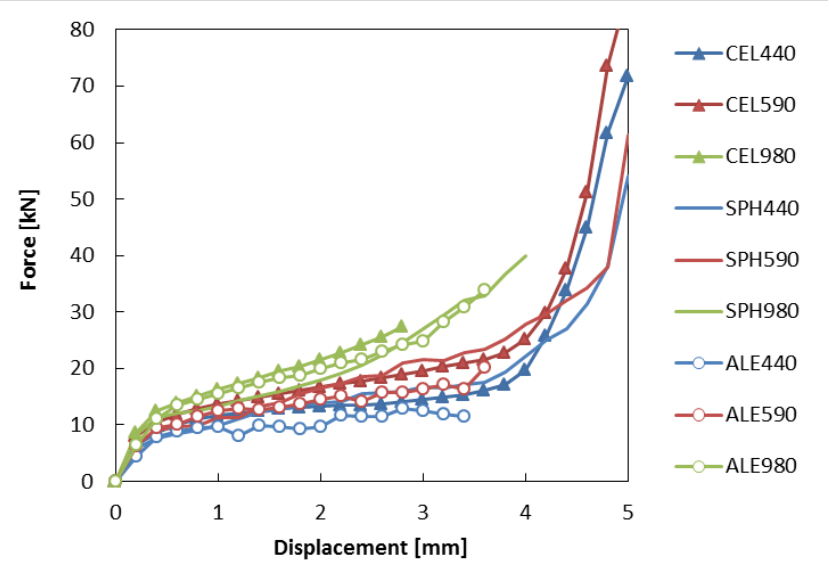

Figure 4: Punch force versus displacement

3.2 Analysis Time

Table 1 shows the analysis time (wallclock time [hh:mm] in the Abaqus log file) with parallel processing under Windows 7 64 bit operating system and a computer having two Intel Xeon E5-2620 (2.10GHz processor six cores). All jobs were analyzed under 12 cores parallel processing with Abaqus version 6.14-5.

Note that all analyses in ALE were not executed completely, and CEL for SPFC980 also ended at 58% of the total phenomenon time.

Table 1: Analysis time

Material for upper sheet	Wall clock time [hh:mm]		
	ALE	CEL	SPH
SPFC440	00:04	12:24	00:17
SPFC580	00:04	12:38	00:17
SPFC980	00:04	8:06	00:15

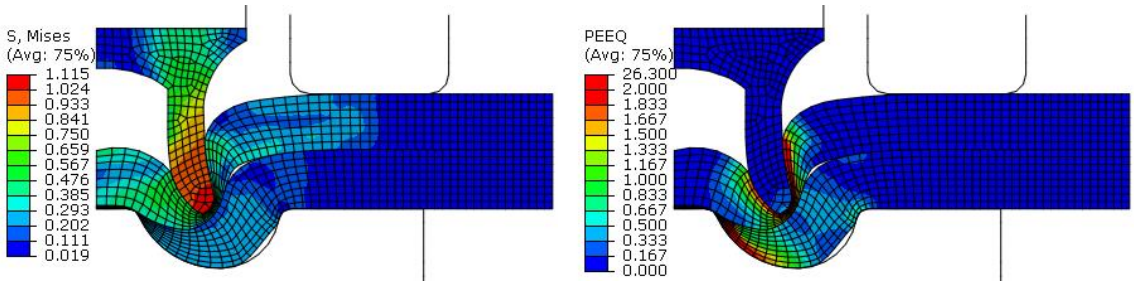

(a) Mises stress (ALE)

(b) Plastic strain (ALE)

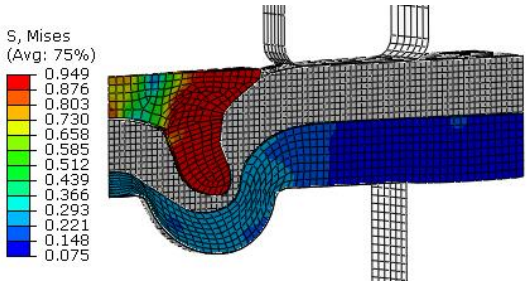

(c) Mises stress (CEL)

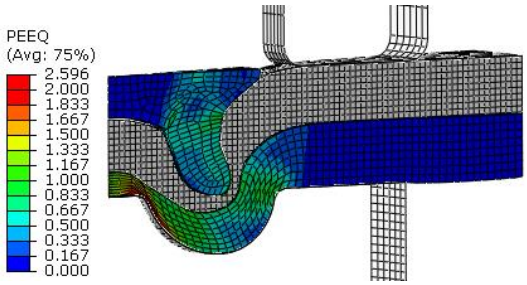

(d) Plastic strain (CEL)

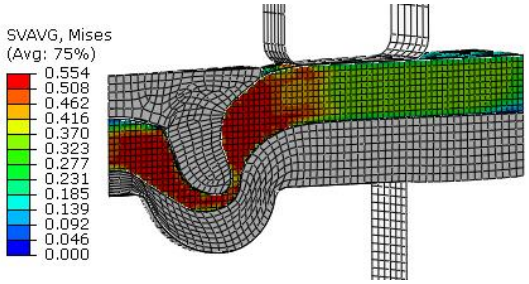

(e) Mises average (CEL)

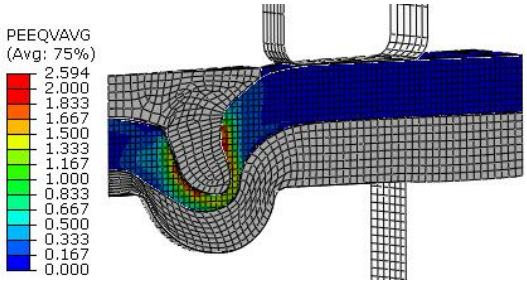

(f) Plastic strain average (CEL)

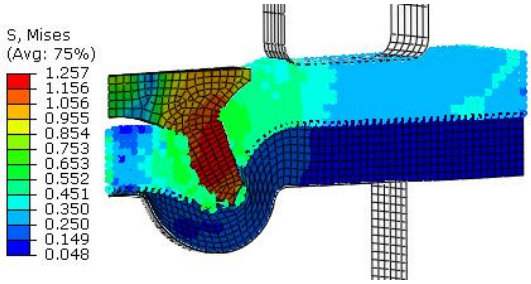

(g) Mises stress (SPH)

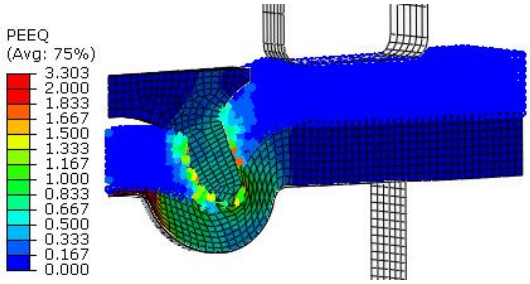

(h) Plastic strain (SPH)

Figure 5: Results of SPFC440

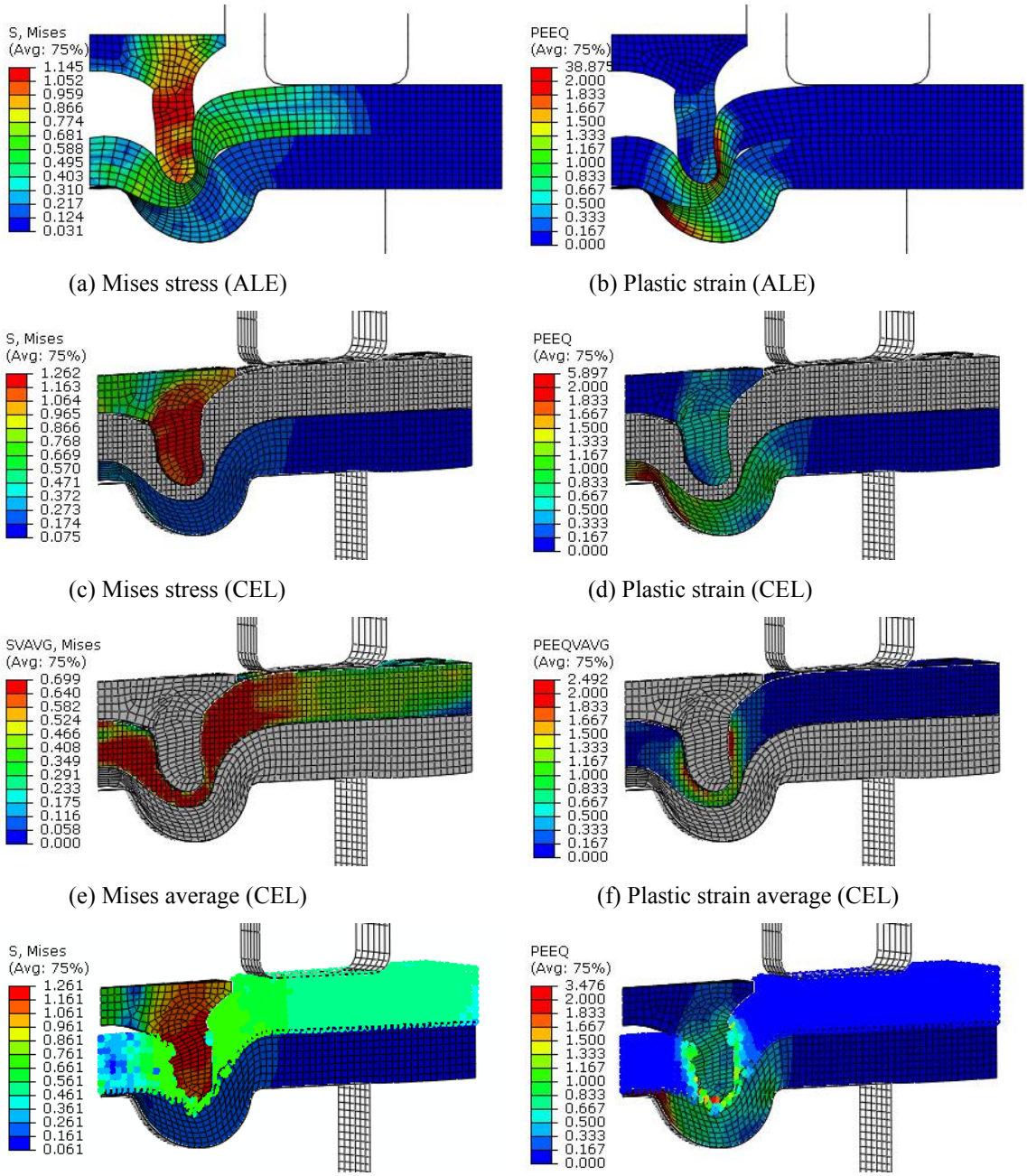

(a) Mises stress (ALE) (b) Plastic strain (ALE)

(c) Mises stress (CEL) (d) Plastic strain (CEL)

(e) Mises average (CEL) (f) Plastic strain average (CEL)

(g) Mises stress (SPH) (h) Plastic strain (SPH)

Figure 6: Results of SPFC590

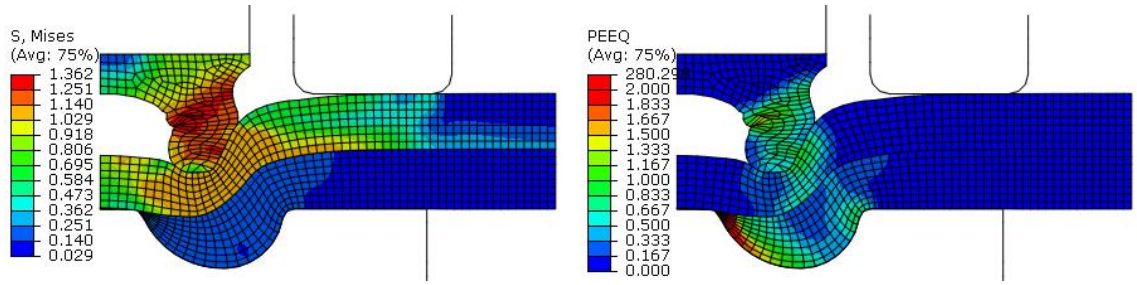

(a) Mises stress (ALE)

(b) Plastic strain (ALE)

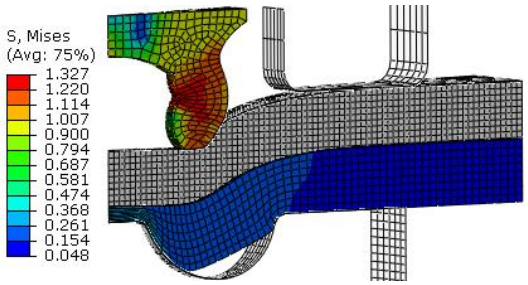

(c) Mises stress (CEL)

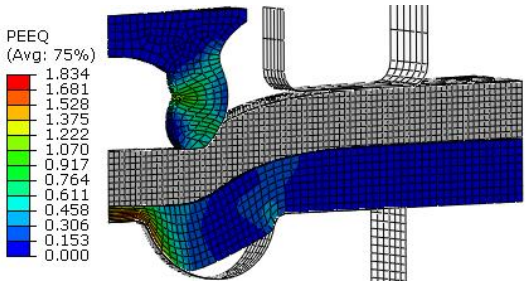

(d) Plastic strain (CEL)

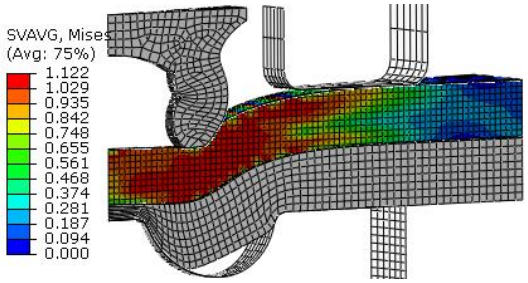

(e) Mises average (CEL)

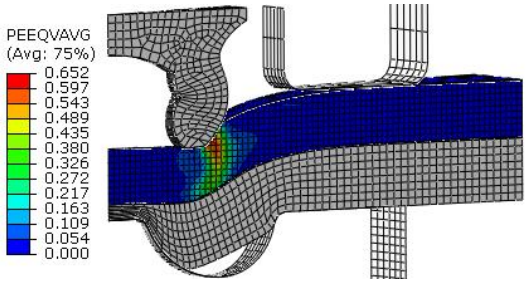

(f) Plastic strain average (CEL)

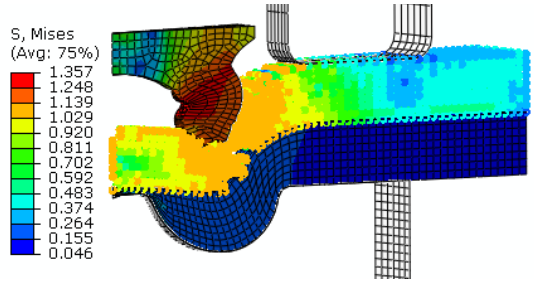

(g) Mises stress (SPH)

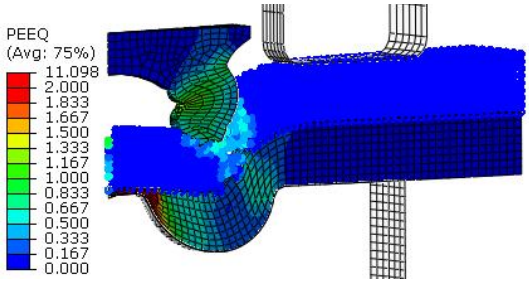

(h) Plastic strain (SPH)

Figure 7: Results of SPFC980

4 DISCUSSION

The focus of our research was to develop the analysis methodology to simulate the SPR forming process. To accomplish our objective we investigated the use of Abaqus/Explicit techniques which avoid the problem of large distortion of element and allow us to enter a new regime. This investigation provided the following important findings.

4.1 ALE

Nodes were relocated to proper position in accordance with deformation in ALE analysis by virtue of adaptive meshing. Since ALE cannot treat damage material, we were not able to see the rivet penetration to upper sheet. But this method is effective even in axisymmetric dimension and is easy to use with low cost. Thus we are able to achieve brief result for SPR process with various materials, die shapes and speeds. In another word, this method is effective to acquire optimal shape design with like Tosca structure.

4.2 CEL

Figure 8 indicated that each analysis method for each SPFC materials showed the same tendency of punch force. However the final forces of CEL were much larger than those of SPH. For instance, the total force of CEL440 was 71.9kN, while SPH440 was 54.1kN. This difference might cause from residual material around the top of rivet in CEL methods.

It was able to find the piercing of rivet in mild SPFC 440 or 590, also the analyses were completely done except hard material SPFC980. On the other hand, this method required enormous CPU time.

4.2 SPH

The rivet could penetrate the upper sheet as shown in Figure 9 (g) (h) for material of SPFC440. This SPH deformation was quite similar to Figure 1 which was a condition almost same as our numerical experiment. This similarity showed that our methodology was appropriate. But our testing condition showed a tendency of no penetration at lower sheet, because we neglected the damage on the lower sheet in this study. If we assume the state of the both sheets rupture, it is necessary to take different technique. Now we cannot use SPH and ALE together, therefore the hybrid method is expected.

SPH method provides insight into the forming mechanism of SPR; moreover the analysis wall time was much less than CEL methods. However it required special care to define the PC3D element for the sake of structure, position and density. For this reason, we developed the way of constructing PC3D elements from nodes composing normal hex diagonal solid elements. We found that our SPH modeling was effective for symmetric condition and we were able to manage particle behavior on the wedge faces for axisymmetric structure such as SPR with few CPU time.

5 CONCLUSION

In conclusion, we examined three methods of Abaqus/Explicit for SPR forming simulation. To acquire the appropriate deformation especially for penetration, we found that SPH method was remarkable way for SPR forming. However, we did not compare analysis and experiment results, therefore we need moreover study including comparison with experiment. As a future work, we have to compare analysis and experimental results. For this purpose, we are trying to do experiment for various shapes and materials, and we will present comparative study in the near future.

REFERENCES

[1] Abaqus Users Manual, Version 6.14-1, Dassault Systémes Simulia Corp., Providence, RI.
[2] Mori, K., "Assessing the suitability of materials for self-piercing riveting(SPR)," Self-piercing riveting Properties processing and applications, edited by Chrysanthou, A., Sun, X., Woodhead Publishing, Oxford, 2014.

XIV International Conference on Computational Plasticity. Fundamentals and Applications
COMPLAS 2017
E. Oñate, D.R.J. Owen, D. Peric and M. Chiumenti (Eds)

OBSERVABILITY OF QUALITY FEATURES OF SHEET METAL PARTS BASED ON METAMODELS

D. HARSCH[1], J. HEINGÄRTNER[1], D. HORTIG[2] AND P. HORA[3]

[1] inspire AG – ivp (Institute of Virtual Manufacturing)
Technoparkstrasse 1, 8005 Zurich, Switzerland,
harsch@inspire.ethz.ch, www.inspire.ethz.ch

[2] Daimler AG,
Käsbrünnlestr., 71059 Sindelfingen, Germany,
dirk.hortig@daimler.com, www.daimler.com

[3] ETH Zurich, Institute of Virtual Manufacturing,
Tannenstrasse 3, 8092 Zurich, Switzerland,
pavel.hora@ivp.mavt.ethz.ch, www.ivp.ethz.ch

Key words: Deep drawing, metamodeling, process window, process robustness.

Abstract. Deep drawn sheet metal parts are increasingly designed to the feasibility limit, thus achieving a robust process is often challenging. The fluctuation of process and material properties often leads to robustness problems. Especially skid impact lines can cause visible changes of the surface fine structure even after painting. Numerical simulations are used to detect critical regions and the influences on the skid impact lines. To enhance the agreement with the real process conditions, the measured material data and the force distribution are taken into account. The simulation metamodel contains the virtual knowledge of a particular forming process, which is determined based on a series of finite element simulations with variable input parameters. Based on these metamodels, innovative process windows can be displayed to determine the influences on the critical regions and on skid impact lines. By measuring the draw-in of the part, sensor positions can be identified. Each sensor observes the accordant quality criterion and is hence able to quantify potential splits, insufficient stretching, wrinkles or skid impact lines. Furthermore the virtual draw-in sensors and quality criteria are particularly useful for the assessment of the process observation of a subsequent process control.

1 INTRODUCTION

The fluctuation of process and material properties, as well as changing environmental conditions and the increasingly tighter tolerance requirements, often lead to robustness problems during series production [1][2]. The factors influencing robustness are not measured systematically, thus online action is limited to a manual intervention on a trial-and-error basis. The major disadvantages are the quality of the outcome is strongly correlated to the experience of the staff and eventual corrections are costly. Furthermore additional circumstances, such as

the reduction of the material thickness, complex geometries with sharp radii and the flexible choice of the press, limit the process stability even further.

The goal of the project is to inspect the critical regions at an early stage regarding robustness problems and to propose improvement measures based on the metamodels. By the use of accurate material models based on experiments, the implementation of digitized tool geometries and the consideration of the press construction, the significance and illustration accuracy of the simulation can be increased.

With the AutoForm version R7 it is possible to compute skid impact lines [3]. Another aim is to identify the influences on the simulatively determined quality criterion and to find a strategy how to avoid skid impact lines without cost-intensive rework and without using die inlets only by changing the press settings.

2 PROCESS DESCRIPTION

The front mudguard by Daimler shows critical behaviour in production, e.g. splits, insufficient stretch respectively hardening through minimal thinning and skid impact lines. Especially variations of the material properties through different batches of blanks have a large impact on the quality of the part. In particular the influence on skid impact lines is very pronounced. Therefore the simulation accuracy is enhanced through a variety of different arrangements.

2.1 Material model

The part is made out of aluminium AA6014 from Novelis (AC170). To approximate the material behaviour various experiments are used in a material model. The tensile experiments are used to capture the characteristic flow behaviour in rolling direction. With additional tensile experiments in 0°, 45° and 90° to rolling direction, the anisotropy coefficient, yield stress, tensile strength and equivalent strain are measured.

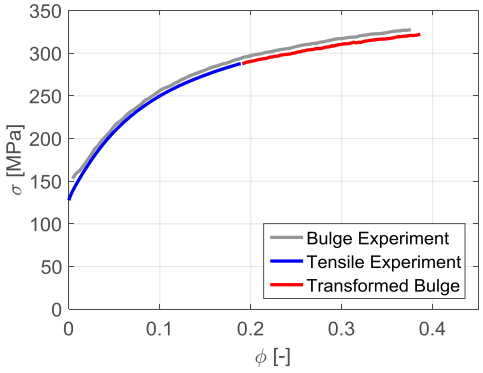

Figure 1: Flow curves of tensile and bulge experiments

This figure above shows the biaxial flow curve (grey). To enhance the prediction of the flow behaviour the biaxial stress state is transformed into a uniaxial stress state, by means of the principle of equivalent work [4]. The flow curve is then fitted with a combined S-H approach (Swift and Hockett-Sherby) [3]. The yield locus is fitted with the BBC model for the measured

data at room temperature. The M-value of the yield locus is assumed to be 8 because of the face-centered cubic crystal structure. The measured values of the anisotropy and of the stress ratios are listed in table 1. The ratio between the biaxial and uniaxial stress state is evaluated at 4% of logarithmic strain because of the measurement uncertainty at the beginning of the bulge test.

Table 1: Measured anisotropy and stress ratios for yield locus

Anisotropy	Values	Stresses	Values
r_0	0.714	σ_0	113.8 MPa
r_{45}	0.498	σ_{45}	112.7 MPa
r_{90}	0.711	σ_{90}	111.9 MPa
r_b	1	σ_b	118.4 MPa

The Forming Limit Curve (FLC) in Figure 2 (c) is measured by doing Nakajima experiments at room temperature. The evaluation method is based on the strain rate evolution by Volk and Hora (Volk 2011b) [5]. For each geometry at least three experiments are evaluated and then averaged. Finally the resulting points of the seven different types of specimen are connected with each other. The resulting line represents the limitation of the forming process because localized necking may occur.

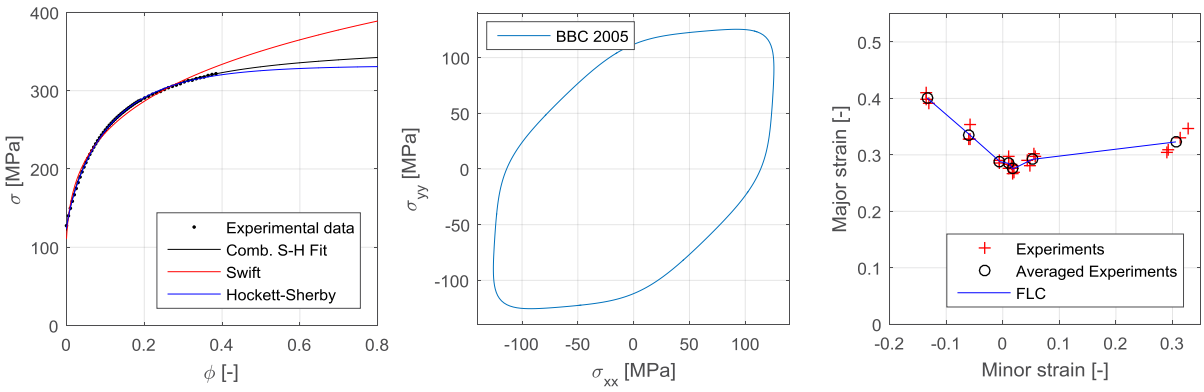

Figure 2: Experimental and fitted flow curve (a), yield locus (b) and FLC (c)

2.2 Tool geometries

After the design of the die addendum and the drawbeads in the method plan, the tool geometries are milled. Afterwards the geometries have to be processed by hand in tool tryout. Especially the drawbead geometries respectively the restraining forces of the drawbeads are adapted to avoid splits, wrinkles, sink marks or skid impact lines. Thereby, in case of a split the drawbeads are smoothed locally to increase the draw-in. Furthermore originally designed radii in the punch and in the die are harmonised. Typically the tryout is done in many loops. After each loop the influences of the made adjustments on the part quality are checked in the tryout press. These quite intense modifications of the tool geometries lead to very different simulation results [8]. Hence, the tools are digitised when tools are ready for serial pressing. The

digitalization is made with a GOM ATOS measurement system. The finalized and re-meshed geometries have a tolerance of maximum 10 microns.

2.3 Press construction

In AutoForm the common simulation setting is to use an initial pressure which is distributed homogenously. In reality the mechanical, single-acting press can be controlled over six die cushion forces, which transmit forces via cushion quills to the binder. Consequently they allow an inhomogeneous force distribution around the binder. Thus, the transmission of the binder force is adjusted in simulation in consideration of the positions of the cushion quills. This measure allows in simulation to redistribute the acting forces inhomogeneously on the binder surface by moving the force application point, in order to better map the set values on serial press [8].

In Figure 3 the positions of the six different die cushions is displayed.

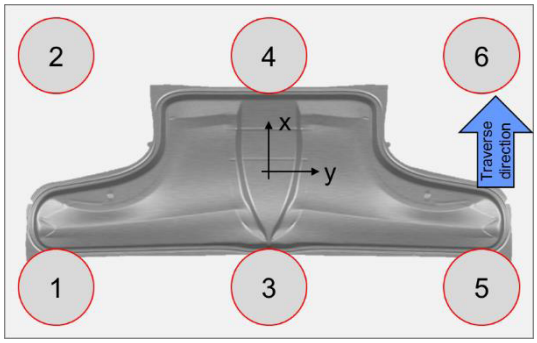

Figure 3: Positions of hydraulic die cushions

The press settings of the six die cushion forces are listed in table 2.

Table 2: Die cushion forces of press

Die cushion nr.	Force [kN]
1 / 3 / 5	470
2 / 4 / 6	450

In simulation the die cushion forces of the die cushions 1, 3 and 5 are reduced because of symmetry to the position of die cushion 3. The same goes for the upper die cushion row to position 4. In simulation this simplification does not influence the simulation result because in AutoForm the tools are assumed to be rigid [3].

Hence, with these two cushion forces it is possible to change the total binder force and the force distribution. The force distribution is computed as a force delta between the lower and the upper die cushion rows (see figure 3). The relation is expressed in equation (1).

$$\Delta F = (F_1+F_3+F_5) - (F_2+F_4+F_6) \quad (1)$$

3 VARIATIONAL SIMULATION

Deep drawing processes are influenced by many different parameters, such as material properties, tool temperature and thus lubrication behaviour. In case the process becomes unstable, the press settings are adjusted. Thereby typical measures are to change the total binder force or the force distribution. Some press operators also change the lubrication amount. In order to model the behaviour of the part when any material or process parameters change, variant simulations are computed.

The range of variation of each parameter has to be defined carefully. The range should correspond to the fluctuations during serial pressing. If the range is too large, the simulation results are unrealistic, thus the metamodels will be distorted. If the range is too small, the metamodel does not map the entire range of fluctuations.

The defined fluctuation range should be varied around a suitable operating point [8], [7]. Therefore a part is removed during serial production after the first deep drawing operation and then compared with the simulation. The material used in simulation corresponds to the used batch of material in production. The friction coefficient, total binder force and force distribution are adjusted to fit the draw-in of the produced part. With these simulation settings the simulated thinning distribution is compared with the measured thickness reduction of the part (see Figure 4). The measurement is performed with a GOM ATOS system in two different regions of the part. The figure below shows one of the regions.

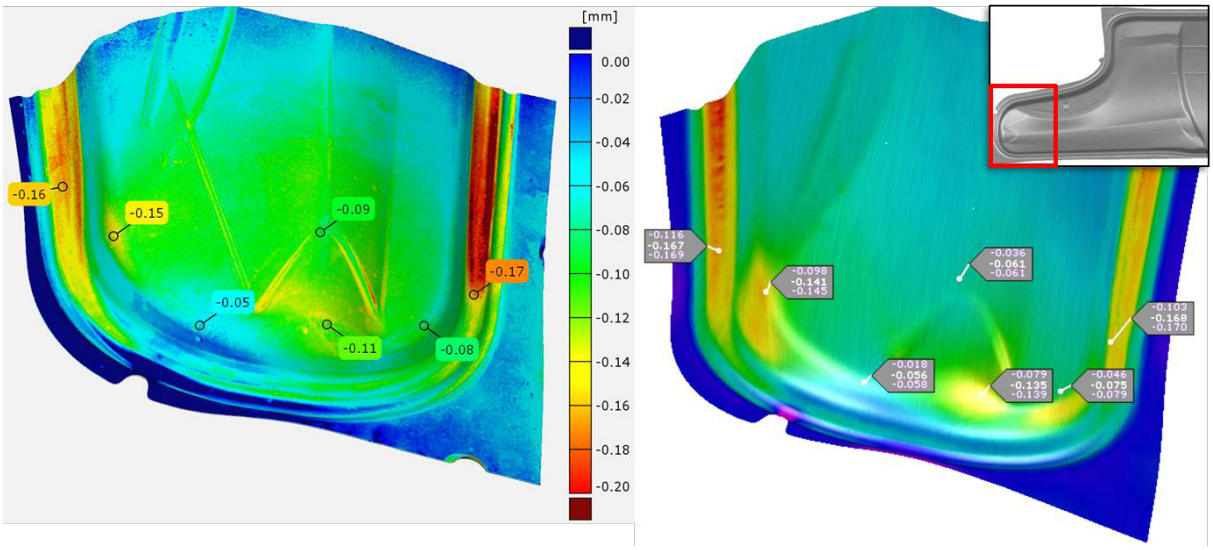

Figure 4: Comparison of thickness reduction between digitised part (left) and simulation (right)

The simulation result from AutoForm R7 is relatively close to the measurement. The deviations are mostly below 0.02 mm. Also the thinning of the material passing through the drawbead can be predicted by the simulation with a good accuracy. Differences in the thinning distribution are based on the simplifications in the simulation, such as the constant friction coefficient, the neglection of the tool deflection but also on the fluctuating initial blank thickness.

In view of the comparison of the thickness reduction, the equalized simulation is a suitable

operating point for the variational simulations. The defined ranges are shown in the table below. The forces are specified based on different press settings during serial production, the friction coefficients based on experience [9] and the material parameters based on the suppliers material data sheets. The design of experiment with 96 simulations is automatically created in AutoForm R7 according to the Latin Hypercube Sampling with six independent variation parameters. Although the variations of yield stress and tensile strength correlate with each other, they are varied independently to simulate low-quality (high yield stress, low tensile strength) and high-quality batches of material.

Table 3: Variation parameters and range

Variation parameter	Minimum	Nominal	Maximum
Binder force F_{tot}	2'000 kN	2760 kN	2'800 kN
Force distribution ΔF	-30 kN	60 kN	300 kN
Friction μ	0.09	0.11	0.13
Yield stress $\sigma_{0.2}$	103.8 MPa	113.8 MPa	123.8 MPa
Tensile strength σ_{ts}	225.4 MPa	235.4 MPa	245.4 MPa
r-values (r_0, r_{45}, r_{90})	-10%	0.71, 0.50, 0.71	+10%

3.1 Simulation criteria

In AutoForm R7 a wide range of result variables are available to quantify a potential quality feature in the part. For example splits can be detected by evaluating the result variables *Thinning* or *Max. Failure* (ratio of major strain to FLC). In the variational simulations three regions with risk of splits could be detected (see Figure 5). Additionally a skid line and a region with insufficient stretch below the skid line are identified to be critical. The criteria are slightly worse in the left half of the part (which corresponds to the mudguard on the right hand side of the car), which is why the following analyses are focused on the left side of the part.

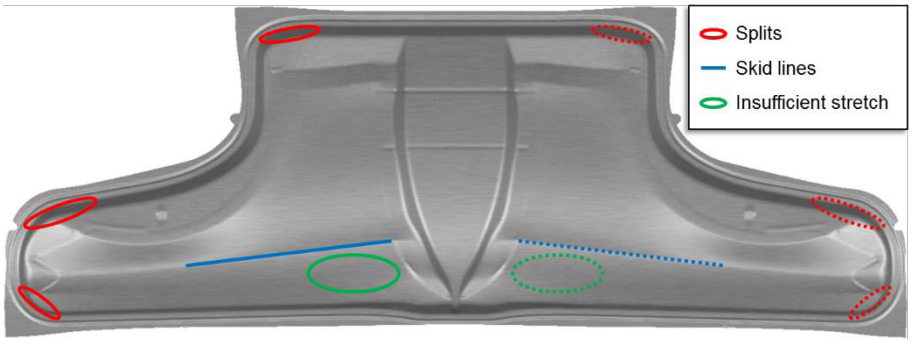

Figure 5: Defined simulation criteria of part

Skid lines represent damage to the sheet metal. They are clearly visible as scratch marks on the finished part. In case the material is dragged against sharp features of the tool after the first contact. They usually arise when the sheet is bended over a sharp angular feature and is subsequently pulled over this feature (e.g. drawbeads, die entry radius) or stretched over the top

of the punch (e.g. design features). If the skid lines are located in the visual range of the finished part, they should be avoided. By adjusting the binder force, changing the addendum design or the retention force of the drawbead through geometrical adaptions, the movement over the radius can be reduced. Thus, skid lines may be reduced or even avoided [3]. As the tools already exist and used for serial production, skid lines should be avoided without cost-intensive rework, therefore only by changing the press settings.

In AutoForm R7 skid lines are computed with two user defined analysis parameters: the maximum tool radius (curvature of tool) and the contact pressure between the tool and the sheet. If the curvature and the contact pressure exceed the predefined radius and pressure values in the same area, a skid line may occur [3].

After computing all simulations, the simulation criteria are defined for the different result variables. For each defined criterion a metamodel is fitted. The used types of metamodels are based on the *Response Surface Methodology*, whereby the polynomial degree is limited to a quadratic base model with interaction coefficients. Every metamodel is validated with the leave-one-out cross validation, to guarantee an appropriate model and to avoid an overfit.

Based on the metamodels the influences of the varied parameters on the defined criteria are quantified by using sensitivity analysis. The applied method is the *Fourier Amplitude Sensitivity Test* (FAST) [10]. The resulting sensitivities are shown in Figure 6.

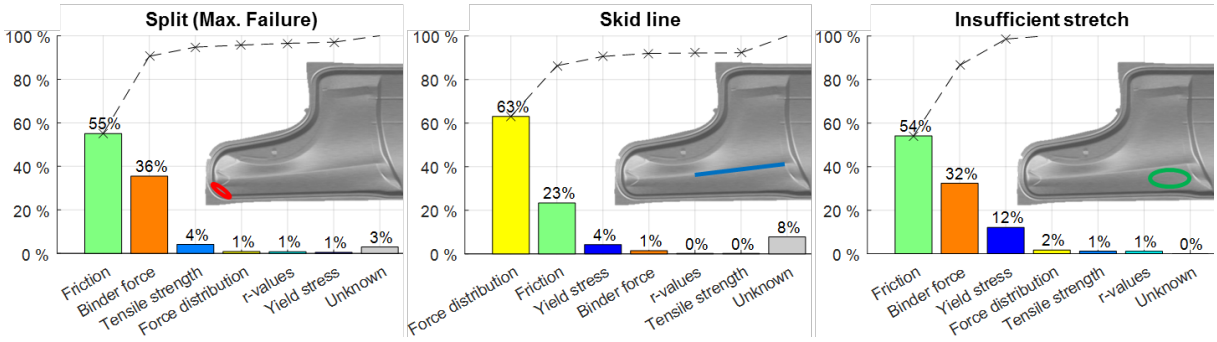

Figure 6: Sensitivities on splits (a), skid impact lines (b) and insufficient stretch (c)

The sensitivities for split criterion (Figure 6 a) point out the friction and binder force to be the most relevant parameters, which is a plausible behaviour. Furthermore the tensile strength shows a relatively small sensitivity. The higher the tensile strength is, the smaller the risk of splits. A similar behaviour could be identified for the insufficient stretch, apart from the not negligible dependence of the yield stress. The higher the yield stress is, the smaller will the stretching in this region turn out. The skid line conversely is primary depending on the force distribution. The metamodel suggest that an increasing friction, due to rising tool temperature during serial pressing, could be corrected by changing the force distribution.

3.2 Process window

In the current state of the art different process windows can be displayed, such as one- and two-dimensional process windows based on conservative minimum/maximum analysis, convex hulls and multi-dimensional hypercubes parallel to the axes. For each of these simplification

methods some information gets lost [11], [12].

Every simulation criteria and hence every metamodel is limited by an upper or lower limitation value, e.g. splits, more specifically the result variable from AutoForm *Max. Failure* [3], at 70% of the major strain in the FLC. By keeping the material properties and the force distribution at a constant value, the metamodel of the criterion is reduced to a three-dimensional surface in dependency of the binder force and the friction. The defined limitation value can now be visualised as a contour line. The projection of this line in the plane of the two remaining parameters (binder force and friction) illustrates the process boundary regarding this specific simulation criterion (see Figure 7, process boundary in red).

This approach is repeated for the remaining simulation criteria and provide further process boundaries. Skid lines are limited at 15 mm (process boundary in blue) and the insufficient stretch criterion at 1% thinning (process boundary in green). *(Note: These limitation values do not necessarily correspond to reality, because the simulation settings can significantly change the numerical results. However, the simulation behaviour shall be assumed to be similar to the real process behaviour.)*

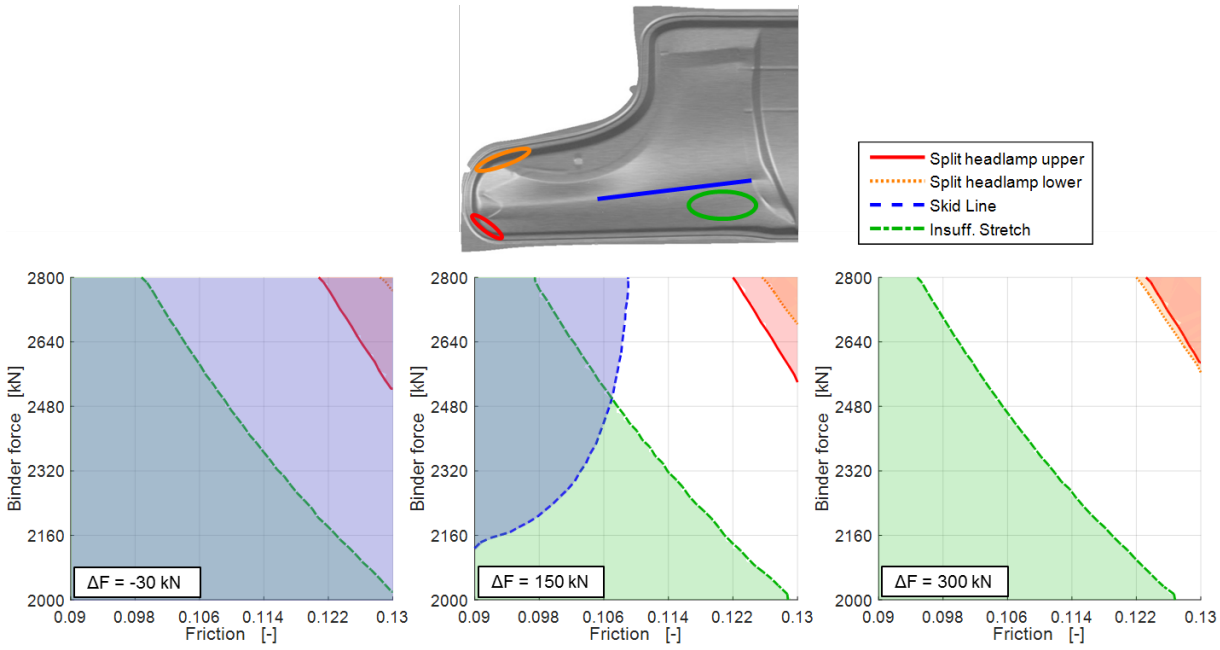

Figure 7: Process windows for different force distributions

The sensitivity analysis (see Figure 6) already pointed out, that the force distribution does not strongly influence the split and the insufficient stretch criteria. The skid lines conversely are significantly affected by changing force distributions. This behaviour can also be observed in Figure 7: If the forces on die cushions 2, 4 and 6 are increased respectively reduced on 1, 3 and 5 (see Figure 3), the skid lines might grow. To avoid skid lines the die cushion forces 1, 3 and 5 should be increased.

At the beginning of the serial production, the tools are cold and thus the friction is low. To reach nevertheless a sufficient stretching for the first part, the total binder force should be

increased at the beginning of the production. After the tools warm up and thereby the friction increases, the binder forces have to be reduced. Otherwise the process would run into risk of splits.

The shown process windows in Figure 7 are only valid for the pre-defined batch of material (see table 3 for nominal material properties). As soon as the material properties change, the process boundaries and thus the process window alters.

3.3 Influence of material on process windows

The fluctuations of the material properties in different batches of material can be very pronounced. Therefore the influences on the process window have to be analysed individually. For this two additional batches of material with various formability are exemplarily analysed. The resulting process windows are shown in Figure 8 below.

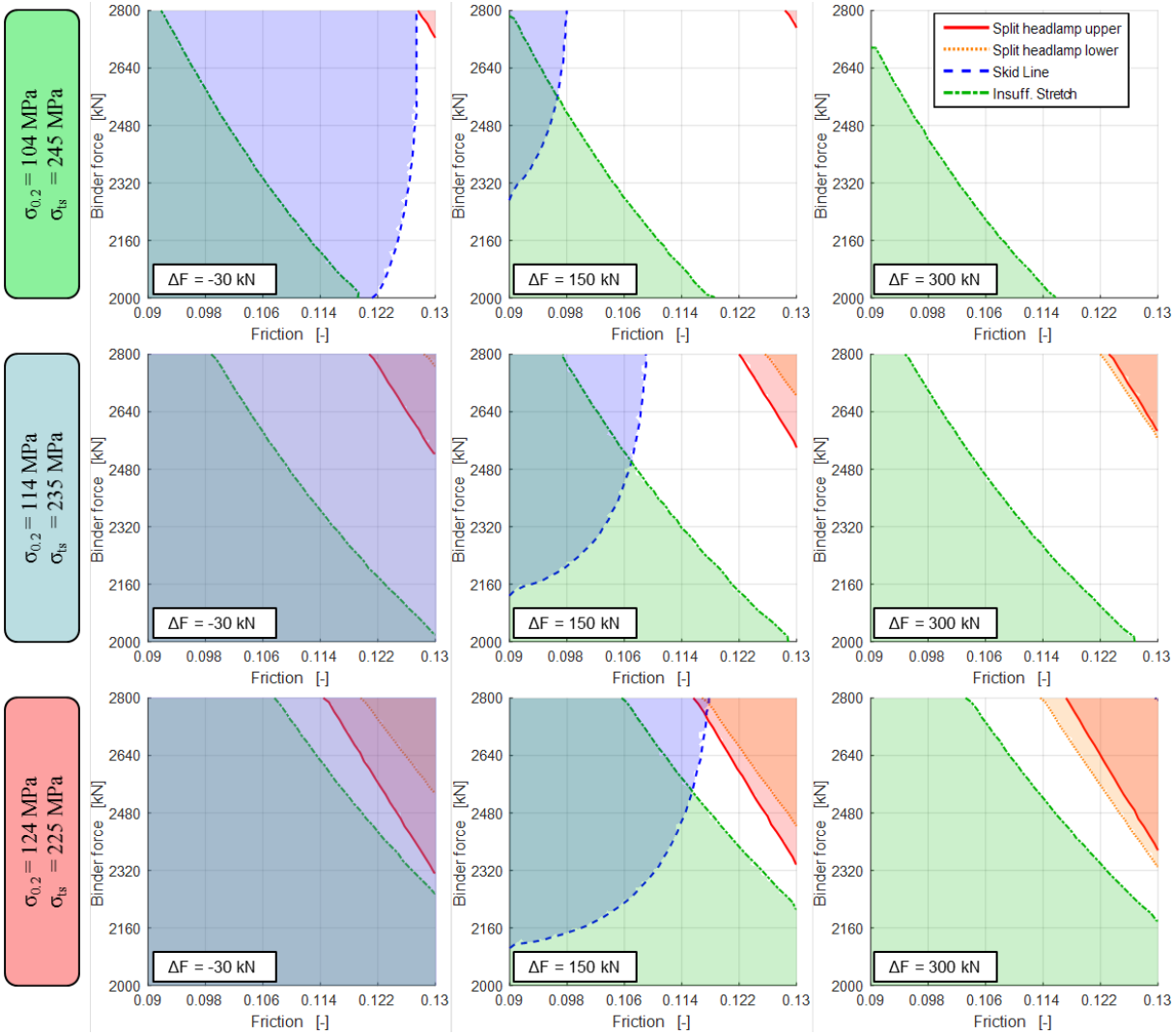

Figure 8: Process windows for three batches of material with different formability

In case a material batch with good formability characteristic (combination of low yield stress and high tensile strength) is used in production, risk of splits are very small. Also the process boundary due to insufficient stretch become less critical. Thus the process window gets bigger the process is more robust.

A material batch with bad formability characteristics (combination of high yield stress and low tensile strength) affects negatively the process boundaries. Although the skid lines can be avoided, the risk of splits and insufficient stretch are getting worse. The remaining process window becomes pretty narrow. Therefore the robustness is reduced, because small changes in friction lead to either risk of splits or insufficient stretch. Hence, the press settings should be adjusted more frequently.

Apart from that, the two different split criteria (red and orange) react differently to the force distribution. While the orange split criterion is getting worse for higher force deltas, the red one is not really affected. For large force deltas the orange split criterion is getting more critical compared to the red split criterion.

4 APPLICATION OF METAMODELS FOR PROCESS CONTROL

During serial pressing the quality criteria cannot be quantified as the simulation does. The part contains either a split or not. A precise statement about a numerical value (e.g. thinning of the material) is associated with high expenditures and costs. A much less expensive and more flexible approach is to measure the draw-in of the part optically in order to enable a quality assessment. For that it is essential to locate the draw-in measurement positions, which allow a reliable conclusion about the defined criteria in the part.

4.1 Selection of draw-in measurement positions

Based on the variation simulations in AutoForm the correlation between the draw-in and the values of the different simulation criteria are calculated [8]. For each criterion the correlations are displayed in colour around the part (see Figure 9).

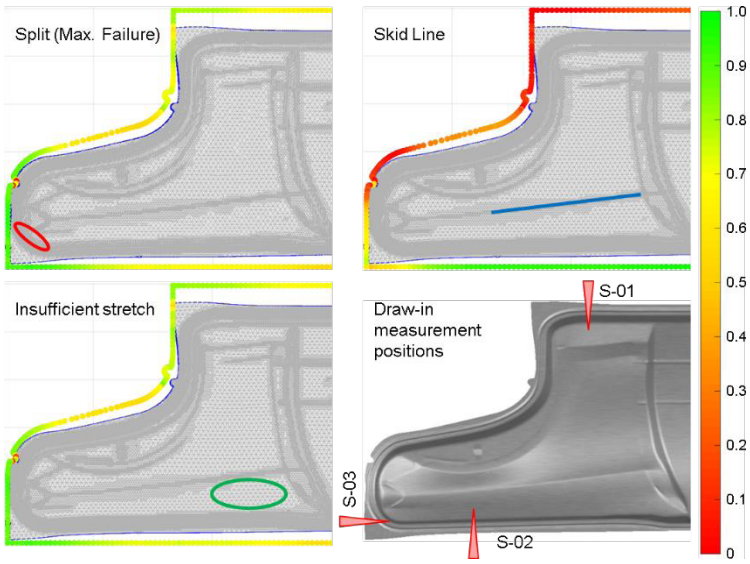

Figure 9: Absolute draw-in correlations and resulting draw-in measurement positions (on bottom right)

The selected draw-in measurement positions are placed in the regions with good correlation values over 0.75 with as many criteria as possible. Consequently some criteria can be observed by more than one draw-in measurement, which increases reliability (see table 4). To fully observe the detected simulation criteria of this part, three measurement positions are sufficient.

Table 4: Correlation values between virtual draw-in sensors and simulation criteria

Simulation criterion	S-01	S-02	S-03
Split headlamp	-0.75	-0.7	-0.91
Skid line	-0.03	0.94	0.7
Insufficient stretch	0.79	0.72	0.88

On the basis of the variational simulations the virtual draw-in measurements are fitted with metamodels. They contain the virtual knowledge how the process settings have to be changed in case the friction increases due to rising tool temperatures or in case another batch of material is processed.

4.2 Feed forward and feedback control

The previously generated knowledge of the process can be used in a feed forward approach to improve the part quality even before the feedback loop would be able to react. The feedback loop is used to compensate all non-measurable effects, such as changing friction conditions due to rising tool temperatures. Therefore the metamodels are evaluated [13].

If another batch of material is processed with different material properties, the strain distribution in the part, and thus the draw-in would change. To suppress a shift in draw-in and to keep the same part quality, the forces have to be adjusted. These adjustments are evaluated based on the corresponding draw-in metamodels [13]. The material properties are measured with an eddy-current measurement system [14].

5 CONCLUSION

With the newly released AutoForm version R7 it is possible to generate all required simulation criteria, though not transferable one-to-one to reality as numerical values. But the behaviour respectively the influences on the criteria can be modelled with sufficient reliability.

Multidimensional systems with different influencing parameters and complex relationships are very difficult for the press operator to get oriented trustworthy and to adjust the press settings accurately in case of any changes in the process. Therefore process windows are used to visualise the influences of the input variables on the simulation criteria. This kind of visualisation simplifies the understanding of the process and provides assistance to adjust the press settings.

For a subsequent process control the simulation results are adequate, because the metamodels are able to map the behaviour of the different input parameters on the draw-in. The metamodels provide a first approach how the press settings should be changed, before the part is produced. Changes in non-measurable effects, such as changing friction conditions, can be corrected based on the metamodels with a feedback control.

ACKNOWLEDGEMENTS

The authors are very grateful to the Daimler AG for providing the material, for digitising the tools and for the great opportunity to perform experiments on the press. The project partner AutoForm Engineering GmbH is also gratefully acknowledged for their support and contributions on the project results.

REFERENCES

[1] D. Hortig. *Experiences with the Robustness of sheet metal forming processes*. Forming Technology Forum 2011, Proceedings, Zürich, 2011.
[2] P. Hora, J. Heingärtner, N. Manopulo, L. Tong. *On the way from an Ideal Virtual Process to the Modelling of the Real Stochastic*. Forming Technology Forum 2011, Proceedings, Zürich, 2011.
[3] AutoForm R7.0.2 Software Manual. AutoForm Engineering GmbH, February 28, 2017.
[4] P. Peters. *Yield functions taking into account anisotropic hardening effects for an improved virtual representation of deep drawing processes*. Diss. ETH Nr. 22707, 2015.
[5] W. Volk, P. Hora. *New algorithm for a robust user-independent evaluation of beginning instability for the experimental FLC determination*. International Journal of Material Forming, Volume 4, Issue 3, pp 339-346, 2011.
[6] P. Fischer, D. Harsch, J. Heingärtner, Y. Renkci, P. Hora. *Inline feedback control for deep drawing applications*. The International Deep Drawing Research Group, Proceedings, 2016
[7] D. Harsch, J. Heingärtner, D. Hortig, P. Hora. *Process Windows for Sheet Metal Parts based on Metamodels*. Journal of Physics: Conference Series, Volume 734, Part B - General Papers, 2016.
[8] D. Harsch, J. Heingärtner, D. Hortig, P. Hora. *Virtual tryout planning in automotive industry based on simulation metamodels.* The International Deep Drawing Research Group, Proceedings, 2016.
[9] J. Krauer. *Erweiterte Werkstoffmodelle zur Beschreibung des thermischen Umformverhaltens metastabiler Stähle.* Diss. ETH Nr. 19070, ISBN 978-3-18-367602-6, 2010.
[10] F. Cannavó. *Sensitivity analysis for volcanic source modeling quality assessment and model selection.* Comput. Geosc., Vol. 44, pp. 52–59. 2012.
[11] C. Annen. *Entwicklung einer neuen Methode zur Ermittlung und Visualisierung von robusten Prozessfenstern in der Blechumformung.* Diss. ETH Nr. 20573, ISBN 978-3-906031-35-4, 2012.
[12] N. Stander, W. Roux, T.Goel, T. Eggleston, and K. Craig. *LS-OPT User's Manual*. Livermore Software Technology Corporation, pp. 9-11, 2009.
[13] P. Fischer , D. Harsch, J. Heingärtner, Y. Renkci, P. Hora. *A knowledge-based control system for the robust manufacturing of deep drawn parts*. International Conference on the Technology of Plasticity, ICTP 2017.
[14] J. Heingärtner, Y. Renkci, P. Hora. *Non-destructive testing of material properties*. 6th Forming Technology Forum, 2013.

XIV International Conference on Computational Plasticity. Fundamentals and Applications
COMPLAS 2017
E. Oñate, D.R.J. Owen, D. Peric and M. Chiumenti (Eds)

PHYSICAL MODELLING OF AMORPHOUS THERMOPLASTIC POLYMER AND NUMERICAL SIMULATION OF MICRO HOT EMBOSSING PROCESS

G. CHENG[*], T. BARRIERE[†], J-C. GELIN[†] AND M. SAHLI[†]

[*] Mechanics and Rheology Laboratory (LMR)
INSA Centre Val de Loire
3 rue de la Chocolaterie, CS 23410, 41034 Blois, France
email: gang.cheng@insa-cvl.fr

[†] FEMTO-ST Institute
Applied Mechanic Department
24 Rue de l'Epitaphe, 25000 Besançon, France
email: thierry.barriere@univ-fcomte.fr, jean-claude.gelin@univ-fcomte.fr, mohamed.sahli@femto-st.fr

Key words: hot embossing, modelling, thermoplastic polymers, viscoelasticity, numerical simulation, microfluidic device.

Abstract. Micro hot embossing process is considered as one of the most promising micro replication processes for manufacturing of polymeric components, especially for the high aspect ratio components and large surface structural components. A large number of hot embossing experimental results have been published, the material modelling and processes simulation to improve the quality of micro replication by hot embossing process are still lacking. This paper consists to 3D modelling of micro hot embossing process with amorphous thermoplastic polymers, including the mechanical characterisation of polymers properties, identification of the viscoelastic behaviour law of the polymers, numerical simulation and experimental investigation of micro hot embossing process. Static compression creep tests have been carried out to investigate the selected polymers' viscoelastic properties. The Generalized Maxwell model has been proposed to describe the relaxation modulus of the polymers and good agreement has been observed. The numerical simulation of the hot embossing process in 3D has been achieved by taking into account the viscoelastic behaviour of the polymers. The microfluidic devices with the thickness of 2 mm have been elaborated by hot embossing process. The hot embossing process has been carried out using horizontal injection/compression moulding equipment, especially developed for this study. A complete compression mould tool, equipped with the heating system, the cooling system, the ejection system and the vacuum system, has been designed and elaborated in our research. Polymer-based microfluidic devices have been successfully replicated by the hot embossing process using the compression system developed. Proper agreement between the numerical simulation and the experimental elaboration has been observed. It shows strong possibility for the development of the 3D numerical model to optimize the micro hot embossing process in the future.

1 INTRODUCTION

Micro hot embossing process is considered as one of the most promising micro replication processes for manufacturing of polymeric components [1]. It is used to elaborate the micro or nano components in diverse fields, thanks to its relatively lower cost for embossing tool, flexibility choice of embossing material and high replication accuracy for small features. In micro hot embossing process, the embossed material is always heated to a certain temperature, which allows the material flow into the cavities of mould insert. For amorphous thermoplastic polymers, the processing temperature is lightly above their glass transition temperature (Tg), which the massive changes in physical properties of polymer occur during this temperature range. More and more micro-components have been fabricated with thermoplastic polymers by micro hot embossing process during recent years, but the lack of the numerical modelling and simulation restricts the further development of the process [2]. The object of this work is to propose a 3D numerical model to investigate the effects of the hot embossing process parameters, such as embossing temperature, embossing pressure, processing time, on the replication accuracy of polymeric components.

Amorphous thermoplastic polymers have a randomly ordered molecular structure, unlike the highly ordered molecular structure of crystalline of semi-crystalline polymers. The amorphous thermoplastic polymers soften gradually as the temperature arises, allowing to a relatively larger moulding temperature range compared to the crystalline polymers. Various behaviour laws have been proposed in the literature in order to describe the physical behaviour of the amorphous thermoplastic polymers used in the micro hot embossing process [3-9]. The viscoelastic model has been widely applied in the numerical simulation of hot embossing process because of its efficiency in numerical computation and its well-fitting with the experimental characterization [10].

This paper consists to 3D modelling of micro hot embossing process with amorphous thermoplastic polymers, including the mechanical characterisation of polymers properties, identification of the viscoelastic behaviour law of the polymers, numerical simulation and experimental investigation of micro hot embossing process. Static compression creep tests have been carried out to investigate the selected polymers' viscoelastic properties. The Generalized Maxwell model has been proposed to describe the relaxation modulus of the polymers and good agreement has been observed. The numerical simulation of the hot embossing process in 3D has been achieved by taking into account the viscoelastic behaviour of the polymers. Different loads have been applied on the mould die insert and the viscoelastic responses of the polymer substrate have been investigated in the simulation. The microfluidic devices with the thickness of 2 mm have been elaborated by hot embossing process. The comparison between the numerical simulation and the experiments shows proper agreement for the prediction of the polymer substrate deformation using the hot embossing process.

2 MODELLING APPROACH

In the numerical simulation of the hot embossing process, the mould die cavity was considered as a rigid body, and the polymer substrate exhibits the viscoelastic behaviour. The related constitutive equations have been implemented in the software. The stress tensor of the viscoelastic material is separated mathematically in two parts [11], the volumetric stress and

the deviatoric stress, as shown in the following equation:

$$\sigma = K_b \varepsilon_v \mathrm{I} + \sigma_d \tag{1}$$

where is K_b the bulk modulus, ε_v is the volumetric strain, I is the identity matrix, and σ_d is the deviatoric stress.

The strain tensor of the viscoelastic material is written as:

$$\varepsilon = \frac{1}{3}\varepsilon_v \mathrm{I} + \varepsilon_d \tag{2}$$

where ε_d is the deviatoric strain, with the volumetric strain given by:

$$\varepsilon_v = trace(\varepsilon_{ij}) \tag{3}$$

The general dependence of the deviatoric stress on the strain history could be expressed in the form:

$$\sigma_d = 2\int_0^t G_{(t-t')}(\partial \varepsilon_d / \partial t')dt' \tag{4}$$

where $G_{(t)}$ is the shear modulus, which could be obtained by the well-known relationship with the elastic modulus for homogeneous isotropic materials:

$$G_{(t)} = E^{cr} / (2(1+\upsilon)) \tag{5}$$

where υ is Poisson's ratio, and E^{cr} is the relaxation modulus identified in the compression creep tests.

3 IDENTIFICATION OF VISCOELALSITC PROPRETIES THERMOPLASTIC POLYMER

The true stress vs. time and true strain vs. time curves of the amorphous polymer PMMA have been obtained from compression creep tests at the hot embossing temperature range from Tg+ 20◦C to Tg+ 40◦C. The relaxation modulus, expressed as the ratio between the true stress and true strain of the polymer specimens during the creep tests, could thereby be obtained. The relaxation moduli of the PMMA are presented in Figure 1. The relaxation modulus of the polymer decreases with respect to time at different testing temperatures in short-term compression creep tests. With the increase of the testing temperature, the relaxation modulus decreases. The relaxation modulus exhibits a sudden decline at the beginning of the compression creep tests and then decreases smoothly with time.

In this study, the Generalized Maxwell model was used to describe the relaxation modulus of the amorphous PMMA specimens with respect to time, as obtained from the compression creep tests. Two relaxation time constants have been characterized to fit the experimental data from the compression creep tests. The compression relaxation modulus E^{cr} of polymer could

be expressed as follows:

$$E^{cr} = E_{\infty}^{cr} + E_1^{cr} \exp\left(\frac{-t}{\tau_1^{cr}}\right) + E_2^{cr} \exp\left(\frac{-t}{\tau_2^{cr}}\right) \tag{6}$$

where E_{∞}^{cr} is the relaxation modulus when time becomes infinite, t represents time, E_1^{cr} and τ_1^{cr} are the relaxation modulus and relaxation time at 1-branch, respectively, and E_2^{cr} and τ_2^{cr} are the relaxation modulus and relaxation time at 2-branch, respectively.

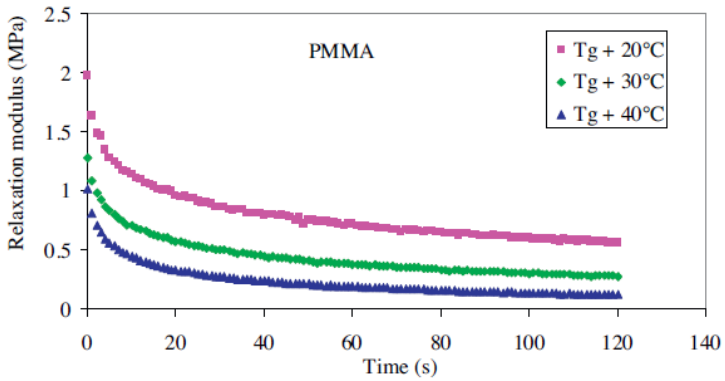

Figure 1: Relaxation modulus of PMMA at Tg+ 20◦C, Tg+ 30◦C and Tg+ 40◦C in short-term compression creep tests.

4 NUMERICAL SIMULATION OF HOT EMBOSSING PROCESS

In this study, a 3D model composed by the polymer substrate and the micro mould die cavity insert was created in the simulation. The mould was considered as a rigid body, which was supposed to be undeformable during the simulation. The polymers substrate was considered as viscoelastic material, described by the Generalized Maxwell model using the identification parameters obtained in compression creep tests. The simulation of the hot embossing process was effectuated at Tg+ 20◦C, Tg+ 30◦C and Tg+ 40◦C. The imposed loads were applied on the mould die cavity insert. The bottom surface of the polymer substrate was fixed, and the displacement of this surface was imposed as 0.

4.1 Hot embossing with fixed compression displacement

The polymer substrate was first compressed with a fixed compression displacement of 0.1 mm with a constant compression speed, shown in Figure 2. The compression tests lasted for 30 s at each compression temperature. Figure 2(a) presents the total displacement of the top surface of the polymer substrate. The reservoir and the channel exhibit almost the same displacement, because the displacement imposed on the mould die insert is the same everywhere. A cutting line in the reservoir zone on the top surface of the polymer substrate, which passes through the center of the reservoir, shown in Figure 2(b), has been selected in order to investigate the displacement profile. Figure 3(c) shows the displacement profile of the polymer PMMA substrate at the cutting line at different compression temperature. The initial height of the polymer substrate is approximately 2 mm and it is compressed by the

mould die insert during the simulation test. The displacement of the polymer substrate in the reservoir zone is approximately 0.1 mm, which is equal to the applied compression displacement. There is not significant difference in the displacement of the polymer substrate among the different compression temperatures. However, the displacement ofthe polymer substrate at Tg+ 40◦C is a little more significant than that at Tg+ 20◦C. This demonstrates that with the same applied compression displacement, the polymer substrate exhibits a larger displacement at a higher compression temperature.

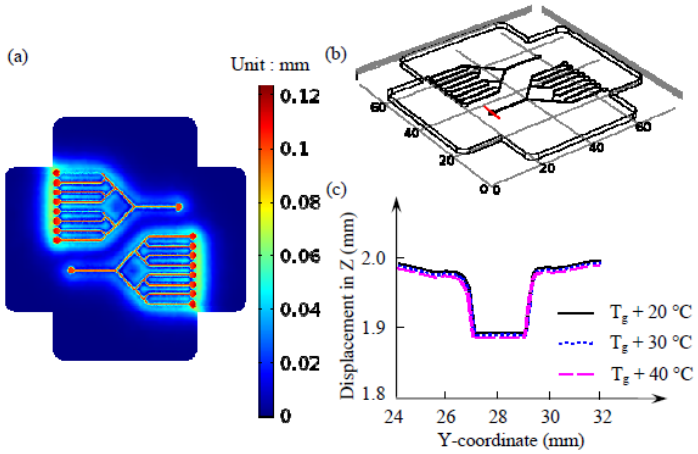

Figure 2: (a) Displacement of the polymer PMMA substrate in the hot embossing simulation with fixed compression displacement 0.1mm at Tg + 20 °C, (b) location of the cutting line on the top surface of the polymer substrate and (c) displacement profile of the cutting line at the end of the testing time at different compression temperature.

4.2 Hot embossing with constant pressure

The polymer substrate was then compressed with a constant pressure of 1 MPa for 30 s at each compression constant pressure of 1 MPa at different compression temperatures, shown in Figure 3. The initial height of the polymer substrate is approximately 2 mm, and it is compressed by the mould die insert at constant pressure during the simulation test. In this test, the difference in the displacement of the polymer substrate in the reservoir zone at different compression temperatures is more significant than in the previous simulation test. Figure 3(a) shows the total displacement of the top surface of the polymer PMMA substrate with applied pressure 0.1 MPa at Tg + 40 °C in the hot embossing simulation. A cutting line in the reservoir zone on the top surface of the polymer substrate, which passes through the centre of the reservoir, shown in Figure 3(b), has been selected in order to investigate the displacement profile. Figure 3(c) shows the displacement profile of the polymer PMMA substrate at the cutting line at different applied pressures. The displacement of the polymer substrate increases with the rise of the compression temperature. When the applied pressure on the mould die insert is fixed at 1 MPa, the displacement of the polymer substrate is approximately 0.8 mm at Tg+ 20◦C, and the displacement increases to approximately 1.6 mm at Tg+ 40◦C. This demonstrates that with the same applied pressure, a polymer substrate exhibits a larger displacement at a higher compression temperature.

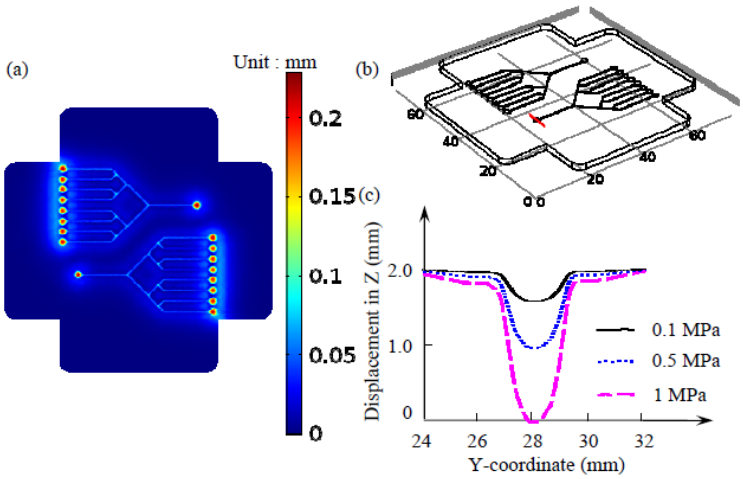

Figure 3: (*a*) Displacement of the polymer PMMA substrate in the hot embossing simulation with constant pressure 1 MPa at Tg + 20 °C, (b) location of the cutting line on the top surface of the polymer substrate and (c) displacement profile of the cutting line at the end of the testing time at different compression temperature.

5 EXPERIMENTAL INVESTIGATION WITH MICROFLUIDIC DEVICE

The replication of microfluidic devices has been effectuated with horizontal electric injection/compression moulding equipment. Mould die inserts with three different cavity dimensions have been developed in this study to obtain microfluidic devices. The height of the micro mould die cavities on the three moulds is approximately 200 µm, 100 µm and 50 µm, respectively.

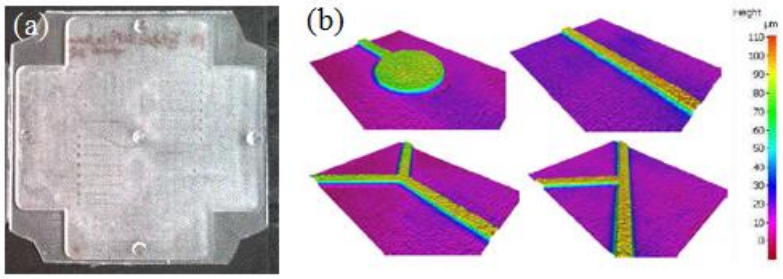

Figure 4: (*a*) PMMA microfluidic devices obtained with the mould die insert (100 µm) by the hot embossing process (b) 3D images of the selected zones of the silicone replicas elaborated from the PMMA microfluidic device.

It shows us that microfluidic devices based on PMMA substrates have been successfully obtained using the three mould die cavities. Figure 4(a) shows the microfluidic device obtained using the mould die cavities with the height of the cavities equal to 100 µm. It seems that the micro cavities in the mould die insert are well filled by the polymer flow. There are no significant replication defects visible on the microfluidic devices. The microfluidic devices produced from thermoplastic polymer substrates are optically transparent, which cause difficulties in measuring their dimensions and surface topography directly with an optical method. Therefore, room temperature vulcanizing (RTV) silicone rubber was used to replicate

the negative micro pattern on the microfluidic devices. Figure 4(b) shows the 3D images of the silicone replicas elaborated from these microfluidic devices. Four zones in the replica were observed to investigate the shape transfer efficiency using the hot embossing process. A proper replication was achieved by effectuating the comparison with the images obtained for micro mould die cavity insert.

A comparison between the numerical results and the experimental results has been made to verify the physical modelling accuracy for the hot embossing process. The identical boundary conditions have been applied for the numerical and experimental tests to make this comparison. PMMA has been compressed at the compression temperature of Tg+ 40◦C for 30 s in the hot embossing process. The displacement imposed on the polymer substrate is fixed at 0.1 mm in the numerical simulation, and the gap imposed is fixed to make sure to compress the polymer substrate by 0.1 mm for the experimental test. One cutting line on the polymer PMMA substrate, located in the reservoir zone, has been drawn to compare the micro cavity geometry after the hot embossing process. The 3D image of the reservoir zone has been obtained by an optical profilometer. The 2D contour of the reservoir has been obtained to enable the comparison of the simulation and numerical results. The 2D contours of the polymer substrate in the same position, both in the numerical and in the experimental results, has been shown in Figure 5. This shows that the diameter of the reservoir is approximately 2000 µm in the numerical simulation, and in the experimental result, the value is approximately 1980 µm. The difference between the simulation result and the experimental result is probably due to the deviation in the selections of the cutting line and the 2D con-tour of the microfluidic device. The simulation results show suitable agreement for the prediction of the polymer substrate deformation in the replication of a microfluidic device using the hot embossing process.

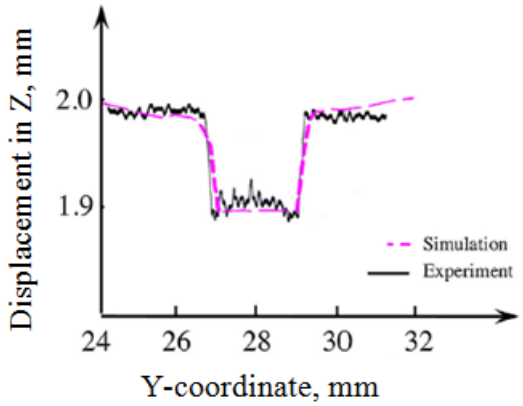

Figure 5: Comparison of the displacement profile on cross section of the reservoir zone of the PMMA microfluidic device obtained by hot embossing process with a fixed compression displacement of 0.1 mm at Tg+ 40◦C.

6 CONCLUSIONS AND PERSPECTIVES

This research work consists on the 3D modelling of the micro hot embossing process using the amorphous thermoplastic polymers. Uniaxial compression creeping tests on cylindrical polymer specimens were carried on in the temperature range from Tg+ 20◦C–Tg+ 40◦C. The relaxation moduli of polymers at Tg+ 20◦C, Tg+ 30◦C and Tg+ 40◦C were obtained with

respect to time. The Generalized Maxwell model with two branches was used to characterize the viscoelastic behaviour of the polymer in the compressing creep tests. Acceptable agreement has been observed by the comparison of experimental data with the fitting models. The Generalized Maxwell model using the parameters identified in the compression creep tests has been used to describe the polymer behaviour in the hot embossing process. The numerical simulation of the filling stage of the hot embossing process has been achieved by taking into account the modelling of the viscoelastic behaviour of amorphous thermoplastic polymers. Polymer-based microfluidic devices have been successfully replicated by the hot embossing process using the compression system developed in our group. Proper agreement between the numerical simulation and the experimental elaboration has been observed. It shows strong possibility for the development of the 3D numerical model to optimise the micro hot embossing process in the future.

REFERENCES

[1] Worgull, W. *Hot Embossing: Theory and Technology of Microreplication*. Elsevier, Burlington (2009).

[2] Worgull, W. and Heckele, M. New aspects of simulation in hot embossing. *Microsyst. Technol.* (2004) **10**:432-437.

[3] Govert L.E., Timmermans P.H.M., Brekelmans W.A.M. The influence of intrinsic strain softening on strain localization in polycarbonate: modeling and experimental validation. *J. Eng. Mater. -T. ASME* (2000) **122**:177-185.

[4] Anand, L. and Gurtin, M.E. A theory of amorphous solids undergoing large deformations with applications to polymeric glasses. *Int. J. Solids Struct.* (2003) **40**:1465-1487.

[5] Anand, L. and Ames, N.M. On modeling the micro-indentation response of anamorphous polymer. *Int. J. Plasticity* (2006) **22**:1123-1170.

[6] Rinaldi R., Gaertner R., Chazeau L. Gauthier C. Modelling of the mechanical behaviour of amorphous glassy polymer based on the Quasi Point Defect theory—Part I: Uniaxial validation on polycarbonate. *Int. J. Nonlinear Mech.* (2011) **46**:496-506.

[7] Srivastava V., Chester S.A., Ames N.M., Anand L. A thermo-mechanically-coupled large deformation theory for amorphous polymers in a temperature range which spans their glass transition. *Int. J. Plasticity* (2010) **26**:1138-1182.

[8] Fleischhauer R., Dal H., Kaliske M., Schneider K. A constitutive model for finite deformation of amorphous polymers. *Int. J. Mech. Sci.*(2012) **65**:48-63.

[9] Holopainen S. Modeling of the mechanical behavior of amorphous glassy polymers under variable loadings and comparison with state-of-the-art model predictions. *Mech. Mater.* (2013) **66**:35-58.

[10] Cheng G., Sahli M., Gelin J.C. and Barrière T. Process parameter effects on dimensional accuracy of a hot embossing process for polymer-based micro-fluidic device manufacturing. *Int. J. Adv Manuf. Technol.* (2014) **75**:225-235.

[11] Cheng G., Sahli M., Gelin J.C. and Barrière T. Physical modelling, numerical simulation and experimental investigation of microfluidic devices with amorphous thermoplastic polymers using a hot embossing process. *J. Mater. Process. Technol.* (2016) **229**:36-53.

XIV International Conference on Computational Plasticity. Fundamentals and Applications
COMPLAS XIV
E. Oñate, D.R.J. Owen, D. Peric & M. Chiumenti (Eds)

3D FINITE ELEMENT SIMULATIONS OF REINFORCED CONCRETE ELEMENTS EXPOSED TO FIRE

Erol Lale*, Chiara Ceccato†

* Department of Civil Engineering
Istanbul Technical University
34469 Maslak Istanbul, Turkey
e-mail: lale@itu.edu.tr

†Dept. of Civil and Environmental Engineering
Hong Kong Polytechnic Univ., Hong Kong, China
e-mail: chiara.ceccato@polyu.edu.hk

Key words: Fire, concrete, transient creep, damage-plasticity, finite elements

Abstract. Fire could dramatically reduce strength of reinforced concrete elements and it is considered one of the major threats for the structural safety of buildings: structural members may even collapse due to intensity and duration of fire. In this study, 3D finite element simulations of reinforced concrete elements under fire loading are presented. A quasi static one-way-coupled thermo-mechanical analysis is carried out, in which a heat transfer simulation is conducted first and then internal forces are computed. A phenomenological constitutive model based on damage-plasticity is used for concrete at high temperature. Transient creep strains are included in the model for elevated temperature. Extended Leon model is used for yield function and isotropic damage is assumed. Numerical results are compared with experimental data found in the literature, showing good agreement.

1 INTRODUCTION

Concrete, as one of the most widely used construction material, is likely exposed to high temperature, in case of extreme events such as explosions and during fire or in special structures such as nuclear vessels. Its mechanical properties, like density, thermal expansion, and thermal conductivity, require a careful evaluation in order for the material performance to be understood under extreme high temperature. In general, strength and stiffness of concrete decrease with the increase of temperature and degradation of concrete mechanical behaviors mainly results from dehydration of concrete at the micro-level [1]. The behavior of concrete though is particularly complex to predict, due to the differences of each constitution in terms of thermal response, with several factors affecting the fire resistance (eg. concrete strength, moisture content, concrete density, aggregate type). For example, high strength concrete (HSC) has lower permeability and water-cement

ratio than normal strength concrete (NSC), therefore, under high temperature exposure, moisture can escape with a slower rate, leading to a faster increase in pore pressure and consequently a major reduction in load bearing capacity [2]. Thus, fire design and assessment of structure has become a fundamental aspect of structural design and, in this contest, urges the development of computational models capable of accurately capturing the behavior of reinforced concrete elements at elevated temperatures.
In this study, a plastic damage model for the simulation of concrete behavior under elevated temperature has been developed. The constitutive model adopted is based on isotropic damage coupled with plasticity in effective stress space. While hardening under compressive loading is modeled within the plasticity framework, softening under both tensile and compressive loadings are taken into account within the damage mechanics framework, where damage is modeled as a function of plastic strains. A sequential coupled thermo-mechanical analysis has been chosen: firstly, a transient heat transfer analysis is carried out to determine the temperature distribution over the specimen; then, based on its results, a mechanical analysis is conducted. For thermal analysis, material parameters such as specific heat, thermal conductivity coefficient are taken from standard design codes or experimental studies found in literature such as [3, 1]. Moisture diffusion and phase change during elevated temperatures are not considered at this stage.

2 Constitutive Model

The total strain tensor can be decomposed into mechanical strain ϵ_σ, free thermal strain ϵ_{fth}, creep strain ε_{cr}, and transient creep strain ε_{tcr}, as shown below:

$$\epsilon_{total} = \epsilon_\sigma + \epsilon_{fth} + \epsilon_{cr} + \epsilon_{tcr} \tag{1}$$

Generally, the creep strain is considerably smaller than the other strain components in fire applications, due to the short duration of a fire events and, therefore, it can be neglected for fire safety assessment of structures [4].

2.1 Constitutive Model at ambitious temperature

According to incremental theory of plasticity, the mechanical strain tensor ϵ_σ can be split into elastic ϵ^e and plastic components, ϵ^p:

$$\epsilon_\sigma = \epsilon_e + \epsilon_p \tag{2}$$

The elastic part is the recoverable portion of the total strain and, considering linear elasticity, it is given by

$$\epsilon_e = D^{-1}\sigma \tag{3}$$

where D and σ are the elasticity tensor and the stress tensor respectively. By using these two equations, stress relation with strain can be defined as:

$$\sigma = D\left(\epsilon - \epsilon_p\right) \tag{4}$$

If we assume that the stiffness degradation is isotropic (scalar), then the stiffness tensor is written as:

$$D = (1 - \omega) D^e \tag{5}$$

where ω is the damage parameter and D^e is the initial elasticity tensor. Substitution of equation (4) into (3) leads to the following equation:

$$\sigma = (1 - \omega) D^e (\epsilon - \epsilon_p) = (1 - \omega) \bar{\sigma} \tag{6}$$

where $\bar{\sigma}$ is the effective stress, defined as:

$$\bar{\sigma} = D^e (\epsilon - \epsilon_p) \tag{7}$$

According to this equation, the constitutive relation for the damage response can be decoupled from the plastic response, providing numerical advantages.

Several combined plasticity and damage models have been developed in recent years. To ensure that a constitutive model remains thermodynamically admissible, the second principle of thermodynamics must be satisfied, which requires non-negative dissipation and this condition leads to certain constraints on the constitutive model. Grassl and Jirasek [5] studied thermodynamic admissibility of different types of coupling of damage and plasticity and have shown that, formulating the plasticity constitutive model in terms of effective stress, the only condition required for the thermodynamic admissibility is the softening plastic modulus not to drop below a critical value, given by the pure plastic model.

2.1.1 Plasticity Formulation

In order to obtain the effective stress due to strain increment, the increase of plastic strain has to be estimated. Plasticity formulations require a yield function, a flow rule and a hardening rule:

$$\begin{aligned} f^p (\bar{\sigma}, \kappa_p) &\leq 0 \\ \dot{\epsilon_p} &= \dot{\lambda} \frac{\delta g^p}{\delta \bar{\sigma}} \\ \dot{\kappa_p} &= \dot{\lambda} H. \end{aligned} \tag{8}$$

The Kuhn-Tucker conditions for loading-unloading need to be satisfied: $f^p (\bar{\sigma}, \kappa_p) \leq 0$,$\dot{\lambda} \geq 0$, $\dot{\lambda} f^p (\bar{\sigma}, \kappa_p) = 0$. Here f^p and g^p denote the yield surface and the plastic potential function respectively, λ_p is the plastic multiplier, $\kappa_p = [\kappa_p^t, \kappa_p^c]$ is (accumulated plastic strains) plastic state variables, and H is the matrix for multiaxial stress situation:

$$H (\bar{\sigma}, \epsilon^p) = \begin{bmatrix} \chi(\hat{\bar{\sigma}}) & 0 & 0 \\ 0 & 0 & -(1 - \chi(\hat{\bar{\sigma}})) \end{bmatrix} \frac{\delta g^p}{\delta \hat{\bar{\sigma}}} \tag{9}$$

where $\hat{\bar{\sigma}}$ denotes the principal effective stress and χ is a weight factor defined as [6] :

$$\chi = \sum_{i=1}^{3} \langle \hat{\bar{\sigma}} \rangle / \sum_{i=1}^{3} |\hat{\bar{\sigma}}| \tag{10}$$

The extended Leon Model, successfully used for the simulation of the concrete behavior under uniaxial, biaxial and multi-axial loadings by many researchers [7, 8, 5, 9], is employed in this study for the definition of the yield surface, which is smooth and convex except for the point where parabolic meridians intersect the hydrostatic axis. The yield function is given in terms of invariant of effective stress tensor, hardening parameter, k and friction parameter, m_0 as follows:

$$f^p = \left[(1-k) \left(\frac{\bar{p}}{f_c} + \frac{\bar{\rho}}{\sqrt{6} f_c} \right)^2 + \sqrt{\frac{3}{2}} \frac{\bar{\rho}}{f_c} \right]^2 + k^2 \, m_0 \left(\frac{\bar{p}}{f_c} + \frac{\bar{\rho} \, r(\theta)}{\sqrt{6} f_c} \right) - k^2 = 0 \tag{11}$$

where $\bar{p} = \bar{I}_1/3$, $\bar{\rho} = \sqrt{2\bar{J}_2}$, $\theta = cos^{-1}\left(3\sqrt{3}/2\bar{J}_3/\bar{J}_2{}^{3/2}\right)/3$ denote the effective mean stress, the deviatoric radius and the Lode angle respectively and $\bar{I}_1$ is the first invariant of stress tensor, $\bar{J}_2$, $\bar{J}_3$ are the second and the third invariant of deviatoric stress tensor. The friction parameter depends on compressive and tensile strength of concrete and it is given by:

$$m_0 = 3 \frac{f_c^2 - f_t^2}{f_c f_t} \frac{e}{e+1} \tag{12}$$

The shape of the deviatoric section is controlled by the function, $r\,(\theta, e)$,

$$r(\theta) = \frac{4\,(1-e^2)\cos^2\theta + (2e-1)^2}{2\,(1-e^2)\cos(\theta) + (2e-1)\sqrt{4\,(1-e^2)\cos^2(\theta) + 5e^2 - 4e}} \tag{13}$$

where e is the eccentricity parameter, calibrated according to the biaxial strength of concrete.

A non-associated flow rule is adopted in order to control excessive dilatancy, which is necessary to guarantee a realistic modeling of cohesive frictional material such as concrete and rocks. The plastic potential function controls the direction of the plastic strains and hence the relative ratios between the plastic strain components. The plastic potential is defined as follows;

$$g^p = \left[(1-k) \left(\frac{\bar{p}}{f_c} + \frac{\bar{\rho}}{\sqrt{6} f_c} \right)^2 + \sqrt{\frac{3}{2}} \frac{\bar{\rho}}{f_c} \right]^2 + k^2 \left(m_g \frac{\bar{p}}{f_c} + m_0 \frac{\bar{\rho}}{\sqrt{6} f_c} \right) - k^2 = 0 \tag{14}$$

where m_g is variable controlling the dilatation of concrete.

The non-linear behavior of concrete in the pre-peak region is described by isotropic hardening. The hardening parameter, $k = f_c/f_{cu}$, which controls the evolution of yield surface under compression, is defined in terms of equivalent plastic strain:

$$\begin{aligned} k = &\quad k_0 + (1-k_0)\sqrt{1-\left(1-\kappa_p^c/\kappa_p^{peak}\right)^2} \quad \text{for} \quad \kappa_p^c \le \kappa_p^{peak} \\ k = &\quad 1 \qquad\qquad\qquad\qquad\qquad\qquad\quad \text{for} \quad \kappa_p^c > \kappa_p^{peak} \end{aligned} \tag{15}$$

$k_0 = f_{c0}/f_{cu}$ is the initial yield strength and κ_p^{peak} the plastic strain value at strength of concrete under uniaxial compression. Softening under compressive loading and tensile behavior is modeled with the damage formulation described in the session below.

2.1.2 Damage Formulation

Elastic stiffness degradation and softening under both compression and tension are formulated using an isotropic damage. Concrete behaves differently under tensile and compressive loading, therefore, two different damage formulations, one for tensile damage ω_t and one for compressive damage ω_c, are defined independently, following Lee and Fenves [6]. Damage is assumed to be depended on the accumulated plastic strain, hence no additional damage surface is required. Internal damage variables are defined equal to the plastic variables, i.e. $\kappa_d^t = \kappa_p^t$, $\kappa_d^c = \kappa_p^c$. Damage evolution law is assumed in the following exponential form:

$$\begin{aligned} \omega_t = &\quad 1 - e^{-\kappa_d^t/a_t} \\ \omega_c = &\quad 1 - e^{-\left(\left(\kappa_d^c - \bar{\epsilon}_0^p\right)/a_c\right)^2} \end{aligned} \tag{16}$$

Where a_t and a_c are material constant for tension and compression loading respectively to be calibrated against uniaxial test results. When tensile and compressive damage parameters are obtained, then the total damage is calculated as follows:

$$\omega = 1 - (1-\omega_t)(1-\omega_c) \tag{17}$$

3 EFFECTS OF TEMPERATURE ON MATERIAL CHARACTERISTICS

3.1 Free Thermal Strain

The free thermal strain of concrete depends on the type of aggregate used. Eurocode [10] suggests the following values for the free thermal strain.

For siliceous aggregates:

$$\begin{aligned} \epsilon_{th} &= -1.8\times10^{-4} + 9\times10^{-6}T + 2.3\times10^{-11}T^3 \quad \text{for} \quad 20°C \le T \le 700°C \\ \epsilon_{th} &= 14\times10^{-3} \qquad\qquad\qquad\qquad\qquad\quad \text{for} \quad 700°C < T \le 1200°C \end{aligned} \tag{18}$$

For calcareous aggregates:

$$\begin{aligned} \epsilon_{th} &= -1.2\times10^{-4} + 6\times10^{-6}T + 1.4\times10^{-11}T^3 \quad \text{for} \quad 20°C \le T \le 700°C \\ \epsilon_{th} &= 12\times10^{-3} \qquad\qquad\qquad\qquad\qquad\quad \text{for} \quad 700°C < T \le 1200°C \end{aligned} \tag{19}$$

In this study, the free thermal strain increment is calculated as follows:

$$\dot{\epsilon}_{fth} = \alpha \dot{T} \boldsymbol{I} \tag{20}$$

where $\boldsymbol{I}$ denotes the second order identity matrix and α the coefficient of free thermal strain which can be obtained from the free thermal strain given by Eurocode. Also Nielsen et al. [11] suggested the following function for coefficient of free thermal strain:

$$\begin{aligned} &\alpha = 6 \times 10^{-5} / \left(7 - \bar{\theta}\right) \quad \text{for} \quad 0 \leq \bar{\theta} \leq 6 \\ &\alpha = 0 \qquad\qquad\qquad\qquad\quad \text{for} \quad \bar{\theta} > 6 \end{aligned} \tag{21}$$

Here $\bar{\theta} = (T - 20)/100$ represents the normalized temperature.

3.2 Transient creep

When concrete is first loaded and then heated, the thermal strain in the material is higher than that experienced by unloaded specimens. This strain difference is called transient creep strain or load induced thermal strain and an exhaustive overview of this phenomenon can be found in Torelli et. al [12]. The transient creep strain, which is an irreversible strains, depends on the temperature reached by the material and it is proportional to the compressive load level. Experimental results have shown that it does not depend on the heating rate or age of concrete [13]. Following De Borst and Peeters [14], it is modeled as follows:

$$\epsilon_{tr} = F_{tr} H_{tr} \frac{\sigma^-}{f_{c,T_0}} \tag{22}$$

where F_{tr} is the transient creep function, σ^- the negative part of effective stress tensors, f_{c,T_0} the concrete strength at ambitious air temperature T_0. H is a fourth order tensor defined as:

$$H_{tr} = -\nu_{tr} \delta_{ij} \delta_{kl} + \frac{1}{2} \left(1 + \nu_{tr}\right) \left(\delta_{ik} \delta_{jl} + \delta_{il} \delta_{jk}\right) \tag{23}$$

Here ν_{tr} is the Poisson ratio for transient creep components. F_{tr} denotes the change of transient creep strain with respect to temperature under uniaxial loading and its function has been described by several different models in the literature. In particular, Pearce et al. [15] have given the following parabolic function:

$$\begin{aligned} &F_{tr} = 0.01 \times \left(2A\bar{\theta} + B\right) \qquad\qquad\quad \text{for} \quad 0 \leq \bar{\theta} \leq \bar{\theta}^* \\ &F_{tr} = 0.01 \times \left[2C\left(\bar{\theta} - \bar{\theta}^*\right) + 2A\bar{\theta}^* + B\right] \quad \text{for} \quad \bar{\theta} > \bar{\theta}^* \end{aligned} \tag{24}$$

$\bar{\theta}^* = 4.5$, $A = 4 - 6‰$, $B = 1 - 1.5‰$ and $C = 7 - 10‰$ values are suggested in the same paper.

3.3 Compressive behavior of Concrete exposed to elevated temperature

The temperature dependency of concrete compressive strength is taken from Eurocode 2. Eurocode provides tabular data for siliceous and calcareous aggregates concrete, which can be approximated by the exponential curve given below:

$$\begin{aligned} f'_{c,T} &= f'_{c,0} \exp\left[-(\bar{T}/5.5)^2\right] \quad \text{for siliceous aggregate} \\ f'_{c,T} &= f'_{c,0} \exp\left[-(\bar{T}/5.5)^{2.5}\right] \quad \text{for calcareous aggregate} \end{aligned} \tag{25}$$

where $\bar{T} = (T - 100)/100$ is the relative temperature.

The ratio of tensile and compressive strength is assumed constant, i.e. degradation of tensile strength is assumed to be equal compressive one.

3.4 Modulus of Elasticity

The modulus of elasticity is assumed to be a function of temperature and the formulation given by Stabler [16] is adopted in this study, as follows:

$$E_c(T) = (1 - \omega_E) E(T_0) \tag{26}$$

where ω_E denotes thermal degradation of Modulus of elasticity and it is formulated as :

$$\begin{aligned} \omega_E = 0.2\bar{T} - 0.01\bar{T}^2 \quad \text{for} \quad 0 \leq \bar{T} \leq 10 \\ \omega_E = 1.0 \quad \text{for} \quad \bar{T} > 10 \end{aligned} \tag{27}$$

where $\bar{T} = (T - T_0)/100$ is relative temperature and $T_0 = 20$ °C.

4 NUMERICAL RESULTS

4.1 Transient creep model

Firstly, an axially restrained cubic specimen is simulated in order to check the implementation of the transient creep formulation. For this simulation, the material parameters have been assumed following Torelli et. al [12]: $v_{tr} = 0.37$, $E = 47000$ MPa (Elastic Modulus), $v = 0.2$ (Poisson ratio), $f_{cu} = 57$ MPa (compressive strength), $f_t = 5.7$ MPa (tensile strength). The specimen is exposed to heating-cooling cycles up to 140 °C and 180 °C and then it is heated up to 220 °.

The numerical results in terms of temperature vs stress curves are shown in figure 1. As soon as the temperature increases, compressive stresses occur in the material, due to the prevented thermal expansion, causing transient creep strain. With the increase of transient creep strain, a stress relaxation is observed, which is the reason for the reduction of stress with the increase of temperature. During the cooling phase, the transient creep strain does not change and does not increase until the temperature values reach the maximum value experienced during the temperature history.

The experimental tests conducted by Anderberg and Thelandersson [17] are simulated to validate the transient creep model. The concrete specimen was loaded first and then heated up a certain temperature level. In particular, the specimen was subjected to different levels of compression: $\zeta = 0$, $\zeta = 0.225$, $\zeta = 0.35$, $\zeta = 0.45$ and $\zeta = 0.675$, with ζ being the ratio between the applied stress and the material strength. In this example,

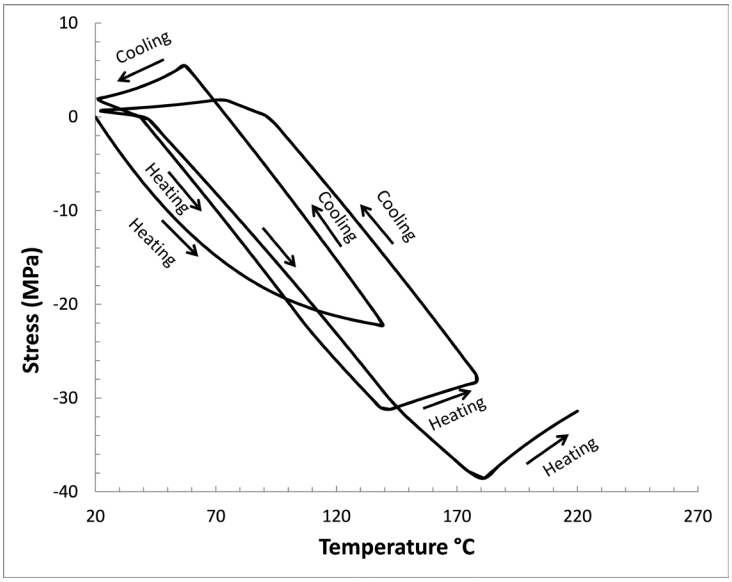

Figure 1: Uniaxially restrained specimen subjected to temperature cycle

the coefficient of free thermal strain is given in Eq. 21 and the following parameters for the transient creep function are adopted: $A = 0.004$, $B = 0.001$ and $C = 0.007$. The numerical results, plotted in Fig. 2, show a good agreement with the experimental data, confirming that the free thermal expansion is well captured by the model.

4.2 Reinforced concrete beam

After the validation of the transient creep model, a reinforced concrete beam has been simulated with the proposed model. A simply supported beam tested by Lin et. al [18] has been selected to compare with numerical results. The beam is characterized by a 6.1 m long span between supports and a 305×355 mm rectangular cross-section, reinforced with $4\phi19$ rebars on the tension side and $2\phi19$ rebars on the compression side. The compressive strength of concrete is $f_{cu} = 29.5$ MPa and yield strength of steel $f_y = 435.8$ MPa. The beam has been loaded up to certain level of load first and then exposed to ASTM E119 fire from three sides. The results of the heat transfer analysis are shown in Fig. 3, in terms of temperature vs. time for the corner rebar. Fig. 4 shows the mid-span deflection of the beam with respect to temperature and, numerical results are in good agreement with experimental ones, confirming the prediction capability of the present model.

5 CONCLUSION

In this study, a damage plasticity model for concrete under elevated temperature has been developed, where the transient creep strain are explicitly obtained. The performance of the model is validated by a comparison with experimental results gathered from the literature: the adopted model for transient creep model has been firstly validated for a concrete specimen and then a 3D reinforced concrete beam has been simulated with the proposed model. The results have shown good agreement, proving that the model can

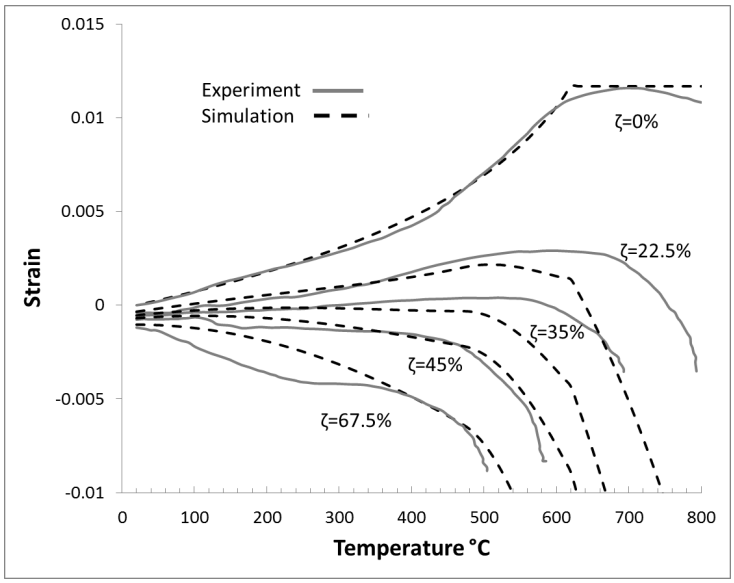

Figure 2: Strain upon heating under constant load levels

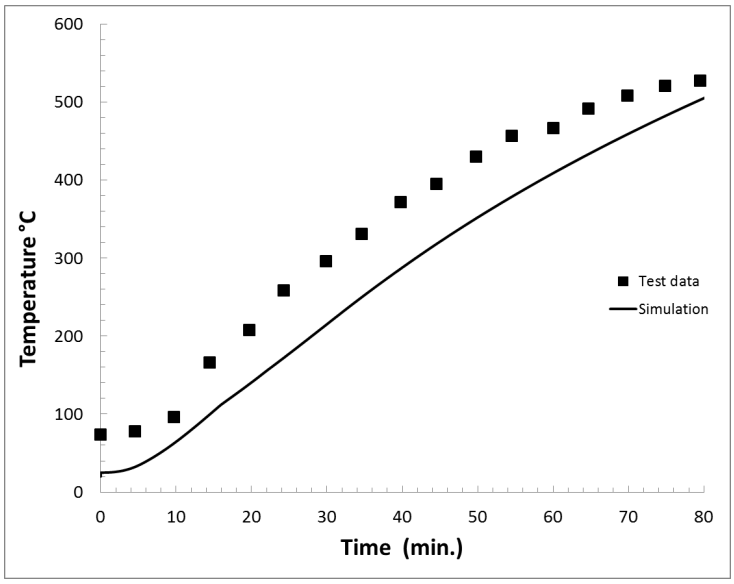

Figure 3: Evaluation of corner rebars temperature with time

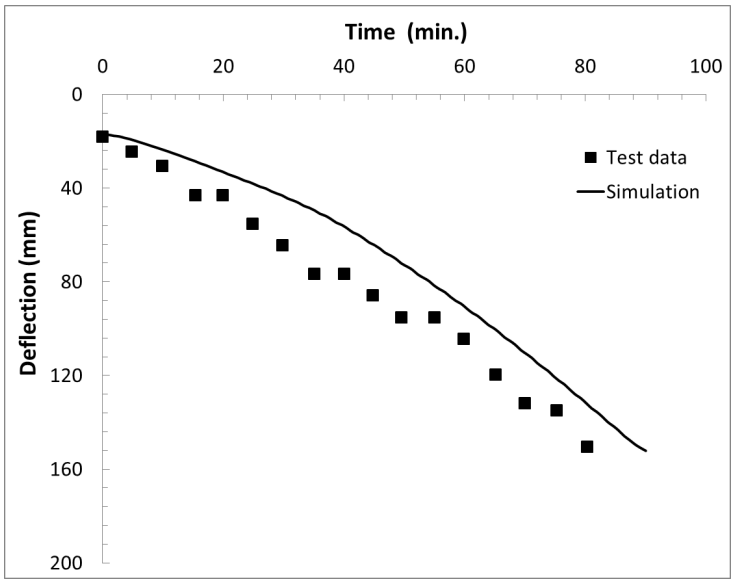

Figure 4: Mid-span deflection of the RC beam

capture the behavior of concrete expose to high temperatures.

In the experimental tests reported in literature, no significant spalling is observed for normal strenght concrete (NSC), but it becomes an important issues for high strength concrete (HSC) due to its low porosity [19]. Consequently, the moisture diffusion in the concrete and spalling will be introduced to model.

REFERENCES

[1] V. Kodur, "Properties of concrete at elevated temperatures," *ISRN Civil engineering*, vol. 2014, 2014.

[2] V. Kodur, "fire performance of high-strength concrete structural members," *Institute for Research in Construction*, 1999.

[3] T. Harmathy, "Thermal properties of concrete at elevated temperatures," *Journal of Materials*, 1970.

[4] T. Gernay, A. Millard, and J.-M. Franssen, "A multiaxial constitutive model for concrete in the fire situation: Theoretical formulation," *International Journal of Solids and Structures*, vol. 50, no. 22, pp. 3659–3673, 2013.

[5] P. Grassl and M. Jirásek, "Damage-plastic model for concrete failure," *International journal of solids and structures*, vol. 43, no. 22, pp. 7166–7196, 2006.

[6] J. Lee and G. L. Fenves, "Plastic-damage model for cyclic loading of concrete structures," *Journal of engineering mechanics*, vol. 124, no. 8, pp. 892–900, 1998.

[7] G. Etse and K. Willam, "Fracture energy formulation for inelastic behavior of plain concrete," *Journal of engineering mechanics*, vol. 120, no. 9, pp. 1983–2011, 1994.

[8] E. Pramono and K. Willam, "Fracture energy-based plasticity formulation of plain concrete," *Journal of Engineering Mechanics*, vol. 115, no. 6, pp. 1183–1204, 1989.

[9] P. Grassl, D. Xenos, U. Nyström, R. Rempling, and K. Gylltoft, "Cdpm2: A damage-plasticity approach to modelling the failure of concrete," *International Journal of Solids and Structures*, vol. 50, no. 24, pp. 3805–3816, 2013.

[10] E. Committee *et al.*, "Eurocode2: Design of concrete structures-part 1-2: General rules-structural fire design," tech. rep., ENV 1992-1-2, 1995.

[11] C. Nielsen, C. Pearce, and N. Bićanić, "Theoretical model of high temperature effects on uniaxial concrete member under elastic restraint," *Magazine of Concrete Research*, vol. 54, no. 4, pp. 239–249, 2002.

[12] G. Torelli, M. Gillie, P. Mandal, and V.-X. Tran, "A multiaxial load-induced thermal strain constitutive model for concrete," *International Journal of Solids and Structures*, vol. 108, pp. 115–125, 2017.

[13] M. Petkovski and R. Crouch, "Strains under transient hygro-thermal states in concrete loaded in multiaxial compression and heated to 250 c," *Cement and Concrete Research*, vol. 38, no. 4, pp. 586–596, 2008.

[14] R. de Borst and P. P. Peeters, "Analysis of concrete structures under thermal loading," *Computer methods in applied mechanics and engineering*, vol. 77, no. 3, pp. 293–310, 1989.

[15] C. J. Pearce, C. V. Nielsen, and N. Bićanić, "Gradient enhanced thermo-mechanical damage model for concrete at high temperatures including transient thermal creep," *International journal for numerical and analytical methods in geomechanics*, vol. 28, no. 7-8, pp. 715–735, 2004.

[16] J. T. Stabler, "Computational modelling of thermo-mechanical damage and plasticity in concrete," 2000.

[17] Y. Anderberg and S. Thelandersson, *Stress and deformation characteristics of concrete at high temperatures*. Lund Institute of Technology. Division of Structural Mechanics and Concrete Construction, 1976.

[18] T. Lin, A. Gustaferro, and M. S. Abrams, "Fire endurance of continuous reinforced concrete beams," *Portland Cement Association RD Bulletin*, 1981.

[19] V. Kodur and M. Dwaikat, "A numerical model for predicting the fire resistance of reinforced concrete beams," *Cement and Concrete Composites*, vol. 30, no. 5, pp. 431–443, 2008.

XIV International Conference on Computational Plasticity. Fundamentals and Applications
COMPLAS 2017
E. Oñate, D.R.J. Owen, D. Peric and M. Chiumenti (Eds)

EFFECT OF THE CURING TIME ON THE NUMERICAL MODELLING OF THE BEHAVIOUR OF A CHEMICALLY STABILISED SOFT SOIL

PAULO J. VENDA OLIVEIRA[*], ANTÓNIO A. S. CORREIA [†] AND LUÍS J.L. LEMOS [#]

[*] ISISE, Department of Civil Engineering, University of Coimbra,
Rua Luís Reis Santos, 3030-788 Coimbra, Portugal
Email: pjvo@dec.uc.pt

† CIEPQPF, Department of Civil Engineering, University of Coimbra,
Rua Luís Reis Santos, 3030-788 Coimbra, Portugal
Email: aalberto@dec.uc.pt

Department of Civil Engineering, University of Coimbra,
Rua Luís Reis Santos, 3030-788 Coimbra, Portugal
Email: llemos@dec.uc.pt

Key words: Modified Cam Clay Model, Von Mises Model, Curing Time, Stabilised Soft Soil, Deep Mixing Columns.

Abstract. The ability of the Modified Cam Clay (MCC) model combined with the Von Mises (VM) model, considering the effect of curing time on the enhancement of the mechanical properties of a chemically stabilised soft soil is examined. The evolution of the strength and stiffness over time is based on the results of undrained compressive strength (UCS) tests carried out for different curing times (from 28 days to 360 days). Initially, the MCC/VM models associated with the effect of curing time are validated by CIU triaxial tests, for curing times of 28 and 90 days. Finally, the behaviour of an embankment built on a soft soil reinforced with deep mixing columns is predicted based on the previously validated models. The results show that the increase of curing time of the DMCs slightly decreases the settlement obtained with a curing time of 28 days.

1 INTRODUCTION

Over the last years, various embankments have been built on soft soils. In general, these types of soils show high compressibility, low undrained shear strength and reduced permeability. One way to solve these problems consists of installing rigid vertical inclusions in the soil foundation, such as: concrete piles, stone columns and deep soil mixing columns (DMCs), i.e., of chemically stabilised soil columns.

Several experimental studies have shown that, due to pozzolanic reactions, the strength and stiffness of the stabilised soils increases over time [1-3]. However, the current design of stabilised soils uses the mechanical properties evaluated for 28 days of curing as a reference [4,

5]. Considering the lack of the numerical studies related to the enhancement of the mechanical properties of stabilised soils over time, it is very pertinent to study the impact of this effect on numerical predictions.

2 SCOPE OF THE WORK

Initially, the performance of the Modified Cam Clay (MCC) model associated with the Von Mises (VM) model and considering the effect of the curing time is validated using the results of triaxial CIU (isotropic consolidation followed by an undrained shear phase) tests for two curing times, 28 and 90 days [1]. Finally, the effect of the curing time on the settlement and the stress concentration ratio of an embankment built on a soft soil reinforced with DMCs is analysed.

A 2-D finite element code with several constitutive models was used, upgraded at the University of Coimbra and capable of carrying out elastoplastic analyses with coupled consolidation and creep.

3 CONSTITUTIVE MODEL

The behaviour of the stabilised soil is simulated by two coupled constitutive models (Figure 1), MCC/VM, which show two yield functions that may be activated either independently or simultaneously. Both models (MCC and VM) assume a linear elastic behaviour inside the yield surface and consider an associated plastic flow rule.

The yield function of the MCC model is represented by an ellipse-shaped surface oriented in line with the p' axis, described by [6, 7]:

$$F = (\lambda - \kappa).\ln\left[p'\left(1+\frac{(q/p')^2}{M^2}\right)\right] - \underbrace{\left[\underbrace{e_{\lambda o} - \underbrace{(e+\kappa.\ln p')}_{e_\kappa}}_{h(e_\kappa)} + \underbrace{(\lambda-\kappa)\times \ln\frac{p'_{c(t_c)}}{p'_{c(t_c=28d)}}}_{\Delta h(t_c)}\right]}_{h(e_k,\,t_c)} \quad (1)$$

where M is the slope of the critical state line (CSL), λ and κ are, respectively, the slope of the virgin consolidation line and the slope of the overconsolidation line in the plot e-lnp' and $e_{\lambda o}$ is the void ratio for p' equal to 1 (Figure 1a). The size of the yield function changes with the hardening rule $h(e_k, t_c)$, related to the isotropic preconsolidation pressure, p'_c (Figure 1b), which depends on the void ratio (e_k) and the curing time (t_c). The t_c promotes the change of $h(e_k, t_c)$ which induces an increase in the apparent p'_c and consequently $e_{\lambda o}$ (Figure 1). The VM model is described by [6, 8]:

$$G = q - \underbrace{q_c}_{h\left(\gamma^p, \varepsilon_v^p, t_c\right)} \quad (2)$$

where $h\left(\gamma^{p}, \varepsilon_{v}^{p}, t_c\right)$ is the hardening rule, represented by the parameter q_c. The hardening rule is evaluated considering that the trace of the yield surface on the q-γ plane is a hyperbola [9, 10]:

$$q_c = \frac{\gamma\, p'_c}{a + b\gamma} R_f \tag{3}$$

where a and b are normalized hyperbolic parameters, and R_f ($q_{failure}/q_{ult}$) is the failure ratio [11].

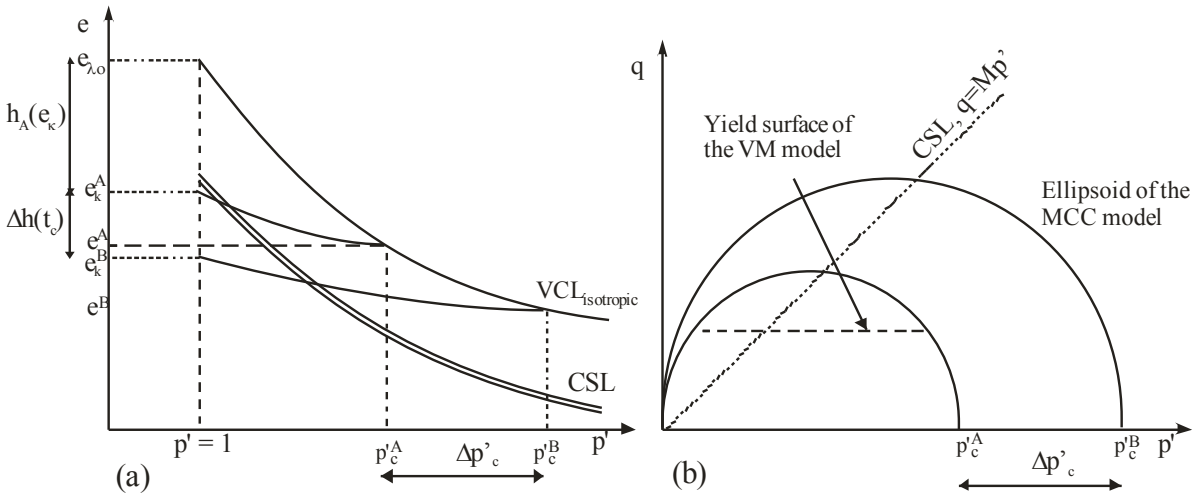

Figure 1: Effect of creep and curing time on the MCC model: a) hardening rule (e-p' plane); b) yield surface (p'-q plane).

4 EFFECT OF CURING TIME ON STABILISED SOIL

Figure 2 depicts the evolution of the unconfined compressive strength ratio ($q_u/q_{u\text{-}28d}$) against curing time (from 28 to 360 days). The results show that $q_u/q_{u\text{-}28d}$ increases faster for shorter curing times, tending to reach a constant value for higher t_c. Thus, for a curing time higher than 360 days, it is assumed that there is no increase of the cementation bonds, i.e., q_u is constant and equal to the value obtained for 360 days.

Considering that the power function presented in Figure 2 reflects the increase of the cementation bonds on the mechanical behaviour, a similar function is used to predict the evolution of the p'_c over t_c:

$$p'_{c(t_c)} = p'_{c(28d)} \times \left[0.4568 \times t_c^{\,0.2438}\right] \qquad (t_c \le 360\,\text{days}) \tag{4}$$

The prediction of Young's modulus (E') over t_c, is based on equation (4), a reduction factor (F_{red} =0.4) is required to match the experimental results, taking the form of:

$$E'_{(t_c)} = E'_{(28d)} \times \left[E'_{(28d)} \times \left(0.4568 \times t_c^{\,0.2438}\right) - E'_{(28d)}\right] \underbrace{x\ 0.4}_{F_{red}} \quad (t_c \le 360\,\text{days}) \tag{5}$$

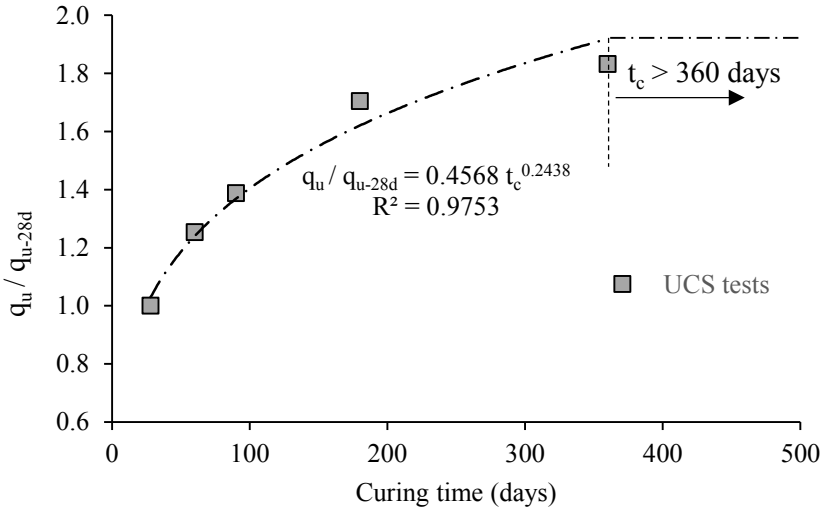

Figure 2: Effect of curing time on the unconfined compressive strength ratio [1].

Equations (4) and (5) are included in the finite element method (FEM) code, in order to take into account the effect of the curing time on the stiffness (E') and the size of the yield surface of the MCC model (p'_c).

5 NUMERICAL PREDICTION OF THE LABORATORY TESTS

Results of triaxial CIU tests were used to validate the CCM/VM model associated with the t_c effect. The numerical predictions were carried out with only 1 FE element (eight-noded isoparametric quadrilateral) and 8 nodes, making the evaluation of the displacement at eight nodes and the excess pore pressure at the four corner nodes possible. Table 1 shows the parameters for the MCC/VM model used in the numerical analyses.

Table 1: Parameters of the soft soil and the stabilised soil (i.e. DMCs) used in the numerical analyses [1].

Soil type		Stabilised soil/DMCs		
Curing time	t_c (days)	28	90	≥ 360
Elastic parameters	E' (MPa)	164.7(*)	189.0(**)	225.2(**)
	v	0.3	0.3	0.3
MCC model	$e_{\lambda 0}$	5.070	5.204(#)	5.349(#)
	e_0	(*)	(*)	(*)
	λ	0.435	0.435	0.435
	κ	0.0074	0.0074	0.0074
	M	1.50	1.50	1.50
VM model	a	0.0013	0.0013	0.0013
	b	1.683	1.683	1.683
	R_f	1.0	1.0	1.0

(*) Depends on the stress level;. (**) Evaluated from equation (5); (#) Evaluated from equations (1), (4).

Figure 3 compares the numerical predictions with the experimental results of the CIU triaxial tests carried out with samples of the stabilised soil, isotropically consolidated with a confining

pressure (p'_0) of 50 kPa, for the curing times of 28 and 90 days. The results obtained show that the numerical models used are able to replicate the significant increase in the strength and the slight increase in the stiffness over curing time, due to the pozzolanic reactions which promote the increase of the cementation bonds. In fact, the stress-strain behaviour (Figure 3) obtained numerically matches the experimental results very well until the peak strength; however, after that, the MCC/VM model does not simulate the softening observed in the laboratory tests.

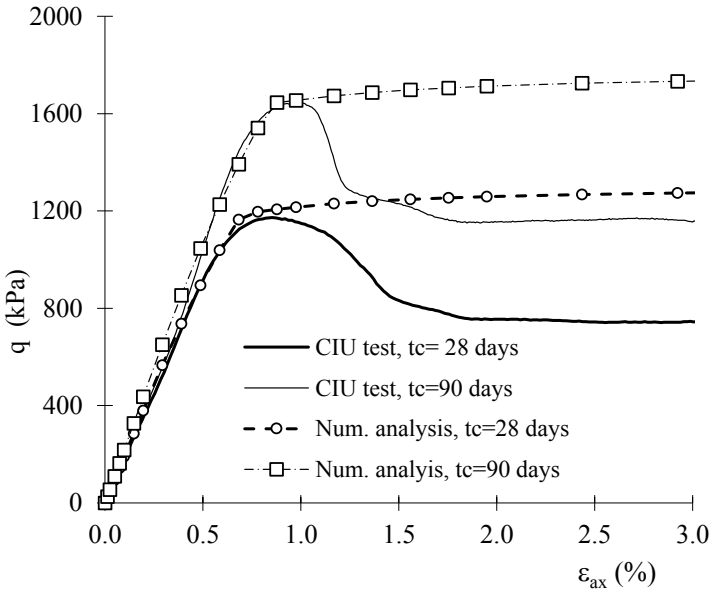

Figure 3: CIU tests with stabilised soil for a curing times of 28 and 90 days.

5 NUMERICAL PREDICTION OF THE BEHAVIOUR OF AN EMBANKMENT

5.1 Materials

The previously tested models are used to study the behaviour of a large-scale embankment built on soft soils reinforced with Deep Mixing Columns (DMCs), simulated by an axisymmetric cylindrical unit cell (Figure 4). The soil foundation is composed by 7.5 metres of soft soil placed under a 0.5 metre thick layer of sand. The water table is on the top of the layer of sand. The construction of the embankment consists of 4 sub-layers, each one with a thickness of 1.0 metre applied with a time delay of 5 days. The construction of the embankment started after a curing time for the DMCs of 28 days, in order to have the strength required in current design.

The finite element (FE) mesh used in the axisymmetric analysis consists of 130 eight-noded isoparametric quadrilateral elements and 355 nodal points. An FE with twenty nodal degrees of freedom was used below the water table, making it possible to simulate the consolidation phenomenon. In terms of boundary conditions of the FE mesh, the bottom boundary was restrained from moving in both directions, both lateral vertical sides were restrained from moving in the horizontal direction, the top boundary of the soil foundation is permeable, while the lateral and the bottom boundaries are impermeable.

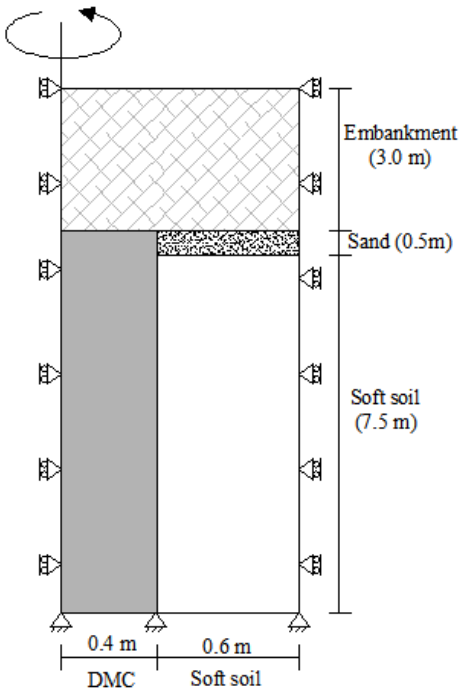

Figure 4: Embankment analysis. FEM mesh used.

The embankment material (γ = 22 kN/m^3) is simulated by an elastic law (E' varies between 15/10/5/1 MPa from the bottom to the top layer; ν'=0.3) associated with the Mohr-Coulomb criterion (c'= 10 kPa; ϕ'= 35º). The behaviour of the sand layer is replicated by a linear elastic law with the parameters: E'=2.0 MPa, ν'=0.3, γ = 15kN/m^3 and k= 10^{-4} m/s. The MCC/VM model is used to predict the behaviour of DMCs; the following parameters, other than those shown in Table 1, are considered: K_0 = 0.8 [12], γ = 16 kN/m^3, k= 3x10^{-10} m/s and k_h/k_v= 1.0. The soft soil is simulated by the MCC model with the parameters: λ = 0.204, κ = 0.03, M = 1.5, $e_{\lambda 0}$= 2.315, K_0 = 0.4, γ = 15 kN/m^3, k= 10^{-9} m/s and k_h/k_v= 3; Young's modulus of the soft soil is calculated by [13]:

$$E' = \frac{3(1+e_0)(1-2\upsilon')}{\kappa} p'_0 \tag{6}$$

where e_0 and p'_0 are the initial void ratio and volumetric effective stress respectively, ν' is the Poisson ratio and κ is the swell-recompression index. The coefficients of the permeability vary with the void ratio according to[14]:

$$k = k_0 x 10^{\frac{e-e_0}{C_k}} \tag{7}$$

where k_0 is the coefficient of permeability corresponding to e_0 and C_k is equal to $e_0/2$ [15].

5.2 Results and discussion

Four cases are modelled in this work. Case A analyses the behaviour of the embankment on

the soft soil without DMCs. Cases B, C and D simulate the reinforcement of the soil foundation with DMCs, considering the properties of the DMCs evaluated for 28 days (Case B), 90 days (case C) and considering the enhancement of the their properties with the curing time (case D).

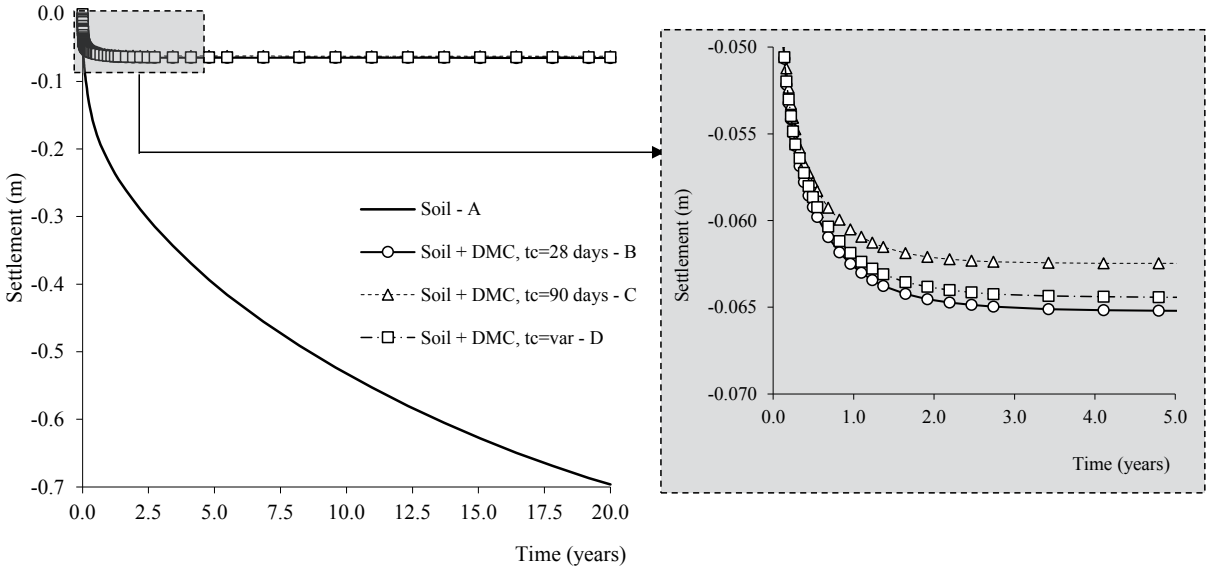

Figure 5: Embankment built on soft soils reinforced with DMCs. Evolution of settlement over time.

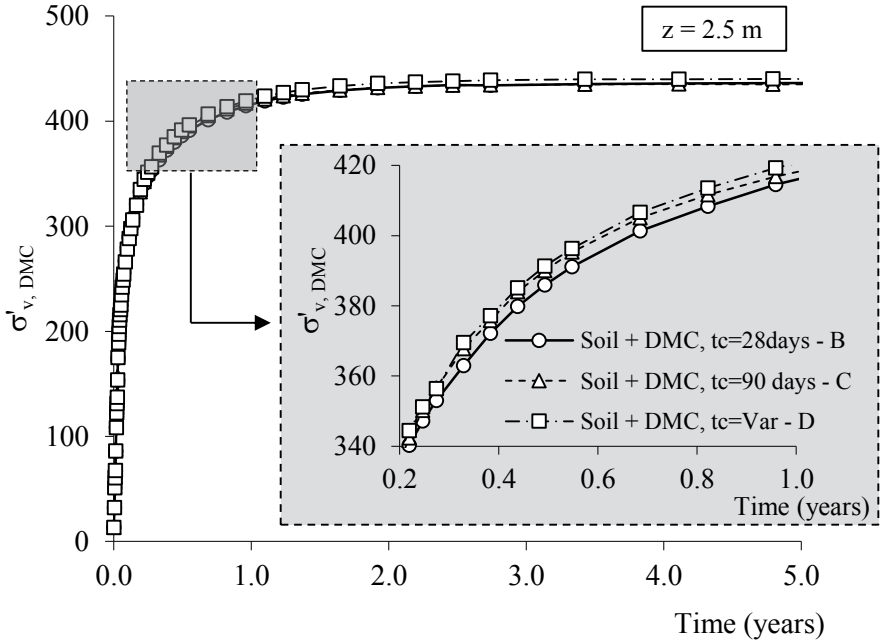

Figure 6: Embankment built on soft soils reinforced with DMCs. Evolution over time of the effective vertical stress on the DMCs.

Figure 5 shows the evolution of the settlement at the top of the soil foundation for the vertical axis of the unit cell over time. Firstly, it should be emphasised that the reinforcement of the soft soil with DMCs decreases the settlement of the embankment significantly, inducing, for a time

of 20 years, a reduction higher than 10 times. Comparison of cases B, C, and D shows that the effect of the curing time has a low impact on the numerically predicted settlement. Indeed, the consideration of the variation of the mechanical properties with t_c (case D) decreases the settlement by about 1% in relation to case B (t_c=28 days), and increases the settlement by about 3% in relation to case C (t_c = 90 days). The high consolidation rate induced by the use of DMCs [4] results in the major part of the settlement occurring in a short period of time (after the placement of the embankment layers), therefore the mechanical properties of the DMCs are similar in cases B and D, which justifies the small differences obtained in both cases.

Figure 6 depicts the evolution over time of the effective vertical stress on the DMCs ($\sigma'_{v,DMC}$) for a depth of 2.5 metres. The results show a slight increase in the $\sigma'_{v,DMC}$ for higher curing times, that is from case B to C and from case C to D. Indeed, the increases of the stiffness, from cases B to D, promote the transference of stresses from the soil to the DMCs as a consequence of the "arching effect" [4].

6 CONCLUSIONS

This work studies the effect of curing time on the mechanical behaviour of a chemically stabilised soft soil. The relationship between the curing time and the undrained shear strength was approximated by a power function, which is used to predict the evolution over time of the effective yield stress, and Young's modulus (with a correction factor of 0.4).

Firstly, the results of triaxial CIU tests, carried out for 28 and 90 days of curing time, were used to validate the constitutive model laws and the effect of curing time. Next, these models were used to predict the behaviour of an embankment built on a soft soil reinforced with DMCs. Some conclusions can be reached:

- The results of the triaxial CIU tests show that the numerical models are able to simulate the stress-strain behaviour until the failure of samples of the stabilised soil, for two curing times (28 and 90 days). However, the softening observed after the peak strength is not predicted by the models.
- Reinforcing the soil foundations with DMCs significantly decreases the settlement of the embankment.
- The curing time has a low impact on the settlement obtained, since the major part of the deformation occurs in the short term, due to the high stiffness of the DMCs.
- The increase of the curing time promotes a slight increase in the effective vertical stress, which is associated with a higher stiffness.

REFERENCES

[1] Correia, A.A.S. (2011). Applicability of deep mixing technique to the soft soil of Baixo Mondego. Ph.D. dissertation, University of Coimbra, Coimbra, Portugal (in Portuguese).

[2] Venda Oliveira, P. J., Correia, A. A. S., and Garcia, M. R. (2012). Effect of organic matter content and curing conditions on the creep behavior of an artificially stabilized soil. Journal of Materials in Civil Engineering, 24(7): 868–875.

[3] Harichane, K., Ghrici, M., Kenai, S. (2011). Effect of curing time on shear strength of cohesive soils stabilized with combination of lime and natural pozzolana. International Journal of Civil Engineering, 9(2): 90-96

[4] Venda Oliveira, P. J., Pinheiro, J. L. P., and Correia, A. A. S. (2011).Numerical analysis of an embankment built on soft soil reinforced with deep mixing columns: Parametric study. Computers and Geotechnics, 38(4): 566–576.

[5] Venda Oliveira, P. J., Correia, A. A. S., and Lemos, L.J.L. (2017). Numerical prediction of the creep behaviour of an unstabilised and a chemically stabilised soft soil. Computers and Geotechnics, 87: 20-31.

[6] Venda Oliveira P.J. (2000). Embankments on soft clays - Numeric analysis. Ph.D. Dissertation, University of Coimbra, Portugal (in Portuguese).

[7] Troung, D.M. and Magnan, J.P. (1977). Application des modèles élastoplastiques de l`Université de Cambridge au calcul du comportement d`un remblai expérimental sur sols mous. Rapport de recherche LPC nº 74, Laboratoire Central des Ponts et Chaussées. Paris.

[8] Hsieh, H.S., Kavazanjian Jr, E. and Borja, R.I. (1990). Double yield surface Cam-Clay plasticity model I: Theory. Journal of Geotechnical Engineering (ASCE), 116(9): 1381-1401.

[9] Morsy M.M., Chan, D.H. and Morgenstern, N.R. (1995). An effective stress model for creep of clay. Canadian Geotechnical Journal, 32(5): 819-834.

[10] Konder, R. L. (1963). Hyperbolic stress-strain response: Cohesive soils. Journal of the Soil Mechanics and Foundation Division, ASCE, 106(6): 611-630.

[11] Duncan, J. M. and Chang, C.Y. (1970). Nonlinear analysis of stress and strain in soils". Journal of the Soil Mechanics and Foundations Division, ASCE, 96(SM 5): 1629-1653.

[13] Atkinson, J.H, Richardson, D. and Stallebrass, S.E. (1990). Effect of recent stress history on the stifness of overconsolidated soil. Géotechnique, 40(4): 531-540.

[14] Åhnberg, H. (2006). Strength of stabilised soils – A laboratory study on clays and organic soils stabilised with different types of binder. Ph.D. thesis, University of Lund, Sweden.

[14] Taylor D.W. (1948). Fundamentals of Soil Mechanics. John Wiley and Sons, Inc., New York.

[15] Tavenas F., Jean P., Leblond P. and Leroueil S. (1983). The permeability of natural soft, part II: permeability characteristics. Canadian Geotechnical Journal, 20(4): 645-660.

XIV International Conference on Computational Plasticity. Fundamentals and Applications
COMPLAS 2017
E. Oñate, D.R.J. Owen, D. Peric and M. Chiumenti (Eds)

MODELLING OF HEAT AND MOISTURE TRANSFER IN CONCRETE AT HIGH TEMPERATURE

M. RODRÍGUEZ* C.M. LÓPEZ* AND I. CAROL*

* Department of Civil and Environmental Engineering
Universidad Politécnica de Cataluña
Jordi Girona 1, Edif. D2, E-08034 Barcelona, Spain
e-mail: mariana.rodriguez@upc.edu,carlos.maria.lopez@upc.edu,ignacio.carol@upc.edu

Key words: High temperature, Concrete, Heat and mass transfer, Numerical model.

Abstract. Moisture diffusion and related fluid pressures play a key role in cracking and spalling of concrete subject to high temperatures. This paper describes recent developments of a mode for moisture and heat transfer in porous materials, to be combined with an existing and well tested meso-mechanical model for concrete. Liquid and gas flows are formulated separately, yet later they can be combined in terms of s single variable, Pv. The material pore distribution curve is taken as the basis for developing a new physically-based desorption isotherm alternative to the traditional Bazant & Thonguthai's model. A simple academic example for temperatures between 27 and 800ºC is presented to show the behaviour of the model.

1 INTRODUCTION

Two are the main mechanisms generally accepted to govern the development of cracking and fracture of concrete exposed to high temperature, for example in the case of fire. The first one is related to the incompatibility of thermal deformations between aggregates and cement paste, which may lead to stresses beyond elastic range. The second one corresponds to the water vapor pressure buildup in the pores, that may take place as the result of heat and water moisture transfer due to temperature and pressure gradients.

Original work of the group in this field was focusing on the first of those mechanisms [1,2] by means of a temperature-driven purely mechanical analysis of a meso-structural model which included cracking via zero-thickness interface elements [3,4]. The present paper describes the recent work on the study of the second of those mechanisms by means of a thermo-hygro model to analyse moisture movement and pore pressure build up as temperature increase.

Analysis of heat and moisture diffusion is generally based on the heat and mass water conservation equations combined with Fourier law (heat flow) and Fick's Law (moisture migration). These two diffusion processes may be considered uncoupled or coupled. The moisture diffusion analysis in turn may be represented with two independent variables (typically the two pressures of gas and water vapor or capillary pressure) [5,6], or be simplified to only one unknown variable [7]. For temperature below the critical point of water

(374.15ºC), one must also distinguish between saturated and non-saturated (partially saturated) concrete; and in this case a constitutive equation for the pore state saturation may be needed. For higher temperature above the critical point, liquid water phase does not exist, and the equations of an ideal gas may be considered.

In the case of partial saturation, additional equations are needed to relate the water content of the pore system, to the partial pressure of the water vapor P_v and the capillary pressure P_c. These relations are a function of temperature T, and typically involve the degree of saturation S and the pore radius r distribution [8]. In the literature, these relations may take different forms; in Geotechnical literature the *water retention curves* relate the degree of saturation to the temperature and capillary pressure $S=S(P_c,T)$; in materials science *sorption-desorption isotherms* relate water content to vapor pressure or relative humidity and temperature $w=w(H,T)$, where $H= P_v/P_{sat}$ and the saturation pressure being a function of temperature $P_{sat} = P_{sat}(T)$.

One of the best known models is that of Bazant & Thonguthai´s [7], which is based on a single primary unknown variable, the vapor pressure P_v, and proposes a set of phenomenological *isothermal desorption curves* $w=w(P_v,T)$. These curves have been used by many other authors, and in particular Tenchev [5] has modified the curves and extended the formulation to consider separate liquid water and water vapor pressures as independent primary variables.

Gawin & Schrefler [6], consider liquid water and water vapor separately in the mass transfer formulation, which are related through the saturation of liquid water, which are defined as a function of capillary pressure, $S=S(P_c)$, for a given temperature.

The present paper describes the new formulation developed to represent the thermal and moisture diffusion in concrete, which should eventually be coupled to the existing meso-mechanical model of the research group, in order to analyze the influence on the concrete damage and cracking due to high temperatures. Due to the many phenomena to be covered in the overall model, it has been established as a priority to try to maintain the representation of moisture diffusion with one single primary variable.

In a recent publication [9], a model was presented which consisted of a modification of the original formulation of Bazant and Tounguthai´s [7] which reduced the excessive pressures. However, although that model managed to reproduce qualitatively the pressure and water content profiles expected in basic 1-D, the formulation exhibited some significant shortcomings such as: (a) consideration of liquid and vapor water as a single phase for most purposes, (b) absence of physical basis for some of the assumptions and in particular the material pore structure was not taken into account, (c) sorption isotherm based on relative humidity H, concept that is not well defined after the critical point of water (374,15ºC), (d) law that allowed the water content w to grow unlimitedly as the vapor pressure was increased, something not physical since water can only fill the available pore space. All these shortcomings have motivated the development of the new model presented in the following sections.

2 THERMAL AND MOISTURE TRANSFER MODEL

Same as in the previous model [9], the formulation may be separated into two parts: (a) desorption isotherm and (b) conservation equations, which are presented in the following

subsections.

2.1 Derivation of a desorption isotherm based on pore distribution and Kelvin equation.

One of the novel aspects of the model, for temperatures below the critical point of water, is the derivation of a desorption isotherm as the result of the combination of the pore distribution curve and some fundamental equations of thermodynamic equilibrium between water vapor and liquid water in the pores.

In the literature one can find different expressions for the degree of saturation of liquid water as a function of the capillary pressure [10-14]. Normally the empirical equations $S=S(P_c)$ proposed are inaccurate when the saturation is close to zero since, in this field not much care is paid to the behavior at very low water content [8].

In the present study, the development starts form the pore size distribution curve $S(r)$, where S has the meaning of the fraction of the pore space which is contained in pores of diameter smaller or equal to r. This is complemented with the assumption that water will fill up first the smallest size pores then progressively larger pores. With this assumption, the curve $S(r)$ can also be interpreted as giving the degree of saturation S for which the pore of radius r is partially filled (and all pores of smaller radii are totally filled, while all pores of radii larger than r are totally empty). Note that Kelvin´s law supports this assumption in a partially saturated porous medium provided enough time has passed so that chemical equilibrium can been reached between water in the menisci and water vapor migrating from larger pores to smaller pores. For fast drying processes, larger pores are emptied first and therefore it seems also reasonable, while for fast wetting processes it may not be so certain to hold and strictly speaking it would require further investigation although here it has been assumed also for convenience.

Assuming an exponential-type expression for $S(r)$, and after combination with Laplace´s and Kelvin´s equations [8], one can obtain a power-type relation between S and P_v valid for temperatures below the critical point of water:

$$S = \left(\frac{P_V}{P_s}\right)^{\beta/m} \tag{1}$$

where P_s is the saturation pressure at the current temperature, and can be known using classical thermodynamic tables (Çengel & Turner, 2001) [15], β is a constant, and exponent m includes the effect of absolute temperature, the density of liquid water and the surface tension of water defined as an equation depending on temperature, as given in [16].

In figure 1, equation $S=S(P_v,T)$ (1) is represented for a various values of temperature.

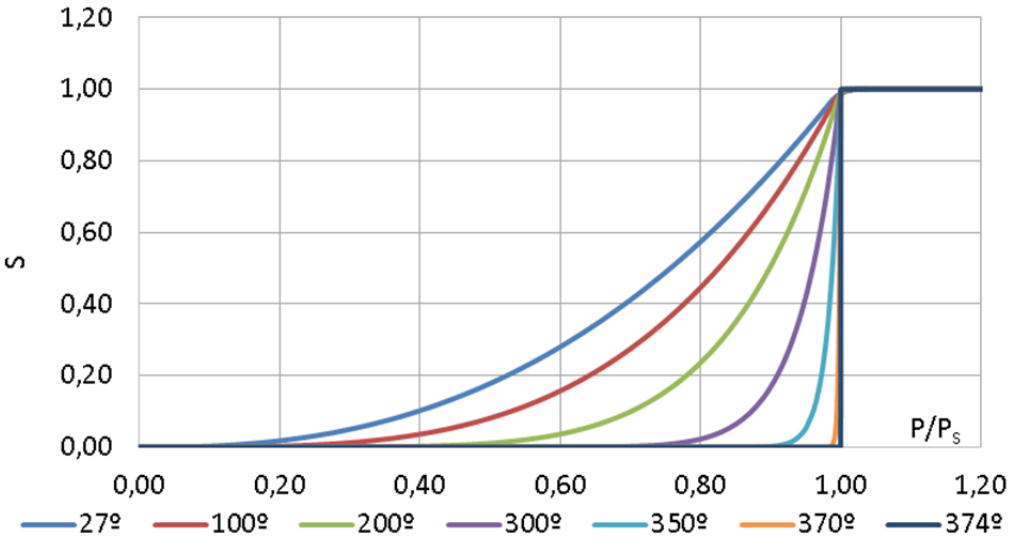

Figure 1: Evolution of the saturation degree in terms of the ratio P_V/P_s for different temperature values.

To obtain finally the total water content, w, must be related to S and P_v. For this purpose, total water content w may be decomposed as the sum of the liquid water, w_L, plus vapor water, w_V:

$$w = \underbrace{\emptyset\, S\, \rho_L}_{w_L} + \underbrace{\emptyset\, (1-S)\, \rho_v}_{w_V} \tag{2}$$

where $\emptyset$ is porosity; S is the degree of saturation, ρ_L is liquid water density [Kg/m^2] which may be obtained from thermodynamic tables in terms of temperature (Çengel & Turner, 2001) [15], and ρ_V is the density of water vapor, which may be taken from the perfect gas equation:

$$\rho_v = \frac{P_V}{R_v T_a} \tag{3}$$

where R_v is the gas constant for water vapor [J/Kg ºK] and T_a is the absolute temperature.

Note that, expressions (1) and (3) replaced into (2) constitute a new physically-motivated desorption isotherm alternative to Bazant and Thongouthai´s [7] for temperatures below the critical point of water. For temperatures above that point, S = 0 and equation (3) simply becomes $w = \emptyset\ \rho_v$.

2.2 Conservation equations

Temperature distributions are obtained from separate thermal diffusion analysis (uncoupled), and only one pressure variable is considered to describe the water transfer process where the water dehydration is included.

The heat and water mass conservation equations may be expressed as:

$$\rho C \frac{\partial T}{\partial t} = -div(-k_T grad T) \tag{4}$$

$$\frac{\partial w}{\partial t} = -div(\bar{J}) + \frac{\partial w_d}{\partial t} \tag{5}$$

in which ρ and C are the mass density [Kg/m^3] and heat capacity of concrete [J/Kg ºC], k_T is the heat conductivity [J/Kg seg ºC], w is the total mass of free water per m^3 of concrete [Kg/m^3]; w_d [Kg/m^3] is the mass of chemically bound water that is released to the pore as a result of the dehydration process (dehydration of the solids in cement paste as a result of heating); and $\bar{J}$ is the total mass flow of water per unit area [Kg/m^2 seg].

Total mass flow of water, $\bar{J}$, may be also decomposed as the sum of the flow of liquid water, $\bar{J}_L$, plus the flow of vapor water, $\bar{J}_V$, both in [Kg/m^2 seg]:

$$\bar{J} = \bar{J}_L + \bar{J}_V \tag{6}$$

where, inserting Fick´s laws for each of them, one obtains:

$$\bar{J}_L = -\emptyset\, S\, \rho_L \frac{k\, k_L}{\mu_L} \nabla P_L \tag{7}$$

$$\bar{J}_V = -\emptyset\, (1-S) \frac{P_V}{R_v\, T_a} \frac{k\, k_V}{\mu_V} \nabla P_V \tag{8}$$

In the previous equations, ∇ indicates gradient, k represents concrete intrinsic permeability [m^2]; k_L and k_V are relative permeabilities of liquid water and water vapor, respectively, μ_L and μ_V are dynamic viscosities for liquid water and water vapor respectively en [Kg/m^2 seg]; and P_L and P_V correspond to the liquid pressure and vapor pressure, both in [Kg/m^2]. Under the critical point of water, these two pressures are related by capillary pressure P_c:

$$P_L = P_V - P_c \tag{9}$$

Combining now equations (7), (8), (9) and Kelvin´s equation, one obtains:

$$\begin{aligned} \bar{J} = -\emptyset\, S\, \rho_L \frac{k\, k_L}{\mu_L} \left[R_V \rho_L ln\left(\frac{P_V}{P_s}\right) + R_V T_a \frac{\partial \rho_L}{\partial T} ln\left(\frac{P_V}{P_s}\right) - R_V T_a \rho_L \frac{1}{P_s} \frac{\partial P_s}{\partial T} \right] \nabla \mathrm{T} \\ - \left[\emptyset\, S\, \rho_L \frac{k\, k_L}{\mu_L} \left(1 + R_V T_a \rho_L \frac{1}{P_V}\right) + \emptyset\, (1-S) \frac{P_V}{R_v\, T_a} \frac{k\, k_V}{\mu_V} \right] \nabla P_V \end{aligned} \tag{10}$$

Note that thanks to assumptions made, only Pv shows up in this final equation.

The dehydration process is assumed to start at about 105ºC, and the expression used is similar to that of Bazant and Thonguthai´s [7]:

$$w_d = w_d^{105}\, f(T) \tag{11}$$

in which w_h^{105} is the hydrated water content at 105ºC and *f(T)* is a function which represents the amount of water that is dehydrated when reaching higher temperature. Function *f(T)* is obtained by fitting experimental data of the weight loss measurements on heated concrete specimens, which can be obtained from the literature [17-19]. The expression used for *f(T)* is the following:

$$f(T) = 1 - exp^{-q\left(\frac{T}{T_r}\right)^p} \tag{12}$$

where *q, p* and T_r are constants fitting parameters which varies for different concretes and T represent the temperature.

With equations (2), (10) and (11) the system is complete and equation (5) may be solved. The model described requires various additional parametric relations. Porosity $\emptyset$ is defined as proposed in [5] in terms of initial porosity $\emptyset_0$ and temperature. Intrinsic permeability of concrete k is also obtained using expression given in [5] in terms of initial intrinsic permeability k_0 and porosity. Expresions for relative permeability of liquid water k_L and vapor k_V correspond to the ones used in [20]. Expresions for dynamic viscosity of liquid water μ_L and vapor $\mu_V$in terms of parameters μ_{V0} y α_v and temperature have been taken from references [10] and [20].

3 RESULTS

The example of application presented in this section is a simplified version the one used in Tenchev *et. al.* (2001) [5] and Davie *et. al.* (2006) [20]. It consists of solving the 1D pressure distribution and water content in the direction perpendicular to the exposed surface, of a thick concrete wall. The numerical analysis is made on a long and narrow 2D FE domain of 20×0.2cm (horizontal×vertical), which is discretized with a single row of 730 linear rectangular elements and the left vertical end corresponds to the exposed surface.

Previous to the moisture calculation, temperature distributions are obtained from a separate thermal diffusion analysis, where the (left vertical) exposed edge is subject to temperature increments from 27 to 800ºC according to the ISO 834 curve [21], condition which is applied *via* mixed Newman-Dirichlet boundary condition (heat flow proportional to the difference of the resulting surface temperature with the desired prescribed value, proportionality constant *h*). Thermal flow is assumed null on the other three faces of the FE domain, and the initial temperature value is 27ºC for all nodes of the mesh. The resulting temperature distribution is then applied as an input for the moisture diffusion analysis, with a constant vapor pressure value assumed prescribed on the (left vertical) exposed edge of the domain (of 1,783e^{-3} MPa which corresponds to a relative humidity of 50% and 27ºC), while moisture flow is assumed null on the other three faces. The initial vapor pressure value was 2,67e^{-3} MPa for all nodes of the mesh, which corresponds a relative humidity of 75% at T_0 = 27ºC.

Thermal parameters used are: ρ= 2300 Kg/m^3*;* C=1171 J/KgºC*;* $k_{T=}$ 66 J/min m ºC and the convective heat transfer coefficient, h = 6500 J/min m^2 ºC. For moisture diffusion analysis, the parameters used are: k_0 = 5e^{-17} m^2; μ_{V0}=1.475e^{-8} Kg min/ m^2; α_v=5.88e^{-11} Kg min/ m^2 ºK; β=2.5; $\emptyset_0$=0.08; R_v=46.15 m/ºK; T_0=27ºC; ρ_L^0 = 1000Kg/m^3. The parameters to obtain the dehydration rate are: w_d^{105}=60 Kg/m^3, T_r =450, q=1 and p=3.

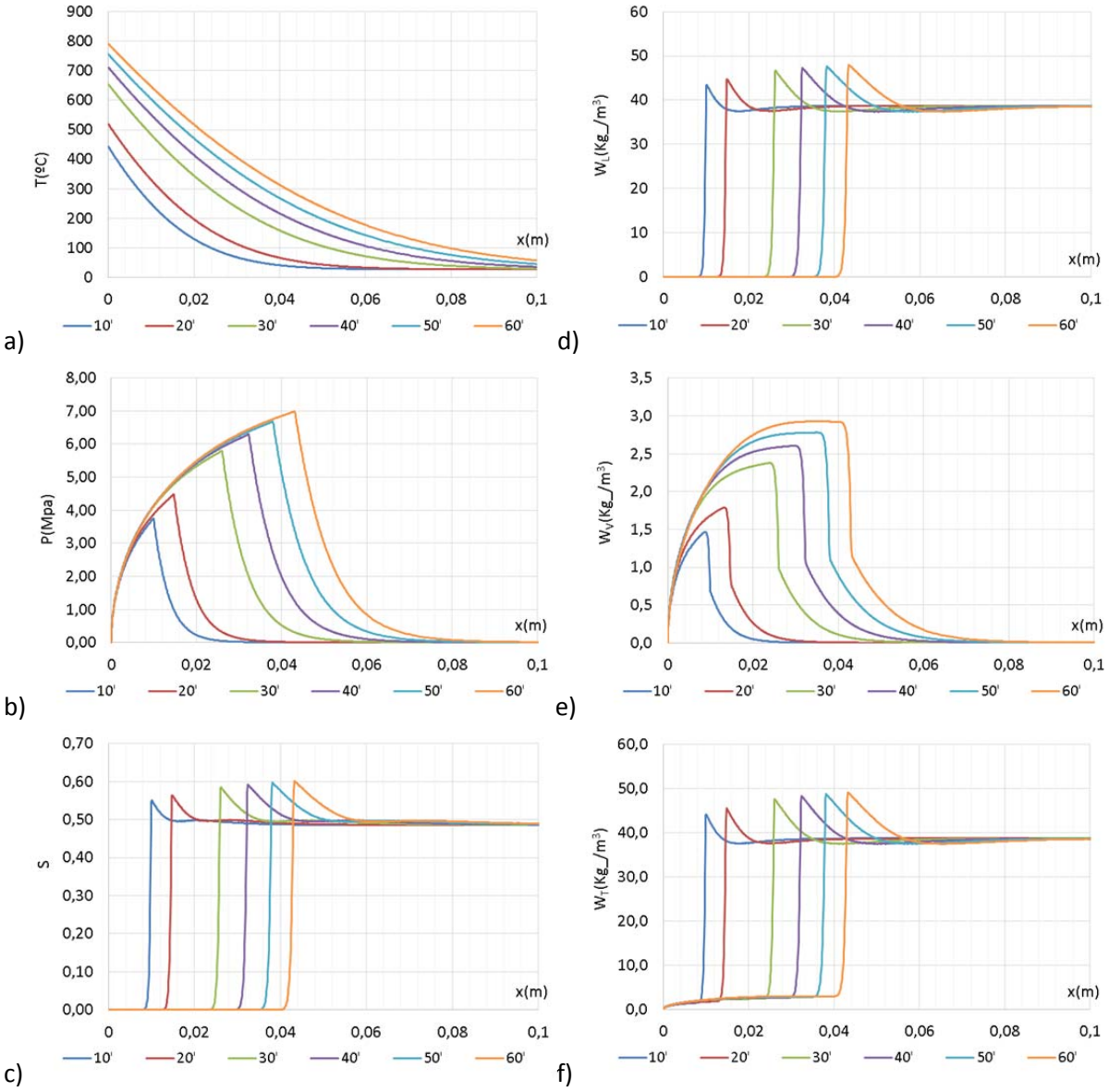

Figure 2: (a) Distribution of temperatures prescribed to the water content analysis; (b) vapor pressure; (c) saturation degree; (d) liquid water content; (e) vapor water content, (f) total water content as a function of the distance from the fire exposed edge for 10, 20, 30, 40, 50 and 60 minutes.

Figure 2 shows the curves of temperature prescribed T (2a), vapor pressure P_V (2b), saturation degree S (2c), resulting liquid water content w_L (2d), vapor water content w_v (2e) and total water content w (2f), as functions of x (depth in the concrete wall), for six different heating times of 10, 20, 30, 40, 50 and 60 minutes. Only the part of the mesh affected by the process is represented (from x=0 to 0.1m), the rest remains in initial conditions. The results turn out qualitatively similar to those obtained in the literature, in which as the high temperatures penetrate the material, a front of low water content and high vapor pressure also moves into the material at around the location of the 250-300ºC front.

In Figure 2, the zone of growing pressures can be seen (fig. 2b) to coincide with the zone of growing water vapor content (Fig. 2e). This is due to a faster rate of water evaporation than liquid water transport. Moreover, the zone where water vapor increases also coincides with the zone where liquid water is practically inexistent. The sudden drop in water vapor content right after the maximum value (Fig. 2e), coincides with the sudden transition from dry to saturated for similar times (Fig. 2d), all of which is dictated by the evolution of the saturation degree (Fig. 2c). For each time, the location of the maximum vapor pressure *p* marks pretty well the limit of the dry zone in corresponding *S* curve.

In Fig. 2d (liquid water distribution), one can clearly identify the four zones from left to right: a) a dry zone where liquid water has totally evaporated, b) a reduced zone of evaporation in which liquid water changes from its initial value (38 kg/m^3) to practically zero; c) a zone of growing liquid water content till a maximum over its initial value of 38 kg/m^3 due to the flow towards the interior of the material due to the pressure gradient, with a condensation front when it reaches the interior zone at lower temperature (*moisture clog*); and d) the inner zone of material not affected by the process, where initial conditions remain.

4 CONCLUDING REMARKS

The model described for moisture diffusion in concrete at high temperatures intends to be a physically-based model capable of representing the most essential aspects of moisture diffusion in concrete, while keeping the formulation simple enough (single-variable) so that eventually it can be implemented in the more general context of a meso-level mechanical model of concrete already developed and verified in a large variety of situations.

In previous work [9], a first attempt made was based on the isothermal sorption curves of Bazant and Thougouthai [7]. However some shortcomings were identified. The new formulation presented in this paper tries to overcome some of those limitations. Flow of water and vapor are initially considered as independent phenomena depending on their respective pressures, although later the use of Kelvin´s equation brings the problem back to a single primary variable P_v. Desorption isotherms are not proposed phenomenologically, but come out as the result of the combination of a pore distribution curve and some fundamental laws such as Laplace and Kelvin´s equations. The model uses the concept of *Ps* (and therefore relative humidity *H*), only for temperatures below the critical point of water, and provides consistent transition to situations above that point, when only water vapor is present in the pores. Water content cannot grow beyond maximum material water capacity given by pore space. These and other advantages, make this model a sounder basis for incorporation into the complex meso-level model which is already under development.

ACKNOWLEDGMENTS

This research is supported by grants BIA2016-76543-R funded by MEC (Madrid), which includes FEDER funds from the European Union, and 2014SGR-1523 from Generalitat de Catalunya (Barcelona).

REFERENCES

[1] Rodríguez, M., López, CM. and Carol, I. High temperature effect in mortar and concrete specimens using a meso-mechanical model with fracture based zero-thickness interface elements. *XI COMPLAS, CD-ROOM* (2011).

[2] Pérez, A., Rodríguez, M., López, CM. and Carol, I. 3D-Mesomechanical analysis of cracking and spalling of concrete subjected to high temperatura. *XII COMPLAS, CD-ROOM* (2013).

[3] Carol, I., Prat, P. C., López, C.M. A normal/shear cracking model. Application to discrete crack analysis. *Engng. Mech.* ASCE **123**: 765−773 (1997).

[4] Carol, I., López, C.M. and Roa, O. Micromechanical analysis of quasi-brittle materials using fracture-based interface elements. *Int. J. Num. Meth. Engng.* **52**:193-215 (2001).

[5] Tenchev, R.T., Li, L.Y. and Purkiss, J.A. Finite element analysis of coupled heat and moisture transfer in concrete subjected to fire. *Numerical Heat Transfer, Part A,* **39**: 685-710 (2001).

[6] Gawin, D. and Schrefler, B.A. Thermo-hygro-mechanicla analysis of partially saturated porous materials. *Engineering Computations* **13**(7): 113-143 (1996).

[7] Bazant, Z.P. and Thonguthai, W. Pore pressure and drying of concrete at high temperature. *Nuclear Engineering Mechanics Division* **104**: 1059-79 (1978).

[8] Baggio, P., Bonacina, C. and Schrefler, B.A. Some considerations of modelling heat and mass transfer in porous media. *Transport in Porous Media* **28**: 233-251 (1997).

[9] M. Rodríguez, C.M. López and I.Carol. Modeling of heat and mass transfer induced by high temperature in concrete. *XIII COMPLAS, CD-ROOM* (2015).

[10] Gawin, D., Majorana, C.E. and Schrefler, B.A. Numerical analysis of hygro-thermal behavior and damage of concrete at high temperature. *Mechanics of Cohesive-Frictional Materials* **4**: 37-74 (1999).

[11] Baroghel-Bouny, V., Mainguy, M., Lassabatere T. and Coussy O. Characterization and identification of equilibrium and transfer moisture properties for ordinary and high-performance cementitious materials. *Cem Con Res*, **29**: 1225-1238 (1999).

[12] Meschke, G. and Grasberger, S. Numerical modeling of coupled hygromechanical degradation of cementitious materials. *Journal of engineering mechanics* **129**(4): 383-392 (2003).

[13] Li, X., Li, R. and Schrefler, B.A. A coupled chemo-thermo-hygro-mechanical model of concrete at high temperature and failure analysis. *International Journal for Numerical and Analytical Methods in Geomechanics* **30**: 635-681 (2006).

[14] Gawin, D., Pasavento, F., and Schrefler, B.A. Modelling of hygro-thermal behavior and damage of concrete at high temperature above the critical point of water. *International Journal for Numerical and Analytical Methods in Geomechanics* **26**: 537-562 (2002).

[15] Cengel, Y.A. and Turner, R.H. *Fundamentals of thermal-fluid sciences*- Second edition. McGraw-Hill (2001).

[16] Vargaftik, N.B., Volkov, B.N. and Voljak, L.D. International tables of the surface tension of water. *J. Phys. Chem. Ref. Data* **12**, (3) (1983).

[17] Alonso, C. and Fernandez, L. Dehydration and rehydration processes of cement paste exposed to high temperature environments. *Journal of Materials Sciences* **39**: 3015-3024 (2004).
[18] Alarcon-Ruiz, L., Platret, G., Massieu, E. and Ehrlacher, A. The use of thermal analysis in assessing the effect of temperature on cement paste. *Cement and Concrete Research* **35**: 609-613 (2005).
[19] Harmathy, T.Z. and Allen, L.W. Thermal properties of selected masonry unit concretes. *Journal of the American Concrete Institute* **70**: 132-142 (1973).
[20] Davie, C.T., Pearce, C.J. and Bicanic, N. Coupled heat and mass moisture transport in concrete at elevated temperatures- Effects of capillary pressure and adsorbed water. *Numerical Heat Transfer, Part A* **49**: 733-763 (2006).
[21] ISO834-1. Fire Resistance Test – *Element of Building constructions*- Part 1: General Requirement (1999).

XIV International Conference on Computational Plasticity. Fundamentals and Applications
COMPLAS XIV
E. Oñate, D.R.J. Owen, D. Peric & M. Chiumenti (Eds)

MULTIPHYSICAL FAILURE PROCESSES IN CONCRETE: A CONSISTENT MULTISCALE HOMOGENIZATION PROCEDURE

Felipe Lopez Rivarola[a], Nicolás Agustín Labanda[abc], and Guillermo J. Etse[ac]

[a]Universidad de Buenos Aires. Facultad de Ingeniería. LMNI-INTECIN (UBA-CONICET), Buenos Aires, Argentina.
e-mail: getse@herrera.unt.edu.ar, web page: http://laboratorios.fi.uba.ar/lame/

[b] SRK consulting and Universidad Nacional de Tucumán, Argentina.
Email: nlabanda@srk.com.ar, web page : http://latam.srk.com/en and http://facet.unt.edu.ar

[c]CONICET - Universidad Nacional de Tucumán, Faculty of Exact Science and Engineering.

Key words: Multiphysical phenomena, poromechanics, multi-scale, failure.

Abstract. Durability and strength capabilities of concrete materials are vastly affected by the combined action of temperature and mechanical loading, which give rise to multiphysical failure processes. Such a phenomenon involves complex cracking, degradation and transport mechanisms on different scale lengths of concrete mixtures which, in turn, depend on the particular properties of the different constituents. Thus, the macroscopic observation of relevant concrete mechanical features such as strength, ductility and durability are the result of several different properties, processes and mechanisms which are not only coupled but moreover, depend on multiple scales. Particularly, regarding the pore pressure and thermal actions, most of the degradation processes in concrete are controlled by the heterogeneities of the microscopic scale. In the case of the mechanical actions both the micro and mesoscales play a relevant role. In this context, multiphysical failure processes in cementitious material-based mixtures like concrete can only and fully be understood and accurately described when considering its multiscale and multiconstituent features. In the realm of the theoretical and computational solid mechanics many relevant proposals were made to model the complex and coupled thermo-hydro-mechanical response behavior of concrete. Most of them are related to macroscopic formulations which account for the different mechanisms and transport phenomena through empirical, dissipative, poromechanical theories. Moreover, although relevant progress was made regarding the formulation of multiscale theories and approaches, none of the existing proposals deal with multiphysical failure processes in concrete. It should be said in this sense that, among the different multiscale approaches for material modeling proposed so far, those based on computational homogenization methods have demonstrated to be the most effective ones due to the involved versatility and accuracy. In this work a thermodynamically consistent semi-concurrent multiscale approach is formulated for modeling the

thermo-poro-plastic failure behavior of concrete materials. A discrete approach is considered to represent the RVE material response. After formulating the fundamental equations describing the proposed homogenizations of the thermodynamical variables, the constitutive models for both the skeleton and porous phases are described. Then, numerical analyses are presented to demonstrate the predictive capabilities of the proposed thermodynamically consistent multiscale homogenization procedure for thermo-mechanical failure processes in concrete mixtures.

1 INTRODUCTION

A thermo-poro-mechanical multi-scale problem to model concrete degradation is presented in this paper and schematically represented in Figure 1. The multi-scale model is stated within the semi-concurrent formulations [1] where the strain tensor $\boldsymbol{\varepsilon}$, the temperature θ and it gradient $\nabla\theta$ is transferred from the coarse scale to the fine scale. The mortar in the micro-scale (or representative volume element **RVE**) is considered a porous media. Biot's poromechanics theory is considered for the mortar simulation, while the aggregate is simulated as a simple elastic material. After solving the boundary value problem in the fine-scale the macro-stress $\boldsymbol{\sigma}(x,t)$, the macro-heat flux $\boldsymbol{q}(x,t)$ and the macro-pore pressure $p(x,t)$ are obtained.

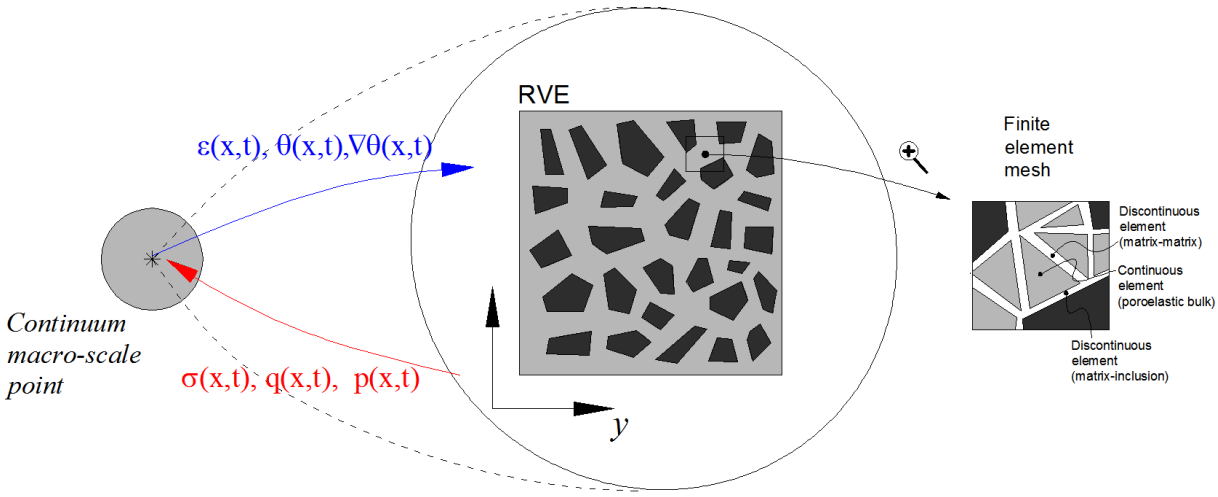

Figure 1: Schematic representation of the proposed multi-scale procedure.

The paper is organized as follow: the themo-poro-mechanic problem in the coarse scale is stated in Section 2. Multi-scale equations are given in Section 3. Fine scale constitutive modelling and some thermodynamics aspects are discussed in Section 4. A numerical example is presented in Section 5 and finally, some conclusions are drawn in Section 6.

2 Thermo-poro-mechanical problem in the coarse scale

In the following section, the equilibrium equations for a thermo-poro-mechanics with undrained hydraulic conditions are presented. It is important to note that all variables with sub-index μ, are those acting in the fine scale.

The thermal problem can be expressed as: *Given a thermal source f, find $\theta \in \Theta$ such that the heat flux $\boldsymbol{q}$ fulfil*

$$\int_{\Omega} \boldsymbol{q} \cdot \nabla_{\boldsymbol{x}} \delta\theta \; d\Omega = \int_{\Omega} f \delta\theta \; d\Omega, \qquad \forall \delta\theta \in \Theta. \tag{1}$$

The poro-mechanical problem can be expressed as: *Given a temperature field θ that satisfied (1) and a load in the Neumann boundary $\boldsymbol{f}$, find $\boldsymbol{u} \in \mathscr{U}$ such that the stress field $\boldsymbol{\sigma}$ fulfil*

$$\int_{\Omega} \boldsymbol{\sigma}\left(\boldsymbol{u}_{\mu}, p_{\mu}, \theta_{\mu}\right) \cdot \nabla^{s}_{\boldsymbol{x}} \delta\boldsymbol{u} \; d\Omega = \int_{\Gamma} \boldsymbol{f} \cdot \delta\boldsymbol{u} \; d\Gamma, \qquad \forall \delta\boldsymbol{u} \in \mathscr{U} \tag{2}$$

where

$$\Theta = \left\{\theta \in \boldsymbol{H}^{1}\left(\Omega\right) : \textit{essential boundary conditions}\right\} \tag{3}$$

$$\mathscr{U} = \left\{\delta\boldsymbol{u} \in \boldsymbol{H}^{1}\left(\Omega\right) : \textit{essential boundary conditions}\right\} \tag{4}$$

In equation 1 it can be seen that the macro stress tensor $\boldsymbol{\sigma}\left(\boldsymbol{u}_{\mu}, p_{\mu}, \theta_{\mu}\right)$ depends on three micro scale variables: the micro-scale displacement $\boldsymbol{u}_{\mu}$, the micro-scale pore pressure p_{μ} and the micro-scale temperature θ_{μ}.

3 Multi-scale framework

Given a point $\boldsymbol{x} \in \Omega$ in the macro scale and being $\boldsymbol{y} \in \Omega_{\mu}$ the coordinate system in the **RVE**, the following scale bridging equations can be formulated.

3.1 Thermal problem

- Axiom 1 - Kinematical admissibility

The following scale transition equation for the temperature gradient is considered

$$\nabla_{\boldsymbol{x}}\theta = \frac{1}{|\Omega_{\mu}|}\int_{\Omega_{\mu}} \nabla_{\boldsymbol{y}}\theta_{\mu} \; d\Omega_{\mu} \;\Rightarrow\; \nabla_{\boldsymbol{x}}\theta = \frac{1}{|\Omega_{\mu}|}\int_{\partial\Omega_{\mu}} \theta_{\mu}\boldsymbol{n} \; d\partial\Omega_{\mu}, \tag{5}$$

being n the external normal of the **RVE** boundary $\partial\Omega_{\mu}$. In the same way, the temperature compatibility between scales is defined

$$\theta = \frac{1}{|\Omega_{\mu}|}\int_{\Omega_{\mu}} \theta_{\mu} \; d\Omega_{\mu}. \tag{6}$$

The insertion of the macro-scale temperature gradient $\nabla_{\boldsymbol{x}}\theta$ in the micro-scale temperature field θ_{μ}, is considered as

$$\theta_{\mu}\left(\boldsymbol{y}\right) = \theta + \nabla_{\boldsymbol{x}}\theta \cdot \left(\boldsymbol{y} - \boldsymbol{y}_{0}\right) + \tilde{\theta}_{\mu}\left(\boldsymbol{y}\right) \;\Rightarrow\; \nabla_{\boldsymbol{y}}\theta_{\mu}\left(\boldsymbol{y}\right) = \nabla_{\boldsymbol{x}}\theta + \nabla_{\boldsymbol{y}}\tilde{\theta}_{\mu} \tag{7}$$

with

$$\boldsymbol{y}_0 = \frac{1}{|\Omega_\mu|}\int_{\Omega_\mu} \boldsymbol{y}\ d\Omega_\mu. \tag{8}$$

Introducing equation (7) in (6) the following constraint over the temperature fluctuation field is obtained

$$\int_{\Omega_\mu} \tilde{\theta}_\mu\ d\Omega_\mu = 0 \tag{9}$$

Finally, the space of kinematically admissible fluctuations in the microscopic temperature field are

$$\tilde{\Theta}_\mu = \left\{ \theta_\mu \in \boldsymbol{H}^1(\Omega_\mu) : \int_{\Omega_\mu} \theta_\mu\ d\Omega_\mu = 0,\ \int_{\partial\Omega_\mu} \theta_\mu \boldsymbol{n}\ d\partial\Omega_\mu = 0 \right\} \tag{10}$$

- Axiom 2 - Multi-scale virtual principle

The thermal multi-scale virtual principle can be written as

$$\boldsymbol{q}\cdot\nabla_{\boldsymbol{x}}\delta\theta = \frac{1}{|\Omega_\mu|}\int_{\Omega_\mu} \boldsymbol{q}_\mu(\theta_\mu)\cdot\nabla_{\boldsymbol{y}}\delta\theta_\mu\ d\Omega_\mu,\quad \forall\ \delta\theta_\mu\ \nabla_{\boldsymbol{x}}\delta\theta\ admissible \tag{11}$$

- Consequence 1 - Thermal equilibrium problem in the **RVE**

Considering $\nabla_{\boldsymbol{x}}\delta\theta = 0$ in equation 11, the thermal equilibrium equation in the micro-scale is obtained

$$\frac{1}{|\Omega_\mu|}\int_{\Omega_\mu} \boldsymbol{q}_\mu(\theta_\mu)\cdot\nabla_{\boldsymbol{y}}\delta\tilde{\theta}_\mu\ d\Omega_\mu = 0,\quad \forall\ \delta\tilde{\theta}_\mu \in \tilde{\Theta}_\mu \tag{12}$$

- Consequence 2 - Homogenization operator for thermal flux

Considering $\delta\tilde{\theta}_\mu = 0$ in equation 11, the homogenization operator for the thermal flux is obtained

$$\boldsymbol{q} = \frac{1}{|\Omega_\mu|}\int_{\Omega_\mu} \boldsymbol{q}_\mu(\theta_\mu)\ d\Omega_\mu. \tag{13}$$

A Fourier law for materials in the fine scale will be considered

$$\boldsymbol{q}_\mu(\theta_\mu) = -\boldsymbol{K}_\mu\nabla_{\boldsymbol{y}}\theta_\mu. \tag{14}$$

3.2 Thermo-poro-mechanical problem

- Axiom 1 - Kinematical admissibility

For the scale transition equations a fractured **RVE** domain noted as Γ_μ with normal $\boldsymbol{n}_\mu$ is considered

$$\boldsymbol{\varepsilon} = \frac{1}{|\Omega_\mu|}\left[\int_{\Omega_\mu} \nabla^s_{\boldsymbol{y}}\boldsymbol{u}_\mu\ d\Omega_\mu + \int_{\Gamma_\mu} [\![\boldsymbol{u}_\mu]\!] \otimes^s \boldsymbol{n}_\mu d\Gamma_\mu\right]. \tag{15}$$

Applying Green's theorem to equation 15, the following equations is obtained

$$\boldsymbol{\varepsilon} = \frac{1}{|\Omega_\mu|} \int_{\partial\Omega_\mu} \boldsymbol{u}_\mu \otimes^s \boldsymbol{n} \; d\partial\Omega_\mu. \tag{16}$$

The insertion of the macro-scale strain tensor $\boldsymbol{\varepsilon}$ in the **RVE** kinematics, is defined as

$$\boldsymbol{u}_\mu = \boldsymbol{u} + \boldsymbol{\varepsilon}\left(\boldsymbol{y} - \boldsymbol{y}_0\right) + \tilde{\boldsymbol{u}}_\mu, \;\Rightarrow\; \nabla^s_{\boldsymbol{y}} \boldsymbol{u}_\mu = \boldsymbol{\varepsilon} + \nabla^s_{\boldsymbol{y}} \tilde{\boldsymbol{u}}_\mu. \tag{17}$$

Finally, the space of kinematically admissible displacement fluctuations are

$$\tilde{\mathscr{U}}_\mu = \left\{ \boldsymbol{u} \in \boldsymbol{H}^1\left(\Omega\right) : \int_{\Omega_\mu} \boldsymbol{u} \; d\Omega_\mu = 0, \; \int_{\partial\Omega_\mu} \boldsymbol{u} \otimes^s \boldsymbol{n} \; d\partial\Omega_\mu = 0 \right\} \tag{18}$$

- Axiom 2 - Multi-scale virtual principle for poro-mechanical problems

The multi-scale virtual principle considering a poro-mechanic material in the **RVE** with undrained hydraulic conditions, can be expressed as

$$\boldsymbol{\sigma} \cdot \nabla^s_{\boldsymbol{x}} \delta\boldsymbol{u} = \frac{1}{|\Omega_\mu|} \int_{\Omega_\mu} \boldsymbol{\sigma}_\mu\left(\boldsymbol{u}_\mu, p_\mu, \theta_\mu\right) \cdot \nabla^s_{\boldsymbol{y}} \delta\boldsymbol{u}_\mu \; d\Omega_\mu + \int_{\Gamma_\mu} \boldsymbol{t}_\mu \cdot [\![\delta\boldsymbol{u}_\mu]\!] d\Gamma_\mu, \quad \forall \delta\boldsymbol{u} \; \delta\boldsymbol{u}_\mu \; admissible, \tag{19}$$

where the last term is the contribution of the activated cohesive elements in the multi-scale virtual power.

- Consequence 1 - Micro-mechanical equilibrium problem

Considering $\nabla^s_{\boldsymbol{x}} \delta\boldsymbol{u} = 0$ in equation 19, the micro-scale equilibrium equation is obtained

$$\int_{\Omega_\mu} \boldsymbol{\sigma}_\mu\left(\boldsymbol{u}_\mu, p_\mu, \theta_\mu\right) \cdot \nabla^s_{\boldsymbol{y}} \delta\tilde{\boldsymbol{u}}_\mu \; d\Omega_\mu + \int_{\Gamma_\mu} \boldsymbol{t}_\mu \cdot [\![\delta\boldsymbol{u}_\mu]\!] d\Gamma_\mu = 0, \quad \forall \delta\tilde{\boldsymbol{u}}_\mu \in \tilde{\mathscr{U}}_\mu \tag{20}$$

- Consequence 2 - Homogenization operator for the stress tensor

Considering $\delta\tilde{\boldsymbol{u}}_\mu = 0$ in equation 19, the homogenization operator for the stress tensor is obtained

$$\boldsymbol{\sigma} = \frac{1}{|\Omega_\mu|} \int_{\Omega_\mu} \boldsymbol{\sigma}_\mu\left(\boldsymbol{u}_\mu, p_\mu, \theta_\mu\right) \; d\Omega_\mu. \tag{21}$$

4 Helmholtz free energy in the RVE

Following Ref. [2], the energetic consistency in the micro-scale is stated considering the Helmholtz free energy as follows

$$\boldsymbol{\psi}_\mu\left(\nabla^s_{\boldsymbol{y}} \boldsymbol{u}_\mu, p_\mu, \theta_\mu\right) = \boldsymbol{\psi}^B_\mu\left(\nabla^s_{\boldsymbol{y}} \boldsymbol{u}_\mu, p_\mu, \theta_\mu\right) + \boldsymbol{\psi}^F_\mu\left(\delta_\mu\right), \tag{22}$$

where $\boldsymbol{\psi}_{\mu}^{B}$ is the Helmholtz free energy for the bulk phase and $\boldsymbol{\psi}_{\mu}^{F}$ is the Helmholtz free energy for the fractured phase, defined as [3, 4]

$$\begin{aligned}\boldsymbol{\psi}_{\mu}^{B}\left(\nabla_{\boldsymbol{y}}^{s}\boldsymbol{u}_{\mu}, p_{\mu}, \theta_{\mu}\right) = \frac{1}{2}\,\mathbb{C}_{\mu}\left(\nabla_{\boldsymbol{y}}^{s}\boldsymbol{u}_{\mu}\right)\cdot\left(\nabla_{\boldsymbol{y}}^{s}\boldsymbol{u}_{\mu}\right) - \boldsymbol{B}_{\mu}\left(\nabla_{\boldsymbol{y}}^{s}\boldsymbol{u}_{\mu}\right)\theta_{\mu} + \\ + \frac{1}{2}M_{w}b_{w}^{2}\left(tr\left(\nabla_{\boldsymbol{y}}^{s}\boldsymbol{u}_{\mu}\right) - \frac{\zeta_{w}}{b_{w}}\right)^{2} + \frac{1}{2}\left(-\frac{\mathscr{C}}{T_{0}} + M_{w}\alpha_{w}^{2}\right)\theta_{\mu}^{2} + \\ - M_{w}b_{w}\left(tr\left(\nabla_{\boldsymbol{y}}^{s}\boldsymbol{u}_{\mu}\right) - \frac{\zeta_{w}}{b_{w}}\right)\alpha_{w}\theta_{\mu} + \chi_{\mu}\rho_{\mu}\zeta_{w},\end{aligned} \tag{23}$$

and

$$\boldsymbol{\psi}_{\mu}^{F}\left(\delta_{\mu}\right) = \begin{cases} G_{c}\frac{\delta_{\mu}}{\delta_{c}}\left(2 - \frac{\delta_{\mu}}{\delta_{c}}\right), & if \quad \delta_{\mu} \leq \delta_{c} \\ G_{c}, & if \quad \delta_{\mu} > \delta_{c} \end{cases}, \quad with \quad \delta_{\mu} = \sqrt{[\![\boldsymbol{u}_{\mu}]\!]\cdot[\![\boldsymbol{u}_{\mu}]\!]}\ . \tag{24}$$

The coefficients needed to calibrate the porous media in the model are: b_w the Biot coefficient, M_w the Biot modulus, $\zeta_w = \phi_w S_w$ the water volumetric fraction being ϕ_w water porosity and S_w the degree of saturation, α_w coefficient of thermal expansion, $\mathscr{C}$ volumetric heat capacity and T_0 the reference temperature. The skeleton part is calibrated using the elastic material operator

$$\mathbb{C}_{\mu} = \frac{E_{\mu}}{1-\nu_{\mu}^{2}}\left[\left(1-\nu_{\mu}\right)\mathbb{I} + \nu_{\mu}\left(\boldsymbol{I}\otimes\boldsymbol{I}\right)\right] \tag{25}$$

and the tensor of thermomechanical expansion of the skeleton

$$\boldsymbol{B}_{\mu} = \frac{\alpha_{\mu}E_{\mu}}{1-\nu_{\mu}^{2}}\left[1 + \nu_{\mu}\left(tr\boldsymbol{I} - 1\right)\right]\boldsymbol{I} \tag{26}$$

Considering Coleman's relations, from equation 22 the following relation can be obtained

$$\begin{aligned}\sigma_{\mu}\left(\nabla_{\boldsymbol{y}}^{s}\boldsymbol{u}_{\mu}, p_{\mu}, \theta_{\mu}\right) = \frac{\partial\boldsymbol{\psi}_{\mu}}{\partial\nabla_{\boldsymbol{y}}^{s}\boldsymbol{u}_{\mu}} = \mathbb{C}_{\mu}\left(\nabla_{\boldsymbol{y}}^{s}\boldsymbol{u}_{\mu}\right) - \boldsymbol{B}_{\mu}\theta_{\mu} + \\ + M_{w}b_{w}\left[b_{w}\left(tr\left(\nabla_{\boldsymbol{y}}^{s}\boldsymbol{u}_{\mu}\right) - \zeta_{w} - \alpha_{w}\theta_{\mu}\right)\boldsymbol{I}\right]\end{aligned} \tag{27}$$

or expressed in term of the pore pressure

$$\sigma_{\mu}\left(\nabla_{\boldsymbol{y}}^{s}\boldsymbol{u}_{\mu}, p_{\mu}, \theta_{\mu}\right) = \mathbb{C}_{\mu}\left(\nabla_{\boldsymbol{y}}^{s}\boldsymbol{u}_{\mu}\right) - \boldsymbol{B}_{\mu}\theta_{\mu} + b_{w}p_{\mu}\boldsymbol{I} \tag{28}$$

It is interesting to note that combining equation 28 with 21 the homogenization of the total stress in the macro scale is the result of the homogenization of the effective stress in the micro-scale plus the homogenization of the porous pressure in the micro-scale

$$\boldsymbol{\sigma} = \boldsymbol{\sigma}' + \boldsymbol{p}, \tag{29}$$

being the effective stress

$$\begin{aligned}\boldsymbol{\sigma}' = &\left(\frac{1}{|\Omega_\mu|}\int_{\Omega_\mu}\mathbb{C}_\mu\ d\Omega_\mu\right)\boldsymbol{\varepsilon} + \frac{1}{|\Omega_\mu|}\int_{\Omega_\mu}\mathbb{C}_\mu\ \left(\nabla^s_{\boldsymbol{y}}\tilde{\boldsymbol{u}}_\mu\right)\ d\Omega_\mu - \left(\frac{1}{|\Omega_\mu|}\int_{\Omega_\mu}\boldsymbol{B}_\mu\ d\Omega_\mu\right)\theta + \\ &- \left(\frac{1}{|\Omega_\mu|}\int_{\Omega_\mu}\boldsymbol{B}_\mu\otimes(\boldsymbol{y}-\boldsymbol{y}_0)\ d\Omega_\mu\right)\cdot\nabla^s_{\boldsymbol{x}}\theta - \frac{1}{|\Omega_\mu|}\int_{\Omega_\mu}\boldsymbol{B}_\mu\tilde{\theta}_\mu\ d\Omega_\mu\end{aligned} \tag{30}$$

and the pore pressure

$$\boldsymbol{p} = \frac{1}{|\Omega_\mu|}\int_{\Omega_\mu} b_w p_\mu\ d\Omega_\mu\boldsymbol{I},\quad with\quad p_\mu = M_w\left[b_w\left(tr\left(\nabla^s_{\boldsymbol{y}}\boldsymbol{u}_\mu\right) - \zeta_w - \alpha_w\theta_\mu\right)\right]. \tag{31}$$

The homogenized constitutive tensor $\mathbb{C}$ retains the classical structure. To compute tensors $\boldsymbol{B}$ and $\boldsymbol{G}$ two extra assumption are considered: a temperature invariant Biot coefficient and a constant fluid mass. The first order thermomechanical contribution to the macroscopic stress tensor is

$$-\frac{\partial\boldsymbol{\sigma}}{\partial\theta} = \boldsymbol{B} = \overline{\boldsymbol{B}} + \tilde{\boldsymbol{B}} + \boldsymbol{B}^p, \tag{32}$$

where

$$\overline{\boldsymbol{B}} = \frac{1}{|\Omega_\mu|}\int_{\Omega_\mu}\boldsymbol{B}_\mu\ d\Omega_\mu,\quad \tilde{\boldsymbol{B}} = -\frac{1}{|\Omega_\mu|}\int_{\Omega_\mu}\mathbb{C}_\mu\ \left(\nabla^s_{\boldsymbol{y}}\frac{\partial\tilde{\boldsymbol{u}}_\mu}{\partial\theta}\right)\ d\Omega_\mu, \tag{33}$$

while the contribution of the pore pressure can be stated as

$$\boldsymbol{B}^p = \frac{1}{|\Omega_\mu|}\int_{\Omega_\mu} b_w\frac{\partial p_\mu}{\partial\theta}\ d\Omega_\mu\boldsymbol{I},\quad with\quad \frac{\partial p_\mu}{\partial\theta} = M_w\left[b_w\left(tr\left(\nabla^s_{\boldsymbol{y}}\frac{\partial\tilde{\boldsymbol{u}}_\mu}{\partial\theta}\right) - \alpha_w\right)\right]. \tag{34}$$

In the same way, the second order thermomechanical contribution to the macroscopic stress can be stated as

$$-\frac{\partial\boldsymbol{\sigma}}{\partial\nabla^s_x\theta} = \boldsymbol{G} = \overline{\boldsymbol{G}} + \tilde{\boldsymbol{G}} + \boldsymbol{G}^p, \tag{35}$$

where

$$\overline{\boldsymbol{G}} = \frac{1}{|\Omega_\mu|}\int_{\Omega_\mu}\boldsymbol{B}_\mu\otimes(\boldsymbol{y}-\boldsymbol{y}_0)\ d\Omega_\mu, \tag{36}$$

$$\begin{aligned}\tilde{\boldsymbol{G}} = &-\left[\frac{1}{|\Omega_\mu|}\int_{\Omega_\mu}\left(\mathbb{C}_\mu\left(\nabla^s_x\left[\frac{\partial\tilde{\boldsymbol{u}}_\mu}{\partial\nabla^s_x\theta}\right]_k\right)\right)_{ij}\ d\Omega_\mu + \right. \\ &\left. -\frac{1}{|\Omega_\mu|}\int_{\Omega_\mu}(\boldsymbol{B}_\mu)_{ij}\left[\frac{\partial\tilde{\theta}_\mu}{\partial\nabla^s_x\theta}\right]_k\ d\Omega_\mu\right](\boldsymbol{e}_i\otimes\boldsymbol{e}_j\otimes\boldsymbol{e}_k),\end{aligned} \tag{37}$$

while the contribution of the pore pressure is

$$\boldsymbol{G}^p = \frac{1}{|\Omega_\mu|}\int_{\Omega_\mu} b_w\frac{\partial p_\mu}{\partial\nabla^s_x\theta}\ d\Omega_\mu\boldsymbol{I}, \tag{38}$$

with

$$\frac{\partial p_\mu}{\partial \nabla_x^s \theta} = M_w \left[b_w \left(tr\left(\nabla_{\boldsymbol{y}}^s \frac{\partial \tilde{\boldsymbol{u}}_\mu}{\partial \nabla_x^s \theta} \right) - \alpha_w \left(\boldsymbol{y} - \boldsymbol{y}_0 + \frac{\partial \tilde{\theta}_\mu}{\partial \nabla_x^s \theta} \right) \right) \right]. \tag{39}$$

The homogenized macroscopic stress can then be calculated as

$$\boldsymbol{\sigma} = \mathbb{C}\boldsymbol{\varepsilon} - \boldsymbol{B}\theta - \boldsymbol{G}\nabla_x^s \theta. \tag{40}$$

5 Numerical examples

Some numerical examples are presented in this section, considering an uncoupled scheme solution for the thermo-poro-mechanical problem. The proposed **RVE** for the analysis in concrete is presented in Figure 2.

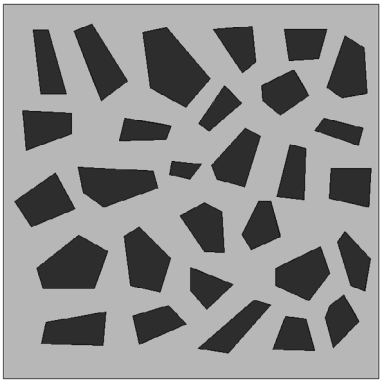

Figure 2: Proposed **RVE** for thermo-poromechanical analysis.

5.1 Multi-scale thermal problem

The considered thermal conductivity tensor for cement mortar and aggregates are

$$\boldsymbol{K}_\mu^{mortar} = \begin{bmatrix} 0.7 & 0 \\ 0 & 0.7 \end{bmatrix} \frac{W}{m\ ^\circ C}, \qquad \boldsymbol{K}_\mu^{aggreg} = \begin{bmatrix} 3.0 & 0 \\ 0 & 3.0 \end{bmatrix} \frac{W}{m\ ^\circ C}. \tag{41}$$

Using the homogenization procedure presented for the thermal problem, the following homogenized thermal conductivity tensors for different sub-spaces of equation 10 are obtained $\left(\text{in } \frac{W}{m\ ^\circ C}\right)$

$$\begin{aligned} \boldsymbol{K}^{Taylor} &= \begin{bmatrix} 1.3696 & 0 \\ 0 & 1.3696 \end{bmatrix}, & \boldsymbol{K}^{Linear} &= \begin{bmatrix} 1.079 & 0.0024854 \\ 0.0024854 & 1.0622 \end{bmatrix}, \\ \boldsymbol{K}^{Periodic} &= \begin{bmatrix} 1.0754 & 0.0023161 \\ 0.0023161 & 1.0573 \end{bmatrix}, & \boldsymbol{K}^{Traction} &= \begin{bmatrix} 1.0724 & 0.0023531 \\ 0.0023531 & 1.0549 \end{bmatrix}. \end{aligned} \tag{42}$$

Considering a temperature gradient of $\nabla_x^s \theta = [1; 0]$ and the homogenized tensors, the macroscopic flux vectors in each case are

$$\begin{aligned} \boldsymbol{q}^{Taylor} &= \begin{bmatrix} 1.3696 \\ 0 \end{bmatrix} \frac{W}{m^2}, & \boldsymbol{q}^{Linear} &= \begin{bmatrix} 1.079 \\ 0.0024854 \end{bmatrix} \frac{W}{m^2}, \\ \boldsymbol{q}^{Periodic} &= \begin{bmatrix} 1.0754 \\ 0.0023161 \end{bmatrix} \frac{W}{m^2}, & \boldsymbol{q}^{Traction} &= \begin{bmatrix} 1.0724 \\ 0.0023531 \end{bmatrix} \frac{W}{m^2}. \end{aligned} \tag{43}$$

It can be seen that the macroscopic thermal flux vectors presented in the last equations have a different direction compared with the introduced macroscopic temperature gradient due to the anisotropy induced by the stochastic nature of the aggregate distribution. The Taylor (classical mixture theory) sub-space is the only one not capable of recognizing this effect, as it does not consider the heterogeneous geometrical conformation of the micro-structure.

Considering the minimally restricted space, or uniform traction space, and introducing a macroscopic temperature of $\theta = 100°C$, figure 3 shows the temperature distribution within the considered **RVE** for different values in $\nabla_x^s \theta$. It can be seen that the average value in the microscopic temperature field θ_μ is the macroscopic introduced temperature.

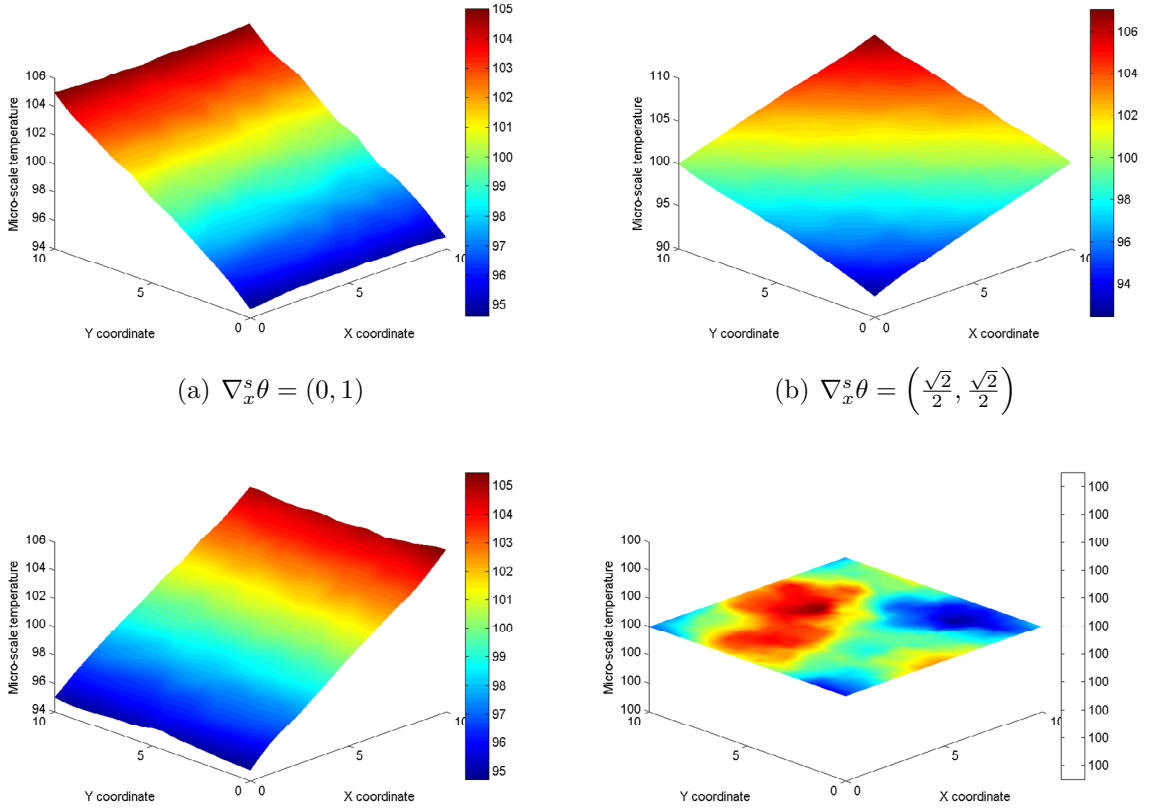

(a) $\nabla_x^s \theta = (0, 1)$ (b) $\nabla_x^s \theta = \left(\frac{\sqrt{2}}{2}, \frac{\sqrt{2}}{2}\right)$

(c) $\nabla_x^s \theta = (1, 0)$ (d) $\nabla_x^s \theta = (0, 0)$

Figure 3: Temperature distribution within the **RVE**.

5.2 Multi-scale thermo-mechanical problem

In order to study the thermo-mechanical problem, a constant thermal distribution in concordance with a temperature gradient $\nabla_x^s \theta = (0, 0)$ is considered. The material parameters used to characterize the components of the micro-scale are presented in Table 1. The macro-scale temperature is increased and then returned to the initial temperature condition, introducing initial damage. Then, a monotonically increasing macro-strain is imposed to de **RVE** until it losses ellipticity.

The final configuration of the proposed **RVE** for different temperatures can be seen in Figure 4, showing a different failure mode for different temperatures. The homogenized stress-strain curves are plotted in Figure 5. It can be seen that the peak stress of the proposed constitutive model is reduced due to the damage induced by the temperature, and there is an increase in ductility. This results coincide with experimental analysis found in literature.

	Mortar	Aggregate	Interface
Young modulus E [MPa]	30800	37000	-
Poisson modulus	0.28	0.16	-
Critical tension σ_c [MPa]	6	-	3
Fracture energy G_c [N/mm]	0.14	-	0.070
Skeleton thermal expansion coefficient α_μ [1/°C]	$7.4e^{-6}$	$12.6e^{-6}$	-
Water thermal expansion coefficient α_w [1/°C]	$207e^{-6}$	-	-
Water porosity ϕ_w	0.16	-	-
Water Biot coefficient b_w	0.4073	-	-
Water Biot modulus M_w [MPa]	9400	-	-
Porous saturation degree S_w	0.5	-	-

Table 1: Properties for concrete.

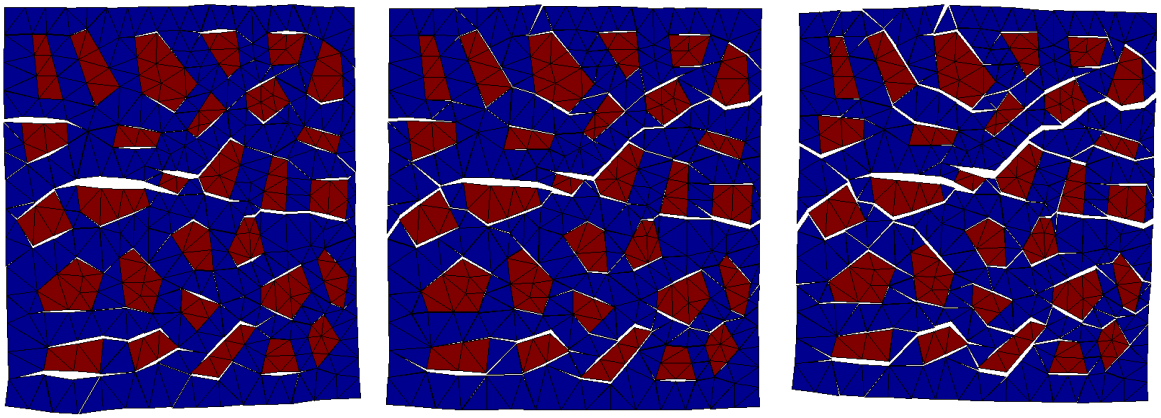

(a) Macro temperature $\theta = 0°C$. Displacement amplified $x500$.

(b) Macro temperature $\theta = 400°C$. Displacement amplified $x150$.

(c) Macro temperature $\theta = 700°C$. Displacement amplified $x100$.

Figure 4: Final configuration of the **RVE** for different temperatures and temperature gradient $\nabla_x^s \theta = (0, 0)$.

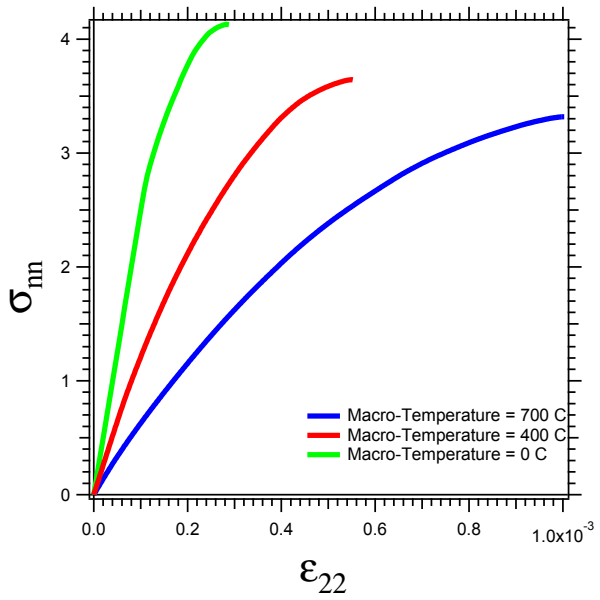

Figure 5: Homogenized stress versus strain curves for different temperatures.

The considered tensors of thermomechanical expansion for cement mortar and aggregates are

$$\boldsymbol{B}_{\mu}^{mortar} = \begin{bmatrix} 0.2072 \\ 0.2072 \\ 0 \end{bmatrix} \frac{MPa}{°C}, \qquad \boldsymbol{B}_{\mu}^{aggreg} = \begin{bmatrix} 0.3709 \\ 0.3709 \\ 0 \end{bmatrix} \frac{MPa}{°C}. \tag{44}$$

Using the homogenization procedure presented, the following homogenized thermal conductivity tensors for different sub-spaces are obtained

$$\boldsymbol{B}^{Taylor} = \begin{bmatrix} 0.2548 \\ 0.2548 \\ 0 \end{bmatrix} \frac{MPa}{^{\circ}C}, \qquad \boldsymbol{B}^{Traction} = \begin{bmatrix} 0.2507 \\ 0.2454 \\ 0.0164 \end{bmatrix} \frac{MPa}{^{\circ}C}. \tag{45}$$

6 Conclusions

A multi-scale model for thermo-poro-mechanic problems has been presented and discussed in this paper. Starting from a semi-concurrent formulation, the Helmholtz free energy of the mortar phase in the micro-scale is reformulated using the Biot theory for porous media to consider the effect of the pore pressure induced by the heat transfer through the material. Some numerical examples showing the homogenized response of a concrete like material are presented and discussed. The lost of resistance of the material due a temperature increasing has been numerically reproduced, and the final damage configuration is presented.

REFERENCES

[1] Blanco P.J., Giusti S.M. Thermomechanical Multiscale Constitutive Modeling: Accounting for Microstructural Thermal Effects, Journal of Elasticity: The Physical and Mathematical Science of Solids, 2013. Vol.111.

[2] López Rivarola F, Etse J.G. and Folino P. On Thermodynamic Consistency of Homogenization-based Multiscale Theories. ASME. J. Eng. Mater. Technol. 2017, doi:10.1115/1.4036243.

[3] Pignatelli Rossella. Modeling of degradation induced by alkali-silica reaction in concrete structures. Ph.D. Thesis, Politecnico di Milano.

[4] Labanda N.A., Giusti S.M. and Luccioni B.M. Meso-Scale Fracture Simulation using an augmented Lagrangian Approach. International Journal of Damage Mechanics, 2016. doi:10.1177/1056789516671092.

XIV International Conference on Computational Plasticity. Fundamentals and Applications
COMPLAS 2017
E. Oñate, D.R.J. Owen, D. Peric and M. Chiumenti (Eds)

CYBER EQUIPPING 4.0 – FE-SIMULATION-BASED SETTING INSTRUCTIONS FOR A ROTARY DRAW-BENDING MACHINE

M. ENG. LINDA SCHULTE [1], DR.-ING. CHRISTOPHER KUHNHEN [1], M. SC. DARWIN ABELE [2], M. SC. SVEN HOFFMANN [3], DR. APARECIDO FABIANO PINATTI DE CARVALHO [3], UNIV.-PROF. DR.-ING. BERND ENGEL [1], PROF.-DR. MARCUS SCHWEITZER [2], UNIV.-PROF. DR. VOLKER WULF [3]

[1] Universität Siegen, Lehrstuhl für Umformtechnik (UTS)
Paul-Bonatz-Straße 9-11, 57076 Siegen
e-mail: linda.schulte@uni-siegen.de, web page: http://www.mb.uni-siegen.de/uts/

[2] Universität Siegen, Lehrstuhl für Technologiemanagement
Unteres Schloß 3, 57072 Siegen
web page: http://www.wiwi.uni-siegen.de/technologiemanagement/

[3] Universität Siegen, Lehrstuhl für Wirtschaftsinformatik und neue Medien
Kohlbettstraße 15, 57072 Siegen
e-mail: sekretariat(at)wineme.fb5.uni-siegen.de, web page: http://www.wineme.uni-siegen.de/

Key words: Equipping process, rotary draw bending, FE simulation, parameter influence, cyber physical systems, industry 4.0

Abstract. The tool setting process for rotary draw-bending is very complex. Only experienced machine operators know which settings lead to a good result in relation to the bending task. Up to seven individual tools can be installed, positioned and set in the process independently. A complete set of tools consists of: pressure die, mandrel, wiper die, inner and outer clamp die as well as the bend die and the collet or piston bend. [1] Furthermore there are the axis settings, which can be adjusted with the parameters distance, force, angle, torque and time. If a defect occurs after the successful set-up process the machine operator has various possibilities to solve the problem. The effects of the different setting parameters and the procedure for the fastest possible elimination of the error are often unclear. The goal is to be able to use an adjustment support for the setting process by means of physical-analytical principles and systematically constructed FE simulations at the bending machine. In order to evaluate the bending result, the condition of the bending component is examined concerning the quality characteristics, cracking, wrinkling, cross-section deformation and elastic deformation. [2] Based on performed and analyzed FE simulations, adjustment recommendations regarding the respective quality characteristics are to be established as well as predictions about possible defects. The simulation and calculation results flow into a database. This is used for the implementation of an electronic expert, who uses a visualization aid to provide the machine operator with information and recommendations on the setup settings. This avoids errors during the equipping process and saves set-up time. Machine operators and particularly trained employees are guided and supported in their work.

1 INTRODUCTION

At present, the set-up process and the adjustment process of the rotary draw bending are mainly based on the knowledge of the machine operators, which can result in high subjectivity. Particularly in the case of work sequences with intensive set-up times, a shortening of this non-value added activity is very important. This fact is multiplied when small series or individual components have to be realized. Interviews revealed that it often takes at least six months until a new trained employee, trained by experienced machine operators, can carry out his first set-up process by herself or himself. The transfer of information is cumbersome and the first economic set-up times are not reached until the employee has acquired his own experience. The aim of the joint research project "Cyber equipping 4.0 - cyber-physical support of humans during the set-up process using the example of a bending process for small-scale production on the basis of a knowledge transfer approach" is the quantification of the machine operator's experience knowledge in order to implement a setting rule and a set-up support for the machine operators using the approach of mental modeling. This set-up support should also be able to capture and process information using new possibilities of visualization, such as augmented reality technology. In order to be able to equip this set-up support with important process knowledge, FE simulations are to illustrate the influence of setting parameters on the quality characteristics of the bending component and to check and evaluate the results for universal validity. The first results of this research project are to be disclosed as followed.

2 THEORY

According to [2], rotary draw bending is a forming process which is shape-related.

1 piston bend or collet
2 mandrel
3 pressure die
4 outer clamp die
5 inner clamp die
6 bend die
7 wiper die

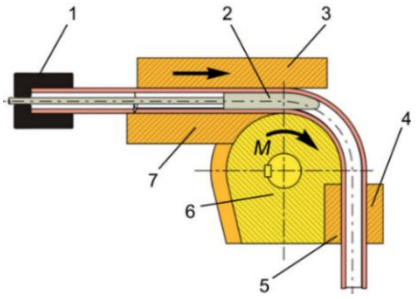

Figure 1: Rotary draw-bending tool kit [1]

Prior to the bending process the tube is pushed over the mandrel from the front and fixed in the piston bend as well as between the inner and outer clamp dies. After that the bend die rotates around the bending center with the required bending angle. The tube is thereby pulled around the bending center while it is in contact with the cavity in the bend die. The outer clamp die rotates around the same center point so that the tube end remains fixed over the entire process. The pressure die serves to absorb the reaction force from the bending moment. Moreover, the pressure die can transmit a force through the tube and the inner mandrel on the wiper die. This passive reaction force superimposes the compressive stresses on the inner arc of the tube bow to prevent wrinkling. In addition to the function as a force-transmitting element, the mandrel serves for geometrically supporting the hollow profile. An ovality can

thus be countered. After the bending process has been completed, the bend part is released from the clamping of the outer and inner clamp dies. After the movements of the machine axes to their basic positions are done, the next bending can be carried out or the component can be removed after releasing the clamp die. The torque required for bending, initiated by the bend die, is transmitted to the plurality of tools and dissipates different reaction forces. This results in a complex force profile along the tube to be bent. In addition, up to seven different tools can be set independently of each other (figure 1). The settings are based on the position (translational displacement and rotational orientation), in selecting the correct speeds, as well as accelerations and the resulting process times. These aspects make the flexural bending process a complicated forming process that reacts very sensitively to parameter variations. Finding connections between setting parameters and bending results and then handing them over to other employees is difficult and time-consuming. There is a great demand for a visualization instrument, which combines know-how with a visual, comprehensible presentation.

2.1 Equipping process

A tool setting process can be subdivided into a static and a dynamic component. The *static tool setting process* includes all in-house activities and necessities, which are indispensable for the actual set-up task. This includes the provision of tools and the maintenance of storage areas, as well as the infrastructure necessary for the correct allocation of tools to bending components. In addition, the static part includes the set-up process itself. This involves dismantling the old tool set and installing the new tool sets. It is also distinguished into a small, as well as a large set-up process, depending on how many tools have to be exchanged. The *dynamic tool setting process* includes all activities which are to be carried out after the static tool setting process. These include in particular parameter variations within the machine control for setting the process, as well as the adjustment of the process due to component faults. For a fast, targeted adjustment of the process parameters, a strong process understanding is necessary.

2.2 Quality characteristics

The VDI 3431 [2] currently comprises over twenty different quality characteristics on the bending component which can be tested both quantitatively and qualitatively according to the customer's requirements (see also [1], [3], [4]).

Table 1: Quality characteristics, extract from VDI 3431 [2]

characteristic	**formular-symbol**
Inner and outer diameter	D_i, D_a
Bending radius	R_{th}
Bending angle	α
Cross-section area	-
Cracking (DIN EN ISO 8785) [3]	-
Roundness of tubes	-
Wall thickness	s

In the context of this publication, the quality characteristics cracking on the outer curve and ovality or cross-section deformation were analyzed using FE simulations.

3 DISCUSSION

3.1 Simulation software

With the aid of the FE simulation program PAM-Stamp 2G of the ESI-Group, Neu-Isenburg Germany, a simulation model was modeled according to the real process of the company Westfalia Metallschlauch GmbH, Hilchenbach Germany.
The quality characteristics explained in chapter 2.2 can be assigned to different process parameters by which these are influenced. The parameters of the rotary draw bending process to be set are listed in table 2. The adjustment parameters were modeled in PAM-Stamp 2G with the semi-finished material 1.4512, a tube outer diameter of D_a = 101.6 mm, a wall thickness of 2 mm, a bending angle of 127.7°, and a bending ratio of 1 × D_a.

3.2 Reference simulation

In order to find out in how far and strong which process parameters influence the bending result, an OFAT study (one factor at a time) was first carried out. For this purpose, a reference simulation was set up, in order subsequently to vary successively individual process parameters. The reference simulation generates a bending result, which is classified as a good part, in accordance with customer's wishes and requirements. A large number of simulations arose, which after evaluation contribute to the improvement of the process understanding. Table 2 shows the values for which the process parameters were set during the reference simulation. Within the contact definition, the COULOMB's coefficient of friction was specified as tangential behavior.

Table 2: Process parameter of the FE-simulation

Process parameter in PAM-Stamp 2G	**Value**	**Unit**
Clamp die force	125	kN
Clamp die coefficient of friction	0.4	-
Piston bend speed	7.5	mm/s
Mandrel position	0	mm
Mandrel speed	19	mm/s
Mandrel coefficient of friction	0.05	-
Presure die displacement	0.15	mm
Pressure die speed	9.4 (= 94 %· v_{Bd})	mm/s
Pressure die coefficient of friction	0.2	-
Wiper die position	0	mm
Wiper die coefficient of friction	0.15	-

In the first 2 s of the simulation time the clamping of the tube is made. Only after the clamping force has reached 100 %, the forming begins. The feed rate is reduced via the piston

bend during the conversion from second 6 (c.f. figure 2 l.h.). This results in less wrinkling. The mandrel is initially left at its starting position during the forming process, which is also shown in figure 2 r.h. In the last 5° of the bending angle, the mandrel is retracted, while at the same time the rotational speed of the bend die and the pressure die displacement in transversal direction (c.f. figure 3 l.h.) are reduced. The paths marked green and red show the setting limits between which a parameter variation was performed.

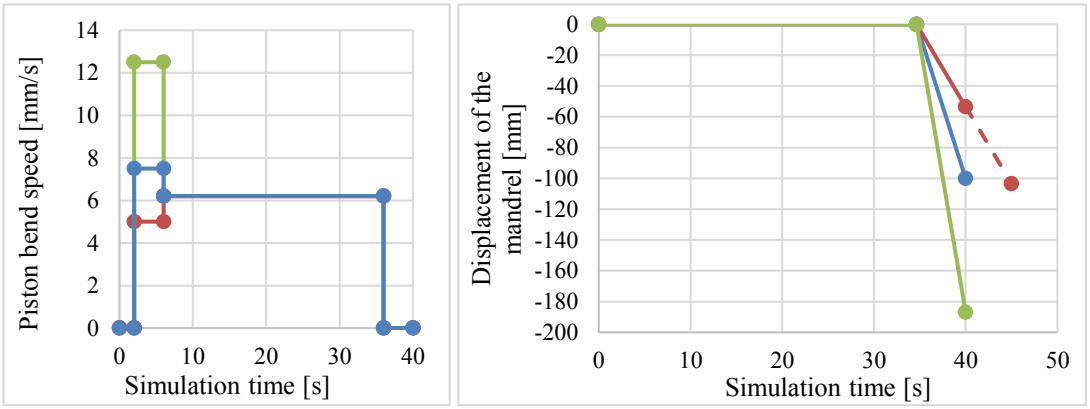

Figure 2: Amplitude profile of the adjustment parameters

The speed of the pressure die v_{Pd} is dependent on the rotational speed of the bend die v_{Bd}, related to the outside radius of the tube bow. For this reason, the coefficient v_{Pd}/v_{Bd} is introduced. If this coefficient is 100 %, the speed of the pressure die is exactly the same as the rotational speed of the outer bow of the tube. In the case of the bending task simulated here, the angular velocity amounts $\omega_{Bd} = 0.0656\, rad/s$ and thus the rotational speed of the outside bow is $v_{Bd} = 10\, mm/s$. In figure 3 r.h., the amplitude profile of the displacement which the pressure die moves in longitudinal direction at specific simulation times is shown. Moreover, the coefficienst $v_{Pd}/v_{Bd}$of the shown velocities are displayed in percent.

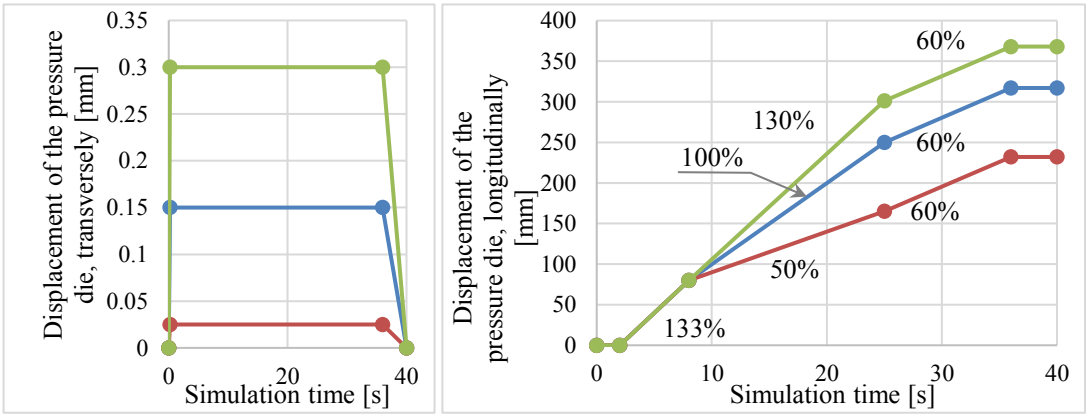

Figure 3: Amplitude profile of the adjustment parameters

At the displacement of the pressure die in longitudinal direction there are three different speed ranges during the bending process. The initial speed, up to second 6, is 33 % above the tube

speed. This is followed by a variable speed up to second 25. If the bending angle is exceeded 90°, a continuously low end speed of 60 % of the tube speed is used. During the last 5° the speed of the pressure die is 0 mm/s.

The forming limit diagram was used for the evaluation of the simulations. This represents the maximum main transformation degree φ_1 over the minimum main transformation degree φ_2. For the failure limit, a simplified calculation model according to [5] with a constant value for the positive range of φ_2 and a constant slope of -1 for the negative range of φ_2 was used. Figure 4 shows the forming limit diagram of the reference simulation.

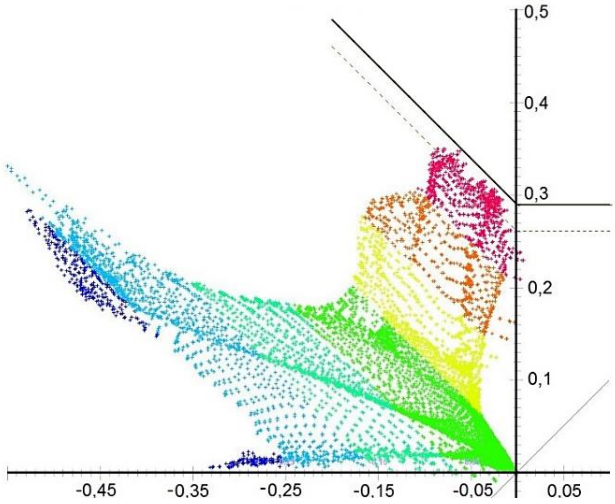

Figure 4: Forming limit diagram of the reference simulation

3.3 Key indicators for assessing the failure criteria

The value FLDCRT, forming limit diagram failure criterion, is used for the failure criterion cracking on the outer radius [6]. The FLDCRT value is calculated for a point A in figure 5 according to equation (1).

$$FLDCRT^A = \frac{\varphi_1^A}{\varphi_1^B} \tag{1}$$

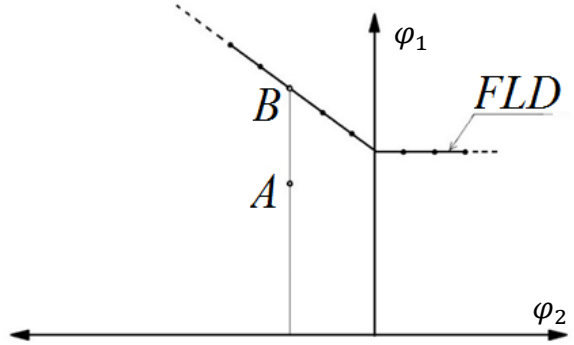

Figure 5: Calculation of the FLDCRT value

In order to be able to compare the simulations, the FLDCRT value is determined from each point of the forming limit diagram. Then the largest value is stored as a comparison characteristic value. If the value of an evaluated simulation is less than 1, the bending part is crack-free. If the value exceeds 1, at least one FLD point has exceeded the limit shape change and the component fails.

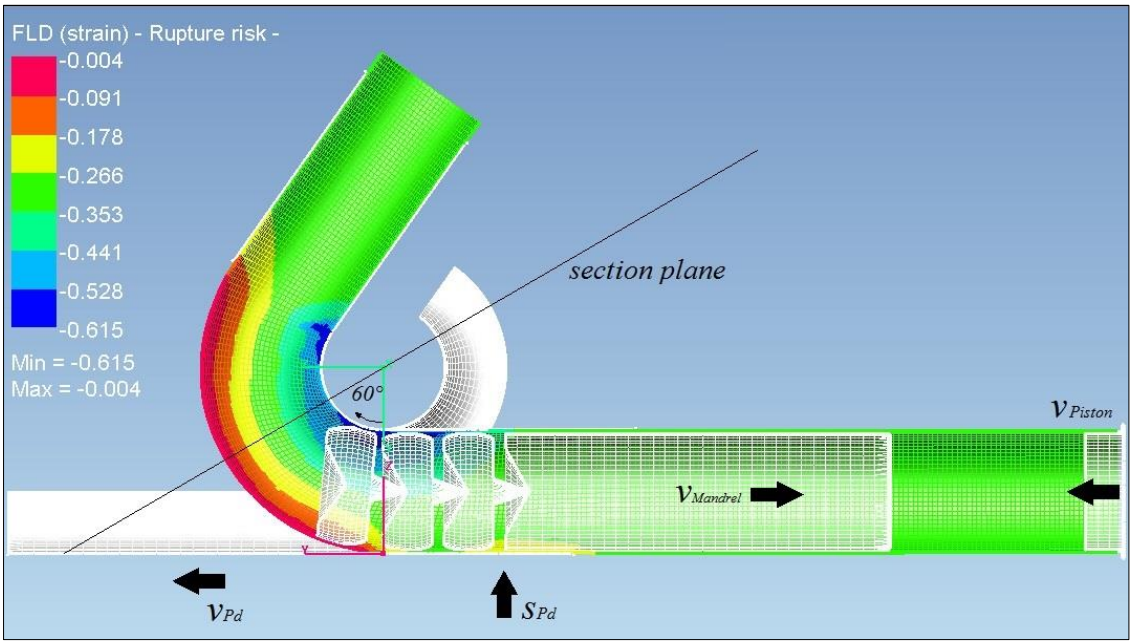

Figure 6: FLD distance value of the reference simulation

Figure 6 shows the FLD distance value of PAM-Stamp 2G, which indicates the distance between point A and point B, where a negative distance corresponds to a point A below the forming limit curve (c.f. figure 5). The FLDCRT value is calculated from this value.

For the failure criterion ovality, the out-of-roundness u is calculated according to VDI 3430 [1] from the coordinates of the simulations at an angle of 60° of the arc. For this purpose, in the simulation program, as shown in figure 6, a cutting plane is laid through the tube at the 60° angle and the coordinates of each node point of the tube cross-section are stored out. Subsequently, the tube outer diameter in the direction of the main axis and the secondary axis are calculated, and the percentage of the out-of-roundness u is determined. The simulated bends pass through a spring back program of PAM-Stamp 2G before being evaluated to measure the comparative values of the unclamped tubes.

3.4 Quality characteristic cracking

The process parameters which are explained in more detail in chapter 3.2 and also displayed in figure 6 are the pressure die displacement s_{Pd}, which corresponds to the adjusting force of the pressure die, the characteristic number v_{Pd}/v_{Bd}, as well as the piston bend speed v_{Piston}. The effects of the variation of these three parameters on the quality characteristic cracking are shown in the following figures.

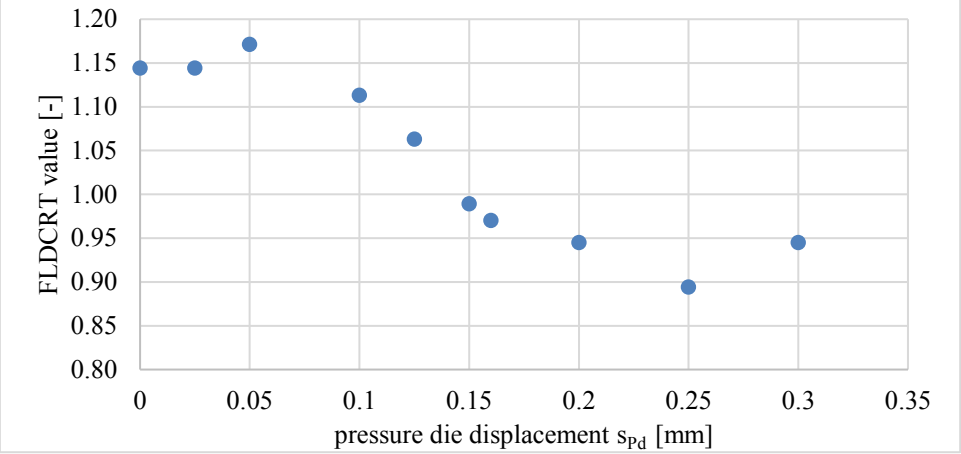

Figure 7: Pressure die displacement influence on the cracking probability

If the pressure die displacement values are less than 0.05, the bending parts are located in the cracking area (FLDCRT> 1), as can be seen in figure 7. At values between 0.05 to 0.25, the cracking probability decreases to FLDCRT = 0.894. At a pressure die displacement of 0.3 mm, the cracking probability increases again. 0.3 mm corresponds to the clearance between the mandrel and inner wall of the tube, which is reduced by the pressure die at a displacement of 0.3 mm to 0 mm. This probably leads to a higher friction.

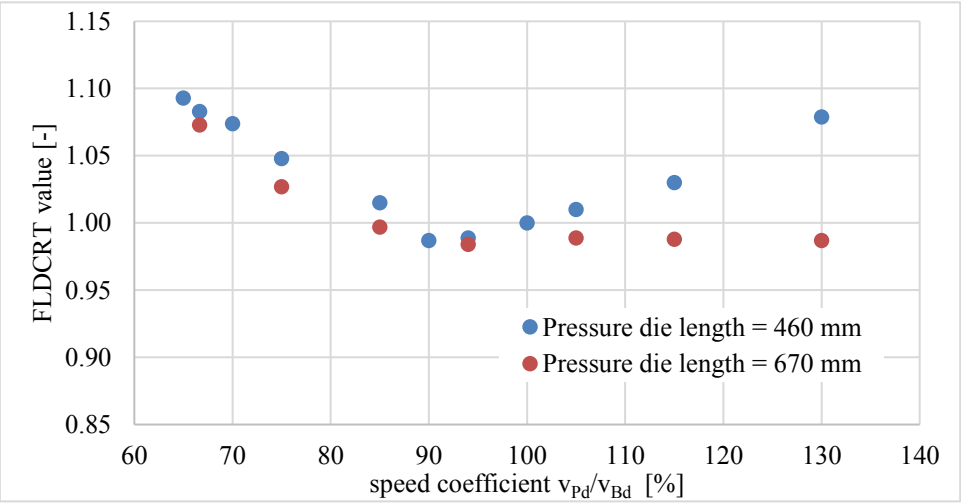

Figure 8: Pressure die speed influence on the cracking probability

As can be seen in figure 8, a raising pressure die speed is lowering the cracking probability. At a pressure die length of 460 mm (blue marking), the supporting effect of the pressure die seems to decrease at the speed coefficient of 90 % therefore the cracking probability is increasing. At a speed coefficient higher than 90 %, the pressure die moves so far that less than 1/3 of its length fits closely to the tube. This reduces the supporting effect. In simulations with a bigger pressure die length of 670 mm (red marking) the cracking probability does not rise at higher speeds. The supporting effect is retrained.

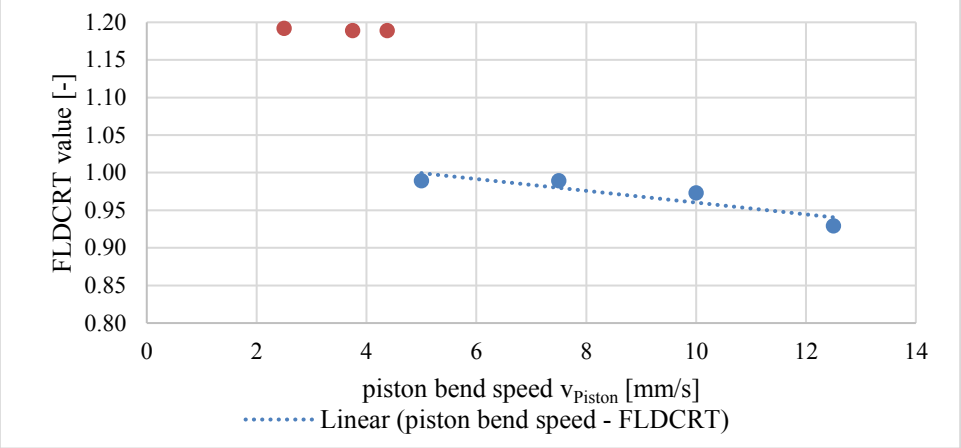

Figure 9: Piston bend speed influence on the cracking probability

As figure 9 shows, the cracking probability decreases with an increasing piston bend speed. The first three, red marked values pertain to simulations, in which the piston bend was slower than the end of the tube, so it has never touched the end face of the tube. Thus the values correspond to a boost speed as good as 0 mm/s. The valuation shows that it is not possible to bend completely without piston bend at this bending task, as, according to the FLDCRT value, the tube will crack.

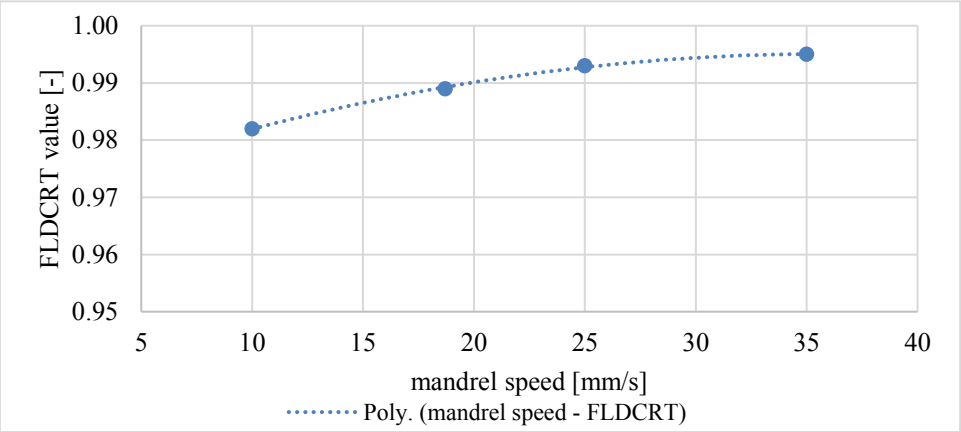

Figure 10: Mandrel speed influence on the cracking probability

A rising speed ensures a slight increase in the probability of cracking, as can be seen in figure 10. A polynomial trend line second degree connects the points.

3.5 Quality characteristic ovality

The three process parameters, already explained in chapter 3.2, have also been varied for the quality characteristic ovality. The effects of the variation to the ovality are shown in the following illustrations.

Figure 11 displays that at a pressure die speed lower than the speed of the tube's outer bow (blue marking 94 %), a rising infeed till 0.15 mm causes an expansion of the ovality, the tube's outer bow might be braked stronger. At a higher pressure die speed, (red marking 130 %), a rising delivery causes a reduction of the ovality. At this point, the boost effect might be strengthened.

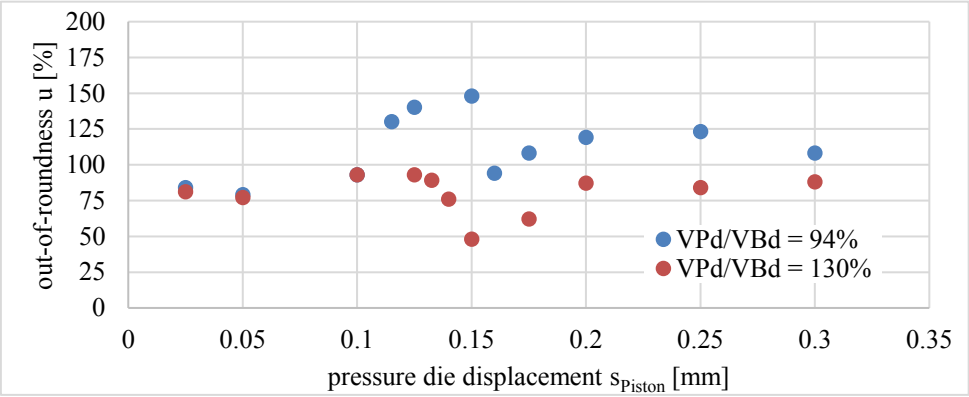

Figure 11: Pressure die displacement influence on the out-of-roundness

At a pressure die displacement of 0.16 mm in figure 11, the out-of-roundness decreases and slowly starts to increase again. The influence of the pressure die displacement to the out-of-roundness *u* seems to be in interaction with the mandrel shaft. The mandrel shaft's diameter amounts to 97.3 mm and the internal tube diameter amounts to 97.6 mm, so the radius has a 0.15 mm clearance. The first contact between the inner wall of the tube and the mandrel shaft is initiated at a displacement of 0.15 mm. If this infeed is increased, the mandrel gets slightly pushed out of its position by the pressure die. The active friction forces increase. At a displacement of 0.3 mm there is no clearance between the mandrel and the inner wall of the tube anymore. Simulations with higher displacements led to oversized, unwanted bulges.

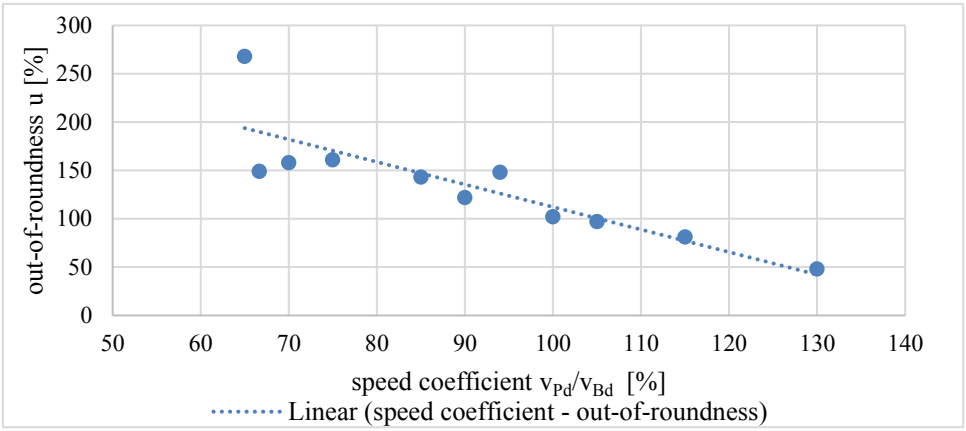

Figure 12: Pressure die speed influence on the out-of-roundness

According to figure 12, the out-of-roundness decreases at a rising pressure die speed. On this bending task, the speed of the tube center has 66 % of the rotation speed of the tube's outer

bow. At a simulated speed of 65 %, the out-of-roundness is at a particular high level.

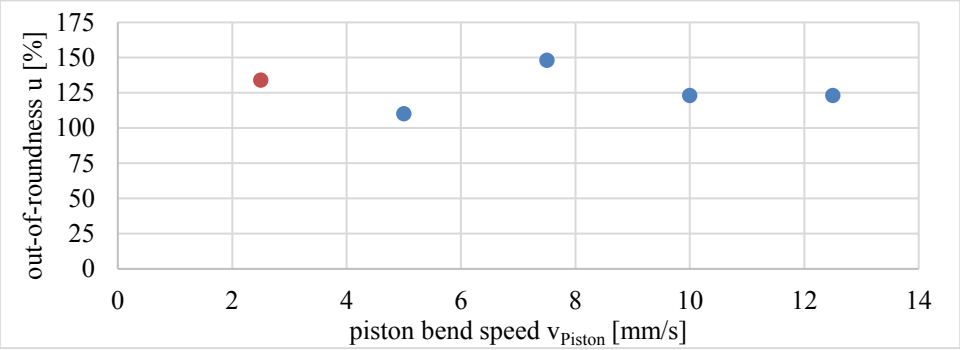

Figure 13: Piston bend speed influence on the out-of-roundness

As can be seen in figure 13, varying the piston bend speed has no clear influence on the out-of-roundness. The first, red marked value pertains to a simulation, in which the piston bend was slower than the end of the tube, so it has never touched the end face of the tube (no boost effect due to the piston bend).

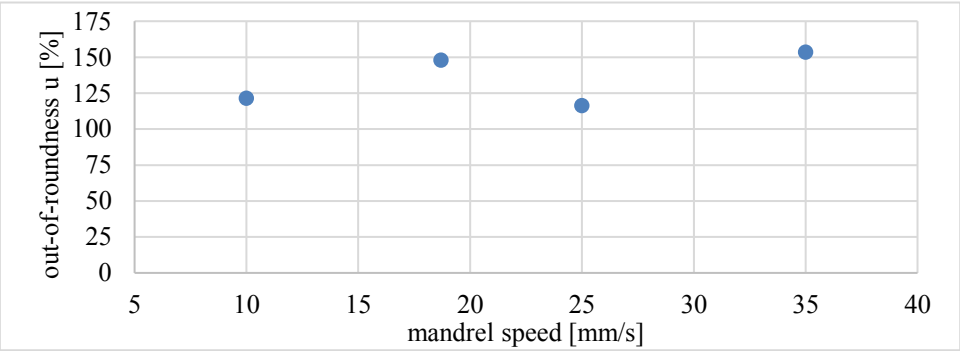

Figure 14: Mandrel speed influence on the out-of-roundness

Figure 14 shows that to vary the mandrel speed does not allow any conclusions to be drawn about the ovality.

4 CONCLUSION

The evaluation of the simulations has shown that the process parameters of the pressure die influence the bending result in a massive way. The piston bend and the mandrel do not have such an important impact to the bending result. This realization underlines the approach of adjusting the process parameters in the course of an equipping process, as previously recommended by our chair of forming technology (also seen in figure 15). This process aims in the first place to increase the pressure die speed and the displacement of the pressure die, till the error pattern is repaired. Thereby, it is important to pay attention to the interaction of the tube's speed at the tube's outer bow and with that to the rotation speed of the bend die, as well as to the interaction of the mandrel shaft's diameter and the resulting clearance to the inner wall of the tube.

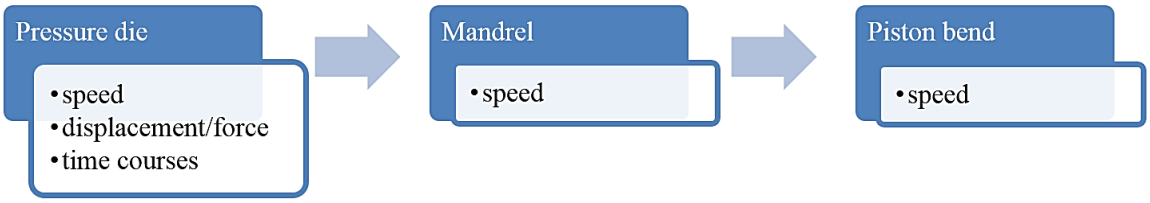

Figure 15: Approach and order of adjusting the process parameters of a rotary draw bending machine

5 OUTLOOK

All of the described investigations highlight the dependency of the configurable process parameters to the quality characteristics of the bending components of cracking and ovality. In the next working steps, actual bending tests will be carried out, based on the bending task shown in this paper, and the results will be compared to the described simulation results. The overall aim of the investigation is to provide the visualization tool, as planned in the project cyber equipping 4.0, with a software, which specifically saves process data of every bending and performs an automatic evaluation. The simulations should provide a knowledge database, which is little by little extended with results of actual bending processes. Based on these results, the visualization tool should output recommendations to parameter corrections, depending on the presented error pattern. The accuracy of the recommendations should increase with growing data quantity. In this way, machine operators and especially trained employees can be guided and supported in their activity.

6 ACKNOWLEDGEMENT AND REMARK

This project is supported by the European Union and the state of North Rhine Westphalia. *Investition in unsere Zukunft – Europäischer Fonds für regionale Entwicklung. EFRE.NRW Investition in Wachstum und Beschäftigung;* www.efre.nrw.de; www.wirtschaft.nrw.de

EFRE.NRW Investitionen in Wachstum und Beschäftigung
EUROPEAN UNION Investing in our Future European Regional Development Fund

Other project partners are:
Westfalia Metallschlauch GmbH, Hilchenbach:
Dipl.-Ing. Oliver Selter, Dipl.-Ing. Marcus Hupertz, Sascha Sckudlarek,
Lachmann und Rink GmbH, Freudenberg:
Dr. Matthias Hebbel, Dipl.-Ing. Stefan Thilo

REFERENCES

[1] VDI 3430 *Rotary draw bending of profiles,* 06.2014
[2] VDI 3431 *Bending of profiles – Testing notes for profile bending elements*, 08.2016
[3] DIN EN ISO 8785 *Geometrische Produktspezifikation (GPS)*, 1990
[4] C. Kuhnhen *Bewertung und quantitative Beschreibung von Rohrbiegebauteilen anhand von Kennziffern zur Feststellung der Rückwirkungen ausgewählter Qualitätsmerkmale auf Produktion und Produktanwendung*, 2016
[5] R. Steinheimer *Prozesssicherheit beim Innenhochdruck-Umformen*, 2005
[6] SIMULIA *Abaqus 6.14*, 04.2017 *(http://50.16.225.63/v6.14/books/usb/default.htm)*

XIV International Conference on Computational Plasticity. Fundamentals and Applications
COMPLAS 2017
E. Oñate, D.R.J. Owen, D. Peric and M. Chiumenti (Eds)

FATIGUE FAILURE ANALYSIS OF VIBRATING SCREEN SPRING BY MEANS OF FINITE ELEMENT SIMULATION: A CASE STUDY

ROSENDO FRANCO*, PEDRO A. FLORES* AND ANGEL A. C. PEINADO*

* Grupo INACOM/Aula PUCP-CIMNE, Sección Ing. Mecánica, Dpto. de Ingeniería
Pontificia Universidad Católica del Perú
Av. Universitaria 1801, 15088 Lima, Perú
e-mail: rofranco@pucp.edu.pe, http://investigacion.pucp.edu.pe/grupos/inacom/

Key words: Fatigue Analysis, High-cycle Loading, Non-proportional Loading.

Abstract. Vibrating screens are often used in the mining industry to separate mineral particles by size. In many designs, spring arrays are used to provide the system with the necessary stiffness for screens to vibrate in a controlled manner. Naturally, these springs are subjected to varying loading cycles, which can cause their premature fatigue failure. This behavior has been studied by means of finite element analysis and compared with data obtained from a real case scenario, in which a helical spring failed. The 3D computational model was developed using the geometric characteristics and material properties of a fractured spring, as well as the loading characteristics of a specific vibrating screen. The meshing and the simulation tasks were performed in the general purpose software ANSYS Mechanical. Given the nature of the helical springs and the high-cycle loading conditions, for the fatigue analysis it was determined that a stress-life approach with constant amplitude and non-proportional loading best fit the investigated phenomenon. In solving the non-proportional loading case, stress values of two static scenarios were required to determine the upper and lower limits. Then, to perform the fatigue calculations a solution combination was used. In addition, in order to correct the effect of mean stress and calculate the stresses component respectively the Goodman and Von Mises theories were employed. Simulation results showed that spring would present failure below the second turn of the coil when working with the full nominal load during nearly forty million cycles. These results strongly agreed with the data extracted from a vibrating screen where fractured spring had been working. Fatigue analysis also predicted that the nominal load should be reduced to 90% in order for the spring to meet the minimum life requirements before failure occur.

1 INTRODUCTION

In the mining industry, vibrating screens play an important role, as they allow the adequate sorting of minerals by their size. Complexity in the design of these machines make numerical techniques a proper tool to study their dynamic behaviour, which could include modal or harmonic response analysis [1].

The operational characteristics of a vibrating screen imply that its components support loading and unloading cycles, which could often activate fatigue mechanisms. As it is well known, these mechanisms could lead to the component failure, even though the stress levels

that they support are below the yield stress of the material.

The springs that are located in the vibrating screen structure are not exempt from these effects, which is why it becomes important to examine the loads that they support. The type of loading in these springs and their geometry, cause the principal stress directions to change over time. This phenomenon is the cause of non-proportional fatigue, which could have great influence over the strength of a material, diminishing it up to 10 times its original value [2].

A general case of non-proportional fatigue, which includes not only change in the principal stress directions, but also a non-constant load amplitude, has been studied in [3]. There, expected life of compression helical springs was predicted based on critical sliding planes on the fracture surface (Fatemi-Socie and Wang-Brown), as well as with methods based on angular strains (Coffin-Manson). A finite element model that simulated the conditions of the experiment later confirmed these results.

An even more detailed analysis on the characteristics of the steel from which compression springs are usually made can be found in [4]. In contrast with the former analysis, these experiments were carried out by bringing test specimens under loading and unloading cycles with varying alternating stress values. The Wöhler curves that were obtain through these tests showed that not only the type of loading has influence on the fatigue stress limits, but it is affected also by the surface finish and environmental conditions in which the material works. As a supplement to these analysis, [5] describes mathematical crack propagation models as functions of the number of cycles that correspond to the results of the experiments. Moreover, [6] introduces changes in the microstructure to such models, as to evaluate their influence on the fatigue stress limits and on crack propagation.

Even though the experiments mentioned up to this point have been useful to determine mechanical properties in helical springs, all of them have been carried out under controlled laboratory conditions. In contrast, [7] presents the analysis of a helical compression spring that belonged to the suspension system of an automobile, which had failed due to fatigue during normal operation. It was confirmed by a FEM analysis that contact stress between the first turn of the spring (where the failure occurred) and the base, as well as the presence of corrosion, were the cause of nucleation and propagation of cracks that ultimately led to the failure.

Similarly to the latter, the analysis in the present article is based on the failure of a spring during normal operation of a vibrating screen. The geometry was modeled after a spring taking its dimensions directly from the fractured specimen. A FEM analysis was then performed using ANSYS Mechanical. In order to consider the weight of the components and the load of the vibrating screen, a static scenario was first evaluated to obtain the mean deformation during operation. Later, the maximum and minimum vibration amplitudes were taken from field data and were added or subtracted from the static deformation, respectively. Together with the spring geometry, they caused the principal stresses to vary over time, which implied a case of non-proportional fatigue that was analyzed using the software Fatigue Tool, considering an adequate correction on the mean stress to predict the life and safety factor of the spring.

2 ANALYSIS METHODOLOGY

The vibrating screen from which the springs were taken presents two types of loading over

them: the first, a static load due to the weight of its components and the material it processes; the second, a dynamic load due to the exciters that produce the screen vibration. The combined effect of both types of loading causes the stress amplitude to oscillate symmetrically around the static stress (pulse loading).

As the dynamic load in terms of force was not directly known, field data concerning the maximum and minimum values of the vibration amplitude were taken. The numerical simulation was based in three scenarios: a first one, considering the static load due to the weight of the screen and its nominal load, which allowed the calculation of the static deformation (and thus, the static force). The second scenario considered the vibration amplitude as contributing to the static load (in the same direction), which gave as result the state of maximum compression over the spring. The last scenario considered the vibration amplitude in the opposite direction of the static load, which gave as result the minimum compression value over the spring.

The results of the static scenarios were finally combined in a single fatigue scenario, which considered the non-proportional effects due to the varying principal stress directions.

3 ANALYSIS PROCEDURE

The following lines contain information about the preprocessing stage of the simulation: geometry, material model and properties, meshing and boundary conditions.

3.1 Geometry

The geometric model was made based on the spring dimensions that operated in the vibrating screen. The shape, as some of the most important dimensions and the 3D model can be observed in figure 1.

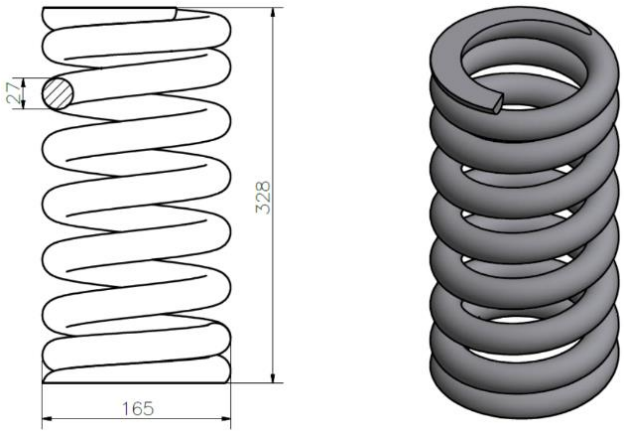

Figure 1: Geometry and 3D model for the analysis

3.2 Meshing

Meshing of the 3D model was performed using tetrahedral, second-order elements that allowed a good adaptation of the numerical model to the existing geometry, as well as a better interpolation between the nodal results. It was also considered convenient a mesh refinement in the coil planar faces. The final mesh had 274124 elements, together with a mean element

quality of 0.83 and a mean aspect ratio of 1.89. Figure 2 shows the final mesh together with the mesh refinement zone.

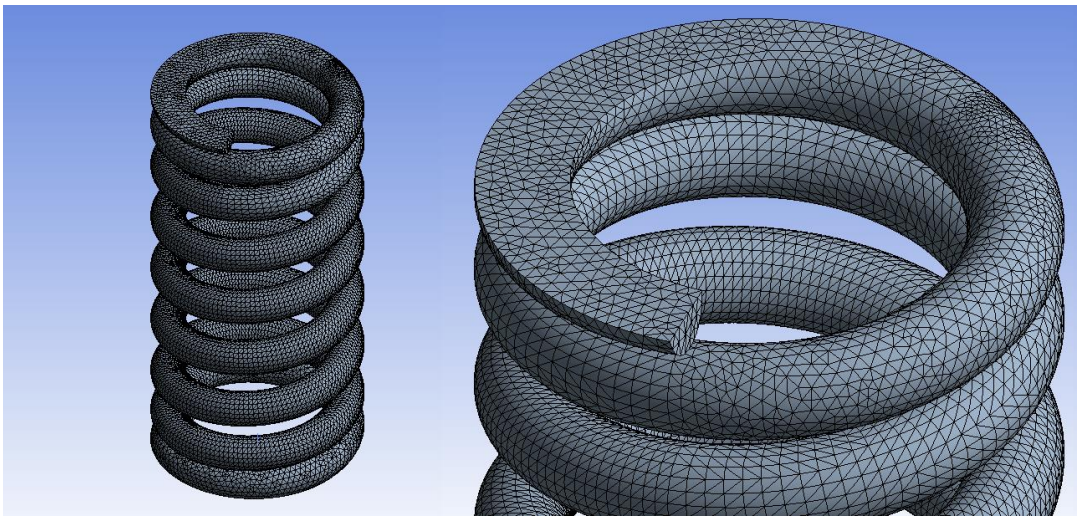

Figure 2: Spring mesh and detail of the mes refinement zone

3.3 Material properties

For the present analysis, a SAE 5160 steel was considered [8]. Table 1 shows some physical and mechanical properties that were taken into account during the simulation. Also, figure 3 shows the S-N curve for this steel, which is necessary to perform the fatigue analysis [9].

Table 1: Physical and mechanical properties of SAE 5160

Density (kg/m^3)	Elastic Modulus (GPa)	Ultimate Stress (MPa)	Yield Stress (MPa)	Poisson's ratio
7850	210	1400	1200	0.3

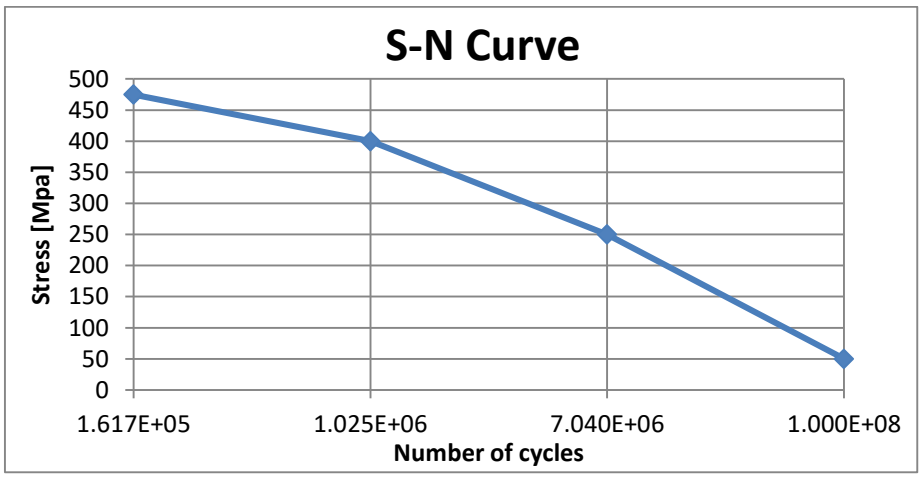

Figure 3: S-N curve for SAE 5160

3.4 Boundary conditions

As the dynamic forces are unknown, displacement boundary conditions over the planar faces of the spring were applied instead. On its base, three displacement restrictions were imposed: null displacement in the normal direction of the planar face, null displacement in the radial and tangent direction of the inner vertex in the planar face and null displacement in the tangent direction of the outer vertex in the planar face. Such displacements can be observed in figure 4.

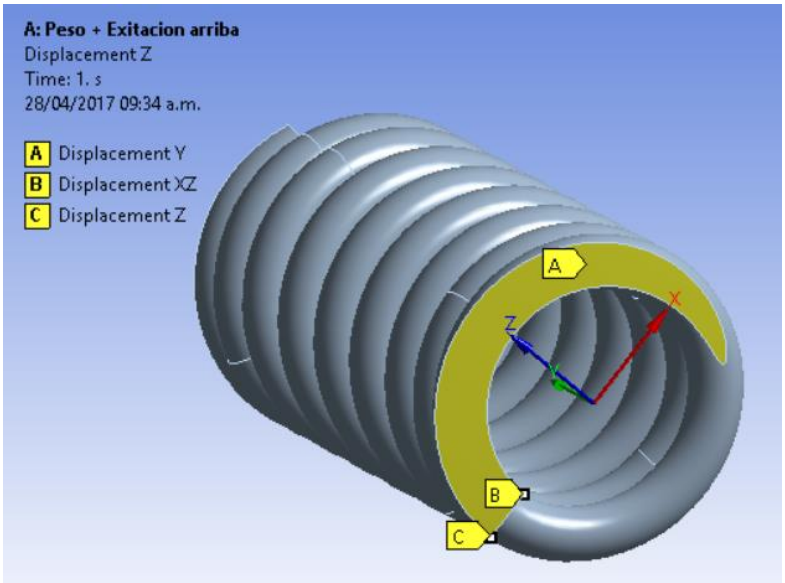

Figure 4: Condiciones de contorno en la base del resorte

To impose the spring load, a displacement was used on the upper planar face of the spring in its normal direction. This displacement value changed according to the scenarios describe in the analysis methodology. Figure 5 shows this boundary condition for one of the analyzed scenarios.

3.4.1 Static scenario due to the weight of the components

The first simulation scenario only considered the weight of the vibrating screen components on the springs. Available field data showed that each spring supported 9810 N. This load was imposed on the upper planar face of the spring in order for the total static deformation to be calculated.

3.4.2 Static scenario for the maximum compression on the spring

In this scenario, the vibration amplitude (4.9 mm) was subtracted to the already negative deformation due to the weight of the components (calculated in the previous scenario). Frictionless contact conditions were also stablished between the first upper and lower turns fo the coil, in order to prevent self-penetration during the simulation. These conditions are shown in figure 6.

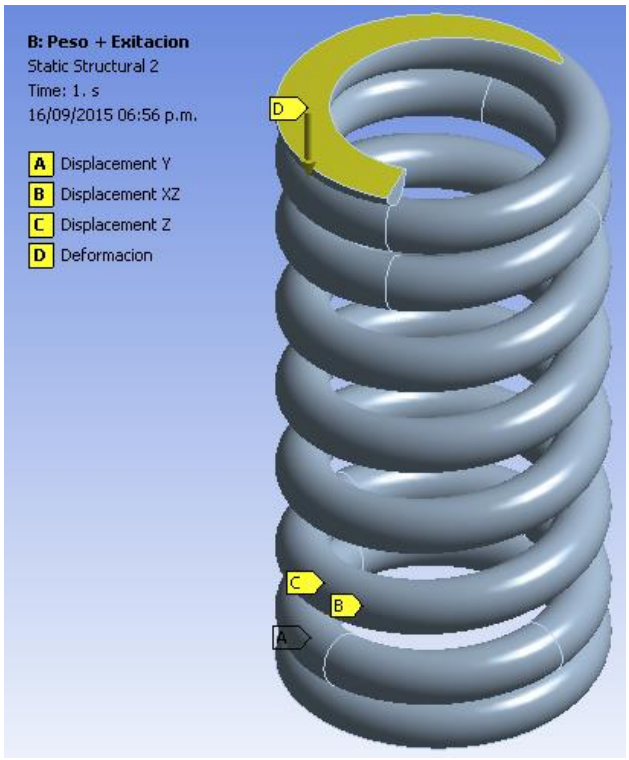

Figure 5: Vertical displacement on the upper planar face of the spring

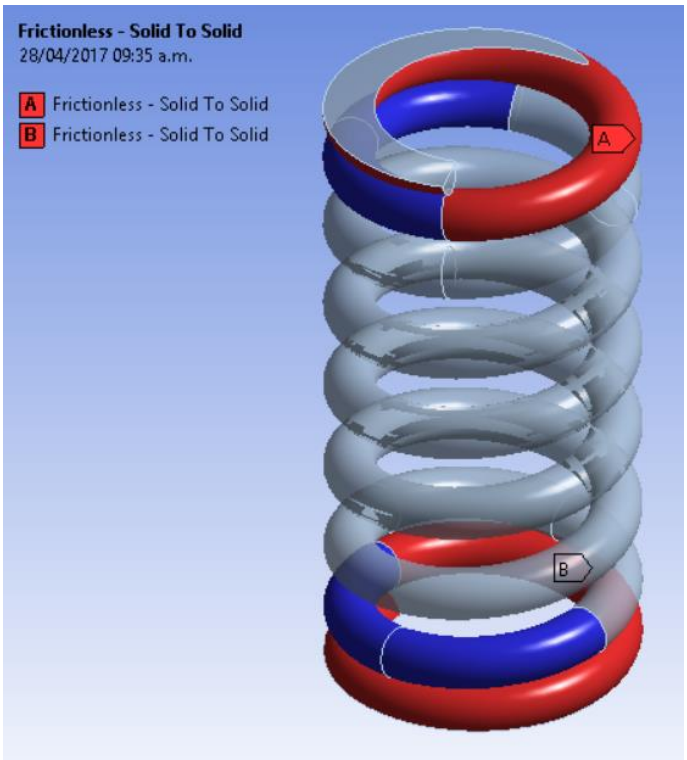

Figure 6: Contact conditions between the coil faces

3.4.2 Static scenario for the minimum compression on the spring

This time, the vibrating amplitude was added to the negative deformation due to the static load, resulting in a lower state of compression. The rest of boundary conditions were similar to the previous scenario.

3.4.2 Fatigue analysis scenario

In this scenario, loads from the previous scenarios were considered cycling and varying over time with constant amplitude. Due to the facts exposed in the first part of the article, the fatigue analysis was defined as non-proportional. Taking into account that vibrating screens usually work at high frequencies, a stress-based approach was used to predict the life of the springs. Goodman theory for mean stress correction was used together with the von Mises equivalent stress. Finally, the highest cycle number in the S-N curve defined infinite life (10^9 cycles).

4 RESULTS

Results of each of the static scenarios were used as inputs to the final fatigue scenario. The results obtained in this last scenario were compared with the actual fractured spring with very good similarities between the numerical model and the component. Also, predicted life had a remarkable correlation with the actual life on which the spring was operational.

4.1 Minimum compression scenario

As previously described, in this scenario the highest displacement was applied (34 mm) and thus, higher equivalent stress values were expected. The higher stresses were obtained from the second upper turn of the coil down to the second lower turn. The stress value in the middle turns was approximately constant. The maximum stress value was 466 MPa. Figure 7 shows the equivalent stress distribution for this scenario.

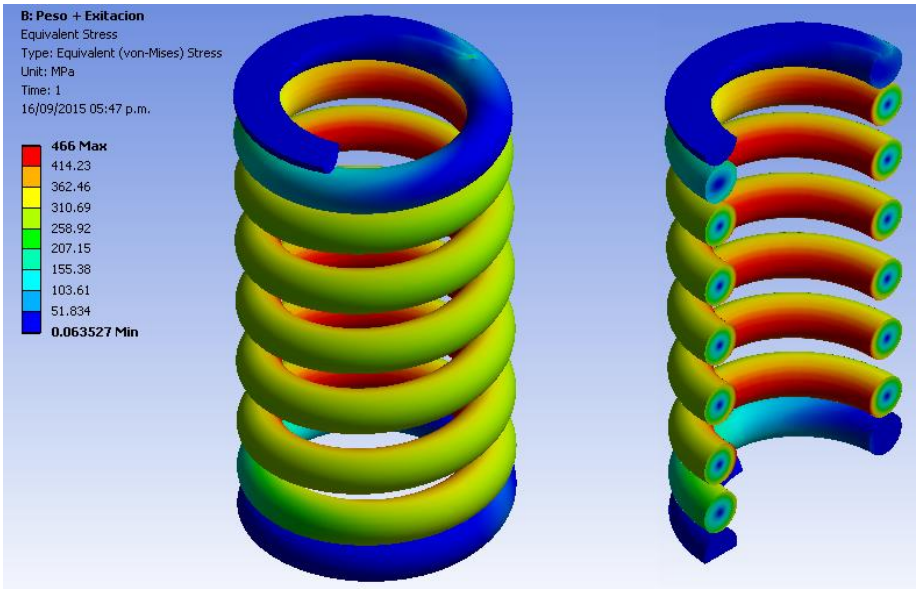

Figure 7: Equivalent stress for the first scenario

4.2 Maximum compression scenario

The imposed displacement was 24 mm. In this case, a very similar stress distribution was obtained compared to the previous scenario. The maximum equivalent stress was 336.6 MPa. The equivalent stress distribution can be observed in figure 8.

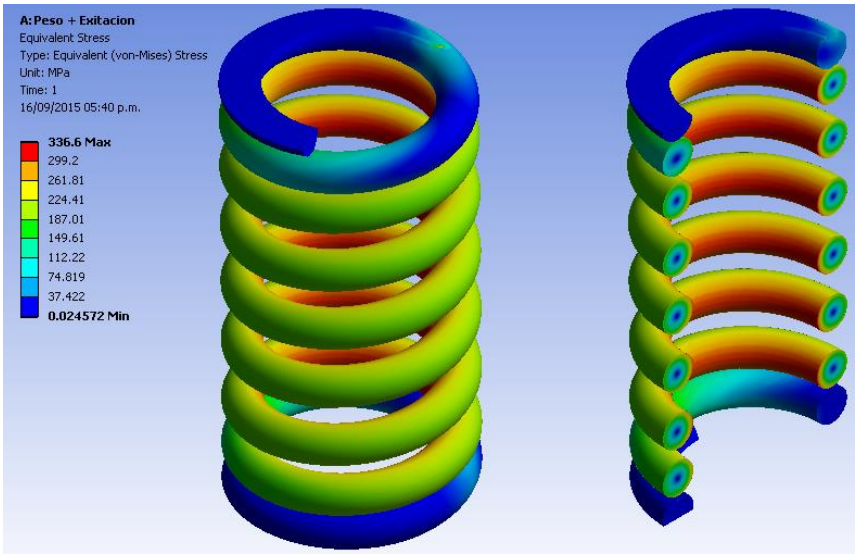

Figure 8: Equivalent stress for this scenario

4.3 Fatigue analysis scenario

Based on the conditions stablished in the analysis methodology, the results of non-proportional fatigue concluded that the spring would have a predicted life of $3.99 \cdot 10^7$ loading cycles before failure. The predicted life for the entire spring can be observed in figure 9.

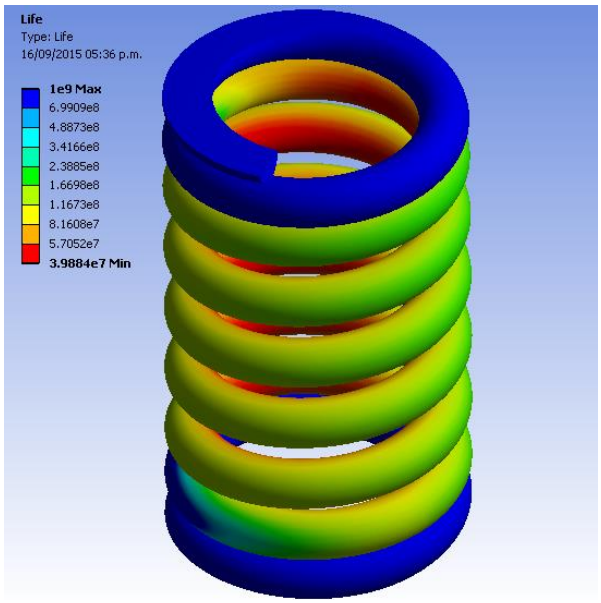

Figure 9: Predicted life of the spring

If it is taken that the spring should have had a working life of 10^9 cycles, its fatigue safety factor was calculated to be 0.25, as shown in figure 10.

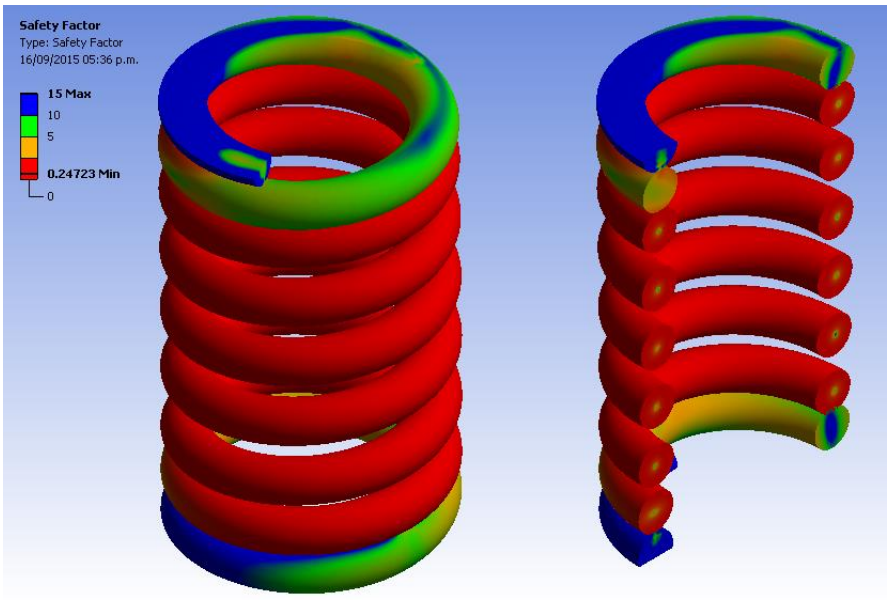

Figure 10: Safety factor for the spring base on the fatigue analysis

A fatigue sensibility study to the load value showed that, for 10^9 cycles, only 20% of the nominal load should be applied. In figure 11, it is shown that if the nominal load is lowered by 10%, the spring can achieve 40 working days.

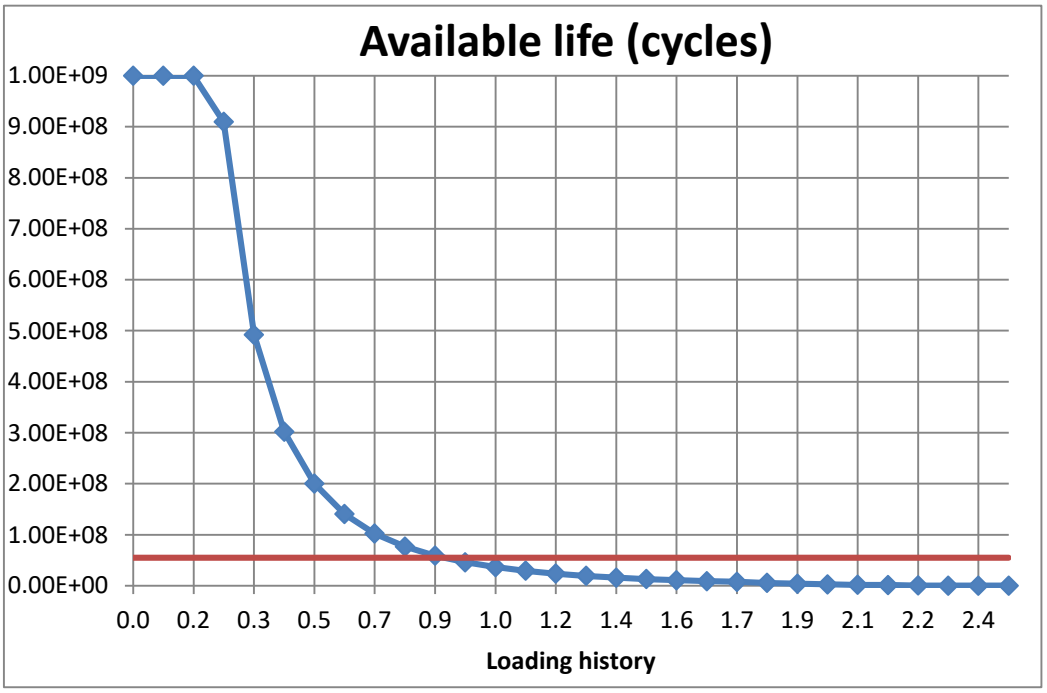

Figure 11: Fatigue sensitivity analysis and limit nominal load for 40 working days (red)

5 CONCLUSIONS

- The different loading scenarios and the spring geometry when the vibrating screen is working with nominal load create the conditions for the spring to be analyzed via a non-proportional fatigue analysis.
- Results obtained through numerical simulation suggest that, when the vibrating screen worked under nominal load, expected life of the springs was about 40 working days, which strongly agreed with actual experience with the fractured specimen.
- The latter also indicates that the stress levels and fatigue life prediction was correct, as the spring presented failure on the turn of the coil in which the numerical simulation showed the highest level of equivalent stress.

REFERENCES

[1] Z. Yue-min, L. Chu-sheng, H. Xiao-mei, Z. Cheng-yong, W. Yi-bin, R. Zi-ting. *Dynamic design theory and application of large vibrating screen*. The 6th International Conference on Mining Science & Technology. Elsevier (2009).

[2] D. Skibicki. *Phenomena and Computational Models of Non-Proportional Fatigue of Materials*. Springer (2014).

[3] L. Del Llano-Vizcaya, C. Rubio-González, G. Mesmacque, T. Cervantes-Hernández. *Multiaxial fatigue and failure analysis of helical compression springs*. Engineering Failure Analysis 13 1303-1313. Elsevier (2006).

[4] D. Angelova, R. Yordanova, T. Lazarova, S. Yankova. *On fatigue behavior of two spring steels. Part I: Wöhler curves and fractured surfaces*. Frattura ed Integrità Strutturale 37 249-257. Gruppo Italiano Frattura (2016).

[5] D. Angelova, R. Yordanova, T. Lazarova, S. Yankova. *On fatigue behavior of two spring steels. Part II: Mathematical models*. Frattura ed Integrità Strutturale 37 258-264. Gruppo Italiano Frattura (2016).

[6] B. Žužek, M. Sedlaček, B. Podgornik. *Effects of segregations on mechanical properties and crack propagation in spring steel.* Frattura ed Integrità Strutturale 34 160-168. Gruppo Italiano Frattura (2015).

[7] Y. Zhu, Y. Wang, Y. Huang. *Failure analysis of a helical compression spring for a heavy vehicle's suspension system*. Case Studies in Engineering Failure Analysis 2 169-173. Elsevier (2014).

[8] L. Pantoja. *Determinación de parámetros óptimos del proceso de temple y revenido del acero SAE 6150 como alternativa para la manufactura de resortes de ballesta*. Universidad Autónoma de Occidente (2006).

[9] F. Cánticus. *Estudio de la resistencia de fatiga del acero SAE 5160 antes y después de proceso shot peening.* Universidad Autónoma de Occidente (2010).

XIV International Conference on Computational Plasticity. Fundamentals and Applications
COMPLAS 2017
E. Oñate, D.R.J. Owen, D. Peric and M. Chiumenti (Eds)

INVESTIGATING DIMENSIONAL AND GEOMETRICAL ACCURACY OF ISOTHERMALLY FORGED BLADES

S. JAVID MIRAHMADI[*] AND MOHSEN HAMEDI[†]

[*] MAPNA Group R&D
MAPNA Group
No. 231, Mirdamad Blvd, Tehran, Iran
e-mail: mirahmadi_j@mapnagroup.com, www.mapnagroup.com

[†] Faculty of Mechanical Engineering
College of Engineering, University of Tehran
North Kargar St., Tehran, Iran
e-mail: mhamedi@ut.ac.ir, www.ut.ac.ir

Key words: Precision Forging, Isothermal Forging, Ti-6Al-4V, Dimensional Accuracy, Compressor Blade.

Abstract. Compressor blades are one of the well-known products made of titanium alloys. They are usually manufactured by a forging process followed by a sequence of machining processes. Precision forging eliminates a considerable amount of machining; however, due to the close tolerances, the process should be designed in a manner to meet dimensional and geometrical tolerances as well as the desired mechanical and metallurgical properties. In this paper, effects of two main process parameters, the process temperature and strain rate, on the dimensional and geometrical accuracy of the isothermally forged blades are investigated experimentally. The results are analyzed by the response surface method (RSM). In order to justify the results and have a tool for further studies, a coupled thermo-mechanical finite element method model is developed and verified by the experimental results. The results show that the process temperature and pressing speed and their interaction have a meaningful effect on the thickness error; however, the interaction effect of the process temperature and pressing speed on the twist error is not considerable and moreover the bow error of the forged blades is not significant. Finally, the results show that for a given geometry, by selection of appropriate process parameters, a sound workpiece with acceptable dimensional and geometrical aspects can be manufactured without any need for a die shape compensation.

1 INTRODUCTION

The titanium and its alloys, including Ti-6Al-4V the workhorse of titanium alloys, have widespread applications in various industries. One of these applications is in the field of compressor blades manufactured by the forging process. Considering the raw material and machining costs, the precision forging may result in reducing the final price of the product. Besides, because of a considerable dependence of its flow stress on the temperature and deformation rate, using the isothermal forging results in a more uniform mechanical and metallurgical properties [1].

Ou and Balendra studied a non-isothermal airfoil forging process, including the airfoil geometrical deviation due to the elastic die deflection numerically [2]. They compensated the airfoil geometrical deviation by modifying the die profile in the opposite direction to the elastic die deflection. Moreover, they studied the effect of preform cross-sections on the elastic die deflection by the 2D finite element method (FEM) [3]. Hu and Balendra studied the airfoil section's form errors arisen from the die elasticity and cooling by the 2D FEM simulations. They concluded that the process temperature had a great impact on the thickness error [4]. Ou et al. simulated a non-isothermal airfoil forging by 2D FEM and presented a compensating factor to adapt the die profile to the airfoil errors [5-10]. Bruschi and Ghiotti investigated the effects of different cooling sequences on the cooling-induced errors of AISI430 forged blade. Their results showed that applying turbulent air to cool down the forged blade, increased the airfoil geometrical stability [11]. Lu et al. compared the application of one or two compensating factors to recompense the forging errors during the non-isothermal forging of a compressor blade by 3D FEM simulations. Their results demonstrated the usefulness of the single factor method to recompense the forging errors [12]. In order to increase the forging accuracy, Lu and Ou studied stochastic aspects of a blade forging process to optimize the systematic and random errors [13]. Lu and Ou presented an approach to assess the contribution of press machine deflections on the accuracy of a forged blade. Their results showed that the press deflection had a considerable effect on the accuracy of the forgings [14]. Makem et al. presented an automated technique to assess the dimensional and geometrical accuracy of the blade forgings in the design and modeling steps [15]. Simonetto et el. developed an approach consist of numerical and experimental studies to evaluate the distortions of stainless steel forged blades in order to optimize the die design [16].

The literature review showed that although the Ti-6Al-4V blades have been manufactured by the forging process since several decades ago, but many researchers are still interested in optimization of various aspects of the blade forging. The process temperature and pressing speed are two main factors that govern the mechanical and metallurgical properties of the forgings; however, the effects of these factor on the geometrical and dimensional aspects of the forgings, which is a significant subject in the case of the precision forging, are not well addressed in the literature. In the current paper, a comprehensive numerical and experimental study of the effects of the temperature and pressing speed on the geometrical aspects of the isothermally forged blade is presented.

2 THE BLADE'S DIMENSIONAL AND GEOMETRICAL ASSESSMENT

2.1 The Blade's Dimensional and Geometrical Errors

During the manufacturing process of the blades, several dimensional and geometrical errors may arise. Some geometrical errors can be eliminated during the subsequent machining processes; however, some of them may not be modifiable which result in scraping the blade. The blade's geometrical errors are shown schematically in Figure 1. The excessive rotation of the airfoil around the x-axis and y-axis results in the *lean* and *tilt* errors, respectively. These errors can often be compensated during the machining processes. The rotation of the tip cross section respect to the platform cross section around the z-axis is defined as the *twist*. The deviation of the twist from its nominal value results in the *twist* error. The out-of-tolerance twist error is not often modifiable by the machining processes. The airfoil thickness is defined

according to Figure 2. The chord line is a straight line between the leading (A) and trailing (B) edges. At a particular distance from the leading edge on the chord line (C), a line perpendicular to the chord line intersects the airfoil section at two points (D and E). The distance between two intersection points (DE) is defined as the airfoil thickness at C.

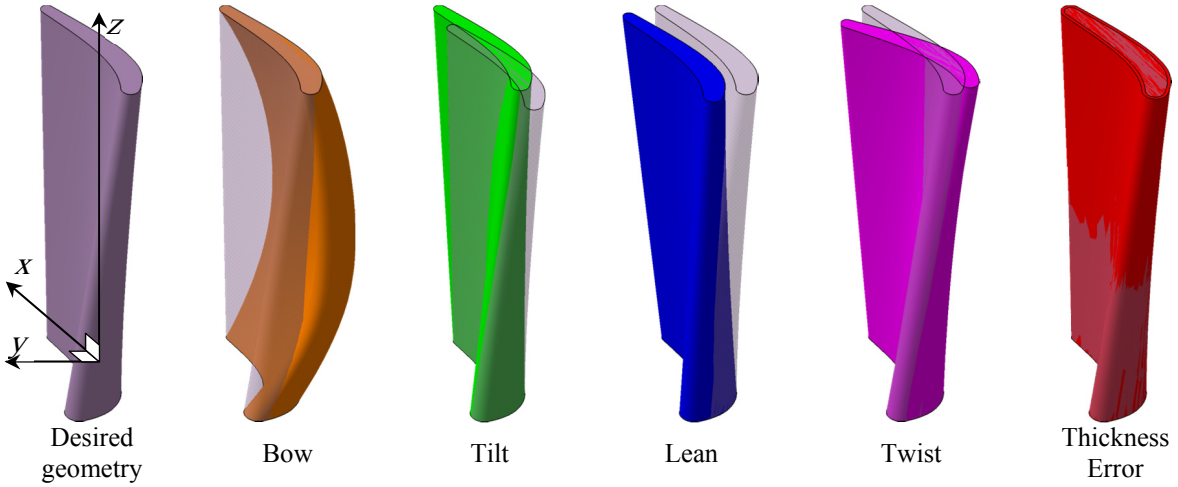

Figure 1: Common geometrical errors arisen during blade manufacturing

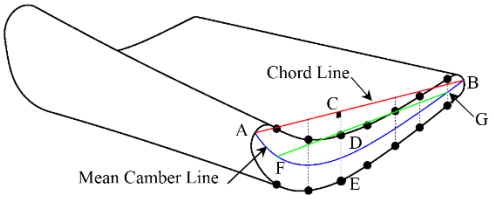

Figure 2: A typical airfoil section

2.2 Error measurement

After the precision forging of the blades, Bow, twist and thickness errors should be considered to be in the permissible tolerance range to prevent the blade scrappage. Behind the forged blades were cooled down and the lubricant removed from their surface, they were subjected to coordinate measurement in order to determine various types of the dimensional and geometrical accuracy. The locating of the blades was done by the 3-2-1 rule at the root as shown in Figure 3. The coordinate measuring was done at four sections from the root to the tip (Figure 3). At each point, the blade's thickness and consequently thickness error was determined. The twist error was calculated by measuring the rotation difference between the first and the last cross-section. The bow, lean and tilt errors were considered at the stacking line.

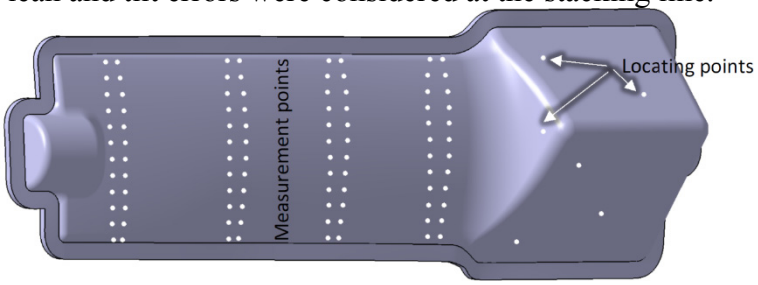

Figure 3: Locating and measuring points of blade.

3 MATERIALS AND METHODS

3.1 Experimental Study

Preform preparation

Forging of compressor blades is a complex forming process that needs an accurate design of the preform to ensure complete die-filling as well as meeting the mechanical and metallurgical properties. In this study, the preforms made of Ti-6Al-4V were formed by using the extrusion process. All the preforms were manufactured with the same processing parameters. Before the isothermal forging process, the preforms were glazed to prevent the formation of alpha-case and also lubricate them.

Experimental setup

In order to carry out the isothermal blade forging process and study the dimensional and geometrical errors during the forging process, there was a need to precisely control the deformation rate and the process temperature; so, a 6 MN hydraulic press was equipped with a servo-hydraulic power-pack and a PLC control system. An electric furnace, isolated from the press bed by water-cooled plates, was used to heat the dies. The dies were fabricated from a nickel-base superalloy to withstand the forging stresses at the high processing temperatures. Both of the preform and dies were held enough in the furnace to remove the temperature gradient inside them. In the die design step, the cavity orientation was chosen in a manner to minimize the lateral forces, in addition, preventing the locating of the preform incorrectly.

Experimental tests

The process temperature and pressing speed are two main factors that govern the forging process of the blades. Inappropriate selection of these factors may result in the unsuitable mechanical and metallurgical properties. In order to assess their effects on the geometrical aspects, a set of experiments was designed based on the face-centered central composite response surface method. The dies and preforms were held enough in the furnace to have a uniform temperature at the test points 890, 920 or 950 °C and then the forging tests were conducted at the mean strain rates 0.179, 0.036 or 0.007 s^{-1} at the middle of the airfoil. All the tests at the factorial and axial points were replicated two times, and three times at the center point in a random sequence. After the cooling sequence of the forged blades and removing the lubricant from their surface, they were subjected to coordinate measurement in order to determine various types of dimensional and geometrical accuracy.

3.2 Numerical Simulations

A finite element method (FEM) model was developed and verified by the experimental results to better understand the mechanisms governing the experimental results and prepare a verified tool for further studies (Figure 4). The workpiece was considered as rigid-viscoplastic and elastic-plastic during the forging and cooling processes, respectively. The flow curves of Ti-6Al-4V were determined by the isothermal compression tests and presented in [17]. The friction factor at the die-workpiece interface was determined as a function of the temperature and deformation rate by the isothermal ring compression tests [18] and implemented in the model. The simulation parameters were chosen as the experimental ones. To simulate the isothermal

forging process, the temperatures of the workpiece, dies, and environment were set to the selected process temperature at the start of the simulation.

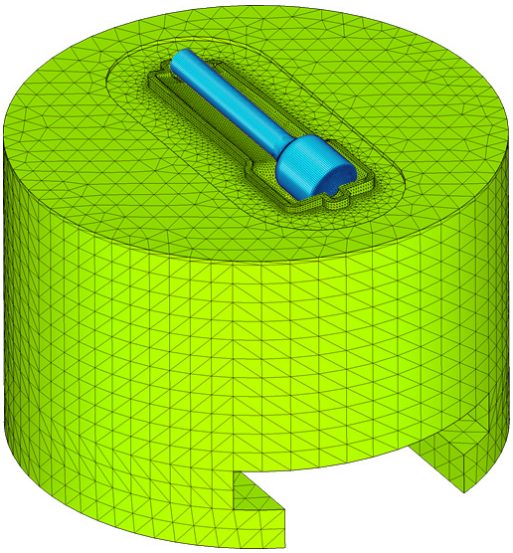

Figure 4: Developed FEM model.

4 RESULTS AND DISCUSSION

After conducting the tests, all the isothermally forged blades were subjected to coordinate measurement to determine the geometrical and dimensional accuracy. The results of various errors are presented and discussed here. The isothermal forged and trimmed blade is shown in Figure 5.

Figure 5: Isothermally forged and trimmed blade.

4.1 Thickness Error

The thickness error in the non-isothermal forging is the most considered aspect of the dimensional accuracy in the literature [2, 5, 6, 8, 9, 12]. As a rule of thumb, an increase of the forging pressure (force) and/or a decrease of the die elastic modulus result in more thickness error; however, how the process temperature and forging speed alter these parameters should be assessed more precisely.

Step-by-step evolution of the elastic die deflection and accordingly thickness error during the isothermal forging process at 890 °C and strain rate 0.179 s^{-1} is shown in Figure 6. As the process proceeds, the forging force increases and thus the die's elastic deflection grows. At the end of the process, the maximum elastic die deflection was 0.131 mm in the middle of the airfoil near the platform. Several parameters affect the elastic die deflection, including the friction factor at the workpiece-die interface, the flow stress of Ti-6Al-4V and the elastic modulus of the dies at the process temperature. Increasing the process temperature results in lower flow

stress and elastic modulus, and higher friction factor [18]. The former results in lower forging force and consequently less die deflection. To consider the elastic die deflection, flow stress has an opposite effect on elastic modulus and friction factor. Increasing deformation rate increases the flow stress, but at the same time decreases the friction factor that has opposite effects on elastic die deflection and consequently thickness error.

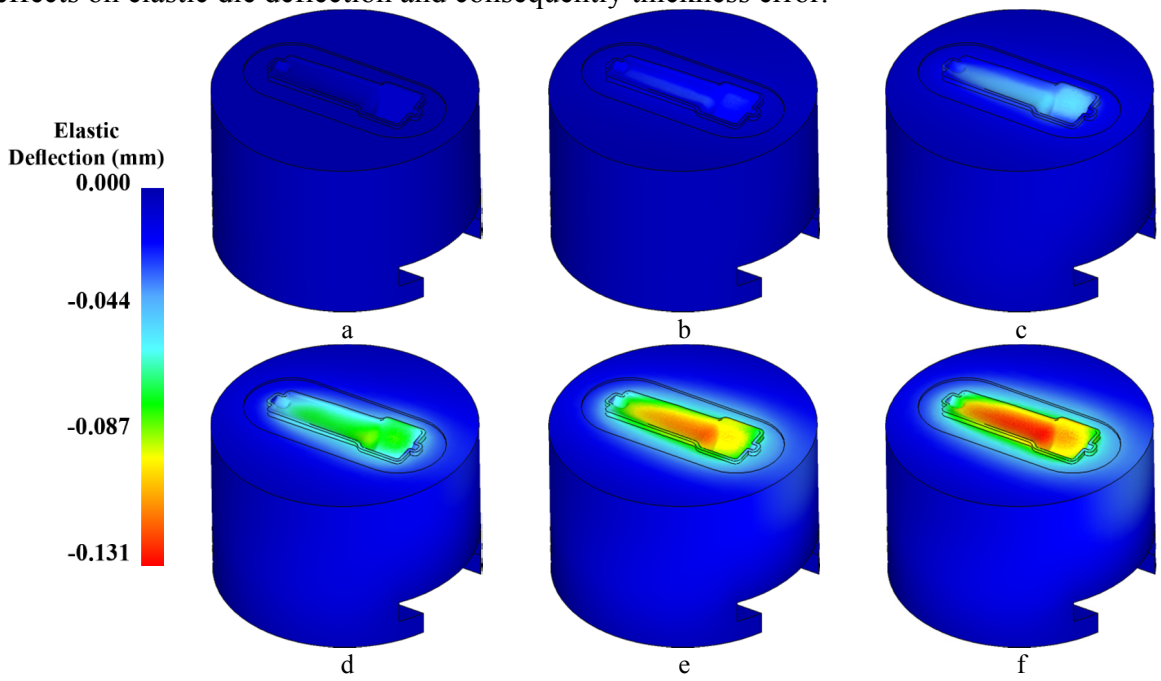

Figure 6: Evolution of die elastic deflection during the isothermal forging at 890 °C and strain rate of 0.179 /s.

By conducting the forging process isothermally at various process temperatures and deformation rates, according to the design of experiments, superimpose of the different effects results in a variety of thickness errors as a function of the process temperature and the strain rate. The effect of the mentioned factors on the thickness error was evaluated by analysis of variance which is presented in Table 1. The modeled response surface is shown in Figure 7.

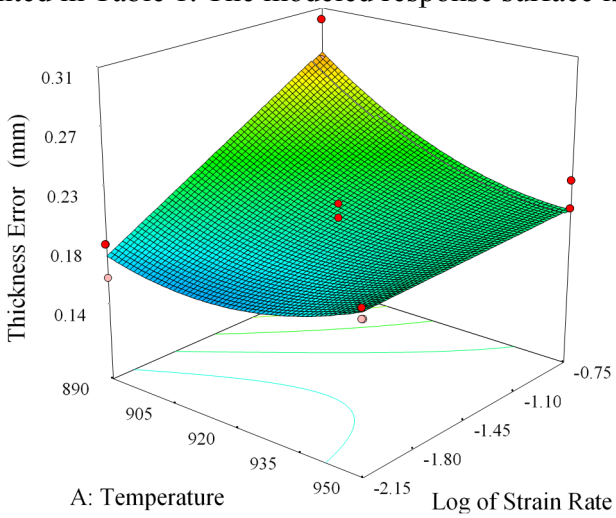

Figure 7: The thickness error as a function of the process temperature and speed.

Table 1: ANOVA table of effective parameters on thickness error

Source	Sum of Squares×10^{-4}	df	Mean Square×10^{-4}	F Value	p-value Prob > F
Model	290.0	4	72.3	16.33	<0.0001
A-Temperature	39.1	1	39.1	8.84	0.0060
B-Strain Rate	130.0	1	130.0	29.97	<0.0001
AB	92.0	1	92.0	20.79	<0.0001
A^2	25.3	1	25.3	5.72	0.0237
Residual	120.0	28	4.4		
Lack of Fit	35.0	10	3.5	0.71	0.7060
Pure Error	88.9	18	4.9		
Cor Total	410.0	32			

According to Figure 7 the maximum elastic deflection and consequently thickness error was taken place at the lower process temperature and the higher deformation rate and was approximately 0.28 mm. At lower strain rates, the effect of the process temperature on the thickness error was not considerable; however, at higher strain rates, the process temperature had a significant effect on the thickness error. From another point of view, at 890 °C, the strain rate had a much more effect on the thickness error rather than 950 °C. Two phenomena govern this finding. First, the measured flow curves showed a more dependence of the flow stress to the strain rate at lower temperatures. Second, at the lower temperature, strain rate doesn't have a considerable effect on friction factor; however at a higher temperature, increasing the strain rate decreases the friction factor significantly that reduces the effect of strain rate on the flow stress and consequently forging force. The results show that by selection of an appropriate region in the process window, acceptable thickness error within the blade's tolerance can be achieved.

4.2 Twist and Bow Errors

The twist and bow errors are two temperature-related errors that happen during the cooling sequence. The initial process temperature, deformation rate, and non-uniform deformation affect the temperature distribution inside the forged blade at the end of the forging process. The leading and trailing edges undergo a more deformation and so a more adiabatic temperature rise (Figure 8). Increasing the deformation rate results in a higher adiabatic temperature rise. Moreover, the lower initial process temperature leads to a more flow stress and a higher adiabatic temperature rise. The temperature distribution coupled with the varying thickness of the airfoil profile results in a non-uniform cooling of the blade and consequently deviation of the airfoil. Because of small thickness in the leading and trailing edges, they cool down faster than the central portion of the airfoil that increases their strength. The contraction of the central area results in the warpage of the airfoil and twist and/or bow formation.

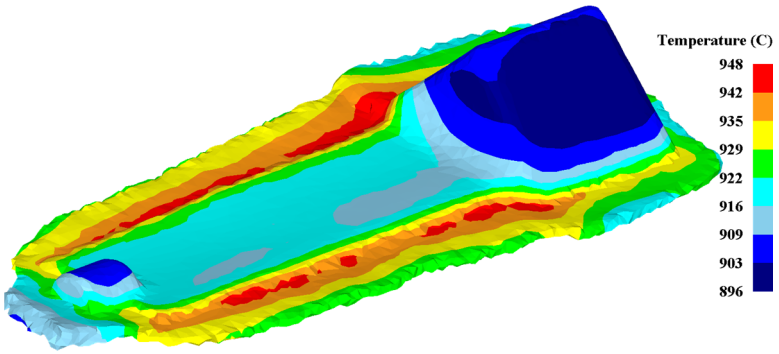

Figure 8: The temperature distribution at the end of forging process for the initial temperature 890 °C and 0.179 s^{-1}.

The resulted response surfaces as a function of the process temperature and speed for the twist and bow errors are presented in Figure 9 and 10, respectively. The results show that both of increasing the initial temperature and decreasing the velocity result in a more uniform temperature at the end of the process that cause a more twist error. This finding shows that the geometry and its effect on the cooling sequence has a significant influence on the warpages after the forging process. In other words, for the temperature-related errors, non-uniform cooling is more important than non-uniform temperature distribution at the end of the process.

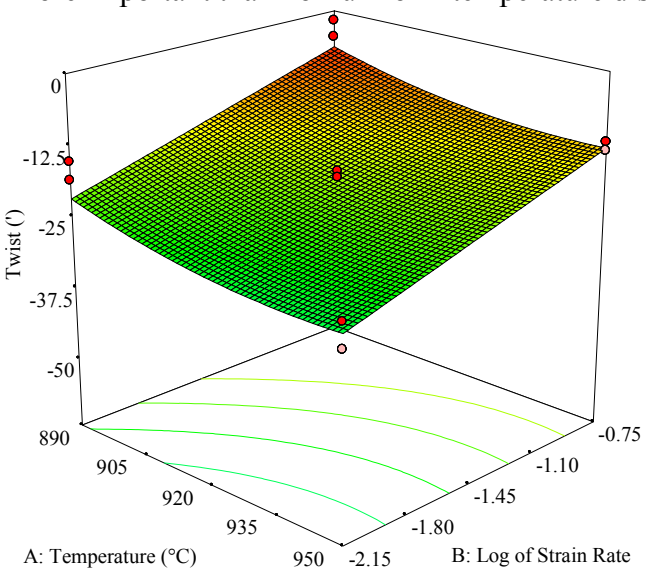

Figure 9: The twist error as a function of the process temperature and speed.

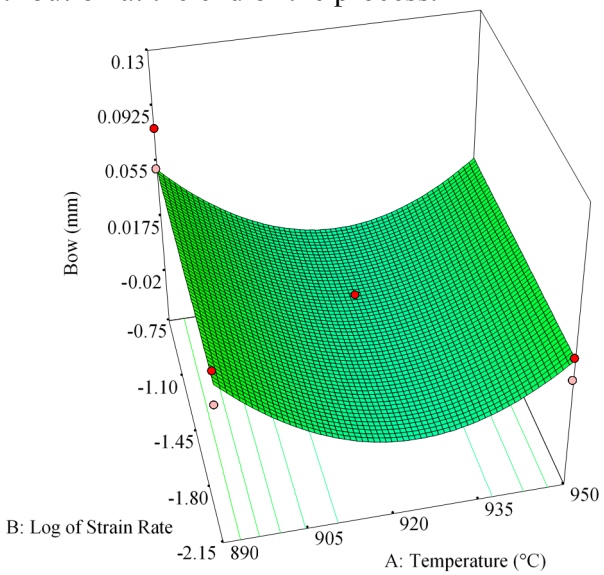

Figure 10: The bow error as a function of the process temperature and speed.

4.3 Tilt and Lean Errors

As stated in the previous section, the non-uniform cooling of the airfoil may result in the buckling of the airfoil. Because of high bending strength around the y-axis in Figure 1, there is no considerable tilt and lean after the process. Moreover, the lean and tilt errors can be readily compensated in the machining process of the blade's root.

5 CONCLUSION

The compressor blades made of titanium alloys are commonly manufactured by forging process. By conducting the process isothermally, the desired control on the geometrical aspects as well as the mechanical and metallurgical properties is achievable. Investigating the temperature and the strain rate effect in the isothermal blade forging revealed their significant interaction effect on the dimensional and geometrical accuracy. Concerned about the thickness error, increasing the process temperature has a positive effect on the flow stress, however, a negative effect on the elastic modulus of the dies and the friction factor. Increasing the forging speed improves the lubricity in the die-workpiece interface, but at the same time rises the flow stress. These parameters have an opposite effect on the die elastic deflection and consequently airfoil thickness error. Such opposite effects govern the geometric deviations. In the other words, increasing the forging speed results in a more thickness error; however, initial process temperature determines the significance of this finding. So, an appropriate selection of process temperature and forging speed will result in acceptable dimensional and geometrical tolerances without any need of die shape compensation.

ACKNOWLEDGEMENT

This research was supported by MAPNA Group and carried out at Mavadkaran engineering company under the supervision of Mr. Mohammad Cheraghzadeh that is sincerely appreciated.

REFERENCES

[1] Ermachenko, A., and Karavayeva, M. High-temperature precision forming of titanium blades. *J. Mater. Eng. Perform.* (1996), 5:589-592.

[2] Ou, H., and Balendra, R. Die-elasticity for precision forging of aerofoil sections using finite element simulation. *J. Mater. Process. Technol.* (1998), 76:56-61.

[3] Ou, H., and Balendra, R. Preform design for forging of aerofoil sections using fe simulation. *J. Mater. Process. Technol.* (1998), 80:144-148.

[4] Lu, X., and Balendra, R. Temperature-related errors on aerofoil section of turbine blade. *J. Mater. Process. Technol.* (2001), 115:240-244.

[5] Ou, H., and Armstrong, C. Die shape compensation in hot forging of titanium aerofoil sections. *J. Mater. Process. Technol.* (2002), 125:347-352.

[6] Ou, H., Armstrong, C., and Price, M. Die shape optimisation in forging of aerofoil sections. *J. Mater. Process. Technol.* (2003), 132:21-27.

[7] Ou, H., Lan, J., Armstrong, C., and Price, M. An fe simulation and optimisation approach for the forging of aeroengine components. *J. Mater. Process. Technol.* (2004), 151:208-216.

[8] Ou, H., Lan, J., Armstrong, C., Walløe, S., and Ward, M. Direct die shape compensation for forging of ni-based aerofoil blades; In *Proceedings of the 8th International Conference on Numerical Methods in Industrial Forming Processes*, 2004: AIP Publishing.

[9] Ou, H., and Armstrong, C. Evaluating the effect of press and die elasticity in forging of aerofoil sections using finite element simulation. *Finite Elem. Anal. Des.* (2006), 42:856-867.

[10] Ou, H., Lan, J., Armstrong, C., Price, M., Walløe, S., and Ward, M. Reduction in post forging errors for aerofoil forging using finite element simulation and optimization. *Modell. Simul. Mater. Sci. Eng.* (2006), 14:179-193.

[11] Bruschi, S., and Ghiotti, A. Distortions induced in turbine blades by hot forging and cooling. *Int. J. Mach. Tool. Manu.* (2008), 48:761-767.

[12] Lu, B., Ou, H., Armstrong, C., and Rennie, A. 3d die shape optimisation for net-shape forging of aerofoil blades. *Mater. Design.* (2009), 30:2490-2500.

[13] Lu, B., and Ou, H. Stochastic finite-element modelling and optimization for net-shape forging of three-dimensional aero-engine blades. *Proc. Inst. Mech. Eng. L J. Mater. Des. Appl.* (2011), 225:71-85.
[14] Lu, B., and Ou, H. Quantification of press elasticity in the forging of three-dimensional complex shapes. *Proc. Inst. Mech. Eng. B J. Eng. Manu.* (2012), 226:466-477.
[15] Makem, J. E., Ou, H., and Armstrong, C. G. A virtual inspection framework for precision manufacturing of aerofoil components. *Comput. Aided Des.* (2012), 44:858-874.
[16] Simonetto, E., Bruschi, S., Ghiotti, A., and Savio, E. Prediction of distortions in hot forged martensitic stainless steel turbine blades by numerical simulation. *Procedia Manu.* (2015), 1:804-813.
[17] Mirahmadi, S. J., Hamedi, M., and Parsa, M. H. Investigation of microstructural uniformity during isothermal forging of Ti-6Al-4V. *J. Mater. Eng. Perform.* (2014), 23:4411-4420.
[18] Mirahmadi, S. J., Hamedi, M., and Cheraghzadeh, M. Investigating friction factor in forging of ti-6al-4v through isothermal ring compression test. *Tribol. T.* (2015), 58:778-785.

XIV International Conference on Computational Plasticity. Fundamentals and Applications
COMPLAS XIV
E. Oñate, D.R.J. Owen, D. Peric & M. Chiumenti (Eds)

3D MODELING OF THE VANE TEST ON A POWER-LAW CEMENT PASTE BY MEANS OF THE PROPER GENERALIZED DECOMPOSITION

CHADY GHNATIOS* AND GERARD-PHILIPPE ZEHIL†

* Notre Dame University - Louaizé
Department of Mechanical Engineering
Zouk Mosbeh, P.O. Box 72, Lebanon
e-mail: cghnatios@ndu.edu.lb

†Notre Dame University - Louaizé
Department of Civil & Environmental Engineering
Zouk Mosbeh, P.O. Box 72, Lebanon
e-mail: gpzehil@ndu.edu.lb

Key words: Cement paste, Vane test, Proper Generalized Decomposition, Power-law fluid, non-linear model

Abstract. The effective modeling of the flow of fresh concrete materials in settings such as that of the vane test is a challenging process that is the object of ongoing research. Previous works modeled concrete and cement pastes as solids subjected to yielding or as Bingham or power-law fluids, both in two or three dimensions [1, 2]. Of the existing models, those implementing power-law fluids in three dimensions carry the best predictive ability considering the typically heterogeneous composition of concrete suspensions and the relatively complex three-dimensional features of their flows.

In this work, we model the vane test in a power-law cement paste using the Proper Generalized Decomposition (PGD). In this framework, the three-dimensional problem is solved as a sequence of $2D \times 1D$ problems, thus alleviating the curse of dimensionality. This choice is supported by experience from previous works using the PGD to simulate Non-Newtonian behavior using iterative resolutions [3, 4]. It is also particularly useful in addressing the inverse problem corresponding to the identification of the material properties of cement pastes from experimental data, as this requires many direct resolutions of the forward problem. The use of the PGD is also appealing because the model parameters can be introduced as extra coordinates of the problem [5].

1 INTRODUCTION

Cement paste characterization is an active field of research. Many cement paste material models currently exist in the relevant literature, based on different physics. Some

works attempt to model cement pastes as solids subjected to yielding [1] while others rely on Brinkman or Power-law fluids [2]. Both types of models have good predictive abilities, although fluid models accounting for suspended particles – such as Non-Newtonian power-law fluids – have a slight advantage.

The conventional vane test consists of a vane rotating inside of a cylinder containing a fluid that must be characterized. The test determines the properties of liquids by measuring the torque on the vane axis [6]. For example, the vane test is used to measure concrete properties based on solid models in [7]. Vane test measurements can also be used to identify the Non-Newtonian power-law properties of cement pastes.

During the vane tests considered in this work, the mixing velocity is increased gradually, at a rate that is sufficiently slow for steady-state conditions to be assumed at every computational time step. To identify material properties using this test, one may need to solve the system of partial differential equations modeling the forward problem at each iteration of an inverse optimization algorithm. The use of the Proper Generalized Decomposition (PGD) is particularly appealing in this case, since the material parameters as well as the angular mixing velocity can be included as extra coordinates of the problem [8, 9]. The result is therefore a "Computational Vademecum" or a "book of solutions," which can be used on the fly to evaluate the quantities of interest during the optimization process of the inverse algorithm.

The PGD's suitability to tackle multidimensional linear problems using the domain separation process is clearly established, with dramatic computational time reductions [10, 11]. However, to the knowledge of the authors, the PGD is not frequently used to resolve multidimensional nonlinear problems. Some works have tackled space domains separations, without including any extra parameters as coordinates of the problem [12, 4]. A few other works have illustrated the ability to simulate nonlinear thermal models using parameters as extra coordinates by combining the PGD and the Proper Orthogonal Decomposition (POD) [9, 13]. In this work, we use the Proper Generalized Decomposition to simulate Non-Newtonian power-law fluid in a vane test while considering the process parameters as extra-coordinates of the problem.

2 MODELING THE VANE TEST

In this section we describe the modeling of the vane test using Non-Newtonian power-law fluids. The modeled vane test has the dimensions shown in Figure 1. Because the problem is not axisymmetric, a three-dimensional simulation is necessary to capture the fluid flow.

Designating by $\mathbf{v}$ the velocity vector, the conservation of mass in the modeled fluid region can be written as:

$$\nabla \cdot \mathbf{v} = 0. \tag{1}$$

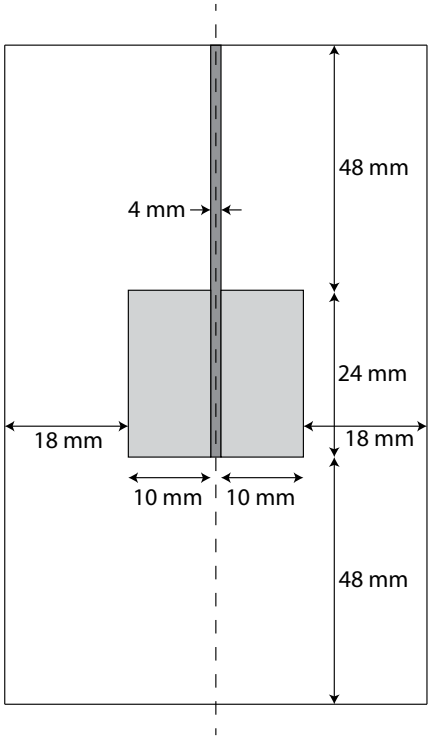

Figure 1: Modeled vane test dimensions.

For the test considered, the angular velocity imposed to the rotating vane changes very slowly. The mixing process is thus modeled assuming steady-state conditions at different velocities. Considering the cement paste as a highly viscous liquid, the momentum balance equation writes:

$$\nabla P = \nabla \cdot (\eta \nabla \mathbf{v}) \,, \tag{2}$$

where P is the fluid pressure and η the apparent viscosity. For Non-Newtonian power-law fluids, the apparent viscosity η can be written as [14]:

$$\eta = K \cdot D_{eq}^{n-1} \cdot \mathbf{D}, \tag{3}$$

K and n being two material parameters, $\mathbf{D}$ the strain rate tensor and D_{eq} the equivalent strain rate tensor given by:

$$D_{eq} = \sqrt{\mathbf{D} : \mathbf{D}}. \tag{4}$$

The symbol " : " corresponds to the tensor product contracted twice. Since the LBB conditions are still unclear in a separated representation framework, the penalty method is used to solve the problem for the velocity field in the domain. This is initiated by expressing the conservation of mass as [15]:

$$\nabla \cdot \mathbf{v} = \lambda P, \tag{5}$$

with λ sufficiently small. Plugging equations (5) and (3) into the momentum balance equation (2), one can write:

$$\nabla \left(\nabla \cdot \mathbf{v} \right) = \lambda \cdot \nabla \cdot \left[\left(K \cdot D_{eq}^{n-1} \cdot \mathbf{D} \right) \nabla \mathbf{v} \right]. \tag{6}$$

Expression (6) represents the main equation to solve. The boundary conditions for the vane test represented in Figure 1 are expressed as:

$$\begin{cases} \mathbf{v} = \mathbf{0} \text{ at } R = 30 \text{ mm (non-slip condition)} \\ \mathbf{v} = \mathbf{0} \text{ at } z = 0 \text{ mm and } z = 120 \text{ mm} \\ \mathbf{v} = \mathbf{R} \times \omega \text{ at the contact with the vane (non-slip condition)} \end{cases} \tag{7}$$

where R is the radius measured from the dashed axis represented in Figure 1 and ω is the angular velocity of the vane.

For the vane test considered, a steady-state modeling approach entails that the problem be solved at each time step with the corresponding value of the angular velocity. The angular velocity is thus introduced as an extra coordinate of the problem, which yields the velocity field as a function of the spatial coordinates x, y, z and the angular velocity ω.

3 SOLVING THE NON LINEAR PROBLEM BY THE PGD

To solve the problem using the PGD, we start by expressing the weak form of equation (6). Denoting by $\mathbf{v}^*$ the test function, the weak form writes:

$$\int_\Omega (\nabla \cdot \mathbf{v}^*) \cdot (\nabla \cdot \mathbf{v}) d\Omega + \lambda \int_\Omega (\nabla \mathbf{D}^*)^T : \eta : \nabla \mathbf{D} d\Omega = 0. \tag{8}$$

The resolution of this four-dimensional problem – which ultimately yields $\mathbf{v}(x, y, z, \omega)$ – starts by a linearization process. The problem is thus solved first for $n = 1$, which is equivalent to considering a Newtonian fluid of apparent viscosity K. Solving the multidimensional problem requires introducing ω which only appears in the boundary conditions, as an extra coordinate. We thus act by means of a change of variables [8] and introduce the variable $\mathbf{F}$ satisfying the boundary conditions expressed in (7), i.e.:

$$\begin{cases} \mathbf{F} = \mathbf{0} \text{ at } R = 30 \text{ mm}, \\ \mathbf{F} = \mathbf{0} \text{ at } z = 0 \text{ mm and } z = 120 \text{ mm}, \\ \mathbf{F} = \mathbf{R} \times \omega \text{ at the contact with the vane, and} \\ \mathbf{F} = \mathbf{0} \text{ on the rest of the domain.} \end{cases} \tag{9}$$

We now define $\mathcal{V} = \mathbf{v} - \mathbf{F}$ and replace $\mathbf{v}$ by $\mathcal{V} + \mathbf{F}$ in equation (6). The problem can hence be resolved for $\mathcal{V}$ using homogeneous boundary conditions [8].

For the specific setting considered in this work, the spacial domain can be separated into a sum of $2D \times 1D$ domains. This said, the reduction in computational time that would result from such a decomposition is not significant because of the geometrical complexity. We thus choose to refrain from implementing any variable separation in 3D and hence to maintain the three-dimensional physical domain as represented in Figure 2. The meshed domain is shown in Figure 3.

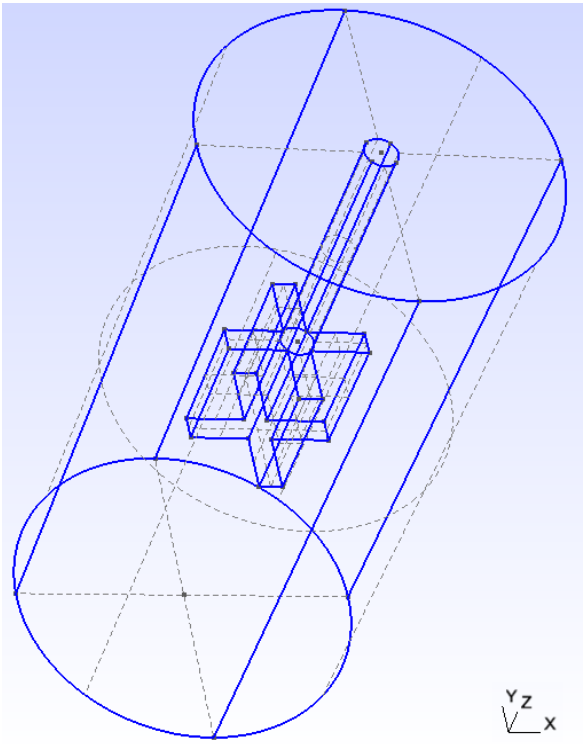

Figure 2: Illustration of the three-dimensional domain considered in the simulation.

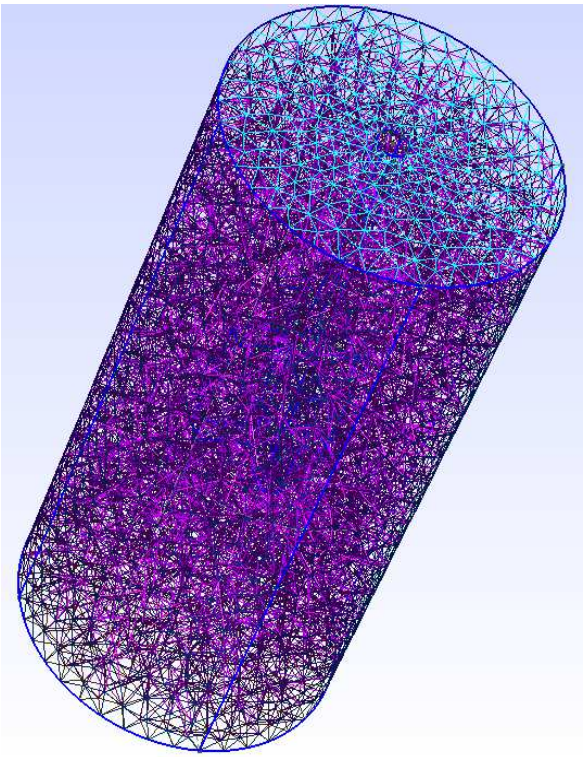

Figure 3: Mesh of the 3D considered domain obtained by using the Gmsh software.

The model's output corresponds to the velocity field $\mathbf{v}$ as a function of the spacial coordinates x, y, z and the angular velocity ω. This field is written in a separated form as:

$$\mathbf{v} = \begin{pmatrix} u(x,y,z,\omega) = \sum_{i=1}^{i=N} U_i(x,y,z) \cdot S_i(\omega) \\ v(x,y,z,\omega) = \sum_{i=1}^{i=N} V_i(x,y,z) \cdot S_i(\omega) \\ w(x,y,z,\omega) = \sum_{i=1}^{i=N} W_i(x,y,z) \cdot S_i(\omega) \end{pmatrix} \tag{10}$$

where u, v and w are the three components of the velocity vector along x, y and z respectively.

A fixed point iterative algorithm is used to solve the problem for Non-Newtonian fluids characterized by $n \neq 1$. The velocity profile obtained from the Newtonian solution is used as a first guess. At each iteration of the fixed point algorithm, a four-dimensional problem is resolved using the PGD. To this aim, all operators should be written in a separated form, including the operator multiplied by the viscosity η. Thus, at each iteration, the four-dimensional viscosity field $\eta(x,y,z,\omega)$ is determined using equation (3); it is then written in a separated form by means of a singular value decomposition (SVD). A new velocity field is finally determined from the separated viscosity result. The iterative process is repeated until the convergence of the viscosity η.

The material parameter K can be introduced as an extra coordinate of the problem at the expense of using a high order singular value decomposition (HOSVD) to write the viscosity in a separated form [16]. The HOSVD generates however approximation errors when writing the viscosity in a separated form and may lead to a dramatic reduction of the PGD's efficiency. The authors therefore prefer to use the PGD to solve $\mathbf{v}(x,y,z,\omega)$ and combine the PGD to a POD during the identification process to keep the problem as simple and accurate as possible.

4 RESULTS AND DISCUSSION

A typical example considering $K = 300$ Pa.s and $\omega = 0.5$ rad/s is retained. For this example, the nonlinear problem corresponding to the weak form in equation (8) is resolved with $n = 0.7$, 0.8, 0.9 and 1 respectively. A horizontal section at mid-height of the vane showing the magnitude superimposed to a quiver plot of the velocity field is provided in Figure 4 for each of these four cases.

Figure 4 reveals striking differences in the velocity fields between the cases corresponding to different values of n. In particular, a shear-thinning behavior can be clearly observed by comparing the cases $n = 0.7$ and $n = 1$, for example. This is for instance revealed by the sharp drop in the magnitude of the velocity field as one moves away from the tips of the blades in the case corresponding to $n = 0.7$ as opposed to the more homogeneous and gradual decrease of the same quantity between the tip of the blades and the outer cylinder

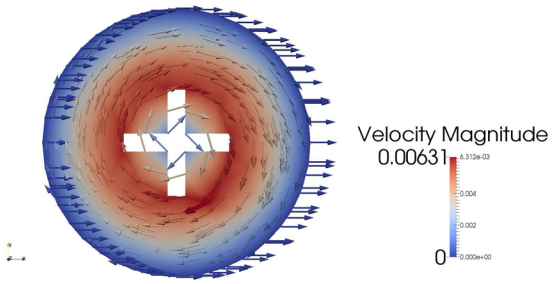

$n = 1$

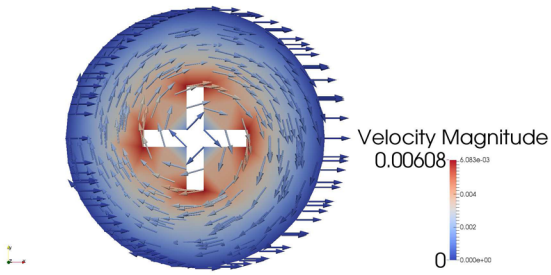

$n = 0.9$

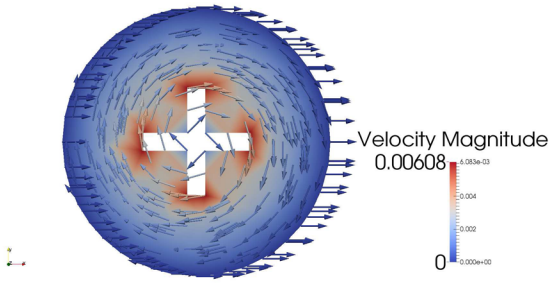

$n = 0.8$

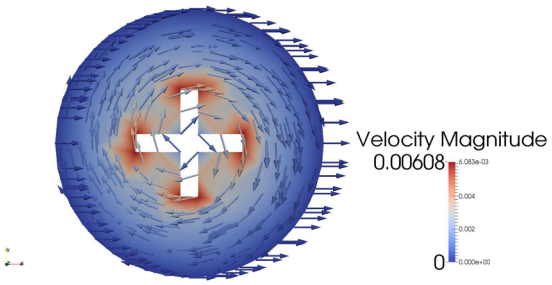

$n = 0.7$

Figure 4: Typical magnitude and quiver plot of the velocity field; $n = 0.7$, 0.8, 0.9 and 1.

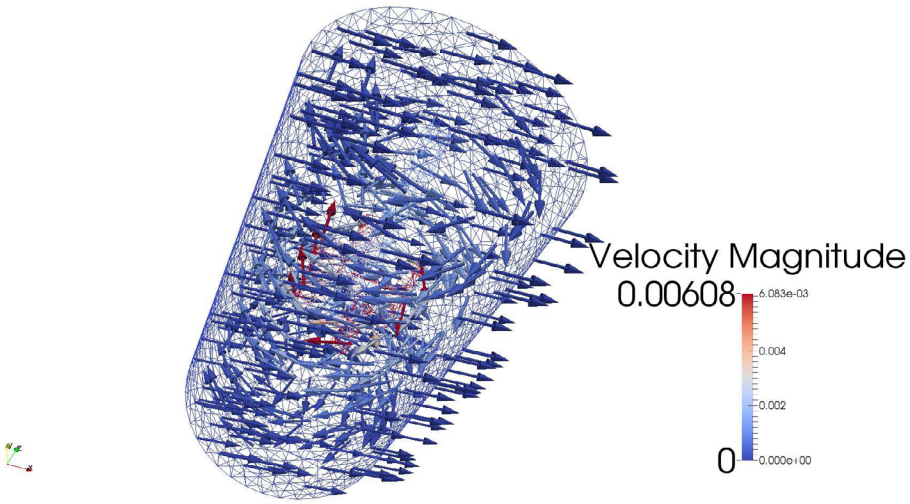

Figure 5: Typical 3D magnitude and quiver plot of the velocity field in the physical domain for $n = 0.7$.

when $n = 1$. A typical three-dimensional magnitude and quiver plot of the velocity field inside of the entire physical domain is also illustrated in Figure 5 at at $\omega = 0.5$ rad/s for $n = 0.7$.

One may also wish to determine the value of the torque applied to the vane – a quantity that is critical to the identification of material parameters from experimental results. To this aim, we distinguish in this work two origins of this torque: (i) the normal pressure field acting on the lateral surfaces of the blades of the vane and (ii) the shear stresses acting on the tips of the blades and on the vane's shaft. The contribution of the shear stresses acting radially on the lateral faces of the blades is neglected due to the their small eccentricity.

The normal pressure on the blades can be determined from equation (5), and thus the corresponding torque T_P expressed as:

$$T_P = \int_{A_1^*} P\mathbf{r} \times d\mathbf{A} - \int_{A_2^*} P\mathbf{r} \times d\mathbf{A}, \tag{11}$$

where A_1^* is the area of the vane surfaces upstream of the fluid flow and A_2^* downstream, $\mathbf{r}$ the radial distance from the axis of the vane to the point of application of the pressure and $d\mathbf{A}$ a differential area at this point. Figure 6 illustrates a typical variation of T_P for $n = 0.7$. The influence of n on the the part T_P of the torque that is due to the normal pressure acting on the lateral surfaces of the blades appears to be marginal.

The second component of the torque T_η that is due to the shear stresses is illustrated

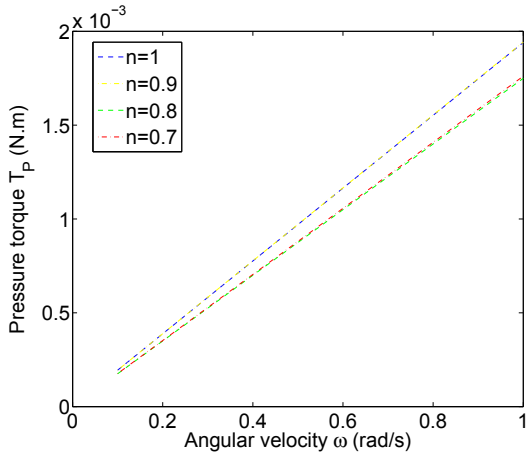

Figure 6: Torque T_p generated by the normal pressure on the blades for $n = 0.7$, 0.8, 0.9 and 1 as a function of ω.

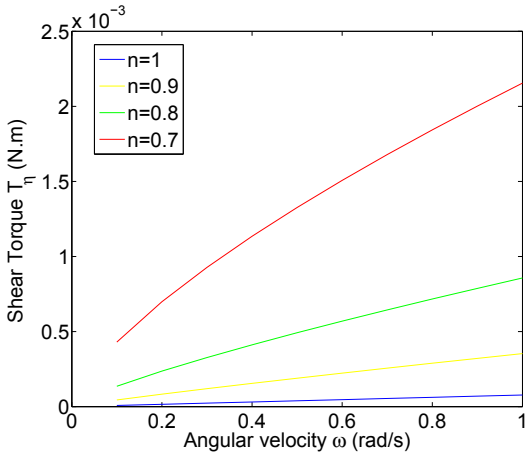

Figure 7: Torque T_η generated by the shear stresses acting on the tips of the blades for $n = 0.7$, 0.8, 0.9 and 1, as a function of ω.

in Figure 7. This component is defined by:

$$T_\eta = \int_{A^\dagger} \eta \cdot \mathbf{r} \times \nabla \mathbf{v} \cdot d\mathbf{A}, \tag{12}$$

where $A^\dagger$ corresponds to the area of the tip of the blades and of the upper circular shaft connecting the blades to the actuator. The dependence of T_η on n and ω appears to be strongly nonlinear. A linear variation of T_η as a function of ω can also be noted for $n = 1$.

In future work, the model's outputs shall be compared to experimental results to identify cement paste material properties K and n.

5 CONCLUSION

A novel approach to the modeling of the vane test on cement pastes using Non-Newtonian power-law fluids is proposed in this work, with the final objective of identifying material properties of the pastes. The PGD is used to simulate the fluid flow in the vane test while introducing the mixing velocity as an extra coordinate. The nonlinear four-dimensional problem is addressed using the PGD by means of a first linearization process using a fixed-point iterative algorithm. The full resolution process – involving 100 nodes in ω and 16050 finite elements discretizing the 3D spatial domain – typically takes a few minutes only, on a normal portable PC.

The proposed model replicates successfully the nonlinear behavior of the torque as a function of the angular velocity. Such behavior is typically observed experimentally when running vane tests on cement pastes.

REFERENCES

[1] G. Ovarlez and N. Roussel. A physical model for the prediction of lateral stress exerted by self-compacting concrete on formwork. *Materials and structures*, 39:269Ű279, 2006.

[2] W. Wang, D. De Kee, and D. Khismatullin. Numerical simulation of power law and yield stress fluid flows in double concentric cylinder with slotted rotor and vane geometries. *Journal of Non-Newtonian Fluid Mechanics*, 166:734–744, 2011.

[3] Chady Ghnatios, Francisco Chinesta, and Christophe Binetruy. 3d modeling of squeeze flows occuring in composite laminates. *International Journal of material forming*, 8(1):73–83, March 2015.

[4] S. Aghighi, A. Ammar, C. Metivier, M. Normandin, and F. Chinesta. Non incremental transient solution of the rayleigh-benard convection model using the pgd. *Journal of Non Newtonian Fluid Mechanics*, 200:65–78, 2013.

[5] Chady Ghnatios, Francoise Masson, Antonio Huerta, Elias Cueto, and Francisco Chinesta. Proper generalized decomposition based dynamic data-driven of thermal processes. *Computer Methods in Applied Mechanics and Engineering*, 213-216:29–41, 2012.

[6] Howard Anthony Barnes and Quoc Dzuy Nguyen. Rotating vane rheometry - a review. *Journal of Non Newtonian Fluid Mechanics*, 98(1):1–14, March 2001.

[7] Petra V. Liddel and David V. Boger. Yield stress measurment with the vane. *Journal of Non-Newtonian Fluid Mechanics*, 63(2-3):235–261, April 1996.

[8] Chady Ghnatios, Francisco Chinesta, Elias Cueto, Adrien Leygue, Arnaud Poitou, Piotr Breitkopf, and Pierre Villon. Methodological approach to efficient modeling and optimization of thermal processes taking place in a die: Application to pultrusion. *Composite Part A : Applied Science and Manufacturing*, 42:1169–1178, May 2011.

[9] Chady Ghnatios. *Modélisation avancée des procédés thermiques rencontrés lors de la mise en forme des composites*. PhD thesis, Ecole Centrale Nantes, October 2012.

[10] Francisco Chinesta, Amine Ammar, and Elias Cueto. Recent advances in the use of the proper generalized decomposition for solving multidimensional models. *Archives of Computational Methods in Engineering*, 17(4):327–350, 2010.

[11] Francisco Chinesta, Amine Ammar, and Elias Cueto. Recent advances and new challenges in the use of the proper generalized decomposition for solving multidimensional models. *Archives of Computational Methods in Engineering*, 17(4):327–350, December 2009.

[12] Etienne Pruliere, Julien Ferec, Francisco Chinesta, and Amine Ammar. An efficient reduced simulation of residual stresses in composite forming processes. *International Journal of Material Forming*, 3:1339–1350, 2010.

[13] Chady Ghnatios. Optimization of composite forming processes using non-linear thermal models and the proper generalized decomposition. In IEEE-xplore, editor, *Third International Conference on Advances in Computational Tools for Engineering Applications (ACTEA)*, 2016.

[14] Jean François Agassant, Pierre Avenas, Jean-Philippe Sergent, Bruno Vergnes, and Michel Vincent. *La mise en forme des matières plastiques*. Lavoisier, 1996.

[15] Jean Donea and Antonio Huerta. *Finite element method for flow problem*. Wiley, 2003.

[16] Tamara G. Kolda and Brett W. Bader. Tensor decompositions and applications. *Society for Industrial and Applied Mathematics*, 51(3):455–500, 2009.

XIV International Conference on Computational Plasticity. Fundamentals and Applications
COMPLAS 2017
E. Oñate, D.R.J. Owen, D. Peric and M. Chiumenti (Eds)

APPLICATION OF CONFIGURATIONAL MECHANICS TO CRACK PROPAGATION

L. CRUSAT AND I. CAROL

ETSECCPB (School of Civil Engineering)
Universitat Politècnica de Catalunya (UPC)
08034 Barcelona, Spain
e-mail: laura.crusat@upc.edu, ignacio.carol@upc.edu

Key words: Configurational mechanics, crack initiation, propagation, fracture mechanics

Abstract. Crack initiation and propagation is an essential aspect in the mechanical behavior of a large variety of materials and structures in all fields of Engineering and, in particular, the prediction of crack trajectories is one of the major challenges of existing numerical methods. Classical procedures to fix crack direction have been based on local criteria such as maximum (tensile) hope stress. However, Fracture Mechanics principles suggest that global criteria should be used instead, such as maximizing structural energy release rates. An emerging trend along this way is based on Configurational Mechanics, which describes a dual version of the mechanical problem in terms of configurational pseudo-stresses, pseudo-forces, etc. all with a physical meaning related to the change in global structural elastic energy caused by changes in the structural geometry (configuration). In the FEM context, these concepts are applied to optimize the total energy of the mesh with respect to reference coordinates using the discrete configurational forces. Configurational stresses given by Eshelby's energy-momentum tensor may be integrated using standard expressions to give configurational nodal forces. Adequate treatment of these forces in the context of iterative FE calculations, may lead to prediction of crack trajectories in terms of global structural energy.

1 INTRODUCTION

The purpose of this paper is to introduce basic ideas of Configurational Mechanics related to crack initiation and propagation. According to Steinmann [1], Configurational Mechanics can be considered from the viewpoints of continuum mechanics or computational mechanics. In the context of continuum mechanics, configurational forces would describe the energy variations due to changes of material configuration, while in a computational context the discrete forces may indicate the quality of a finite element mesh. In both cases, configurational analysis consists of evaluating the energy variations due to changes of the material configuration (original geometry of the structure or mesh). Configurational mechanics may be used to solve a large variety of problems, such is mechanics of dielectrics, thermodynamic problems, or mechanical problems with presence of dislocations and fractures, etc.

Configurational forces are derived combining the energy and momentum balance, with the

so called pseudo-momentum balance or configurational force balance. The original concept is due to Eshelby [2], who introduced the so called energy-momentum tensor $\mathbf{\Sigma} = \mathrm{W}\mathbf{I} - \mathbf{F}^{\mathrm{T}}\mathbf{P}$. In the fifties, Eshelby developed the driving forces for elastic singularities, defining the well-known "Maxwell tensor of elasticity". Configurational forces are the negative gradient of total energy with respect to the position of a point or defect, so forces are used to evaluate imperfections, dislocations, etc.

In addition, configurational forces may take a special meaning in the context of the Finite Element Method, because the FEM yields only approximate solutions which depend on discretization. The equilibrium equation is approximated but not exactly satisfied, and energy is also approximated but not exactly evaluated, and the error may depend on the chosen discretization. The concept of finite element mesh optimization using configurational forces is described in [1, 3, 4, 5, 6, 7], with application to remeshing methods or r-adaptivity methods [3, 7].

2 CONFIGURATIONAL MECHANICS IN THE CONTEXT OF THE FINITE ELEMENT METHOD

Configurational forces show the direction in which the original position of the nodes of mesh would have to be moved, so that the overall energy in the mesh would decrease. Energy variation can be caused by physical changes such as changes in dimensions of geometry of the domain (if the nodes changing location are at the boundary for instance), or changes of the mesh discretization (if the nodes changing location are in the interior of the domain and their location does not affect the boundaries but only the internal arrangement of the mesh).

Nevertheless, both can be represented by configurational forces which are the gradient of the total domain elastic energy ψ with respect to original nodal location $\mathbf{X}$ (Eq. 1). Since, in general, energy is a function of original location as well as final node position after deformation $\mathbf{x}$, i.e. $\psi = \psi(\mathbf{X}, \mathbf{x})$, this means that configurational forces are evaluated at constant $\mathbf{x}$:

$$\hat{\mathbf{f}} = \left.\frac{\partial \psi}{\partial \mathbf{X}}\right|_{\mathbf{x=ct}} \tag{1}$$

In the finite element context, energy may be expressed as an integral over the domain, of the specific energy per unit volume, which leads to the following integral expression of the configurational forces:

$$\hat{\mathbf{f}} = \int \mathbf{B}^{T}(\mathrm{W}\mathbf{I} - \mathbf{F}^{\mathrm{T}}\mathbf{P})\mathrm{dV} \tag{2}$$

where $\mathbf{B}$ is the traditional FE matrix, W is the specific elastic energy per unit volume of original configuration, $\mathbf{I}$ is the 3x3 unit matrix, $\mathbf{F}$ is the deformation gradient and $\mathbf{P}$ is the first Piola-Kirchoff stress.

Equation (2) may be obtained by combining the basic definition of configurational forces (Eq.1) with finite element equations, or by alternative procedures as it is developed in some articles [4, 5, 6, 7].

Expression (2) contains the well-known Eshelby's stress tensor, also called energy-momentum tensor, which is defined as:

$$\boldsymbol{\Sigma} = \mathrm{W}\mathbf{I} - \mathbf{F}^{\mathrm{T}}\mathbf{P} = \mathrm{W}\mathbf{I} - \mathbf{C}\mathbf{S} \tag{3}$$

Note the alternative expression of $\boldsymbol{\Sigma}$ in terms of symmetric tensors, second Piola-Kirchhoff ($\mathbf{S} = \mathbf{F}^{-1}\mathbf{P}$) and symmetric right Cauchy-Green strain tensor ($\mathbf{C} = \mathbf{F}^{\mathrm{T}}\mathbf{F}$).

Notice that the definition of configurational forces is similar to mechanical forces in the classical (deformational) finite element formulation. In this case, instead of the physical stress the integral is over shape function derivatives and the Eshelby's stress tensor.

$$\mathbf{f} = \int \mathbf{B}^T \boldsymbol{\sigma}\, dV \;\rightarrow\; \hat{\mathbf{f}} = \int \mathbf{B}^T \boldsymbol{\Sigma}\, dV \tag{4}$$

As said, configurational forces indicate the direction in which nodes should be configurationally moved (original coordinates changed) in order to decrease the overall domain elastic energy, and eventually reach the minimal energy configuration. On the basis of that, an r-adaptivity method has been implemented. It is an iterative process which consists of changing nodal location until material forces vanish. The change of location for each iteration is calculated via Eq.(5), using a small value for constant c multiplying the configurational forces with minus sign (logical, since being those forces the gradient of the energy, their positive direction would indicate energy increase):

$$\mathrm{X}_i = \mathrm{X}_{i-1} - c\hat{f}_{i-1} \tag{5}$$

In this equation, X are the nodal coordinates, $\hat{f}$ the configurational forces and subindex i indicates the current configurational iteration.

The r-adaptivity procedure provides energetically optimized meshes, where number of elements remains constant and connectivity as well. These may be great advantages in comparison to other more complex methods such as h-adaptivity methods [7].

3 NUMERICAL EXAMPLES

3.1 Example 1

This example has been often used in configurational mechanics papers [4]. It consists on a homogeneous block (E=1085.7 MPa and ν =0.3571) with a constrained tensile displacement on the top side and fixed on the bottom (Figure 1a). It is discretized with a structured mesh of 16 regular quadrilateral elements as shown in Figure 1b, where the solid nodes also indicate the nodes that are "configurationally fixed" (i.e. those that will not be allowed to move even if configurational forces are applied on them), while the hollow ones are "configurationally free" to change location through configurational iterations.

In this problem, configurational forces (with minus sign) are concentrated on the boundary nodes that are configurationally fixed (Figure 2a), with such proportion that if scale is adjusted to those, the forces on inner nodes cannot be even visualized. Physically this means that, if domain dimensions would be increased slightly (but final node positions would remain constant), total energy would decrease. To explain this, one has to take into account two counteracting effects. On one side, tensile deformations would be lower (because initial and final positions of nodes would be closer) and therefore volumetric energy density would be lower, but on the other side total volume would be larger. Out of those effects, the decrease of specific energy would be dominant because is a quadratic relation. From the r-adaptivity

method itself, it makes sense to fix configurational movements on the boundary so that domain dimensions will not change and only internal configurational forces (Figure 2b) are allowed to change the material configuration, and therefore node relocations will reflect only the mesh rearrangement to reach an energy minimum

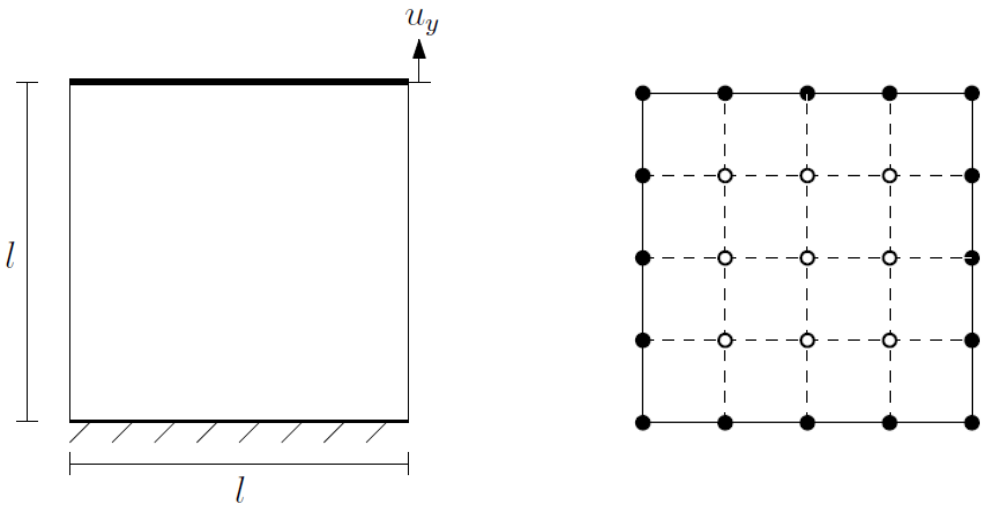

(a) (b)

Figure 1: (a) Boundary conditions of example 1 (b) Finite element discretization, with indication of nodes that are "configurationally fixed" (solid) and "configurationally free" (hollow).

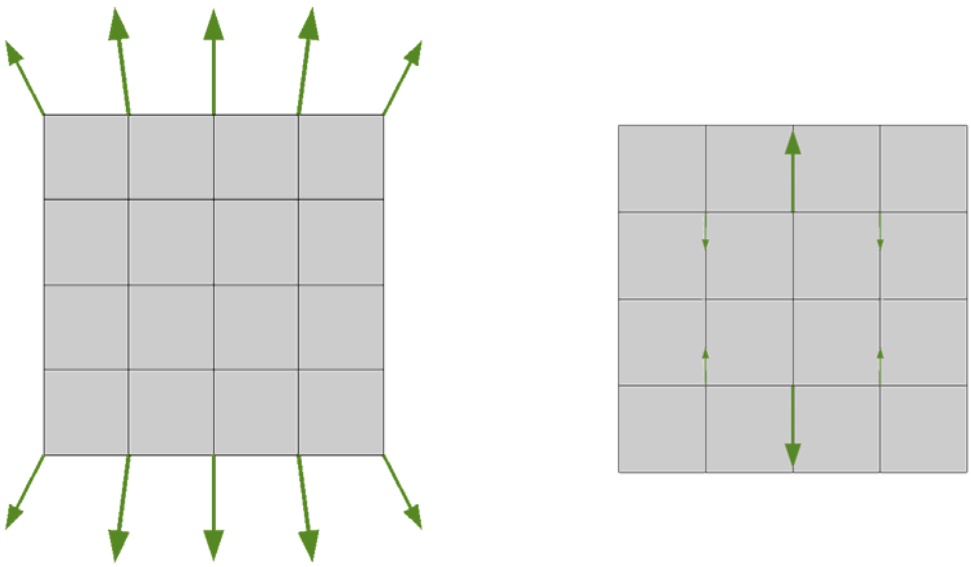

(a) (b)

Figure 2: (a) Configurational forces (with minus sign) on all nodes of the mesh, at the scale dictated by larger forces on the boundary nodes, (b) same only for internal nodes, at a larger scale in which forces on those nodes would be represented.

Finally, applying equation (5) in various steps with an appropriate value of c leads to the optimized mesh. As Figure 3a shows, nodes with larger configurational forces exhibit larger position changes. Since this optimal corresponds, not to a real geometry change of the domain but to the optimization of the FE discretization error, this solution turns out not trivial and might be different for other meshes or element types. Figure 3b depicts the total energy of the mesh as a function of the y-coordinate position of the most relevant node in this example, and Figure 3c the norm of the configurational forces of internal nodes, also as a function of the same vertical position of the relevant node. It can be seen as the node approaches it optimal position, energy comes to a minimum and forces are reduced to zero norm.

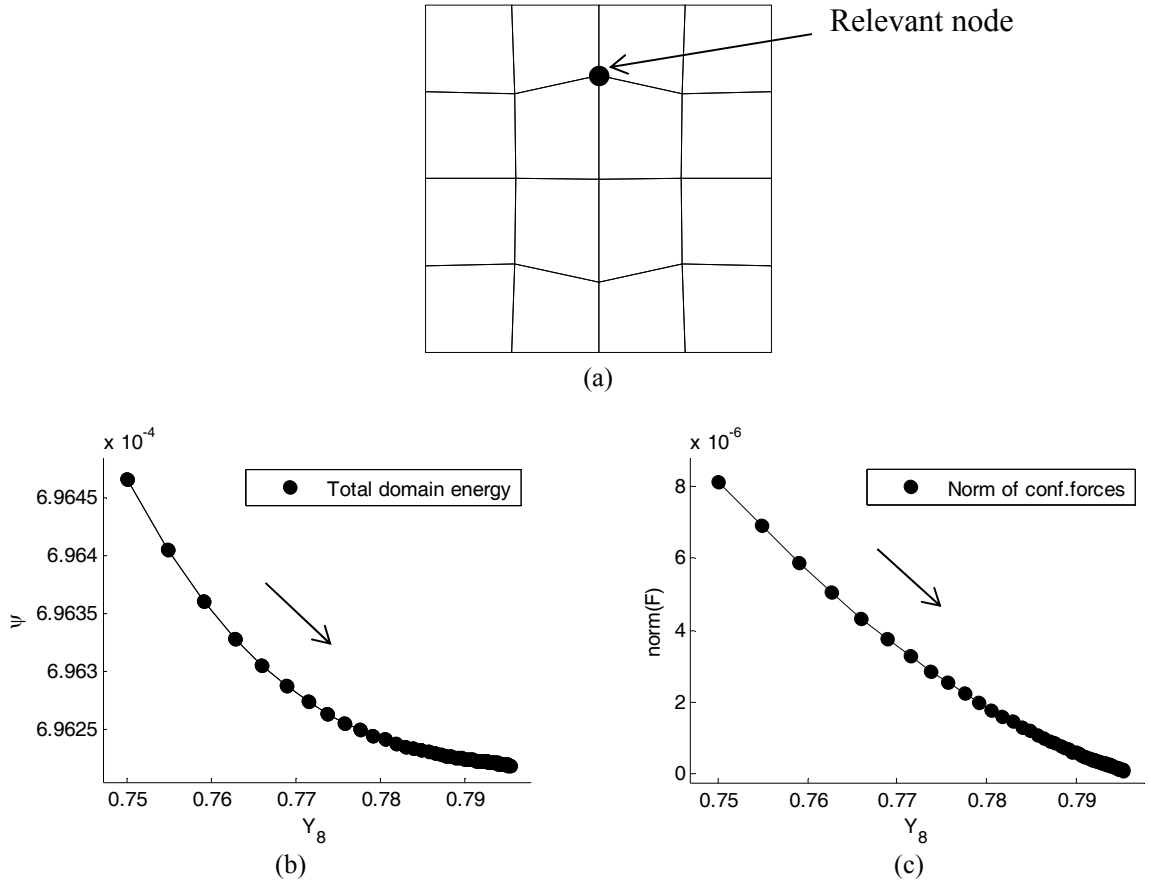

Figure 3: (a) Optimal mesh configuration. (b) Total mesh energy with respect to relevant node vertical position, and (c) norm of configurational forces with respect to relevant node vertical position.

3.2 Example 2

The second example is a notched beam with a prescribed displacement on the top. In this case the point where displacement is imposed is not aligned with the notch, in order to observe the path followed by the central top node of the notch (Figure 4). Material properties are $\lambda = 1000$, $\mu = 400$ (Lamé Constants, which correspond to E=1085.7 MPa and ν =0.3571) and plane strain is assumed.

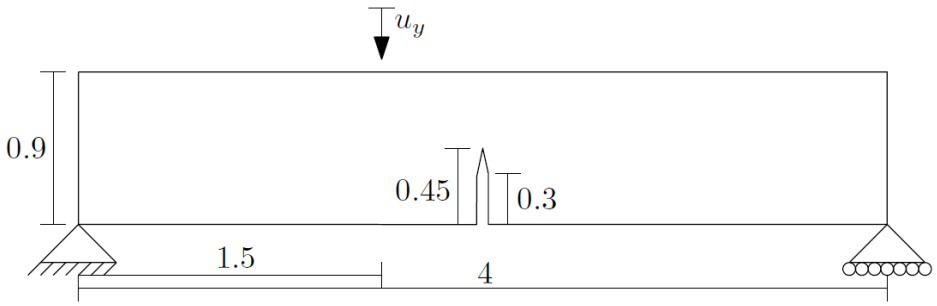

Figure 4: Notched beam on two supports with a punctual displacement imposed on the top.

The mesh discretization used to analyze path evolution in vertical and horizontal direction is shown in Figure 5, there are six quadrangular elements. The advantage of using that simple structure is is that only one node is not configurationally fixed, and therefore it is easier to understand energy distribution and configurational force effects depending on its position.

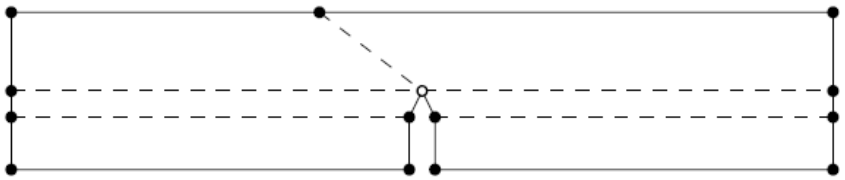

Figure 5: Finite element mesh used on example 2.

As the interactive procedure starts, configurational forces drive the central node progressively to its optimal energetic position. As it is represented in Figure 8a, the optimal position is at the point of coordinates $X = 1.5$ and $Y = 0.9$, which is the application point of the imposed displacement. Figures 6, 7 and 8 confirm that solution because there is a minimum of energy and the norm of configurational forces are near zero at the point $X = 1.5$ and $Y = 0.9$.

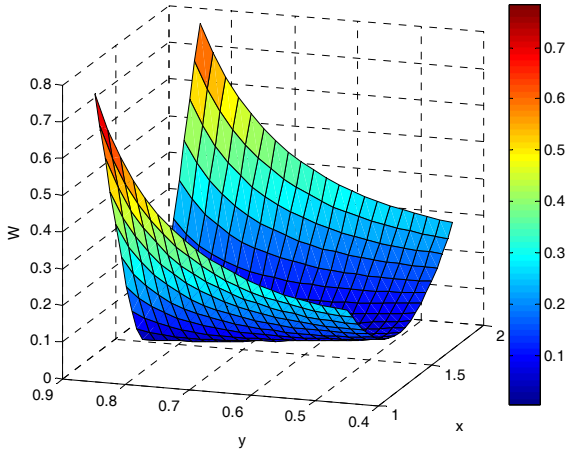

Figure 6: Total domain energy as a function of the central node position.

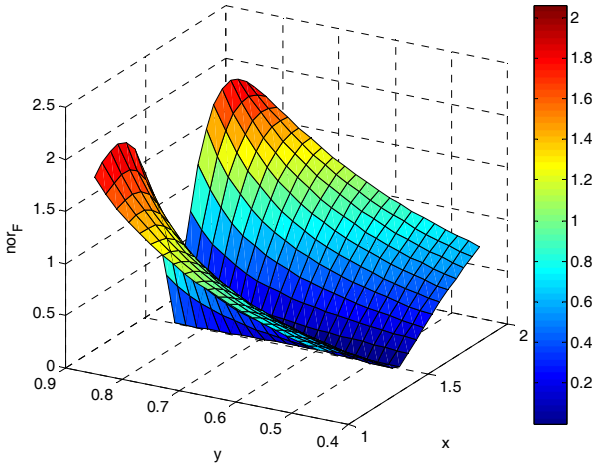

Figure 7: Configurational force norm as a function of the central node position.

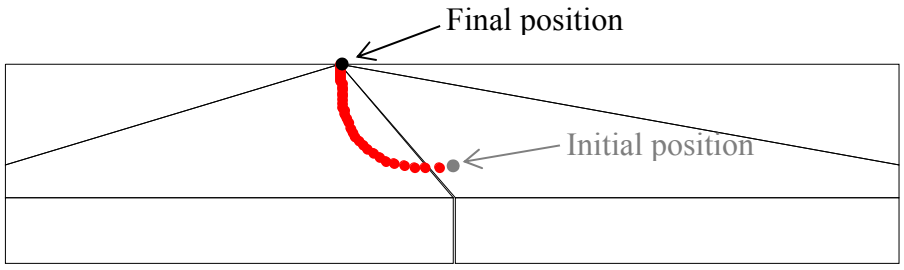

(a)

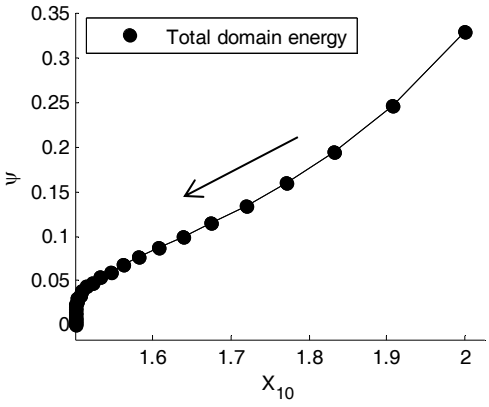

(b)

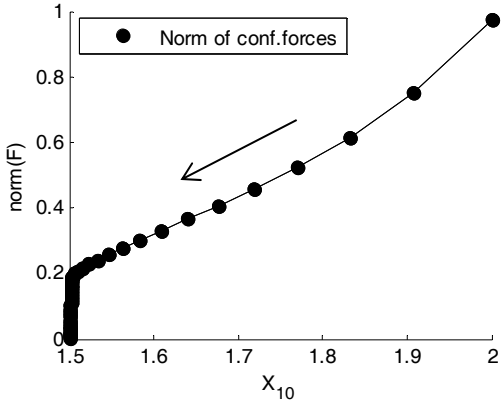

(c)

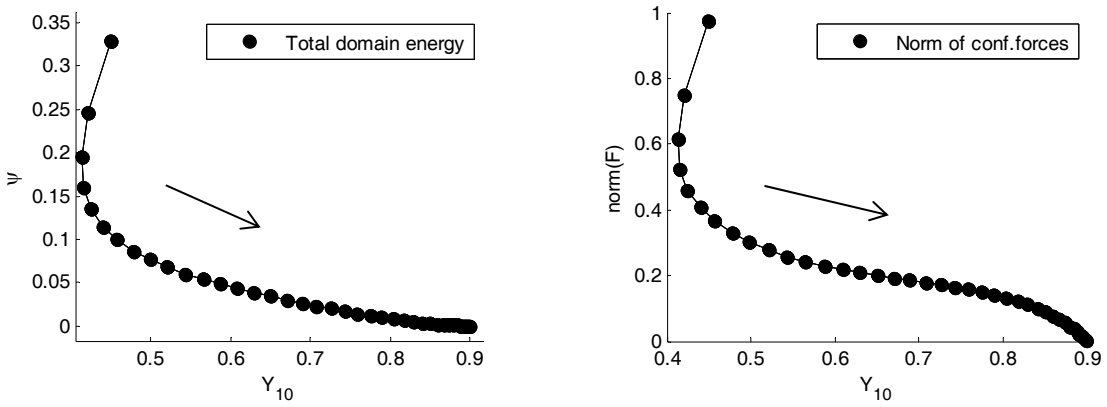

(d) (e)

Figure 8: (a) Optimal mesh distribution, the path is represented in red. (b) Total energy with respect to the relevant node horizontal position. (c) Norm of configurational forces with respect to the relevant node horizontal position. (d) Total energy with respect to the relevant node vertical position. (e) Norm of configurational forces with respect to the relevant node vertical position.

4 CONCLUDING REMARKS

In this article the application of configurational mechanics to FE meshes has been introduced. Configurational forces are used to know the direction in which the nodes original positions would have to be moved, in order to decrease the total domain energy and eventually reach the minimum energy configuration. Using this concept as an r-adaptive strategy, nodal coordinates may be modified leading to the optimal mesh (in the energy sense). From a physical point of view, configurational forces may also be used to indicate the direction of crack tip propagation for minimal energy and therefore help predict the most probable path on crack trajectories. In example 1, a simple mesh optimization was performed reaching the minimum total energy for some non-trivial configuration. On the other hand, the second example was useful to illustrate how configurational forces can be applied to evaluate optimal crack paths. Note that in this academic example the notch was allowed to move (and therefore the crack could grow) without restrictions or energy consumption, only driven by configurational forces exclusively, that is only responding to the direction of crack extension that will reduce more effectively the total energy of the domain. This is why, the minimum is reached for zero total energy, when the crack tip arrives to the point of prescribed displacement, configuration that actually corresponds to a hinge mechanism. But physically, crack extension requires energy consumption. And this is precisely one of the focus of on-going work, complementing configurational mechanics with the restrictions imposed by the principles of fracture mechanics that dictate the balance between energy released from the structure and energy consumption required for crack propagation.

ACKNOWLEDGMENTS

The work was partially supported by research grants BIA2016-76543-Rfrom MEC (Madrid), which includes FEDER funds from the European Union, and 2014SGR-1523 from Generalitat de Catalunya (Barcelona). The first author acknowledges MICINN (Madrid) for her FPI doctoral fellowship.

REFERENCES

[1] P. Steinmann, M. Scherer, and R. Denzer, "Secret and joy of configurational mechanics: From foundations in continuum mechanics to applications in computational mechanics" *ZAMM-Journal of Applied Mathematics and Mechanics*, **89**, 614-630 (2009).

[2] J.D. Eshelby, "The elastic energy-momentum tensor" *Journal of Elasticity* **5.3-4,** 321-335 (1975).

[3] C. Miehe, and E. Gürses. "A robust algorithm for configurational-force-driven brittle crack propagation with R-adaptive mesh alignment." *International Journal for Numerical Methods in Engineering* **72.2**, 127-155 (2007).

[4] R. Mueller, and G.A. Maugin. "On material forces and finite element discretizations" *Computational mechanics*, **29.1**, 52-60 (2002).

[5] R Mueller, S. Kolling, and D. Gross. "On configurational forces in the context of the finite element method." *International Journal for Numerical Methods in Engineering*, **53.7**, 1557-1574 (2002).

[6] R. Mueller, D. Gross and G. A. Maugin. "Use of material forces in adaptive finite element methods." *Computational Mechanics*, **33.6**, 421-434 (2004).

[7] R. Mueller and D. Gross. "Discrete Material Forces in the Finite Element Method." *In Mechanics of Material Forces* (pp. 105-114). Springer US (2005).

XIV International Conference on Computational Plasticity. Fundamentals and Applications
COMPLAS 2017
E. Oñate, D.R.J. Owen, D. Peric and M. Chiumenti (Eds)

APPLICATION OF LIFECYCLE ASSESSMENT AND FINITE ELEMENT ANALYSIS IN THE DESIGN OF RAISED ACCESS FLOOR PRODUCTS

You Wu[1], Daizhong Su[1], Wenjie Peng[1] and Qianren Zhang[2]

[1] Advanced Design and Manufacturing Engineering Centre (ADMEC)
University of Nottingham Trent University
50 Shakespeare Street, Nottingham, NG1 4FQ, UK
E-mail: you.wu2013@my.ntu.ac.uk, daizhong.su@ntu.ac.uk, wenjie.peng02@ntu.ac.uk

[2] Chongqing Polycomp International Corp
Zone B, Jianqiao Industrial Park, Dadukou District, Chongqing, 400082, China
E-mail: zhangqianren@cpicfiber.com

Key words: Finite Element Analysis, Lifecycle Assessment, Raised Access Floor Product Sustainable Design, Product Design

Abstract: In this research, lifecycle assessment (LCA) and finite element analysis (FEA) are applied in raised access floor product design. LCA is conducted to assess the product's sustainable features, while the FEA is carried out to ensure that the product meets the required strength. The materials used to develop the floor panel is Sheet Moulding Compound (SMC) with 30% glass fibres. The product is modelled in SolidWorks software package. Based on the CAD model of the product, the LCA and FEA are then conducted. The LCA results revealed that the materials contribute significant impacts in the four environmental impact categories: 84% in carbon footprint, 91% in total energy consumed, 73% in air acidification, and 66% in water eutrophication. The LCA evaluation results not only clarify the optimized design targets, but also enable to benchmark values for design iterations. According to the FEA, the deformation values are less than 2.5 mm with 3000 N loading forces on the central of the panel and stringer, which meet the flooring product's deformation criteria of Class A, as defined by the British Standards.

1 INTRODUCTION

A typical raised access floor comprises of load bearing floor panels laid in a horizontal grid supported by adjustable vertical pedestals, which provides an underfloor space for the housing and distribution of services in a building. The floors generally consist of 600mm X 600mm panel supported at each corner by pedestal jacks, each jack locating and supporting the corners of four adjacent panels. A raised access floor product system is shown in Figure 1. The floor panels are readily removable to allow quick access to the underfloor services. The adopting raised floor products provide flexibility in the design and layout of telephone, electrical, electronic communication cables and air-conditioning systems, which are easily routed below the floor panels.

The materials to make the floor panel normally includes particle board, plywood, aluminium, steel, or a combination of metal and non-metal. The particle board or plywood panels are usually covered with thin sheet steel or aluminium for implementation of fire protection. In some cases the steel is in the form of a tray, depending on the bonding adhesive used between

the wood product and the steel, it can increase the structural strength of the panel. SMC (Sheet Moulding Compound) materials are used for producing the floor panel in this project, because of its strong performance in mechanical properties, fire resistance, and stiffness. The physical properties of the selected SMC material are presented in Table 1.

This paper presents a computational approach to develop this floor product system. The approach include 3D CAD modelling, lifecycle assessment (LCA) and finite element analysis of the product (FEA).

Figure 1: A generic raised access floor product system [1]

Table 1: SMC physical properties

properties	values
Density of the selected SMC	1800 kg/m^3
Flexural modules	1.3 GPa
Poisson's ratio	0.3
Yield strength	250 MPa
Tensile strength	150 MPa

2 INITIAL DESIGN AND MODELLING

The modelling of the raised access floor system involves the design of a floor panel and pedestals, as shown in Figure 2. The standard size (600 mm x 600 mm x 40 mm) is applied for the raised access floor panel in this project. The dimensions of the design prototype are presented in Table 2, which meet the criteria of the British Standard 12825 [5]. The pedestal design prevents excessive movement of the panel, by which the stability of the raised access floor system is enhanced.

Table 2: Dimensions for the initial design

Component dimensions of raised flooring product	
items	**values**
Height of pedestal	100 mm
Square base plate	100 mm x 100 mm
Diameter of circular plate at the top	90 mm
Size of the floor panel	600 mm x 600 mm x 40 mm
Weight of the floor panel	25.92 kg

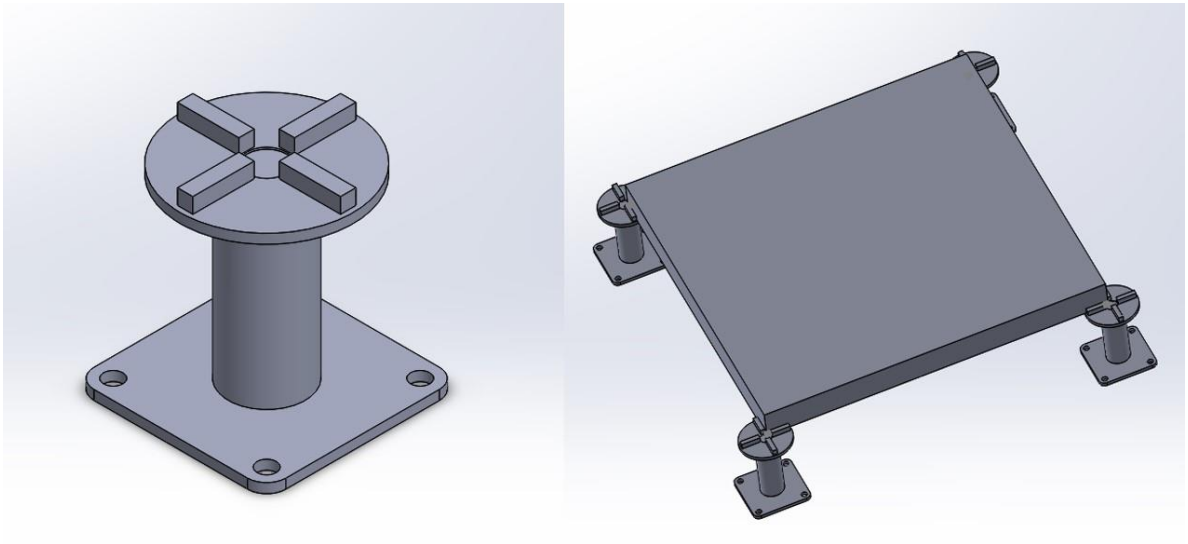

Figure 2: Initial design for the pedestal unit (left) and the raised access floor system (right)

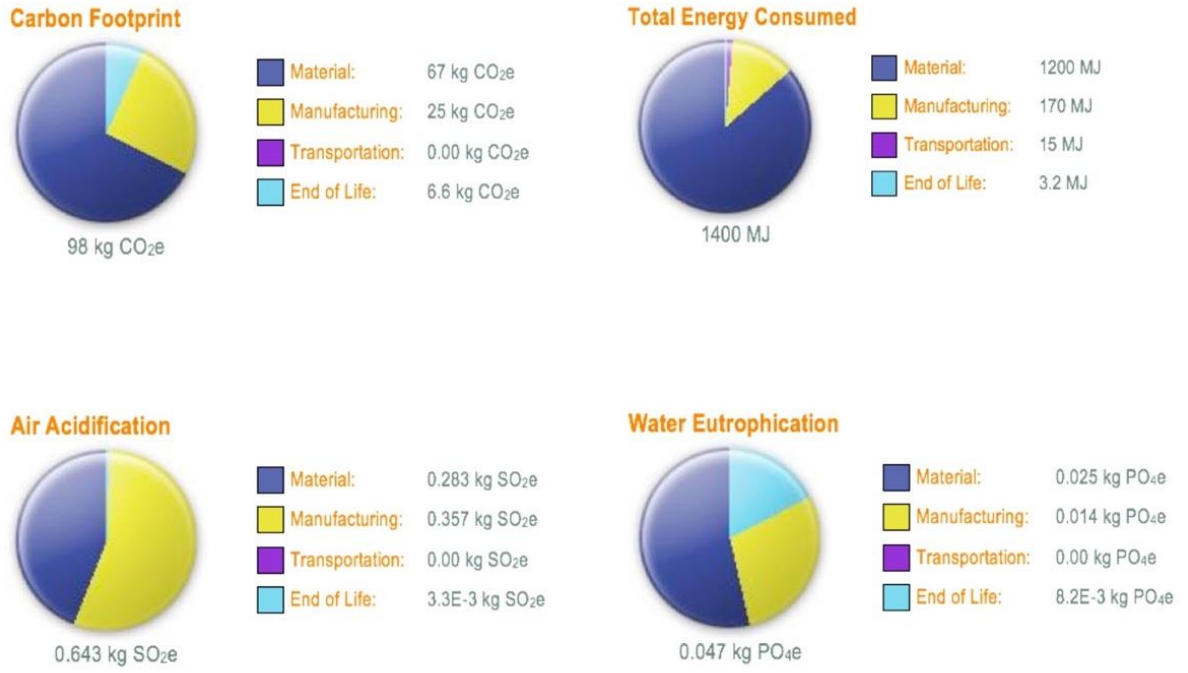

Figure 3: The LCA results by applying CML methodology in SolidWorks 2015

The weight of the floor panel is 25.92 kg, which is obtained by calculating the design dimensions and SMC density. This is much over the weight, 11 kg, of the existing product in the market with the same size and made of chip board covered by metal sheets. And hence re-design has to be considered in order to reduce the weight.

CML and TRACI are LCA based methodologies, which are embedded in the sustainability package of SolidWorks 2105. The CML method is applied in this phase, and the results show

that the materials contribute major negative impacts in the four environmental impact categories: 84% in Carbon Footprint, 91% in Total Energy Consumed, 73% in Air Acidification, and 66% in Water Eutrophication. The pie chart of the LCA analytic results are presented in Figure 3.

3 RE-DESIGN

According to the initial design, the floor panel is over-weight. Therefore, reducing the weight of the floor panel is the prioritized task in this phrase. In addition, necessary LCA and FEA have to be conducted in order to ensure the product meets the required functions.

3.1 Refinement of the raised access floor system

In order to achieve an effective design, the floor panel requires strong outer edges with the side of the panels connected by ribs, hence, the strategy of designing ribs for the floor panel is confirmed. The optimum design of the floor panel has same size squares with 3 mm ribs between them, and the layout and dimensions of these squares are shown in Figure 4 and Table 3, respectively.

Table 3: Main components' dimensions and weight in detail design phrase

Component dimensions and weight in detail design	
Items	**Values**
Square	94.7 mm X 94.7 mm x 94.7 mm
Thickness of ribs	3 mm
Thickness of the floor panel	30 mm
Size of the stringer	600 mm x 600 mm x 37 mm
Thickness of the string edge and beam	3 mm
Component weight for detailed design	
Items	**Values**
Floor panel	3.52 kg
Stringer	3.55 kg
Pedestal unit	0.99 kg
Total mass	8.06 kg

The thickness of the floor panel is cut from 40 mm to 12 mm in the design comprising rectangles' size and ribs' thickness, therefore the strength performance of the floor panel is reduced. The solution of placing a steel stringer under the floor panel is employed, as this design not only sustains the strength performance of the floor system, but also provides the facility of recycle or reuse for the steel stringer. The stringer design is shown in Figure 4, and its dimensions are shown in Table 3. With this optimum design, the total weight of this raised access floor system has been reduced to 8.06 kg, which is lighter than the average weight of a raised access flooring product. The refinement of the raised access floor system is presented in Figure 4.

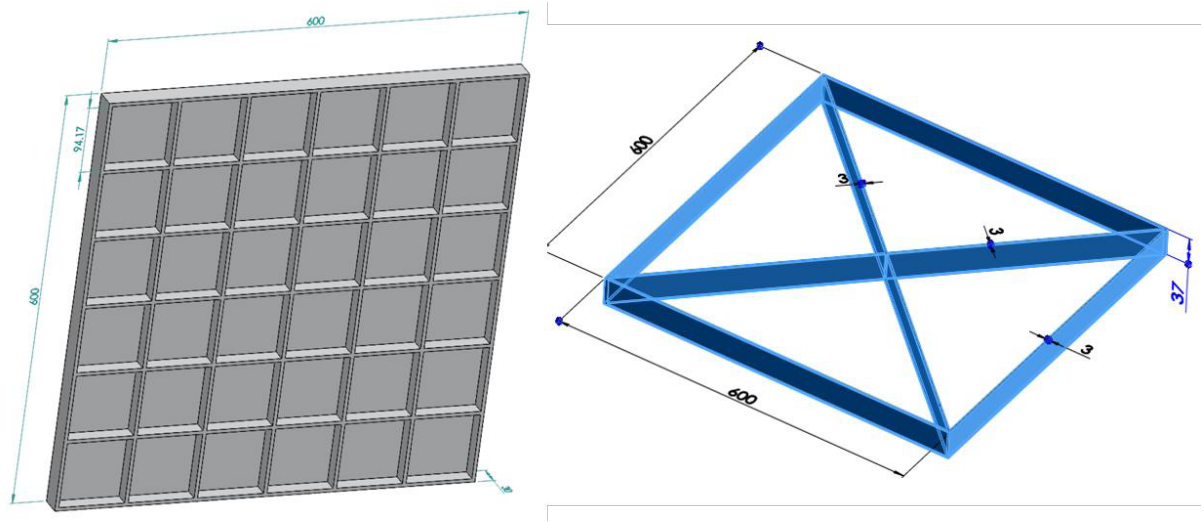

Figure 4: The design of the floor panel (left) and stringer (right) in detail design phrase

3.2 LCA of the raised access floor system

LCA is conducted in order to assess the product's sustainability, and, in particular, to identify the environmental impacts of materials and manufacturing processes, which will enable to set up optimization strategies for design and production process optimisation.

3.2.1 LCA modelling

Considering the available data and objectives of this research, the examined life cycle processes of the raised access floor system include: Materials, Production, Distribution and End of Life, which are described as follows:

Materials: The main ingredients of SMC are glass fibre and polymers. The pedestal unit and stringer are manufactured with normal steel. The floor panel is packaged with wood pallets and PVC films

Production: The examined processes of producing SMC include: heating of resin and moulding, which follows the information of the SMC product specification [2]. The examined processes of producing the floor panel include: heating, cutting ribs and edges. The examined processes of producing the pedestal unit and stringer include: extrusion of steel, and steel turning. The main process not covered in this phrase is the production of glass fibre, which usually include raw material extraction, glass melting and refining, and fibre forming and finishing [3].

Transportation: The examined distribution scenarios are from manufacturing site to retailers or construction sites in England, and this distance is an average of 200 km (suggested by the floor panel prototype manufacturer). The neglected distribution scenarios are the delivery of SMC ingredients from suppliers to manufacturers, and the delivery of packaging materials from suppliers to flooring product manufactures.

End of Life: This study refers for the waste treatment and management figures in England that are provided by the UK DEFRA [4].

3.2.2 Lifecycle impact assessment (LCIA) results

The environmental impact assessment of the raised access floor system is carried out using SolidWorks 2015 with CML method. The assessment results are shown in Figure 5.

As revealed in Figure 5, within the total impacts, the major negative impacts are generated by the Materials (80.6%) and the Manufacturing (13.6%). The Transportation and End of Life

share the 0.6% negative environmental impacts within the Carbon Footprint impact. Within the Total Energy Consumed, Materials cause 74.5% energy consumption, and Manufacturing steps have 25% consumptions, and the Transportation and End of Life total share 0.048% consumptions. Within Air Acidification impact, the Materials have the major impacts (59.2%), and Manufacturing cause 37.9% impacts. The impacts caused by the Transportation and End of Life are 2.79%. Within Water Eutrophication impact, Materials, Manufacturing , and Transportation and End of Life cause 68.7% , 9%, 3% and 17% impacts, respectively.

Compared with the environmental performance evaluation results between initial design and re-design, the four environmental impacts with CML methodology, Carbon Footprint (10.2%), Total Energy Consumed (29.2%), Air Acidification (67.2%), and Water Eutrophication (31.9%) have been improved. This shows the optimum design have achieved, which performs improved environmental impacts while meets the quality and requirements of the floor product standards.

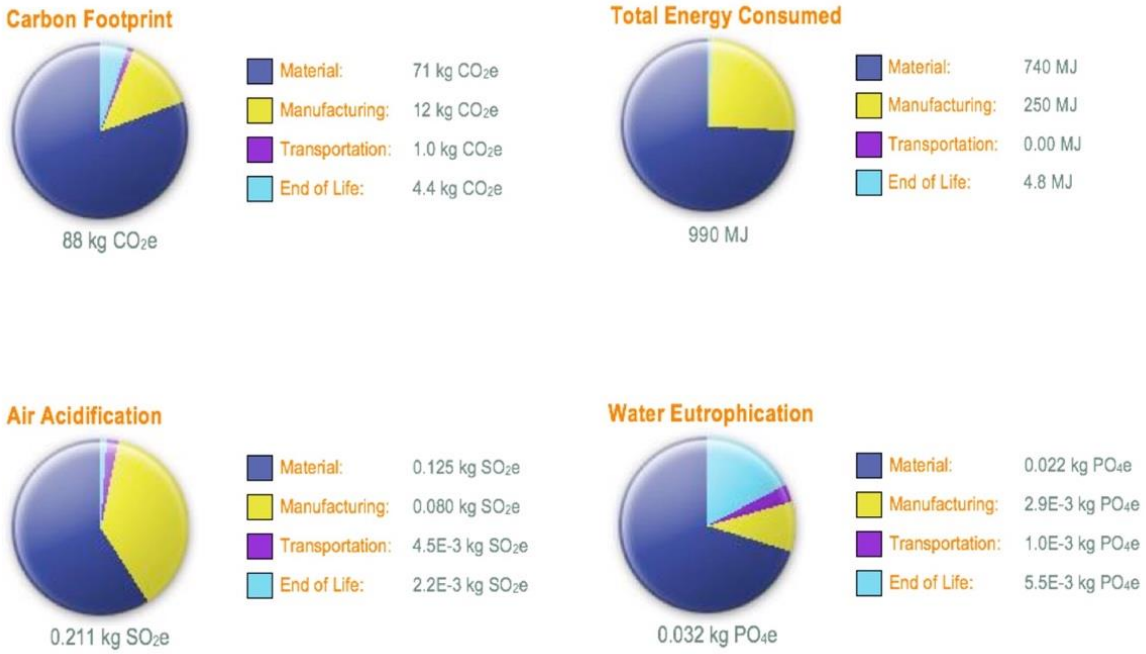

Figure 5: The LCA results by applying CML methodology in SolidWorks 2015 for the improved design

3.2.3 Analysis of the results

As the End of Life and Distribution share relatively small negative impacts in the life cycle of the raised access floor system, the target of design improvement should be placed at the Materials and manufacturing. The following strategies are proposed to achieve this objective through exploring the findings of the LCIA.

The mass of negative impacts caused by the main flows within the three environmental impact categories, which could be used as benchmarking values in the next iterations of design. For example, in the case of investigating alternative main materials, the total mass of negative impacts can be used as the key benchmarking value to examine the potential material's environmental performance.

The Materials has the most negative impacts, and the Distribution stage has the smallest negative impacts, which proves the design improvement strategy on reducing the mass of materials is correct, and in order to achieve further design improvement, the design on the ribs and rectangles of floor panel could be elaborated, for example, reducing the thickness of ribs, or increasing the depth of each rectangles.

The Injection moulding process causes the highest negative impacts among all the production processes, so an improvement strategy would be to cutting the overall moulding cycle time, and improve the mould speed.

4 PROTOTYPING AND TESTING

4.1 The prototype

In this phase, the prototype of the raised access floor system is manufactured and analysed to confirm that the product meets the required environmental impact and strength. The prototype of the raised access floor system is shown in Figure 6. The fire safety test must be conducted under controlled conditions, and by an external fire safety test company, which is not reported in this paper. The following section is to report the Finite Element Analysis for the floor product prototype.

4.2 Finite element analysis

Finite element analysis module of SolidWorks 2015 is used to assess the strength of the product in this phrase. With the FEA results, the relationship between the force and deflection of the floor system can be identified.

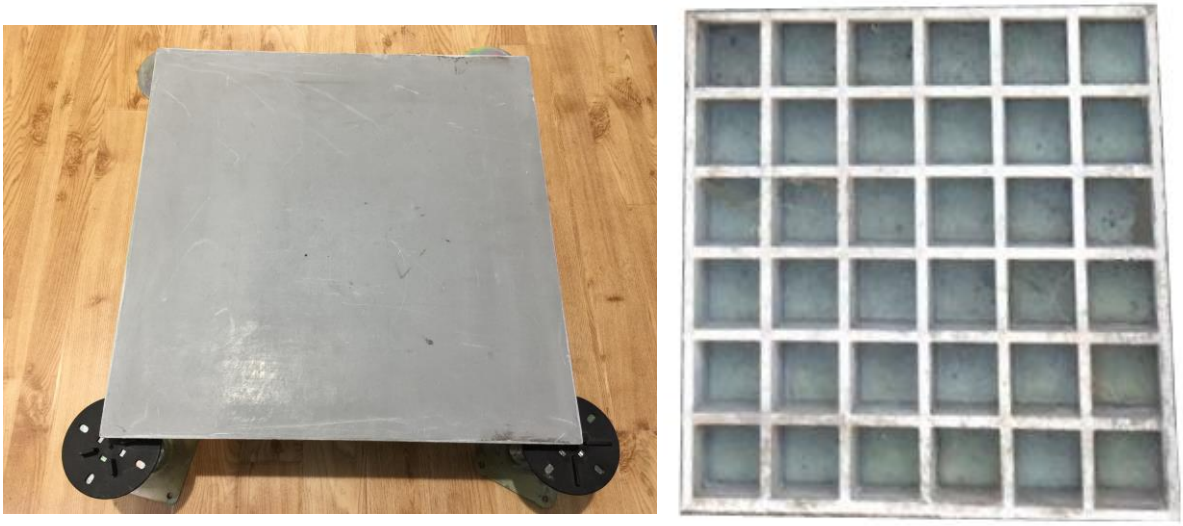

Figure 6: The prototype of the raised access floor product system (Left) and the back of the floor panel (right)

Two key indicators for FEA are maximum yielding stress (von Mises stress) and maximum deformation. According to the Fourth Strength theory of material mechanics, the flooring product starts to yield at a location when the maximum yielding stress becomes equal to the yielding strength, which is the upper limit of yielding stress. For the flooring product developed by this project, the yielding strength is obtained utilising the physical properties of the floor panel and stringer. The maximum yielding stresses of the panel and stringer are required to be less than 94MPa and 250MPa respectively, while the maximum deformation of the panel and stringer should be lower than 2.5mm. According to the requirements of British Standards BSEN 12825:2001 [5] and Platform Floors (Raised Access Floors) Performance Specification [6], 3000 N working loads are required to place at the centre of the floor panel.

As Figure 7 shows, the deformation values are less than 2.5 mm with 3000 N loading forces on the central of the panel and stringer, which satisfy the flooring product's deformation criteria of Class A, as defined by the British Standard requirements. Therefore, under 300 N of working

loads, the designed flooring product is able to work properly within the scope of elastic deformation.

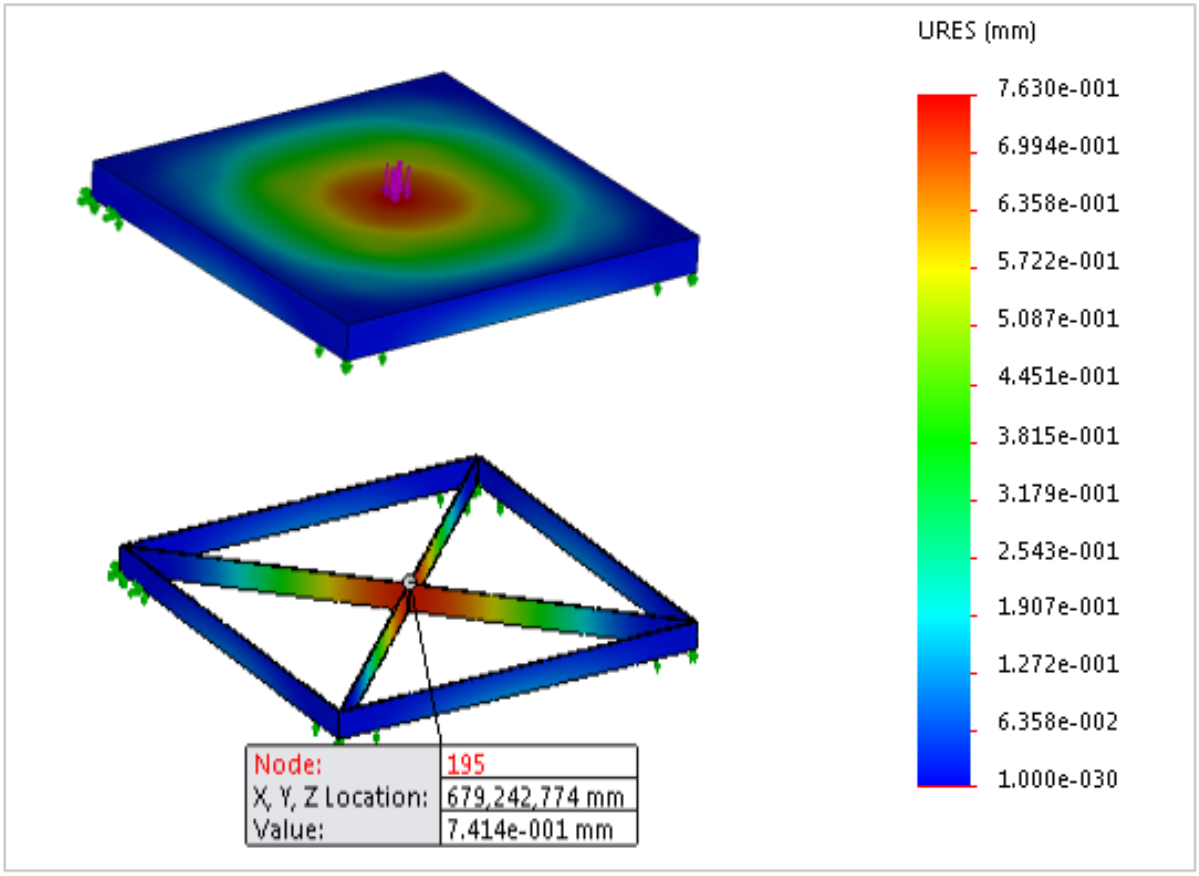

Figure 7: Max deformation for the floor panel and stringer with loading 3000N forces at the centre panel

5 CONCLUSIONS

A new type of raised flooring product is developed, which consists of a rib-supported floor panel made of SMC materials, a metal stringer and pedestals. 3D CAD modelling, LCA and FEA were conducted. The assessment results confirm that the product meets required LCA and FEA performance.

The floor panel has achieved 44% weight reduction compared with the traditional raised access floor panel. The prototype passed the strength test and met the environmental requirements stipulated by the regulations and standards on manufacturing floor products in the EU and UK market. CML methodology and SolidWorks software are applied to evaluate the life cycle environmental performance of the flooring product, the results show that the major environmental impacts are related to the SMC material and manufacturing process.

ACKNOWLEDGEMENTS

The authors acknowledge the research grant received from the Ministry of Science and Technology, China (Grant No. 2015DFA51330), which supported the research presented in this paper.

REFERENCES

[1] Kingspan Access Floors Limited, 2016. TL3 Europed Raised Access Flooring System. pp.1–13. Available at: http://gryphon.environdec.com/data/files/6/11497/epd802%20TL3%20Europed.pdf [Accessed April 5, 2017].
[2] Menzolit, 2016. SMC :: menzolit moulding compounds. Available at: http://www.menzolit.com/products/smc/ [Accessed July 24, 2016].
[3] EPA, 1985. Glass Fiber Manufacturing. Available at: https://www3.epa.gov/ttn/chief/ap42/ch11/final/c11s13.pdf [Accessed December 31, 2016].
[4] DEFRA, 2015. ENV23 - UK statistics on waste. Available at: https://www.gov.uk/government/statistical-data-sets/env23-uk-waste-data-and-management [Accessed June 5, 2016].
[5] BSI, British Standard Institution, 2001. *BS EN 12825:2001 - Raised access floors*, London.
[6] PSA Specialist Services, 1990. *Platform Floors (Raised Access Floors) Performance Specification*, MOB Focal Point.

XIV International Conference on Computational Plasticity. Fundamentals and Applications
COMPLAS XIV
E. Oñate, D.R.J. Owen, D. Peric & M. Chiumenti (Eds)

CLOSED FORM SOLUTION OF THE RETURN MAPPING ALGORITHM IN ELASTOPLASTICITY

FABIO DE ANGELIS*, ROBERT L. TAYLOR†

* Department of Structures for Engineering and Architecture
University of Naples Federico II
Via Claudio 21, 80125 Naples, Italy
e-mail: fabio.deangelis@unina.it

†Department of Civil and Environmental Engineering
University of California, Berkeley
714 Davis Hall, Berkeley, CA 94720-1710, USA
e-mail: rlt@ce.berkeley.edu

Key words: Exact Closed Form Solution, Return Mapping Algorithm, Computational ElastoPlasticity.

Abstract. In the present work a return mapping algorithm is discussed for small strain elastoplasticity boundary value problems with an exact closed form solution of the local constitutive equations. Nonlinear kinematic hardening rules are adopted in modelling kinematic hardening behavior of ductile materials. The local solution of the constitutive equations is expressed by only one nonlinear scalar equation which is subsequently reduced to a single variable algebraic equation. Due to the straightforward form of the nonlinear scalar equation the analytical solution of the algebraic equation is found in exact closed form. A remarkable advantage of the present approach is that no iterative solution method is used to solve the local constitutive equations in three-dimensional elastoplasticity. Numerical applications and computational results are reported in order to illustrate the robustness and effectiveness of the proposed algorithmic procedure.

1 INTRODUCTION

In the present work a return mapping algorithm is discussed for small strain elastoplasticity boundary value problems with an exact closed form solution of the local constitutive equations, see De Angelis and Taylor [1]. Nonlinear kinematic hardening rules are adopted in modelling kinematic hardening behavior of ductile materials, see e.g. Armstrong and Frederick [2]. In fact, saturation hardening rules of the exponential type do not properly represent nonlinear kinematic hardening behavior since upon unloading and reloading the simulation does not suitably reproduce the material behavior in which it is exhibited renewed plasticity prior to the state at which unloading occurred.

One of the advantages of the present algorithmic procedure is to reduce the local solution of the constitutive equations to only one nonlinear scalar equation. In the literature other proposals have been presented which reduce the local constitutive equations to one nonlinear scalar equation. However in the present work a particularly simple form of nonlinear scalar equation is derived. In fact, herein the local constitutive equations are reduced to a single variable algebraic (polynomial) equation. Moreover, in the present approach due to the straightforward form of the nonlinear scalar equation the analytical solution of the algebraic equation is found in exact closed form. Accordingly, a remarkable advantage of the present approach is that no iterative solution method is used to solve the local constitutive equations in three-dimensional elastoplasticity.

The consistent tangent operator associated to the proposed formulation is derived for elastoplasticity models, thus ensuring a quadratic rate of asymptotic convergence when used with the Newton Raphson iterative method for the global solution procedure of the structural problem, see e.g. Zienkiewicz Taylor and Fox [3] and Simo and Hughes [4].

Numerical applications and computational results for cyclic loading conditions are finally reported in order to illustrate the robustness and effectiveness of the proposed algorithmic scheme. Accordingly, the robustness and effectiveness of the proposed computational procedure is illustrated with specific numerical examples.

2 THE CONTINUUM MODEL

We assume the body $\mathcal{B}$ in the reference configuration $\Omega \subset \Re^n$, with $1 \leq n \leq 3$, and we denote with $\mathcal{T} \subset \Re_+$ the time interval of interest and with $\boldsymbol{V}$ the space of displacements, $\boldsymbol{D}$ the strain space and $\boldsymbol{S}$ the dual stress space. Let us also indicate with $\mathbf{u} : \Omega \times \mathcal{T} \to \boldsymbol{V}$ the displacement and with $\boldsymbol{\sigma} : \Omega \times \mathcal{T} \to \boldsymbol{S}$ the stress tensor. The compatible strain tensor is defined as $\boldsymbol{\varepsilon} = \nabla^s \mathbf{u} : \Omega \times \mathcal{T} \to \boldsymbol{D}$, where ∇^s is the symmetric part of the gradient operator. We consider the stress tensor as additively decomposed into a deviatoric and a spherical part so that $\boldsymbol{\sigma} = \mathbf{s} + p\,\mathbf{1}$, where $\mathbf{s} \stackrel{\text{def}}{=} \text{dev}\boldsymbol{\sigma} = \boldsymbol{\sigma} - p\,\mathbf{1}$ is the stress deviator, $p \stackrel{\text{def}}{=} \frac{1}{3} tr(\boldsymbol{\sigma})$ is the pressure of the spherical part $p\,\mathbf{1}$ and $\mathbf{1}$ is the rank two identity tensor. The strain tensor is similarly decomposed into the deviatoric and volumetric parts $\boldsymbol{\varepsilon} = \mathbf{e} + \frac{1}{3}\theta\,\mathbf{1}$, where $\mathbf{e} \stackrel{\text{def}}{=} \text{dev}\boldsymbol{\varepsilon} = \boldsymbol{\varepsilon} - \frac{1}{3}\theta\,\mathbf{1}$ is the strain deviator and $\theta \stackrel{\text{def}}{=} tr(\boldsymbol{\varepsilon})$ is the change in volume. The relation between the spherical part of the stress and the volumetric part of the strain is described by $p = K\,\theta$, where K is the bulk modulus.

The linear elastic relation between the stress deviator and the elastic deviatoric strain is expressed by

$$\mathbf{s} = 2G\,\mathbf{e}^e = 2G[\mathbf{e} - \mathbf{e}^p], \tag{1}$$

in which G is the shear modulus, and the deviatoric part of the total strain has been additively decomposed into an elastic and a plastic part $\mathbf{e} = \mathbf{e}^e + \mathbf{e}^p$. The relative stress $\boldsymbol{\Sigma}$ is also expressed by

$$\boldsymbol{\Sigma} = \mathbf{s} - \boldsymbol{\alpha}, \tag{2}$$

where $\boldsymbol{\alpha}$ represents the deviatoric back stress.

A J_2 material behavior is assumed herein. Accordingly, a von Mises yield criterion is

adopted in the form

$$f(\boldsymbol{\sigma}, \boldsymbol{\alpha}, \kappa) = \|\mathrm{dev}\boldsymbol{\sigma} - \boldsymbol{\alpha}\| - \kappa(\chi_{iso}) = \|\mathbf{s} - \boldsymbol{\alpha}\| - \sqrt{\tfrac{2}{3}}(\sigma_{yo} + \chi_{iso}) \leq 0, \tag{3}$$

where $\kappa(\chi_{iso}) = \sqrt{\frac{2}{3}}\,\sigma_y = \sqrt{\frac{2}{3}}(\sigma_{yo} + \chi_{iso})$ is the current radius of the yield surface in the deviatoric plane and σ_{yo} is the uniaxial yield stress of the virgin material. The static internal variable for isotropic hardening is specified by $\chi_{iso} = H_{iso}\overline{e}^p$, where H_{iso} is the isotropic hardening modulus and where we assumed $\chi_{iso} \stackrel{\text{def}}{=} R$, being R the increment of the yield stress with respect to the uniaxial yield stress of the virgin material and $\overline{e}^p$ representing the equivalent (accumulated) plastic strain $\overline{e}^p \stackrel{\text{def}}{=} \int_0^t \sqrt{\frac{2}{3}}\|\dot{\mathbf{e}}^p\|\,\mathrm{d}\,t$. For a finer representation of the isotropic hardening it is often assumed

$$\chi_{iso} = H_{iso}(\overline{e}^p)^m, \qquad \text{or} \qquad R = R_\infty(1 - \mathrm{e}^{-b\,\overline{e}^p}), \tag{4}$$

where m, R_∞ and b are material parameters.

The evolutive flow law for the deviatoric plastic strain rate is expressed by

$$\dot{\mathbf{e}}^p = \dot{\gamma}\,\frac{\partial f}{\partial \boldsymbol{\sigma}} = \dot{\gamma}\,\frac{\partial f}{\partial \boldsymbol{\Sigma}} = \dot{\gamma}\,\mathbf{n}, \tag{5}$$

where $\dot{\gamma}$ is the plastic rate multiplier and $\mathbf{n} \stackrel{\text{def}}{=} \dfrac{\boldsymbol{\Sigma}}{\|\boldsymbol{\Sigma}\|}$ is the normal to the yield surface. Consequently, the equivalent plastic strain rate is supplied by $\dot{\overline{e}}^p = \sqrt{\frac{2}{3}}\,\dot{\gamma}$.

The rate of the back stress can be expressed by the Prager law [5]

$$\dot{\boldsymbol{\alpha}} = \tfrac{2}{3}\,H_{kin}\,\dot{\mathbf{e}}^p, \tag{6}$$

where H_{kin} is the kinematic hardening modulus. For a nonlinear kinematic hardening behavior it is often adopted the model proposed by Armstrong and Frederick [2]

$$\dot{\boldsymbol{\alpha}} = \tfrac{2}{3}\,H_{kin}\,\dot{\mathbf{e}}^p - H_{nl}\,\dot{\overline{e}}^p\,\boldsymbol{\alpha}, \tag{7}$$

where H_{nl} is a non-dimensional material dependent parameter. The second term of equation (7) is a recall term and $H_{nl} = 0$ stands for a linear kinematic hardening behavior. For a better approximation several models can be added with different recall constants (see e.g. [6])

$$\boldsymbol{\alpha} = \sum_{i=1}^{M} \boldsymbol{\alpha}_i, \qquad\qquad \dot{\boldsymbol{\alpha}}_i = \tfrac{2}{3}\,H_{kin,i}\,\dot{\mathbf{e}}^p - H_{nl,i}\,\dot{\overline{e}}^p\,\boldsymbol{\alpha}_i. \tag{8}$$

The Kuhn-Tucker optimality conditions

$$\dot{\gamma} \geq 0, \qquad f(\boldsymbol{\sigma}, \boldsymbol{\alpha}, \kappa) \leq 0, \qquad \dot{\gamma} f(\boldsymbol{\sigma}, \boldsymbol{\alpha}, \kappa) = 0, \tag{9}$$

represent the loading-unloading conditions and they complete the evolutive model in plasticity, see e.g. [3] and [4].

3 Algorithmic formulation

In the finite element formulation we adopt a *strain driven* approach. Accordingly, by knowing the strain and the solution at time t_n, represented by the set $(\mathbf{s}_n, \mathbf{e}_n, \mathbf{e}^p_n, \overline{e}^p_n, \boldsymbol{\alpha}_n)$, we need to determine the solution at time t_{n+1} represented by the set $(\mathbf{s}, \mathbf{e}, \mathbf{e}^p, \overline{e}^p, \boldsymbol{\alpha})$. By adopting a backward Euler integration scheme, the evolutive equation for the deviatoric plastic strain rate (5) and the equivalent plastic strain rate are given respectively by

$$\mathbf{e}^p = \mathbf{e}^p_n + \lambda\,\mathbf{n}, \qquad\qquad \overline{e}^p = \overline{e}^p_n + \sqrt{\tfrac{2}{3}}\,\lambda, \tag{10}$$

where we have set $\lambda \stackrel{\text{def}}{=} \Delta\gamma_{n+1} = \dot{\gamma}_{n+1}\Delta t$.

The discrete form of the evolution law for the back stress is given by

$$\boldsymbol{\alpha} - \boldsymbol{\alpha}_n = \tfrac{2}{3}\,H_{kin}\lambda\mathbf{n} - H_{nl}\sqrt{\tfrac{2}{3}}\lambda\boldsymbol{\alpha}, \tag{11}$$

which can be expressed as

$$\boldsymbol{\alpha} = T^\lambda\boldsymbol{\alpha}_n + \tfrac{2}{3}\,H_{kin}T^\lambda\lambda\mathbf{n}, \tag{12}$$

where we have set

$$R^\lambda = (1 + \sqrt{\tfrac{2}{3}}\,H_{nl}\lambda), \qquad\qquad T^\lambda = \frac{1}{R^\lambda} = \frac{1}{(1 + \sqrt{\frac{2}{3}}\,H_{nl}\lambda)}. \tag{13}$$

In the above expressions we have adopted the superscript λ to denote a dependence on the increment of the plastic rate multiplier in the step $t_n \to t_{n+1}$.

Taking into account equation $(10)_1$ the deviatoric stress is given by

$$\mathbf{s} \;= 2G[\mathbf{e} - \mathbf{e}^p_n] - 2G\lambda\mathbf{n}, \tag{14}$$

and, by considering equation (12), the relative stress is expressed by

$$\boldsymbol{\Sigma} \;= \mathbf{s} - \boldsymbol{\alpha} = 2G[\mathbf{e} - \mathbf{e}^p_n] - T^\lambda\boldsymbol{\alpha}_n - U^\lambda\mathbf{n}, \tag{15}$$

where we have set

$$U^\lambda = [2G + \tfrac{2}{3}\frac{H_{kin}}{R^\lambda}]\lambda = [2G + \tfrac{2}{3}H_{kin}T^\lambda]\lambda. \tag{16}$$

An elastic predictor-plastic corrector scheme is adopted by means of a return mapping algorithm. By enforcing the satisfaction of the limit equations at time t_{n+1} the increment λ of the plastic rate parameter is computed. The variables are then updated according to the equations

$$\begin{cases} \mathbf{e}^p = \mathbf{e}^{p,TR} + \lambda\mathbf{n} \\ \overline{e}^p = \overline{e}^{p,TR} + \sqrt{\frac{2}{3}}\lambda \\ \boldsymbol{\alpha} = T^\lambda\boldsymbol{\alpha}^{TR} + \frac{2}{3}H_{kin}T^\lambda\lambda\mathbf{n} \\ \mathbf{s} \;= \mathbf{s}^{TR} - 2G\lambda\mathbf{n} \\ \boldsymbol{\Sigma} \;= \mathbf{s}^{TR} - T^\lambda\boldsymbol{\alpha}^{TR} - U^\lambda\mathbf{n}. \end{cases} \tag{17}$$

The relative stress $(17)_5$ is also expressed by

$$\boldsymbol{\Sigma} = \boldsymbol{\Sigma}^{TR} + (1 - T^{\lambda})\boldsymbol{\alpha}^{TR} - U^{\lambda}\mathbf{n}, \tag{18}$$

where $\boldsymbol{\Sigma}^{TR} \stackrel{\text{def}}{=} \mathbf{s}^{TR} - \boldsymbol{\alpha}^{TR}$ is the trial value of the relative stress typically adopted in plasticity with linear kinematic hardening.

In the proposed approach for plasticity with nonlinear kinematic hardening rules we find useful to introduce a trial-like value of the relative stress

$$\boldsymbol{\Sigma}^{\lambda}_{NLK} \stackrel{\text{def}}{=} \mathbf{s}^{TR} - T^{\lambda}\boldsymbol{\alpha}^{TR} \tag{19}$$

Accordingly, equation (18) can be expressed by

$$\boldsymbol{\Sigma} = \boldsymbol{\Sigma}^{\lambda}_{NLK} - U^{\lambda}\mathbf{n}, \tag{20}$$

Herein, we emphasize that for plasticity with nonlinear kinematic hardening the trial-like value $\boldsymbol{\Sigma}^{\lambda}_{NLK}$ depends upon λ, whereas the conventional trial value $\boldsymbol{\Sigma}^{TR}$ adopted in plasticity with linear kinematic hardening is independent of λ. The second rank tensor $\mathbf{n}$ is expressed by

$$\mathbf{n} = \frac{\partial f}{\partial \boldsymbol{\sigma}} = \frac{\partial f}{\partial \boldsymbol{\Sigma}}\frac{\partial \boldsymbol{\Sigma}}{\partial \boldsymbol{\sigma}} = \frac{\partial f}{\partial \boldsymbol{\Sigma}}\frac{\partial(\mathrm{dev}\boldsymbol{\sigma} - \boldsymbol{\alpha})}{\partial \boldsymbol{\sigma}} = \frac{\partial \|\boldsymbol{\Sigma}\|}{\partial \boldsymbol{\Sigma}}\mathbf{I}_{dev} = \frac{\boldsymbol{\Sigma}}{\|\boldsymbol{\Sigma}\|}\mathbf{I}_{dev} = \frac{\boldsymbol{\Sigma}}{\|\boldsymbol{\Sigma}\|}, \tag{21}$$

where $\mathbf{I}_{dev} = \mathbf{I} - \frac{1}{3}(\mathbf{1}\otimes\mathbf{1})$. Given the expressions (19) and (20), the tensor $\mathbf{n}$ also depends upon λ. This is at variance with respect to plasticity with linear kinematic hardening, where $\mathbf{n}$ is independent from λ. Accordingly, the algorithmic procedure for plasticity with nonlinear kinematic hardening is more complex.

We note from equation (21) that $\boldsymbol{\Sigma}$ is collinear with $\mathbf{n}$. From equation (20) we also derive that $\boldsymbol{\Sigma}^{\lambda}_{NLK}$ must be collinear with $\mathbf{n}$, and therefore $\boldsymbol{\Sigma}^{\lambda}_{NLK} = \|\boldsymbol{\Sigma}^{\lambda}_{NLK}\|\mathbf{n}$. Accordingly, we observe that in plasticity with nonlinear kinematic hardening it results

$$\mathbf{n}(\lambda) = \frac{\boldsymbol{\Sigma}(\lambda)}{\|\boldsymbol{\Sigma}(\lambda)\|} = \frac{\boldsymbol{\Sigma}^{\lambda}_{NLK}(\lambda)}{\|\boldsymbol{\Sigma}^{\lambda}_{NLK}(\lambda)\|}. \tag{22}$$

Consequently, the present approach to plasticity with nonlinear kinematic hardening has the advantage that the equation (20) preserves a nonlinear scalar equation in λ

$$\|\boldsymbol{\Sigma}\| = \|\boldsymbol{\Sigma}^{\lambda}_{NLK}\| - U^{\lambda}. \tag{23}$$

As shown in the following section the above equation represents an algebraic (polynomial) equation in the single variable λ. Once the increment λ of the plastic rate parameter is determined the variables are updated at time t_{n+1} by considering equations (17) and taking into account equation (22).

4 Nonlinear scalar equation in λ

Equation (23) yields the novel expression of the nonlinear scalar equation which is solved for determining the increment λ of the plastic rate parameter. Accordingly, in the present approach the local solution of the constitutive equations reduces to only one nonlinear scalar equation. In the literature other proposals have been presented in which the constitutive equations are reduced to a nonlinear scalar equation, see e.g. Hartmann Luhrs and Haupt [7] and Kobayashi and Ohno [8]. With respect to such proposals, the present approach has the advantage that the constitutive equations are reduced to only one *single variable algebraic (quartic) equation* which is a particularly simple form of nonlinear scalar equation. Remarkably, in the present approach no numerical procedures are required to accelerate convergence for the solution of the nonlinear scalar equation, such as for instance the Aitken's process adopted in [8]. In fact, in the proposed formulation the search for the analytical solutions of the nonlinear scalar equation is pursued in exact closed form, i.e. with no recourse to iterative methods. This particular feature ensures efficiency and robustness to the overall computational procedure.

The limit function (3) is expressed as $\|\boldsymbol{\Sigma}\| - \sqrt{\frac{2}{3}}\sigma_y = 0$. Accordingly, the equation (23) supplies

$$\|\boldsymbol{\Sigma}^{\lambda}_{NLK}\| - U^{\lambda} - \sqrt{\tfrac{2}{3}}\sigma_y = 0, \tag{24}$$

and by setting

$$\begin{aligned} S_{ss} &= \mathbf{s}^{TR} \cdot \mathbf{s}^{TR} = \|\mathbf{s}^{TR}\|^2 \\ S_{s\alpha} &= \mathbf{s}^{TR} \cdot \boldsymbol{\alpha}^{TR} \\ S_{\alpha\alpha} &= \boldsymbol{\alpha}^{TR} \cdot \boldsymbol{\alpha}^{TR} = \|\boldsymbol{\alpha}^{TR}\|^2, \end{aligned} \tag{25}$$

after some algebra (see De Angelis and Taylor [1]) we obtain the quartic algebraic equation

$$g(\lambda) = C_1\lambda^4 + C_2\lambda^3 + C_3\lambda^2 + C_4\lambda + C_5 = 0, \tag{26}$$

where the coefficients of the quartic equation are given by De Angelis and Taylor [1]. For more details see De Angelis and Taylor [1] and De Angelis and Taylor [9] where a comprehensive treatment of the present approach is illustrated.

The present form of nonlinear scalar equation is at variance from the nonlinear scalar equation presented by Auricchio and Taylor [10] since it is generated by a different algorithmic scheme. Further, in [10] the solution of the nonlinerar scalar equation was performed by a Newton's iterative method, which for complex constitutive equations and highly nonlinear scalar equations sometimes experiences failures due to the occurring high gradients and the resulting round-off errors. One of the advantages of the present algorithmic scheme is that the local constitutive equations condense in a particularly simple form of nonlinear scalar equation, that is a *quartic algebraic equation*. Consequently, in the present approach the solutions of the quartic algebraic equation are determined in exact closed form, see among others Abramowitz [11], Beyer [12], and Hacke [13], and no iterative procedure is required to solve the local constitutive problem. Accordingly,

the increment λ of the plastic rate parameter in the step $t_n \to t_{n+1}$ is evaluated as the smallest positive real root of the quartic algebraic equation (26).

For more details see De Angelis and Taylor [1]. An alternative formulation resulting in a different algorithmic scheme associated to a different algorithmic form of the consistency condition and a different consistent tangent operator has also been presented by De Angelis and Taylor [9].

5 Consistent tangent operator

In the present section we illustrate the expression of the consistent tangent operator associated to the present algorithmic scheme which ensures a fast and robust numerical solution procedure for the iterative solution of the structural problem in elastoplasticity. The proposed numerical scheme ensures a quadratic rate of asymptotic convergence to the Newton Raphson iterative method for the solution of the global structural problem.

The linearization of the discrete forms of the evolutive equations for the stress deviator and the back stress yields a consistent tangent operator expressed by

$$\begin{aligned}\mathbf{D}_{discr} = \big\{ & K(\mathbf{1}\otimes\mathbf{1}) + [2G\ (1 - C^{NLK}_{discr})]\,\mathbf{I}_{dev} + [2G\,(C^{NLK}_{discr} - A^{NLK}_{discr}) \\ & + B^{NLK}_{discr}(\mathbf{n}\cdot\boldsymbol{\alpha})](\mathbf{n}\otimes\mathbf{n}) - B^{NLK}_{discr}(\boldsymbol{\alpha}\otimes\mathbf{n})\big\}\,,\end{aligned} \tag{27}$$

where we have set

$$\begin{aligned} a &= \frac{2G\,\lambda}{\|\boldsymbol{\Sigma}\|}, & b &= \tfrac{2}{3}\,\frac{H_{kin}\lambda}{\|\boldsymbol{\Sigma}\|}, \\ R^\lambda &= (1 + \sqrt{\tfrac{2}{3}}\,H_{nl}\lambda), & T^\lambda &= \frac{1}{R^\lambda}, & W^\lambda &= b + R^\lambda + aR^\lambda, \\ A^{NLK}_{discr} &= \frac{2G}{[2G + \frac{2}{3}H_{iso} + \frac{2}{3}H_{kin}T^\lambda - \sqrt{\frac{2}{3}}H_{nl}T^\lambda(\mathbf{n}\cdot\boldsymbol{\alpha})]}, \\ B^{NLK}_{discr} &= A^{NLK}_{discr}T^\lambda C^{NLK}_{discr}\sqrt{\tfrac{2}{3}}H_{nl}, & C^{NLK}_{discr} &= a\frac{R^\lambda}{W^\lambda}. \end{aligned} \tag{28}$$

The expression of the consistent tangent operator results to be non-symmetric due to the last term of equation (27), as is typically in elastoplasticity with nonlinear kinematic hardening rules. For more details on the development of the consistent tangent operator see De Angelis and Taylor [1].

For the derivation of the consistent tangent operator associated to the algorithmic procedure it is necessary to perform matrix inversions. At variance with respect to such usual approach, an alternative algorithmic formulation which is able to provide a consistent tangent operator without the necessity to perform matrix inversions has been presented by De Angelis and Taylor [9].

Other various algorithmic formulations have been presented e.g. by Nukala [14], Artioli Auricchio and Beirao da Veiga [15], De Angelis and Cancellara [16], De Angelis and Taylor [17], Artioli and Bisegna [18], Artioli Castellazzi and Krysl [19], Castellazzi Artioli and Krysl [20].

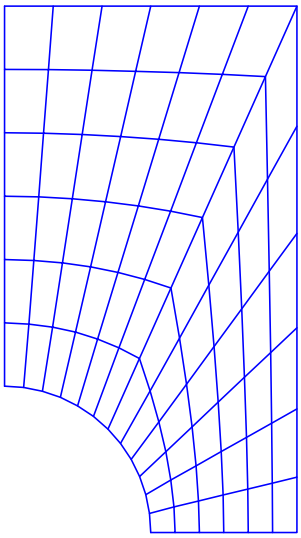

Figure 1: Perforated strip. Geometry and finite element mesh.

6 Computational results

The algorithmic formulation illustrated in the present work may be used for any 2-d or 3-d element which accepts a strain-driven approach. In our analysis we use 4-node quadrilateral elements with 2×2 Gaussian quadrature and the mixed approach described in Sec. 2.6.2 of Zienkiewicz Taylor and Fox [3]. The numerical scheme is implemented into the Finite Element Analysis Program (FEAP), see Zienkiewicz Taylor and Fox [3], and Taylor [21].

6.1 Numerical example: perforated strip

In the numerical example we consider the problem of an infinitely long rectangular strip with a circular hole in its axial direction, subject to increasing extension in a direction perpendicular to the axis of the strip and parallel to one of its sides. The geometry of the problem is illustrated in Fig. 1. For symmetry reasons only 1/4 of the strip needs to be considered. The dimensions of the rectangular section containing 1/4 of the strip are 18 mm for the long side and 10 mm for the short side. The radius of the circular hole is 5 mm. The adopted mesh consists of 91 nodes and 72 elements.

The mechanical properties of the material are: elastic modulus $E = 208000$ MPa, Poisson's ratio $\nu = 0.3$, yield limit $\sigma_{yo} = 170$ MPa, kinematic hardening modulus $H_{kin} = 41080$ MPa, nonlinear kinematic hardening parameter $H_{nl} = 525$, isotropic hardening modulus $H_{iso} = 2100$ MPa. The prescribed displacement at the top boundary is $u_o = 0.0025$ mm. The evolution with time of the proportional load coefficient $p(t)$ amplifies the prescribed displacement and illustrates the loading history according to equation $u(t) = p(t)u_o$.

In the numerical example we consider a cyclic loading program in tension with increasing mean value of the loading. The assumed loading program is illustrated in Fig. 2. For

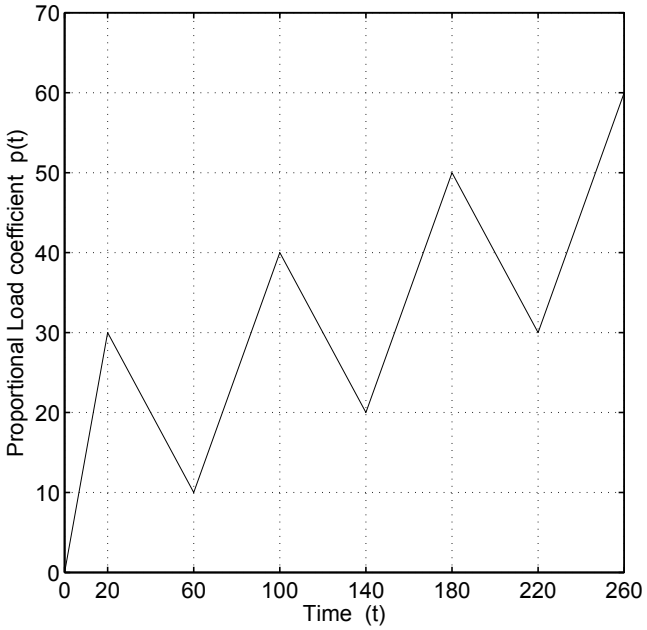

Figure 2: Cyclic loading program in tension with increasing mean value of the loading.

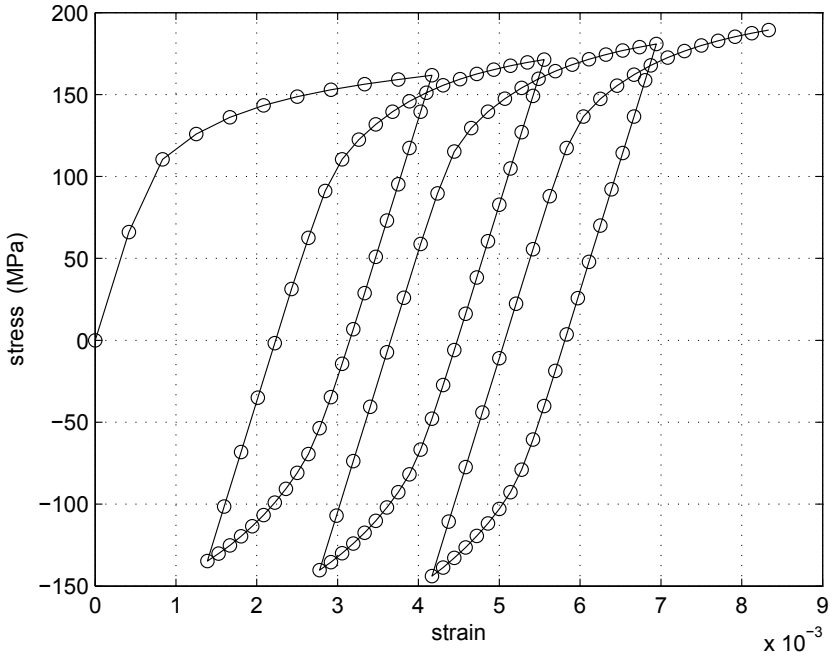

Figure 3: Average end stress versus average strain for the cyclic loading program given in Fig. 2. In the analysis a doubled time increment $\Delta t = 2$ has been adopted with $t_{max} = 260$.

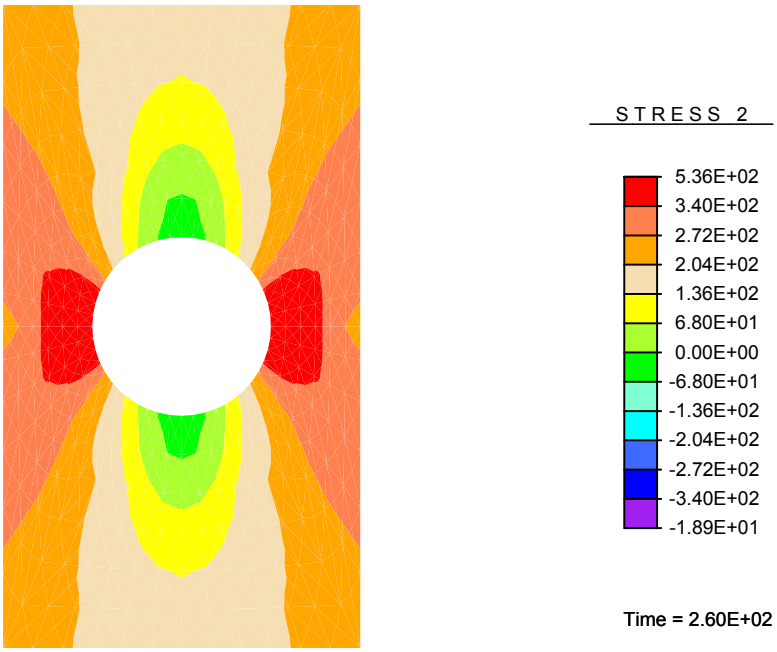

Figure 4: Contour plot of vertical stress in the strip for $t_{max} = 260$. Cyclic loading program in tension with loading program given in Fig. 2.

this loading program the average end stress versus the average strain is illustrated in Fig. 3. Herein the stress is averaged as the sum of the reactions on the boundary upper edge over the related area, the strain is averaged as the displacement at the boundary upper edge over the height. By exploiting symmetry properties, the final contour plot of the vertical stress in the strip is illustrated in Fig. 4 for $t_{max} = 260$.

The computational analysis of the Newton Raphson iterative procedure for the global structural problem shows a quadratic rate of asymptotic convergence. For more details on the convergence properties of the proposed algorithmic scheme, see De Angelis and Taylor [1] where a comprehensive treatment is presented.

7 CONCLUSIONS

In this work we presented an exact closed form solution of the return mapping algorithm in elastoplasticity with nonlinear kinematic hardening behavior, see also De Angelis and Taylor [1]. Nonlinear kinematic hardening rules have been adopted for modelling kinematic hardening behavior of ductile materials, see e.g. [2].

One of the advantages of the proposed formulation is to reduce the local constitutive equations of three-dimensional elastoplasticity problems to only one nonlinear scalar equation which ultimately condenses in a *quartic algebraic equation*. The formulation allows to find the analytical solution of the algebraic equation in exact closed form and, consequently, no iterative method is required to solve the local constitutive equations in three-dimensional elastoplasticity. The consistent tangent operator associated to the

proposed algorithmic scheme has been derived. The algorithmic formulation ensures a quadratic rate of asymptotic convergence for the global structural problem in elastoplasticity. The effectiveness of the proposed algorithmic scheme has been suitably illustrated by reporting numerical applications and computational results for complex and cyclic loading conditions.

REFERENCES

[1] De Angelis, F., and Taylor, R.L., "An efficient return mapping algorithm for elastoplasticity with exact closed form solution of the local constitutive problem", *Engineering Computations*, **32** (8), 2259 - 2291, (2015).

[2] Armstrong, P.J., and Frederick, C.O., "A mathematical representation of the multiaxial Bauschinger effect", Report RD/B/N731, CEGB, *Central Electricity Generating Board,* Berkeley, UK, (1966). Reprint in: Frederick, C.O., and Armstrong, P.J., "A mathematical representation of the multiaxial Bauschinger effect", *Mater. High Temp.*, **24** (1), 1-26, (2007).

[3] Zienkiewicz, O.C., Taylor, R.L., and Fox, D.D. *The Finite Element Method for Solid and Structural Mechanics*, 7th ed., Elsevier, Oxford, (2013).

[4] Simo, J.C., and Hughes, T.J.R., *Computational Inelasticity*, Springer-Verlag, Berlin, (1998).

[5] Prager, W., "Recent developments in the mathematical theory of plasticity", *J. Appl. Phys.*, **20**, (3), 235-241, (1949).

[6] Chaboche, J.L., "A review of some plasticity and viscoplasticity constitutive theories", *Int. J. Plasticity*, **24**, 1642-1693, (2008).

[7] Hartmann, S., Lührs, G., and Haupt, P., "An efficient stress algorithm with applications in viscoplasticity and plasticity", *Int. J. Num. Meth. Engrg.*, **40**, 991-1013, (1997).

[8] Kobayashi, M., and Ohno, N., "Implementation of cyclic plasticity models based on a general form of kinematic hardening", *Int. J. Num. Meth. Engrg.*, **53**, 2217-2238, (2002).

[9] De Angelis, F., Taylor, R.L., "A nonlinear finite element plasticity formulation without matrix inversions", *Finite Elements in Analysis and Design*, **112**, 11-25 , (2016).

[10] Auricchio, F., and Taylor, R.L., "Two material models for cyclic plasticity: nonlinear kinematic hardening and generalized plasticity", *Int. J. Plasticity*, **11**, 65-98, (1995).

[11] Abramowitz, M., "Solutions of quartic equations", in *Handbook of mathematical functions with formulas, graphs and mathematical tables*, M. Abramowitz and I.A. Stegun (Editors), 17-18, §3.8.3, Dover, New York, (1972).

[12] Beyer, W.H. *CRC Standard mathematical tables*, 28th ed., 12, CRC Press, Boca Raton, FL, (1987).

[13] Hacke, J.E. Jr., "A simple solution of the general quartic", *The American Mathematical Monthly*, **48**, (5), 327-328 , (1941).

[14] Nukala, P.K.V.V., "A return mapping algorithm for cyclic viscoplastic constitutive models" *Comput. Methods Appl. Mech. Engrg.*, **195**, 148-178, (2006).

[15] Artioli, E., Auricchio, F., and Beirao da Veiga, L., "Second-order accurate integration algorithms for the von-Mises plasticity with a nonlinear kinematic hardening mechanism" *Comput. Methods Appl. Mech. Engrg.*, **196**, 1827-1846, (2007).

[16] De Angelis, F., and Cancellara, D., "Multifield variational principles and computational aspects in rate plasticity", *Computers and Structures*, **180**, 27-39 , (2017).

[17] De Angelis, F., and Taylor, R.L., "Numerical algorithms for plasticity models with nonlinear kinematic hardening", in *11th World Congress on Computational Mechanics, WCCM XI, and 5th European Conference on Computational Mechanics, ECCM V*, Eds.: E. Onate, J. Oliver and A. Huerta, 20-25 july, 2014, EBook **VI**, 6560-6570, CIMNE, Barcellona, Spain, (2014).

[18] Artioli, E., Bisegna, P., "An incremental energy minimization state update algorithm for 3D phenomenological internal-variable SMA constitutive models based on isotropic flow potentials" *Int. J. Num. Meth. Engrg.*, **105** (3), 197-220, (2016).

[19] Artioli, E., Castellazzi, G., Krysl, P., "Assumed strain nodally integrated hexahedral finite element formulation for elastoplastic applications" *Int. J. Num. Meth. Engrg.*, **99** (11), 844-866, (2014).

[20] Castellazzi, G., Artioli, E., Krysl, P., "Linear tetrahedral element for problems of plastic deformation" *Meccanica*, **50** (12), 3069-3086, (2015).

[21] Taylor, R.L., "FEAP - A Finite Element Analysis Program, User Manual (Vers: 8.4)", `http://www.ce.berkeley.edu/feap`, (2017).

XIV International Conference on Computational Plasticity. Fundamentals and Applications
COMPLAS XIV
E. Oñate, D.R.J. Owen, D. Peric & M. Chiumenti (Eds)

FAST COMPUTATION: A STEADY-STATE SIMULATION OF RAILWAYS BALLASTED TRACK SETTLEMENT

THIBAULT BADINIER[*,†], SIEGFRIED MAÏOLINO[*] AND HABIBOU MAÏTOURNAM[†]

[*] Geological and Geotechnical Hazards Research Team
Cerema Centre Est, Département Laboratoire de Lyon
25 avenue François Mitterrand, 69500 Bron, France
web page: http://www.centre-est.cerema.fr

[†]Institut des Sciences de la Mécanique et Applications Industrielles (IMSIA; UMR 9219)
Unité de Mecanique (UME), ENSTA ParisTech
828 Boulevard des Maréchaux, 91120, France
Web page: http://www.imsia.cnrs.fr/

Key words: Computational Plasticity, Railway, Ballast, Geomaterials, Finites Elements Methods, Steady State

Abstract. Geometry of ballasted railways track is a major concern in railroads safety and efficiency. Settlement of railways ballast has been studied to help railway infrastructure managers to keep infrastructures in shape and to prevent accidents.

In this paper, we present an innovative numerical approach to study railways ballast settlement. Commonly used models representing a moving load need huge computation time. On the other hand, assuming static cyclic loading representation leads to discrepancies. Indeed, it does not conceder particularities of moving load. With this new model we want to avoid the drawbacks of previously developed methods.

We developed a steady state algorithm to compute plastic strain in geomaterials and to study behaviour of ballasted railways track with an Eulerian approach. This way we improved model efficiency by drastically reducing computation time while considering mobile load specificities.

1 INTRODUCTION

Railway tracks are usually composed of rails, sleepers and ballast. Rails support and guide the train, sleepers maintain rails and transmit load to the ballast, and ballast keeps sleepers in place, distributes load over the ground, and maintains all geometric aspects of the tracks. Geometry of tracks is a major concern in railways safety. A deviation of some millimetres with the normative prescription could lead to derailment and potential accidents.

In this paper we study railways settlement via a continuous approach, computing plastic strain in ballast layer under train traffic. The purpose of this paper is to evaluate the pros and cons of different numerical computational methods.

We chose to study impact of a moving load on the structure in opposition with other classical methods which use a static load, varying in sinusoidal cycles for example. Those simplified load cycle representations hides particular yielding condition due to load movement. This could lead to major discrepancies during computation.

We developed two different algorithms, using two different methods to represent load movement. First, a classical Step-by-Step method, representing movement with many small incremental displacements. And secondly, an innovative Steady-Sate method, using Eulerian assumption and representing continuous flow movement.

We tested both algorithm on the same railways model to be able to compare the results in the same conditions, especially the computation time.

2 RAILWAYS BALLAST BEHAVIOUR

Although ballast is composed of a multitude of smalls blocks, we focus on global behaviour. The ballast layers are modelled using a continuous materials assumptions and studied with Finites Element Methods (FEM) which is easier to implement and needs less computational time than Discrete Elements Methods (DEM). The continuous approach is useful to study structure deformation as an accumulation of plastic strain. This approach has already been used to study ballasted track in different works [1, 2, 3]

2.1 Elastic-Plastic behaviour

We suppose infinitesimal strain which means additive decomposition between elastic and plastic strain tensor (equation 1).

$$\underline{\underline{\varepsilon}} = \underline{\underline{\varepsilon}}^e + \underline{\underline{\varepsilon}}^p \tag{1}$$

Relation between elastic strain $\underline{\underline{\varepsilon}}^e$ and stress tensor $\underline{\underline{\sigma}}$ [1] are supposed to be isotropic linear elastic behaviour, described with Hooke's equation. Young's Modulus and Poisson coefficient are taken from Profillidis study [4], *i.e.* $E = 110\text{MPa}$ and $\nu = 0.2$.

Plastic strain $\underline{\underline{\varepsilon}}^p$ evolution is described using plastic criterion written as a yield function $f(\underline{\underline{\sigma}})$ ($f(\underline{\underline{\sigma}}) < 0$ stress state is acceptable ; $f(\underline{\underline{\sigma}}) = 0$ plastic strain can grow ; stress state is not acceptable $f(\underline{\underline{\sigma}}) > 0$). For simplification reason, we consider ballast with a "standard" bahaviour, *i.e.* flow rule is described as a gradient of the yield function :

$$\dot{\underline{\underline{\varepsilon}}}^p = \lambda \frac{\partial f(\underline{\underline{\sigma}})}{\partial \underline{\underline{\sigma}}} \tag{2}$$

1. **Sign convention** : Traction are positive, and principal stresses are ordered as follows : $\sigma_I \geq \sigma_{II} \geq \sigma_{III}$

2.2 Commonly used criteria

Geomaterial behaviour description commonly uses dedicated criteria such as the Mohr-Coulomb criterion, the Matsuoka-Nakai criterion[5] and the Drucker-Prager criterion[6] (Figure 1).

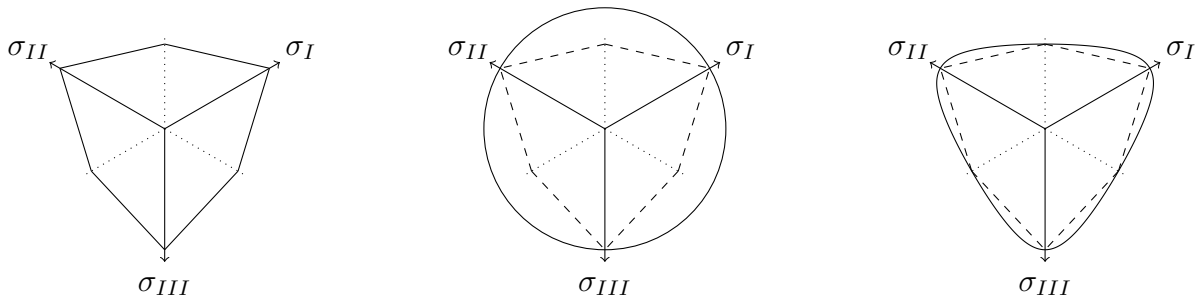

(a) Mohr-Coulomb criterion

(b) Drucker-Prager Criterion compression fitted on Mohr-Coulonb

(c) Matsuka-Nakain criterion fitted on Mohr-Coulomb

Figure 1: Commonly used Criteria represented din Pi-plane

The Mohr-Coulomb criterion is the most commonly used criterion in geo-technical engineering. Its parameters (cohesion C and internal friction angle ϕ) are easy to deduce from laboratory tests and meaningful for engineers. They are commonly used to describe material and Fitting parameter can be described to use other criterion

The Drucker-Prager criterion is the simplest geo-technical criterion, with a circular conical yield surface. It allow direct computation of plastic strain using radial return[7, 8].

The Matsuoka-Nakai criterion is a more complex criterion, with a smooth conical yield surface. It avoids angular problem during flow rule computation in opposition with Mohr-Coulomb . Moreover, this criterion seems to excellently fit to real tri-axial tests [5]. This criterion easily fits on Mohr-Coulomb (see figure 1(c)).

In previous works [9, 10, 11] we compared those three criteria. Firstly, Drucker-Prager improve computation speed of plastic strain. Secondly, despite its induced mist-estimated resistance of materials, a wisely chosen Drucker-Prager fitting keeps discrepancies to an acceptable level. For this reason we use the compression fitted Drucker-Prager criterion (figure 1(b)). We use yield function from equation (3) with mean stress σ_m and deviatoric stress amplitude J_2. Fitting parameters are gives in equation (4).

For this study we will use $\phi = 40^\circ$ [12] and $C = 5\text{Pa}$ [2].

$$f(\underline{\underline{\sigma}}) = 3\alpha(\sigma_m - H) + \sqrt{J_2} \tag{3}$$

$$\alpha = \frac{2\sin\phi}{\sqrt{3}(3+\sin\phi)} \text{ and } H = \frac{C}{\tan\phi} \tag{4}$$

2. The ballast is supposed to be cohesion-less but we take a negligible C value to avoid zero division issues during the computation process.

3 COMPUTATIONAL METHODS

Computation of $\underline{\underline{\varepsilon}}^p$ depends on stress path followed by particles during load cycle. Many classical cyclic loading models commonly use 2D or 3D structure with a static sinusoidal loading which induces increasing and decreasing stress path following a determined way. Mobile load, such as train on railways, induce a particular strain path witch has a major importance for plastic strain determination.

Here, we propose here two different methods to compute plastic strain under a mobile load.

For following part we will suppose that our structure is a $\vec{x}$ axial structure and the load move downstream on the structure. *i.e.* load speed is $\vec{V} = -V\vec{x}$, constant.

3.1 Step-by-Step Computation Methods and Algorithms

The step-by-step algorithm is a classical method to compute influence of a mobile load on a structure based on an incremental displacement of the load (see figure 3(a)).

We focus on a central part of the structure. Before loading cycle, initial plastic strain are taken from previous load passing or are induced by the weight of the structure itself. We start by locating the load before the considered section of the structure, on abscissa X_0, and we compute elastic-plastic strain state on the entire structure.

At time t the structure is on a $\underline{\underline{\varepsilon}}^p_t$ plastic strain state, and abscissa of the load is X_t. At the next step, time is $t + \Delta t$, the load is now at abscissa $X_{t+\delta t} = X_t - V \cdot \delta t$ (see figure 3(a)). For the new configuration, we compute plastic strain $\underline{\underline{\varepsilon}}^p_{T+\delta t}$ taking account previous plastic strain $\underline{\underline{\varepsilon}}^p_t$. (Equation 5)

$$\underline{\underline{\varepsilon}}^p_{t+\delta t} = \underline{\underline{\varepsilon}}^p_t + \lambda \frac{\partial f(\underline{\underline{\sigma}})}{\partial \underline{\underline{\sigma}}} \tag{5}$$

On each Gauss point the plastic strain are searched by closest point projection process[13, 7] until stress state are acceptable. When stress-strain state for the time t are validated, we move the load decreasing abscissa from X_t to X_{t+1}.

The load moves this way from before to after the studied part of the structure on T different steps. After the T computation phases we stop the computational process and we consider that stress-strain state of the studied element (usually central elements) is representative of the global stress-strain state of the entire structure after the loading cycle.

This method is limited because of the non continuous loading of the structure. To ensure a correct stress path description we need to use small δt steps which multiply the number of steps. Remembering that the entire strain state has to be computed on each step, computational time is also multiplied and can be huge.

3.2 Steady-State Computation

The steady-state is an Eulerian methods which allows stress-strain state computation of a structure under a moving load. This method is based on the works of Nguyen and

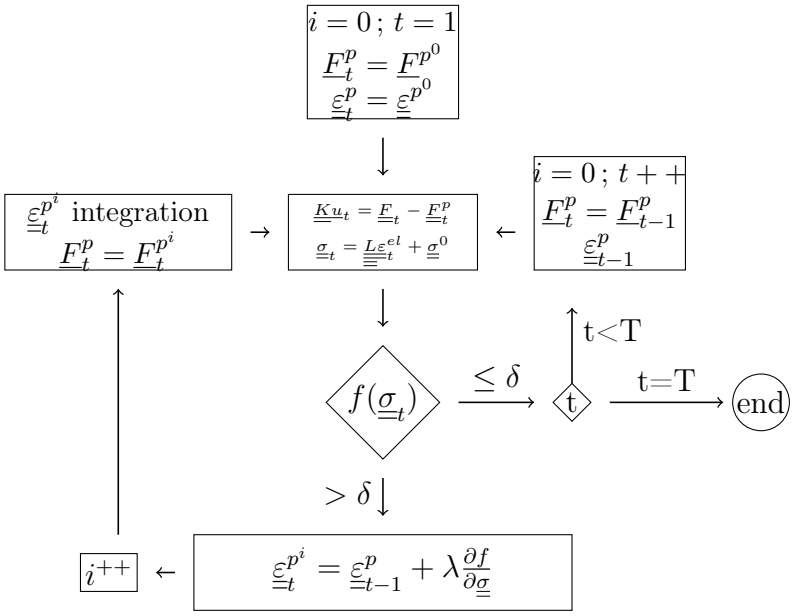

Figure 2: Step-By-Step Algorithm

Rahimian [14](1981) and Dang Van et al. [15](1985) who described the theoretical framework and first applications of the method. It has been used to various problems involving moving loads, such as the impact of rolling on rail heads [16], interaction between rock and cutting tool [17], automotive brake disk [18], tunnelling [19, 20]. But it as been never used to study ballast behaviour under train traffic.

3.2.1 Basic Concept

The method is based on a load point of view focus, the structure is then seen as material flow that goes under the load (see figure 3(b)). Primary, the method supposes that the structure is continuous and invariant along $\vec{x}$ axis. It also supposes that the load speed $\vec{V}$ and the load intensity are constant during a passage.

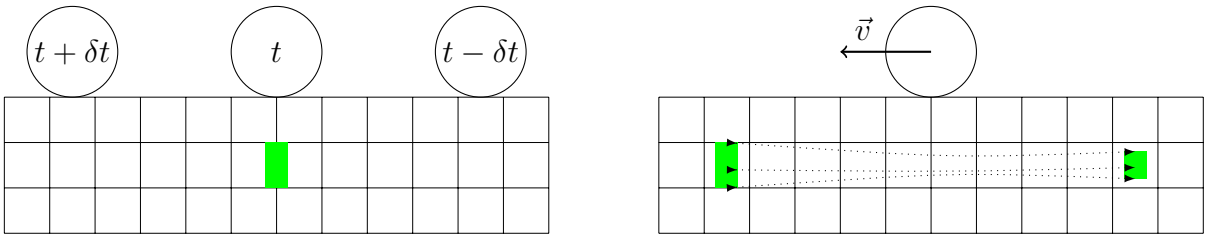

(a) Step-by-Step computation methods (b) Steady-State computational methods

Figure 3: Difference between Step-by-Step and Steady-State

It is possible to use a modified algorithm to compute non constant load or load at non constant speed. The TRC algorithm (Transitoire dans le Repère de Chargement)

developed by Nguyen-Tajan [21](2002) allows such particularities. In case of an periodic structure, such as railways tracks using sleepers, we can use another modified steady state algorithm. This particular aspect is not the purpose of this paper, it will be the subject of future work.

3.2.2 Computational Methods

Under a moving load the time derivative of a tonsorial quantity $\underline{\underline{A}}$ can be written as equation (6) from the structure point of view, and be rewritten as equation (7) from a load point of view.

$$\dot{\underline{\underline{A}}} = \frac{\partial \underline{\underline{A}}}{\partial t} + \vec{V} \cdot \vec{grad} \underline{\underline{A}} \tag{6}$$

$$\dot{\underline{\underline{A}}} = V \frac{\partial \underline{\underline{A}}}{\partial x} \tag{7}$$

In a steady-state method the plastic flow rules can be rewritten :

$$\dot{\underline{\underline{\varepsilon}}}^p = \lambda \frac{\partial f}{\partial \underline{\underline{\sigma}}} \tag{8}$$

With $\lambda \cdot f = 0$, $\lambda \cdot \dot{f} = 0$, $\lambda \geq 0$ and $f \leq 0$.

$$\frac{\partial \underline{\underline{\varepsilon}}^p}{\partial x} = \Lambda \frac{\partial f}{\partial \underline{\underline{\sigma}}} \tag{9}$$

With $\Lambda > 0$ if $f = 0$ and $\frac{\partial f}{\partial x} = 0$ or $\Lambda = 0$ otherwise.

Steady state methods consider that stress path during the loading cycle can be described by following the stress state on a line parallel to the structure axis. Plastic strain are then computed on the integrations points (Gauss points) which are lined because of quadrilateral mesh construction.

Gauss points are then noted and sorted on many parallels lines along the structure. To compute the plastic strain at point n we use the plastic strain state on the previous Gauss point $n-1$, because we assume the continuous yielding during the movement (see figure 4). Equation (10) is used to compute the plastic strain in point n.

$$\underline{\underline{\varepsilon}}^p_n = \underline{\underline{\varepsilon}}^p_{n-1} + \Lambda \frac{\partial f}{\partial \underline{\underline{\sigma}}} \tag{10}$$

3.2.3 Steady-State Algorithm

For the steady state algorithm we consider a central load over the structure that does not move. Before the loading cycle, initial plastic strain are taken from the previous load passes or are those induced by the weight of the structure itself.

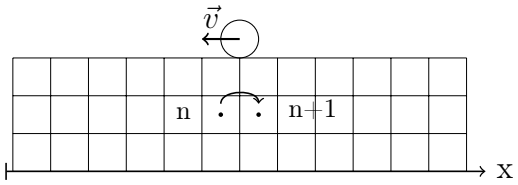

Figure 4: Plastic strain computation process on Gauss point

The plastic strain are then computed and integrated along each of Gauss points line flowing the particular computation process of Steady-State algorithm. The plastic strain are searched by the closest point projection process [13, 7] until stress state are acceptable all along the line. If it's not, the plastic strain integration is started over on the entire line.

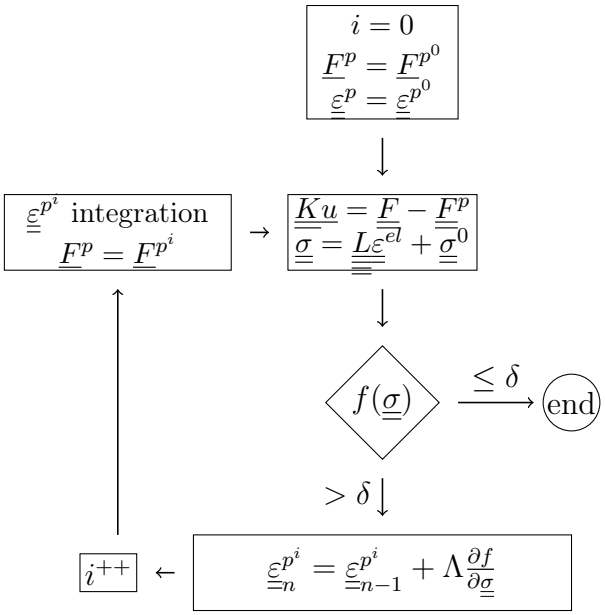

Figure 5: Steady-State Algorithm

At the end of the process, *i.e.* when stress state is acceptable on the entire structure, we identify the final plastic strain at the end of the structure, we consider that this stress-strain state is representative of the global stress-strain state of the entire structure.

For a multi-cycle loading computation, the process is repeated N times for the N loading cycles needed.

4 RAILWAYS MODELLING

We will illustrate the different computation methods using a 3D model of a Railways track. The Model is build in COMSOL Multiphysics FEM software and the computation is led with a Matlab routine. The two softwares communicated using Matlab LiveLink tools of COMSOL's software.

4.1 3D Model

The 3D model represent half of a symmetric 15m long railways track. The 2D transversal shape represent a 50cm hight ballast layers. Over it, a 25cm height and 1.1m wide half single block sleeper is disposed. On the side a 50cm shoulders, and die down slope with a 2/3 ratio are made. (See figure 6)

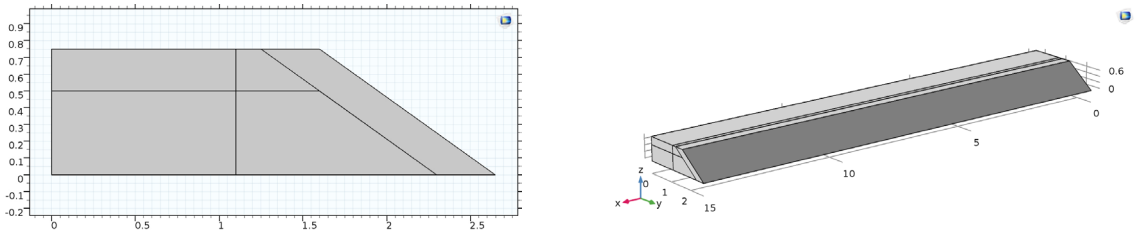

(a) 2D transversal shape (b) Full model

Figure 6: 3D Model of half a railway track

We focus on plastic strain under the sleepers, *i.e.* only in the 50cm bottom layer. Plastic strain are not significant in the rest of the structure and are not computed.

4.2 Meshing

The meshing use quadrilateral elements along the structure. The elements are built lined due to the steady-state computation assumption. Mesh element has to be smaller near the load to correctly describe stress repartition. Because the structure can be loaded on multiple spots, the Step-by-step model uses equally dense mesh. The Steady-state model uses a gradually dense mesh, denser in the middle of the structure, to limit the number of elements and improve computation time. Here we use three time fewer elements.

4.3 Load

Before any loading, the structure stability is computed supporting its own weight. The gravity will continue to affect the entire structure during all computation.

For this work the main load will correspond to a classical maximal load for our half track model. Because our model does not feature rail or sleepers, we will use an equivalent load continuously applied on the top of the bottom layers of ballast. The load repartition is taken from Profillidis work [4], and is interpolated to build a continuous loading (see figure 7). The total load is 10t, (20t for full axle load).

The load is placed on the middle of the structure for the Steady-State computed model, or can be moved along the structure with a parametrised position for the Step-by-Step de computed model.

For the Step-by-Step method we describe 57 steps equally distant from 20cm to ensure load zone covering step after step.

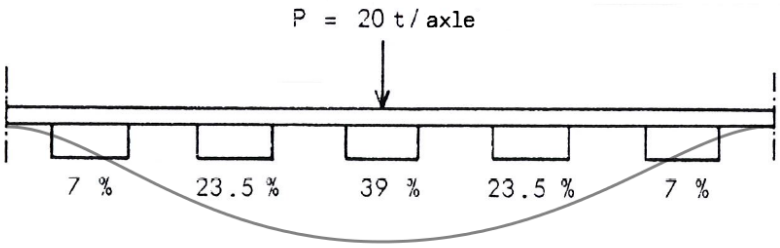

Figure 7: Load reparation on sleepers [4]

5 RESULT AND DISCUSSION

In the following part we will plot and compare plastic strain magnitude define as $\boldsymbol{\epsilon}^p = Tr(\underline{\underline{\varepsilon}}^p \cdot \underline{\underline{\varepsilon}}^p)$. Comparison of other measure of plastic strain has led to same conclusion and will not be presented.

5.1 Longitudinal representation

On figure 8, we represent plastic strain magnitude in the centre of a longitudinal slice of the model, for the Steady-State method and for the last steps of the Step-by-Step method. Those representations give us information on computation process accuracy and plastic strain distribution.

The steady-state algorithm figure shows plastic strain evolution from before to after the load passing. It also shows perfectly a regular and continuous plastic strain distribution after the load.

In opposition the step-by-step figure does not show us plastic strain evolution. To do so, we have to study plastic strain repartition on each step of the computation process. It also shows us an irregular and not continuous repartition of plastic strain. This is due to the jumping representation of load movement. The irregularities are not critical for the study but show a limitation of this methods.

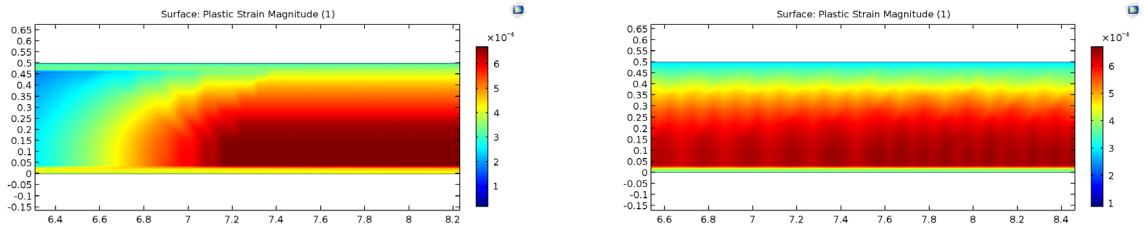

(a) Steady-State (b) Step-by-Step

Figure 8: Longitudinal repartition of plastic Strain for both methods

5.2 Transversal representation

On figure 9, we represent the transversal repartition of plastic strain magnitude in the representatives zones. Shape of the figure and measured values of plastic strain are totally comparable. For example, maximal magnitudes are $\boldsymbol{\varepsilon}^p = 6.76E^{-4}$ for steady-state and $\boldsymbol{\varepsilon}^p = 6.52E^{-4}$ for step-by-step, *i.e.* less than 5% discrepancies.

Both methods can be used to study plastic strain in railway ballast under train load. Small advantage for the Steady-State method who provide cleaner results and more informations.

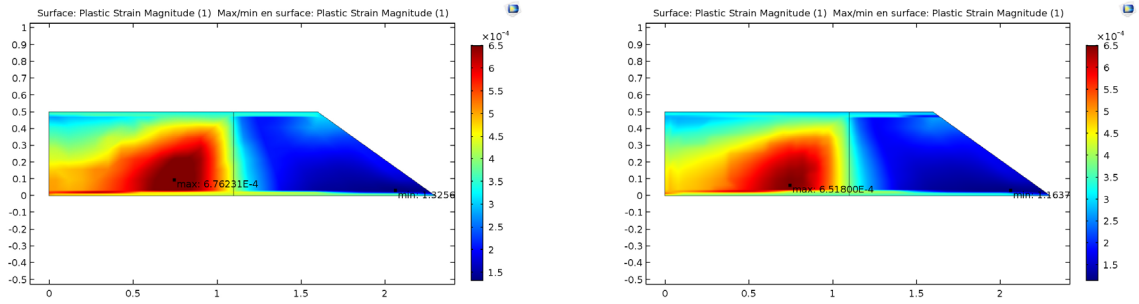

(a) Steady-State (b) Step-by-Step

Figure 9: Longitudinal repartition of plastic Strain for both methods

5.3 Computation time

For this model the step-by-step computation process had run for $395015s$ ($4d$, $13h$ and $43min$), the steady-state had run for $1940s$ ($32min$) [3]. This huge difference remain logical and can be explained as follow :

On one hand, the steady-state process correspond to a single full computation step of 24 iterations and both iteration takes about $80s$.

On the other hand, the step-by-step process correspond to 57 full computation steps. Each step needs about 24 iterations and each iteration takes about $260s$.

Those number are logical, by construction the Step-by-Step needs the same amount of computation on each steps as a full steady-state. Moreover, because of the 3 times denser meshing each iteration of a Step-by-Step need 3 times more time than a Steady-State iteration.

The same result was found with other tested model, independently from the different models and parameters.

Finally, the comparison of the computational time give a huge advantage to the Steady-State process over the Step-by-Step process.

3. These numbers may vary depending on the software and the computer, there are given to illustrate the comparison using same tools and conditions.

6 CONCLUSIONS

In this paper we studied possibilities of using the Steady-State computational methods for studying ballasted track settlement with a continuous approach. Considering the major importance of accurate moving load representation, we have looked for plastic strain computation methods under train circulation.

In that purpose we developed two algorithms using COMSOL Multiphysics and Livelink for Matlab. The first algorithm uses a classical computational method, Step-By-step methods, based on the movement representation via multiples small incremental displacements. The second algorithm uses an innovative Eulerian method, the Seady-State method, based on a load centred point of view and assuring the continuous yielding of the structure.

Using and comparing both methods showed minor differences between the results, with a small advantage for the Steady-State methods which provide homogeneous result. More importantly, comparing computational times showed a strong advantage for Eulerian method over the incremental method with a drastic computation time reducing, which let us see great potential for the Steady-State algorithms. Moreover, because our examples and models are quite simple, this advantage could be even more important for more complex model, including viscous-plastic behaviour for example.

The Steady-State algorithm give us many others potential advantage, including precise plastic strain and plastic work study during cycle, or cyclic structure study. Those improvements will be subject of further work and development in near future.

RÉFÉRENCES

[1] Profillidis, V. *La voie ferrée et sa fondation - Modélisation mathématique.* Theses, Ecole nationale des ponts et chaussées - ENPC (1983). URL `https://pastel.archives-ouvertes.fr/pastel-00693511`.

[2] Suiker, A. *The mechanical behavior of ballasted railway tracks (DUP Science).* Ph.D. thesis, PhD Thesis, Technische Universiteit Delft (2002).

[3] Paderno, C. *Comportement du ballast sous l'action du bourrage et du trafic ferroviaire.* Ph.D. thesis (2010).

[4] Profillidis, V. and Humbert, P. Étude en élastoplasticité par la méthode des éléments finis du comportement de la voie ferrée et de sa fondation. *Bulletin Liaison du Laboratoire des Ponts et Chaussées* **141** (1986).

[5] Matsuoka, H. and Nakai, T. Stress-deformation and strength characteristics of soil under three different principal stresses. In *Proc. JSCE*, vol. 232, 59–70 (1974).

[6] Drucker, D. C. and Prager, W. Soil mechanics and plastic analysis or limit design. *Quarterly of applied mathematics* **10** (1952).

[7] Krieg, R. and Key, S. Implementation of a time independent plasticity theory into structural computer programs. *Constitutive equations in viscoplasticity : Computational and engineering aspects* 125–137 (1976).

[8] Wilkins, J. L. Calculation of Elastic-plastic Flow. *Methods of Compuational Physics* **8** (1964).

[9] Maiolino, S. and Luong, M. P. Measuring discrepancies between coulomb and other geotechnical criteria : Drucker–prager and matsuoka–nakai. In *7th Euromech solid mechanics conference, Lisbon, Portugal*, 09–07 (2009).

[10] Badinier, T. and Maïolino, S. Computation of ballasted track damage : A comparison of Coulomb, Drucker Prager and Matsuoka Nakai criteria. In Pombo, J. (ed.) *The Third International Conference on Railway Technology : Research, Development and Maintenance* (Civil-Comp Press, 2016). URL `http://dx.doi.org/10.4203/ccp.110.21`. Paper 21.

[11] Badinier, T. and Maïolino, S. Limiting discrepancies in substitution of Mohr-Coulomb with fast computation smooth criteria : Application to ballast layer (Submitted).

[12] Suiker, A. S., Selig, E. T. and Frenkel, R. Static and cyclic triaxial testing of ballast and subballast. *Journal of geotechnical and geoenvironmental engineering* **131**, 771–782 (2005).

[13] Simo, J. and Hughes, T. J. Computational inelasticity, volume 7 of interdisciplinary applied mathematics (1998).

[14] Nguyen, Q. S. and Rahimian, M. Mouvement permanent d'une fissure en milieu élasto-plastique. *Journal de Mécanique appliquée* **5**, 95–120 (1981).

[15] Van, K. D., Inglebert, G. and PROIX, J. Sur un nouvel algorithme de calcul de structure élastoplastique en régime stationnaire. In *3ème Colloque :" Tendances actuelles en calcul de structures", Bastia* (1985).

[16] Maitournam, H. *Résolution numérique des problèmes élastoplastiques stationnaires.* Ph.D. thesis, Thèse de Doctorat de l'ENPC (1989).

[17] Geoffroy, H. *Etude de l'interaction roche/outil de forage : influence de l'usure sur les paramètres de coupe.* Ph.D. thesis (1996).

[18] Nguyen-Tajan, M.-L., Maitournam, H. and Thomas, J.-J. Une méthode de calcul de structures soumises à des chargements mobiles : Application au freinage automobile. *Revue Européenne des Eléments* **11**, 247–261 (2002).

[19] Corbetta, F. *Nouvelles méthodes d'étude des tunnels profonds : calculs analytiques et numériques.* Ph.D. thesis, EMP (1990).

[20] Maiolino, S. *Fonction de charge générale en géomécanique : application aux travaux souterrains.* Ph.D. thesis, Ecole Polytechnique X (2006).

[21] Nguyen-Tajan, T. M.-L. *Modélisation thermomécanique des disques de frein par une approche eulérienne.* Ph.D. thesis, Ecole Polytechnique X (2002).

XIV International Conference on Computational Plasticity. Fundamentals and Applications
COMPLAS 2017
E. Oñate, D.R.J. Owen, D. Peric and M. Chiumenti (Eds)

FLEXIBILITY OF APPROXIMATION IN PIES APPLIED FOR SOLVING ELASTOPLASTIC BOUNDARY PROBLEMS

AGNIESZKA BOŁTUĆ

Faculty of Mathematics and Informatics
University of Bialystok
K. Ciołkowskiego 1M, 15-245 Białystok, Poland
e-mail: aboltuc@ii.uwb.edu.pl

Key words: Approximation, Local vs. global, Elastoplastic, Boundary problems, PIES.

Abstract. The paper presents the flexibility of approximation in PIES applied for solving elastoplastic boundary value problems. Three various approaches to approximation of plastic strains have been tested. The first one bases on the globally applied Lagrange polynomial. The two remaining are local: inverse distance weighting (IDW) method and approximation in different zones by locally applied Lagrange polynomials. Some examples are solved and results obtained are compared with analytical solutions. Conclusions on the effectiveness of presented approaches have been drawn.

1 INTRODUCTION

The main issue of solving boundary value problems by the finite element method (FEM) [1,2] and the boundary element method (BEM) [3,4] is discretization. The approach called parametric integral equation system (PIES)[5] has been developed as an alternative to mentioned methods. It is characterized by analytical incorporation of curves and surfaces into the integral equation, which results in separation of approximations: the shape from the solutions. It means that more effective methods for both approximations can be applied. PIES with mentioned advantages has been applied for solving various problems e.g. acoustic [6], elastic [7,8] or lately elasto-plastic [9].

Solving elasto-plastic problems, in PIES like in BEM, only the plastic region has to be modelled. It is defined globally using surface patches known from computer graphics [10,11]. In most cases only single surface is enough. For this reason also approximation of plastic strains is done globally using various polynomials (e.g. the Lagrange polynomial). Such an approach has pros and cons. Advantageous is simple global integration with a bit more number of weights in the quadrature and without the necessity of calculating integrals over small regular areas and summing them. The second benefit is flexibility of obtaining plastic strains at any point of the considered domain, because it is done continuously using only one formula. On the other hand, it is known that plastic strains occur locally. Even if the defined surface covers only the estimated plastic zone, a part of it is characterized by a zero plastic deformations. Using global approximation every calculated value is more or less affected by values from all interpolation nodes. It means that there is no possibility to obtain exactly zero at nodes which are not plastic, but only a value that oscillates around zero. The accuracy of

the results obtained using the global approach depends on the number of interpolation nodes. The more interpolation nodes with zero plastic strains, the more accurate results in the vicinity of zero can be obtained between them. When a lot of nodes have to be taken in order to guarantee appropriate accuracy, a local approximation should be considered. However, in order not to lose the main advantage of PIES, local approximation cannot be associated with shape discretization.

The main aim of this paper is to develop and test various methods of local approximation without the necessity of dividing the domain into elements or cells. At the beginning, approximation is separated into two or more zones depending on the distribution of plastic strains. This division is done only on the interpolation nodes level. However, there are also problems that require totally local approach around the considered node only. The inverse distance weighting (IDW) method is an example of the method using this approach and it can be easily adapted to PIES. Some examples are solved using both approaches. The results obtained confirm the effectiveness of proposed methods of approximation.

2 PIES AND THE INTEGRAL IDENTITY FOR STRESSES

The parametric integral equation system (PIES) in the initial-strain approach was derived and presented in [9]. The resulting form of PIES is given by

$$0.5\dot{\boldsymbol{u}}_l(\bar{s}) = \sum_{j=1}^{n} \int_{s_{j-1}}^{s_j} \left\{ \overline{\boldsymbol{U}}_{lj}^{\,*}(\bar{s},s)\dot{\boldsymbol{p}}_j(s) - \overline{\boldsymbol{P}}_{lj}^{\,*}(\bar{s},s)\dot{\boldsymbol{u}}_j(s) \right\} J_j(s)ds + \int_{v_{d-1}}^{v_d}\int_{w_{d-1}}^{w_d} \overline{\boldsymbol{\sigma}}_l^{\,*}(\bar{s},v,w)\dot{\boldsymbol{\varepsilon}}^p(v,w)J_d(v,w)dvdw, \tag{1}$$

where $s_{l-1} \le \bar{s} \le s_l$, $s_{j-1} \le s \le s_j$, $v_{d-1} \le v \le v_d, w_{d-1} \le w \le w_d$. Variable n is the number of segments that built a boundary, while m is the number of surfaces that built a domain, therefore $l = 1,2,.....n$ and $d = 1,2,....., m$.

As is stated in the introduction, boundary segments in PIES can be defined by any curves $\boldsymbol{\Gamma}_j(s)$ (e.g. Bézier, Hermite, B-spline or NURBS curves) and s_{l-1} and s_{j-1} correspond to the beginning of lth and jth segments, while s_l and s_j to the end of these segments. Consequently, a domain in PIES can be defined by surface patches (e.g. Bézier surface patches) and $v_{d-1}, v_d, w_{d-1}, w_d$ are respectively the beginning and the end of the domain of dth surface. For the sake of simplicity, it should be remembered that the domain of the surface is a unit square $[0,1]\times[0,1]$. Mapping integral intervals require introduction of scaling factors (Jacobians), which can be presented as follows

$$J_j(s) = \left[\left(\frac{\partial \Gamma_j^{(1)}(s)}{\partial s} \right)^2 + \left(\frac{\partial \Gamma_j^{(2)}(s)}{\partial s} \right)^2 \right]^{0.5}, \qquad \text{for a boundary segments,} \tag{2}$$

and

$$J_d(v,w) = [A_1^2(v,w) + A_2^2(v,w) + A_3^2(v,w)]^{0.5}, \qquad \text{for a domain,} \tag{3}$$

where functions $A_1(v,w), A_2(v,w), A_3(v,w)$ represent the combination of the partial derivatives of mathematical functions that describe surfaces [10,11].

Functions $\dot{\boldsymbol{p}}_j(s), \dot{\boldsymbol{u}}_j(s)$ from (1) are parametric boundary functions defined or searched on each segment of the boundary, while $\dot{\boldsymbol{\varepsilon}}^p(v,w)$ are plastic strains. Since PIES is solved using the collocation method, $\bar{s}$ stands for a collocation point.

Equation (1) contains three kernels. The first kernel $\overline{\boldsymbol{U}}^*_{lj}(\bar{s},s)$ for the plane strain case is presented in the following matrix form [9]

$$\overline{\boldsymbol{U}}^*_{lj}(\bar{s},s) = -\frac{1}{8\pi(1-\nu)\mu}\begin{bmatrix} (3-4\nu)\ln(\eta)-\dfrac{\eta_1^2}{\eta^2} & -\dfrac{\eta_1\eta_2}{\eta^2} \\ -\dfrac{\eta_1\eta_2}{\eta^2} & (3-4\nu)\ln(\eta)-\dfrac{\eta_2^2}{\eta^2} \end{bmatrix}, \qquad l,j=1,2,.....n, \tag{4}$$

where $\eta=[\eta_1^2+\eta_2^2]^{0.5}$, $\eta_1=\Gamma_j^{(1)}(s)-\Gamma_l^{(1)}(\bar{s})$, $\eta_2=\Gamma_j^{(2)}(s)-\Gamma_l^{(2)}(\bar{s})$, while ν is Poisson's ratio and μ is a shear modulus.

The next kernel $\overline{\boldsymbol{P}}^*_{lj}(\bar{s},s)$ in (1) can be presented by the expression [9]

$$\overline{\boldsymbol{P}}^*_{lj}(\bar{s},s) = -\frac{1}{4\pi(1-\nu)\eta}\begin{bmatrix} P_{11} & P_{12} \\ P_{21} & P_{22} \end{bmatrix}, \quad l,j=1,2,.....n, \tag{5}$$

where

$$P_{11}=\left\{(1-2\nu)+2\frac{\eta_1^2}{\eta^2}\right\}\frac{\partial\eta}{\partial n}, \quad P_{12}=\left\{2\frac{\eta_1\eta_2}{\eta^2}\frac{\partial\eta}{\partial n}-(1-2\nu)\left[\frac{\eta_1}{\eta}n_2(\mathrm{s})+\frac{\eta_2}{\eta}n_1(\mathrm{s})\right]\right\},$$

$$P_{21}=\left\{2\frac{\eta_2\eta_1}{\eta^2}\frac{\partial\eta}{\partial n}-(1-2\nu)\left[\frac{\eta_2}{\eta}n_1(\mathrm{s})+\frac{\eta_1}{\eta}n_2(\mathrm{s})\right]\right\}, \quad P_{22}=\left\{(1-2\nu)+2\frac{\eta_2^2}{\eta^2}\right\}\frac{\partial\eta}{\partial n},$$

$$\frac{\partial\eta}{\partial n}=\frac{\partial\eta_1}{\partial\eta}n_1(\mathrm{s})+\frac{\partial\eta_2}{\partial\eta}n_2(\mathrm{s}),$$

and $n_1(s)$ and $n_2(s)$ are the direction cosines of the external normal to j*th* segment of the boundary.

Both kernels (4) and (5) take into account (in their mathematical formalism) the shape of the boundary defined by any parametric curves $\boldsymbol{\Gamma}(s)$. The shape of the domain defined by any parametric surfaces $\boldsymbol{B}(v,w)$ is integrated into the integrand $\overline{\boldsymbol{\sigma}}^*_l(\bar{s},v,w)$ from (1). For the plane strain case that function can be presented as follows [9]

$$\overline{\sigma}^*_l(\bar{s},v,w) = -\frac{1}{4\pi(1-\nu)\overline{\eta}}\begin{bmatrix} (1-2\nu)\dfrac{\overline{\eta}_1}{\overline{\eta}}+2\dfrac{\overline{\eta}_1^3}{\overline{\eta}^3}-2\nu\dfrac{\overline{\eta}_1}{\overline{\eta}} & (1-2\nu)\dfrac{\overline{\eta}_2}{\overline{\eta}}+2\dfrac{\overline{\eta}_1^2\overline{\eta}_2}{\overline{\eta}^3} \\ -(1-2\nu)\dfrac{\overline{\eta}_2}{\overline{\eta}}+2\dfrac{\overline{\eta}_1^2\overline{\eta}_2}{\overline{\eta}^3}-2\nu\dfrac{\overline{\eta}_2}{\overline{\eta}} & (1-2\nu)\dfrac{\overline{\eta}_1}{\overline{\eta}}+2\dfrac{\overline{\eta}_2^2\overline{\eta}_1}{\overline{\eta}^3} \\ (1-2\nu)\dfrac{\overline{\eta}_2}{\overline{\eta}}+2\dfrac{\overline{\eta}_2\overline{\eta}_1^2}{\overline{\eta}^3} & -(1-2\nu)\dfrac{\overline{\eta}_1}{\overline{\eta}}+2\dfrac{\overline{\eta}_2^2\overline{\eta}_1}{\overline{\eta}^3}-2\nu\dfrac{\overline{\eta}_1}{\overline{\eta}} \\ (1-2\nu)\dfrac{\overline{\eta}_1}{\overline{\eta}}+2\dfrac{\overline{\eta}_2^2\overline{\eta}_1}{\overline{\eta}^3} & (1-2\nu)\dfrac{\overline{\eta}_2}{\overline{\eta}}+2\dfrac{\overline{\eta}_2^3}{\overline{\eta}^3}-2\nu\dfrac{\overline{\eta}_2}{\overline{\eta}} \end{bmatrix}^{\mathrm{T}}, \tag{6}$$

where $\overline{\eta}=[\overline{\eta}_1^2+\overline{\eta}_2^2]^{0.5}$, $\overline{\eta}_1=B^{(1)}(v,w)-\Gamma_l^{(1)}(\bar{s})$ and $\overline{\eta}_2=B^{(2)}(v,w)-\Gamma_l^{(2)}(\bar{s})$.

Formula (1) allows obtaining displacements and forces on the boundary. To determine other quantities within the domain the integral identity is required. In order to calculate stresses the following expression has to be used

$$\dot{\boldsymbol{\sigma}}(\boldsymbol{x}) = \sum_{j=1}^{n} \int_{s_{j-1}}^{s_j} \{\hat{\hat{\boldsymbol{D}}}_j^*(\boldsymbol{x},s)\dot{\boldsymbol{p}}_j(s) - \hat{\hat{\boldsymbol{S}}}_j^*(\boldsymbol{x},s)\dot{\boldsymbol{u}}_j(s)\} J_j(s)ds + \\ + \int_{v_{d-1}}^{v_d} \int_{w_{d-1}}^{w_d} \hat{\hat{\boldsymbol{\Sigma}}}^*(\boldsymbol{x},v,w)\dot{\boldsymbol{\varepsilon}}^p(v,w) J_d(v,w)dvdw + \hat{\hat{\boldsymbol{f}}}\dot{\boldsymbol{\varepsilon}}^p(\boldsymbol{x}) \tag{7}$$

Kernels $\hat{\hat{\boldsymbol{D}}}_j^*(\boldsymbol{x},s)$, $\hat{\hat{\boldsymbol{S}}}_j^*(\boldsymbol{x},s)$, $\hat{\hat{\boldsymbol{\Sigma}}}^*(\boldsymbol{x},v,w)$ and also a free term are given in explicit form in [9].

3 DEFINING THE DOMAIN

As is stated in section 2, the domain in the proposed method is modeled globally using surface patches [10,11]. Till now only Bézier surfaces were applied, but the approach gives flexibility in choosing the type of patch. In PIES, like in BEM, only the yield region is defined, because the domain integrals are zero elsewhere. In order to show the way of modeling in PIES two different shapes are considered. The first domain is polygonal, the second curvilinear and both of them are presented in [12]. Figure 1 and 2 present them discretized in BEM and defined in PIES. White circles ○ represent nodes required to define the boundary, while black ● are those which are necessary for the yield region modeling.

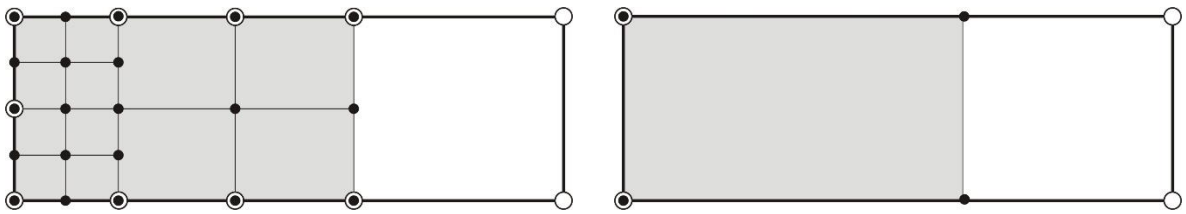

a) b)

Figure 1: Modeling a cantilever beam in: a) BEM, b) PIES

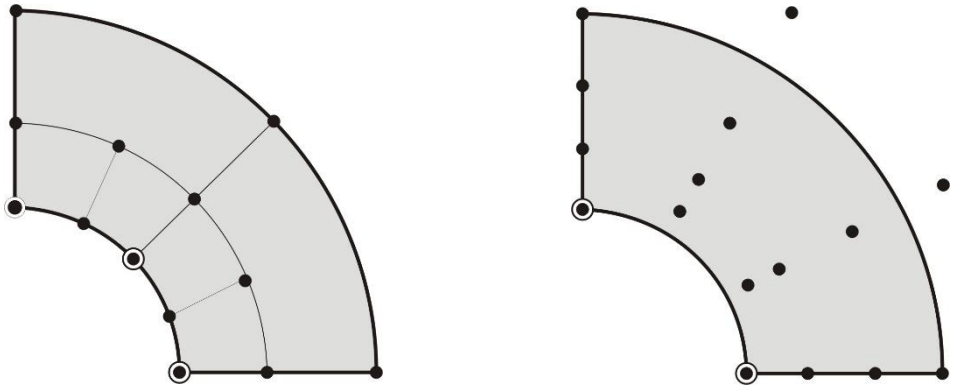

a) b)

Figure 2: Modeling a circular hole in an infinite domain in: a) BEM, b) PIES

As can be seen in Fig. 1a and 2a, the discretization requires division of yield region into cells. They model the geometry, but also their number and type are responsible for the accuracy of obtained solutions. Therefore, even if the shape can be modeled using smaller number of cells, sometimes (or even very often) they have to be multiplied in order to maintain satisfactory level of results. Thus, the yield region in the cantilever beam (Fig. 1a) in BEM is defined by 12 linear cells and 21 nodes, while in fact it can be modeled using only one bilinear surface and 4 corner points (Fig. 1b). The same situation is when the curved shape is defined. In BEM there is the necessity of applying 6 linear cells (Fig. 2a), while PIES requires only one bicubic surface (Fig. 2b).

Concluding, the number of data required for modeling the domain in PIES depends only on the complexity of a shape. The accuracy of approximation is guaranteed by the number of expressions in approximation series presented in the next section. Proposed method solves also another complication occurring in BEM. The extent of the yield region is not known a priori, therefore very often generous proportion of it are assumed initially. For this reason the greater number of cells has to be defined. In PIES that problem does not exists, because as it is presented in Fig.1b using the same number of nodes even entire domain can be modeled as an initial yield region. Thus, it is more effective to assume quite large proportions than performing pilot studies.

4 APPROXIMATION OF PLASTIC STRAINS

4.1 Global approximation using Lagrange polynomials

As is mentioned in section 3, approximations of the shape and solutions in PIES are performed independently. Therefore, the domain can be modeled globally using only minimal number of data needed for accurate definition of the shape. A consequence of the global modeling of the plastic zone is the possibility of global approximation of plastic strains. For this purpose any 2D method can be used. Till now I have applied the approximation series with Chebyshev basis functions and Lagrange polynomials. The first approach has one disadvantage i.e. it requires solving of the system of equations. This feature can be unfavorable especially when the system is ill-conditioned. The second way is not characterized by this defect, and therefore is more efficient.

Using the Lagrange polynomials the plastic strains $\dot{\boldsymbol{\varepsilon}}^p(\boldsymbol{x})$ can be approximated by the following approximation series

$$\dot{\boldsymbol{\varepsilon}}^p(\boldsymbol{x}) = \sum_{r=0}^{R_1-1}\sum_{w=0}^{R_2-1} \dot{\boldsymbol{\varepsilon}}^{p,rw}(\boldsymbol{x}) L_{rw}(\boldsymbol{x}) \,, \tag{8}$$

where

$$L_{rw}(\boldsymbol{x}) = L_r(x_1) L_w(x_2),$$

$$L_r(x_1) = \prod_{o=0,o\neq r}^{R_1-1} \frac{x_1 - x_{1o}}{x_{1r} - x_{1o}}, \quad L_w(x_2) = \prod_{o=0,o\neq w}^{R_2-1} \frac{x_2 - x_{2o}}{x_{2w} - x_{2o}},$$

and $N = R_1 \cdot R_2$ is the given number of interpolation nodes, while $\dot{\boldsymbol{\varepsilon}}^{p,rw}(\boldsymbol{x})$ is the value of plastic strain at the node (x_{1r}, x_{2w}).

One of the most crucial elements of the approximation is arrangement of interpolation nodes. Taking into account the domain of approximation – a unit square – it is very easy to distribute nodes in any order. Some orders that were previously successfully used are:

uniform and at zeros of Chebyshev polynomial. Using the first method and quite large number of interpolation nodes Runge's phenomenon may occur. Therefore, the most efficient and safe is the second proposition. Nodes placed in the unit square have to be transformed into the actual domain in order to obtain values of plastic strains for approximation. This is also simple, because each surface is described by some formulas, which translate coordinates from the parametric domain of the surface to Cartesian coordinate system.

After substituting formula (8) into (1) and using approximating series for the boundary functions (presented in [9]) we obtain approximating form of PIES for elastoplastic problems

$$0.5\dot{\boldsymbol{u}}_l(\bar{s}) = \sum_{j=1}^{n}\sum_{k=0}^{M-1}\left\{\dot{\boldsymbol{p}}_j^{(k)}\int_{s_{j-1}}^{s_j}\overline{\boldsymbol{U}}_{lj}^{\,*}(\bar{s},s) - \dot{\boldsymbol{u}}_j^{(k)}\int_{s_{j-1}}^{s_j}\overline{\boldsymbol{P}}_{lj}^{\,*}(\bar{s},s)\right\} t_j^{(k)}(s)J_j(s)ds + \\ + \int_{v_{d-1}}^{v_d}\int_{w_{d-1}}^{w_d}\overline{\boldsymbol{\sigma}}_l^{*}(\bar{s},v,w)J_d(v,w)\sum_{r=0}^{R_1-1}\sum_{w=0}^{R_2-1}\dot{\boldsymbol{\varepsilon}}^{p,rw}(\boldsymbol{x})L_{rw}(v,w)dvdw. \tag{9}$$

As can be seen in (9), the domain integral is calculated on the basis of values returned by the formula (8), which is used globally (one formula for the whole surface). The advantage of the approach is that we have only one polynomial by which plastic strains at arbitrary points of the plastic region can be obtained. On the other hand, this approach may not reflect the local character of strains. It means that every point which does not yield has plastic strains only around zero, but not exactly zero. It comes from the fact, that all interpolation nodes have influence on searched values. Therefore, maybe it is reasonable to separate approximation into two or more zones depending on the distribution of plastic strains.

4.2 Local approximation

4.2.1 Different Lagrange polynomials in different zones

In PURC separation of approximations is very easy, because approximation of the domain and approximation of the plastic strains are independent. Thus, the shape still is modeled by the surface, interpolation nodes are generated in its domain (the unit square) and approximation is done by manipulating these nodes. Such an approach allows to separate two sets of nodes and for approximation of strains to use two approximation polynomials. Most expected division is the one, which separates zone with nonzero plastic strains from that where they are zero. The example of such a division for the Lame problem is presented in Fig. 3. The analytical solution for this problem is known, therefore the boundary of the division is drawn as the boundary between elastic and plastic regions.

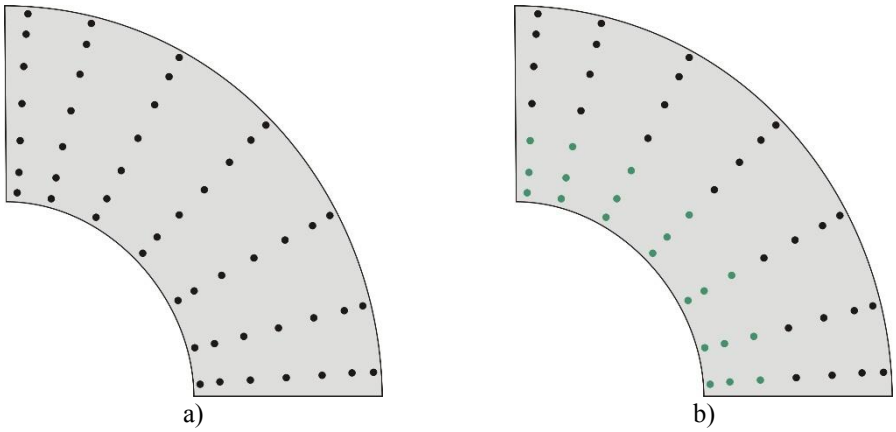

Figure 3: a) An arrangement of interpolation nodes, b) split into two sets of nodes

Each point for which plastic strains are required has to be assigned to one of the approximation zones and depending on the choice its value should be approximated with the appropriate polynomial. Zone boundaries can be arbitrarily chosen, however, it seems intuitively that it should divide the domain evenly between the extreme nodes of the designated sets of nodes. Dividing a plastic region into zones is straightforward in the proposed method, since approximation takes place in the unit square, which is a domain of the surface. An example of division into zones of influence of individual approximation polynomials is shown in Fig. 4.

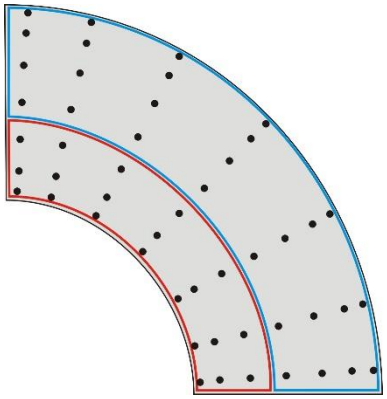

Figure 4: Two zones for which are used different approximation series

As can be seen in Fig. 4, for all points included in the red and blue zones different polynomials have to be used.

The PIES approximation form described by (9) has to be modified, and the last term of the equation

$$\int_{v_{d-1}}^{v_d}\int_{w_{d-1}}^{w_d} \overline{\boldsymbol{\sigma}}_l^*(\bar{s},v,w)J_d(v,w)\sum_{r=0}^{R_1-1}\sum_{w=0}^{R_2-1}\dot{\boldsymbol{\varepsilon}}^{p,rw}(\boldsymbol{x})L_{rw}(v,w)dvdw,$$

is replaced by

$$\int_{v_{d-1}}^{v_d}\int_{w_{d-1}}^{w_d} \overline{\boldsymbol{\sigma}}_l^*(\bar{s},v,w)J_d(v,w)\sum_{r=0}^{T_1-1}\sum_{w=0}^{T_2-1}\dot{\boldsymbol{\varepsilon}}^{p,rw}(\boldsymbol{x})L_{rw}(v,w)dvdw, \tag{10}$$

where T_1, T_2 are numbers of interpolation points assigned to the corresponding Lagrange polynomial. Considering the example presented in Fig.4 the first polynomial is characterized by $T_1 = 3$ and $T_2 = 7$, while the second by $T_1 = 4$ and $T_2 = 7$. Which of the polynomials will be used to approximate $\dot{\boldsymbol{\varepsilon}}^p(v,w)$ in (10) depends on the location of point $\boldsymbol{x}$.

Similar modifications should also be made to the last element of the approximation form of the integral identity for stress (7). The situation is a little more complicated here, because the integral over the domain is strongly singular. In [9], the algorithm described in [13] was used for its determination. It consists in transforming the singular integral into two

$$\begin{aligned}&\int_{v_{d-1}}^{v_d}\int_{w_{d-1}}^{w_d} \hat{\overline{\boldsymbol{\Sigma}}}^*(\boldsymbol{x},v,w)\dot{\boldsymbol{\varepsilon}}^p(v,w)J_d(v,w)dvdw= \\ &\int_{v_{d-1}}^{v_d}\int_{w_{d-1}}^{w_d} \hat{\overline{\boldsymbol{\Sigma}}}^*(\boldsymbol{x},v,w)[\dot{\boldsymbol{\varepsilon}}^p(v,w)-\dot{\boldsymbol{\varepsilon}}^p(\boldsymbol{x})]J_d(v,w)dvdw+\dot{\boldsymbol{\varepsilon}}^p(\boldsymbol{x})\int_{v_{d-1}}^{v_d}\int_{w_{d-1}}^{w_d} \hat{\overline{\boldsymbol{\Sigma}}}^*(\boldsymbol{x},v,w)J_d(v,w)dvdw\end{aligned} \tag{11}$$

The first integral is weakly singular and can be evaluated by subdivision technique, while the second has been transformed into a boundary integral with no singularity. In both integrals it is necessary to use the approximation series (8) twice to calculate the plastic strains at the point $\boldsymbol{x}$ and for all points (v,w). And again like in (10), one should use polynomials that correspond to positions of both points.

The advantage of the proposed strategy is that the number of interpolation nodes in a polynomial can be quite effectively controlled. For example, if one of the polynomials is used to approximate strains where most of them are zero, it can be built with smaller number of nodes. An example of the strategy is presented in Fig. 5.

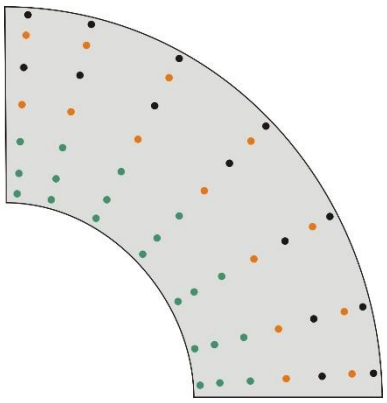

Figure 5. Interpolation nodes used in two approximation series

As shown in Fig. 5, green nodes have been used in one of the polynomials, while in the second is considered only every second row of nodes marked by orange.

The strategy described in this section, despite being based on globally generated nodes and a globally modeled plastic region, is zonally local. However, there are issues that require approximation to be completely local to the selected point. There are many local

approximation algorithms, most of which can be easily adapted to PIES. One of the simplest examples is the inverse distance weighting (IDW) method.

4.2.2 Inverse distance weighting

Inverse distance weighting (IDW), also known as the Shepard method, is used for interpolation with an irregularly-spaced interpolation nodes [14]. Unknown values are calculated with a weighted average of the values available at the known nodes. A general form of finding an interpolated value $\dot{\boldsymbol{\varepsilon}}^p(\boldsymbol{x})$ at a given point $\boldsymbol{x}$ based on plastic strains $\dot{\boldsymbol{\varepsilon}}^p(\boldsymbol{x}_r)$ ($r = 0,1,...R$) at R interpolation points using IDW is

$$\dot{\boldsymbol{\varepsilon}}^p(\boldsymbol{x}) = \begin{cases} \dfrac{\sum_{r=0}^{R} \omega_r(\boldsymbol{x}) \dot{\boldsymbol{\varepsilon}}^p(\boldsymbol{x}_r)}{\sum_{r=0}^{R} \omega_r(\boldsymbol{x})}, & if\ d(\boldsymbol{x},\boldsymbol{x}_r) \neq 0\ \ for\ all\ r \\ \dot{\boldsymbol{\varepsilon}}^p(\boldsymbol{x}_r), & if\ d(\boldsymbol{x},\boldsymbol{x}_r) = 0\ \ for\ some\ r \end{cases}, \tag{12}$$

where

$$\omega_r(\boldsymbol{x}) = \frac{1}{d(\boldsymbol{x},\boldsymbol{x}_r)^p}, \tag{13}$$

is a simple IDW weighting function, d is a given distance from the known point $\boldsymbol{x}_r$ to the unknown point $\boldsymbol{x}$ and p is a positive real number, called the power parameter.

The main idea of IDW is that things that are close to one another are more alike than those that are farther apart. To predict a value for any unmeasured location, IDW uses the measured values surrounding the prediction location (from so-called neighborhood of influence). It is known that using such an approach the accuracy depends on the arrangement of interpolation nodes and the way of determination of the mentioned neighborhood. In the simplest case the neighborhood of influence can be specified using maximal distance from point of interest and it is just a spatially fixed shape e.g. circle. Selection of interpolation nodes could be much more complex, but also more effective especially in cases with highly nonregularly distributed nodes [15].

In the paper, the simplest method of determining the neighborhood of influence is used. Fig. 6 presents nodes used for approximation of plastic strain at point $\boldsymbol{x}$.

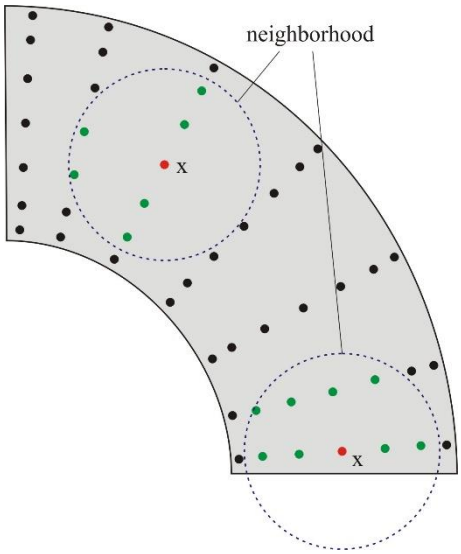

Figure 6: Neighborhood determines nodes for approximation at points $\boldsymbol{x}$

Another factor affecting the accuracy of the approximation in IDW is the power parameter p. Greater values of p assign greater influence to values closest to the approximated point.

5 RESULTS

5.1 Different Lagrange polynomials in different zones

The first example concerns a thick-walled cylinder subjected to internal pressure under plain strain conditions. The radius of inner face is $a = 100$, while outer face is $b = 200$. The whole domain is defined by one bicubic Bézier surface. The Von-Mises yield criterion with perfect plasticity and the following material constants $\sigma_Y = 30 MPa$, $E = 21000 MPa$, $v = 0.3$ are assumed.

Initially, the problem was solved using global approach with 25 and 36 interpolation nodes placed at roots of Chebyshev polynomials. For those two cases, radial and circumferential stress distribution for a specific ($p = 20.9 MPa$) internal pressure were calculated. Values obtained at 100 internal points are used to calculate a norm L_2

$$\|e\| = \frac{1}{\left|\overline{\sigma}_r^w\right|_{\max}} \sqrt{\frac{1}{100} \sum_{w=1}^{100} (\sigma_r^w - \overline{\sigma}_r^w)^2} \times 100\% , \tag{14}$$

where σ_r^w represents radial stresses obtained by PIES at 100 interior points, while $\overline{\sigma}_r^w$ are exact solutions [16]. Values of norm for two assumed numbers of interpolation nodes are presented in Table 1.

Table 1: Norms for radial and circumferential stress distribution – global approximation

	25	**36**
$\|e\|_{\sigma_r}$	0.4432	0.1923
$\|e\|_{\sigma_q}$	2.4478	1.4653

As can be seen in Table 1 value of norm is smaller for higher number of interpolation nodes, but it still can be better (especially for σ_q). For this reason the first technique described in section 4.2.1 is applied. Three different cases are considered: two of them with 36 and one with 25 interpolation nodes. Figure 7 presents nodes used to create two approximation polynomials and also the division of the domain into zones for which different polynomials have to be applied.

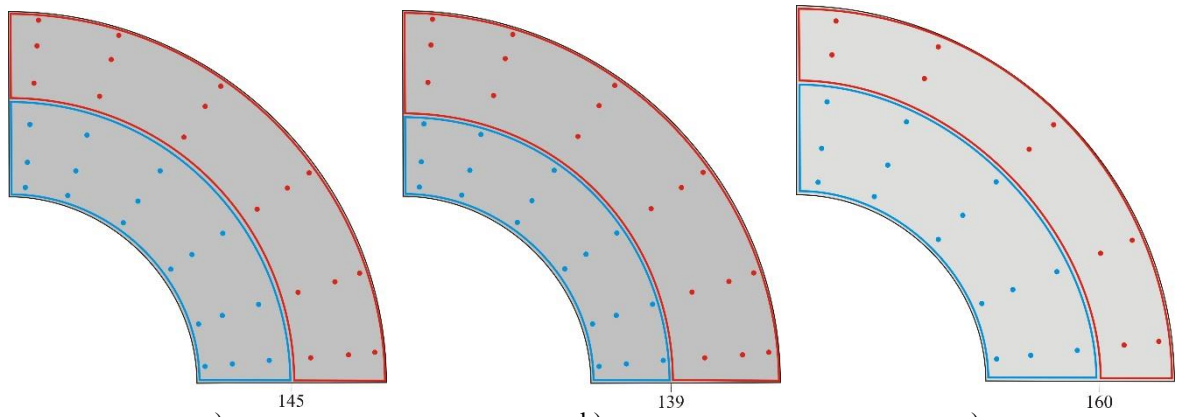

Figure 7: Different approaches for zonally local approximation

Figure 7a present arrangement of 36 interpolation nodes, which are divided into two groups for two approximation polynomials. In both of polynomials $T_1 = 3$ and $T_2 = 6$. Values of plastic strains at points from the zone with outer face with $r = 145$ are calculated using the first polynomial, while the rest using the second one. In the case presented in Fig. 7b the first zone of influence is reduced to favor the other ($r = 139$). This test is to check whether the maximum reduction of the zone with non-zero plastic strains affects the final results. The last from presented cases concerns approximation with 25 nodes. The first polynomial has $T_1 = 3$ and $T_2 = 5$, while the second $T_1 = 2$ and $T_2 = 5$. Zones of influence of individual polynomials are defined by the radius $r = 160$.

For the individual cases described above, the value of norm (14) has been determined. The results are presented in Table 2.

Table 2: Norms for radial and circumferential stress distribution – local approximation

	25,r=160	**36, r=145**	**36,r=139**
$\|e\|_{\sigma_r}$	0.3235	0.1561	0.1613

$\|e\|_{\sigma_\varphi}$	1.5861	1.0146	0.9195

Comparing the results presented in Tables 1 and 2, the following conclusions can be drawn:

a) the norm for radial stress reduces its value by 27%, while for circumferential stress by 35% when dividing into two polynomials and using totally 25 interpolation nodes,

b) for 36 nodes and the boundary between zones in $r = 145$ norms are reduced by 19% and 30% respectively for radial and circumferential stress (comparing to the global approach),

c) moving the boundary to $r = 139$ only affects the improvement of the norm for circumferential stress (in comparison to values obtained for $r = 145$).

As can be seen, there is an improvement in the results after dividing the domain into two approximating zones. Another important benefit is the shortening of calculation time. Thus, the calculations for 25 interpolation node divided into two polynomials is about 2.5 times shorter than for the global case. Taking into account the 36 interpolation nodes, the time is even shorter by 3.5 times.

5.2 Inverse distance weighting

Second example concerns the cantilever beam presented in Fig. 8. The beam is end-loaded and is considered as plane stress. The material parameters for this example are: $E = 2*10^{11} Pa$ and $v = 0.25$. The Von Mises yield criterion is assumed to apply with $\sigma_Y = 20 Pa$ and $H' = 0$.

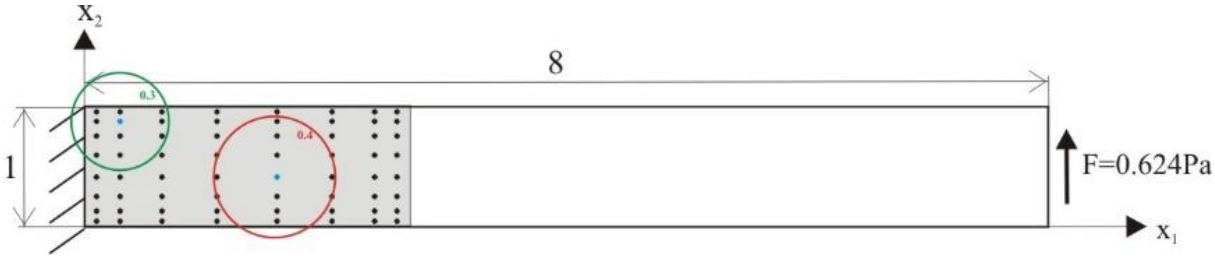

Figure 8: The considered cantilever beam

In the proposed method, like in BEM, only the plastic region is modeled. The considered example is described by the analytical solution, therefore the spread of that region is known a priori. Thus, not the whole domain must be defined, only its part presented in Fig. 8 (filled with gray). This requires only one Bézier bilinear surface with four corner points.

In [17] analytical formulas for elastic-plastic boundary and tip deflection are presented. In order to obtain those quantities using PIES 64 interpolation nodes are placed at roots of Chebyshev polynomials. Two methods of approximation are applied: the global approximation using Lagrange polynomial and IDW method. The power parameter is assumed as $p = 2$, while the radius of the neighborhood of influence are 0.3 and 0.4 (they are marked in Fig. 8 by green and red circles respectively). Of course it should be remembered that both radii are defined in the basic unit area. Obtained force-deflection values are presented in Fig. 9.

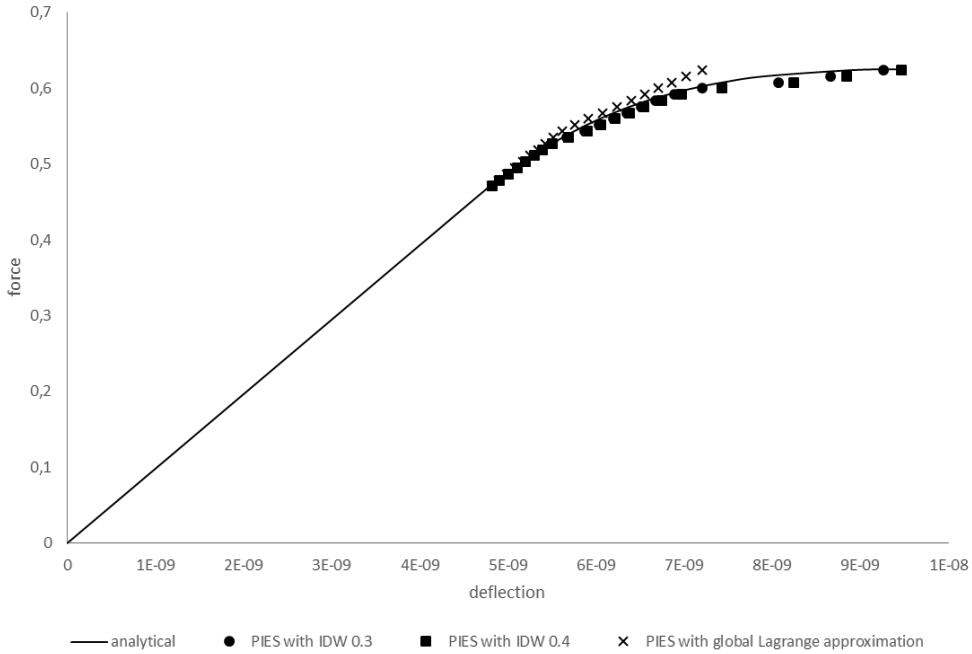

Figure 9: Force-deflection values for the cantilever beam

As can be seen in Fig. 9 solutions obtained by IDW with larger radius of neighborhood are slightly more accurate than those with a smaller radius. Both of them are more closer to analytical than those generated using global approximation with Lagrange polynomial. The latter reflect those obtained by FEM in [17].

Taking into account that slightly better results are obtained using larger radius of neighborhood in IDW method, the elastic-plastic boundary is determined using only this configuration. The boundary of the plastic zone determined analytically in comparison to plastified points obtained by PIES is presented in Fig. 10.

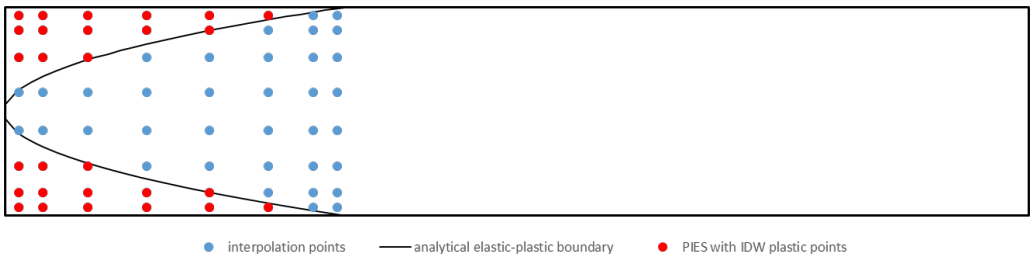

Figure 10: Comparison of plastic zones obtained by various method of approximation

As presented in Fig. 10, the spread of the plastic zone obtained by PIES with IDW method overlaps with analytical results. Having in mind also values of deflection shown above, it can be stated that the local approximation used in PIES method is very promising alternative to global approximation by various polynomials (e.g. Lagrange like in this paper).

6 CONCLUSIONS

The paper presents various methods of approximation of plastic strains in PIES. The PIES method is characterized by the global modeling of the plastic region, what gives the flexibility in application different approaches to approximation of solutions. Therefore, in the paper global and two local methods of approximation have been used. The first is zonally local, while the second takes into account only the influence of neighboring nodes.

Two examples were solved and results obtained were compared with analytical solutions. Moreover, numerical results obtained in the global manner are compared with the local one using different parameters.

It can be stated that using more than one approximation polynomial zonally is beneficial, because solutions obtained are more accurate. There was an improvement in accuracy up to 35%. Moreover, the time of calculations has decreased significantly (up to 3.5 times). Considering the IDW method applied to cantilever beam it is also shown that solutions obtained by local approach are more accurate than those received using global approximation.

REFERENCES

[1] Zienkiewicz, O.C. *The Finite Element Methods*. McGraw-Hill, (1977).

[2] Ameen, M. *Computational elasticity*. Alpha Science International Ltd., (2005).

[3] Aliabadi, M.H. *The boundary element method. Vol. 2. Applications in Solids and Structures*. John Wiley & Sons Ltd., (2002).

[4] Becker, A.A. *The boundary element method in engineering. A complete course*. McGraw-Hill, (1992).

[5] Zieniuk, E. Potential problems with polygonal boundaries by a BEM with parametric linear functions. *Engineering Analysis with Boundary Elements* (2001) **25(3)**: 185-190.

[6] Zieniuk, E. and Bołtuć, A. Bézier curves in the modeling of boundary geometry for 2D boundary problems defined by Helmholtz equation. *Journal of Computational Acoustics* (2006) **14(3)**: 353-367.

[7] Zieniuk, E. and Bołtuć, A. Non-element method of solving 2D boundary problems defined on polygonal domains modeled by Navier equation. *International Journal of Solids and Structures* (2006) **43(25-26)**: 7939-7958.

[8] Boltuc, A. and Zieniuk, E. Numerical approximation strategy for solutions and their derivatives for two-dimensional solids. *Applied Mathematical Modelling* (2015) **39(18)**: 5370-5391.

[9] Boltuc, A. Parametric integral equation system (PIES) for 2D elastoplastic analysis. *Engineering Analysis With Boundary Elements* (2016) **69**: 21-31.

[10] Farin, G. *Curves and surfaces for CAGD: A practical Guide*. Morgan Kaufmann Publishers, (2002).

[11] Salomon, D. *Curves and Surfaces for Computer Graphics*. Springer, (2006).

[12] Beer, G. and Smith, I. and Duenser, C. *The Boundary Element Method with Programming. For Engineers and Scientists*. Springer-Verlag Wien, (2008).

[13] Gao, X.W. Evaluation of regular and singular domain integrals with boundary-only discretization – theory and Fortran code. *Journal of Computational and Applied Mathematics* (2005) **175**: 265-290.

[14] Shepard, D. A two-dimensional interpolation function for irregularly-spaced data. Proceedings of the 1968 ACM National Conference (1968) 517–524, doi:10.1145/800186.810616.
[15] Liu, G.R. *Meshfree Methods: Moving Beyond the Finite Element Method*. CRC Press, (2009).
[16] Prager, R.M. and Hodge, P.G. *Theory of Perfectly Plastic Solids*. Dover Publications, (1951).
[17] Lubliner, J. *Plasticity theory*. Macmillan Publishing Company, (1990).

XIV International Conference on Computational Plasticity. Fundamentals and Applications
COMPLAS XIV
E. Oñate, D.R.J. Owen, D. Peric & M. Chiumenti (Eds)

IMPROVED APPROXIMATION OF ARBITRARY SHAPES IN DEM SIMULATIONS WITH MULTI-SPHERES

FABIAN WESTBRINK* AND ANDREAS SCHWUNG†

* South Westphalia University of Applied Sciences
Lübecker Ring 2, 59494 Soest, Germany
e-mail: westbrink.fabian@fh-swf.de, web page: http://www.fh-swf.de/cms/fat

†South Westphalia University of Applied Sciences
Lübecker Ring 2, 59494 Soest, Germany
e-mail: schwung.andreas@fh-swf.de, web page: http://www.fh-swf.de/cms/fat

Key words: Discrete Element Method (DEM), Multi-sphere, Clustering, Fuzzy C-means, Clump

Abstract. DEM simulations are originally made for spherical particles only. But most of real particles are anything but not spherical. Due to this problem, the multi-sphere method was invented. It provides the possibility to clump several spheres together to create complex shape structures. The proposed algorithm offers a novel method to create multi-sphere clumps for the given arbitrary shapes. Especially the use of modern clustering algorithms, from the field of computational intelligence, achieve satisfactory results. The clustering is embedded into an optimisation algorithm which uses a pre-defined criterion. A mostly unaided algorithm with only a few input and hyperparameters is able to approximate arbitrary shapes.

1 INTRODUCTION

Modern Discrete Element Method (DEM) simulation tools provide the use of multi-spheres instead of only spherical particles to approximate the shape of real material more precisely. The use of multi-spheres is a method of clumping several spheres together. The total number of spheres, positions, radii and overlapping between spheres in a clump can be adjusted to obtain a broad range of arbitrary shapes. Some modern simulation tools offer inherent functions to create custom clumps or present a range of several different templates. Also, the use of super-quadrics instead of multi-spheres is another way to obtain non-spherical particles which are available in some DEM tools. To be not restricted by vendors specifications, e.g. LIGGGHTS [1] offers the possibility to include user-defined clumps. These clumps are saved in files which only consists of the local Cartesian coordinates and the radius of each sphere of the multi-sphere clump. A creation of these files by approximate desired shapes and transfer them into sphere constellations needs an appropriate algorithm. This algorithm requires several different steps to create proper

approximations. It begins with analysing the given shape, initial filling of these shape with random spheres, efficient clustering and observing the obtained result. Generally, there are three objectives which have to be fulfilled within the approximation. To save computation time in DEM simulations, a sufficient approximation of desired shapes by using a minimum number of spheres per clump is required. Secondly, the number of spheres must be large enough to achieve an adequate surface representation. And finally, the applicability of this algorithm for expected shapes and an acceptable algorithm cycle time is to be ensured. A user-friendly functioning along with a minimum number of possible adjustments and mostly automatic algorithm is desired. The complete algorithm is currently based on a MATLAB script, but generally translatable to other programming languages.

2 MULTI-SPHERE APPROXIMATION

Often real shapes are given as 3D surface representation by using laser scan technology or stereo photogrammetry. The stereolithography (STL) file format is the standard presentation form in this context and represents the shape as complete mesh consisting of a distinct number of triangles. Also, standard CAD tools are usually able to translate drawings into this file format. Due to possible complex shape structures, appropriate algorithms are required to define and place single spheres converging to a multi-sphere clump. In general, there a three approaches to fill 3D shapes. Phillips et al. explain that in a two-dimensional space, by using either mono-disperse or poly-disperse disks, an approximation of shapes is possible by packing, covering or filling [2]. These approaches can also be converted into the three-dimensional space. Packing does not allow an overlapping of spheres and protruding the surface of the shape, covering allows overlapping as well as protruding to cover the complete surface and filling only allows overlapping of spheres but no protruding of the surface edges. Due to the fact that overlapping is not possible, packing usually requires a much higher amount of spheres to reach the desired approximation instead of using overlapping spheres. Only covering and filling provide the performance for modern approximation algorithms.
The general approach to approximate shapes and generate spheres starts with placing distinct or randomly chosen spheres within the shape's volume. Afterwards, an optimisation problem defines different criteria which are used to cluster and reduce afterwards the total number of spheres. Some algorithms have to consider the inertia and centre of gravity during the creation of the resulting clumps. Deviations in these properties from the original body and clump can significantly change the clump behaviour in the DEM simulation itself. The DEM tool LIGGGHTS offers, therefore, the opportunity to set these properties independently from the clump shape. This reduces the effort enormously during the approximation. Most attention is thus on the exact surface and volume representation.

2.1 Related work

A current clump generation tool developed by Price et al. is made with randomised sphere positions to fill initially thousands of spheres into a shape. The spheres are placed

assuming that it needs exactly four random points of the shape, nodes of the mesh, to form a distinct sphere with the centre position and radius. This filling yields finally to the issue, that most of the spheres are deleted afterwards because their centre is often outside the shape. So the post processing starts first with deleting of unnecessary spheres and then starts clustering the spheres [3]. The algorithm by [4], uses only three different parameters, the minimum distance between surface nodes and spheres, the minimum radii of spheres, the percentage number of nodes which are covered and uses thus no need of post processed clustering at all. Clustering methods in recent works are often based on heuristic algorithms, [5, 6] present their clustering as flow chart algorithms which use individual conditions to cluster the spheres to appropriate clumps. One way of validating the results is the off-volume criterion. This criterion, which is also used by [7], compares the original shape volume with the approximated volume of the final clump representation.
The algorithms often need a relatively large number of spheres per clump for proper approximation results. It depends on the one hand on the optimisation indicators or the possible hyperparameters and on the other hand on the clustering methodologies how much spheres per clump are computed. Particularly the clustering methods offer space for optimisation. But also the prior steps, filling and observing of the given mesh, up to the quality analysis have the potential for improvements. A complete algorithm for arbitrary shapes, which uses only a minimum of spheres for the approximation is not developed yet.

2.2 Problem Statement

The presented algorithms offer different ways to approximate shapes into multi-sphere clumps for DEM simulations. Creation of multi-sphere clumps is always a compromise between accuracy of approximation and the total number of spheres per clump. With increasing approximation quality the number of spheres increases as well. The quality of an approximation can be assumed as a grade of similarity to the original shape. With an infinite number of spheres an identical approximation can be achieved. With fewer spheres, a good approximation is performed when the dimensions of the shape are completely filled and the roughness of the obtaining sphere constellation is relatively smooth. How much spheres are needed for a proper approximation always depends on the complexity of the desired shape and the allowed multi-sphere method, overlapping or non-overlapping method. To reduce the computation time of DEM simulations there is basically the idea of minimising the number of spheres in complete DEM simulation. Increasing number of spheres always extend the total computation time. Due to the simulation purposes, the desired approximation quality varies significantly. A general rule is that with a rising number of clumps within one simulation run in the DEM simulation, the quality of the approximation, respectively number of sphere per clumps is negligible reduced. But otherwise, when the degree of approximation is of particular importance, the shape approximation requires more spheres per clump, hence the total number of clumps in DEM is there relatively small.
Summarised there are four requirements defined which have to be fulfilled by the improved approximation algorithm:

- Minimum number of spheres per clump to achieve short DEM simulation time
- Approximation for arbitrary shapes with overlapping multi-spheres with sufficient approximation quality
- Minimised number of possible input parameters - highly autonomous approximation

3 FILLING

The improved algorithm presented in this paper is based on the filling approach. The spheres of the multi-sphere clump may protrude the shapes surface or other spheres. These overlaps to other spheres increase, compared to non-overlapping spheres, the accuracy and smoothness of the surface representation as well as decreases the total number of spheres by the same roughness.The initial filling is made generally with random spheres. There it is also ensured that all of these sphere's centres are within the surface of the shape. Compared to the algorithm of [3], it is not necessary to delete unfitting spheres. Each sphere with its centre and radius covers or is in contact with at least one node. When a prior defined number of nodes is covered with spheres, is the filling process ended. Depending on the quality of the mesh and the total number of nodes in it, the number of the filled spheres may very significantly. This node based filling ensures compared to a distinct number of initial spheres that the mesh is appropriately filled. A variation of the percentage nodes which are covered is adjustable to reach optimal filling with a sufficient number of spheres by using arbitrary shapes. A restriction of too close centres is not required because of the clustering afterwards and the different radii of each sphere. The radii of all initial spheres, where each radius is defined as the minimum distance to next available node of the shapes mesh, are computed. This distance is defined as the euclidean distance in the three-dimensional space, for each centre to its closest node, which is defined as:

$$d(n, c) = \sum_{i=1}^{3} \sqrt{(n_i - c_i)^2}. \tag{1}$$

To find the minimum distance and thus the closest node, each sphere compares the distances to all nodes iteratively. These smallest distances are now set as radii. Figure 1 shows a randomly set sphere inside a STL mesh, which radius is adapted to the distance D to the closest node. This sphere covers not only the contacted node but surrounding nodes as well. Depending on the shapes structure and the meshing quality it makes sense to increase the radius with a particular offset to ensure that most of the nodes are covered. When the desired number of nodes is covered with spheres, the filling process usually ends with up to several thousand spheres.

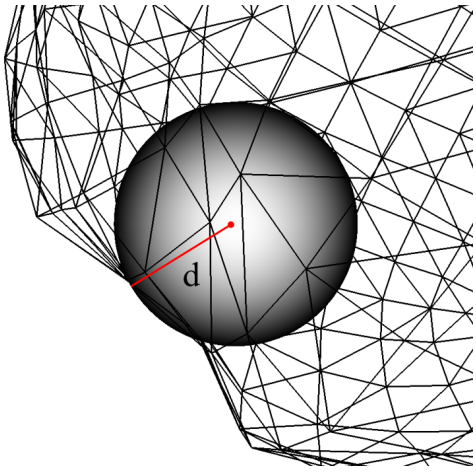

Figure 1: Define radius of initial sphere

The complete filling of the given shape by using this large number of spheres close to optimal. Figure 2a shows the original shape of a common piece of stone. This shape consists of close to 400 nodes, and thus moderate accuracy or quality. The few thousands of spheres in 2b are in the next step clustered and the total number reduced by using an optimisation algorithm and the off-volume criterion. To run the optimisation algorithm and thus the clustering properly, it is necessary to calculate or estimate the resulting volume of the clump in each optimisation step.

(a) Original shape

(b) Randomly filled clump

Figure 2: Initial filling

4 OPTIMISATION

Considering only two circles which are overlapping, calculating the entire volume of this resulting shape is trivially done by adding the volume of both circles and subtract once the intersection sector. This methodology can be also transferred into the three-dimensional space by using spheres instead of circles. But this analytical calculation is only possible with the intersection of maximum two spheres. When n spheres overlap together in one intersection, only a numerical volume estimation is possible . A recent methodology is the use of a Monte Carlo estimation by using random numbers. Another possibility is a discretized scan of the clump area into sufficiently small pieces with a

regular grid, which eliminates the uncertain factor of random numbers but needs more computation time. Depending on the dimensions of the shape, it is ensured that the grid is precise enough to compute the resulting volume sufficiently accurate.
One option to define the quality of an approximation is to observe the accuracy of the volume representation. The volume criterion, in general, does not give any information about the clump's roughness or surface quality. But when the resulting volume of multiple spheres reaches as close as possible the original volume, particularly when the dimensions of the spheres protrude the original mesh, the surface quality is also sufficient. The volume criterion is following defined as the ratio between the calculated off-volume of the resulting clump and the original volume of the input shape,

$$C_{vol}(n) = \frac{V_{off}(n)}{V_{Original}}, \tag{2}$$

where the off-volume changes with the total number of spheres n in the clump. This volume criterion or off-volume ratio is used as optimisation hyperparameter. The optimum is found when the ratio between off-volume and original volume is exactly one. It can be assumed that, as closer this ratio becomes to one, the quality of the approximation rises. The original volume, if unless not already available, is either read out with appropriate CAD software tools or computed with a convex hull of the mesh in the MATLAB script itself. Depending on the allowed protruding and on the complexity of the given shape, an off-volume ratio between $0.85 - 1$ yields to sufficient approximations.
The optimisation reduces the number of spheres by clustering them. As already said the volume criterion is used as hyperparameter for this optimisation. When the resulting clump grows up to the prior defined off-volume ratio, the clustering stops and outputs the final clump. Hence, this optimisation starts with a low number of clusters and increases them iteratively.

5 CLUSTERING

After the initial filling process, the shape approximation is made with several thousand spheres. Often the spheres centres are very close to each other, create dense areas, or the spheres overlap for the most part. In these cases, an exchange of these spheres against one single sphere, which represents a similar extension, is an advantage. These grouping of spheres, or data sets, is called clustering.
In the field of computational intelligence or machine learning, clustering belongs to the subfield of unsupervised learning. Instead of supervised learning, unsupervised learning considers only the input data without any consideration of the output information. Clustering always uses input data sets with n dimensions as vectors $x_1, ..., x_n$. In this application, the centre x_c, y_c, z_c and the radius r of each sphere are used as the input vector. The resulting clusters then also consist of a centroid with an appropriate radius. The most common and simplest clustering algorithm is the k-means clustering. As firstly explained by [8], this algorithm uses k numbers of clusters. To start the algorithm the total amount of k clusters and its centroids are priorly defined in the data set space. With every optimisation step, the input sets are assigned to nearest centroid by calculat-

ing the euclidean distance between them. After the assignment is done for all sets, the centroids position is updated according to the arithmetic mean of all assigned sets. This cost function is defined in the following equation:

$$J = \sum_{i=1}^{k} \sum_{x_j \in S_i} ||x_j - \mu_i||^2, \tag{3}$$

where J is the objective function which should be minimised with the sum of squares from each cluster k with its mean μ_k to every data point of S_i [8]. Due to this, it is clear that this clustering needs a prior defined number of different clusters. Because the clusters also define the number and positions of the spheres in the clump afterwards, a prediction of the number of spheres which are necessary for an arbitrary shape needs to be performed. But this prediction, especially for very complex structures, cannot be done easily. With different numbers of spheres, the expected volume and surface roughens changes. So, an overall optimisation, which increases the number of spheres iteratively and checks at each iteration the volume criterion is assigned to it. A major disadvantage of k-means clustering to obtain spheres properties for multi-sphere approximation is that the resulting clusters do not overlap at all. Each input data set is only assigned to one distinct cluster. And non-overlapping clump requires significantly more spheres to reach the same volume instead of overlapping clumps which is not feasible with k-means clustering. Therefore, for an optimal approximation, another clustering method is recommended.

5.1 Fuzzy clustering

Fuzzy clustering or fuzzy c-means clustering is an enhanced version of the conventional k-means clustering, developed first by [9]. This clustering algorithm extends the hard clustering k-means by a soft, fuzzy, attribute. Instead of a distinct assignment of each input data set to only one cluster, fuzzy c-means clustering allows an assignment to several clusters at the same time. How much percent one input set belongs to different clusters is defined as membership degree. Generally, the algorithm works similar to k-means, with defining a number of clusters, in this case, c, place them initially and optimise the mean of assigned sets, but with the enhancement of degree of membership and results following as

$$J = \sum_{i=1}^{C} \sum_{j=1}^{N} \mu_{ij}^{m} ||x_i - c_j||^2, \tag{4}$$

where for each cluster, the membership degree is defined as u_{ik} between 0 and 1, but the sum of all membership degrees is always 1 [9]. The partition matrix m can be set between 1 and ∞ and defines the degree of memberships. When m equals to 1, it represents hard clustering and the results are identical to k-means, if it is close to infinity the membership degree for all sets becomes equal. An adjustment of the m parameter defines the grade of membership or overlapping [9]. The grade of overlapping can be used afterwards to define how close the different centroids are placed and how much spheres per clump fit to the

volume criterion. It has been shown that values of m between 1.5 to 3.0 yield an optimal approximation. Compared to k-means clustering, fuzzy c-means clustering requires more computation time, especially when the partition matrix is also iteratively optimised.

6 APPROXIMATION PROCESS

The described improved approximation algorithm of arbitrary shapes with the overlapping multi-sphere method can be analysed in four steps. The first step analyses the desired shape, observes its nodes and defines its volume. The second step fills the shape's dimension with random spheres. These spheres are defined to cover almost one node of the shape's mesh and the radii are equal to the distance to the closest node. The filling stops when a distinct percentage of nodes is covered by spheres. Thirdly runs the optimisation with fuzzy clustering which reduces the total number of spheres rapidly. The fuzzy c-means clustering is implemented, due to the fact that overlapping of spheres can be represented by a partition matrix which fits perfectly for the creation of multi-spheres. By changing the value of the membership degree the grade of overlapping can be set. The partition matrix is changed iteratively to find a sufficient overlapping. When the desired volume criterion is reached, the optimisation stops automatically. The complete algorithm is shown as pseudo code in algorithm 1. There it is also shown that the resulting clump, with all necessary information, is stored afterwards in a file which fits the requirements of the LIGGGHTS DEM simulation tool.

Algorithm 1 Shape Approximation

Input Shape as STL file
Create Bounding Box
$V_{Original} = Volume(STL)$
while $NodesCovered <= NodesPercentage$ **do**
    $i = 0$
    $Sphere_{Centre}(i) = Random(BoundingBox)$ ▷ Centre in Bounding Box
    if $inhull = (Sphere_{Centre}(i), STL)$ **then** ▷ Centre inside STL mesh
        $Sphere_{Radius}(i) = EuclideanDistance(Sphere_{Centre}(i), STL)$
    $NodesCovered = Cover(Sphere_{Centre}(i), Sphere_{Radius}(i), STL)$
    i++
$clusters = 1$
while $Volume_{Criterion} >= V_{Off}/V_{Original}$ **do** ▷ Optimisation with volume criterion
    for $m = 1.5$ to $m = 3.0$ **do**
        $Cluster(Centre, Radius) = Fuzzy(Sphere_{Centre}, Sphere_{Radius}, m, clusters)$
        $V_off = Volume(Cluster)$
    $clusters++$
$WriteMultiSphere(Clusters)$ ▷ Create Multi-Sphere file

7 RESULTS

The approximation algorithm is generally made for every arbitrary shape, which is available as STL files. Shapes with other file formats are previously to export in binary or ASCII STL format. It starts with a random placement of spheres inside the mesh until the particular percentage of all node is covered with spheres. The given shapes as STL mesh can be arbitrary, but for a huge number of nodes in the mesh, the computational time significantly increases. Therefore, in some cases, the mesh has to be simplified and the number of nodes to be reduced.

It is shown in figure 3 that different arbitrary shapes can be approximated appropriately by using a different number of overlapping spheres. Especially the approximations in figures 3b and 3c, with very complex meshes, are well approximated with only a few spheres. A prior adjustment of the approximation can be done by defining, on the one hand, the percentage of nodes which are covered with spheres in the initial phase and on the other hand the value of the off-volume criterion. Also, it is possible to let the spheres protrude out of the shape to decrease the surface roughness. The approximation in figure 3 is made with 90% covered nodes of the original mesh and an off-volume criterion of 90%. Be defining only these three parameters it is possible to get sufficient approximations for nearly each shape by considering the inherent inaccuracies of the multi-sphere method itself. The number of resulting sphere per clump is an appropriate range to simulate multi-spheres in DEM simulation shortly, also with a large number of clumps. Figure 4 shows how the number of spheres per clump varies with the different off-volume criteria.

A shape approximation of < 0.7 off-volume ratio often gives poor results and is useless for appropriate DEM simulations. The quality increases noticeably in the range between $0.7 - 0.9$ and the number of spheres is an adequate range. In the range of $0.95 - 1$, the number of spheres is significantly high and the approximation benefits are hardly present. Furthermore, the computation time of the approximation algorithm itself and later the DEM simulation becomes comparatively too high. After satisfactory results from the clustering algorithm, the spheres properties are stored in an input file for the DEM simulation. The clustering algorithm creates the Cartesian coordinates as the position of the spheres in the clump. Finally, the information about the centre coordinates with their radii is stored in a file which is readable in LIGGGHTS. As specified in section 2, information about the centre of mass or inertia tensor could be additional set in the LIGGGHTS input script. LIGGGHTS changes internally the density of each sphere in the clump to fit these mechanical properties.

To employ the algorithm for other DEM tools is not a tedious task. The multi-sphere file is modifiable for all necessary data types and thus usable for other DEM tools.
The computation time of the approximation depends on several criteria. Firstly, the quality of the shape, the complexity and the accuracy or resolution of the mesh influences the computation time. Also, the desired off-volume ration, which is mostly responsible for the number of spheres in the clump, is a factor for computation time. For arbitrary shapes, the default parameter values create sufficient results, but for well-known shapes,

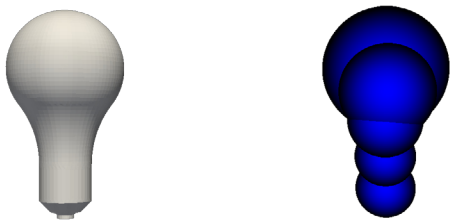

(a) Light bulb; $n = 12 spheres$

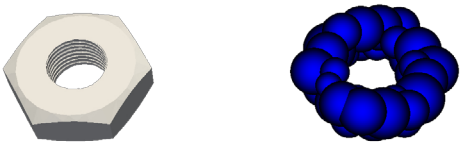

(b) Nut; $n = 36 spheres$

(c) Stone; $n = 37 spheres$

Figure 3: Shape approximations

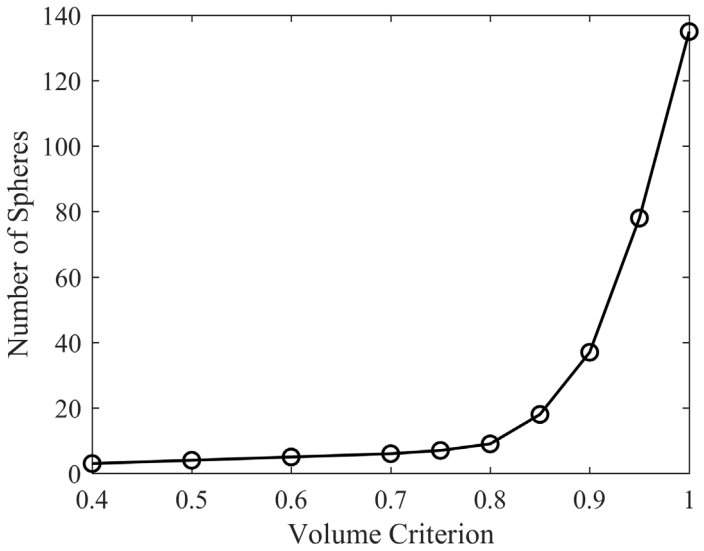

Figure 4: Changing number of spheres with volume criterion

the parameters can be improved to obtain faster computation time and better results.

8 CONCLUSIONS

The presented algorithm offers the ability to approximate arbitrary shapes with a low number of spheres. An optimisation with the volume criteria shows good results not only for the complete filling of the desired shape but also a smooth surface roughness. The upcoming need of arbitrary shapes in DEM simulation reasons rising effort of improved approximation algorithms. Especially the use of fuzzy c-means clustering performs inherent good results for overlapping multi-sphere representations.

Further improvements shall translate the MATLAB script into a LIGGGHTS in-build function. This would offer the possibility to call the desired shape as STL mesh within the LIGGGHTS input script and an approximation runs inside the DEM simulation. Also, other clustering algorithms like density bases clustering are under observation. Especially improvements in the roughness quality of the approximation and reducing of the computation time of the algorithm are foreseen.

REFERENCES

[1] C. Kloss, C. Goniva, A. Hager, S. Amberger, and S. Pirker, "Models, algorithms and validation for opensource dem and cfd-dem," *Progress in Computational Fluid Dynamics, An International Journal*, vol. 12, no. 2/3, p. 140, 2012.

[2] C. L. Phillips, J. A. Anderson, G. Huber, and S. C. Glotzer, "Optimal filling of shapes," *Physical review letters*, vol. 108, no. 19, p. 198304, 2012.

[3] M. Price, V. Murariu, and G. Morrison, "Sphere clump generation and trajectory comparison for real particles," *Proceedings of Discrete Element Modelling 2007*, 2007.

[4] J.-F. Ferellec and G. R. McDowell, "A method to model realistic particle shape and inertia in dem," *Granular Matter*, vol. 12, no. 5, pp. 459–467, 2010.

[5] X. Garcia, J.-P. Latham, J. Xiang, and J. P. Harrison, "A clustered overlapping sphere algorithm to represent real particles in discrete element modelling," *Géotechnique*, vol. 59, no. 9, pp. 779–784, 2009.

[6] C.-Q. Li, W.-J. Xu, and Q.-S. Meng, "Multi-sphere approximation of real particles for dem simulation based on a modified greedy heuristic algorithm," *Powder Technology*, vol. 286, pp. 478–487, 2015.

[7] S. Amberger, M. Friedl, C. Gonvia, S. Pirker, and C. Kloss, "Approximation of objects by spheres for multisphere simulations in dem," *ECCOMAS*, 2012.

[8] J. MacQueen, "Some methods for classification and analysis of multivariate observations," in *Proceedings of the Fifth Berkeley Symposium on Mathematical Statistics and Probability, Volume 1: Statistics*. University of California Press, 1967, pp. 281–297.

[9] J. C. Bezdek, *Pattern Recognition with Fuzzy Objective Function Algorithms*, ser. Advanced Applications in Pattern Recognition. Boston, MA: Springer, 1981.

XIV International Conference on Computational Plasticity. Fundamentals and Applications
COMPLAS XIV
E. Oñate, D.R.J. Owen, D. Peric & M. Chiumenti (Eds)

LIMIT ANALYSIS PROBLEM AND ITS PENALIZATION

Stanislav Sysala*

* Institute of Geonics, Czech Academy of Sciences
Department of Applied Mathematics and Computer Sciences & Department IT4Innovations
Studentská 1768, 708 00 Ostrava, Czech Republic
e-mail: stanislav.sysala@ugn.cas.cz - web page: http://www.ugn.cas.cz/˜sysala

Key words: perfect plasticity, limit analysis, truncation method, indirect incremental method

Abstract. The contribution is focused on solution of the kinematic limit analysis problem within associative perfect plasticity. It is a constrained minimization problem describing a collapse state of an investigated body. Two different penalization methods are presented and interpreted as the truncation method and the indirect incremental method, respectively. It is shown that both methods are meaningful even within the continuous setting of the problem. Convergence with respect to penalty and discretization parameters is discussed. The indirect incremental method can be simply implemented within current elastoplastic codes.

1 Introduction

Existence of the limit load is a feature of elastic-perfectly problems. It is well-known that an investigated body collapses when the limit value of a load parameter is exceeded [4, 16]. Strip-footing collapse or slope stability are traditional geotechnical applications, where the limit load analysis is important (see, e.g., [3, 5, 10]). We focus only on associative perfect plasticity, although the limit analysis is also meaningful for nonassociative elastoplastic models with internal variables [10, 17].

The collapse state can be described by a special variational problem, the so-called *limit analysis problem* [4, 16, 17]. It leads to a minimization of a convex functional subject to various constraints, when the kinematic approach is considered. The constraints depend on a prescribed yield function and they can cause locking phenomena. Therefore, mixed finite elements are often used for solution of such problems [1, 4].

In order to suppress the constraints, we introduce two different penalization methods for the kinematic limit analysis problem. These methods can be interpreted as the truncation method and the indirect incremental method, respectively. Both methods have been analyzed in recent papers [2, 7, 8, 15, 14], can be used for various yield criteria and lead to simple numerical techniques. Here, we recapitulate main results of these papers and slightly generalize the indirect method of incremental limit analysis.

The rest of the contribution is organized as follows. In Section 2, evolution variational formulations of the associative elastic-perfectly plastic problem with an abstract yield criterion are summarized. The implicit Euler discretization of the problem is introduced in Section 3. In Section 4, the static and kinematic limit analysis problems are formulated. In Section 5, the truncation and indirect incremental methods are derived by penalization of the kinematic limit analysis problem. The finite element approximation is discussed. In Section 6, the indirect method of incremental limit analysis is combined with Newton-like method.

2 Associative elastic-perfectly plastic problem

Assume that the investigated body occupies a bounded domain $\Omega \subset \mathbb{R}^3$ with the Lipschitz continuous boundary $\partial\Omega = \bar{\Gamma}_f \cup \bar{\Gamma}_u$ where Γ_f, Γ_u are open in $\partial\Omega$, mutually disjoint and $\Gamma_u \neq \emptyset$. On Γ_f, Γ_u, we prescribe the Neumann and the homogeneous Dirichlet boundary conditions, respectively.

We denote $\mathbb{R}^{3\times3}_{sym}$ as the space of symmetric second order tensors. The biscalar product and the corresponding norm in $\mathbb{R}^{3\times3}_{sym}$ will be denoted by $\boldsymbol{e} : \boldsymbol{\eta} = e_{ij}\eta_{ij}$ and $|\boldsymbol{e}|^2 = \boldsymbol{e} : \boldsymbol{e}$ for any $\boldsymbol{e}, \boldsymbol{\eta} \in \mathbb{R}^{3\times3}_{sym}$, respectively. Let

$$V = \{\boldsymbol{v} \in W^{1,2}(\Omega;\mathbb{R}^3) \mid \boldsymbol{v}|_{\Gamma_u} = \boldsymbol{0}\} \quad \text{and} \quad Q = L^2(\Omega;\mathbb{R}^{3\times3}_{sym}) \tag{1}$$

be the spaces of for displacement and stress (strain) fields with respect to the space variable $\boldsymbol{x} \in \Omega$. Suitable functional spaces with respect to the pseudo-time variable $t \in (0,T)$ can be found e.g. in [6].

We use the standard notation $\boldsymbol{\sigma}$, $\boldsymbol{\varepsilon}$, $\boldsymbol{\varepsilon}^p$, $\boldsymbol{u}$ for a stress tensor, a strain tensor, a plastic strain tensor, and a displacement vector, respectively, and assume that these unknown quantities depend on $\boldsymbol{x} \in \Omega$ and $t \in (0,T)$. Under the small strain assumption, we arrive at $\boldsymbol{\varepsilon} := \varepsilon(\boldsymbol{u})$, where $\varepsilon(\boldsymbol{v}) = \frac{1}{2}(\nabla\boldsymbol{v} + (\nabla\boldsymbol{v})^T)$ for any $\boldsymbol{v} \in V$. Further, we consider the linear relation between the stress and the elastic strain: $\boldsymbol{\sigma} = \mathbb{C}(\boldsymbol{\varepsilon} - \boldsymbol{\varepsilon}^p)$, where $\mathbb{C}$ denotes the fourth order elastic tensor representing the Hooke law.

The load functional

$$\ell_t(\boldsymbol{v}) = \int_\Omega \boldsymbol{F}\cdot\boldsymbol{v}\,d\boldsymbol{x} + \int_{\Gamma_f} \boldsymbol{f}\cdot\boldsymbol{v}\,d\boldsymbol{s}, \quad \boldsymbol{v} \in V,\ t \in (0,T),$$

consists of the volume forces $\boldsymbol{F} := \boldsymbol{F}(\boldsymbol{x},t)$ and the surface forces $\boldsymbol{f} := \boldsymbol{f}(\boldsymbol{x},t)$ applied on the part Γ_f of the boundary $\partial\Omega$. Then the weak formulation of the equilibrium equation reads as

$$\int_\Omega \boldsymbol{\sigma} : \varepsilon(\boldsymbol{v})\,d\boldsymbol{x} = \ell_t(\boldsymbol{v}) \quad \forall \boldsymbol{v} \in V,\ \forall t \in (0,T). \tag{2}$$

In order to introduce the plastic flow rule, we define at first the set

$$B = \{\boldsymbol{\tau} \in \mathbb{R}^{3\times3}_{sym} \mid \varphi(\boldsymbol{\tau}) \le 0\}, \tag{3}$$

of plastically admissible stress tensors. We let the function $\varphi\colon \mathbb{R}^{3\times3}_{sym} \to \mathbb{R}$ in an abstract form and assume that φ is convex and satisfies $\varphi(\boldsymbol{0}) < 0$. Using the principle of maximum

plastic dissipation, the plastic flow rule reads as

$$\dot{\boldsymbol{\varepsilon}^p} : (\boldsymbol{\tau} - \boldsymbol{\sigma}) \leq 0 \quad \forall \boldsymbol{\tau} \in B,\ \forall t \in (0,T). \tag{4}$$

Notice that the flow rule can also be defined in literature by different ways. For example, one can use the Karush-Kuhn-Tucker conditions and write [5, 12, 13]:

$$\dot{\boldsymbol{\varepsilon}^p} \in \dot{\lambda} \partial \varphi(\boldsymbol{\sigma}), \quad \dot{\lambda} \geq 0,\ \ \varphi(\boldsymbol{\sigma}) \leq 0,\ \ \dot{\lambda}\varphi(\boldsymbol{\sigma}) = 0,$$

where $\partial\varphi(\boldsymbol{\sigma})$ denotes the subdifferential of φ at $\boldsymbol{\sigma}$ and $\dot{\lambda}$ is the plastic multiplier. Making use of the convex duality, one can also write the flow rule as follows [6]:

$$-\boldsymbol{\sigma} : (\boldsymbol{q} - \dot{\boldsymbol{\varepsilon}^p}) + I_B^*(\boldsymbol{q}) - I_B^*(\dot{\boldsymbol{\varepsilon}^p}) \geq 0 \quad \forall q \in \mathbb{R}^{3\times 3}, \tag{5}$$

where

$$I_B^*(\boldsymbol{q}) := \sup_{\boldsymbol{\tau} \in B} \boldsymbol{\tau} : \boldsymbol{q} \tag{6}$$

denotes the dissipation potential and simultaneously, the dual function to the indicator function I_B of the set B.

To complete the model, we consider the following initial conditions:

$$\boldsymbol{u}(0) = \boldsymbol{u}_0,\ \ \boldsymbol{\varepsilon}^p(0) = \boldsymbol{\varepsilon}_0^p,\ \ \boldsymbol{\varepsilon}(0) = \varepsilon(\boldsymbol{u}_0),\ \ \boldsymbol{\sigma}(0) = \mathbb{C}(\varepsilon(\boldsymbol{u}_0) - \boldsymbol{\varepsilon}_0^p) \quad \text{in } \Omega. \tag{7}$$

The elastoplastic problem in terms of stresses leads to the following evolution variational inequality:

$$\begin{cases} \text{find } \boldsymbol{\sigma} := \boldsymbol{\sigma}(t) \in \Lambda_t \cap P: \quad \int_\Omega \mathbb{C}^{-1}\dot{\boldsymbol{\sigma}} : (\boldsymbol{\tau} - \boldsymbol{\sigma})\, d\boldsymbol{x} \geq 0 \quad \forall \boldsymbol{\tau} \in \Lambda_t \cap P,\ \ \forall t \in (0,T), \\ \Lambda_t = \{\boldsymbol{\tau} \in Q \mid \int_\Omega \boldsymbol{\tau} : \varepsilon(\boldsymbol{v})\, d\boldsymbol{x} = \ell_t(\boldsymbol{v}) \quad \forall \boldsymbol{v} \in V\},\ \ P = \{\boldsymbol{\tau} \in Q \mid \boldsymbol{\tau}(\boldsymbol{x}) \in B,\ \forall \boldsymbol{x} \in \Omega\}. \end{cases} \tag{8}$$

Notice that problem (8) can be derived inserting $\dot{\boldsymbol{\varepsilon}}^p = \mathbb{C}^{-1}\dot{\boldsymbol{\sigma}} - \varepsilon(\dot{\boldsymbol{u}})$ to the flow rule (4), integrating over Ω and using the definition of Λ_t. One can analyze existence and uniqueness of the solution to (8) under the assumption on the *save load condition* [6]:

$$\forall t \in (0,T)\ \exists \boldsymbol{\tau} \in \Lambda_t \cap P. \tag{9}$$

As we will see, the verification of (9) is closely related to the limit load analysis.

The problem can also be formulated in terms of displacements and plastic strains by using the dual flow rule (5) and inserting $\boldsymbol{\sigma} = \mathbb{C}(\varepsilon(\boldsymbol{u}) - \boldsymbol{\varepsilon}^p)$ to (2) and (5):

$$\int_\Omega \mathbb{C}(\varepsilon(\boldsymbol{u}) - \boldsymbol{\varepsilon}^p) : [\varepsilon(\boldsymbol{v} - \dot{\boldsymbol{u}}) - (\boldsymbol{q} - \dot{\boldsymbol{\varepsilon}^p})]\, d\boldsymbol{x} + \int_\Omega I_B^*(\boldsymbol{q})\, d\boldsymbol{x} - \int_\Omega I_B^*(\dot{\boldsymbol{\varepsilon}^p})\, d\boldsymbol{x} \geq \ell_t(\boldsymbol{v} - \dot{\boldsymbol{u}}), \tag{10}$$

for any $(\boldsymbol{v}, \boldsymbol{q}) \in V \times Q$ and any $t \in (0,T)$. It is well-known that (10) is a dual problem to (8) and its solvability cannot be studied on the Sobolev space V but on BD-spaces with bounded deformations [16] similarly as other problems formulated below in terms of displacements.

3 Implicit discretization of the quasistatic problem

As we shall see, the limit analysis problem presented in Section 4 is independent of the pseudo-time parameter t. Despite this fact, we introduce a time discretization of the problem since it will be useful for an interpretation a penalty method studied in Section 5.

Consider a partition $0 = t_0 < t_1 < \ldots < t_N = T$ of the interval [0,T] and approximate the plastic strain rate by the implicit Euler scheme:

$$\dot{\boldsymbol{\varepsilon}}^p(t_k) \approx \frac{\boldsymbol{\varepsilon}_k^p - \boldsymbol{\varepsilon}_{k-1}^p}{t_k - t_{k-1}}, \quad \boldsymbol{\varepsilon}_k^p := \boldsymbol{\varepsilon}^p(t_k), \quad k = 1, 2, \ldots, N.$$

It is well-known that discrete counterparts of problems (8) and (10) can be arranged as the following minimization problems, respectively [6]:

$$\left\{ \begin{array}{c} \text{given } \boldsymbol{\sigma}_{k-1} \in Q, \text{ find } \boldsymbol{\sigma}_k \in \Lambda_k \cap P: \quad \mathcal{J}_k^*(\boldsymbol{\sigma}_k) \le \mathcal{J}_k^*(\boldsymbol{\tau}) \quad \forall \boldsymbol{\tau} \in \Lambda_k \cap P, \\ \mathcal{J}_k^*(\boldsymbol{\tau}) = \frac{1}{2}\int_\Omega \mathbb{C}^{-1}\boldsymbol{\tau} : \boldsymbol{\tau}\, d\boldsymbol{x} - \int_\Omega \mathbb{C}^{-1}\boldsymbol{\sigma}_{k-1} : \boldsymbol{\tau}\, d\boldsymbol{x}, \quad \Lambda_k \equiv \Lambda_{t_k}, \end{array} \right. \tag{11}$$

$$\left\{ \begin{array}{c} \text{given } \boldsymbol{\varepsilon}_{k-1}^p \in Q, \text{ find } (\boldsymbol{u}_k, \boldsymbol{\varepsilon}_k^p) \in V \times Q: \quad \mathcal{I}_k(\boldsymbol{u}_k, \boldsymbol{\varepsilon}_k^p) \le \mathcal{I}_k(\boldsymbol{v}, \boldsymbol{q}) \quad \forall (\boldsymbol{v}, \boldsymbol{q}) \in V \times Q, \\ \mathcal{I}_k(\boldsymbol{v}, \boldsymbol{q}) = \frac{1}{2}\int_\Omega \mathbb{C}(\varepsilon(\boldsymbol{v}) - \boldsymbol{q}) : (\varepsilon(\boldsymbol{v}) - \boldsymbol{q})\, d\boldsymbol{x} + \int_\Omega I_B^*(\boldsymbol{q} - \boldsymbol{\varepsilon}_{k-1}^p)\, d\boldsymbol{x} - \ell_k(\boldsymbol{v}). \end{array} \right. \tag{12}$$

Unlike the evolution problem, the discretized problem can also be formulated only in terms of displacements. To this end, we introduce the mapping $\Pi_B : \mathbb{R}^{3\times3}_{sym} \to B$ such that

$$\Pi_B : \boldsymbol{e} \mapsto \boldsymbol{\sigma}, \quad (\boldsymbol{e} - \mathbb{C}^{-1}\boldsymbol{\sigma}) : (\boldsymbol{\tau} - \boldsymbol{\sigma}) \le 0 \quad \forall \boldsymbol{\tau} \in B. \tag{13}$$

It is easy to see that $\Pi_B(\boldsymbol{e})$ represents the closest projection of $\mathbb{C}\boldsymbol{e}$ onto B with respect to the scalar product $\mathbb{C}^{-1}\boldsymbol{\tau} : \boldsymbol{e}$ in $\mathbb{R}^{3\times3}_{sym}$. Comparing (13) with (4), the discrete flow rule can be written as follows:

$$\boldsymbol{\sigma}_k = \Pi_B(\varepsilon(\boldsymbol{u}_k) - \boldsymbol{\varepsilon}_{k-1}^p). \tag{14}$$

Inserting (14) to the equilibrium equation (2), we arrive at the following problem:

$$\text{given } \boldsymbol{\varepsilon}_{k-1}^p \in Q, \text{ find } \boldsymbol{u}_k \in V: \quad \int_\Omega \Pi_B(\varepsilon(\boldsymbol{u}_k) - \boldsymbol{\varepsilon}_{k-1}^p) : \varepsilon(\boldsymbol{v})\, d\boldsymbol{x} = \ell_k(\boldsymbol{v}) \quad \forall \boldsymbol{v} \in V. \tag{15}$$

Further, it is well-known that there exists the potential to Π_B (see, e.g., [11]):

$$\Psi_B(\boldsymbol{e}) = \sup_{\boldsymbol{\tau} \in B}\{\boldsymbol{\tau} : \boldsymbol{e} - \frac{1}{2}\mathbb{C}^{-1}\boldsymbol{\tau} : \boldsymbol{\tau}\}, \quad \boldsymbol{e} \in \mathbb{R}^{3\times3}_{sym}, \tag{16}$$

i.e., $\partial\Psi_B(\boldsymbol{e})/\partial\boldsymbol{e} = \Pi_B(\boldsymbol{e})$. Hence, problem (17) can be equivalently rewritten as the minimization problem

$$\mathcal{J}_k(\boldsymbol{u}_k) \le \mathcal{J}_k(\boldsymbol{v}) \ \ \forall \boldsymbol{v} \in V, \quad \mathcal{J}_k(\boldsymbol{v}) = \int_\Omega \Psi_B(\varepsilon(\boldsymbol{u}_k) - \boldsymbol{\varepsilon}_{k-1}^p)\, d\boldsymbol{x} - \ell_k(\boldsymbol{v}). \tag{17}$$

Notice that the functionals $\mathcal{I}_k$ and $\mathcal{J}_k$ are related as follows:

$$\min_{\boldsymbol{q} \in Q} \mathcal{I}_k(\boldsymbol{v}, \boldsymbol{q}) = \mathcal{J}_k(\boldsymbol{v}) \quad \forall \boldsymbol{v} \in V, \ \forall k = 0, 1, 2, \ldots$$

4 Limit load analysis

From now on, we consider the load functional in the form

$$\ell_t(\boldsymbol{v}) = L_0(\boldsymbol{v}) + tL(\boldsymbol{v}), \quad \boldsymbol{v} \in V, \tag{18}$$

where the functionals L_0 and L_1 are independent of t and satisfy:

$$\exists \boldsymbol{\tau}_0 \in P: \quad \int_\Omega \boldsymbol{\tau}_0 : \varepsilon(\boldsymbol{v})\, d\boldsymbol{x} = L_0(\boldsymbol{v}) \quad \forall \boldsymbol{v} \in V, \tag{19}$$

$$\exists \hat{\boldsymbol{v}} \in V: \quad L(\hat{\boldsymbol{v}}) \neq 0. \tag{20}$$

Under the assumption (19), the following implication holds:

$$\text{if} \quad \Lambda_T \cap P \neq \emptyset \quad \text{then} \quad \Lambda_t \cap P \neq \emptyset \ \ \forall t \in (0,T). \tag{21}$$

Hence, $\Lambda_T \cap P \neq \emptyset$ is a sufficient condition for the save load (9).

Within the limit analysis, the fixed value T is not prescribed. Instead of this, the limit value t^* of the parameter t is searched:

$$t^* = \sup\{t \geq 0 \mid \Lambda_t \cap P \neq \emptyset\} = \sup_{\boldsymbol{\tau} \in P} \inf_{\substack{\boldsymbol{v} \in V \\ L(\boldsymbol{v})=1}} \left\{ \int_\Omega \boldsymbol{\tau} : \varepsilon(\boldsymbol{v})\, d\boldsymbol{x} - L_0(\boldsymbol{v}) \right\}. \tag{22}$$

The problem (22) is known as the static principle of the limit analysis. The kinematic principle is dual to the static one and leads to the following minimization problem:

$$\bar{t} = \inf_{\substack{\boldsymbol{v} \in V \\ L(\boldsymbol{v})=1}} \sup_{\boldsymbol{\tau} \in P} \left\{ \int_\Omega \boldsymbol{\tau} : \varepsilon(\boldsymbol{v})\, d\boldsymbol{x} - L_0(\boldsymbol{v}) \right\} = \inf_{\substack{\boldsymbol{v} \in V \\ L(\boldsymbol{v})=1}} \left\{ \int_\Omega I_B^*(\varepsilon(\boldsymbol{v}))\, d\boldsymbol{x} - L_0(\boldsymbol{v}) \right\}, \tag{23}$$

where I_B^* is defined by (6). From the duality, it follows that

$$t^* \leq \bar{t}, \tag{24}$$

i.e., $\bar{t}$ is an upper bound of t^*. Nevertheless, the equality in (24) was shown for bounded sets B (see [8]) and some unbounded ones representing, e.g., by the von Mises, Tresca [16, 4] or Drucker-Prager yield criteria [9]. Further, it is readily seen that problems (22) and (23) are independent of the time variable and thus the same problems can also be introduced for the discretized problem defined in Section 3 or for the generalized Hencky problem [16, 4, 7, 8]. The limit analysis problems are also independent of the elastic tensor $\mathbb{C}$ and describe the collapse state of the body.

The kinematic limit analysis problem defined by (23) contains the linear equality constraint on the load L and other eventual constraints depending on the set B as follows from the definition of I_B^*. We introduce two examples of B for illustration (see, e.g., [8, 14]).

1. If the von Mises yield criterion is considered then $B = \left\{\boldsymbol{\tau} \in \mathbb{R}^{3\times 3}_{sym} \mid |\boldsymbol{\tau}^D| \leq \gamma\right\}$, where $\boldsymbol{\tau}^D$ denotes the deviatoric part of $\boldsymbol{\tau}$ and $\gamma > 0$ represents the initial yield stress. The related limit analysis problem reads:

$$\bar{t} = \inf_{\substack{\boldsymbol{v}\in V,\ \operatorname{div}\boldsymbol{v}=0 \\ L(\boldsymbol{v})=1}} \left\{ \int_\Omega \gamma|\varepsilon(\boldsymbol{v})|\, d\boldsymbol{x} - L_0(\boldsymbol{v}) \right\}, \quad \operatorname{div}\boldsymbol{v} = \operatorname{trace}\varepsilon(\boldsymbol{v}). \tag{25}$$

2. If the Drucker-Prager yield criterion is considered then

$$B = \left\{ \boldsymbol{\tau} \in \mathbb{R}^{3\times 3}_{sym} \mid \frac{a}{3}\operatorname{trace}\boldsymbol{\tau} + |\boldsymbol{\tau}^D| \leq \gamma \right\}, \quad a, \gamma > 0.$$

The related limit analysis problem reads:

$$\bar{t} = \inf_{\substack{\boldsymbol{v}\in V,\ L(\boldsymbol{v})=1 \\ \operatorname{div}\boldsymbol{v}\geq a|\varepsilon^D(\boldsymbol{v})|}} \left\{ \int_\Omega \frac{\gamma}{a}\operatorname{div}\boldsymbol{v}\, d\boldsymbol{x} - L_0(\boldsymbol{v}) \right\}. \tag{26}$$

5 Penalization of the kinematic limit analysis problem

We have illustrated that the kinematic limit analysis problem can contain very difficult constraints at each point of Ω causing locking phenomena. To eliminate these constraints, we introduce two possible ways of penalization to the problem (23).

5.1 Truncation method

The first penalization is based on replacing unbounded B by its bounded, convex subset B_m and thus can be interpreted as the truncation method. Notice that the function $I^*_{B_m}$ is real-valued for any $\boldsymbol{\tau} \in \mathbb{R}^{3\times 3}_{sym}$ and thus the penalized problem

$$\bar{t}_m = \inf_{\substack{\boldsymbol{v}\in V \\ L(\boldsymbol{v})=1}} \left\{ \int_\Omega I^*_{B_m}(\varepsilon(\boldsymbol{v}))\, d\boldsymbol{x} - L_0(\boldsymbol{v}) \right\}, \tag{27}$$

contains only the basic constraint on L. Let t^*_m denote the static limit load parameter from (22), where B_m is used instead of B. Then the following relations hold [8, 14]:

$$t^*_m = \bar{t}_m \leq t^* \leq \bar{t}. \tag{28}$$

We see that the penalized limit load parameters $\bar{t}_m$ and t^*_m coincide and that they are lower bounds of t^* and $\bar{t}$.

For the bounded set B_m, we have also stronger convergence results with respect to the (space) discretization parameter than for unbounded B, see [7, 8, 14]. Denote V_h as a finite element approximation of V and assume that the system $\{V_h\}_h$ is limit dense in V. Then $\bar{t}_{m,h} \to \bar{t}_m$ as $h \to 0_+$, where $\bar{t}_{m,h}$ denotes the the discrete limit load parameter obtained by the finite element approximation of problem (27).

The discrete counterpart to problem (27) can be solved, e.g., by the indirect incremental method presented below. We refer to [7, 8, 14] for some illustrative numerical examples.

5.2 Indirect incremental method

The indirect method of incremental limit analysis was originally introduced in [15, 2] for the discretized Hencky problem containing the von Mises yield criterion. Their extension for continuous setting of the Hencky problem and an abstract yield criterion was done in [7, 8]. This method was interpreted as the penalization method to the limit analysis problem in [14]. Here, we generalize the method for $L_0 \neq 0$ and relate it to the problem (17).

This penalization is based on the following relations between the functions I_B^* and Ψ_B:

$$\lim_{\alpha\to+\infty} \frac{1}{\alpha}\Psi_B(\alpha \boldsymbol{e} - \boldsymbol{\eta}) = I_B^*(\boldsymbol{e}) \quad \forall \boldsymbol{e}, \boldsymbol{\eta} \in \mathbb{R}^{3\times 3}_{sym}, \quad \frac{1}{\alpha}\Psi_B(\alpha \boldsymbol{e}) \leq I_B^*(\boldsymbol{e}) \quad \forall \alpha > 0. \tag{29}$$

To be in accordance with Section 3, we choose $\boldsymbol{\eta} = \boldsymbol{\varepsilon}^p_{k-1}$ in (29) and define the following penalization of problem (23):

$$\left\{ \begin{array}{c} \text{given } \alpha > 0,\ \boldsymbol{\varepsilon}^p_{k-1} \in Q,\ \text{find } \boldsymbol{u}_k^\alpha \in V,\ L(\boldsymbol{u}_k^\alpha) = 1 : \\ \mathcal{J}_k^\alpha(\boldsymbol{u}_k^\alpha) \leq \mathcal{J}_k^\alpha(\boldsymbol{v}) \quad \forall \boldsymbol{v} \in V,\ L(\boldsymbol{v}) = 1, \\ \mathcal{J}_k^\alpha(\boldsymbol{v}) = \int_\Omega \frac{1}{\alpha}\Psi_B(\alpha \boldsymbol{e} - \boldsymbol{\varepsilon}^p_{k-1})\, d\boldsymbol{x} - L_0(\boldsymbol{v}). \end{array} \right. \tag{30}$$

Enforcing the constraint $L(\boldsymbol{v}) = 1$ by a Lagrange multiplier and using the differentiability of Ψ_B, we arrive from (30) at the following saddle point system:

$$\left\{ \begin{array}{c} \text{given } \alpha > 0,\ \boldsymbol{\varepsilon}^p_{k-1} \in Q,\ \text{find } t_k := t_k(\alpha),\ \boldsymbol{u}_k^\alpha \in V : \\ \int_\Omega \Pi_B(\varepsilon(\alpha \boldsymbol{u}_k^\alpha) - \boldsymbol{\varepsilon}^p_{k-1}) : \varepsilon(\boldsymbol{v})\, d\boldsymbol{x} = L_0(\boldsymbol{v}) + t_k L(\boldsymbol{v}) \quad \forall \boldsymbol{v} \in V, \\ L(\boldsymbol{u}_k^\alpha) = 1. \end{array} \right. \tag{31}$$

Recalling $\ell_k = L_0 + t_k L$ and comparing (31) with (17), we observe that the following statements hold. If $(t_k, \boldsymbol{u}_k^\alpha) \in \mathbb{R}_+ \times V$ is a solution to (31) then $\boldsymbol{u}_k = \alpha \boldsymbol{u}_k^\alpha$ solves (17) for $t_k := t_k(\alpha)$. Conversely, if $\boldsymbol{u}_k \in \mathbb{V}$ is a solution to (17) satisfying $L(\boldsymbol{u}_k) > 0$ for given $t_k > 0$ then $(t_k, \boldsymbol{u}_k^\alpha)$, where $\boldsymbol{u}_k^\alpha = \boldsymbol{u}_k / L(\boldsymbol{u}_k)$, solves (31) for $\alpha = L(\boldsymbol{u}_k)$.

The direct method of incremental limit analysis is based on an adaptive construction of the sequence

$$0 < t_0 < t_1 < \ldots < t_k < \ldots < t^*$$

depending on the solvability of problem (17). Within the indirect method, an unbounded sequence

$$\alpha_0 < \alpha_1 < \ldots < \alpha_k < \ldots$$

is constructed and the corresponding sequence $\{t_k\}$ of solutions to (31) is computed. One can expect that the sequence $\{t_k\}$ is nondecreasing and tending to t^* as $k \to +\infty$. This was shown in [7] under the following simplified assumptions:

$$L_0 = 0 \quad \text{and} \quad \boldsymbol{\varepsilon}^p_{k-1} = \boldsymbol{0}, \quad k = 1, 2, \ldots. \tag{32}$$

Moreover, (32) and (21) imply that the mapping $\alpha \mapsto t_k(\alpha) \equiv t(\alpha)$ is uniquely defined, continuous and $t(\alpha) \to 0$ as $\alpha \to 0$ from above [7].

As above, consider the system $\{V_h\}_h$ of finite element approximations of the space V. Then the discrete counterpart $t_h := t_h(\alpha)$ has analogous properties as $t := t(\alpha)$. Moreover, the following pointwise convergence holds for any $\alpha > 0$: $t_h(\alpha) \to t(\alpha)$ as $h \to 0_+$.

In order to extend these results to nontrivial L_0, it seems to be sufficient to assume that there exists $\boldsymbol{u}_0 \in \mathbb{V}$ satisfying

$$\int_\Omega \Pi_B(\varepsilon(\boldsymbol{u}_0)) : \varepsilon(\boldsymbol{v})\, d\boldsymbol{x} = L_0(\boldsymbol{v}) \quad \forall \boldsymbol{v} \in V \quad \text{and} \quad L(\boldsymbol{u}_0) \geq 0. \tag{33}$$

Notice that $(33)_1$ implies the assumption (19) while $(33)_2$, ensures $t(\alpha) \to 0$ as $\alpha \to 0$.

6 Newton-like method for the indirect incremental method

The finite element approximation of problem (31) leads to the following algebraic system:

$$\text{given } \alpha_k > 0, \text{ find } (\boldsymbol{u}_k, t_k) \in \mathbb{R}^n \times \mathbb{R}_+ : \quad \begin{cases} \boldsymbol{F}_k(\boldsymbol{u}_k) = \boldsymbol{l}_0 + t_k \boldsymbol{l}, \\ \boldsymbol{l}^T \boldsymbol{u}_k = 1. \end{cases} \tag{34}$$

Notice that the nonlinear function $\boldsymbol{F}_k \colon \mathbb{R}^n \to \mathbb{R}^n$ is assembled using the operators Π_B at each integration point and depends on the solution from the previous step t_{k-1} and the given value α_k. Since Π_B is not smooth everywhere, the same also holds for $\boldsymbol{F}_k$. On the other hand, one can study the semismoothness of Π_B or $\boldsymbol{F}_k$, and introduce generalized derivatives of these functions [11, 12, 13]. The generalized derivative of Π_B is known as the consistent tangent operator in literature. Using this operator, one can assemble the generalized derivative of $\boldsymbol{F}_k$, which is represented by a mapping $\boldsymbol{K}_k : \mathbb{R}^n \to \mathbb{R}^{n \times n}$.

A nonsmooth (or semismooth) version of the Newton method to problem (34) leads to the following algorithm:

Algorithm 1 (ALG-α)

1: initialization: $\boldsymbol{u}_k^0$, t_k^0
2: **for** $i = 0, 1, 2, \ldots$ **do**
3: find $\boldsymbol{v}^i,\ \boldsymbol{w}^i \in \boldsymbol{V}$: $\boldsymbol{K}_k(\boldsymbol{u}_k^i)\boldsymbol{v}^i = \boldsymbol{l}_0 + t_k^i \boldsymbol{l} - \boldsymbol{F}_k(\boldsymbol{u}_k^i),\ \ \boldsymbol{K}_k(\boldsymbol{u}_k^i)\boldsymbol{w}^i = \boldsymbol{l}$
4: compute $\delta t^i = [1 - \boldsymbol{l}^T(\boldsymbol{u}_k^i + \boldsymbol{v}^i)]/\boldsymbol{l}^T\boldsymbol{w}^i$
5: compute $\delta \boldsymbol{u}^i = \boldsymbol{v}^i + \delta t^i \boldsymbol{w}^i$
6: set $\boldsymbol{u}_k^{i+1} = \boldsymbol{u}_k^i + \delta \boldsymbol{u}^i$, $t_k^{i+1} = t_k^i + \delta t^i$
7: **if** $\|\delta \boldsymbol{u}^i\|/(\|\boldsymbol{u}_k^{i+1}\| + \|\boldsymbol{u}_k^i\|) \leq \epsilon_{Newton}$ **then stop**
8: **end for**
9: set $\boldsymbol{u}_k = \boldsymbol{u}_k^{i+1}$, $t_k = t_k^{i+1}$.

Further, we initialize ALG-α using the linear extrapolation of the solutions from two previous steps $k-2$ and $k-1$, $k \geq 2$ [13]:

$$\boldsymbol{u}_k^0 = \boldsymbol{u}_{k-1} + \frac{\alpha_k - \alpha_{k-1}}{\alpha_{k-1} - \alpha_{k-2}}(\boldsymbol{u}_{k-1} - \boldsymbol{u}_{k-2}), \quad t_k^0 = t_{k-1} + \frac{\alpha_k - \alpha_{k-1}}{\alpha_{k-1} - \alpha_{k-2}}(t_{k-1} - t_{k-2}).$$

We observe that this initialization is more convenient than $\boldsymbol{u}_k^0 = \boldsymbol{u}_{k-1}$, $t_k^0 = t_{k-1}$.

Local superlinear convergence of ALG-α was analyzed in [2]. There was also proposed some modifications of the algorithm in order to receive global convergence results.

We refer to [2, 7, 8, 14, 13] for some illustrative numerical examples on the indirect method of the incremental limit analysis. For unbounded B, we observe that it is more convenient to use higher order finite elements. In the case of $P1$ or $Q1$ elements, we recommend to combine the indirect incremental method with the truncation method to reduce expected locking phenomena.

Acknowledgements

The work was supported by The Ministry of Education, Youth and Sports of the Czech Republic from the National Programme of Sustainability (NPU II) project "IT4Innovations excellence in science - LQ1602".

REFERENCES

[1] Caboussat, A. and Glowinski, R. Numerical solution of a variational problem arising in stress analysis: the vector case. *Discrete Contin. Dyn. Syst* (2010) **27**: 1447–1472.

[2] Cermak, M., Haslinger, J., Kozubek, T., Sysala, S. Discretization and numerical realization of contact problems for elastic-perfectly plastic bodies. PART II - numerical realization, limit analysis. *ZAMM - Z. Angew. Math. Mech.* (2015) **95**: 1348–1371.

[3] Chen, W.F. and Liu, X. *Limit analysis in soil mechanics*. Elsevier, 2012.

[4] Christiansen, E. Limit analysis of collapse states, in: *Handbook of numerical analysis* (P.G. Ciarlet and J.L. Lions eds., Vol IV, Part 2), North-Holland, 1996, pp. 193–312.

[5] de Souza Neto, E. A., Perić, D., Owen, D. R. J.: *Computational methods for plasticity: theory and application*. Wiley, (2008).

[6] Han W, Reddy BD. *Plasticity: mathematical theory and numerical analysis*. Springer, 1999.

[7] Haslinger, J., Repin, S., Sysala S. A reliable incremental method of computing the limit load in deformation plasticity based on compliance: Continuous and discrete setting. *Journal of Computational and Applied Mathematics* (2016) **303**: 156–170.

[8] Haslinger, J., Repin, S., Sysala S. Guaranteed and computable bounds of the limit load for variational problems with linear growth energy functionals. *Applications of Mathematics* (2016) **61**: 527–564.

[9] Repin, S. and Seregin, G. Existence of a weak solution of the minimax problem arising in Coulomb-Mohr plasticity. *Nonlinear evolution equations* (N.N. Uraltseva, ed.), *Translations of the American Mathematical Society*, Series 2 (1995) **164**: 189–220.

[10] Sloan, S. Geotechnical stability analysis, *Géotechnique* (2013) **63**, 531–572.

[11] Sysala, S. Properties and simplifications of constitutive time-discretized elastoplastic operators. *ZAMM - Z. Angew. Math. Mech.* (2014) **94**: 233–255.

[12] Sysala, S., Cermak, M., Koudelka, T., Kruis, J., Zeman, J., Blaheta, R. Subdifferential-based implicit return-mapping operators in computational plasticity. *ZAMM - Z. Angew. Math. Mech.* (2016) **96**: 1318–1338.

[13] Sysala, S., Cermak, M., Ligurský, T. Subdifferential-based implicit return-mapping operators in Mohr-Coulomb plasticity. (Submitted in 2017), http://arxiv.org/abs/1508.07435.

[14] Sysala, S. and Haslinger, J. Truncation and indirect incremental methods in Hencky's perfect plasticity, in: *Mathematical Modelling in Solid Mechanics*, Springer, 2017, pp. 265–284.

[15] Sysala, S., Haslinger, J., Hlaváček, I., Cermak, M. Discretization and numerical realization of contact problems for elastic-perfectly plastic bodies. PART I - discretization, limit analysis. *ZAMM - Z. Angew. Math. Mech.* (2015) **95**: 333–353.

[16] Temam, R.: *Mathematical Problems in Plasticity*. Gauthier-Villars, Paris, (1985).

[17] N. Zouain, I. Pontes Filho, L. Borges, and L. M. da Costa, Plastic collapse in non-associated hardening materials with application to cam-clay. *International journal of solids and structures* (2007) **44**: 4382–4398.

XIV International Conference on Computational Plasticity. Fundamentals and Applications
COMPLAS XIV
E. Oñate, D.R.J. Owen, D. Peric & M. Chiumenti (Eds)

LMIT AND SHAKEDOWN ANALYSIS BASED ON SOLID SHELL MODELS

LEONARDO LEONETTI *, GIOVANNI GARCEA.* DOMENICO MAGISANO * FRANCESCO LIGUORI*

* Dipartimento di Ingegneria Informatica, Modellistica, Elettronica e Sistemistica
Universit della Calabria 87036 Rende (Cosenza), Italy
web page: http://www.labmec.unical.it/

Key words: Computational Plasticity, Shakedown, Optimization, Solid Shells

Abstract. The paper treats the formulation of the shakedown problem and, as special case, of the limit analysis problem, using solid shell models and ES-FEM discratization technology. In this proposal the Discrete shear gap method is applied to alleviate the shear locking phenomenon.

1 INTRODUCTION

Shakedown analysis plays an important role in assessing the safety of structures in presence of many independent load combinations [1] against plastic collapse, loss in functionality due to excessive deformation (ratcheting) or collapse due to low cycle fatigue.

Nowadays, due to the growing attention of the scientific community, solid-shell elements have reached a high level of efficiency and accuracy. It has been shown that solid-shell finite elements give some advantages in linear and nonlinear context of analysis [2]. When compared to shell elements, solid-shell formulations present a simpler structure since only displacement degrees-of-freedom are employed. They can automatically account for 3D constitutive relations and are able to model through the thickness behaviours more accurately without the need to resort plane-stress assumptions, which often occurs in shell elements including rotation degrees-of-freedom. Solid-shell formulations also present important advantages when considering double-sided contact situations and in treating large deformations, since no rotation degrees-of-freedom are involved. However in addition to the classical shear, membrane and volumetric lockings, in the solid-shell exhibits thickness and trapezoidal locking. The latter is typical only of low order FEM. Assumed Natural Strain, Enhanced Assumed Strain and mixed (hybrid) formulations have been proposed for resolving these locking phenomena. In the context of triangular grids, the Assumed Natural Strain doesn't solve at all the shear locking [3] and a good alternative seems to be the so-called Discrete Shear Gap method [4]. Particularly for these models, to be competitive, it is better to improve the behaviour of lower-order finite elements due to its low computational cost when moderately fine meshes are required. To this aim linear

triangular (T_3) discretization [5] is highly suitable for describing complicated data and shows little sensitivity to the mesh distortion.

In order to alleviate the overstiffness of lower order FEMs various solutions have been proposed in the literature and smoothed finite element methods (SFEM) represent a a quite recent and effective numerical strategy. It is based on the idea of defining a smoothing domain through the discretization with different patterns, i.e. cells, nodes, edges or faces of a background mesh. More recently, the smoothing concept has been extended to elements with higher order shape functions [6, 7] simply obtained by using a mixed method. For an exhaustive description of the S-FEM method and a complete list of references, the authorship can find in [8].

Obviating the need to perform a cumbersome incremental elasto-plastic analysis [9, 10, 11], direct methods has been proved to be one of the most powerful tools to estimate the shakedown safety load of practical engineering structures.

The aim of this paper is to present a mixed shakedown (limit) analysis formulation for solid-shells. The proposed mixed element is based on a Edge Smoothed representation of the displacement field and piece-wise constant description of the stress field. The mixed nature of the element gives coherent equilibrium equations suitable for the simple application to the shakedown analysis and prevents volumetric locking problem. The assumed piece-wise constant description of the stress field allows the discontinuities inherent in the plastic solution. Furthermore, the model is particularly simple and easy to implement while providing accurate solutions of the plastic collapse analysis. Among other benefits the proposed MES-FEM model resolves also the dependency of state-of-art triangular solid shell elements on the adaptation of the cross-diagonal mesh. It is constructed by using a mixed format as described in [6, 7], and is suitable to perform well also in geometrically nonlinear context [12, 2, 13].

The yield criteria are borrowed from classical shell shear deformable shell models rewritten in terms of the variables used in defining the solid shell model used.

Another FEM model based on the so-called composite concept [14, 15, 16] is derived and compared with the ES-FEM ancestor.

2 THE SOLID-SHELL FINITE ELEMENT

In this section we briefly recall the kinematics of solid-shell finite element following the description of Sze et al. [17, 3].

2.1 Kinematics in convective frame

The convective coordinates $\zeta = \{\xi, \eta, \zeta\}$ are used to express the FE interpolation. A position vector in the initial or current configuration are denoted by $\mathbf{X}[\zeta] \equiv \{\mathbf{X_1}[\zeta], \mathbf{X_2}[\zeta], \mathbf{X_3}[\zeta]\}$ and $\mathbf{Y}[\zeta] \equiv \{\mathbf{Y_1}[\zeta], \mathbf{Y_2}[\zeta], \mathbf{Y_3}[\zeta]\}$ respectively and are linked by the displacement field $\mathbf{d}[\zeta]$

$$\mathbf{Y}[\zeta] = \mathbf{X}[\zeta] + \mathbf{d}[\zeta] \tag{1}$$

Adopting the convention of summing on repeated indexes, the covariant Green-Lagrange

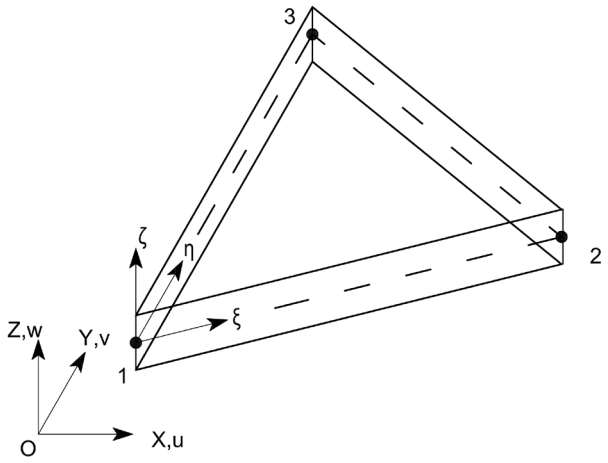

Figure 1: Linear triangular based solid-shell element

strain measure components are

$$\bar{\varepsilon}_{ij} = \frac{1}{2}\left(\mathbf{X}_{,\mathbf{i}}\cdot\mathbf{d}_{,\mathbf{j}} + \mathbf{d}_{,\mathbf{i}}\cdot\mathbf{X}_{,\mathbf{j}} + \mathbf{d}_{,\mathbf{i}}\cdot\mathbf{d}_{,\mathbf{j}}\right) \quad \text{with} \quad i,j = \xi,\eta,\zeta \tag{2}$$

where a comma followed by k denotes the derivative with respect to kth component of ζ and $(\cdot)$ denotes the scalar product.

The shell, with constant thickness, is conveniently described using a bi-dimensional frame

$$\mathbf{X}[\zeta] = \mathbf{X_0}[\xi,\eta] + \zeta\mathbf{X_n}[\xi,\eta] = \mathbf{N_d}[\zeta]\mathbf{X_e}, \qquad \mathbf{d}[\zeta] = \mathbf{d_0}[\xi,\eta] + \zeta\mathbf{d_n}[\xi,\eta] = \mathbf{N_d}[\zeta]\mathbf{d_e} \tag{3}$$

where vectors $\mathbf{d_e}$ and $\mathbf{X_e}$ collect the element nodal displacements and coordinates. The matrix $\mathbf{N_d}[\zeta]$ collects the interpolation functions

$$\mathbf{N_d}[\zeta] \equiv \left[\mathbf{N}, \zeta\mathbf{N}\right] = \mathbf{N_{d0}} + \zeta\mathbf{N_{dn}} \tag{4}$$

where $\zeta \in [-1,+1]$, $\mathbf{N_{d0}} = [\mathbf{N}[\mathbf{r},\xi,\eta], \mathbf{0}]$ and $\mathbf{N_{dn}} = [\mathbf{0}, \mathbf{N}[\mathbf{r},\xi,\eta]]$ that for linear triangular grids, the bi-dimensional shape functions $\mathbf{N} \equiv \left[N_1, \quad N_2, \quad N_3\right]$ are as usual

$$N_1 = r = 1 - \xi - \eta, \;\; N_2 = \xi, \;\; N_3 = \eta \tag{5}$$

Adopting a Voigt notation the infinitesimal covariant strain components in Eq.(2) are collected in vector $\bar{\varepsilon} \equiv [\bar{\varepsilon}_{\xi\xi}, \bar{\varepsilon}_{\eta\eta}, 2\bar{\varepsilon}_{\xi\eta}, \bar{\varepsilon}_{\zeta\zeta}, 2\bar{\varepsilon}_{\eta\zeta}, 2\bar{\varepsilon}_{\xi\zeta}]^T$ that, exploiting Eq.(3), becomes

$$\bar{\varepsilon} \equiv \begin{bmatrix} \mathbf{X_e^T}\mathbf{N_{d,\xi}^T}\mathbf{N_{d,\xi}} \\ \mathbf{X_e^T}\mathbf{N_{d,\eta}^T}\mathbf{N_{d,\eta}} \\ \mathbf{X_e^T}(\mathbf{N_{d,\xi}^T}\mathbf{N_{d,\eta}} + \mathbf{N_{d,\eta}^T}\mathbf{N_{d,\xi}}) \\ \mathbf{X_e^T}\mathbf{N_{d,\zeta}^T}\mathbf{N_{d,\zeta}} \\ \mathbf{X_e^T}(\mathbf{N_{d,\zeta}^T}\mathbf{N_{d,\eta}} + \mathbf{N_{d,\eta}^T}\mathbf{N_{d,\zeta}}) \\ \mathbf{X_e^T}(\mathbf{N_{d,\xi}^T}\mathbf{N_{d,\zeta}} + \mathbf{N_{d,\zeta}^T}\mathbf{N_{d,\xi}}) \end{bmatrix} \mathbf{d_e}, \tag{6}$$

The covariant strains can be conveniently linearized with respect to ζ in the following form

$$\bar{\varepsilon} \approx \begin{bmatrix} \bar{\mathbf{e}}[\xi,\eta] + \zeta\ \bar{\chi}[\xi,\eta] \\ \bar{\varepsilon}_{\zeta\zeta}[\xi,\eta] \\ \bar{\boldsymbol{\gamma}}[\xi,\eta] \end{bmatrix} \tag{7}$$

and collected in the vector $\bar{\rho}[\zeta] = \bar{\rho}[\xi,\eta] \equiv [\bar{\mathbf{e}}, \bar{\varepsilon}_{\zeta\zeta}, \bar{\chi}, \bar{\boldsymbol{\gamma}}]^T$

where

$$\bar{\mathbf{e}}[\xi,\eta] \equiv \begin{bmatrix} \bar{\varepsilon}_{\xi\xi} \\ \bar{\varepsilon}_{\eta\eta} \\ 2\bar{\varepsilon}_{\xi\eta} \end{bmatrix} \quad \bar{\chi}[\xi,\eta] \equiv \begin{bmatrix} \bar{\varepsilon}_{\xi\xi,\zeta} \\ \bar{\varepsilon}_{\eta\eta,\zeta} \\ 2\bar{\varepsilon}_{\xi\eta,\zeta} \end{bmatrix} \quad \bar{\boldsymbol{\gamma}}[\xi,\eta] \equiv \begin{bmatrix} 2\bar{\varepsilon}_{\eta\zeta} \\ 2\bar{\varepsilon}_{\xi\zeta} \end{bmatrix}$$

By partitioning the vectors $\mathbf{d_e} = [\mathbf{d_{0e}}, \mathbf{d_{en}}]^{\mathbf{T}}$ and $\mathbf{d_e} = [\mathbf{X_{e0}}, \mathbf{X_{ne}}]^{\mathbf{T}}$ the components of generalized covariant strains (7) have the following form

$$\begin{aligned} \bar{\mathbf{e}}_1 &= \mathbf{X_e^T Q^m_{\xi\xi} d_e},\ \bar{\mathbf{e}}_2 = \mathbf{X_e^T Q^m_{\eta\eta} d_e},\ \bar{\mathbf{e}}_3 = \mathbf{X_e^T Q^m_{\xi\eta} d_e} \\ \bar{\chi}_1 &= \mathbf{X_e^T Q^b_{\xi\xi} d_e},\ \bar{\chi}_2 = \mathbf{X_e^T Q^b_{\eta\eta} d_e},\ \bar{\chi}_1 = \mathbf{X_e^T Q^b_{\xi\eta} d_e} \\ \bar{\varepsilon}_{\zeta\zeta} &= \mathbf{X_e^T Q_{\zeta\zeta} d_e},\ 2\bar{\varepsilon}_{\xi\zeta} = \mathbf{X_e^T Q_{\xi\zeta} d_e},\ 2\bar{\varepsilon}_{\eta\zeta} = \mathbf{X_e^T Q_{\eta\zeta} d_e} \end{aligned} \tag{8}$$

It can be shown that the operators involved in previous equations are of compact shape.

2.2 Remedies for shear and trapeziodal locking

A way of resolving shear locking is the Assumed Natural Strain method in which the natural transverse shear strains are sampled at some discrete element points and then interpolated. As shown in [3, 18] also after this treatment triangular elements based on ANS still have a moderate chance of exhibiting shear locking.

The so-called Discrete Shear Gap method [4] that can be classified as an ANS method is another effective strategy of resolving shear locking gives some advantage. The element formulation is automatic for any kind of element, regardless of shape and polynomial order, there is no need to choose an interpolation for the shear strains or to specify any sampling points. The process to construct DSG is similar for both triangles and quadrangles whereas in applying the ANS to triangles a proper choice of feasible sampling points proves to be more problematic than for rectangles [4].

The DSG algorithm is employed in this finite element formulation

- Evaluation of the discrete shear gaps by integrating the transverse shear strains, or equivalently the corresponding matrices $\mathbf{Q}$s (8)

$$\begin{aligned} \Delta\gamma^1_{\xi z} = 0,\ \ \Delta\gamma^2_{\xi z} = \int_{\xi_1}^{\xi_2} \bar{\mathbf{Q}}_{\xi\zeta} d\xi,\quad \Delta\gamma^3_{\xi z} = \int_{\xi_1}^{\xi_3} \bar{\mathbf{Q}}_{\xi\zeta} d\xi \\ \Delta\gamma^1_{\eta z} = 0,\ \ \Delta\gamma^2_{\eta z} = \int_{\eta_1}^{\eta_2} \bar{\mathbf{Q}}_{\eta\zeta} d\eta,\quad \Delta\gamma^3_{\eta z} = \int_{\eta_1}^{\eta_3} \bar{\mathbf{Q}}_{\eta\zeta} d\eta \end{aligned} \tag{9}$$

  $\bar{\mathbf{Q}}_{\xi\zeta}$ and $\bar{\mathbf{Q}}_{\eta\zeta}$ are obtained from compatibility relations (3). It is worth mentioning that these integrals are carried out apriori analitically

- Interpolation of the discrete shear gaps across the element in order to obtain the suitable discrete form

$$\begin{aligned}\mathbf{Q}_{\xi\zeta} &= \frac{\partial \mathbf{N_2}}{\partial \xi}\boldsymbol{\Delta}\gamma^{\mathbf{2}}_{\xi\mathbf{z}} + \frac{\partial \mathbf{N_3}}{\partial \xi}\boldsymbol{\Delta}\gamma^{\mathbf{3}}_{\xi\mathbf{z}} \\ \mathbf{Q}_{\eta\zeta} &= \frac{\partial \mathbf{N_2}}{\partial \eta}\boldsymbol{\Delta}\gamma^{\mathbf{2}}_{\eta\mathbf{z}} + \frac{\partial \mathbf{N_3}}{\partial \eta}\boldsymbol{\Delta}\gamma^{\mathbf{3}}_{\eta\mathbf{z}}\end{aligned} \tag{10}$$

Similarly to shear locking, the excessive number of sampled thickness strains lead to trapezoidal locking. It can be reduced in the system level by sampling the strain along the element edges [19], namely

$$\mathbf{Q}_{\zeta\zeta} = \mathbf{r}\bar{\mathbf{Q}}\big|_{\boldsymbol{\xi}=\mathbf{0},\eta=\mathbf{0}} + \xi\bar{\mathbf{Q}}\big|_{\mathbf{r}=\mathbf{0},\eta=\mathbf{0}} + \eta\bar{\mathbf{Q}}\big|_{\boldsymbol{\xi}=\mathbf{0},\mathbf{r}=\mathbf{0}} \tag{11}$$

In this way the element is free from trapezoidal locking and is immune to shear locking as the other standard three-node degenerated shell elements [18, 20]

2.3 Dual variables of generalized strain components

Once the kinematic model is assumed (or vice versa) the related stress variables are automatically given by assuring the invariance of the internal work. By collecting the contravariant stress components $\bar{\sigma} \equiv [\bar{\sigma}_{\xi\xi}, \bar{\sigma}_{\eta\eta}, 2\bar{\sigma}_{\xi\eta}, \bar{\sigma}_{\zeta\zeta}, 2\bar{\sigma}_{\eta\zeta}, 2\bar{\sigma}_{\xi\zeta}]^T$ the work conjugate variables with $\bar{\rho}$ are obtained by

$$\mathcal{W} = \int_V \bar{\varepsilon}^T \bar{\sigma} dV = \int_\Omega \left(\bar{\mathcal{N}}^T \bar{\mathbf{e}} + \bar{\mathcal{M}}^T \bar{\chi} + \bar{s}_{\zeta\zeta}\bar{\varepsilon}_{\zeta\zeta} + \bar{\mathcal{T}}^T \bar{\boldsymbol{\gamma}}\right) \tag{12}$$

The generalized contravariant stresses are then

$$\bar{\mathcal{N}} \equiv \frac{1}{2}\int_{-1}^{1} \sigma_{\mathbf{p}} \mathbf{d}\zeta \quad \bar{\mathcal{M}} \equiv \frac{1}{2}\int_{-1}^{1} \zeta\sigma_{\mathbf{p}} \mathbf{d}\zeta \quad \bar{\mathbf{s}}_{\zeta\zeta} \quad \equiv \frac{1}{2}\int_{-1}^{1} \sigma_{\zeta\zeta} d\zeta \bar{\mathcal{T}} \quad \equiv \frac{1}{2}\int_{-1}^{1} \tau \mathbf{d}\zeta \tag{13}$$

with

$$\bar{\sigma}_p = \begin{bmatrix} \bar{\sigma}_{\xi\xi} \\ \bar{\sigma}_{\eta\eta} \\ \bar{\sigma}_{\xi\eta} \end{bmatrix} \quad \bar{\tau} = \begin{bmatrix} \bar{\sigma}_{\xi\zeta} \\ \bar{\sigma}_{\eta\zeta} \end{bmatrix} \text{ and } \quad \bar{\mathbf{t}} \equiv \left[\bar{\mathcal{N}}, \bar{s}_{\zeta\zeta}, \bar{\mathcal{M}}, \bar{\mathcal{T}}\right]^T$$

The way of performing the integral $\int_\Omega(\cdots)$ defines the finite element formulation.

2.4 The mapping to physical coordinates

A physical coordinate system is used to describe the material properties that can be different for each patch (subdomain) in which the domain may be partitioned. It is assumed that $x-y$ plane is coincident with the mid-plane of the shell ($\zeta = 0$, ζ parallel to z). With these assumptions the generalized Cartesian strain and stresses are obtained from the natural ones as

$$\begin{aligned}\mathbf{t} &= \mathbf{T}_\sigma \bar{\mathbf{t}} \\ \rho &= \mathbf{T}_\epsilon \bar{\rho} = \mathbf{T}_\sigma^{-\mathbf{T}} \bar{\rho}\end{aligned} \quad \text{with} \quad \mathbf{T}_\sigma = \begin{bmatrix} \mathbf{T_p} & 0 & 0 & 0 \\ 0 & T_z & 0 & 0 \\ 0 & 0 & \mathbf{T_p} & 0 \\ 0 & 0 & 0 & \mathbf{T_t} \end{bmatrix} \tag{14}$$

where $T_z = z_{,\zeta}^2 = \frac{h^2}{4}$ and where h is the thickness of the shell and

$$\mathbf{T_p} = \begin{bmatrix} x_{,\xi}^2 & y_{,\eta}^2 & 2x_{,\xi}x_{,\eta} \\ y_{,\xi}^2 & y_{,\eta}^2 & 2y_{,\xi}y_{,\eta} \\ x_{,\xi}y_{,\xi} & x_{,\eta}y_{,\eta} & x_{,\xi}y_{,\eta} + x_{,\eta}y_{,\xi} \end{bmatrix} \qquad \mathbf{T_t} = z_{,\zeta} \begin{bmatrix} x_{,\xi} & x_{,\eta} \\ y_{,\xi} & y_{,\eta} \end{bmatrix} \tag{15}$$

and $\mathbf{x}_\xi = \mathbf{R}\mathbf{X_0}_{,\xi}$, $\mathbf{x}_\eta = \mathbf{R}\mathbf{X_0}_{,\eta}$. The matrix $\mathbf{R} = [\boldsymbol{i}_x^T, \boldsymbol{i}_y^T, \boldsymbol{i}_z^T]^T$ collects by row the unit vectors along the axis of the local Cartesian coordinates

$$\boldsymbol{i}_x = \frac{\mathbf{X_0}_{,\xi}}{\|\mathbf{X_0}_{,\xi}\|} \text{ or provided as input,} \quad \boldsymbol{i}_y = \frac{\mathbf{X_0}_{,\eta}}{\|\mathbf{X_0}_{,\eta}\|}, \quad \boldsymbol{i}_z = \boldsymbol{i}_x \times \boldsymbol{i}_y$$

Being the Jacobian matrix $\mathbf{J}$

$$\mathbf{J_0}[\xi, \eta] = \begin{bmatrix} \mathbf{X_0}_{,\xi} & \mathbf{X_0}_{,\eta} & \mathbf{X_0}_{,\zeta} \end{bmatrix} = \begin{bmatrix} x_{,\xi} & y_{,\xi} & 0 \\ x_{,\eta} & y_{,\eta} & 0 \\ 0 & 0 & h/2 \end{bmatrix} \tag{16}$$

constant with ζ its determinant can be evaluated as $det(\mathbf{J}) = \mathbf{Ah}$ where $2A = x_{,\xi}y_{,\eta} - y_{,\xi}x_{,\eta}$

2.5 Edge smoothed element topology

The solid shell model is based on a description of a bi-dimensional domain using three-dimensional strain measure. Many advantages in employing Smoothed FEM (S-FEM) have been proven [8, 21] but standard formulation still show some drawback. Is the authors opinion that the generation of the mesh for S-FEM-type elements, including edge imbricate FEM (EI-FEM) [22] is not trivial. Recently in [23] a nice method for an automatic mesh generation for S-FEM have been developed. It is also the authors opinion also that the simplest, automatic and costless way to describe the S-FEM models based on first order grids (T_3 or Q_4) is to use a quadratic grids and stress assumption [6] instead of strain assumptions. In this way the method can be easily generalized to higher shape functions and the preprocessing is simple.

Similarly to ES-FEM, we start from a geometrical discretization of the two-dimensional domain (*grid*), by means of three node triangles (*parts*). Each part can be subdivided into three triangular *subparts* identified by each edge and the centroid of the part. On this grid the *element* is defined by the union of the subparts adjacent to each edge of the grid (see [6]). The union of all the elements defines the *mesh*. Each part contributes to the elements corresponding to its sides, so the mesh (of the elements) is not coincident with the grid (of the parts).

To obtain the numerical model in each part the stress components are collected as $\mathbf{t}_e = [\mathbf{t}_e^1, \mathbf{t}_e^3, \mathbf{t}_e^3]$ with $\mathbf{t}^i = \left[\mathcal{N}^\mathbf{i}, \mathbf{s}_{\zeta\zeta}^\mathbf{i}, \mathcal{M}^\mathbf{i}, \mathcal{T}^\mathbf{i}\right]^T$, where superscripts denote each triangle subpart, and the displacement parameters are collected as

$$\mathbf{d_e} = [\mathbf{u_1}...\mathbf{u_3}, \mathbf{v_1}...\mathbf{v_3}, \mathbf{w_1}...\mathbf{w_3}, \mathbf{u_{n1}}..., \mathbf{u_{n3}}, \mathbf{v_{n1}}..., \mathbf{v_{n3}}, \mathbf{w_{n1}}..., \mathbf{w_{n3}}]^\mathbf{T} \tag{17}$$

where subscripts $1, 2, 3$ denote the vertex of the triangular part. With the same shape is assumed the vector $\mathbf{X_e}$

3 CONSTITUTIVE EQUATIONS AND YIELD CRITERIA

The perfectly-plastic material assumption restrains the stress σ to belong to a fix admissible domain

$$\mathbb{E} \equiv \{\sigma : \mathbf{f}[\sigma] \leq \mathbf{0}, \text{with} \mathbf{f}[\mathbf{0}] < \mathbf{0}\} \tag{18}$$

where the function $f[\sigma]$ is a convex yield function. Exploiting its convexity the constitutive relation follows

$$\dot{\varepsilon^{\mathbf{p}}} = \dot{\mu} \frac{\partial f[\sigma]}{\partial \sigma} \Big|_{f(\sigma)=\mathbf{0}} \tag{19}$$

due to Drucker condition

$$(\sigma_{\mathbf{y}} - \sigma)^{\mathbf{T}} \dot{\varepsilon}^{\mathbf{p}} \geq \mathbf{0} \quad \forall \sigma \in \mathbb{E}$$

3.1 Von Mises yield criterion

The classical H. V. Mises yield criterion for metal shells, generalized in terms of stress resultants (13) can be expressed as [24]

$$\frac{1}{2} \mathbf{t}^T \mathbf{P_e} \mathbf{t} \leq \sigma_{\mathbf{y}}^{\mathbf{2}} \tag{20}$$

where

$$\mathbf{P_e} = \begin{bmatrix} 2 & -1 & \cdot & -1 & \cdot & \cdot & \cdot & \cdot & \cdot \\ -1 & 2 & \cdot & -1 & \cdot & \cdot & \cdot & \cdot & \cdot \\ \cdot & \cdot & 6 & \cdot & \cdot & \cdot & \cdot & \cdot & \cdot \\ -1 & -1 & \cdot & 2 & \cdot & \cdot & \cdot & \cdot & \cdot \\ \cdot & \cdot & \cdot & \cdot & 2h^2 & -h^2 & \cdot & \cdot & \cdot \\ \cdot & \cdot & \cdot & \cdot & -h^2 & 2h^2 & \cdot & \cdot & \cdot \\ \cdot & \cdot & \cdot & \cdot & \cdot & \cdot & 6h^2 & \cdot & \cdot \\ \cdot & \cdot & \cdot & \cdot & \cdot & \cdot & \cdot & \frac{3h^2}{2} & \cdot \\ \cdot & \cdot & \cdot & \cdot & \cdot & \cdot & \cdot & \cdot & \frac{3h^2}{2} \end{bmatrix}, \tag{21}$$

Note that the terms of $\frac{3h^2}{2}$ in the matrix $\mathbf{P}$ are the transverse shear components.

4 SHAKEDOWN ANALYISIS

We refer to the analysis of a body subjected to volume forces $\partial\Omega$ and tractions $\mathbf{f}$, both increasing with the same load multiplier λ.

The proncipal virtual work equation becomes

$$W[\sigma, \mathbf{u}] = \int_{\Omega} \sigma^{\mathbf{T}} \mathbf{D} \mathbf{u} \, \mathbf{d\Omega} - \int_{\mathbf{\Omega}} \mathbf{b}^{\mathbf{T}} \mathbf{u} \, \mathbf{d\Omega} - \int_{\mathbf{\Gamma}}^{\mathbf{T}} \mathbf{u} \, \mathbf{d\Gamma} \tag{22}$$

where $\mathbf{D}$ is the compatibility operator. By introducing the interpolation the part contribution to the

$$W_e[\boldsymbol{\beta}_e, \mathbf{d_e}] = \boldsymbol{\beta}_{\mathbf{e}}^{\mathbf{T}} \mathbf{D_e} \mathbf{d_e} - \mathbf{d}_{\mathbf{e}}^{\mathbf{T}} \mathbf{p_e} \tag{23}$$

and $\mathbf{D_e}$ is the discrete compatibility operator, $\mathbf{p_e}$ is the load vector furnished by the integration of the external load components weighted with the shape functions of the displacement interpolations.

The global compatibility operator $\mathbf{Q}$ and load vector $\mathbf{p}$ are obtained by assembling the element contributions through the element incidence operators for displacements $\mathbf{u_e} = \mathbf{T_u q}$ and stresses $\boldsymbol{\beta}_e = \mathbf{T}_\beta \boldsymbol{\beta}$, where $\boldsymbol{\beta}$ is the global stress vector and $\mathbf{q}$ is the global displacement vector.

The material is assumed to be elastic-perfectly plastic, therefore the stress field is constrained to satisfy plastic admissibility inequalities which are independent of the plastic strain. The shakedown analysis can be solved using an evolutive analysis through the solution of a sequence of incremental elasto-plastic problems [9] and the shakedown multiplier λ_s is evaluated as the limit value for the equilibrium path. The shakedown analysis theorems offer an alternative way which is directly addressed to compute the lower and upper approximations of the safety multiplier. In this case, following [9] the shakedown multiplier is individuated as a solution of the nonlinear mathematical programming problem

$$\begin{aligned} &\text{maximize} && \lambda \\ &\text{subject to} && \mathbf{Q^T}\boldsymbol{\beta} - \lambda \mathbf{p} = \mathbf{0} \\ & && \phi[\boldsymbol{\beta}] \leq \mathbf{0} \end{aligned} \tag{24}$$

where the equality constraints are represented by the equilibrium equations, described through the global equilibrium operator $\mathbf{Q^T}$ and the load vector $\mathbf{p}$ collecting the body forces and tractions. The plastic admissibility inequalities are expressed through the vector ϕ, which collects the local restrictions imposed by the assumed yield condition over the stress state $\mathbf{t}^i$ of the N_r regions of the domain

$$\phi_i[\mathbf{t}^i, \lambda] \leq 0, \quad i = 1..N_r \tag{25}$$

For more details in the formulation of the shakedown problem the reader is encouraged to see [9].

5 NUMERICAL RESULTS

The performances of the proposed mixed finite element model in evaluating plastic collapse states have been tested by the numerical experiments reported in the following subsections.

5.1 Cook membrane

The well-known Cook's membrane, depicted in Figure 2 is used to show some preliminary results of the in-plane behaviour. The convergence of the numerical solution has been tested by using three meshes obtained by successive refinements initiated by a coarse mesh of 2 elements for each side.

Table 1 reports a comparison of the computed values of the plastic collapse multiplier. The reference result [11] was obtained using a mesh having 1024 elements and 2178 dofs

while the finest mesh used in the present analysis has 512 triangular elements and 1649 dofs.

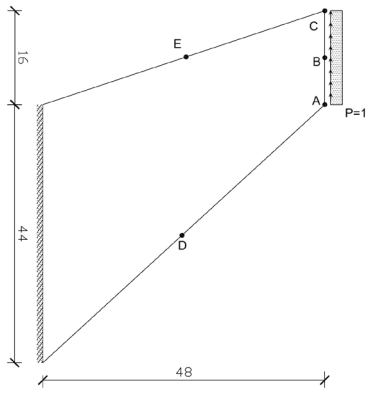

Figure 2: Cook membrane data.

Table 1: Cook membrane. Plane stress limit analysis.

	mesh 1	*mesh 2*	*mesh 3*
	λ	λ	λ
Present	0.4151	0.4012	0.3970
$N-S$	0.3888	0.3883	0.3935
ref. [11]			0.3956

5.2 Square plate under uniform transverse load

The transverse performances are tested by exercising the simply supported (SS) and clamped (CL) square plates as described in Fig. 3 subject to uniform transverse load $q = 1$. Owing to its symmetry, only a quarter of the plate is modelled with respectively 8, 12 and 16 elements for each side. To appreciate the effectiveness in resolving the shear locking, different ratios L/h are considered. A unitary yield moment $m_y = \frac{\sigma_y h^2}{4}$ is considered. The collapse multipliers are given normalized with respect the yield moment divided by qL^2 where $q = 1$ is the transversal uniform load.

Tables 2 and 3 compare the present results with those obtained in [25], showing good agreement between solutions obtained by two methods.

6 CONCLUSIONS

The paper proposes an MES-FEM solid shell element for application in shakedown and limit analysis. The model is adapt, simple and accurate, to solve the problem also

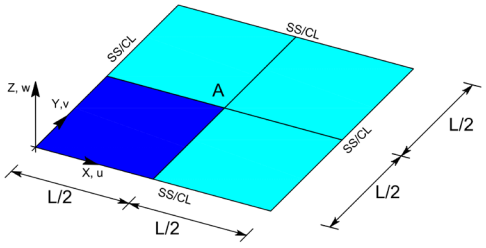

Figure 3: Square plate data. $L = 10$.

Table 2: Clamped square plate: computed plastic collapse load using uniform meshes

L/t	*mesh 1*	*mesh 2*	*mesh 3*	
	λ	λ	λ	Uniform mesh [25]
1	9.29	9.09	9.00	9.02
4	32.03	31.11	30.64	31.46
10	44.81	43.16	42.37	43.37
40	49.43	47.35	46.41	46.57
50	49.69	47.50	46.54	-
100	50.73	47.90	46.78	46.84

in conic formulation of mathematical programs. The main features of the model are its simplicity and easy implementation within existing computational tools. Nevertheless fully capitalizes its features in the analysis of plastic problems. The piece-wise constant description of the stress field address the discontinuities inherent in the plastic solution.

The numerical experiments show the good performance of the proposed model. It is worth noting that the model proves to be able to furnish very accurate results by employing moderately fine meshes using few variables and nonlinear constraints in the formulation of the mathematical program used to perform the analysis, and this is of great interest in technical applications.

The accurate results achieved in the evaluation of the collapse multiplier and in the description of the collapse mechanism demonstrate that the element is able to approximate well the discontinuous fields generated by the plastic behaviour without drawbacks and locking phenomena also for small thickness.

REFERENCES

[1] L. Leonetti, R. Casciaro, G. Garcea, Effective treatment of complex statical and dynamical load combinations within shakedown analysis of 3d frames, Computers AND Structures 158 (2015) 124 – 139.

[2] D. Magisano, L. Leonetti, G. Garcea, Advantages of the mixed format in geometrically nonlinear analysis of beams and shells using solid finite elements, International Journal for Numerical Methods in Engineering 109 (9).

Table 3: Simply supported square plate: computed plastic collapse load using uniform meshes

L/t	*mesh 1*	*mesh 2*	*mesh 3*	Uniform mesh [25]
	λ	λ	λ	λ
1	9.27	9.08	8.99	9.03
4	23.52	23.43	23.41	23.88
10	24.95	24.81	24.76	24.85
40	25.36	25.12	25.06	25.03
50	25.41	25.14	25.07	-
100	25.67	25.20	25.09	25.05

[3] A six-node pentagonal assumed natural strain solidshell element, Finite Elements in Analysis and Design 37 (8) (2001) 639 – 655.

[4] A unified approach for shear-locking-free triangular and rectangular shell finite elements, Computers and Structures 75 (3) (2000) 321 – 334.

[5] O. Zienkiewicz, R. Taylor, The finte element method, McGraw-Hill, 1989.

[6] L. Leonetti, G. Garcea, H. Nguyen-Xuan, A mixed edge-based smoothed finite element method (mes-fem) for elasticity, Computers and Structures 173 (2016) 123 – 138.

[7] L. Leonetti, G. Garcea, H. Nguyen-Xuan, A mixed node-based smoothed finite element method (mns-fem) for elasticity, Computer with Engineering (2017) in press.

[8] W. Zeng, G. R. Liu, Smoothed finite element methods (s-fem): An overview and recent developments, Archives of Computational Methods in Engineering (2016) 1–39.

[9] G. Garcea, L. Leonetti, A unified mathematical programming formulation of strain driven and interior point algorithms for shakedown and limit analysis, Int. J. Numer. Methods Eng.

[10] G. G. Bilotta A, Leonetti L, An algorithm for incremental elastoplastic analysis using equality constrained sequential quadratic programming, Computers and Structures.

[11] A. Bilotta, L. Leonetti, G. Garcea, Three field finite elements for the elastoplastic analysis of 2d continua 47 (2011) 1119–1130.

[12] D. Magisano, L. Leonetti, L. Garcea, How to improve efficiency and robustness of the newton method in geometrically non-linear structural problem discretized via displacement-based finite elements, Computer Methods in Applied Mechanics and Engineering 313 (2017) 986 – 1005.

[13] D. Magisano, L. Leonetti, G. Garcea, Koiter asymptotic analysis of multilayered composite structures using mixed solid-shell finite elements, Composite Structures 154 (2016) 296 – 308.

[14] L. Leonetti, M. Aristodemo, A composite mixed finite element model for plane structural problems, Finite Element Analysis and Design 94 (2015) 33–46.

[15] L. Leonetti, C. Le, Plastic collapse analysis of mindlin-reissner plates using a composite mixed finite element, International Journal for Numerical Methods in Engineering 105 (2016) 915–935.

[16] A. Bilotta, G. Garcea, L. Leonetti, A composite mixed finite element model for the elasto-plastic analysis of 3d structural problems, Finite Element Analysis and Design 113 (2016) 43–53.

[17] K. Sze, A. Ghali, Hybrid hexahedral element for solids, plates, shells and beams by selective scaling, International Journal for Numerical Methods in Engineering 36 (9) (1993) 1519–1540.

[18] A. F. Saleeb, T. Y. Chang, S. Yingyeunyong, A mixed formulation of c0-linear triangular plate/shell elementthe role of edge shear constraints, International Journal for Numerical Methods in Engineering 26 (5).

[19] K. Y. Sze, L. Q. Yao, S. Yi, A hybrid stress ans solid-shell element and its generalization for smart structure modelling. part iismart structure modelling, International Journal for Numerical Methods in Engineering 48 (4).

[20] Hybrid strain based three-node flat triangular shell elements, Finite Elements in Analysis and Design 17 (3) (1994) 169 – 203.

[21] H. Nguyen-Xuan, S. Bordas, H. Nguyen-Dang, Smooth finite element methods: convergence, accuracy and properties, International Journal for Numerical Methods in Engineering 74 (2008) 175–208.

[22] F. Cazes, G. Meschke, An edge-based imbricate finite element method (ei-fem) with full and reduced integration, Computers and Structures 106-107 (2012) 154–175.

[23] Y. Li, J. Yue, R. Niu, G. Liu, Automatic mesh generation for 3d smoothed finite element method (s-fem) based on the weaken-weak formulation, Advances in Engineering Software 99 (2016) 111 – 120.

[24] P. Papadopoulos, R. Taylor, An analysis of inelastic reissner-mindlin plates, Finite Elements Analysis and Design 10 (1991) 221–223.

[25] C. Le, A stabilized discrete shear gap finite element for adaptive limit analysis of mindlin-reissner plates, International Journal for Numerical Methods in Engineering 96 (2013) 231–246.

XIV International Conference on Computational Plasticity. Fundamentals and Applications
COMPLAS 2017
E. Oñate, D.R.J. Owen, D. Peric and M. Chiumenti (Eds)

MATERIAL POINT METHOD FOR DETERIORATING INELASTIC STRUCTURES

CHRISTOS D. SOFIANOS[1], VLASIS K. KOUMOUSIS[2]

[1] National Technical University of Athens
Institute of Structural Analysis & Aseismic Research
Zografou Campus, 15780 Athens, Greece
e-mail: sofianoschristos@yahoo.gr

[2] National Technical University of Athens
Institute of Structural Analysis & Aseismic Research
Zografou Campus, 15780 Athens, Greece
e-mail: vkoum@central.ntua.gr

Key words: Material Point Method, Plasticity.

Abstract. The material point method (MPM) is one of the latest developments in particle in cell methods (PIC). The structure is discretized into a number of material points that hold all the state variables of the system [1] such as stress, strain, velocity, displacement etc. These properties are then mapped to a temporary background grid and the governing equations are solved. The momentum conservation equations (together with energy and mass conservation considerations) are solved at the grid nodes. The state variables of the particles are then updated by transferring the solutions from the grid nodes back to the material points. Since the background grid is used only to solve the governing equations at the end of each computational step it can be reset to its undistorted form and thus mesh distortion and element entanglement are avoided.

In this work an explicit MPM accounting for elastoplastic material behavior with degradations is proposed. The stress tensor is decomposed into an elastic and a hysteretic – plastic part [5] where the hysteretic part of the stresses evolves according to a Bouc-Wen type hysteretic rule [2]. The inelastic constitutive material law provides a smooth transition from the elastic to the inelastic regime and accounts for the different phases during elastic loading, unloading, yielding and stiffness and strength degradation. Heaviside type functions are introduced that act as switches, incorporate the yield criterion and the terms for stiffness and strength degradation as in the Bouc-Wen model of hysteresis [2]. The resulting constitutive law relates stresses and strains with the use of the tangent modulus of elasticity, which now includes the Heaviside functions and gathers all of the governing inelastic degrading behavior.

1 INTRODUCTION

In the Material Point Method, the domain is discretized into a set of material points or particles. Each particles represents a fraction of the volume of the material and carries all the

properties and the state of the material (mass, stress, density strain etc.). In addition to the material points a background grid is employed. This is in most cases structured, but it can also be arbitrary. The grid is static and does not deform and it is reset to its original form after each computational step. It is used to solve the governing equations of motion. The properties of the material points are mapped to the background grid using shape functions similar to FEM. After the solution is obtained in the background grid nodes, the updated quantities are mapped back to the material points.

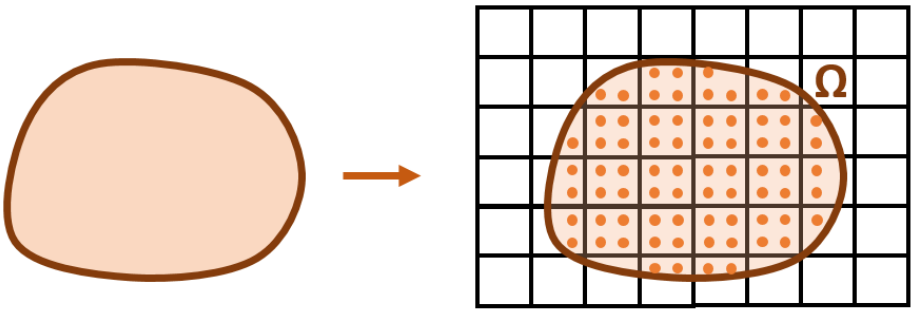

Figure 1: MPM discretization.

In this work cubic B-Splines shape functions are used [3]. They have been shown to reduce quadrature errors and the grid crossing errors that occur when a material point crosses between two elements of the background grid if the gradients of the shape functions are discontinuous [4].

2 THE MATERIAL POINT METHOD

In the MPM algorithm the following steps are considered: firstly, the element of the background grid that each material point lies in, is identified and the corresponding shape functions are evaluated. The material point masses M_p and momenta $(Mv)_p$ are mapped to the background grid and the nodal masses m_i and momenta $(mv)_i$ are calculated:

$$\begin{aligned} m_i &= \sum_{p=1}^{N_p} M_p N_i \\ (mv)_i &= \sum_{p=1}^{N_p} (Mv)_p N_i \end{aligned} \tag{1}$$

where N_i are the corresponding shape functions. The nodal internal forces F_i^{int} are calculated on the background grid based on the material point stresses and using the gradient of the shape functions:

$$F_i^{\text{int}} = -\sum_{p=1}^{N_p} \frac{M_p}{p_p} \sigma_p \nabla N_i \tag{2}$$

where p_p is the density of the material point p. The total nodal force vector F_i, on the background grid is calculated and the appropriate boundary conditions are applied:

$$F_i = F_i^{ext} + F_i^{\text{int}} \tag{3}$$

The momenta at the background grid nodes are updated:

$$(mv)_i = (mv)_i + F_i dt \tag{4}$$

The properties are mapped back to the material points and their positions and velocities are updated as follows:

$$\begin{aligned} v(x_p) &= v(x_p) + \left(\sum_{i=1}^{N} \frac{F_i N_i}{m_i} \right) dt \\ x_p &= x_p + \left(\sum_{i=1}^{N} \frac{(mv)_i N_i}{m_i} \right) dt \end{aligned} \tag{5}$$

The final step is to calculate the strain increments and from those the stress increments. Using the Modified Update Stress Last (MUSL), that has been shown to conserve energy better, the grid nodal momenta are recalculated based on the new particle velocities and the particle strain increments $\Delta\varepsilon_p$ are calculated based on the new nodal velocities:

$$\begin{aligned} (mv)_i &= \sum_{p=1}^{N_p} M_p v(x_p) N_i \\ v_i &= \frac{(mv)_i}{m_i} \\ \Delta\varepsilon_p &= \sum_{i=1}^{N} v(x_p) \nabla N_i dt \\ \Delta\sigma_p &= [D] \Delta\varepsilon_p \end{aligned} \tag{6}$$

where $[D]$ is the plane stress elasticity matrix:

$$[D] = \begin{bmatrix} \frac{E}{(1-\nu^2)} & \frac{E\nu}{(1-\nu^2)} & 0 \\ \frac{E\nu}{(1-\nu^2)} & \frac{E}{(1-\nu^2)} & 0 \\ 0 & 0 & \frac{E}{2(1+\nu)} \end{bmatrix} \tag{7}$$

3 PLASTICITY MODEL WITH DEGRADATIONS

The mechanical analogue of the Bouc – Wen [2] hysteretic model for a Single Degree of Freedom system is presented in Figure 2.

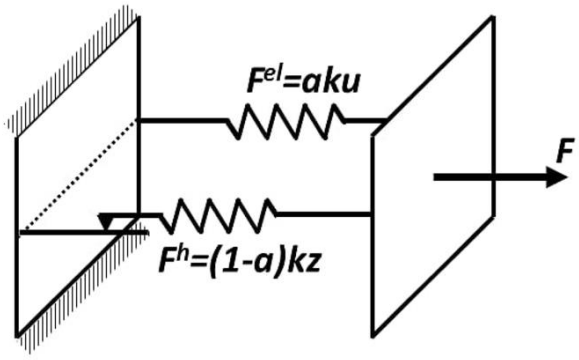

Figure 2: Mechanical analogue of Bouc-Wen model.

The model can be visualized as the parallel combination of two components, one being a linear spring with reduced stiffness ak, where a is the ratio of the post yield stiffness to the initial elastic one. The second element consists of a linear spring and a slider that are connected in series. If the force that acts on the system is smaller than the yield force, then the system behaves elastically with its initial stiffness. If, however, the yield force is exceeded, then the force in the second element stays constant and equal to the yield force and the linear spring provides the additional hardening.

The differential equations of the Bouc-Wen model for the single degree of freedom system are:

$$\begin{aligned} F &= F^{el} + F^{h} = \alpha K u + (1-\alpha) K z \\ \dot{z} &= \left[1 - \left| \frac{z}{z_y} \right|^{n} \left(\beta + \gamma \operatorname{sgn}(z\dot{u}) \right) \right] \dot{u} \end{aligned} \tag{8}$$

where z is the hysteretic parameter, z_y is the maximum value of the hysteretic parameter, sgn is the signum function, K is the stiffness of the spring and a is the ratio of the post yield stiffness to the initial elastic one. The total force is uncoupled into an elastic one and a hysteretic one.

The Bouc – Wen model as explained in the previous paragraph is generalized herein regarding the stress tensor which is now decomposed into an elastic a hysteretic part as:

$$\{\sigma\} = [\alpha]\{\sigma^{e}\} + ([I] - [\alpha])\{\sigma^{h}\} \tag{9}$$

where $[a]$ is a diagonal matrix that hold the ratio of the post yield stiffness to the elastic one and $[I]$ is the identity matrix. The elastic part of the stresses relates to the strains with the use of the classic constitutive matrix $[D]$:

$$\{\sigma^{e}\} = [D]\{\varepsilon\} \tag{10}$$

The hysteretic part of the stresses follows a Bouc-Wen type hysteretic rule and thus:

$$\{\dot{\sigma}^{h}\} = [D]([I] - H_1 H_2 [R])\{\dot{\varepsilon}\} \tag{11}$$

where H_1, H_2 are Heaviside type functions and $[R]$ is the interaction matrix. Its formulation stands from the theory of classical plasticity and can be found in [5] and [7] and contains no hardening related terms [6]. The Heaviside type functions are given as:

$$H_1 = \left|\frac{\Phi}{\Phi_0}\right|^n \quad , \qquad H_2 = 0.5 + 0.5 sign\left(\{\varepsilon\}^T \{\dot{\sigma}\}\right) \tag{12}$$

where Φ is the yield criterion. These functions essentially smooth the transition from the elastic to the inelastic regime and control loading and unloading behaviour. The rate form of equation (9), using equation (11), can be written as:

$$\{\dot{\sigma}\} = [\alpha][D]\{\dot{\varepsilon}\} + ([I] - [\alpha])[D]([I] - H_1 H_2 [R])\{\dot{\varepsilon}\} \tag{13}$$

Two additional parameters are added into the model to account for stiffness degradation and strength deterioration. These parameters where first introduced by Baber and Wen [8] and equation (13) now becomes:

$$\{\dot{\sigma}\} = [\alpha][D]\{\dot{\varepsilon}\} + \frac{1}{n_s}([I] - [\alpha])[D]([I] - v_s H_1 H_2 [R])\{\dot{\varepsilon}\} \tag{14}$$

where:

$$\begin{aligned} n_s &= 1 + c_n e^h \\ v_s &= 1 + c_v e^h \end{aligned} \tag{15}$$

Regarding the parameters in the previous relations, c_n and c_v are the model parameters that need to be identified, while e^h is the accumulated hysteretic energy due to plastic energy dissipation. It is calculated from the hysteretic stresses as:

$$e^h = \int \{\sigma^h\} d\{\varepsilon\} \tag{16}$$

Finally, the constitutive equation can be written as:

$$\begin{aligned} \{\dot{\sigma}\} &= [E^t]\{\dot{\varepsilon}\}, \\ [E^t] &= \left[[\alpha][D] + \frac{1}{n_s}([I] - [\alpha])[D]([I] - v_s H_1 H_2 [R])\right] \end{aligned} \tag{17}$$

where $[E^t]$ can be considered as a tangent matrix effectively controlling the smooth transition from the elastic to the inelastic regime, loading and unloading, as well as accounting for stiffness and strength degradation. This matrix can now substitute the classic elasticity matrix in (6) and extend the MPM to account for plasticity and degradations.

4 NUMERICAL EXAMPLES

In order to verify the proposed model within the MPM framework a cantilever beam is considered. Material is steel with *E=210GPa*, and yield strength of s_y*=240MPa*. The dimensions of the beam are *1m* by *0.2m*. In this analysis the beam was discretized with 320 material points using 4 points per element. The discretized beam and the employed background

grid can be seen in Figure 3. A sinusoidal force is applied at the free end of the beam during a time of 5 secs with a maximum value ok 375kN and a period of 2π to simulate one full cycle. The results are plotted in Figure 4 regarding the stress strain diagram of the material point closest to fixed end both with and without degradations. In addition, the Von Mises stresses of the beam at its maximum displaced position are plotted in Figure 5. Results show that the formulation is able to capture accurately the main features of plasticity together with degradation phenomena.

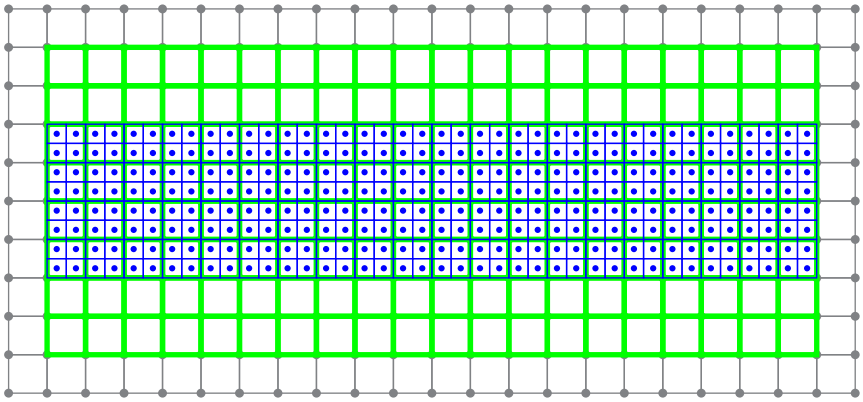

Figure 3: MPM discretization of the beam with 320 material points.

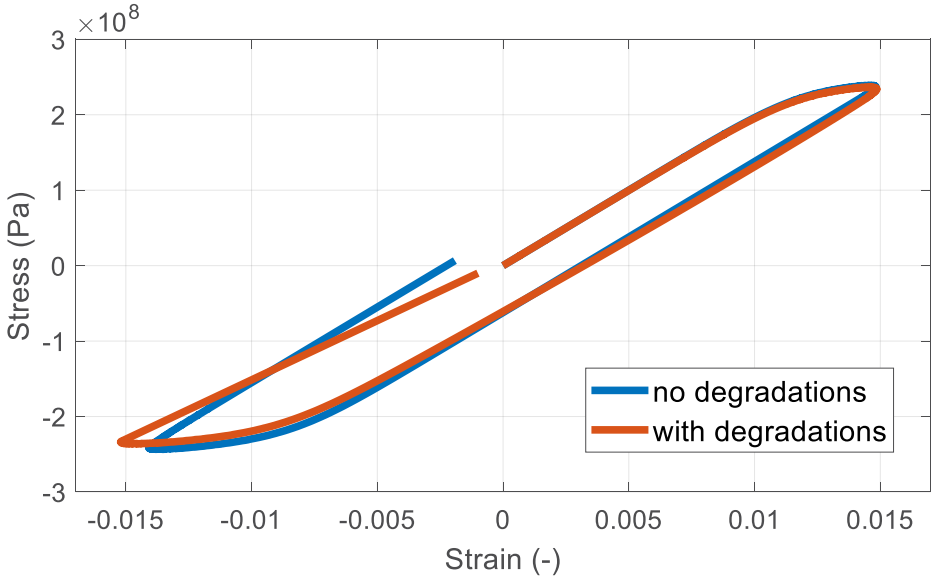

Figure 4: Stress strain diagram for the material point closest to the fixed end.

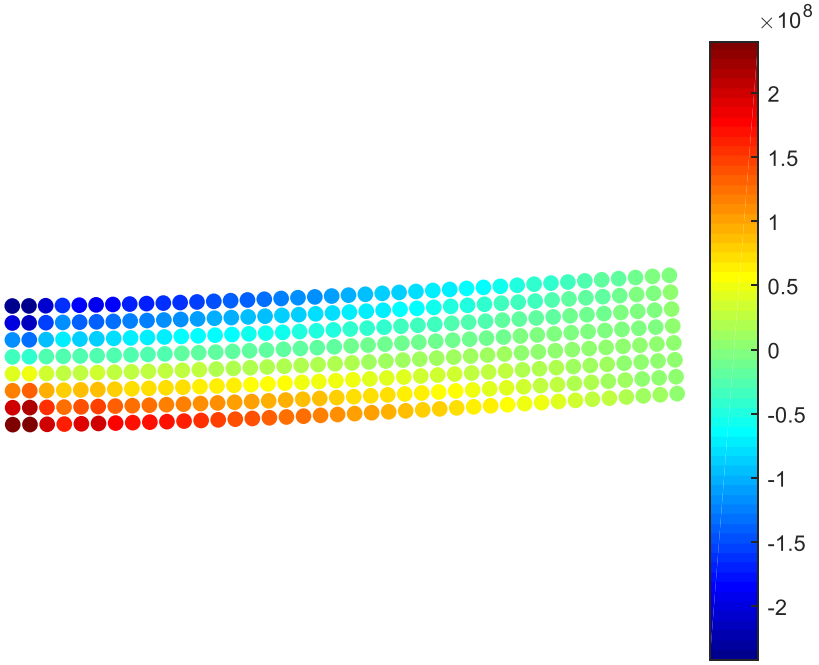

Figure 5: Von Mises stresses.

5 CONCLUSIONS

- The Material Point Method is used in an explicit formulation scheme to model plasticity with degradation phenomena.
- Use of higher order cubic B-Splines effectively minimizes the grid crossing errors and improves the accuracy of the MPM method.
- The hysteretic - plasticity model for nonlinear analysis accounts for smooth transition from the elastic to the inelastic regime.
- The model accounts for stiffness degradation and strength deterioration. and has been incorporated into the MPM framework by modifying the tangent modulus of elasticity.
- Numerical examples are presented that verify the proposed model ability to simulate plastic and damage phenomena.

6 AKNOWLEDGMENTS

The authors would like to acknowledge the support from the “RESEARCH PROJECTS FOR EXCELLENCE IKY/SIEMENS”.

REFERENCES

[1] Sulsky, D., Chen Z. and Schreyer H.L., *A particle method for history-dependent materials*. Comput. Methods, Appl. Mech. Eng. 118,179 (1994).

[2] Bouc R. *Forced vibration of mechanical system with hysteresis*. Proc. 4th Conf. on Nonlinear Oscillation, Prague

[3] Andersen S., Andersen L., *Analysis of spatial interpolation in the material-point method*.

Computers and Structures 88 (2010), 506-518.
[4] Steffen M, Kirby RM, Berzins M. *Analysis and reduction of quadrature errors in the material point method (MPM)*. International Journal for Numerical Methods in Engineering;76:(2008), 922–48
[5] Triantafyllou S., Koumousis V., *Bouc-Wen Hysteretic Plane Stress Element*, Journal of Engineering Mechanics, 138 (2012), 235-246
[6] Casciati F. *Stochastic dynamics of hysteretic media*. In: Krée P., Wedig W. (eds) Probabilistic Methods in Applied Physics. Lecture Notes in Physics, vol 451. Springer, Berlin, Heidelberg, (1995)
[7] Sofianos, C. and Koumousis, V., Hysteretic model for the explicit material point method. 6th ECCOMAS Thematic Conference on Computational Methods in Structural Dynamics and Earthquake Engineering, COMPDYN 2017, Rhodes Island, Greece, (2017)
[8] Baber, T. T., Yi-Kwei Wen.. *Seismic response of hysteretic degrading structures*, Publ. Turk. Natl. Comm. on Earthquake Eng., (1980) Volume 7:457-464.

XIV International Conference on Computational Plasticity. Fundamentals and Applications
COMPLAS XIV
E. Oñate, D.R.J. Owen, D. Peric & M. Chiumenti (Eds)

NONLINEAR STATIC AND DYNAMIC ANALYSIS OF MIXED CABLE ELEMENTS

MIQUEL CRUSELLS-GIRONA*,
FILIP C. FILIPPOU* **AND ROBERT L. TAYLOR***

* Department of Civil and Environmental Engineering
University of California, Berkeley
94720 Berkeley, CA, USA
e-mail: miquel.crusells@berkeley.edu

Key words: Cables, Mixed FEM, Weak Compatibility, Nonlinear Dynamics

Abstract. This paper presents a family of finite elements for the nonlinear static and dynamic analysis of cables based on a mixed variational formulation in curvilinear coordinates and finite deformations. This formulation identifies stress measures, in the form of axial forces, and conjugate deformation measures for the nonlinear catenary problem. The continuity requirements lead to two distinct implementations: one with a continuous axial force distribution and one with a discontinuous. Two examples from the literature on nonlinear cable analysis are used to validate the proposed formulation for St Venant-Kirchhoff elastic materials. These studies show that displacements and axial forces are captured with high accuracy for both the static and the dynamic case.

1 INTRODUCTION

Cable structures are of great interest in many engineering applications because they offer numerous advantages, such as high ultimate strength, light weight or prestressing capabilities, among others. Nonetheless, a highly nonlinear behavior arises in this type of structures because of their high flexibility. For analyzing cable structures, two families of elements have traditionally been considered: truss elements and catenary elements.

For truss elements, the cable is discretized in a series of straight 2-node elements. In this case, the geometric nonlinearity is often accounted for by a corotational formulation, involving the transformation of the node kinematic variables under large displacements. Truss elements suffer from excessive mesh refinement to obtain accurate results, especially when assuming a constant axial force distribution in the element. Moreover, they may exhibit snap-through instabilities at states of nearly singular stiffness.

Catenary elements use linear kinematics to discretize the cable into a series of curved elements that satisfy the catenary equation. These elements solve the global balance of linear momentum by explicit integration and assuming linear elasticity [1]. As a result, loads are not adjusted with the cable elongation, so that these elements cannot be extended to nonlinear elasticity or inelasticity. Recently, the authors have proposed a general

formulation for a catenary element in finite deformations and curvilinear coordinates [2] that overcomes these limitations.

2 MIXED FORMULATION OF THE CATENARY PROBLEM

2.1 Kinematics

Fig. 1 shows the motion of a cable from a reference configuration $\mathcal{P}_0$ to a current configuration $\mathcal{P}$. Define an orthogonal frame $\{\mathbf{G}_i\}_{i=1}^3$ with associated coordinates $\{\xi^i\}_{i=1}^3$ at any point $P \in \mathcal{P}_0$, such that

$$\mathbf{G}_1 = \frac{d\mathbf{X}}{d\xi^1} \;\; ; \;\; \mathbf{G}_1 \cdot \mathbf{G}_2 = 0 \;\; ; \;\; \|\mathbf{G}_2\| = 1 \;\; ; \;\; \mathbf{G}_3 = \frac{\mathbf{G}_1 \times \mathbf{G}_2}{\|\mathbf{G}_1 \times \mathbf{G}_2\|} \tag{1}$$

where ξ^1 is the parameter describing the curve. Under the motion $\mathbf{x} = \boldsymbol{\chi}(\mathbf{X})$, this frame is convected to the orthogonal frame $\{\mathbf{g}_i\}_{i=1}^3$. Let upper case letters denote variables in the reference configuration and lower case letters, variables in the current configuration.

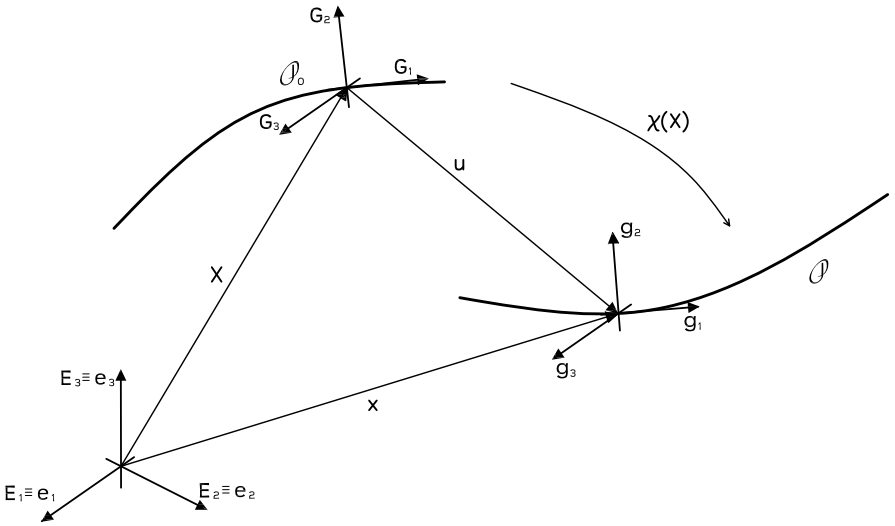

Figure 1: Motion $\mathbf{x} = \boldsymbol{\chi}(\mathbf{X}(\xi^1))$ of the cable $\mathcal{C}$.

The relevant stretch and Green-Lagrange strain of the problem, in the $\mathbf{g}_1$ direction, are

$$\lambda = \frac{\|\mathbf{g}_1\|}{\|\mathbf{G}_1\|} \qquad ; \qquad \mathrm{E} = \frac{1}{2}(\lambda^2 - 1)\|\mathbf{G}_1\|^2 \tag{2}$$

The displacement vector $\mathbf{u}$ depends only on the curvilinear coordinate ξ^1,

$$\mathbf{u}(\mathbf{X}(\xi^1)) = \mathbf{x}(\mathbf{X}(\xi^1)) - \mathbf{X}(\xi^1) = u_A(\xi^1)\mathbf{E}_A \tag{3}$$

Therefore, the relationship between the displacement field $\mathbf{u}$ and the relevant Green-Lagrange strain E can be computed [2] as

$$\mathrm{E} = \frac{d\mathbf{u}}{d\xi^1} \cdot \mathbf{G}_1 + \frac{1}{2}\left|\frac{d\mathbf{u}}{d\xi^1}\right|^2 = \frac{d\mathbf{u}}{d\xi^1} \cdot \left(\mathbf{G}_1 + \frac{1}{2}\frac{d\mathbf{u}}{d\xi^1}\right) = \frac{1}{2}\frac{d\mathbf{u}}{d\xi^1} \cdot (\mathbf{G}_1 + \mathbf{g}_1) \tag{4}$$

It is relevant to observe that the frame $\{\mathbf{G}_i\}_{i=1}^3$ is orthogonal, but not orthornomal in general. Indeed, the metric tensor $G_{ij} = \mathbf{G}_i \cdot \mathbf{G}_j$ is not necessarily the identity operator and the Green-Lagrange strain E may not be physical. Nevertheless, one can construct an orthonormal basis $\{\hat{\mathbf{G}}_A\}_{A=1}^3 = \{\mathbf{G}_i/\|\mathbf{G}_i\|\}_{i=1}^3$ such that

$$\mathbf{E} = \mathrm{E}_{ij}\mathbf{G}^i \otimes \mathbf{G}^j = \hat{\mathrm{E}}_{AB}\hat{\mathbf{G}}_A \otimes \hat{\mathbf{G}}_B \tag{5}$$

Hence, the components

$$\hat{\mathrm{E}}_{AB} = \mathrm{E}_{ij}(\hat{\mathbf{G}}_A \cdot \mathbf{G}^i)(\hat{\mathbf{G}}_B \cdot \mathbf{G}^j) \tag{6}$$

are physical quantities.

2.2 Equilibrium and principle of virtual work

For expressing the equilibrium equation of the cable in finite deformations, let $\mathbf{n}$ denote the axial force in the current configuration, thus a Cauchy representation. Observe that the first Piola-Kirchhoff and the Cauchy representations of the axial force coincide for the problem in hand, which does not account for changes in the cross section dimensions.

The Cauchy axial force can be pulled back to the reference configuration to obtain a second Piola-Kirchhoff representation of the axial force, $\mathbf{N}$. It can be shown [2] that, using the orthonormal basis in Eq. 5, namely with components $\mathbf{n} = \hat{\mathrm{n}}\hat{\mathbf{g}}_1$ and $\mathbf{N} = \hat{\mathrm{N}}\hat{\mathbf{G}}_1$,

$$\hat{\mathrm{n}} = \lambda\hat{\mathrm{N}} \tag{7}$$

Denoting by s and S the arc-length coordinates in the current and reference configurations, respectively, the cable distributed load can be described as

$$\mathbf{w}ds = \hat{\mathbf{W}}dS = \mathbf{W}d\xi^1 \tag{8}$$

Then, global equilibrium for the cable in the current configuration $\mathcal{P}$ states

$$\mathbf{n}(s) - \mathbf{n}(0) + \int_0^s \mathbf{w}\, ds = \int_0^s \rho\mathbf{a}\, ds \tag{9}$$

where ρ is the material density in the current configuration and $\mathbf{a}$, the total acceleration. The corresponding local statement in the current configuration can be obtained with the fundamental theorem of calculus and the localization theorem

$$\frac{d}{ds}(\mathrm{n}\mathbf{g}_1) + \mathbf{w} = \rho\mathbf{a} \tag{10}$$

or, in the reference configuration,

$$\frac{d}{dS}(\hat{\mathrm{N}}\sqrt{G^{11}}\mathbf{g}_1) + \hat{\mathbf{W}} = \rho_0\mathbf{a} \tag{11}$$

where $G^{ij} = \mathbf{G}^i \cdot \mathbf{G}^j$ represents the dual metric tensor and $\rho_0 = \lambda\rho$.

In summary, if $\hat{\mathrm{N}} = \Psi(\hat{\mathrm{E}})$ is a frame-indifferent constitutive relation between the physical Green-Lagrange strain $\hat{\mathrm{E}}$ and the physical 2nd Piola-Kirchhoff axial force $\hat{\mathrm{N}}$, the pair of fields $(\mathbf{u}, \hat{\mathrm{N}})$ will be the solution of the cable problem, if and only if, they satisfy

$$\begin{cases} G^{11}\dfrac{d\mathbf{u}}{d\xi^1}\cdot\left(\mathbf{G}_1+\dfrac{1}{2}\dfrac{d\mathbf{u}}{d\xi^1}\right)-\hat{\mathrm{E}}=0 & \text{in } \Omega=(0,L) \\ \dfrac{d}{dS}\left(\sqrt{G^{11}}\hat{\mathrm{N}}\mathbf{g}_1\right)+\hat{\mathbf{W}}=\rho_0\mathbf{a} & \text{in } \Omega=(0,L) \\ \hat{\mathrm{N}}-\Psi(\hat{\mathrm{E}})=0 & \text{in } \Omega=(0,L) \\ \mathbf{u}=\bar{\mathbf{u}} & \text{on } \Gamma_u \\ \sqrt{G^{11}}\hat{\mathrm{N}}\mathbf{g}_1=\bar{\mathbf{T}} & \text{on } \Gamma_q \end{cases} \tag{12}$$

for $0 < S < L$ equivalent to $\xi_1^1 < \xi^1 < \xi_2^1$.

The corresponding two-field weak statement of Eq. 12 can be obtained by considering any variation $\delta\mathbf{u} \in \mathcal{V}$, the space of displacement test functions, any variation $\delta\hat{\mathrm{N}} \in \mathcal{W}$, the space of axial force test functions, and integrating the equilibrium equation by parts,

$$\begin{cases} \displaystyle\int_0^L \delta\hat{\mathrm{N}}\left\{G^{11}\frac{d\mathbf{u}}{d\xi^1}\cdot\left(\mathbf{G}_1+\frac{1}{2}\frac{d\mathbf{u}}{d\xi^1}\right)-\hat{\mathrm{E}}\right\}dS=0 \\ \displaystyle\int_0^L \frac{d(\delta\mathbf{u})}{dS}\cdot\hat{\mathrm{N}}\sqrt{G^{11}}\mathbf{g}_1\,dS+\int_0^L\delta\mathbf{u}\cdot\rho_0\mathbf{a}\,dS=\left[\delta\mathbf{u}\cdot\bar{\mathbf{T}}\right]_{\Gamma_q}+\int_0^L\delta\mathbf{u}\cdot\hat{\mathbf{W}}\,dS \end{cases} \tag{13}$$

where the constitutive relation is imposed strongly. The spaces for the trial solutions of the displacements and axial forces, $\mathcal{S}$ and $\mathcal{N}$, respectively, are

$$\begin{aligned} \mathcal{S} &= \{\mathbf{u}\in H^1(0,L)\,|\,\mathbf{u}=\bar{\mathbf{u}} \text{ on } \Gamma_u\} \\ \mathcal{N} &= \left\{\hat{\mathrm{N}}\in H^0(0,L)\,|\,\hat{\mathrm{N}}>0, \text{ and } \hat{\mathrm{N}}=g^{11}\sqrt{G_{11}}\bar{\mathbf{T}}\cdot\mathbf{g}_1 \text{ on } \Gamma_q\right\} \end{aligned} \tag{14}$$

Similarly, the spaces for the test functions of the displacements and the axial forces, $\mathcal{V}$ and $\mathcal{W}$, respectively, become

$$\begin{aligned} \mathcal{V} &= \{\delta\mathbf{u}\in H^1(0,L)\,|\,\delta\mathbf{u}=0 \text{ on } \Gamma_u\} \\ \mathcal{W} &= \{\delta\hat{\mathrm{N}}\in H^0(0,L)\,|\,\delta\hat{\mathrm{N}}=0 \text{ on } \Gamma_q\} \end{aligned} \tag{15}$$

where $H^k(\Omega)$ is the Sobolev space for the $k-$th weak derivative in the $L^2(\Omega)$ norm.

As a result, there are no continuity requirements for the axial force field $\hat{\mathrm{N}}$. This implies the possibility of exploring cable finite elements with continuous or discontinuous axial force distribution.

3 FINITE-ELEMENT IMPLEMENTATION

3.1 Discretization

The discretization of the governing equations requires interpolations for $\hat{\mathrm{N}}(\xi^1)$, $\mathbf{u}(\xi^1)$ and $\mathbf{a}(\xi^1)$. Assume a k-th order Galerkin interpolation for the axial forces

$$\hat{\mathrm{N}} = \boldsymbol{\varphi}^t\hat{\mathbf{N}} = \hat{\mathbf{N}}^t\boldsymbol{\varphi} \tag{16}$$

and an l-th order Galerkin interpolation for the displacement and acceleration fields

$$\mathbf{u} = \boldsymbol{\phi}^t \hat{\mathbf{u}} \quad ; \quad \mathbf{a} = \boldsymbol{\phi}^t \hat{\mathbf{a}} \tag{17}$$

Then, using the same shape functions for the reference configuration, the current configuration is obtained as

$$\mathbf{x} = \mathbf{X} + \mathbf{u} = \boldsymbol{\phi}^t(\hat{\mathbf{X}} + \hat{\mathbf{u}}) = \boldsymbol{\phi}^t \hat{\mathbf{x}} \tag{18}$$

With these interpolation functions, one can discretize the weak statement in Eq. 13 for a finite element Ω_e and a time step n as

$$\begin{cases} \displaystyle\int_{\Omega_e} \delta\hat{\mathbf{N}}^t \boldsymbol{\varphi} \left\{ G^{11} \hat{\mathbf{u}}_n^t \boldsymbol{\phi}' \left(\mathbf{G}_1 + \frac{1}{2} (\boldsymbol{\phi}')^t \hat{\mathbf{u}}_n \right) - \hat{\mathrm{E}}(\hat{\mathbf{N}}_n) \right\} dS = 0 \\ \displaystyle\int_{\Omega_e} \delta\hat{\mathbf{u}}^t \boldsymbol{\phi}' G^{11} \boldsymbol{\varphi}^t \hat{\mathbf{N}}_n \hat{\mathbf{g}}_n \, dS + \int_{\Omega_e} \delta\hat{\mathbf{u}}^t \rho_0 \boldsymbol{\phi} \boldsymbol{\phi}^t \hat{\mathbf{a}}_n \, dS = \left[\delta\hat{\mathbf{u}}^t \boldsymbol{\phi} \bar{\mathbf{T}}_n \right]_{\partial\Omega_e} + \int_{\Omega_e} \delta\hat{\mathbf{u}}^t \boldsymbol{\phi} \hat{\mathbf{W}}_n \, dS \end{cases} \tag{19}$$

where $(\cdot)'$ represents the derivative with respect to the curvilinear coordinate ξ^1 and $\hat{\mathbf{g}}_n = \mathbf{G}_1 + (\boldsymbol{\phi}')^t \hat{\mathbf{u}}_n$ is the numerical counterpart to $\mathbf{g}_1$.

3.2 Time integration and consistent linearization

Once the discretization of the problem has been performed, the corresponding time-dependent equations need to be solved. As stated before, one can consider cable finite elements with a continuous or a discontinuous axial force field.

3.2.1 Mixed cable element with continuous axial force

For the element with continuous axial force distribution, the cable is subdivided into e elements of k-th order in axial forces and l-th order in displacements. By defining the expanded stress divergence term $\mathbf{R} = (\mathbf{R}_1, \mathbf{R}_2)$ with components

$$\begin{aligned} \mathbf{R}_1(\hat{\mathbf{N}}_n, \hat{\mathbf{u}}_n) &= \int_{\Omega_e} \boldsymbol{\varphi} \left(G^{11} \hat{\mathbf{u}}_n^t \boldsymbol{\phi}' \left(\mathbf{G}_1 + \frac{1}{2} (\boldsymbol{\phi}')^t \hat{\mathbf{u}}_n \right) - \hat{\mathrm{E}}(\hat{\mathbf{N}}_n) \right) dS \\ \mathbf{R}_2(\hat{\mathbf{N}}_n, \hat{\mathbf{u}}_n) &= \int_{\Omega_e} G^{11} \boldsymbol{\varphi}^t \hat{\mathbf{N}}_n \, \boldsymbol{\phi}' \hat{\mathbf{g}}_n \, dS \end{aligned} \tag{20}$$

and the mass matrix $\mathbf{M}$ as

$$\mathbf{M} = \int_{\Omega_e} \rho_0 \boldsymbol{\phi} \boldsymbol{\phi}^t \, dS \tag{21}$$

one can rewrite Eq. 19 in an implicit scheme as

$$\begin{bmatrix} \mathbf{R}_1(\hat{\mathbf{N}}_{n+1}, \hat{\mathbf{u}}_{n+1}) \\ \mathbf{R}_2(\hat{\mathbf{N}}_{n+1}, \hat{\mathbf{u}}_{n+1}) \end{bmatrix} + \begin{bmatrix} \mathbf{0} \\ \mathbf{M}\hat{\mathbf{a}}_{n+1} \end{bmatrix} = \begin{bmatrix} \mathbf{0} \\ \mathbf{F}_{ext,n+1} \end{bmatrix} \tag{22}$$

where $\mathbf{F}_{ext,n+1}$ refers to the external forces considered at the time step $n+1$.

Introducing Newmark's time integrator [3], one obtains the system of equations

$$\begin{aligned}\frac{1}{\beta\Delta t_n^2}\begin{bmatrix}\mathbf{0}\\ \mathbf{M}\hat{\mathbf{u}}_{n+1}\end{bmatrix}+\begin{bmatrix}\mathbf{R}_1(\hat{\mathbf{N}}_{n+1},\hat{\mathbf{u}}_{n+1})\\ \mathbf{R}_2(\hat{\mathbf{N}}_{n+1},\hat{\mathbf{u}}_{n+1})\end{bmatrix}\\ =\begin{bmatrix}\mathbf{0}\\ \mathbf{F}_{ext,n+1}\end{bmatrix}+\frac{1}{\beta\Delta t_n^2}\begin{bmatrix}\mathbf{0}\\ \mathbf{M}(\hat{\mathbf{u}}_n+\Delta t_n\hat{\mathbf{v}}_n)\end{bmatrix}+\frac{1-2\beta}{2\beta}\begin{bmatrix}\mathbf{0}\\ \mathbf{M}\hat{\mathbf{a}}_n\end{bmatrix}\end{aligned} \tag{23}$$

Hence the consistent linearization of the former equation, namely $\mathbf{\Phi}(\hat{\mathbf{u}}_{n+1},\hat{\mathbf{N}}_{n+1})=\mathbf{0}$, around a point $\bar{\mathbf{V}}_{n+1}=(\hat{\mathbf{u}}_{n+1},\hat{\mathbf{N}}_{n+1})$ and for the k-th iterate establishes

$$\mathcal{L}\mathbf{\Phi}=\mathbf{\Phi}|^{(k)}_{\bar{\mathbf{V}}_{n+1}}+\underbrace{\frac{\partial\mathbf{\Phi}}{\partial\hat{\mathbf{V}}_{n+1}}\bigg|_{\bar{\mathbf{V}}^{(k)}_{n+1}}(\hat{\mathbf{V}}^{(k+1)}_{n+1}-\bar{\mathbf{V}}^{(k)}_{n+1})}_{\mathrm{D}\mathbf{\Phi}(\bar{\mathbf{V}}^{(k)}_{n+1},\Delta\mathbf{V}_{n+1})}=\mathbf{0} \tag{24}$$

where the Fréchet derivative $\partial\mathbf{\Phi}/\partial\hat{\mathbf{V}}_{n+1}|_{\hat{\mathbf{V}}^{(k)}_{n+1}}$ corresponds to the dynamic stiffness $\mathbf{K}$ of the problem, with components

$$\begin{aligned}\mathbf{K_{NN}}&=-\int_{\Omega_e}\boldsymbol{\varphi}\frac{\partial\hat{\mathrm{E}}}{\partial\hat{\mathbf{N}}_{n+1}}\,dS=-\int_{\Omega_e}\boldsymbol{\varphi}\frac{\partial\hat{\mathrm{E}}}{\partial\hat{\mathrm{N}}}\boldsymbol{\varphi}^t\,dS\\ \mathbf{K_{Nu}}&=\int_{\Omega_e}G^{11}\boldsymbol{\varphi}\hat{\mathbf{g}}^t_{n+1}(\boldsymbol{\phi}')^t dS=\mathbf{K}^t_{\mathbf{uN}}\\ \mathbf{K}^s_{\mathbf{uu}}&=\int_{\Omega_e}G^{11}\boldsymbol{\varphi}^t\hat{\mathbf{N}}_{n+1}\boldsymbol{\phi}'(\boldsymbol{\phi}')^t dS\\ \mathbf{K}^d_{\mathbf{uu}}&=\frac{1}{\beta\Delta t_n^2}\mathbf{M}+\mathbf{K}^s_{\mathbf{uu}}\end{aligned} \tag{25}$$

in the form

$$\mathbf{K}=\frac{\partial\mathbf{\Phi}}{\partial\hat{\mathbf{V}}_{n+1}}\bigg|_{\bar{\mathbf{V}}^{(k)}_{n+1}}=\begin{bmatrix}\mathbf{K_{NN}}&\mathbf{K_{Nu}}\\ \mathbf{K_{uN}}&\mathbf{K}^d_{\mathbf{uu}}\end{bmatrix} \tag{26}$$

In order to satisfy stability of the solution scheme, it is necessary [2] that

$$\ker\left(\mathbf{K_{NN}}-\mathbf{K_{Nu}}(\mathbf{K}^s_{\mathbf{uu}})^{-1}\mathbf{K}^t_{\mathbf{Nu}}\right)=\mathbf{0} \tag{27}$$

3.2.2 Mixed cable element with discontinuous axial force

For the element with discontinuous axial force distribution, the cable is also subdivided into e elements of k-th order in axial forces and l-th order in displacements. In this case, however, the axial forces are treated as internal degrees of freedom, and are consequently condensed out at the element level before assembly of the element response. This generates a discontinuity in the axial forces, which is allowed by the condition $\hat{\mathrm{N}}\in H^0(0,L)$. The stress divergence term $\mathbf{R}(\hat{\mathbf{N}}_n,\hat{\mathbf{u}}_n)$ is then understood as

$$\mathbf{R}(\hat{\mathbf{N}}_n(\hat{\mathbf{u}}_n),\hat{\mathbf{u}}_n)=\int_{\Omega_e}G^{11}\boldsymbol{\varphi}^t\hat{\mathbf{N}}_n\,\boldsymbol{\phi}'\hat{\mathbf{g}}_n\,dS \tag{28}$$

and one can rewrite Eq. 19 in an implicit scheme as

$$\mathbf{R}(\hat{\mathbf{u}}_{n+1}) + \mathbf{M}\hat{\mathbf{a}}_{n+1} = \mathbf{F}_{ext,n+1} \tag{29}$$

Introducing Newmark's time integrator [3], one obtains the system of equations

$$\frac{1}{\beta\Delta t_n^2}\mathbf{M}\hat{\mathbf{u}}_{n+1} + \mathbf{R}(\hat{\mathbf{u}}_{n+1}) = \mathbf{F}_{ext,n+1} + \frac{1}{\beta\Delta t_n^2}\mathbf{M}(\hat{\mathbf{u}}_n + \Delta t_n\hat{\mathbf{v}}_n) + \frac{1-2\beta}{2\beta}\mathbf{M}\hat{\mathbf{a}}_n \tag{30}$$

Hence the consistent linearization of the former equation, namely $\mathbf{\Phi}(\hat{\mathbf{u}}_{n+1}) = \mathbf{0}$, around a point $\bar{\mathbf{u}}_{n+1}$ and for the k-th iterate establishes

$$\mathcal{L}\mathbf{\Phi} = \mathbf{\Phi}|_{\bar{\mathbf{u}}_{n+1}^{(k)}} + \underbrace{\left.\frac{\partial\mathbf{\Phi}}{\partial\hat{\mathbf{u}}_{n+1}}\right|_{\bar{\mathbf{u}}_{n+1}^{(k)}}(\hat{\mathbf{u}}_{n+1}^{(k+1)} - \bar{\mathbf{u}}_{n+1}^{(k)})}_{\mathrm{D}\mathbf{\Phi}(\bar{\mathbf{u}}_{n+1}^{(k)},\Delta\mathbf{u}_{n+1})} = \mathbf{0} \tag{31}$$

where the Fréchet derivative $\partial\mathbf{\Phi}/\partial\hat{\mathbf{u}}_{n+1}|_{\bar{\mathbf{u}}_{n+1}^{(k)}}$ corresponds to the condensed dynamic stiffness $\mathbf{K}$ of the problem

$$\mathbf{K} = \mathbf{K}_{\mathbf{uu}}^{d} - \mathbf{K}_{\mathbf{uN}}\mathbf{K}_{\mathbf{NN}}^{-1}\mathbf{K}_{\mathbf{Nu}} \tag{32}$$

with the components defined in Eq. 25.

The stability condition of the solution scheme reads [2] in this case as

$$\ker\left(\mathbf{K}_{\mathbf{uu}}^{s} - \mathbf{K}_{\mathbf{uN}}\mathbf{K}_{\mathbf{NN}}^{-1}\mathbf{K}_{\mathbf{Nu}}\right) = \mathbf{0} \tag{33}$$

4 NUMERICAL EXAMPLES

The proposed formulation is implemented in two cable elements with continuous and discontinuous axial force distributions. The elements, deployed in the general purpose finite element program FEAP [4] and Matlab toolbox FEDEASLab [5], use a linear approximation for the axial forces ($k = 1$) and a quadratic approximation for the displacements ($l = 2$). The two-dimensional element results in eight degrees of freedom (DOFs), six displacement DOFs and two axial force DOFs, while the three-dimensional element results in eleven DOFs, nine displacement DOFs and two axial force DOFs.

Both elements are implemented with a St Venant - Kirchhoff elastic material model with stored energy $\mathcal{U}$ in terms of the stretch λ and the generalized Young's modulus E

$$\mathcal{U} = \frac{E}{8}(\lambda^2 - 1)^2 \tag{34}$$

Thus, if A is the area of the cross section and $\hat{\mathrm{N}}_0$ the prestressing force,

$$\hat{\mathrm{N}} - \hat{\mathrm{N}}_0 = (EA)\hat{\mathrm{E}} \tag{35}$$

with constant material stiffness $\partial\hat{\mathrm{N}}/\partial\hat{\mathrm{E}} = EA$.

4.1 Example 1: Stability of a 3d pulley system

The first example investigates the stability of a 3d cable supported by a pulley that was previously studied by Impollonia *et al* [6]. The structural model, whose geometric and material properties are shown in Table 1, consists of a cable anchored at both ends and supported by an intermediate roller. In this case, the inertia forces in Eq. 19 and the mass term of the stiffness are not considered as the problem is analyzed in a static manner.

Property	**Value**
Cross-sectional area	805 mm^2
Elastic modulus	16.0 kN/mm^2
Cable self-weight	62.0679 N/m
Cable length	500 m

Table 1: Geometry and Material Properties for Example 1.

The objective of this example is to determine the equilibrium configurations of the cable under the assumptions that the pulley is free to move horizontally and that the pulley radius and friction are negligible. For the nonlinear analysis, the cable is subdivided into two segments, one for each span, with the reference curvilinear coordinate ξ^1 of the pulley as problem unknown. This curvilinear coordinate ξ^1 is used to construct the finite element mesh in each iteration.

Following the form finding procedure by Argyris *et al* [2, 7], the analysis starts from a straight reference configuration, and imposes a displacement $\mathbf{u} = (-200, 0, 50)$ m at the right support and a pair of displacements $u_2 = 50$ m and $u_3 = 100$ m at the intermediate roller. Because friction is not considered, the jump in the Cauchy axial force at the roller support must be zero. As a result, the problem is solved by iterating over the curvilinear coordinate ξ^1 so that the jump in the Cauchy axial force at the pulley becomes zero.

	Impollonia *et al* [6]	**Present work (continuous)**	**Present work (discontinuous)**
ξ_1^1 (m)	126.12	126.26	126.25
N_1 (kN)	14.12	8.31-13.99	8.31-13.99
ξ_2^1 (m)	219.98	219.46	219.47
N_2 (kN)	10.79	4.02-10.68	4.02-10.68
ξ_3^1 (m)	424.76	424.70	424.70
N_3 (kN)	17.42	10.25-17.28	10.25-17.28

Table 2: Results for Example 1 from different studies.

Table 2 summarizes the results for the equilibrium configurations with ξ_i^1 refering to the curvilinear coordinate of the pulley and N_i, to the axial force. Because the study by Impollonia *et al* [6] does not consider finite deformations, ξ_i^1 and N_i correspond to

infinitesimal deformations. For the present study, ξ_i^1 corresponds to the reference configuration and N_i, to the Cauchy axial force. While the values of the present study agree well with those by Impollonia *et al* [6], it is worth noting the variation of the Cauchy axial force that the current formulation captures, as indicated by the range of axial force values in Table 2. In contrast, the model in [6] overestimates the axial force by reporting a value corresponding to the maximum of the current formulation.

Three equilibrium states result from the analysis, as Fig. 2 shows: three stable configurations denoted with solid lines (C_1 and C_3), and one unstable configuration, denoted with a dashed line (C_2), as reflected in the change of direction for the horizontal component of the reaction at the pulley. The x_1 positions of the pulley for these equilibrium states in Fig. 2 are $x_1^1 = 56.54/56.53$ m, $x_1^2 = 134.00/134.01$ m and $x_1^3 = 274.31/274.31$ m for the continuous and the discontinuous formulations, respectively.

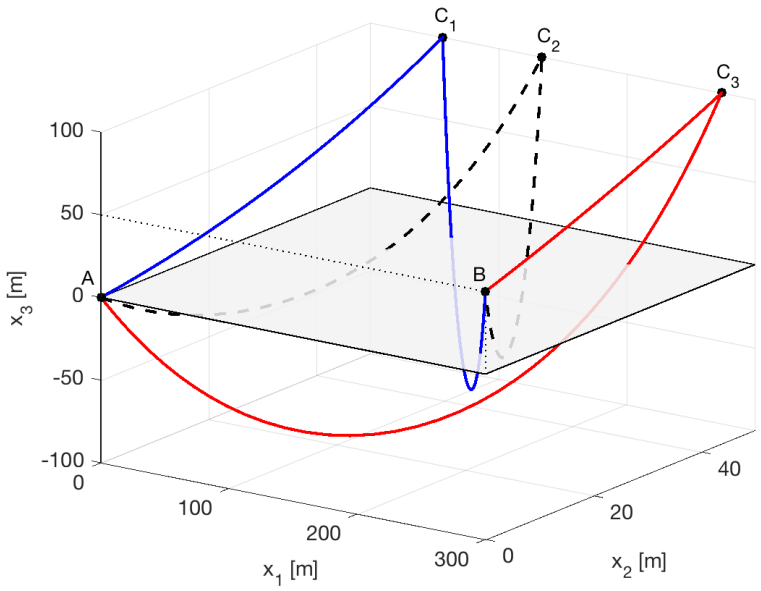

Figure 2: Deformed shape (30 elements) of equilibrium states for Example 1.

4.2 Example 2: Free vibration in finite deformations

The second example studies the large-amplitude free vibration of two cables with different sag/span ratio that were investigated by Srinil *et al* [8]. The structural model consists of a cable anchored at both ends and spanning 850 m in both cases. Table 3 summarizes the geometric and material properties of the cables denoted by C1 and C2.

First, following the shape finding procedure by Argyris *et al* [7], the equilibrium configuration and the first two natural modes of vibration around this configuration are obtained for both cables by solving the standard eigenvalue problem

$$\det[\mathbf{K}(\mathbf{u}_{eq}) - w^2\mathbf{M}] = 0 \tag{36}$$

Property	**C1**	**C2**
Cross-sectional area	0.1159 m^2	0.1159 m^2
Elastic modulus	17.94 GPa	17.94 GPa
Density	8337.9 kg/m^3	8337.9 kg/m^3
Cable length	840.48 m	870.51 m
Prestressing	-	345 kN

Table 3: Geometry and Material Properties for Example 1.

where w is the angular frequency, $\mathbf{u}_{eq}$ refers to the displacement field at the equilibrium state, and $\mathbf{K}$ and $\mathbf{M}$ correspond to the static stiffness and mass matrices of the formulation in Sec. 3.2. Both cables are discretized with a mesh of 14 elements. Results are presented in Table 4, where the end tension is given in the Cauchy representation, and "S" and "A" refer to the symmetric and antisymmetric modes, respectively. Fig. 3 shows the normalized first symmetric and antisymmetric modes of both cables. From this figure, it is interesting to note that, when the sag/span ratio increases, the single extremum for the symmetric mode divides into three because of increasing horizontal displacements.

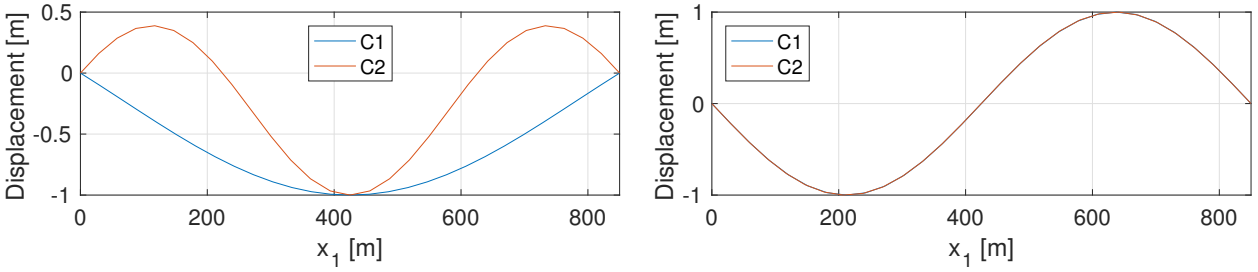

(a) First symmetric mode (b) First antisymmetric mode

Figure 3: Normalized vertical eigenvectors for Example 2.

	C1		**C2**	
	Present	Srinil *et al* [8]	Present	Srinil *et al* [8]
Sag [m]	28.01	28.39	89.28	89.57
Sag/span [-]	1/30	1/30	1/9.5	1/9.5
End tension [kN]	30432	30000	10500	10500
Frequency (1st S) [Hz]	0.124	0.123	0.158	0.158
Frequency (1st A) [Hz]	0.208	0.206	0.112	0.112

Table 4: Results for equilibrium configurations and natural vibration in Example 2.

To evaluate the large-amplitude free vibration, an initial displacement field is imposed corresponding to an amplified first symmetric mode, $\mathbf{u}_0 = \alpha \mathbf{u}_{m1}$, where $\mathbf{u}_{m1}$ is the normalized first symmetric mode. The parameters for Newmark's method are $\beta = 0.25$, $\gamma = 0.5$ and $\Delta t = 0.05$ s. No differences are observed between the continuous and the discontinuous formulations as the problem in hand is symmetric in geometry and loads.

Fig. 4(a) shows the normalized vertical displacements and Cauchy axial forces for cable C1 and $\alpha = 15$. The evolution of the energy for this case is presented in Fig. 5(a). Likewise, Fig. 4(b) and Fig. 5(b) present the normalized vertical displacements and Cauchy axial forces, and energy evolution, respectively, for cable C2 and $\alpha = 15$. While cable C1 behaves linearly in displacements, cable C2 shows a high dependence on high-frequency modes. Also, high-frequency contributions are observed in both cases for the axial force, becoming more relevant for the large sag/span ratio, as observed by Srinil *et al* [6]. The total energy is conserved for cable C1, whereas it shows minor oscillations for cable C2.

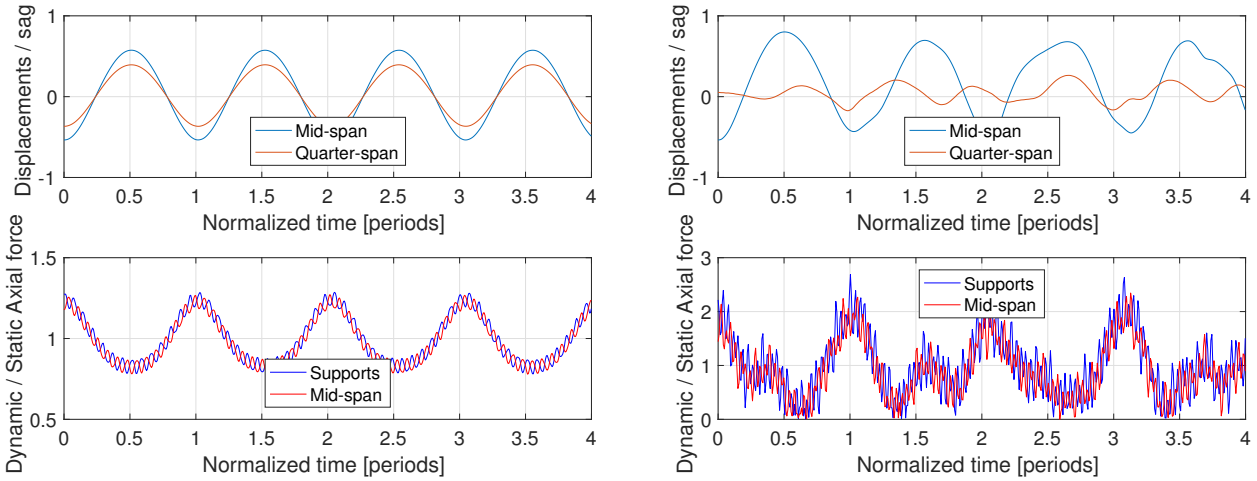

(a) Cable C1 (b) Cable C2

Figure 4: Normalized vertical displacements and Cauchy axial forces for Example 2.

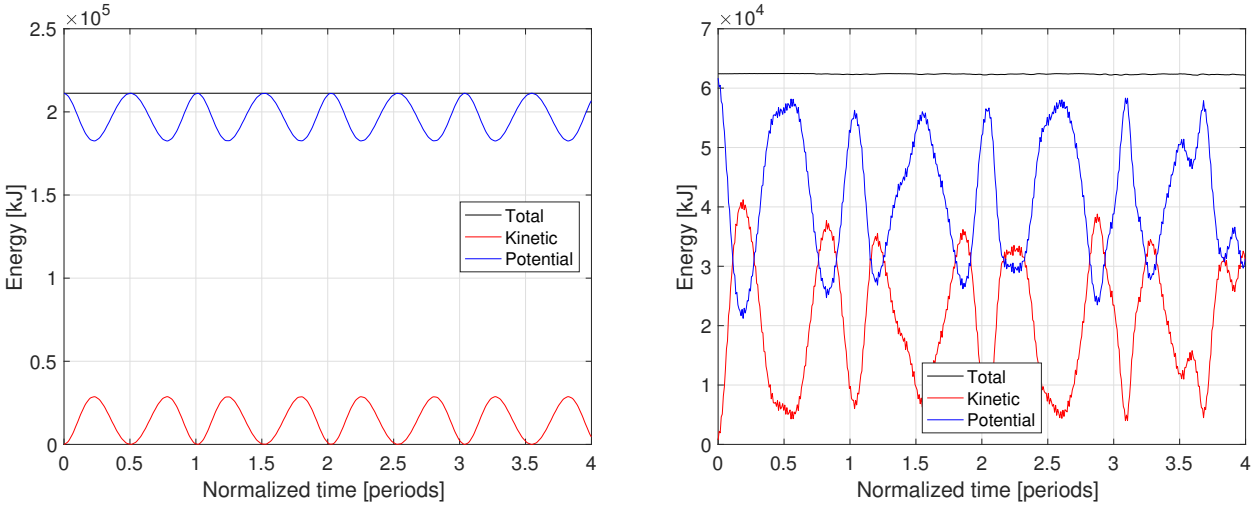

(a) Cable C1 (b) Cable C2

Figure 5: Energy evolution for Example 2.

5 CONCLUSIONS

The paper presents a general formulation of catenary elements based on finite deformations and curvilinear coordinates for the nonlinear static and dynamic analysis of cables. From the weak statement of the problem, two implementations are derived: one with a continuous axial force distribution and one with a discontinuous.

As demonstrated by the first example, the formulation is capable of determining equilibrium configurations of three-dimensional cable arrangements with high accuracy, especially in axial forces, compared to other elements in the literature which do not distinguish between Cauchy and 2nd PK axial forces. Furthermore, the second example shows that the natural modes of vibration around equilibrium configurations can also be obtained by the proposed formulation. Because the energy is conserved in the analyzed range of sag/span ratios, Newmark's implicit method can be used to solve the nonlinear dynamic problem. Nevertheless, as observed in the literature, high-frequency contributions in the axial force appear in the analysis, with their amplitude increasing with the sag/span ratio.

In conclusion, because of their consistency and versatility, the proposed catenary elements seem well suited for the nonlinear static and dynamic analysis of nonlinear elastic cables under general loading.

REFERENCES

[1] Andreu, A., Gil, L. and Roca, P. A new deformable catenary element for the analysis of cable net structures. *Comp. Struct.* (2006) **84**:882–1890.

[2] Crusells-Girona, M., Filippou, F.C. and Taylor, R.L. A mixed formuation for nonlinear analysis of cable structures. *Comp. Struct.* (2017) **186**:50–61.

[3] Newmark, N. A method of computation for structural dynamics. *J. Eng. Mech.-ASCE* (1959) **85**:67–94.

[4] Taylor, R.L. *FEAP - Finite Element Analysis Program*. Univ. of California, Berkeley (2014). http://www.ce.berkeley/feap.

[5] Filippou, F. C. *FEDEASLab - Finite Elements in Design, Evaluation and Analysis of Structures*. Univ. of California, Berkeley (2007). http://www.ce.berkeley.edu/˜filippou/Courses/FEDEASLab.htm.

[6] Impollonia, N., Ricciardi, G. and Saitta, F. Statics of elastic cables under 3D point forces. *Int. J. Solids Struct.* (2011) **48**:1268–1276.

[7] Argyris, J. H., Angelopoulos, T. and Bichat, B. A general method for the shape finding of lightweight tension structures. *Comp. Meth. Appl. Mech. Eng.* (1974) **3**:135–149.

[8] Srinil, N., Rega, G. and Chucheepsakul, S. Three-dimensional non-linear coupling and dynamic tension in large-amplitude free vibrations of arbitrarily sagged cables. *J. Sound Vib.* (2004) **269**:823–852.

XIV International Conference on Computational Plasticity. Fundamentals and Applications
COMPLAS 2017
E. Oñate, D.R.J. Owen, D. Peric and M. Chiumenti(Eds)

ELECTROMAGNETIC PROCESSING OF METAL AS COUPLING OF MULTI-PHYSICS PHENOMENA

VICTOR B. DEMIDOVICH[*], FEDOR V. TCHMILENKO[*], YURI YU. PEREVALOV[*] AND IRINA I. RASTVOROVA[†]

[*] St.Petersburg Electrotechnical University (LETI),
prof. Popov 5, St.Petersburg, Russia
e-mail: vbdemidovich@mail.ru, web page: http://www.eltech.ru

[†] Saint-Petersburg Mining University, 21 Line, 2, St.Petersburg, Russia,
e-mail: rastvorova@mail.ru web page: http://www.spmi.ru

Key words: Coupled Electromagnetic and Temperature Fields, Multiphysics Problems, Induction heating, Electromagnetic processing of metals.

Abstract. Effective numerical models of induction heat treatment are developed. They include two-dimensional modeling of coupling electromagnetic and temperature fields in cylindrical systems for processing of tubes and rolls. Also thermal tension during heating and cooling of tubes and rolls are simulated. These data allow defining structure, hardness, the size of grain and other properties of the tubes and rolls. They allow optimizing design and a choice of equipment, a heat treatment mode for the purpose of achievement of the maximum quality and minimization of energy consumption. The developed two-dimensional models were used not only for the design of induction heat treatment systems of tubes and rolls, but also for a digital control of these complexes.

1 INTRODUCTION

The aim of induction hardening is to increase the hardness of the boundary layers of a workpiece by rapid heating and subsequent quenching. This heat treatment leads to a change in the microstructure, which produces the desired hardening effect.

In the case of induction heating, a current in the induction coil induces eddy currents inside the workpiece. Eddy currents lead to an increase of the temperature in the boundary layers of the workpiece due to Joule and Skin effects. After that the current is switched off and the workpiece is quenched by spray-water cooling.

In spite of the fact that induction hardening has successfully been applied in industry for many years, there is a growing demand in industry for a more precise process control. This circumstance is linked with the growing complexity of the quenched components, reduction of the workpiece thickness due to modern weight requirements, etc. Using of computer simulation is a powerful and necessary approach for solving these problems. From the physical point of view the induction hardening is a very complicated process (Figure 1). We

should include all the significant phenomena in the mathematical description to achieve an acceptable calculation result. Moreover, it is very important to understand that all phisical phenomena are linked with each other.

It is obvious that induction hardening mathematical description should include the electromagnetic, thermal and phase transformations phenomena. But the resulting workpiece properties are strongly depend on stress-strain state (residual stress) due to summation stress effect with the external load. Moreover, stress is an additional driving force for the phase transformation (Figure 1). That's why it is desirable to describe this phenomenon too.

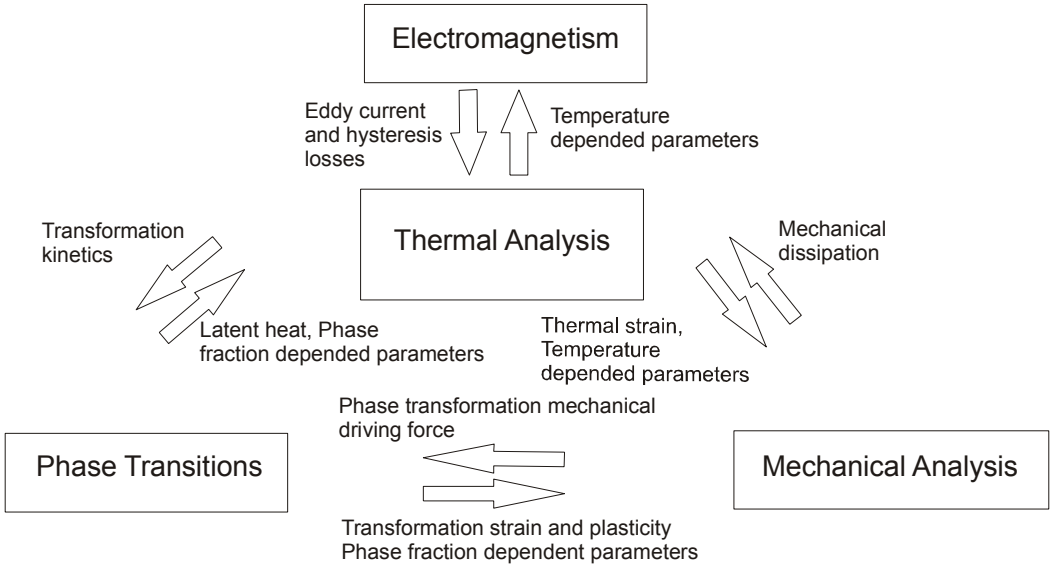

Figure 1. Heat treatment physical phenomena

2 ELECTROMAGNETIC AND THERMAL ANALYSIS

A simulation of the induction heating process includes a computation of electromagnetic and temperature fields. In the case of ferrous steel heating, some features should be taken into account because of very strong non-linearity in the system.

Codes for the simulation of induction heating should provide the capability to solve the tightly coupled (inter-related) computations of electromagnetic and heat transfer phenomena. In order to create this feature, a special computational algorithm has been developed [1]. This algorithm is based on jointly solving a system of two non-linear differential equations, which describe the electromagnetic and temperature fields, and provides a reliable coupling of both phenomena.

Electromagnetic field in the workpiece can be described by the following equation

$$rot\left(\rho rotH\right)=-\mu\mu_0\frac{\partial H}{\partial t}, \qquad (1)$$

where:

H is the strength of magnetic field, ρ is the electrical resistivity of metals, μ is the relative magnetic permeability, μ_0 is the permeability of free space. The electrical resistivity of a metal is temperature dependent. In addition, the relative magnetic permeability is a function

of two parameters: magnetic field intensity and temperature.

It is important to note that common approach of using the first harmonic for the computation of the electromagnetic field in induction heating systems can result in a low accuracy in the ferrous workpiece heating analysis. For more accurate computations, equation (1) should be used for the simulation of a non-sinusoidal distribution of the electromagnetic field in a workpiece. Very strong dependence of magnetic permeability on temperature is very important for the simulation induction heating.

Accurate data of this dependence are not readily available, though in many cases it could be approximated as follows:

$$\mu(T,H) = 1 + (\mu - 1) \times \left[1 - \left(\frac{T}{T_C} \right)^n \right], \quad T \langle T_c \qquad (2)$$

$$\mu(T,H) = 1, \qquad T \geq T_C$$

where:

T_c - temperature of Curie, n - index.

The most reliable data that is supported by experimental investigations correlate with an index *n* between 4 and 6.

The transient heat transfer process in a steel tubes and rolls can be described by the nonlinear Fourier equation:

$$C_V \frac{\partial T}{\partial t} = div(\lambda grad T) + w, \qquad (3)$$

where:

T is the temperature, C_V is the volume specific heat, λ is thermal conductivity of the metal, and w is the heat source density that is generated in the case of induction heating process. The thermal conductivity and specific heat of metal are each functions of temperature.

The coupling algorithm jointly solves the system of two non-linear differential equations for the electromagnetic (1) and temperature fields (3) with either the Finite Element Method (FEM) or the Finite Difference Method (FDM). The algorithm calls for an iterative process consisting of an electromagnetic computation and followed by a re-calculation of the heat sources in order to make an updated heat transfer computation. This assumes that temperature variations are not significant in each time step that the material properties remain approximately the same, and the temperature fields can be computed without correcting the heat sources. The temperature distribution within the workpiece, obtained from the time-stepped heat transfer computation, is used to update the values of specific heat and thermal conductivity in each time step. As soon as the heat source variations become significant (due to the variations of electrical conductivity; magnetic permeability, change of the current in the inductors, etc.) the convergence condition will no longer be satisfied and a re-calculation of the electromagnetic field and heat sources will take place.

In general case all the coefficients in (3) are depended on temperature. This circumstance leads to a non-linearity thermal analyses problem which should be solved by using one of the iteration numerical methods.

Moreover, these coefficients are depended on instant phase mixture during the process of heating or cooling of the workpiece. Thus, it is desirable to use the temperature dependencies of the thermal coefficients for all the possible phases in coupling with additivity concept, which allow us to calculate the mean coefficient quantity. The experimental data for the thermal properties of each phase are absent in available reference-literature, but the modern state of computational material science allows us to use specialized for this purposes software like JMatPro [2].

3 PHASE TRANSITIONS

Time-temperature-transformation (TTT) diagrams (Figure 2) are used for the description of experimental research in steel phase transformations. Continuous-cooling-transformation (CCT) diagram is built under the continuous cooling (or heating) conditions (Figure 2,*a*, 2,*b*). Isothermal-transformation (IT) diagram is built under the isothermal conditions (Figure 2,*c*).

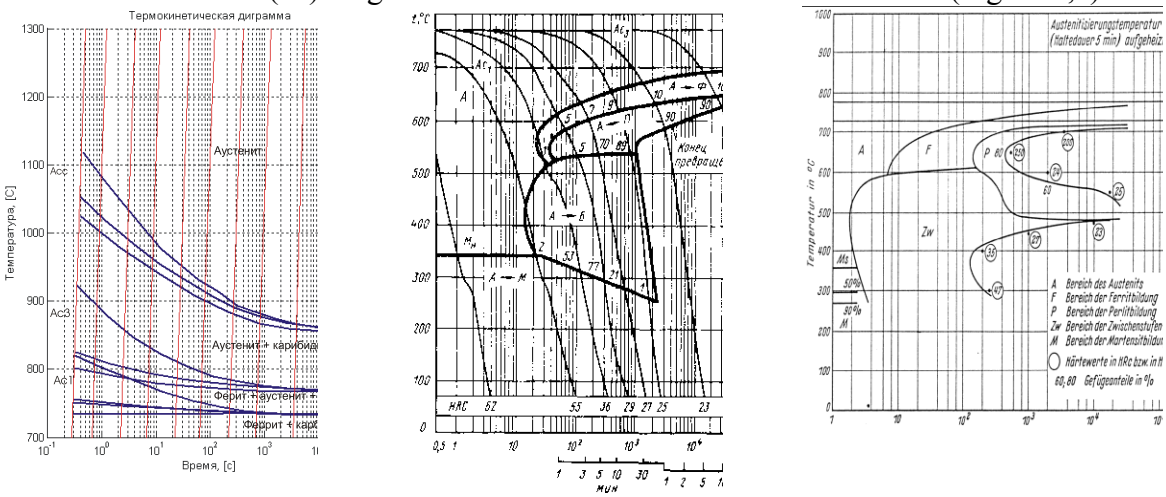

a) b) c)

Figure 2. Examples of typical TTT-diagrams

a – CCT diagram of heating; b – CCT digram of cooling; c – IT diagram of cooling

Nowadays the experimental diagrams using is wide spread for the induction heat treatment process analysis and development. Most of the calculation approaches based on the combination of Scheil rule for the continuous conditions analysis and Avrami-type kinetics parametric equation [3]. In this case the model is based on the IT diagrams only. But there are several problems for this approach:

- Scarce phase solubility data – necessity of thermodynamics using for the correct calculation of the ferrite, pearlite transformation. Moreover, the maximum volume fraction of bainite is complicated for calculation [4].
- Lack of the grain size kinetics influence information.

- Absence of the mechanical driving force influence information.
- TTT diagrams do not reflect a simultaneous phase transformation.

Thus, for solving these problems it would be suitable to develop a mathematical model which allows us to calculate of cooling or heating diagram for arbitrary steel, taking into account composition, microstructure and stress-strain station. It is possible to use a modern computational material science for these purposes [5]. These theories based on combination of thermodynamics and kinetics and could be used for the calculation of:

- Incubation time for the certain phase.
- Nucleation rate and the type of grain geometry.
- Growth mechanism and rate.
- Ac3, Ac1, Ms points.

Usually these calculations are used in combination with thermodynamics theory and CALPHAD method [6]. There are several program tools which implements this method (MTDATA, ThermoCalc, etc).

4 MECHANICAL ANALYSIS

It is very important to analyze the residual stress because it is an additional component of loading during the exploitation of the part. Moreover, it is important to evaluate stresses during the induction heating technological process to avoid cracks and large deformations.

The classification of the stresses based on the scale of continuity is shown on Figure 3:

- Stresses of type *I* vary continuously over large distances (σ_{Macro}).
- Type *II* (intergranular stresses) vary over the grain scale (σ_{II}).
- Type *III* – atomic scale (σ_{III}).

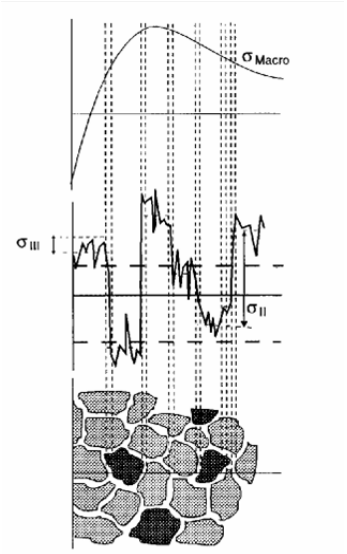

Figure 3. Stress classification

We concentrate on analysis of type *I* stresses because their importance and direct influence on exploitation part properties.

On the other hand the classification based on causes of stress is needed for the development of the valid mathematical model of stress-strain state. This type of classification could be done by the Figure 1. In compliance with it, there are three main sources of the residual stresses:

- Thermal stresses.
- Misfits in different phases density and their thermal expansion coefficients.
- Transformation induced plasticity (TRIP).

All of this sources cause the residual stress. One of the main problems in induction heating simulation by the general-purpose FEM programs is adequately calculation of the residual stress. It is necessary to calculate phase transformation phenomenon for TRIP and phase transformation stresses analysis.

It is obvious that elastic solution of this problem is being of no favor because all of the interesting effects are linked with the plasticity. In case of the plasticity calculation it is necessary to determine the yield criterion. It is good idea to use von Mises criterion for the steels [7]. Besides that, we need to determine the type of hardening. Kinematic hardening is taking place during the cycle loading only. Moreover it is complicated to determine phenomenological coefficients for this type of hardening. We use the isotropic hardening rule.

Thus, we have a mathematical description based on von Mises criterion and isotropic hardening rule. For solving this problem it is possible to use J_2-plasticity model [8]. This algorithm does not require a difference approximation of partial differentials in tangential matrix. This circumstance reduces a computational complexity.

5 CONCLUSIONS

The effectiveness of induction heat treatment computation is related to the numerical methods which are used. In the most practical cases it is impossible to use a "general" method for all the phenomenon description. We have shown that it could be combination based on FEM, thermodynamic analysis, etc. It is convenient and appropriate to use individual approach for all the physical phenomena in induction heat treatment process.

The publication was carried out in the framework of the state work "Organization of Scientific Research" (assignment No.8.6037.2017 / VU Ministry of Education and Science of Russia).

REFERENCES

[1] Demidovitch, V. (1996) Special Software IndHeat for Modeling Induction Heating Processes, *Proceedings of 3rd International Workshop on ELECTRIC AND MAGNETIC FIELDS EMF`96*, Liege, Belgium, p. 273-278.

[2] Saunders, N., Li, X., Miodownik, A., & Schille, J.-P. (2001). *Materials Design Approaches and Experiences.* (J.-C. Z. al., Ed.) Warrendale: PA:TMS.

[3] Kurek, K., & Dołęga, D. (2003). Modeling of Induction Hardening. *International Scientific Colloquium "Modeling for Electromagnetic Processing"*, (125-130). Hannover.

[4] Reti, T., Fried, Z., & Felde, I. (2001). Computer simulation of steel quenching process using a multi-phase transformation model. *Comutational Materials Science* , 261-278.

[5] Bhadeshia, H. (2001). *Bainite in steels* (2nd Edition). London: IOM Communications Ltd.

[6] Saunders, N., & Miodownik, A. (1991). *CALPHAD - Calculation of Phase Diagrams* (Vol. 1). (R. Cahn, Ed.) Oxford: Elsevier Science.

[7] Edited by E. Steck, R. Ritter, U. Peil, A. Ziegenbein. (2001). *Plasticity of Metals: Experiments, Models, Computation.* Wiley-VCH Verlag GmbH.

[8] Zienkievich O.C., Taylor R.L. (2000). *The Finite Element Method. Volume 2: Solid Mechanics* (5th Edition). Butterworth-Heinemann.

XIV International Conference on Computational Plasticity. Fundamentals and Applications
COMPLAS XIV
E. Oñate, D.R.J. Owen, D. Peric & M. Chiumenti (Eds)

A NEW INTERPRETATION OF THE GLOBAL TRACKING ALGORITHM IN THE CONTEXT OF THE STRONG DISCONTINUITY APPROACH

F. RICCARDI* AND B. RICHARD†

* DEN-Service d'études mécaniques et thermiques (SEMT), CEA, Université Paris-Saclay, F-91191, Gif-sur-Yvette, France. e-mail: francesco.riccardi@cea.fr

†DEN-Service d'études mécaniques et thermiques (SEMT), CEA, Université Paris-Saclay, F-91191, Gif-sur-Yvette, France. e-mail: benjamin.richard@cea.fr

Key words: Tracking, strong discontinuity, E-FEM, Cast3M, damage, strain localization

Abstract. The numerical simulation of two-dimensional fracture processes of quasi-brittle materials by means of the Embedded Finite Element Method is dealt with. The attention is paid to the coupling with the global crack-tracking strategy often used to ensure the crack path continuity. It has been proposed in the literature in the form of a heat conduction-like problem. It turns out that the stiffness-like matrix associated with this formulation is singular and a numerical perturbation has to be introduced in order to overcome the ill-posedness of the problem. The sensitivity of the solution on this parameter may represent a limitation for the global tracking approach. In addition, it is found that if the root of each discontinuity is not updated during an incremental analysis, a loss of continuity of the crack path may appear when principal stress directions rotate. This contribution aims to provide a solution to the aforementioned issues. A new interpretation of the mathematical problem based upon Navier-Stokes equations is proposed in order to link the diffusive contribution to a characteristic mesh length. Furthermore, a modified crack-tracking algorithm, considering the evolution of the root for the identification of the crack path, is proposed. The numerical assessment of the proposed tracking strategy is reported by means of benchmark tests at the structural level.

1 INTRODUCTION

In the last decade, the Embedded Finite Element Method (E-FEM) has gained wide popularity for the description of cracking phenomena [1]. Due to the local nature of the kinematic enrichment, this approach presents some advantages concerning the computational effort with respect, for example, to the Extended Finite Element Method (X-FEM) [2]. Indeed the additional degrees of freedom can be statically condensed, since they are expressed at the element level in terms of crack opening displacement components [3], thus leaving unchanged the dimension of the global system of equations. As a counterpart, since no information is available in

the vicinity of cracked elements, the continuity of the crack path is not intrinsically guaranteed and a loss in objectivity may be encountered in numerical simulations. For this reason, the E-FEM is usually associated with the adoption of tracking algorithms leading to C^0-continuous crack paths [4, 5]. Different crack-tracking strategies can be found in the literature. In general, two families may be distinguished: local tracking and global tracking algorithms [6].

Local tracking relies on geometry-based or energy-based schemes, which are applied for each element able to crack. The main difference between the two strategies stands in the evaluation of the direction of the propagating discontinuity. In case of a geometrical approach, the crack orientation is given by the assumed failure criterion, e.g. accordingly to Rankine it is supposed to be perpendicular to the maximum tensile principal direction [7], whereas in case of an energetic approach, it is computed from linear-elastic fracture mechanics (LEFM) by minimization of the mechanical energy. From the knowledge of the root of each discontinuity, i.e. the material point experiencing failure and not associated to any pre-existing crack path, it is possible to make the input point of the crack inside an element match the output point of the crack present in an adjacent element. Local tracking techniques are able to reproduce continuous crack paths in a robust manner by exploiting the informations of nearby elements. Nevertheless, their implementation in the case of multiple crack problems may be cumbersome and this strategy can loose much of its robustness.

Global tracking has been introduced to overcome the limits of local strategies when dealing with multi-cracking modelling [3]. The main idea is to trace the envelopes of the tangent vector field to the discontinuities as the isovalues of the temperature field of a heat conduction-like problem in the case of steady state conditions and no internal sources. Dirichlet and Neumann boundary conditions must be prescribed on the respective portions of the boundary, in terms of fixed temperature values and (null) heat flux. Once the assumed failure criterion is fulfilled for the first time in a certain material point, the latter becomes the root of a new discontinuity line, which can be traced as the isovalue passing through that point. Numerical applications can be found in [8]. The main advantage of this approach is the fact that no information from the neighbourhood of the cracked elements is required to perform the analysis: indeed, since the isovalues are available at every point of the domain, only root element coordinates shall be provided in order to ensure a continuous crack path.

The finite element formulation of the heat conduction-like problem is straightforward. However, the stiffness-like matrix deduced from the anisotropic conductivity tensor reveals to be singular and a user-defined perturbation (isotropic algorithmic conductivity) is introduced in numerical simulations to circumvent this drawback. The dependence of the solution on this parameter may then represents a limitation for the application of global tracking, since its value changes for each specific structural problem. In addition, it is found out that the capability of the thermal-like isovalues to envelop the vector tangent field is reduced as soon as cracking occurs.

This fact, due to the rotation of the principal stress directions outside the region crossed by the discontinuity, may lead to a loss of continuity of the crack path and, in the worst case, to a wrong evaluation of the enriched shape functions whenever the element domain is not decomposed properly. Such a circumstance becomes increasingly critical as the evolution of the principal stress field is important.

The objective of this paper is to provide an alternative formulation of the global crack-tracking strategy able to improve the performance of this technique with respect to the aforementioned issues. This paper is organized as follows. In Section 2 a new physical interpretation of the problem is given in terms of Navier-Stokes equations, where the concept of numerical diffusion is introduced in order provide a stable and consistent solution of the initially ill-posed descrete problem. A revised algorithm for ensuring continuous crack paths in case of step-by-step analysis is presented in Section 3, considering the evolution of the root for the choice of the isovalue enveloping the propagating discontinuity. Section 4 investigates the application of the proposed model to the E-FEM by means of a structural case study. Section 5 then concludes with a critical comparison between the proposed approach and the original formulation.

2 GLOBAL EQUATIONS

The problem of tracing the envelopes of a vector field $\mathbf{T}(\mathbf{x})$ in a domain Ω is dealt with. For the sake of simplicity, let us focus upon the bi-dimensional case. If we indicate with $\mathbf{N}(\mathbf{x})$ the normal vector field to $\mathbf{T}(\mathbf{x})$, we can consider a scalar function $\theta(\mathbf{x})$ whose gradient is parallel to $\mathbf{N}(\mathbf{x})$, i.e. such that:

$$\mathbf{N}(\mathbf{x}) = \frac{\nabla\theta(\mathbf{x})}{\|\nabla\theta(\mathbf{x})\|} \quad , \quad \mathbf{x} \in \Omega \tag{1}$$

Hence, the following partial differential equation will hold in the domain Ω:

$$\mathbf{T}(\mathbf{x}) \cdot \nabla\theta(\mathbf{x}) = 0 \tag{2}$$

Since the level contours of the function $\theta(\mathbf{x})$ are orthogonal to the gradient, the envelope of the vector field $\mathbf{T}(\mathbf{x})$ passing through a generic point P can be defined as:

$$\Gamma_P = \{\mathbf{x} \in \Omega | \theta(\mathbf{x}) = \theta_P\} \tag{3}$$

The envelopes of the vector field $\mathbf{T}$ thus provide C^0-continuous curves, which are well-suited to model crack-paths within the framework of the E-FEM. From now on the dependence of all the quantities on $\mathbf{x}$ will be omitted.

2.1 Heat conduction-like problem

Equation (2) can be manipulated by multiplying it by the vector field $\mathbf{T}$. After some analytical computations and using the same notations as in [4], the previous problem can be reformulated as the following boundary value problem for the unknown function θ:

$$\begin{cases} \nabla \cdot \mathbf{q} = 0 & \forall \mathbf{x} \in \Omega \quad (4a) \\ \mathbf{q} = -\mathbb{K} \cdot \nabla\theta & \forall \mathbf{x} \in \Omega \quad (4b) \\ \mathbf{q} \cdot \boldsymbol{\nu} = 0 & \forall \mathbf{x} \in \partial_q\Omega \quad (4c) \\ \theta = \theta^* & \forall \mathbf{x} \in \partial_\theta\Omega \quad (4d) \end{cases}$$

with:

$$\mathbb{K} := \mathbf{T} \otimes \mathbf{T} \tag{5}$$

where $\otimes$ denotes the tensor product. The boundary value problem (4) defines a heat conduction-like problem in the domain Ω, where θ is the temperature field and where $\mathbf{q}$ is the conduction flux vector. Boundary conditions are prescribed on the boundary $\partial\Omega = \partial_q\Omega \cup \partial_\theta\Omega$ such that $\partial_q\Omega \cap \partial_\theta\Omega = \emptyset$. More precisely, equation (4c) expresses the Neumann condition of a null heat flux on the set $\partial_q\Omega$, whereas equation (4d) represents the Dirichlet condition of fixed temperature values on the boundary $\partial_\theta\Omega$.
From expression (5), it turns out that the conductivity tensor $\mathbb{K}$ is singular. In order to avoid the ill-posedness of the conduction problem, the following isotropic perturbation is introduced [4, 3]:

$$[\mathbb{K}]_\epsilon = \begin{bmatrix} T_x^2 & T_xT_y \\ T_xT_y & T_y^2 \end{bmatrix} + \epsilon \begin{bmatrix} 1 & 0 \\ 0 & 1 \end{bmatrix} \tag{6}$$

where T_x and T_y are the Cartesian components of the vector field $\mathbf{T}$ and where ϵ is a user-defined numerical parameter. No rigorous criterion is available for its choice. However, it should be as small as possible in order to fulfil equation (4a), but sufficiently large to break down the singularity of $\mathbb{K}$. The dependence of the results on this numerical parameter may then limit the applicability of global tracking, eventually leading to numerical instability issues.

2.2 Heat convection-diffusion-like problem

With the aim of overcoming the aforementioned limitation, a new interpretation of the original problem defined by equation (2) is here proposed. To start with, let us consider a convection-diffusion-like problem, which consists in finding a temperature field θ such that:

$$\begin{cases} \underbrace{\mathbf{T} \cdot \nabla\theta}_{\text{Convective term}} - \underbrace{\mathbf{div}(\alpha\nabla\theta)}_{\text{Diffusive term}} = 0 & \forall \mathbf{x} \in \Omega \quad (7a) \\ J = -\alpha\nabla T \cdot \boldsymbol{\nu} = 0 & \forall \mathbf{x} \in \partial_J\Omega \quad (7b) \\ \theta = \theta^* & \forall \mathbf{x} \in \partial_\theta\Omega \quad (7c) \end{cases}$$

where α is a diffusion coefficient and $\boldsymbol{\nu}$ the unit outward normal vector to the boundary. Problem (7) can be derived from Navier-Stokes equations in case of incompressible fluids. In this context, the vector field $\mathbf{T}$ takes the physical meaning of a fluid velocity. Therefore equation (7a) describes a heat transfer process where

two contributions can be distinguished: the first one of convective nature, the second one of diffusive nature. Boundary condition (7b) expresses the Neumann condition on the diffusive flux J, while equation (7c) assumes the same meaning as in problem (4). However, since $\mathbf{T}$ is now a velocity field, Dirichlet boundary conditions should be prescribed only on the portions of the boundary where the former is directed inward the domain Ω. In order to better understand the preceding formulation, let us focus upon the one-dimensional case. Assuming a constant diffusion coefficient and considering, on the one hand, a first order upwind scheme for the convective term and, on the other hand, a second order centered scheme for the diffusive term, equation 7a is discretized as:

$$T\frac{\theta_i - \theta_{i-1}}{\Delta x} - \alpha\frac{\theta_{i+1} - 2\theta_i + \theta_{i-1}}{\Delta x^2} = 0 \tag{8}$$

where Δx is the one-dimensional spatial discretization step. If we consider now a centered discretization of the convective term, it turns out that the difference between the upwind discretization and the aforementioned one is given by:

$$\begin{aligned}\left[T\frac{\partial\theta}{\partial x}\right]_{Upwind} - \left[T\frac{\partial\theta}{\partial x}\right]_{Centered} &= T\frac{\theta_i - \theta_{i-1}}{\Delta x} - T\frac{\theta_{i+1} - \theta_{i-1}}{2\Delta x} \\ &= -\frac{T\Delta x}{2}\frac{\theta_{i+1} - 2\theta_i + \theta_{i-1}}{\Delta x^2} \\ &= \left[\frac{T\Delta x}{2}\frac{\partial^2\theta}{\partial x^2}\right]_{Centered}\end{aligned} \tag{9}$$

Equation (9) shows that the discretized expression of the convective term by means of the *first order upwind scheme* is equal to the *second order centered scheme* discretization of the same term plus an additional diffusive contribution. By comparing equations (8) and (9), we notice that a numerical diffusive term comes out naturally and it is characterized by a diffusion coefficient $\frac{T\Delta x}{2}$ which is function of a mesh characteristic length - Δx in the case of one-dimensional problems. This term is similar to the numerical conductivity coefficient ϵ introduced in equation (6) but it is no more user-defined and it tends towards zero as $\Delta x \to 0$, which means that the centered and the upwind discretization schemes are consistent. This observation constitutes the fundamentals of upwind discretization methods, classically used in fluid mechanics. Higher dimensional extensions of the concept of numerical diffusion have been well-established in fluid mechanics in the case of finite element discretizations. More precisely, two formulations are considered in this study. Given the vector field $\mathbf{T}(\mathbf{x})$, the following bi-dimensional extension of the concept of numerical diffusion has been proposed (Streamline Upwind method - SU):

$$\begin{cases} \mathbf{T}\cdot\nabla\theta - \mathbf{div}\left(\dfrac{h_T\|\mathbf{T}\|}{2}\nabla\theta\right) = 0 & \forall\mathbf{x}\in\Omega \quad (10a) \\ J = \left(-\dfrac{h_T\|\mathbf{T}\|}{2}\cdot\nabla\theta\right)\cdot\boldsymbol{\nu} = 0 & \forall\mathbf{x}\in\partial_J\Omega \quad (10b) \\ \theta = \theta^* & \forall\mathbf{x}\in\partial_\theta\Omega \quad (10c) \end{cases}$$

where h_T is a mesh characteristic length. Problem (10) describes the numerical diffusion as an isotropic process and this may lead to imprecise results if coarse meshes are adopted. As a matter of fact, since in this case a large amount of diffusion is introduced in all directions, the isovalues of the temperature-like field do not longer envelop the tangent vector field. Another formulation, which considers an anisotropic numerical diffusion only in the direction of the vector field $\mathbf{T}$ (Streamline Upwind Petrov Galerkin method - SUPG) has also been proposed:

$$\begin{cases} \mathbf{T}\cdot\nabla\theta - \mathbf{div}\left(\dfrac{h_T\|\mathbf{T}\|}{2}\dfrac{\mathbf{T}\otimes\mathbf{T}}{\|\mathbf{T}\|^2}.\nabla\theta\right) = 0 & \forall\mathbf{x}\in\Omega \quad (11a) \\ J = \left(-\dfrac{h_T\|\mathbf{T}\|}{2}\dfrac{\mathbf{T}\otimes\mathbf{T}}{\|\mathbf{T}\|^2}\cdot\nabla\theta\right)\cdot\boldsymbol{\nu} = 0 & \forall\mathbf{x}\in\partial_J\Omega \quad (11b) \\ \theta = \theta^* & \forall\mathbf{x}\in\partial_\theta\Omega \quad (11c) \end{cases}$$

It can be demonstrated that the tensor $\frac{\mathbf{T}\otimes\mathbf{T}}{\|\mathbf{T}\|^2}$ has only one non-zero eigenvalue associated to $\mathbf{T}$ as eigenvector. The product $\frac{\mathbf{T}\otimes\mathbf{T}}{\|\mathbf{T}\|^2}.\nabla\theta$ then retains only the part of $\nabla\theta$ parallel to $\mathbf{T}$.

3 CRACK TRACKING ALGORITHM

In Section 2.2 the problem of tracing the envelopes of a vector field $\mathbf{T}(\mathbf{x},t)$ has been formulated in terms of Navier-Stokes equations for incompressible fluids. As for the heat-conduction-like formulation, the scalar function $\theta(\mathbf{x},t)$ represents the temperature field whose isovalues describe all the possible discontinuity lines in the domain Ω.

The choice of the right isovalue stands on the stress distribution at time t. In particular, global tracking associates to each discontinuity line Γ_i a root r_i, i.e. the material point (or the element) at time t_0 not belonging to any crack path and satisfying for the first time the activation condition [4, 3]. The discontinuity is thus represented as follows:

$$\begin{cases} \Gamma_i(t) = \{\mathbf{x}\in\Omega | \theta(\mathbf{x},t) = \theta(\mathbf{x}_{r_i},t)\} & (12a) \\ \mathbf{x}_{r_i}\in\Omega | \left\|\underline{\underline{\sigma}}(\mathbf{x}_{r_i},t_0)\right\| \geq f_t & (12b) \end{cases}$$

where the activation condition is expressed in terms of a certain tensorial norm $\|.\|$ and the material strength f_t. The reference isovalue is considered to pass through the centroid of the root element of the discontinuity [4, 3].

The previous definition implicitly assumes that the portion of isovalue associated to the *active part* of the crack, i.e. with points characterized by $[\![\mathbf{u}]\!]_{\Gamma_i}\neq 0$, does not change any more. In reality, due to the approximative nature of the finite element solution, this is not generally guaranteed: indeed, since principal stress directions are free to rotate where the material is linear elastic, the isovalues of the thermal field may evolve also inside the elements already exhibiting a crack. As a consequence,

the nodes of the element domain Ω_e traversed by the crack may be incorrectly separated, with a loss of continuity of the crack-path and stress-locking effects taking place. A possible solution would be to freeze the nodal temperature of the cracked element by imposing additional Dirichlet boundary conditions [9]. However, the initial boundary value problem (4) or (10) would be contradicted with respect to the initial boundary conditions and local techniques should be adopted in order to perform the analysis at each time step.

This drawback can be found if the root r_i is not updated for $t \geq t_0$. Thus, the tracking procedure should explicitly take into account both the active part Γ_{i_a} and the potential part Γ_{i_p} of each discontinuity Γ_i and, at the same time, impose the match between the root r_i, used to trace the prosecution of the crack, and the crack-tip. In this circumstances, the reference point for tracing the isovalue defining Γ_{i_p} does not coincide with the root element centroid but instead with a point belonging to one of the root element edges, i.e. the crack-tip. If we consider a time discretization $\{t_0, ..., t_k, ..., t_n\}$, the total discontinuity Γ_i at time t_n can then be represented as:

$$\begin{cases} \Gamma_i = \Gamma_{i_a} \cup \Gamma_{i_p} = \bigcup_{k=0}^{n-1} \tilde{\Gamma}_i^{(k)} \cup \tilde{\Gamma}_i^{(n)} & \text{(13a)} \\ \tilde{\Gamma}_i^{(k)} = \left\{ \mathbf{x} \in \Omega | \theta(\mathbf{x}, t_k) = \theta(\mathbf{x}_{r_i}^{(k)}, t_k), [\![\mathbf{u}(\mathbf{x}, t_k)]\!] \neq 0 \right\} & \text{(13b)} \\ \tilde{\Gamma}_i^{(n)} = \left\{ \mathbf{x} \in \Omega | \theta(\mathbf{x}, t_n) = \theta(\mathbf{x}_{r_i}^{(n)}, t_n), [\![\mathbf{u}(\mathbf{x}, t_n)]\!] = 0 \right\} & \text{(13c)} \\ \mathbf{x}_{r_i}^{(k)} \in \Omega | \left\| \underline{\underline{\sigma}}(\mathbf{x}_{r_i}^{(k)}, t_k) \right\| \geq f_t & \text{(13d)} \end{cases}$$

From the previous definition, the potential part of the discontinuity Γ_{i_p} has been defined as the portion of the isovalue triggered off the root r_i at time t_n and characterized by linear elastic behavior. Consequently, only the portion of the isovalue that does not cross the element associated to r_i should be taken into account. Since root r_i divides the potential line into two parts, in order to avoid ambiguity, it seems convenient to orient the curve by setting the origin at the root itself and assume as positive the direction of the propagating discontinuity. This can be done by means of a curvilinear abscissa s_i, whose origin is set to coincide with root r_i (see Fig. 1).

Thus, the prosecution of the crack path Γ_i at time t_n will be associated to the positive values of s_i, with origin at the root r_i. This procedure can be translated by the following steps:

1. Make the input point I_{Γ_i} match the crack-tip.
2. Trace of the isovalue passing trough I_{Γ_i}.
3. Create the curvilinear abscissa s_i with origin in I_{Γ_i} and with positive values in the sense of the propagating discontinuity.
4. Choose the potential continuation of discontinuity Γ_i as the part of isovalue associated to $s_i > 0$.

The algorithms derived by problem (12) and problem (13) are now compared. The geometry is depicted in Fig. 2 and consists in a concrete specimen under

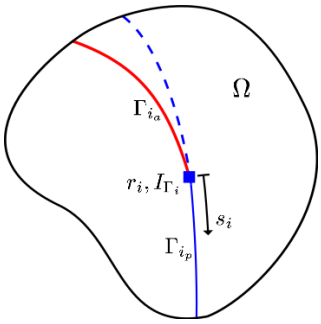

Figure 1: Crack path tracking in a bi-dimensional domain by means of the variable-root algorithm.

tension, characterized by two notches with an offset in the direction of the load. An imposed displacement δ is applied horizontally on the right side of the structure, while the left side is fixed in this direction. A hinged support is introduced at the upper left corner in order to forbid any rigid body motion.

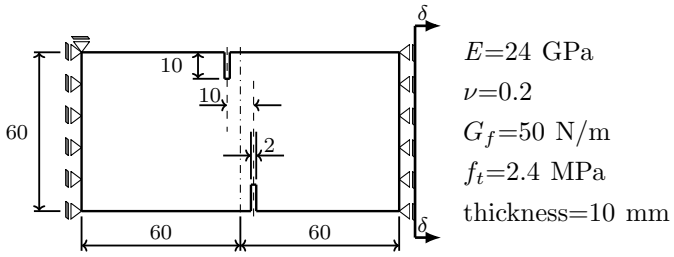

Figure 2: Tension test on double-edge notched specimen - dimensions in mm.

In Fig. 3a the case of fixed roots r_1 and r_2 for the crack paths Γ_1 and Γ_2 is shown. It appears that the evolution of the reference isovalues due to the rotation of the principal stress directions inside linear elastic elements may lead to an imprecise evaluation of the propagating discontinuities. In particular, even if the principal stress directions are freezed inside cracked elements, the isovalues may no longer be able to envelop the tangents to the active part of the discontinuities. A change in the decomposition mode of the elemental domain Ω_e may then occur whenever the nodes shared by adjacent elements do not belong to the same sub-domain Ω_e^+ or Ω_e^-. If the root of each discontinuity is updated, it is possible to separate its active part from its potential prosecution. This strategy allows to enforce the continuity of the crack path even if the isovalue distribution evolves during the analysis. As depicted in Fig. 3b, the requirement of a domain of unique decomposition is attained for all the cracked elements.

4 STRUCTURAL CASE STUDY

The first example is the same as the double-edge notched specimen under tension that has been preliminarily studied in Section 3. The formation of two principal crack paths has been observed experimentally. A correct evaluation of the propagating discontinuities is essential in order to properly simulate the structural response. Firstly, the fixed-root algorithm deriving from equations (12) is applied in the case

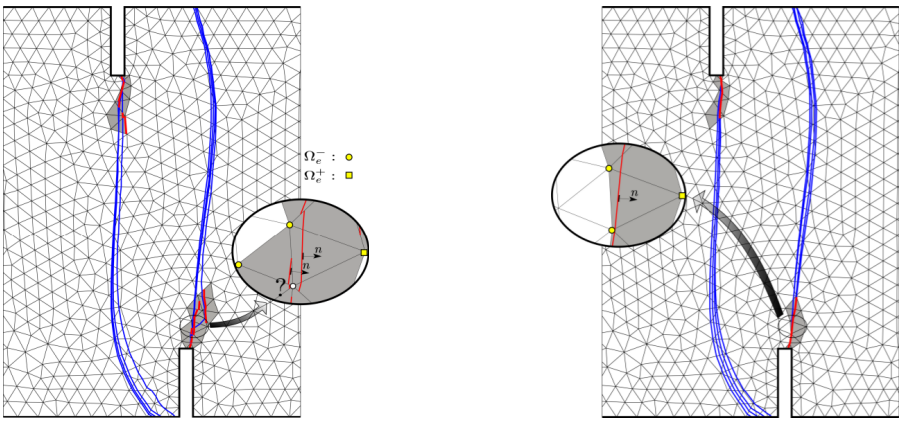

(a) Fixed-root algorithm (b) Variable-root algorithm

Figure 3: Crack propagation scheme.

of the formulation presented above. Three discretizations counting 496, 1691 and 6762 3-node triangular elements respectively have been considered. The corresponding load-displacement curves are plotted in Fig. 4a. The localization zones at the end of each simulation are depicted in Fig. 4b.

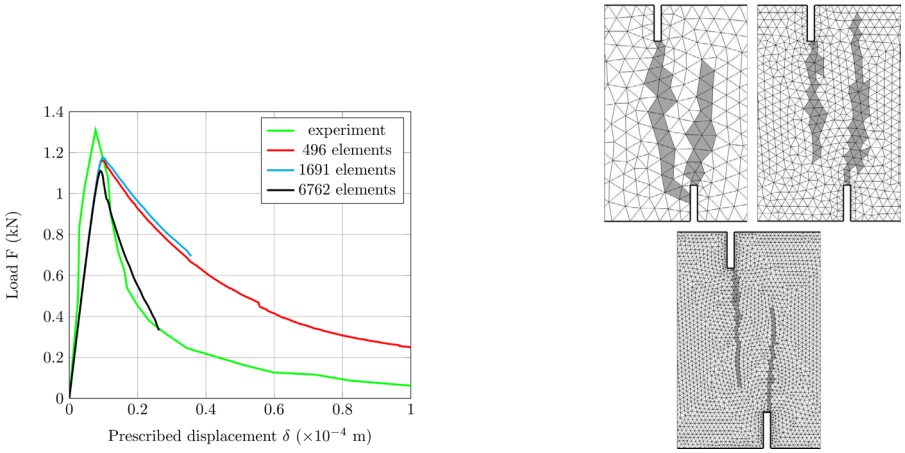

(a) Load-displacement curves (b) Localization zones

Figure 4: Results of the fixed-root global tracking algorithm for the Shi's test.

It can be noticed that the crack paths start developing correctly from the notches, but then, as the distance from the respective root element increases, a loss of continuity occurs in all the three simulations. As it can be observed in Fig. 4b, the localizations zones are not always defined by simple bands of elements, which means that stress-locking and spurious cracking take place. Consequently the knowledge of the crack-tip position is lost and the constitutive response is not well evaluated. In addition, numerical issues are encountered already at early stages in particular when fine meshes are adopted. These drawbacks may constitute a limitation to the applicability of the global tracking scheme.
If the variable-root algorithm derived from equations (13) is adopted, the position of the crack-tip is always available during the analysis. This information allows to impose the continuity of each crack path by separating it into an active part and

a potential part without the use of any further strategy. As shown in Fig. 5a, the numerical simulations fit pretty well with the experimental result in terms of load-displacement curves, denoting a good mesh-size independence. The localization zones, depicted in Fig. 4b, consist in a fully developed crack-band initiating at the upper notch and a partially developed crack-band starting from the lower notch.

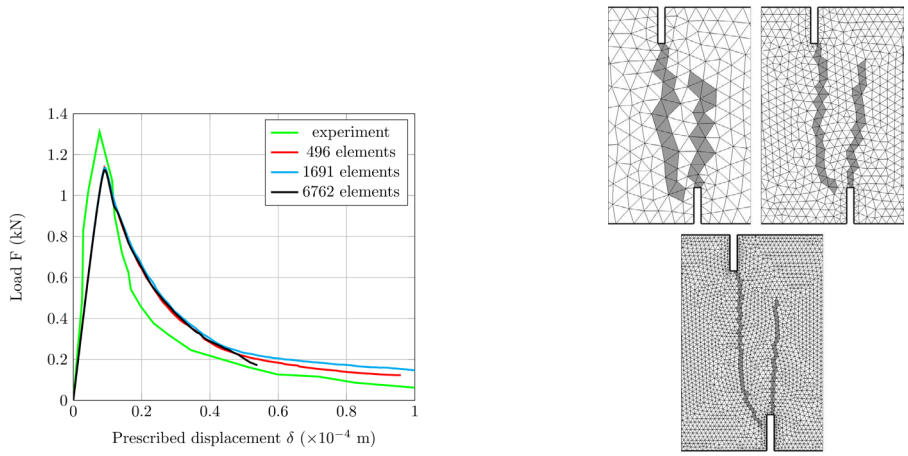

(a) Load-displacement curves (b) Localization zones

Figure 5: Results of the variable-root global tracking algorithm for the Shi's test.

The mathematical formulation is now discussed. A comparison between the heat conduction-like problem and the heat convection-diffusion-like problem is drawn in case of the variable-root global tracking. The load-displacement curves and the localizations zones are shown in Fig. 6 and 7 for the intermediate mesh containing 1691 elements. The global structural response shows minor differences between the two simulations, in particular it seems that the former approach allows a better energy dissipation in the final stage of the analysis. By observing the crack trajectories, it appears that an asymmetrical propagation takes place for the heat-convection-diffusion problem, whereas two almost identical crack paths are found for the former problem, which is coherent with the fact that the stress distribution is symmetrical with respect to the vertical axis. This discrepancy may be due to the different physical meaning of the mathematical formulation. In particular, for the heat-conduction-diffusion problem the tangent vector field represents a fluid velocity, deduced from the principal stress directions. Therefore, the solution is affected by the sense given to the velocity field. Such operation may lead to less accurate results with respect to the heat-conduction formulation if not properly done, especially in presence of singular points or high gradients in the stress distribution.

5 CONCLUSION

In this paper a modified global crack-tracking strategy has been applied to the E-FEM simulation of quasi-brittle materials. The following conclusions can be drawn:

- Independently from the mathematical formulation of the thermal-like prob-

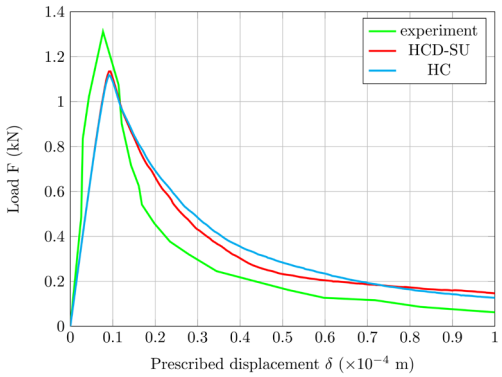

Figure 6: Load-displacement curve comparison of the heat-conduction and heat-convection-diffusion formulations for the Shi's test.

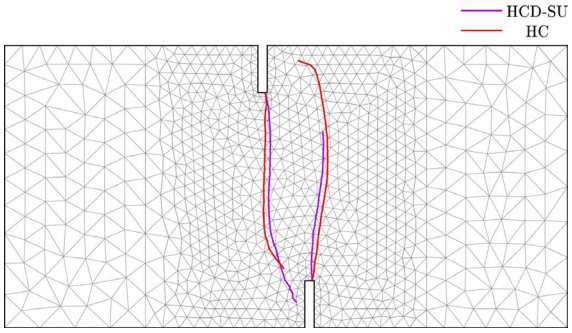

Figure 7: Crack path comparison of the heat-conduction and heat-convection-diffusion formulations for the Shi's test.

lem, a fixed-root scheme does not prevent the loss of continuity of the crack path due to the rotation of the isovalues. As a consequence, spurious cracking appears and both stress-locking effects and numerical instability issues occur;

- The variable-root scheme is able to provide a C^0-continuous crack path at no additional computational cost and without integrating any further technique;
- A good agreement with the experiments is found when coupling the variable-root algorithm to the heat-convection-diffusion formulation, although in the case of coarse meshes its precision is reduced with respect to the heat conduction-like approach. However, from the authors' experience, good results have been obtained for all the spatial discretizations adopted in the analysis;
- Attention must be paid to the sense of the tangent vector field, especially in the case of strong gradients of the stress distribution. This consideration is important since Dirichlet boundary conditions can be applied only on the portions of the boundary where the velocity field is directed inward the domain;
- The heat-convection-diffusion formulation provides better stability performances with respect to the heat-conduction formulation. The latter is strongly dependent on the numerical conductivity parameter, which may be not sufficient to guarantee stable solutions and therefore to perform the global tracking procedure.

The applicability of the variable-root heat-convection-diffusion tracking strat-

egy to three-dimensional problems has not been investigated yet, in particular the variable-root algorithm could be object of further studies. The extension of the proposed approach to branching scenarios should be also evaluated, such as the possibility to handle intersecting cracks.

6 ACKNOWLEDGEMENTS

The authors wish to express their most grateful thanks to CEA/DEN for its financial support. The work carried out under the SINAPS@ project has benefited from French funding managed by the National Research Agency under the program Future Investments (SINAPS@ reference No. ANR-11-RSNR-0022). This work has also been supported by the SEISM Institute (http://www.institut-seism.fr).

REFERENCES

[1] J. Oliver, M. Cervera, O. Manzoli, Strong discontinuities and continuum plasticity models: the strong discontinuity approach, International journal of plasticity 15 (3) (1999) 319–351.

[2] N. Moës, T. Belytschko, Extended finite element method for cohesive crack growth, Engineering fracture mechanics 69 (7) (2002) 813–833.

[3] J. Oliver, A. Huespe, E. Samaniego, E. Chaves, Continuum approach to the numerical simulation of material failure in concrete, International Journal for Numerical and Analytical Methods in Geomechanics 28 (7-8) (2004) 609–632.

[4] J. Oliver, A. Huespe, E. Samaniego, E. Chaves, On strategies for tracking strong discontinuities in computational failure mechanics, in: Fifth World Congress on Computational Mechanics, 2002.

[5] G. Meschke, P. Dumstorff, Energy-based modeling of cohesive and cohesionless cracks via x-fem, Computer Methods in Applied Mechanics and Engineering 196 (21) (2007) 2338–2357.

[6] P. Jäger, P. Steinmann, E. Kuhl, Modeling three-dimensional crack propagationa comparison of crack path tracking strategies, International Journal for Numerical Methods in Engineering 76 (9) (2008) 1328–1352.

[7] J. Alfaiate, G. Wells, L. Sluys, On the use of embedded discontinuity elements with crack path continuity for mode-i and mixed-mode fracture, Engineering Fracture Mechanics 69 (6) (2002) 661–686.

[8] F. Dufour, G. Pijaudier-Cabot, M. Choinska, A. Huerta, Extraction of a crack opening from a continuous approach using regularized damage models, Computers & Concrete 5 (4) (2008) 375–388.

[9] J. Oliver, A. Huespe, Continuum approach to material failure in strong discontinuity settings, Computer Methods in Applied Mechanics and Engineering 193 (30) (2004) 3195–3220.

XIV International Conference on Computational Plasticity. Fundamentals and Applications
COMPLAS XIV
E. Oñate, D.R.J. Owen, D. Peric & M. Chiumenti (Eds)

EFFICIENT MULTI-SCALE MODELLING OF PATH DEPENDENT PROBLEMS – COMPLAS 2017

NINA ZUPAN*, JOŽE KORELC†

* Faculty of Civil and Geodetic Engineering
University of Ljubljana
Jamova cesta 2, 1000 Ljubljana, Slovenia
e-mail: nina.zupan@fgg.uni-lj.si, web page: http://www3.fgg.uni-lj.si

† Faculty of Civil and Geodetic Engineering
University of Ljubljana
Jamova cesta 2, 1000 Ljubljana, Slovenia
e-mail: joze.korelc@fgg.uni-lj.si, web page: http://www3.fgg.uni-lj.si

Key words: Multi-scale, MIEL, sensitivity analysis, path dependent

Abstract. With growing capabilities of computers use of multi-scale methods for detailed analysis of response with respect to material and geometric nonlinearities is becoming more relevant. In this paper focus is on MIEL (mesh-in-element) multi-scale method and its implementation with *AceGen* and *AceFEM* based on analytical sensitivity analysis. Such implementation enables efficient multi-scale modelling, consistency and quadratic convergence also for two-level path following methods for the solution of path dependent problems.

1 INTRODUCTION

Implementation of multi-scale methods is possible in various ways. Here, the numerical scheme for implementation of MIEL multi-scale method based on sensitivity analysis is presented. Implementation is done with the *Mathematica* packages *AceGen* and *AceFEM* [1]. Programs enable analytical sensitivity analysis of first and second order [2], that can be used for efficient implementation of multi-scale finite element methods, eg. FE^2 or MIEL.

2 AUTOMATIC DIFFERENTIATION BASED (ADB) NOTATION

AceGen is advanced automatic code generator, where automatic differentiation technique, automatic code optimization and generation are combined with computer algebra system *Mathematica*[3]. Size of code is reduced through control of expression swell[4]. The *AceFEM* package is a general finite element environment designed to solve multi-physics and multi-field problems.

Automation of primal and sensitivity analysis is done with *AceGen*. The automatic differentiation technique (AD) can be used for the evaluation of the exact derivatives of any arbitrary complex function via chain rule and represents an alternative solution to the numerical differentiation and symbolic differentiation. The result of AD procedure is called "computational derivative" and is written as $\frac{\hat{\delta} f(\mathbf{a})}{\hat{\delta}\mathbf{a}}$. The AD operator $\frac{\hat{\delta} f(\mathbf{a})}{\hat{\delta}\mathbf{a}}$ represents partial derivative of a function $f(\mathbf{a})$ with respect to variables $\mathbf{a}$. If, for example, alternative or additional dependencies for a set of intermediate variables $\mathbf{b}$ have to be considered for differentiation, then the AD exception is indicated by the following formalism

$$\left.\frac{\hat{\delta} f(\mathbf{a},\mathbf{b})}{\hat{\delta}\mathbf{a}}\right|_{\frac{D\mathbf{b}}{D\mathbf{a}}=\mathbf{M}}, \tag{1}$$

which indicates that during the AD procedure, the total derivatives of variables $\mathbf{b}$ with respect to variables $\mathbf{a}$ are set to be equal to matrix $\mathbf{M}$. The automatic differentiation exceptions are the basis for the ADB formulation of computational problem. The ADB notation can be directly translated to the *AceGen* input and is part of numerically efficient code automation. Details of the method and of the corresponding software *AceGen* can be found in [4], [2] and [5].

The automation of multi-scale analysis requires the automation of primal and sensitivity analysis. In primal analysis the response of the system is evaluated, whereas in sensitivity analysis the derivatives of the response, e.g. displacements, strains, stresses or work, with respect to arbitrary design parameter ϕ_i are sought. The primal problem is solved by the standard Newton-Raphson iterative procedure (see e.g. [2]). For the automation of the multi-scale methods the sensitivity analysis with respect to prescribed essential boundary conditions is needed.

3 MULTI-SCALE METHODS

Multi-scale methods are nowadays widespread in computational mechanics [6, 7, 8]. They usually originate from the demand to model heterogeneous materials, like fiber reinforced composites, particle reinforced adhesives, concrete and even metal. FE^2 is a standard two-level finite element homogenization approach [9], that is appropriate for the problems where scales are separated far enough and are only weakly coupled. FE^2 method is already implemented in *AceFEM* using sensitivity analysis, for details reader is referred to [10, 11]. In some cases for example when difference between two scales is finite, or when in the region of high gradients, the FE^2 multi-scale approach fails, thus we need to use some sort of domain decomposition method. One possibility is the mesh-in-element or MIEL scheme described e.g. by Markovič and Ibrahimbegović in [12].

3.1 MIEL method

MIEL method is variant of domain decomposition methods. Here its implementation based on sensitivity analysis is presented. The finite element models at different scales communicate between each other through degrees of freedom of the finite element at

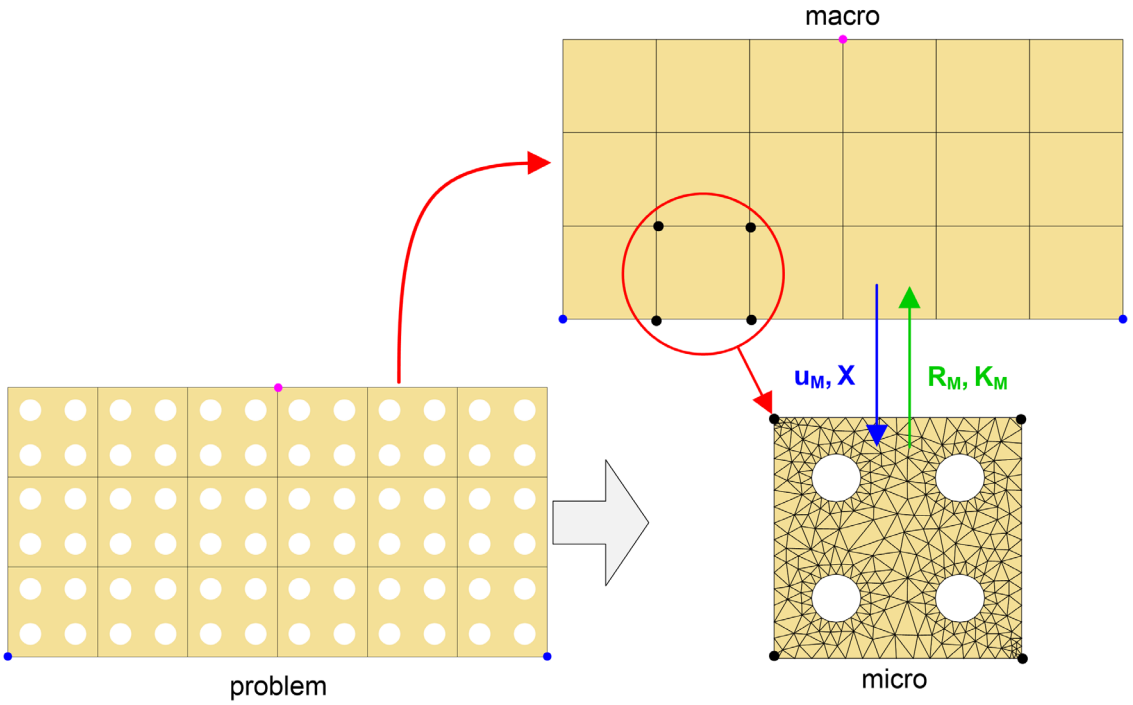

Figure 1: MIEL, problem, micro and macro level

the macro-scale. The residual and tangent matrix are for each macro element obtained directly from the micro-scale problem. Each macro element thus represents one micro problem, see Fig. 1. Macro element performs only proper transfer of components of the macro element residual vector and tangent matrix from micro scale to macro scale finite element assembly procedure. At the macro level residual and tangent are assembled from individual macro elements and macro response is calculated. Macro tangent matrix is typically evaluated using the Schur complement of the global micro matrix, which is numerical expensive operation. Here it is calculated through sensitivity analysis with respect to prescribed essential boundary conditions. Implementation in *AceFEM* enables this approach that is numerical more efficient for dense micro finite element meshes. Correctly done sensitivity analysis at micro level leads to algorithmically consistent macro tangent matrix. Quadratic convergence of problem is with that ensured also for examples, that are dependent on load-path.

Let $\mathbf{p}_{Me}$ be a vector of unknowns in the nodes of the macro element, $\mathbf{p}_{me}$ a vector of unknowns in the nodes of the characteristic micro problem element and W strain energy function. The outer shape of the micro problem is the same as the shape of the corresponding macro element. The prescribed essential boundary conditions (displacements) are identical to the displacements at the boundary of the corresponding macro element. The integration point contribution (g-th integration point in the e-th element of the micro

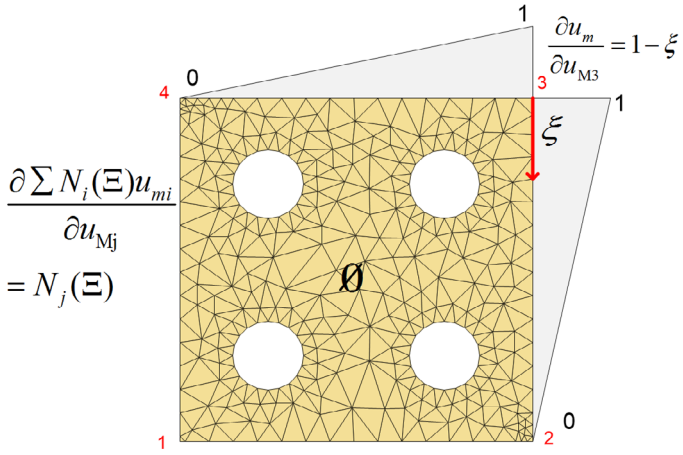

Figure 2: Characteristic velocity field for MIEL

mesh) to the macro residual and macro tangent matrix is then

$$\mathbf{R}_{Mg} = \frac{\partial W(\mathbf{p}_{me}(\mathbf{p}_{Me}))}{\partial \mathbf{p}_{Me}} = \frac{\partial W}{\partial \mathbf{p}_{me}} \frac{D\mathbf{p}_{me}}{D\mathbf{p}_{Me}} \tag{2}$$

$$\mathbf{K}_{Mg} = \frac{\partial \mathbf{R}_{Mg}}{\partial \mathbf{p}_{Me}} = \frac{\partial^2 W}{\partial \mathbf{p}_{me}{}^2} \frac{D\mathbf{p}_{me}}{D\mathbf{p}_{Me}} + \frac{\partial W}{\partial \mathbf{p}_{me}} \frac{D^2\mathbf{p}_{me}}{D\mathbf{p}_{Me}^2}. \tag{3}$$

The implicit dependencies $\frac{D\mathbf{p}_{me}}{D\mathbf{p}_{Me}}$ and $\frac{D^2\mathbf{p}_{me}}{D\mathbf{p}_{Me}^2}$ are obtained by the first and second order sensitivity analysis. Thus, the sensitivity analysis based automation of the MIEL scheme requires the second order sensitivity analysis for a set of sensitivity parameters $\mathbf{p}_{Me}$. The ADB form of (2) and (3) then leads to

$$\mathbf{R}_{Mg} = \left. \frac{\hat{\delta} \mathbf{W}}{\hat{\delta} \mathbf{p}_{Me}} \right|_{\frac{D\mathbf{p}_{me}}{D\mathbf{p}_{Me}} = D_{\mathbf{p}_{Me}} \mathbf{p}_{me}} \tag{4}$$

$$\mathbf{K}_{Mg} = \left. \frac{\hat{\delta} \mathbf{R}_{Mg}}{\hat{\delta} \mathbf{p}_{Me}} \right|_{\frac{D\mathbf{p}_{me}}{D\mathbf{p}_{Me}} = D_{\mathbf{p}_{Me}} \mathbf{p}_{me}, \frac{D(D_{\mathbf{p}_{Me}} \mathbf{p}_m)}{D\mathbf{p}_{Me}} = D_{\mathbf{p}_{Me} \mathbf{p}_{Me}} \mathbf{p}_{me}} \tag{5}$$

where data structures $D_{\mathbf{p}_{Me}} \mathbf{p}_{me} = \frac{D\mathbf{p}_{me}}{D\mathbf{p}_{Me}}$ and $D_{\mathbf{p}_{Me} \mathbf{p}_{Me}} \mathbf{p}_{me} = \frac{D^2\mathbf{p}_{me}}{D\mathbf{p}_{Me}^2}$ are the results of the first and second order sensitivity analysis.

For the complete formulation of the prescribed boundary condition sensitivity problem, we need the first and second order prescribed boundary condition velocity fields $D_{\phi_i} \bar{\mathbf{p}}_e$ and $D_{\phi_i \phi_j} \bar{\mathbf{p}}_e$ for details see e.g.[2]. Let $\bar{\mathbf{p}}_m$ be a vector of unknowns at the boundary of micro problems with prescribed essential boundary conditions, thus $\bar{\mathbf{p}}_m = \bar{\mathbf{p}}_m(\mathbf{p}_{Me})$. The set of sensitivity parameters of the MIEL problem is $\boldsymbol{\phi} = \mathbf{p}_{Me}$. The components of $D_{\phi_i} \bar{\mathbf{p}}_e$ are obtained by the differentiation of $\bar{\mathbf{p}}_m(\mathbf{p}_{Me})$ with respect to $\mathbf{p}_{Me}$. Let us assume the standard interpolation of the unknown field u on the boundary of the macro element

$$u = \sum N_i(\boldsymbol{\Xi})\, u_i, \tag{6}$$

where $N_i(\boldsymbol{\Xi})$ are the shape functions and u_i the nodal unknowns and $\frac{\partial u}{\partial u_i} = N_i(\boldsymbol{\Xi})$. Thus, the components of the first order boundary condition velocity field $D_{\phi_i}\bar{\mathbf{p}}_e$ are the values of the macro element shape functions at the position of the boundary nodes of the micro mesh, see Fig. 2. For boundary condition in form of linear combination (6), the second order velocity field is zero $D_{\phi_i\phi_j}\bar{\mathbf{p}}_e = \mathbf{0}$.

4 EFFICIENCY IMPROVEMENT

Numerical efficiency of multi-scale methods can be improved in different ways. First improvement was done at individual macro problem, with replacing calculation of Schur complement with sensitivity analysis based calculation of macro tangent matrix. For densely meshed micro-structure calculation of the Schur complement inflicts high memory allocation and is time consuming, which is not the case for the sensitivity analysis based implementation. In case of MIEL method this is due to the fact that the number of sensitivity parameters remains the same, regardless of the density of the micro mesh, whereas the size of the Schur complement grows with the number of the nodes on the boundary of the micro problem.

Further optimisation can be done with use of unified sensitivity based approach to multi-scale modelling, that is enabled by automatic-differentiation-based (ADB) formulation for an arbitrary nonlinear, time dependent coupled problem (e.g. general finite strain plasticity). Different multi-scale methods FE^2, MIEL and also single scale schemes can be used together in one model. With that optimal domain discretization is possible. For example, MIEL that is numerically most demanding can be used only where it is needed, other ways FE^2 or single-scale method can be used.

In *AceFEM* solving of nonlinear problems is done implicitly with a Newton-Raphson type iterative solution procedure. Since we have two scales, we have in general a path following procedure at both scales, resulting in two-level path following procedure. Traditionally, each step at macro level is followed by only one step at micro level. Sensitivity analysis based multi-scale analysis allows extension to more general case, where each macro step can be followed by an arbitrary number of micro substeps.

Implementation of the presented multi-scale computational approach in *AceFEM* is fully parallelized for multi-core processors. Micro problems are distributed on kernels by evaluating each individual micro problem always at the same kernel. With parallelized computation, computational time for complex problems can be significantly reduced. The setup is also appropriate for the implementation on clusters.

5 NUMERICAL EXAMPLE

Multi-scale MIEL method was tested on Cook membrane benchmark problem, to verify consistency and efficiency of micro-macro coupling. The homogeneous micro structure is chosen intentionally for the benchmark purposes. Effect of macro mesh density and use of different finite elements were investigated. With *AceGen*, the codes of analytical first and second order sensitivity analysis are generated automatically. Examples were calculated with *AceFEM*, where whole MIEL scheme is implemented including communication

between macro and micro scale. Essential boundary condition of macro mesh are sent to micro problem and interpolated over the edge. Important is that essential boundary condition velocity fields are set correctly.

5.1 Description of example

In Tab. 1 characteristics of problem on macro and micro level are described. Geometry, constraints and load are defined at macro level, whereas material properties are defined at micro level. Displacements are fixed on one side and on the other distributed load in vertical direction is added. Division of macro mesh had been variated, while division on micro level was the same in all computations. For mesh at macro and micro level two-dimensional quadrilateral elements with 4 nodes Q1 and with 8 nodes Q2S were used. Converged mesh density on micro level was used, so that results for different macro mesh densities can be compared.

Table 1: Macro and micro problem for MIEL

macro problem	micro problem
Geometry $h_1 = 44$ mm; $h_2 = 16$ mm; $l = 48$ mm; $t = 1$ mm Constraints: $X = 0$: $u = v = 0$ Load: $q = 0.1$ N/mm^2 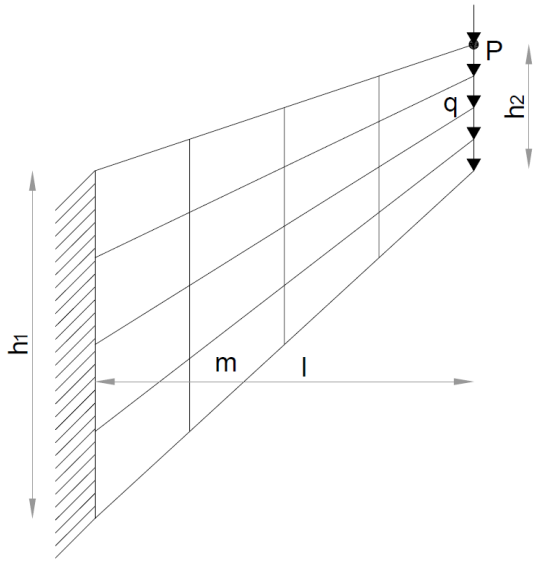	Material $E = 1$ N/mm^2 $\nu = 0$ *micro mesh of macro element marked with m 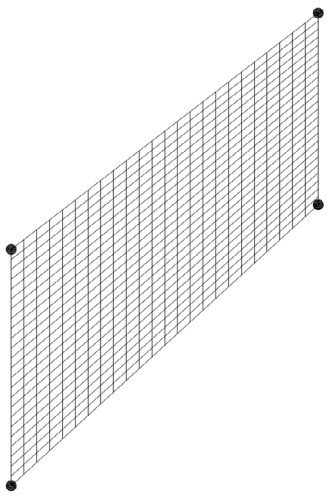

5.2 Consistency of micro-macro coupling

Consistent coupling between micro and macro scale was verified with comparison of upper right point P displacement on the Cook membrane test. Vertical displacement was compared for different macro mesh densities. For single scale analysis results for linear and quadratic elements are shown. For MIEL three combinations were investigated. MIEL Q1-Q1: Q1 element at macro and Q1 element at micro level, MIEL Q2S-Q1: Q2S element at macro and Q1 element at micro level and MIEL Q2S-Q2S: Q2S element at macro and Q2S element at micro level. Convergence of result is faster for MIEL, than for single-scale analysis, comparison is shown in Fig. 3. Overall convergence of Q2S elements with quadratic interpolation is faster than with Q1. Results show that for meshing at micro level use of Q2S elements is not preferable, because small improvement of convergence does not compensate for increased computational time. In Fig. 4 results for strain Exx of example MIEL Q2S-Q1 are shown.

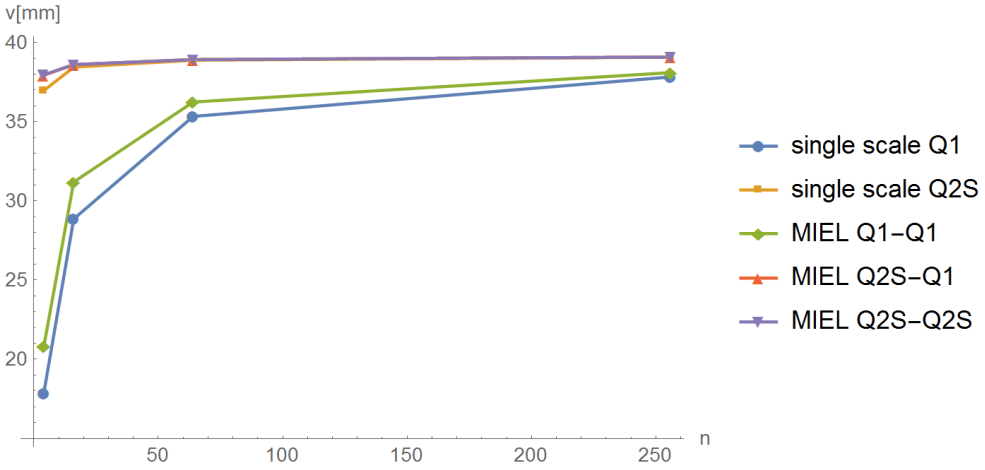

Figure 3: Convergence of result for vertical displacement

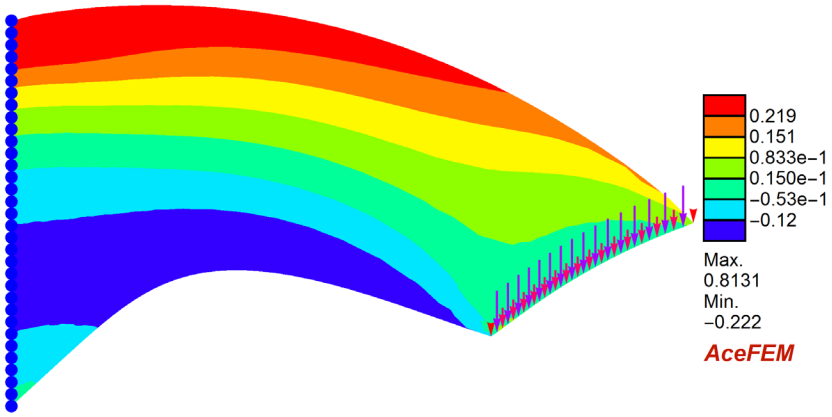

Figure 4: Results for strains Exx

6 CONCLUSIONS

In this work, basic principles of multi-scale MIEL method and possibilities for numerical improvement were described. In a conventional way of computing macroscopic tangent matrix a Schur complement is needed. As an alternative, the boundary condition sensitivity analysis was used to obtain macroscopic tangent matrix, for which second order sensitivity is needed. Numerical examples were calculated with *AceFEM*. Consistency of micro-macro coupling was shown on a Cook membrane example. Use of finite elements with quadratic interpolation is recommended for macro elements, whereas for micro mesh, elements with linear interpolation are preferred. Codes of the finite element for analytical first and second order sensitivity analysis are generated automatically with *AceGen*. For densely meshed micro-structures, the sensitivity analysis based calculation is numerically more efficient than Schur complement. This is due to the fact that the size of the Schur complement grows with the number of the nodes on the boundary of the micro problem, whereas the number of sensitivity parameters remains the same regardless of the density of the micro mesh. Traditionally, in multi-scale methods solved with two-level path-following procedure one macro time step is followed by one micro time step. Sensitivity analysis based multi-scale analysis allows that each macro step can be followed by an arbitrary number of micro substeps.

Acknowledgement The financial support for this work was obtained from the Slovenian Research Agency within the PhD Grant Agreement (annex No: 630-34/2015-7).

REFERENCES

[1] Korelc, J., Wriggers, P.: Automation of finite element methods. Springer, Switzerland (2016)

[2] Korelc, J.: Automation of primal and sensitivity analysis of transient coupled problems. Computational Mechanics. **44**, 631-649 (2009)

[3] Mathematica 11, Wolfram Research Inc., http://www.wolfram.com (2016)

[4] Korelc, J.: Automatic generation of finite-element code by simultaneous optimization of expressions. Theoretical computer science. **187**, 231-248 (1997)

[5] Korelc, J.: AceFEM and AceGen user manuals, http://symech.fgg.uni-lj.si/ (2017)

[6] Fèyel, F.: Multiscale FE^2 elastoviscoplastic analysis of composite structures. Computational Materials Science. **16**, 344-354 (1999)

[7] Geers, M.G.D., Kouznetsova, V.G., Brekelmans, W.A.M.: Multi-scale computational homogenization: Trends and challenges. Journal of Computational and Applied Mathematics. **234**, 2175-2182 (2010)

[8] Lamut, M., Korelc, J., Rodič, T.: Multiscale modelling of heterogeneous materials. Materials and technology. **45**, 421-426 (2011)

[9] Kouznetsova, V., Brekelmans, W.A.M., Baaijens F.P.T.: An approach to micro-macro modelling of heterogeneous materials. Computational Machanics. **27**, 37-48 (2001)

[10] Miehe, C., Schotte, J., Schröder, J.: Computational Micro-Macro Transitions and Overall Moduli in the Analysis of Polycrystals at Large Strains. Computational Materials Science. **16**, 372-382 (1999)

[11] Šolinc, U., Korelc, J.: A simple way to improved formulation of FE^2 analysis. Computational Mechanics. **56**, 905-915 (2015)

[12] Markovič, D., Ibrahimbegović, A.: On micro-macro interface conditions for micro scale based FEM for inelastic behaviour of heterogeneous materials. Computer methods in applied mechanics and engineering. **193**, 5503-5523 (2004)

XIV International Conference on Computational Plasticity. Fundamentals and Applications
COMPLAS XIV
E. Oñate, D.R.J. Owen, D. Peric & M. Chiumenti (Eds)

EIGENSTRAIN-BASED REDUCED ORDER HOMOGENIZATION MODELS FOR POLYCRYSTAL PLASTICITY: ADDRESSING SCALABILITY

Xiang Zhang*, **Caglar Oskay**†

*Department of Civil and Environmental Engineering
Vanderbilt University
Nashville, TN 37235
e-mail: xiang.zhang@vanderbilt.edu, web page: https://my.vanderbilt.edu/xiangzhang/

†Department of Civil and Environmental Engineering
Vanderbilt University
Nashville, TN 37235
e-mail: caglar.oskay@vanderbilt.edu, web page:https://my.vanderbilt.edu/mcml/

Key words: Sparse, Scalable, Reduced order model, Grain cluster, Multiscale model, Polycrystal plasticity

Abstract. In this manuscript, accelerated, sparse and scalable eigenstrain-based reduced order homogenization models have been developed for computationally efficient multiscale analysis of polycrystalline materials. The proposed model is based on the eigenstrain based reduced order homogenization (EHM) approach, which takes the concept of transformation field theory that pre-computes certain microscale information and considers piece-wise constant inelastic response within partitions (e.g., grains) of the microstructure for model order reduction.The acceleration is achieved by introducing sparsity into the linearized reduced order system through selectively considering the interactions between grains based on the idea of grain clustering. The proposed approach results in a hierarchy of reduced models that recovers original EHM, when full range of interactions are considered, and degrades to the Taylor model, when all grain interactions are neglected. The resulting sparse system is solved efficiently using both direct and iterative sparse solvers, both of which show significant efficiency improvements compared to the full EHM. A layer-by-layer neighbor grain clustering scheme is proposed and implemented to define ranges of grain interactions. Performance of the proposed approach is evaluated by comparison with the original full EHM and crystal plasticity finite element (CPFE) simulations.

1 INTRODUCTION

Concurrent multiscale modeling for polycrystalline materials that couples the mechanical behavior at the grain scale to structural scale poses significant challenges. First is the tremendous computational costs associated with evaluating complex polycrystalline morphologies, especially in the context of a multiscale analysis. Second is the development of constitutive models

that accurately capture the physics at the material microstructures. This manuscript addresses the former challenge.

CPFE is a powerful tool to solve various crystal plasticity problems (e.g., see Zhang and Oskay [14]). However, high computational cost of CPFE simulations on a polycrystalline representative volume element (RVE) makes its use in concurrent multiscale modeling frameworks (e.g., computational homogenization [6]) for structural scale analysis impractical. Reduced order representation of the microstructural behavior is therefore essential for structural scale analysis that takes into account the grain level behavior.

Early attempts for reduced order modeling of polycrystal plasticity are based on the iso-strain or iso-stress assumption[10, 11], which either fails compatibility or equilibrium. To overcome these drawbacks, grain-cluster [2], VPSC [5] and FFT [4] method have been developed and widely used. Eigendeformation-based reduced order homogenization (EHM) has been recently extended to polycrystal plasticity by the authors [13]. EHM is based on the transformation field theory [1] and operates in the context of computational homogenization. EHM pre-computes certain microstructure information (i.e., concentration tensors, interaction tensors) and approximates the microscale problem using a much smaller basis by prescribing spatial variation of inelastic response fields over the microstructure.

This manuscript extends the original EHM to an accelerated, sparse and scalable formulation for computationally efficient multiscale analysis of polycrystalline materials. Specifically, the grain-cluster concept is used to identify a cluster of neighboring grains for each grain, between which the interactions (i.e., short-range interactions) are considered, while interactions between grains far away from each other (i.e., long-range interactions) are neglected. Computationally, this strategy introduces sparsity into the linearized reduced order system, facilitating the use of sparse solvers. We thoroughly assessed the performance of the sparse EHM model for a range of microstructure sizes using direct and iterative sparse solvers.

2 EHM for polycrystal plasticity

EHM starts from a two-scale analysis of the governing equation, resulting in the classical form of coupled nonlinear microscale and the homogenized macroscale problem. Model order reduction is achieved by first expressing the microscale component of the displacement field in terms of "influence functions", which define its variation over the microstructure. The influence functions are numerical Green's functions computed by solving linear-elastic problems defined over the RVE prior to macroscale analysis. Next, the inelastic strain field within a microstructure are approximated by a coarse discretization. Similar to finite elements, the discretization (i.e., each coefficient) is associated with a subdomain (part) of the microstructure domain. Employing the microscale displacement discretization and the eigenstrain approximation, the reduced order microscale problem is obtained as in Box 1 (see Ref. [13] for details).

2.1 Computational Implementation Overview

The reduced order microscale system defined in Box 1 serves as the macroscale constitutive relationship and has been implemented as a User supplied MATerial (UMAT) subroutine within the finite element solver Abaqus.The constitutive equation, along with, the evolution equations for

Given: coefficient tensors $\mathbf{M}^{(\beta)}$, $\mathbf{P}^{(\alpha\beta)}$, $\mathbf{A}^{(\beta)}$, part-wise parameters $\mathbf{n}^{s(\alpha)}$, $\mathbf{m}^{s(\alpha)}$, $g_{sa}^{s(\alpha)}$, $\dot{\gamma}_0^{s(\alpha)}$, $h_0^{(\alpha)}$, $g_{s0}^{s(\alpha)}$, $\dot{\gamma}_{s0}^{(\alpha)}$, volume fraction $c^{(\beta)}$, macroscale strain $\bar{\varepsilon}_{kl}$ and its increment $\Delta\bar{\varepsilon}_{kl}$
Find: macroscale stress $\bar{\sigma}_{kl}$

• Constitutive equation:

$$M_{ijkl}^{(\beta)}\dot{\sigma}_{kl}^{(\alpha)}(\mathbf{x},t)-\sum_{\alpha=1}^{n}[P_{ijkl}^{(\alpha\beta)}-\delta^{(\alpha\beta)}I_{ijkl}]\dot{\mu}_{kl}^{(\alpha)}(\mathbf{x},t)=A_{ijkl}^{(\beta)}\dot{\bar{\varepsilon}}_{kl}(\mathbf{x},t)$$

$$\bar{\sigma}_{ij}=\sum_{\beta=1}^{n}c^{(\beta)}\sigma_{ij}^{(\beta)}$$

• Kinematics:

$$\dot{\mu}_{ij}^{(\alpha)}(\mathbf{x},t)=\sum_{s=1}^{N}\dot{\gamma}^{s(\alpha)}(\mathbf{x},t)\,Z_{ij}^{s(\alpha)}$$

• Flow rule:

$$\dot{\gamma}^{s(\alpha)}(\mathbf{x},t)=\dot{\gamma}_0\left(\frac{|\tau^{s(\alpha)}(\mathbf{x},t)|}{g^{s(\alpha)}(\mathbf{x},t)}\right)^{1/m}\operatorname{sgn}(\tau^{s(\alpha)}(\mathbf{x},t))$$

• Hardening rule:

$$\dot{g}^{s(\alpha)}(\mathbf{x},t)=h_0\left(\frac{g_{sa}^{s(\alpha)}-g^{s(\alpha)}(\mathbf{x},t)}{g_{sa}^{s(\alpha)}-g_0^{s(\alpha)}}\right)\sum_{s=1}^{N}|\dot{\gamma}^{s(\alpha)}(\mathbf{x},t)|$$

• Schmid's law:

$$\tau^{s(\alpha)}(\mathbf{x},t)=\boldsymbol{\sigma}^{(\alpha)}(\mathbf{x},t):\mathbf{Z}^{s(\alpha)}\quad\mathbf{Z}^{s(\alpha)}=\mathbf{n}^{s(\alpha)}\otimes\mathbf{m}^{s(\alpha)}$$

Box 1: Reduced order microscale problem.

slip and hardening constitutes a nonlinear system, evaluated using the N-R method. Evaluating the system with the part-average stresses, $\boldsymbol{\sigma}^{(\alpha)}$, as unknown, the system Jacobian is:

$$\mathbf{J}=\begin{bmatrix}
\frac{\partial\boldsymbol{\phi}^{(1)}}{\partial\boldsymbol{\sigma}^{(1)}} & \frac{\partial\boldsymbol{\phi}^{(1)}}{\partial\boldsymbol{\sigma}^{(2)}} & \cdots & \frac{\partial\boldsymbol{\phi}^{(1)}}{\partial\boldsymbol{\sigma}^{(\bar{\alpha})}} & \cdots & \frac{\partial\boldsymbol{\phi}^{(1)}}{\partial\boldsymbol{\sigma}^{(\bar{\beta})}} & \cdots & \frac{\partial\boldsymbol{\phi}^{(1)}}{\partial\boldsymbol{\sigma}^{(n)}} \\
\frac{\partial\boldsymbol{\phi}^{(2)}}{\partial\boldsymbol{\sigma}^{(1)}} & \frac{\partial\boldsymbol{\phi}^{(2)}}{\partial\boldsymbol{\sigma}^{(2)}} & \cdots & \frac{\partial\boldsymbol{\phi}^{(2)}}{\partial\boldsymbol{\sigma}^{(\bar{\alpha})}} & \cdots & \frac{\partial\boldsymbol{\phi}^{(2)}}{\partial\boldsymbol{\sigma}^{(\bar{\beta})}} & \cdots & \frac{\partial\boldsymbol{\phi}^{(2)}}{\partial\boldsymbol{\sigma}^{(n)}} \\
\vdots & \vdots & \ddots & \vdots & \ddots & \vdots & \ddots & \vdots \\
\frac{\partial\boldsymbol{\phi}^{(\bar{\alpha})}}{\partial\boldsymbol{\sigma}^{(1)}} & \frac{\partial\boldsymbol{\phi}^{(\bar{\alpha})}}{\partial\boldsymbol{\sigma}^{(2)}} & \cdots & \frac{\partial\boldsymbol{\phi}^{(\bar{\alpha})}}{\partial\boldsymbol{\sigma}^{(\bar{\alpha})}} & \cdots & \frac{\partial\boldsymbol{\phi}^{(\bar{\alpha})}}{\partial\boldsymbol{\sigma}^{(\bar{\beta})}} & \cdots & \frac{\partial\boldsymbol{\phi}^{(\bar{\alpha})}}{\partial\boldsymbol{\sigma}^{(n)}} \\
\vdots & \vdots & \ddots & \vdots & \ddots & \vdots & \ddots & \vdots \\
\frac{\partial\boldsymbol{\phi}^{(\bar{\beta})}}{\partial\boldsymbol{\sigma}^{(1)}} & \frac{\partial\boldsymbol{\phi}^{(\bar{\beta})}}{\partial\boldsymbol{\sigma}^{(2)}} & \cdots & \frac{\partial\boldsymbol{\phi}^{(\bar{\beta})}}{\partial\boldsymbol{\sigma}^{(\bar{\alpha})}} & \cdots & \frac{\partial\boldsymbol{\phi}^{(\bar{\beta})}}{\partial\boldsymbol{\sigma}^{(\bar{\beta})}} & \cdots & \frac{\partial\boldsymbol{\phi}^{(\bar{\beta})}}{\partial\boldsymbol{\sigma}^{(n)}} \\
\vdots & \vdots & \ddots & \vdots & \ddots & \vdots & \ddots & \vdots \\
\frac{\partial\boldsymbol{\phi}^{(n)}}{\partial\boldsymbol{\sigma}^{(1)}} & \frac{\partial\boldsymbol{\phi}^{(n)}}{\partial\boldsymbol{\sigma}^{(2)}} & \cdots & \frac{\partial\boldsymbol{\phi}^{(n)}}{\partial\boldsymbol{\sigma}^{(\bar{\alpha})}} & \cdots & \frac{\partial\boldsymbol{\phi}^{(n)}}{\partial\boldsymbol{\sigma}^{(\bar{\beta})}} & \cdots & \frac{\partial\boldsymbol{\phi}^{(n)}}{\partial\boldsymbol{\sigma}^{(n)}}
\end{bmatrix} \tag{1}$$

where each component is a 6×6 block expressed as:

$$\left(\frac{\partial\phi^{(\beta)}}{\partial\sigma^{(\alpha)}}\right)_{IK}=\left(\delta^{(\alpha\beta)}I_{IJ}-P_{IJ}^{(\beta\alpha)}\right)\sum_{s=1}^{N}\Omega^{s(\alpha)}Z_J^{s(\alpha)}Z_K^{s(\alpha)}+\delta^{(\alpha\beta)}\frac{M_{IK}^{(\beta)}}{\Delta t} \tag{2}$$

2.2 Analysis of EHM scalability

The efficiency of EHM compared to CPFE (i.e., ratio between simulation time of CPFE and EHM) as a function of RVE sizes is evaluated using uniaxial tension tests on a series of increasing

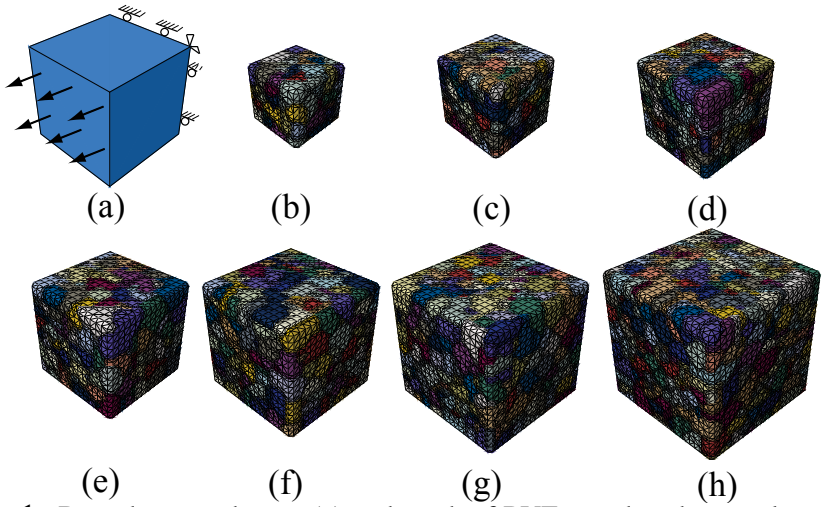

Figure 1: Boundary conditions (a) and mesh of RVEs used in the simulation with $n = 85, 154, 242, 347, 487, 629, 938$ (b-h).

Table 1: EHM efficiency compared with CPFE

n	n_{element}	n_{node}	$T_{\text{CPFE}}(s)$	$T_{\text{EHM}}(s)$	R_{DOF}	R_{Time}
85	29369	5627	2128.7	19.1	33.1	111.7
154	53149	9983	4034.0	74.85	32.4	53.9
242	84642	15583	7052.8	265.1	32.20	26.6
347	128716	23339	10371.3	662.1	33.63	15.7
487	176415	31777	13998.8	1671.5	32.63	8.4
629	238216	42651	19435.0	3434.2	33.90	5.7
938	337818	60122	29451.2	11240.6	32.05	2.6

size RVEs as shown in Fig. 1. The reduced order models consider uniform inelastic strain in each grain (i.e., n =number of grains) in the current study. The macroscale mesh consists of a single hexahedron with reduced order integration regularized by hourglass stiffness. The reference CPFE analysis is performed over the fully resolved microstructure discretized with trilinear tetrahedron elements.

The comparison between CPFE and EHM are listed in Table 1 and the efficiency of EHM compared with CPFE reduces as microstructure size increases as shown in Fig. 2. Number of grains in a RVE is often between $O(10^2)$ to $O(10^3)$ in literature. Maintaining high efficiency of EHMs with n within this range is therefore critical and motives the the current research.

The primary cause of the efficiency degradation with increasing n is the dense and unsymmetric structure of the linear system in Eq. (1), which requires $0.67(6n)^3 = 144.72n^3$ floating-point operations (FLOPs) when solved using direct solver (e.g., LAPACK LU decomposition routines). This explains the cubic increase in simulation time for the EHM as n increases.

We also investigate the effect of using iterative solver in the N-R iterations using the flexible General Minimum Residual method (FGMRES) combined with Gauss-Seidel pre-conditioning. The efficiency of EHM using FGMRES compared with CPFE is plotted in Fig. 2(b), which

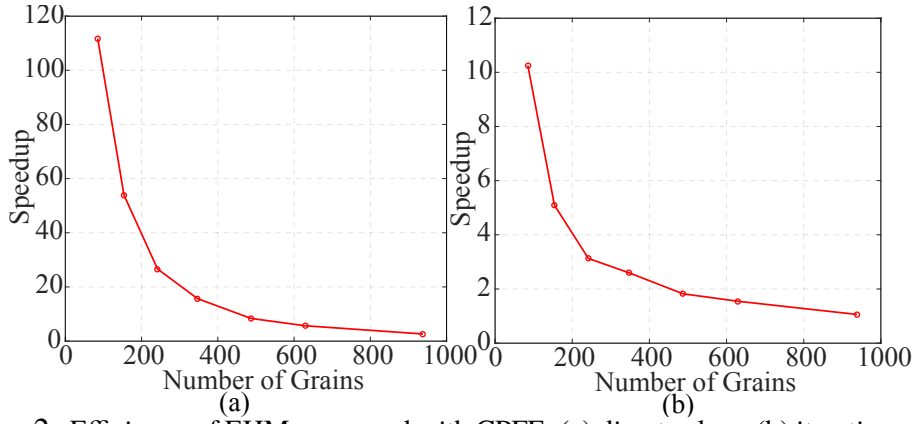

Figure 2: Efficiency of EHM compared with CPFE: (a) direct solver; (b) iterative solver.

shows lower efficiency than direct solver and similar degradation trend.

3 A sparse and scalable EHM formulation

To maintain the efficiency of EHM, one possible solution is to introduce sparsity into the linearized EHM system and decrease the FLOPs for solving the system substantially. By examing Eq. (2), one can find that, two 6×6 zero blocks will be introduced in to the Jacobian matrix (highlighted in Eq. (1)) when $\mathbf{P}^{(\bar{\alpha}\bar{\beta})} = \mathbf{P}^{(\bar{\beta}\bar{\alpha})} = \mathbf{0}$. Following this finding, a structurally symmetric sparse linear system can be obtained by setting interaction interaction tensors between a group of selected grain pairs to be zero. Zero $\mathbf{P}^{(\bar{\alpha}\bar{\beta})}$ and $\mathbf{P}^{(\bar{\beta}\bar{\alpha})}$ indicates there is no interactions between grain $\bar{\alpha}$ and $\bar{\beta}$. This section investigate the consequence of neglecting interactions between a pair of grains, $\bar{\alpha}$ and $\bar{\beta}$ and the strategy for determining a cluster of grains between which the interactions are negligible.

3.1 Coefficient tensors considering partial interactions

In the case of piecewise uniform fields, Dvorak [1] derived the following properties for the coefficient tensors:

$$\text{Kinematic consistency} : \sum_{\alpha=1}^{n} \mathbf{P}^{(\beta\alpha)} = \mathbf{I} - \mathbf{A}^{(\beta)} \tag{3}$$

$$\text{Simultaneous iso} - \text{stress/strain condition} : \sum_{\alpha=1}^{n} \mathbf{P}^{(\beta\alpha)}\mathbf{M}^{(\alpha)} = \mathbf{0} \tag{4}$$

$$\text{Elastic reciprocity} : c^{(\beta)}\mathbf{P}^{(\beta\alpha)}\mathbf{M}^{(\alpha)} = c^{(\alpha)}\mathbf{M}^{(\beta)}\mathbf{P}^{(\alpha\beta),T} \tag{5}$$

$$\text{Strain compatibility} : \sum_{\alpha=1}^{n} c^{(\alpha)}\mathbf{P}^{(\alpha\beta)} = \mathbf{0} \tag{6}$$

In addition, the concentration tensors $\mathbf{A}^{(\alpha)}$ satisfies the well-known Hill relation:

$$\sum_{\alpha=1}^{n} c^{(\alpha)}\mathbf{A}^{(\alpha)} = \mathbf{I} \tag{7}$$

In general, concentration (**A**) and interaction tensors (**P**) are computed from the elastic Green's function through linear elastic analysis on the microstructure domain. Our goal here is to derive a new set of coefficient tensors from the original ones when interaction between a chose pair of grains are neglected that enforce Eqs. (3)-(7) as much as possible. By applying this formulation on a group of selected grains, one can obtain a sparse EHM model.

While enforcing Eqs. (3)- (7) simultaneously is not successful to the best knowledge of the authors, we now introduce two models that will either enforce the kinematic consistency or simultaneous iso-stress/strain condition, namely kinematically (ϵ-EHM) and simultaneous iso-stress/strain constrained sparse EHM (σ-EHM), respectively. For both models, the compliance tensors remain unchanged. The new coefficient tensors for ϵ-EHM are:

$$\mathbf{P}'^{(\alpha\beta)} = \begin{cases} \mathbf{0} & \{\alpha,\beta\} = \{\bar{\alpha},\bar{\beta}\} \\ \mathbf{P}^{(\bar{\alpha}\bar{\alpha})} + \frac{c^{(\bar{\beta})}}{c^{(\bar{\alpha})}}\mathbf{P}^{(\bar{\beta}\bar{\alpha})} & \{\alpha,\beta\} = \{\bar{\alpha},\bar{\alpha}\} \\ \mathbf{P}^{(\bar{\beta}\bar{\beta})} + \frac{c^{(\bar{\alpha})}}{c^{(\bar{\beta})}}\mathbf{P}^{(\bar{\alpha}\bar{\beta})} & \{\alpha,\beta\} = \{\bar{\beta},\bar{\beta}\} \\ \mathbf{P}^{(\alpha\beta)} & \text{otherwise} \end{cases} \tag{8}$$

$$\mathbf{A}'^{(\alpha)} = \begin{cases} \mathbf{A}^{(\alpha)} & \alpha \notin \{\bar{\alpha},\bar{\beta}\} \\ \mathbf{A}^{(\bar{\alpha})} + \mathbf{P}^{(\bar{\alpha}\bar{\beta})} - \frac{c^{(\bar{\beta})}}{c^{(\bar{\alpha})}}\mathbf{P}^{(\bar{\beta}\bar{\alpha})} & \alpha = \bar{\alpha} \\ \mathbf{A}^{(\bar{\beta})} + \mathbf{P}^{(\bar{\beta}\bar{\alpha})} - \frac{c^{(\bar{\alpha})}}{c^{(\bar{\beta})}}\mathbf{P}^{(\bar{\alpha}\bar{\beta})} & \alpha = \bar{\beta} \end{cases} \tag{9}$$

while the coefficient tensors for σ-EHM are:

$$\mathbf{P}'^{(\alpha\underline{\beta})} \begin{cases} \mathbf{0} & \{\alpha,\beta\} = \{\bar{\alpha},\bar{\beta}\} \\ \mathbf{P}^{(\bar{\alpha}\bar{\alpha})} + \frac{c^{(\bar{\beta})}}{c^{(\bar{\alpha})}}\mathbf{M}^{(\bar{\alpha})}\mathbf{P}^{(\bar{\beta}\bar{\alpha}),T}\mathbf{M}^{(\bar{\alpha}),-1} & \{\alpha,\beta\} = \{\bar{\alpha},\bar{\alpha}\} \\ \mathbf{P}^{(\bar{\beta}\bar{\beta})} + \frac{c^{(\bar{\alpha})}}{c^{(\bar{\beta})}}\mathbf{M}^{(\bar{\beta})}\mathbf{P}^{(\bar{\alpha}\bar{\beta}),T}\mathbf{M}^{(\bar{\beta}),-1} & \{\alpha,\beta\} = \{\bar{\beta},\bar{\beta}\} \\ \mathbf{P}^{(\alpha\beta)} & \text{otherwise} \end{cases} \tag{10}$$

$$\mathbf{A}'^{(\underline{\alpha})} \begin{cases} \mathbf{A}^{(\alpha)} & \alpha \notin \{\bar{\alpha},\bar{\beta}\} \\ \mathbf{A}^{(\bar{\alpha})} + \mathbf{P}^{(\bar{\alpha}\bar{\beta})} - \frac{c^{(\bar{\beta})}}{c^{(\bar{\alpha})}}\mathbf{M}^{(\bar{\alpha})}\mathbf{P}^{(\bar{\beta}\bar{\alpha})}\mathbf{M}^{(\bar{\alpha}),-1} & \alpha = \bar{\alpha} \\ \mathbf{A}^{(\bar{\beta})} + \mathbf{P}^{(\bar{\beta}\bar{\alpha})} - \frac{c^{(\bar{\alpha})}}{c^{(\bar{\beta})}}\mathbf{M}^{(\bar{\beta})}\mathbf{P}^{(\bar{\alpha}\bar{\beta})}\mathbf{M}^{(\bar{\beta}),-1} & \alpha = \bar{\beta} \end{cases} \tag{11}$$

Remark. *ϵ-EHM can be deemed as a model between Taylor model and full EHM. It can be shown, when all transmitted interactions are neglected ($\mathbf{P}^{(\alpha,\beta)} = \mathbf{0}$, $\alpha \neq \beta$), the self-induced interaction tensors become zero and concentration tensors will become identity tensor, leading to a diagonal system in Eq.* (2) *and recovers the classical Taylor model.*

3.2 A consistent grain clustering scheme

In the current study, we employe a nearest neighbor based algorithm to consistently eliminate weak interactions between grains that are far from each other. Let $\Theta_1^{(\alpha)}$ denote the domain of all grains in the immediate neighborhood of the grain, α, with domain, $\Theta^{(\alpha)}$. The immediate neighborhood of $\Theta_1^{(\alpha)}$ is denoted as $\Theta_2^{(\alpha)}$ and constitutes the secondary influence zone of grain

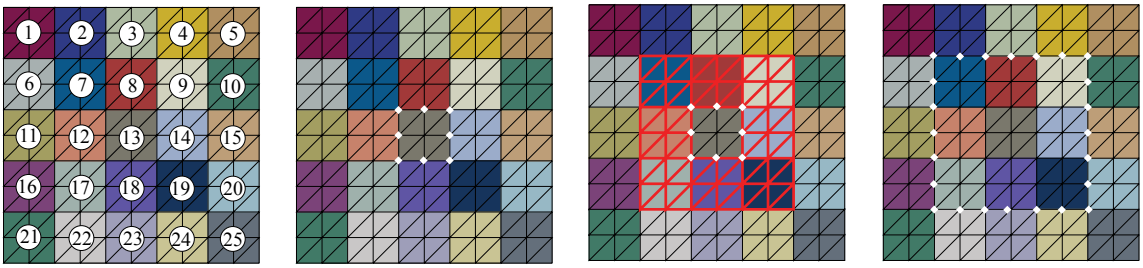

Figure 3: Schematic demonstration of the clustering scheme.

α. Following the same argument for higher order influence zones, n_c-layer grain cluster for grain α is defined as:

$$\Omega_{n_c}^{(\alpha)} = \Theta^{(\alpha)} \bigcup_{i=1}^{n_c} \Theta_i^{(\alpha)} \tag{12}$$

The algorithm for constructing the grain clusters is schematically illustrated in Fig. 3. The index of each grain is illustrated in Fig. 3(a). For each grain within the microstructure, the boundary nodes are identified (Fig. 3(b)). An element connectivity based search is conducted to identify all grains that contain at least one of the boundary nodes to build $\Theta_1^{(\alpha)}$ (Fig. 3(c)). To build the second layer of neighbors, $\Theta_2^{(\alpha)}$, the above process is repeated by replacing $\Theta^{(\alpha)}$ with $\Theta_1^{(\alpha)}$ (Fig. 3(d)).

4 Computational implementation

The nonlinear numerical procedures for the sparse EHM models are similar to the full EHM (detailed in Ref. [13]). The characteristics of the linearized equations of the sparse EHM system is exploited to efficiently evaluate the reduced order models. In particular, we leverage the structural symmetry (Fig. 4(a)-(b)), sparsity, compressed storage and reordering (Fig. 4(c)-(d)) of the equation system for computational efficiency.

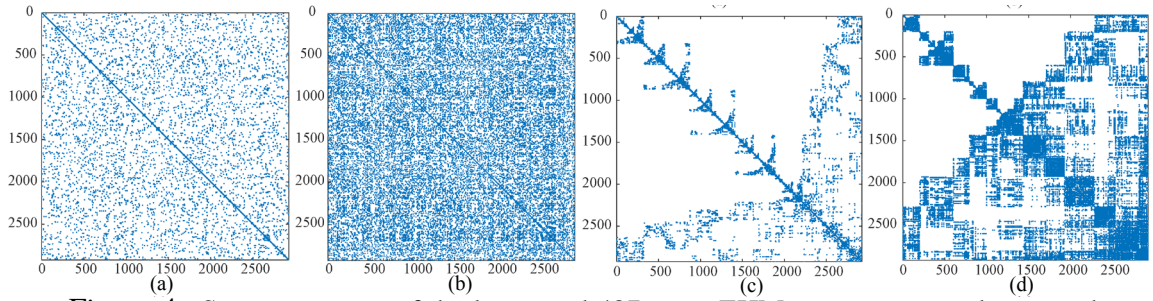

Figure 4: Sparsity pattern of the linearized 487-grain EHM system: original one- and two-layer sparse EHM and their reordered versions (c)-(d).

The implementation is performed in two stages: (1) preprocessing; and (2) multiscale analysis. Particular attention is paid on obtaining as much information as possible in the preprocessing stage (e.g., CRS format and reordering as well as analysis and symbolic factorization in the case

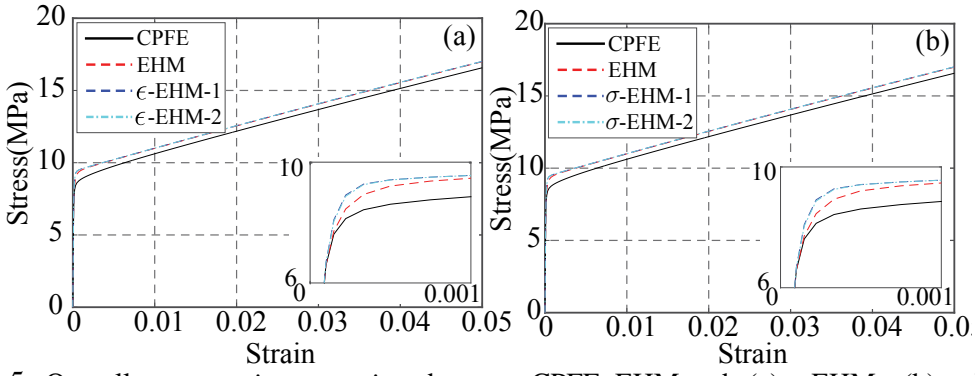

Figure 5: Overall stress-strain comparison between CPFE, EHM and: (a) ϵ-EHMs; (b) σ-EHMs.

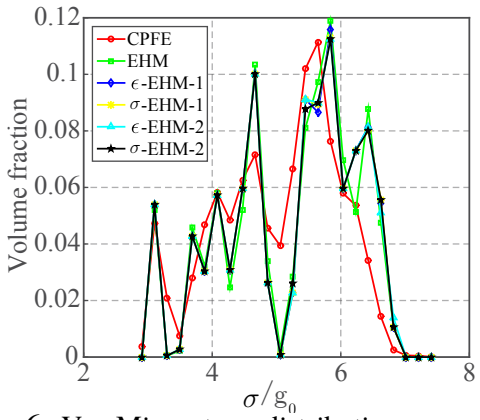

Figure 6: Von Mises stress distribution comparison.

of direct solver) and directly use them in the later on N-R process since the sparsity pattern of the system remain unchanged. Both direct (PARDISO) and iterative solver (FGMRES) are implemented for maximum efficiency (parallel disabled) in the multiscale analysis stage and the details are skipped here for simplicity.

5 Numerical verification

5.1 Accuracy and efficiency evaluation

The material considered is pure aluminum with material parameters from Ref. [13]. The RVE is taken to consist of 487 grains and the microstructure is shown in Fig. 1(f) under uniaxial tension. The overall stress-strain response obtained by the CPFE, full EHM, ϵ-EHM and σ-EHM models are compared in Fig. 6. Both ϵ-EHM and σ-EHM models provide almost identical results as the full EHM model. The local von Mises stress distribution (i.e., stress distribution of all the grains within the RVE, normalized by g_0) computed with the CPFE and the proposed models within the RVE is plotted in Fig. 6. The discrepancies between the stress distribution for different EHMs are negligible, and the distribution match the results from the reference CPFE simulation with reasonable accuracy.

The efficiency characteristics of the EHM models are assessed by performing simulations with microstructures shown in Fig. 1. The speedup of different EHM models compared with

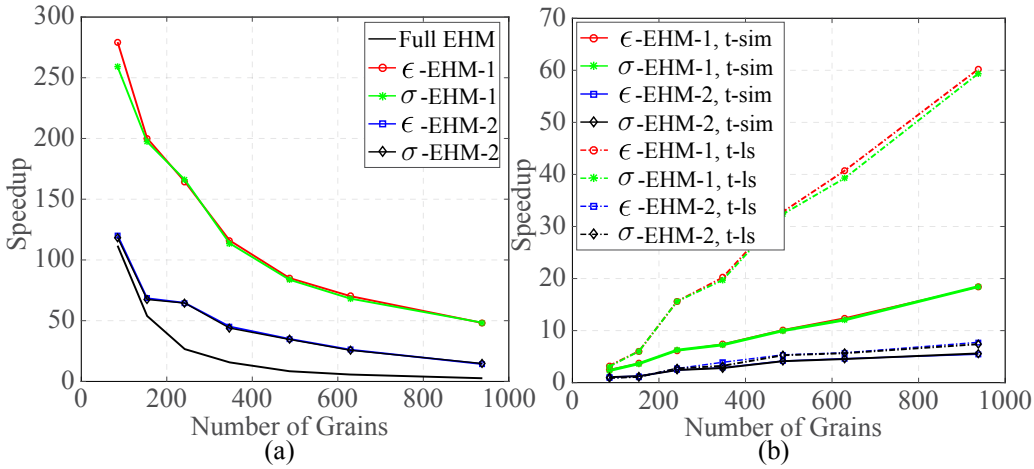

Figure 7: Efficiency comparison: (a) full and sparse EHMs compared with CPFE; (b) sparse EHM compared with full EHM.

CPFE are listed in Table 1 and plotted in Fig. 7. One-layer sparser EHMs (ϵ-EHM-1 and σ-EHM-1) provide significant speedup compared with full EHM and a much slower efficiency degradation as the microstructure size increases.

The speedup of sparse EHMs compared with the full EHM are plotted in Fig. 7(b), together with the the speedup of linear solver portion (accumulated CPU time spent for linear solver only). It is observed that the speedup of one-layer sparse EHM compared with full EHM increases linearly as n increases. The speedup of the two-layer sparse EHM compared with EHM, shows a sub-linear relationship with n. This is because sparsity decreases fast from the one-layer sparse EHM to the two-layer sparse EHM and the FLOPs of solving a sparse linear system increase fast as the decrease of the sparsity. The behavior of speedup for the linear solver portion is generally similar to the total simulation times, but the curves show much higher slopes. This is because the other procedures (i.e., computation of slip resistance evolution, matrix constructions etc.) are of similar order for all models, including the full EHM and sparse EHM.

Figure 8 shows the efficiency of ϵ-EHM-1 using the iterative solver as a function of n. It clearly shows that sparsity also significantly increase the efficiency of EHM when using iterative solver, while the speedup is less than the case of direct solver in the cases we studied.

5.2 A structural example: plate with hole under bolt load

To demonstrate the capability of sparse EHM in solving structural scale problems, we investigated the response of a plate subjected to bolt pressure as shown in Fig. 9(a). Half of the plate is discretized due to symmetry with 27,680 tri-linear eight-noded hexahedron elements (Fig. 9(b)). The microstructure is the 938-grain RVE as shown in Fig. 1 (h). The simulation therefore tracks 25,963,840 grains throughout the domain of the plate and the one-layer ϵ-EHM is used in this study.

The stress-contour of the plate at the end of loading is shown in Fig. 9(c). The reaction force versus the displacement at the far end (i.e., $\theta = 0^o$) of the hole is shown in Fig. 10(a). 12 elements at each position as shown in Fig. 9(a) are selected (probing 11,256 grains at each

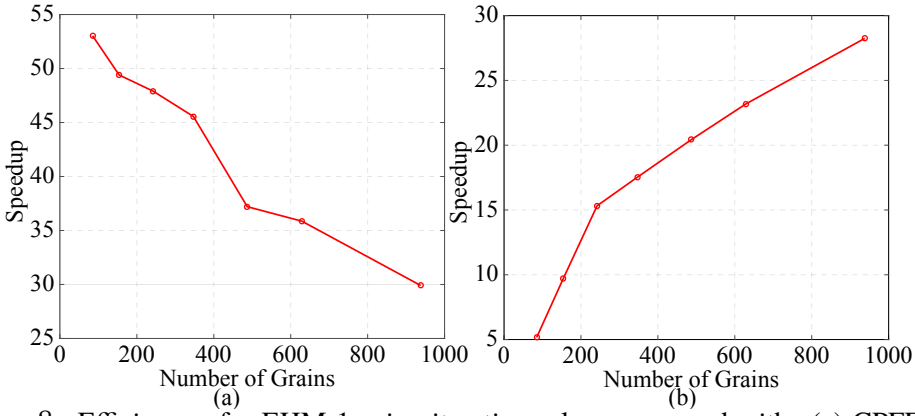

Figure 8: Efficiency of ϵ-EHM-1 using iterative solver compared with: (a) CPFE and (b) full EHM using iterative solver.

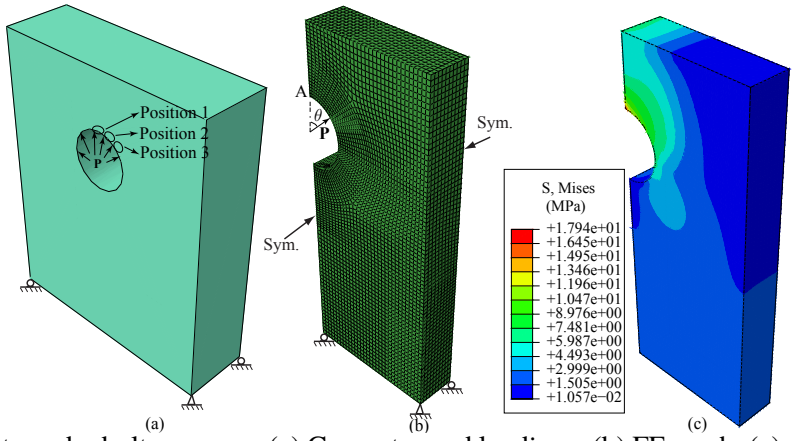

Figure 9: Plate under bolt pressure: (a) Geometry and loadings; (b) FE mesh; (c) stress contour.

position), and the von Mises stress (normalized by initial slip resistance, g_0) histograms of the microscale grains at each position are plotted in Fig. 10(b). Microscale stress histograms show a decreasing grain level von Mises stress from position 1, 2 to 3, consistent with the macroscale stress at position 1, 2 and 3 as shown in Fig. 9(c).

6 Conclusions and future research interests

We presented a grain-cluster accelerated eigenstrain-based reduced-order homogenization model for computationally efficient modeling of complex polycrystal microstructures through selectively considering grain-to-grain interactions. It is found that the proposed sparse EHM can maintain the high efficiency better as the RVE size increases and with negligible differences compared with full EHM for both overall stress-strain response and local response. The concept of the sparse EHM is also beneficial for other reduced models (e.g., [9, 7, 8, 3, 12]) when higher resolution (i.e., number of parts is relative large) is required. Future work will consider incorporating of the sparse EHM concept into these models for efficiency improvement.

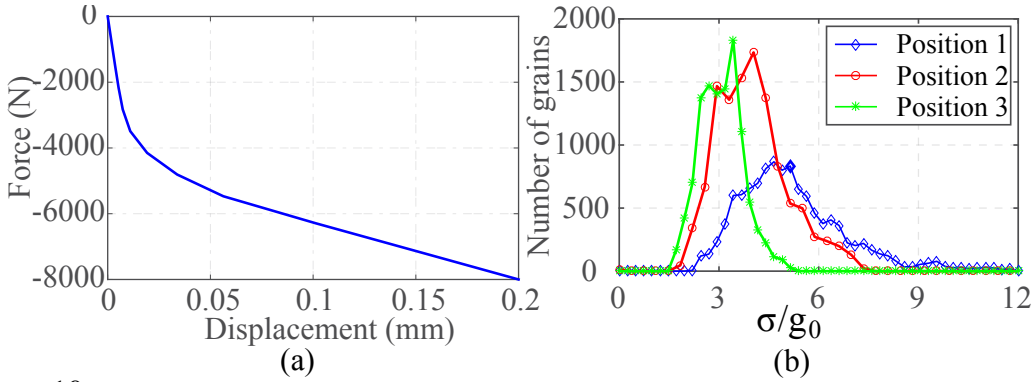

Figure 10: Response of the plate: (a) force-displacement; (b) local von Mises stress histogram.

References

[1] G. J. Dvorak. Transformation field analysis of inelastic composite materials. *Proc. Math. Phys. Eng. Sci.*, 437:311–327, 1992.

[2] P. V. Houtte. On the equivalence of the relaxed taylor theory and the bishop-hill theory for partially constrained plastic deformation of crystals. *Mater. Sci. Eng*, 55:69–77, 1982.

[3] T. Hui and C. Oskay. A high order homogenization model for transient dynamics of heterogeneous media including micro-inertia effects. *Comput. Methods Appl. Mech. Engrg.*, 273:181–203, 2014.

[4] R. A. Lebensohn. N-site modeling of a 3d viscoplastic polycrystal using fast fourier transform. *Acta Mater.*, 49:2723–2737, 2001.

[5] R.A. Lebensohn and C.N. Tome. A self-consistent anisotropic approach for the simulation of plastic deformation and texture development of polycrystals: Application to zirconium alloys. *Acta Meta. Mater.*, 41:2611–2624, 1993.

[6] C. Miehe, J. Schroder, and J. Schotte. Computational homogenization analysis in finite plasticity simulation of texture development in polycrystalline materials. *Comput. Methods Appl. Mech. Engrg.*, 171:387–418, 1999.

[7] C. Oskay. Variational multiscale enrichment for modeling coupled mechano-diffusion problems. *Int. J. Numer. Meth. Engng*, 89:686–705, 2012.

[8] C. Oskay. Variational multiscale enrichment method with mixed boundary conditions for modeling diffusion and deformation problems. *Comput. Methods Appl. Mech. Engg.*, 264: 178–190, 2013.

[9] C. Oskay and M. Haney. Computational modeling of titanium structures subjected to thermo-chemo-mechanical environment. *Int. J. Solids Struct.*, 47(24):3341–3351, 2010.

[10] G. Sachs. Zur ableitung einer fliessbedingung. *Ver. Dtsch. Ing.*, 72:734–736, 1928.

[11] G.I. Taylor. Plastic Strain in Metals. *J. Inst. Met.*, 62:307–324, 1938.

[12] S. Zhang and C. Oskay. Reduced order variational multiscale enrichment method for elasto-viscoplastic problems. *Comput. Methods Appl. Mech. Engg.*, 300:199–224, 2016.

[13] X. Zhang and C. Oskay. Eigenstrain based reduced order homogenization for polycrystalline materials. *Comput. Methods Appl. Mech. Engrg.*, 297:408–436, 2015.

[14] X. Zhang and C. Oskay. Polycrystal plasticity modeling of nickel-based superalloy in 617 subjected to cyclic loading at high temperature. *Modelling Simul. Mater. Sci. Eng.*, 24: 055009, 2016.

XIV International Conference on Computational Plasticity. Fundamentals and Applications
COMPLAS XIV
E. Oñate, D.R.J. Owen, D. Peric & M. Chiumenti (Eds)

RESIDUAL STRESS DEVELOPMENT AND EVOLUTION IN TWO-PHASE CRYSTALLINE MATERIAL: A DISCRETE DISLOCATION STUDY

T. N. Tak[*,a], A. Prakash [†], A. Lodh[††], I. Samajdar[†], and P. J. Guruprasad[*]

[*] Department of Aerospace Engineering,
Indian Institute of Technology Bombay,
Mumbai 400076, India
[a]e-mail: tawqeer.nasir@aero.iitb.ac.in

[†]Department of Metallurgical Engineering and Materials Science
Indian Institute of Technology Bombay,
Mumbai 400076, India

[††]IITB-Monash Research Academy,
Indian Institute of Technology Bombay,
Mumbai 400076, India

Key words: Residual Stress, Discrete Dislocation Dynamics, Geometrically Necessary Dislocations

Abstract. Crystalline materials undergo heterogeneous deformation upon the application of external load, which results in the development of incompatible elastic strains in the material as soon as the load is removed. The presence of heterogeneous distribution of elastic strains in the absence of any form of external load results in the building up of stresses referred to as residual stresses. The heterogeneity of strain is attributed either to the presence of multiple phases or to the orientation gradients across the sample volume. This paper is an endeavour to model the presence of second phase in a two-dimensional discrete dislocation dynamics framework, which already contains constitutive rules to include three-dimensional mechanisms, such as line tension and dynamic junction formation. The model is used to investigate residual stress development in single crystals subjected to plane strain loading and then subsequently unloaded to study residual stresses. The dislocation accumulation around the second phase and its effect on the mechanical properties is studied. The orientation dependence of residual stresses as a function of the underlying defect substructure has also been explored. A variety of results are obtained. In particular, the development of stresses as a function of underlying defect substructure is also presented and found to depend upon the orientation of the crystal.

1 INTRODUCTION

Metals and metallic alloys are essentially multiphase materials. The presence of multiple phases in a material completely changes the mechanical behaviour of the system ranging from the macroscopic stress versus strain response to the microscopic defect structure development, which in turn affects the life of a component by accelerating or decelerating failure. Presence of a brittle phase in a crystalline matrix may be detrimental as it tends to be a potential site for failure by giving rise to residual stress, due to the difference in properties between the two phases [1].

Residual stress development in metals and metallic alloys mainly depends upon the manufacturing process. These stresses can be removed by subjecting the material to a wide variety of treatments but cannot be completely nullified, which makes it important to study the development and evolution of the stresses of this type, more so in case of multiphase alloys where they play a crucial role in the failure of a material.

This paper is an endeavour to model residual stresses in a multiphase material using discrete dislocation dynamics (DDD), a framework that models the plastic deformation in crystalline materials as a collective motion of individual dislocations in an imposed displacement field [2], thus exploring a relation between the stress development as a function of defect substructure and establishing a signature of residual stress. Preliminary results that show interesting trends have been presented.

2 DISCRETE DISLOCATION PLASTICITY

The formulation constitutes of a framework for solving quasi-static initial/boundary value problems in which plastic flow is a direct consequence of collective motion of large number of dislocations [3]. The formulation presented here is valid for a material characterised by a linear elastic constitutive relation undergoing small deformation. The formulation is applicable for three-dimensional solids, but the implementation is carried out for plane strain problems.

A linear elastic body of volume V comprising of an elastic inclusion of volume V^* is considered. The matrix material contains a distribution of dislocations, modelled as line defects in elastic continuum. The elastic properties of the matrix and the inclusion are governed by the fourth order tensors $\boldsymbol{\mathcal{L}}$ and $\boldsymbol{\mathcal{L}}^*$ respectively. Each dislocation $\mathbf{i}$ is characterised by its Burgers vector, $\mathbf{b_i}$ and unit normal, $\mathbf{n_i}$ of its slip plane. The body with boundary $S_u \cup S_f$ is now considered to be subject to time dependent traction and displacement boundary conditions $\boldsymbol{T} = \boldsymbol{T_0}(\boldsymbol{t})$ on S_f and $\boldsymbol{u} = \boldsymbol{u_0}(\boldsymbol{t})$ on S_u respectively.

The ensuing deformation is assumed to be quasi-static and is limited only to small strains. The deformation process will lead to motion of dislocations, generation of new dislocations by nucleation and mutual annihilation, and their pinning at obstacles. The analysis of the deformation process is performed in an incremental manner in time where

the incremental step at any time step involves three main computational stages. The first of them involving the computation of the current dislocation configuration and the associated stress and strain values for current configuration; the second step comprises of determining the Peach-Koehler force, driving force for change in dislocation structure, and the third being the determination of instantaneous rate of change of dislocation structure, computed on the basis of a set of constitutive equations for motion, annihilation and generation of dislocations.

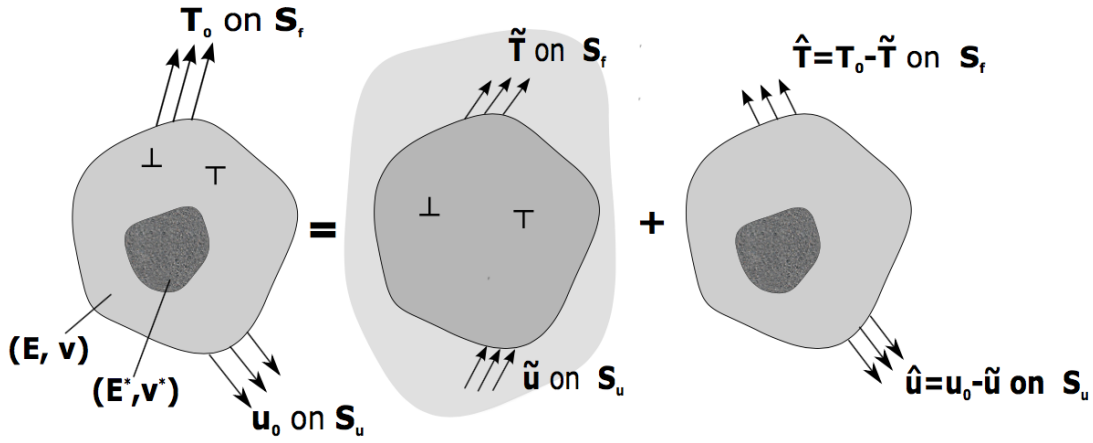

Figure 1: Decomposition of a problem for a body with dislocations and an inclusion into a problem of interacting dislocations in the infinite solid and a complementary field for the non-homogenous body without dislocations.

The formulation is based on decomposing the problem into two equivalent problems as shown in figure 1, one solving for the fields due to individual dislocations ($\sim$) and the other for the fields ($\wedge$) due to the external boundary conditions. After solving for the individual fields, the solutions are superposed. The first step, determining the instantaneous state of the body, involves determination of the current state of the body, which follows the formulation of [4] to determine the present dislocation structure and compute the current state of the body in terms of the displacement, strain and stress fields corresponding to the underlying dislocation substructure, and is written as the superposition of two fields,

$$\boldsymbol{u} = \tilde{\boldsymbol{u}} + \hat{\boldsymbol{u}} \qquad \boldsymbol{\epsilon} = \tilde{\boldsymbol{\epsilon}} + \hat{\boldsymbol{\epsilon}} \qquad \boldsymbol{\sigma} = \tilde{\boldsymbol{\sigma}} + \hat{\boldsymbol{\sigma}} \tag{1}$$

where ($\sim$) fields are associated with n dislocations in their current configuration but in an infinitely large medium of homogenous matrix material, and are obtained by superposition of fields of individual dislocations. Standard equations of linear elasticity are supposed to be valid outside the dislocation core area. These fields are obtained by superposition of fields $(\boldsymbol{u}^i, \boldsymbol{\epsilon}^i, \boldsymbol{\sigma}^i)$ associated with each individual dislocation,

$$\tilde{\boldsymbol{u}} = \Sigma \boldsymbol{u}^i \qquad \tilde{\boldsymbol{\epsilon}} = \Sigma \boldsymbol{\epsilon}^i \qquad \tilde{\boldsymbol{\sigma}} = \Sigma \boldsymbol{\sigma}^i \tag{2}$$

The governing equations for ($\sim$) fields can therefore be summarised as:

$$\nabla \cdot \tilde{\boldsymbol{\sigma}} = \mathbf{0} \qquad \tilde{\boldsymbol{\epsilon}} = \nabla \tilde{\boldsymbol{u}} \qquad \tilde{\boldsymbol{\sigma}} = \boldsymbol{\mathcal{L}} : \tilde{\boldsymbol{\epsilon}} \qquad \text{in} \quad V^M \cup V^* \tag{3}$$

with following boundary conditions on S,

$$\boldsymbol{\nu} \cdot \tilde{\boldsymbol{\sigma}} = \tilde{\boldsymbol{T}} \quad \text{on} \quad S_f \quad \text{and} \tag{4}$$

$$\boldsymbol{u} = \tilde{\boldsymbol{u}} \quad \text{on} \quad S_u \tag{5}$$

where ν is the outer unit normal to S. The absence of boundary conditions facilitates the finding of solution of the ($\sim$) fields. Since the formulation has been restricted to the modelling of edge dislocations alone, the solutions are available in textbooks [5]. The ($\wedge$) fields take care of the actual boundary conditions as well as the presence of inclusion. The governing equations may be written as follows:

$$\nabla \cdot \hat{\boldsymbol{\sigma}} = \mathbf{0} \qquad \hat{\boldsymbol{\epsilon}} = \nabla \hat{\boldsymbol{u}} \qquad \text{in} \quad V^M \cup V^* \tag{6}$$

$$\hat{\boldsymbol{\sigma}} = \boldsymbol{\mathcal{L}} : \hat{\boldsymbol{\epsilon}} \quad \text{in} \quad V^M \tag{7}$$

$$\hat{\boldsymbol{\sigma}} = \boldsymbol{\mathcal{L}}^* : \hat{\boldsymbol{\epsilon}} + (\boldsymbol{\mathcal{L}}^* - \boldsymbol{\mathcal{L}}) : \tilde{\boldsymbol{\epsilon}} \tag{8}$$

It is important to notice the contribution of polar stresses to the ($\sim$) fields in the inclusion, which results due to the dislocation strain fields and the difference in the elastic properties between matrix and inclusion.

$$\boldsymbol{\nu} \cdot \hat{\boldsymbol{\sigma}} = \hat{\boldsymbol{T}} = \boldsymbol{T_0} - \tilde{\boldsymbol{T}} \quad \text{on} \quad S_f \tag{9}$$

$$\boldsymbol{u} = \hat{\boldsymbol{U}} = \boldsymbol{u_0} - \tilde{\boldsymbol{U}} \quad \text{on} \quad S_u \tag{10}$$

μ and B are used to denote the shear and bulk moduli of the matrix material where as μ^* and B^* represent the respective moduli for the second phase. The displacement fields due to the presence of dislocations in the matrix are assumed to remain smooth across the interface of the matrix and second phase, which makes the problem a well posed one and can be solved by using Finite Element Method.

For any dislocation configuration to be stable in a deformed body, it has to fulfil the conditions for thermodynamic equilibrium, which makes the rearrangement of dislocations a vital activity in a deformation process. The dislocations will time and again have to reorganise themselves to minimise the energy of the system. The rearrangement takes place under the action of a gliding force, referred to as Peach-Koehler force, which essentially can be described as the change of the potential energy of the body associated with an infinitesimal variation of the dislocation position in the glide plane. The expression for the Peach-Koehler force, f^i may be written as:

$$f^i = \boldsymbol{m^i} \cdot \{\hat{\boldsymbol{\sigma}} + \sum_{\boldsymbol{j \neq i}} \boldsymbol{\sigma^j}\} \cdot \boldsymbol{b^i} \tag{11}$$

Short range interactions are accounted for by a set of constitutive rules for (i) dislocation nucleation, (ii) dislocation annihilation, (iii) dislocation obstacles, (iv) dislocation glide, (v) junction formation and (vi) dynamic sources. The three-dimensional interactions are modelled through constitutive rules.

In case of a two dimensional analysis, performed here, an initial density of sources and obstacles is specified a priori, each of them being a point source on a slip plane. Dislocations are nucleated in the form of dipoles when the magnitude of Peach-Koehler force at the location of the source i exceeds a critical value, for a prescribed time t_0. During the deformation, dislocations get pinned at these locations and are released only when the Peach-Koehler force exceeds $\tau_{obs} b_i$. While the number of sources remain constant throughout the entire deformation, the case is different in actual conditions, i.e., (i) the density of sources and obstacles increases as the dislocation density increases and (ii) line tension acts to restrict dislocation multiplication. These mechanisms are captured in two dimensions following the approach given in [6], wherein they have successfully been able to include key features of these interactions into two dimensional simulations to enable the dislocation source and obstacle population to evolve dynamically. This is achieved by modelling the formation of junctions upon the interaction of dislocations on intersecting planes. A junction, once formed, can act as a source or an obstacle to dislocations gliding on the slip plane, thus increasing the density of sources and obstacles with ensuing deformation.

3 RESULTS

To implement the framework discussed above using finite element method, a boundary value problem to simulate the uniaxial deformation of a planar crystal is formulated. A crystal of FCC type with dimensions, L x H with a second phase with dimensions w x h, as shown in figure 2, is subjected to compression followed by unloading along x_1-axis. Plane strain condition is invoked. A uniform displacement of $u_1 = \pm U/2$ and vanishing shear stress at $x_1 = \pm L/2$ is prescribed while a traction free condition is maintained at surfaces, $x_2 = \pm H/2$.

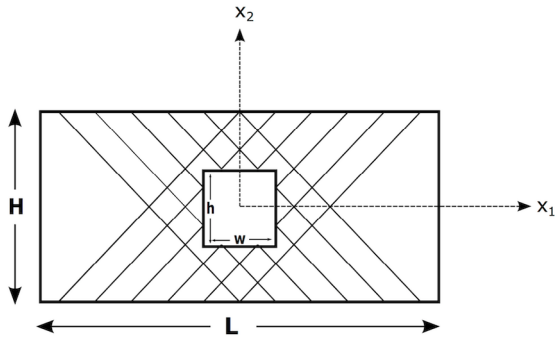

Figure 2: Geometry of the compression problem analysed for an FCC crystal with an inclusion oriented for double slip.

For the present simulations, a sample of dimensions 8μm x 4μm with a precipitate volume fraction $v_f^p = 0.03$ and dimensions 1μm x 1μm was used. The simulations were initially carried out for a single orientation with two slip systems oriented at $\phi = \pm 54.75^o$ to the loading x_1 axis. The slip planes are such that they extend from one free surface to another without intersecting the surfaces where the displacement boundary conditions are prescribed. The material was initially assumed to be dislocation free with initial source and obstacle density, $\rho_s = \rho_o = 1.56$ x 10^{13}m^{-2}. The static obstacles were assigned a constant strength $\tau_{obs} = 150$ MPa. The mean nucleation strength was taken to be $\tau_{nuc} = 17$ MPa. Standard values for other material parameters like Young's modulus $E = 70$ GPa, Poisson's ratio $\nu = 0.3$, drag factor $B = 10^{-4}$ Pa s, Burger's vector, $b = 0.25$nm, were used. For the second phase, the values for Young's Modulus and Poisson's ratio were taken to be $E = 500$ GPa and $\nu = 0.17$ respectively. Nucleation time remains fixed at $t_{nuc} = 10ns$.

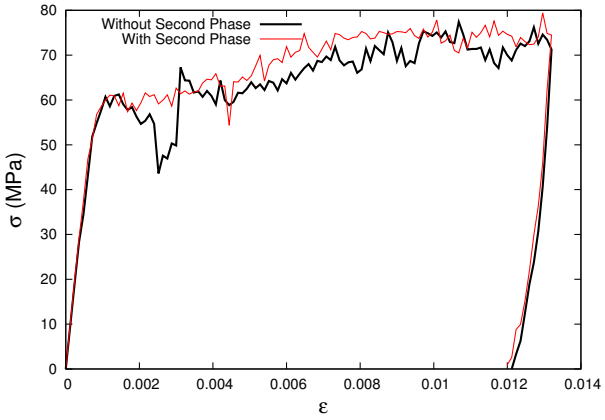

Figure 3: Representative stress versus strain response for an FCC crystal, with and without second phase, during loading and unloading.

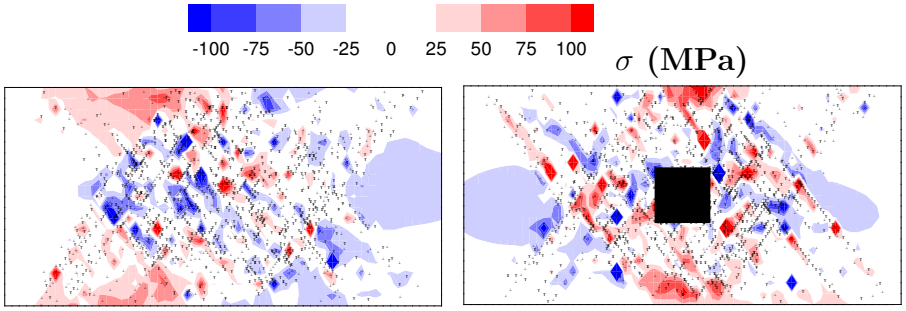

(a) (b)

Figure 4: Contours showing residual stress distribution in a deformed sample after unloading for (a) without a second phase (b) with second phase

A nominal strain rate of the order of $10^4 s^{-1}$ was applied. The sample was loaded in simple uniaxial compression. With the nucleation of first dislocation loop, the material begins to yield. In order to demonstrate the effect of presence of a second phase particle in a material, two cases (i) a sample without a second phase and (ii) a sample with a second phase present in it, were simulated. Both the samples were loaded in compression up to a strain, $\epsilon = 0.012$ followed by unloading to a zero value of macroscopic stress, by reversing the direction of the applied load. Representative stress versus strain response was plotted, as given in figure 3.

From the results given in figure 3, it can be seen that the presence of a second phase in an otherwise homogenous matrix changes the mechanical response of the material; the sample with a second phase hardens more than the one without a second phase. This happens as a result of the obstruction to the flow of dislocations in the matrix caused by the presence of the second phase. It was observed that unloading to a zero value of finite body stresses doesn't make the material completely stress free. The average value of stress present in the sample in presence of a second phase, after unloading, was found to be $\sigma = 2.67$ MPa, which is more than $\sigma = 1.968$ MPa, the value obtained for the sample without a second phase. In order to relate the presence of these stresses with the underlying defect substructure, the geometrically necessary dislocation (GND) density was computed for both the cases. The GND density values for the sample with a second phase was found to be $\rho_{GND} = 2.67$ x 10^{12} m^{-2}, which is more than $\rho_{GND} = 1.96$ x 10^{12} m^{-2} observed in the sample without a precipitate, which suggests a correlation between the residual stress development and the GND density. This has also been illustrated by representing the dislocation configuration superimposed upon the stresses contours as shown in figure 4. It can be seen that in a material with second phase, the dislocation pile ups around the second phase lead to the accumulation of more residual stresses.

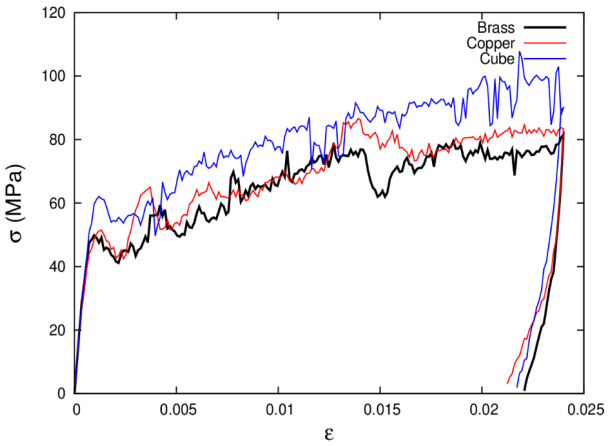

Figure 5: Representative stress versus strain response for an FCC single crystal with a second phase under compressive load for three different matrix orientations.

Additional simulations were carried out to study the orientation dependence of resid-

ual stress development in a material. Uniaxial compression tests, for three different matrix orientations, viz., Cube ($\{100\} < 001 >$), Brass ($\{011\} < 211 >$), and Copper ($\{112\} < 111 >$) were carried out. The samples were deformed upto a strain, $\epsilon = 0.023$ and were subsequently unloaded to a zero value of macroscopic stress as shown in figure 5. It was observed that the samples, after unloading, show a different distribution of residual stresses depending on their orientation, which is illustrated in the contours given in figure 6. The average values of residual stresses for the three different orientations were computed. It was found that Cube orientation develops the maximum residual stress, $\sigma_{Cube} = 4.93$ MPa, and Copper develops the least, $\sigma_{Copper} = 3.97$ MPa, while the residual stress value in the Brass orientation, $\sigma_{Brass} = 4.24$ MPa was found to lie midway between the two, which establishes the hypothesis that residual stress development in a two phase alloy is orientation dependent. A similar behaviour was observed for Bauschinger effect as well.

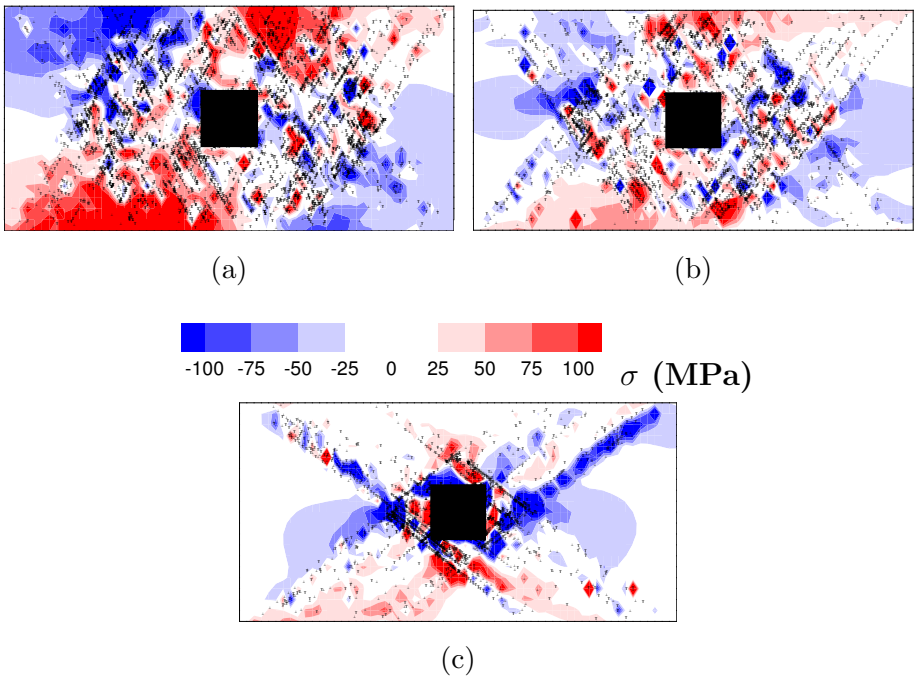

Figure 6: Contours showing residual stress distribution in a deformed sample after unloading for three different orientations (a) Cube (b) Brass (c) Copper

4 SUMMARY

A mechanism based discrete dislocation dynamics model was used to simulate the development of residual stresses in a two phase face centred cubic (FCC) material. It was observed that the presence of a harder phase in the matrix changes the mechanical behaviour of the material, which can be observed from a representative stress versus strain response, and leads to the hardening of material and development of residual stresses in a material. Moreover, it was also observed that the residual stress development in a two

phase crystalline material not only depends upon the mechanical properties of the second phase but also the orientation of the matrix. A trend between the development of residual stress and defect substructure was observed.

REFERENCES

[1] Withers, P.J. and Bhadeshia, H.K.D.K. Residual Stress Part 1- Measurement techniques. *Mater. Sci. Technol.* (2001) **17**:355–365.

[2] Cleveringa, H.H.M., Van der Giessen, Erik, Needleman, A. A discrete dislocation analysis of residual stresses in a composite material. *Phil. Mag.* (1999) **79**(4): 893-920

[3] Van der Giessen, E. and Needleman, A. Discrete dislocation plasticity: a simple planar model. *Modelling Simul. Mater. Sci. Eng.* (1995) **3**(5):689

[4] Lubarda, V.A., Blume, J.A. and Needleman, A. An analysis of equilibrium dislocation distributions. *Acta Mater* (1993) **41**:625 - 642

[5] Dieter, G. E. *Mechanical Metallurgy.* McGraw-Hill Book Co. Newyork, Vol. I., (1986).

[6] Benzerga, A. A., Brèchet, Y., Needleman, A. and Van der Giessen, E. Incorporating three-dimensional mechanisms into two-dimensional dislocation dynamics *Modelling Simul. Mater. Sci. Eng.* (2004) **12**(3):557

XIV International Conference on Computational Plasticity. Fundamentals and Applications
COMPLAS 2017
E. Oñate, D.R.J. Owen, D. Peric and M. Chiumenti (Eds)

COMPUTER SIMULATION OF SURFACE MODIFICATION OF AL CRYSTALLITE UNDER HIGH ENERGY TREATMENT

DMITRIJ S. KRYZHEVICH, ALEKSANDR V. KORCHUGANOV AND KONSTANTIN P. ZOLNIKOV

International Institute of Strength Physics and Materials Science of Siberian Branch of Russian Academy of Sciences (ISPMS SB RAS)
Akadenicheskii 2/4, 634055 Tomsk, Russia
e-mail: root@ispms.tomsk.ru, web page: http://ispms.ru/en

Key words: Ion implantation, Surfaces, Molecular dynamics, Structural defects, Grain Boundaries.

Abstract. The simulation of structural changes in the surface region of Al crystallite during self-ion bombardment was carried out. The calculations were performed on the base of the molecular dynamics method. A many-body potential calculated in the approximation of the embedded atom method was used to describe the interatomic interactions. It is shown that atomic displacement cascades in the near-surface region were generated under ion irradiation. At relatively low energies the impact of the atomic displacement cascades not only lead to the generation of Frenkel pairs, but also to the nucleation of plastic deformation. That is due to the high-rate heating of the grains, causing their expansion and deformation in the stained conditions with the formation of stacking faults. Melting of surface layers takes place at high energies of irradiation. A crystallization process and a formation of a grain structure of the surface layers will be determined by the characteristics of the propagation of the crystallization front, which shape depends on the relative location, size and orientation of grains on the boundary of the liquid and solid phases.

1 INTRODUCTION

Modification of the surface by ion beams is widely used to improve the operating characteristics of metals and alloys [1,2]. The change in physical and mechanical properties is due both to the process of surface alloying of the material by chemical elements from the beam, and to the structural changes of the near-surface layer.

Irradiation by ions can cause not only fragmentation of grains but also lead to melting of the surface layer. The thickness of the modified layer depends on the energy of the ion beam. It may reach to several tens of microns at the irradiation by ion beams with energy of more than 3 MeV. We note that fragmentation takes place in a layer with several micrometers of thickness for beams with energies less than 1 MeV.

In this case, the thickness of the modified layer with the changed defect structure can reach more than 100 μm. Due to the long-range effect, the depth of the modified layer exceeds not only the mean free path of the incident ions, but also the average grain size. The occurrence of high stresses at the boundaries and grain joints causes the fragmentation of the surface layer

upon irradiation [1,3]. Irradiation with high-energy ions leads to the generation of shock waves and strong elastic fields [4-6]. As a result, nonequilibrium micro- and nanostructural layers can form in the near-surface region of metals. Different competing mechanisms connected with phase transitions, structural transformations, plastic deformation, fragmentation in the near-surface region, lay on the base of the relaxation process of the irradiated material.

Experimental study of the dynamics of such processes may face considerable difficulties in view of the small spatial and temporal scales of their occurrence Modeling of these processes allows to overcome these difficulties and to obtain detailed information on the dynamics of structural changes during irradiation and relaxation of the material [7-9]

In this paper, we investigate the features of structural transformations in the surface layer both in single crystals with different orientations of the irradiated surface and in nanocrystalline aluminum samples under ion irradiation.

2 METHODS

The method of molecular dynamics [10,11] was used to solve the problem posed in this paper. The simulation was carried out in the software package LAMMPS [12]. The potential of the interatomic interaction for aluminum was described in the framework of the embedded atom method [13]. The simulated samples contained from 75 000 to 1 000 000 atoms. The initial temperature of the samples was set equal to 300 K. The mono- and nanocrystalline samples of aluminum were subjected to irradiation. The {100}, {110} and {111} surfaces were irradiated in the case of single-crystal samples. The nanocrystalline samples consisted of 6 and 10 grains with an average size of 7.5 and 6.5 nm, respectively. Ion irradiation was simulated by the bombardment of aluminum atoms on a free surface. In the case of a single crystal, the energy of incident atoms on the free surface was 60 eV. Total number of incident atoms was 540. Both mechanically unloaded crystallites and elastically deformed samples were irradiated. In the case of nanocrystalline samples, the number of incident atoms varied from 16 to 80. The energy of each atom was 1.5 keV. Analysis of structural changes in irradiated samples was based on the Common Neighbor Analysis [14] and the Dislocation Extraction Algorithm [15]. Visualization of investigated structures was performed in the OVITO software [16].

3 SIMULATION RESULTS

Calculations showed that ion irradiation with the above energies leads to sputtering of individual atoms and atomic clusters from the irradiated surfaces of the crystallite. Under this irradiation regime, the number of implanted atoms was less than the number of atoms sputtering from the surface. It was found that the process of atom sputtering occurred most intensively at exposing of the {111} surface.

During the irradiation, the temperature of the near-surface layer of the crystallite exceeded the melting point. Temperature dependency on time for the layer with a thickness of 10 lattice parameters near the {111} surface is shown in Fig. 1. After irradiation, the temperature of this layer decreases quite rapidly and is characterized by pronounced oscillations. We note that irradiation of the surface leads to the generation of shock waves in the crystallite. Due to this fact the periodicity of the temperature oscillations correlates well with the time of passage of

the shock waves from the loaded surface to the rear one and back.

Crystallites with the {100} irradiated surfaces are the most stable to structural changes in the near-surface layers. In this case, only a small number of surface layers involved in cascades of atomic displacements locally change the symmetry of the nearest environment (Fig. 2a). It was noted that dislocations, stacking faults, interstitial dumbbells are not formed in crystallites. The elastic deformation of the investigated crystallites before irradiation had little effect on the structural changes in the surface layer.

When the {111} surfaces of the undeformed crystallite are irradiated, the stacking faults are formed in the near-surface region in the (111) planes. If the crystallite is pre-deformed, the stacking faults are also generated in adjacent planes (Fig. 1b). In the case of irradiation of the {110} surface, the local symmetry of the nearest environment changes for many atoms, which can subsequently lead to the generation of stacking faults (Fig. 3). The sizes of the defects increase with the growth of preliminary elastic deformation of the crystallite. In this case, stacking faults are formed in adjacent planes and vacancy chains can be formed at their intersection (Fig. 3b, c).

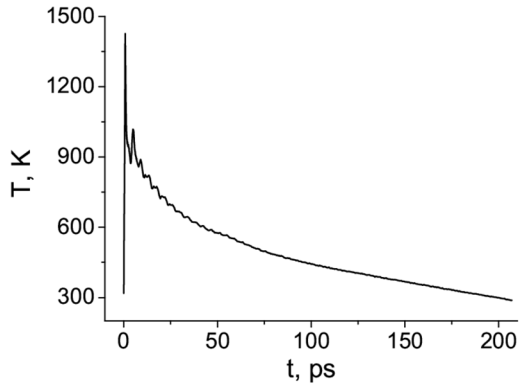

Figure 1: Dependence of the temperature of the surface layer versus time at the irradiation of the {111} surface. Sample was preliminary deformed to 4%

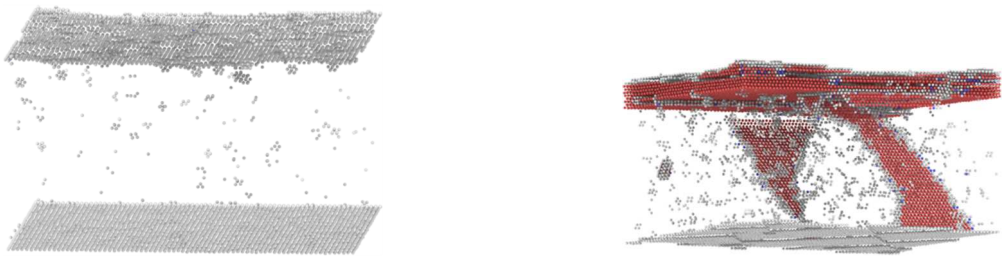

Figure 2: The structure of the samples after irradiation of the {100} (a) and {111} (b) surfaces. Samples were deformed by 4%. Atoms with hcp and an uncertain symmetry of the nearest environment are indicated by pink and gray colors, respectively. Atoms with fcc symmetry of the

nearest environment are invisible

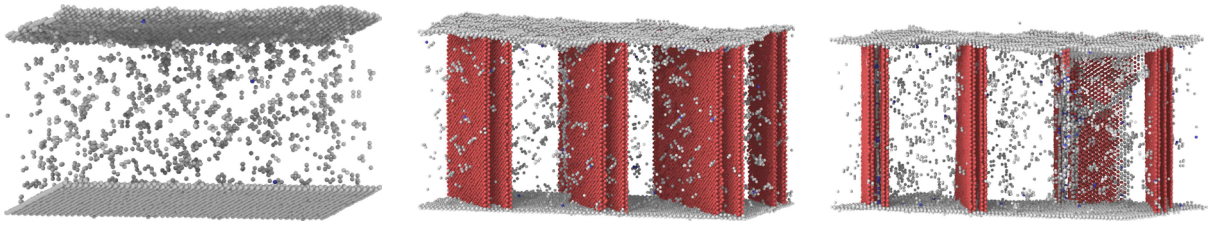

Figure 3: Structure of the crystallite after irradiation of the {110} surface. The value of the preliminary deformation is: a) 0%; b) 4%; c) 5%. Atoms with fcc symmetry of the nearest environment are not shown. Pink and gray spheres are atoms with a hcp and an uncertain symmetry of the nearest environment, respectively

Irradiation dose have a significant effect on the structural changes in a nanocrystalline sample. Small dose of irradiation (16-40 atoms with energy of 1.5 keV) do not change the sizes and positions of grains in the sample. At the irradiation of the nanocrystalline samples stacking faults are generated in grain boundary regions and begin to propagate into the grain interior. This is due to the fact that the incident atoms generate cascades of atomic displacements (Fig. 4a, c). This leads to high-rate local heating of the grains and the formation of shock waves [4,17]. As a result, the interaction of shock waves with grain boundaries causes a local increase in stresses and generation of stacking faults. At the same time, the density of stacking faults in grains increases with increasing number of incident atoms (Fig. 4). The stacking faults locating in parallel slip planes were formed only in few grains at irradiation by 16 atoms (Fig. 4b). When the irradiation dose was increased to 40 atoms with energy of 1.5 keV, the stacking faults are formed in all grains in a larger number. In this case, their slip planes have indices of different signs (Fig. 4d).

If the radiation dose is increased, the surface layer will melt. At the stage of relaxation, the crystallization front propagates from the boundary of the liquid and crystalline phases. As a result, the formed grain structure in the surface layer differs significantly from the structure before irradiation. Analysis of the calculation results shows that after crystallization, the number of grains in the simulated sample is changed (Fig. 5). This is clearly seen in the histogram, which shows the change in grain size distribution after irradiation of the sample with 80 atoms with energy of 1.5 keV. The grain sizes in the near-surface layer of the sample are increased. This is due to the fact that the atoms of the molten region were adjusted to the grain structure at the crystallization front and increased their size. Note that craters formed on the surface of the irradiated sample, which size increases with increasing radiation dose.

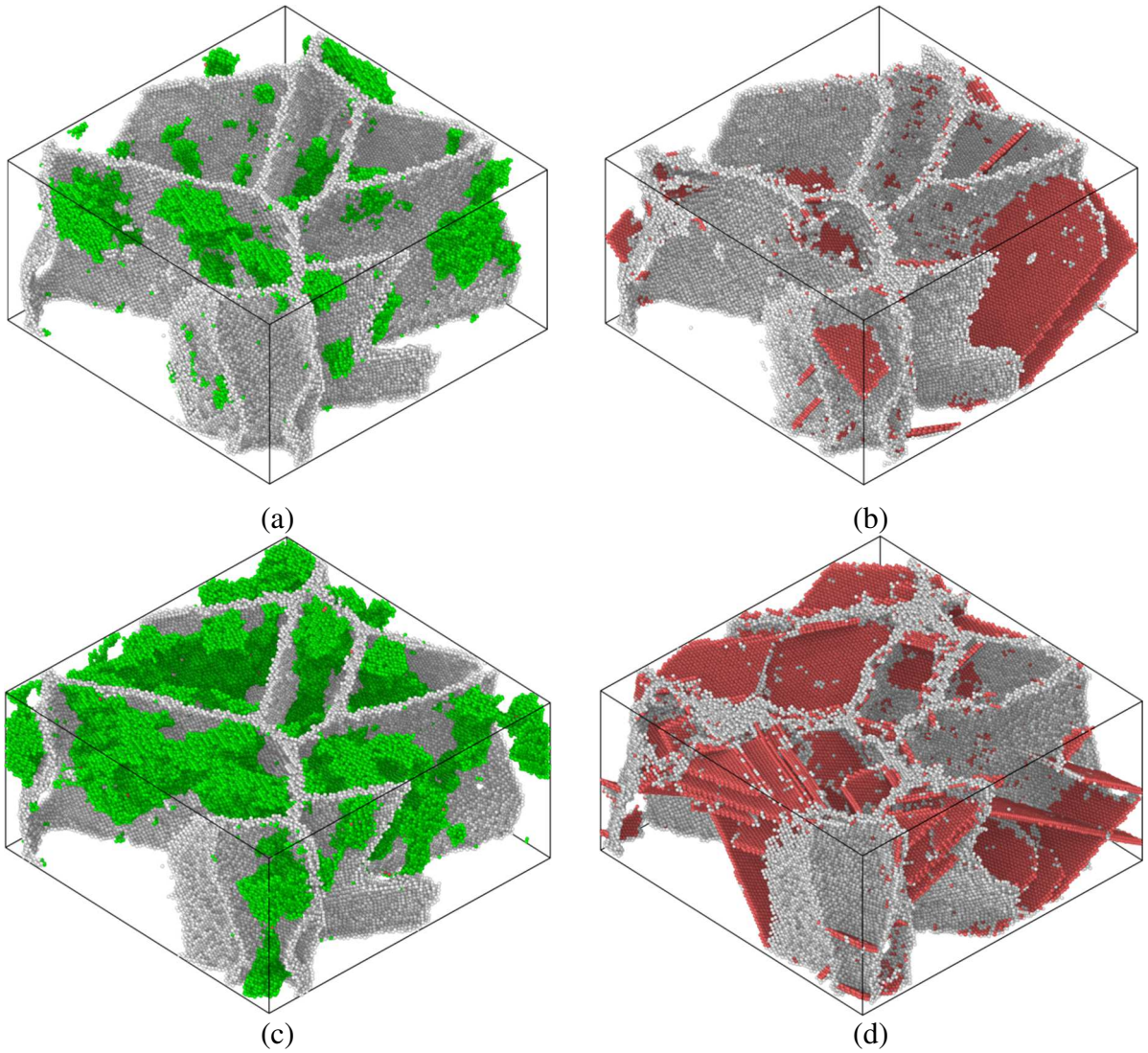

Figure 4: Structure of irradiated sample with 6 grains before (a and c) and after relaxation (b and d). The upper and lower rows of figures refer to the irradiation by 16 and 40 atoms, respectively. The grain boundaries, defects formed by cascades and stacking faults are shown in gray, green and pink, respectively. Atoms with fcc symmetry of the nearest environment are invisible

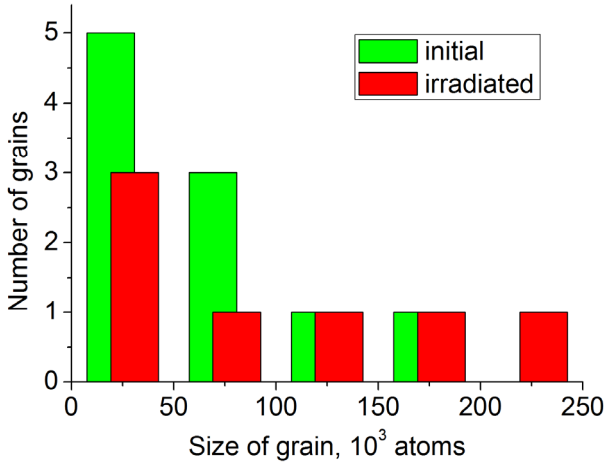

Figure 5: Distribution of grains in size before (green bars) and after irradiation (red bars) of the sample

4 SUMMARY

It is shown that the nature of structural changes in the surface layer of an aluminum single crystal upon irradiation is largely determined by the crystallographic orientation of the irradiated surface. The {100} surfaces undergo the smallest structural changes under irradiation. Irradiation of the {111} and {110} surfaces results in formation a large number of stacking faults in the surface layer. On the basis of this, it can be assumed that an increase in the irradiation dose can cause fragmentation of the surface layer of the crystallite. Irradiation of a nanocrystalline sample with small doses leads to the formation of stacking faults in grains. Their number increases with increasing radiation dose. At higher doses, the surface layer melts. Crystallization of the molten layer increases the grain size in the near-surface region. This is due to the fact that the atoms of the molten layer are adjusted to the crystal structure of grains at the boundary of the liquid and crystalline phases.

ACKNOWLEDGMENTS

The work is supported by the Programme of Presidium of Russian Academy of Sciences No 13 “Thermophysics of high energy densities”.

REFERENCES

[1] Meisner, S.N., Meisner, L.L., Lotkov, A.I. and Tverdokhlebova, A.V. Surface Modification of titanium nickelide after bombardment by silicon ions. *Steel Transl* (2015) **45**(4):258–261.
[2] Gleiter, H. Nanocrystalline materials. *Progr. Mater. Sci* (1969) **33**:223.
[3] Psakhie, S.G., Kryzhevich, D.S. and Zolnikov, K.P. Local structural transformations in copper crystallites under nanoindentation. *Tech. Phys. Lett* (2012) **38**:634–637.
[4] Korchuganov, A.V., Zolnikov, K.P., Kryzhevich, D.S., Chernov, V.M. and Psakhie, S.G.

Generation of shock waves in iron under irradiation. *Nucl. Instr. Meth. B* (2015) **352**:39–42.

[5] Korchuganov, A.V., Zolnikov, K.P., Kryzhevich, D.S., Chernov, V.M. and Psakhie, S.G., MD simulation of plastic deformation nucleation in stressed crystallites under irradiation. *Physics of Atomic Nuclei* (2016) **79**(7):1193-1198.

[6] Psakh'e, S.G. and Zol'nikov, K.P. Possibility of a vortex mechanism of displacement of the grain boundaries under high-rate shear loading. *Combust. Explos. Shock Waves* (1998) **34**(3):366–368.

[7] Psakhie, S.G., Zolnikov, K.P., Kryzhevich, D.S., Abdrashitov, A.V. and Lerner, M.I. Stage character of cluster formation in metal specimens in electrothermal pulse dispersion. *Phys. Mesomech* (2010) **13**(3-4):184–188.

[8] Psakhie, S.G., Korostelev, S.Y., Negreskul, S.I., Zolnikov, K.P., Wang, Z. and Li, S. Vortex mechanism of plastic-deformation of grain-boundaries - computer-simulation. *Physica Status Solidi B-Basic Research* (1993) **176**(2):K41-K44.

[9] Zolnikov, K.P., Psakhe, S.G. and Panin, V.E. Alloy phase diagrams using temperature, concentration and density as variables. *J. Phys. F: Met. Phys* (1986) **16**(8) 1145–1152.

[10] Psakhe, S.G., Zolnikov, K.P. and Korostelev, S.Y. Nonlinear response of materials under the high-speed deformation. Atomic level. *Pisma v Zhurnal Tekhnicheskoi Fiziki* (1995) **21**(13):1-5.

[11] Zolnikov, K.P., Psakhie, S.G., Negreskul, S.I. and Korostelev, S.Y. Computer simulation of plastic deformation in grain boundary region under high rate loading. Journal of *Materials Science & Technology* (1996) **12**(3):235-237.

[12] Plimpton, S. J. Fast Parallel Algorithms for Short-Range Molecular Dynamics. *Comp. Phys* (1995) **117**:1–19.

[13] Mendelev, M.I., Kramer, M.J., Becker, C.A. and Asta, M. Analysis of semi-empirical interatomic potentials appropriate for simulation of crystalline and liquid Al and Cu. *Philos. Mag* (2008) **88**(12):1723–1750.

[14] Honeycutt, J.D. and Andersen, H.C. Molecular dynamics study of melting and freezing of small Lennard-Jones clusters. *The Journal of Physical Chemistry* (1987) **91**:4950-4963.

[15] Stukowski, A. and Albe, K. Extracting dislocations and non-dislocation crystal defects from atomistic simulation data. *Modell. Simul. Mater. Sci. Eng* (2010) **18**:085001.

[16] Stukowski, A. Visualization and analysis of atomistic simulation data with OVITO – the Open Visualization Tool. *Modelling Simul. Mater. Sci. Eng* (2010) **18**:015012.

[17] Zol'nikov, K.P., Uvarov, T.Y., Lipnitskii, A.G., Saraev, D.Yu. and Psakh'e, S.G. Characteristics of cleavage fracture during interaction of nonlinear waves with the free surface of a copper single crystal. *Tech. Phys. Lett* (1999) **25**(12):936-937.

XIV International Conference on Computational Plasticity. Fundamentals and Applications
COMPLAS 2017
E. Oñate, D.R.J. Owen, D. Peric and M. Chiumenti (Eds)

ELASTIC PROPERTIES OF CARBON NANOTUBES AND THEIR HETEROJUNCTIONS

N.A. SAKHAROVA[*], J.M. ANTUNES[*†], A.F.G. PEREIRA[*], B.M. CHAPARRO[†] AND J.V. FERNANDES[*]

[*] CEMMPRE – Department of Mechanical Engineering, University of Coimbra,
Rua Luís Reis Santos, Pinhal de Marrocos
3030-788 Coimbra, Portugal
e-mail: {nataliya.sakharova, andre.pereira, valdemar.fernandes}@dem.uc.pt,
www.uc.pt/en/iii/research_centers/CEMUC

[†] Escola Superior de Tecnologia de Abrantes, Instituto Politécnico de Tomar
Rua 17 de Agosto de 1808-2200 Abrantes, Portugal
email: jorge.antunes@ipt.pt, bruno.chaparro@sapo.pt, http://www.esta.ipt.pt

Key words: Carbon Nanotubes, Carbon Nanotubes Heterojunctions, Elastic Properties, Numerical simulation.

Abstract. Comprehensive studies on the modelling and numerical simulation of the mechanical behaviour under tension, bending and torsion of single-walled carbon nanotubes and their heterojunctions are performed. It is proposed to deduce the mechanical properties of the carbon nanotubes heterojunctions from the knowledge of the mechanical properties of the single-walled carbon nanotubes, which are their constituent key units.

1 INTRODUCTION

Systematic research has been conducted for studying nano-materials such as carbon nanotubes (CNTs) that are efficient components for designing new materials with required electronic and mechanical properties [1] and building blocks for optical and electronic nanodevices [2]. The CNT heterojunctions (two connected CNTs) are necessary constituents for such nanodevices as circuits, amplifiers, switches and nanodiodes [3]. The understanding of the CNTs' mechanical properties is indispensable in order to design composites reinforced with CNTs and CNT-based devices, since their stability and efficiency are dependent on the mechanical properties of the constituents, i.e. CNTs and CNT heterojuctions.

The elastic properties of CNTs can be assessed using experimental techniques (atomic force microscopy (AFM) and transmission electron microscopy (TEM) [4]) and computational approach. There are three main groups of methodologies for the modelling of CNTs mechanical behaviour: the atomistic approach, the continuum mechanics approach and the nanoscale continuum mechanics approach. In case of the nanoscale continuum modelling approach (NCM) each carbon-carbon (C-C) bond is replaced by a solid element, e.g. a beam element, whose behaviour is described by elasticity theory (see, [5, 6]).

A considerable part of the theoretical investigations has been devoted to the predicting of

the Young's modulus of single-walled carbon nanotubes (SWCNTs) [5, 6]. Less attention has been paid to understanding the mechanical behaviour of nanotube heterojunctions.

The present work is focused on the characterisation of mechanical properties of SWCNTs in a wide range of chiral indices, diameters as well as SWCNT cone-heterojunctions by modelling their structure and mechanical behaviour, using nanoscale continuum approach [5].

2 ATOMIC STRUCTURE OF CNTS AND THEIR HETEROJUNCTIONS

An ideal single-walled nanotube can be seen as a rolled-up graphene sheet, whose surface is composed by the repeated periodically hexagonal [2]. The symmetry of the atomic structure of a nanotube is characterized by the chirality, which is defined by the chiral vector $\boldsymbol{C_h}$:

$$\boldsymbol{C_h} = n\boldsymbol{a_1} + m\boldsymbol{a_2} \tag{1}$$

where n and m are integers, and $\boldsymbol{a_1}$ and $\boldsymbol{a_2}$ are the unit vectors of the hexagonal lattice.

The length of the unit vectors is defined as $a = \sqrt{3}a_{C-C}$ with the equilibrium carbon-carbon (C-C) covalent bond length a_{C-C} usually taken to be 0.1421 nm [2]. The nanotube circumference, L_c, and diameter, D_n are:

$$L_c = |\boldsymbol{C_h}| = a\sqrt{n^2 + nm + m^2} \tag{2}$$

$$D_n = \frac{L_c}{\pi} \tag{3}$$

The chiral angle, θ, is defined by the angle between the chiral vector $\boldsymbol{C_h}$ and the direction (n, 0) [2] and it is given by:

$$\theta = \sin^{-1}\frac{\sqrt{3}m}{2\sqrt{n^2 + nm + m^2}} \tag{4}$$

Three major categories of carbon nanotubes can be defined based on the chiral angle θ: zigzag ($\theta = 0°$), armchair ($\theta = 30°$) and chiral ($0° < \theta < 30°$) SWCNTs. Three main symmetry groups can be also defined based on the chiral indices. In this case for armchair structure $n = m$, for zigzag structure $m = 0$, and for chiral structure $n \neq m$.

The CNT heterojunction can be represented as two CNTs that are connected by introducing an intermediate region with Stone–Wales defects [7]. Similarly to SWCNT structures, the geometrical parameters of heterojunctions (HJs) are the chirality, and diameter. There are two main heterojunction configurations [7]: (i) cone-heterojunctions (HJs of nanotubes with a given chiral angle but different radii) as armchair – armchair and zigzag – zigzag HJs, and (ii) radius-preserving heterojunctions (HJs preserving the radii, but with different chiral angles of the constituent nanotubes) as armchair – zigzag or chiral – armchair (or zigzag) HJs. According to the study of Yao *et al.* [8] most HJs (>95%) are cone-heterojunctions type.

The overall length of the heterojunction is defined as follows:

$$L_{HJ} = L_1 + L_2 + L_3 \tag{5}$$

where L_1, L_2 are the lengths of the narrower and wider SWCNTs regions, respectively, and L_3 is the length of the connecting region (see, Fig. 1).

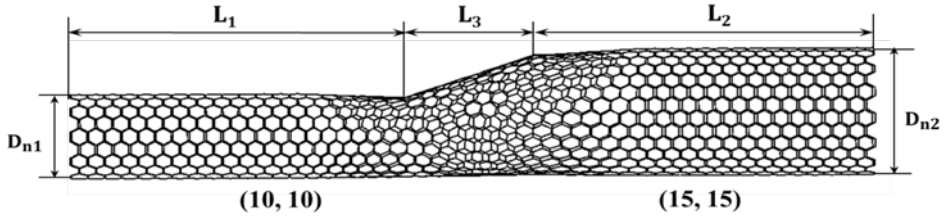

Figure 1: Geometry of cone armchair – armchair (10, 10) – (15, 15) HJ, obtained by using academic software CoNTub 1.0 © [7]

When the heterojunction consists of two SWCNTs with different diameters (i.e. cone-heterojunction), the diameter of HJ can be characterised by the average of the narrower and wider diameters (see for example: [7]):

$$\overline{D}_{HJ} = \frac{1}{2}(D_{n1} + D_{n2}) \tag{6}$$

And the aspect ratio of the cone-heterojunction is defined as [9]:

$$\eta = \frac{L_3}{\overline{D}_{HJ}} \tag{7}$$

The length of the connecting region, L_3, can be deduced basing on geometrical analysis [9]:

$$L_3 = \frac{\sqrt{3}}{2}\pi(D_{n2} - D_{n1}) = 2.7207(D_{n2} - D_{n1}) \tag{8}$$

where D_{n1} and D_{n2} are diameters of the narrow and wider nanotubes, respectively.

Other relationship for the connecting region, which follows a linear function with $(D_{n2} - D_{n1})$, for armchair – armchair and zigzag – zigzag cone-heterojunctions was previously proposed [10]:

$$L_3 = 2.9157(D_{n2} - D_{n1}) \tag{9}$$

3 NUMERICAL SIMULATION AND ANALYSIS

3.1 Finite element modelling of CNTs' structures

The NCM approach that replaces the carbon-carbon bonds of CNT by equivalent beam elements is used for modelling SWCNTs and SWCNT HJs. The finite element (FE) method uses the coordinates of the carbon atoms for generating the nodes and their suitable connection creates the beam elements. The relationships between the inter-atomic potential energies of the molecular CNT structure and strain energies of the equivalent continuum structure, consisting of beam elements undergoing axial, bending and torsional deformations, are the basis for the application of continuum mechanics to the analysis of the mechanical behaviour of SWCNTs and SWCNT HJs [5].

The meshes of the SWCNTs and SWCNT HJs structures to be used in the FE analyses, were built using the CoNTub 1.0 software [7]. This code generates ASCII files, describing atom positions and their connectivity that enter as input data in available commercial and in-

house FE codes. A previously developed in-house application, designated *InterfaceNanotubes* [6], was used to convert the ASCII files, acquired from the CoNTub 1.0 software, into the format compatible with the ABAQUS® commercial FE code. The geometrical characteristics of the SWCNTs used in the current FE analyses are summarized in Table 1. The nanotube length used in the numerical simulations was 30 times bigger than the outer diameter, so that the mechanical behaviour can be independent of the length [11].

Table 1: Geometrical characteristics of SWCNTs under study.

SWCNT type	(n,m)	D_n, nm	$\theta°$	SWCNT type	(n,m)	D_n, nm	$\theta°$
armchair	(5, 5)	0.678	30	zigzag	(14, 0)	1.096	0
	(10, 10)	1.356			(23,0)	1.802	
	(15, 15)	2.034			(32,0)	2.507	
	(20, 20)	2.713			(41,0)	3.212	
	(25, 25)	3.390			(50,0)	3.916	
	(30, 30)	4.068			(59,0)	4.618	
	(35, 35)	4.746			(77,0)	5.323	
	(40, 40)	5.424			(68,0)	6.027	
	(45, 45)	6.101			(86,0)	6.732	
	(50, 50)	6.780			(95,0)	7.436	
	(55, 55)	7.457					

The geometrical characteristics of SWCNT HJs used in the present FE analyses are summarized in Table 2. The HJs were constructed such that the lengths of the constituent nanotubes are almost equal to each other and their value is about two orders of magnitude of the length of the junction region.

Numerical simulations of conventional tensile, bending and torsion tests were carried out in order to study the mechanical properties of the SWCNTs and SWCNT HJ. In the latter case, two loading conditions, which consist of fixing the narrower and the wider side of the HJ structure, were considered.

3.2 Molecular interactions and equivalent properties of beam elements

The NCM approach uses the direct relationships between the structural mechanics parameters, i.e. tensile, E_bA_b, bending, E_bI_b, and G_bJ_b, torsional rigidities, and the bond force field constants, k_r, k_θ, and k_τ as follows [5]:

$$\frac{E_bA_b}{l} = k_r \tag{10}$$

$$\frac{E_bI_b}{l} = k_\theta \tag{11}$$

$$\frac{G_bJ_b}{l} = k_\tau \tag{12}$$

where l is the beam length equal to 0.1421 nm; E_b and G_b are the beam Young's and shear

moduli, respectively; A_b is the beam cross-sectional area; I_b and J_b are the beam moment of inertia and polar moment of inertia, respectively; and k_r, k_θ, and k_τ, are the bond stretching, bond bending and torsional resistance force constants, respectively.

Table 2: Geometrical characteristics of SWCNT HJs under study.

HJ	$(n_1, m_1) – (n_2, m_2)$	$\overline{D}_{HJ}$, nm	η	L_1, nm	L_2, nm	L_3, nm
armchair	(5, 5) – (10, 10)	1.018	1.940	100.01	99.95	1.97
	(10, 10) – (15, 15)	1.696	1.166	100.06	100.00	1.98
	(15, 15) – (20, 20)	2.375	0.833	100.00	100.01	1.98
zigzag	(5, 0) – (10, 0)	0.588	1.950	99.92	99.96	1.15
	(10, 0) – (15, 0)	0.979	1.177	100.14	100.12	1.15
	(15, 0) – (20, 0)	1.371	0.843	100.03	100.00	1.16

Equations 10 – 12 are the base for the application of continuum mechanics to the analysis of the mechanical behaviour of SWCNTs and SWCNT HJs. The input material and geometrical parameters of the beam element (see refs. [36, 37] from [12]) for the numerical simulations was previously summarised by the authors (see, for example [6, 10 – 12]).

4 ELASTIC PROPERTIES OF THE SINGLE-WALLED CARBON NANOTUBES

4.1 Rigidities of SWCNTs

The values of the tensile, EA, bending, EI, and torsional, GJ, rigidities were obtained from the respective numerical simulation tests results as described in the following. The tensile rigidity, EA, of SWCNT is determined as:

$$EA = \frac{F_x L}{u_x} \tag{13}$$

where F_x, is the tensile axial force applied at one nanotube end, leaving the other end fixed, L is the nanotube length and u_x is the axial displacement taken from the FE analysis.

Similarly, the bending rigidity of the nanotube, EI, is represented as:

$$EI = \frac{F_y L^3}{3u_y} \tag{14}$$

where F_y is the transverse force applied at one end of the nanotube, leaving the other fixed, u_y is the transverse displacement, taken from the FE analysis. Finally, the torsional rigidity of the nanotube, GJ, is determined as:

$$GJ = \frac{TL}{\varphi} \tag{15}$$

where T is torsional moment applied at one end of the nanotube, leaving the other fixed and φ is the twist angle, taken from the FE analysis. In case of torsion, the nodes under loading, at the end of the nanotube, are prevented from moving in the radial direction.

The evolutions of the tensile, EA, bending, EI, and torsional, GJ, rigidities with the nanotube diameter, D_n, were studied for the SWCNTs presented in Table 1. These evolutions are shown in Fig. 2. In previous studies [6, 12], the evolutions of the rigidities with nanotube diameter, D_n, were represented by a linear function for the case of the tensile rigidity, EA, and by a cubic power function for the cases of bending, EI, and torsional, GJ, rigidities, for armchair, zigzag and chiral SWCNTs, with diameters up to 2.713 nm. The fitting equations were expressed as follows, regardless of the nanotube chirality:

$$EA = \alpha(D_n - D_0) \tag{16}$$

$$EI = \beta(D_n - D_0)^3 \tag{17}$$

$$GJ = \gamma(D_n - D_0)^3 \tag{18}$$

The values of the fitting parameters [6, 12] were: $\alpha = 1131.66\ nN/nm$, $\beta = 143.48\ nN/nm$, $\gamma = 130.39\ nN/nm$ and $D_0 = 3.5 \cdot 10^{-3}\ nm$.

Figure 3 shows that the current results, up to nanotube diameters equal to 7.457 nm, also follows the trends described by Eqs. 16 – 18. The values of the fitting parameters calculated based on the results of the Fig. 3 are: $\alpha = 1121.20\ nN/nm$, $\beta = 140.25\ nN/nm$ and $\gamma = 130.39\ nN/nm$, which are close to those above mentioned. Given that the value of D_0 is negligible when compared with D_n, it was discarded in the fitting of the equations (i.e. D_0 was considered equal to zero).

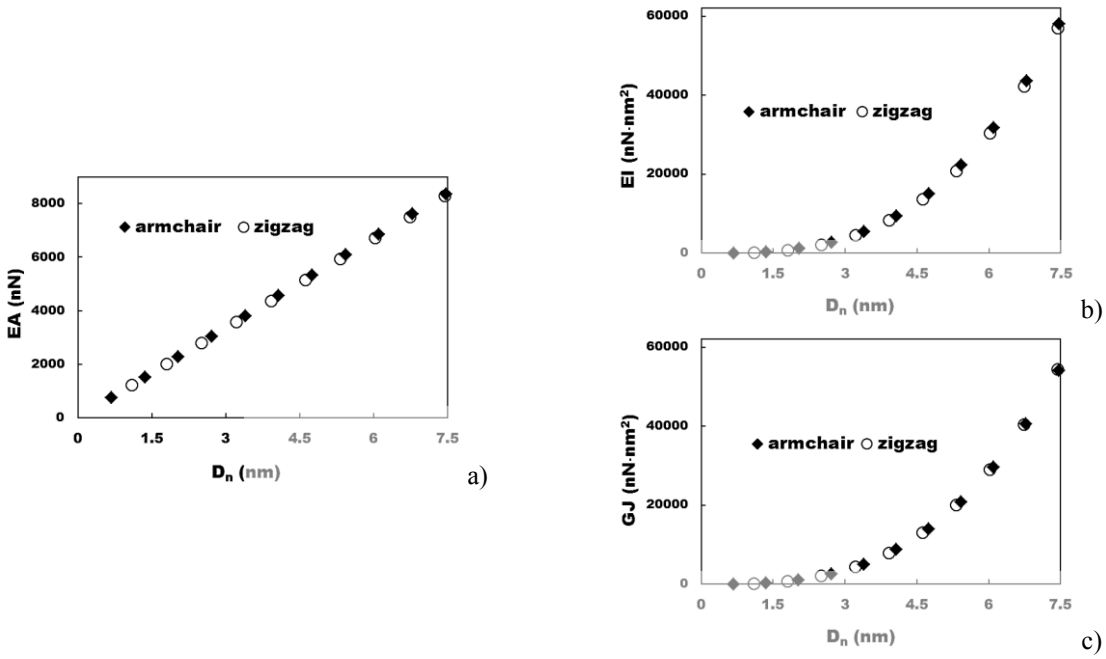

Figure 2: Evolution of: (a) the tensile, EA, (b) bending, EI, and (c) torsional, GJ, rigidities as a function of the nanotube diameter, D_n, for armchair and zigzag SWCNTs.

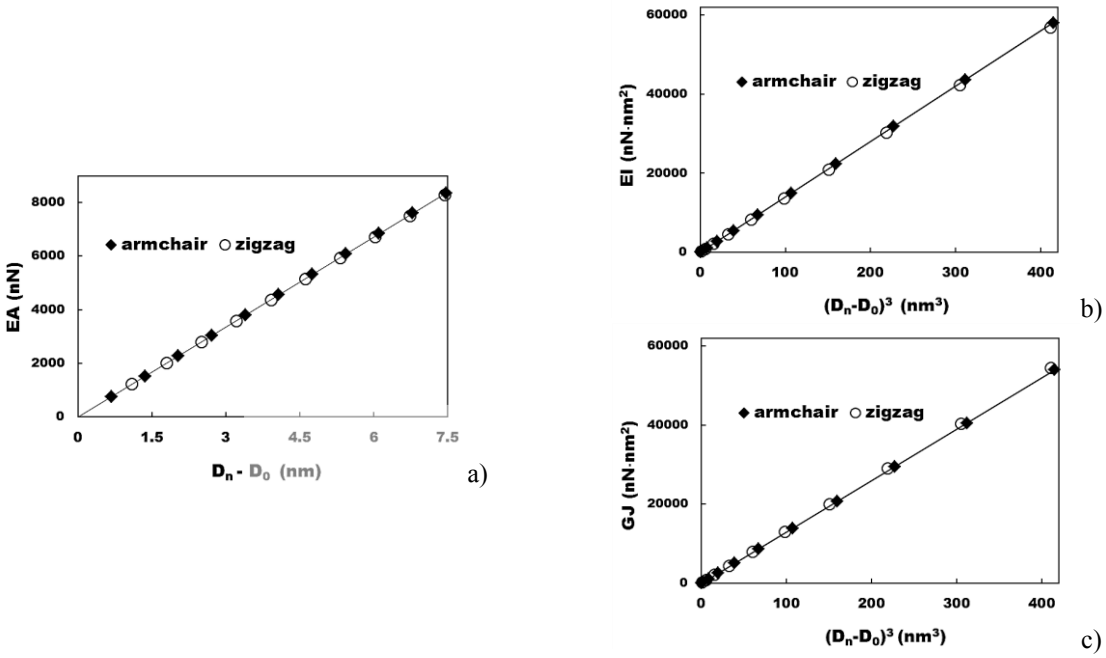

Figure 3: Evolution of: (a) the tensile, EA, rigidity as a function of $D_n - D_0$ and (b) bending, EI, and (c) torsional, GJ, rigidities, as a function of $(D_n - D_0)^3$ for armchair and zigzag SWCNTs.

The linear dependence of Eq. 16 can be understood on the base of the linear relationship between cross-sectional area and the nanotube diameter:

$$A = \frac{\pi}{4}[(D_n + t_n)^2 - (D_n - t_n)^2] = \pi D_n t_n \tag{19}$$

where t_n is the value wall thickness, which in the current study is $0.34\,nm$, equal to the interlayer spacing of graphite. In a similar way, the cubic dependences of Eqs. 17 – 18 can be understood based on the quasi-cubic relationships between the moment of inertia or the polar moment of inertia and the nanotube diameter (neglecting the value of $(t_n/D_n)^2$ in the following equations):

$$I = \frac{\pi}{64}[(D_n + t_n)^4 - (D_n - t_n)^4] = \frac{\pi D_n^3 t_n}{8}\left[1 + \left(\frac{t_n}{D_n}\right)^2\right] \tag{20}$$

$$J = \frac{\pi}{32}[(D_n + t_n)^4 - (D_n - t_n)^4] = \frac{\pi D_n^3 t_n}{4}\left[1 + \left(\frac{t_n}{D_n}\right)^2\right] \tag{21}$$

4.2 Young's and shear moduli of SWCNTs

The Young's modulus of the SWCNT is calculated, taking into account the tensile, EA, and bending, EI, rigidities, using the following expression [6]:

$$E = \frac{EA}{A} = \frac{EA}{\pi t_n \sqrt{8\left(\frac{EI}{EA}\right) - t_n^2}} \tag{22}$$

The shear modulus of the SWCNT is calculated, taking into account the tensile, EA, bending, EI, and torsional, GJ, rigidities by following equation [12]:

$$G = \frac{GJ}{J} = \frac{GJ}{2\pi t_n \left(\frac{EI}{EA}\right)\sqrt{8\left(\frac{EI}{EA}\right) - t_n^2}} \tag{23}$$

The relationships 16 – 18 and the knowledge of the values of the parameters α, β, γ allow the easy evaluation of the Young's and the shear moduli as a function of the nanotube diameter, without resorting to the numerical tests (D_0 was neglected in these equations):

$$E = \frac{\alpha D_n}{\pi t_n \sqrt{8\frac{\beta}{\alpha} D_n^2 - t_n^2}} \tag{24}$$

$$G = \frac{\gamma D_n}{2\pi t_n \left(\frac{\beta}{\alpha}\right)\sqrt{8\frac{\beta}{\alpha} D_n^2 - t_n^2}} \tag{25}$$

In the Fig. 4 (a, b) the values of the Young's modulus and shear modulus calculated by Eqs. 22 and 23, are plotted as a function of the nanotube diameter, D_n. The evolutions of the Young's modulus and shear modulus, obtained by Eqs. 24 and 25, are also shown in Fig. 4. The Young's modulus of SWCNTs decreases with increase of the nanotube diameter, and with further increase of the nanotube diameter, the Young's modulus tends to an approximately constant value as it is shown in the Fig. 4a. The same trend is observed for the evolution of the shear modulus with D_n (see, Fig. 4b). These trends in the evolution of the Young's and shear moduli with nanotube diameter extend up to diameters of about 7.5 nm, the trends already described for SWCNTs with diameters up to about 2.7 nm [6, 12]. Eqs. 24 and 25 allow obtaining acurate evolutions of the Young's and shear moduli, respectively, without resorting to the numerical simulation.

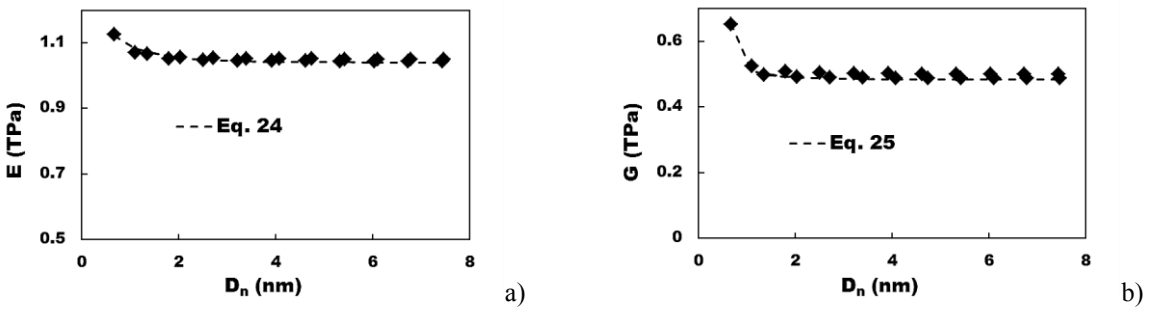

Figure 4: Evolution of: (a) Young's modulus, E, and (b) shear modulus, G, of SWCNTs as a function of the nanotube diameter, D_n.

5 ELASTIC PROPERTIES OF THE SINGLE-WALLED CARBON NANOTUBES HETEROJUNCTIONS

5.1 Rigidities of SWCNT HJs

The analysis of the mechanical behaviour of the armchair – armchair and zigzag – zigzag HJs, pointed out the occurrence of redundant bending deformation during the tensile test, making it difficult to analyse this test [10]. Therefore, we analyse the mechanical behaviour under bending and torsion.

The bending rigidity, $(EI)_{HJ}$, is obtained from the respective numerical simulation tests results as follows:

$$(EI)_{HJ} = \frac{F_y {L_{HJ}}^3}{3u_y} \tag{26}$$

where L_{HJ} is the heterojunction length, F_y is the transverse force applied at one end of the nanotube, leaving the other fixed, u_y is the transverse displacement, taken from the FE analysis. The torsional rigidity, $(GJ)_{HJ}$, is determined by:

$$(GJ)_{HJ} = \frac{TL_{HJ}}{\varphi} \tag{27}$$

where T is torsional moment applied at one end of the nanotube, leaving the other fixed and φ is the twist angle, taken from the FE analysis. The nodes under loading, at the end of the nanotube, are prevented from moving in the radial direction.

The $(EI)_{HJ}$ and $(GJ)_{HJ}$ rigidities for armchair-armchair and zigzag-zigzag HJs were plotted in Fig. 5 as a function of the heterojunction aspect ratio, $\eta = L_3/\bar{D}_{HJ}$ (see Fig. 1). Both rigidities, $(EI)_{HJ}$ and $(GJ)_{HJ}$ for armchair-armchair and zigzag-zigzag HJs increase with the increasing of the η. The bending and torsional rigidities for armchair-armchair HJs are higher than those for zigzag-zigzag HJs. The difference between the $(EI)_{HJ}$ values for armchair – armchair HJs and zigzag – zigzag HJs is more significant when the force is applied to the narrower nanotube. On the contrary, the evolution of the torsional rigidity with the aspect ratio, η is not sensitive to the loading condition: the $(GJ)_{HJ}$ values are at about the same whether the torsional moment is applied to the wider or narrower nanotube.

The bending, $(EI)_{HJ}$, and torsional, $(GJ)_{HJ}$, rigidities of the HJ structures can be calculated knowing the rigidities of the constituent SWCNTs. In fact, using Eq. 26 (or more suitably the equation of beam deflection) and Eq. 27, it is possible to obtain both rigidities for the HJs structures, considering that the respective transverse displacement (bending test) or the twist angle (torsion test) are equal to the sums of the corresponding transverse displacements or twist angles of each SWCNT constituent of the HJs:

$$(EI)_{HJ} = \frac{L_{HJ}^3}{\left(\frac{L_a^3}{(EI)_a} + \frac{3L_a^2 L_f + 3L_a L_f^2 + L_f^3}{(EI)_f}\right)} \tag{28}$$

$$(GJ)_{HJ} = \frac{L_{HJ}}{\left(\frac{L_a}{(GJ)_a} + \frac{L_f}{(GJ)_f}\right)} \tag{29}$$

where L_{HJ} is the overall length of HJ; $(EI)_a$ and $(EI)_f$ are the bending rigidities of the constituent SWCNTs and $(GJ)_a$ and $(GJ)_f$ are their torsional rigidities; L_a and L_f are the lengths of the constituent SWCNTs; the letters a and f refer to the nanotubes to which the force is applied and is fixed, respectively.

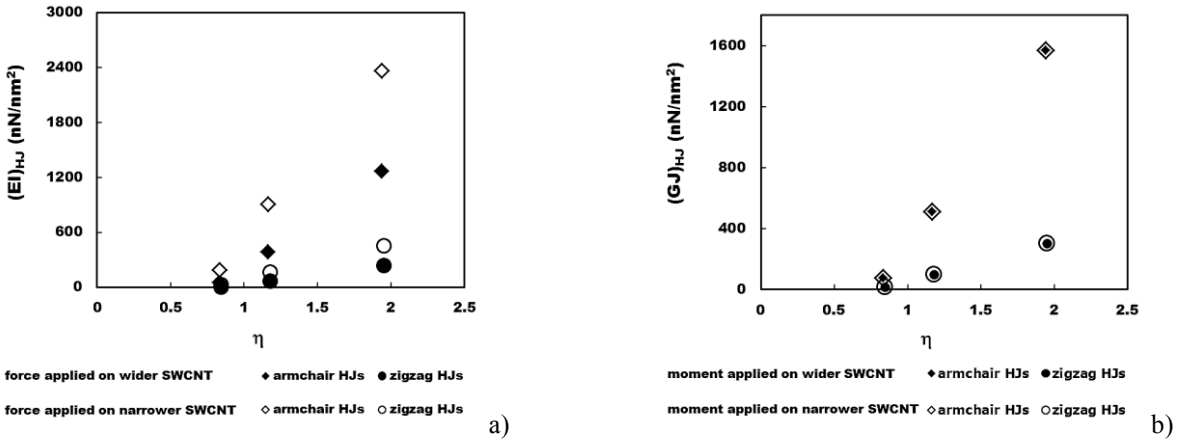

Figure 5: Evolution of: (a) $(EI)_{HJ}$ rigidity and (b) $(GJ)_{HJ}$ rigidity with the heterojunction aspect ratio, η, for armchair – armchair and zigzag – zigzag HJs.

Figure 6 compares the values of the rigidities ($(EI)_{HJ}$ – Fig. 6a; $(GJ)_{HJ}$ – Fig. 6b) obtained from FE analysis (Eqs. 26 and 27) and those calculated with help of Eqs. 28 and 29. The results of the Fig. 6 evidence the accuracy of the proposed analytical solutions for evaluation of the bending and torsional rigidities of armchair – armchair and zigzag – zigzag heterojunctions. The mean difference between the values of rigidities, evaluated by Eqs. 28 and 29 and those obtained from FE analysis, is 1.22% for the $(EI)_{HJ}$ rigidity and 1.74% for the $(GJ)_{HJ}$ rigidity.

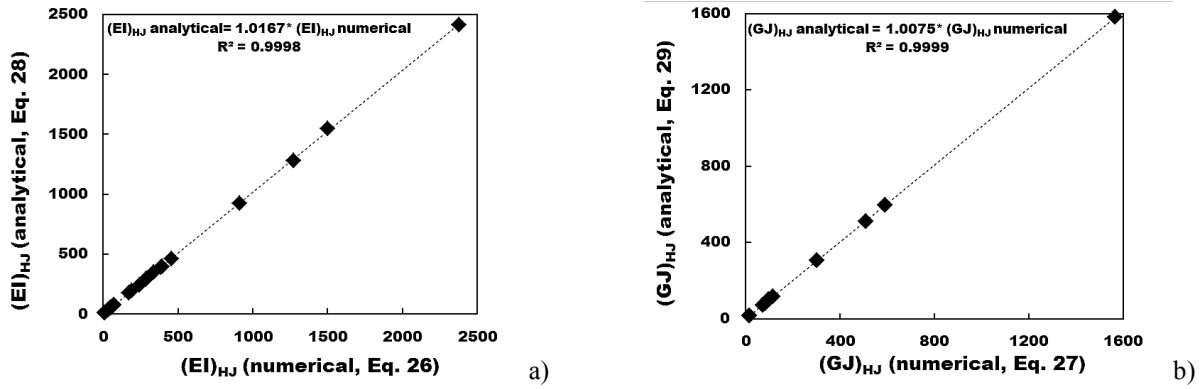

Figure 6: Comparison of: (a) bending, $(EI)_{HJ}$ and (b) torsional, $(GJ)_{HJ}$ rigidities obtained from FE analysis and evaluated by Eqs. 28 and 29, for armchair – armchair and zigzag – zigzag HJs.

5.2 Young's and shear moduli of SWCNT HJs

The bending and torsional rigidities obtained from FE analysis were used for the evaluation of the heterojunction Young's, E_{HJ}, and shear, G_{HJ}, moduli equivalent to a SWCNT with diameter given by $\bar{D}_{HJ} = \frac{1}{2}(D_{n1} + D_{n2})$, respectively:

$$E_{HJ} = \frac{(EI)_{HJ}}{I_{HJ}} = \frac{(EI)_{HJ}}{\frac{\pi}{64}\left[\left(\bar{D}_{HJ} + t_n\right)^4 - \left(\bar{D}_{HJ} - t_n\right)^4\right]} \tag{30}$$

$$G_{HJ} = \frac{(GJ)_{HJ}}{J_{HJ}} = \frac{(GJ)_{HJ}}{\frac{\pi}{32}\left[\left(\bar{D}_{HJ} + t_n\right)^4 - \left(\bar{D}_{HJ} - t_n\right)^4\right]} \tag{31}$$

where $t_n = 0.34\ nm$ is the value of the nanotube wall thickness.

The Young's modulus and shear modulus of armchair-armchair and zigzag-zigzag SWCNT HJs were plotted as a function of the heterojunction aspect ratio, η (Fig. 7). Both, Young's modulus and shear modulus decrease with increasing of the HJ aspect ratio. Also, the Young's modulus of HJs is sensitive to the loading condition: the value of E_{HJ} is higher when the force is applied on the narrower nanotube. The difference between the E_{HJ} values of armchair – armchair HJs and zigzag – zigzag HJs is less significant when the force is applied on the narrower nanotube. On the contrary, shear modulus of HJs is insensitive to the loading condition: the value of G_{HJ} does not change when the torsional moment is applied on the wider or narrower nanotube. The difference observed between shear modulus of armchair HJs and zigzag HJ is relatively small.

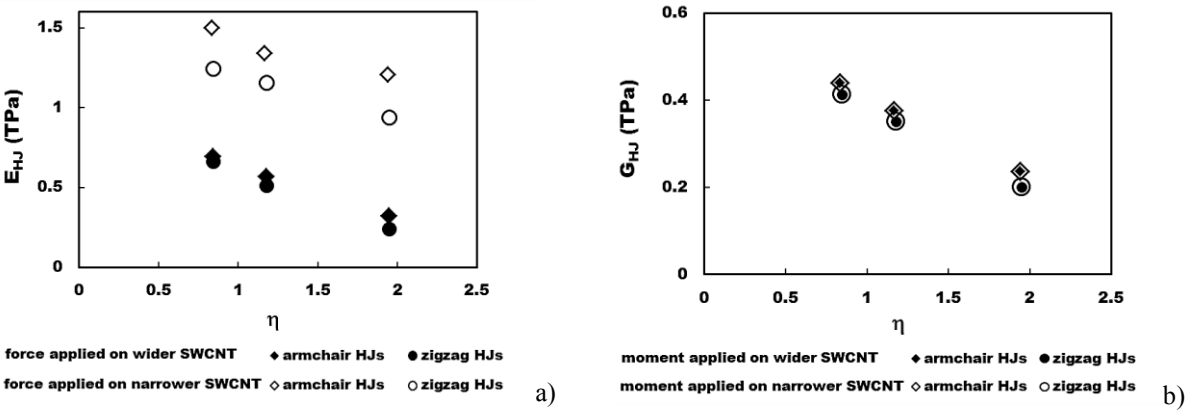

Figure 7: Evolution of the Young's modulus (a) and shear modulus (b) with the heterojunction aspect ratio for armchair – armchair and zigzag – zigzag HJs.

6 CONCLUSIONS

- Equations 16 – 18 establishing relationships between each of three rigidities and the nanotube diameter allowing the easy evaluation of the Young's modulus and shear modulus of SWCNTs by using Equations 24 and 25, without resorting to numerical simulation;
- Equations 28 and 29 allow the easy evaluation of the bending and torsion rigidities of

HJs structures, from the respective rigidities of the constituents SWCNT. These allows the accurate evaluation of the Young's and shear moduli of the SWCNTs, equivalent to the HJs structures.

ACKNOLEDGEMENTS

The authors gratefully acknowledge the financial support of the Portuguese Foundation for Science and Technology (FCT), Portugal, via Projects PTDC/EMS-TEC/0702/2014 (POCI-01-0145-FEDER-016779), PTDC/EMS-TEC/6400/ 2014 (POCI-01-0145-FEDER-016876), and UID/EMS/00285/ 2013, by UE/FEDER through Program COMPETE2020. N. A. Sakharova and A. F. G. Pereira were supported by a grant for scientific research from the Portuguese Foundation for Science and Technology (refs. SFRH/BPD/107888/ 2015, and SFRH/BD/102519/2014, resp.). All supports are gratefully acknowledged.

REFERENCES

[1] Robertson, J. Realistic applications of CNTs. *Mater Today* (2004) **7**: 46-52.
[2] Dresselhaus, M.S., Dresselhaus, G., Avouris, Ph. *Carbon Nanotubes: Synthesis, Structure, Properties, and Applications*, Springer Book Series: Topics in Applied Physics, Springer-Verlag Berlin Heidelberg, Germany, 80, (2001).
[3] Wei, D.C. and Liu, Y.Q. The intramolecular junctions of carbon nanotubes. *Adv Mater* (2008) **20**: 2815-2841.
[4] Wang, L., Zhang, Z., Han, X. In situ experimental mechanics of nanomaterials at the atomic scale. *NPG Asia Mater* (2013) **5**: e40-11.
[5] Li, C. and Chou, T.W. A structural mechanics approach for the analysis of carbon nanotubes. *Int J Solids Struct* (2003) **40**: 2487-2499.
[6] Sakharova, N.A., Pereira, A.F.G., Antunes, J.M., Brett, C.M.A., Fernandes, J.V. Mechanical characterization of single-walled carbon nanotubes: Numerical simulation study. *Compos Part B-Eng*. (2015) **75**: 73-85.
[7] Melchor, S. and Dobado, J.A. CoNTub: An algorithm for connecting two arbitrary carbon nanotubes. *J Chem Inf Comp Sci* (2004) **44**: 1639-1646.
[8] Yao, Y.G., Li, Q.W., Zhang, J., Liu, R., Jiao, L.Y., Zhu, Y.T., Liu, Z.F. Temperature-mediated growth of single-walled carbon-nanotube intramolecular junctions. *Nat Mater* (2007) **6**: 283-286.
[9] Qin, Z., Qin, Q.-H., Feng, X.-Q. Mechanical property of carbon nanotubes with intramolecular junctions: Molecular dynamics simulations. *Phys Lett A* (2008) **372**: 6661-6666.
[10] Sakharova, N.A., Pereira, A.F.G., Antunes, J.M., Fernandes, J.V. Numerical simulation of the mechanical behaviour of single-walled carbon nanotubes heterojunctions. *J Nano Res* (2016) **38**: 73- 87.
[11] Sakharova, N.A., Pereira, A.F.G., Antunes, J.M., Fernandes, J.V. Numerical simulation on the mechanical behaviour of the multi-walled carbon nanotubes. *J Nano Res* (2017) **47**: 106-119.
[12] Pereira, A.F.G., Antunes, J.M., Fernandes, J.V., Sakharova, N.A. Shear modulus and Poisson's ratio of single-walled carbon nanotubes: numerical evaluation. *Phys Status Solidi B* (2016) **253**: 366-376.

XIV International Conference on Computational Plasticity. Fundamentals and Applications
COMPLAS 2017
E. Oñate, D.R.J. Owen, D. Peric and M. Chiumenti (Eds)

FEATURES OF NUCLEATION AND EVOLUTION OF DEFECT STRUCTURE IN VANADIUM UNDER CONSTRAINED DEFORMATION

ALEKSANDR V. KORCHUGANOV, KONSTANTIN P. ZOLNIKOV AND DMITRIJ S. KRYZHEVICH

Institute of Strength Physics and Materials Science (ISPMS)
2/4 pr. Akademicheskii, 634055, Tomsk, Russia
e-mail: root@ispms.ru, www.ispms.ru/en/

Key words: Plastic Deformation, Twins, Structure Fragmentation, Molecular Dynamics.

Abstract. Atomic mechanisms of structural transformations leading to fragmentation in vanadium under deformation in constrained conditions without changing its volume are investigated on the basis of the molecular dynamics method. The process of formation of a fragmented structure in a deformed specimen can be divided into two stages. At the first stage, twins nucleate and grow in the crystallite. In the second stage, the orientation of lattice in twins may change due to the intersection of twins leading to their anisotropic deformation. In this case, the directions of stretching and compression of the crystal lattice in the deformed twin quite closely lie in the directions of stretching and compression of the whole crystallite.

1 INTRODUCTION

The mechanical load when large deformations are reached can lead to a fragmentation of the microstructure of the metallic materials. For this purpose, various methods of severe plastic deformation (SPD) are most frequently used, for example rolling, equal-channel angular pressing and torsion under high pressure [1,2]. It is believed that the main mechanism determining deformation-induced fragmentation of grains is dislocation activity such as multiplication and interaction of dislocations, as well as the formation of various configurations of dislocation boundaries. The formation of these dislocation boundaries is due to the fact that dislocation sliding is the prevailing deformation regime in majority of metals when loaded by SPD methods at room temperature with ordinary deformation rates ($<1\ s^{-1}$).

Deformation twinning also plays an important role in deformation of metals [3,4]. It becomes the main regime of plastic deformation at low temperatures and/or at high deformation rates [5,6]. It is due to the fact that the critical shear stress for twinning becomes lower than stress required for dislocation glide. In this case plastic deformation results in the generation of numerous deformation twins in the grains and the spacing between neigboring twin boundaries may reach an order of nanometers. Further deformation leads to the formation of equiaxed grains from twin lamellae. Thus, deformation twinning can be considered as a process preceding the nanoscale fragmentation of material.

The onset and evolution of plastic deformation on a microscopic level determines the deformation behavior of materials at higher scale levels. In view of the smallness of the spatial and temporal scales of the processes computer simulation is a powerful tool for

studying the dynamics of structural transformations at the micro level [7-9]. It should be noted that some of the grains in the bulk can be in the constrained conditions during the deformation of polycrystalline materials that affect their mechanical response under load. In this work, we study the atomic mechanisms of fragmentation of vanadium crystallite under deformation in constrained conditions.

2 SIMULATION DETAILS

The calculations were based on the molecular dynamics method [10,11]. The interatomic interaction in vanadium was described by the Finnis-Sinclair potential [12]. The initial crystallite had a parallelepiped shape and was heated to the room temperature. Periodic boundary conditions were applied in all directions. To simulate the constrained deformation the crystallite was uniformly stretched in one direction and compressed in other two directions without changing its volume. The crystallite was stretched along one of following crystallographic directions: X - $[11\bar{2}]$, Y - [111] and Z - $[1\bar{1}0]$. An analysis of the simulated crystallite structure of was carried out using Common Neighbor Analysis (CNA) [13] and the Dislocation Extraction Algorithm (DXA) [14]. Visualization of obtained structures was performed in the OVITO software [15].

3 RESULTS AND DISCUSSION

It is shown that structural defects begin to nucleate in the material when the threshold value of tensile strain is reached. This value depends on the crystallographic direction of loading. It is minimal when stretching the specimen along the Y direction and maximum for the Z direction. When the threshold value of tensile strain is reached, the potential energy of the simulated crystallite decreases abruptly (Fig. 1).

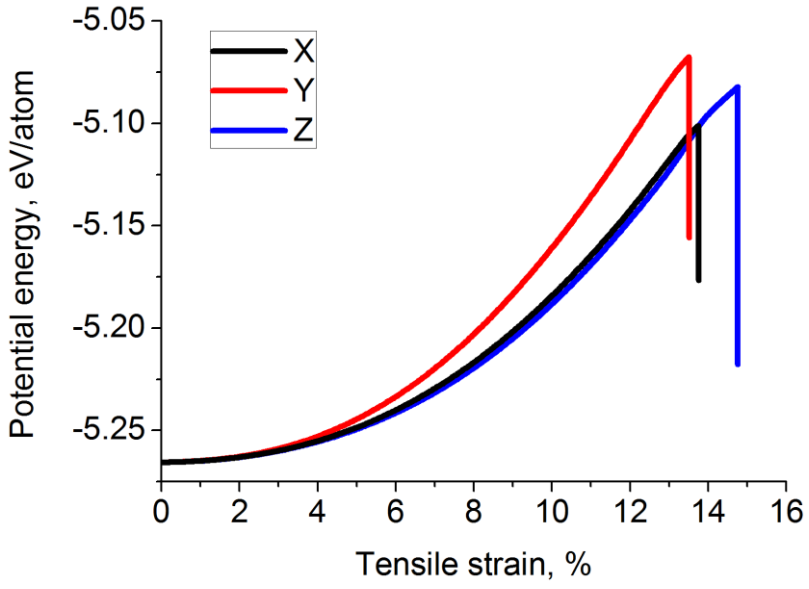

Figure 1: Dependence of the specimen potential energy per atom on the tensile strain along different crystallographic directions

The process of structural rearrangements in the deformed specimens can be divided into two stages. In the first stage, twins nucleate in the specimen, the growth of which is accompanied by the generation of the 1/2 <111> and <100> dislocations. The density of the 1/2<111> dislocations formed is much larger. Dislocations are nucleated at twin boundaries and propagate into the volume of matrix. The dislocation density inside the twins is much lower than in the surrounding volume. Formed twins grow until they intersect with other counterparts. In the second stage, a redistribution of the stresses occurs in the vicinity of intersected twins. This can lead to a reorientation of the crystal lattice in the region of twins and/or a decrease in their dimensions, until they disappear completely. The typical structure of the specimens stretched to a threshold value along different directions is shown in Fig. 2. It is seen in the figure that a large twin is formed when tension is applied along the X direction (Fig. 2a). Stretching along Y and Z directions leads to the formation of a large number of fragments. Moreover, when stretching along the Z direction, the largest number of fragments with the smallest average size is formed (Fig. 2c). The results of calculations showed that the total volume of fragments for specimens stretched along Y and Z directions is practically the same and they occupy approximately 4% of the simulated crystallite volume. The twin formed in the specimen stretched along the X direction occupies 10% of crystallite volume.

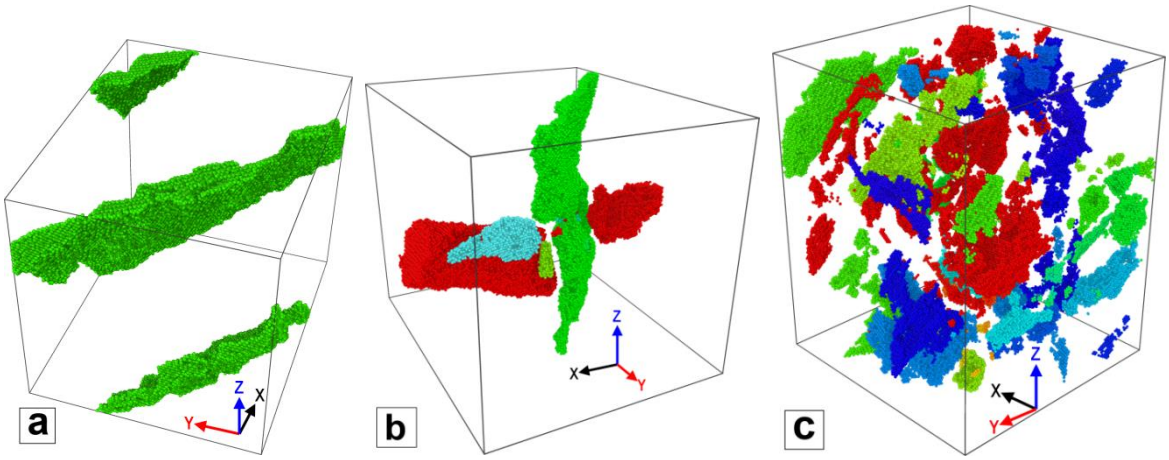

Figure 2: The defect structure of specimens stretched to a threshold value along the X $[11\bar{2}]$ (a), Y [111] (b) and Z $[1\bar{1}0]$ (c) directions. Specimen fragments reoriented relative to the initial lattice are shown. Each fragment has its own color

We have carried out a comparative analysis of the fragment size distribution in specimens stretched along different directions. For this purpose, 10 calculations for each direction were performed and the results were summed. On the basis of these data, two intervals can be distinguished in which the number of fragments differs significantly for various streching directions. Calculations showed that small fragments that contain less than 10 thousand atoms are formed in a larger amount in a specimen stretched along the Z direction than along the Y one. There are no small fragments in a specimen stretched along the X direction (Fig. 3a). For large fragments containing more than 10 thousand atoms, the size distribution is directly opposite: the largest fragments are typical for specimens stretched along the X direction. Their dimensions are 2-3 times larger than the size of fragments for specimens stretched along

X and Y directions (Fig. 3b). The number of such fragments is larger in specimens stretched along the Y direction.

The difference in the number and size of the fragments is related to the orientation of the preferred slip systems with respect to the direction of stretching. As a consequence, at the stage of plastic deformation nucleation a different number of twin nuclei is formed in the crystallite for different load directions. When stretching along the X direction, a twin is formed in one of the {112} planes, which subsequently crosses the entire specimen. When loaded along the Y direction, one nucleus is formed, consisting of two twins oriented at an angle to each other. These twins subsequently become the largest fragments, such as the red and green fragments in Fig. 2b. When stretching along the Z direction, a large number of twins with a thickness of several atomic layers are formed in one region. Their growth is accompanied by the generation of new twins at the periphery of the defective area. Moreover, the rate of increase in their longitudinal dimensions (area) is much higher than the rate of increase in their transverse dimensions (thickness). As a result, the intersection of these twins leads to the formation of a structure consisting of small size fragments (Fig. 2c).

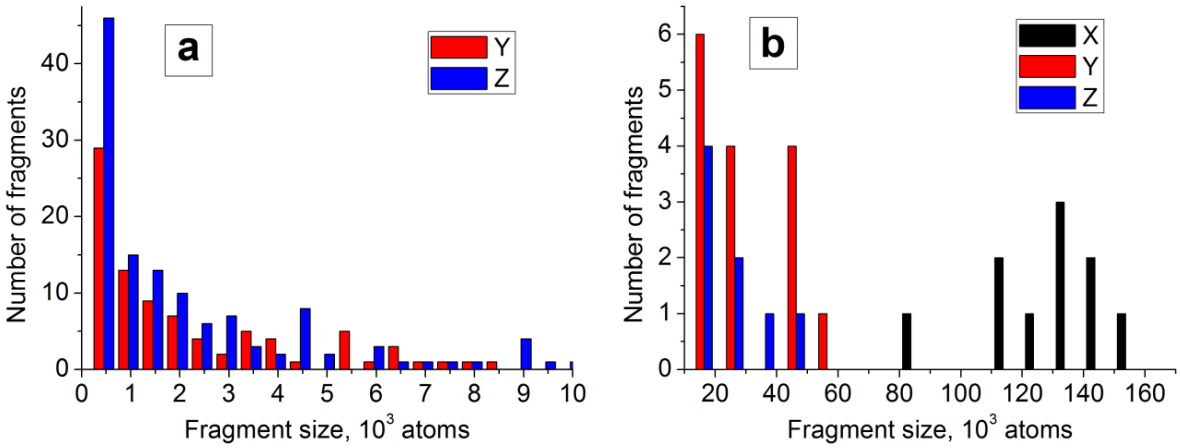

Figure 3: Distribution of fragments by their sizes (<10^4 atoms (a), >10^4 atoms (b)) in specimens for different directions of stretching

All reoriented fragments are formed due to the growth and interaction of twins. Some of them have orientations that differ from twinning ones. Fig. 4 shows such a fragment in a specimen stretched along the Z direction. Initially, when the specimen was loaded, a twin was formed (indicated by the arrow in Fig. 4a). As a result of the twin growth and its interaction with other defects, the orientation of the region in which the twin nucleated has changed. This region and its surroundings are highlighted with a red border in Fig. 4b and are shown in Fig. 4c. The orientation of this fragment does not correspond to the twin, which is clearly seen from comparing the structures in Fig. 4c and Fig. 4d. The latter shows a part of the twin considered, which retained its orientation. An analysis of the structure change in the central region in Fig. 4c showed that its crystal lattice is elastically deformed according to the scheme shown in the inset of Fig. 4a. In the insert, green and blue atoms from two {110} planes are shown, the lines indicate the cross section of the elementary bcc cell by the {110} plane. The arrows show that the lattice is compressed in the <110> direction and stretched in the <100>

direction. It should be noted that the directions of stretching and compression of the crystal lattice in the twin are sufficiently close to the directions of preliminary stretching and compression of the entire specimen. The resulting lattice structure in the reoriented fragment is shown in the inset of Fig. 4b, the cross section of the elementary bcc cell by the {100} plane is highlighted by lines. Thus, the reorientation of fragments of the specimen can occur due to deformation of the formed twins. This deformation is elastic and is realized by the compression and stretching in different directions by a different value. This leads to the formation of a new crystallographic orientation of the lattice without significant rotation of the fragment as a whole.

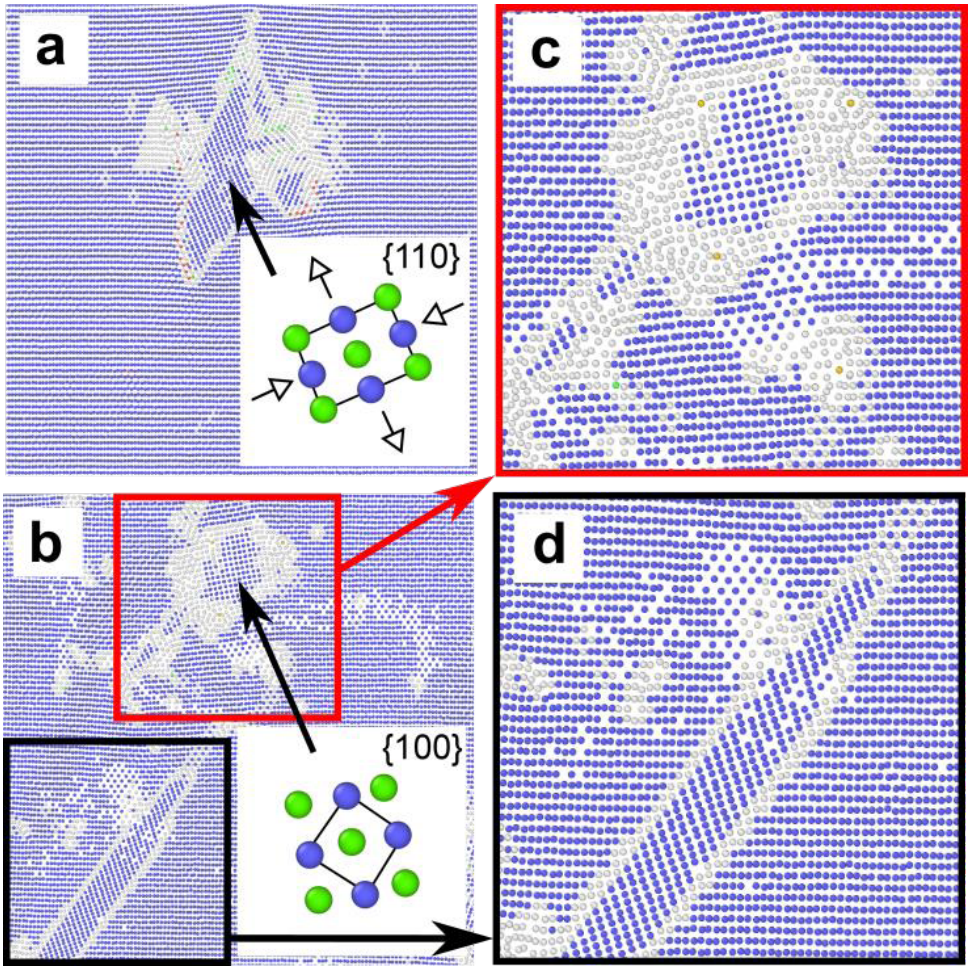

Figure 4: Structure of the two {110} atomic planes of the specimen, stretched along the Z [$1\,\bar{1}\,0$] direction by 14.75%, after stopping the loading in: a) 10 ps b) 70 ps. Figures c and d show enlarged areas in red and black frames in figure b, respectively

4 CONCLUSIONS

The vanadium crystallite behavior under constrained deformation without changing its volume was studied by means of molecular dynamics simulation. Loading of the crystallite leads to nucleation and growth of twins, which is accompanied by the generation of

dislocations. The formation and interaction of twins leads to the fragmentation of the crystallite.

The difference in the number and size of the fragments is related to the orientation of the preferred slip systems with respect to the direction of streching. The twin of maximum size is formed by stretching along the X direction. Stretching along Y and Z directions leads to the formation of a large number of fragments. The greatest number of fragments is formed in the specimen stretched along the Z direction. The volumes of fragmented parts of the specimens stretched along Y and Z directions are almost the same.

The process of fragmentation of the deformed specimens can be divided into two stages. In the first stage, twins nucleate in the specimen, the growth of which is accompanied by the generation of dislocations. Formed twins grow until they intersect with each other. In the second stage, a redistribution of the stresses occurs in the vicinity of intersected twins. This can lead to a reorientation of the crystal lattice in the region of twins and/or a decrease in their dimensions, until they disappear completely.

It is shown that the process of the lattice reorientation in fragments can be realized due to anisotropic deformation of the formed twins. The directions of stretching and compression of the crystal lattice in the deformed twin quite closely lie in the directions of stretching and compression of the whole crystallite.

ACKNOWLEDGEMENTS

The work has been done in the framework of the Programme of fundamental research of state academies of Sciences for 2013-2020.

REFERENCES

[1] Tyumentsev, A.N., Ditenberg, I.A., Korotaev, A.D. and Denisov, K.I. Lattice curvature evolution in metal materials on meso- and nanostructural scales of plastic deformation. *Phys. Mesomech* (2013) **16**(4):319-334.

[2] Litovchenko, I.Yu., Tyumentsev, A.N., Zahozheva, M.I. and Korznikov, A.V. Direct and reverse martensitic transformation and formation of nanostructured states during severe plastic deformation of metastable austenitic stainless steel. *Rev. Adv. Mater. Sci* (2012) **31**(1): 47-53.

[3] Tyumentsev, A.N., Litovchenko, I.Yu., Pinzhin, Yu.P., Korotaev, A.D., Girsova, S.L. and Nesterenkov, V.A. A new mechanism of localization of deformation in austenitic steels: II. Effect of twinning on the reorientation regularities of the crystal lattice in localized deformation bands. *Phys. Metals Metallogr* (2003) **95**(3): 291-299.

[4] Korchuganov, A.V., Zolnikov, K.P., Kryzhevich, D.S., Chernov, V.M. and Psakhie, S.G. MD simulation of plastic deformation nucleation in stressed crystallites under irradiation. *Phys. Atom. Nuclei* (2016) **79**(7):1193-1198.

[5] Beyerlein, I.J., Zhang, X. and Misra, A. Growth twins and deformation twins in metals. *Annu. Rev. Mater. Res* (2014) **44**:329-363.

[6] Gray III, G.T. High-strain-rate deformation: mechanical behavior and deformation substructures induced. *Annu. Rev. Mater. Res* (2012) **42**:285-303.

[7] Psakhe, S.G., Zolnikov, K.P. and Korostelev, S.Y. Nonlinear response of materials under the high-speed deformation. Atomic level. *Pisma v zhurnal tekhnicheskoi fiziki* (1995)

21(13):1-5.
[8] Psakhie, S.G., Kryzhevich, D.S and Zolnikov, K.P. Local structural transformations in copper crystallites under nanoindentation. *Tech. Phys. Lett* (2012) **38**(7):634-637.
[9] Psakhie, S.G., Korostelev, S.Yu., Negreskul, S.I., Zolnikov, K.P., Wang, Z. and Li, S. Vortex mechanism of plastic-deformation of grain-boundaries - computer-simulation. *Phys. Stat. Sol. (B)* (1993) **176**(2):K41-K44.
[10] Zolnikov, K.P., Psakhe, S.G. and Panin, V.E. Alloy phase-diagrams using temperature, concentration and density as variables. *J. Phys. F: Met. Phys* (1986) **16**(8):1145-1152.
[11] Psakhie, S.G., Zolnikov, K.P., Kryzhevich, D.S., Abdrashitov, A.V. and Lerner, M.I. Stage character of cluster formation in metal specimens in electrothermal pulse dispersion. *Phys. Mesomech* (2010) **13**(3-4):184-188.
[12] Sivak, A.B., Chernov, V.M. and Romanov V.A. Energetic, kinetic and crystallographic characteristics of self-point defects in vanadium and iron crystals *Joint International Topical Meeting on Mathematics & Computation and Supercomputing in Nuclear Applications (M&C + SNA 2007),* Monterey, California, April 15-19 (2007) on CD-ROM.
[13] Honeycutt, J.D. and Andersen, H.C. Molecular dynamics study of melting and freezing of small Lennard-Jones clusters. *J. Phys. Chem* (1987) **91**:4950-4963.
[14] Stukowski, A. and Albe, K. Extracting dislocations and non-dislocation crystal defects from atomistic simulation data. *Modelling Simul. Mater. Sci. Eng* (2010) **18**:085001.
[15] Stukowski, A. Visualization and analysis of atomistic simulation data with OVITO – the Open Visualization Tool. *Modelling Simul. Mater. Sci. Eng* (2010) **18**:015012.

XIV International Conference on Computational Plasticity. Fundamentals and Applications
COMPLAS 2017
E. Oñate, D.R.J. Owen, D. Peric and M. Chiumenti (Eds)

MOLECULAR DYNAMICS SIMULATION OF NUCLEATION AND GROWTH OF DEFECTS IN THE ALLOY FE-CR IN THE CONDITIONS OF HIGH-ENERGY LOADING

KONSTANTIN P. ZOLNIKOV, ALEKSANDR V. KORCHUGANOV AND DMITRIJ S. KRYZHEVICH

Institute of Strength Physics and Materials Science of Siberian Branch of Russian Academy of Sciences (ISPMS SB RAS)
Akadenicheskii 2/4, 634055 Tomsk, Russia
e-mail: root@ispms.tomsk.ru, web page: http://ispms.ru/en

Key words: Radiation Damage, Molecular Dynamics, Free Surface, Cascade of Atomic Displacements.

Abstract. Features of primary radiation damages in the near-surface layers of the Fe-Cr crystallite were investigated. The calculations were based on the molecular dynamics method. It was found that the number of surviving defects at the generation of atomic displacement cascades near the free surfaces is almost twice their number than in case of cascade generation far away from the various interfaces. Besides it the cascades can knock out some atoms from the free surfaces and form some specific structural defects: craters, adatom islands, dislocation loops of vacancy type. The crystallographic orientation of the irradiated surfaces has a significant influence on the features of the material damage. Craters are much more frequently formed at the irradiation of the (111) surface. There is a correlation between the size of the vacancy loops and the number of adatoms on the free surface. The size of the vacancy loops formed by the irradiation of the (111) surface is slightly larger than the number of adatoms. The inverse relationship was found at the irradiation of the (110) surface of Fe-Cr crystallite.

1 INTRODUCTION

The primary radiation damage of materials is determined by the evolution of cascades of atomic displacements, which are generated in collisions of the decay particles with lattice atoms. The internal structure of the material, as well as the chemical composition has a significant impact on the nature of radiation damage. So, the survived radiation defects near the free surfaces, interfacial and grain boundaries differ in the amount and type from radiation defects in the material with ideal structure [1-4]. Grain boundaries accumulate in their regions the greatest number of the generated radiation defects [5,6]. They formed the largest clusters of point defects. Features of the radiation damage evolution near the free surfaces associated with the formation of craters and adatom islands on the surface of the irradiated material, as well as the escape of the generated defects onto the surface. As a result of collision of the decay particles and atoms of the surface layer, usually a certain number of atoms is knocked out from a sample.

It is expected that the generation of atomic displacement cascades with energies less than 50 keV in the surface region most significantly affects the radiation damage of the material. This is due to the fact that the evolution of the cascade occurs in the vicinity of the surface. The aim of this work is investigation of peculiarities of the radiation defect evolution in the atomic displacement cascades in the Fe-10Cr crystallite near free surfaces with different crystallographic orientations.

2 FORMALISM

Primary radiation damage near free surfaces of the Fe-10Cr alloy was studied on the base of the molecular dynamics method [7-9]. Simulations were performed in the LAMMPS package [10]. The interaction between atoms was described by the many-body potential constructed according to the concentration-dependent embedded atom method [11]. The collision of decay particle with the crystallite was simulated by setting a momentum to the one of surface atoms – the primary knocked atom (PKA). Direction of PKA momentum was perpendicular to the free surface. Periodic boundary conditions were applied in other two directions. The PKA energy was equal to 20 keV. Simulated crystallites had the cubic shape with 20 nm edges. The irradiated free surface had the (110) or (111) indices. The temperature of the crystallite before irradiation was 300 K. Concentration of Cr was 10 at.% which is close to concentrations for majority of steels applied in nuclear power plants. About 40 calculations with different PKA positions for each irradiated surface were made. The occupancy of Wigner-Seitz cells was calculated to identify point defects in irradiated crystallites. Analysis of extended defects, such as craters and dislocation loops was based on the Common Neighbor Analysis [12] and the Dislocation Extraction Algorithm [13]. Visualization of investigated structures was performed in the OVITO software [14].

3 RESULTS AND DISCUSSION

The evolution of cascades of atomic displacements can be characterized by three stages. The ballistic stage lasts from the generation of cascade of atomic displacements until a number of defects in the cascade reaches its maximum size. At the recombination stage, the number of radiation defects decreases as a result of annihilation of the formed self-interstitial atoms (SIAs) and vacancies. It finishes when the number of radiation defects reaches saturation. At the steady stage, the number of radiation defects is subject to weak fluctuations, associated only with thermal and diffusion processes in the material.

Calculations showed that twice more radiation damage is formed at the steady stage of cascade with an energy of 20 keV near the free surface, than at the same energy cascade in the volume far from the interfaces. This is due to the knockout of atoms from the surface of the sample and the formation of a number of specific structural defects: craters, dislocation loops of a vacancy type, adatom islands. Approximately 250 point defects survive (this is without taking into account surface defects such as adatoms and craters) in the near-surface region of the material. In the case of cascade generation in the material bulk, approximately 110 point defects survive and some of which form small clusters.

The Table 1 presents the calculation results of the number of survived radiation defects at the generation of cascades of atomic displacements in the volume of the material and in the regions of the (111) and (110) free surfaces. The number of vacancies, without taking into

account vacancy loops, is approximately the same for cascades near irradiated surfaces, and for cascades in the bulk of the material. The number of SIAs survived in the free surface regions is approximately half that in the volume of the material. This is explained by the SIAs escape onto the free surfaces and by the knocking out of atoms from the irradiated surface at the ballistic stage of the cascade. It can be seen from the table that the number of adatoms on the (110) surface is somewhat higher than on the (111) surface.

Table 1: The number of radiation defects in the steady stage formed by cascades of atomic displacements with energy of 20 keV in different regions of Fe-Cr crystallite

Cascade type	Number			Average size, vacancies		
	Vacancies	SIAs	Adatoms	Crater	½<111> loop	<100> loop
Bulk cascade	54±3	54±3	-	-	-	-
(110) surface cascade	46±3	26±2	176±26	-	63±8	101±12
(111) surface cascade	53±3	28±2	127±18	105±16	113±18	75±9

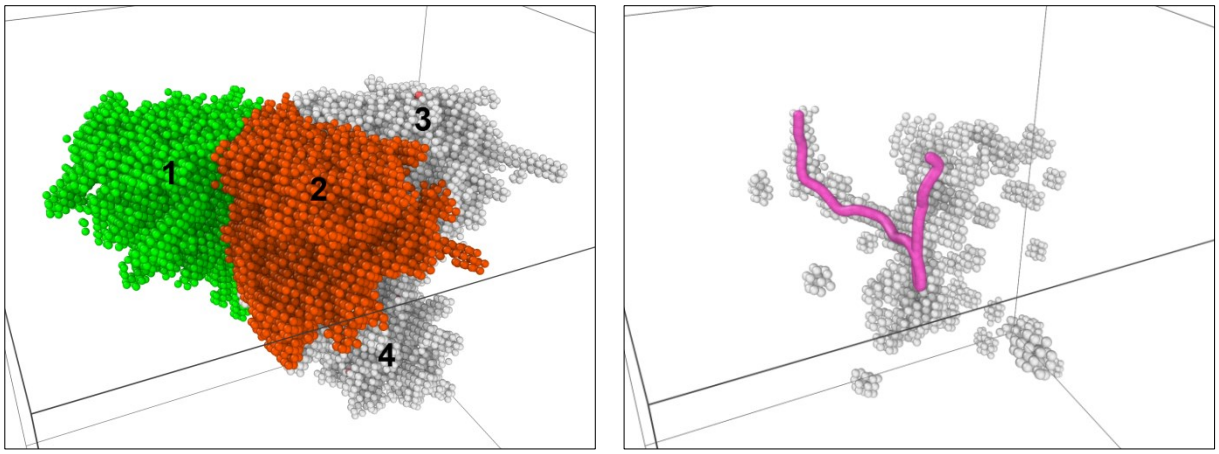

a) b)

Figure 1: The defect structure of the crystallite with the irradiated (110) surface at different stages of cascade evolution: a) the end of the ballistic stage, b) the steady state. Only atoms which symmetry of the nearest environment is different from the bcc lattice are shown. Subcascades are numbered by digits. The pink line shows the <100> dislocation

The simulation results showed that near-surface cascades lead to the formation of sufficiently large vacancy loops with the 1/2 <111> and <100> Burgers vectors. When the (110) surface is irradiated, the <100> vacancy loops are mainly formed in the material. In the case of the (111) surface, the 1/2 <111> vacancy loops are formed. The loop size was determined by the number of vacancies from which they are consisted. The average size of vacancy loops depends on the orientation of the irradiated surface. It should be noted that the cascades of atomic displacements generated in the bulk of the material do not lead to the formation of vacancy loops (Table). Calculations showed that craters, as a rule, are formed

during the generation of cascades of atomic displacements on the (111) surface. The formation of craters on the (110) surface is much less frequent. The results of the simulation are in good agreement with experimental [15,16] and theoretical data [1,2].

A cascade of atomic displacements near the (110) free surface at different stages of evolution is shown in Fig. 1. At the ballistic stage, the cascade consists of four subcascades (Fig. 1a). The displaced atoms in the region of the main subcascades, whose energy exceeds 50% of the kinetic energy of the whole cascade, are colored green and orange. At the end of the recombination stage, the largest vacancy loop is formed in this region (Fig. 1b).

The character of the radiation damage of the crystallite structure after the cascade generation on the (110) and (111) free surfaces is shown in Fig. 2. It is clearly seen that the crater is formed on the (111) surface and the vacancy loops arise in the near-surface regions.

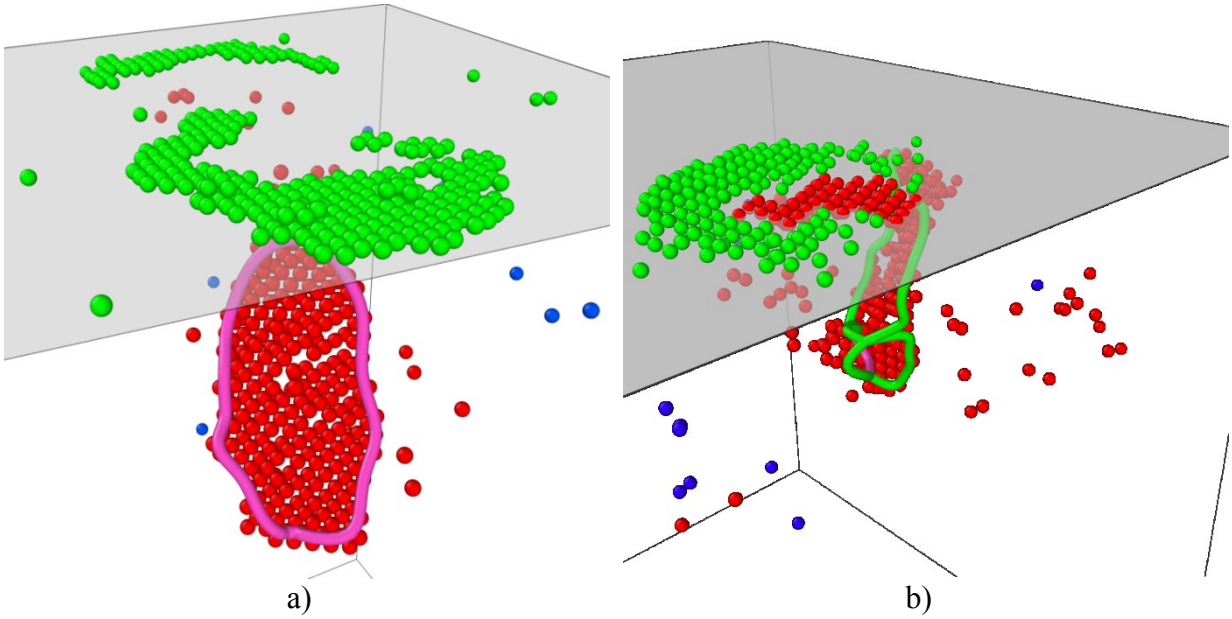

Figure 2: Radiation damage in the crystallite on the (110) (a) and (111) (b) surfaces. Adatoms are shown in green, vacancies in red, and SIAs in blue. The pink and green lines show the <100> and 1/2 <111> dislocations, correspondingly. The free surface is colored by grey

Analysis of the results of calculations shows that there is a correlation between the size of the vacancy loops and the number of adatoms. Thus, the number of adatoms on the free surface is approximately equal to the size of the vacancy loop (Fig. 3). Deviations from this ratio are associated with a small number of surviving point defects and clusters formed from them in the crystallite bulk. It is found that the number of adatoms on the (110) surface is slightly larger than the number of vacancies that make up the loop. The number of adatoms on the (111) surface is, as a rule, smaller than the size of the loop. A sufficiently large number of loops left the (111) free surface in the process of crystallite relaxation.

It follows from the calculations that there is a correlation between the sizes of the surviving vacancy loop and the crater on the free surface. So, the smaller the size of the surviving vacancy loop, the larger the crater size on the free surface. It was found that the higher the kinetic energy of the main subcascade of atomic displacements, the larger the size of the

vacancy loop.

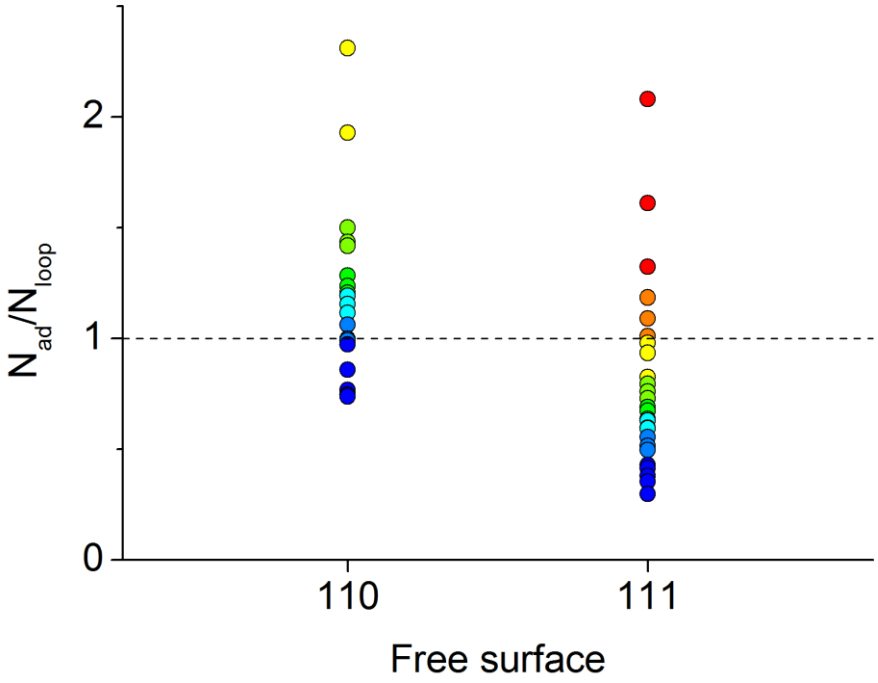

Figure 3: The ratio between the number of adatoms and the size of dislocation loops at the steady stage of cascade development near the (110) and (111) surfaces. Colors mean different calculations

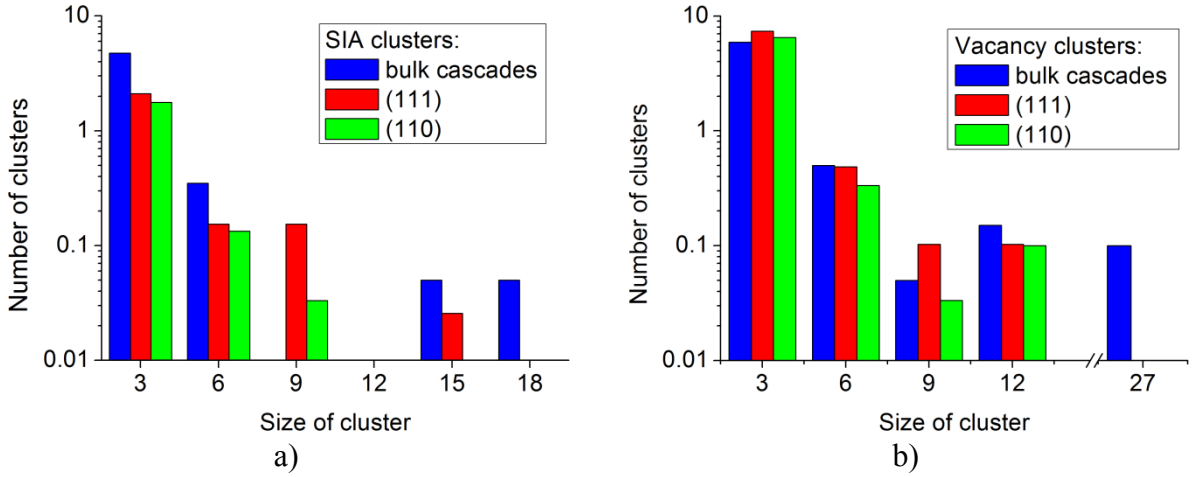

Figure 4: Distribution of survived SIA (a) and vacancy (b) clusters by their size for cascades generated near the (111) и (110) free surfaces and in the bulk

Since free surfaces are a region of a point defect sink, the number of survived clusters consisting of SIAs at irradiation of free surfaces is less than when cascades of atomic displacements develop in the bulk of the material (Fig. 4a). Note that the largest clusters are

formed by cascades of atomic displacements which are far from free surfaces. In this case clusters with size up to 18 SIAs can survive in the bulk of the material. This is almost twice the size of clusters in the near-surface regions. The number of clusters of SIAs larger than 6 is always less for the (110) surface than for the (111) one. The number of single dumbbells is the same for both surfaces. The number of survived vacancies and vacancy clusters with size of ≤12 is approximately the same for the generation of cascades in the near-surface region and in the bulk. This is due to their low mobility. Figure 4b shows that the largest vacancy clusters (except dislocation loops) are formed in the bulk of the material. It should be noted that an increase of the atomic volume at constant temperature and pressure can lead to a change in the phase composition of the region [17].

4 CONCLUSION

The cascades of atomic displacements near the free surface generate twice as many radiation defects as cascades developing in the bulk far from different interfaces. This is due to the fact that the generation of cascades of atomic displacements in the near-surface region leads to knockout of atoms from the free surface, as well as the formation of craters, adatom islands and dislocation loops of the vacancy type. The nature of the radiation damage of the near-surface region depends on the crystallographic orientation of the irradiated surfaces. In the samples with the (111) irradiated surface, as a rule, craters are formed. In the (111) near-surface region, the 1/2 <111> dislocations are mainly formed, and <100> dislocations arise in regions with the (110) orientation. There is a correlation between the number of adatoms on the free surface and the size of the vacancy loops. When the (111) surface is irradiated, the size of the vacancy loop is somewhat larger than the number of adatoms, while for the (110) surface the inverse ratio is observed. A greater number of vacancy loops from the radiation-damaged region escape on the (111) free surface than on the (110) surface.

ACKNOWLEDGMENTS

The work was carried out with the financial support of RFBR grant No. 16-08-00120.

REFERENCES

[1] Aliaga, M.J., Schäublin, R., Löffler, J.F. and Caturla, M.J. Surface-induced vacancy loops and damage dispersion in irradiated Fe thin films. *Acta Mater* (2015) **101**:22-30.

[2] Osetsky, Y.N., Calder, A.F. and Stoller, R.E. How do energetic ions damage metallic surfaces? *Curr. Opin. Solid State Mater. Sci* (2015) **19**(5):277-286.

[3] Psakhe, S.G., Zolnikov, K.P. and Korostelev, S.Y. Nonlinear response of materials under the high-speed deformation. Atomic level. *Pisma v zhurnal tekhnicheskoi fiziki* (1995) **21**(13):1-5.

[4] Zolnikov, K.P., Korchuganov, A.V, Kryzhevich, D.S., Chernov, V.M. and Psakhie, S.G. Structural changes in elastically stressed crystallites under irradiation. *Nucl. Instr. Meth B* (2015) **352**:43-46.

[5] Korchuganov, A.V., Zolnikov, K.P., Kryzhevich, D.S., Chernov, V.M. and Psakhie, S.G., MD simulation of plastic deformation nucleation in stressed crystallites under irradiation. *Physics of Atomic Nuclei* (2016) **79**(7):1193-1198.

[6] Psakhie, S.G., Zolnikov, K.P., Kryzhevich, D.S., Zheleznyakov, A.V. and Chernov, V.M. Evolution of atomic collision cascades in vanadium crystal with internal structure. *Crystallogr. Rep* (2009) **54**:1002–10.
[7] Psakhie, S.G., Kryzhevich, D.S and Zolnikov, K.P. Local structural transformations in copper crystallites under nanoindentation. *Tech. Phys. Lett* (2012) **38**(7):634-637.
[8] Psakhie, S.G., Korostelev, S.Yu., Negreskul, S.I., Zolnikov, K.P., Wang, Z. and Li, S. Vortex mechanism of plastic-deformation of grain-boundaries - computer-simulation. *Physica Status Solidi B-Basic Research* (1993) **176**(2):K41-K44.
[9] Psakhie, S.G., Zolnikov, K.P., Kryzhevich, D.S., Abdrashitov, A.V. and Lerner, M.I. Stage character of cluster formation in metal specimens in electrothermal pulse dispersion. *Phys. Mesomech* (2010) **13**(3-4):184-188.
[10] Plimpton, S. Fast Parallel Algorithms for Short-Range Molecular Dynamics. *J. Comput. Phys* (1995) **117**:1-19.
[11] Stukowski, A., Sadigh, B., Erhart, P. and Caro, A. Efficient implementation of the concentration-dependent embedded atom method for molecular-dynamics and Monte-Carlo simulations. *Modelling Simul. Mater. Sci. Eng* (2009) **17**:075005.
[12] Honeycutt, J.D. and Andersen, H.C. Molecular dynamics study of melting and freezing of small Lennard-Jones clusters. *The Journal of Physical Chemistry* (1987) **91**:4950-4963.
[13] Stukowski, A. and Albe, K. Extracting dislocations and non-dislocation crystal defects from atomistic simulation data. *Modell. Simul. Mater. Sci. Eng* (2010) **18**:085001.
[14] Stukowski, A. Visualization and analysis of atomistic simulation data with OVITO – the Open Visualization Tool. *Modell. Simul. Mater. Sci. Eng* (2010) **18**:015012.
[15] Prokhodtseva, A., Décamps, B. and Schäublin, R. Comparison between bulk and thin foil ion irradiation of ultra high purity Fe. *J. Nucl. Mater* (2013) **442**:S786– S789.
[16] English, C.A. and Jenkins, M.L. Molecular ion irradiations of molybdenum. *Philos. Mag* (2010) **90**:821–43.
[17] Zolnikov, K.P., Psakhe, S.G. and Panin, V.E. Alloy phase-diagrams using temperature, concentration and density as variables. *Journal of physics F – Metal physics* (1986) **16**(8):1145-1152.

XIV International Conference on Computational Plasticity. Fundamentals and Applications
COMPLAS XIV
E. Oñate, D.R.J. Owen, D. Peric & M. Chiumenti (Eds)

MATLAB PARALLEL CODES FOR 3D SLOPE STABILITY BENCHMARKS

MARTIN CERMAK* AND VACLAV HAPLA* AND DAVID HORAK*†

* VSB-TU Ostrava
IT4Innovations National Supercomputing Center (IT4I)
Studentska 6231/1b, 708 00 Ostrava, Czech Republic
email: martin.cermak@vsb.cz - web page: http://www.it4i.cz

† VSB-TU Ostrava
Department of Applied Mathematics
17. listopadu 15/2172, 708 00 Ostrava, Czech Republic

Key words: Computational Plasticity, TFETI, MATLAB, Parallel implementation, Mohr-Coulomb

Abstract. This contribution is focused on a description of implementation details for solver related to the slope stability benchmarks in 3D. Such problems are formulated by the standard elastoplastic models containing the Mohr-Coulomb yield criterion and by the limit analysis of collapse states. The implicit Euler method and higher order finite elements are used for discretization. The discretized problem is solved by non-smooth Newton-like methods in combination with incremental methods of limit load analysis.

In this standard approach, we propose several innovative techniques. Firstly, we use recently developed sub-differential based constitutive solution schemes. Such an approach is suitable for non-smooth yield criteria, and leads better return-mapping algorithms. For example, a priori decision criteria for each return-type or simplified construction of consistent tangent operators are applied.

The parallel codes are developed in MATLAB using Parallel Computing Toolbox. For parallel implementation of linear systems, we use the TFETI domain decomposition method. It is a non-overlapping method where the Lagrange multipliers are used to enforce continuity on the subdomain interfaces and satisfaction of the Dirichlet boundary conditions.

1 INTRODUCTION

In our paper, we focus on parallel implementation of the new approach introduced in [12], which is based on MATLAB codes. The parallelization is based on the TFETI domain decomposition method [5], which is a modification of the original FETI method proposed by Farhat and Roux [7].

We investigated the parallel implementation of a solver for small-strain, quasi-static elastoplastic problem that contains the Mohr-Coulomb yield criterion, associative flow rule, and perfect plasticity. The incremental constitutive problem is usually solved by the elastic predictor/plastic corrector method. The plastic correction is also called (implicit) return-mapping scheme. The improved scheme in [12] is based on the sub-differential formulation of the plastic flow rule. It leads to a priori information whether the unknown stress tensor lies on the smooth portion, on the "left" edge, on the "right" edge, or at the apex of the pyramidal yield surface, even if the nonlinear isotropic hardening is considered within the model.

The procedure of solving the problem in parallel is very similar to the classical solution. The main differences are: a) the original mesh is partitioned by METIS [10] into subdomains, and it is necessary to assemble the TFETI objects for each subdomain such as the equality constraint matrix and the kernel matrix, and these matrices do not change during the computation process [13]; b) the stiffness matrix, right hand side and other objects are assembled for each subdomain in each Newton step; c) in each Newton step, the dual formulation in the Lagrange multipliers is solved instead of the primal formulation in displacement; d) in contrast to the approach introduced in [12] where two loops (loading step, Newton step) are considered, we add another loop for the iterative solver (conjugate gradient) which solved the linearized problem in each Newton iteration.

In the text, we assume a deformable body from an elastoplastic material. The material model contains the Mohr-Coulomb yield criterion, the associative flow rule, and the nonlinear hardening law as in [2, 4]. For the sake of simplicity, consider an elasto-plastic problem in 3D. Let Ω be a polygonal 3D domain and $\mathcal{T}_h$ denote its triangulation. Further, consider linear and conforming elements. So the displacement fields are approximated by continuous and piecewise linear functions, and the strain, stress and isotropic hardening fields are approximated by piecewise constant functions.

The paper is organized as follows. In Section 2, we introduce the initial value constitutive problem for the Mohr-Coulomb plastic criterion with the implicit Euler time discretization; in Section 3, we summarize the TFETI domain decomposition method and algebraic formulation of our investigated problem; in Section 4, several implementation details for the parallel code in MATLAB are briefly summarized. We illustrate the performance of our algorithm on the slope stability benchmark in 3D in Section 5.

2 THE CONSTITUTIVE INITIAL VALUE PROBLEM OF THE MOHR-COULOMB CRITERION AND THE IMPLICIT EULER DISCRETIZATION

The initial value constitutive problem reads:

Given the history of the strain tensor $\boldsymbol{\varepsilon} = \boldsymbol{\varepsilon}(t)$, $t \in [0, t_{\max}]$, *and the initial values* $\boldsymbol{\varepsilon}^p(0) = \boldsymbol{\varepsilon}^p_0$, $\bar{\varepsilon}^p(0) = \bar{\varepsilon}^p_0$, *find* $(\boldsymbol{\sigma}(t), \boldsymbol{\varepsilon}^p(t), \bar{\varepsilon}^p(t))$ *such that the conditions*

$$\left.\begin{aligned} \boldsymbol{\sigma} = \mathbb{D}_e : (\boldsymbol{\varepsilon} - \boldsymbol{\varepsilon}^p), \quad \kappa = H(\bar{\varepsilon}^p), \\ \dot{\boldsymbol{\varepsilon}^p} \in \dot{\lambda} \partial g(\boldsymbol{\sigma}), \quad \dot{\bar{\varepsilon}}^p = -\dot{\lambda} \tfrac{\partial f(\boldsymbol{\sigma}, \kappa)}{\partial \kappa}, \\ \dot{\lambda} \geq 0, \quad f(\boldsymbol{\sigma}, \kappa) \leq 0, \quad \dot{\lambda} f(\boldsymbol{\sigma}, \kappa) = 0. \end{aligned}\right\} \tag{1}$$

hold for each instant $t \in [0, t_{\max}]$.

Here, $\boldsymbol{\sigma}, \boldsymbol{\varepsilon}^p, \bar{\varepsilon}^p, \lambda$ denote the Cauchy stress tensor, the plastic strain, the hardening variable, and the plastic multiplier, respectively. The dot symbol means the pseudo-time derivative of a quantity. The functions f and g represent the yield function and the plastic potential for the Mohr-Coulomb model, respectively. They are defined as:

$$f(\boldsymbol{\sigma}, \kappa) = (1 + \sin\phi)\omega_1(\boldsymbol{\sigma}) - (1 - \sin\phi)\omega_3(\boldsymbol{\sigma}) - 2(c_0 + \kappa)\cos\phi, \tag{2}$$

$$g(\boldsymbol{\sigma}) = (1 + \sin\psi)\omega_1(\boldsymbol{\sigma}) - (1 - \sin\psi)\omega_3(\boldsymbol{\sigma}), \tag{3}$$

where ω_1 and ω_3 are the maximal and minimal eigenvalue functions, and $\partial f(\boldsymbol{\sigma}, \kappa)/\partial\kappa = -2\cos\phi$.

Further, the fourth order tensor $\mathbb{D}_e$ represents the linear isotropic elastic law

$$\boldsymbol{\sigma} = \mathbb{D}_e : \boldsymbol{\varepsilon}^e = \frac{1}{3}(3K - 2G)(\boldsymbol{I} : \boldsymbol{\varepsilon}^e)\boldsymbol{I} + 2G\boldsymbol{\varepsilon}^e, \quad \mathbb{D}_e = \frac{1}{3}(3K - 2G)\boldsymbol{I} \otimes \boldsymbol{I} + 2G\mathbb{I}, \tag{4}$$

where $\boldsymbol{\varepsilon}^e = \boldsymbol{\varepsilon} - \boldsymbol{\varepsilon}^p$, K and G $(K, G > 0)$ denote the elastic part of the strain tensor, bulk and shear moduli, respectively.

Finally, we let the function H representing the non-linear isotropic hardening in an abstract form and assume that it is a nondecreasing, continuous, and piecewise smooth function satisfying $H(0) = 0$.

It is worth mentioning that the value t_{max} need not be always known. Let

$$0 = t_0 < t_1 < \ldots < t_k < \ldots < t_N = t_{\max}$$

be a partition of the interval $[0, t_{\max}]$ and denote $\boldsymbol{\sigma}_k := \boldsymbol{\sigma}(t_k)$, $\boldsymbol{\varepsilon}_k := \boldsymbol{\varepsilon}(t_k)$, $\boldsymbol{\varepsilon}^p_k := \boldsymbol{\varepsilon}^p(t_k)$, $\bar{\varepsilon}^p_k := \bar{\varepsilon}^p(t_k)$, $\bar{\varepsilon}^{p,tr}_k := \bar{\varepsilon}^p(t_{k-1})$, $\boldsymbol{\varepsilon}^{tr}_k := \boldsymbol{\varepsilon}(t_k) - \boldsymbol{\varepsilon}^p(t_{k-1})$, and $\boldsymbol{\sigma}^{tr}_k := \mathbb{D}_e : \boldsymbol{\varepsilon}^{tr}_k$. Here, the superscript tr denotes the so-called trial variables (see, e.g., [4]) which are known. If it is clear that the step k is fixed, then we will omit the subscript k and write $\boldsymbol{\sigma}$, $\boldsymbol{\varepsilon}$, $\boldsymbol{\varepsilon}^p$, $\bar{\varepsilon}^p$, $\bar{\varepsilon}^{p,tr}$, $\boldsymbol{\varepsilon}^{tr}$, and $\boldsymbol{\sigma}^{tr}$ to simplify the notation. The k-th step of the incremental constitutive problem discretized by the implicit Euler method reads:

Given $\boldsymbol{\sigma}^{tr}$ *and* $\bar{\varepsilon}^{p,tr}$*, find* $\boldsymbol{\sigma}$*,* $\bar{\varepsilon}^p$*, and* $\triangle\lambda$ *satisfying*

$$\left.\begin{aligned} \boldsymbol{\sigma} = \boldsymbol{\sigma}^{tr} - \triangle\lambda\mathbb{D}_e : \boldsymbol{\nu}, \quad \boldsymbol{\nu} \in \partial g(\boldsymbol{\sigma}), \\ \bar{\varepsilon}^p = \bar{\varepsilon}^{p,tr} + \triangle\lambda(2\cos\phi), \\ \triangle\lambda \geq 0, \quad f(\boldsymbol{\sigma}, H(\bar{\varepsilon}^p)) \leq 0, \quad \triangle\lambda f(\boldsymbol{\sigma}, H(\bar{\varepsilon}^p)) = 0. \end{aligned}\right\} \tag{5}$$

Unlike Problem (1), the unknown $\boldsymbol{\varepsilon}^p$ is not introduced in (5). It can be simply computed from the formula $\boldsymbol{\varepsilon}^p(t_k) = \boldsymbol{\varepsilon}(t_k) - \mathbb{D}_e^{-1} : \boldsymbol{\sigma}(t_k)$ and used as the input parameter for the next step. To solve the incremental problem, we use the standard elastic predictor/plastic corrector method.

The elastic predictor. First, we verify whether the trial generalized stress $(\boldsymbol{\sigma}^{tr}, \bar{\varepsilon}^{p,tr})$ is admissible:

$$f(\boldsymbol{\sigma}^{tr}, H(\bar{\varepsilon}^{p,tr})) \leq 0. \tag{6}$$

If this inequality holds, then we set

$$\boldsymbol{\sigma} = \boldsymbol{\sigma}^{tr}, \quad \bar{\varepsilon}^p = \bar{\varepsilon}^{p,tr}, \quad \triangle\lambda = 0.$$

It is readily seen that the triplet $(\boldsymbol{\sigma}, \bar{\varepsilon}^p, \triangle\lambda)$ solves the incremental problem.

The plastic corrector (the implicit return-mapping scheme). Let (6) not hold and assume that the incremental constitutive problem has a solution. Then clearly $\triangle\lambda > 0$, and the problem reduces into the following form:
Given $\boldsymbol{\varepsilon}^{e,tr}$ and $\bar{\varepsilon}^{p,tr}$ such that $f(\boldsymbol{\sigma}^{tr}, H(\bar{\varepsilon}^{p,tr})) > 0$, find $\boldsymbol{\sigma}$, $\bar{\varepsilon}^p$ and $\triangle\lambda > 0$ satisfying

$$\left.\begin{aligned} \boldsymbol{\sigma} = \boldsymbol{\sigma}^{tr} - \triangle\lambda\mathbb{D}_e : \boldsymbol{\nu}, \quad \boldsymbol{\nu} \in \partial g(\boldsymbol{\sigma}), \\ \bar{\varepsilon}^p = \bar{\varepsilon}^{p,tr} + \triangle\lambda(2\cos\phi), \\ f(\boldsymbol{\sigma}, H(\bar{\varepsilon}^p)) = 0. \end{aligned}\right\} \tag{7}$$

If the plastic potential g is differentiable on the yield surface, then the flow direction $\boldsymbol{\nu}$ is always single valued, and the return-mapping scheme leads to solving a system of nonlinear equations. In [12] you can find details how to return to the smooth portion, to the "left" edge, to the "right" edge, and to the apex of the pyramidal yield surface, as well as how to construct nonlinear and tangential operators. The algebraic formulation of the elastoplastic problem is formulated in [3] for the Drucker-Prager criterion and in [14] for the von Mises criterion in combination with TFETI, which is summarized in the following section.

As we mentioned above, we solved the nonlinear system of equations in each time step. The semi-smooth Newton method [11] is applied to the nonlinear system of equations in order to linearize it.

After preparing the tangential stiffness matrix and load vectors according to [12], we can formulate the following problem:
Find increment of displacement $\triangle\boldsymbol{u}_{k+1} \in \boldsymbol{V}$ so that

$$\boldsymbol{v}^T \left(\boldsymbol{F}_k(\triangle\boldsymbol{u}_{k+1}) - \triangle\boldsymbol{f}_{k+1}\right) = 0 \quad \forall \boldsymbol{v} \in \boldsymbol{V}, \tag{8}$$

where $\triangle\boldsymbol{f}_{k+1}$ is the increment of the load vector, $\boldsymbol{F}_k$ is the nonlinear operator, and $\boldsymbol{V}$ is the set of admissible displacements

$$\boldsymbol{V} = \{\boldsymbol{v} \in \mathbb{R}^n | \boldsymbol{B}_U\boldsymbol{v} = \boldsymbol{o}\}.$$

The relation $\boldsymbol{B}_U\boldsymbol{v} = \boldsymbol{o}$ represents the Dirichlet boundary conditions. The nonlinear equations (8) can be linearized by the semi-smooth Newton method.

3 TFETI AND ALGEBRAIC FORMULATION OF THE PROBLEM FOR ELASTO-PLASTIC BODIES

To apply the Total FETI (TFETI) domain decomposition method (DDM), we tear the body from the part of the boundary with the Dirichlet boundary condition, decompose it into subdomains, assign each subdomain a unique number, and introduce new "gluing"

conditions on the artificial subdomain interfaces and on the boundaries with the imposed Dirichlet condition. Let s denote the total number of the subdomains.

In the case of TFETI, the global stiffness matrix $\mathbf{K}$ and right-hand side $\mathbf{f}$ are assembled only subdomain-wise, and take the form

$$\mathbf{K} = \mathrm{diag}(\mathbf{K}^1, \ldots, \mathbf{K}^s),$$
$$\mathbf{f} = [(\mathbf{f}^1)^T, \ldots, (\mathbf{f}^s)^T]^T,$$

where $\mathbf{K}^p$ and $\mathbf{f}^p$, $p = 1, \ldots, s$, are the fully assembled stiffness matrix and load vector of the subdomain Ω^p, respectively. Then also the unknown vector of displacements $\mathbf{u}$ can be subdivided as

$$\mathbf{u} = [(\mathbf{u}^1)^T, \ldots, (\mathbf{u}^s)^T]^T,$$

where $\mathbf{u}^p$, $p = 1, \ldots, s$, is the vector of displacements of subdomain Ω^p.

TFETI is a dual approach, which means that the interface compatibility is enforced by introducing the Lagrange multipliers. In the case of TFETI, also the Dirichlet boundary conditions are enforced (see Figure 1) in this way whereas $\mathbf{K}^p$ remains unchanged, and hence it is singular. The resulting equality constraints can be written as

$$\mathbf{B}\mathbf{u} = \mathbf{o},$$

where $\mathbf{B}$ is a signed Boolean matrix. It can be split vertically into two blocks corresponding to the gluing part $\mathbf{B}_G$ and the Dirichlet part $\mathbf{B}_D$.

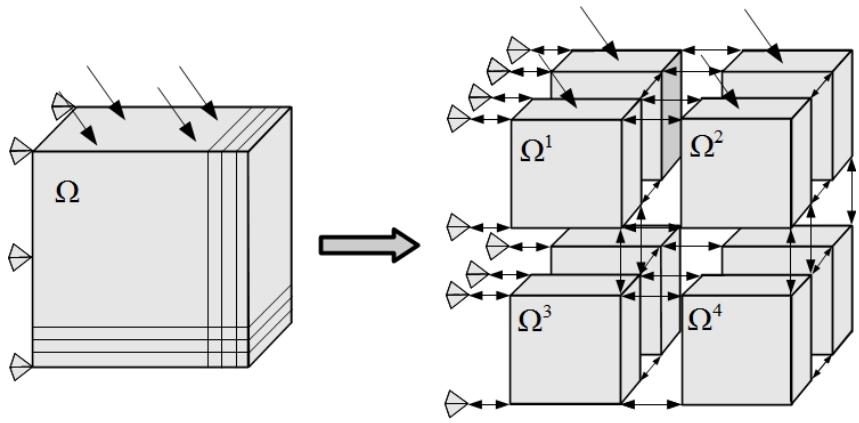

Figure 1: The TFETI domain decomposition method for unit cube.

Introducing the Lagrange multipliers $\boldsymbol{\lambda}$ to enforce the interface compatibility, the global problem takes the equivalent primal-dual form

$$\begin{bmatrix} \mathbf{K} & \mathbf{B}^T \\ \mathbf{B} & \mathbf{O} \end{bmatrix} \begin{bmatrix} \mathbf{u} \\ \boldsymbol{\lambda} \end{bmatrix} = \begin{bmatrix} \mathbf{f} \\ \mathbf{o} \end{bmatrix}. \tag{9}$$

Let us establish notation

$$\mathbf{F} = \mathbf{B}\mathbf{K}^{\dagger}\mathbf{B}^{T}, \quad \mathbf{G} = -\mathbf{R}^{T}\mathbf{B}^{T}, \quad \mathbf{d} = \mathbf{B}\mathbf{K}^{\dagger}\mathbf{f}, \quad \mathbf{e} = -\mathbf{R}^{T}\mathbf{f}.$$

$\mathbf{K}^{\dagger}$ denotes a generalized inverse of $\mathbf{K}$, satisfying $\mathbf{K}\mathbf{K}^{\dagger}\mathbf{K} = \mathbf{K}$. Notice $\mathbf{K}^{\dagger}$ inherits the block-diagonal structure from $\mathbf{K}$ and each block $(\mathbf{K}^{\dagger})^{p}$ is the generalized inverse of $\mathbf{K}^{p}$. We obtain a new linear system with unknowns $\boldsymbol{\lambda}$ and $\boldsymbol{\alpha}$

$$\begin{bmatrix} \mathbf{F} & \mathbf{G}^{T} \\ \mathbf{G} & \mathbf{O} \end{bmatrix} \begin{bmatrix} \boldsymbol{\lambda} \\ \boldsymbol{\alpha} \end{bmatrix} = \begin{bmatrix} \mathbf{d} \\ \mathbf{e} \end{bmatrix}. \tag{10}$$

For more details about solving this system and preconditioning, see [6, 1].

4 IMPLEMENTATION DETAILS

Our parallel implementation is based on the TFETI DDM. To apply this method, the original domain is partitioned into subdomains first. One of the widely used software tools for this task is METIS [10], which allows meshes to be partitioned in 2D and 3D. This software returns the number of subdomains for each element in the original mesh. Based on this partitioning, we assemble the objects for each individual subdomains independently. The local-to-global maping is constructed and the elements and nodes belonging to the interface are identified in order to assemble the equality constraint matrix B.

The equality constraint matrix $\mathbf{B}$ consists of the Dirichlet part $\mathbf{B}_D$ and the gluing part $\mathbf{B}_G$. We have three ways how to assemble the gluing part $\mathbf{B}_G$: redundant, non-redundant and orthonormal case, see [8]. In our code we allow all options but we recommend a) and c) for better convergence.

Two well known preconditioners were implemented: Dirichlet and lumped, see [6, 1]. The Dirichlet preconditioner needs a smaller number of CG iterations but is more expensive than the lumped one.

In our implementation, we use three loops: the outer loop for the loading process represents the direct method; the middle loop for the semi-smooth Newton method; and the inner loop for the linear iteration solver, more specifically the preconditioned conjugate gradient method with projector (PCGP). The first two loops were introduced in [12] in detail and the last one in [14].

For parallel computation, we use MATLAB Distributed Computing Server and MATLAB Parallel Toolbox for sending and receiving data via its Message Passing Interface (MPI) wrappers.

5 NUMERICAL EXPERIMENTS

We implemented the direct method of incremental limit analysis in MATLAB for the 3D slope stability problem. The code is parallelized by MATLAB Parallel Toolbox as we mentioned in the previous section, and includes the improved return-mapping scheme for the Mohr-Coulomb model. The available options include a) several types of finite elements with appropriate numerical quadratures; b) locally refined meshes with various densities; c) different preconditioners; d) different types of the equality constraint matrix.

We consider the extension of the benchmark for the plane strain problem introduced in [4, Page 351] for the 3D case. Further, we set $E = 20\,000\,\text{kPa}$, $\nu = 0.49$, $\phi = 20°$ and $c = 50\,\text{kPa}$, where c denotes the cohesion for the perfect plastic model. The stopping tolerance of the Newton and CG loops are set to $\epsilon_{Newton} = 10^{-7}$ and $\epsilon_{CG} = 10^{-12}$, respectively.

All numerical experiments were computed on the Salomon supercomputer. The Salomon cluster consists of 1008 compute nodes, totaling 24,192 compute cores with 129 TB RAM and giving over 2 Pflop/s theoretical peak performance. Each node is a powerful x86-64 computer, equipped with 24 cores, at least 128 GB RAM. The nodes are interconnected by 7D Enhanced hypercube InfiniBand network and equipped with the Intel Xeon E5-2680v3 processors. The Salomon cluster consists of 576 nodes without accelerators and 432 nodes equipped with the Intel Xeon Phi MIC accelerators.

Within this slope stability experiment, we compared the loading paths for the Q1 and Q2 hexahedral elements with 8 and 20 nodes, respectively, simillarly as in [12]. We consider $2 \times 2 \times 2$ and $3 \times 3 \times 3$ nodes integration quadratures for these element types, respectively. For the Q1 elements, the meshes contain 5103 and 37597 nodal points. For the Q2 elements, the meshes contain 19,581 and 147,257 nodal points. We use the direct method of the incremental limit analysis which is terminated when the computed settlement exceeds 4 meters. For parallel computing, we use 4 and 20 cores on Salomon for level 1 and 2, respectively.

The corresponding loading paths are depicted in Figure 2. We can see that the loading paths are very similar to loading paths which were introduced in [12]. Figure 3 illustrates a failure at the end of the loading process for the Q2 elements and the finer mesh.

The computation time of our approach is worse than the time which we need for the sequential version of the code in MATLAB, but this implementation gives us the opportunity to compute bigger problems and guidelines how to implement it more efficiently for example in our PERMON toolbox [9].

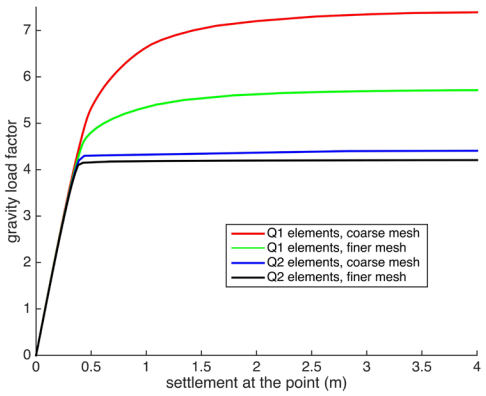

Figure 2: Comparison of the loading paths for $Q1$ and $Q2$ elements.

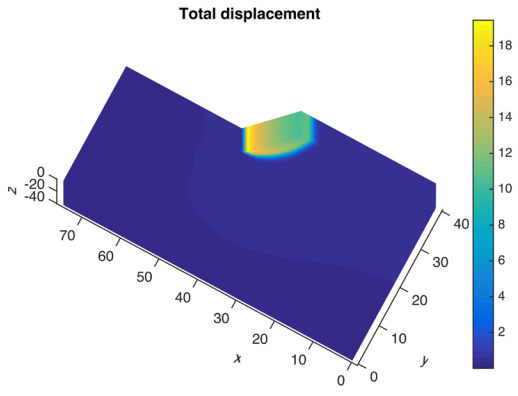

Figure 3: Total displacement and original shape at the end of the loading process.

6 CONCLUSIONS

In this paper, we have briefly summarized our parallel implementation of the Mohr-Coulomb plastic criterion, which is based on the new approach introduced in [12] and the TFETI DDM. This approach allows us to compute bigger benchmarks and estimate the limit value to get closer to the expected value of 4.045 (which is the experimentally measured limit value of the slope stability experiment).

ACKNOWLEDGEMENTS

The work was also supported by The Ministry of Education, Youth and Sports from the National Programme of Sustainability (NPU II) project "IT4Innovations excellence in science - LQ1602" and from the Large Infrastructures for Research, Experimental Development and Innovations project "IT4Innovations National Supercomputing Center LM2015070"; by the internal student grant competition project SP2017/169 "PERMON toolbox development III". The authors acknowledge the Czech Science Foundation (GACR) project no. 15-18274S.

REFERENCES

[1] M. Cermak, V. Hapla, J. Kruzik, A. Markopoulos, and A. Vasatova. Comparison of different FETI preconditioners for elastoplasticity. *Computers & Mathematics with Applications*, forthcoming.

[2] M. Cermak and S. Sysala. How to simplify return-mapping algorithms in computational plasticity: Part 1-main idea. In *Proceedings of the 8th International Conference on Computational Plasticity - Fundamentals and Applications, COMPLAS 2015*, pages 843–854, 2015.

[3] M. Cermak and S. Sysala. How to simplify return-mapping algorithms in computational plasticity: Part 2 - implementation details and experiments. In *Proceedings of the 8th International Conference on Computational Plasticity - Fundamentals and Applications, COMPLAS 2015*, 2015.

[4] E. A. de Souza Neto, D. Peri, and D. R. J. Owen. *Computational Methods for Plasticity*. Wiley-Blackwell, oct 2008.

[5] Z. Dostál, D. Horák, and R. Kučera. Total FETI – an easier implementable variant of the FETI method for numerical solution of elliptic PDE. *Communications in Numerical Methods in Engineering*, 22(12):1155–1162, 2006.

[6] C. Farhat, J. Mandel, and F.-X. Roux. Optimal convergence properties of the FETI domain decomposition method. *Computer Methods in Applied Mechanics and Engineering*, 115:365–385, 1994.

[7] C. Farhat and F.-X. Roux. A method of finite element tearing and interconnecting and its parallel solution algorithm. *International Journal for Numerical Methods in Engineering*, 32(6):1205–1227, 1991.

[8] Y. Fragakis and M. Papadrakakis. The mosaic of high performance domain decomposition methods for structural mechanics: formulation, interrelation and numerical efficiency of primal and dual methods. *Computer Methods in Applied Mechanics and Engineering*, 192(35-36):3799–3830, 2003.

[9] V. Hapla et al. PERMON (Parallel, Efficient, Robust, Modular, Object-oriented, Numerical) web pages, 2015.

[10] G. Karypis and V. Kumar. A fast and high quality multilevel scheme for partitioning irregular graphs. *SIAM Journal on Scientific Computing*, 20(1):359–392, 1998.

[11] L. Qi and J. Sun. A nonsmooth version of newton's method. *Mathematical Programming*, 58(1-3):353–367, jan 1993.

[12] S. Sysala and M. Cermak. Subdifferential-based implicit return-mapping operators in mohr-coulomb plasticity. *ZAMM Zeitschrift fur Angewandte Mathematik und Mechanik*, forthcoming.

[13] M. Čermák, V. Hapla, D. Horák, M. Merta, and A. Markopoulos. Total-FETI domain decomposition method for solution of elasto-plastic problems. *Advances in Engineering Software*, 84(0):48–54, 2015.

[14] M. Čermák, T. Kozubek, S. Sysala, and J. Valdman. A TFETI domain decomposition solver for elastoplastic problems. *Applied Math. and Comp*, 231:634–653, 2014.

AUTHORS INDEX

CIMNE

International Center
for Numerical Methods in Engineering